**รายงานวิจัยฉบับสมบูรณ์**

# โครงการ: นาโนเทคโนโลยีในอุตสาหกรรมปิโตรเคมี: การออกแบบสังเคราะห์และวิเคราะห์ วัสดุนาโนที่มีรูพรุน


โดย

นาย จำรัส ลิ้มตระกูล



15 กันยายน พ.ศ. 2551 ถึง 14 กันยายน พ.ศ. 2554

สัญญาเลขที่ DBG5180027

# รายงานวิจัยฉบับสมบูรณ์

# โครงการ: นาโนเทคโนโลยีในอุตสาหกรรมปิโตรเคมี: การออกแบบสังเคราะห์และวิเคราะห์ วัสดุนาโนที่มีรูพรุน

**คณะผู้วิจัย**

**นายจำรัส ลิ้มตระกูล**

**สังกัด**

**ภาควิชาเคมี คณะวิทยาศาสตร์**

**มหาวิทยาลัยเกษตรศาสตร์**

**สนับสนุนโดยสำนักงานกองทุนสนับสนุนการวิจัย**

(ความเห็นในรายงานนี้เป็นของผู้วิจัย สกว. ไม่จำเป็นต้องเห็นด้วยเสมอไป)

# สารบัญ

**บทคัดย่อ**

การออกแบบตัวเร่งปฏิกิริยาและการศึกษากระบวนการเร่งปฏิกิริยาเคมีระดับโมเลกุล เป็นงานวิจัยด้านหนึ่งที่มีบทบาทและเป็นประโยชน์อย่างมาก ต่อการพัฒนาอุตสาหกรรมเคมีและปิโตรเคมี ซึ่งจากการศึกษาโดยอาศัยความรู้ด้านนาโนเทคโนโลยีของวัสดุนาโนที่มีรูพรุน พบว่า ตัวเร่งปฏิกิริยาที่มีโครงสร้างในระดับนาโนเมตรแสดงสมบัติพิเศษแตกต่างไป เช่น มีความว่องไวสูงและมีคุณสมบัติที่ดีในการเลือกเกิดปฏิกิริยาที่จำเพาะกับขนาดและรูปร่างของโมเลกุล ดังนั้นการออกแบบตัวเร่งปฏิกิริยาเพื่อให้ได้คุณสมบัติตามต้องการและมีประสิทธิภาพสูงสุดนั้น จำเป็นอย่างยิ่งที่จะต้องเข้าใจโครงสร้างระดับนาโนเมตร อิทธิพลของโครงสร้างต่อสมบัติทางเคมีและสมบัติทางกายภาพและกลไลการเกิดปฏิกิริยาเคมีในระดับโมเลกุล

คณะวิจัยได้ดำเนินงานวิจัยอย่างต่อเนื่องเพื่อพัฒนางานวิจัยด้านการออกแบบ สังเคราะห์และวิเคราะห์วัสดุที่มีโครงสร้างระดับนาโนเมตร โดยเฉพาะอย่างยิ่งวัสดุนาโนที่มีรูพรุนในกลุ่มซีโอไลต์ เพราะเป็นตัวเร่งปฏิกิริยาที่มีประสิทธิภาพสูงในหลากหลายปฏิกิริยาที่มีความสำคัญในอุตสาหกรรมเคมีและปิโตรเคมี โดยได้ทำการปรับปรุงโครงสร้างของซีโอไลต์ทั้งขนาดผลึกและขนาดของรูพรุน เพื่อแก้ปัญหาเกี่ยวการแพร่ของสารตั้งต้นหรือสารผลิตภัณฑ์ที่มีขนาดใหญ่ เช่น โมเลกุลไฮโดรคาร์บอนในน้ำมันดิบจากแหล่งปิโตรเลียมธรรมชาติ ซึ่งมีผลให้ซีโอไลต์มีประสิทธิภาพในการเร่งปฏิกิริยาดีขึ้น นอกเหนือจากการสังเคราะห์และทดสอบประสิทธิภาพของตัวเร่งปฏิกิริยาในห้องปฏิบัติการจริงแล้ว คณะวิจัยยังได้ศึกษาทางทฤษฎีด้วยการคำนวนทางเคมีคอมพิวเตอร์ควบคู่กัน โดยการจำลองแบบโครงสร้างซีโอไลต์ที่ถูกดัดแปลงซึ่งมีผลต่อประสิทธิภาพในการเร่งปฏิกิริยาที่ศึกษา เสนอและอธิบายกลไกการเกิดปฏิกิริยา คำนวณค่าคงที่ทางจลนพลศาสตร์และอุณหพลศาสตร์ ในแต่ละขั้นตอนของปฏิกิริยาพื้นฐานเพื่อทำนายผลการทดลอง ซึ่งการวิเคราะห์ข้อมูลต่างๆเหล่านี้นำไปสู่การพัฒนาตัวเร่งปฏิกิริยาซีโอไลต์ได้อย่างมีประสิทธิผลมากขึ้น นอกจากนี้คณะวิจัยยังได้ศึกษาวัสดุนาโนที่มีรูพรุนอื่นๆ เช่น Nanoporous carbons, Metal-organic frameworks และ Nanoporous alkali halide polymophs เพื่อให้ได้ข้อมูลอันเป็นแนวทางในการประยุกต์ใช้งานด้านต่างๆ อาทิเช่น ด้านอิเลคทรอนิกส์ พลังงาน และการแพทย์

ตลอดระยะเวลา 3 ปีของการดำเนินโครงการ คณะวิจัยสามารถตีพิมพ์ผลงานในวารสารวิชาการนานาชาติชั้นนำจำนวนทั้งสิ้น 29 ผลงาน โดยเป็นงานวิจัยที่เกี่ยวข้องกับการออกแบบโครงสร้างเพื่อพัฒนาคุณสมบัติของตัวเร่งปฏิกิริยาซีโอไลต์มากถึง 13 ผลงาน และงานวิจัยด้านวัสดุนาโนรูพรุนชนิดอื่นๆ อีก 16 ผลงาน ซึ่งผลผลิตจากคณะวิจัยโครงการฯนี้ ถือเป็นองค์ความรู้ที่สำคัญและเป็นประโยชน์อย่างยิ่งต่อภาคการผลิตในอุตสาหกรรมเคมีและปิโตรเคมี ซึ่งจะนำไปสู่ความร่วมมือด้านงานวิจัยของประเทศต่อไปในอนาคต

**Abstract**

Our research project has been carefully developed to focus on molecular design, fabrication and characterization of nanostrcutured and nanoporous materials, in particular, on design, synthesis and reaction mechanism of the industrially important zeolite catalysts. Our newly developed synthetic methods are able to effectively control their crystals and pore sizes for facilitating the diffusion of the large chemical molecules such as the long chain hydrocarbon compounds. These excellent properties are very important and one of the essential key factors for cracking reactions frequently undertaken in Thai chemical industries. In addition to this, fine experiments, either state-of-the-art syntheses or the high performance of catalysts, the Nanoscale ab initio electronic structure theory and cutting-edge simulations are also employed as effective tools to design the molecular structure and reaction mechanisms and, more importantly, to derive kinetic and thermodynamic parameters which are employed to predict the feasibility of reaction. Thus, the combined state-of-the-art methods lead to the fabrication of novel and high efficiency nanoporous and nanostructured materials. Moreover, other porous materials including nanoporous carbons, metal-organic frameworks and nanoporous alkali halide polymophs are investigated. Such systematic and accurate findings provide not only reliable data for experimental and theoretical researchers for further development, but real-time beneficial information for utilizing them as nano-materials for many important areas such as, chemical, electronic, energy and medical applications.

Our small project of 3 MB could generate 29 articles published in prestige international journals, each with a very high impact factor, including the American Chemical Society Journals and Royal Society of Chemistry, England. These scientific outputs are crucial and indeed beneficial information for creating nano-materials used in chemical and petrochemical industries and do lead to collaboration between academic and industrial sections to propel the development of the potential researches in Thailand.

**หน้าสรุปโครงการ (Executive Summary)**
**ทุนวิจัยพื้นฐานแบบกำหนดทิศทาง**
**"นาโนศาสตร์และนาโนเทคโนโลยี"**

---

**1. ชื่อโครงการ:** (ภาษาไทย) โครงการ: นาโนเทคโนโลยีในอุตสาหกรรมปิโตรเคมี: การออกแบบ สังเคราะห์และวิเคราะห์ วัสดุนาโนที่มีรูพรุน

(ภาษาอังกฤษ) Applications of Nanotechnology to Petrochemical Industries: Molecular Design, Fabrication and Characterization of Nanostrcutured and Nanoporous Materials

**2. ชื่อหัวหน้าโครงการ:** ศ.ดร. จำรัส ลิ้มตระกูล

**ที่อยู่:** ภาควิชาเคมี คณะวิทยาศาสตร์ มหาวิทยาลัยเกษตรศาสตร์
50 ถนนงามวงศ์วาน แขวงลาดยาว เขตจตุจักร กรุงเทพฯ 10900
โทรศัพท์: 02-562-5555 ต่อ 2169, โทรสาร: 02-562-5555 ต่อ 2176
e-mail: fscijrl@ku.ac.th

**3. สาขาที่ทำการวิจัย:** สาขาเคมีเชิงฟิสิกส์

**4. ปัญหาที่ทำการวิจัย และความสำคัญของปัญหา:**

วัสดุนาโนที่มีรูพรุนโดยเฉพาะอย่างยิ่งวัสดุประเภทซีโอไลต์ มีความสำคัญอย่างมากต่ออุตสาหกรรมปิโตรเคมี โดยมีการใช้งานกันอย่างกว้างขวางทั้งเป็นตัวเร่งปฏิกิริยา เป็นตัวดูดซับ และใช้ในการแลกเปลี่ยนไอออน ซีโอไลต์ Y (FAU) เป็นชนิดที่มีการใช้งานมากที่สุดในกระบวนการ Fluid Catalytic Cracking (FCC) เพื่อแตกโมเลกุลไฮโดรคาร์บอนขนาดใหญ่ในน้ำมันดิบจากแหล่งปิโตรเลียมธรรมชาติ ให้ได้เป็นเชื้อเพลิงและผลิตภัณฑ์ที่เป็นประโยชน์อื่นๆ สำหรับซีโอไลต์ชนิด ZSM-5 (MFI) ซึ่งมีความเป็นกรดที่แรงกว่าและมีขนาดรูพรุนที่เล็กกว่า จะช่วยในการแตกโมเลกุลน้ำมันดิบให้ได้ผลิตภัณฑ์เป็นโอลิฟินขนาดเล็ก เช่น ethylene, propylene ซึ่งเป็นสารตั้งต้นที่สำคัญในอุตสาหกรรมพอลิเมอร์ ปัจจัยสำคัญที่มีผลต่อการใช้งานตัวเร่งปฏิกิริยาซีโอไลต์ได้แก่ลักษณะจำเพาะทางโครงสร้าง ขนาดและรูปร่างของรูพรุน สมบัติความเป็นกรด และความจำเพาะในการเลือกเกิดปฏิกิริยาตามขนาดโมเลกุล (Shape Selectivity) ซึ่งเป็นสมบัติที่เกิดจากขนาดรูพรุนซีโอไลต์ที่เล็กใกล้เคียงกับขนาดของโมเลกุลที่เข้าทำปฏิกิริยา แต่ในขณะเดียวกันขนาดของรูพรุนที่เล็กมากๆ ก็เป็นข้อจำกัดของการใช้งานซีโอไลต์ สารโมเลกุลใหญ่ไม่สามารถเข้าทำปฏิกิริยาได้และเกิดปัญหาเกี่ยวการแพร่ของสารเข้า-ออกจากรูพรุนของซีโอไลต์ ทำให้ในบางกรณี

อัตราการเกิดปฏิกิริยาถูกจำกัดด้วยอัตราการแพร่ที่ช้า และในบางกรณีการแพร่ของสารที่ช้าทำให้โมเลกุลที่เข้าทำปฏิกิริยาอยู่ในรูพรุนของซีโอไลต์นานเกินไป จนเกิดปฏิกิริยาต่อเนื่องเป็นสารอื่นที่ไม่ต้องการหรือกลายเป็น Coke อุดตันรูพรุนทำให้ซีโอไลต์เสื่อมสภาพ มีการศึกษาพบว่าถ้าสามารถลดระยะทางในการแพร่เข้า-ออกจากผลึกของซีโอไลต์ได้ จะทำให้ซีโอไลต์มีประสิทธิภาพดีขึ้น มีอัตราการเร่งปฏิกิริยาดีขึ้น มีความจำเพาะในการเลือกเกิดผลิตภัณฑ์ที่ต้องการสูงขึ้น และลดการเกิดปฏิกิริยาต่อเนื่องไปเป็นสารที่ไม่ต้องการ

โครงการวิจัยนี้เสนอการศึกษาการพัฒนาซีโอไลต์โดยเน้นที่ประเภท FAU, LTA และ MFI เพื่อลดปัญหาในการแพร่ของสารเคมีที่เข้าทำปฏิกิริยา โดยการสังเคราะห์เป็นผลึกขนาดนาโนเมตร และ/หรือ เติมรูพรุนขนาดมีโซพอร์ (Mesopore 2-50 nm) ในโครงการวิจัยนี้จะใช้ความก้าวหน้าทางเทคโนโลยีคอมพิวเตอร์ช่วยในการศึกษาร่วมกับการปฏิบัติทดลอง เพื่อสร้างความเข้าใจในปฏิกิริยาที่เกิดขึ้น และเข้าใจปัจจัยที่มีผลต่ออัตราการเกิดปฏิกิริยาและชนิดของผลิตภัณฑ์ที่ได้ สร้างเป็นฐานความรู้ในการพัฒนาปรับปรุงตัวเร่งปฏิกิริยา และกระบวนการทำปฏิกิริยาให้มีประสิทธิภาพดียิ่งขึ้น รวมถึงศึกษาผลของการปรับปรุงโครงสร้างของซีโอไลต์ดังกล่าวต่อกระบวนการดูดซับ การแลกเปลี่ยนไอออนและการเร่งปฏิกิริยา โดยเน้นที่ปฏิกิริยาพื้นฐานได้แก่ Isomerization และ Cracking ของ Butene ซึ่งเป็นปฏิกิริยาที่เหมาะสมในการศึกษาผลกระทบจากการดัดแปลงโครงสร้างผลึกซีโอไลต์ ความเป็นกรดของซีโอไลต์ต่อความจำเพาะในการเลือกเกิดปฏิกิริยา และยังเป็นปฏิกิริยาพื้นฐานในกระบวนการ Catalytic cracking ซึ่งมีความสำคัญในอุตสาหกรรม สร้างฐานความรู้ที่สำคัญเกี่ยวกับ การแพร่ การดูดซับ กลไกการเกิดปฏิกิริยา และจลนพลศาสตร์ของปฏิกิริยาของสารประกอบไฮโดรคาร์บอนในซีโอไลต์ โดยใช้เคมีคอมพิวเตอร์เพื่อศึกษากลไกปฏิกิริยา คำนวณค่าคงที่ทางจลนพลศาสตร์และอุณหพลศาสตร์ควบคู่ไปกับการศึกษาวิจัยในห้องปฏิบัติการ ดังนั้นผลของโครงการวิจัยนี้จะเป็นการสร้างองค์ความรู้ในด้านการพัฒนาซีโอไลต์ในอุตสาหกรรม เป็นประโยชน์ในการพัฒนาการผลิตซีโอไลต์เพื่อเป็นตัวดูดซับ ตัวแลกเปลี่ยนไอออน และใช้ในกระบวนการเร่งปฏิกิริยา อีกทั้งเป็นการสร้างความร่วมมือในด้านงานวิจัยและให้คำปรึกษาแก่ภาคอุตสาหกรรมในการใช้เคมีคอมพิวเตอร์ในการพัฒนาตัวเร่งปฏิกิริยา และปรับปรุงกระบวนทำปฏิกิริยาให้มีประสิทธิภาพสูงสุด

**5. วัตถุประสงค์**

5.1 สร้างความเชื่อมโยงอย่างเป็นรูปธรรมระหว่างสถาบันการศึกษากับภาคอุตสาหกรรม เพื่อผลักดันให้เกิดงานวิจัยที่เป็นประโยชน์ต่อภาคอุตสาหกรรมโดยตรง

5.2 พัฒนาการสังเคราะห์ซีโอไลต์ขนาดนาโนเมตร โดยเน้นที่ซีโอไลต์ประเภท FAU, LTA และ MFI

5.3 สร้างฐานความรู้เกี่ยวกับ การแพร่และการดูดซับ และกลไกปฏิกิริยา และคำนวณค่าคงที่ทางจลนพลศาสตร์และอุณหพลศาสตร์ ของปฏิกิริยาระหว่างไฮโดรคาร์บอนในซีโอไลต์ เพื่อประโยชน์ในการพัฒนาซีโอไลต์สำหรับกระบวนการดูดซับ การแลกเปลี่ยนไอออน และการเร่งปฏิกิริยา

5.4 ให้คำปรึกษาและพัฒนาศักยภาพของนักวิจัยจากภาคอุตสาหกรรม ในการประยุกต์ใช้เทคโนโลยีคอมพิวเตอร์เพื่อการพัฒนาในอุตสาหกรรมปิโตรเคมี

5.5 ผลิตบุคลากรที่มีความรู้และความเชี่ยวชาญตรงกับความต้องการของภาคอุตสาหกรรม

**6. สรุปผลการดำเนินการของโครงการ**

จากการดำเนินงานโครงการฯ ในระยะเวลา 3 ปี ภายใต้การสนับสนุนจากทุนวิจัยพื้นฐานแบบกำหนดทิศทาง “นาโนศาสตร์และนาโนเทคโนโลยี” นั้น คณะวิจัยโครงการฯ ได้มุ่งเน้นศึกษาการออกแบบ การสังเคราะห์และการวิเคราะห์ วัสดุนาโนที่มีรูพรุน โดยเฉพาะอย่างยิ่งวัสดุในกลุ่มซีโอไลต์ รวมไปถึงโครงสร้างที่มีรูพรุนชนิดอื่นๆ เช่น Nanoporous carbons, Metal organic frameworks และ Nanoporous alkali halide polymophs โดยอาศัยการทดลองขั้นสูงในห้องปฏิบัติการจริงพัฒนากระบวนการสังเคราะห์แบบใหม่ เพื่อดัดแปลงขนาดของผลึกให้เล็กลงอยู่ในระดับนาโนเมตรและเพิ่มขนาดรูพรุนของซีโอไลต์ให้เป็นแบบมีโซพอร์ ซึ่งลักษณะของผลึกซีโอไลต์ดังกล่าว มีความเหมาะสมต่อปฏิกิริยาการแตกโมเลกุลไฮโดรคาร์บอนขนาดใหญ่ที่มีอยู่ในน้ำมันดิบให้ได้เป็นผลิตภัณฑ์ที่เป็นประโยชน์ต่ออุตสาหกรรมเคมีและปิโตรเคมี เนื่องจากช่วยปรับปรุงอัตราการแพร่ของสารตั้งต้นและสารผลิตภัณฑ์ ซึ่งเป็นการช่วยลดการเกิดสารอื่นๆที่ไม่ต้องการอีกด้วย นอกจากนี้ยังมีการศึกษาทางทฤษฎีโดยใช้ระเบียบวิธีทางเคมีคอมพิวเตอร์ควบคู่กัน ทำการจำลองแบบโครงสร้างและวิเคราะห์ปัจจัยต่างๆ เช่น ขนาดของรูพรุน ลักษณะของรูพรุน และองค์ประกอบทางเคมีของตัวเร่งปฏิกิริยาซีโอไลต์ ต่อการดูดซับ กลไกการเกิดปฏิกิริยาเคมี จลนพลศาสตร์และอุณหพลศาสตร์ของปฏิกิริยาเคมี เพื่อให้เกิดความเข้าใจถึงอิทธิพลของปัจจัยต่างๆเหล่านั้นต่อการเกิดปฏิกิริยาอย่างละเอียดลึกซึ้ง ซึ่งนำไปสู่การดัดแปลงโครงสร้างของตัวเร่งปฏิกิริยาซีโอไลต์ให้มีประสิทธิภาพสูงสุด สำหรับวัสดุนาโนที่มีรูพรุนชนิดอื่นๆนั้น ได้มีการออกแบบโครงสร้างใหม่ๆ เพื่อปรับปรุงคุณสมบัติการใช้งานในด้านต่างๆ อาทิเช่น ด้านอิเลคทรอนิกส์ พลังงาน และการแพทย์ เป็นต้น ซึ่งงานทั้งหมดดังกล่าวจะเป็นแนวทางนำไปสู่ในการพัฒนางานวิจัยและความร่วมมือในภาคการศึกษาและภาคอุตสาหกรรมที่เกี่ยวข้องต่อไป

ผลลัพธ์ของโครงการฯ ทำให้เกิดงานวิจัยที่สามารถถูกตีพิมพ์ในวารสารวิชาการนานาชาติ
ทั้งสิ้นจำนวน 29 เรื่อง

**เนื้อหางานวิจัย**

คณะวิจัยโครงการฯ ได้มุ่งเน้นศึกษาการสังเคราะห์วัสดุนาโนที่มีรูพรุนอย่างซีโอไลต์ ซึ่งถูกใช้เป็นตัวเร่งปฏิกิริยาที่มีความสำคัญในอุตสาหกรรมเคมีและปิโตรเคมี เช่น การแตกโมเลกุลน้ำมันดิบให้ได้ผลิตภัณฑ์เป็นโอลิฟินขนาดเล็ก เช่น Ethylene และ Propylene ซึ่งเป็นสารตั้งต้นที่สำคัญในอุตสาหกรรมพอลิเมอร์ คณะวิจัยได้ทำการสังเคราะห์ซีโอไลต์ชนิด ZSM-5 ด้วยกระบวนการสังเคราะห์แบบใหม่เพื่อลดปัญหาการแพร่ของสารเคมีที่เข้าทำปฏิกิริยา โดยทำให้เป็นผลึกขนาดนาโนเมตรและเติมรูพรุนมีโซพอร์ (Mesopore 2-50 nm) ปัจจัยที่สำคัญในการสังเคราะห์ผลึกขนาดนาโนเมตรคือ ต้องเพิ่มอัตราการเกิด nuclei (nucleation rate) และลดอัตราการเติบโตของผลึก (Crystal growth) ซึ่งสามารถทำได้โดยการใช้สารละลายความเข้มข้นสูงเพื่อให้เกิด Nuclei จำนวนมาก สำหรับการดัดแปลงโครงสร้างผลึกโดยเติมรูพรุนขนาดมีโซพอร์นั้น ได้สังเคราะห์ซีโอไลต์จากสารตั้งต้นที่เป็นสารผสมของซิลิกาและคาร์บอน (Si/C) ซึ่งมีคุณสมบัติพิเศษคือนอกจากเป็นแหล่งให้ซิลิกา (Silica source) ที่เป็นองค์ประกอบหลักในโครงสร้างแล้ว อนุภาคคาร์บอนในสารผสมดังกล่าวยังทำหน้าที่เป็นแม่แบบเพื่อให้เกิดรูพรุนขนาดมีโซพอร์ (Mesoporous template) อีกด้วย โดยอนุภาคคาร์บอนนี้จะถูกเผาทิ้งภายหลังการสังเคราะห์ผลึกจากกระบวนการ Hydrothermal ซึ่งจะทำให้เกิดเป็นรูพรุนขนาดมีโซพอร์อยู่ภายใน ซึ่งการวิจัยนี้ได้ควบคุมปัจจัยต่างๆ ให้เหมาะสมที่สามารถทำให้เกิดช่องว่างรูพรุนขนาด 2-50 นาโนเมตร (Mesopore) ได้แก่ ชนิดของก๊าซที่เป็นแหล่งกำเนิดคาร์บอน, อัตราส่วนของ Si:C ซึ่งแปรผันกับระยะเวลาในการเผาไหม้และความเข้มข้นของก๊าซขณะเผาไหม้

นอกเหนือจากการสังเคราะห์และวิเคราะห์ตัวเร่งปฏิกิริยาในห้องปฏิบัติการจริงแล้ว คณะผู้วิจัยยังได้ศึกษาทางทฤษฎีด้วยระเบียบวิธีทางเคมีคอมพิวเตอร์ควบคู่กัน ในการออกแบบโครงสร้างของวัสดุและตัวเร่งปฏิกิริยาที่มีขนาดระดับนาโนเมตรเพื่อปรับปรุงคุณสมบัติที่ต้องการให้ดียิ่งขึ้น โดยทำการศึกษาการดูดซับของสารตั้งต้นในปฏิกิริยาที่สำคัญต่างๆบนตัวเร่งปฏิกิริยาซีโอไลต์ ซึ่งถือว่าเป็นขั้นแรกของกระบวนการเร่งปฏิกิริยาและศึกษากลไกการเกิดปฏิกิริยาในระดับโมเลกุล รวมถึงวิเคราะห์ปัจจัยต่างๆที่มีผลต่อการเกิดปฏิกิริยาซึ่งมีรายละเอียดดังนี้

- ศึกษาผลของความเป็นกรดของตัวเร่งปฏิกิริยาซีโอไลต์ชนิด ZSM-5 ต่อการเกิดปฏิกิริยา Beckmann Rearrangement ของสารประกอบ Cyclohexanone Oxime ไปเป็นสารประกอบ ε-caprolactam ซึ่งเป็นสารตั้งต้นที่สำคัญในการผลิต Nylon-6 polymer ที่ใช้ในอุตสาหกรรมเคมีสิ่งทอ
- ศึกษากลไกของปฏิกิริยาการเติมหมู่ Methyl ไปยังโมเลกุลของ Ethylene ด้วย Methanol และ Dimethyl Ether โดยใช้ซีโอไลต์ชนิด H-ZSM-5 เป็นตัวเร่งปฏิกิริยา และศึกษากลไกปฏิกิริยาการเติมหมู่ Methyl ด้วย Methanol ไปยังโมเลกุลของ 2-methylnaphthalene โดยใช้

ซีโอไลต์ชนิด H-BEA เป็นตัวเร่งปฏิกิริยา ซึ่งทั้งสองปฏิกิริยาดังกล่าวเป็นกระบวนการเปลี่ยน Methanol ที่เป็นสารพลอยได้จากกระบวนการเปลี่ยนก๊าซธรรมชาติหรือถ่านหินไปเป็นน้ำมันเชื้อเพลิงในอุตสาหกรรมปิโตรเลียม ให้กลายเป็นสารประกอบไฮโดรคาร์บอนที่สำคัญในอุตสาหกรรมปิโตรเคมี

- ศึกษากลไกปฏิกิริยาการ Isomerization บนตัวเร่งปฏิกิริยา β-ซีโอไลต์ ของ 1,5-Dimethylnaphthalene ไปเป็น 2,6-Dimethylnaphthalene ซึ่งเป็นโมโนเมอร์สำคัญในการผลิตพอลิเมอร์ชนิด Polyethylene naphthalate (PEN) ที่มีคุณสมบัติพิเศษและนิยมใช้ในการผลิตไฟเบอร์ ฟิล์ม และบรรจุภัณฑ์
- ศึกษาผลของโครงสร้างซีโอไลต์ ZSM-5 ต่อการดูดซับสารประกอบ Unsaturated Aliphatic, Aromatic, และ Heterocyclic ซึ่งทั้งหมดเป็นสารประกอบสำคัญที่ถูกใช้ในอุตสาหกรรมเคมี รวมถึงศึกษาปฏิกิริยาการแลกเปลี่ยนอะตอมไฮโดรเจนบนสารประกอบ Aromatic ซึ่งเป็นปฏิกิริยาพื้นฐานในการต่อยอดงานวิจัยที่เกี่ยวข้องต่อไป
- ศึกษาอิทธิพลของความเป็นกรดในซีโอไลต์ชนิด H-FER, H-ZSM-5 และ H-MCM-22 ต่อประสิทธิภาพการดูดซับและการเกิดปฏิกิริยา Tautomerization ของ Acetone ไปเป็นสารประกอบในรูป Enol ซึ่งเป็นขั้นตอนแรกของการเกิดปฏิกิริยา Aldol condensation ในการสังเคราะห์สารอินทรีย์ที่สำคัญหลายชนิด
- ศึกษาอิทธิพลทางโครงสร้างของตัวเร่งปฏิกิริยาซีโอไลต์ชนิด H-FAU and H-ZSM-5 ต่อปฏิกิริยาการแตกพันธะของ Hexane ซึ่งปฏิกิริยาการแตกพันธะคาร์บอนในลักษณะนี้เป็นปฏิกิริยาสำคัญในอุตสาหกรรมปิโตรเคมี ที่ใช้สำหรับเปลี่ยนไฮโดรคาร์บอนสายโซ่ยาวให้เป็นไฮโดรคาร์บอนสายสั้นลงเพื่อนำไปผลิตเชื้อเพลิง
- ศึกษากลไกการเกิดปฏิกิริยา Oxidative Dehydrogenation บนตัวเร่งปฏิกิริยาซีโอไลต์ชนิด MCM22 ของ Propane ไปเป็น Propene ซึ่งเป็นสารตั้งต้นสำคัญในอุตสาหกรรมพอลิเมอร์
- ศึกษากลไกการเกิดปฏิกิริยา Dehydration บนตัวเร่งปฏิกิริยาซีโอไลต์ H-ZSM-5 ของ Glycerol ไปเป็นสารประกอบ Acrolein ที่เป็นสารตั้งต้นสำคัญและนิยมใช้ในอุตสาหกรรมผลิตสารเคมีหลายชนิด เช่น DL-Methionine, Acrylic acid, Super absorber polymers, และ Detergents
- ศึกษาอิทธิพลของโลหะทรานซิชั่น Cu, Ag และ Au ในโครงสร้างของซีโอไลต์ชนิด FAU ต่อการเกิดปฏิกิริยา Carbonyl-ene ของสารประกอบ Formaldehyde

พบว่าปัจจัยด้านโครงสร้าง อาทิเช่น ขนาดของรูพรุน ลักษณะของรูพรุน ตำแหน่งและลักษณะของ Active site รวมถึงองค์ประกอบทางเคมีของซีโอไลต์ ส่งผลอย่างมากต่อค่าพลังงานดูดซับ พลังงานกระตุ้นและพลังงานของปฏิกิริยา ดังนั้นการที่จะเลือกตัวเร่งปฏิกิริยามาใช้ประโยชน์จำเป็น

ที่จะต้องศึกษาให้เข้าใจกลไกการเกิดปฏิกิริยา และปัจจัยต่างๆที่มีผลต่อการเกิดปฏิกิริยาอย่างละเอียด เพราะจะทำให้ได้ข้อมูลที่จะนำไปสู่การออกแบบดัดแปลงโครงสร้าง รวมถึงการพัฒนากระบวนการเคมีให้มีประสิทธิภาพสูงสุด นอกจากนี้การเลือกระเบียบวิธีการคำนวณให้เหมาะสมกับระบบที่ศึกษาถือเป็นอีกปัจจัยหนึ่งที่มีผลต่อความน่าเชื่อถือของข้อมูลที่ได้รับ โดยกรณีที่ระบบที่ต้องการศึกษาประกอบด้วยโมเลกุลที่ถูกดูดซับซึ่งมีขนาดใกล้เคียงกับรูพรุนของซีโอไลต์ และเป็นโมเลกุลไม่มีขั้ว พลังงานการดูดซับที่ได้นั้นจะเกิดจากแรงดึงดูดแบบ van der Waals ระหว่างโมเลกุลกับผนังรูพรุนของซีโอไลต์เป็นส่วนใหญ่ อย่างไรก็ตามเมื่อโมเลกุลที่ถูกดูดซับเป็นโมเลกุลมีขั้วแรงดึงดูดแบบ van der Waals จะมีผลต่อพลังงานการดูดซับน้อยลง แต่ผลของแรงดึงดูดแบบ Electrostatic จากโครงผลึกของซีโอไลต์จะเพิ่มขึ้น ดังนั้นเมื่อต้องการศึกษาการดูดซับของสารประกอบอะโรมาติกส์บนตัวเร่งปฏิกิริยาซีโอไลต์ จึงควรเลือกใช้ระเบียบวิธีที่รวมอิทธิพลของแรงดึงดูดแบบ van der Waals ไว้ด้วย ซึ่งวิธีหนึ่งที่ประหยัดเวลาและให้ผลที่เชื่อถือได้คือ DFT:UFF Hybrid method ในขณะที่ระบบมีสารดูดซับเป็นโมเลกุลมีขั้ว เช่น น้ำหรือเมทานอล ควรเลือกใช้ระเบียบวิธีที่รวมผลของแรงดึงดูดแบบ electrostatic ไว้ด้วย เช่น SCREEP method อย่างไรก็ดี ถึงแม้ DFT:UFF และ SCREEP Hybrid methods จะสามารถใช้ศึกษาการดูดซับของโมเลกุลบนตัวเร่งซีโอไลต์ได้ดี แต่ทั้งสองวิธีนี้ยังมีข้อจำกัด โดยเฉพาะอย่างยิ่งเมื่อต้องการศึกษากลไกการเร่งปฏิกิริยาของซีโอไลต์ที่เกี่ยวข้องกับ Transition states หรือ Intermediates ที่มีโครงสร้างเกะกะและมีประจุ การใช้แบบจำลองที่มีเพียงแรงดึงดูดแบบ van der Waals หรือ Electrostatic อย่างใดอย่างหนึ่งจึงไม่เพียงพอที่จะอธิบายโครงสร้างที่ไม่เสถียรเหล่านี้ได้ คณะผู้วิจัยจึงได้พัฒนาระเบียบวิธีใหม่บนพื้นฐานของระเบียบวิธีเดิมคือ การรวมอิทธิพลของแรงดึงดูดแบบ van der Waals และ Electrostatic ไว้ในแบบจำลองเดียวกัน เพื่อเปรียบเทียบการดูดซับและการเร่งปฏิกิริยาของซีโอไลต์ที่มีโครงสร้างผลึกต่างกันและเรียกแบบจำลองนี้ว่า Embedded ONIOM method รวมถึงการใช้ระเบียบวิธีการคำนวณที่มีความถูกต้องสูง และมีการพัฒนาอย่างต่อเนื่องให้เหมาะสมกับการศึกษาปฏิกิริยาเคมีในโครงสร้างของซีโอไลต์อย่าง M06-L อีกด้วย

นอกเหนือจากตัวเร่งปฏิกิริยาซีโอไลต์แล้ว คณะผู้วิจัยยังได้ศึกษาวัสดุที่มีรูพรุนอย่างโครงสร้างของ Metal-organic frameworks ในการดูดซับสารตั้งต้นที่สำคัญในอุตสาหกรรมเคมีอย่าง Formaldehyde ซึ่งทำให้ได้ข้อมูลที่เป็นประโยชน์ในการปรับปรุงโครงสร้างเพื่อนำไปใช้เป็นตัวเร่งปฏิกิริยาที่เกี่ยวข้องต่อไป นอกจากนี้ยังได้ศึกษาวัสดุที่มีโครงสร้างระดับนาโนเมตรอย่างคาร์บอนนาโนทิวบ์ โดยการดัดแปลงโครงสร้างด้วยการเติมหมู่ฟังก์ชั่นหรือโลหะเพื่อปรับปรุงคุณสมบัติของคาร์บอนนาโนทิวบ์ให้เหมาะสมกับการนำไปประยุกต์ใช้งานด้านต่างๆ อาทิเช่น ตัวเร่งปฏิกิริยาและตัวตรวจจับสารเคมี (Sensor) โดยพบว่าคาร์บอนนาโนทิวบ์เป็นตัวกลางที่ดีในการถ่ายเทอิเล็กตรอน เช่น อิเล็กตรอนจากปฏิกิริยา Oxidation ของ Anthraquinonyl สามารถถ่ายเทผ่านคาร์บอนนาโนทิวบ์ไปเกิดปฏิกิริยา Reduction ของ 4-arylhydroxyl amine ได้ สำหรับคาร์บอนนา

โนทิวบ์ที่ถูกปรับปรุงโครงสร้างด้วยโลหะทรานซิชั่นไปบนผนังท่อ ยังสามารถแสดงการเปลี่ยนแปลงสมบัติทางไฟฟ้าได้อย่างเด่นชัด ในกระบวนการตรวจจับสารพิษและสารก่อมลพิษอย่าง Ammonia และ Nitrogen dioxide และเนื่องด้วยโครงสร้างที่มีลักษณะเป็นท่อ คณะวิจัยจึงได้ทำการศึกษาการเคลื่อนที่ของโมเลกุลขนาดเล็กอย่างน้ำภายในท่อคาร์บอนนาโนทิวบ์ ซึ่งได้ข้อมูลเชิงลึกและเป็นประโยชน์ ในการประยุกต์ใช้คาร์บอนนาโนทิวบ์ทำหน้าที่กักเก็บและถ่ายเทสารบางชนิดได้ สำหรับวัสดุนาโนที่มีรูพรุนอีกชนิดที่ได้ทำการศึกษาคือ สารประกอบ Alkali halide โดยได้พยายามออกแบบและวิเคราะห์สารประกอบ alkali halide หลายชนิด เช่น LiF, NaBr, KCl และ RbI เป็นต้น เพื่อให้ได้รูปแบบโครงสร้างที่เสถียรในการนำไปสังเคราะห์และใช้ประโยชน์ต่อไป

**ผลลัพธ์ที่ได้จากโครงการ**

1. สรุปผลงานที่ได้รับการตีพิมพ์ในวารสารวิชาการนานาชาติในตลอดระยะเวลา 3 ปี ของการดำเนินโครงการ อันได้แก่

   1.1 บทความทางวิชาการที่เกี่ยวข้องกับตัวเร่งปฏิกิริยาซีโอไลต์ จำนวน 13 ผลงาน

   1.1.1 Jakkapan Sirijaraensrea, Jumras Limtrakul, **Effect of the acidic strength on the vapor phase Beckmann rearrangement of cyclohexanone oxime over the MFI zeolite: An embedded ONIOM study**. *Physical Chemistry Chemical Physics,* **2009**, *11*, 578–585.

   1.1.2 Thana Maihom, Bundet Boekfa, Jakkapan Sirijaraensre, Tanin Nanok, Micael Probst, Jumras Limtrakul, **Reaction mechanisms of the methylation of ethene with methanol and dimethyl Ether over H-ZSM-5: An ONIOM study**. *The Journal of Phyicals. Chemistry C,* **2009**, *113*, 6654–6662.

   1.1.3 Chawanwit Kumsapaya, Karan Bobuatong, Pipat Khongpracha, Yuthana Tantirungrotechai, Jumras Limtrakul, **Mechanistic investigation on 1,5- to 2,6-Dimethylnaphthalene isomerization catalyzed by acidic β zeolite: ONIOM study with an M06-L functional**. *The Journal of Phyical Cheistrry C,* **2009**, *113,* 16128–16137.

   1.1.4 Bundet Boekfa, Saowapak Choomwattana, Pipat Khongpracha, Jumras Limtrakul, **Effects of the zeolite framework on the adsorptions and hydrogen-exchange reactions of unsaturated aliphatic, aromatic, and heterocyclic compounds in ZSM-5 zeolite: A combination of perturbation**

**theory (MP2) and a newly developed density functional theory (M06-2X) in ONIOM scheme**. *Langmuir*, **2009**, *25*, 12990–12999.

1.1.5 Bundet Boekfa, Piboon Pantu, Michael Probst, Jumras Limtrakul, **Adsorption and tautomerization reaction of acetone on acidic zeolites: the confinement effect in different types of zeolites**. *Journal of Physical Chemistry C,* **2010**, *114*, 15061–15067.

1.1.6 Thana Maihom, Piboon. Pantu, Chaiwat Tachakritikul, Michael Probst, Jumras Limtrakul, **Effect of the zeolite nanocavity on the reaction mechanism of n-Hexane cracking: A density functional theory study**. *Journal of Physical Chemistry C,* **2010**, *114*, 7850–7856.

1.1.7 Sippakorn Wannakao, Bundet Boekfa, Pipat Khongpracha, Michael Probst, Jumras Limtrakul, **Oxidative dehydrogenation of propane over a $VO_2$-exchanged MCM-22 zeolite: A DFT Study**. *ChemPhysChem*, **2010,** *11*, 3432-3438.

1.1.8 Karan Bobuatong, Michael Probst, Jumras Limtrakul, **Structures and energetics of the methylation of 2-methylnaphthalene with methanol over H-BEA Zeolite**. *Journal of Physical Chemistry C*, **2010,** *114*, 21611-21617.

1.1.9 Kanokwan Kongpatpanich, Tanin Nanok, Bundet Boekfa, Michael Probst, Jumras Limtrakul, **Structures and reaction mechanisms of glycerol dehydration over H-ZSM-5 zeolite: A density functional theory study.** *Physical Chemistry Chemical Physics*, **2011,** *13*, 6462-6470.

1.1.10 Siriporn Jungsuttiwong, Jarun Lomratsiri, Jumras Limtrakul, **Characterization of acidity in [B], [Al], and [Ga] isomorphously substituted ZSM-5: Embedded DFT/UFF approach**. *International Journal of Quantum Chemistry*, **2011**, *111*, 2275-2282.

1.1.11 Oranit Phuakkong, Karan Bobuatong, Piboon Pantu, Bundet Boekfa, Michael Probst, Jumras Limtrakul, **Glycine peptide bond formation catalyzed by Faujasite**. *ChemPhysChem*, **2011**, *12*, 2160-2168.

1.1.12 Sippakorn Wannakao, Pipat Khongpracha, Jumras Limtrakul, **Density functional theory study of the carbonyl-ene reaction of encapsulated**

**formaldehyde in Cu(I), Ag(I), and Au(I) exchanged FAU zeolites**. *Journal of Physical Chemistry A,* **2011**, *115*, 12486-12492.

1.1.13 Chularat Wattanakit, Chompunuch Warakulwit, Piboon Pantu, Boonruen Sunpetch, Metta Charoenpanich, Jumras Limtrakul, **The versatile synthesis method for hierarchical micro- and mesoporous zeolite: an embedded nanocarbon cluster approach**. *The Canadian Journal of Chemical Engineering,* **Inpress**.

1.2 บทความทางวิชาการที่เกี่ยวข้องกับวัสดุที่มีรูพรุนชนิดอื่นๆ จำนวน 16 ผลงาน

1.2.1 Panvika Pannopard, Pipat Khongpracha, Michael Probst, Jumras Limtrakul, **Gas sensing properties of platinum derivatives of single-walled carbon nanotubes: A DFT analysis**. *Journal of Molecular Graphics and Modelling,* **2009**, *28*, 62–69.

1.2.2 Tanin Nanok, Nongnuch Artrith, Piboon Pantu, Philippe A. Bopp, Jumras Limtrakul, **Structure and dynamics of water confined in single-wall nanotubes**. *The Journal of Phyical Cheistrry A,* **2009**, *113,* 2103–2108.

1.2.3 Winyoo Sangthong, Jumras Limtrakul, Francesc Illasa, Stefan Thomas Bromley, **Stable nanoporous alkali halide polymorphs: a first principles bottom-up study**. *Journal of Materials Chemistry,* **2008***, 18,* 5871–5879.

1.2.4 Winyoo Sangthong, Jumras Limtrakul, Francesc Illas, Stefan T. Bromley, **Predicting transition pressures for obtaining nanoporous semiconductor polymorphs: oxides and chalcogenides of Zn, Cd and Mg**. *Physical Chemistry Chemical Physics,* **2010**, *12,* 8513-8520.

1.2.5 G. Loget, G. Larcade, V. Lapeyre, P. Garrigue, C. Warakulwit, J. Limtrakul, M.-H. Delville, V. Ravaine, A. Kuhn, **Single point electrodeposition of nickel for the dissymmetric decoration of carbon tubes**. *Electrochimica Acta*, **2011**, *55*, 8116-8120.

1.2.6 Winyoo Sangthong, Jumras Limtrakul, Francesc Illas, Stefan T. Bromley, **Persistence of magic cluster stability in ultra-thin semiconductor nanorods**. *Nanoscale,* **2010**, *2*, 72–77.

1.2.7 Teeranan Nongnual, Somkiat Nokbin, Pipat Khongpracha, Philippe Anthony Bopp, Jumras Limtrakul, **Density functional theory evidence for an electron hopping process in single-walled carbon nanotube-mediated redox reactions**. *Carbon*, **2010**, *48*, 1524 –1530.

1.2.8 Amporn Sane, Jumras Limtrakul, **Formation of retinyl palmitate-loaded poly(l-lactide) nanoparticles using rapid expansion of supercritical solutions into liquid solvents (RESOLV)**. *Journal of Supercritical Fluids,* **2009**, *51*, 230–237.

1.2.9 Natcha Injan, Tuende Megyes, Tamas Radnai, Imre Bako, Szabolcz Balint, Jumras Limtrakul, Daniel Spangberg, Michael Probst, **Potential energy surface and molecular dynamics simulation of gold(I) in liquid nitromethane**. *Journal of Molecular Liquids*, **2009**, *147*, 64-70.

1.2.10 Chan Inntam, Jumras Limtrakul, **Adsorption of M species and M2 dimers (M = Cu, Ag, and Au) on the pristine and defective single-walled carbon nanotubes: A density functional theory study**. *Journal of Physical Chemistry C*, **2010**, *114*, 21327-21337.

1.2.11 Teeranan Nongnual, Jumras Limtrakul, **Healing of a vacancy defect in a single-walled carbon nanotube by carbon monoxide disproportionation**. *Journal of Physical Chemistry C*, **2011,** *115*, 4649-4655.

1.2.12 Fattah Z., Loget G., Lapeyre V., Garrigue P., Chompunuch Warakulwit, Jumras Limtrakul, Bouffier L., Kuhn A., **Straightforward single-step generation of microswimmers by bipolar electrochemistry**. *Electrochimica Acta*, **2011**, 56, 10562-10566.

1.2.13 Natcha Injan, Tuende Megyes, Tamas Radnai, Imre Bako, Szabolcz Balint, Jumras Limtrakul, Michael Probst, **$Au(CN)_2(CH_3NO_2)_n$ cluster anions: Energetics and geometrical features**. *Journal of Molecular Liquids*, **2011,** *159*, 38-41.

1.2.14 Gabriel Loget, Veronique Lapeyre, Patrick Garrigue, Chompunuch Warakulwit, Jumras Limtrakul, Marie-Helene Delville, Alexander Kuhn**, Versatile Procedure for Synthesis of Janus-Type**. *Chemistry of Materials*, **2011**, *23*, 2595-2599.

1.2.15 Norawit Krainara, Jumras Limtrakul, Francesc Illas, Stefan T. Bromley, **Structural and electronic bistability in ZnS single sheets and single-walled nanotubes**. *Physical Review B: Condensed Matter and Materials Physics*, **2011**, *83*, 233305/1-233305/4.

1.2.16 Thana Maihom, Saowapak Choomwattana, Pipat Khongpracha, Michael Probst, Jumras Limtrakul, **Formaldehyde Encapsulated in Lithium-Decorated Metal-Organic Frameworks: A Density Functional Theory Study**. *ChemPhysChem*, **Inpress**.

2. สรุปผลงานในการประชุมนานาชาติตลอดระยะเวลา 3 ปี ของการดำเนินโครงการ อันได้แก่

2.1 งานวิจัยที่นำเสนอในการประชุมวิชาการนานาชาติ “Nanotech Conference 2009” ณ เมือง Houston ประเทศสหรัฐอเมริกา ระหว่างวันที่ 3-7 พฤษภาคม 2552 จำนวน 8 เรื่อง

2.1.1 Bundet Boekfa, Saowapak Choomwattana, Phornpimon Maitarad, Jumras Limtrakul, **The quantum confinement effect on the adsorption and reaction of aliphatic and aromatic hydrocarbons on ‘nano reactor’ ZSM-5 zeolite: A newly developed density functional theory (DFT) investigation**.

2.1.2 Chawanwit Kumsapaya, Karan Bobuatong ,Saowapak Choomwattana, Pipat Khongpracha,Yuthana Tantirungrotechai, Jumras Limtrakul, **A mechanistic investigation on 1,5- to 2,6-Dimethylnaphthalene isomerization catalyzed by acidic Beta zeolite: An ONIOM study with a newly developed density functional theory**.

2.1.3 Jittima Meeprasert, Saowapak Choomwattana, Piboon Pantu, Jumras Limtrakul, **Dehydration of ethanol into ethylene over H-MOR: A quantum chemical investigation of possible reaction mechanisms in the presence of water**.

2.1.4 Karan Bobuatong, Jakkapan Sirijaraensre, Pipat Khongpracha, Piboon Pantu, Jumras Limtrakul, **The Theoretical Investigation of Oxidative dehydrogenation of ethane to ethene over Fe-ZSM-5: A QM/MM study**.

2.1.5 Sudarat Yadnum, Saowapak Choomwattana, Pipat Khongpracha, Jumras Limtrakul, **structures and mechanism of MOF-505 and Cu-ZSM-5 promoted Mukaiyama aldol reaction: An ONIOM study**.

2.1.6 Chompunuch Warakulwit, M.-H. Delville, V. Ravaine, Jumras Limtrakul, Alexander Kuhn, **Dissymetric metal deposition on carbon nanotubes**.

2.1.7 Teeranan Nongnual, Saowapak Choomwattana, Somkiat Nokbin, Pipat Khongpracha, Jumras Limtrakul, **Electron hopping process in SWCNT-mediated redox reaction: An evidence observed by DFT theory**.

2.1.8 Winyoo Sangthong, Jumras Limtrakul, Francesc Illasa, Stefan Thomas Bromley, **Comparing the stabilities of nanoclusters and cluster-based materials: alkali halides and the first row element compounds**.

2.2 งานวิจัยที่นำเสนอในการประชุมวิชาการนานาชาติ “ 239th American Chemical Society National meeting & Exposition” ณ เมือง San Francisco ประเทศสหรัฐอเมริกา ระหว่างวันที่ 21-25 มีนาคม 2553 จำนวน 11 เรื่อง

2.2.1 Sarawoot Impeng, Thana Maihom, Pipat Kongpracha, Somkiat Nokbin, Jumras Limtrakul, **Propane cracking reaction over different types of nanostructured zeolites: A newly developed DFT approach**.

2.2.2 Supalak Khueanphet, Bundet Boekfa, Tanin Nanok, Jumras Limtrakul, **Adsorption of a basic probe molecule over nanostructured zeolitic catalysts (H-FAU, H-MOR, and H-MCM-22): A newly developed density functional M06-2X study**.

2.2.3 Chularat Wattanakit, Butdet Boekfa, Somkiat Nokbin, Piboon Pantu, Jumras Limtrakul, **Skeletal isomerization of 1-Butene over ferrierite zeolite: A quantum chemical analysis of structures and reaction mechanisms**.

2.2.4 Kanokwan Kongpatpanich, Tanin Nanok, Bundet Boekfa, Jumras Limtrakul**, Structures and reaction mechanisms of glycerol dehydration over H-ZSM-5 zeolites**.

2.2.5 Bundet Boekfa, Piboon Pantu, Pailin Limtrakul, Michael Probst, Jumras Limtrakul, **Application of newly developed M06-2X functional for identifying A suitable industrially important petrochemical zeolite catalyst for a particular reaction**.

2.2.6 Pemikar Srifa, Somkiat Nokbin, Bundet Boekfa, Jumras Limtrakul, **Quantum-chemical analysis of reactions between Pyridine and the industrially important petrochemical zeolite catalyst**.

2.2.7 Sippakorn Wannakao, Bundet Boekfa, Pipat Kongpracha, Jumras Limtrakul, **Oxidative dehydrogenation of propane over a $VO_2$-exchanged MCM-22: A newly developed DFT study**.

2.2.8 Thana Maihom, Piboon Pantu, Chaiwat Tachakrittikul, Jumras Limtrakul, **Adsorption and cracking reaction of n-Hexane over H-ZSM-5: A M06-2X study**.

2.2.9 Sudarat Yadnum, Soawapak Choomwattana, Pipat Kongpracha, Jumras Limtrakul, **Density functional study of epoxide ring-opening reaction with methanol promoted by dicopper carboxylate in metal-organic framework.**

2.2.10 Chardchalerm Raksakoon, Saowapak Choomwattana, Jumras Limtrakul, **Molecular dynamics simulation of otho-, para- and meta-xylenes diffusion in MOF-5 with a model potential of Zn-O bonds for MOF materials**.

2.2.11 Panvika Pannopard, Pipat Kongpracha, Chompunuch Warakulwit, Jumras Limtrakul**, Decomposition of nitrous oxide on transition metal-doped carbon nano-tubes**.

2.3 งานวิจัยที่นำเสนอในการประชุมวิชาการนานาชาติ "240th American Chemical Society National meeting & Exposition" ณ เมือง Boston ประเทศสหรัฐอเมริกา ระหว่างวันที่ 22-26 สิงหาคม 2553 จำนวน 6 เรื่อง

2.3.1 Bundet Boekfa, Thana Maihom, Sippakorn Wannakao, Karan Bobuatong, Jumras Limtrakul, **Structures and reaction mechanisms of propene oxide isomerization to propanal on H-FER zeolite: A theoretical study using the newly developed density functional theory**.

2.3.2 Bundet Boekfa, Thana Maihom, Sippakorn Wannakao, Pailin Limtrakul, Jumras Limtrakul, **Catalytic dehydrogenation of ethylbenzene to styrene over Fe-ZSM-5 zeolite: A newly developed density functional theory (M06-L) in ONIOM scheme**.

2.3.3 Karan Bobuatong, Bundet Boekfa, Sippakorn Wannakao, Jumras Limtrakul, **Structures and Reaction pathways of Methylation of 2-methylnaphthalene with Methanol over HBEA zeolite**.

2.3.4 Sippakorn Wannakao, Thana Maihom, Winyoo Sangthong, Bundet Boekfa, Pipat Khongpracha, Jumras Limtrakul, **DFT study of oxidative dehydrogenation of propane over a VO2-exchanged MCM-22 and ZSM-5 zeolites**.

2.3.5 Thana Maihom, Bundet Boekfa, Sippakorn Wannakao, Jumras Limtrakul, **Reaction mechanisms of ethene formation via ethanol dehydration catalyzed by Fe-ZSM-5 zeolite: An ONIOM study with an M06-L functional**.

2.3.6 Winyoo Sangthong, Sippakorn Wannakao, Saowapak Choomwattana, Thana Maihom, , Bundet Boekfa, Jumras Limtrakul, **Quantum chemical calculation of the hydrogenation reaction of encapsulated formaldehyde in Na-FAU zeolite**.

2.4 งานวิจัยที่นำเสนอในการประชุมวิชาการนานาชาติ “Nanothailand 2010: Nanotechnology for a Sustainable World” ณ โรงแรมรามา การ์เด้นส์ กรุงเทพฯ ประเทศไทย ระหว่างวันที่ 18-20 พฤศจิกายน 2553 จำนวน 15 เรื่อง

2.4.1 Teeranan Nongnual, Jmras Limtrakul, **Healing of a vacancy defect in a Single-Walled Carbon Nanotube by carbon monoxide disproportionation**.

2.4.2 Sippakorn Wannakao, Pipat Khongpracha, Jumras Limtrakul, **Carbonyl-ene reaction of encapsulated formaldehyde in Cu(I), Ag(I) and Au(I) exchanged FAU zeolites**.

2.4.3 Thana Maihom, Jumras Limtrakul, **Theoretical investigation of the effect of the zeolite acidic strength on the reaction mechanism of n-Hexane cracking**.

2.4.4 Anawat Thivasasith, Panvika Pannopard, Pipat Khongpracha, Chompunuch Warakulwit, Jumras Limtrakul, **H-Bond formation assisted by a single Au atom and an $Au_{13}$ cluster: A DFT study**.

2.4.5 Boonruen Sunpetch, Bundet Boekfa, Piboon Pantu, Jumras Limtrakul, **Theoretical studies of nitrous oxide decomposition reaction in transition metals (TM) ion exchanged ZSM-5 zeolite**.

2.4.6 Winyoo Sangthong, Jumras Limtrakul, **Corporative effect of zeolite framework and cation on dehydrogenation of methanol over Na-exchanged faujasite zeolite: A newly developed density functional (M06-2X)**.

2.4.7 Bundet Boekfa, Jumras Limtrakul, **The confinement effect of the zeolite framework on the isomerization reaction of propene oxide over nanostructured H-FER zeolite catalyst using a newly developed "Embedded MP2:M06" method**.

2.4.8 Chularat Wattanakit, Somkiat Nokbin, Bundet Boekfa, Piboon Pantu, Jumras Limtrakul, **Structures and reaction mechanisms of skeletal isomerization of 1-Butene over ferrierite zeolite: An embeded nanocluster approach**.

2.4.9 Sudarat Yadnum, Saowapak Choomwattana, Pipat Khongpracha, Chompunuch Warakulwit, Jumras Limtrakul, **DFT analysis of the MOF catalyzed ring-opening reaction of epoxides: An important process in alkoxy alcohol synthesis.**

2.4.10 Chadchalerm Raksakoon, Saowapak Choomwattana, Jumras Limtrakul, **First-principle-derived potential energy function for $Zn_4O$ tetrahedron-based metal-organic frameworks**.

2.4.11 Pemikar Srifa, Somkiat Nokbin, Bundet Boekfa, Jumras Limtrakul, **Density functional analysis of the confinement effect in nanoporous MCM-22 petrochemical catalyst: nanocluster model approach**.

2.4.12 Panida Singra, Pipat Khongpracha, Jumras Limtrakul, **Reaction mechanisms for ETBE production catalyzed by H-BEA as nanoporous zeolite**.

2.4.13 Supalak Khueanphet, Bundet Boekfa, Tanin Nanok, Jumras Limtrakul, **Adsorption of a basic probe molecule over nanoporous catalysts (H-FAU and H-MOR): An embedded nanocluster approach**.

2.4.14 Patanachai Janthon, Teeranan Nongnual, Piboon Pantu, Jumras Limtrakul, **Catalytic dehydrogenation of ethylbenzene to styrene over a tetrahedral platinum nanocluster: A DFT study**.

2.4.15 Saowapak Choomwattana, Jakkapan Sirijaraensre, Jumras Limtrakul, **DFT study on the effect of phosphate ionic core on basicity of $PW_{12}O_{40}^{3-}$ Polyoxometalate.**

2.5 งานวิจัยที่นำเสนอในการประชุมวิชาการนานาชาติ "241th American Chemical Society National meeting & Exposition" ณ เมือง Anaheim ประเทศสหรัฐอเมริกา ระหว่างวันที่ 27-31 มีนาคม 2554 จำนวน 12 เรื่อง

2.5.1 Bundet Boekfa, Kanokwan Kongpatpanich, Pailin Limtrakul, Jumras Limtrakul, **Skeletal isomerization of 1-butene to isobutene on H-ZSM-5 zeolite: A newly developed density functional theory study**.

2.5.2 Jitwadee Wiangngean, Kanokwan Kongpatpanich, Sippakorn Wannakao, Bundet Boekfa, Jumras Limtrakul, **Structures and reaction mechanisms of n-butyl alcohol conversion to isobutylene over theta-1 zeolite: A DFT study**.

2.5.3 Kulwadee Theanngern, Bundet Boekfa, Pipat Khongpracha, Jumras Limtrakul**, Quantum effect on the reaction mechanism of propene oxide isomerization in H-ITQ-22: A DFT investigation**.

2.5.4 Thittaya Yutthalekha, Kanokwan Kongpatpanich, Thana Maihom, Bundet Boekfa, Jumras Limtrakul, **Structures and reaction mechanisms of butadiene cycloaddition over metal-exchanged faujasite**.

2.5.5 Patanachai Janthon, Teeranan Nongnual, Piboon Pantu, Jumras Limtrakul, **Catalytic dehydrogenation of ethylbenzene to styrene over a tetrahedral platinum nanocluster: A DFT study.**

2.5.6 Panida Singra, Kanokwan Kongpatpanich, Pipat Khongpracha, Jumras Limtrakul, **Density functional theory study of possible mechanisms of isooctene formation via isobutene dimerization over acidic beta zeolite.**

2.5.7 Bundet Boekfa, Jumras Limtrakul, **The acid location of the Bronsted acid site in ITQ-22 zeolite: A newly developed density functional theory study**.

2.5.8 Bundet Boekfa, Jumras Limtrakul, **Strength and Bronsted acid sites of ITQ-34/pyridine complexes: A newly developed density functional theory study**.

2.5.9 Sippakorn Wannakao, Kanokwan Kongpatpanich, Pipat Khongpracha, Jumras Limtrakul, **Activities of Au and Au2 cation-exchanged zeolite for methane C-H bond activation: A DFT study**.

2.5.10 Phornphimon Maitarad, Pimpa Hormnirun, Pipat Khongpracha, Jumras Limtrakul, **Structure activity relationship and the electronic property of bis(phenoxyimine) ligated zirconium catalysts for ethylene polymerization: A combined CoMFA and DFT study**.

2.5.11 Thana Maihom, Jumras Limtrakul, **Formaldehyde encapsulated in lithium-decorated metal-organic frameworks: A DFT study**.

2.5.12 Supawadee Namuangruk, Pipat Khongpracha, Jumras Limtrakul, **Theoretical study of the oxidative dehydrogenation of ethylbenzene to styrene over Fe-ZSM-5**.

2.6 งานวิจัยที่นำเสนอในการประชุมวิชาการนานาชาติ "242$^{th}$ American Chemical Society National meeting & Exposition" ณ เมือง Denver ประเทศสหรัฐอเมริกา ระหว่างวันที่ 28 สิงหาคม -1 กันยายน 2554 จำนวน 10 เรื่อง

2.6.1 Bundet Boekfa, Piti Treesukol, Jumras Limtrakul, **Reaction mechanism of isomerization of 1-butene to isobutene over multipore H-ITQ-22 zeolite: a DFT study**.

2.6.2 Anawat Thivasasith, Pipat Khongpracha, Chompunuch Warakulwit, Jumras Limtrakul, **Decomposition of nitrous oxide on Au-embedded graphene**.

2.6.3 Saowapak Choomwattana, Thana Maihom, Jumras Limtrakul, **Density functional theory study on catalytic cracking of n-hexane on heteropoly acid comparison with FAU zeolite.**

2.6.4 Sarawoot Impeng, Amporn Sane, Chompunuch Warakulwit1, Panvika Pannopard, Boonruen Sunpetch, Pipat Khongpracha, Jumras Limtrakul, **Synthesis of precisely size-controlled gold nanoparticles and their infusion into mesoporous silica SBA-15 by compressed carbon dioxide solution technique.**

2.6.5 Sippakorn Wannakao, Thana Maihom, Pipat Khongpracha, Bundet Boekfa, Jumras Limtrakul, **Oxidation of carbon monoxide by nitrous oxide decomposition on Fe-embedded graphene.**

2.6.6 Sudarat Yadnum, Pipat Khongpracha, Chompunuch Warakulwit, Jumras Limtrakul, **Precisely size-controlled metal nanoparticles (Au, Pd and Pt) inserted into metal-organic frameworks (MOFs): synthesis and catalytic properties**.

2.6.7 Supakit Tiewcharoen, Bundet Boekfa, Piti Treesukol, Thana Maihom, Jumras Limtrakul, **Shape-selective hydrocarbon cracking of n-hexane on MCM-22 zeolite**.

2.6.8 Thana Maihom, Pipat Khongpracha, Jumras Limtrakul, **Activity of gold-supported MFI zeolites for nitrous oxide decomposition: a density functional study**.

2.6.9 Thittaya Yutthalekha, Bundet Boekfa, Jumras Limtrakul**, Structures and reaction mechanisms of butadiene cycloaddition over metal-exchanged faujasite**.

2.6.10 Winyoo Sangthong, Jumras Limtrakul, **Catalytic dehydrogenation of propane over Au(I) exchanged ZSM-5: density functional theory calculations**.

# ภาคผนวก

# บทความที่ตีพิมพ์
# ในวารสารวิชาการต่างประเทศ
# จำนวน 29 ผลงาน

# บทความทางวิชาการที่เกี่ยวข้องกับ
# ตัวเร่งปฏิกิริยาซีโอไลต์
# จำนวน 13 ผลงาน

# Effect of the acidic strength on the vapor phase Beckmann rearrangement of cyclohexanone oxime over the MFI zeolite: an embedded ONIOM study†

**Jakkapan Sirijaraensre[ab] and Jumras Limtrakul*[ab]**

***Received 22nd May 2008, Accepted 7th October 2008***
***First published as an Advance Article on the web 5th November 2008***
**DOI: 10.1039/b808662a**

The mechanism and energetic profile of the Beckmann rearrangement reaction of cyclohexanone oxime to ε-caprolactam catalyzed by the H-[Al]-MFI and H-[B]-MFI zeolites were investigated by both the bare cluster and the ONIOM models at the B3LYP/6-31G(d,p) and the B3LYP/6-31G(d,p) : MNDO levels of theory, respectively. In order to improve the energetic properties and take into account the whole zeolite framework effect, single point calculations are undertaken at the embedded ONIOM2 schemes; MP2/6-311G(d,p) : HF/6-31G(d) with an additional long-range electrostatic potential from the extended zeolite framework. The reaction mechanism of the Beckmann rearrangement over the acid site of zeolites consists of three steps: the 1,2 H shift, the rearrangement and the tautomerization. The activation energies for the Beckmann rearrangement of cyclohexanone oxime on the H-[Al]-MFI zeolite are calculated to be 31.46, 16.15 and 18.95 kcal $mol^{-1}$, for the first, second and third steps, respectively, whereas in the H-[B]-MFI zeolite, the energy barriers for each step of the reaction are 24.33, 7.46 and 20.43 kcal $mol^{-1}$, respectively. The rate-determining step of the reaction is the first step, which is the transformation from the N-ended cyclohexanone oxime adsorption complex and the O-ended one. These results signify the important role that the acid strength of zeolites plays in altering the energy profile of the reaction. The results further indicate that the weak Brønsted acid sites in the [B]-MFI zeolite could better catalyze the Beckmann rearrangement of cyclohexanone oxime than the strong acid sites in the [Al]-MFI zeolite, as compared with the quantitatively low activation energy of most steps. However, the turnover reaction of the H-[B]-MFI zeolite might be delayed by the quantitatively high desorption energy of the product as compared to the adsorption energy of the reactant.

## Introduction

The Beckmann rearrangement[1–6] is one of the most important industrial reactions for producing the ε-caprolactam, an important intermediate for the production of the Nylon-6 polymer. In the conventional method, this process uses acid solution, ammonia and cyclohexane as the principal raw materials. However, it is both environmentally unfavorable; due mainly to the use of corrosive sulfuric acid, instrument corrosion occurs and wastes the resources; and ammonium sulfate, a by-product formed during the neutralization process, is produced at approximately 1–5 times that of ε-caprolactam. Hence, a range of heterogeneous catalysts are used in this reaction with the objective of overcoming these problems. Zeolites have been widely investigated on this reaction, for example MFI,[7–16] FAU,[15–20] Beta,[20–25] and MOR[15,16,20] zeolites. From previous studies, it is of interest to note that porous catalysts like zeolites show both high activity and provide a highly selective product. As a result of these investigations, Sumitomo Chemical Co., Ltd., have industrialized the production of ε-caprolactam, using high-silica MFI zeolite as the catalyst for the vapor phase Beckmann rearrangement. This process does not produce any ammonium sulfate, a by-product through the Beckmann rearrangement without a catalyst.

The Beckmann rearrangement catalyzed by solid catalysts (usually called the vapor-phase Beckmann rearrangement) has been the subject of many researchers who have developed suitable experimental and computational techniques for finding an efficient catalyst which can enhance the process of manufacturing the desired product. In earlier studies,[18,19,23,26,31] strong Brønsted acid sites in zeolites were suggested as playing a crucial role in catalyzing this reaction by protonating the oxime molecule, whereas external silanols appear to be nonreactive, while in some previous works,[8,11,12,21,32,33] they have reported that the weak acidic groups in zeolites such as high-silica MFI, [B]-MFI and [B]-Beta are also active catalysts for the rearrangement reaction with high activity and selectivity toward ε-caprolactam.

[a] *Laboratory for Computational and Applied Chemistry, Chemistry Department, Faculty of Science, Kasetsart University, 10900 Bangkok, Thailand. E-mail: fscijrl@ku.ac.th*
[b] *Center of Nanotechnology, Kasetsart University Research and Development Institute, Kasetsart University, 10900 Bangkok, Thailand. E-mail: fscijrl@ku.ac.th*

† Electronic supplementary information (ESI) available: Additional experimental details. See DOI: 10.1039/b808662a

 

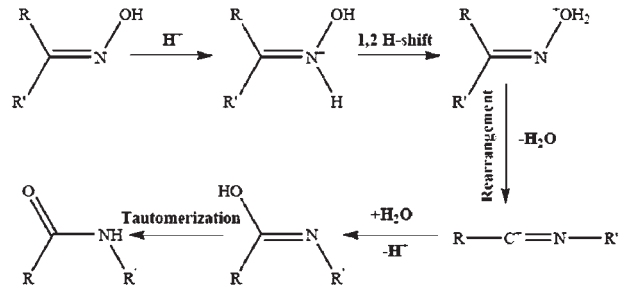


**Scheme 1** The reaction mechanism for the Beckmann rearrangement.

Therefore, the role of the acid site strength in the Beckmann rearrangement is a matter of debate.

The reaction mechanism over the Brønsted acid site of zeolite catalysts is intensively investigated both experimentally[22,23,34–36] and theoretically.[26–28,36,37] The reaction mechanism, commonly suggested for the Beckmann rearrangement, is described in Scheme 1 as follows:

The reaction initially involves the protonation of the oxime molecule at the nitrogen atom of the oxime molecule (designated by N-Bound). Then, in the first TS step, named the 1,2 H-shift step, the hydrogen is transferred from the nitrogen-end to the oxygen atom of the oxime molecule (designated as O-Bound) and followed by migration of an R group (R = alkyl, aryl or hydrogen), which is *anti* to both the hydroxyl group and to the nitrogen atom, and a water molecule is displaced. This second step is called the rearrangement step. Subsequently, the displaced water molecule binds to the carbon atom, simultaneously transferring a proton to the acid catalyst. The last transforming step is the tautomerization from the enol–amide complex to the amide complex and desorption of the amide molecule in the final step. Recently, theoretical investigations reveal that the transfer of proton from the nitrogen-end to the oxygen-end of oxime molecules is the rate-determining step of the reaction when it occurs over zeolite catalysts. Nevertheless, the theoretical investigation of the Beckmann rearrangement on zeolite systems is not yet well-founded.

The aim of this work is to investigate the effect of the Brønsted acid site strength in isomorphously substituted MFI zeolites: H-[Al]-MFI and H-[B]-MFI zeolites, on the reaction mechanism and the energetic profile of the Beckmann rearrangement of cyclohexanone oxime. To the best of our knowledge, no theoretical study has investigated the Beckmann rearrangement mechanism of cyclohexanone oxime catalyzed by as large a unit cell zeolite as MFI zeolite. This finding can provide more insight into the role of the acidic strength of zeolite on the Beckmann rearrangement reaction. The interaction of the MFI zeolite and the oxime molecule has been investigated by using the bare cluster and embedded ONIOM approaches.

## Computational details

To determine the adsorbed structure of cyclohexanone oxime molecules in H-[Al]-MFI and H-[B]-MFI zeolites, the ONIOM models were used. The T12 site, which has been widely used to model the active site of MFI in many theoretical studies, is substituted with two different types of trivalent atoms; $Al^{3+}$ and $B^{3+}$. Either B substitution or Al substitution introduces a net negative charge in the zeolite framework which is compensated by a proton acting as a Brønsted acid site to preserve neutrality. Due mainly to the large unit cell of the MFI zeolite, the use of periodic calculation is computationally too expensive and even impractical. Recently, hybrid methods such as the embedded cluster,[26,27,38–46] QM-Pot[47–49] as well as the ONIOM methods[50–59] have been used for including the framework effects of zeolite with the benefit of the computational cost becoming economically feasible. In the ONIOM2 scheme, the MFI zeolite is represented by the 128T model which covers the nanometer-sized cavity that is the intersection of the main and sinusoidal channels and the location of the active site of MFI zeolite. The 128T ONIOM model (see Fig. 1) is divided into two layers: only the small active region (12T) located at the intersection of the main and sinusoidal channel is accessible to the adsorbates (see Fig. 1a–b), the active site of the H-MFI zeolite was treated accurately with the density functional theory (B3LYP) with the 6-31G(d,p) basis set, while the contribution of influences from the rest of the model was approximated by a less expensive method (MNDO). This combination was previously used to investigate the adsorption of $NH_3$ and $H_2O$ in H-CHA zeolite.[59] These results showed that the adsorbed structures obtained from the ONIOM2(B3LYP : MNDO) scheme are in agreement with those obtained from periodic calculations. In order to obtain more accurate adsorption energies, single point calculations were carried out at the ONIOM2(MP2/6-311G(d,p) : HF/6-31G(d)) level of theory. Attempts have been made to demonstrate that the geometry constraints imposed in this work do not influence the results. Some test calculations on cyclohexanone oxime over the H-[Al]-MFI and H-[B]-MFI zeolite have been performed using two different sizes of QM region: 12T and 30T atoms with a different degree of relaxation in QM regions (see ESI, Fig. S1 and Table S1).† It was found that no significant structural differences were obtained when using 5T, 8T and 24T clusters during optimization. Furthermore, the combination of B3LYP and UFF, which has shown good results in predicting the structural parameters and reaction energies in previous works, is preformed to compare the results with the MNDO environment. The B3LYP : UFF combination[60–65] has been found to provide a good description of the short range van der Waals

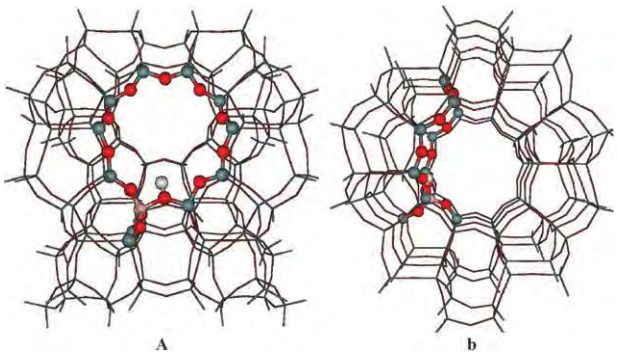


**Fig. 1** Presentation of the 128T ONIOM2 model of H-MFI zeolite. The atoms belonging to the high-level region are presented as bonds and sticks, while the rest of the atoms belong to the low-level region.

interactions. The ONIOM calculation using B3LYP : MNDO with the 12T : 128T cluster leads to geometry similar to that obtained from the B3LYP : UFF calculations. The adsorption energy computed from MP2/6-311G(d,p) : HF/6-31G(d) single point calculations at the B3LYP/6-31G(d,p) : MNDO optimized structures, is also in agreement with the B3LYP : UFF value. Consequently, the use of the MP2/6-311G(d,p) : HF/6-31G(d)//B3LYP/6-31G(d,p) : MNDO approach seems to be a good strategy to model this system (see ESI, Table S2).† All optimizations have been preformed on the 12T/5T cluster embedded in the 116T cluster treated by the MNDO method. However, the 128T ONIOM model neglects the long-range effects from the remaining infinite lattice of zeolite (excluding the 128T ONIOM model). Hence, in order to fulfil the entire behavior of the adsorption properties of the probe molecule in the zeolite pore, the ONIOM model is embedded in the zeolitic Madelung potential field which is represented by two sets of point charges generated by the SCREEP method.[26,27,40–46] The detailed description of the SCREEP method which reproduces the correct Madelung potential calculated from the Ewald-sum method was previously reported elsewhere.[38,40] This new model can take into consideration the long-range effects extended from the general ONIOM model. The combination of the SCREEP and ONIOM approach is called the embedded-ONIOM approach (e-ONIOM) which is a sufficiently accurate and practical model for studying reaction mechanisms on zeolite systems.[64,66,67] Verification that the optimized transition state connects the intended reactant and product, was made by normal mode analysis. All calculations were carried out using the Gaussian 03 program.[68]

## Results and discussion

### The local structure of the isomorphously substituted MFI structure

Selected parameters of the active sites of both zeolites are listed in Table 1 and illustrated in Fig. 2a–b. It is obvious that the type of trivalent atom substituted into the zeolite framework has a significant effect on the structure of the zeolite framework and the length of the O–H bond of the Brønsted acid site. For the acid site structure, the O–H bond distance of the H-[B]-MFI zeolite is slightly shorter than that of the H-[Al]-MFI zeolite by 0.003 Å. The negligible difference of the O1–H1 bond distance has an effect on the charge-population changes for the H1 atom (0.5419 *vs.* 0.5755), suggesting that the acid site of the H-[Al]-MFI zeolite is more acidic than that of the H-[B]-MFI zeolite. Some significant differences are found in the bond distances and bond angles of the zeolite framework. The distances between the silicon atom and the bridging oxygen atom (Si–O bond distance) of the H-[B]-MFI zeolite are slightly longer than those of the H-[Al]-MFI zeolite and the angles between the substituted site and neighboring silicon atoms ($M^{3+}$–O–Si) in the H-[B]-MFI zeolite are larger than those in the [Al]-MFI by around 10–13°. The distances between the substituted site and the bridging oxygen atoms ($M^{3+}$–O) in the H-[B]-MFI are significantly shorter than those in the [Al]-MFI zeolite by 0.02 and 0.26 Å for the $M^{3+}$–O1 and $M^{3+}$–O2 bond distances, respectively. Because of the small size of the $B^{3+}$ cation, the length of the B–O1 bond distance no bonding occurs between the B and the bridging hydroxyl group, and the structure is in the form of a trigonal $BO_3$ and a terminal silanol group is formed in the H-[B]-MFI zeolite. These observations are consistent with previous experimental and theoretical studies.[69–74]

**Table 1** Optimized geometries and proton affinity (PA) of H-[B]-MFI and H-[Al]-MFI at the ONIOM2(B3LYP : 6-31G(d,p) : MNDO) scheme

| Parameters | H-[B]-MFI | H-[Al]-MFI |
|---|---|---|
| O1–H1 | 0.970 | 0.973 |
| Si1–O1 | 1.656 | 1.653 |
| $M^{3+}$–O1 | 1.782 | 1.802 |
| Si–O2 | 1.607 | 1.582 |
| $M^{3+}$–O2 | 1.402 | 1.663 |
| M–H | 2.195 | 2.301 |
| ∠Si1–O1–M | 137.6 | 127.8 |
| ∠Si2–O2–M | 149.2 | 133.8 |
| $q$(H1)[a] | 0.5419 | 0.5755 |

[a] The atomic charges from the Mulliken population analysis were carried out by single point calculations with the full quantum calculation, HF/6-31G(d) level of theory.

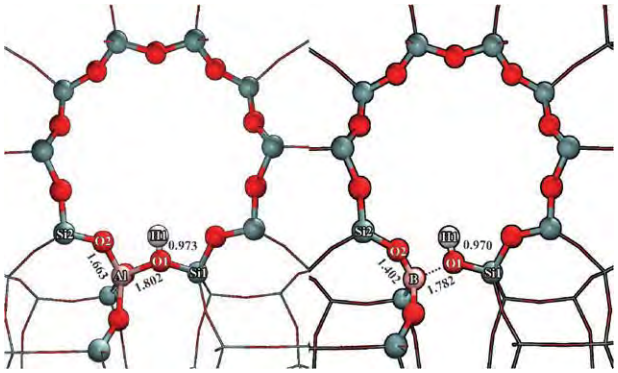


**Fig. 2** Optimized geometric parameters of the 128T ONIOM model of zeolites at the B3LYP/6-31G(d,p) : MNDO scheme: (a) H-[Al]-MFI zeolite and (b) H-[B]-MFI zeolite.

### The Beckmann rearrangement on an isomorphously substituted MFI structure

**The 1,2 H-shift step.** The geometrical parameters of the N-bound complex, the H-shift transition state and the O-bound complexes calculated by the ONIOM2 scheme are illustrated in Fig. 3a–c for the H-[Al]-MFI zeolite and Fig. 3d–f for the H-[B]-MFI zeolite. At the initial step, the cyclohexanone oxime molecule interacts with the acidic site of the zeolite *via* its nitrogen atom. The reaction subsequently proceeds in three consecutive steps. The first step is called 1,2 H-shift step. The initial adsorption complex; N-bound complex on both zeolites: H-[Al]-MFI and H-[B]-MFI zeolites, is in the form of a protonated complex, which is consistent with previous experimental studies[23,34] that observed the protonated form of cyclohexanone oxime over the Brønsted acid site. In both zeolitic systems, the O1–H1 bond in the N–bond complex is lengthened to 1.775 and 1.764 Å to form the N–H1 single bond. The N–H1 bond distance is predicted to be 1.035 and 1.043 Å for the H-[Al]-MFI and the H-[B]-MFI systems,

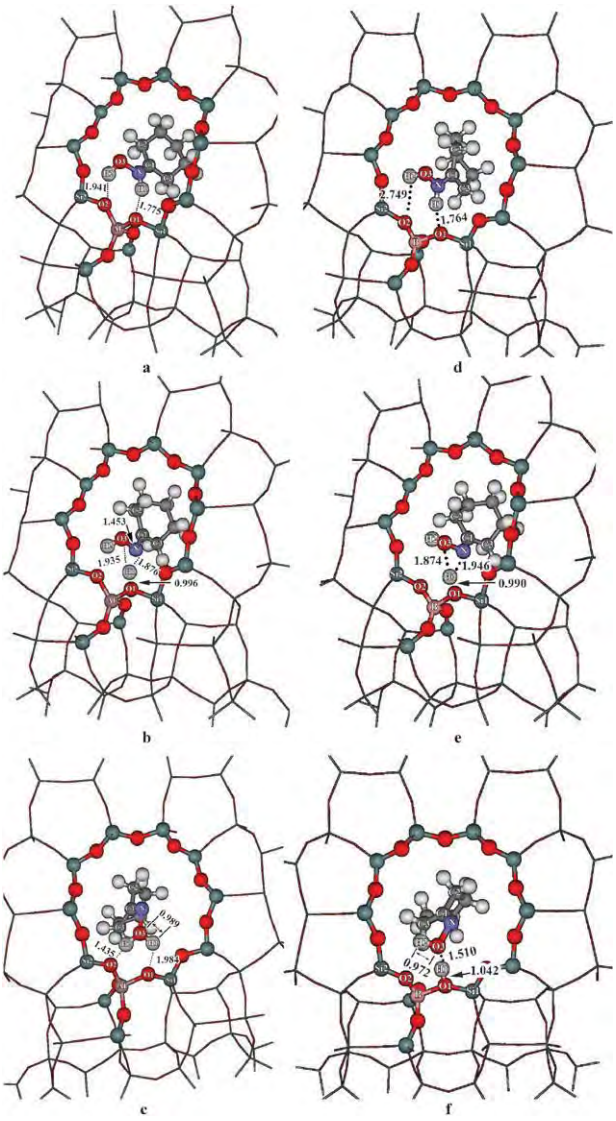


**Fig. 3** Optimized geometrical parameters of the stationary points corresponding to 1,2 H-shift step of cyclohexanone oxime: (a) N-bound complex, (b) 1,2 H-shift transition state complex and (c) O-bound complex, respectively. They are catalyzed by the H-[Al]-MFI zeolite. Sections (d)–(f) present the corresponding complexes on the H-[B]-MFI zeolite.

respectively. This complex consists of the two strong hydrogen bond interactions between O5–H2–O2 and N–H1–O1 and corresponds to the previous theoretical studies on the MFI[26] and FAU[27] zeolites. The adsorption energy of this complex is calculated to be −50.67 and −39.91 kcal mol$^{-1}$ for the H-[Al]-MFI and H-[B]-MFI systems, respectively. The difference of the adsorption energy of this complex is due mainly to the acidic strength of the Brønsted acid sites of both zeolites. Due to the H-[Al]-MFI zeolite being more acidic than the H-[B]-MFI zeolite, the adsorption energy of cyclohexanone oxime on the H-[Al]-MFI zeolite is more exothermic. The transition state (*cf*. Fig. 3b and e) of the first step is the transfer of the active proton (H1) from the nitrogen-ended site to the oxygen-ended site of the cyclohexanone oxime. The structural changing from the N-bound complex to the other one in this transition state can be observed from the N–H1, O3–H1 and N–O3 bond distances. At the TS, the N–O3 bond distance is elongated by about 0.08 and 0.06 Å for the H-[Al]-MFI and H-[B]-MFI systems, respectively. For the active H1 atom, the bond distance between it and the nitrogen atom is broken and located in the midway point between the N and O atoms, with the N–H1 and O3–H1 active distances being 1.876 and 1.935 Å for the H-[Al]-MFI system, and 1.946 and 1.874 Å for the H-[B]-MFI system. These distances correspond to a previous observation in the zeolitic systems: MOR[28] (1.90 Å), MFI[26] (1.95 Å) and FAU[27] (1.85 Å). With assistance from the zeolite framework in shuttling the proton, the barrier height of this step is 31.5 and 24.3 kcal mol$^{-1}$ for the H-[Al]-MFI and H-[B]-MFI zeolites, respectively. They are quantitatively similar to the activation energies of the oximes in the zeolite systems in previous studies[26–28] by 21–31 kcal mol$^{-1}$. The reduction of the activation energy for this step in the H-[B]-MFI zeolite, as compared to that in the H-[Al]-MFI zeolite, is due mainly to the decrease of the acidity of Brønsted site of the zeolite that leads to a significantly weak interaction in the initial-state adsorption of reaction, N-bound complex. This observation is consistent with previous works,[26,27] concluding that the barrier height of this step corresponds to the strength of the adsorption in the N-bound complex. Subsequently, after the 1,2 H-shift process, the O-bound complex, which is an interaction between the oxygen atom of cyclohexanone oxime and the Brønsted acid site of zeolite, is formed with the adsorption energy of −31.51 and −18.91 kcal mol$^{-1}$. Contrary to the N-bound complex, it can be seen clearly from Fig. 3c and f that only the H-[Al]-MFI zeolite promotes the protonation of the O-bound complex, whereas the corresponding complex on the H-[B]-MFI system is in a molecularly adsorbed state. In the [Al]-MFI system, the protonated-oxygen cyclohexanone oxime interacts with the bridging oxygens of zeolite *via* two strong hydrogen bonds: O1···H1–O3 and O2···H2–O3 (1.984 and 1.435 Å), while for the [B]-MFI system, the physisorbed oxime molecule is stabilized by one strong O3···H1–O1 hydrogen bond (1.510 Å) and one weaker O2···H2–O3 hydrogen bond (2.414 Å). The difference between the geometrical O-bound complex and the calculated heat of adsorption values corresponds to the acidic strength of the Brønsted acid site of the zeolites.

**The rearrangement step.** The key parameters of the rearrangement transition state and the corresponding intermediate product are illustrated in Fig. 4a–b for the H-[Al]-MFI zeolite and Fig. 4c–d for the H-[B]-MFI, respectively. In the transition state of the [Al]-MFI zeolite, the C1–C2 bond is broken and the C2 is shifted toward the N atom and located above the C1–N bond, causing a shortening of the N–C1 bond distance from 1.280 to 1.187 Å. The bond distances of the C1–C2 and N–C2 bonds are predicted to be 1.864 and 1.995 Å, respectively. Concurrently with the breaking of the C1–C2 bond, the N–O3 bond is broken and a water molecule is separated from the rest of the molecules. The intermolecular N–O bond distance is significantly elongated to 2.545 Å. The O3–H1 and O3–H2 bond distances are shortened to 0.966 and 0.976, respectively, and the bond angle of H1–O2–H2 is slightly spread from 103.0 to 103.7°, while in the rearrangement TS step over the H-[B]-MFI zeolite, the

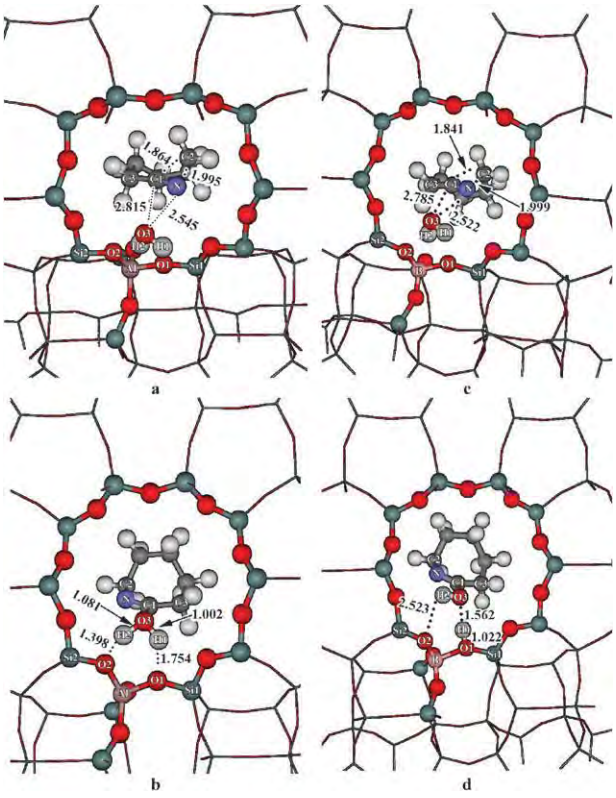


**Fig. 4** Optimized geometrical parameters of the stationary points corresponding to the rearrangement step of cyclohexanone oxime: (a) the rearrangement transition state complex and (b) the enol–amide adsorption complex, respectively. Those are catalyzed by the H-[Al]-MFI zeolite. Sections (c) and (d) present the corresponding complexes on the H-[B]-MFI zeolite.

elimination of the C1–C2 bond and the transfer of the C2 to the N atom take place with low activation energy. The C2 atom is located in between the C1 atom and N atom with bond distances of 1.841 and 1.999 Å for the C1–C2 and N–C2 bond lengths, respectively. Furthermore, comparing the rearrangement transition state between both zeolitic systems, we found that the protonation occurred during the rearrangement in the H-[B]-MFI zeolite. The activation energy for this step is calculated to be 16.15 and 7.46 kcal $mol^{-1}$ for the H-[Al]-MFI and the H-[B]-MFI zeolites, respectively. The reduction of the energy barrier for this step is due mainly to the adsorption strength of the O-bound complex. In the H-[B]-MFI zeolite, this complex is in the neutral form complex, whereas in the other zeolite, it is in the protonated complex. Therefore, the effects from the zeolite framework have a much larger degree of stabilization of the O-bound complex in the H-[Al]-MFI zeolite than that in the H-[B]-MFI zeolite. Our results compare well to the periodic calculation[28] that predicted the activation energies to be 21.05 and 15.31 kcal $mol^{-1}$ for the 1,2 H-shift and rearrangement steps on the Brønsted acid site of MOR zeolite. After the rearrangement process, the enol–amide complex is formed. The distances of the forming bonds, N–C2 and C1–O3, are 1.465 and 1.469 Å, respectively, resulting in slight shortening of the N–C1 bond. The adsorbed complex is in a protonated form, forming two slightly stronger hydrogen bonds to the bridging oxygen atoms of zeolite with the $–OH_2$ group. The intermolecular O1–H1 and O2–H2 bond distances are 1.754 and 1.398 Å, respectively. In the H-[B]-MFI zeolite, the enol–amide complex is in the neutral complex consisting of only a strong hydrogen bond between the O3 atom and the Brønsted acid site of [B]-MFI zeolite. The distances of the newly formed N–C2, C1–O3 and O3–H1 bonds are 1.460, 1.402 and 1.562 Å, respectively. The adsorption energies are predicted to be −59.86 and −52.19 kcal $mol^{-1}$ for H-[Al]-MFI and H-[B]-MFI zeolites, respectively. The difference in the adsorption energies of these complexes is in agreement with their structural adsorption complexes, as shown in Fig. 4b and d.

**Tautomerization step.** The optimized structures of this state are illustrated in Fig. 5a–b for H-[Al]-MFI zeolite and Fig. 5c–d for H-[B]-MFI, respectively. The transition state of this step (*cf*. Fig. 5a and c) is the migration of the H atom from the –OH group to the N atom to form the ε-caprolactam. In the H-[Al]-MFI system, the migrating proton (H2) is close to the midway point between the O3 and N atoms (the distances of O3–H2 and N–H2 bonds are 1.218 and 1.414 Å) where it is nearly in the same plane with the O3 and N atoms of the enol–amide complex (the N–C1–O3–H2 dihedral angle is 3.0°; see Fig. 5a and c). These take place simultaneously with shortening of the C–O bond (by about 0.05 Å) and the slight elongation of the N–C1 bond (by about 0.02 Å) for transferring to the amide compound, the keto–amide complex. Whilst in the H-[B]-MFI zeolite, the migration proton is located in a

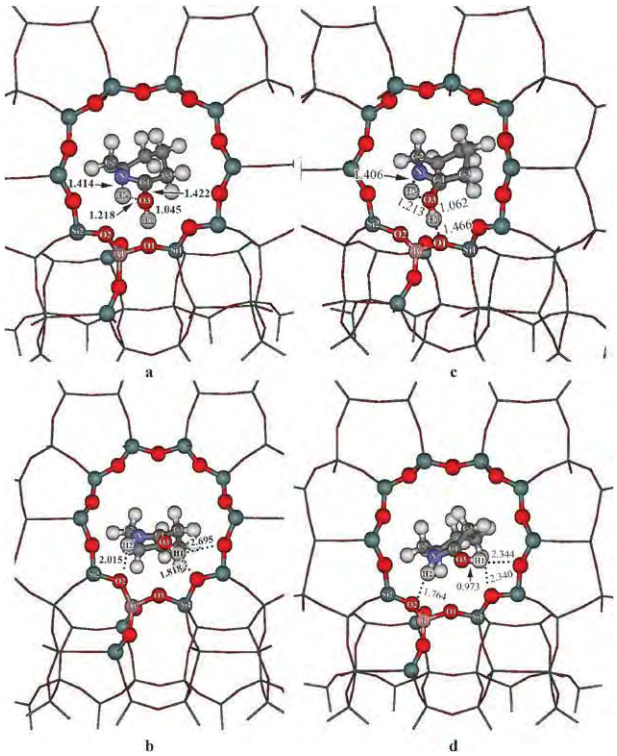


**Fig. 5** Optimized geometric parameters of the complexes corresponding to the tautomerization step of cyclohexanone oxime: (a) the tautomerization transition state complex and (b) the keto–amide adsorption complex, respectively. Those are catalyzed by the H-[Al]-MFI zeolite. Sections (c) and (d) present the corresponding complexes on the H-[B]-MFI zeolite.

similar geometry as that found in the H-[Al]-MFI zeolite. The N–H2 and O3–H2 bond distances are 1.406 and 1.213 Å, respectively. These are quantitatively similar to the corresponding bonds in the H-[Al]-MFI zeolite. Concurrently with the migration of the H2 atom, the proton of the Brønsted acid site is transferred to protonate the O2 atom of the enol–amide complex during the transition state. The activation energy for this step, using the embedded-ONIOM2 model, is evaluated to be 18.95 and 20.43 kcal $mol^{-1}$ for the H-[Al]-MFI and H-[B]-MFI zeolites, respectively. The barrier for this step in the H-[Al]-MFI zeolite is slightly lower than that in the H-[B]-MFI zeolite because of the enhancement of the acidity of the H2 atom caused by the protonation at the oxygen atom of the enol–amide product. After the tautomerization process, the keto–amide product or ε-caprolactam is formed (*cf*. Fig. 5b and d). The interaction between the keto–amide complex and the Brønsted acid site of both zeolites is in the form of a protonated complex which agrees well with the experiment observation[34,37] that the O-protonated ε-caprolactam is formed over the Brønsted acid sites of zeolite. The desorption energy of the ε-caprolactam molecule is calculated to be −44.96 and −39.11 kcal $mol^{-1}$ for the H-[Al]-MFI and H-[B]-MFI zeolites, respectively. The high value of the desorption energy indicates that the desorbing process of the reaction product from the zeolites possibly obstructs the adsorption of the oxime molecule in the first step of the reaction. These results agree well with previous experimental studies,[14,15] concluding that the reaction on the strong Brønsted acid of MFI is very active in the rearrangement of the cyclohexanone oxime to the ε-caprolactam, but a problem will be encountered due to a difficulty in the desorption step, which also leads to the catalyst deactivation because of coke deposition in the zeolite pores. Because the produced ε-caprolactam remains on the acid sites, it is converted to an oligomer, which could be a precursor of coke.

A comparison of the results of the embedded ONIOM model and the bare cluster model (see ESI),† reveals that the effects from the zeolite framework play an important role in lowering the activation energies in each step of the reaction, excepting the 1,2 H-shift step. It is because of the zeolite framework effect having a much larger degree of stabilization of the adsorption complex, N-bound complex, than at the TS complex. Consequently, this step is the rate-determining step of the reaction in both zeolites which have activation energies of 31.46 and 24.33 kcal $mol^{-1}$ for the H-[Al]-MFI and H-[B]-MFI zeolites, respectively (*cf*. Fig.6). The largest effect is at the rearrangement step, which is the connection between the O-bound complex and the enol–amide complex. The zeolite framework effects lower the energy barrier by about 10 and 25 kcal $mol^{-1}$ for the H-[Al]-MFI and H-[B]-MFI zeolites, respectively.

## Conclusions

In this work, we have examined both the role of acid strength and the zeolite framework effects on the Beckmann rearrangement of cyclohexanone oxime catalyzed by the isomorphously substituted MFI zeolites: the H-[Al]-MFI and the H-[B]-MFI zeolites. All of these systems have been investigated by both the bare cluster and the ONIOM2 scheme. By use of the ONIOM2 scheme in combination with the electrostatic potential

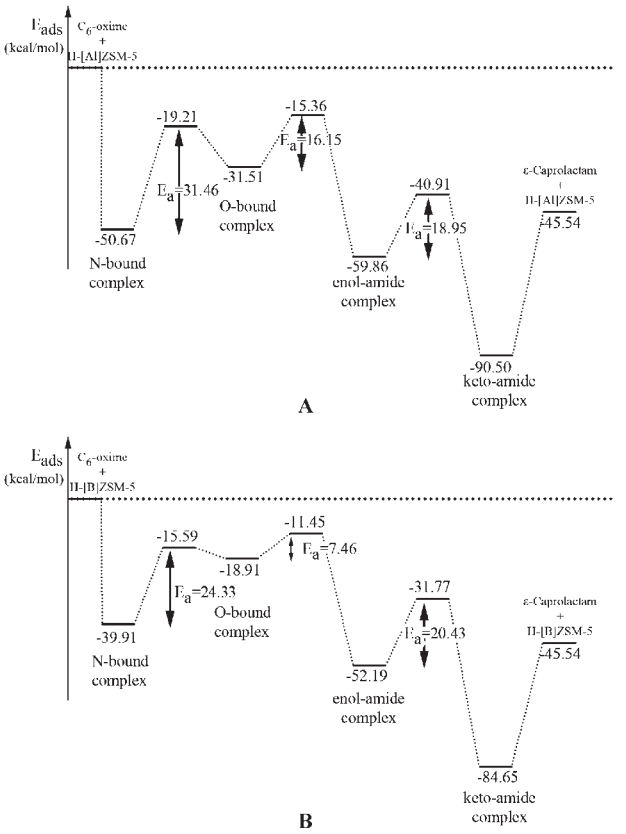


**Fig. 6** The energetic profile along the pathway of the Beckmann rearrangement of the cyclohexanone oxime molecule on zeolites at the embedded ONIOM2 scheme (MP2/6-311G(d,p):HF/6-31G(d)//B3LYP/6-31G(d,p):MNDO) level of theory: (a) H-[Al]-MFI zeolite, (b) H-[B]-MFI zeolite. The energetic changes for complexes are in kcal $mol^{-1}$.

obtained from the SCREEP method, it demonstrates that the electrostatic potential from the extended zeolite framework plays a dominant function in the reduction of the energy barrier. The reaction is initiated by the strong interaction of the N-ended cyclohexanone oxime on the acid sites of the zeolite. The N-ended adsorption complex is transformed to the O-ended adsorption complex *via* the 1,2 H-shift step. Subsequently, the ε-caprolactam is yielded rapidly *via* the rearrangement step and the tautomerization step, respectively. From the embedded ONIOM2 scheme, the rate determining step of the reaction is the 1,2 H-shift step which has an energy barrier of 31.46 and 24.33 kcal $mol^{-1}$ for the H-[Al]-MFI and the H-[B]-MFI zeolites, respectively (*cf*. Fig.6). Furthermore, we found that the protonation of the reaction product ε-caprolactam occurs in both zeolites H-[Al]-MFI and H-[B]-MFI. This leads to a strong adsorption on the catalyst surface. It should be noted that the catalyst deactivation might take place due to the irreversibly adsorbed ε-caprolactam molecule. One may expect that the addition of diluting solvents may play a crucial role in the desorption of the products from the zeolite micorpores, and, consequently, decrease the deactivation of the catalyst.

## Acknowledgements

This work was supported in part by grants from the Thailand Research Fund (to J.S. and J.L.) and the Science Research

Fund (ScRF) from the Faculty of Science, Kasetsart University (to J.S.) as well as the Commission of Higher Education, Ministry of Education under Postgraduate Education and Research Programs in Petroleum and Petrochemicals, and Advanced Materials. Support from the National Nanotechnology Center (NANOTEC Center of excellence and CNC) under the National Science and Technology Development Agency is also acknowledged.

## References


1 E. Beckmann, *Chem. Ber*., 1886, **19**, 988–993.
2 A. H. Blatt, *Chem. Rev*., 1933, **12**, 215–260.
3 B. Jones, *Chem. Rev*., 1944, **35**, 335–350.
4 H. E. Ungnade and D. A. McLaren, *J. Org. Chem*., 1945, **10**, 29–33.
5 D. E. Pearson and J. D. Bruton, *J. Org. Chem*., 1954, **19**, 957–963.
6 W. Z. Heldt, *J. Org. Chem*., 1961, **26**, 1695–1702.
7 H. Ichihashi and H. Sato, *Appl. Catal., A*, 2001, **221**, 359–366.
8 Y. Izumi, H. Ichihashi, Y. Shimazu, M. Kitamura and H. Sato, *Bull. Chem. Soc. Jpn*., 2007, **80**, 1280–1287.
9 H. Ichihashi, M. Ishida, A. Shiga, M. Kitamura, T. Suzuki, K. Suenobu and K. Sugita, *Catal. Surveys Asia*, 2003, **7**, 261–270.
10 C. Flego and L. Dalloro, *Microporous Mesoporous Mater*., 2003, **60**, 263–271.
11 G. P. Heitmann, G. Dahlhoff and W. F. Holderich, *J. Catal*., 1999, **186**, 12–19.
12 G. P. Heitmann, G. Dahlhoff, J. P. M. Niederer and W. F. Holderich, *J. Catal*., 2000, **194**, 122–129.
13 H. Ichihashi and M. Kitamura, *Catal. Today*, 2002, **73**, 23–28.
14 T. Takahashi, T. Kai and E. Nakao, *Appl. Catal., A*, 2004, **262**, 137–142.
15 P. O'Sullivan, L. Forni and B. K. Hodnett, *Ind. Eng. Chem. Res*., 2001, **40**, 1471–1475.
16 T. Takahashi, M. N. A. Nasution and T. Kai, *Appl. Catal., A*, 2001, **210**, 339–344.
17 L. Dai, K. Koyama, M. Miyamoto and T. Tatsumi, *Appl. Catal., A*, 1999, **189**, 237–242.
18 C. Ngamcharussrivichai, P. Wu and T. Tatsumi, *Chem. Lett*., 2004, **33**, 1288–1289.
19 C. Ngamcharussrivichai, P. Wu and T. Tatsumi, *Appl. Catal., A*, 2005, **288**, 158–168.
20 L.-X. Dai, Y. Iwaki, K. Koyama and T. Tatsumi, *Appl. Surf. Sci*., 1997, **121/122**, 335–338.
21 G. P. Heitmann, G. Dahlhoff and W. F. Holderich, *Appl. Catal., A*, 1999, **185**, 99–108.
22 Y.-M. Chung and H.-K. Rhee, *J. Mol. Catal. A: Chem*., 2000, **159**, 389–396.
23 Y. M. Chung and H. K. Rhee, *J. Mol. Catal. A: Chem*., 2001, **175**, 249–257.
24 Y. Zhang, Y. Wang and Y. Bu, *Microporous Mesoporous Mater*., 2008, **107**, 247–251.
25 P. Botella, A. Corma, S. Iborra, R. Monton, I. Rodriguez and V. Costa, *J. Catal*., 2007, **250**, 161–170.
26 J. Sirijaraensre, T. N. Truong and J. Limtrakul, *J. Phys. Chem. B*, 2005, **109**, 12099–12106.
27 J. Sirijaraensre and J. Limtrakul, *ChemPhysChem*, 2006, **7**, 2424–2432.
28 T. Bucko, J. Hafner and L. Benco, *J. Phys. Chem. A*, 2004, **108**, 11388–11397.
29 C. Ngamcharussrivichai, P. Wu and T. Tatsumi, *J. Catal*., 2005, **235**, 139–149.
30 A. Fernandez, A. Marinas, T. Blasco, V. Fornes and A. Corma, *J. Catal*., 2006, **243**, 270–277.
31 M. A. Camblor, A. Corma, H. Garcia, V. Semmer-Herledan and S. Valencia, *J. Catal*., 1998, **177**, 267–272.
32 B. Bonelli, L. Forni, A. Aloise, J. B. Nagy, G. Fornasari, E. Garrone, A. Gedeon, G. Giordano and F. Trifiro, *Microporous Mesoporous Mater*., 2007, **101**, 153–160.
33 L. Forni, E. Patriarchi, G. Fornasari, F. Trifiro, A. Katovic, G. Giordano and B. Nagy, *Stud. Surf. Sci. Catal*., 2005, **155**, 281–290.
34 V. R. R. Marthala, Y. Jiang, J. Huang, W. Wang, R. Glaeser and M. Hunger, *J. Am. Chem. Soc*., 2006, **128**, 14812–14813.
35 G. A. Fois, G. Ricchiardi, S. Bordiga, C. Busco, L. Dalloro, G. Spano and A. Zecchina, *Stud. Surf. Sci. Catal*., 2001, **135**, 2477–2484.
36 A. B. Fernandez, M. Boronat, T. Blasco and A. Corma, *Angew. Chem., Int. Ed*., 2005, **44**, 2370–2373.
37 A. B. Fernandez, I. Lezcano-Gonzalez, M. Boronat, T. Blasco and A. Corma, *J. Catal*., 2007, **249**, 116–119.
38 J. M. Vollmer, E. V. Stefanovich and T. N. Truong, *J. Phys. Chem. B*, 1999, **103**, 9415–9422.
39 I. H. Hillier, *THEOCHEM*, 1999, **463**, 45–52.
40 E. V. Stefanovich and T. N. Truong, *J. Phys. Chem. B*, 1998, **102**, 3018–3022.
41 J. Limtrakul, S. Jungsuttiwong and P. Khongpracha, *J. Mol. Struct*., 2000, **525**, 153–162.
42 J. Limtrakul, P. Khongpracha, S. Jungsuttiwong and T. N. Truong, *J. Mol. Catal. A: Chem*., 2000, **153**, 155–163.
43 J. Limtrakul, T. Nanok, S. Jungsuttiwong, P. Khongpracha and T. N. Truong, *Chem. Phys. Lett*., 2001, **349**, 161–166.
44 J. Limtrakul, S. Nokbin, P. Chuichay, P. Khongpracha, S. Jungsuttiwong and T. N. Truong, *Stud. Surf. Sci. Catal*., 2001, **135**, 2469–2476.
45 P. Treesukol, K. Srisuk, J. Limtrakul and T. N. Truong, *J. Phys. Chem. B*, 2005, **109**, 11940–11945.
46 S. Jungsuttiwong, J. Limtrakul and T. N. Truong, *J. Phys. Chem. B*, 2005, **109**, 13342–13351.
47 M. Sierka and J. Sauer, *J. Phys. Chem. B*, 2001, **105**, 1603–1613.
48 M. E. Franke, M. Sierka, U. Simon and J. Sauer, *Phys. Chem. Chem. Phys*., 2002, **4**, 5207–5216.
49 O. Bludsky, M. Silhan, P. Nachtigall, T. Bucko, L. Benco and J. Hafner, *J. Phys. Chem. B*, 2005, **109**, 9631–9638.
50 K. Bobuatong and J. Limtrakul, *Appl.Catal., A*, 2003, **253**, 49–64.
51 S. Kasuriya, S. Namuangruk, P. Treesukol, M. Tirtowidjojo and J. Limtrakul, *J. Catal*., 2003, **219**, 320–328.
52 S. Namuangruk, P. Pantu and J. Limtrakul, *J. Catal*., 2004, **225**, 523–530.
53 S. Pabchanda, P. Pantu and J. Limtrakul, *J. Mol. Catal. A: Chem*., 2005, **239**, 103–110.
54 W. Panjan and J. Limtrakul, *J. Mol. Struct*., 2003, **654**, 35–45.
55 P. Pantu, S. Pabchanda and J. Limtrakul, *ChemPhysChem*, 2004, **5**, 1901–1906.
56 C. Raksakoon and J. Limtrakul, *THEOCHEM*, 2003, **631**, 147–156.
57 R. Rungsirisakun, B. Jansang, P. Pantu and J. Limtrakul, *J. Mol. Struct*., 2004, **733**, 239–246.
58 W. Sangthong, M. Probst and J. Limtrakul, *J. Mol. Struct*., 2005, **748**, 119–127.
59 X. Solans-Monfort, M. Sodupe, V. Branchadell, J. Sauer, R. Orlando and P. Ugliengo, *J. Phys. Chem. B*, 2005, **109**, 3539–3545.
60 P. Pantu, B. Boekfa, B. Sunpetch and J. Limtrakul, *Chem. Eng. Commun*., 2008, **195**, 1477–1485.
61 B. Jansang, T. Nanok and J. Limtrakul, *J. Phys. Chem. C*, 2008, **112**, 540–547.
62 W. Panyaburapa, T. Nanok and J. Limtrakul, *J. Phys. Chem. C*, 2007, **111**, 3433–3441.
63 P. Pantu, B. Boekfa and J. Limtrakul, *J. Mol. Catal. A: Chem*., 2007, **277**, 171–179.
64 J. Lomratsiri, M. Probst and J. Limtrakul, *J. Mol. Graphics Modell*., 2006, **25**, 219–225.
65 B. Jansang, T. Nanok and J. Limtrakul, *J. Mol. Catal. A: Chem*., 2007, **264**, 33–39.
66 N. Injan, N. Pannorad, M. Probst and J. Limtrakul, *Int. J. Quantum Chem*., 2005, **105**, 898–905.
67 B. Jansang, T. Nanok and J. Limtrakul, *J. Phys. Chem. B*, 2006, **110**, 12626–12631.
68 M. J. Frisch, G. W. Trucks, H. B. Schlegel, G. E. Scuseria, M. A. Robb, J. R. Cheeseman, J. J. A. Montgomery, T. Vreven, K. N. Kudin, J. C. Burant, J. M. Millam, S. S. Iyengar, J. Tomasi, V. Barone, B. Mennucci, M. Cossi, G. Scalmani, N. Rega, G. A. Petersson, H. Nakatsuji, M. Hada, M. Ehara, K. Toyota, R. Fukuda, J. Hasegawa, M. Ishida, T. Nakajima, Y. Honda, O. Kitao, H. Nakai, M. Klene, X. Li, J. E. Knox, H. P. Hratchian,


 

J. B. Cross, V. Bakken, C. Adamo, J. Jaramillo, R. Gomperts, R. E. Stratmann, O. Yazyev, A. J. Austin, R. Cammi, C. Pomelli, J. W. Ochterski, P. Y. Ayala, K. Morokuma, G. A. Voth, P. Salvador, J. J. Dannenberg, V. G. Zakrzewski, S. Dapprich, A. D. Daniels, M. C. Strain, O. Farkas, D. K. Malick, A. D. Rabuck, K. Raghavachari, J. B. Foresman, J. V. Ortiz, Q. Cui, A. G. Baboul, S. Clifford, J. Cioslowski, B. B. Stefanov, G. Liu, A. Liashenko, P. Piskorz, I. Komaromi, R. L. Martin, D. J. Fox, T. Keith, M. A. Al-Laham, C. Y. Peng, A. Nanayakkara, M. Challacombe, P. M. W. Gill, B. Johnson, W. Chen, M. W. Wong, C. Gonzalez and J. A. Pople, *GAUSSIAN 03*, Gaussian, Inc., Wallingford CT, 2004.

69 L. Regli, S. Bordiga, C. Lamberti, K. P. Lillerud, S. I. Zones and A. Zecchina, *J. Phys. Chem. C*, 2007, **111**, 2992–2999.

70 Y. Wang, D. Zhou, G. Yang, S. Miao, X. Liu and X. Bao, *J. Phys. Chem. A*, 2004, **108**, 6730–6734.

71 S. P. Yuan, J. G. Wang, Y. W. Li and H. Jiao, *THEOCHEM*, 2004, **674**, 267–274.

72 S. P. Yuan, J. G. Wang, Y. W. Li and H. Jiao, *J. Phys. Chem. A*, 2002, **106**, 8167–8172.

73 R. C. Deka, N. Tajima and K. Hirao, *THEOCHEM*, 2001, **535**, 31–38.

74 H. Berndt, A. Martin, H. Kosslick and B. Luecke, *Microporous Mater.*, 1994, **2**, 197–204.

# Reaction Mechanisms of the Methylation of Ethene with Methanol and Dimethyl Ether over H-ZSM-5: An ONIOM Study

**T. Maihom,[†,‡] B. Boekfa,[†,‡] J. Sirijaraensre,[†,‡] T. Nanok,[†,‡] M. Probst,[§] and J. Limtrakul*[,†,‡]**

*Laboratory for Computational and Applied Chemistry, Department of Chemistry, Faculty of Science and Center of Nanotechnology, Kasetsart University Research and Development Institute, and NANOTEC Center of Excellence, National Nanotechnology Center, Kasetsart University, Bangkok 10900, Thailand, and Institute of Ion Physics and Applied Physics, University of Innsbruck, A-6020 Innsbruck, Austria*

*Received: November 2, 2008; Revised Manuscript Received: February 16, 2009*

The mechanisms of ethene methylation with methanol and dimethyl ether have been investigated using a 128T cluster of ZSM-5 zeolite modeled by ONIOM(B3LYP/6-31G(d,p):UFF) and ONIOM(M06-2X/6-311+G(2df,2p):UFF) calculations. The effects of the infinite zeolitic framework on the model of the zeolite nanopocket, which consisted of a quantum cluster of 34 tetrahedral units and of 128 tetrahedral units modeled on the UFF level, were also included. The zeolitic Madelung potential was reproduced by a set of point charges generated by the SCREEP method. The energies for the adsorption of methanol and dimethyl ether on H-ZSM-5 from an ONIOM2(M06-2X/6-311+G(2df,2p):UFF)+SCREEP calculation are −26.3 and −29.4 kcal/mol, respectively, which are in good agreement with the experimental data. Dissociative and associative mechanisms of the ethene methylation by methanol and dimethyl ether have been considered. For the dissociative mechanism, the methylation reaction of ethene starts with the protonation of methanol or dimethyl ether by the acidic zeolite proton to form a surface methoxide intermediate, which subsequently reacts with an ethene molecule forming a propoxide intermediate. The propoxide intermediate is then deprotonated to form the propene product. The activation energies for the first step are computed to be 41.2 and 42.9 kcal/mol for methanol and dimethyl ether, respectively. The activation energies for the subsequent second and third reaction steps are 21.4 and 26.5 kcal/mol, respectively. For the associative mechanism, protonation and methylation take place simultaneously without formation of a surface methoxide. The calculated activation barriers are 29.0 and 33.0 kcal/mol for methanol and dimethyl ether, respectively, suggesting that methanol should be slightly more reactive than dimethyl ether for the methylation of ethene. The final step in the associative mechanism, the deprotonation of the propoxide intermediate to give the adsorbed propene product, has an activation energy of 25.4 kcal/mol. The results indicate that the associative pathway is favored over the dissociative one and that the rate-determining step of this reaction is the ethene methylation step.



## 1. Introduction

Methylation is one of a number of reactions that increase the number of C atoms in a hydrocarbon chain. Methyl halides ($CH_3I$, $CH_3Br$, and $CH_3Cl$), dimethyl ether, and methanol are important conventional methylating agents. Among these, methanol is the one used most frequently in the petrochemical industry. It is supplied as a feedstock in the conversion process of methanol to hydrocarbons (MTH),[1,2] an industrial process making use of heterogeneous catalysis invented by Chang and Silvestri[3] in 1977. Presently, the MTH technology is the most interesting process besides the transformation of natural gas or coal into olefins or gasoline because the synthesis gas (CO and $H_2$) generated from the transformation processes of natural gas or coal can be reused in the synthesis of methanol.

The mechanistic aspects of the MTH process have been reported in many publications.[2,4−15] More than 20 different mechanisms have been suggested. However, during the past decade, the conversion mechanism of methanol to hydrocarbons over acidic zeolites through "the hydrocarbon pool mechanism" has been verified as the dominating route. This mechanism was originally proposed by Dahl and Kolboe.[16−18] The reaction proceeds via repeated methylations and dealkylations of carbonaceous compounds. Light alkenes are formed from these compounds via an elimination process. It is observed that the initial C−C bond formation leading to the formation of organic compounds is one of the important steps in the hydrocarbon pool mechanism. Therefore, this work studies the C−C bond formation between methanol and ethene, which is one of the hydrocarbon pool species.

Experimental and theoretical efforts have been carried out to gain an understanding of the methylation reaction of small olefins with methanol over the zeolite catalysts. Experimental studies[19−23] found that the methoxide intermediate can be observed inside the cavity of zeolites during the conversion of methanol. This species is generated from methanol dissociation on the acid site of zeolites. The surface methoxide intermediate is able to act as a reactive species for the C−C bond formation in the hydrocarbon-pool mechanism and could thus react directly with alkanes, alkenes, and aromatics molecules.[14,19−23] However, some studies[14,24−26] indicated that the coadsorption of methanol (end-on adsorption) and the alkene molecule on the acid site of zeolite is responsible for the methylation. Recently, Svelle et al.[10,11] have studied the methylation of ethene, propene, and

* Corresponding author. Tel.: +66-2-562-5555 ext 2159. E-mail: jumras.l@ku.ac.th.
[†] Department of Chemistry, Kasetsart University.
[‡] National Nanotechnology Center, Kasetsart University.
[§] University of Innsbruck.

10.1021/jp809746a CCC: $40.75 
Published on Web 03/31/2009

*n*-butylene with methanol on acidic ZSM-5 by means of an isotopic label technique. They found that the intrinsic activation energies for the methylation of ethene, propene, and *n*-butene are 32.3, 26.3, and 21.5 kcal/mol, respectively. In theoretical studies,[4,9,27−31] it was shown that the methylation reaction proceeds via either a stepwise or a concerted mechanism. In the stepwise mechanism, the intermediates are consecutively generated along the reaction path. The formation of methoxide species is the first step of the reaction, followed by the methylation of alkenes and arenes. In the concerted mechanism, the methylation takes place in a single step. The C−O bond dissociation of methanol occurs simultaneously with the C−C bond formation without the formation of an intermediate. Vos et al.[31] have studied the methylation of benzene and toluene theoretically using a 4T quantum cluster model of H-ZSM-5 at the B3LYP/6-31G(d,p) level of theory. They found that the reaction occurs preferably via the concerted mechanism rather than via the stepwise mechanism. However, the stepwise pathway was found to be entropically favored over the concerted mechanism because only one molecule is required to interact with the active site. In other works, the methylation of some alkenes and arenes with methanol and dimethylether was investigated by a quantum chemical cluster model at the MP2/6-311G(d)//B3LYP/6-31G(d) level of theory via the concerted pathway only.[9,30] However, in these works, the acidic zeolite lattice was represented by an unconstrained 4T cluster model, and therefore the short- and long-range effects of the zeolite framework were neglected. Previously, it had been found[32−34] that the long-range effect of the zeolite framework must be taken into account for accurate results.[35] To account for the effects of the zeolite framework, various techniques such as periodic ab initio calculations and quantum mechanics/molecular mechanics (QM/MM) hybrid methods have been widely used. The former approach is computationally too expensive and impractical for studying the large unit cell zeolites. The recent development of QM/MM hybrid methods, such as the embedded cluster methods,[36−41] QM/MM methods with coupling Hamiltonians,[32,42−44] as well as the ONIOM methods,[45−57] were employed to keep the calculations feasible. These methods can properly describe the effect of the zeolite framework. Especially, the ONIOM method has been used successfully to investigate the adsorption of hydrocarbons such as ethene, benzene, and ethylbenzene[45−47] and the reactions of organic molecules over zeolites.[48−54]

In the present study, the ONIOM2 method was employed for investigating the formation of propene via the methylation of ethene with methanol and dimethyl ether over H-ZSM-5 zeolite. This reaction can, in principle, proceed via a dissociative (stepwise) or an associative (concerted) mechanism, and both mechanisms are considered. We have investigated the effects of the zeolite framework on the energetic profiles of both the dissociative and the associative routes. Dimethyl ether was chosen as a reactant in this work because it can be generated easily by the reversible condensation of two methanol molecules.

## 2. Models and Methods

The crystal lattice of the acidic ZSM-5 zeolite is represented by a 128T (127 tetrahedral atoms of Si and 1 tetrahedral atom of Al) cluster model, which covers the intersection of the straight and zigzag channels, as shown in Figure 1a. One silicon atom at the T12 site is replaced with an aluminum atom to generate the Brønsted acid site. For computational efficiency, the 128T cluster model is subdivided into two layers according to the ONIOM2 scheme. The inner layer comprises 12T atoms and is considered as the active region and is treated at the B3LYP/6-31G(d,p) level of theory. The outer layer, which is the rest of the 128T cluster, is treated with a computationally less expensive method, the universal force field (UFF) to represent the confinement effect[58−60] of the zeolite pore structure. This force field has been reported to give a good description of the short-range van der Waals interactions. During geometry optimizations, only the 5T cluster of the active region, [(≡SiO)$_3$Al(OH)Si≡], and the adsorbing molecules are relaxed. The frequency calculations are performed at the same level of theory to ensure that transition state structure has only one imaginary frequency that corresponds to the desired reaction coordinate. We have made attempts to cover the dispersion interaction in the zeolite system. Some test calculations on adsorbing molecules (methanol and dimethyl ether) over the Brønsted acid site of MFI zeolite have been performed using MP2 and the newly developed density functional, M06-2X,[61−64] which we expected to be able to reproduce adsorption on zeolites. Single-point calculations with M06-2X and MP2 at B3LYP-optimized complex geometries yield very similar results (27.7 vs 29.8 kcal/mol for adsorption energies of dimethyl ether and 25.2 vs 26.5 for methanol complexes; see Table S1 of the Supporting Information). This indicates that the M06-2X functional can indeed recover the dispersion interaction in these zeolite systems as reliably as the MP2 method with the benefit of feasible computational costs. To cover both the active Brønsted acid site and the nanopocket surrounding the reactive center, 34T QM clusters were employed in the ONIOM scheme: 34T/128T (see Figure 1b and c).

To include the electrostatic effect of the infinite zeolitic framework, the zeolite nanopockets were embedded in a set of point charges, generated by the SCREEP method, that reproduce the zeolitic Madelung potential. A detailed description of the method to optimized magnitude and positions of the point charges that accurately reproduce the electrostatic effect of the infinite lattice has been given previously.[65,66] This embedded scheme (see Figure 1d) has been successfully used in our previous studies on unsaturated hydrocarbons adsorption[54,57,67] and on the mechanisms of the Beckmann rearrangement over H-MFI zeolites.[68] With 34T/128T single point calculation using the ONIOM2(M06-2X/6-311+G(2df,2p):UFF)+SCREEP combination, the adsorption energies of methanol and dimethyl ether over the H-ZSM-5 zeolite were computed to be −26.3 and −29.4 kcal/mol, respectively, in good agreement with the experimental data.[69] While the adsorption energy of methanol is insensitive to the size of the QM region, the confinement effects from the zeolite framework significantly affect the adsorption energy of dimethyl ether. This is due mainly to the size of the adsorbing molecule inside the nanocavity of zeolite. Hence, ONIOM2(M06-2X/6-311+G(2df,2p):UFF) seems to be well suited to investigate adsorption properties and reaction mechanisms of the methylation of ethene with methanol and dimethyl ether over H-ZSM-5. All calculations were performed using the Gaussian 03 code.[70]

## 3. Results and Discussion

The catalytic methylation of ethene with methanol and dimethyl ether over H-ZSM-5 was systematically investigated, and the results were compared to experimentally established facts whenever possible.[10] Two previously proposed mechanisms, dissociative and associative, were theoretically investigated within the model described above. The side-on structure, the weak adsorption mode (cf., Figure 2b), was taken as the starting geometry for the dissociative mechanism, while the end-

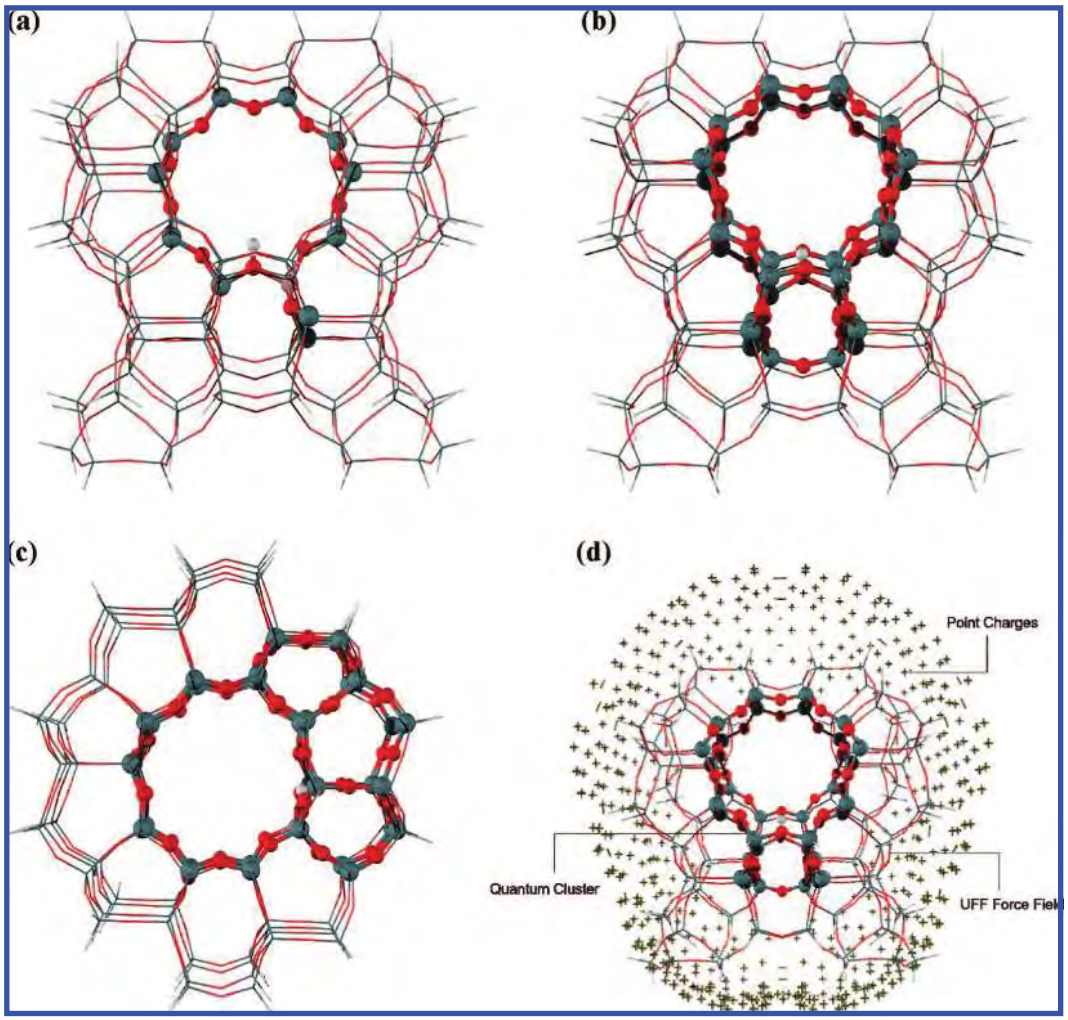


**Figure 1.** ONIOM2 model of the 128T cluster from H-ZSM-5 zeolite. Atoms belonging to the quantum region in the ONIOM2 scheme are drawn as bond and stick models: (a) 12T/128T ONIOM model, (b) sinusoidal channel view, and (c) straight channel view of 34T/128T ONIOM model and (d) SCREEP embedded model.



on structure, the strong adsorption mode (cf., Figure 2a), was used to describe the initial step of the associative mechanism.

**3.1. Structures and Energetics of Methanol and Dimethyl Ether Adsorption.** The optimized adsorption structures of methanol on the Brønsted acid site of H-ZSM-5 are shown in Figure 2a and b. It can be seen that methanol is adsorbed on the acid site by either the end-on (Ads1_M_S) or the side-on (Ads2_M_S) hydrogen-bond complex structure, in agreement with the theoretical studies mentioned above.[4,31,53,71−74] In the side-on structure, there is only one strong hydrogen bond between the OH group of methanol and the OH group of zeolite, whereas in the end-on geometry methanol is stabilized by two strong hydrogen bonds. The adsorption energies, for the side-on and end-on structures, are calculated to be 24.2 and 26.3 kcal/mol, respectively, which are consistent with the experimental observation that methanol adsorbed by the side-on structure is weaker than that by the end-on structure.[14] The later estimated adsorption energy is in good agreement with the reported experimental adsorption heat of end-on adsorption of methanol in H-ZSM-5 of 27.5 ± 1 kcal/mol.[69] The acidic O−H bond of zeolite is stretched upon adsorption of methanol by 0.07 and 0.10 Å for the weak and strong adsorption modes, respectively (O···H−O intermolecular distance: 2.53 and 2.48 Å). The O−H bond of methanol is virtually unaffected by the adsorption. It is stretched from the isolated gas phase by 0.01 and 0.02 Å, for side-on and end-on adsorption, respectively.

Figure 2c shows the adsorption structure of dimethyl ether (Ads_D_S) on the Brønsted acid site of H-ZSM-5, which resembles the end-on adsorption structure of methanol. Two methyl groups are weakly bound to the zeolite oxygen framework. No stable side-on structure could be obtained from the ONIOM2(12T/128T) scheme. The end-on adsorption energy is calculated to be −29.4 kcal/mol. The interatomic distance between the oxygen atom of dimethyl ether and the acidic hydrogen atom of zeolite (O3···H1 = 1.51 Å) is longer than that of the corresponding O3···H1 distances in the methanol case (1.49 and 1.41 Å for side-on and end-on structures, respectively), and, consequently, also the elongation of the zeolite O−H bond (1.03 Å) is less. These overall consistent results make it likely that the structures from the 12T/128T ONIOM2(B3LYP/6-31G(d,p)//UFF) model with the single point calculation at the 34T/128T embedded-ONIOM2(M06-2X/6-311+G(2df,2p)//UFF) model constitute a suitable QM/MM hybrid method for studying the adsorption of small polar molecules in zeolites, to be used to study ethene methylation, as discussed in the following sections.

**3.2. Reaction and Mechanism of Ethene Methylation with Methanol and Dimethyl Ether.** Experimental reports seem to indicate that the methylation of toluene by methanol and dimethyl ether that are adsorbed side-on onto the Brønsted acid site of zeolite takes place through the dissociative mechanism, while the methylation of end-on adsorbed molecules proceeds

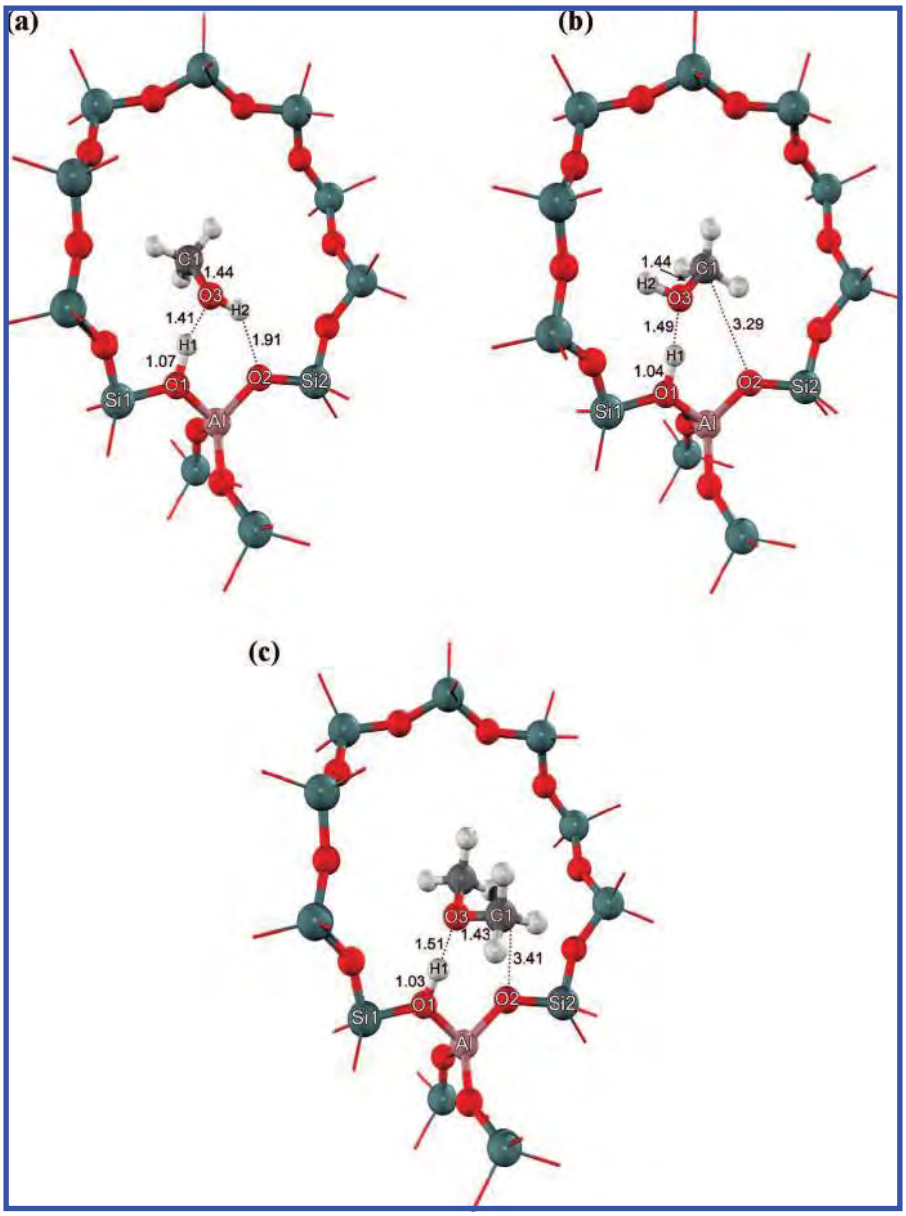


**Figure 2.** Optimized geometries of the adsorption complexes on 12T/128T ONIOM model: (a) end-on methanol adsorption, (b) side-on methanol adsorption, and (c) dimethyl ether adsorption.

through the associative mechanism.[14] In the dissociative mechanism, the surface methoxide species is generated as the key intermediate prior to the methylation process. This species was found to react with water and methanol at room temperature.[19−23] However, in the absence of other species, it remains stable up to a temperature of 523 K.[19−23]

***3.2.1. Dissociative Reaction Pathway.*** *3.2.1.1. Surface Methoxide Intermediate Formation.* The surface methoxide intermediate formed by methanol is illustrated in Figure 3a, and selected geometrical parameters are listed in Table S2 (Supporting Information). This reaction is initiated by the adsorption of methanol on the active acidic site of ZSM-5 through the formation of a strong hydrogen bond between the alcoholic oxygen atom of methanol and the OH group of zeolite ("side-on" adsorption complex, Ads2_M_S). Here, its adsorption energy is −24.2 kcal/mol. The O1−H1 bond of ZSM-5 is lengthened from 0.97 to 1.04 Å. In the methanol molecule, the C1−O3 length increases by 0.02 Å because it is weakened by the hydrogen-bond formation and the subsequent electron transfer from O3 to H1.

The H-bonded adsorption complex reacts to form the surface methoxide intermediate via the transition state TS1_M_S shown in Figure 2c. In this transition state, the Brønsted proton H1 is transferred to the methanol oxygen atom O, and the C−O bond of methanol is cleaved leading to the formation of a water molecule. The leaving methyl group is stabilized by the bridging oxygen O2 of the zeolite. This results in an elongation of the C1−O3 bond distance from 1.44 to 1.94 Å. The C1···O2 distance is reduced to 2.16 Å, while the O2−C1−O3 angle stays nearly linear (171°). The activation energy for this transition state is 41.2 kcal/mol, considerably lower than what has been reported for the bare cluster models (51−54 kcal/mol).[4,71,75−77] This shows that the transition state is stabilized by the confinement effect of the zeolitic framework. Relative to the methanol end-on adsorption complex, the transition state is 43.2 kcal/mol higher in energy.

TS1_M_S proceeds then by the formation of a covalent C1−O2 bond (bond length 1.50 Å) to the surface methoxide product (Int1_M_S). In it, the Si−O2 and Al−O2 bonds are shortened by 0.08 and 0.13 Å, respectively, as are the Si1−O1

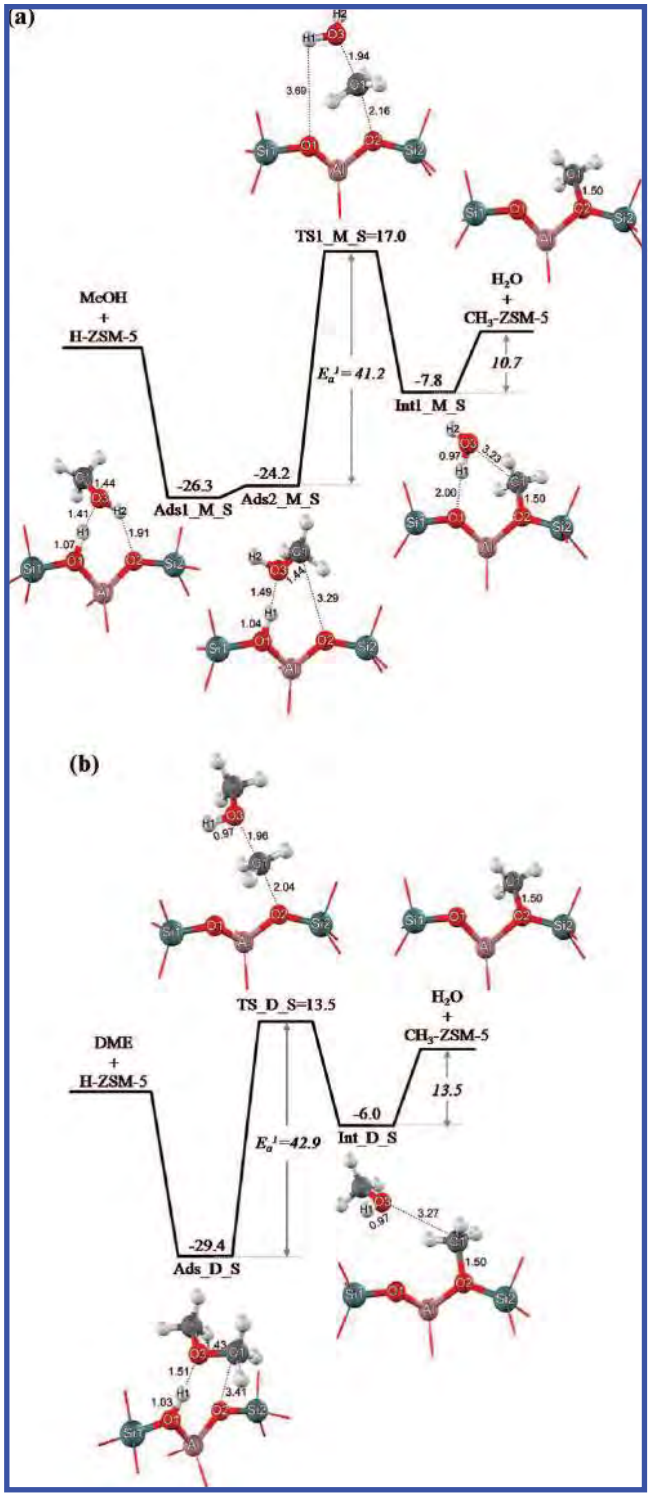


**Figure 3.** Energy profiles for the surface methoxide intermediate formation step of the dissociative mechanism for the embedded 34T/128T cluster calculated with the ONIOM2(M06-2X/6-311+G(2df,2p):UFF) model: (a) methanol protonation and (b) dimethyl ether protonation (energies in kcal/mol).

and Al−O1 bonds (0.06 and 0.13 Å, respectively). The Al−O1−Si1 angle decreases by 4.6°. The adsorption energy of the methoxide−water complex with respect to the isolated reactants is −7.8 kcal/mol, significantly less than the adsorption energy of methanol. The fact that the covalent bond between the methoxide intermediate and the zeolite is weak is also in agreement with experiments[19] and has been related to the steric forces of the zeolite pore walls in previous studies.[78−81] It is an active, unstable species that can easily interact with incoming molecules such as ethene.

If we consider now the corresponding surface methoxide formation from dimethyl ether, the reaction starts with the adsorption of dimethyl ether on the Brønsted acid active site of ZSM-5 zeolite, as the end-on adsorption complex. The energy profile for this reaction is shown in Figure 3b, and selected geometrical parameters are listed in Table S3 (Supporting Information). The dimethyl ether adsorbs on the acidic site through the hydrogen-bonding interaction between its oxygen and H1. The H1−O1 distance, therefore, increases from 0.97 to 1.03 Å (Ads_D_S). Similar to the methanol case, electron density is transferred from the O3 to the H1 atom, and C1−O3 is slightly lengthened by 0.02 Å. The adsorption energy of this complex is −29.4 kcal/mol. Next, the C1−O3 bond of the adsorbed dimethyl ether is cleaved and the H1−O3 bond is formed. Again, the surface methoxide species and a methanol molecule are generated on the zeolite framework. In the transition state TS_D_S, the proton (H1) is transferred to the oxygen of dimethyl ether to form the leaving methanol molecule. Its oxygen atom O3, C1, and the surface oxygen atom, O2, are aligned in a linear way (173.4° for the O3−C1−O2 bond angle). The breaking C1−O3 bond is elongated from 1.43 to 1.96 Å, and the C1···O2 distance decreases to 1.37 Å. The activation energy for the protonation step is 42.9 kcal/mol, which is close to the one for the methanol protonation reported above. The surface C1−O2 distance in the surface methoxide species is 1.50 Å (Int_D_S). Again, the calculated adsorption energy of the methoxide−methanol complex calculated is quite small, −6.0 kcal/mol, even less than for methanol. We can summarize that the reaction of dimethyl ether proceeds in the same way as for methanol and also that the energetics are similar.

*3.2.1.2. Methylation and Deprotonation Reaction Step.* Subsequently, the surface methoxide species in the zeolite pore structure acts as a methylating agent. It is assumed that an ethene molecule diffuses into the zeolite pore and adsorbs on the reactive methoxide intermediate, enabling the formation of an ethene−methoxide coadsorption complex (Ads3_M_S). The calculated energy profile of this part of the overall reaction is shown in Figure 4; geometric parameters are listed in Table S4 (Supporting Information). Ethene and the methoxide coadsorption complex are interacting only weakly (−10.5 kcal/mol) in this coadsorption complex. Next, the reaction proceeds via the transition state TS2_M_S that involves the concerted bond breaking of the C1−O2 bond and the formation of the C1−C2 bond. The C1−O2 distance increases from 1.50 to 2.19 Å. The length of the newly formed C1−C2 bond in Ads3_M_S is 2.23 Å, and the C2−C3 bond distance is slightly increased by 0.02 Å. The activation energy is 21.4 kcal/mol. The small primary carbocation $CH_3CH_2CH_2^+$, which is produced by the methylation of ethene, has the opportunity to stay in the zeolite nanocavity. However, theoretical studies indicate that carbocation intermediates formed by catalytic processes in zeolite are short-lived when the positive charge of the carbon atom can be approached by atoms of the framework.[82]

The propoxide intermediate produced for methylation of ethene by the methyl group is formed with a covalent bond to the O1 oxygen bridging atom of the zeolite framework (Int2_M_S). The C3−O1 bond length is 1.54 Å. The C1−C2 and C2−C3 bond distances of 1.53 and 1.52 Å, respectively, are typical for C−C single bonds. The adsorption energy of the propoxide intermediate is −36.8 kcal/mol. In the last step, the propene product is formed via the deprotonation transition state (TS3_M_S) in which the breaking of the C3−O1 bond

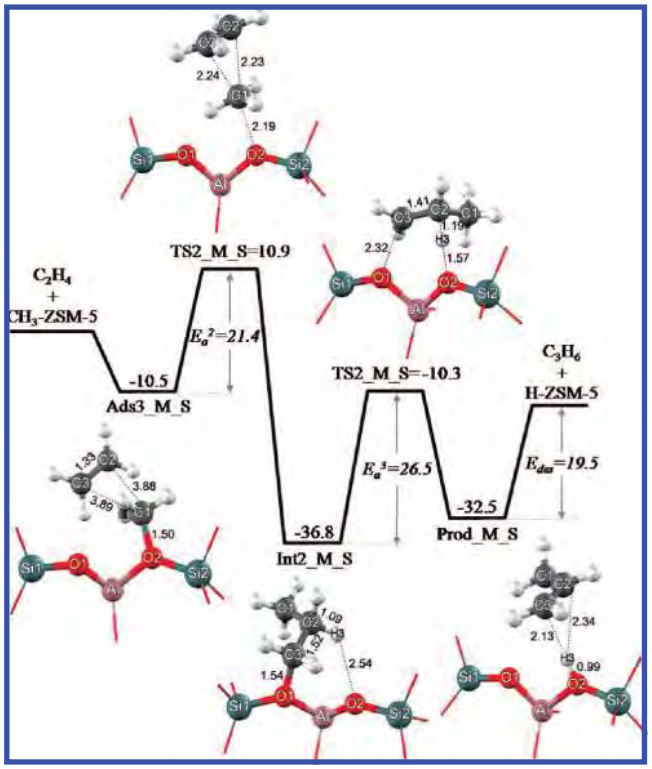


**Figure 4.** Energy profiles for the ethene methylation and deprotonation reaction step of the dissociative mechanism for the embedded 34T/128T cluster calculated with the ONIOM2(M06-2X/6-311+G(2df,2p):UFF model (energies in kcal/mol).

and the H3 proton transfer from propoxide to the oxygen bridging atom of zeolite begin. This transition state is very similar to the carbenium−ion complex. The C3−O1 and C2−H3 bond distances are elongated by 0.78 and 0.10 Å, respectively, while the O2···H3 distance decreases to 1.57 Å. The predicted activation energy of this step of 26.5 kcal/mol is again lower than the one obtained with a small 10T cluster model (33.4 kcal/mol)[83] due to the effects of the zeolite framework. After the back-migration of the proton to the zeolite framework, the propene product is formed (Prod_M_S). It is adsorbed on the acidic site of the zeolite through a $\pi$-bond interaction with an adsorption energy of −32.5 kcal/mol. Finally, the propene product is desorbed. This endothermic step requires 19.5 kcal/mol.

***3.2.2. Associative Reaction Pathway.*** An associative reaction mechanism is an alternative for the ethene methylation with methanol or dimethyl ether. For the ethene methylation with methanol, the energy profile is shown in Figure 5a, and selected geometrical parameters are listed in Table S5 (Supporting Information). This reaction is also initialized by the coadsorption complex between methanol and ethene over the Brønsted acid site (Ads_M_C). Next, however, ethene is methylated directly by methanol without the formation of the methoxide intermediate. Methanol is adsorbed on the acidic proton in the end-on formation via two hydrogen bonds. The neighboring ethene molecule is adsorbed weakly. The O1−H1 distance increases from 0.97 to 1.08 Å upon absorption, and the C1−O3 bond distance increases by approximately 0.03 Å. The C1···C2 and C1···C3 intermolecular distances between the methanol and the ethene molecule are 3.99 and 4.05 Å, respectively. The coadsorption energy of the methanol and ethene on the acidic site of ZSM-5 zeolite with respect to isolated reactants is calculated to be −36.6 kcal/mol. In the transition state (TS1_M_C) of this step, methanol is protonated by the H1 of zeolite and

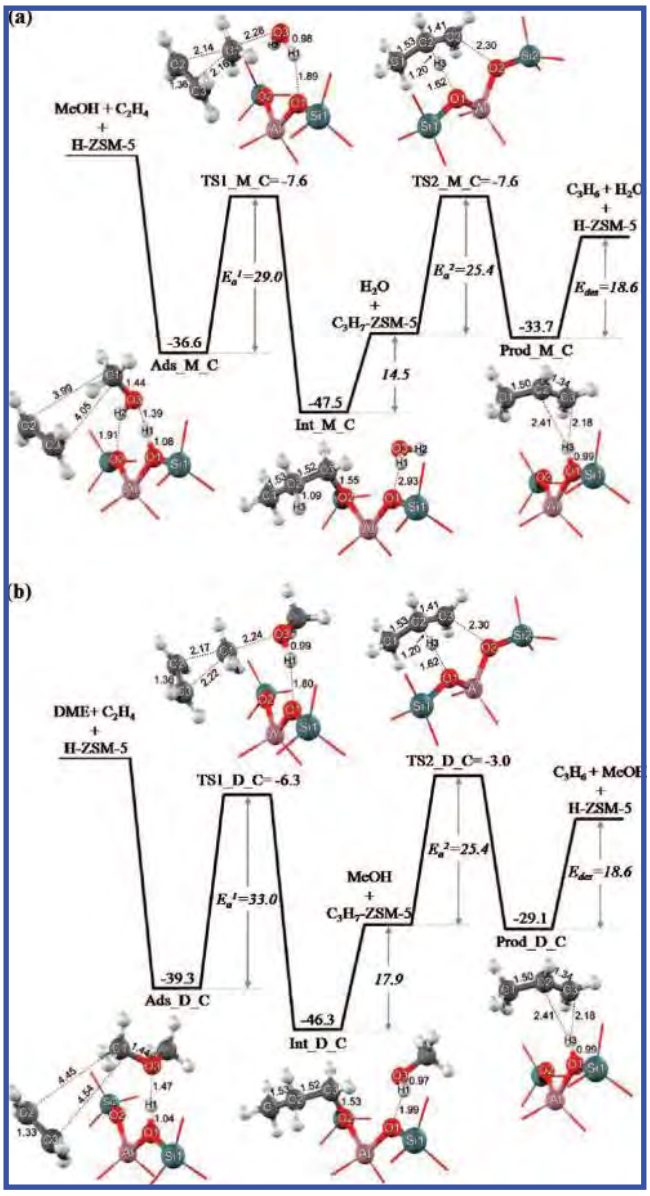


**Figure 5.** Energy profiles for the associative ethene methylation pathway. The calculations on the embedded 34T/128T cluster were performed with the ONIOM2(M06-2X/6-311+G(2df,2p):UFF) method: (a) methanol and (b) dimethyl ether (energies in kcal/mol).

simultaneously the C1−O3 bond is broken to give a methoxonium cation, which at the same time reacts with the C2 of ethene to form the primary alkoxide. As a result, the methanol C1−O3 bond is broken, while the C1···C2 and C1···C3 distances decrease (2.14 and 2.16 Å, respectively). The activation energy of this step is 29.0 kcal/mol, which compares well with the experimental results of Svell et al.[10] (approximately 32.3 kcal/mol). On the product side, the primary propoxide is formed with a neighboring water molecule adsorbed in the zeolite pore with the C3−O2 distance of 1.55 Å (Int_M_C). This propoxide−water complex is even more strongly adsorbed (−47.5 kcal/mol) than methanol at the beginning of the process. Finally, the desorbtion of the water molecule requires 14.5 kcal/mol.

The energy profile of the equivalent ethene methylation with dimethyl ether is shown in Figure 5b, and selected geometrical parameters are listed in Table S6 (Supporting Information). This reaction proceeds like the one with methanol discussed above. Ads_D_C shows the dimethyl ether−ethene coadsorption complex. In this complex, the O1−H1 bond length increases

slightly less (0.08 Å) than when interacting with methanol. The adsorption energy of this complex is −39.3 kcal/mol. Next, the adsorbed dimethyl ether is protonated at the O3 atom, and the free methyl group is transferred to react with the C2 of the ethene molecule leading to the formation of the propoxide intermediate (TS1_D_C). The H1−O1 bond and C1−O3 distances are elongated to 1.80 and 2.24 Å, respectively, and the O3···H1 distance is shortened to 0.99 Å. These and the other geometrical changes follow the trends found for methanol. The calculated activation energy of 33.0 kcal/mol is slightly higher than the activation energy of the methanol reaction (29.0 kcal/mol). After the transition state, TS1_D_C, the propoxide−methanol complex (Int_D_C) is formed with a C3−O2 bond length of 1.53 Å and an adsorption energy of −46.3 kcal/mol. Finally, desorption of the methanol molecule from propoxide requires 17.9 kcal/mol.

After the active primary propoxide is generated by eliminating water or methanol, the H3 proton connects to O1. This reaction to the final propene product is formed via the transition state TS2_M_C. In the reaction as well, the breaking of the C2−H3 and C3−O2 bonds starts by an increase of their lengths from 1.54 to 2.30 and 1.09 to 1.20 Å, respectively. The C2−C3 bond distance is shortened by 0.11 Å, reflecting its double bond character. The activation energy of this step is 25.4 kcal/mol. −33.7 and −29.1 kcal/mol are then gained by formation of the final product bound to the zeolite for ethene methylation with methanol and dimethyl ether, respectively. The desorption of the $\pi$-complexed product requires 18.6 kcal/mol.

## 4. Comparison of Dissociative and Associative Pathways

From the energetic profiles for the dissociative and associative reaction pathways of ethene methylation with methanol and dimethyl ether, it can be seen that the protonation of methanol and dimethyl ether to form the active methoxide intermediate is found to be the rate-determining step in the stepwise mechanism with activation energies of 41.2 and 42.9 kcal/mol, respectively. The methoxide intermediate is stabilized by the framework of zeolite that is active for the incoming molecule as ethene. Therefore, the methylation of ethene with the methoxide intermediate and the deprotonation step of the subsequent reaction are more facile than the methanol protonation step with lower activation energy barriers of 21.4 and 26.5 kcal/mol, respectively. However, considering the energy barrier for the ethene methylation reaction and for the hydrolysis reaction of the methoxide species, it is found that the hydrolysis reaction, reversing the methoxide complex to the methanol molecule, is kinetically and thermodynamically favored over the ethene methylation. Furthermore, the water molecule is more strongly adsorbed on the methoxide than is the ethene molecule. Therefore, an ethene molecule cannot easily be inserted into the methoxide active site. For the associative mechanism of ethene methylation with methanol or dimethyl ether, the simultaneous protonation and C−C bond formation reaction is regarded as the rate-determining step with activation energies of 29.0 and 33.0 kcal/mol, respectively. These results indicate that methanol is more reactive than dimethyl ether (DME) as a methylating agent in our system. This is in disagreement with a previous study,[9] which was performed on a cluster consisting of only four tetrahedral units, showing that such a model is too small. In this work, we found that the zeolite lattice has an important effect on both the reaction mechanism and the energetic profile. The coadsorption of the dimethyl ether and ethene molecules is stronger than that of methanol (MeOH) and ethene molecules. Considering the transition state (TS) structure of the ethene methylation with methanol as compared to that of ethene methylation with DME, it was found that the TS of the ethene + MeOH complex forms two hydrogen bonds between the leaving water and the bridging oxygens of zeolite (H1···O1 and H2···O2), while the TS structure of the ethane + DME complex forms only one hydrogen bond between the leaving water and the oxygen of zeolite (H1···O1). This indicates that the TS of the ethene + methanol complex is more stable than the TS of the other complex. The weaker coadsorption in the adsorption step and the more stable TS state both lead to the lower activation energy of the methylation of ethene with MeOH as compared to that of the methylation of ethene with DME. However, experimentally an activation energy of DME that is about 1.2 kcal/mol lower than the one for the methanol complex has been found.[9] Also, the conversion of methanol into DME in the methanol + propene system is observed to be around 20%, which is higher than the conversion of methylation process. This implies that the coadsorption of methanol can occur in the MFI zeolite favorably. As results, it might be expected that, although the methanol is more reactive than the DME in methylation reaction, the sizable turnover of a reaction catalyzed by the methanol might be delayed by the coadsorption of methanol over the acid sites of zeolite. In fact, the nature of the methanol coadsorption complex is found to strongly interact with the Brønsted acid sites and is stronger than the coadsorption of the methanol and ethene molecules. From this behavior, it leads to obstruct the methylation process of alkenes. That might be one of the reasons why the activity of DME is higher than that of methanol in experiments.

## 5. Conclusions

The reaction mechanism of ethene methylation with methanol or with dimethyl ether over H-ZSM-5 zeolite has been investigated by applying two ONIOM schemes: one with a popular density functional, ONIOM2(B3LYP/6-31G(d,p):UFF), and one with a newly developed density functional, ONIOM2(M06-2X/6-311+G(2df,2p):UFF). Two different pathways, the dissociative and associative mechanism, were considered in this study. For the dissociative mechanism, the methylation of ethene initiates from the protonation of methanol or dimethyl ether leading to the surface methoxide intermediate formation, which is followed by the C−C formation between the methoxide and the incoming ethene molecule to produce a propoxide intermediate. This intermediate is finally deprotonated to form the propene product. The calculated energy barrier for the rate-determining protonation step is 41.2 and 42.9 kcal/mol, respectively. The subsequent reactions, the methylation and the deprotonation, require the energy barriers of 21.4 and 26.5 kcal/mol, respectively.

For the associative mechanism, the simultaneous C−O bond breaking and C−C bond formation occur in the single step without the methoxide intermediate. The activation energy of this step is calculated to be 29.0 and 33.0 kcal/mol for methanol and for dimethyl ether, respectively. In the case of methylation with methanol, this is consistent with the experimental value of 32.3 kcal/mol. The deprotonation of the propoxide intermediate to give the adsorbed propene product has an activation energy of 25.4 kcal/mol.

The calculated pathways and energetics suggest that the ethene methylation reaction with methanol and the one with dimethyl ether proceeded preferably via the dissociative mechanism. Our calculations also demonstrated the important effect of the zeolite framework in lowering the activation barriers for these reactions.

**Acknowledgment.** This work was supported in part by grants from the National Science and Technology Development Agency (NSTDA Chair Professor and NANOTEC Center of Excellence), the Thailand Research Fund and the Kasetsart University Research and Development Institute (KURDI), the Commission on Higher Education, Ministry of Education, under the Postgraduate Education and Research Programs in Petroleum and Petrochemicals, and Advanced Materials, as well as the Sandwich Program (CHE-PhD-SW-INDV to T.M.). We are grateful to Donald G. Truhlar and Yan Zhao for support with the M06-2X functional.

**Supporting Information Available:** Table S1: Comparison of the calculated adsorption energies of methanol and dimethyl ether with the different methods and basis sets, SCREEP contributions not included. Tables S2−S6: Selected geometric parameters for the ethene methylation with methanol and dimethyl ether. This material is available free of charge via the Internet at http://pubs.acs.org.



## References and Notes

(1) Stocker, M. *Microporous Mesoporous Mater.* **1999**, *29*, 3.
(2) Haw, J. F.; Song, W.; Marcus, D. M.; Nicholas, J. B. *Acc. Chem. Res.* **2003**, *36*, 317.
(3) Chang, C. D.; Silvestri, A. J. *J. Catal.* **1977**, *47*, 249.
(4) Andzelm, J.; Govind, N.; Fitzgerald, G.; Maiti, A. *Int. J. Quantum Chem.* **2003**, *91*, 467.
(5) Keil, F. J. *Microporous Mesoporous Mater.* **1999**, *29*, 49.
(6) Fougerit, J. M.; Gnep, N. S.; Guisnet, M. *Microporous Mesoporous Mater.* **1999**, *29*, 79.
(7) Cui, Z. M.; Liu, Q.; Song, W. G.; Wan, L. J. *Angew. Chem., Int. Ed.* **2006**, *45*, 6512.
(8) Svelle, S.; Joensen, F.; Nerlov, J.; Olsbye, U.; Lillerud, K. P.; Kolboe, S.; Bjorgen, M. *J. Am. Chem. Soc.* **2006**, *128*, 14770.
(9) Svelle, S.; Kolboe, S.; Swang, O.; Olsbye, U. *J. Phys. Chem. B* **2005**, *109*, 12874.
(10) Svelle, S.; Ronning, P. O.; Kolboe, S. *J. Catal.* **2004**, *224*, 115.
(11) Svelle, S.; Ronning, P. O.; Olsbye, U.; Kolboe, S. *J. Catal.* **2005**, *234*, 385.
(12) Mikkelsen, O.; Kolboe, S. *Microporous Mesoporous Mater.* **1999**, *29*, 173.
(13) Arstad, B.; Nicholas, J. B.; Haw, J. F. *J. Am. Chem. Soc.* **2004**, *126*, 2991.
(14) Ivanova, I. I.; Corma, A. *J. Phys. Chem. B* **1997**, *101*, 547.
(15) Bjørgen, M.; Svelle, S.; Joensen, F.; Nerlov, J.; Kolboe, S.; Bonino, F.; Palumbo, L.; Bordiga, S.; Olsbye, U. *J. Catal.* **2007**, *249*, 195.
(16) Dahl, I. M.; Kolboe, S. *Catal. Lett.* **1993**, *20*, 329.
(17) Dahl, I. M.; Kolboe, S. *J. Catal.* **1994**, *149*, 458.
(18) Dahl, I. M.; Kolboe, S. *J. Catal.* **1996**, *161*, 304.
(19) Wang, W.; Buchholz, A.; Seiler, M.; Hunger, M. *J. Am. Chem. Soc.* **2003**, *125*, 15260.
(20) Wang, W.; Jiang, Y.; Hunger, M. *Catal. Today* **2006**, *113*, 102.
(21) Wang, W.; Jiao, J.; Jiang, Y.; Ray, S. S.; Hunger, M. *ChemPhysChem* **2005**, *6*, 1467.
(22) Wang, W.; Seiler, M.; Hunger, M. *J. Phys. Chem. B* **2001**, *105*, 12553.
(23) Wang, W.; Hunger, M. *Acc. Chem. Res.* **2008**, *41*, 895.
(24) Vinek, H.; Derewinski, M.; Mirth, G.; Lercher, J. A. *Appl. Catal.* **1991**, *68*, 277.
(25) Mirth, G.; Lercher, J. A. *J. Phys. Chem.* **1991**, *95*, 3736.
(26) Mirth, G.; Lercher, J. A. *J. Catal.* **1991**, *132*, 244.
(27) Svelle, S.; Kolboe, S.; Olsbye, U.; Swang, O. *J. Phys. Chem. B* **2003**, *107*, 5251.
(28) Arstad, B.; Kolboe, S.; Swang, O. *J. Phys. Chem. B* **2002**, *106*, 12722.
(29) Svelle, S.; Kolboe, S.; Swang, O. *J. Phys. Chem. B* **2004**, *108*, 2953.
(30) Svelle, S.; Arstad, B.; Kolboe, S.; Swang, O. *J. Phys. Chem. B* **2003**, *107*, 9281.
(31) Vos, A. M.; Nulens, K. H. L.; Proft, F. D.; Schoonheydt, R. A.; Geerlings, P. *J. Phys. Chem. B* **2002**, *106*, 2026.
(32) Brändle, M.; Sauer, J. *J. Am. Chem. Soc.* **1998**, *120*, 1556.
(33) Sinclair, P. E.; de Vries, A. H.; Sherwood, P.; Catlow, C. R. A.; R. A., v. S. *J. Chem. Soc., Faraday Trans.* **1998**, *94*, 3401.
(34) Clark, L. A.; Sierka, M.; Sauer, J. *J. Am. Chem. Soc.* **2003**, *125*, 2136.
(35) Derouane, E. G.; Chang, C. D. *Microporous Mesoporous Mater.* **2000**, *425*, 35.
(36) Treesukol, P.; Truong, T. N.; Srisuk, K.; Limtrakul, J. *J. Phys. Chem. B* **2005**, *109*, 11940.
(37) Sirijaraensre, J.; Limtrakul, J.; Truong, T. N. *J. Phys. Chem. B* **2005**, *109*, 12099.
(38) Jungsuttiwong, S.; Truong, T. N.; Limtrakul, J. *J. Phys. Chem. B* **2005**, *109*, 13342.
(39) Hillier, I. H. *J. Mol. Struct. (THEOCHEM)* **1999**, *463*, 45.
(40) Sirijaraensre, J.; Limtrakul, J. *ChemPhysChem* **2006**, *7*, 2424.
(41) Ketrat, S.; Limtrakul, J. *Int. J. Quantum Chem.* **2003**, *94*, 333.
(42) Greatbanks, S. P.; Hillier, I. H.; Burton, N. A.; Sherwood, P. *J. Chem. Phys.* **1996**, *105*, 3770.
(43) Limtrakul, J.; Jungsuttiwong, S.; Khongpracha, P. *J. Mol. Struct.* **2000**, *525*, 153.
(44) Treesukol, P.; Lewis, J. P.; Limtrakul, J.; Truong, T. N. *Chem. Phys. Lett.* **2001**, *350*, 128.
(45) Kasuriya, S.; Namuangruk, S.; Treesukol, P.; Tirtowidjojo, M.; Limtrakul, J. *J. Catal.* **2003**, *219*, 320.
(46) Namuangruk, S.; Khongpracha, P.; Tantanak, D.; Limtrakul, J. *J. Mol. Catal. A* **2006**, *256*, 113.
(47) Pantu, P.; Boekfa, B.; Limtrakul, J. *J. Mol. Catal. A* **2007**, *277*, 171.
(48) Pabchanda, S.; Pantu, P.; Limtrakul, J. *J. Mol. Catal. A* **2005**, *239*, 103.
(49) Pantu, P.; Pabchanda, S.; Limtrakul, J. *ChemPhysChem* **2004**, *5*, 1901.
(50) Namuangruk, S.; Khongpracha, P.; Pantu, P.; Limtrakul, J. *J. Phys. Chem. B* **2006**, *110*, 25950.
(51) Namuangruk, S.; Pantu, P.; Limtrakul, J. *ChemPhysChem* **2005**, *6*, 1333.
(52) Jansang, B.; Nanok, T.; Limtrakul, J. *J. Phys. Chem. B* **2006**, *110*, 12626.
(53) Jansang, B.; Nanok, T.; Limtrakul, J. *J. Phys. Chem. C* **2008**, *112*, 540.
(54) Maihom, T.; Namuangruk, S.; Nanok, T.; Limtrakul, J. *J. Phys. Chem. C* **2008**, *112*, 12914.
(55) Panjan, W.; Limtrakul, J. *J. Mol. Struct.* **2003**, *654*, 35.
(56) Raksakoon, C.; Limtrakul, J. *J. Mol. Struct. (THEOCHEM)* **2003**, *631*, 147.
(57) Lomratsiri, J.; Probst, M.; Limtrakul, J. *J. Mol. Graphics Modell.* **2006**, *25*, 219.
(58) Derouane, E. G. *J. Catal.* **1986**, *100*, 541.
(59) Derouane, E. G.; Andre, J. M.; Lucus, A. A. *J. Catal.* **1988**, *110*, 58.
(60) Zicovich-Wilson, C. M.; Corma, A.; Viruela, P. *J. Phys. Chem.* **1994**, *98*, 10863.
(61) Zhao, Y.; Truhlar, D. G. *J. Phys. Chem. C* **2008**, *112*, 6860.
(62) Zhao, Y.; Truhlar, D. G. *Acc. Chem. Res.* **2008**, *41*, 157.
(63) Zhao, Y.; Schultz, N. E.; Truhlar, D. G. *J. Chem. Theory Comput.* **2006**, *2*, 364.
(64) Zhao, Y.; Truhlar, D. G. *Theor. Chem. Acc.* **2008**, *120*, 215.
(65) Stefanovich, E. V.; Truong, T. N. *J. Phys. Chem. B* **1998**, *102*, 3018.
(66) Vollmer, J. M.; Stefanovich, E. V.; Truong, T. N. *J. Phys. Chem. B* **1999**, *103*, 9415.
(67) Jansang, B.; Nanok, T.; Limtrakul, J. *J. Mol. Catal. A* **2006**, *264*, 33.
(68) Sirijaraensre, J.; Limtrakul, J. *Phys. Chem. Chem. Phys.* **2009**, *11*, 578.
(69) Lee, C. C.; Gorte, R. J.; Farneth, W. E. *J. Phys. Chem. B* **1997**, *101*, 3811.
(70) Frisch, M. J.; Trucks, G. W.; Schlegel, H. B.; Scuseria, G. E.; Robb, M. A.; Cheeseman, J. R.; Montgomery, J. A., Jr.; Vreven, T.; Kudin, K. N.; Burant, J. C.; Millam, J. M.; Iyengar, S. S.; Tomasi, J.; Barone, V.; Mennucci, B.; Cossi, M.; Scalmani, G.; Rega, N.; Petersson, G. A.; Nakatsuji, H.; Hada, M.; Ehara, M.; Toyota, K.; Fukuda, R.; Hasegawa, J.; Ishida, M.; Nakajima, T.; Honda, Y.; Kitao, O.; Nakai, H.; Klene, M.; Li, X.; Knox, J. E.; Hratchian, H. P.; Cross, J. B.; Adamo, C.; Jaramillo, J.; Gomperts, R.; Stratmann, R. E.; Yazyev, O.; Austin, A. J.; Cammi, R.; Pomelli, C.; Ochterski, J. W.; Ayala, P. Y.; Morokuma, K.; Voth, G. A.; Salvador, P.; Dannenberg, J. J.; Zakrzewski, V. G.; Dapprich, S.; Daniels, A. D.; Strain, M. C.; Farkas, O.; Malick, D. K.; Rabuck, A. D.; Raghavachari, K.; Foresman, J. B.; Ortiz, J. V.; Cui, Q.; Baboul, A. G.; Clifford, S.; Cioslowski, J.; Stefanov, B. B.; Liu, G.; Liashenko, A.; Piskorz, P.; Komaromi, I.; Martin, R. L.; Fox, D. J.; Keith, T.; Al-Laham, M. A.; Peng, C. Y.; Nanayakkara, A.; Challacombe, M.; Gill, P. M. W.; Johnson, B.; Chen, W.; Wong, M. W.; Gonzalez, C.; Pople, J. A. *Gaussian 03*, revision B.05; Gaussian, Inc.: Pittsburgh, PA, 2003.
(71) Blaszkowski, S. R.; van Santen, R. A. *J. Phys. Chem.* **1995**, *99*, 11728.
(72) Blaszkowski, S. R.; van Santen, R. A. *J. Am. Chem. Soc.* **1996**, *118*, 5152.

(73) Blaszkowski, S. R.; van Santen, R. A. *J. Am. Chem. Soc.* **1997**, *119*, 5020.

(74) Solans-Monfort, X.; Sodupe, M.; Mo, O.; Yanez, M.; Elguero, J. *J. Phys. Chem. B* **2005**, *109*, 19301.

(75) Blaszkowski, S. R.; van Santen, R. A. *J. Phys. Chem. B* **1997**, *101*, 2292.

(76) Zicovich-Wilson, C. M.; Viruela, P.; Corma, A. *J. Phys. Chem.* **1995**, *99*, 13224.

(77) Geerlings, P.; Vos, A. M.; Schoonheydt, R. A. *J. Mol. Struct. (THEOCHEM)* **2006**, *762*, 69.

(78) Boronat, M.; Zicovich-Wilson, C. M.; Viruela, P.; Corma, A. *J. Phys. Chem. B* **2001**, *105*, 11169.

(79) Rozanska, X.; Demuth, T.; Hutschka, F.; Hafner, J.; van Santen, R. A. *J. Phys. Chem. B* **2002**, *106*, 3248.

(80) Namuangruk, S.; Pantu, P.; Limtrakul, J. *J. Catal.* **2004**, *225*, 523.

(81) Boronat, M.; Viruela, P. M.; Corma, A. *J. Am. Chem. Soc.* **2004**, *126*, 3300.

(82) Boronat, M.; Corma, A. *Appl. Catal., A: General* **2008**, *336*, 2.

(83) Bhan, A.; Joshi, Y. V.; Delgass, W. N.; Thomson, K. T. *J. Phys. Chem. B* **2003**, *107*, 10476.

JP809746A

# Mechanistic Investigation on 1,5- to 2,6-Dimethylnaphthalene Isomerization Catalyzed by Acidic $\beta$ Zeolite: ONIOM Study with an M06-L Functional

**Chawanwit Kumsapaya,[†,‡] Karan Bobuatong,[†,‡] Pipat Khongpracha,[†,‡] Yuthana Tantirungrotechai,[§] and Jumras Limtrakul*[,†,‡]**

*Laboratory for Computational and Applied Chemistry, Chemistry Department, Faculty of Science, Kasetsart University, Bangkok 10900, NANOTEC Center of Excellence, National Nanotechnology Center (NANOTEC), Kasetsart University Research and Development Institute, Bangkok 10900, and NANOTEC, National Science and Technology Development Agency, Khongluang, Pathumthani 12120, Thailand*

*Received: May 3, 2009; Revised Manuscript Received: July 3, 2009*

The isomerization of 1,5- to 2,6-dimethylnaphthalene (DMN) over $\beta$ zeolite has been investigated by applying a newly developed density functional named M06-L, incorporated into the ONIOM scheme: M06-L/6-31G(d,p): UFF. Two consecutive reaction mechanisms over the extended zeolite framework have been carefully examined: the 1,5- to 1,6-DMN isomerization followed by the 1,6- to 2,6-DMN isomerization. Both catalytic processes take place via the same mechanism. The isomerization process starts from the protonation of the DMN step, creating the naphthalynic carbocation. Subsequently, the intramolecular methyl shift occurs from the $\alpha$-position to the adjacent $\beta$-position of the naphthalynic carbocation. In the final step, the anionic zeolite framework takes a proton away from the naphthalynic carbocation, yielding a desired 1,6-DMN or 2,6-DMN molecule. The methyl migrations are the rate-determining steps and require activation barriers of 25.69 and 21.05 kcal/mol for the 1,5- to 1,6-DMN and 1,6- to 2,6-DMN processes, respectively. The calculated reaction profiles are in agreement with the experimental prediction that the 1,5- to 1,6-DMN isomerization is the kinetically controlled step. The results in this study show the excellent performance of a combination of the newly developed functional and the confinement effect represented by the universal force field (M06-L/6-31G(d,p): UFF) for investigating the transformations of aromatic species in the zeolite system.



## Introduction

Polyethylene naphthalate (PEN) is a thermoplastic polyester which shows very good gas barrier, mechanical, thermal, and electrical properties. These properties are indicative of promising innovative applications such as high-performance fibers and films and novel packaging, e.g., plastic beer bottles.[1−3] The current production process involves the condensation polymerization of ethylene glycol and dimethyl 2,6-napthalenedicarboxylate (2,6-NDC). The 2,6-NDC is in turn prepared from 2,6-dimethylnaphthalene (2,6-DMN).[4] However, the low availability and high production cost of 2,6-DMN result in the price of PEN being higher than that of polyethylene terephthalate (PET).[4] These, unfortunately, limit the successful commercialization of PEN, even though it shows superior properties in comparison with the widely used PET polymer. Current large-scale production (30 kton/year) of 2,6-DMN is made by BP-Amoco using its patented process. The employed process based on butadiene and *o*-xylene involves four subsequent reaction stages in four separate reactors: alkylation, cyclization, dehydrogenation, and finally catalytic isomerization from 1,5- to 2,6-DMN.[2,5] The 1,5- to 2,6-DMN isomerization step is thought to be a limiting step which leads to the low availability and the high cost of 2,6-DMN.[6] Although there are some available reports concerning the detailed investigation of this limiting step, there is no study that provides sufficient information on this reaction at the molecular level.[2,6−8] A better understanding of this reaction at the molecular level which would help increase the yield of 2,6-DMN is crucial for the improvement of the 2,6-DMN production process, hence lowering the cost of 2,6-DMN and also of PEN production.

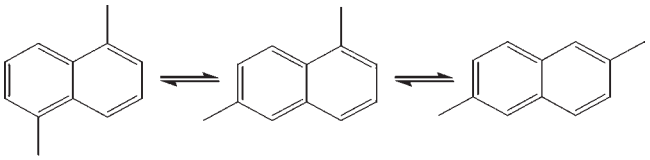


**Figure 1.** Isomerization reaction of 1,5-DMN to 2,6-DMN proceeding via an intramolecular 1,2-methyl shift.

The isomerization of 1,5-DMN to a more profitable 2,6-DMN molecule occurs via the intramolecular 1,2-methyl shift; i.e., the methyl group migrates one at a time from the $\alpha$-position to the $\beta$-position (see Figure 1).[9−11] The intramolecular 1,2-methyl shift is widely recognized as a key mechanistic step in the rearrangements of methylbenzenes, trimethylbenzenes, tetramethylbenzenes,[9,10] methylnaphthalenes, and dimethylnaphthalenes. From the isomer distribution at the thermodynamic equilibrium sets,[1,11,12] the shift of a methyl group from the $\alpha$-position to the $\beta$-position of the naphthalene nucleus in the same ring is observed to be facile. A single methyl shift of 1,5-DMN leads to 1,6-DMN. A further methyl shift of 1,6-DMN leads to 2,6-DMN. The reaction can be promoted by both Lewis and Brønsted acids. Thus, catalysts such as $BF_3 \cdot HF$ and zeolite can be used to speed up the reaction and, therefore, reduce the cost of the 2,6-DMN production.

When new "green chemistry" industrial processes are being developed, the heterogeneous catalyst is considered more

[†] Faculty of Science, Kasetsart University.
[‡] Kasetsart University Research and Development Institute.
[§] National Science and Technology Development Agency.

10.1021/jp904098t CCC: $40.75 
Published on Web 08/17/2009

favorable than its homogeneous counterpart. Zeolite is a unique choice of catalyst for this purpose. Its porous structure can provide specific pathways to desirable products. Several zeolites are candidates for catalyzing this isomerization reaction.[4] Recently, Kraikul et al. conducted a catalytic activity test of three zeolites, H-$\beta$, H-mordenite, and H-ZSM-5, on the isomerization of 1,5-DMN to 2,6-DMN.[6] Among the tested catalysts, the H-$\beta$ zeolite was found to be the best catalyst which provided the highest yield of 2,6-DMN. They observed that no 2,6-DMN was detected when using H-ZSM-5 as a catalyst under the testing condition. This finding demonstrates the framework selectivity of zeolitic materials. Millini et al. conducted a molecular dynamics simulation to estimate the diffusional energy barrier of DMN in zeolites.[13] The H-ZSM-5 pore structure has a very high diffusional energy barrier, rendering it difficult for DMN to move in and out of the framework. For H-mordenite and H-$\beta$ zeolite, the diffusional energy barriers are much less than that of H-ZSM-5. For the porous systems considered, the diffusivity of the DMN isomer is in the order 2,6-DMN > 1,6-DMN > 1,5-DMN.[13]

At 265 °C, when using H-$\beta$ zeolite as the catalyst to isomerize 1,5-DMN, the equilibrium composition of 1,5-DMN:1,6-DMN:2,6-DMN is 9.33:43.52:47.16, respectively. The percentage of 2,6-DMN is greater than that of 1,6-DMN. An analysis of the reaction quotient at 1 h and the equilibrium constant led Kraikul et al. to conclude that the 1,5- to 1,6-DMN isomerization is the kinetically limiting step for the 1,5- to 2,6-DMN conversion process.[6] However, no chemical kinetics parameter can be deduced from their study. On the other hand, Suld and Stuart studied the isomerization kinetics of several di- and monomethylnapthalenes catalyzed by $BF_3 \cdot HF$.[11] For a set of 2,6-DMN, 1,6-DMN, and 1,5-DMN molecules, they deduced the rate of isomerization to be in the temperature range of 20−50 °C. Assuming the reversible first-order kinetics, the activation energies for the 2,6- to 1,6-DMN and the 1,6- to 1,5-DMN steps were estimated to be 20.1 ± 1 and 20.3 ± 1 kcal/mol, respectively.

To our knowledge, there is no report on the activation energy of this reaction catalyzed by heterogeneous catalysts, zeolite in particular, available in the literature. In addition, although the isomerization from 1,5-DMN into 2,6-DMN over the heterogeneous catalysts is known to occur with two single methyl shift steps, the reaction mechanism has not been investigated in detail. In this paper, we report a detailed reaction mechanism of 1,5- to 2,6-DMN isomerization catalyzed by acidic $\beta$ zeolite by means of the hybrid quantum mechanics/molecular mechanics (QM/MM) approach.



## Computational Methods and Material Models

**Computational Methods.** Quantum chemical calculation is accepted nowadays by practical chemists as a very useful tool to provide insights into reaction mechanisms at the molecular level.[14] It is the only practical way to comprehend the transition states and intermediates of a complex reaction. The density functional theory (DFT) is by far the most common choice of method for chemical applications. As one deals with complex reactions taking place in a heterogeneous catalyst of infinite size, a certain approach is required to incorporate the framework effect while keeping the computational cost as low as possible. A periodic DFT is a straightforward approach, but it is very computationally demanding.[15] The typical zeolites, such as ZSM-5 and $\beta$ zeolite, possess hundreds of atoms per unit cell, making a periodic calculation too expensive to be employed for these systems. At the other extreme, a bare cluster calculation, taking only the catalytic active site and the reactants, ignores all of the framework effect. A practical approach is one that incorporates the framework effect on the chemically active region in some approximate way. Examples are the embedded cluster or a combined quantum mechanics/molecular mechanics (QM/MM) approach,[16−20] as well as the more general ONIOM (our-Own-N-layered-Integrated molecular Orbital and molecular Mechanics) method.[21−27] We adopted the ONIOM approach in this work. Several reports by our groups indicate its good performance on modeling the adsorption and reaction mechanism in zeolite.[28−38]

The ONIOM scheme we adopted consists of an inner layer of the active region calculated by the M06-L/6-31G(d,p) level and a large outer layer of the framework calculated by the universal force field (UFF). The M06-L functional, as developed by the Minnesota group,[39] uses the meta generalized gradient approximation in which the density functional includes the spin densities gradient and spin kinetic energy densities and their reduced gradient.[39−41] This local functional allows the use of density fitting algorithms and plane wave algorithms that require much less computational effort than the best algorithms for the nonlocal functional; thus, it is preferred for practical computations on large systems.[41] All calculations were performed by using the Gaussian 03 code[42] incorporated with the Minnesota density functionals module 3.1 by Yan Zhao and Donald G. Truhlar.

**Material Models.** The extended 120T cluster, covering the active region, of the H-$\beta$ zeolite is used to represent the Brønsted acid site and the zeolite framework in this investigation. This was taken from the H-$\beta$ zeolite crystal lattice structures.[43,44] It includes the 12-membered ring (12MR) representing the main gateway to the intersection of two perpendicular 12MR channel systems, where the reactions normally take place (see Figure 2b). A silicon atom at a T5 position in the $\beta$ zeolite is substituted by an aluminum atom. A proton is added to the bridging oxygen atoms bonded directly to the aluminum atom, conventionally called the O5 position but is designated as the O1 position in this study.[43]

In the ONIOM model, an inner layer consists of a 14T cluster including the 12-membered ring and the other two Si atoms around the Al atom and the DMN molecules. The DFT treatment in this region accounts for the interactions of the adsorbates with the Brønsted acid site of the $\beta$ zeolite. A large outer layer consists of the remainder of the extended framework up to 120T. This layer takes the confinement of the extended zeolite structure and the effect of the framework into account. The UFF that is selected to represent the effect in this layer also accounts for the van der Waals interaction.[45] This interaction is the dominant contribution for adsorption−desorption mechanisms in zeolites.[45−48] During optimization, only the 5T region [$(\equiv SiO)_3Al(OH)Si\equiv$] was allowed to relax while the rest of the model was fixed along the crystallographic coordinates.

From our previous work,[49] attempts have been made to demonstrate that the geometries of reaction intermediates in the zeolite system do not influence the results. Several test calculations on zeolite models have been performed using different zeolite models: 5T, 12T, 34T, 46T, and 128T QM clusters. It was found that some important structural parameters (e.g., O1−Hz and Al···Hz) are insignificantly different on those five zeolite models. The estimates for the geometry error of the method are 0.966 ± 0.001 A for O1−Hz and 2.364 ± 0.02 Å for Al···Hz. From these findings, one could propose that the 14T QM size is reliable enough in the ONIOM model for studying such a complicated reaction mechanism in the bulk

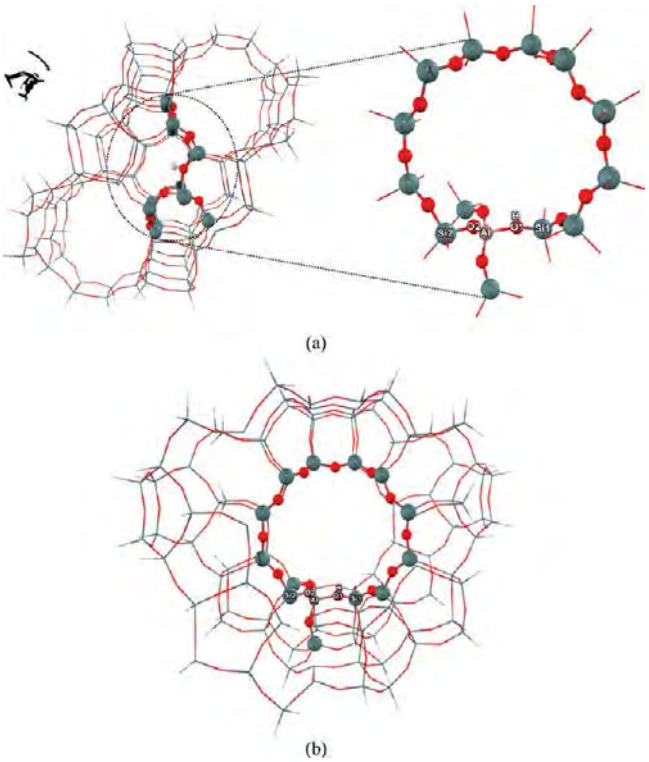


**Figure 2.** Extended 120T cluster model of H-$\beta$ zeolite considered in this study. (a) The oval dashed line encloses an intersection of two perpendicular 12-membered ring (12MR) channel systems which serves as a nanoreactor. The ball-and-stick graphics represent the 14T active region including the main gateway to a channel intersection of H-$\beta$ zeolite (12MR) where the DMN isomerization takes place. (b) View along the main channel.

catalytic system. Furthermore, to improve the energetic properties and take into account the whole zeolite framework effect, single-point energy calculations at a high level of theory on the prior optimized structures by the ONIOM method have been performed to cover the drawbacks of ONIOM models observed via the so-called *S* values,[50] being in the range of 0.00826−0.01864 au for the adsorption energy (see Table S2 of the Supporting Information). The adsorption energy computed from M06-L/6-31g(d,p) single-point calculations of 120T extended along the reaction coordinate at the ONIOM(M06-L/6-31G(d,p):UFF) optimized structures has been found to provide a good description of dispersion interactions and is also in agreement with the experimental data.[51] Consequently, the use of the 120T M06-L/6-31G(d,p)//14T ONIOM(M06-L/6-31G(d,p):UFF) approach seems to be a good strategy to model this system (see Figure 10).

The isomerization reaction from 1,5-DMN to 2,6-DMN is shown in Figure 3. This reaction mechanism is proposed on the basis of the 1,2-methyl shift in methylbenzene and dimethylnaphthalene catalyzed by acid solution.[9,11] It involves successive intramolecular 1,2-methyl shift reactions from 1,5-DMN to 1,6-DMN and finally to 2,6-DMN. Each reaction is basically a shift of a single methyl group from the α- to the $\beta$-position that is catalyzed by the acidic proton. We do not consider the situation in which the shift of two methyl groups takes place simultaneously since it is unlikely to find two acidic protons at the right position. Each reaction begins with the adsorption of DMN on the Brønsted acid site followed by the protonation, methyl shift, and proton back-donation to become the neutral adsorbed product. The geometry optimizations were performed on all important species along the reaction coordinate. These include the isolated reactant, adsorbed reactant, intermediate, transition state, adsorbed product, and isolated product.

## Results and Discussion

**Reaction Mechanism of 1,5- to 1,6-DMN Isomerization.** Figure 3a summarizes the reaction mechanism of 1,5- to 1,6-DMN isomerization. In this mechanism, the 1,5-DMN molecule is first adsorbed at the Brønsted acid site of the acidic $\beta$ zeolite. Then the adsorbed 1,5-DMN complex is protonated to form a $\sigma$-complex (Int_1). This is followed by the intramolecular methyl shift between the adjacent C5 and C6 positions. This results in the formation of a new $\sigma$-complex (Int_2) which donates a proton back to the zeolite framework, yielding the 1,6-DMN molecule in the adsorbed state (Prod_1). The following subsections describe the structural and energetic information for each step of the 1,5- to 1,6-DMN isomerization.

***Protonation of the 1,5-DMN Adsorption Complex.*** The optimized geometric parameters of species in the 1,5-DMN protonation step are documented in Table S2 of the Supporting Information. The C5−C6 and C6−H2 bond lengths of the isolated 1,5-DMN are 1.379 and 1.088 Å, respectively. These bond lengths compare well with the corresponding experimental bond lengths of benzene of 1.397 and 1.084 Å, respectively. The adsorption mode takes place with the C5−C6 double bond interacting with the acidic proton (H1) with C5−H1 and C6−H1 distances of 2.901 and 2.576 Å, and the O1−H1 bond length increases from 0.967 to 0.980 Å (see Table S2 and Figure 4). The 1,5-DMN molecule shows few structural changes. The 1,5-DMN molecule was slightly perturbed by the zeolite cavity when adsorbed at the Brønsted acid site. The C5−C6 double bond lengthens only slightly by 0.005 Å. No change is observed in the C6−H2 bond length. Furthermore, this weak interaction does not significantly perturb the zeolite structure. Compared with the isolated zeolite, the Al−O1, Al−O2, and Si2−O2 bond distances are decreased only by 0.005, 0.004, and 0.009 Å, respectively, while the Si1−O1 bond distance is increased only by 0.002 Å. The Si1−O1−Al bond angle decreases by 2.4°, whereas the Si2−O2−Al bond angle increases by 2.0°.

The adsorption energy of 1,5-DMN is computed to be −22.13 kcal/mol. There is, unfortunately, no report of an experimental adsorption energy of this molecule in the literature. Nevertheless, this value is in accord with the experimental adsorption energy of −20.4 kcal/mol for the adsorption of ethylbenzene[51] in H-Y zeolites. Our calculated adsorption energy for the 1,5-DMN molecule is larger than the experimental report for ethylbenzene. This is due to the fact that 1,5-DMN is a more basic molecule than the ethylbenzene molecule. Therefore, the adsorption energy of 1,5-DMN on a highly acidic $\beta$ zeolite should be larger than that of ethylbenzene adsorbed on a less acidic H−Y zeolite. These results show that the 120T M06-L/6-31G(d,p)//14T ONIOM(M06-L/6-31G(d,p):UFF) model is reasonable for investigating the interactions between the adsorbate and the zeolite catalyst.

In the next step, the protonation of the adsorbed 1,5-DMN complex, Ads_1, takes place at the C5 position. A new $\sigma$-bond is formed, and the original conjugation is disrupted. Figure 4 shows the calculated energy profile for the protonation step. Selected geometric parameters of the transition state and the intermediate of the first part of the isomerization are tabulated in Table S2 of the Supporting Information. The protonated 1,5-DMN is in the form of a carbenium ion in which the positive charge can delocalize over the remaining five carbon atoms of a benzene ring in DMN. At the transition state, TS_1, the zeolite proton moves toward a carbon atom of 1,5-DMN as evidenced

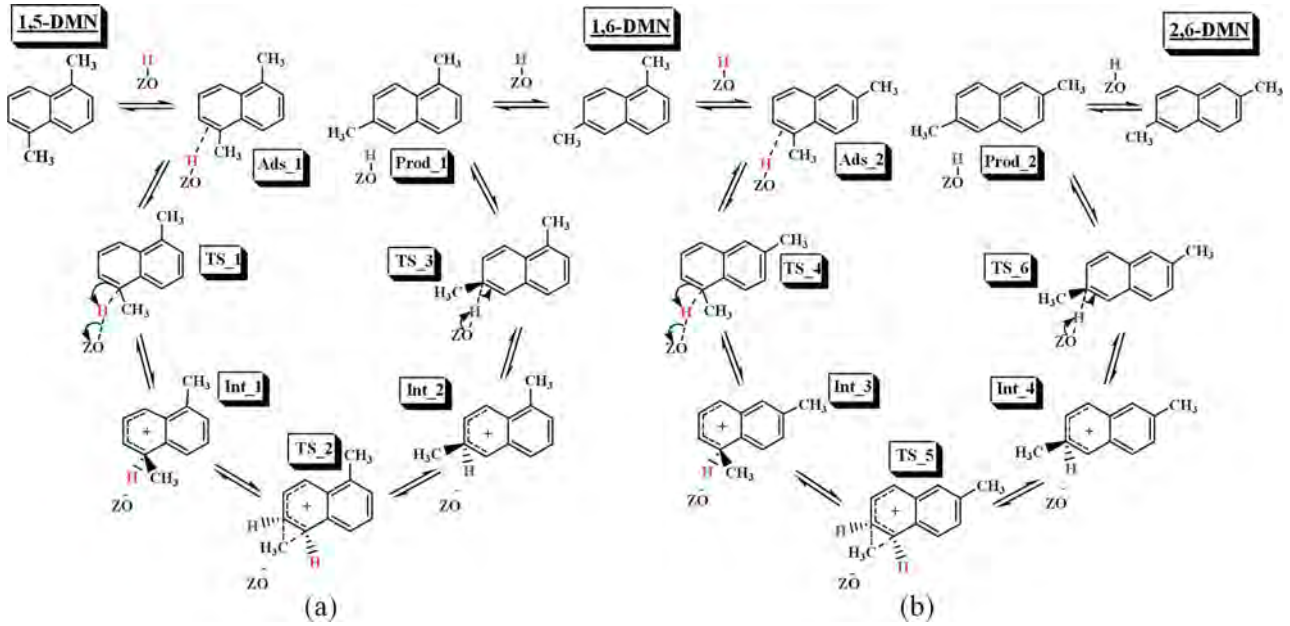


**Figure 3.** Reaction mechanism of (a) the 1,5- to 1,6-DMN and (b) the 1,6- to 2,6-DMN isomerizations over H-$\beta$ zeolite. Schematically they consist of protonation, methyl shift, and proton back-donation of the adsorbed species.

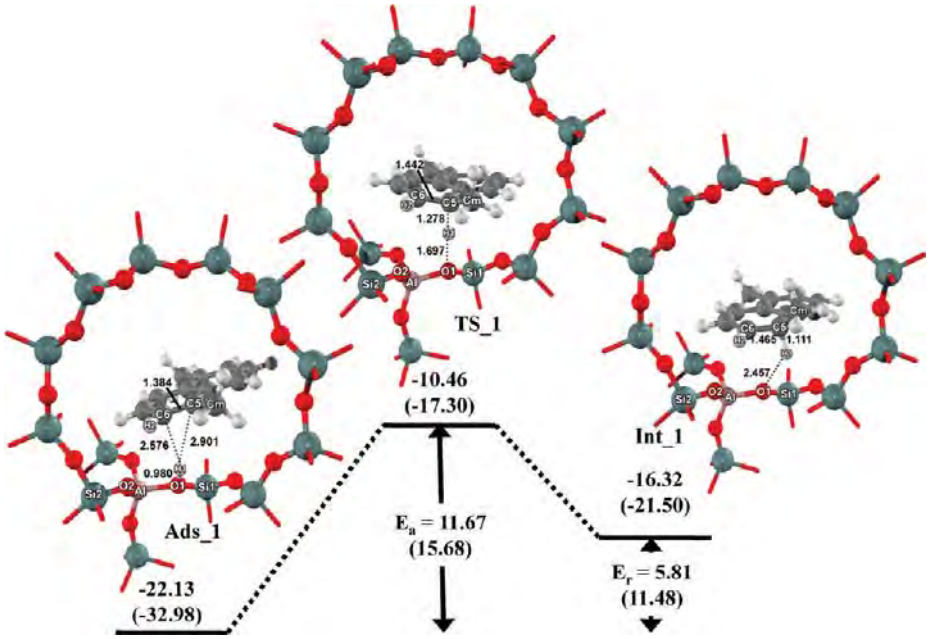


**Figure 4.** 120T M06-L/6-31G(d,p)//14T ONIOM(M06-L/6-31G(d,p):UFF) energy profile (kcal/mol) for the protonation step of the 1,5- to 1,6-DMN isomerization over H-$\beta$ zeolite. The sum of isolated 1,5-DMN and 120T zeolite cluster energies is taken as a reference. The values in parentheses are calculated at 14T ONIOM(M06-L/6-31G(d,p):UFF). Only DMN and the 14T active region are displayed.

by a great reduction of the C5−H1 distance from 2.901 to 1.278 Å. The O1−H1 and C5−C6 bond lengths are also elongated by 0.717 and 0.058 Å with respect to those of the Ads_1 complex. It is then transformed to a stabilized intermediate, Int_1. This dimethylnaphthalenonium ion is stabilized by the resonance energy of the intact benzenoid nucleus.[11]

The energy barrier for the protonation is 11.67 kcal/mol, and the corresponding reaction energy is endothermic by 5.81 kcal/mol. The formation of the $\sigma$-bonded complex is accompanied by the structural changes of the zeolite. The Al−O1, Si1−O1, and Si2−O2 bond distances are decreased by 0.091, 0.069, and 0.009 Å, respectively, whereas the Al−O2 bond distance increases by 0.020 Å. The Si2−O2−Al angle increases by 3.3° compared with those of the adsorbed 1,5-DMN (Ads_1). We observe that the geometry of the transition state, TS_1, is more similar to that of Int_1 than to that of Ads_1. This results in the reaction tendency to proceed with the forward direction to the methyl shift step (cf Table S2 of the Supporting Information).

***Methyl Shift Step of Protonated 1,5-DMN.*** The reversible intramolecular 1,2-methyl shift moves a methyl group from the α-position to the adjacent $\beta$-position. With reference to Figure 5, this is the formation of a second intermediate (Int_2) from the first intermediate (Int_1). The selected geometrical parameters of Int_1, the transition state (TS_2), and Int_2 are reported in Table S3 (Supporting Information), while the reaction profile is illustrated in Figure 5. The TS_2 transition structure has the shifting methyl group located in between with a C5−*Cm*−C6 bond angle of 45.4° and a C5−C6 bond distance of 1.412 Å. At this unstable tricentric transition state, the methyl group is moving slightly toward the C6 carbon atom with *Cm*−C5 and

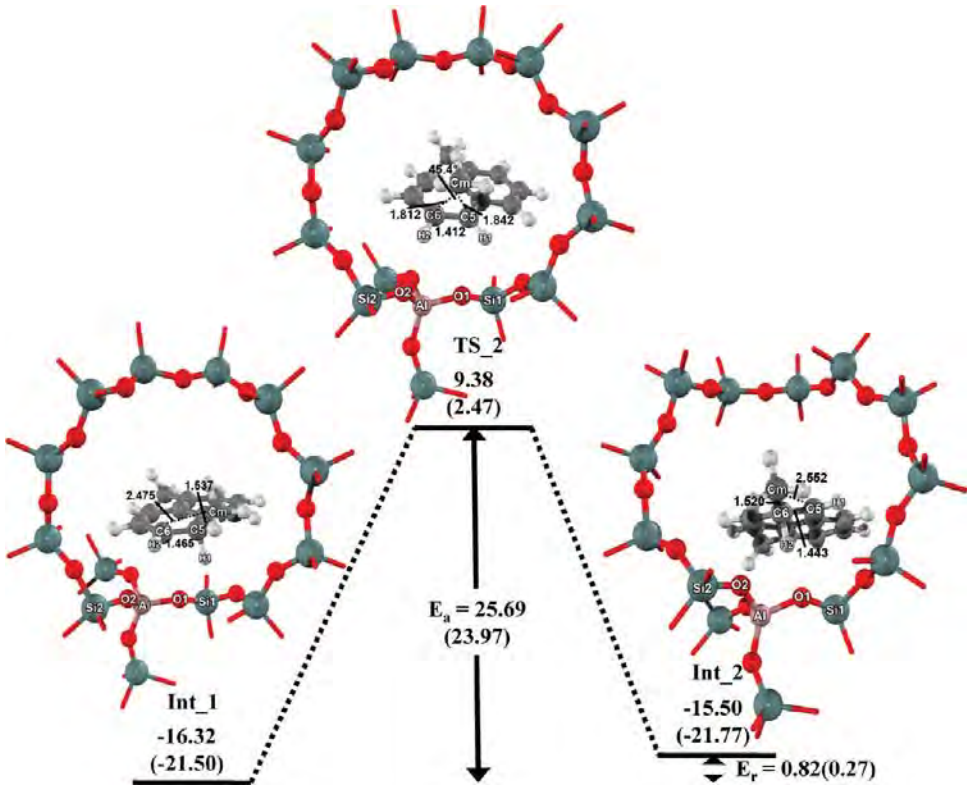


**Figure 5.** 120T M06-L/6-31G(d,p)//14T ONIOM(M06-L/6-31G(d,p):UFF) energy profile (kcal/mol) for the methyl shift of the 1,5- to 1,6-DMN isomerization over H-$\beta$ zeolite.



*Cm*−C6 distances of 1.842 and 1.812 Å, respectively. In the Int_2 structure, a *Cm*−C6 bond of 1.520 Å is formed. This process causes rather insignificant perturbation on the zeolitic structure (see Table S3). The Al−O1, Al−O2, and Si2−O2 bond lengths are increased by 0.005, 0.006, and 0.004 Å, respectively, while the Si1−O1 bond length is decreased by 0.002 Å. The Si1−O1−Al bond angle increases by 0.4° and the Si2−O2−Al bond angle decreases by 1.8° with respect to those of Int_1.

The calculated binding energy of Int_2 is −15.50 kcal/mol (see Figure 5). This is slightly less stable than that of Int_1 by 0.82 kcal/mol. Therefore, the reaction energy is almost thermoneutral. This may be attributed to the reduction of steric hindrance between the methyl group in the naphthalene ring and the zeolitic pore. The activation energy for the 1,5- to 1,6-DMN methyl migration step is 25.69 kcal/mol. This actually compares well with the reported experimental activation energy of 20.3 ± 1 kcal/mol of Suld and Stuart.[11]

***Proton Back-Donation to the Zeolite Framework.*** The final stage of the 1,5- to 1,6-DMN isomerization involves the proton back-donation from Int_2 to the zeolite framework. This leads to the 1,6-DMN molecule adsorbed on the Brønsted acid site. Figure 6 shows the energy profile for this step and the geometric parameters of all species involved: Int_2, the transition state (TS_3), and adsorbed 1,6-DMN (Prod_1) are documented in Table S4 of the Supporting Information. The H2 atom of Int_2 is transferred from C6 back to the active oxygen O1 site of the zeolite framework to form adsorbed 1,6-DMN. This is accompanied by an increase of the C6−H2 distance from 1.213 Å in TS_3 to 2.528 Å in Prod_1 and a decrease of the O1−H2 distance from 1.765 Å in TS_3 to 0.988 Å in Prod_1. The TS_3 transition-state configuration is very similar to that of Int_2. This proton back-donation occurs very fast as evidenced by the predicted energy barrier being only 2.64 kcal/mol. The reaction energy for this step is exothermic by 12.95 kcal/mol. This indicates that the proton prefers to sit on the zeolite framework.

The proton back-donation process has a slight impact on the zeolite framework. With reference to the Int_2 configuration, the Al−O1, Si1−O1, and Si2−O2 bond distances increase by 0.012, 0.009, and 0.001 Å, respectively, while the Al−O2 bond distance and the Si1−O1−Al and Si2−O2−Al bond angles are decreased by 0.005 Å, 0.5°, and 0.4°, respectively. The back-transferred proton forms a chemical bond with the O1 atom with a distance of 0.988 Å. The C6−H2 and C5−H2 bond distances of the adsorbed product are 2.528 and 2.252 Å, respectively. The C5−C6 bond is shortened to 1.384 Å, which resembles the double bond. Finally, a desorption energy of 28.36 kcal/mol is required to remove the 1,6-DMN product from the Brønsted acid site (see Figure 6).

The energy profile for all steps of the 1,5- to 1,6-DMN isomerization is summarized in Figure 10a (see also Table 1). The results show that the rate-determining step of the isomerization from 1,5- to 1,6-DMN is the methyl shift step. This step has the highest activation energy of 25.69 kcal/mol compared with 11.67 and 2.64 kcal/mol for the protonation and the proton back-donation steps. These results are in good agreement with the experimental observation in which the acid-catalyzed intramolecular 1,2-methyl shift is the rate-determining step for this isomerization with an activation energy of 20.3 kcal/mol.[11]

**Reaction Mechanism of 1,6- to 2,6-DMN Isomerization.** The reaction mechanism of 1,6- to 2,6-DMN isomerization is outlined in Figure 3. Once 1,5-DMN is converted to 1,6-DMN, the 1,6-DMN molecule isomerizes further to become 2,6-DMN over the same Brønsted acid site of the $\beta$ zeolite catalyst. However, 1,6-DMN must orientate itself inside the pore and point another methyl group at the α-position toward the acidic proton for the reaction to occur. The considered mechanism

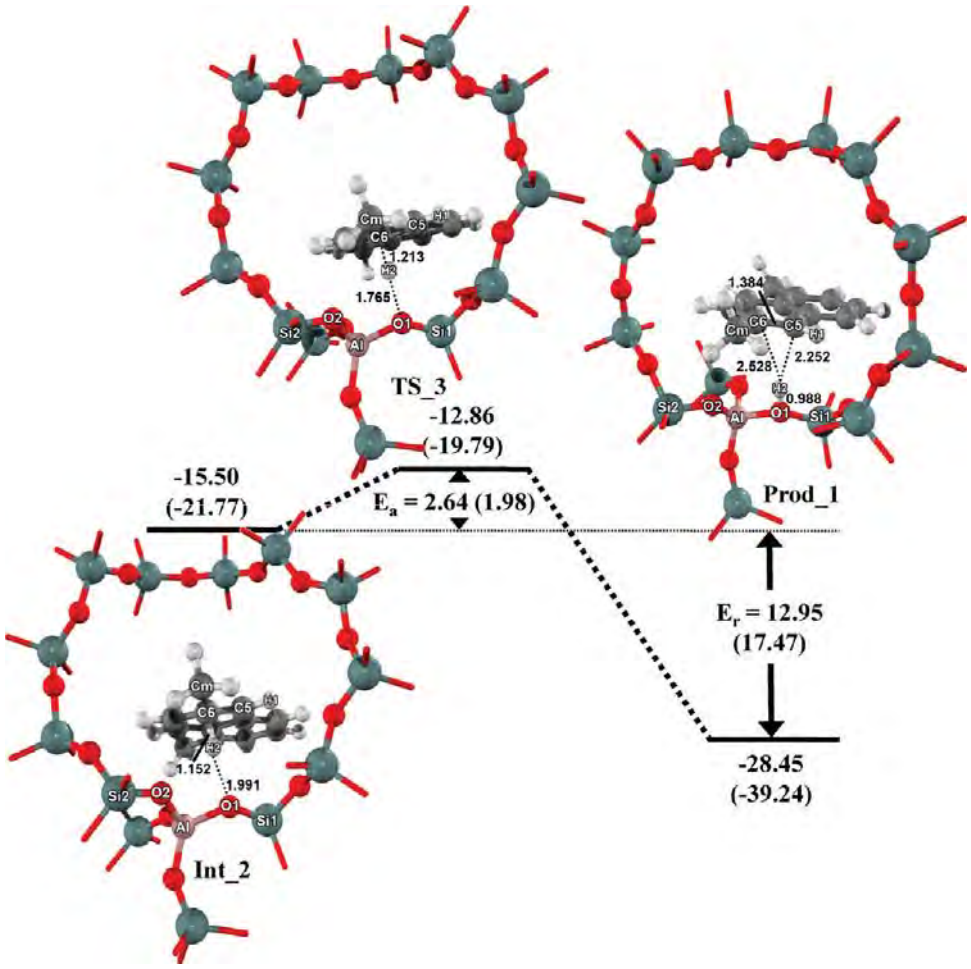


**Figure 6.** 120T M06-L/6-31G(d,p)//14T ONIOM(M06-L/6-31G(d,p):UFF) energy profile (kcal/mol) for the proton back-donation step of the 1,5- to 1,6-DMN isomerization over H-$\beta$ zeolite.

**TABLE 1: Summary of the 14T ONIOM(M06-L/6-31G(d,p):UFF) and 120T M06-L/6-31G(d,p) Energies of the Important Species along the Reaction Coordinate of the 1,5- to 2,6-DMN Isomerization over H-$\beta$ Zeolite (See Figure 10)[a]**

| complex | ONIOM(M06-L/6-31G(d,p):UFF) | M06-L/6-31G(d,p) |
|---|---|---|
| Ads_1 | −32.98 | −22.13 |
| TS_1 | −17.30 | −10.46 |
| Int_1 | −21.50 | −16.32 |
| TS_2 | 2.47 | 9.38 |
| Int_2 | −21.77 | −15.50 |
| TS_3 | −19.79 | −12.86 |
| Prod_1 | −39.24 | −28.45 |
| Ads_2 | −33.12 | −21.43 |
| TS_4 | −18.36 | −11.37 |
| Int_3 | −20.44 | −13.90 |
| TS_5 | 0.44 | 7.14 |
| Int_4 | −23.13 | −16.89 |
| TS_6 | −19.45 | −12.95 |
| Prod_2 | −38.78 | −27.72 |

[a] The 120T M06-L/6-31G(d,p) energies reported are the single-point energies at the ONIOM(M06-L/6-31G(d,p):UFF)-optimized structures.

begins with the adsorption of orientated 1,6-DMN over the acid site (Ads_2). Then the acidic proton is transferred to form the $\sigma$-complex (Int_3) followed by the intramolecular 1,2-methyl shifts from the adjacent $C_\alpha$ to $C_\beta$ positions. This step leads to a new $\sigma$-complex (Int_4) which can transfer a proton back to the zeolite framework, yielding the adsorbed 2,6-DMN (Prod_2). Finally the adsorbed 2,6-DMN desorbs from the zeolite framework to become an isolated 2,6-DMN molecule.

***Protonation of the 1,6-DMN Adsorption Complex.*** Within a $\beta$ micropore, the 1,6-DMN molecule orientates its α-methyl group toward a Brønsted proton at the 12-membered ring channel intersection. The adsorbed complex Ads_2 has its geometric parameters given in Table S5 of the Supporting Information. The C1−C2 double bond of the 1,6-DMN molecule interacts with the acidic proton (H3) with C1−H3 and C2−H3 distances of 3.272 and 3.528 Å. Upon adsorption, the Brønsted O1−H3 bond is weakened with the bond length lengthened by 0.005 Å. The structure of the $\beta$ zeolite is slightly perturbed upon interacting with 1,6-DMN. With reference to the isolated zeolite framework, the Al−O1 and Si1−O1 bond distances increase by 0.837 and 0.006 Å, respectively, as the Si2−O2−Al bond angle is increased by 1.4°. The Al−O2 and Si2−O2 bond distances are decreased by 0.156 and 0.087 Å, respectively, and the Si1−O1−Al bond angle is decreased by 1.7°.

The calculated adsorption energy for the adsorbed 1,6-DMN complex prior to isomerization is −21.43 kcal/mol. This is close to the −22.13 kcal/mol energy of 1,5-DMN and approximately close to the −20.4 kcal/mol energy of ethylbenzene[51] in H-Y zeolite. The adsorbed 1,6-DMN complex, Ads_2, is protonated to initiate the second isomerization. The protonation step leads to dimethylnaphthalenonium ion (Int_3) via the transition state (TS_4). For this transition-state (TS_4) configuration, the C1−H3 bond distance is significantly decreased from 3.272 to 1.222 Å, as the O1−H3 and C1−C2 bond distances increase by 0.955 and 0.073 Å, respectively. The TS_4 transition state has its structure closer to that of Int_3 than to that of Ads_2

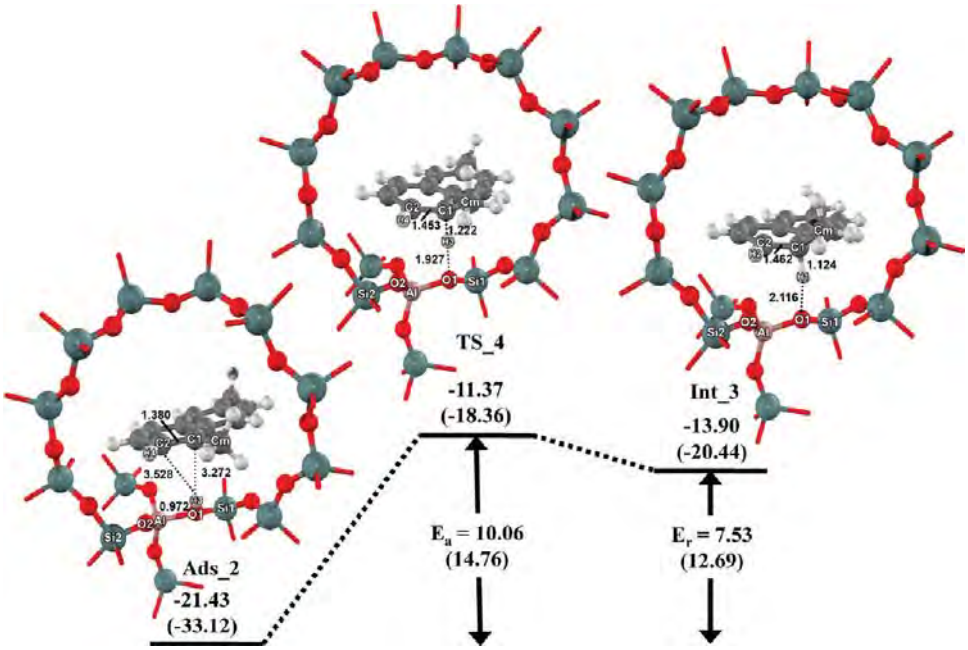


**Figure 7.** 120T M06-L/6-31G(d,p)//14T ONIOM(M06-L/6-31G(d,p):UFF) energy profile (kcal/mol) for the protonation step of the 1,6- to 2,6-DMN isomerization over H-$\beta$ zeolite. The sum of isolated 1,6-DMN and 120T zeolite cluster energies is taken as a reference. The values in parentheses are calculated at 14T ONIOM(M06-L/6-31G(d,p):UFF). Only DMN and the 14T active region are displayed.

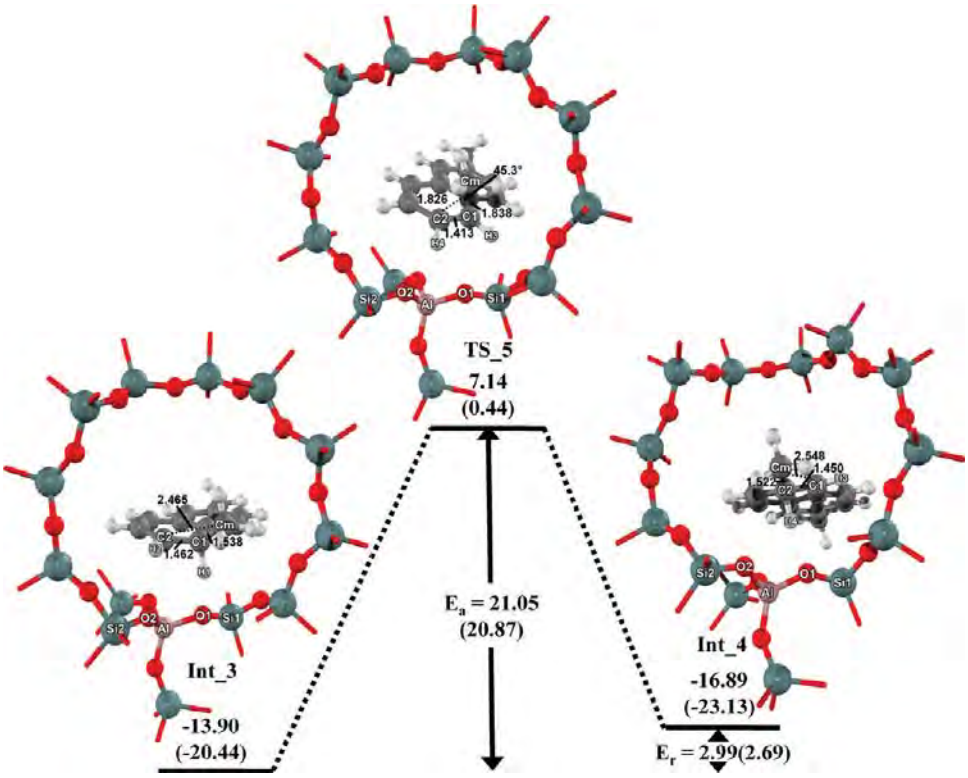


**Figure 8.** 120T M06-L/6-31G(d,p)//14T ONIOM(M06-L/6-31G(d,p):UFF) energy profile (kcal/mol) for the methyl shift step of the 1,6- to 2,6-DMN isomerization over H-$\beta$ zeolite.

(see Figure 7 and Table S5, Supporting Information). The activation energy for the protonation step is 10.06 kcal/mol, and the reaction energy is endothermic by 7.53 kcal/mol. In comparison with the protonation step in the earlier reaction, the protonation step of Ads_2 takes up less energy than that of Ads_1 because of the steric hindrance inside the zeolite of the two methyl groups at the α-positions of 1,5-DMN.[13]

***Methyl Shift Step of Protonated 1,6-DMN.*** The formation of the fourth intermediate (Int_4) via the intramolecular 1,2-methyl shift follows the protonation step. The optimized geometric parameters of all species in this step, Int_3, transition state (TS_5), and Int_4, are reported in Table S6 of the Supporting Information together with the reaction profile shown in Figure 8. This step shares common features with the methyl shift step of the 1,5- to 1,6-DMN isomerization. At the TS_5 transition state, the *Cm*−C1 distance increases from 1.538 to 1.838 Å, while the *Cm*−C2 distance decreases from 2.465 to 1.826 Å. The tricentric transition state also has a C1−C2 bond

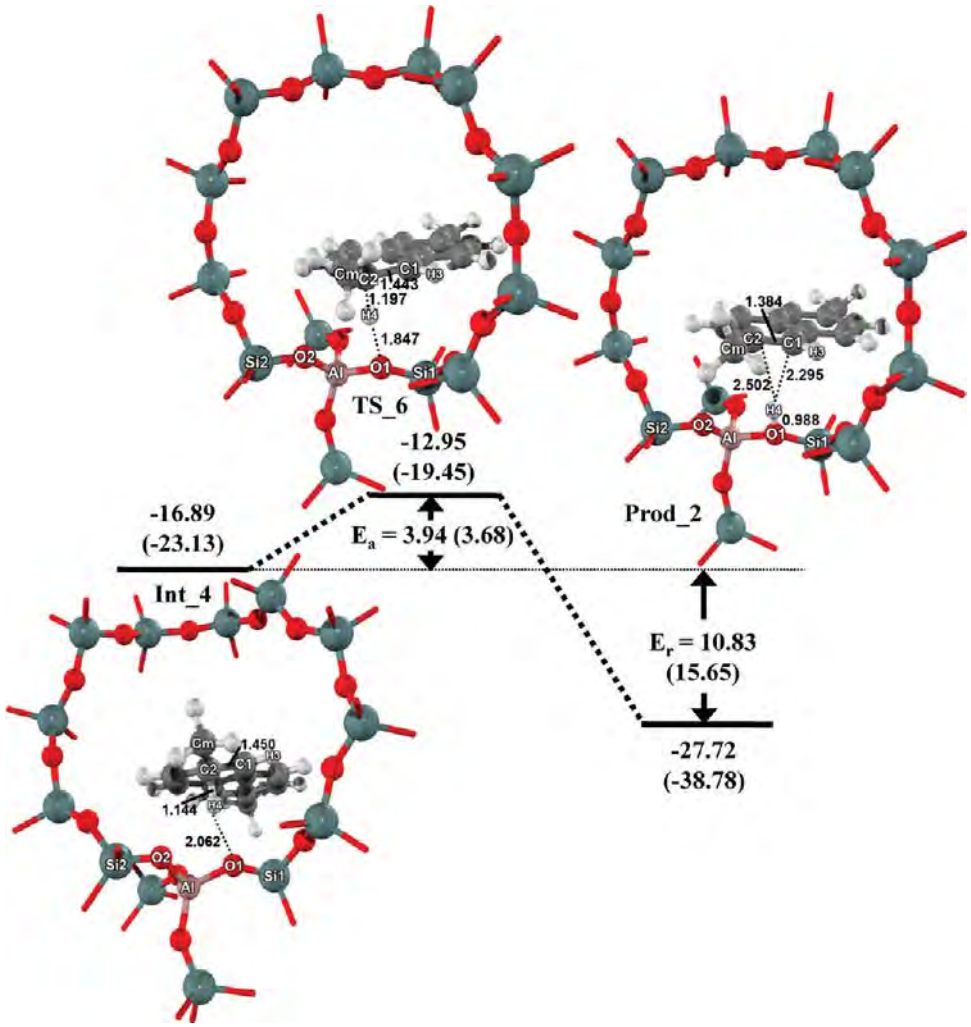


**Figure 9.** 120T M06-L/6-31G(d,p)//14T ONIOM(M06-L/6-31G(d,p):UFF) energy profile (kcal/mol) for the proton back-donation step of the 1,6- to 2,6-DMN isomerization over H-$\beta$ zeolite.

distance of 1.413 Å and a C1−*Cm*−C2 bond angle of 45.3°. Most of the structure constraints seen in this tight transition state are relieved when a $\sigma$-complex (Int_4) is formed.

The zeolitic structure is slightly changed when Int_4 is formed. The Al−O1 and Si1−O1 bond distances are incresed by 0.003 and 0.002 Å, while both Al−O2 and Si2−O2 bond distances decrease by 0.001 Å. The Si2−O2−Al bond angle increases by 0.5°, whereas the Si1−O1−Al bond angle decreases by 0.1°. The Int_4 structure has a binding energy of −16.89 kcal/mol; it is more stable than the Int_3 intermediate by 2.99 kcal/mol. The energy barrier for the methyl shift step is 21.05 kcal/mol. This is less than that of 25.69 kcal/mol of the 1,5 to 1,6-DMN isomerization. The reaction energy is exothermic by 2.99 kcal/mol. Although there is no report of an experimental activation energy for the 1,6- to 2,6-DMN reaction, the activation energy of 19.2 kcal/mol can be estimated from the experimental activation energy of the reverse 2,6- to 1,6-DMN reaction (20.1 kcal/mol).[11] Our activation energy agrees well with this estimated activation energy. Both experimental and theoretical results agree with the fact that the activation energy for the methyl shift step in 1,5- to 1,6-DMN is greater than that in 1,6- to 2,6-DMN.

***Proton Back-Donation to the Zeolite Framework.*** The proton is transferred back to the zeolite framework from protonated 2,6-DMN in this step. The optimized geometric parameters of species involved in this proton back-donation step are listed in Table S7 of the Supporting Information. The corresponding reaction profile is shown in Figure 9. In this step, a proton of Int_4 is transferred back to a zeolite-bridging oxygen (O1) at the acid site, hence leading to the adsorbed 2,6-DMN (Prod_2). This differs from the data obtained in the 1,5- to 1,6-DMN isomerization. The energy profile indicates that this proton back-donation step is very fast. The calculated activation energy in this second isomerization process is 3.94 kcal/mol, which is greater than that in the first isomerization. This proton back-donation step releases an energy of 10.83 kcal/mol. With reference to the Int_4 configuration, this proton back-donation step does not perturb the zeolite structure significantly. The Al−O1, Si1−O1, and Si2−O2 bond lengths increase by 0.106, 0.082, and 0.011 Å, respectively. The Al−O2 bond length and the Si1−O1−Al and Si2−O2−Al bond angles decrease by 0.027 Å, 0.6°, and 4.0°, respectively. For the geometry of 2,6-DMN, the C2−H4 distance increases from 1.144 to 2.502 Å, indicating C2−H4 bond breaking and O1−H4 bond formation. The O1−H4 bond length is now 0.988 Å. The C1−C2 bond shows double bond character as supported by the reduced bond length of 1.384 Å from 1.450 Å. The 2,6-DMN is now in the adsorbed state with the Brønsted acid site. The adsorbed 2,6-DMN product is subsequently separated from the framework by a desorption energy of 27.48 kcal/mol.

For convenient discussion, the energetic profiles for the overall steps of the 1,6- to 2,6-DMN isomerization are sum-

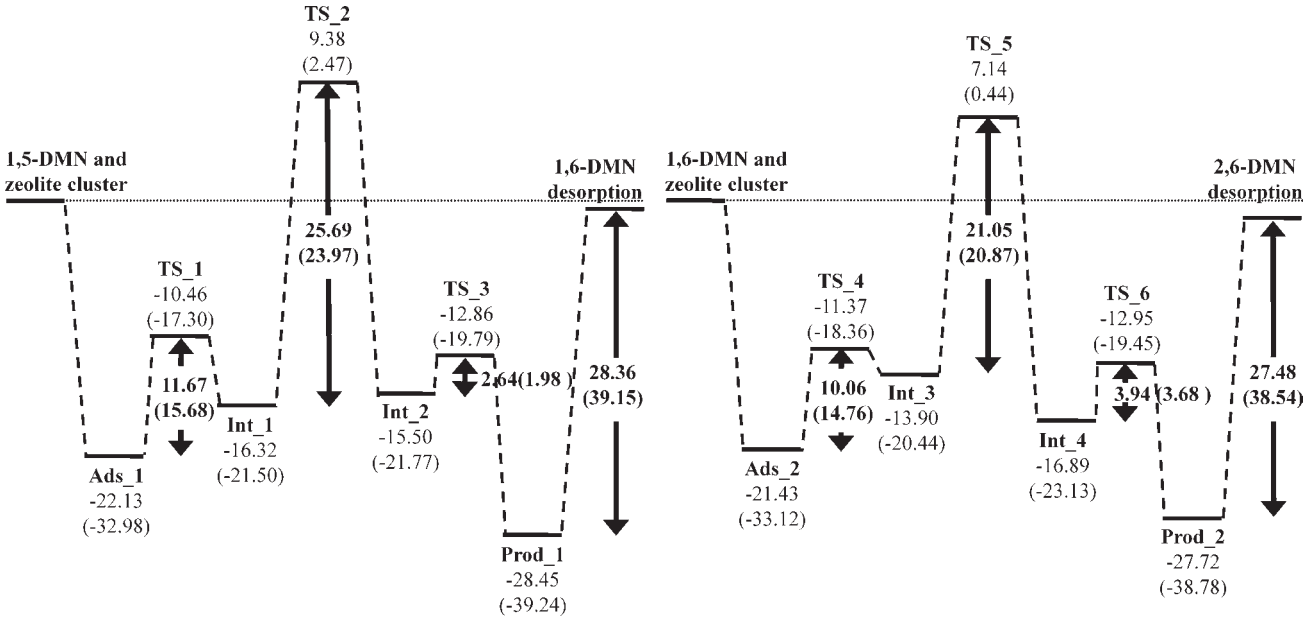


**Figure 10.** Summary of the overall 120T M06-L/6-31G(d,p)//14T ONIOM(M06-L/6-31G(d,p):UFF) energy profile (kcal/mol) of the (a) 1,5- into 1,6-DMN and (b) 1,6- into 2,6-DMN isomerizations over H-$\beta$ zeolite. The values in parentheses are calculated at 14T ONIOM(M06-L/6-31G(d,p):UFF).



marized in Figure 10b (see also Table 1). The reaction starts with 1,6-DMN adsorbed on the acidic proton of zeolite (Ads_2). The subsequent step is the protonation to form the Int_3 intermediate with an activation barrier of 10.06 kcal/mol. The following step is the 1,2-methyl shift within bonded C−C atoms, leading to Int_4 with an energy barrier of 21.05 kcal/mol. This is followed by the proton back-donation step to generate the adsorbed 2,6-DMN product (Prod_2) with a rather low reaction barrier of 3.94 kcal/mol. The methyl shift step is considered to be the rate-determining step for the 1,6- to 2,6-DMN isomerization. This finding corresponds well with the work of Suld and Stuart.[11]

Comparison between the complete energy profiles of the 1,5- to 1,6-DMN and subsequent 1,6- to 2,6-DMN isomerization reactions can be made with the data from Figure 10 and Table 1. The methyl migration step is the rate-determining step in both reactions. The activation energy of the 1,5- to 1,6-DMN reaction is 25.69 kcal/mol, which is greater than the 21.05 kcal/mol energy of the 1,6- to 2,6-DMN reaction. This suggests that, for successive 1,5- to 1,6-DMN and 1,6- to 2,6-DMN reactions, the former isomerization reaction takes place more slowly than in the latter. This conclusion is in line with the thermodynamic view observed by Kraikul et al. that the 1,6-DMN to 2,6-DMN isomerization occurs rapidly with a higher isomerization rate.[6]

These results agree with the observation that the catalytic 1,5- to 1,6-DMN isomerization over H-$\beta$ zeolite is the kinetically limiting step for the production of 2,6-DMN from 1,5-DMN. Under a thermodynamic condition as performed by Kraikul et al., the ratio of 2,6-DMN to 1,6-DMN product can be rationalized from the Boltzmann distribution of the two species. Our M06-L/6-31G(d,p) calculation indicates that the 2,6-DMN:1,6-DMN ratio is greater than 1, which agrees with the experimental observation that 2,6-DMN is obtained in a higher percentage than 1,6-DMN.[6] Although only the 14T cluster representing the active site of zeolite and the adsorbate are allowed to relax in this 120T M06-L/6-31G(d,p)//14T ONIOM(M06-L/6-31G(d,p):UFF) model, the energetic information of the isomerization reaction such as the adsorption energies and the activation energies are rational and compared well with experimental data reports in the literature.[6,9,11,13,51,52]

## Conclusion

The isomerization of 1,5-DMN into 2,6-DMN over the acidic $\beta$ zeolite is investigated at the molecular level by using the 120T M06-L/6-31G(d,p)//14T ONIOM(M06-L/6-31G(d,p):UFF) method. The isomerization reaction involves two consecutive methyl shift processes through the conversion of 1,5- into 1,6-DMN and of 1,6- into 2,6- DMN, respectively. The reaction mechanism begins with the adsorption of the reactant on a Brønsted acid site of the $\beta$ zeolite followed by the protonation, 1,2-methyl shift, and proton back-donation steps and the product desorption. The methyl shift is shown to be the rate-determining step, with the 1,5- to 1,6-DMN isomerization reaction having a greater activation barrier than the 1,6- to 2,6-DMN reaction (25.69 vs 21.05 kcal/mol). The predicted activation barriers are in agreement with the available experimental data. Under thermodynamic control, 2,6-DMN is expected to be the main product of the isomerization reaction.

The present work is another successful example for the ONIOM approach, with proper selection of each layer that can be used to study the chemical reaction catalyzed by acidic zeolite. The M06-L/6-31G(d,p)//ONIOM(M06-L/6-31G(d,p):UFF) method of the 120T cluster is recommended to be used as an accurate and practical model to explore the structure, adsorption, and reaction mechanisms of $\beta$ zeolite.

**Acknowledgment.** This work was supported in part by grants from the National Science and Technology Development Agency (NSTDA Chair Professor and NANOTEC Center of Excellence), the Thailand Research Fund, the Kasetsart University Research and Development Institute (KURDI), and the Commission on Higher Education, Ministry of Education, under the Postgraduate Education and Research Programs in Petroleum and Petrochemicals and Advanced Materials as well as the Sandwich Program (Grant CHE-PhD-SW-INDV to C.K.). We are grateful to Donald G. Truhlar and Yan Zhao for supporting us with the M06-L functional.

**Supporting Information Available:** Table S1 containing substituent values (*S* values) and their differences between the

real and model systems at the M06-L/6-31G(d,p) and UFF levels for the partitioning schemes in the isomerization of 1,5- to 2,6-DMN on H-$\beta$ zeolite and Tables S2−S7 giving the selected geometric parameters for the mechanistic investigation on 1,5- to 2,6-dimethylnaphthalene isomerization catalyzed by acidic $\beta$ zeolite. This material is available free of charge via the Internet at http://pubs.acs.org.

## References and Notes


(1) Pu, S. B.; Inui, T. *Appl. Catal., A* **1996**, *146*, 305.
(2) Lillwitz, L. D. *Appl. Catal., A* **2001**, *221*, 337.
(3) *2,6-Dimethylnaphthalene (2,6-DMN)*; ChemSystems Report 99/00S7; Nexant: White Plains, NY, 2000.
(4) Song, C. *CATTECH* **2002**, *6*, 64.
(5) Tanabe, K.; Holderich, W. F. *Appl. Catal., A* **1999**, *181*, 399.
(6) Kraikul, N.; Rangsunvigit, P.; Kulprathipanja, S. *Chem. Eng. J.* **2005**, *114*, 73.
(7) Kraikul, N.; Rangsunvigit, P.; Kulprathipanja, S. *Appl. Catal., A* **2006**, *312*, 102.
(8) Ferino, I.; Monaci, R.; Pedditzi, L.; Rombi, E.; Solinas, V. *React. Kinet. Catal. Lett.* **1996**, *58*, 307.
(9) McCaulay, D. A.; Lien, A. P. *J. Am. Chem. Soc.* **1952**, *74*, 6246.
(10) Kilpatrick, M.; Bett, J. A. S.; Kilpatrick, M. L. *J. Am. Chem. Soc.* **1963**, *85*, 1038.
(11) Suld, G.; Stuart, A. P. *J. Org. Chem.* **1964**, *29*, 2939.
(12) Glaeser, R.; Li, R.; Hunger, M.; Ernst, S.; Weitkamp, J. *Catal. Lett.* **1998**, *50*, 141.
(13) Millini, R.; Frigerio, F.; Bellussi, G.; Pazzuconi, G.; Perego, C.; Pollesel, P.; Romano, U. *J. Catal.* **2003**, *217*, 298.
(14) Dykstra, C. E.; Frenking, G.; Kim, K. S.; Scuseria, G. *Theory and Applications of Computational Chemistry*; Elsevier: New York, 2005.
(15) van Santen, R. A.; Neurock, M. *Molecular Heterogeneous Catalysis*; Wiley-VCH: New York, 2006.
(16) Braendle, M.; Sauer, J. *J. Am. Chem. Soc.* **1998**, *120*, 1556.
(17) Hillier, I. H. *J. Mol. Struct.: THEOCHEM* **1999**, *463*, 45.
(18) Limtrakul, J.; Jungsuttiwong, S.; Khongpracha, P. *J. Mol. Struct.: THEOCHEM* **2000**, *525*, 153.
(19) Khaliullin, R. Z.; Bell, A. T. *J. Phys. Chem. A* **2001**, *105*, 10454.
(20) Limtrakul, J.; Nanok, T.; Khongpracha, P.; Jungsuttiwong, S.; Truong, T. N. *Chem. Phys. Lett.* **2001**, *349*, 161.
(21) Maseras, F.; Morokuma, K. *J. Comput. Chem.* **1995**, *16*, 1170.
(22) Humbel, S.; Sieber, S.; Morokuma, K. *J. Chem. Phys.* **1996**, *105*, 1959.
(23) Matsubara, T.; Sieber, S.; Morokuma, K. *Int. J. Quantum Chem.* **1996**, *60*, 1101.
(24) Svensson, M.; Humbel, S.; Froese, R. D. J.; Matsubara, T.; Sieber, S.; Morokuma, K. *J. Phys. Chem.* **1996**, *100*, 19357.
(25) Svensson, M.; Humbel, S.; Froese, R. D. J.; Matsubara, T.; Sieber, S.; Morokuma, K. *J. Chem. Phys.* **1996**, *105*, 3654.
(26) Dapprich, S.; Komaromi, I.; Byun, K. S.; Morokuma, K.; Frisch, M. J. *J. Mol. Struct.: THEOCHEM* **1999**, *461*, 1.
(27) Vreven, T.; Morokuma, K. *J. Comput. Chem.* **2000**, *21*, 1419.
(28) Bobuatong, K.; Limtrakul, J. *Appl. Catal., A* **2003**, *253*, 49.
(29) Panjan, W.; Limtrakul, J. *J. Mol. Struct.: THEOCHEM* **2003**, *654*, 35.
(30) Raksakoon, C.; Limtrakul, J. *J. Mol. Struct.: THEOCHEM* **2003**, *631*, 147.
(31) Namuangruk, S.; Pantu, P.; Limtrakul, J. *J. Catal.* **2004**, *225*, 523.
(32) Sirijaraensre, J.; Truong, T. N.; Limtrakul, J. *J. Phys. Chem. B* **2005**, *109*, 12099.
(33) Namuangruk, S.; Khongpracha, P.; Pantu, P.; Limtrakul, J. *J. Phys. Chem. B* **2006**, *110*, 25950.
(34) Jansang, B.; Nanok, T.; Limtrakul, J. *J. Phys. Chem. B* **2006**, *110*, 12626.
(35) Panyaburapa, W.; Nanok, T.; Limtrakul, J. *J. Phys. Chem. C* **2007**, *111*, 3433.
(36) Pantu, P.; Boekfa, B.; Limtrakul, J. *J. Mol. Catal. A* **2007**, *277*, 171.
(37) Jansang, B.; Nanok, T.; Limtrakul, J. *J. Phys. Chem. C* **2008**, *112*, 540.
(38) Maihom, T.; Namuangruk, S.; Nanok, T.; Limtrakul, J. *J. Phys. Chem. C* **2008**, *112*, 12914.
(39) Zhao, Y.; Truhlar, D. G. *J. Chem. Phys.* **2006**, *125*, 194101.
(40) Zhao, Y.; Truhlar, D. G. *Acc. Chem. Res.* **2008**, *41*, 157.
(41) Zhao, Y.; Truhlar, D. G. *Theor. Chem. Acc.* **2008**, *120*, 215.
(42) Frisch, M. J.; Trucks, G. W.; Schlegel, H. B.; Scuseria, G. E.; Robb, M. A.; Cheeseman, J. R.; Montgomery, J. J. A.; Vreven, T.; Kudin, K. N.; Burant, J. C.; Millam, J. M.; Iyengar, S. S.; Tomasi, J.; Barone, V.; Mennucci, B.; Cossi, M.; Scalmani, G.; Rega, N.; Petersson, G. A.; Nakatsuji, H.; Hada, M.; Ehara, M.; Toyota, K.; Fukuda, R.; Hasegawa, J.; Ishida, M.; Nakajima, T.; Honda, Y.; Kitao, O.; Nakai, H.; Klene, M.; Li, X.; Knox, J. E.; Hratchian, H. P.; Cross, J. B.; Bakken, V.; Adamo, C.; Jaramillo, J.; Gomperts, R.; Stratmann, R. E.; Yazyev, O.; Austin, A. J.; Cammi, R.; Pomelli, C.; Ochterski, J. W.; Ayala, P. Y.; Morokuma, K.; Voth, G. A.; Salvador, P.; Dannenberg, J. J.; Zakrzewski, V. G.; Dapprich, S.; Daniels, A. D.; Strain, M. C.; Farkas, O.; Malick, D. K.; Rabuck, A. D.; Raghavachari, K.; Foresman, J. B.; Ortiz, J. V.; Cui, Q.; Baboul, A. G.; Clifford, S.; Cioslowski, J.; Stefanov, B. B.; Liu, G.; Liashenko, A.; Piskorz, P.; Komaromi, I.; Martin, R. L.; Fox, D. J.; Keith, T.; Al-Laham, M. A.; Peng, C. Y.; Nanayakkara, A.; Challacombe, M.; Gill, P. M. W.; Johnson, B.; Chen, W.; Wong, M. W.; Gonzalez, C.; Pople, J. A. *Gaussian 03*, revision C.02; Gaussian, Inc.: Wallingford, CT, 2004.
(43) de Vries, A. H.; Sherwood, P.; Collins, S. J.; Rigby, A. M.; Rigutto, M.; Kramer, G. J. *J. Phys. Chem. B* **1999**, *103*, 6133.
(44) Rungsirisakun, R.; Jansang, B.; Pantu, P.; Limtrakul, J. *J. Mol. Struct.: THEOCHEM* **2005**, *733*, 239.
(45) Derouane, E. G.; Chang, C. D. *Microporous Mesoporous Mater.* **2000**, *35*, 425–36.
(46) Pelmenschikov, A.; Leszczynski, J. *J. Phys. Chem. B* **1999**, *103*, 6886.
(47) Clark, L. A.; Sierka, M.; Sauer, J. *J. Am. Chem. Soc.* **2003**, *125*, 2136.
(48) Rozanska, X.; van Santen, R. A.; Hutschka, F.; Hafner, J. *J. Am. Chem. Soc.* **2001**, *123*, 7655.
(49) Boekfa, B.; Choomwattana, S.; Maitarad, P.; Limtrakul, P.; Limtrakul, J. *NSTI-Nanotech 2009* **2009**, *3*, 268.
(50) Morokuma, K. *Bull. Korean Chem. Soc.* **2003**, *24*, 797.
(51) Ruthven, D. M.; Goddard, M. *Zeolites* **1986**, *6*, 275.
(52) Barthomeuf, D.; Ha, B. H. *J. Chem. Soc., Faraday Trans.* **1973**, *69*, 2158.


JP904098T

Langmuir
Article
pubs.acs.org/Langmuir


# Effects of the Zeolite Framework on the Adsorptions and Hydrogen-Exchange Reactions of Unsaturated Aliphatic, Aromatic, and Heterocyclic Compounds in ZSM-5 Zeolite: A Combination of Perturbation Theory (MP2) and a Newly Developed Density Functional Theory (M06-2X) in ONIOM Scheme

Bundet Boekfa,[†,‡,§] Saowapak Choomwattana,[†,‡,§] Pipat Khongpracha,[†,‡,§] and Jumras Limtrakul*[,†,‡,§]

[†]*Laboratory for Computational and Applied Chemistry, Chemistry Department, Faculty of Science, Kasetsart University, Bangkok 10900, Thailand,* [‡]*Center of Nanotechnology, Kasetsart University Research and Development Institute, Kasetsart University, Bangkok 10900, Thailand, and* [§]*NANOTEC Center of Excellence, National Nanotechnology Center, Bangkok 10900, Thailand*

*Received May 22, 2009. Revised Manuscript Received July 10, 2009*

The confinement effect on the adsorption and reaction mechanism of unsaturated aliphatic, aromatic and heterocyclic compounds on H-ZSM-5 zeolite has been investigated by the four ONIOM methods (MP2:M06-2X), (MP2:B3LYP), (MP2:HF), and (MP2:UFF). The H-ZSM-5 'nanoreactor' porous intersection, where chemical reactions take place, is represented by a quantum cluster of 34 tetrahedral units. Ethene, benzene, ethylbenzene, and pyridine are chosen to represent reactions of various adsorbates of aliphatic, aromatic and heterocyclic compounds. Among the four combined methods, (MP2:M06-2X) outperforms the others. The results confirm that the method that takes weak interactions, especially the van der Waals interaction, into account is essential for describing the confinement effect from the zeolite framework. The effects of the infinite zeolitic framework on the cluster model are also included by a set of point charges generated by the embedded ONIOM model. The energies for the adsorption of ethene, benzene, ethylbenzene, and pyridine on H-ZSM-5 from an embedded ONIOM(MP2:M06-2X) calculation are predicted to be −14.0, −19.8, −24.7, and −48.4 kcal/mol, respectively, which are very close to available experimental observations. The adsorption energy of pyridine agrees well with the experiment data of −47.6 kcal/mol. We also applied the same computational methodology on the systematic investigation of the H/H exchange reaction of benzene and ethylbenzene with the acidic H-ZSM-5 zeolite. The H/H exchange reaction was found to take place in a single concerted step. The calculated apparent activation energies for benzene and ethylbenzene are 12.6 and 4.9 kcal/mol, which can be compared to the experimental estimates of 11.0 and 6.9 kcal/mol, respectively. The confinement effect of the extended zeolite framework has been clearly demonstrated not only to stabilize the adsorption complexes but also to improve their corresponding activation energies to approach the experimental benchmark.

## 1. Introduction

Zeolite, one of the industrially important microporous catalysts, is of great interest for its range of applications in adsorption and separation, particularly for catalysis. One of the most notable catalyst zeolites for modern petrochemical processes is ZSM-5. With its size- and shape-selectivity, thermal stability and the ability of ion-exchange, ZSM-5 is the catalyst of choice for important hydrocarbon reactions such as cracking, isomerization, and oligomerization.[1−8]

Theoretical study can offer a practical tool that provides clear insight to the reaction mechanism complementing experimental investigations or, in certain cases, offering an understanding that is not possible by experimental investigations. Most of the theoretical studies of chemical reactions on heterogeneous catalysts are based on the use of wave function methods and density functional theory (DFT). Wave function methods, especially post-Hartree−Fock methods such as configuration interaction, coupled cluster, and Møller−Plesset perturbation theory, certainly give accurate results. However, the high accuracy comes with the price of higher computational cost. DFT has gained increasing interest by providing good predictions of important properties for a wide range of applications in chemistry with a lower required computational demand. However, the conventional DFT functionals are not able to properly describe van der Waals effects, which are very important in the interactions of host/guest systems. The selection of the functional in DFT is crucial for correctly exploring the properties and reaction mechanisms of chemical reactions. Considerable effort has been invested to overcome this severe deficiency of DFT. Grimme[9] has proposed a new semiempirical functional by introducing atom-pairwise dispersion corrections to the generalized gradient

*Corresponding author.

(1) Smit, B.; Maesen, T. L. M. *Nature* (*London, U. K.*) **2008**, *451*, 671.
(2) Bhan, A.; Iglesia, E. *Acc. Chem. Res.* **2008**, *41*, 559.
(3) Luzgin, M. V.; Rogov, V. A.; Arzumanov, S. S.; Toktarev, A. V.; Stepanov, A. G.; Parmon, V. N. *Angew. Chem., Int. Ed.* **2008**, *47*, 4559.
(4) Corma, A. *J. Catal.* **2003**, *216*, 298.
(5) Chen, C. S. H.; Bridger, R. F. *J. Catal.* **1996**, *161*, 687.
(6) Yaluris, G.; Rekoske, J. E.; Aparicio, L. M.; Madon, R. J.; Dumesic, J. A. *J. Catal.* **1995**, *153*, 65.
(7) Andy, P.; Gnep, N. S.; Guisnet, M.; Benazzi, E.; Travers, C. *J. Catal.* **1998**, *173*, 322.
(8) Venuto, P. B. *Microporous Mater.* **1994**, *2*, 297.
(9) Grimme, S. *J. Comput. Chem.* **2006**, *27*, 1787.

approximation (GGA) part of the B97 functional. Zhao and Truhlar[10−13] have recently developed the M06 family of local (M06-L) and hybrid (M06, M06-2X) meta-GGA functionals that show promising performance for studying main group thermochemistry, kinetics, noncovalent interactions, excited states, and transition elements.

Nevertheless, zeolites that have high impacts in industrial processes usually possess hundreds of atoms per unit cell, making the use of sophisticated methods, such as periodic ab initio calculations, computationally too expensive and even impractical when very large zeolites are concerned. Therefore, the electronic properties of zeolites are usually modeled with quantum chemical methods for relatively small clusters where only the most important part of the zeolites is focused on.[14−19] Such limited models do not take into account the effect of the framework, which can significantly change the structure and energetics of the system and has been shown to lead to discrepancies between the cluster results and the actual zeolite behaviors.[20,21]

The confinement effect was proposed to explain the interactions between the zeolite framework and the adsorbed molecule, which is confined within the pore of the zeolite.[22,23] The confinement effects play an important role on the sorption and catalytic properties of zeolites by stabilizing adsorbed molecules, intermediates, and reaction transition states. The quantum mechanics/molecular mechanics (QM/MM) scheme was successfully applied to study the interactions and reactions of hydrocarbon molecules on zeolites.[14−19] Those calculated adsorption and activation energies are very close to the available experimental benchmarks. One of the successful combined approaches in our previous works is the ONIOM(B3LYP:UFF). This method usually gives surprisingly good results for studying systems in which confinement effects play a significant role on adsorptions and reactions in the zeolite pore.[16] However, it is due to the fact that the overestimated van der Waals interactions represented by the universal force field compensate for the weak interactions from small quantum cluster calculations treated by the B3LYP method. One could expect worse results by increasing the size of the quantum cluster. In order to avoid these unfavorable errors, we have to find another method that is more reliable and also economically viable for studying the chemistry of zeolites.

We performed the quantum chemical calculation to study (1) the adsorption of chosen molecules not only to represent various industrially important hydrocarbons and heterocyclic compounds, but also because they are known to be common failures for conventional DFT calculations: unsaturated aliphatic (ethene), aromatics (benzene and ethylbenzene), and heterocycles (pyridine) and (2) the hydrogen exchange reaction of aromatics (benzene and ethylbenzene). The hydrogen exchange is chosen because of its simplicity; it consists of a single concerted step, and

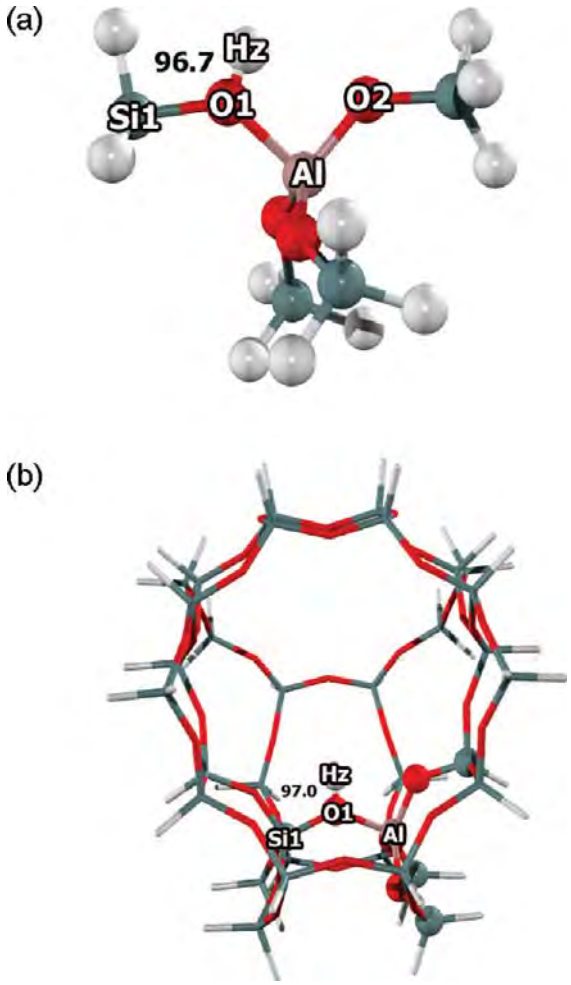


**Figure 1.** Presentation of H-ZSM-5 models in different sizes: (a) 5T quantum cluster and (b) 5T:34T ONIOM model. Atoms treated with the MP2 level of theory are shown in balls, whereas the area treated with a lower level of calculation is symbolized with wireframes.

the availability of experimental data. To investigate the confinement effect, the ONIOM scheme on the widely used 34T model was chosen specifically. The active site is calculated with the MP2 method, whereas the outer part is treated with different approaches: M06-2X, B3LYP, HF methods and UFF force field. The discrepancy between the benchmark of experimental data and our calculated results in the adsorption and reaction energies of probe molecules are discussed below.

## 2. Method

The adsorption and reaction of ethene, benzene, ethylbenzene, and pyridine on H-ZSM-5 have been initially studied with a five tetrahedral unit (5T) model. The Al atom is selected to substitute a Si atom at the T12 position, which is the most energetically favored position.[15,17,19] Afterward, the zeolite framework is expanded to become the 34T quantum cluster ($AlSi_{33}O_{46}H_{45}$) to cover the so-called "nanocavity", which is the intersection between straight and zigzag channels. For computational cost efficiency, the ONIOM scheme[24] is applied on this 34T model. The 5T quantum region of the Brønsted acid site, illustrated in Figure 1a, is assigned to be the inner layer, whereas the extended

(10) Zhao, Y.; Schultz, N. E.; Truhlar, D. G. *J. Chem. Theory Comput.* **2006**, *2*, 364.
(11) Zhao, Y.; Truhlar, D. G. *Theor. Chem. Acc.* **2008**, *120*, 215.
(12) Zhao, Y.; Truhlar, D. G. *Acc. Chem. Res.* **2008**, *41*, 157.
(13) Zhao, Y.; Truhlar, D. G. *J. Phys. Chem. C* **2008**, *112*, 6860.
(14) Kasuriya, S.; Namuangruk, S.; Treesukol, P.; Tirtowidjojo, M.; Limtrakul, J. *J. Catal.* **2003**, *219*, 320.
(15) Lomratsiri, J.; Probst, M.; Limtrakul, J. *J. Mol. Graphics Modell.* **2006**, *25*, 219.
(16) Pantu, P.; Boekfa, B.; Limtrakul, J. *J. Mol. Catal. A: Chem.* **2007**, *277*, 171.
(17) Raksakoon, C.; Limtrakul, J. *THEOCHEM* **2003**, *631*, 147.
(18) Namuangruk, S.; Pantu, P.; Limtrakul, J. *ChemPhysChem* **2005**, *6*, 1333.
(19) Panjan, W.; Limtrakul, J. *J. Mol. Struct.* **2003**, *654*, 35.
(20) Sinclair, P. E.; de Vries, A.; Sherwood, P.; Catlow, C. R. A.; van Santen, R. A. *J. Chem. Soc., Faraday Trans.* **1998**, *94*, 3401.
(21) Braendle, M.; Sauer, J. *J. Am. Chem. Soc.* **1998**, *120*, 1556.
(22) Derouane, E. G. *J. Mol. Catal. A Chem.* **1998**, *134*, 29.
(23) Zicovich-Wilson, C. M.; Corma, A.; Viruela, P. *J. Phys. Chem.* **1994**, *98*, 10863.
(24) Dapprich, S.; Komiromi, I.; Byun, K. S.; Morokuma, K.; Frisch, M. J. *THEOCHEM* **1999**, *461−462*, 1.

34T model is the outer layer. Only the active region ($AlSi_4O_4H$) and the probe molecule are allowed to relax while the rest is kept fixed with the crystallographic structure.[25] The various combinations of methods for the ONIOM scheme are compared to find the best approach for the best prediction. The full quantum calculation of the 5T inner layer of the ONIOM model is optimized with the MP2 method. A lower level of calculation for the outer layer is varied with M06-2X, B3LYP, HF, and UFF approaches. Therefore, the four combined ONIOM schemes, (MP2:M06-2X), (MP2:B3LYP), (MP2:HF), and (MP2:UFF) methods, are compared. All geometry optimizations in each method were performed by using the 6-31G(d,p) basis set. Curtiss et al. reported the close agreement between the adsorption results of MP2/6-31G(d,p) and the more accurate G2(MP2, SVP) [effectively QCISD(T)/6-311+G(3df,2p)+ ZPVE] for the adsorption complex of ethane and small 3T and 5T clusters of zeolite, which appears to be a cancellation of the high level effects: correlation, basis set and zero-point energies.[26,27] Thus, the MP2/6-31G(d,p) adsorption energy may be reasonably reliable. To obtain more reliable interaction energies, the single-point energy calculations at the 5T quantum cluster with the MP2/6-311+G(2df,2p)//MP2/6-31G(d,p) level and the 5T:34T with the ONIOM(MP2/6-311+G(2df,2p):M06−2X/6-31G(d,p)//MP2/6-31G(d,p):M06−2X/6-31G(d,p)) method are carried out. However, the long-range effects from the extended framework that is neglected in any truncated finite quantum cluster are essential for exploring adsorption and reaction properties in the zeolite systems. We have also incorporated the long-range electrostatic potential from the infinite zeolite lattice to our systems by performing single-point calculations with the electronic embedding approach. The Madelung potential from the extended lattice is reproduced by well-calibrated point charges enclosed around the 34T quantum cluster.[28−31] The ONIOM and optimized point charges embedded method called the embedded-ONIOM (e-ONIOM) approach has been successfully applied to predict adsorptions and reaction mechanisms in several zeolite systems.[15,30−34] All calculations were carried out using the Gaussian 03 program[35] incorporated with the Minnesota Density Functionals module 3.1 by Zhao and Truhlar.

## 3. Results and Discussion

**3.1. Molecular Cluster and Nanocluster Models of Zeolites.** Before giving details on the molecular adsorptions of our chosen adsorbates, we first clarify how the Brønsted acid in H-ZSM-5 is modeled. It is known that the proton can reside on any of the four nonequivalent neighboring oxygen atoms at a given Al T-site.[36] From the total of 96 tetrahedral centers and 12 topologically distinct sites in a unit cell of ZSM-5, T12 is found to be the most favored for an aluminum (Al) substitution.[37] One proton, known as Brønsted acid, is required to compensate the charge of the Al-substituted framework. From the Al position, the proton then points to the 10T ring, thus providing a catalytic cavity for acid-mediated reactions.[17,38,39] The Brønsted active site is therefore chemically composed of $AlSi_4O_4H_{13}$, called a 5T cluster, illustrated in Figure 1a. The zeolite model is further expanded to represent the more realistic system, i.e., the 34T cluster for the components of zigzag and straight channels connected with the intersection, shown in Figure 1b. With the extended framework, dominant interactions for adsorbate molecules can be taken into account. From our previous studies,[17,19] the adsorption site for small molecules such as ethene is in the zigzag channel, whereas a larger molecule such as benzene is generally located at the intersection of the channel system.

For our theoretical study of the effects of the framework on the adsorption and H/H exchange of hydrocarbons on the nanostructured zeolite, we evaluate the method combined into the ONIOM scheme to find the approach that gives the best prediction. The quantum calculation of the 5T cluster optimized with the MP2 method is performed to analyze the energy contribution from the high level of calculation in ONIOM schemes with four combined computational methods: (MP2:M06-2X), (MP2:B3LYP), (MP2:HF), and (MP2:UFF).

From the bare H-ZSM-5, the optimized structural parameters of the 5T cluster and ONIOM model with different approaches [the (MP2:M06-2X), (MP2:B3LYP), (MP2:HF), and (MP2:UFF) methods] are listed in Table S1 in the Supporting Information. It is found that a different lower level of calculation leads to a different result on the acidity of the zeolite active site. As was expected, the 5T cluster gives an underestimated Brønsted O1-Hz bond length of 96.7 pm, which is smaller than the value from all of the ONIOM approaches. The bond distance is predicted with the ONIOM methods to be in the range of 96.8−97.0 pm. The difference of those calculated bond lengths reveals the influence of the extended framework on the optimized structure and the effective reactivity of the acid site. In this case, the framework is found to enhance the acidity. To evaluate the quality of the method combination, the computed values of the Al···Hz distances are compared to the experimental observation (238.0−248.0 ± 4 pm).[40,41] The Al···Hz distance from the MP2:B3LYP (235.9 pm), MP2:HF (235.7 pm), and MP2:UFF (228.5 pm) ONIOM approaches are underestimated. The most comparable computed value is from the ONIOM(MP2:M06-2X) (236.4 pm) method.

**3.2. Adsorptions of Aliphatic (Ethene), Aromatic (Benzene, Ethylbenzene) and Heterocyclic Compounds (Pyridine) with H-ZSM-5.** Adsorption is one of the most important chemical

(25) Van Koningsveld, H.; Van Bekkum, H.; Jansen, J. C. *Acta Crystallogr., Sect. B: Struct. Sci.* **1987**, *B43*, 127.
(26) Curtiss, L. A.; Zygmunt, S. A.; Iton, L. E. *Proc. Int. Zeolite Conf., 12th* **1999**, *1*, 415.
(27) Zygmunt, S. A.; Curtiss, L. A.; Zapol, P.; Iton, L. E. *J. Phys. Chem. B* **2000**, *104*, 1944.
(28) Stefanovich, E. V.; Truong, T. N. *J. Chem. Phys.* **1996**, *104*, 2946.
(29) Allavena, M.; Seiti, K.; Kassab, E.; Ferenczy, G.; Angyan, J. G. *Chem. Phys. Lett.* **1990**, *168*, 461.
(30) Dungsrikaew, V.; Limtrakul, J.; Hermansson, K.; Probst, M. *Int. J. Quantum Chem.* **2003**, *96*, 17.
(31) Injan, N.; Pannorad, N.; Probst, M.; Limtrakul, J. *Int. J. Quantum Chem.* **2005**, *105*, 898.
(32) Boekfa, B.; Pantu, P.; Limtrakul, J. *J. Mol. Struct.* **2008**, *889*, 81.
(33) Maihom, T.; Boekfa, B.; Sirijaraensre, J.; Nanok, T.; Probst, M.; Limtrakul, J. *J. Phys. Chem. C* **2009**, *113*, 6654.
(34) Sirijaraensre, J.; Limtrakul, J. *Phys. Chem. Chem. Phys.* **2009**, *11*, 578.
(35) Frisch, M. J.; Trucks, G. W.; Schlegel, H. B.; Scuseria, G. E.; Robb, M. A.; Cheeseman, J. R.; Montgomery, J. A., Jr.; Vreven, T.; Kudin, K. N.; Burant, J. C.; Millam, J. M.; Iyengar, S. S.; Tomasi, J.; Barone, V.; Mennucci, B.; Cossi, M.; Scalmani, G.; Rega, N.; Petersson, G. A.; Nakatsuji, H.; Hada, M.; Ehara, M.; Toyota, K.; Fukuda, R.; Hasegawa, J.; Ishida, M.; Nakajima, T.; Honda, Y.; Kitao, O.; Nakai, H.; Klene, M.; Li, X.; Knox, J. E.; Hratchian, H. P.; Cross, J. B.; Adamo, C.; Jaramillo, J.; Gomperts, R.; Stratmann, R. E.; Yazyev, O.; Austin, A. J.; Cammi, R.; Pomelli, C.; Ochterski, J. W.; Ayala, P. Y.; Morokuma, K.; Voth, G. A.; Salvador, P.; Dannenberg, J. J.; Zakrzewski, V. G.; Dapprich, S.; Daniels, A. D.; Strain, M. C.; Farkas, O.; Malick, D. K.; Rabuck, A. D.; Raghavachari, K.; Foresman, J. B.; Ortiz, J. V.; Cui, Q.; Baboul, A. G.; Clifford, S.; Cioslowski, J.; Stefanov, B. B.; Liu, G.; Liashenko, A.; Piskorz, P.; Komaromi, I.; Martin, R. L.; Fox, D. J.; Keith, T.; Al-Laham, M. A.; Peng, C. Y.; Nanayakkara, A.; Challacombe, M.; Gill, P. M. W.; Johnson, B.; Chen, W.; Wong, M. W.; Gonzalez, C.; Pople, J. A. *Gaussian 03, revision B.05*; Gaussian, Inc.: Pittsburgh, PA, 2003.
(36) Derouane, E. G.; Fripiat, J. G. *J. Phys. Chem.* **1987**, *91*, 145.
(37) Lonsinger, S. R.; Chakraborty, A. K.; Theodorou, D. N.; Bell, A. T. *Catal. Lett.* **1991**, *11*, 209.
(38) Brand, H. V.; Curtiss, L. A.; Iton, L. E. *J. Phys. Chem.* **1993**, *97*, 12773.
(39) Simperler, A.; Bell, R. G.; Foster, M. D.; Gray, A. E.; Lewis, D. W.; Anderson, M. W. *J. Phys. Chem. B* **2004**, *108*, 7152.
(40) Klinowski, J. *Chem. Rev.* **1991**, *91*, 1459.
(41) Freude, D.; Klinowski, J.; Hamdan, H. *Chem. Phys. Lett.* **1988**, *149*, 355.

processes that lead to numerous chemical reactions. Ethene, the simplest molecule with $\pi$-bonding, thus representing intermolecular $\pi$ interaction, was studied to represent the unsaturated hydrocarbon adsorption. Benzene and ethylbenzene were chosen to study aromatic hydrocarbons adsorption on H-ZSM-5. Ethylbenzene was considered for the influence of the substitution on the aromatics adsorption. Finally, the acidity of the zeolite is observed with pyridine, which is known as the basic probe molecule.

*3.2.1. Unsaturated Hydrocarbon Adsorption: Ethene*. The ethene molecule weakly adsorbs over the Brønsted acid site forming a $\pi$-adsorption complex. The ONIOM(MP2:M06-2X) optimized structure of the adsorption is illustrated in Figure 2. The key geometrical parameters of the adsorption complexes are shown in Table S2 in the Supporting Information. Almost symmetrical distances between Hz···C1 (218.8 pm) and Hz···C2 (218.1 pm) can be found in the optimized 5T adsorption complex. When the framework is extended to be the 34T in the ONIOM scheme, the unsymmetrical impact on the Hz···C distance from the framework is observed (216.3 pm vs 220.5 pm). In all models, the structures of Brønsted acid sites and the ethene molecule have little perturbation upon the adsorption. Focusing on the O−Hz parameter, the acid bond length is elongated during the adsorption, corresponding with the slightly elongated C1═C2 bond of ethene, from 133.5 to 134.3 pm. From the MP2 optimization for the 5T model, the O−Hz distance was extended from 96.7 to 98.1 pm. The structural change from other methods is found to have the same trend.

As for the MP2 calculation on the 5T quantum cluster, the predicted adsorption energy is just −8.7 kcal/mol. The values from the ONIOM scheme are −13.3, −10.5, −10.4, and −16.6 kcal/mol for ONIOM(MP2:M06-2X), (MP2:B3LYP), (MP2:HF) and (MP2:UFF) methods, respectively. Due to the lack of information for ethene adsorption on H-ZSM-5 zeolite, we select the ethene adsorption on H-FAU zeolite to make a validation for our calculated values. Ethene adsorbs on H-FAU with the adsorption energy of −9.0 kcal/mol.[42] It is known that the acidity of H-ZSM-5 is higher than that of H-FAU. The interaction energy of ethene on H-ZSM-5 is expected to be stronger than that on H-FAU and should be greater than a value of 10 kcal/mol. Since then, the (MP2:M06-2X) and (MP2:UFF) methods are found to give reasonable results.

*3.2.2. The Aromatic Hydrocarbon Adsorption: Benzene and Ethylbenzene*. Benzene and ethylbenzene also interact with the zeolite acid site via $\pi$-interaction, illustrated in Figures 3 and 4. Selected structural parameters of the benzene and ethylbenzene molecules are shown in Tables S3 and S4 in the Supporting Information. In order to discuss this in a concise manner, only the structure complexes at the most reliable and well-calibrated ONIOM(MP2: M06-2X) scheme will be the main focus . The C═C double bond in the benzene ring that forms the $\pi$-interaction with the zeolite is slightly increased and the acidic O1−Hz bond distance is slightly increased from 97.0 to 98.4 and 98.3 pm for both benzene and ethylbenzene adsorption complexes, respectively. Similar to the adsorption of ethene, the zeolite structural parameters are slightly changed by the weak interactions (changes in bond distances and bond angles are less than 0.02 Å, and 2°, respectively).

As for the bare 5T quantum cluster, the interaction of benzene calculated with the MP2 method is −12.1 kcal/mol. Considering the surrounding framework, the calculation with the ONIOM scheme gives adsorption energies of −18.4, −12.9, −11.8, and

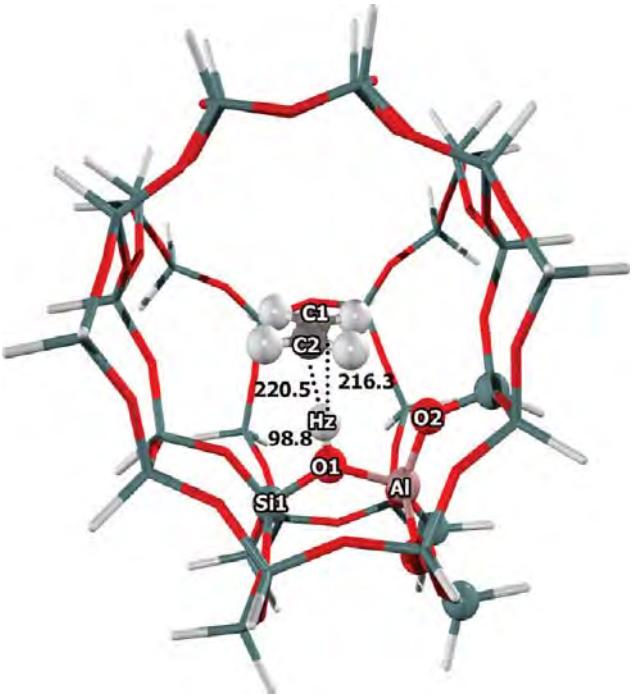


**Figure 2.** Presentation of an ethene molecule adsorbed on the 5T:34T model of H-ZSM-5 zeolite. Atoms treated with the MP2 level of theory are shown in balls, whereas the area treated with a lower level of calculation is symbolized with wireframes. Bond lengths are in picometers.

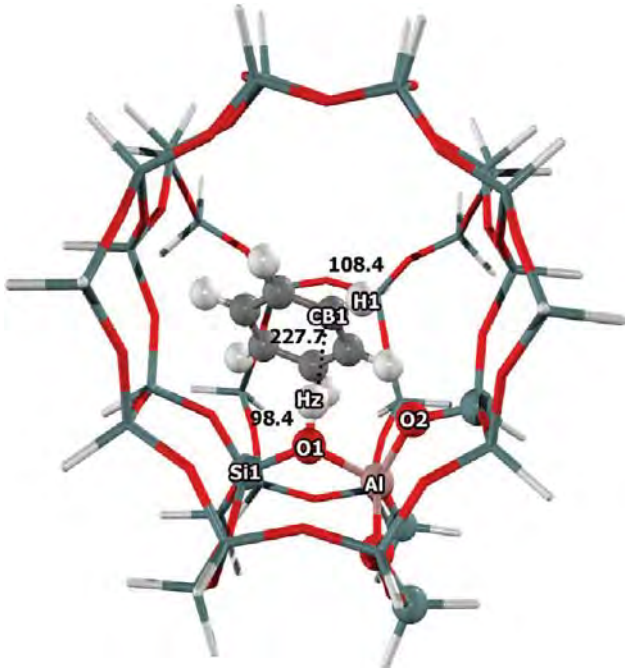


**Figure 3.** Presentation of a benzene molecule adsorbed on the 5T:34T model of H-ZSM-5 zeolite. Atoms treated with the MP2 level of theory are shown in balls, whereas the area treated with a lower level of calculation is symbolized with wireframes. Bond lengths are in picometers.

−26.0 kcal/mol for the ONIOM(MP2:M06-2X), (MP2:B3LYP), (MP2:HF), and (MP2:UFF) methods, respectively. The energies that are larger than those from the quantum cluster are mainly attributed to "nonlocal interactions", which are the van der Waals

(42) Cant, N. W.; Hall, W. K. *J. Catal.* **1972**, *25*, 161.

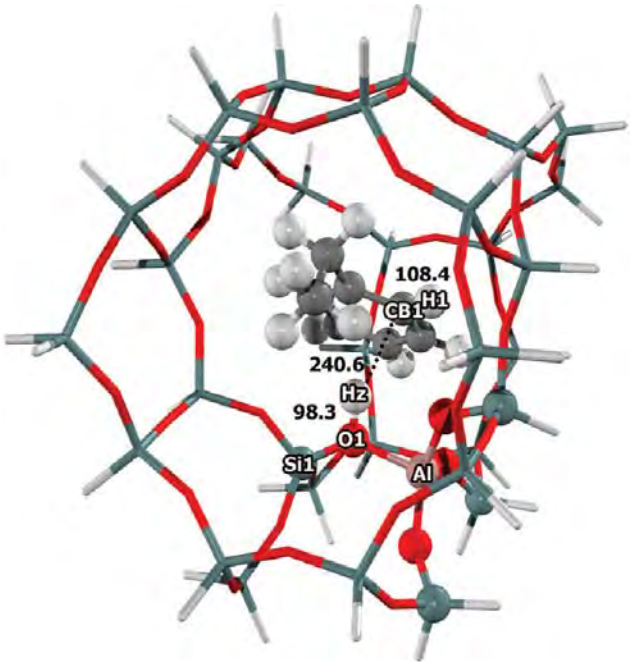


**Figure 4.** Presentation of an ethylbenzene molecule adsorbed on the 5T:34T model of H-ZSM-5 zeolite. Atoms treated with the MP2 level of theory are shown in balls, whereas the area treated with a lower level of calculation is symbolized with wireframes. Bond lengths are in picometers.

interactions, due to confinement of the zeolite. According to the nonpolarity of benzene, only the van der Waals interactions are expected to be significant. Since only the adsorption energy, measured as −15.3 kcal/mol for H-FAU zeolite, is available[43] and the ZSM-5 zeolite pore is smaller, the interaction inside its pore should be stronger than the value in the H-FAU system. Only the energy from the ONIOM(MP2:M06-2X) gives a reasonable adsorption energy.

The adsorption energies for ethylbenzene on H-ZSM-5 were calculated to be −13.9, −23.3, −13.3, −11.6, and −35.3 kcal/mol with the full 5T quantum MP2 and ONIOM(MP2:M06−2X), (MP2:B3LYP), (MP2:HF), and (MP2:UFF) methods, respectively. Obviously, the van der Waals interaction for the case of benzene is weaker than for the ethylbenzene adsorption and, hence, the corresponding adsorption energies at ONIOM(MP2:M06-2X) are −18.4 and −23.3 kcal/mol for benzene and ethylbenzene, respectively. These values compare well with the experimental values of −15.3 and −19.6 kcal/mol[43] for the adsorption of benzene and ethylbenzene in a weaker acid zeolite, and H−Y zeolite, respectively. This discrimination of adsorption energies is due partly to the confinement effect of H-ZSM-5 being larger than the H−Y zeolite. The accurately predicted adsorption energies clearly demonstrate that the ONIOM(MP2:M06-2X) model used in this work can represent the interactions between the adsorbates and zeolite very well. The combination of the MP2 method at the active region embedded in the extended structure modeled by the M06-2X apparently works well in representing van der Waals interactions in the zeolite system as compared to B3LYP and HF. The adsorption results of the ONIOM(MP2:UFF) tend to yield overestimated values (see Table 1).

*3.2.3. Heterocyclic Compounds Adsorption: Pyridine.* The acidity of the H-ZSM-5 zeolite can be studied with pyridine, known as the basic probe molecule. The molecule also has been widely studied as the representative for the heterocyclic molecule. Pyridine is held over the Brønsted acid site of the H-ZSM-5 zeolite with the ion pair intermolecular interaction, illustrated in Figure 5a. Selected structural parameters of the pyridine molecule on H-ZSM-5 are shown in Table S5 in the Supporting Information. From the calculation of the 5T model, the nitrogen atom of pyridine is spontaneously protonated by the zeolite proton. The formation of an ion pair consisting of a pyridinium cation and the deprotonated zeolite can be seen by the bond distance between N and the acidic proton Hz of 110.2 pm, concurrently with the increase of its distance to O1 from 96.7 to 144.5 pm. The results are in accordance with Gutmann's rules,[44] i.e., a lengthening of the O1−Hz bond, a shortening of Al−O1, and a lengthening of Al−O2 (not adjacent to the bridging O1−Hz). Similar structural changes are also found from the ONIOM calculation on the model with the extended framework. The intermolecular O1···N distance of the pyridine/zeolite adduct increases on the model expansion from 253.7 pm (5T) to 257.4−274.7 pm (ONIOM).

The experimentally determined adsorption energy of pyridine on the acidic H-ZSM-5 zeolite of 47.6 kcal/mol[45] is considered as the benchmark. We computed the adsorption energy on the 5T model with the MP2/6-31G(d,p) level of theory to be −24.9 kcal/mol. Once the model is expanded up to 34T, the adsorption energies are considerably increased to −43.7, −39.1, −38.7, and −38.6 kcal/mol for the ONIOM(MP2:M06−2X), (MP2:B3LYP), (MP2:HF), and (MP2:UFF) methods, respectively. As in the former cases, the ONIOM(MP2:M06−2X) result most closely approaches the benchmark. As expected, this result is due to the M06-2X method

**Table 1. The Contribution Analysis on Adsorption Energies of Ethene, Benzene, Ethylbenzene, and Pyridine Molecules on 5T Models Calculated with MP2 Full Quantum Calculation and the 5T:34T Model with Different ONIOM Approaches[a]**

| model | method | ethene | benzene | ethylbenzene | pyridine |
|---|---|---|---|---|---|
| 5T | MP2[b] | −8.7 | −12.1 | −13.9 | −24.9 |
| 5T:34T | ONIOM(MP2:M06−2X)[c] | −13.3 | −18.4 | −23.3 | −43.7 |
| | high level | −8.8 | −11.7 | −12.8 | −23.6 |
| | low level | −4.5 | −6.7 | −10.5 | −20.1 |
| 5T:34T | ONIOM(MP2:B3LYP)[d] | −10.5 | −12.9 | −13.3 | −39.1 |
| | high level | −9.1 | −11.0 | −12.0 | −24.2 |
| | low level | −1.4 | −1.9 | −1.3 | −14.9 |
| 5T:34T | ONIOM(MP2:HF)[e] | −10.4 | −11.8 | −11.6 | −38.7 |
| | high level | −9.0 | −10.7 | −11.8 | −23.9 |
| | low level | −1.4 | −1.1 | 0.2 | −14.8 |
| 5T:34T | ONIOM(MP2:UFF)[f] | −16.6 | −26.0 | −35.3 | −38.6 |
| | high level | −8.5 | −10.9 | −11.8 | −26.3 |
| | low level | −8.1 | −15.1 | −23.5 | −12.3 |
| Expt | H-ZSM-5 | | | | −47.6 |
| | FAU | −9 | −15.3 | −19.6 | −43.1 |

[a] Energies are in kcal/mol. (high level means contribution from a high level of theory: $\triangle E$(model,high); low level means contribution from a low level of theory: $\triangle E$(real, low) − $\triangle E$(model, low)). [b] MP2/6-311+G(2df,2p)//MP2/6-31G(d,p). [c] ONIOM(MP2/6-311+G(2df,2p):M06−2X/6-31G(d,p)//MP2/6-31G(d,p):M06−2X/6-31G(d,p)). [d] ONIOM(MP2/6-311+G(2df,2p):B3LYP/6-31G(d,p)//MP2/6-31G(d,p):B3LYP/6-31G(d,p)). [e] ONIOM(MP2/6-311+G(2df,2p):HF/6-31G(d,p)//MP2/6-31G(d,p):HF/6-31G(d,p)). [f] ONIOM(MP2/6-311+G(2df,2p):UFF//MP2/6-31G(d,p):UFF).

(43) Coker, E. N.; Jia, C.; Karge, H. G. *Langmuir* **2000**, *16*, 1205.

(44) Gutmann, V. *The Donor-Acceptor Approach to Molecular Interactions*; Plenum Press: New York, 1978.

(45) Parrillo, D. J.; Lee, C.; Gorte, R. J. *Appl. Catal., A* **1994**, *110*, 67.

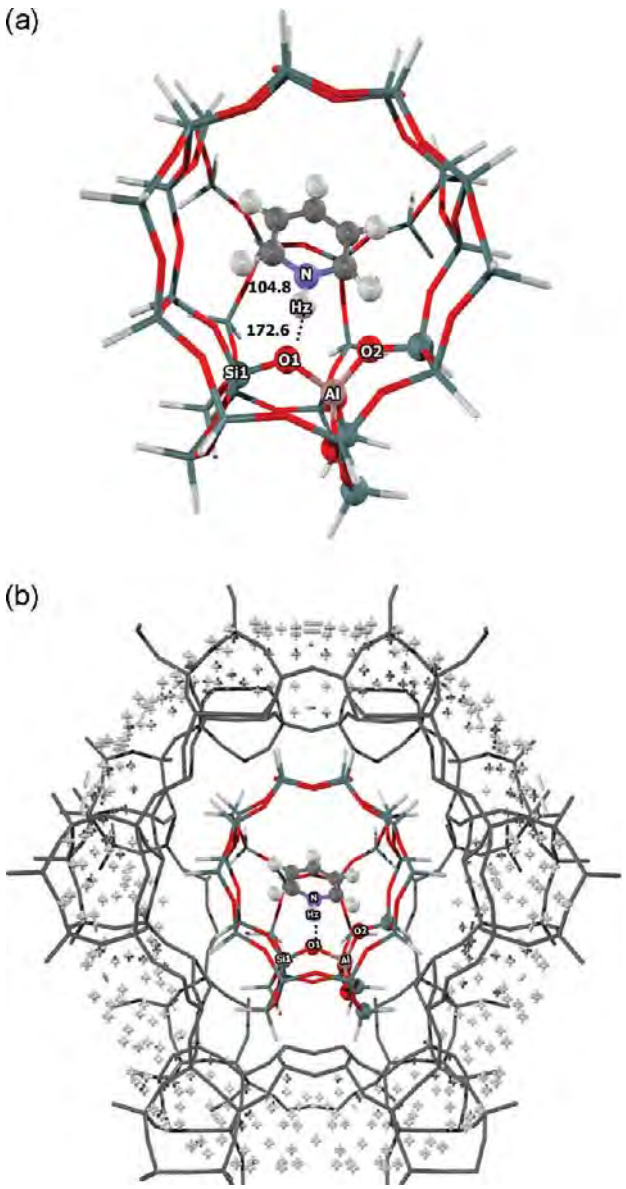


**Figure 5.** Presentation of a pyridine molecule adsorbed on the 5T:34T model of H-ZSM-5 zeolite (a) without charge embedding and (b) with well-calibrated charge embedding. Atoms treated with the MP2 level of theory are shown in balls, whereas the area treated with a lower level of calculation is symbolized with wireframes. Bond lengths are in picometers.

including the nonlocal interactions, which are a vital contribution from the outer framework, into the calculation.

By using the ONIOM(MP2:M06-2X) scheme in combination with the embedded approach, referred to here as the "embedded ONIOM", we demonstrate that the electrostatic potential from the extended framework plays a much larger role in the stabilization of the adsorption complex of the ion-pair of pyridine cation interacted with anionic zeolite than at the other neutral complexes. Consequently, the zeolite framework effects bring the adsorption energy of the ion-pair complex close to the experimental observation.

Confirmation of the convergence of the model size is listed in Table 2. The ONIOM(5T:128T) calculations were performed for all nonpolar adsorbates and found to give no difference in the energy (−13.3 vs −13.6 kcal/mol for ethene, −18.4 vs −19.0 kcal/mol for benzene, and −23.3 vs −23.6 kcal/mol for ethylbenzene). Therefore, the ONIOM(5T:34T) model is large enough for the chemical prediction. From the table, we also found that adsorption energies derived from those of the ONIOM(5T:128T) (−47.0 kcal/mol) and embedded ONIOM (−48.4 kcal/mol), where long-range electrostatic interactions have been included, can be compared well with the experimental data (−47.6 kcal/mol) for the case of the ion-pair system. Moreover, it should be noted that adsorption energies from M06-2X/6-31G(d,p) with the 34T quantum cluster and the ONIOM(MP2:M06-2X) with the 5T:34T are in good agreement with each other.

**3.3. Benzene and Ethylbenzene Hydrogen Exchange in ZSM-5 Reaction.** The well thought-out combined method of ONIOM(MP2:M06-2X) with the 34T model is used to study the H/H exchange reaction of the adsorbates. Generally, the H/D exchange can be described as an electrophilic aromatic substitution.[46−49] The reaction mechanism is composed of (1) the attack of the Brønsted proton at the aromatic ring, which is protonated to yield a $\sigma$ complex, and (2) the decomposition of the complex by transferring a proton to the negatively charged framework oxygen in the local structure. One can also consider that the adsorbates and the zeolite active site exchange their protons, as presented in the chemical eq 1.

$$\mathrm{RCH} + \mathrm{Z(O\mathbf{Hz})} \rightarrow \mathrm{RC\mathbf{Hz}} + \mathrm{Z(OH)} \qquad (1)$$

where RCH in our study represents benzene and ethylbenzene, Z(O**Hz**) is the active site, and **Hz** is the Brønsted proton.

Since ethene and pyridine proceed differently for further chemical steps, only the reactions of benzene and ethylbenzene are investigated. Our prediction is then evaluated with the benchmark of experimental data.[47]

The proton exchange reaction takes place at the bridging OH group of the zeolite. Considering the transition state of the reaction between benzene and the active site, the $sp^3$ hybridized CB1 atom can be generated from the orginal $sp^2$ carbon of the benzene. The CB1−H1 bond dissociation is found to correspond to the O2−H1 bond formation. The Brønsted proton (Hz) is leaving the zeolite acid site (O1) for the three-coordinated carbon (CB1). The transition structure is proposed to be in the benzenium cation ($C_6H_7^+$).[48] Receiving the hydrogen atom from benzene, the O2 oxygen acts as a Lewis base. For the orbital insight, it is the $sp^3$ hybridized carbon (CB1) that proceeds to full aromatization restoration. Similar to the methane case,[49−51] the protonated carbon (CB1) stays in the main plane of the active site and becomes a six-membered transition structure, as shown in Scheme 1.

Figure 6 illustrates the optimized structures of the adsorption, the transition state, and the product for the hydrogen exchange reaction of benzene on the zeolite model. From the normal-mode analysis, one imaginary frequency is identified to confirm the transition structure. Key structural parameters for these structures are shown in Tables S6 and S7 in the Supporting Information.

The reaction starts with the benzene adsorption (AD) over the Brønsted acid site of H-ZSM-5 zeolite, demonstrated in Figure 6. The structural parameters are shown in Table S6. From the

(46) Goncalves, V. L. C.; Rodrigues, R. C.; Lorencato, R.; Mota, C. J. A. *J. Catal.* **2007**, *248*, 158.
(47) Huang, J.; Jiang, Y.; Marthala, V. R. R.; Wang, W.; Sulikowski, B.; Hunger, M. *Microporous Mesoporous Mater.* **2007**, *99*, 86.
(48) Nicholas, J. B. *Top. Catal.* **1997**, *4*, 157.
(49) Ryder, J. A.; Chakraborty, A. K.; Bell, A. T. *J. Phys. Chem. B* **2000**, *104*, 6998.
(50) Zheng, X.; Blowers, P. *J. Mol. Catal. A: Chem.* **2005**, *242*, 18.
(51) Zheng, X.; Blowers, P. *J. Mol. Catal. A: Chem.* **2006**, *246*, 1.

**Table 2. Comparison of Model Size and Computational Approach on Adsorption Energies of Ethene, Benzene, Ethylbenzene, and Pyridine Molecule on H-ZSM-5 Zeolite[a]**

| model | method | ethene | benzene | ethylbenzene | pyridine |
|---|---|---|---|---|---|
| 5T:34T | ONIOM(MP2:M06-2X)[b] | −13.2 | −17.7 | −22.2 | −43.2 |
| 5T:34T | ONIOM(MP2:M06-2X)[c] | −13.3 | −18.4 | −23.3 | −43.7 |
| 5T:128T | ONIOM(MP2:M06-2X)[c] | −13.6 | −19.0 | −23.6 | −47.0 |
| 5T:34T | embedded ONIOM(MP2:M06-2X)[c] | −14.0 | −19.8 | −24.7 | −48.4 |
| 34T | M06-2X[d] | −14.0 | −18.2 | −22.8 | −41.5 |
| Expt | H-ZSM-5 | | | | −47.6 |
| | FAU | −9 | −15.3 | −19.6 | −43.1 |

[a] The ONIOM(MP2:M06-2X) method on the 5T:34T and 5T:128T models, the embedded ONIOM(MP2:M06-2X) method on the 5T:34T model, and the M06-2X quantum calculation on the 34T model. Energies are in kcal/mol. [b] ONIOM(MP2/6-31G(d,p):M06−2X/6-31G(d,p)). [c] ONIOM(MP2/6-311+G(2df,2p):M06-2X/6-31G(d,p)//MP2/6-31G(d,p):M06-2X/6-31G(d,p)). [d] M06-2X/6-31G(d,p)//ONIOM(MP2/6-31G(d,p):M06−2X/6-31G(d,p)).

**Scheme 1**

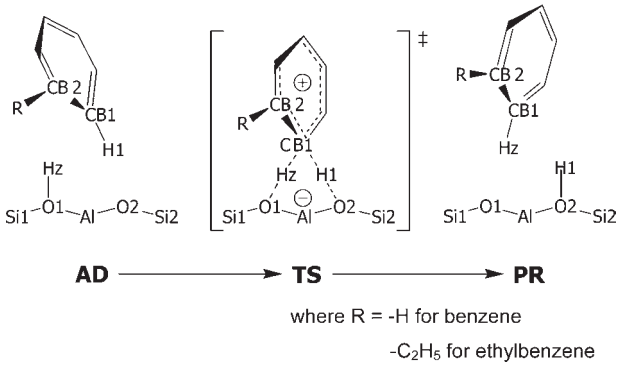


adsorption state, the acidic proton points to the benzene ring. The intermolecular distances were measured from the CB1 and CB2 of benzene to the zeolite acid. From the optimized structure with the ONIOM calculation, the adsorption distances grow significantly larger to 227.7 and 246.5 pm. Moreover, the acidity of the framework-included model in the adsorption state is more pronounced as the acid bond length is increased from 97.8 to 98.4 pm. The O−Hz bond length in the adsorption complex is barely changed from the bare model (97.0 pm). From the transition structure (TS), the optimized geometry is consistent with the asymmetric exchange of the protons. Hz···CB1 was found to be 118.2 pm long, whereas the H1···CB1 distance is 122.4 pm. The extended O1−Hz bond of 151.4 pm corresponds to the shortened Hz−CB1 intermolecular distance of 118.2 pm. The aromaticity of the benzene remains the same as the CB1−CB2 distance and is constant along the reaction. From a frequency calculation of the transition state geometry, the imaginary frequency of 605i $cm^{-1}$ corresponds to the exchange. In the product formation (PR) shown in Figure 6, CB1···H1 becomes the definition of the intermolecular distance for the product/zeolite complex. It is calculated to be 234.0 pm, similar to the Hz···CB1 and Hz···CB2 values in the adsorption state. Like the reactant adsorption, benzene in the product state is located at the nanocavity, close to the zigzag channel, owing to the influence from the zeolite framework.

Now we will discuss the energetics of the reaction. The calculated energies are reported in Table 3. As mentioned in the previous section, the adsorption energies, before and after the framework addition, are −12.1 and −18.4 kcal/mol, respectively. The framework inclusion not only stabilizes the molecular adsorption, but also the transition structure. Thus, the reaction energies from both the quantum cluster and the ONIOM scheme are insignificantly different. The relative energy of the transition is also found to be greatly reduced from 22.7 to 12.6 kcal/mol while the surrounding framework is considered with the ONIOM calculation. The calculated apparent activation energy of 12.6 kcal/mol corresponds with the experimental apparent activation energy of 11.0 kcal/mol.[47] Because of the lack of information for adsorption energy from experiment, we could not compare the calculated actual activation energy with the experimental one. From the energies of the adsorption and transition, the actual activation energy is found to be 31.0 kcal/mol. It is logical that less energy is required for the reaction of benzene than methane and ethane since the electron delocalization of the benzene ring stabilizes the transition state structure. The reaction is found to be 4.1 kcal/mol endothermic. From the accurate apparent activation energy, it is obvious that using the M06-2X method for taking the framework effect into account for the calculation remarkably improves the computational prediction.

For the reactant with a larger molecular size, ethylbenzene is studied. Its adsorption and reaction are analogous with the benzene case. It was reported that *meta*-substituted alkylbenzenes showed noticeably less exchange than the *ortho* or *para* isomers.[52] Further considering the steric hindrance, the *ortho* postition is the most preferential for the proton exchange. At the site, the H1 transfer from ethylbenzene to zeolite oxygen (O2) is simultaneous with the Hz transfer back to the adsorbate (CB1). The mechanism is illustrated in Scheme 1.

Upon the adsorption (AD), the zeolite acid bond length is elongated as in the previous cases and becomes even more elongated when the framework is taken into account. From Table S7 in the Supporting Information, the distances are 97.9 pm for the 5T cluster (from 96.7 pm) and 98.3 pm for the ONIOM model (from 97.0 pm). A more distinct change is found compared to the benzene adsorption. A less asymmetric exchange of the protons is observed from the transition structure (TS), compared to the benzene case. Optimized with the ONIOM calculation, the Hz···CB1 was found to be 117.2 pm long, whereas the H1···CB1 distance is 119.5 pm. We found that the O1−Hz bond (153.6 pm) is more extended than the one in the benzene reaction (151.4 pm). This leads us to expect that both the activation energy and the energy barrier will be lower than the values of the previous reaction. Other structural changes correspond to the reaction coordinate. During the transition, the aromaticity of ethylbenzene is stable as the CB1−CB2 distance hardly changes. The imaginary frequency of 282i $cm^{-1}$ of the transition geometry corresponds to the exchange. When the product is completely formed (PR), the intermolecular distance (CB1···H1) was predicted to be 296.4 pm, which is slightly larger than the value in the first step (240.6 pm). The illustration of the product adsorption at the active site is presented in Figure 7. Like the reactant adsorption, the product is held over the intersection close to the zigzag channel.

(52) Hawthorne, S. B.; Miller, D. J. *Anal. Chem.* **1985**, *57*, 694.

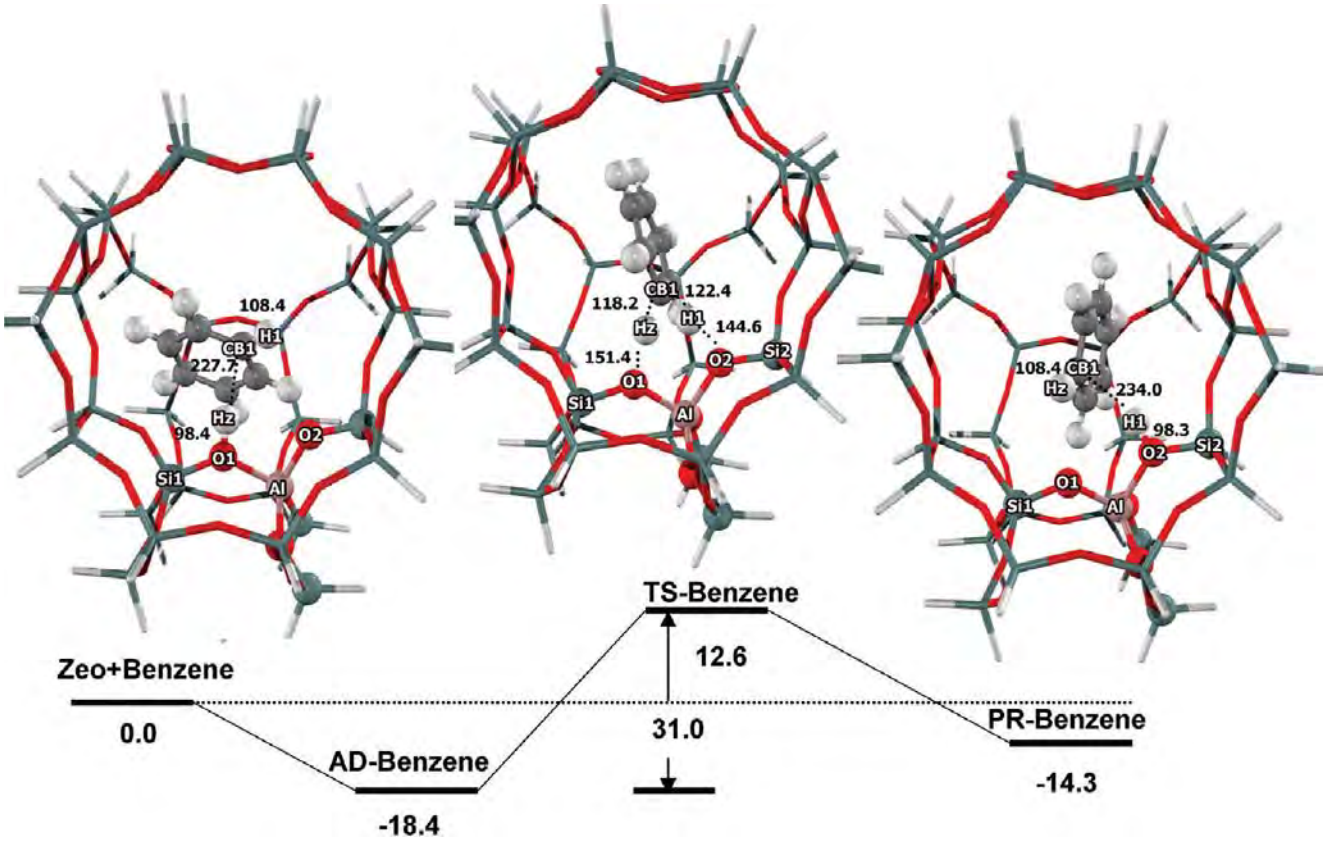


**Figure 6.** Energy profile for the proton exchange of benzene on the 5T:34T model of H-ZSM-5 zeolite calculated by the ONIOM(MP2/6-311+G(2df,2p):M06-2X/6-31G(d,p)//MP2/6-31G(d,p):M06-2X/6-31G(d,p)) method. Atoms treated with the MP2 level of theory are shown in balls, whereas the area treated with a lower level of calculation is symbolized with wireframes. Bond lengths are in picometers and energies are in kcal/mol.

**Table 3. Reaction Energies for the H/H Exchange Reaction of Benzene and Ethylbenzene on Various Models of H-ZSM-5 Zeolite Calculated with Different Methodologies**[a]

| | | benzene | | | ethyl benzene | | |
|---|---|---|---|---|---|---|---|
| model | method | AD | TS | PR | AD | TS | PR |
| 5T | MP2[b] | −12.1 | **22.7** (34.8) | −8.6 | −13.9 | **19.8** (33.7) | −10.4 |
| 5T:34T | ONIOM(MP2:M06-2X)[c] | −18.4 | **12.6** (31.0) | −14.3 | −23.3 | **4.6** (27.9) | −20.6 |
| 5T:128T | ONIOM(MP2:M06-2X)[c] | −19.0 | **12.6** (31.6) | −13.7 | −23.6 | **4.9** (28.5) | −20.6 |
| 5T:34T | embedded ONIOM(MP2:M06-2X)[c] | −19.8 | **10.4** (30.2) | −14.1 | −24.7 | **1.9** (26.6) | −21.9 |
| 34T | M06-2X[d] | −18.2 | **13.5** (31.7) | −14.2 | −22.8 | **4.9** (27.7) | −20.0 |
| Expt | H-ZSM-5 | | **11.0** | | | **6.9** | |

[a] Apparent activation energies are presented in bold type, while intrinsic activation energies are in parentheses. Energies are in kcal/mol. [b] MP2/6-311+G(2df,2p)//M06-2X/6-31G(d,p). [c] ONIOM(MP2/6-311+G(2df,2p):M06-2X/6-31G(d,p)//MP2/6-31G(d,p):M06-2X/6-31G(d,p)). [d] M06-2X/6-31G(d,p)//ONIOM(MP2/6-31G(d,p):M06-2X/6-31G(d,p)).

The calculated energies for the reaction are reported in Table 3. The adsorption energy almost doubled as a result of the framework effect, from −13.9 to −23.3 kcal/mol, as previously discussed. The explanation of this is given in the discussion on the benzene reaction. The relative energy for the transition structure is found to be 19.8 and 4.6 kcal/mol for bare quantum 5T and ONIOM(5T:34T) models, respectively. Considering the experimental estimate of the apparent activation energy (6.9 kcal/mol), the ONIOM(MP2:M06−2X) method gives us the prediction for the value of 4.6 kcal/mol, which is comparable to the benchmark. The energy barrier is calculated to be 27.9 kcal/mol. Compared to the predicted barrier of the benzene reaction (31.0 kcal/mol), it is

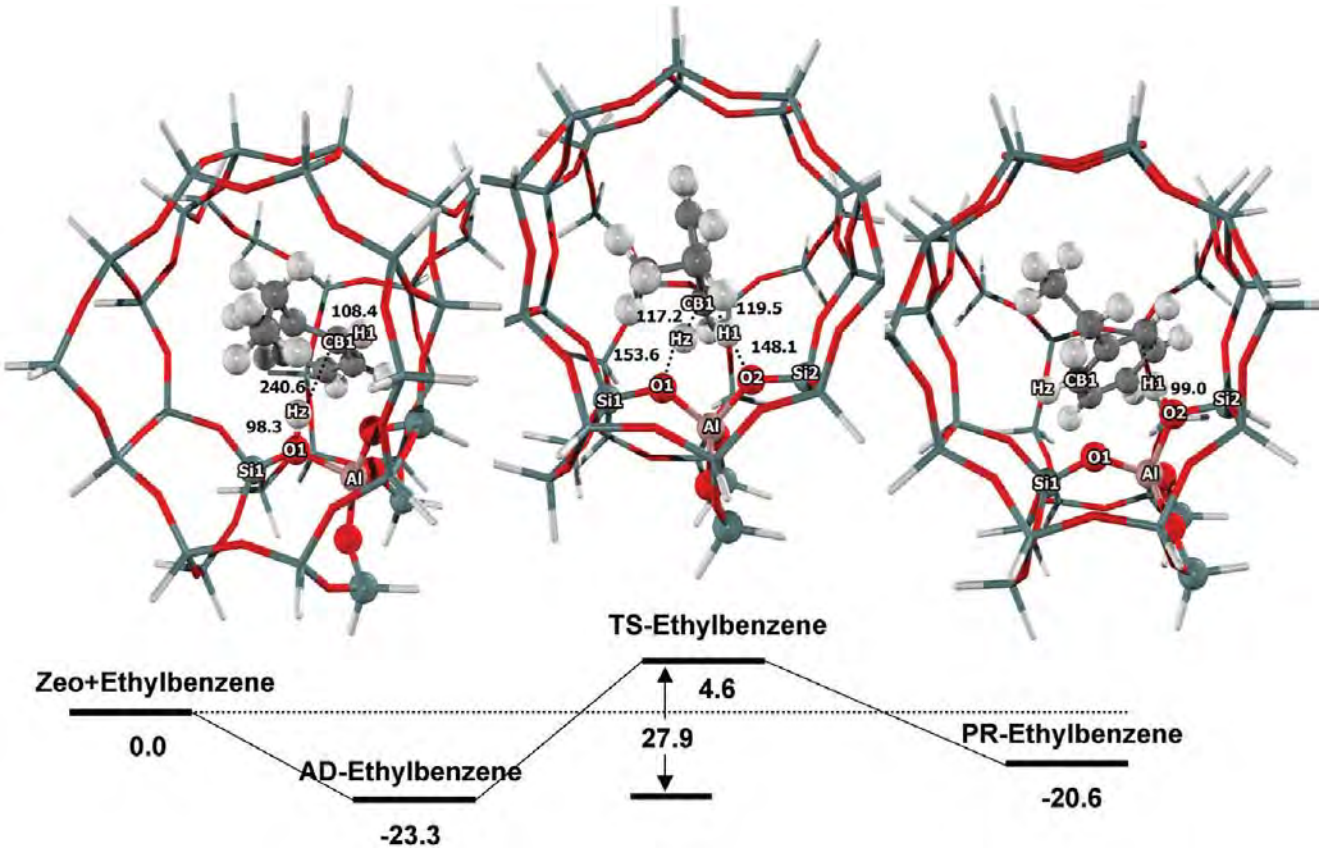


**Figure 7.** Energy profile for the proton exchange of ethylbenzene on the 5T:34T model of H-ZSM-5 zeolite calculated using the ONIOM-(MP2/6-311+G(2df,2p):M06-2X/6-31G(d,p)//MP2/6-31G(d,p):M06-2X/6-31G(d,p)) method. Atoms treated with the MP2 level of theory are shown in balls, whereas the area treated with a lower level of calculation is symbolized with wireframes. Bond lengths are in picometers and energies are in kcal/mol.

in good agreement with an alkyl group bound to aromatic rings that decrease the energy barrier for the ring protonation or methylation.[46,53]

The energy prediction for the proton exchange reactions of benzene and ethylbenzene to the H-ZSM-5 zeolite with the ONIOM(MP2:M06-2X) approach successfully reproduced the experimental observations. The energies for the adsorption, transition state, and product are computed to be −18.4, 12.6, and −14.3 kcal/mol for benzene (see Figure 6) and −23.3, 4.6, and −20.6 kcal/mol for ethylbenzene (see Figure 7), respectively. The apparent activation energy (the same as the transition structure's relative energy) agrees well with the experimental data for both reactions.[47] We therefore propose that the combined methodology of the ONIOM(MP2:M06-2X) method and the 5T:34T model is practical for the study of the framework effect on the adsorption and the reaction for such molecules in the zeolite pore.

## 4. Conclusions

Chemical insight on the adsorption and the H/H exchange reaction of ethene, benzene, ethylbenzene, and pyridine on H-ZSM-5 zeolite were investigated with the ONIOM scheme associated with the combination of the MP2 method and various lower level approaches including M06-2X, B3LYP, HF, UFF. This is the first time that a newly developed density functional, M06-2X, is combined with the MP2 method to perform the ONIOM calculation. The H-ZSM-5 model was carefully calibrated to be 5T:34T for the ONIOM(MP2:M06-2X) calculation. The adsorption energies of ethene, benzene, ethylbenzene, and pyridine on H-ZSM-5 from the ONIOM(MP2:M06-2X) plus long-range electrostatic contributions corrected, are predicted to be −14.0, −19.8, −24.7, and −48.4 kcal/mol, respectively, which are very close to experimental observations if available. The adsorption energy of pyridine agrees well with the experiment data of −47.6 kcal/mol. The ONIOM(MP2:M06-2X) approach can well describe the reaction mechanisms for the proton exchange reactions of benzene and ethylbenzene on H-ZSM-5 zeolite and successfully reproduce experimental observations. Energies for adsorption, transition state, and product are computed to be −18.4, 12.6, and −14.3 kcal/mol for benzene and −23.3, 4.6, and −20.6 kcal/mol for ethylbenzene, respectively. Therefore, the ONIOM(MP2:M06-2X) approach is recommended to represent the framework effect on the reacting molecule within the zeolite pore for both studies of adsorption and reaction.

**Acknowledgment.** This work was supported in part by grants from the National Science and Technology Development Agency, (NSTDA Chair Professor and NANOTEC Center of Excellence), the Thailand Research Fund and the Kasetsart University Research and Development Institute (KURDI), the Commission on Higher Education as well as the Ministry of Education, under the Postgraduate Education and Research Programs in Petroleum and Petrochemicals, and Advanced Materials. The authors are grateful to Donald G. Truhlar and Yan Zhao for their support with the M06-2X functional.

(53) March, J. *Advanced Organic Chemistry: Reactions, Mechanisms, and Structure*, 4th ed.; McGraw-Hill Press: New York, 1992.

**Supporting Information Available:** Tables S1−S7: Selected geometrical parameters for adsorption and reaction mechanism of ethene, benzene, ethylbenzene, and pyridine on H-ZSM-5 zeolite with various methods. Tables S8−S11: The adsorption and reaction energies of ethene, benzene, ethylbenzene, and pyridine on H-ZSM-5 zeolite with various methods. Table S12: comparison of CPU time for different zeolite models at different levels of theory. This material is available free of charge via the Internet at http://pubs.acs.org.

# Adsorption and Tautomerization Reaction of Acetone on Acidic Zeolites: The Confinement Effect in Different Types of Zeolites

**Bundet Boekfa,[†,‡,§] Piboon Pantu,[†,‡,§] Michael Probst,[⊥] and Jumras Limtrakul*[,†,‡,§]**

*Laboratory for Computational and Applied Chemistry, Department of Chemistry, Faculty of Science, Kasetsart University, Bangkok 10900, Thailand, Center of Nanotechnology, Kasetsart University Research and Development Institute, Kasetsart University, Bangkok 10900, Thailand, NANOTEC Center of Nanotechnology, National Nanotechnology Center, Kasetsart University, Bangkok 10900, Thailand, and Institute of Ion Physics and Applied Physics, University of Innsbruck, A-6020 Innsbruck, Austria*

*Received: June 26, 2010; Revised Manuscript Received: August 4, 2010*

The adsorption and tautomerization reaction of acetone in H-FER, H-ZSM-5, and H-MCM-22 zeolites has been studied using full quantum calculations at the M06-2X/6-311+G(2df,2p) level of theory. The combination of a large quantum cluster and this meta-hybrid density functional results in reasonably accurate adsorption energies of −26.9, −28.1, and −23.9 kcal/mol for acetone adsorption in H-FER, H-ZSM-5, and H-MCM-22, respectively. Due to the acidity of the zeolite and the framework confinement effect, the tautomerization of acetone proceeds through a much lower activation barrier than in the isolated gas phase or in the presence of water molecules alone. The activation energies are calculated to be 24.9, 20.5, and 16.6 kcal/mol in H-FER, H-ZSM-5 and H-MCM-22, respectively. The endothermic reaction energy decreases with increasing of the zeolite pore sizes and amounts to 22.7, 17.6, and 15.9 kcal/mol for the reaction in H-FER, H-ZSM-5 and H-MCM-22, respectively. In addition, the adsorbed acetone enol is found to be highly unstable in the zeolite framework and readily reverse-transforms to adsorbed acetone with a very small activation energy. The activity trend and relative stabilities of the adsorbed keto and enol forms are well correlated with the interactions within the Brønsted acid site.

## 1. Introduction

Aldol condensation is one of the most important C−C bond forming reactions for organic synthesis.[1−3] Aldol condensation of acetone can be readily catalyzed by acidic or basic reagents. In a confined space of microporous zeolites, reactions of acetone over the Brønsted acid site selectively produce mesityl oxide.[4−7] The mesityl oxide can be hydrogenated to produce methyl isobutyl ketone, which is widely used as a solvent for paints, lacquers, and certain types of polymers and resins. The process can be carried out in a single step over bifunctional catalysts (e.g., Pt/H-ZSM-5,[8] Pd/H-MCM-22,[9] etc.). Aldol condensation is very important for the transformation of acetone to methyl isobutyl ketone.[4−6]

Acetone tautomerization to the enol form is an important initial step of aldol condensation and many reactions of acetone.[1−3] The activity of tautomerization dependents on the acidity and the ionic strength of the reaction media. The fundamental steps of the aldol condensation in acidic zeolites are believed to be similar to the reaction in solution.[4−7] The mechanism consists of the acid-catalyzed tautomerization of acetone. Acetone is transformed to an $\alpha,\beta$-unsaturated carbonyl compound. A number of theoretical studies on keto−enol tautomerization of acetaldehyde and acetone have been reported.[10−15] Previous theoretical calculations reported that in the gas phase, acetone tautomerization requires a high activation energy of 64.0−69.2 kcal/mol.[11−15] In solvent-assisted systems, the presence of water molecules can greatly reduce the energy barrier by about 20−30 kcal/mol.[12−15] Theoretical results for the tautomerization reaction over a zeolite catalyst have also been reported[15,16] with the synergistic functions of Brønsted acid and Lewis basic sites on H-ZSM-5, drastically reducing the barrier height for the tautomerization of acetaldehyde to 20.2 kcal/mol.[15]

The interaction between the zeolite framework and an adsorbed molecule, which is generally called the confinement effect,[17,18] also plays an important role for the adsorptions and reactions on zeolites.[17−23] Therefore, the details of the interactions between the reactants and the active site in the zeolite's framework and the influence of the topology close to the active site are important to completely understand the reaction mechanism inside zeolite pores. Recently, the role of the zeolite confinement effect on reactions of unsaturated aliphatic, aromatic and heterocyclic compounds has been successfully studied[24] by using full quantum calculations with the new density functional M06-2X.[25−27]

In this work, we study the mechanism of acetone tautomerization and relative stabilities of the keto and enol form in the isolated phase, in the presence of assisting water molecules, and in zeolite-catalyzed environments. Our aim is to investigate the effects of confinement in different zeolite structures on the tautomerization of acetone. Three different zeolites (H-FER, H-ZSM-5, and H-MCM-22) with different dimensions of pores and cavities are selected for this investigation. Sufficiently large clusters are used to represent the zeolite structures, and the full quantum chemical calculations using the M06-2X method are performed to attempt to account for all interactions between

* Corresponding author. Phone: +66-2-562-5555 ext 2159. E-mail: jumras.l@ku.ac.th.
† Department of Chemistry, Kasetsart University.
‡ Kasetsart University Research and Development Institute, Kasetsart University.
§ National Nanotechnology Center, Kasetsart University.
⊥ Institute of Ion Physics and Applied Physics, University of Innsbruck.

10.1021/jp1058947 
Published on Web 08/19/2010

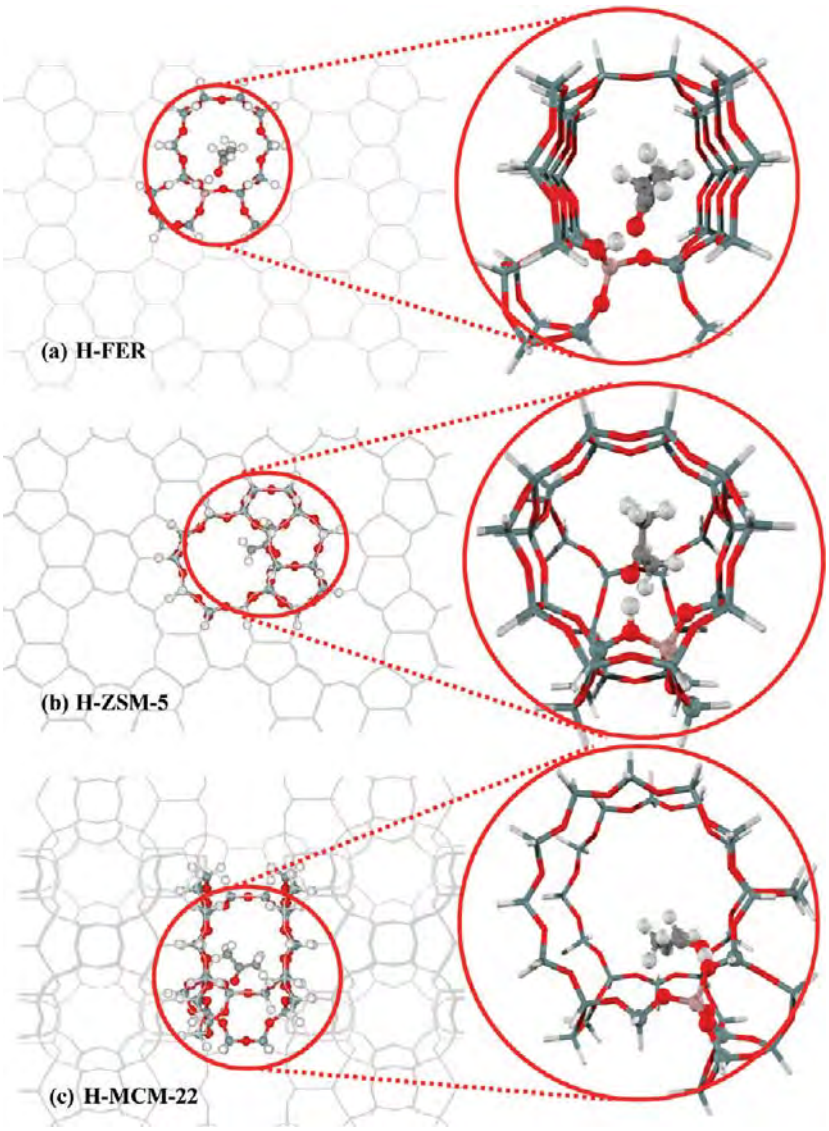


**Figure 1.** Optimized structures of acetone adsorbed on the 34T model of (a) H-FER, (b) H-ZSM-5, and (c) H-MCM-22 zeolites.

the reactive intermediates and the zeolite acid site and surrounding pore walls.

## 2. Methodology

34T clusters were taken from crystallographic data of H-FER, H-ZSM-5, and H-MCM-22 zeolites.[28−30] The cluster model of H-FER zeolite covers the 10-membered ring main channel (4.2 × 5.4 Å) that is intersected with the 8-membered ring channel (3.5 × 4.8 Å), as shown in Figure 1a. One silicon atom at the T2 site[31] is replaced with an aluminum atom to represent the Brønsted acid site. The model of H-ZSM-5 represents the intersection cavity where the straight channel (5.4 × 5.6 Å) and the zigzag channel cross (5.1 × 5.4 Å), as shown in Figure 1b. A silicon atom was substituted with an aluminum atom at the most favorable position (T12).[32] The cluster model of H-MCM-22 represents the 12-membered ring channels of the supercage (7.1 × 7.1 × 18.4 Å), as shown in Figure 1c. The substituted aluminum atom is located at the T1 site.[33]

The M06-2X density functional is used in all calculations. During geometry optimizations, only the 5T active region of ≡SiOHAl(OSi)$_2$OSi≡ and the reacting molecule are allowed to relax, while the rest of the structure is kept fixed at the crystallographic coordinates. We also study the reaction of an isolated acetone molecule and the reaction in the presence of water molecules. For geometry optimizations, the 6-31G(d,p) basis set was used. To obtain more accurate interaction energies, single-point calculations with the 6-311+G(2df,2p) basis set were carried out. Transition states were located with the Berny algorithm[34,35] and were checked to confirm that they had one imaginary frequency corresponding to the reaction coordinate. We did not include the zero-point vibrational contributions (ZPVE) to the energies, since the systems are too large to calculate the matrix of second energy derivatives with the M06-2X functional in reasonable time. We are also not aware that this has been performed on systems of similar size. Curtis et al. have performed a study on ethane absorbed on small 3T and 5T clusters.[36,37] They found close agreement between results from G2(MP2) (including ZPVE) and MP2/6-31G(d,p) calculations not including ZPVE, due to cancellation of various effects. We assume that also in our work, the relative changes caused by inclusion of the ZPVE are less than the errors inherent in the functional and basis set. All calculations were performed with the Gaussian 03 code[38] modified to incorporate the Minnesota Density Functionals module 3.1 by Zhao and Truhlar.

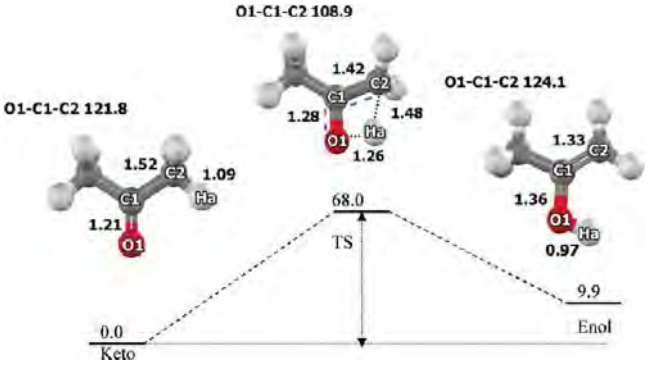


**Figure 2.** Molecular structures and energy profile of the tautomerization of acetone in an uncatalyzed gas phase environment (M06-2X/6-311+G(2df,2p)//M06-2X/6-31G(d,p) calculations). Distances and energies are given in Å and kcal/mol.

## 3. Results and Discussion

**3.1. Tautomerization of Acetone in the Gas Phase.** The uncatalyzed tautomerization of acetone has been extensively studied and was found to occur via a concerted mechanism.[11−15] In this study, we therefore examine the concerted tautomerization mechanism of acetone to validate the applicability of the new density functional M06-2X. Figure 2 shows the potential energy profile and the geometries of acetone, the transition state, and the enol product computed at the M06-2X/6-311+G(2df,2p)//M06-2X/6-31G(d,p) level of theory. At the transition state, the intramolecular proton transfer from the methyl group to the carbonyl oxygen atom takes place. The C2−Ha bond distance increases to 1.48 Å and the O1−Ha decreases to 1.26 Å. At the same time, the C1−O1 carbonyl bond increases from 1.21 to 1.28 Å and the C1−C2 bond length decreases from 1.52 to 1.42 Å. The activation energy is calculated to be 68.0 kcal/mol, and the reaction energy is 9.9 kcal/mol. The computed activation energy and reaction energy agree well with previous theoretical studies that employed the Møller−Plesset perturbation theory.[12,14] In those studies, the activation energies were found to be 64.0 and 69.2 kcal/mol, and the reaction energies were 11.6 and 13.1 kcal/mol. The reaction energies computed in this study are also in reasonable agreement with the experimental results of 12 ± 2 kcal/mol.[39,40]

**3.2. Tautomerization of Acetone in Aqueous Solution.** For aqueous solutions, it has previously been reported that water molecules can reduce the energy barrier by stabilizing the transition state with hydrogen bonds.[11−15] The tautomerization reaction occurs via cyclic proton transfer networks with water molecules acting as proton donors and acceptors facilitating the reaction. The optimized geometries and energy profiles are presented in Figure 3. The reaction is considered to proceed via the concerted mechanism similar to the reaction in the isolated gas phase. In the presence of a water molecule, acetone interacts with the water molecule by forming 2 hydrogen bonds. Then two protons are transferred simultaneously through the hydrogen bonding network. With two and three additional water molecules, stronger and larger hydrogen bonding networks are formed, as indicated by shorter hydrogen bond distances and angles that are closer to the linear angles of the hydrogen bonds (O···H···O). The addition of water molecules results in a significant reduction of activation energy. The computed activation energies at the M06-2X/6-311+G(2df,2p)//M06-2X/6-31G(d,p) level of theory are 40.2, 32.7, and 33.6 kcal/mol and the reaction energies are 9.7, 7.8, and 8.2 kcal/mol, for the presence of 1, 2, and 3 water molecules, respectively. These results agree well with a previous theoretical study[14] at the MP2/cc-pVTZ//MP2/6-31G(d,p) level, which included the zero-point vibrational energy correction and reported activation energies of 37.5, 30.4, and 29.1 kcal/mol for the presence of 1, 2, and 3 water molecules, respectively. The computed reaction energies in the presence of water molecules were reported to be similar to the reaction energy in the gas phase. The measured reaction enthalpy in aqueous solution was reported as 10.3 ± 0.4 kcal/mol,[41] very close to the gas phase value. Therefore, we conclude that the M06-2X method can give reasonably accurate results for the activation energy and reaction energy of acetone tautomerization as compared with the high level of calculations.

**3.3. Tautomerization of Acetone in Zeolites.** ***3.3.1. Structure of the Zeolites.*** In this study, we examine the tautomerization of acetone in three different zeolites.[25−27] These three zeolites can be synthesized with a high Si/Al ratio. Therefore, for the sake of model simplicity, we use a single Brønsted acid as an active site for these high silica zeolites. The Brønsted acid is placed on the favorable sites predicted by previous theoretical studies.[31−33] H-FER zeolite has a two-dimensional pore structure with a main straight channel and a smaller channel. The two channels are perpendicular and intersected. In the model used in this study, the Brønsted acid is located at the most favorable position (T2)[31] at the intersection of the 10T main channel (4.2 × 5.4 Å in diameter) and the 8T channel (3.5 × 4.8 Å in diameter) (see Figure 1a). The O1−Hz bond leans toward the middle of the small 8T channel with an angle of about 30° to the axial direction of the 10T main channel.

H-ZSM-5 zeolite is a three-dimensional pore zeolite. The Brønsted acid is located at the T12 position[32] on the window of the zigzag channel that is connected to the intersection cavity. The employed model represents the intersection cavity of ∼9 Å in diameter where the straight channel (10-membered ring, 5.4 × 5.6 Å in diameter) and the zigzag channel (10-membered ring, 5.1 × 5.4 Å in diameter) intersect (see Figure 1b).

H-MCM-22 is also a three-dimensional pore zeolite. The main straight channel is a 10-membered ring having dimensions of 4.0 × 5.5 Å in diameter. It opens to a large cavity called the supercage (7.1 × 7.1 × 18.4 Å). In this study, we consider the acid site to be located on the 12-membered ring in the supercages.

Despite different pore structures, the O1−Hz Brønsted acid bond distance is approximately the same at 0.97 Å in all three zeolite models. The Al···Hz distances are in the range of 2.30−2.43 Å, which compared well with the experimental values of 2.38−2.48 ± 0.04 Å.[42,43]

***3.3.2. Acetone Adsorption on H-FER, H-ZSM-5 and H-MCM-22.*** The optimized structures of acetone adsorbed on the three zeolites are shown in Figure 1, and selected geometric parameters are given in Table 1. In H-FER, an acetone molecule forms a hydrogen bond between its carbonyl oxygen (O3) and the Brønsted acidic proton (Hz). The adsorbed acetone molecule is located in the 10T main channel. The O1−Hz−O3 hydrogen bond angle is 165.8°. This deviation from the linear hydrogen bond angle is due to the alignment of the Brønsted O−H that initially leans toward the small 8T window. The adsorption energy is computed to be −26.9 kcal/mol. In the H-ZSM-5 zeolite, the acetone molecule adsorbs by forming a strong hydrogen bond with the Brønsted acid site. The O1−Hz−O3 bond angle (177.6°) is close to linear, and the adsorption energy is computed to be −28.1 kcal/mol. This value agrees reasonably with an experimental report of the adsorption energy of acetone in H-ZSM-5 of −31.1 kcal/mol.[44] In the large cavity of H-MCM-22, acetone also forms a strong hydrogen bond with the Brønsted acid site on the 12T-membered ring of the

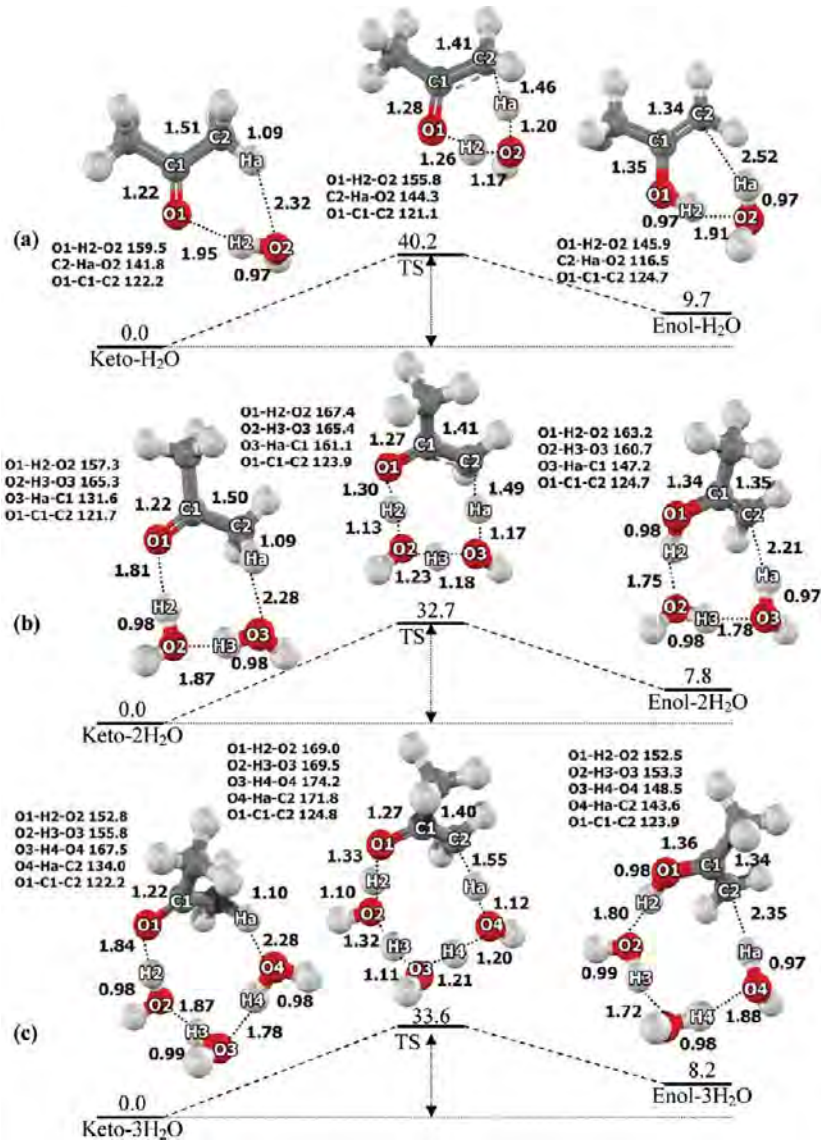


**Figure 3.** Energy profile and complex geometries in the water-assisted tautomerization of acetone from M06-2X/6-311+G(2df,2p)//M06-2X/6-31G(d,p) calculations: (a) one, (b) two, and (c) three water molecules.

supercage. The O1−Hz−O3 bond angle (171.7°) is also close to linear. The adsorption energy is −23.9 kcal/mol.

The computed adsorption energy is found to be dependent on the pore dimension and also on the local geometry of the Brønsted acid site. H-FER is a medium-pore zeolite with a smaller pore dimension as compared with H-ZSM-5, but the geometry of the Brønsted acid site is not suitable for the adsorption of the acetone molecule. Initially, the acid site bond points toward the small 8T window that is too small to accommodate an acetone molecule. The adsorbed acetone molecule has to be located in the 10T main channel. Therefore, the O1−Hz−O3 hydrogen bond angle deviates from linearity. As a result, the interaction of acetone with the Brønsted acid site in H-FER is not as strong as in H-ZSM-5. The adsorption energy in the medium pore H-ZSM-5 is higher than the large pore H-MCM-22 mainly due to the pore confinement effect.

In our previous work,[20] we demonstrated that in studies of the adsorption of carbonyl compounds in zeolites both van der Waals and electrostatic interactions have to be carefully accounted for. We were able to calculate the adsorption energies of acetaldehyde and acetone in H-ZSM-5 by using the embedded ONIOM(B3LYP:UFF) method. With small cluster models, the computed adsorption energy is underestimated by as much as 16 kcal/mol. In the embedded ONIOM(B3LYP:UFF) method, the UFF force field was used to explicitly account for the short-range van der Waals interactions with the surrounding pore walls, and the embedded Madelung potential was used to account for the long-range electrostatic interactions with the zeolite framework. It has been demonstrated that the short-range van der Waals interactions and the long-range electrostatic interactions with the zeolite framework are both very important to the stabilization of the adsorbed carbonyl compounds in zeolite.

In this work, aiming at higher accuracy, we decided to use a large quantum cluster (34T) model calculated with the meta-hybrid M06-2X method that can account for those two important interactions in the zeolite framework simultaneously. The computed results compared well with the experimental measurement, especially in the case of H-ZSM-5. Therefore, we believe that the combination of models and methods presented here is appropriate for investigation of the interactions and reactions of acetone with the Brønsted acid site of zeolites.

**TABLE 1: Optimized Structural Parameters of the Acetone/Zeolite Cluster Complexes in the Three Zeolites As Obtained from M06-2X/6-31G(d,p) Calculations**

| | H-FER | | | | **H-ZSM-5** | | | | H-MCM-22 | | | |
|---|---|---|---|---|---|---|---|---|---|---|---|---|
| | bare | AD | TS | PR | bare | AD | TS | PR | bare | AD | TS | PR |
| | | | | | | Distance | | | | | | |
| Si1−O1 | 1.67 | 1.64 | 1.59 | 1.59 | 1.65 | 1.63 | 1.59 | 1.58 | 1.67 | 1.63 | 1.60 | 1.60 |
| Si2−O2 | 1.58 | 1.57 | 1.64 | 1.66 | 1.59 | 1.57 | 1.62 | 1.64 | 1.60 | 1.59 | 1.64 | 1.65 |
| O1−Al | 1.87 | 1.81 | 1.72 | 1.71 | 1.82 | 1.78 | 1.71 | 1.69 | 1.80 | 1.75 | 1.69 | 1.68 |
| O2−Al | 1.67 | 1.67 | 1.79 | 1.82 | 1.68 | 1.69 | 1.77 | 1.80 | 1.67 | 1.68 | 1.76 | 1.77 |
| Al ··· Hz | 2.30 | 2.44 | 2.93 | 3.01 | 2.35 | 2.45 | 3.19 | 3.52 | 2.43 | 2.43 | 3.06 | 3.08 |
| O1−Hz | 0.97 | 1.10 | 1.74 | 1.83 | 0.97 | 1.11 | 1.80 | 2.08 | 0.97 | 1.16 | 1.90 | 1.94 |
| Hz ··· O3 | | 1.36 | 0.99 | 0.98 | | 1.32 | 0.99 | 0.97 | | 1.24 | 0.98 | 0.97 |
| O1 ··· O3 | | 2.43 | 2.71 | 2.80 | | 2.42 | 2.74 | 2.91 | | 2.39 | 2.70 | 2.73 |
| O3−C1 | 1.21 | 1.23 | 1.32 | 1.34 | 1.21 | 1.23 | 1.31 | 1.33 | 1.21 | 1.24 | 1.31 | 1.32 |
| C1−C2 | 1.52 | 1.50 | 1.38 | 1.36 | 1.52 | 1.49 | 1.38 | 1.36 | 1.52 | 1.49 | 1.38 | 1.37 |
| C2−Ha | 1.09 | 1.09 | 1.56 | 1.92 | 1.09 | 1.10 | 1.43 | 1.76 | 1.09 | 1.09 | 1.50 | 1.60 |
| C1 ··· Ha | 2.14 | 2.14 | 2.24 | 2.46 | 2.14 | 2.10 | 2.07 | 2.25 | 2.14 | 2.14 | 2.19 | 2.23 |
| Ha ··· O2 | | 2.36 | 1.14 | 1.02 | | 2.67 | 1.20 | 1.04 | | 2.81 | 1.14 | 1.09 |
| O1 ··· O2 | 2.56 | 2.59 | 2.65 | 2.66 | 2.49 | 2.52 | 2.54 | 2.52 | 2.60 | 2.63 | 2.62 | 2.61 |
| C1 ··· O1 | | 3.23 | 3.30 | 3.37 | | 3.23 | 3.27 | 3.37 | | 3.20 | 3.21 | 3.23 |
| C1 ··· O2 | | 3.60 | 3.20 | 3.31 | | 3.09 | 3.09 | 3.19 | | 3.64 | 3.18 | 3.18 |
| C2 ··· O2 | | 3.33 | 2.67 | 2.89 | | 2.99 | 2.63 | 2.79 | | 3.03 | 2.63 | 2.68 |
| | | | | | | Angle | | | | | | |
| Al−O1−Si1 | 141.8 | 139.5 | 141.5 | 141.1 | 130.6 | 128.4 | 127.6 | 127.4 | 125.0 | 123.5 | 123.4 | 123.2 |
| Al−O2−Si2 | 150.7 | 153.0 | 146.3 | 146.8 | 133.3 | 135.8 | 133.0 | 133.0 | 124.5 | 125.8 | 126.0 | 126.2 |
| O1−Hz−O3 | | 165.8 | 167.1 | 167.8 | | 177.6 | 156.8 | 142.0 | | 171.7 | 137.3 | 136.1 |
| O1−Al−O2 | 92.5 | 95.8 | 98.0 | 97.8 | 90.4 | 93.1 | 93.7 | 92.4 | 97.2 | 100.0 | 98.8 | 98.4 |

***3.3.3. Tautomerization of Acetone on H-FER, H-ZSM-5 and H-MCM-22.*** The tautomerization of acetone on the Brønsted acid site of zeolite starts by the adsorption of acetone on the active site shown in Figure 4. The acetone molecule is stabilized by forming a hydrogen bond complex with the zeolite acid site. The computed adsorption energies are in the following order: −23.9, −26.9, and −28.1 for H-MCM-22, H-FER, and H-ZSM-5, respectively. These adsorption energies would suggest that the hydrogen bond between the adsorbed acetone and zeolite acid site on H-ZSM-5 is the strongest and on the H-MCM-22 is the weakest. However, when looking at the structural parameters of the optimized complex, it is observed that the hydrogen bond distance (O1···O3) in the H-MCM-22 is the shortest at 2.39 Å and the hydrogen bond angle (O1-Hz-O3) is also close to the linear angle (171.7°), indicating a very strong hydrogen bond interaction. In H-MCM-22, the adsorption causes the Brønsted O1−Hz bond distance to be significantly lengthened from 0.97 to 1.16 Å. The carbonyl double bond (O3−C1) is lengthened from 1.21 to 1.24 Å, and the C1−C2 single bond distance is decreased from 1.52 to 1.49 Å, indicating that the adsorbed acetone is activated. In H-ZSM-5, the hydrogen bond distance (O1···O3) is longer than in H-MCM-22 (2.42 Å). Therefore, the adsorbed acetone is somewhat less activated. The carbonyl double bond (O3−C1) is lengthened to 1.23 Å, and the C1−C2 single bond distance is decreased to 1.49 Å. The hydrogen bond complex in H-FER is observed to have the weakest hydrogen bond interaction. The hydrogen bond angle (O1−Hz−O3) is 165.8°, and the hydrogen bond distance (O1···O3) is 2.43 Å. The adsorbed acetone is, thus, least activated. The O3−C1 bond distance is lengthened to 1.23 Å and the C1−C2 bond distance is slightly decreased to 1.50 Å. At the transition state, the Brønsted proton is completely transferred to the carbonyl oxygen atom. For example, in the case of H-MCM-22, the O1−Hz bond elongates from 1.16 to 1.90 Å. The O3−C1 bond distance increases to 1.31 Å as the O3−Hz hydroxyl bond is formed with a bond length of 0.98 Å. The C1−C2 bond distance is reduced to 1.38 Å, indicating the double bond formation.

The activation energy of acetone tautomerization on the zeolite acid site is much smaller than in the isolated gas phase and in the water-assisted system. The zeolite acid site can greatly reduce the activation barrier. The computed activation energies are 16.6, 20.5, and 24.9 kcal/mol for the reaction in H-MCM-22, H-ZSM-5, and H-FER, respectively. The activation energies for acetone enolization in zeolites are in the same range with the free energy of activation for the reaction catalyzed by diluted mineral acid in aqueous solutions of 23.6 kcal/mol (at 298 K).[41] The activation energy trend is directly related to the strength of the hydrogen bond interactions between the adsorbed acetone and the Brønsted acid site but not to the overall adsorption interactions.

In these three representative cases, the adsorbed acetone molecule can get closer to the acid site in a geometry with larger pores and, thus, form a stronger hydrogen bonds and more activated adsorption complexes. The reaction energies for the transformation of adsorbed keto to enol of acetone are found to be 15.9, 17.6, and 22.7 kcal/mol in H-MCM-22, H-ZSM-5, and H-FER, respectively. These values are significantly higher than the reaction energy observed in diluted solutions of mineral acids (10.3 kcal/mol).[41] The higher endothermic reaction energy is due to the fact that the adsorbed acetone is highly stabilized by a strong hydrogen bond with the acid site but the produced acetone enol is weakly adsorbed on the acid site by a weak $\pi$ interaction. Among these three zeolites, the difference in the energies between adsorbed acetone and acetone enol decrease with the increase of pore dimensions. However, the observed reaction energy trend is not simply due to the confinement effect of the zeolite walls. It is more likely to be related to the local interaction of the adsorbed enol form with the Brønsted acid site. The large cavity of H-MCM-22 can better accommodate the bulkier acetone enol, as reflected by a closer intermolecular distance of the C2 carbon atom of the adsorbed enol to the Ha proton of the acid site. The distances are 1.60, 1.76, and 1.92 Å for H-MCM-22, H-ZSM-5, and H-FER, respectively.

It is noticed that the structures of the transition state and the product are very similar and the reverse reaction to transform

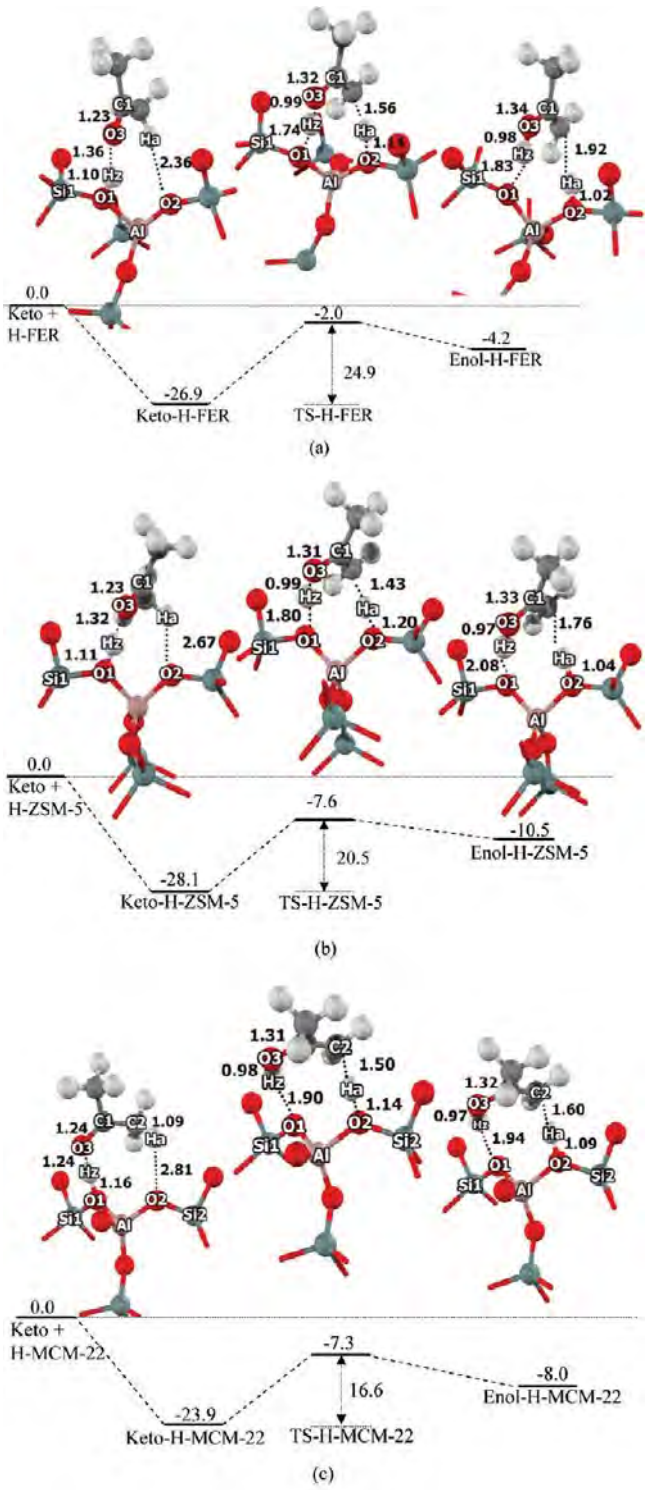


**Figure 4.** Molecular structures and energy profile of the tautomerization of acetone in a 34T model of (a) H-FER, (b) H-ZSM-5 and (c) H-MCM-22 as obtained from M06-2X/6-31+G(2df,2p)//M06-2X/6-31G(d,p) calculations. Distances and energies are given in Å and kcal/mol.

the adsorbed enol to the adsorbed keto form is very facile on zeolite surfaces with a small activation barrier. The activation energy of the ketonization process in these zeolites is calculated to be 0.7, 2.9, and 2.2 kcal/mol for H-MCM-22, H-ZSM-5, and H-FER, respectively, although the activation barrier for acetone ketonization in diluted mineral acid was experimentally measured to be 12.3 kcal/mol.[41] The reason for the small reverse activation energies and their trend among these three zeolites should be due to the relative stability of the adsorbed enol compared with the adsorbed acetone on the zeolite acid site. Acetone enol is much less stabilized than the adsorbed acetone on the zeolite acid site. This observation is in agreement with several experimental studies of reactions of carbonyl compounds in zeolites in which the enol form could not be detected.[4,5,45] The involvement of the enol form in carbonyl transformations was experimentally suggested by the observation of H/D exchange[45] and chlorination of acetone on the Brønsted acid site of zeolites.[5] These experimental results would indicate that the reaction of acetone would be processed through the enol form, which, however, is highly unstable in the zeolite framework. Our results clearly illustrate the relative stabilities of keto and enol forms of acetone in these three zeolites. The energies of reactants, transition states and products have also been calculated with the B3LYP functional. As expected, these adsorption energies are much smaller or there is no binding at all. Their values are given in the Supporting Information.

## 4. Conclusions

The effect of zeolite pore confinement on the tautomerization of acetone has been studied on three zeolites with different pore sizes. The use of a large cluster model with M06-2X/6-311+G(2df,2p)//M06-2X/6-31G(d,p) level of theory is found to be sufficient to account for interactions of acetone with the zeolite acid site and pore environments. The adsorption energies are calculated to be −26.9, −28.1, and −23.9 kcal/mol for H-FER, H-ZSM-5, and H-MCM-22, respectively, which agree well with the available experimental data for H-ZSM-5. Due to the involvement of the zeolite Brønsted acid site and the confinement effect, the tautomerization of acetone in zeolite proceeds through a much lower activation barrier than in the isolated gas phase and in the presence of water molecules. The activation energies and reaction energies decrease with the increase in the zeolite pore sizes, which are 24.9, 20.5, and 16.6 kcal/mol and 22.7, 17.6, and 15.9 kcal/mol, for the reaction in H-FER, H-ZSM-5, and H-MCM-22, respectively. The fact that the adsorption energy and activation energy trends are not correlated but rather in opposite directions indicates that the interaction with the acid site and the confinement effect of the pore walls are equally important and must be carefully accounted for to understand this reaction in zeolites. These trends are more related to the relative strength of the interactions of the active intermediates with the Brønsted acid site than to the confinement effect of the zeolite walls. The large pore of H-MCM-22 allows the adsorbed acetone and acetone enol to be closer to the acid site for stronger interactions. Therefore, both acetone enolization and (reverse) ketonization are very facile in this large-pore zeolite.

**Acknowledgment.** This work was supported in part by grants from the National Science and Technology Development Agency (2009 NSTDA Chair Professor funded by the Crown Property Bureau under the management of the National Science and Technology Development Agency and NANOTEC Center of Excellence funded by the National Nanotechnology Center), The Thailand Research Fund, the Commission of Higher Education, Ministry of Education ("the National Research University Project of Thailand (NRU)" and "Postgraduate Education and Research Programs in Petroleum and Petrochemicals and Advanced Materials"). Support from the Kasetsart University Research and Development Institute (KURDI) and Graduate School Kasetsart University are also acknowledged. The authors are grateful to Donald G. Truhlar and Yan Zhao

for their support with the M06-2X functional. M.P. acknowledges support from the Austrian Ministry of Science BMWF as part of the Uni-Infrastrukturprogramm of the research platform Scientific Computing at LFU Innsbruck.

**Supporting Information Available:** Table S1: Selected geometrical parameters for adsorption and reaction mechanism of acetone on H-FER, H-ZSM-5, and H-MCM-22 zeolites. Table S2: The adsorption and reaction energies of acetone on H-FER, H-ZSM-5, and H-MCM-22 zeolites with various methods. This material is available free of charge via the Internet at http://pubs.acs.org.

## References and Notes

(1) Evans, D. A.; Nelson, J. V.; Vogel, E.; Taber, T. R. *J. Am. Chem. Soc.* **1981**, *103*, 3099.
(2) Salvapati, G. S.; Ramanamurty, K. V.; Janardanarao, M. *J. Mol. Catal.* **1989**, *54*, 9.
(3) Li, C. J. *Chem. Rev. (Washington, DC)* **1993**, *93*, 2023.
(4) Xu, T.; Munson, E. J.; Haw, J. F. *J. Am. Chem. Soc.* **1994**, *116*, 1962.
(5) Biaglow, A. I.; Sepa, J.; Gorte, R. J.; White, D. *J. Catal.* **1995**, *151*, 373.
(6) Panov, A. G.; Fripiat, J. J. *J. Catal.* **1998**, *178*, 188.
(7) Dumitriu, E.; Hulea, V.; Fechete, I.; Auroux, A.; Lacaze, J. F.; Guimon, C. *Microporous Mesoporous Mater.* **2001**, *43*, 341.
(8) Melo, L.; Giannetto, G.; Cardozo, L.; Llanos, A.; Garcia, L.; Magnoux, P.; Guisnet, M.; Alvarez, F. *Catal. Lett.* **1999**, *60*, 217.
(9) Yang, P.; Shang, Y.; Yu, J.; Wang, J.; Zhang, M.; Wu, T. *J. Mol. Catal. A: Chem.* **2007**, *272*, 75.
(10) Rodriguez-Santiago, L.; Vendrell, O.; Tejero, I.; Sodupe, M.; Bertran, J. *Chem. Phys. Lett.* **2001**, *334*, 112.
(11) Wu, C.-C.; Lien, M.-H. *J. Phys. Chem.* **1996**, *100*, 594.
(12) Lee, D.; Kim, C. K.; Lee, B.-S.; Lee, I.; Lee, B. C. *J. Comput. Chem.* **1997**, *18*, 56.
(13) Cucinotta, C. S.; Ruini, A.; Catellani, A.; Stirling, A. *ChemPhysChem* **2006**, *7*, 1229.
(14) Zakharov, M.; Masunov, A. E.; Dreuw, A. *J. Phys. Chem. A* **2008**, *112*, 10405.
(15) Solans-Monfort, X.; Bertran, J.; Branchadell, V.; Sodupe, M. *J. Phys. Chem. B* **2002**, *106*, 10220.
(16) Rattanasumrit, A.; Ruangpornvisuti, V. *J. Mol. Catal. A: Chem.* **2005**, *239*, 68.
(17) Zicovich-Wilson, C. M.; Corma, A.; Viruela, P. *J. Phys. Chem.* **1994**, *98*, 10863.
(18) Derouane, E. G. *J. Mol. Catal. A: Chem.* **1998**, *134*, 29.
(19) Derouane, E. G.; Chang, C. D. *Microporous Mesoporous Mater.* **2000**, *35*−*36*, 425.
(20) Boekfa, B.; Sirijareansre, J.; Pantu, P.; Limtrakul, J. *Stud. Surf. Sci. Catal.* **2004**, *154B*, 1582.
(21) Pantu, P.; Boekfa, B.; Limtrakul, J. *J. Mol. Catal. A: Chem.* **2007**, *277*, 171.
(22) Namuangruk, S.; Khongpracha, P.; Pantu, P.; Limtrakul, J. *J. Phys. Chem. B* **2006**, *110*, 25950.
(23) Namuangruk, S.; Pantu, P.; Limtrakul, J. *ChemPhysChem* **2005**, *6*, 1333.
(24) Boekfa, B.; Choomwattana, S.; Khongpracha, P.; Limtrakul, J. *Langmuir* **2009**, *25*, 12990.
(25) Zhao, Y.; Truhlar, D. G. *Theor. Chem. Acc.* **2008**, *120*, 215.
(26) Zhao, Y.; Truhlar, D. G. *J. Phys. Chem. C* **2008**, *112*, 6860.
(27) Maihom, T.; Boekfa, B.; Sirijaraensre, J.; Nanok, T.; Probst, M.; Limtrakul, J. *J. Phys. Chem. C* **2009**, *113*, 6654.
(28) Morris, R. E.; Weigel, S. J.; Henson, N. J.; Bull, L. M.; Janicke, M. T.; Chmelka, B. F.; Cheetham, A. K. *J. Am. Chem. Soc.* **1994**, *116*, 11849.
(29) Van Koningsveld, H.; Van Bekkum, H.; Jansen, J. C. *Acta Crystallogr., Sect. B: Struct. Sci.* **1987**, *B43*, 127.
(30) Kennedy, G. J.; Lawton, S. L.; Rubin, M. K. *J. Am. Chem. Soc.* **1994**, *116*, 11000.
(31) Nieminen, V.; Sierka, M.; Murzin, D. Y.; Sauer, J. *J. Catal.* **2005**, *231*, 393.
(32) Lonsinger, S. R.; Chakraborty, A. K.; Theodorou, D. N.; Bell, A. T. *Catal. Lett.* **1991**, *11*, 209.
(33) Zhou, D.; Bao, Y.; Yang, M.; He, N.; Yang, G. *J. Mol. Catal. A: Chem.* **2006**, *244*, 11.
(34) Schlegel, H. B. *J. Comput. Chem.* **1982**, *3*, 214.
(35) Gonzalez, C.; Bernhard Schlegel, H. *J. Chem. Phys.* **1989**, *90*, 2154.
(36) Curtiss, L. A.; Zygmunt, S. A.; Iton, L. E. *Proc. Int. Zeolite Conf.* **1999**, *1*, 415.
(37) Zygmunt, S. A.; Curtiss, L. A.; Zapol, P.; Iton, L. E. *J. Phys. Chem. B* **2000**, *104*, 1944.
(38) Frisch, M. J.; Trucks, G. W.; Schlegel, H. B.; Scuseria, G. E.; Robb, M. A.; Cheeseman, J. R.; Montgomery, J. A., Jr.; Vreven, T.; Kudin, K. N.; Burant, J. C.; Millam, J. M.; Iyengar, S. S.; Tomasi, J.; Barone, V.; Mennucci, B.; Cossi, M.; Scalmani, G.; Rega, N.; Petersson, G. A.; Nakatsuji, H.; Hada, M.; Ehara, M.; Toyota, K.; Fukuda, R.; Hasegawa, J.; Ishida, M.; Nakajima, T.; Honda, Y.; Kitao, O.; Nakai, H.; Klene, M.; Li, X.; Knox, J. E.; Hratchian, H. P.; Cross, J. B.; Adamo, C.; Jaramillo, J.; Gomperts, R.; Stratmann, R. E.; Yazyev, O.; Austin, A. J.; Cammi, R.; Pomelli, C.; Ochterski, J. W.; Ayala, P. Y.; Morokuma, K.; Voth, G. A.; Salvador, P.; Dannenberg, J. J.; Zakrzewski, V. G.; Dapprich, S.; Daniels, A. D.; Strain, M. C.; Farkas, O.; Malick, D. K.; Rabuck, A. D.; Raghavachari, K.; Foresman, J. B.; Ortiz, J. V.; Cui, Q.; Baboul, A. G.; Clifford, S.; Cioslowski, J.; Stefanov, B. B.; Liu, G.; Liashenko, A.; Piskorz, P.; Komaromi, I.; Martin, R. L.; Fox, D. J.; Keith, T.; Al-Laham, M. A.; Peng, C. Y.; Nanayakkara, A.; Challacombe, M.; Gill, P. M. W.; Johnson, B.; Chen, W.; Wong, M. W.; Gonzalez, C.; Pople, J. A. *Gaussian 03, revision B.05*; Gaussian, Inc.: Pittsburgh, PA, 2003.
(39) Holmes, J. L.; Lossing, F. P. *J. Am. Chem. Soc.* **1982**, *104*, 2648.
(40) Turecek, F.; Havlas, Z. *J. Org. Chem.* **1986**, *51*, 4066.
(41) Chiang, Y.; Kresge, A. J.; Schepp, N. P. *J. Am. Chem. Soc.* **1989**, *111*, 3977.
(42) Klinowski, J. *Chem. Rev.* **1991**, *91*, 1459.
(43) Freude, D.; Klinowski, J.; Hamdan, H. *Chem. Phys. Lett.* **1988**, *149*, 355.
(44) Sepa, J.; Lee, C.; Gorte, R. J.; White, D.; Kassab, E.; Evleth, E. M.; Jessri, H.; Allavena, M. *J. Phys. Chem.* **1996**, *100*, 18515.
(45) Xu, M.; Wang, W.; Hunger, M. *Chem. Commun. (Cambridge, U. K.)* **2003**, 722.

JP1058947

# Effect of the Zeolite Nanocavity on the Reaction Mechanism of *n*-Hexane Cracking: A Density Functional Theory Study

**T. Maihom,[†,‡] P. Pantu,[†,‡] C. Tachakritikul,[§] M. Probst,[||] and J. Limtrakul*[,†,‡]**

*Laboratory for Computational and Applied Chemistry, Department of Chemistry, Faculty of Science and Center of Nanotechnology, Kasetsart University Research and Development Institute, Kasetsart University, Bangkok 10900, Thailand, NANOTEC Center of Excellence, National Nanotechnology Center, Kasetsart University, Bangkok 10900, Thailand, PTT Research and Technology Institute, PTT Public Company Limited, Wang Noi, Phra Nakhon Si Ayutthaya, Thailand, and Institute of Ion Physics and Applied Physics, University of Innsbruck, A-6020 Innsbruck, Austria*

*Received: December 11, 2009; Revised Manuscript Received: February 9, 2010*

The effects of the zeolite framework on the mechanism of *n*-hexane monomolecular cracking have been investigated with M06-2X/6-311+G(2df,2p)//M06-2X/6-31G(d,p) calculations. M06-2X is a recently developed hybrid-meta functional that is parametrized to include the London dispersion energy. The 38T H-FAU and 34T H-ZSM-5 nanocluster models where T atoms are either Si or Al atoms are used to represent H-FAU and H-ZSM-5 zeolites. The adsorption energies of hexane are predicted to be −10.8 and −18.2 kcal/mol for H-FAU and H-ZSM-5, respectively, in good agreement with experimental measurements. This indicates that the confinement effects on different types of zeolites can be well represented by the M06-2X functional. The reaction is assumed to proceed in two steps. In the first step, the central C−C bond of adsorbed *n*-hexane is protonated to form a hexonium intermediate. The adsorbed 3-C-hexonium is highly unstable and can be rapidly decomposed to produce the products. The first step is found to be the rate-determining step with activation energies of 45.7 and 45.8 kcal/mol for H-FAU and H-ZSM-5, respectively. For step two, the activation energies are calculated to be 8.6 and 9.9 kcal/mol for H-FAU and H-ZSM-5, respectively. The results clearly demonstrate that the reaction of *n*-hexane cracking is intrinsically the same in these large- and medium-pore zeolites. The different apparent activities can be explained by the different adsorption energies which are mainly due to the van der Waals interactions with the zeolite walls.

## 1. Introduction

The catalytic cracking of hydrocarbons is an important reaction in the petrochemical industry. It is used to break down large hydrocarbons in crude oil into light hydrocarbons for the production of fuels. Zeolite catalysts, especially Y and ZSM-5, are widely used in cracking processes due to their advantages of high catalytic activity and selectivity. Because of the molecular shape selectivity, zeolites are also widely used in many other petrochemical processes, for example, hydrocracking, isomerization, and alkylation of hydrocarbons and aromatics.[1,2]

The catalytic cracking of hydrocarbons is proposed to occur via a bimolecular and a monomolecular mechanism.[3–5] The classical bimolecular mechanism involves hydride transfer between an alkane and an adsorbed carbenium ion followed by isomerization and $\beta$-scission. This mechanism prevails under high partial pressure of hydrocarbons and low reaction temperature. Monomolecular cracking is believed to be an important mechanism for the cracking reaction of hydrocarbons under low partial pressure of hydrocarbons and high reaction temperature.[3,4] In this mechanism, the reaction proceeds through a high-energy carbonium ion which is formed by the direct protonation of Brønsted acid to the C−C bond.[3,4] Subsequently, the carbonium ion collapses, leading to the scission of the C−C bond to produce alkane and alkene products. Many theoretical studies[6–12] have attempted to explain monomolecular cracking of alkanes in zeolites and reported that the nonclassical two-electron three-center carbonium ions are the transition states of the reactions. Collins and O'Malley[6,7] have suggested that a pathway involving a carbenium ion intermediate could also exist for the protolytic cracking of alkanes. Kazansky et al.[13] were able to locate adsorbed carbonium ions as local minima in hydride transfer between methyl and methane and between ethyl and ethane on the zeolite surface. However, for hydride transfer involving secondary and tertiary alkyl cations, carbonium ions are only present as transition states. The adsorbed carbonium ions are highly unstable and easily decomposed to give products with a very small activation energy or presumably without an energy barrier. Boronat et al.[14,15] have reported that the C−H−C bridged carbonium ions, for example, 1-C-butonium and 2-C-butonium, can be reaction intermediates for hydride transfer, alkylation, and cracking of alkanes on zeolites. They have concluded that only carbonium ions whose positive charges are delocalized and inaccessible to oxygen atoms on the zeolite surface can exist as true reaction intermediates.

To understand hydrocarbon reactions, it is of particular interest to study the reactivity and stability of the carbonium ions as transition states or reaction intermediates on the zeolite surface. It is expected that the zeolite framework should have profound effects on reactive intermediates and the reaction

* To whom correspondence should be addressed. E-mail: jumras.1@ku.ac.th. Telephone: +66-2-562-5555 ext 2159.
[†] Laboratory for Computational and Applied Chemistry, Department of Chemistry, Faculty of Science and Center of Nanotechnology, Kasetsart University Research and Development Institute, Kasetsart University.
[‡] NANOTEC Center of Excellence, National Nanotechnology Center, Kasetsart University.
[§] PTT Research and Technology Institute, PTT Public Company Limited.
[||] Institute of Ion Physics and Applied Physics, University of Innsbruck.

10.1021/jp911732p 
Published on Web 04/13/2010

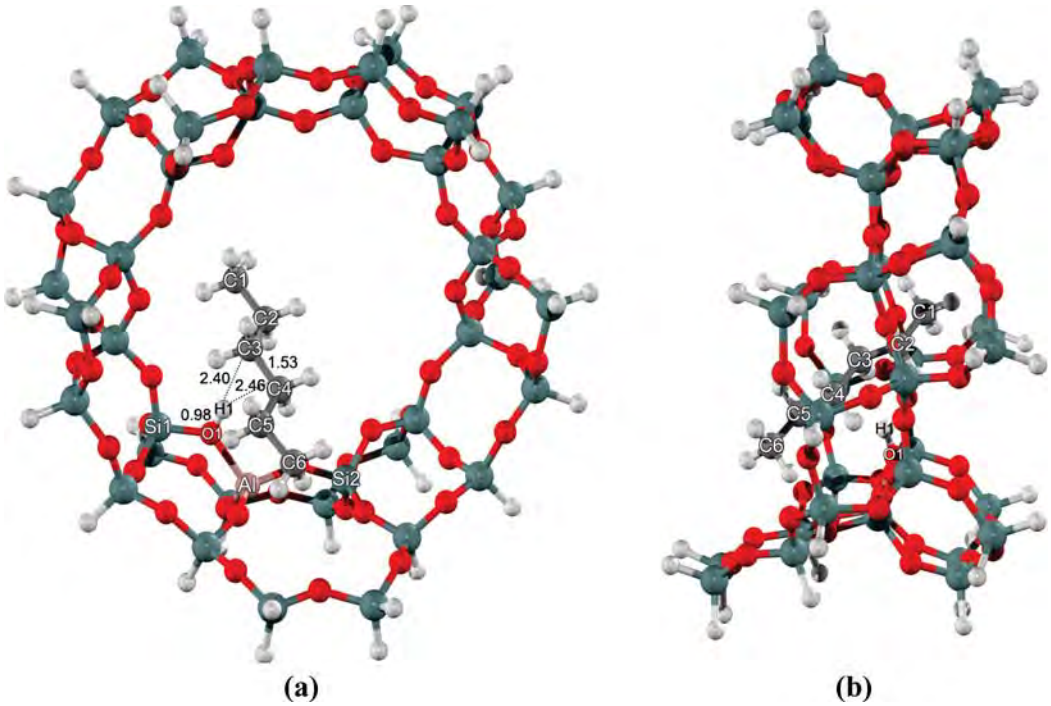


**Figure 1.** 38T cluster model of H-FAU zeolite with adsorbed *n*-hexane: (a) front view and (b) side view.

mechanism for catalytic reactions over zeolite catalysts.[16,17] Recently, Hansen et al.[18] have indicated that to be able to locate highly reactive intermediates, carbenium or carbonium ions, it is necessary to use a sufficiently large model. In that report, they have found protonated ethyl benzene as a stable intermediate only when a large cluster of zeolite (33T) was used for the calculations. That finding emphasizes that both short-range van der Waals interactions and long-range electrostatic interactions with the zeolite pore walls can significantly affect relative stabilities of intermediates and transition states of reactions and, thus, the overall reaction mechanisms. Due to a large number of atoms per unit cell of zeolites, the periodic ab initio calculations usually are computationally too expensive and even impractical when very large zeolites are concerned. Conventional density functional methods are known to be unable to describe dispersion (van der Waals) forces.[19] Therefore, it is not certain that density functional theory (DFT) calculations on large zeolite clusters will give the right answer. Previously, we have successfully used the ONIOM method[20] to study several reaction mechanisms in zeolites.[21–26] The success of the ONIOM method is, however, strongly dependent on the right partition of the active region and the environment, and the right combination of high and low level methods. Recently, the new meta-hybrid density functional M06 series[27,28] have been developed and shown to accurately compute binding energies of adsorbates covalently and noncovalently interacting with the zeolite acid site. The results were comparable to MP2 calculations at a high basis set but at much more affordable computer times. Recently, we have demonstrated that the zeolite confinement effect on reactions of unsaturated aliphatic, aromatic, and heterocyclic compounds could be successfully studied[29] by performing full quantum calculations on sufficiently large clusters using the M06-2X method. This approach is, in principle, not only more accurate compared to the ONIOM method, but it also makes the selection of zeolite models more general and systematic.

In this work, we report the theoretical investigation on the mechanism of *n*-hexane protolytic cracking of H-ZSM-5 and H-FAU zeolites by employing relatively large cluster models to realistically represent the framework of zeolites and using the M06-2X method. The reaction mechanism and relative energies and structures of intermediates and transition states are discussed to understand the effect of the zeolite pore confinement on the protolytic cracking reaction. *n*-Hexane is chosen as a reactant in this work because it is widely used experimentally as a benchmark in cracking reactions to study the zeolite acidity and the effect of different zeolite frameworks.[30,31] Theoretical studies of the protolytic cracking of *n*-hexane on different types of zeolites utilizing realistic models have not been performed previously.

## 2. Models and Method

38T H-FAU and 34T H-ZSM-5 cluster zeolite models were generated from their lattice structures.[32,33] The 38T cluster model of H-FAU, illustrated in Figure 1, covers the 12-membered-ring window connecting two supercages of faujasite. It is symmetrically extended from the 12T of the 12-membered-ring to include 38 tetrahedral atoms. Silicon at the T2 position was replaced by aluminum to model a Brønsted acid site. For the ZSM-5 zeolite, the 34T quantum cluster model (see Figure 2) covers the intersection at the interconnection between the straight channel and the zigzag channel. One aluminum atom was substituted for a silicon atom at the T12 site to generate the Brønsted acid site.

The M06-2X density functional is used in all calculations. During geometry optimizations, only the 5T active region of "$SiOHAl(OSi)_2OSi$" and the reacting molecule are allowed to relax while the rest of the structure is kept fixed at the crystallographic coordinates. For geometry optimizations, the 6-31G(d,p) basis set was used. In order to obtain more accurate interaction energies, single point calculations with the 6-311+G(2df,2p) basis set were carried out. Transition states were confirmed to have one imaginary frequency corresponding to the reaction coordinate. Furthermore, the internal reaction coordinate (IRC) method[34,35] was used to verify that the transition states are

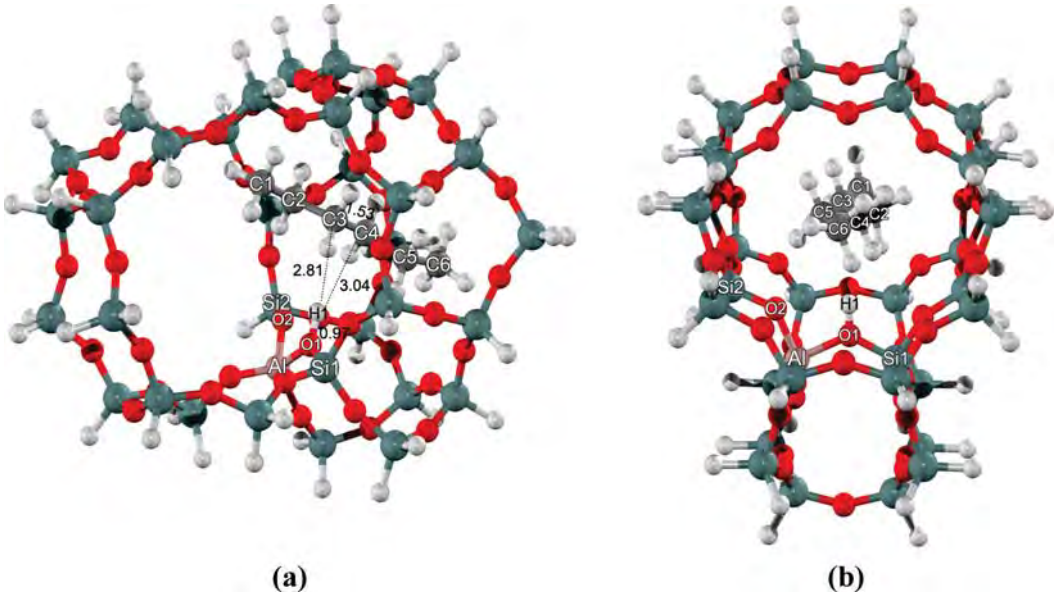


**Figure 2.** 34T cluster model of H-ZSM-5 zeolite with adsorbed *n*-hexane via the two methylene carbon atoms: (a) straight channel view and (b) sinusoidal channel view.

**TABLE 1: Optimized Geometrical Parameters of the Species Involved in the *n*-Hexane Cracking on FAU Zeolite**

| parameter | isolated cluster | hexane adsorption (Ads_FAU) | transition state (TS1_FAU) | 3-C-hexonium intermediate (Int_FAU) | transition state (TS2_FAU) | product (Prod_FAU) |
|---|---|---|---|---|---|---|
| | | | **distances (Å)** | | | |
| O1−H1 | 0.97 | 0.98 | 1.79 | 2.15 | 2.45 | |
| Al−O1 | 1.97 | 1.96 | 1.83 | 1.81 | 1.79 | 1.74 |
| Al−O2 | 1.72 | 1.72 | 1.77 | 1.78 | 1.80 | 1.94 |
| H1−C3 | | 2.40 | 1.25 | 1.24 | 1.71 | |
| H1−C4 | | 2.46 | 1.39 | 1.26 | 1.13 | 1.09 |
| C2−C3 | 1.53 | 1.53 | 1.52 | 1.51 | 1.43 | 1.34 |
| C3−C4 | 1.53 | 1.53 | 1.72 | 1.91 | 2.70 | 4.06 |
| O2−H2 | | 3.85 | 4.02 | 4.32 | 1.81 | 1.01 |
| C2−H2 | | 1.10 | 1.10 | 1.09 | 1.14 | 2.11 |
| C3−H2 | | 2.16 | 2.14 | | 2.01 | 1.98 |
| C3−O1 | | 3.37 | 2.93 | 3.14 | 2.90 | 3.23 |
| C3−O2 | | 4.47 | 2.89 | 4.40 | 3.57 | 2.98 |
| C4−O1 | | 3.32 | 2.89 | 3.04 | 3.15 | 3.17 |
| C4−O2 | | 3.53 | 3.12 | 3.10 | 3.61 | 4.53 |
| | | | **angles (deg)** | | | |
| O2−Al−O1 | 106.2 | 107.1 | 109.3 | 109.6 | 109.1 | 104.8 |
| Si1−O1−Al | 132.3 | 131.5 | 128.3 | 129.9 | 133.1 | 132.3 |
| C3−H1−C4 | | 35.0 | 81.2 | 100.1 | 144.0 | 138.7 |

connected with the minima. In order to reduce the computational cost of the frequency and IRC calculations, 14T H-FAU and 12T H-ZSM-5 models based on 38T H-FAU and 34T H-ZSM-5 optimized structures were employed. Profiles of the energy and of important distances along the reaction coordinate are given as Supporting Information. All calculations were performed with the Gaussian 03 code[36] modified to incorporate the Minnesota Density Functionals module 3.1 by Zhao and Truhlar.

## 3. Results and Discussion

**3.1. Adsorption of *n*-Hexane on H-FAU and H-ZSM-5 Zeolites.** Optimized structures of *n*-hexane adsorption on H-FAU and H-ZSM-5 zeolites obtained from the M06-2X/6-31G(d,p) calculations are shown in Figures 1 and 2, respectively. Selected geometrical structures for the adsorption complexes are tabulated in Tables 1 and 2. An *n*-hexane molecule is weakly adsorbed on zeolite through interactions between two methylene carbon atoms and the Brønsted acid site (O1−H1). In this study, we focus only on the adsorption on the central C−C bond of *n*-hexane because the protolytic cracking of this bond will lead to the formation of propane and propene molecules which are the main products of *n*-hexane cracking.[37–40] The adsorption interactions are weak so that the structures of the zeolites and the adsorbed *n*-hexane are not significantly changed. The bond distance in the acidic O−H bond and the C−C bond of *n*-hexane differ slightly from the isolated molecules. In H-FAU, the distances between the carbon atoms of the adsorbed *n*-hexane and the zeolite proton are 2.40 and 2.46 Å for H1···C3 and H1···C4, respectively. The calculated adsorption energy is −10.8 kcal/mol, which agrees well with an experimental measurement of −12.7 kcal/mol.[41] In the ZSM-5 zeolite, the calculated adsorption energy is −18.2 kcal/mol. This computed adsorption energy is also in good agreement with the experimental measurement of −19.6 kcal/mol.[41]

Analogous calculations were also performed with the widely used B3LYP density functional. Selected geometrical parameters of the complexes and the corresponding adsorption energies obtained from B3LYP are listed in Table S1 in the Supporting

**TABLE 2: Optimized Geometrical Parameters of All Species Involved in the *n*-Hexane Cracking on H-ZSM-5 Zeolite**

| parameter | isolated cluster | hexane adsorption (Ads_ZSM-5) | transition state (TS1_ ZSM-5) | 3-C-hexonium intermediate (Int_ZSM-5) | transition state (TS2_ZSM-5) | product (Prod_ZSM-5) |
|---|---|---|---|---|---|---|
| | | | **distances (Å)** | | | |
| O1−H1 | 0.97 | 0.97 | 1.74 | 2.01 | 2.31 | |
| Al−O1 | 1.82 | 1.82 | 1.73 | 1.72 | 1.71 | 1.68 |
| Al−O2 | 1.68 | 1.68 | 1.70 | 1.71 | 1.72 | 1.81 |
| H1−C3 | | 2.81 | 1.31 | 1.26 | 1.88 | |
| H1−C4 | | 3.04 | 1.32 | 1.26 | 1.11 | 1.09 |
| C2−C3 | 1.53 | 1.53 | 1.52 | 1.52 | 1.42 | 1.34 |
| C3−C4 | 1.53 | 1.53 | 1.76 | 1.86 | 2.72 | 3.38 |
| O2−H2 | | 2.90 | 2.53 | 2.67 | 1.87 | 1.01 |
| C2−H2 | | 1.10 | 1.09 | 1.09 | 1.15 | 2.10 |
| C3−H2 | | 2.15 | 2.14 | | 1.95 | 2.03 |
| C3−O1 | | 3.77 | 2.87 | 2.96 | 3.01 | 3.32 |
| C3−O2 | | 3.96 | 3.34 | 3.31 | 3.47 | 3.03 |
| C4−O1 | | 3.95 | 2.85 | 3.00 | 3.21 | 3.46 |
| C4−O2 | | 3.81 | 2.98 | 2.99 | 3.18 | 3.57 |
| | | | **angles (deg)** | | | |
| O2−Al−O1 | 90.4 | 90.5 | 94.3 | 94.2 | 95.0 | 91.6 |
| Si1−O1−Al | 130.5 | 130.1 | 126.1 | 127.5 | 128.8 | 128.8 |
| C3−H1−C4 | | 30.0 | 83.7 | 95.0 | 129.3 | 115.1 |

Information. While the geometric differences are small, B3LYP leads to adsorption energies of −1.65 and 1.06 kcal/mol for H-FAU and H-ZSM-5, respectively, which are much too low compared to the experimental values given above. This is not surprising, given the lack of dispersion interactions in B3LYP which leave exchange repulsion as the only short-range *n*-hexane/zeolite interaction.

**3.2. Reaction Mechanism of *n*-Hexane Protolytic Cracking.** The adsorbed *n*-hexane molecule is considered to undergo a two-step protolytic cracking, consisting of the protonation of *n*-hexane and the decomposition of the hexonium intermediate to produce propane and propene products.

***3.2.1. Protonation of n-Hexane.*** In the first step, the adsorbed *n*-hexane molecule is protonated by the acidic proton at the central C−C bond to form the adsorbed 3-C-hexonium intermediate. Selected geometrical parameters for this reaction step are shown in Tables 1 and 2, and optimized structures are shown in Figures 3 and 4 for reactions in H-FAU and H-ZSM-5, respectively. The energy profiles are shown in Figure 5. At the transition state, the H1 proton is protonated to the C3−C4 bond of *n*-hexane. In H-FAU, the Brønsted O1−H1 bond distance is elongated from 0.98 to 1.79 Å while the C3−C4 bond distance is increased to 1.72 Å. The C3−H1 and C4−H1 distances are 1.25 and 1.39 Å, respectively. The activation energy of this step is 45.7 kcal/mol. The transition state structure in H-ZSM-5 is very similar to that in H-FAU. The activation energy for *n*-hexane protonation in H-ZSM-5 is also almost the same (45.8 kcal/mol). The existence of true transition states has been confirmed by frequency calculations resulting in one imaginary frequency at −548.3i and −470.2i $cm^{-1}$ for H-FAU and H-ZSM-5 zeolites, respectively, related to the movement of the acidic proton of zeolite (H1) to the *n*-hexane C3−C4 bond and the breaking of the C3−C4 bond. IRC calculations (see Figures S1 and S2 in the Supporting Information) were performed to illustrate the continuous change from products to the transition state. They also confirm that the C3−C4 bond of *n*-hexane is broken by the attacking of the zeolite H1 proton leading to the formation of the 3-C-hexonium intermediates.

The 3-C-hexonium intermediate is adsorbed on the zeolite surface by forming hydrogen bond interactions with the negatively charged oxygen atom (O1) of the zeolite. The distance H1···O1 is at 2.15 and 2.01 Å in H-FAU and H-ZSM-5, respectively. The structure of the adsorbed C3−H1−C4 bridge hexonium intermediate becomes symmetrical. The C3−H1 and C4−H1 bond distances are almost equal at 1.24 and 1.26 Å, respectively. The C3−C4 bond distance is 1.91 Å and the C3−H1−C4 angle is 100.1° in H-FAU. In H-ZSM-5, the C3−H1−C4 bridge angle is narrower at 95.0° and, consequently, the C3−C4 bond distance is shorter at 1.86 Å. The C3−H1 and C4−H1 bond distances are the same at 1.26 Å. Kazansky et al.[13] have pointed out that the C3−H1−C4 bridge angle is related to the hydride character of the central H atom. The Mulliken population analysis for the partial atomic charge of the H1 atom is 0.294 and 0.322 in H-FAU and H-ZSM-5, respectively, and in agreement with the Kazansky et al.[13] report.

The formation of the adsorbed 3-C-hexonium intermediate is highly endothermic. The reaction energies with respect to the isolated reactants are 33.6 and 26.9 kcal/mol, in H-FAU and H-ZSM-5, respectively. The adsorbed 3-C-hexonium intermediate is only 1.3 and 0.7 kcal/mol more stable than its preceding transition state, in H-FAU and H-ZSM-5, respectively.

***3.2.2. Decomposition of the Hexonium Intermediate.*** The adsorbed 3-C-hexonium intermediates in both zeolites are unstable and highly reactive. They can be decomposed back to adsorbed *n*-hexane with a very small activation barrier. Therefore, it would be extremely difficult to locate this intermediate experimentally. The conversion to produce propane and propene products proceeds through a more energetic transition state (TS2). At the transition state, the H1 atom is moved toward a carbon atom (C4) and the C3−C4 bond is dissociated. The Mulliken population analysis indicates that at the transition state the H1 atom has a higher hydride character than in its previous adsorption complex. The partial atomic charge of the H1 atom is 0.051 and 0.115 in H-FAU and H-ZSM-5, respectively. At this transition state, the H2 proton on the carbon next to the C3 atom is elongated to be transferred to the oxygen atom of the zeolite framework. Simultaneously, the C3−C2 bond is contracted. In H-FAU, the C4−H1 distance is reduced to 1.13 Å while the C3−C4 bond is increased to 2.70 Å. The C2−H2 is elongated from 1.09 to 1.14 Å, and the C2−C3 bond distance is decreased from 1.51 to 1.43 Å. The TS2 structure in H-ZSM-5 is also similar but a little bit closer to the product state. The C2−C3 and C4−H1 are a little bit shorter while the C3−C4 and C2−H2 distances are slightly longer than what was observed in the TS2 of H-FAU. Normal mode analysis reveals one

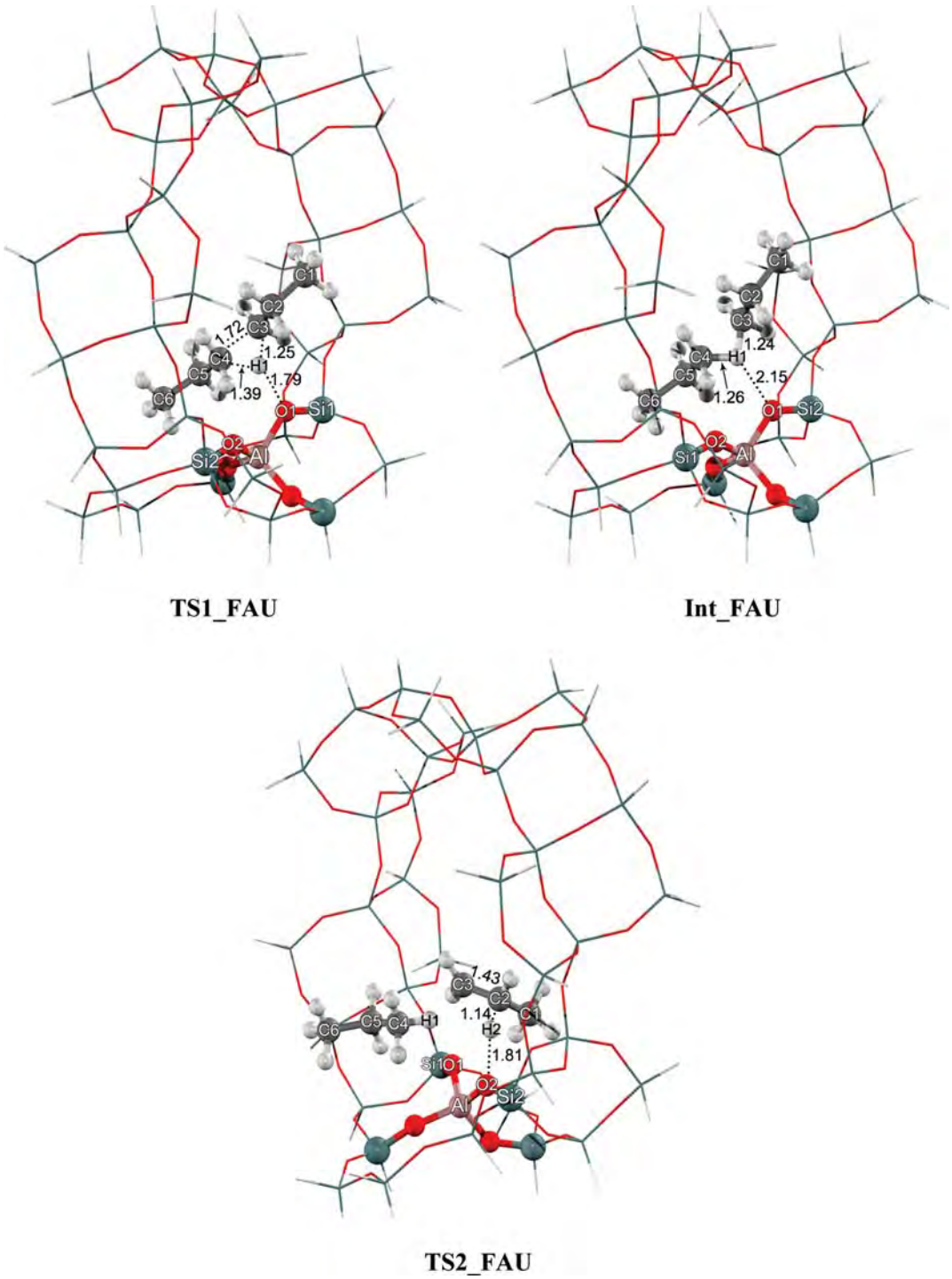


**Figure 3.** Optimized structures of transition states and intermediates involved in the protolytic cracking of *n*-hexane over H-FAU.

imaginary frequency at −294.9i and −197.7i $cm^{-1}$ associated with the TS2 of H-FAU and H-ZSM-5 zeolites, respectively, which corresponds to movement along the reaction coordinate in which the C2−H2 bond breaks and the H2−O2 bond forms simultaneously. The energy barriers for this step are 8.6 and 9.9 kcal/mol for the reaction in H-FAU and H-ZSM-5, respectively. After the decomposition is completed, a propane molecule and a propene molecule are produced. The propene molecule remains adsorbed on the acidic site of the zeolite through a $\pi$-bond interaction. The desorption of products requires an amount of energy of 20.4 and 26.2 kcal/mol in H-FAU and H-ZSM-5, respectively.

The intrinsic activation energies for the protonation of *n*-hexane and the decomposition of the 3-C-hexonium intermediate are found to be almost the same in both zeolites (cf. Figure 5). The overall reaction barrier is considered to be the energy difference between the adsorbed *n*-hexane and the TS2 and is found to be 53.0 and 55.0 kcal/mol for the reaction in H-FAU and H-ZSM-5, respectively. These values are very close to the experimentally estimated intrinsic activation energies of about 56 kcal/mol in these two zeolites.[39,40] The energy profiles of the reactions in these two zeolites contain very similar features. However, due to the confinement effect, the reaction intermediates and transition states in H-ZSM-5 are 6−8 kcal/mol lower in energies than those stationary points in H-FAU. Therefore, the apparent reaction barrier would be 36.8 and 42.2 kcal/mol for the reaction in H-ZSM-5 and H-FAU, respectively. The predicted apparent reaction barriers are also very close to the

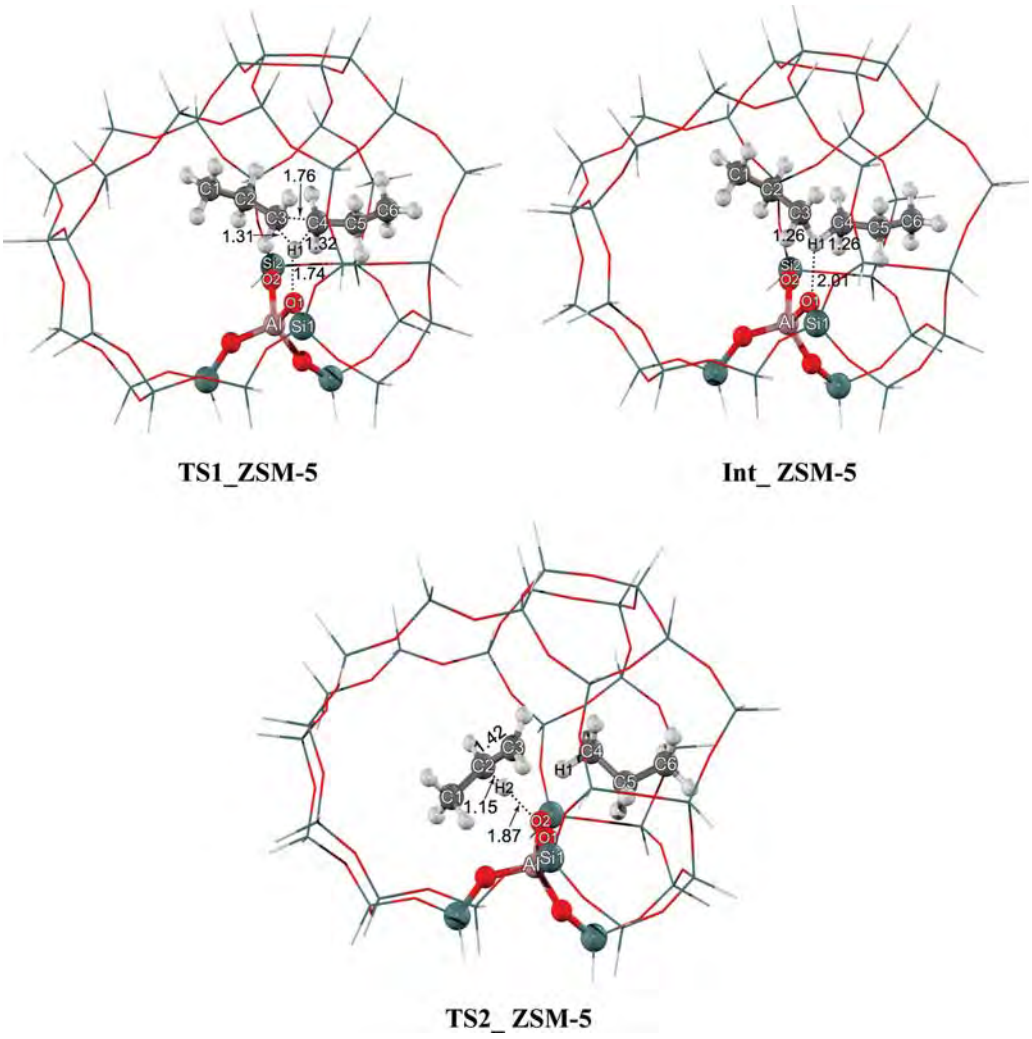


**Figure 4.** Optimized structures of transition states and intermediates involved in the protolytic cracking of *n*-hexane over H-ZSM-5.

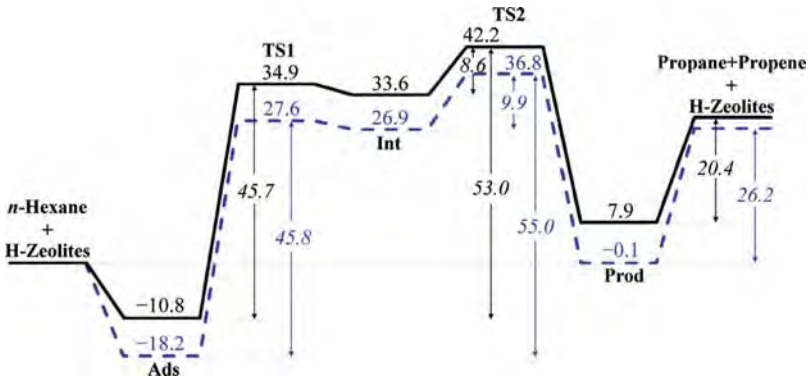


**Figure 5.** Energy profile for the *n*-hexane cracking mechanisms for both zeolites: H-FAU zeolite (solid line) and H-ZSM-5 zeolite (dashed line) (energies are in kcal/mol).

values reported in recent experimental studies[39,40] which reported the apparent activation energies of 35.5 and 44.4 kcal/mol for the monomolecular cracking of *n*-hexane in H-ZSM-5 and H-FAU, respectively. Since the computed intrinsic activation energies of the two reaction steps are very similar in these two zeolites, the different cracking activity on these two zeolites can only be explained by the different adsorption energies of the *n*-hexane reactant. The computed deprotonation energies of these two models of zeolites are also comparable (295.9 and 293.8 kcal/mol, for H-ZSM-5 and H-FAU, respectively). Therefore, the intrinsic catalytic activity of zeolites for *n*-hexane cracking is not dependent on the type of zeolites, even if their pores are quite different in shape and size. This confirms previous experimental results,[37–40] and the mechanism underlying this unexpected behavior can now be better understood.

## 4. Conclusion

The cracking reaction of *n*-hexane over two different types of zeolite has been investigated by utilizing the 38T H-FAU and 34T H-ZSM-5 cluster models calculated at the M06-2X/6-311+G(2df,2p)//M06-2X/6-31G(d,p) level of theory. These

calculations give adsorption energies which are in good agreement with experimental data. After the adsorption, the acidic proton of the zeolites is directly protonated to a C−C bond of *n*-hexane and the 3-C-hexonium intermediate is formed in the nanocavity. In the second step, the 3-C-hexonium is readily decomposed to form propane and propene molecules. The computational results indicate the plausible existence of 3-C-hexonium intermediates in the zeolites for the protolytic cracking of *n*-hexane. The structures and relative stabilities of the 3-C-hexonium intermediates in these two zeolites are very similar. The protonation step is found to be the rate-determining step. The apparent activation energies are computed to be 42.2 and 36.8 kcal/mol in H-FAU and H-ZSM-5, respectively, which are very close to the apparent activation energies for monomolecular cracking of *n*-hexane reported in literature.[39,40] The results confirm that relatively large quantum clusters are needed for the study of hydrocarbon reactions in zeolites. The M06-2X method is well-suited for this case, while reference calculations show that functionals such as B3LYP are not. The different activities of the two zeolites can only be explained by the different adsorption energies which are mainly due to the van der Waals interactions between *n*-hexane and the zeolite walls.

**Acknowledgment.** This work was supported in part by grants from the National Science and Technology Development Agency (NSTDA Chair Professor and NANOTEC Center of Excellence), the Thailand Research Fund (to J.L.), the Kasetsart University Research and Development Institute (KURDI), the Commission on Higher Education, Ministry of Education ("National Research University of Thailand" and "Postgraduate Education and Research Programs in Petroleum and Petrochemicals and Advanced Materials"), under the program Strategic Scholarships for Frontier Research Network for the Joint Ph.D. Program Thai Doctoral degree from the Office of the Higher Education Commission, Thailand (to T.M.), as well as PTT Research and Technology Institute, PTT Public Company Limited. The authors are grateful to Donald G. Truhlar and Yan Zhao for supporting them with the code for the M06-2X functional.

**Supporting Information Available:** Table S1: Selected geometric parameters and adsorption energies of the *n*-hexane adsorption obtained from B3LYP. Figures S1 and S2: IRC calculation for protonation of *n*-hexane over H-ZSM-5 and H-FAU zeolites, respectively. This material is available free of charge via the Internet at http://pubs.acs.org.

## References and Notes

(1) Weitkamp, J. *Solid State Ionics* **2000**, *131*, 175.
(2) Stocker, M. *Microporous Mesoporous Mater.* **2005**, *82* (3), 257.
(3) Haag, W. O.; Dessau, R. M. In *Proceedings, 8th International Congress on Catalysis Berlin, 1984*; Ertl. G., Ed.; Dechema: Frankfurt-am-Main, 1984; Vol. 2, p 305.
(4) Kotrel, S.; Knözinger, H.; Gates, B. C. *Microporous Mesoporous Mater.* **2000**, *35*−*36*, 11.
(5) Corma, A.; Orchilles, A. V. *Microporous Mesoporous Mater.* **2000**, *35*−*36*, 21.
(6) Collins, S. J.; O'Malley, P. J. *J. Catal.* **1995**, *153*, 94.
(7) Collins, S. J.; O'Malley, P. J. *Chem. Phys. Lett.* **1995**, *246*, 555.
(8) Kazansky, V. B.; Senchenya, I. N.; Frash, M. V.; van Santen, R. A. *Catal. Lett.* **1994**, *27*, 345.
(9) Blaszkowski, S. R.; Nascimento, M. A. C.; van Santen, R. A. *J. Phys. Chem. A* **1996**, *100* (9), 3463.
(10) Frash, M. V.; van Santen, R. A. *Top. Catal.* **1999**, *9*, 191.
(11) Zheng, X.; Blowers, P. *J. Phys. Chem. A* **2005**, *109*, 10734.
(12) Zheng, X.; Blowers, P. *J. Mol. Catal. A: Chem.* **2005**, *229*, 77.
(13) Kazansky, V. B.; Frash, M. V.; van Santen, R. A. *Catal. Lett.* **1997**, *48*, 61.
(14) Boronat, M.; Viruela, P.; Corma, A. *J. Phys. Chem. B* **2000**, *104*, 1944.
(15) Boronat, M.; Corma, A. *Appl. Catal., A* **2008**, *336*, 2.
(16) Zicovich-Wilson, C. M.; Corma, A.; Viruela, P. *J. Phys. Chem. B* **1994**, *98*, 10863.
(17) Derouane, E. G. *J. Mol. Catal. A: Chem.* **1998**, *134*, 29.
(18) Hansen, N.; Brüggemann, T.; Bell, A. T.; Keil, F. J. *J. Phys. Chem. C* **2008**, *112*, 15402.
(19) Wesolowski, T. A.; Parisel, O.; Ellinger, Y.; Weber, J. *J. Phys. Chem. A* **1997**, *101* (42), 7818.
(20) Svensson, M.; Humbel, S.; Froese, R. D. J.; Matsubara, T.; Sieber, S.; Morokuma, K. *J. Phys. Chem. A* **1996**, *100*, 19357.
(21) Namuangruk, S.; Pantu, P.; Limtrakul, J. *J. Catal.* **2004**, *225*, 523.
(22) Namuangruk, S.; Pantu, P.; Limtrakul, J. *ChemPhysChem* **2005**, *6* (7), 1333.
(23) Maihom, T.; Namuangruk, S.; Nanok, T.; Limtrakul, J. *J. Phys. Chem. C* **2008**, *112*, 12914.
(24) Maihom, T.; Boekfa, B.; Sirijaraensre, J.; Nanok, T.; Probst, M.; Limtrakul, J. *J. Phys. Chem. C* **2009**, *113*, 6654.
(25) Jansang, B.; Nanok, T.; Limtrakul, J. *J. Phys. Chem. B* **2006**, *110*, 12626.
(26) Namuangruk, S.; Khongpracha, P.; Pantu, P.; Limtrakul, J. *J. Phys. Chem. B* **2006**, *110* (51), 25950.
(27) Zhao, Y.; Truhlar, D. G. *J. Phys. Chem. C* **2008**, *112*, 6860.
(28) Zhao, Y.; Truhlar, D. G. *Acc. Chem. Res.* **2008**, *41*, 157.
(29) Boekfa, B.; Choomwattana, S.; Khongpracha, P.; Limtrakul, J. *Langmuir* **2009**, *25* (22), 12990.
(30) Bourdillon, G.; Gueguen, C.; Guisnet, M. *Appl. Catal.* **1990**, *61*, 123.
(31) Lercher, J. A.; Jentys, A.; Brait, A. *Mol. Sieves Sci. Technol.* **2008**, *6*, 153.
(32) Alberti, A.; Davoli, P.; Vezzalini, G. Z. *Z. Kristallogr.* **1986**, *175*, 249.
(33) van Koningsveld, H.; Bekkum, H. v.; Jansen, J. C. *Acta Crystallogr., Sect. B: Struct. Sci.* **1987**, *43*, 127.
(34) Gonzalez, C.; Schlegel, H. B. *J. Chem. Phys.* **1989**, *90*, 2154.
(35) Gonzalez, C.; Schlegel, H. B. *J. Phys. Chem.* **1990**, *94*, 5523.
(36) Frisch, M. J.; Trucks, G. W.; Schlegel, H. B.; Scuseria, G. E.; Robb, M. A.; Cheeseman, J. R.; Montgomery, J. A., Jr.; Vreven, T.; Kudin, K. N.; Burant, J. C.; Millam, J. M.; Iyengar, S. S.; Tomasi, J.; Barone, V.; Mennucci, B.; Cossi, M.; Scalmani, G.; Rega, N.; Petersson, G. A.; Nakatsuji, H.; Hada, M.; Ehara, M.; Toyota, K.; Fukuda, R.; Hasegawa, J.; Ishida, M.; Nakajima, T.; Honda, Y.; Kitao, O.; Nakai, H.; Klene, M.; Li, X.; Knox, J. E.; Hratchian, H. P.; Cross, J. B.; Adamo, C.; Jaramillo, J.; Gomperts, R.; Stratmann, R. E.; Yazyev, O.; Austin, A. J.; Cammi, R.; Pomelli, C.; Ochterski, J. W.; Ayala, P. Y.; Morokuma, K.; Voth, G. A.; Salvador, P.; Dannenberg, J. J.; Zakrzewski, V. G.; Dapprich, S.; Daniels, A. D.; Strain, M. C.; Farkas, O.; Malick, D. K.; Rabuck, A. D.; Raghavachari, K.; Foresman, J. B.; Ortiz, J. V.; Cui, Q.; Baboul, A. G.; Clifford, S.; Cioslowski, J.; Stefanov, B. B.; Liu, G.; Liashenko, A.; Piskorz, P.; Komaromi, I.; Martin, R. L.; Fox, D. J.; Keith, T.; Al-Laham, M. A.; Peng, C. Y.; Nanayakkara, A.; Challacombe, M.; Gill, P. M. W.; Johnson, B.; Chen, W.; Wong, M. W.; Gonzalez, C.; Pople, J. A. *Gaussian 03*, revision B.05; Gaussian, Inc.: Pittsburgh, PA, 2003.
(37) Narbeshuber, T. F.; Vinek, H.; Lercher, J. A. *J. Catal.* **1995**, *157*, 388.
(38) Kotrel, S.; Rosynek, M. P.; Lunsford, J. H. *J. Phys. Chem. B* **1999**, *103*, 818.
(39) Babitz, S. M.; Williams, B. A.; Miller, J. T.; Snurr, R. Q.; Haag, W. O.; Kung, H. *Appl. Catal., A* **1999**, *179*, 71.
(40) van Bokhoven, J. A.; Williams, B. A.; Ji, W.; Koningsberger, D. C.; Kung, H. H.; Miller, J. T. *J. Catal.* **2004**, *224*, 50.
(41) Eder, F.; Stockenhuber, M.; Lercher, J. A. *J. Phys. Chem. B* **1997**, *101*, 5414.

JP911732P

CHEMPHYSCHEM

DOI: 10.1002/cphc.201000586

# Oxidative Dehydrogenation of Propane over a $VO_2$-Exchanged MCM-22 Zeolite: A DFT Study

Sippakorn Wannakao,[a, b] Bundet Boekfa,[b, c] Pipat Khongpracha,[a, b, c] Michael Probst,[d] and Jumras Limtrakul*[a, b, c]

The adsorption and the mechanism of the oxidative dehydrogenation (ODH) of propane over $VO_2$-exchanged MCM-22 are investigated by DFT calculations using the M06-L functional, which takes into account dispersion contributions to the energy. The adsorption energies of propane are in good agreement with those from computationally much more demanding MP2 calculations and with experimental results. In contrast, B3LYP binding energies are too small. The reaction begins with the movement of a methylene hydrogen atom to the oxygen atom of the $VO_2$ group, which leads to an isopropyl radical bound to a HO–V–O intermediate. This step is rate determining with the apparent activation energy of 30.9 kcal mol$^{-1}$, a value within the range of experimental results for ODH over other silica supports. In the propene formation step, the hydroxyl group is the more reactive group requiring an apparent activation energy of 27.7 kcal mol$^{-1}$ compared to that of the oxy group of 40.8 kcal mol$^{-1}$. To take the effect of the extended framework into account, single-point calculations on 120T structures at the same level of theory are performed. The apparent activation energy is reduced to 28.5 kcal mol$^{-1}$ by a stabilizing effect caused by the framework. Reoxidation of the catalyst is found to be important for the product release at the end of the reaction.

## 1. Introduction

Propene is one of the most important starting materials for many processes in the chemical industry. It is, for example, used for polymer production and the scarcity of natural resources will most likely lead to a significant increase in the demand for propene in the near future.[1] However, the conventional propene production processes exhibit many disadvantages. For example, due to thermodynamic constraints, larger amounts of ethylene than propene are produced in the steam cracking process even though the demand for ethylene is not growing as much as that for propene. Moreover, industrial steam cracking is a high energy-consuming process that also produces $CO_2$.[2] Dehydrogenation also has the problem of rapid deactivation of the catalyst by coke production. Thus, finding competitive ways to produce propene has high priority and the oxidative dehydrogenation (ODH) of propane has, in principle, the advantages of low energy consumption, lower coke and $CO_x$ by-products, and high selectivity of the desired product compared to the conventional dehydrogenation process.[3]

Vanadia-supported catalysts have proven to be active and selective for this reaction.[1,3,4] Silica-supported vanadium oxide catalysts especially are highly selective because they do not favor direct combustion of the propane reactant to $CO_x$ species, compared to alumina and titania supports.[1,4j] Zeolites and mesoporous silicas, which are industrially important catalysts, can also be used as the silica support catalysts.[1,5] To understand the mechanistic scheme of the reaction, many theoretical studies of the propane ODH over vanadium oxides and silica-supported catalysts have been conducted. Engeser et al. found a product allyl complex ($\eta^3$-$C_3H_5$)V(O)–(OH)$^+$ when they studied alkane oxidation by $VO_2^+$ in a gas-phase system.[6] Systems consisting of clusters systematically selected from the bulk structure have also been studied theoretically.[7] Rozanska et al. identified possible reaction pathways for ODH of propane by vanadium oxide sites on a silica support cluster.[7b] They found that the first hydrogen abstraction at the O=V site was the rate-limiting step. In another study on a (001) periodic surface of $V_2O_5$, Fu et al. found that the propene formation step was rate limiting.[8] From these observations, one can say that different systems cause different controls of the rate-determining step even when they have the same active species. Although porous silica supports have been widely used in many experimental studies, to the best of our knowledge their atom-

[a] S. Wannakao, Dr. P. Khongpracha, Prof. Dr. J. Limtrakul
Laboratory for Computational and Applied Chemistry
Department of Chemistry, Faculty of Science and Center of Nanotechnology
Kasetsart University Research and Development Institute
Kasetsart University, Bangkok 10900 (Thailand)
Fax: (+66) 2-562-5555
E-mail: Jumras.l@ku.ac.th

[b] S. Wannakao, Dr. B. Boekfa, Dr. P. Khongpracha, Prof. Dr. J. Limtrakul
NANOTEC Center of Excellence, National Nanotechnology Center
Kasetsart University, Bangkok 10900 (Thailand)

[c] Dr. B. Boekfa, Dr. P. Khongpracha, Prof. Dr. J. Limtrakul
Center for Advanced Studies in Nanotechnology and its Applications in Chemical, Food, and Agricultural Industries
Kasetsart University, Bangkok 10900 (Thailand)

[d] Prof. Dr. M. Probst
Institute of Ion Physics and Applied Physics
University of Innsbruck, 6020 Innsbruck (Austria)

Supporting information for this article is available on the WWW under http://dx.doi.org/10.1002/cphc.201000586.

istic details have never been studied computationally. In reactions such as adsorption and catalysis processes in confined spaces, van der Waals interactions play an important role. In previous calculations on various reactions in zeolites, ONIOM (B3LYP:UFF) was found to be an economical method,[9] able to reproduce experimental data for such systems. Its good performance is, however, partially due to the compensation between the overestimated framework confinement effect and the underestimated interaction in the active region. Recently, Zhao and Truhlar have developed a new type of density functional (M06 series) in which London dispersion is taken into account in the parameterization.[10] This method has been shown to be very useful for studying adsorption and reaction mechanisms in zeolite and metal oxide systems in which van der Waals interactionspredominate.[11]

To understand such a reaction in a confined space, we used a well-calibrated $VO_2$-exchanged MCM-22 ($VO_2$-MCM22) model that has been recently studied experimentally.[5c] We studied propane adsorption and the reaction mechanism of the propane ODH reaction over the catalyst by means of DFT calculations with the M06-L functional, which Zhao and Truhlar have shown to be both accurate for transition metals and practical for large-system studies. The reaction can be divided into three main steps: 1) methylene ($-CH_2-$) hydrogen activation, 2) propene formation, and 3) reoxidation of the catalyst by using $N_2O$ as an oxidizing agent.

## 2. Results and Discussion

### 2.1. Propane Adsorption over the Catalyst

A $VO_2$-MCM-22 cluster, the vanadium oxide component of which acts as an active site and is embedded in the intersection cavity at the 12T-membered ring of the supercage, was used in this study (Figure 1). The cluster model is similar to

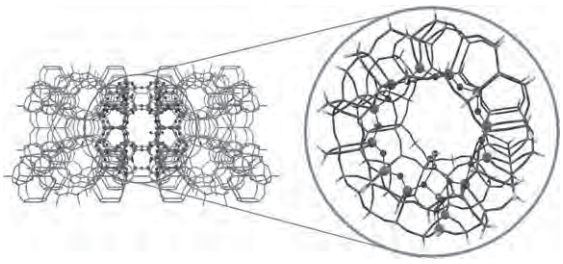

**Figure 1.** Structure of $VO_2$-MCM-22. Balls represent the 14T optimized site and sticks represent the extended framework on which single-point calculations were performed.

that used in our previous study on isolated metal oxide on zeolite.[12] The [$VO_2$] ionic group lies between the two bridging oxygen atoms of the zeolite framework forming a tetrahedral arrangement at the vanadium atom, which is the most stable configuration. With the M06-L functional and the 6-31G(d,p) basis set, the optimized V–O bond lengths are 1.59, 1.59, 1.98, and 1.98 Å for V–O1, V–O2, V–Oa, and V–Ob, respectively. The distance between V and the Al atoms is 2.78 Å. With the B3LYP functional, V–O and V–Al distances were the same as those obtained from the M06-L functional. Geometry optimizations with the MP2 method gave longer V–O distances, that is, V–O1 and V–O2 are 1.66 Å and V–Oa and V–Ob are 2.03 Å with a V–Al distance of 2.82 Å.

Although the M06-L functional leads to nearly the same structure of the active site as the B3LYP functional, when the van der Waals probe molecule propane was interacting with the site the relation of the structure obtained with each method was different. Optimized geometries of the adsorption complexes and their energies obtained from M06-L and B3LYP functional and MP2 calculations are illustrated in Figure 2. The

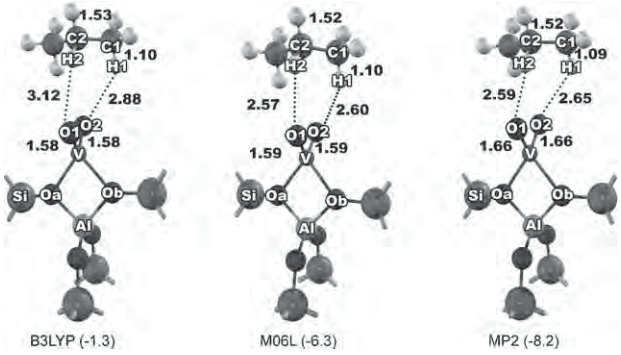


**Figure 2.** Optimized adsorption structures from the three methods. The adsorption energies are given in parentheses [kcal mol$^{-1}$].

propane molecule is weakly adsorbed on the catalyst with H2 binding to O1 and H1 to O2. The M06-L and MP2 methods lead to about the same O1–H2 and O2–H1 distances (2.57 and 2.59 Å, respectively). The weaker interaction from the B3LYP functional leads to a longer O1–H2 distance of 3.12 Å.

Not only the structure but also the energies from M06-L ($-6.3$ kcal mol$^{-1}$) are close to those obtained from the (much more CPU time-consuming) MP2 calculations ($-8.2$ kcal mol$^{-1}$). The adsorption energy from B3LYP is, in contrast, very small ($-1.3$ kcal mol$^{-1}$). The experimental value for the heat of propane adsorption over supported vanadium oxide material is about $-8$ kcal mol$^{-1}$.[5d,13] These results indicate that M06-L is suitable for studying systems of transition metals in which the van der Waals interaction plays an important role, as originally suggested.[10b]

### 2.2. Methylene Hydrogen Abstraction

The M06-L functional was used to study the reaction mechanism of the propane ODH over $VO_2$-MCM-22. The reaction begins with the activation of the methylene C–H bond by an oxygen atom of the $VO_2$ group. The transition structure shows distortion from the original tetrahedral one (Figure 3). At the transition state (TS1), the O1–H2 and C2–H2 distances are 1.21 and 1.45 Å, respectively. The V–O1 distance changes from 1.59 Å in the bare catalyst to 1.68 Å. The imaginary frequency of 1372i cm$^{-1}$ of the transition state corresponds to the move-

  

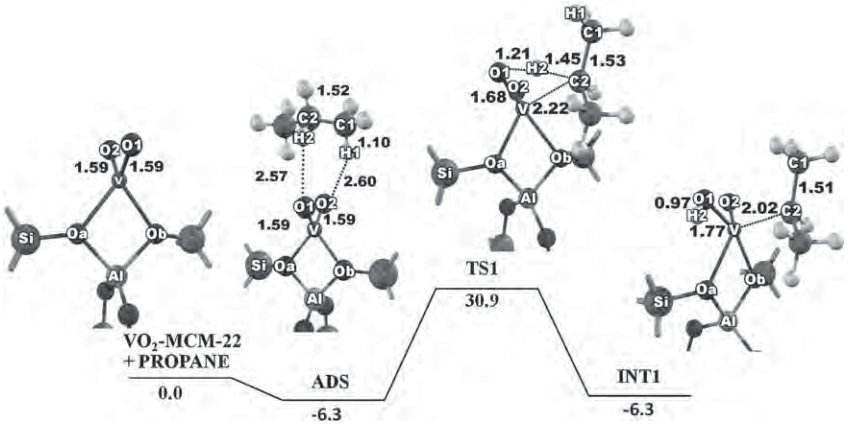


**Figure 3.** Energy profile for the first hydrogen abstraction step of the ODH of propane over $VO_2$-MCM-22 (M06-L/6-31G(d,p) calculations on a 14T model).

ment of the H2 atom between the O1 and C2 atoms. This step requires an intrinsic activation energy of 37.2 kcal mol$^{-1}$ while the apparent activation energy is 30.9 kcal mol$^{-1}$ (see Figure 3). The product of this step, the isopropyl radical intermediate (INT1), has a relative energy of −6.3 kcal mol$^{-1}$. It is closely coordinated to the vanadium atom with a V–C2 distance of 2.02 Å. It is interesting to note that in $V_2O_5$ bulk[8] and clusters,[7a,b] the intermediate was found to be not coordinated to the vanadium atom but that our intermediate is rather similar to the one predicted for gas-phase $VO_2^+$,[6] thus indicating the flexibility of the active site.

### 2.3. Propene Formation

The isopropyl radical intermediate (INT1) can be converted to propene via abstraction of the hydrogen atom from C1 to the hydroxyl group (O1H2) or to the O2 oxygen atom on the vanadium atom, to yield an adsorbed water molecule and dihydroxy vanadium intermediates (INT2-O2), respectively. For the former, the C1–H1 bond of the isopropyl radical is elongated from 1.09 to 1.37 Å and correspondingly, H1–O1 decreases from 2.74 to 1.32 Å. The normal-mode analysis shows one imaginary frequency at 1445i cm$^{-1}$ corresponding to the movement of H1 in the formation of the O1–H1 bond and the breaking of the C1–H1 bond.

The second pathway proceeds through the transition state TS2-O2, and H1 is transferred towards O2 and the C1–H1 and H1–O2 bond lengths become 1.46 and 1.26 Å, respectively. The associated imaginary frequency at the transition state is 1529i cm$^{-1}$. The first pathway is kinetically preferred over the second one with a required apparent activation energy of 27.7 kcal mol$^{-1}$, which is 13.1 kcal mol$^{-1}$ lower than that for the second pathway. Moreover, the water formation intermediate (INT2) is more stable than the dihydroxy vanadium one (see Figure 4). During this step, the isopropyl radical intermediate can react with the hydroxyl group (O1H2) of the active site to

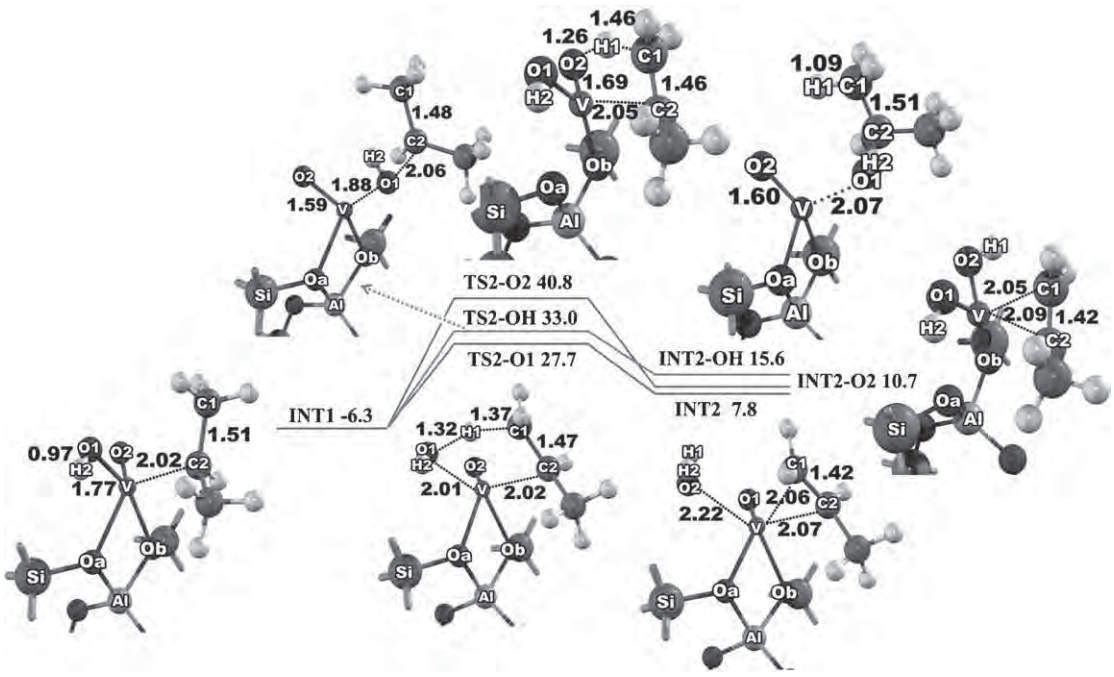


**Figure 4.** Energy profiles of the three possible reactions at the propene formation step (M06-L/6-31G(d,p) calculations on a 14T model).

  

form an oxygenated product, which leads to a reduced selectivity towards propene. This step was found to proceed via a triplet state, consistent with the literature.[7b] However, the calculation shows that propene formation is favored by 5.3 kcal mol$^{-1}$ energy and thus this pathway is kinetically and thermodynamically preferred. This agrees with observations from Fu et al. in which the formation of isopropoxide at the vanadyl oxygen site was found to be unlikely.[8] The driving force of this step is the highly endothermic change of the V oxidation state from +5 ($d^0$) to +3 ($d^2$), thus overcompensating the exothermic conversion of propane and oxygen to propene and water.[14] It is noted that for the transition structure TS2-OH, the oxygen atoms are tetrahedrally coordinated to the V atom, which is different from the distorted square-planar structure for the other transition states (TS2-O2 and TS2-O1).

### 2.4. Reoxidation of the Catalyst

Nitrous oxide ($N_2O$) was used as the reoxidizing agent for the catalyst recovery step because it has been proven that it provides a higher selectivity than molecular oxygen.[7c] After the propene formation step, the water molecule needs 24.9 kcal mol$^{-1}$ to desorb while propene is even more strongly coordinated at the vanadia site (41.9 kcal mol$^{-1}$).

The reaction profile for this step is shown in Figure 5. In the beginning of the reoxidation step, $N_2O$ adsorbs on the vanadium atom with N2–O3 and O3–V distances of 1.20 and 2.47 Å, respectively. Its adsorption sets 8.5 kcal mol$^{-1}$ free. After that, the O3 of $N_2O$ interacts with vanadium causing elongation of the N2–O3 bond to 1.35 Å while O3–V contracts to 1.90 Å. This requires an intrinsic activation energy of 15.9 kcal mol$^{-1}$. The intermediate is stabilized by a relative energy of −37.5 kcal mol$^{-1}$. This indicates that the active site strongly prefers the fivefold coordination over the fourfold one. Finally, removal of nitrogen and propene from the catalyst requires 5.3 and 14.0 kcal mol$^{-1}$, respectively. From these results, it can be implied that the reoxidation step is not rate limiting but that the reduction of the product desorption energy is needed to recover the active site.

### 2.5. The Framework Effect

The 120T nanocluster model was used for single-point calculations, to evaluate how the MCM-22 framework affects reaction energies during the ODH process. It was found that all structures are stabilized by the extended framework. The adsorption energy of propane over the catalyst increases from −6.3 kcal mol$^{-1}$ for the 14T cluster to −7.0 kcal mol$^{-1}$ for the 120T model. In the methylene hydrogen abstraction step, which is considered to be a rate-limiting step for this reaction, the apparent activation energy was reduced from 30.9 to 28.5 kcal mol$^{-1}$. This is in accordance with the 20–30 kcal mol$^{-1}$ from experiments on propane ODH over supported vanadia catalysts.[4i,15] However, when the reduction of the adsorption energy is considered, the true activation energy of this system remains nearly unchanged by the confinement effect of the MCM-22 framework. This overall shift is similar to the propene formation step (see Table 1).

Single-point calculations were also performed for the structures without the whole zeolitic framework. Three model structures containing $VO_2^+$ and the probe molecule were formed from the 14T optimized geometries (see Figure 6). In these models $VO_2^+$ was neutralized by $OH^-$ (**1**), ($H_2O$)($OH^-$) (**2**), and $Al(OH)_4^-$ (**3**) and each structure was fixed at the 14T optimized geometry. The adsorption energies of the three models were similar to each other (−2.4, −2.6, and −2.2 kcal mol$^{-1}$ for models **1**–**3**, respectively). Taking into account the value of −6.3 kcal mol$^{-1}$ for the cluster with the framework, one can estimate that the framework contribution to the adsorption energy of propane on the catalyst is about 60%. The desorption energy of the propene product is 8.1 and 8.2 kcal mol$^{-1}$ for models **2** and **3**, respectively, and 16.4 kcal mol$^{-1}$ for model **1**. The strong interaction obtained for model **1** might be due to the unsaturated fourfold coordination that is found to be the same as in the initial desorption of propene before the reconstruction of the active site takes place. When considering only models **2** and **3**, one can state

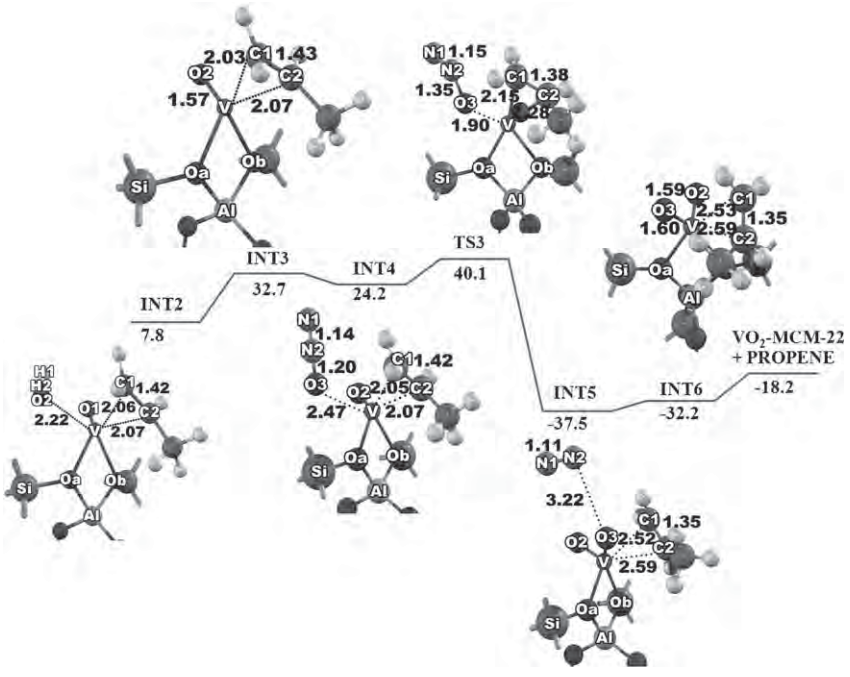


**Figure 5.** Reaction profile for the reoxidation step.

  

**Table 1.** Energies of the components in the ODH process, given relative to the energy of the reactants.

| System | Relative Energy [kcal mol$^{-1}$] 14T M06-L/6-31G(d,p) (Optimized) | 120T M06-L/6-31G(d,p) (Single Point) |
|---|---|---|
| VO2-MCM-22 + propane + $N_2O$ | 0.0 | 0.0 |
| ADS | −6.3 | −7.0 |
| TS1 | 30.9 | 28.5 |
| INT1 | −6.3 | −10.8 |
| TS2 | 27.7 | 23.1 |
| INT2 | 7.8 | 1.1 |
| INT3 | 32.7 | 28.1 |
| INT4 | 24.2 | 19.9 |
| TS3 | 40.1 | 36.9 |
| INT5 | −37.5 | −42.4 |
| INT6 | −32.2 | −36.8 |
| $VO_2$-MCM-22 + propene + $N_2$ | −18.2 | −18.2 |

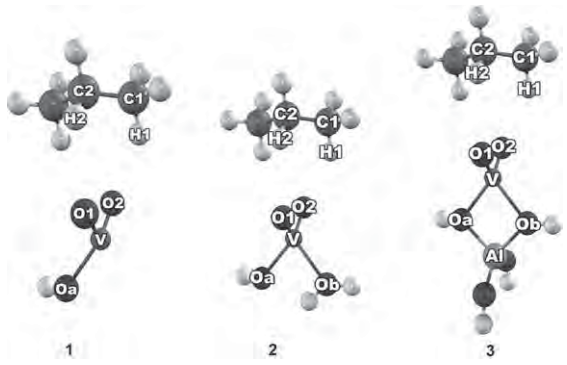


**Figure 6.** Three small models of the active site saturated and neutralized by $OH^-$ (**1**), $(H_2O)(OH^-)$ (**2**), and $Al(OH)_4^-$ (**3**). See text for explanation.

that the framework contribution for the propene desorption energy is less than about 40%, a result of the strong π bond between alkene and the metal.

Finally, to obtain additional information about the interactions in our system we performed an approximate energy decomposition[16] of the zeolite–adsorbate system. In this scheme, the self-consistent field (SCF) energy between the zeolite model and propane is "deconstructed" into: 1) the interaction between the two parts, each with its own frozen wavefunction, 2) the mutual polarization due to orbital relaxation, still with independent wavefunctions, 3) charge transfer, and 4) the change due to orbital delocalization after the wavefunctions are allowed to mix. Since in M06-L the dispersion-like interactions are parameterized into the basic energy expression of the functional, they ought to appear in part (1). Indeed, the zeolite–propane interaction energy (1) between the frozen parts is −9 kcal mol$^{-1}$ for M06-L and +2 kcal mol$^{-1}$ for B3LYP in their respective geometries (partially optimized as described above). The small overall attractive energy in the case of B3LYP is mostly a result of SCF delocalization (4). The energy decomposition analysis thus confirms the nature of the improvements resulting from M06-L. The calculations were performed with the Q-Chem 3.22 program[17] and, for technical reasons, the SBKJC basis set.[18]

### 2.6. Rate Constants

Rate constants ($k_r$) and equilibrium constants ($K_{eq}$) were calculated for the rate-limiting C–H activation step and are summarized in Table 2. Values of $k_r$ and $K_{eq}$ were calculated in the range of 300–800 °C, a typical temperature range for experiments. It was found that $k_r$ for the forward reaction increases dramatically when the temperature increases; $K_{eq}$ increases gradually from 0.255 to 0.418. This finding is consistent with the experimentally observed temperature dependence of the propane conversion rate.[5c]

**Table 2.** Kinetic and equilibrium constants of the reaction in the temperature range between 300 and 800 °C.

| Temperature [°C] | $k_r$ (FWD) | $k_{-r}$ (REV) | $K_{eq}$ |
|---|---|---|---|
| 300 | $4.27\times10^{-1}$ | $1.67\times10^{0}$ | 0.255 |
| 350 | $5.33\times10^{0}$ | $1.99\times10^{1}$ | 0.268 |
| 400 | $4.63\times10^{1}$ | $1.65\times10^{2}$ | 0.281 |
| 450 | $3.01\times10^{2}$ | $1.02\times10^{3}$ | 0.296 |
| 500 | $1.55\times10^{3}$ | $4.96\times10^{3}$ | 0.312 |
| 550 | $6.56\times10^{3}$ | $2.00\times10^{4}$ | 0.328 |
| 600 | $2.37\times10^{4}$ | $6.87\times10^{4}$ | 0.345 |
| 650 | $7.51\times10^{4}$ | $2.07\times10^{5}$ | 0.363 |
| 700 | $2.12\times10^{5}$ | $5.56\times10^{5}$ | 0.381 |
| 750 | $5.43\times10^{5}$ | $1.36\times10^{6}$ | 0.399 |
| 800 | $1.28\times10^{6}$ | $3.06\times10^{6}$ | 0.418 |

## 3. Conclusions

The adsorption and the ODH reaction mechanism of the propane/$VO_2$-MCM-22 system have been investigated by DFT calculations with the M06-L functional. The adsorption energies of propane are comparable to those derived from computationally much more demanding MP2 calculations and to experimental results while, as expected, the values from the B3LYP functional are too small.

For the reaction mechanism, two main steps were considered. The reaction begins with the rate-determining step, the abstraction of the methylene hydrogen. The calculated apparent activation energy for this system is 30.9 kcal mol$^{-1}$, which is within the range of the experimental values reported for propane ODH over supported vanadium catalysts. We find that the formation of propene is indeed preferred over the competing oxygenated product on the $VO_2$-MCM-22 nanocatalyst. A single-point calculation showed that the activation energy with a larger 120T model is 2.4 kcal mol$^{-1}$ lower than it is in the 14T cluster, which indicates the amount of stabilization due to the framework.

For the propane adsorption step the framework dominates the energetics, while for the propene desorption the metal site dominates. As a consequence, the reoxidation of the vanadium

  

site by $N_2O$ greatly reduces the amount of energy needed for propene desorption due to the strong interaction of the unsaturated active site. From the very different adsorption energies of propane and propene, one can suggest this catalyst to be usable for separating the alkene product from the alkane. A subsequent study will consider the activity and selectivity of this reaction on further modified catalysts.

## Computational Methods

The geometry of the MCM-22 zeolite cluster was obtained from the crystal structure,[19] represented by a cluster of 14 tetrahedrally coordinated Si or Al atoms (14T). The cluster covers the 12-membered ring at the intersection of two channels, which is considered to be an appropriate active site of the catalyst (see Figure 1). An Al atom is located at the T1 position, its most stable configuration in this model.[20] The vanadium oxide species $[VO_2]^+$ is adsorbed at the highly accessible Brønsted acid site. All geometry optimizations were performed by the M06-L functional using the 6-31G(d,p) basis set for H, C, O, Al, and Si atoms, whereas the Stuttgart effective core potentials (ECPs)[21] were employed for the V atom. Calculations with the B3LYP functional and with Møller–Plesset perturbation theory (MP2) with the same basis set were performed for comparison. During geometry optimization, only the active sites of the catalyst ($VO_2/AlSi_4O_4$) and the probe molecule were allowed to relax, while the rest were kept fixed at the original crystal structure. A normal-mode analysis of the transition states shows only one imaginary frequency, the mode of which corresponds to the designated reaction. The total spin state was assumed to be a singlet, which was found to be the most stable state.[6] Rate constants were calculated by classical transition-state theory (TST) using Equation (1):

$$k_r = \frac{k_B T}{h}\frac{q_{TS}}{q_{Int}}\exp(-\Delta E_a/RT) \quad (1)$$

where $\Delta E_a$ is the activation energy, $k_B$ is Boltzmann's constant, $h$ is Plank's constant, $T$ is the temperature, $R$ is the universal gas constant, and $q_{TS}$ and $q_{Int}$ are the total partition functions for the transition state and intermediate complex, respectively.

Finally, to cover the confinement effect from the zeolite framework, the model was extended to a 120T structure which included a supercage of MCM-22. All calculations were performed by the Gaussian 03 package[22] modified to incorporate the Minnesota Density Functionals module 3.1 by Zhao and Truhlar.

## Acknowledgements

*This work was supported in part by grants from the National Science and Technology Development Agency (NSTDA Chair Professor and NANOTEC Center of Excellence), the Thailand Research Fund (to J.L.), the Kasetsart University Research and Development Institute (KURDI), the Commission on Higher Education, Ministry of Education ("the National Research University Project of Thailand (NRU)" and "Postgraduate Education and Research Programs in Petroleum and Petrochemicals and Advanced Materials"), under the Royal Golden Jubilee Ph.D. program from the Thailand Research Fund (to S.W.). The authors are grateful to Donald G. Truhlar and Yan Zhao for supplying them with the code for the M06-L functional. M.P. acknowledges an infrastructure grant of the Austrian Ministry of Science to the LFU scientific computing platform.*

**Keywords:** density functional calculations · oxidative dehydrogenation · propene · vanadium oxide · zeolites

[1] F. Cavani, N. Ballarini, A. Cericola, *Catal. Today* **2007**, *127*, 113 – 131.
[2] T. Ren, M. Patel, K. Blok, *Energy* **2006**, *31*, 425 – 451.
[3] a) G. Centi, F. Cavani, F. Trifirò, *Selective Oxidation by Heterogeneous Catalysis*, Kluwer Academic, New York, **2001**; b) T. Blasco, J. M. Lopez Nieto, *Appl. Catal. A* **1997**, *157*, 117 – 142; c) E. A. Mamedov, V. Cortés Corberán, *Appl. Catal. A* **1995**, *127*, 1 – 40.
[4] a) M. A. Chaar, D. Patel, H. H. Kung, *J. Catal.* **1988**, *109*, 463 – 467; b) A. Corma, J. M. Lopez Nieto, N. Paredes, *J. Catal.* **1993**, *144*, 425 – 438; c) F. D. Hardcastle, I. E. Wachs, *J. Mol. Catal.* **1988**, *46*, 173 – 186; d) I. E. Wachs, B. M. Weckhuysen, *Appl. Catal. A* **1997**, *157*, 67 – 90; e) J. G. Eon, R. Olier, J. C. Volta, *J. Catal.* **1994**, *145*, 318 – 326; f) A. Khodakov, B. Olthof, A. T. Bell, E. Iglesia, *J. Catal.* **1999**, *181*, 205 – 216; g) A. Khodakov, J. Yang, S. Su, E. Iglesia, A. T. Bell, *J. Catal.* **1998**, *177*, 343 – 351; h) E. V. Kondratenko, M. Baerns, *Appl. Catal. A* **2001**, *222*, 133 – 143; i) M. D. Argyle, K. Chen, A. T. Bell, E. Iglesia, *J. Catal.* **2002**, *208*, 139 – 149; j) E. V. Kondratenko, M. Cherian, M. Baerns, *Catal. Today* **2006**, *112*, 60 – 63.
[5] a) A. Julbe, D. Farrusseng, J. C. Jalibert, C. Mirodatos, C. Guizard, *Catal. Today* **2000**, *56*, 199 – 209; b) S. A. Karakoulia, K. S. Triantafyllidis, G. Tsilomelekis, S. Boghosian, A. A. Lemonidou, *Catal. Today* **2009**, *141*, 245 – 253; c) A. A. Teixeira-Neto, L. Marchese, G. Landi, L. Lisi, H. O. Pastore, *Catal. Today* **2008**, *133–135*, 1 – 6; d) A. Dinse, S. Khennache, B. Frank, C. Hess, R. Herbert, S. Wrabetz, R. Schlögl, R. Schomäcker, *J. Mol. Catal. A* **2009**, *307*, 43 – 50.
[6] M. Engeser, M. Schlangen, D. Schröder, H. Schwarz, T. Yumura, K. Yoshizawa, *Organometallics* **2003**, *22*, 3933 – 3943.
[7] a) M. J. Cheng, K. Chenoweth, J. Oxgaard, A. Van Duin, W. A. Goddard III, *J. Phys. Chem. C* **2007**, *111*, 5115 – 5127; b) X. Rozanska, R. Fortrie, J. Sauer, *J. Phys. Chem. C* **2007**, *111*, 6041 – 6050; c) X. Rozanska, E. V. Kondratenko, J. Sauer, *J. Catal.* **2008**, *256*, 84 – 94.
[8] H. Fu, Z. P. Liu, Z. H. Li, W. N. Wang, K. N. Fan, *J. Am. Chem. Soc.* **2006**, *128*, 11114 – 11123.
[9] a) T. Maihom, S. Namuangruk, T. Nanok, J. Limtrakul, *J. Phys. Chem. C* **2008**, *112*, 12914 – 12920; b) B. Jansang, T. Nanok, J. Limtrakul, *J. Phys. Chem. C* **2008**, *112*, 540 – 547; c) S. Choomwattana, T. Maihom, P. Khongpracha, M. Probst, J. Limtrakul, *J. Phys. Chem. C* **2008**, *112*, 10855 – 10861; d) B. Jansang, T. Nanok, J. Limtrakul, *J. Mol. Catal. A* **2007**, *264*, 33 – 39; e) S. Namuangruk, D. Tantanak, J. Limtrakul, *J. Mol. Catal. A* **2006**, *256*, 113 – 121; f) S. Namuangruk, P. Khongpracha, P. Pantu, J. Limtrakul, *J. Phys. Chem. B* **2006**, *110*, 25950 – 25957; g) J. Lomratsiri, M. Probst, J. Limtrakul, *J. Mol. Graphics Modell.* **2006**, *25*, 219 – 225; h) S. Kasuriya, S. Namuangruk, P. Treesukol, M. Tirtowidjojo, J. Limtrakul, *J. Catal.* **2003**, *219*, 320 – 328; i) K. Bobuatong, J. Limtrakul, *Appl. Catal. A* **2003**, *253*, 49 – 64.
[10] a) Y. Zhao, D. G. Truhlar, *Theor. Chem. Acc.* **2008**, *120*, 215 – 241; b) Y. Zhao, D. G. Truhlar, *Acc. Chem. Res.* **2008**, *41*, 157 – 167.
[11] a) T. Maihom, B. Boekfa, J. Sirijaraensre, T. Nanok, M. Probst, J. Limtrakul, *J. Phys. Chem. C* **2009**, *113*, 6654 – 6662; b) B. Boekfa, S. Choomwattana, P. Khongpracha, J. Limtrakul, *Langmuir* **2009**, *25*, 12990 – 12999; c) C. Kumsapaya, K. Bobuatong, P. Khongpracha, Y. Tantirungrotechai, J. Limtrakul, *J. Phys. Chem. C* **2009**, *113*, 16128 – 16137; d) R. Valero, J. R. B. Gomes, D. G. Truhlar, F. Illas, *J. Chem. Phys.* **2008**, *129*, 124710; e) R. Valero, J. R. B. Gomes, D. G. Truhlar, F. Illas, *J. Chem. Phys.* **2010**, *132*, 104701.
[12] P. Pantu, S. Pabchanda, J. Limtrakul, *ChemPhysChem* **2004**, *5*, 1901 – 1906.
[13] A. Kämper, A. Auroux, M. Baerns, *Phys. Chem. Chem. Phys.* **2000**, *2*, 1069 – 1075.
[14] J. Sauer, J. Döbler, *Dalton Trans.* **2004**, 3116 – 3121.
[15] a) K. Chen, A. T. Bell, E. Iglesia, *J. Phys. Chem. B* **2000**, *104*, 1292 – 1299; b) E. Heracleous, M. Machli, A. A. Lemonidou, I. A. Vasalos, *J. Mol. Catal. A* **2005**, *232*, 29 – 39.

  

[16] R. Z. Khaliullin, E. A. Cobar, R. C. Lochan, A. T. Bell, M. Head-Gordon, *J. Phys. Chem. A* **2007**, *111*, 8753 – 8765.
[17] Y. Shao, L. F. Molnar, Y. Jung, J. Kussmann, C. Ochsenfeld, S. T. Brown, A. T. B. Gilbert, L. V. Slipchenko, S. V. Levchenko, D. P. O'Neill, R. A. DiStasio, Jr., R. C. Lochan, T. Wang, G. J. O. Beran, N. A. Besley, J. M. Herbert, C. Y. Lin, T. Van Voorhis, S. H. Chien, A. Sodt, R. P. Steele, V. A. Rassolov, P. E. Maslen, P. P. Korambath, R. D. Adamson, B. Austin, J. Baker, E. F. C. Byrd, H. Dachsel, R. J. Doerksen, A. Dreuw, B. D. Dunietz, A. D. Dutoi, T. R. Furlani, S. R. Gwaltney, A. Heyden, S. Hirata, C. P. Hsu, G. Kedziora, R. Z. Khalliulin, P. Klunzinger, A. M. Lee, M. S. Lee, W. Liang, I. Lotan, N. Nair, B. Peters, E. I. Proynov, P. A. Pieniazek, Y. M. Rhee, J. Ritchie, E. Rosta, C. D. Sherrill, A. C. Simmonett, J. E. Subotnik, H. L. Woodcock III, W. Zhang, A. T. Bell, A. K. Chakraborty, D. M. Chipman, F. J. Keil, A. Warshel, W. J. Hehre, H. F. Schaefer III, J. Kong, A. I. Krylov, P. M. W. Gill, M. Head-Gordon, *Phys. Chem. Chem. Phys.* **2006**, *8*, 3172 – 3191.
[18] a) T. R. Cundari, W. J. Stevens, *J. Chem. Phys.* **1993**, *98*, 5555 – 5565; b) W. J. Stevens, H. Basch, M. Krauss, *J. Chem. Phys.* **1984**, *81*, 6026 – 6033; c) W. J. Stevens, M. Krauss, H. Basch , P. G. Jasien, *Can. J. Chem.* **1992**, *70*, 612.
[19] M. E. Leonowicz, J. A. Lawton, S. L. Lawton, M. K. Rubin, *Science* **1994**, *264*, 1910 – 1913.
[20] D. Zhou, Y. Bao, M. Yang, N. He, G. Yang, *J. Mol. Catal. A* **2006**, *244*, 11 – 19.
[21] M. Dolg, U. Wedig, H. Stoll, H. Preuss, *J. Chem. Phys.* **1987**, *86*, 866 – 872.
[22] Gaussian 03, Revision B.05, M. J. Frisch, G. W. Trucks, H. B. Schlegel, G. E. Scuseria, M. A. Robb, J. R. Cheeseman, J. A. Montgomery, Jr., T. Vreven, K. N. Kudin, J. C. Burant, J. M. Millam, S. S. Iyengar, J. Tomasi, V. Barone, B. Mennucci, M. Cossi, G. Scalmani, N. Rega, G. A. Petersson, H. Nakatsuji, M. Hada, M. Ehara, K. Toyota, R. Fukuda, J. Hasegawa, M. Ishida, T. Nakajima, Y. Honda, O. Kitao, H. Nakai, M. Klene, X. Li, J. E. Knox, H. P. Hratchian, J. B. Cross, V. Bakken, C. Adamo, J. Jaramillo, R. Gomperts, R. E. Stratmann, O. Yazyev, A. J. Austin, R. Cammi, C. Pomelli, J. W. Ochterski, P. Y. Ayala, K. Morokuma, G. A.Voth, P. Salvador, J. J. Dannenberg, V. G. Zakrzewski, S. Dapprich, A. D. Daniels, M. C. Strain, O. Farkas, D. K. Malick, A. D. Rabuck, K. Raghavachari, J. B. Foresman, J. V. Ortiz, Q. Cui, A. G. Baboul, S. Clifford, J. Cioslowski, B. B. Stefanov, G. Liu, A. Liashenko, P. Piskorz, I. Komaromi, R. L. Martin, D. J Fox, T. Keith, M. A. Al-Laham, C. Y. Peng, A. Nanayakkara, M. Challacombe, P. M. W. Gill, B. Johnson, W. Chen, M. W. Wong, C. Gonzalez, J. A. Pople, Gaussian, Inc., Wallingford, CT, **2004**.

Received: July 20, 2010
Published online on October 25, 2010

  

# Structures and Energetics of the Methylation of 2-Methylnaphthalene with Methanol over H-BEA Zeolite

**Karan Bobuatong,[†,‡,§,⊥] Michael Probst,[¶] and Jumras Limtrakul*[,†,‡,§,⊥]**

*Laboratory for Computational and Applied Chemistry, Department of Chemistry, Faculty of Science, Kasetsart University, Bangkok 10900, Thailand, Center of Nanotechnology, Kasetsart University Research and Development Institute, Kasetsart University, Bangkok 10900, Thailand, NANOTEC Center of Nanotechnology, National Nanotechnology Center, Kasetsart University, Bangkok 10900, Thailand, Center for Advanced Studies in Nanotechnology and Its Applications in Chemical, Food and Agricultural Industries, Kasetsart University, Bangkok 10900, Thailand, and Institute of Ion Physics and Applied Physics, University of Innsbruck, A-6020 Innsbruck, Austria*

*Received: September 8, 2010; Revised Manuscript Received: October 24, 2010*

The methylation of 2-methylnaphthalene (2-MN) with methanol to the 2,6 (2,6-DMN) and 2,7 (2,7-DMN) dimethylnaphthalenes catalyzed over nanoporous BEA zeolite has been investigated quantum chemically using the M06-2X density functional. The catalytic cycle consists of three elementary steps: (1) formation of a methoxy species from methanol that is bound to a zeolite oxygen atom, (2) methylation of 2-MN to DMN with methoxy leading to naphthalynic carbocations, and (3) formation of DMN by proton back-donation from naphthalynic carbocations. The reaction profiles are similar for both the 2,6 and the 2,7 isomer and are in agreement with the experimental observation that they are produced in equal amounts on acidic BEA zeolite. A possible side reaction, the formation of dimethyl ether via the self-activation of methanol, is also discussed. The stability of the intermediates inside the pores is, to a large extent, governed by the steric constraints and the van der Waals dispersion interactions induced by the pore structure of BEA zeolite. These are the key parameters for understanding the relationship between zeolite topology and catalytic activity.

## 1. Introduction

The catalytic conversion of aromatic molecules via methylation, alkylation and isomerization is a very important process in the petrochemical industry.[1] Nowadays, zeolites are used industrially for this purpose. These remarkable aluminosilicate minerals are capable of catalyzing chemical reactions that take place in their well-defined nanostructured pore cavity, and also often provide numerous advantages over the traditional Friedel−Crafts catalyst due to their high selectivity to the desired products and their thermal properties. In addition, the use of heterogeneous inorganic catalysts like zeolites facilitates the design of clean technologies and applications that have to take into consideration environmental concerns.

In the past decade, the demand for 2,6-naphthalenedicarboxylic acid (2,6-NDA) as a raw material for the manufacture of a high-performance polyethylene naphthalene (PEN)[2,3] has increased significantly. 2,6-Dimethylnaphthalene (2,6-DMN) is considered as the most suitable feedstock with its high reactivity toward oxidation into 2,6-NDA.[4] Therefore, the synthesis of 2,6-DMN from the ten DMN isomers has been studied.[4−7] The alternative process of 2,6-DMN production, the methylation of methylnaphthalene (MN), has also been investigated[8−12] intensively.

In all these studies, ZSM-5 showed a high $\beta$- and/or $\beta,\beta$-selectivity, approximately 80%. T. Inui et al.[13] optimized the performance of H-ZSM-5 by a mechanochemical method leading to a significant improvement in the life of the catalyst as well as the improvement of the shape-selectivity. However, the ratio of 2,6-DMN/2,7-DMN produced on ZSM-5 was almost 1, and their yields were still not high. S.-B. Pu et al.[11] studied the same reaction over MFI metallosilicates, as well as over some large-pore zeolites, to improve especially the 2,6-DMN/2,7-DMN ratio. They reported that these large-pore zeolites significantly increase the yield of 2,6-DMN. In all the zeolites used, BEA showed the highest yield of 2,6-DMN and its deactivation was more gradual than the one of ZSM- 12 and Y. A three-dimensional large-pore structure without a supercage as is present in BEA, is necessary for binuclear aromatic hydrocarbon conversion. Furthermore, the catalytic life of BEA can be prolonged markedly by using tetralin as the solvent for $\beta$-MN. This is caused by the dehydrogenation of tetralin in the vicinity of the active sites to prevent coke formation and/or remove the coke formed. However, the reaction mechanisms of this reaction inside the zeolite pores are not well understood.

Computational methods based on quantum chemistry have become reliable techniques to clarify the microstructural properties of various chemical systems.[14] Especially, the computational investigation of the catalytic mechanisms in zeolites is of considerable practical importance. Nevertheless, zeolites that have a high impact in industrial processes usually possess hundreds of atoms per unit cell, which makes the use of sophisticated methods, such as periodic DFT calculations,

* Corresponding author. E-mail: jumras.l@ku.ac.th. Telephone: +66-2-562-5555, ext 2159.
† Laboratory for Computational and Applied Chemistry, Department of Chemistry, Faculty of Science, Kasetsart University.
‡ Center of Nanotechnology, Kasetsart University Research and Development Institute, Kasetsart University.
§ NANOTEC Center of Nanotechnology, National Nanotechnology Center, Kasetsart University.
⊥ Center for Advanced Studies in Nanotechnology and Its Applications in Chemical, Food and Agricultural Industries, Kasetsart University.
¶ Institute of Ion Physics and Applied Physics, University of Innsbruck.

10.1021/jp108566c 
Published on Web 11/17/2010

computationally too expensive. Most DFT calculations do not take into account the van der Waals (vdW) contributions to the interaction energy.[15] For example, the popular B3LYP functional has an unsatisfactory performance for such reactions. Besides issues such as an underestimation of reaction barrier heights, it is unable to describe van der Waals complexes bound by medium-range interactions, and it also exhibits incorrect trends in the bond energies of organometallic catalytic systems.[16,17]

Recently, Zhao and Truhlar[18−21] have developed the M06 class of hybrid functionals, and they suggest that they are suitable for general-purpose applications. Both M06-L and M06 are intended for applications in transition metal chemistry and perform markedly better than B3LYP for main-group thermochemistry, barrier heights, and noncovalent interactions. M06-2X has an improved performance in these areas as compared with M06-L and M06, but it is not suitable for describing transition metal chemistry. In recent works[22−24] it has been demonstrated that the zeolite confinement effect on reactions of unsaturated aliphatic, aromatic, and heterocyclic compounds can be studied by performing full quantum chemical calculations on sufficiently large clusters using the M06-2X method. This leads to a better overall accuracy than the somewhat arbitrary QM/MM schemes like the ONIOM method. Furthermore, it makes the selection of zeolite models more general and systematic.

The purpose of the present study is to examine the reaction mechanisms of the methylation of 2-methylnaphthalene (2-MN) in a model of a large zeolite cluster. The reaction path for the side reaction, the formation of dimethyl ether, has also been studied.

## 2. Computational Details

The crystal lattice structure of H-BEA was taken from the work of J. B. Higgins, et al.[25] An extended 34T (34 tetrahedral sites) zeolite cluster, covering the active region of the H-$\beta$ zeolite is used to represent the Brønsted acid site and the zeolite framework. It includes the 12-membered ring representing the main gateway to the intersection of two perpendicular 12 MR channel systems, where the reactions normally take place (See Figure 1). A silicon atom at a T5 position in $\beta$ zeolite is substituted by an aluminum atom. A proton is added to the bridging oxygen atoms bonded directly to the aluminum atom, conventionally called the O5 position, which is the O1 position in this study.

The M06-2X functional and the 6-31G(d,p) basis set were applied for the 34T zeolite cluster. In order to obtain more reliable results, single point calculations at the M06-2X/6-311+G(2df,2p) level of theory were also carried out. All calculations have been performed using the Gaussian 03 code.[26] During the structure optimization, the 5T portion of the active-site region [≡SiO(≡SiO)$_2$AlO(H)OSi≡] and the adsorbates are allowed to relax while the rest of the active region is kept at the crystallographic coordinates.

## 3. Results and Discussion

The results are organized in the following way. First, we examine the mechanism of the methylation of 2-MN to 2,6-DMN and 2,7-DMN, the main issue of the present work. Finally, we explore the possibility of dimethyl ether formation as a competitive reaction to the methylation of 2-MN.

**3.1. The Methylation of 2-Methyl Naphthalene.** A graph of the reaction mechanism is depicted in Scheme 1. The energy profile containing all species involved is plotted in Figure 2. In the following, we employ the notation that a postfix 'a' (as in Int_1a) denotes the 2,6-isomer, while a postfix 'b' is used for the 2,7-isomer. When energy values are followed by a second value in parentheses (as 2.6 (2.7) kcal/mol), this also refers to the 2,6- and 2.7-isomers. In addition, the optimized geometries of all species in this study are shown in the Supporting Information (Figure S1). This reaction is initiated by the adsorption of a methanol molecule on the acidic proton of H-BEA (denoted Ads in Scheme 1). The adsorption complex is stabilized by two hydrogen bonds between the OH group of methanol and the Brønsted acid site (O1−H1) of the zeolite: one between the Brønsted proton (H1) and the methanol oxygen atom (O4), and another between the methanol hydrogen atom

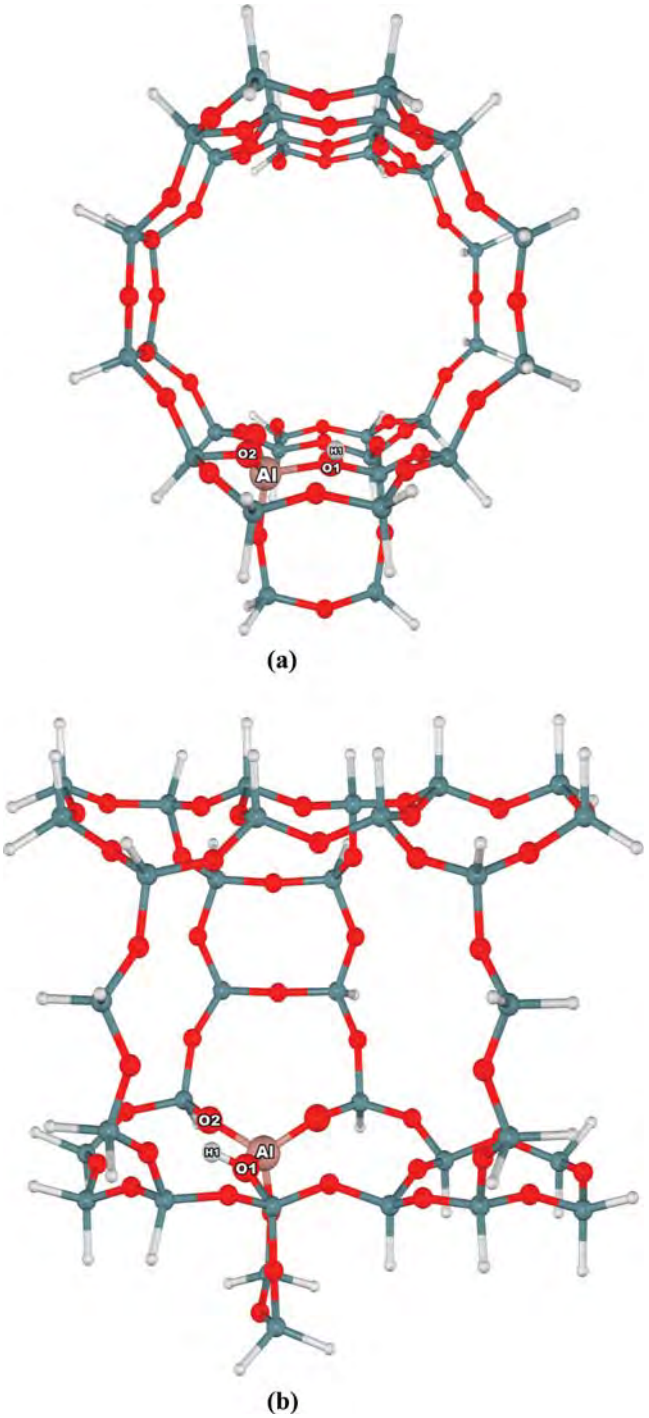


**Figure 1.** 34T cluster models of H-BEA. (a) 34T quantum cluster viewed from the direction of the pore axis. (b) 34T quantum cluster viewed from the direction of the side pore.

**SCHEME 1: Catalytic Cycles of the Methylation of 2-MN to 2,6-DMN and 2,7-DMN over H-BEA Zeolite; Initiation Step Is the Adsorption of Methanol (Ads)**

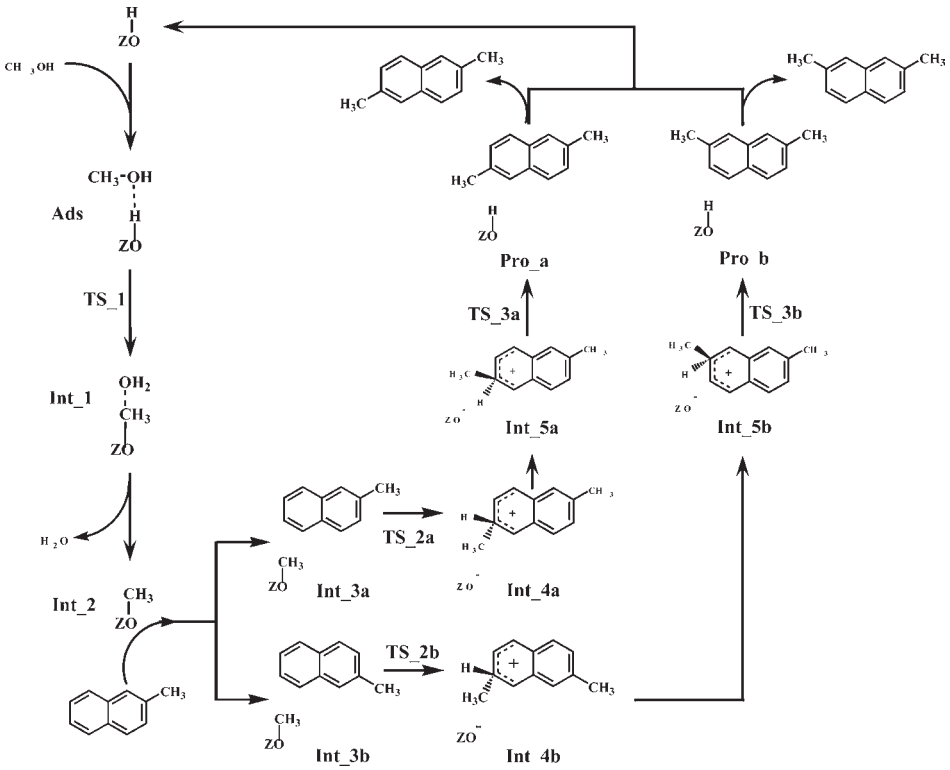


(H2) and the basic oxygen atom of the zeolite active site (O3). No protonation of methanol by the Brønsted site is observed. Similar configurations have also been described in previous studies.[27−30] The adsorption of methanol on the hydrogen form of ZSM-5 was studied in a calorimetric experiment by Gorte et al.[31] At 80% coverage of the Brønsted sites, a value of 27.5 ± 1.2 kcal/mol (115 ± 5 kJ/mol) was reported. The average acidic strength of the ZSM-5 zeolite was found to be similar to or stronger than that of the BEA zeolite, as determined by various spectroscopic techniques,[32−34] or $NH_3$-TPD[33] and hydrocarbon cracking.[32,34,35] The calculated adsorption energy of −24.2 kcal/mol therefore seems reliable. It is also compatible with typical van der Waals contributions inside the zeolite pore.

At the first transition state, the methanol C−O bond is activated by the attack of the Brønsted proton H1 on the methanol oxygen atom O4. The protonated methanol OH group is leaving as the methyl group is being attacked by the active zeolite O atom (Figure S1b, Supporting Information). We observe the dissociation of the C1−O4 bond and the association of the C1−O2 bond, respectively. As summarized in Table 1, the C1−O4 bond is lengthened from 1.44 to 1.91 Å, whereas the C1−O2 distance contracts to 2.05 Å. The corresponding O4−C1−O2 angle is 171.4°. In this configuration, the geometry of the methyl group is altered from tetrahedral to trigonal planar. The active-site structure of the zeolite is only slightly affected in the course of the progression of the reaction.

The activation barrier taken with respect to the adsorption of one methanol molecule at the acidic site (Ads) is predicted to be 39.8 kcal/mol (Figure 2a). This value is lower than the 51.4 kcal/mol obtained in previous calculations on smaller zeolite clusters.[36,37] The stabilizing effect of the zeolite micropore on the ionic transition state is well-known and can reach 10−30% of the activation barrier as was found for small zeolite clusters.[38] Upon methanol dehydration, methoxy species and a water molecule are created and coadsorb at the active site of BEA zeolite, Int_1. The water molecule then desorbs (Int_2) and is replaced by the incoming 2-MN. The relative energies of the coadsorption complexes are exothermic by −20.2 (Int_3a; 2,6-DMN) and −19.3 kcal/mol (Int_3b; 2,7-DMN).

After the coadsorption, the methyl group from the zeolite framework is transferred to the $\beta$-position of 2-MN via transition states TS_2a and TS_2b. The barriers for this reaction are 29.5 and 28.1 kcal/mol for 2,6-DMN and 2,7-DMN, respectively. The transition states are also shown in Figure 2a. The normal mode corresponding to the single imaginary frequency was also calculated and indicates the proceeding of the methylation of 2-MN. In the transition structures, which have the characteristics of methyl carbocations with a trigonal planar geometry, the C−C bond between $CH_3$ and MN starts to form. The C1−O2 bond of the methoxy species is elongated from 1.48 Å (1.49 Å) to 2.17 Å (2.12 Å) for 2,6-DMN and 2,7-DMN, respectively. Simultaneously, the lengths of the C1−C2 and C1−C3 bonds decrease from 3.77 Å to 2.20 Å and 3.35 Å to 2.20 Å for 2,6-DMN and 2,7-DMN, respectively. The transition states lead to the formation of the key intermediates, 2,6- and 2,7-naphthalenium (Int_4a and Int_4b). These are adsorbed on the active site by −14.6 (−11.3) kcal/mol. The difference of the adsorption energies can be explained by the fact that the 2,6-naphthalenium intermediate is located closer to the active site than the 2,7-isomer. The existence of aromatic cations in the zeolite cavity has been disclosed by the results of N. Hansen et al.[38] and X. Rozanska et al.[39] They found the aromatic carbocation as a reaction intermediate and concluded that large models of medium and micropore zeolites are able to stabilize the benzylic ionic intermediate.

Our results from above show that the naphthalenium intermediates will stay adsorbed to the active site and can undergo a proton back-donation process, as shown in Figure 2b. The hydrogen atoms at the carbon center of the naphthalenium intermediates are not in close proximity to the three oxygen

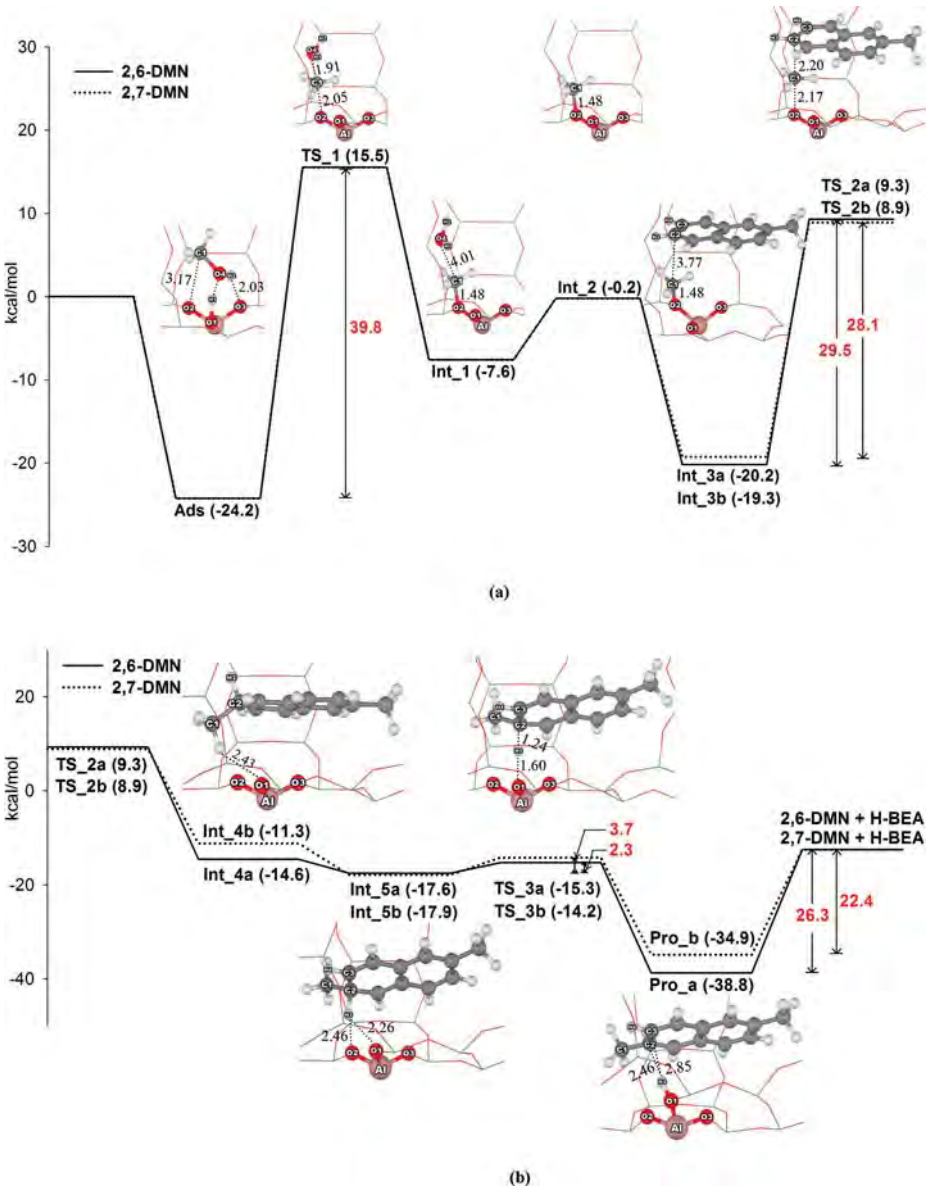


**Figure 2.** The calculated energy profile for the methylation of 2-MN to 2,6-DMN and 2,7-DMN (kcal/mol). Due to its size, this figure is split into parts (a) and (b).

**TABLE 1: Geometrical Parameters from the 34T Model (M06-2X/6-311+G(2df,2p)//M06-2X/6-31G(d,p)) Calculations of the H-BEA Zeolite, Adsorption Complex (Ads), Transition States (TS_1 to TS_3b), Reaction Intermediates (Int_1 to Int_5b), and Products (Pro_a and Pro_b) for the Methylation of 2-MN to 2, 6-DMN and 2,7-DMN over H-BEA Zeolite[a]**

| parameter | H-BEA | Ads | TS_1 | Int_1 | Int_2 | Int_3a | TS_2a | Int_4a | Int_5a | TS_3a | Pro_a | Int_3b | TS_2b | Int_4b | Int_5b | TS_3b | Pro_b |
|---|---|---|---|---|---|---|---|---|---|---|---|---|---|---|---|---|---|
| O1−H1 | 0.98 | 1.10 | 3.76 | 4.61 | – | – | – | – | – | – | – | – | – | – | – | – | – |
| C1−O2 | – | 3.17 | 2.05 | 1.48 | 1.48 | 1.48 | 2.17 | 3.12 | 3.38 | 3.24 | 3.18 | 1.49 | 2.12 | 3.20 | 3.36 | 3.32 | 3.45 |
| C1−O4 | – | 1.44 | 1.91 | 4.01 | – | – | – | – | – | – | – | – | – | – | – | – | – |
| C1−C2 | – | – | – | – | – | 3.92 | 2.20 | 1.54 | 1.54 | 1.54 | 1.51 | 3.58 | 2.75 | 2.55 | 2.55 | 2.51 | 2.53 |
| C1−C3 | – | – | – | – | – | 3.77 | 2.81 | 2.52 | 2.55 | 2.56 | 2.53 | 3.35 | 2.20 | 1.53 | 1.54 | 1.55 | 1.51 |
| C2−H3 | – | – | – | – | – | 1.09 | 1.09 | 1.16 | 1.13 | 1.24 | 2.46 | 1.09 | 1.09 | 1.12 | 1.13 | 1.26 | 2.56 |
| O1−H3 | – | – | – | – | – | 6.08 | 4.88 | 4.57 | 2.26 | 1.60 | 0.99 | 5.69 | 5.01 | 4.36 | 2.24 | 1.68 | 0.99 |
| Al−O1 | 1.85 | 1.81 | 1.72 | 1.69 | 1.69 | 1.69 | 1.68 | 1.72 | 1.72 | 1.72 | 1.84 | 1.69 | 1.71 | 1.72 | 1.72 | 1.71 | 1.84 |
| Al−O2 | 1.70 | 1.70 | 1.76 | 1.86 | 1.86 | 1.86 | 1.71 | 1.71 | 1.72 | 1.72 | 1.69 | 1.85 | 1.75 | 1.71 | 1.72 | 1.72 | 1.69 |
| Al−O3 | 1.68 | 1.72 | 1.70 | 1.69 | 1.69 | 1.69 | 1.67 | 1.72 | 1.72 | 1.72 | 1.69 | 1.69 | 1.71 | 1.72 | 1.72 | 1.72 | 1.69 |
| ∠O1−Al−O2 | 93.1 | 97.1 | 97.2 | 94.3 | 94.3 | 94.4 | 96.7 | 100.0 | 99.1 | 98.8 | 94.9 | 94.6 | 97.8 | 99.9 | 99.1 | 99.16 | 94.9 |

[a] Distances are in Å, and angles are in degrees.

atoms around the active site. To allow for the regeneration of the active site in the final step, the naphthalenium intermediates need to rotate along the zeolite pore axis which causes these hydrogen atoms to get closer to the active site. Due to the lack of data, we use an experimentally derived approximate value of 6.9 kcal/mol[40,41] for the barriers of rotation of the protonated species around C2. The reoriented naphthalenium intermediates stick to the active site (Int_5a and Int_5b) with adsorption energies of −17.6 and −17.9 kcal/mol, respectively.

2,6-DMN and 2,7-DMN can be generated through direct proton transfer from the tetrahedral carbon center of the naphthalenium intermediates to an oxygen atom attached to the

**SCHEME 2: Diagram Showing the Possible Competition between the Dimethyl Ether Formation and the Methylation of 2-MN over H-BEA Zeolite**

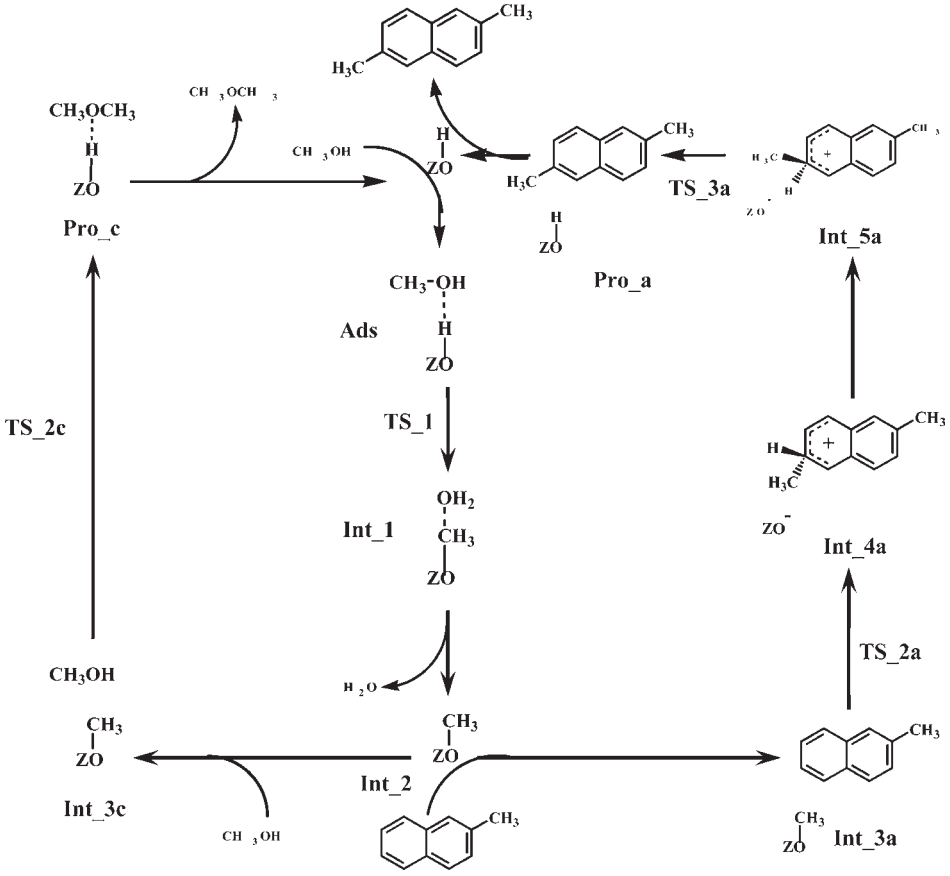


aluminum atom at the active sites (TS_3a and TS_3b) with calculated barriers of 2.3 and 3.7 kcal/mol. The transition states are slightly perturbed by the zeolite framework which causes the optimized structures to be very close to the intermediates. At the transition state TS_3 where the C−H cleavage occurs, the C−H bond distances of the naphthalenium intermediates are elongated from 1.13 Å (1.13 Å) to 1.24 Å (1.26 Å). Finally, after this third transition state, the products, 2,6-DMN and 2,7-DMN are adsorbed at the acidic active site via a $\pi$-bond interaction by −38.8 and −34.9 kcal/mol, respectively. These predicted reactions are exothermic, and finally 2,6-DMN and 2,7-DMN require desorption energies of 26.3 and 22.4 kcal/mol, respectively. Overall, the reaction profiles for the formation of 2,6-DMN and 2,7-DMN are similar to each other, in agreement with the experimental observation[11] that there is no preference for either of them when synthesized over acidic BEA zeolite.

**3.2. Dimethyl Ether Formation.** Finally, we consider another possible reaction of methanol over zeolite catalysts that could compete with the naphthalene methylation. It has been shown earlier[37] that at low coverage the methoxy species described above can react with a second methanol molecule to dimethyl ether (DME).

The proposed reaction mechanism of the dimethyl ether formation involves two elementary steps and is shown in Scheme 2. Its energetics are presented in Figure 3. We use the postfix 'c', when appropriate, for this reaction cycle. The first step starts with the initial adsorption of one methanol molecule at the zeolite acidic site, which is then dehydrated, leaving a methyl group attached to the basic oxygen of the zeolite. This step has been discussed already in section 3.1. The dehydration process is now followed by the activation of another methanol molecule by the methoxy species. The adsorption of the second methanol to the methoxy intermediate (Int_3c) is exothermic by −10.3 kcal/mol. The adsorption energy of this structure is 9.9 kcal/mol higher than the coadsorbed methoxy species and 2-MN (Int_3a), indicating a weaker interaction with the BEA zeolite cavity. The transition state (TS_2c) has the characteristics of a methyl carbocation with a trigonal planar geometry that leads to the formation of the C−O bond with the methanol molecule. The distance between C1 and O2 of methoxy increases from 1.49 to 1.98 Å, and the C1 and O5 distance decreases from 3.22 to 1.92 Å as their bond is formed (Table 2). Here, the zeolite framework plays an important role in stabilizing both the adsorption complex and the transition structure, with the energy barrier lowered by 3.6 kcal/mol compared to the value obtained from the 3T quantum cluster model[37] (Table 2). From the reaction profile in Figure 3 it can be seen that DME requires 26.2 kcal/mol to desorb from the active site. The rate-limiting step for DME formation according to this pathway is the dehydration of the first methanol molecule which requires 39.8 kcal/mol. The activation barrier in the latter step is 5.1 (6.4) kcal/mol higher than the methylation of 2-MN to 2,6-DMN (2,7-DMN). Therefore, also the second side reaction discussed here, the self-activation of methanol to dimethyl ether, is not supposed to be competitive with the methylation of 2-MN.

## 4. Conclusions

In this theoretical investigation we have shown how steric constraints and van der Waals contributions of the zeolite

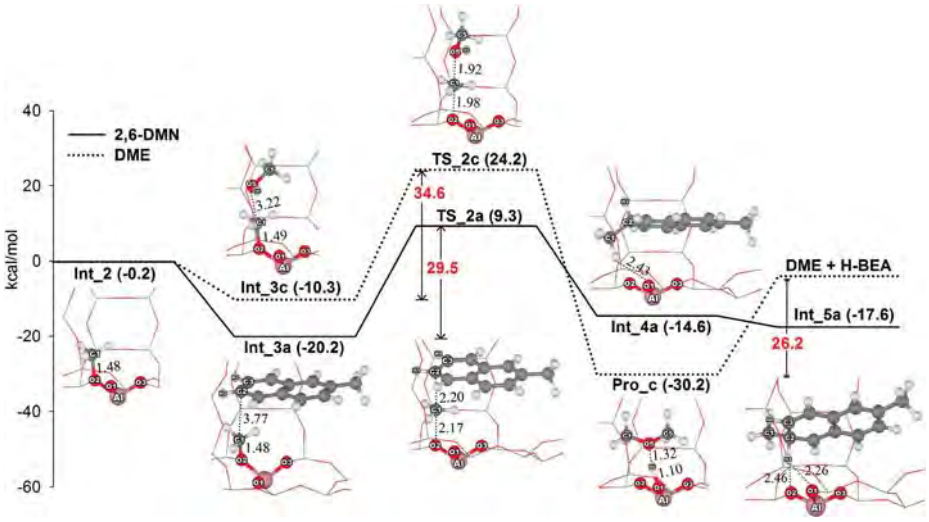


**Figure 3.** The energy profile comparing the methylation of 2-MN to 2,6-DMN and the dimethyl ether (DME) formation.

**TABLE 2: Geometrical Parameters from the 34T Model (M06-2X/6-311+G(2df,2p)//M06-2X/6-31G(d,p)) Calculations of the Intermediates (Int_2 and Int_3c), Transition State (TS_2c), and Product (Pro_c) for the Dimethyl Ether Formation over H-BEA[a]**

| parameters | H-BEA | Int_2 | Int_3c | TS_2c | Pro_c |
|---|---|---|---|---|---|
| O1−H1 | 0.98 | − | − | − | − |
| C1−O2 | − | 1.48 | 1.49 | 1.98 | 2.99 |
| C1−O5 | − | − | 3.22 | 1.92 | 1.43 |
| C4−O5 | − | − | 1.41 | 1.44 | 1.43 |
| O5−H5 | − | − | 0.97 | 0.97 | 1.51 |
| O1−H5 | − | − | 4.05 | 3.97 | 1.10 |
| Al−O1 | 1.85 | 1.69 | 1.66 | 1.71 | 1.80 |
| Al−O2 | 1.70 | 1.86 | 1.80 | 1.77 | 1.70 |
| Al−O3 | 1.68 | 1.69 | 1.65 | 1.71 | 1.70 |
| ∠O1−Al−O2 | 93.1 | 94.3 | 93.0 | 98.1 | 95.8 |

[a] Distances are in Å and angles are in degrees.

framework can affect the reaction pathways of the methylation of 2-methylnaphthalene and of competing reactions. Our results can be summarized as follows:

(1) The methylation of 2-MN to 2,6-DMN and 2,7-DMN is initiated by the adsorption of a methanol molecule at the zeolite acidic site, which is then dehydrated, leaving a methyl group attached to the basic oxygen of the zeolite. Subsequently, the methyl group from the zeolite framework transfers to 2-MN at the $\beta$-positions yielding naphthalenium intermediates. Eventually, 2,6- and 2,7-DMN are generated by direct proton transfer from the naphthalenium intermediates to the active site. The formation of the methoxy species is considered to be the rate-determining step.

(2) The zeolitic framework plays an important role in the stabilization of the adsorption complexes, transition states, and intermediates. The calculated adsorption energies are in good qualitative agreement with experimental results. The stabilizing effect of the zeolite micropore on the ionic transition state causes the activation barrier to be about 20% lower than what has been calculated for small clusters lacking these contributions. The 34T cluster that is used to model BEA zeolite stabilizes the key reaction intermediates, the naphthalenium cations.

(3) The energy profiles for the formation of 2,6- and 2,7-DMN formation are similar and in agreement with the experimental data that showed no preference for either of them.

(4) Considering a possibly competing process, the self-activation barrier of methanol to DME is unfavorably high for the C−O bond-formation step, compared to that for the formation of the C−C bond in 2-MN.

**Acknowledgment.** This work was supported in part by grants from the National Science and Technology Development Agency (2009 NSTDA Chair Professor funded by the Crown Property Bureau under the management of the National Science and Technology Development Agency and NANOTEC Center of Excellence funded by the National Nanotechnology Center), The Thailand Research Fund (to J.L.), the Commission on Higher Education, Ministry of Education (the "National Research University Project of Thailand (NRU)" and the "National Center of Excellence for Petroleum, Petrochemical and Advanced Materials (NCE-PPAM)"). The support from the Kasetsart University Research and Development Institute (KURDI) and the Graduate School Kasetsart University (to K.B.) are also acknowledged. We are grateful to Donald G. Truhlar and Yan Zhao for their support concerning the M06-2X code. M.P. acknowledges an infrastructure grant from the Austrian Ministry of Science to the LFU scientific computing platform.

**Supporting Information Available:** All Cartesian coordinates of the species in the paper. This material is available free of charge via the Internet at http://pubs.acs.org.

## References and Notes

(1) Jacobs, P. A.; Martens, J. A. In *Studies in Surface Science and Catalysis*; van Bekkum, H., Flanigen, E. M., Jansen, J. C., Eds.; Elsevier: Amsterdam, 1991; Vol. 58, Chapter 12, pp 445−496.

(2) Lillwitz, L. D. *Appl. Catal., A* **2001**, *221*, 337.

(3) Song, C.; Schobert, H. H. *Fuel Process. Technol.* **1993**, *34*, 157.

(4) Horita, H.; Takeuchi, G. *Petrotech* **1995**, *18*, 844.

(5) Kraikul, N.; Rangsunvigit, P.; Kulprathipanja, S. *Chem. Eng. J.* **2005**, *114*, 73.

(6) Kraikul, N.; Rangsunvigit, P.; Kulprathipanja, S. *Appl. Catal., A* **2006**, *312*, 102.

(7) Sikkenga, D. Zaenger, I. C.; Williams, G. S. U.S. Patent 4,962,260, 1990.

(8) Fraenkel, D.; Cherniavsky, M.; Ittah, B.; Levy, M. *J. Catal.* **1986**, *101*, 273.

(9) Komatsu, T.; Araki, Y.; Namba, S.; Yashima, T. In *Studies in Surface Science and Catalysis*; Weitkamp, J., Karge, H. G., Pfeifer, H., Hölderich, W., Eds.; Elsevier: Amsterdam, 1994; Vol. 84, Part 3, p 1821.

(10) Popova, Z.; Yankov, M.; Dimitrov, L. In *Studies in Surface Science and Catalysis*; Weitkamp, J., Karge, H. G., Pfeifer, H., Hölderich, W., Eds.; Elsevier: Amsterdam, 1994; Vol. 84, Part 3, p 1829.

(11) Pu, S.-B.; Inui, T. *Appl. Catal., A* **1996**, *146*, 305.

(12) Weitkamp, J.; Neuber, M. In *Studies in Surface Science and Catalysis*; Tomoyuki lnui, S. N., Takashi, T., Eds.; Elsevier: Amsterdam, 1991; Vol. 60, p 291.
(13) Inui, T.; Pu, S.-B.; Kugai, J.-i. *Appl. Catal., A* **1996**, *146*, 285.
(14) Schwabe, T.; Grimme, S. *Acc. Chem. Res.* **2008**, *41*, 569.
(15) Zhang, I. Y.; Wu, J.; Xu, X. *Chem. Commun.* **2010**, *46*, 3057.
(16) Tsipis, A. C.; Orpen, A. G.; Harvey, J. N. *Dalton Trans.* **2005**, 2849.
(17) Zhao, Y.; Truhlar, D. G. *Org. Lett.* **2007**, *9*, 1967.
(18) Zhao, Y.; Truhlar, D. G. *J. Chem. Phys.* **2006**, *125*, 194101.
(19) Zhao, Y.; Truhlar, D. G. *J. Phys. Chem. A* **2006**, *110*, 13126.
(20) Zhao, Y.; Truhlar, D. *Theor. Chem. Acc* **2008**, *120*, 215.
(21) Zhao, Y.; Truhlar, D. G. *Acc. Chem. Res.* **2008**, *41*, 157.
(22) Boekfa, B.; Choomwattana, S.; Khongpracha, P.; Limtrakul, J. *Langmuir* **2009**, *25*, 12990.
(23) Maihom, T.; Boekfa, B.; Sirijaraensre, J.; Nanok, T.; Probst, M.; Limtrakul, J. *J. Phys. Chem. C* **2009**, *113*, 6654.
(24) Maihom, T.; Pantu, P.; Tachakritikul, C.; Probst, M.; Limtrakul, J. *J. Phys. Chem. C* **2010**, *114*, 7850.
(25) Higgins, J. B.; LaPierre, R. B.; Schlenker, J. L.; Rohrman, A. C.; Wood, J. D.; Kerr, G. T.; Rohrbaugh, W. J. *Zeolites* **1988**, *8*, 446.
(26) Frisch, M. J.; Trucks, G. W.; Schlegel, H. B.; Scuseria, G. E.; Robb, M. A.; Cheeseman, J. R.; Montgomery, Jr., J. A.; Vreven, T.; Kudin, K. N.; Burant, J. C.; Millam, J. M.; Iyengar, S. S.; Tomasi, J.; Barone, V.; Mennucci, B.; Cossi, M.; Scalmani, G.; Rega, N.; Petersson, G. A.; Nakatsuji, H.; Hada, M.; Ehara, M.; Toyota, K.; Fukuda, R.; Hasegawa, J.; Ishida, M.; Nakajima, T.; Honda, Y.; Kitao, O.; Nakai, H.; Klene, M.; Li, X.; Knox, J. E.; Hratchian, H. P.; Cross, J. B.; Bakken, V.; Adamo, C.; Jaramillo, J.; Gomperts, R.; Stratmann, R. E.; Yazyev, O.; Austin, A. J.; Cammi, R.; Pomelli, C.; Ochterski, J. W.; Ayala, P. Y.; Morokuma, K.; Voth, G. A.; Salvador, P.; Dannenberg, J. J.; Zakrzewski, V. G.; Dapprich, S.; Daniels, A. D.; Strain, M. C.; Farkas, O.; Malick, D. K.; Rabuck, A. D.; Raghavachari, K.; Foresman, J. B.; Ortiz, J. V.; Cui, Q.; Baboul, A. G.; Clifford, S.; Cioslowski, J.; Stefanov, B. B.; Liu, G.; Liashenko, A.; Piskorz, P.; Komaromi, I.; Martin, R. L.; Fox, D. J.; Keith, T.; Al-Laham, M. A.; Peng, C. Y.; Nanayakkara, A.; Challacombe, M.; Gill, P. M. W.; Johnson, B.; Chen, W.; Wong, M. W.; Gonzalez, C.; Pople, J. A. *Gaussian 03*, revision C.02; Gaussian, Inc.: Wallingford, CT, 2004.
(27) Haase, F.; Sauer, J.; Hutter, J. *Chem. Phys. Lett.* **1997**, *266*, 397.
(28) Stich, I.; Gale, J. D.; Terakura, K.; Payne, M. C. *Chem. Phys. Lett.* **1998**, *283*, 402.
(29) Haase, F.; Sauer, J. *Microporous Mesoporous Mater.* **2000**, *35*−*36*, 379.
(30) Svelle, S.; Tuma, C.; Rozanska, X.; Kerber, T.; Sauer, J. *J. Am. Chem. Soc.* **2008**, *131*, 816.
(31) Lee, C. C.; Gorte, R. J.; Farneth, W. E. *J. Phys. Chem. B* **1997**, *101*, 3811.
(32) Kotrel, S.; Lunsford, J. H.; Knozinger, H. *J. Phys. Chem. B* **2001**, *105*, 3917.
(33) Pinto, R. R.; Borges, P.; Lemos, M. A. N. D. A.; Lemos, F.; Védrine, J. C.; Derouane, E. G.; Ribeiro, F. R. *Appl. Catal., A* **2005**, *284*, 39.
(34) Suzuki, K.; Noda, T.; Katada, N.; Niwa, M. *J. Catal.* **2007**, *250*, 151.
(35) Kotrel, S.; Rosynek, M. P.; Lunsford, J. H. *J. Phys. Chem. B* **1999**, *103*, 818.
(36) Blaszkowski, S. R.; van Santen, R. A. *J. Am. Chem. Soc.* **1996**, *118*, 5152.
(37) Blaszkowski, S. R.; van Santen, R. A. *J. Phys. Chem. B* **1997**, *101*, 2292.
(38) Hansen, N.; Bruggemann, T.; Bell, A. T.; Keil, F. J. *J. Phys. Chem. C* **2008**, *112*, 15402.
(39) Rozanska, X.; van Santen, R. A.; Hutschka, F.; Hafner, J. *J. Am. Chem. Soc.* **2001**, *123*, 7655.
(40) Sato, T.; Kunimori, K.; Hayashi, S. *Phys. Chem. Chem. Phys.* **1999**, *1*, 5.
(41) Jobic, H.; Bee, M.; Renouprez, A. *Surf. Sci.* **1984**, *140*, 307.

JP108566C

PCCP

View Online
Dynamic Article Links

Cite this: *Phys. Chem. Chem. Phys.*, 2011, **13**, 6462–6470

www.rsc.org/pccp

**PAPER**

# Structures and reaction mechanisms of glycerol dehydration over H-ZSM-5 zeolite: a density functional theory study†

**Kanokwan Kongpatpanich,[abcd] Tanin Nanok,[abcd] Bundet Boekfa,[bcd] Michael Probst[e] and Jumras Limtrakul*[abcd]**

***Received 5th September 2010, Accepted 27th January 2011***
**DOI: 10.1039/c0cp01720e**



The initial stage of glycerol conversion over H-ZSM-5 zeolite has been investigated using density functional theory (DFT) calculations on an embedded cluster model consisting of 128 tetrahedrally coordinated atoms. It is found that glycerol dehydration to acrolein and acetol proceeds favourably *via* a stepwise mechanism. The formation of an alkoxide species upon the first dehydration requires the highest activation energy (42.5 kcal $mol^{-1}$) and can be considered as the rate determining step of the reaction. The intrinsic activation energies for the first dehydration are virtually the same for both acrolein and acetol formation, respectively, suggesting the competitive removal of the primary and secondary OH groups. A high selectivity to acrolein at moderate temperatures can be attributed to the selective activation of the stronger adsorption mode of glycerol through the secondary OH group and the kinetically favoured subsequent consecutive steps. In addition, the less reactive nature of acrolein relative to acetol precludes it from being converted to other products upon conversion to glycerol. In accordance with typical endothermic reactions, the forward rate constant for glycerol dehydration significantly increases with increasing reaction temperature.

## 1. Introduction

Biomass conversion can partially replace petroleum-based chemical processes.[1] Among the biomass-based raw materials, glycerol has gained much attention because of its continuous overproduction from the biodiesel production process and its capability of being a sustainable and biodegradable raw material to synthesize various chemicals.[2]

While there are many recent attempts concerning the utilization of glycerol by means of oxidation, hydrogenolysis, pyrolysis, transesterification, esterification, polymerization and dehydration, one of the most interesting catalytic processes is the catalytic conversion of glycerol to acrolein by double dehydration. This process could offer a route to the sustainable production of acrolein, which has broad industrial and agricultural applications.[3] Acrolein is an essential and versatile starting chemical widely used in the production of DL-Methionine, acrylic acid, super absorber polymers, and detergents. Furthermore, it can be directly used as bactericides in the petroleum drilling branch. Various homogeneous and heterogeneous acid catalysts have been investigated for glycerol dehydration in the liquid phase, especially in near- or supercritical water, and in the gas phase. The main advantage of using supercritical water is the capability to adjust its physical properties by varying the pressure and temperature.[4–7] However, a heterogeneous catalyst is often more preferable because of its easy separation at the end of the process. Moreover, the use of supercritical water results in high investments because processes dealing with supercritical conditions need high-quality equipment. Therefore, the development of a high-performance heterogeneous catalyst and a practical gas phase reaction is still of great interest.

The dehydration of glycerol in the gas phase can be accomplished by three categories of solid acid catalysts:

The first one is supported inorganic acids, including heteropolyacids.[8] The properties required to design effective catalysts of that type[9] are well understood. Although their selectivity for acrolein is high, these catalysts often lose their activity quite rapidly. The second group is the mixed-oxide type catalyst.

[a] *Laboratory for Computational and Applied Chemistry, Department of Chemistry, Faculty of Science, Kasetsart University, Bangkok 10900, Thailand*
[b] *Center for Advanced Studies in Nanotechnology and Its Applications in Chemical, Food and Agricultural Industries, Kasetsart University, Bangkok 10900, Thailand*
[c] *Center of Nanotechnology, Kasetsart University Research and Development Institute, Kasetsart University, Bangkok 10900, Thailand*
[d] *NANOTEC Center of Nanotechnology, National Nanotechnology Center, Kasetsart University, Bangkok 10900, Thailand. E-mail: jumas.l@ku.ac.th; Fax: +66-2562-5555 ext 2159; Tel: +66-2562-5555 ext 2176*
[e] *Institute of Ion Physics and Applied Physics, University of Innsbruck, A-6020 Innsbruck, Austria*
† Electronic supplementary information (ESI) available: See DOI: 10.1039/c0cp01720e

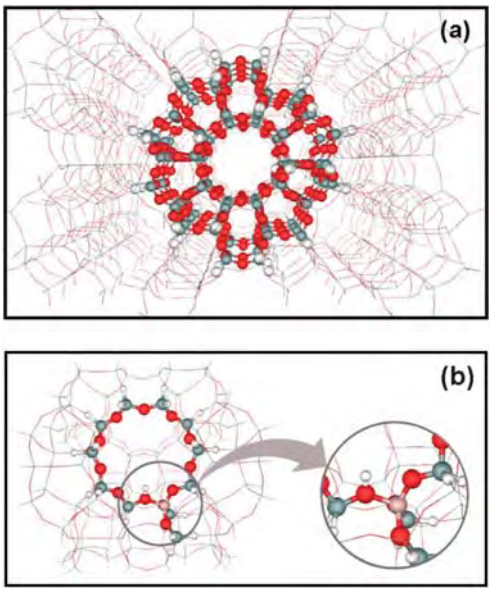


**Fig. 1** (a) The model of the 128T cluster of H-ZSM-5 zeolite. Atoms belonging to the 128T region and wires represent the rest of the lattice structure. (b) Selection of the 12T active site region and the 128T clusters from the lattice structure of the H-ZSM-5 zeolite.

Mixed-oxide catalyst types are currently called into question because they have not been extensively studied.[10–12] The last group is acidic zeolites. These groups have been extensively studied for glycerol dehydration for more than three years.[13–16] Their general advantages are high catalytic activity, shape selectivity and thermal stability. The catalytic activity originates from the presence of the Brønsted acid site in the confined space.[17] Its acidity and, therefore, performance, can be controlled by tuning the Si/Al ratio. Experimental studies suggest that the H-ZSM-5 zeolite is one of the best for glycerol conversion, especially in the gas phase.

It is quite difficult to get comprehensive information about the detailed mechanism of glycerol dehydration in zeolites solely from experiments. This is due to the complexity of their nanoporous structures that prevents them from being investigated by conventional techniques. The most comprehensive study has been performed by Corma and co-workers.[14] These authors proposed a complex reaction network to explain the formation of all the observed products. The first dehydration step in glycerol dehydration leads to either acetol or 3-hydroxypropionaldehyde. The latter further dehydrates in a second dehydration step to yield acrolein. The progress of the reaction can be briefly observed experimentally by the in-situ FTIR study. IR spectra interpretation proved that acrolein is the major product of the glycerol dehydration over H-ZSM-5 zeolite. The reaction towards acrolein is found to be more favorable than towards acetol.[18]

There are theoretical studies on glycerol dehydration over homogeneous catalysts[19] but, to the best of our knowledge, there are no theoretical studies reported about the detailed reaction mechanism of glycerol dehydration over solid acid in the gas phase, which may offer a different mechanism from the conventional ones. Therefore, a computational investigation of the reaction mechanisms with a reliable method should be useful. In this work we investigate and compare the different possible reaction mechanisms and product formation pathways by means of cluster calculations using a density functional that includes dispersion energy.

## 2. Computational details

The cluster approach is commonly used to describe the interaction between organic molecules and the active sites of zeolites. Nevertheless, its accuracy is limited to only small polar molecules in which the effect caused by the extended zeolite lattice is negligible. For non-polar molecules, the confinement effect by the zeolite framework becomes important, particularly, when the molecular size of adsorbing molecules is comparable to the dimension of zeolite pores. To take into account the short- and medium-range effects by the zeolite framework, a 128T (T = Si and Al tetrahedral sites) cluster model of the ZSM-5 zeolite, covering the straight channel, the zigzag channel, and the channel intersection, was used in this study. The reaction was assumed to mainly take place at the cavity that emerged at the channel intersection. One silicon atom of 12 different tetrahedral sites (T1 to T12) was substituted by an aluminum atom to generate the Brønsted acidic site. An aluminum atom was chosen to reside at the T12 site located at the 10-membered ring window open to both straight and zigzag channels. In that position it is accessible to the diffusing molecules from both types of the channel. Our previous studies showed that the density functional theory using the M06-2X functional[20,21] provided quite good results compared to functionals without dispersion energy terms for the interaction energy of organic molecules in the zeolite systems.[22–26] The performance of M06-2X has also been evaluated favourably in other studies. For example, it was found[27] that short-to medium range correlation effects are well reproduced and that it's accuracy for reaction enthalpies is often comparable to much more expensive methods[28] This functional is, therefore, also used in our present study.

Because the adsorption complex between the 128T cluster model of zeolite and the adsorbing molecule constitutes a large and computationally demanding system, we considered the 12T cluster as the smallest unit required to represent the active site of zeolite (see Fig. 1). The dangling bonds created from the cluster trimming process, aligning exactly in the same direction of the corresponding Si–O bonds from the crystallographic structure, were saturated with hydrogen atoms. During the geometry optimization, all atoms of the 12T zeolite cluster model were frozen at their initial position except atoms located within the second coordination shell of the aluminum centre. The adsorbing molecule was permitted to fully relax. All stationary points along the reaction paths were located by eigenvector following and verified by performing frequency calculations at the M06-2X/6-31G(d,p) level of theory.[29] A negative frequency of the normal mode motion corresponding to the desired reaction coordinate observed in all transition states confirmed that our transition states were located at the saddle point. No negative frequency was found in the reactants and products. The optimized structure of each stationary point was then inserted in the rest of the 128T cluster to impose the realistic short- and medium-range effects of the zeolite framework. The model was further augmented

with the long-range electrostatic potential from the periodic zeolite lattice. For this, the 128T quantum cluster was surrounded with point charges derived from the surface charge representation of the electrostatic embedding potential (SCREEP)[30] method to reproduce the Madelung potential. The energy was then calculated in a single-point calculation. This embedding scheme provides a cost-effective way of treating the extended framework effects on the adsorption and reaction of organic molecules in zeolites.[22,31]

Standard enthalpies and free energy changes of all structures in the rate determining step were obtained from frequency calculations. These data were used to predict the rate and equilibrium constants for the rate determining step of the reaction. The rate constants were evaluated over the temperature range of 473–773 K with an interval of 50 K using simple transition state theory (TST). The equation for calculating the reaction rate constant is:

$$k(T) = \frac{k_B T}{h} \exp\left(-\frac{\Delta G^{\neq}}{RT}\right)$$

Where $\Delta G^{\#}$ is the free energy of activation, $k_B$ is Boltzmann's constant, $h$ is Plank's constant, $T$ is the temperature in Kelvin and $R$ is the universal gas constant. Thermodynamic data at the temperature range of 473 to 773 K were listed in Table S6 (see Supporting Information). All calculations were performed using the Gaussian 03 code[32] modified to include the Minnesota density functionals module 3.1 by Zhao and Truhlar.

## 3. Results and discussions

### 3.1 Glycerol adsorption onto the Brønsted acid site

Glycerol has a highly flexible $C_3$-backbone structure with three hydroxyl (OH) groups in vicinal positions. A variation in the orientation of the three OH groups leads to different conformations of its gas phase molecule. Recently, it has been reported that the most stable conformer of glycerol is the one in which all three of its OH groups form a linear-chain structure of intramolecular hydrogen bonds.[33,34]

Adsorption of glycerol onto the zeolite acid site can probably take place through either its primary or secondary OH groups. Fig. 2a and b show the optimized geometries of glycerol adsorption through primary (**ads_1**) and secondary (**ads_2**) OH groups, respectively. The nearly linear O1–Hz–O5 and O1–Hz–O4 angles (177.2° for both structures) suggest a strong hydrogen bond between glycerol and the zeolite which normally increases the proton transfer capability. As can be seen, the O1–Hz bond separation (1.07 and 1.06 Å for the primary and secondary OH groups, respectively) increases significantly from that of an isolated zeolite (0.97 Å). The close contact of one glycerol OH group with the zeolite Brønsted proton Hz results in a significant lengthening and weakening of its corresponding C–O bond (1.44 and 1.43 Å for **ads_1** and **ads_2**, respectively) with respect to the other two C–O bond distances (an average of 1.42 Å).

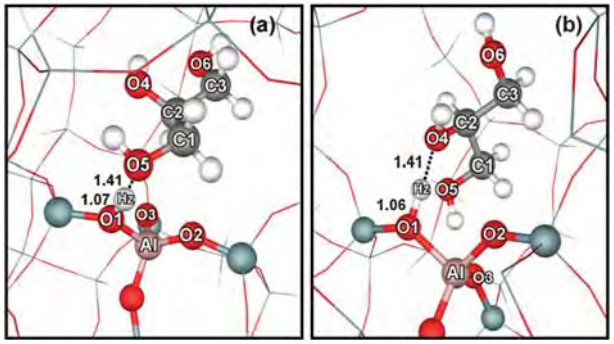


**Fig. 2** Optimized structures of glycerol adsorption using (a) the primary OH group **ads_1** and (b) the secondary OH group **ads_2**.

As a result, the protonation of glycerol by the zeolite could give support to enhancing the glycerol dehydration. However, we could not locate the completely protonated form, an ion-pair complex, as a stable intermediate, even when carrying out the geometry optimization using the 34T quantum cluster at the same level of theory. This situation is similar to the monomolecular adsorption of small alcohols on the proton zeolites.[22,35] The adsorption energies for the **ads_1** and **ads_2** structures are estimated to be −39.4 and −42.5 kcal mol$^{-1}$, respectively.

These values are considerably higher than the experimental values for simple alcohols on the H-ZSM-5 zeolite of −27.5 and −31.1 kcal mol$^{-1}$ for methanol and ethanol, respectively.[36] The higher value for glycerol adsorption indicates a stronger interaction with the zeolite, which results mostly from two additional hydrogen-bondings of the non-adsorbed OH groups with the partially negatively charged oxygen atoms of the zeolite framework. The dehydration of **ads_1** is believed to result in the acetol formation, while acrolein is formed upon the dehydration of **ads_2**. Statistically, from the number of primary and secondary OH groups in a glycerol molecule, the possibility for acetol formation would be twice that for acrolein formation. Recently, the product distribution[14] and FT-IR studies[18] of glycerol conversion at low temperatures (< 646 K) have revealed that the H-ZSM-5 zeolite is selective to acrolein formation, whereas the selectivity to acetol is only very small. To clarify if the removal of the secondary OH group is more favourable than that of the primary OH group, the detailed mechanisms of the initial reaction pathways for glycerol dehydration to acrolein and acetol are to be explored and discussed in the reaction mechanism sections.

### 3.2 Conversion of glycerol to acrolein

As mentioned above, the conversion of glycerol to acrolein is presumably initialized from **ads_2**. Based on the previous FT-IR study,[18] the reaction mechanism for acrolein formation consecutively proceeds through the three main steps: (1) the removal of the secondary OH group of glycerol by the dehydration reaction to produce an enol-intermediate, (2) the tautomerization of the enol into the keto-intermediate, and (3) the removal of the primary OH group from the keto-intermediate to form the acrolein product. Each step of the reaction is considered to take place in the monomolecular fashion. The water molecules developed in the dehydration process are assumed not to be further involved in the reaction progress. The three steps for acrolein formation are shown in Scheme 1.

 

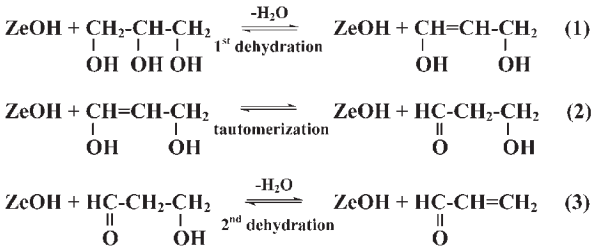


**Scheme 1** The reaction pathway of glycerol dehydration: the acrolein formation pathway.

**3.2.1 Dehydration at the secondary OH group (the first dehydration).** In the first dehydration step, the adsorbed glycerol is protonated by the acidic proton of the zeolite at the secondary OH group. This results in the weakening of the secondary C–O bond and promotes the removal of the secondary OH group as a water molecule. The dehydration can in principle proceed through either the stepwise or the concerted mechanism.

For the stepwise mechanism, the water molecules are developed upon the formation of alkoxide species. It is noted that the attempt to locate the transition state closely related to the corresponding adsorption complex **ads_2** is discarded by the proton back donation from the adsorbed glycerol to the zeolite. The proton exchange is also expected to occur readily under normal experimental conditions. We, therefore, propose an activated complex as shown in Fig. 3a for the first transition state structure, **ts_dehyd_1**. The secondary carbon C2 is centred between the protonated OH group and the zeolite lattice oxygen O2. The protonated glycerol is ionized by the assistance of the basic zeolite oxygen to form a secondary carbocation.

However, it is found that the secondary carbocation created at the transition state does not exist as an intermediate. From the vibrational mode with an imaginary frequency, it can be seen that the transition state already indicates the formation of a water molecule and the alkoxide. The secondary surface alkoxide species, **alk_1**, and a water molecule are the stable products of the first elementary step. The transition state requires an activation energy of 42.5 kcal $mol^{-1}$. From the bond distance parameters, the formation of a water molecule is more advanced (C2–O4 = 2.40 Å) than the formation of the alkoxide species (C2–O2 = 2.28 Å). With respect to the adsorption complex **ads_2**, the alkoxide formation is endothermic by 27.7 kcal $mol^{-1}$. This is consistent with the Hammond–Leffler postulate[37] which states that for an endothermic reaction the transition state structure resembles the final products. To shift the reaction forwards, it is essential that the water molecule generated in this step is desorbed from the system. The desorption energy of a water molecule adsorbed nearby the surface alkoxide is estimated to be 16.3 kcal $mol^{-1}$. This value is close to the reported desorption energy of a water molecule from the Brønsted active site of about 12–14 kcal $mol^{-1}$.[38,39] After the water molecule is eliminated from the system, the surface alkoxide, **alk_1**, can readily desorb from the zeolite surface by undergoing the proton back donation to regenerate the zeolite Brønsted active site. The hydrogen atom attached to the alkoxy primary carbon C1 is abstracted by the basic zeolite oxygen O3 to release 1,3-dihydroxypropene, **hyd_enol_1**, as a resulting product. This elementary step proceeds through the transition state **ts_alk_1** as depicted in Fig. 3b and requires an activation energy of 19.7 kcal $mol^{-1}$. 1,3-dihydroxypropene has an enol-form structure and binds strongly to the zeolite Brønsted active site using its vinyl hydroxyl group. As a result, the transformation of the alkoxide species to 1,3-dihydroxypropene adsorbed onto the zeolite Brønsted active site is an exothermic elementary step.

In the concerted mechanism, the water elimination and the enol formation occur without passing through the alkoxide intermediate. 1,3-dihydroxypropene is, therefore, obtained in a single elementary step. Fig. 4a shows the transition state structure, **tsc_dehyd_1**, for the E2 mechanism. The secondary glycerol OH group is protonated by the Brønsted proton at the same time that the primary hydrogen is abstracted by the basic zeolite oxygen. In concomitance with the elongation of the C2–O4 bond distance from 1.43 to 2.20 Å upon glycerol protonation, the C1–C2 bond distance is contracted to 1.39 Å upon the primary hydrogen abstraction. Such a simultaneous action of two functions (proton donor and proton acceptor) of the zeolite active site requires an activation energy of 72.0 kcal $mol^{-1}$, which is higher than that required in the stepwise mechanism (42.5 and 19.7 kcal $mol^{-1}$). A slightly smaller amount of the energy (14.3 kcal $mol^{-1}$) relative to that used to desorb a water molecule from the alkoxide intermediate (16.3 kcal $mol^{-1}$) is necessitated for extracting a water molecule from its coadsorption with 1,3-dihydroxypropene in the zeolite pore.

**3.2.2 Tautomerization of 1,3-dihydroxypropene to 3-hydroxypropionaldehyde.** 1,3-dihydroxypropene can isomerize to its keto-form through the tautomerization reaction. The π-bonding interaction of the double bond with the Brønsted acid site is considered to facilitate a double proton transfer and leads to the formation of 3-hydroxypropanal. As shown in Fig. 3c, the transition state, **ts_tauto_1**, for the tautomerization involves the concerted action of the zeolite active sites. The acidic proton at the zeolite O3 transfers to the C2 of glycerol at the same time that the hydroxyl proton on the glycerol O6 transfers back to the zeolite O1 to regenerate the acidic site. A small activation energy of 3.6 kcal $mol^{-1}$ implies that the keto-enol tautomerization of 1,3-dihydroxypropene to 3-hydroxypropionaldehyde on the acidic site occurs readily under the experimental conditions. As it is typical for the tautomerization of the enol-form to the keto-form, the reaction is exothermic. The keto-product strongly adsorbs onto the Brønsted acid site with its carbonyl group, **keto_CO**, *via* the hydrogen bonding interaction.

**3.2.3 Dehydration of at the primary OH group (the second dehydration).** In order to stimulate the second dehydration, the orientation of the strongly adsorbed keto-form is readjusted to the weaker adsorption mode, **keto_OH**. The interaction of its OH group with the Brønsted acid site is adopted as the starting geometry for the second dehydration step. Similar to the first dehydration step, the OH group is protonated by the zeolite and acts as a leaving group. The dehydration can proceed through either the stepwise or concerted mechanism.

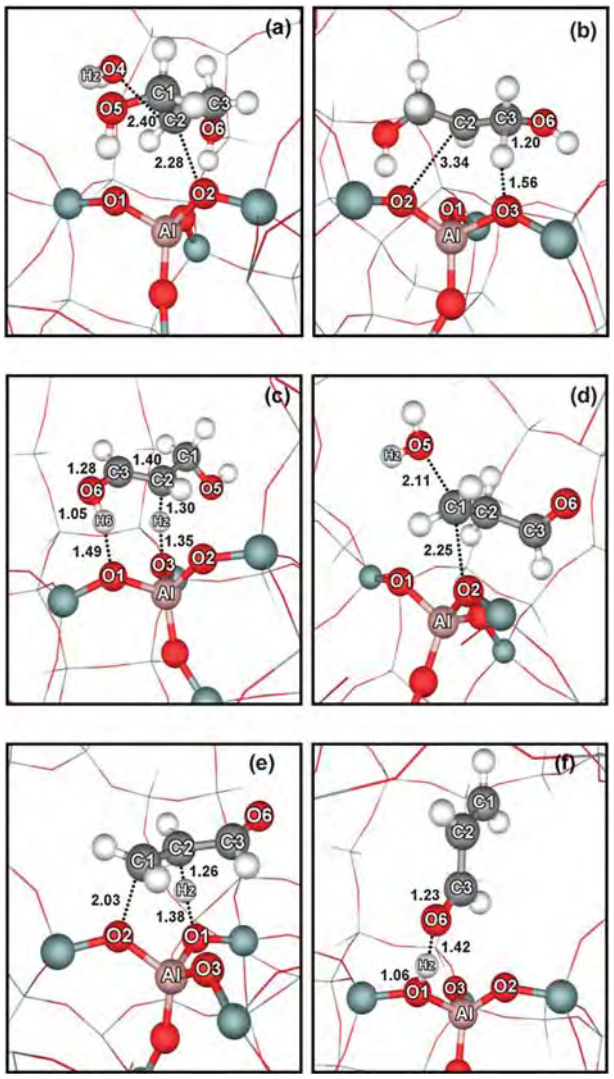


**Fig. 3** Optimized structures of the transition states and a product (acrolein) along the stepwise mechanism for glycerol conversion to acrolein: (a) **ts_dehyd_1** (b) **ts_alk_1** (c) **ts_tauto_1** (d) **ts_alk_2** (e) **ts_acrolein** and (f) **acrolein**.

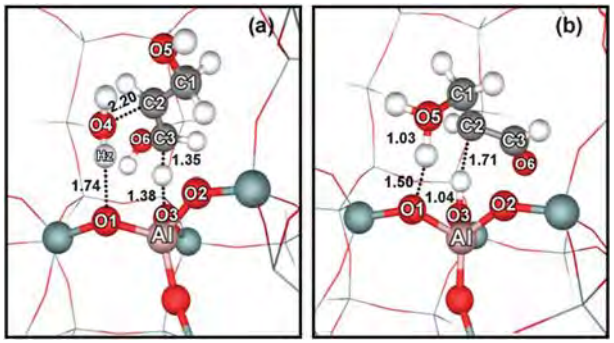


**Fig. 4** Optimized structures of the transition states along the concerted mechanism for glycerol conversion to acrolein: (a) **tsc_dehyd_1** (b) **tsc_dehyd_2**.

For the stepwise mechanism, the attack of the 3-hydroxypropanal primary carbon by the basic zeolite oxygen takes place in concomitance with the elimination of a water molecule, generating the primary alkoxide intermediate **alk_2**. The transition state **ts_alk_2** (see Fig. 3d) requires an activation energy of 35.8 kcal/mol. The primary alkoxide intermediate **alk_2** generated from this step is coadsorbed by a single water molecule. To remove an adsorbed water molecule from the alkoxide species requires the desorption energy of 12.6 kcal $mol^{-1}$. The dehydrated alkoxide species undergoes proton back donation from the secondary carbon to the basic zeolite oxygen leading to the acrolein product formation. The corresponding transition state **ts_acrolein** (see Fig. 3e) requires an activation energy of 24.0 kcal $mol^{-1}$. Finally, the desorption of acrolein from the zeolite surface requires the energy of 30.5 kcal $mol^{-1}$.

In the concerted mechanism, the elimination of the protonated primary OH group occurs simultaneously with the hydrogen abstraction at the secondary carbon atom. The single imaginary frequency of $-1145i$ $cm^{-1}$ indicates that at the transition state **tsc_dehyd_2** the protonation is more complete than the hydrogen abstraction. This can be confirmed by the selected bond distances depicted in Fig. 4b. The concerted activation energy for the second dehydration is estimated to be 39.3 kcal $mol^{-1}$, which is still higher than the activation energies in the stepwise case. The coadsorption complex of a water molecule and acrolein are the final products of this mechanism. These two constituents require the energy of 41.4 kcal $mol^{-1}$ to desorb from the zeolite framework.

### 3.3 Comparison of the stepwise mechanism with the concerted mechanism

The energetic profiles for the stepwise and the concerted mechanisms are shown in Fig. 5 and 6. Elementary steps in Fig. 5 refers to the first and the second steps of Scheme 1 while Fig. 6 relates to the third step of Scheme 1. It can be seen that the production of acrolein from glycerol is an endothermic process. The first dehydration reaction requires the highest activation energy and is therefore the rate determining step for both reaction mechanisms. Since the dehydration is thermodynamically and kinetically unfavourable, it is necessary to introduce a sufficiently high temperature to the system.[14,40] The selectivity to acrolein is, however, significantly decreased when increasing the reaction temperature while the selectivity to products resulting from the combustion and cracking of the coke such as CO, $CO_2$, light olefins, methane, and hydrocarbons become dominant.[14] On the other hand, when the reaction is carried out under low to moderate temperatures, selectivity close to 60% can be achieved for acrolein as the major product. Therefore, the large amount of energy (39.5–42.5 kcal $mol^{-1}$) released by glycerol adsorption could also be an additional internal energy for driving the conversion at low and moderate temperatures. From our calculated activation energies, it is apparent that the dehydration of glycerol in a stepwise mechanism is more favoured than that in a concerted mechanism. In addition, our result is also in agreement with experiments that have detected stable alkoxide intermediates for methanol and ethanol dehydration on zeolites.[41]

The temperature dependence of the rate constants of the reaction is often useful for understanding the reaction

 

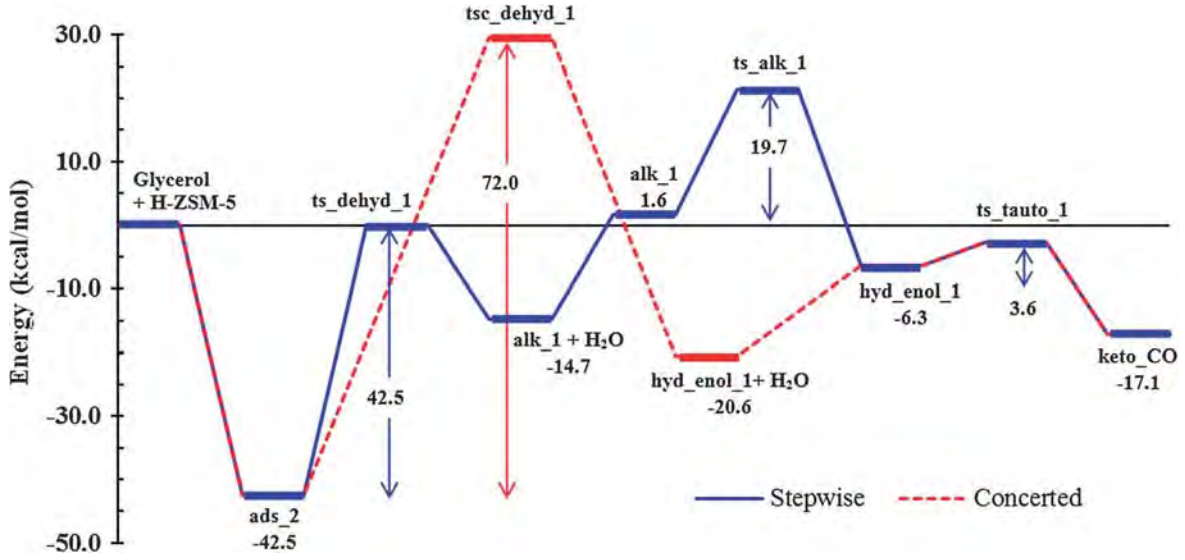


**Fig. 5** Energy profile for the glycerol dehydration to acrolein calculated using the M06-2X/6-31G(d,p) method including SCREEP charges on the 128T//12T cluster of H-ZSM-5 zeolite for the first two steps (the first dehydration and the keto-enol tautomerization). Energies are in kcal $mol^{-1}$.

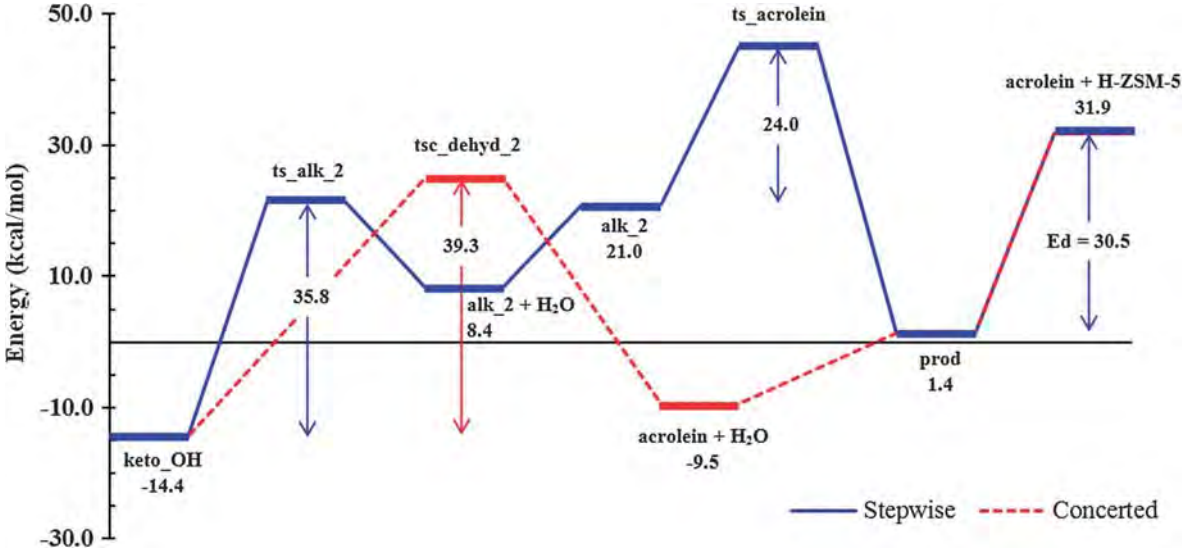


**Fig. 6** Energy profile for the glycerol dehydration to acrolein calculated using the M06-2X/6-31G(d,p) method including SCREEP charges on the 128T//12T cluster of H-ZSM-5 zeolite for the first two steps (the second dehydration, and the product desorption). Energies are in kcal $mol^{-1}$.

mechanism. In this study, the forward and reverse rate constants ($k$) as well as the equilibrium constants ($K$) for the first dehydration step of glycerol have been calculated by using the transition state theory (TST)[42] based on thermodynamic parameters obtained from the simplified 12T cluster. Over a temperature range of 473–773 K, the rate constant for both forward and reverse reactions increases with increasing the temperature (see Fig. 7), in an accordance with the typical endothermic reaction behavior. No related experiment on reaction rates over the H-ZSM-5 zeolite has been reported and so we provide only a qualitative discussion of the results. At an optimal temperature of 563 K, we find that the reaction rate for the alkoxide formation is about eight orders of magnitude lower than the alkoxide decomposition. However, since the free energy for water desorption from the zeolite surface is −4.10 kcal $mol^{-1}$ lower than the one for adsorption on the surface alkoxide implies that the water molecule developed from the first dehydration will be suddenly desorbed from the zeolite surface at this temperature. As a result, the hydration rate must be considerably very slow to shift the reaction backwards. This is consistent with results obtained from previous reaction optimization experiments which require a continuous feed reactor for shifting the reaction forwards.[3,14] Since the water molecule generated by the dehydration process can readily react with the active alkoxide intermediate, the continuous removal of water from the system is another crucial point. We can also note that these results can well explain why the gas phase reaction is preferred over the liquid phase.

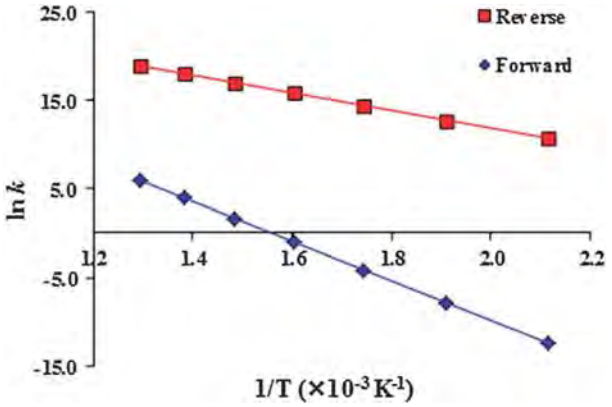


**Fig. 7** Arrhenius Plot for the rate determining step.

### 3.4 Conversion of glycerol to acetol

The reaction pathway for glycerol conversion to acetol is proposed to consist of two main steps. The results of reaction mechanisms for acrolein formation demonstrated that the analogous dehydration of glycerol could favor the stepwise mechanism. Therefore, only the stepwise mechanism is considered for glycerol conversion to acetol. Two steps of acetol formation are shown in Scheme 2.

For the first step, the adsorbed glycerol, **ads_1**, loses its primary OH group upon the attack of the zeolite basic oxygen at the primary carbon through the transition state **TS1** shown in Fig. 8a. Similar to the removal of the secondary OH group, the water formation is more advanced than the alkoxide formation. The primary OH group is already protonated by the zeolite and readily eliminated as a water molecule while the primary carbon C1 is forming a covalent bond with the zeolite basic oxygen O2. The activation energy for the removal of the primary OH group is calculated to be 42.3 kcal $mol^{-1}$. Subsequently, the alkyl group is covalently bound to the basic oxygen atom of zeolite (C1–O2 = 1.49 Å) forming the alkoxide intermediate, **ALK**. The removal of a water molecule from the system requires the energy of 13.3 kcal $mol^{-1}$. During the alkoxide intermediate being desorbed from the zeolite surface, it returns the proton back to regenerate the zeolite active site through the transition state **TS2** (see Fig. 8b). This process requires an activation energy of 26.8 kcal $mol^{-1}$. The one imaginary frequency exhibits the simultaneous actions of the proton back donation to the zeolite surface and the double bond formation of the resulting enol product.

In the second step, the adsorbed enol tautomerizes to its corresponding keto-form leading to the formation of acetol. The tautermerization of the enol-form proceeds through a

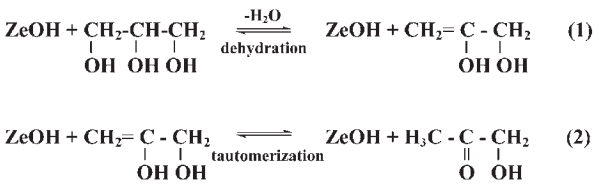


**Scheme 2** The reaction pathway of glycerol dehydration: the acetol formation pathway.

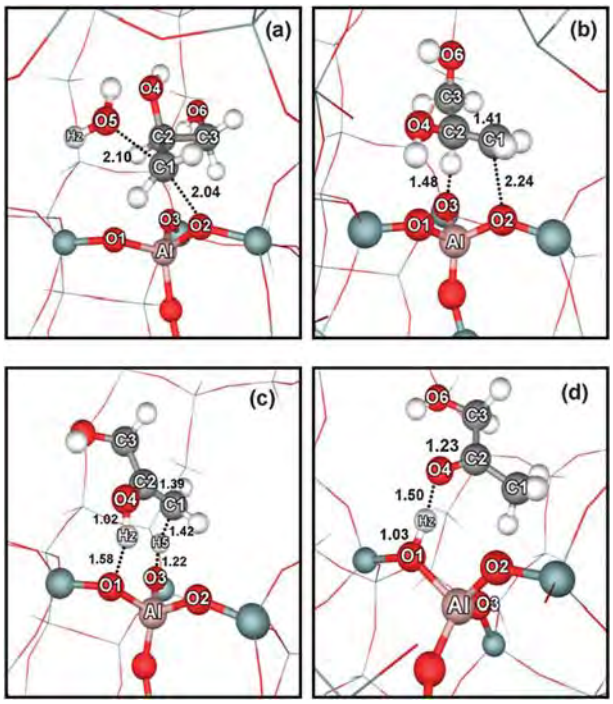


**Fig. 8** Optimized structures of the transition states and a by-product (acetol) for glycerol conversion to acetol (a) **TS1** (b) **TS2** (c) **TS3** and (d) **acetol**.

transition state **TS3** (see Fig. 8c). The hydrogen abstraction by the zeolite basic oxygen occurs simultaneously with the protonation of the secondary carbon by the zeolite Brønsted proton. The activation energy for this step is 11.3 kcal $mol^{-1}$. Desorption of acetol from the zeolite active site requires 30.9 kcal $mol^{-1}$.

Fig. 9 shows the energy profiles of acrolein and acetol formation in a stepwise mechanism. The first two elementary steps in Fig. 9 are equal to the first step in Scheme 2. It can be seen that the first dehydration is the rate determining step for both acrolein and acetol formation. The removal of the primary and secondary OH groups competes with one another with virtually the same activation energy. Therefore, the selective dehydration is determined by the binding strength of the primary and secondary OH groups to the Brønsted acid site. Our adsorption results support the selective removal of the glycerol secondary OH group over H-ZSM-5.[18] The selectivity to acrolein formation becomes more noticeable after the first dehydration has taken place. Desorption of the secondary surface alkoxide to regenerate the zeolite acid site requires less energy than for the primary surface alkoxide. This is due to the smaller steric hindrance in the primary hydrogen abstraction than in the secondary hydrogen abstraction by the basic oxygen of the zeolite. In contrast to the hydrogen abstraction, upon the keto-enol tautomerization, the protonation by the zeolite proceeds more readily at the secondary carbon atom than on the primary one. These results indicate that acrolein formation is more kinetically favored over acetol formation. In addition, the study of acetol conversion reveals that, even at the moderate temperature, acetol is almost completely converted to other products.[14] From this information,

 

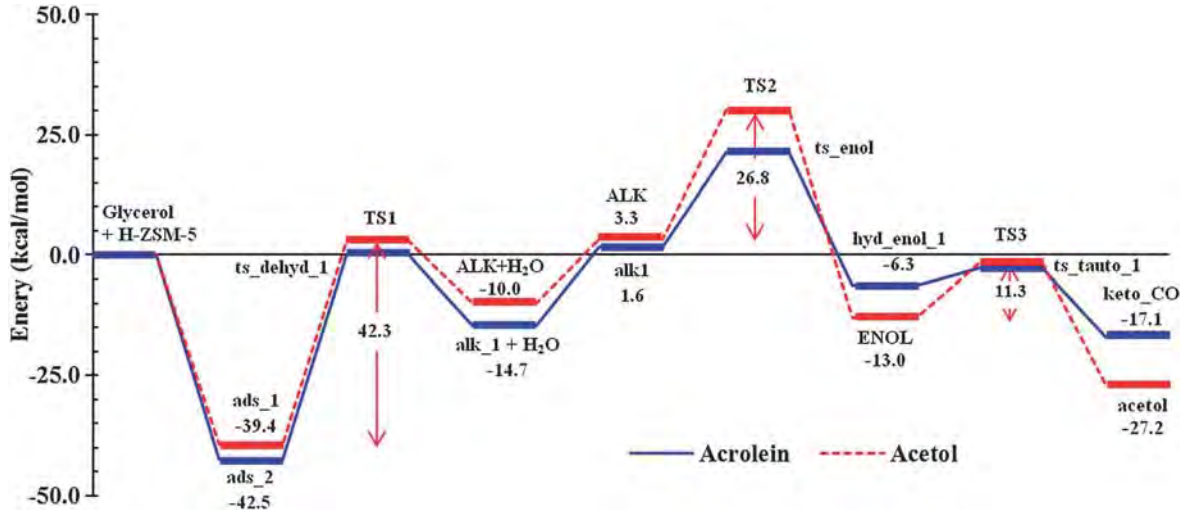


**Fig. 9** Energy profile for the acetol formation calculated using the M06-2X/6-31G(d,p) method on the 128T/12T cluster of H-ZSM-5 zeolite. Energies are in kcal $mol^{-1}$.

one can conclude that acetol is more reactive than acrolein and it is further converted to other products during the glycerol conversion.

## 4. Conclusions

The structures and reaction mechanisms for the initial stage of glycerol dehydration over the H-ZSM-5 zeolite are investigated. The effects of the zeolite framework imposed on the reaction mechanism are described by using the embedded M06 approach utilizing a 128T cluster. As proposed by the recent experimental studies,[14] the glycerol dehydration mechanism is started with two different glycerol adsorption modes. The adsorption with the primary OH group leads to acetol formation, while the adsorption with the secondary OH group directs to acrolein formation. The dehydration through the alkoxide formation in the stepwise mechanism is apparently more favourable than that in the concerted mechanism. The first dehydration is considered as the rate determining step for both acrolein and acetol formation with the intrinsic activation energies of 42.5 and 42.3 kcal $mol^{-1}$, respectively. These results imply that the removal of the primary OH group competes with the removal of the secondary OH group in the glycerol dehydration. However, modes of glycerol adsorption onto the zeolite Brønsted site might exhibit selective dehydration. The stronger adsorption of glycerol through its secondary OH group favourably supports the secondary OH dehydration. Details of the reaction mechanism subsequent to the first dehydration reveal that acrolein formation is more kinetically favoured over the competitive formation of acetol. Also, it is expected that acrolein is less reactive than acetol and, at moderate temperatures, it is not converted to other products, thus remaining the major product for glycerol conversion. Consistent with experimental findings, conversion of glycerol to acrolein or acetol is an endothermic reaction. The increase of reaction temperature causes a more significant increase in the forward rate than that in the reverse rate. Further studies of the reaction network of acrolein and acetol conversion could lead to a better understanding of the experimental product selectivity of glycerol conversion. We believe that such information can be important as a guideline to find the best reaction conditions.

## Acknowledgements

This work was supported in part by grants from the National Science and Technology Development Agency (2009 NSTDA Chair Professor funded by the Crown Property Bureau under the management of the National Science and Technology Development Agency and NANOTEC Center of Excellence funded by the National Nanotechnology Center), The Thailand Research Fund, the Commission on Higher Education, Ministry of Education (“National Research University of Thailand” and “Postgraduate Education and Research Programs in Petroleum and Petrochemicals and Advanced Materials”). The support from the Kasetsart University Research and Development Institute (KURDI) and the Graduate School Kasetsart University are also acknowledged. The authors are grateful to Donald G. Truhlar and Yan Zhao for their support concerning the M06-2X code. MP acknowledges support from the Austrian Ministry of Science *via* an infrastructure grant to the LFU scientific computing platform and from the RFBR-FWF projects 09-03-91001-a and I200-N19.

## References

1 A. Corma Canos, S. Iborra and A. Velty, *Chem. Rev. (Washington, DC, U. S.)*, 2007, **107**, 2411–2502.
2 M. Pagliaro, R. Ciriminna, H. Kimura, M. Rossi and C. Della Pina, *Angew. Chem., Int. Ed.*, 2007, **46**, 4434–4440.
3 B. Katryniok, S. Paul, M. Capron and F. Dumeignil, *ChemSusChem*, 2009, **2**, 719–730.
4 S. Ramayya, A. Brittain, C. DeAlmeida, W. Mok and M. J. Antal Jr, *Fuel*, 1987, **66**, 1364–1371.
5 W. Bühler, E. Dinjus, H. J. Ederer, A. Kruse and C. Mas, *J. Supercrit. Fluids*, 2002, **22**, 37–53.
6 L. Ott, M. Bicker and H. Vogel, *Green Chem.*, 2006, **8**, 214–220.
7 V. Lehr, M. Sarlea, L. Ott and H. Vogel, *Catal. Today*, 2007, **121**, 121–129.
8 A. Alhanash, E. F. Kozhevnikova and I. V. Kozhevnikov, *Appl. Catal., A*, 2010, **378**, 11–18.

9 W. Suprun, M. Lutecki, T. Haber and H. Papp, *J. Mol. Catal. A: Chem.*, 2009, **309**, 71–78.
10 S. H. Chai, H. P. Wang, Y. Liang and B. Q. Xu, *J. Catal.*, 2007, **250**, 342–349.
11 F. Wang, J. L. Dubois and W. Ueda, *J. Catal.*, 2009, **268**, 260–267.
12 F. Wang, J. L. Dubois and W. Ueda, *Appl. Catal., A*, 2010, **376**, 25–32.
13 C. J. Zhou, C. J. Huang, W. G. Zhang, H. S. Zhai, H. L. Wu and Z. S. Chao, *Stud. Surf. Sci. Catal.*, 2007, **165**, 527–530.
14 A. Corma, G. W. Huber, L. Sauvanaud and P. O'Connor, *J. Catal.*, 2008, **257**, 163–171.
15 C. J. Jia, Y. Liu, W. Schmidt, A. H. Lu and F. Schüth, *J. Catal.*, 2010, **269**, 71–79.
16 Y. T. Kim, K. D. Jung and E. D. Park, *Microporous Mesoporous Mater.*, 2010, **131**, 28–36.
17 R. A. Van Santen and G. J. Kramer, *Chem. Rev. (Washington, DC, U. S.)*, 1995, **95**, 637–660.
18 E. Yoda and A. Ootawa, *Appl. Catal., A*, 2009, **360**, 66–70.
19 M. R. Nimlos, S. J. Blanksby, X. Qian, M. E. Himmel and D. K. Johnson, *J. Phys. Chem. A*, 2006, **110**, 6145–6156.
20 Y. Zhao and D. G. Truhlar, *Acc. Chem. Res.*, 2008, **41**, 157–167.
21 Y. Zhao and D. G. Truhlar, *J. Phys. Chem. C*, 2008, **112**, 6860–6868.
22 T. Maihom, B. Boekfa, J. Sirijaraensre, T. Nanok, M. Probst and J. Limtrakul, *J. Phys. Chem. C*, 2009, **113**, 6654–6662.
23 C. Kumsapaya, K. Bobuatong, P. Khongpracha, Y. Tantirungrotechai and J. Limtrakul, *J. Phys. Chem. C*, 2009, **113**, 16128–16137.
24 T. Maihom, P. Pantu, C. Tachakritikul, M. Probst and J. Limtrakul, *J. Phys. Chem.C*, 2010, **114**, 7850–7856.
25 B. Boekfa, P. Pantu, M. Probst and J. Limtrakul, *J. Phys. Chem. C*, 2010, **114**, 15061–15067.
26 S. Wannakao, B. Boekfa, P. Khongpracha, M. Probst and J. Limtrakul, *ChemPhysChem*, 2010, **11**, 3432–3438.
27 E. G. Hohenstein, S. T. Chill and C. D. Sherrill, *J. Chem. Theory Comput.*, 2008, **4**, 1996–2000.
28 S. Rayne and K. Forest, *THEOCHEM*, 2010, **948**, 102–107.
29 C. Peng, P. Y. Ayala, H. B. Schlegel and M. J. Frisch, *J. Comput. Chem.*, 1996, **17**, 49–56.
30 E. V. Stefanovich and T. N. Truong, *J. Phys. Chem. B*, 1998, **102**, 3018–3022.
31 B. Boekfa, S. Choomwattana, P. Khongpracha and J. Limtrakul, *Langmuir*, 2009, **25**, 12990–12999.
32 M. J. Frisch, G. W. Trucks, H. B. Schlegel, G. E. Scuseria, M. A. Robb, J. R. Cheeseman, J. Montgomery, T. J. A. Vreven, K. N. Kudin, J. C. Burant, J. M. Millam, S. S. Iyengar, J. Tomasi, V. Barone, B. Mennucci, M. Cossi, G. Scalmani, N. Rega, G. A. Petersson, H. Nakatsuji, M. Hada, M. Ehara, K. Toyota, R. Fukuda, J. Hasegawa, M. Ishida, T. Nakajima, Y. Honda, O. Kitao, H. Nakai, M. Klene, X. Li, J. E. Knox, H. P. Hratchian, J. B. Cross, V. Bakken, C. Adamo, J. Jaramillo, R. Gomperts, R. E. Stratmann, O. Yazyev, A. J. Austin, R. Cammi, C. Pomelli, J. W. Ochterski, P. Y. Ayala, K. Morokuma, G. A. Voth, P. Salvador, J. J. Dannenberg, V. G. Zakrzewski, S. Dapprich, A. D. Daniels, M. C. Strain, O. Farkas, D. K. Malick, A. D. Rabuck, K. Raghavachari, J. B. Foresman, J. V. Ortiz, Q. Cui, A. G. Baboul, S. Clifford, J. Cioslowski, B. B. Stefanov, G. Liu, A. Liashenko, P. Piskorz, I. Komaromi, R. L. Martin, D. J. Fox, T. Keith, M. A. Al-Laham, C. Y. Peng, A. Nanayakkara, M. Challacombe, P. M. W. Gill, B. Johnson, W. Chen, M. W. Wong, C. Gonzalez and J. A. Pople, *Gaussian 03, revision B.05*, Gaussian, Inc., Wallingford CT, 2004.
33 R. Chelli, F. L. Gervasio, C. Gellini, P. Procacci, G. Cardini and V. Schettino, *J. Phys. Chem. A*, 2000, **104**, 11220–11222.
34 R. Chelli, F. L. Gervasio, C. Gellini, P. Procacci, G. Cardini and V. Schettino, *J. Phys. Chem. A*, 2000, **104**, 5351–5357.
35 M. Hunger and T. Horvath, *J. Am. Chem. Soc.*, 1996, **118**, 12302–12308.
36 C. C. Lee, R. J. Gorte and W. E. Farneth, *J. Phys. Chem. B*, 1997, **101**, 3811–3817.
37 G. S. Hammond, *J. Am. Chem. Soc.*, 1955, **77**, 334–338.
38 A. Ison and R. J. Gorte, *J. Catal.*, 1984, **89**, 150–158.
39 S. A. Zygmunt, L. A. Curtiss, L. E. Iton and M. K. Erhardt, *J. Phys. Chem.*, 1996, **100**, 6663–6671.
40 Y. Izumi, *Catal. Today*, 1997, **33**, 371–409.
41 W. Wang and M. Hunger, *Acc. Chem. Res.*, 2008, **41**, 895–904.
42 D. G. Truhlar, B. C. Garrett and S. J. Klippenstein, *J. Phys. Chem.*, 1996, **100**, 12771–12800.




 

# Characterization of Acidity in [B], [Al], and [Ga] Isomorphously Substituted ZSM-5: Embedded DFT/UFF Approach

**SIRIPORN JUNGSUTTIWONG,[1] JARUN LOMRATSIRI,[1] JUMRAS LIMTRAKUL[2]**

[1]*Department of Chemistry, Ubon Ratchathani University, Ubon Ratchathani 34190, Thailand*

[2]*Department of Chemistry and NANOTEC Center of Excellence, Kasetsart University, Bangkok 10900, Thailand*

*Received 8 November 2009; accepted 23 November 2009*
*Published online 2 March 2010 in Wiley Online Library (wileyonlinelibrary.com).*
*DOI 10.1002/qua.22531*

**ABSTRACT:** The structure and electronic properties of the Brønsted acid site in B, Al or Ga isomorphously substituted ZSM-5 zeolites were studied by using quantum cluster and embedded ONIOM approaches. In the former approach, zeolites are modeled by 5T and 12T quantum clusters, where T represents a Si or Al atom. In the latter model, called "Embedded ONIOM", the long-range interactions of the zeolite lattice beyond the 12T quantum cluster is included via optimized point charges added to the ONIOM(B3LYP/6-31G(d,p):UFF). Inclusion of the extended zeolitic framework covering the nanocavity has an effect on the structure and adsorption properties. We found that the OH distances and v OH of the acidic proton in zeolite obtained from both models can predict the trend of acid strength as: B-ZSM-5 < Ga-ZSM-5 < Al-ZSM-5, which is in very good agreement with the experimental sequence. Furthermore, the PA data calculated from E-ONIOM is also consistent with the experimental trend: B-ZSM-5 < Ga-ZSM-5 < Al-ZSM-5. It has, therefore, been demonstrated that our embedded ONIOM model provides accurate performance and can be one of the useful and affordable methods for future mechanistic studies involving petrochemical reactions. ©2010 Wiley Periodicals, Inc. Int J Quantum Chem 111: 2275–2282, 2011

**Key words:** embedded ONIOM; DFT; isomorphous substituted ZSM-5

*Correspondence to:* S. Jungsuttiwong; e-mail: jsiriporn_2000@yahoo.com

Contract grant sponsors: The Thailand Research Fund (TRF-CHE Research Grant for New Scholar), Ubon Ratchathani University and NANOTEC Center of Excellence, Kasetsart University.

## Introduction

Since the introduction of synthetic zeolites as catalysts in fluid catalytic cracking of heavy petroleum distillates in 1962, catalysis has become the single most financially-important application of zeolites in terms of financial impact. Driven by the potential economic impact, progress in zeolite catalysis has focused largely on the synthesis, postsynthesis modification, physiochemical characterization, and testing. Much less has been achieved in improving the fundamental understanding of the structure and functions of zeolites and their catalytic roles. This is indicated by the fact that there are a very large number of zeolite topologies are known today, yet only a very limited number of such zeolites are actually used in applications [1–7]. Fundamental molecular-level understanding of structure–function relationships of the catalytic activity of zeolites and mechanisms of reactions at the active sites have a significant impacts on catalytic and process design and thus drastically improve the industrial competitive edge. The presence of Al replacing Si in zeolite structure generates a bridging hydroxyl group so called ["Brønsted acid site" (BAS)]. Many of the catalytic properties of zeolites can be directly related to this Brønsted acidity. In fact, heteroatoms such as B, Ga, Fe, and Zn can be introduced into the framework of zeolite [8–12] by the replacement of Si atoms. Many of these studies were focused on predicting the acid strength of isomorphously substituted ZSM-5. The ability to vary the acidity of the catalyst is of importance in determining the extent and selectivity of the catalytic process. In previous experiments in which results were mostly obtained by IR spectroscopy and TPD of $NH_3$, Chu and Chang [9] predicted that the Brønsted acidity of substituted ZSM-5 increases in the order B-ZSM-5 $\ll$ Fe-ZSM-5 $<$ Ga-ZSM-5 $<$ Al-ZSM-5, indicating that the catalytic properties can be tuned for a particular reaction. There have been several theoretical studies on zeolite structure and reactivity [3, 8, 13–16] using the cluster method.

The cluster methodology recognizes the most important region of the chemistry of the system as that surrounding the active site and the adsorbate, and treats it explicitly within full quantum mechanical formalism as an isolated system and ignoring the effects of the remaining crystal framework. Therefore the cluster methodology cannot provide information on the effects of the zeolite framework. Periodic electronic structure methods, on the other hand, provide an accurate framework to model interactions in extended systems such as crystals or surfaces [17, 18]. Zeolites often have large unit cells; for instance, the unit cell for ZSM-5 has 288 atoms (96 silicon atoms and 192 oxygen atoms). Because of the large number of reactions involved in this mechanism, the use of accurate periodic electronic structure methods is limited due to the demand of enormous computational resources and time. The only alternative is to use the embedded cluster approach. This approach recognizes the most important region of the chemistry of the system as that surrounding the active site and the adsorbate and thus treats it explicitly within full quantum mechanical formalism and adding the effects of the crystal framework in the Hamiltonian of the quantum region in an approximated manner. Some previous works employed a charge representation of the external electrostatic potential [19–23]. The electrostatic component of the Madelung potential, which makes the largest contribution, is represented by a set of surface charges. This is done by the SCREEP method [24–27]. However, in several systems, it was found to be technically difficult to obtain an accurate Madelung potential for the cluster embedded inside by means of surface charges [28]. To obtain a more accurate method, as in the study of the structure of BAS, the E-ONIOM method has been used to improve the energetic information.

In this article, the focus was on using the ONIOM embedded [29] approach in fine tuning the strength of the acid sites of the isomorphously substituted zeolites. This technique is a simple method that uses only the atomic positions of the lattice and is, therefore, easy to use while requiring a similarly small computational effort compared with periodic calculations. The structure and electronic properties of the BAS in [B], [Al], and [Ga] isomorphously substituted ZSM-5 zeolites were studied by using the ONIOM embedded approach with the B3LYP/6-31G (d,p) level of theory.

## Computational Details

There are three different models that have been used to study the isomorphously substituted zeolites. The first model is the small 5T cluster model

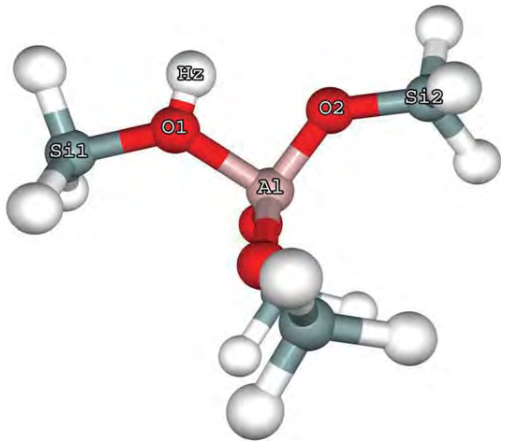


**FIGURE 1.** The 5T cluster model of H-ZSM-5. [Color figure can be viewed in the online issue, which is available at wileyonlinelibrary.com.]

(see Fig. 1), which are parts of the 10-membered ring of ZSM-5 zeolites, consisting of five tetrahedrally coordinated atoms (Si, Al). They were taken from the crystal structure of the ZSM-5 lattice [30]. These rings are at the intersections of the channels and are accessible to the adsorbates. Hydrogen atoms were used to cap the dangling bonds. These capped hydrogen atoms are located along the direction of corresponding Si—O bonds. The resulting 5T clusters, Si4AlO4H13, have a total of 22 atoms. The second models are a larger 12T clusters, Si11AlO12H25, consisting of a total of 49 atoms (see Fig. 2). They were selected to study the effects of unphysical interactions between small adsorbates and capped hydrogen atoms. These effects were remarkably observed in 5T cluster models. The T12 site was selected to represent the active site of ZSM-5 because it was found to be among the most stable sites for Al substitution [29, 31], and this site provides sufficient space and can be accessed easily by small adsorbates. Most previous theoretical works have also chosen the T12 site as the Al substitution site for ZSM-5.

The third model is termed "embedded ONIOM"[29] and is used to include the long-range interactions of the zeolite lattice beyond 12T (see Fig. 3). As point charges close to the quantum region can easily cause problems, we place our point charges only in a region defined by a minimal distance to the center of the quantum region and a maximal distance that determines the number of point charges. This finite number of point charges is further divided into an inner and an

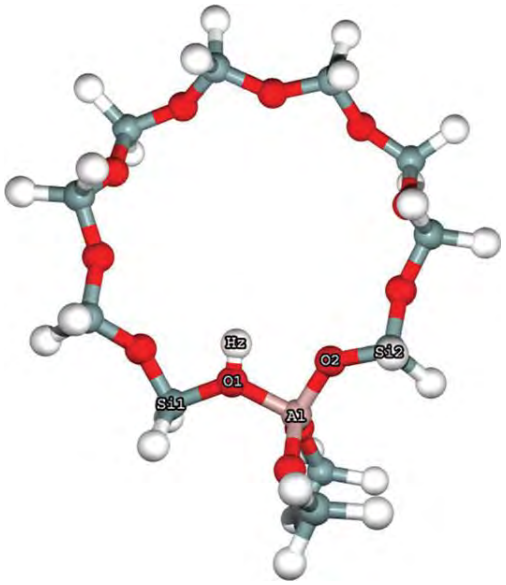


**FIGURE 2.** 12T-[Al]-ZSM-5 cluster model. [Color figure can be viewed in the online issue, which is available at wileyonlinelibrary.com.]

outer zone. Point charges in the inner zone (which might be a shell with a typical thickness of 5–10 Å and a few hundred point charges) are not optimized and have values one-half the formal charges of the zeolite atoms. Such "effective" charges $Q_{Si} = +2$ and $Q_O = -1$ are often used for a supermolecule such as zeolite and appear to be more realistic than the formal charges. The point charges in the outer region, which is a shell region immediately adjacent to the zone of the fixed charges, are

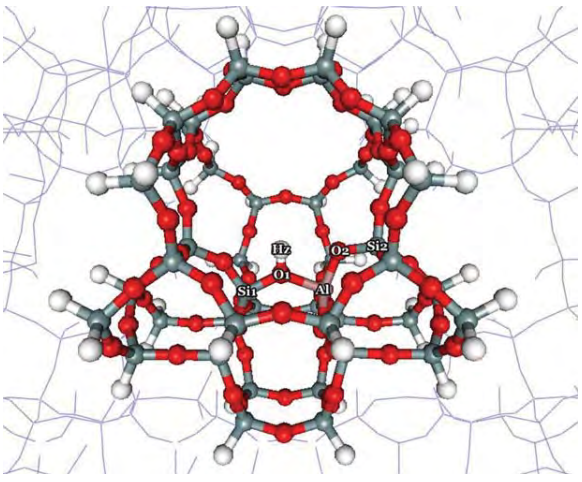


**FIGURE 3.** Embedded ONIOM 12T-[Al]-ZSM-5 model. [Color figure can be viewed in the online issue, which is available at wileyonlinelibrary.com.]

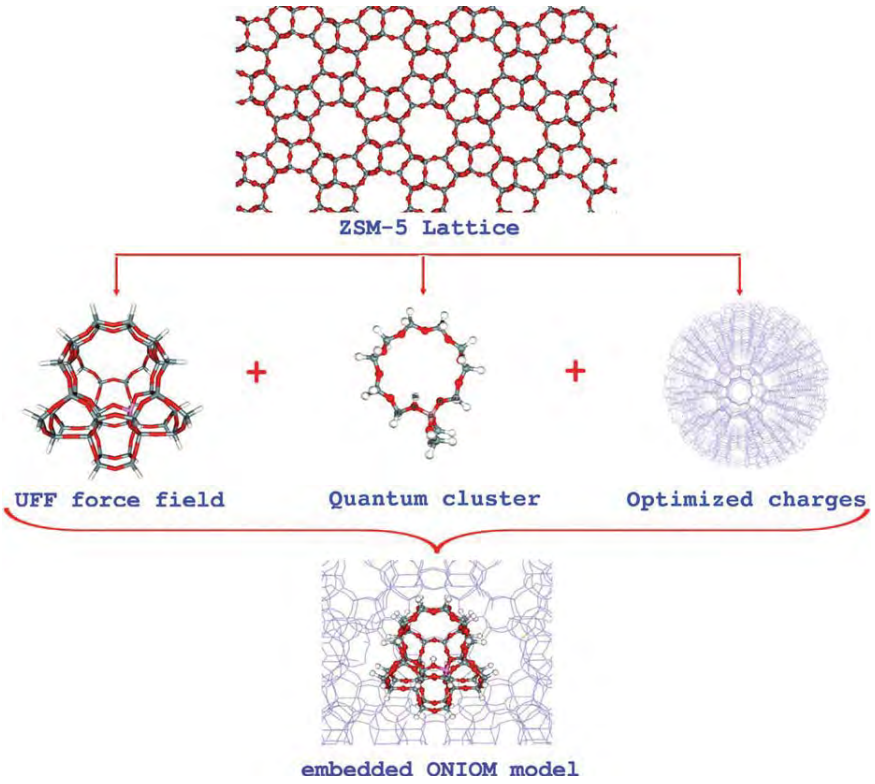


**FIGURE 4.** Embedded ONIOM Scheme. [Color figure can be viewed in the online issue, which is available at wileyonlinelibrary.com.]

optimized (typically there are a few thousand of them). We can define them by ΔQ, the vector of deviations from the values

$$Q'_{\text{outer}} = Q_{\text{outer}} + \Delta Q'' \tag{1}$$

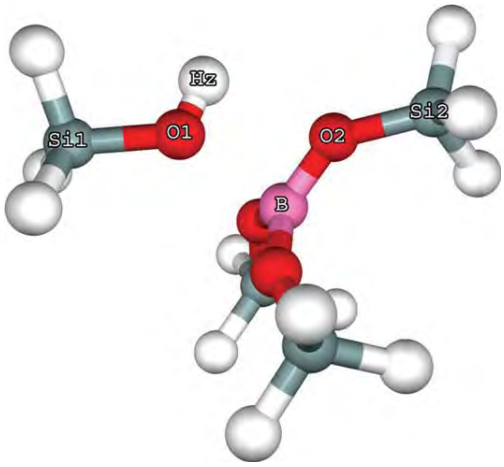


**FIGURE 5.** 5T-[B]-ZSM-5 cluster model. [Color figure can be viewed in the online issue, which is available at wileyonlinelibrary.com.]

where ΔQ is derived in the following way. The electrostatic potential from the infinite crystal is calculated at the grid points using the Ewald method. The electrostatic potential from the zeolite cluster and from the point charges in both zones are then subtracted from it as follows:

$$V_{\text{outside}} = V_{\text{ewald}} - V_{\text{cluster}} - V_{\text{inner/outer}} \tag{2}$$

We find the ΔQ that reproduces $V_{\text{outside}}$ by solving the matrix of simultaneous linear equations:

$$A \cdot \Delta Q = V_{\text{outside}} \tag{3}$$

**TABLE I**

**The distances (pm) of T—O1 in isolated H-ZSM-5 with B3LYP/6-31G (d, p) level of theory.**

| Level of theory | Al—O1 | B—O1 | Ga—O1 |
|---|---|---|---|
| 5T Cluster | 185.60 | 207.16 | 193.22 |
| 12T Cluster | 183.98 | 204.57 | 191.61 |
| 12T E-ONIOM | 179.40 | 176.88 | 187.46 |

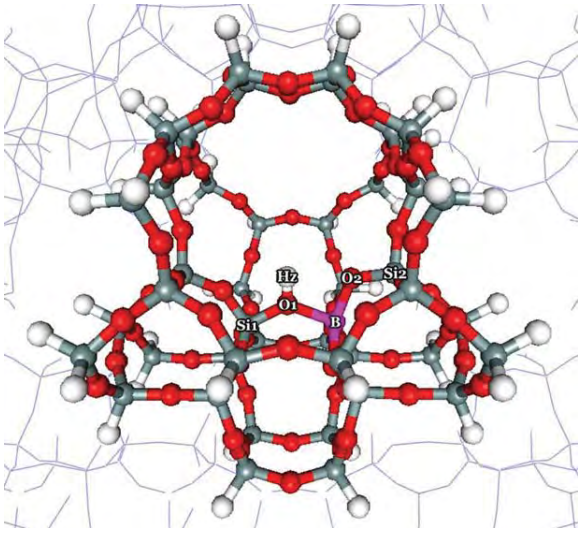


**FIGURE 6.** Embedded ONIOM 12T-[B]-ZSM-5 model. [Color figure can be viewed in the online issue, which is available at wileyonlinelibrary.com.]

$$A_{if} = 1/|R_i - R_j| \cdot R_i$$

where $V_{\text{outside}}$ is a column matrix with $m$ rows and $m$ is the number of grid points. $A$ is the distance matrix having $m$ rows and $n$ (the number of charges in the outer zone) columns. Its elements are defined as $R_i$ being the position of grid point $i$, and $R_j$ is the position of charge $j$. The Embedded ONIOM scheme is shown in Figure 4. We now have a complete set of charges consisting of the point charges in the inner zone and the optimized point charges in the outer zone and their respective positions. This allows us to add the crystal potential to the quantum region. The system of equations described in Eq. (3) also contains the four equations needed to guarantee the overall neutrality of charges and vanishing dipole moments along $x$, $y$, and $z$ [31]. In all three models, the geometry optimizations were done at the B3LYP/6-31G (d, p) level. All calculations were performed using the GAUSSIAN 03 program [32].

**TABLE III**

**PA and $\nu_{OH}$ calculated with B3LYP/6-31G (d, p) level of theory.**

| Substituted ZSM-5 | PA (kcal/mol) | |
|---|---|---|
| | 12T Cluster | E-ONIOM 12T |
| B-ZSM-5 | 320.12 | 363.69 |
| Ga-ZSM-5 | 313.36 | 362.31 |
| Al-ZSM-5 | 308.98 | 357.68 |
| Acidity sequence | B-ZSM-5 < Ga-ZSM-5 < Al-ZSM-5 | |

## Results and Discussion

### THE EFFECTS OF THE ZEOLITE LATTICE FRAMEWORK

To take into account the effects of the electron correlation of a large basis set and of the BSSE correction in the determinations, the effects of the lattice framework were included by the use of the embedded ONIOM (E-ONIOM) method. It is outlined in Figure 1. It was found that the 5T cluster with the fully optimized model at B3LYP/6-31G (d, p) level of theory leads to structures that did not resemble experimental zeolite geometry, see Figure 5. The T—O1 distances are listed in Table I. However, the inclusion of the Madelung potential, which was determined by improving optimized point charges to reproduce the infinite zeolitic lattice crystal integrated into the ONIOM (E-ONIOM method), the optimized model with electron correlation, and the large basis set, B3LYP/6-31G (d, p), resulted in more accuracy (see Figure 6). Furthermore, OH distances and the acidic proton in zeolite obtained from embedded ONIOM models were able to predict the trend of acid strength as: B-ZSM-5 < Ga-ZSM-5 <

**TABLE II**

**The distanced of O—H (pm) in isolated H-ZSM-5 with B3LYP/6-31G (d, p) level of theory.**

| Level of theory | Al-ZSM-5 | B-ZSM-5 | Ga-ZSM-5 | Acidity |
|---|---|---|---|---|
| 5T Cluster | 96.80 | 96.45 | 96.83 | B < Al < Ga |
| 12T Cluster | 96.98 | 96.66 | 97.01 | B < Al < Ga |
| 12T E-ONIOM | 97.07 | 96.93 | 97.06 | B < Ga < Al |
| Experimental sequence of acid strength | | B-ZSM-5 < Ga-ZSM-5 < Al-ZSM-5 | | |

**TABLE IV**

**The distances (pm) of O—$H_z$ in isolated H-ZSM-5 with B3LYP/6-31G (d, p) level of theory.**

| Level of theory | Al | B | Ga | Acidity trend |
|---|---|---|---|---|
| 5T Cluster | 96.80 | 96.45 | 96.83 | B < Al < Ga |
| 12T Cluster | 96.98 | 96.66 | 97.01 | B < Al < Ga |
| 12T E-ONIOM | 97.08 | 96.93 | 97.06 | B < Ga < Al |
| $\nu_{OH}$ ($cm^{-1}$) calculated IR frequency | 3604 | 3616 | 3608 | B < Ga < Al |

Al-ZSM-5, showing strong agreement with the experimental sequence (see Table II).

## PROTON AFFINITY OF THE SUBSTITUTED ZSM-5

Proton affinity (PA) can serve as a measure of the acid strength of ZSM-5. While direct experiments related to PA are not feasible, the data can be easily obtained from quantum calculation in which PA is considered as the energy required to remove the acidic proton from the zeolite structure. This is calculated by equation (4):

$$PA = E_{ZO} - E_{ZOH} \quad (4)$$

In this equation, $E_{ZO}$ and $E_{ZOH}$ are the energies of the deprotonated and the neutral clusters, respectively. It is obvious that the larger the PA, the weaker the acidity of the bridged hydroxyl group. The predicted PA data listed in Table II are calculated from two models, the 12T cluster and the 12T E-ONIOM giving the same trends of acid strength. These results are consistent with the experimental trend: B-ZSM-5 < Ga-ZSM-5 < Al-ZSM-5. It is obvious that the larger the PA, the weaker the acidity of the bridged hydroxyl group. The PA data calculated from the three models 12T cluster, 12T ONIOM, and 12T E-ONIOM give the same trends of acid strength, which is consistent with the experimental trend: B-ZSM-5 < Ga-ZSM-5 < Al-ZSM-5 (see Table III).

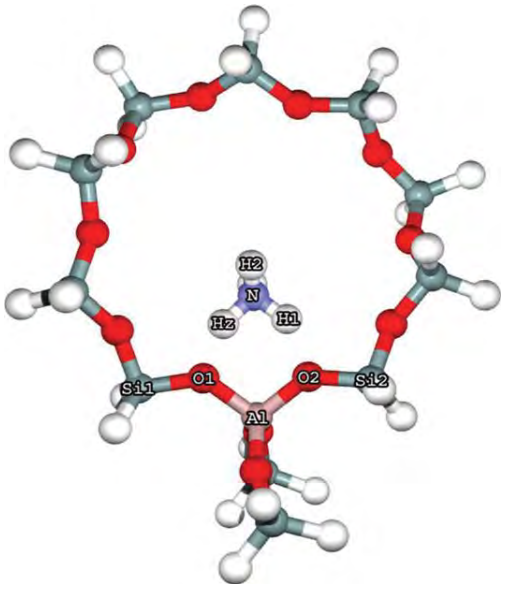


**FIGURE 7.** NH3/12T-[Al]-ZSM-5 complex. [Color figure can be viewed in the online issue, which is available at wileyonlinelibrary.com.]

## OH STRETCHING FREQUENCY

It is generally accepted that the stretching frequency of the OH bond ($\nu_{OH}$) can be taken as an indicator of Brønsted acidity [16]; and that the lower wave number of $\nu_{OH}$ is related to weaker O—H bond strength and hence corresponds to stronger acid strength. The calculations were performed directly after the geometry optimization by the B3LYP method with three different 12T models: cluster, ONIOM, and E-ONIOM. Positions of $\nu_{OH}$ are given in Table IV. The data calculated with 6–31G (d,p) require scaling by 0.950 [33]. It was shown that the

**TABLE V**

**The charged form NBO population analysis using 12T E-ONOM model with B3LYP/6-31G (d,p) level of theory.**

| Substituted ZSM-5 | NBO population analysis | | | |
|---|---|---|---|---|
| | *q*(M) | *q* (Hz) | *q*(O1) | Electronegativity |
| [B]-ZSM-5 | 1.3610 | 0.5722 | −1.0415 | 2.01 |
| [Ga]-ZSM-5 | 1.8265 | 0.5851 | −1.1238 | 1.82 |
| [Al]-ZSM-5 | 2.0013 | 0.5905 | −1.1390 | 1.47 |
| Acidity sequence | B-ZSM-5 < Ga-ZSM-5 < Al-ZSM-5 | | | |

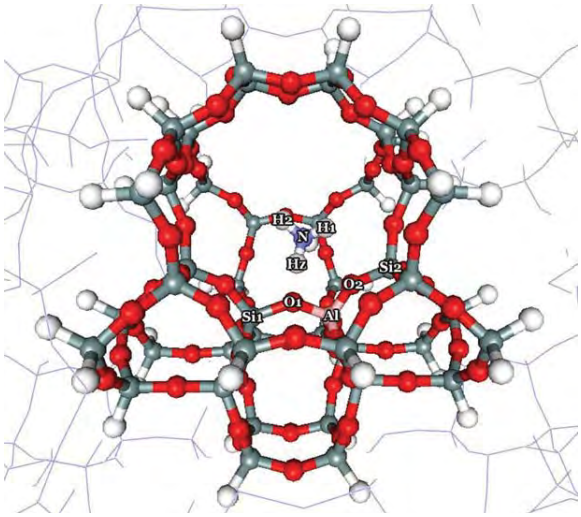


**FIGURE 8.** NH3/Embedded ONIOM-[Al]-ZSM-5 complex. [Color figure can be viewed in the online issue, which is available at wileyonlinelibrary.com.]

three different methods give different acidity sequences. The $\nu_{OH}$ calculated from the 12T E-ONIOM provide trends corresponding to the experimental result; and the results of this study also supported the $\nu_{OH}$ in the region 3600–3700 $cm^{-1}$ suggested by Chu and Chang [9] as the fingerprint for Brønsted OH species. It was shown that the DFT method with the 12T E-ONIOM model was sufficient for this article.

## THE NATURAL BOND ORBITAL POPULATION ANALYSIS OF ATOMIC CHARGE

The atomic charges from natural bond orbital (NBO) population analysis with M (M = B, Al, Ga), O1, and Hz (acidic proton) are presented in Table V. It has been shown that $q$(M), charges on heteroatom M, increase with the decrease of its electronegativity (1.47, 1.82, and 2.01 for Al, Ga, and B, respectively). The charge on the oxygen bridge atom (O1), $q$(O1), increase with the increases with the escalation of $q$M, leading to a boost in the charges on the acidic proton (qHz) corresponding with an increase of the acidity. It can be stated from the $q$(Hz) data that the acid strength of the substituted ZSM-5 increases in order: B-ZSM-5 < Ga-ZSM-5 < Al-ZSM-5, which is consistent with the PA.

**TABLE VI**

**The calculated $\nu_{OH}$ with B3LYP/6-31G (d,p) level of theory.**

| | | Tetrahedral atom | | |
|---|---|---|---|---|
| $\nu_{OH}$ ($cm^{-1}$) | Acidity trend | Al | Ga | B |
| 12T E-ONIOM | B < Ga < Al | 3604 | 3608 | 3616 |
| 12T Cluster | B < Al < Ga | 3614 | 3612 | 3658 |
| $\nu_{OH}$ [33] 8T cluster | B < Ga < Al | 3816 | 3825 | 3830 |
| $\nu_{OH}$ from IR [9] | B < Ga < Al | 3610 | 3620 | 3725 |

## ADSORPTION OF $NH_3$ ON ZSM-5

The optimized adsorption structures of $NH_3$ on ZSM-5 are shown in Figures 7 representing the cluster model and Figure 8 showing the E-ONIOM model. Table VI illustrates the energy of the adsorption of $NH_3$ on the acid site of the substituted ZSM-5 zeolites calculated by Eq. (5)

$$\Delta E_{ads} = E(\text{complex}) - E(\text{ZOH}) - E(NH_3) \quad (5)$$

The relative acid strength predicted by the adsorption energy of $NH_3$ is shown to be

**TABLE VII**

**Comparisons of calculated adsorption energies of $NH_3$/zeolite including BSSE at 6-311++G (d, p) basis set with previous theoretical and experimental results.**

| | Level of theory | Cluster | Model | $\Delta E$ |
|---|---|---|---|---|
| Al | B3LYP/6-31G (d,p) | 12T | E-ONIOM | 33.98 |
| Al [16] | B3LYP/3-21G | 8T | Cluster | 50.7 |
| Al [33] | Experiment | | | 33.5–35.6 |
| Ga | B3LYP/6-31G (d,p) | 12T | E-ONIOM | 31.43 |
| Ga [16] | B3LYP/3-21G | 8T | Cluster | 50.0 |
| Ga [33] | Experiment | | | 34.52–36.90 |
| B | B3LYP/6-31G (d,p) | 12T | E-ONIOM | 24.86 |
| B [16] | B3LYP/3-21G | 8T | Cluster | 41.0 |

consistent with that derived from the PA and $\nu_{OH}$ of this article, B-ZSM-5 < Ga-ZSM-5 < Al-ZSM-5. Moreover, the adsorption energies calculated with B3LYP/6-31G (d,p) for the 12T E-ONIOM model more strongly correspond with the experimental results compared to those of previous work [16, 33] (see Table VII).

## Conclusions

It was shown that the acidity is the adsorption energy of $NH_3$ which showed that the acid strength of the substituted ZSM-5 increases in the sequence: B-ZSM-5 < Ga-ZSM-5 < Al-ZSM-5, in strong agreement with experimental results. The interaction of $NH_3$ with the BAS indicated that $NH_3$ becomes protonated in contact with the zeolite cluster and the configurations in which the protonated $NH_3$ interacts with two lattice oxygen atoms are favored energetically. In addition, the calculated adsorption energy of $NH_3$ on Al-ZSM-5 is comparable with the experimental data. This indicates that it is essential to take into account the effects of the Madelung potential due to atoms outside the quantum cluster by using the E-ONIOM method are essential to be taken into account. Furthermore, the results show a prospective trend to predict properties of metal-substituted zeolites, with a special emphasis on the Bronsted acid strength of zeolites.

## References


1. Pirngruber, G. D.; Seshan, K.; Lercher, J. A. J Catal 2000, 190, 338.
2. Cerqueira, H. S.; Mihindou-Koumba, P. C.; Magnoux, P.; Guisnet, M. Ind Eng Chem Res 2001, 40, 1032.
3. Li, H.-Y.; Pu, M.; Liu, K.-H.; Zhang, B.-F.; Chen, B.-H. Chem Phys Lett 2005, 404, 384.
4. Ivanov, P.; Papp, H. Chem Ing Tech 2000, 72, 1213.
5. Kuznetsov, P. N. J Catal 2003, 218, 12.
6. Davis, R. J. J Catal 2003, 216, 369.
7. Coudurier, G.; Vedrine, J. C. Pure Appl Chem 1986, 58, 1389.
8. Alverado Swasigood, A. E.; Barr, M. K.; Hay, P. J.; Redondo, A. J Phys Chem 1991, 95, 10031.
9. Chu Cynthia, T. W.; Change, C. D. J Phys Chem 1985, 89, 1569.
10. Dong, M.; Wang, J.; Sun, Y. Micropor Mesopor Mater 2001, 43, 237.
11. Fricke, R.; Kosslick, H.; Lischke, G.; Richter, M. Chem Rev 2000, 100, 2303.
12. Langenaeker, W.; Coussement, N.; De Proft, F.; Geerlings, P. J Phys Chem 1994, 98, 3010.
13. White, J. C.; Hess, A. C. J Phys Chem 1993, 97, 8703.
14. Brand, H. V.; Curtiss, L. A.; Iton, L. E. J Phys Chem 1992, 96, 7725.
15. O'Malley, P. J.; Dwyer, J. J Phys Chem 1988, 92, 3005.
16. Yuan, S. P.; Wang, J. G.; Li, Y. W.; Peng, S. Y. J Mol Catal A: Chem 2002, 178, 267.
17. Shah, R.; Gale, J. D.; Payne, M. C. Chem Commun (Camb.) 1997, 131.
18. Jeanvoine, Y.; Angyan, J. G.; Kresse, G.; Hafner, J. J Phys Chem B 1998, 102, 5573.
19. Allouche, A. J Phys Chem B 1996, 100, 17915.
20. Ferrari, A. M.; Pacchioni, G. J Phys Chem B 1996, 100, 9032.
21. Allouche, A. J Phys Chem B 1996, 100, 1820.
22. Saunders, V. R.; Freyria-Fava, C.; Dovesi, R.; Salasco, L.; Roetti, C. Mol Phys 1992, 77, 629.
23. Ferro, Y.; Allouche, A.; Cora, F.; Pisani, C.; Girardet, C. Surf Sci 1995, 325, 139.
24. Stefanovich, E. V.; Truong, T. N. J Phys Chem B 1998, 102, 3018.
25. Limtrakul, J.; Jungsuttiwong, S.; Khongpracha, P. J Mol Struct 2000, 525, 153.
26. Limtrakul, J.; Khongpracha, P.; Jungsuttiwong, S.; Truong, T. N. J Mol Catal A 2000, 153, 155.
27. Treesukol, P.; Limtrakul, J.; Truong, T. N. J Phys Chem B 2001, 105, 2421.
28. Greatbanks, S. P.; Sherwood, P.; Hillier, I. H. J Phys Chem B 1994, 98, 8134.
29. Injan, N.; Pannorad, N.; Probst, M.; Limtrakul, J. Int J Quantum Chem 2005, 105, 898.
30. Derouane, E. G.; Fripiat, J. G. Zeolites 1985, 5, 165.
31. Derenzo, S. E.; Klintenberg, M. K.; Weber, M. J. J Chem Phys 2074, 2000, 112.
32. Frisch, M. J.; Trucks, G. W.; Schlegel, H. B.; Scuseria, G. E.; Robb, M. A.; Cheeseman, J. R.; Zakrzewski, V. G.; Montgomery, J. A.; Stratmann, R. E., Jr.; Burant, J. C.; Dapprich, S.; Millam, J. M.; Daniels, A. D.; Kudin, K. N.; Strain, M. C.; Farkas, O.; Tomasi, J.; Barone, V.; Cossi, M.; Cammi, R.; Mennucci, B.; Pomelli, C.; Adamo, C.; Clifford, S.; Ochterski, J.; Petersson, G. A.; Ayala, P. Y.; Cui, Q.; Morokuma, K.; Salvador, P.; Dannenberg, J. J.; Malick, D. K.; Rabuck, A. D.; Raghavachari, K.; Foresman, J. B.; Cioslowski, J.; Ortiz, J. V.; Baboul, A. G.; Stefanov, B. B.; Liu, G.; Liashenko, A.; Piskorz, P.; Komaromi, I.; Gomperts, R.; Martin, R. L.; Fox, D. J.; Keith, T.; Al-Laham, M. A.; Peng, C. Y.; Nanayakkara, A.; Challacombe, M.; Gill, P. M. W.; Johnson, B.; Chen, W.; Wong, M. W.; Andres, J. L.; Gonzalez, C.; Head-Gordon, M.; Replogle, E. S.; Pople, J. A. Gaussian 03, revision B.05; Gaussian, Inc.: Pittsburgh, PA, 2001.
33. Parrillo, D. J.; Lee, C.; Gorte, R. J.; White, D.; Farneth, W. E. J Phys Chem 1995, 99, 8745.

CHEMPHYSCHEM

DOI: 10.1002/cphc.201100047

# Glycine Peptide Bond Formation Catalyzed by Faujasite**

Oranit Phuakkong,[a, b, c] Karan Bobuatong,[a, b, c] Piboon Pantu,[a, b, c] Bundet Boekfa,[b, c, d] Michael Probst,[e] and Jumras Limtrakul*[a, b, c]

The catalysis of peptide bond formation between two glycine molecules on H-FAU zeolite was computationally studied by the M08-HX density functional. Two reaction pathways, the concerted and the stepwise mechanism, starting from three differently adsorbed reactants, amino-bound, carboxyl-bound, and hydroxyl-bound, are studied. Adsorption energies, activation energies, and reaction energies, as well as the corresponding intrinsic rate constants were calculated. A comparison of the computed energetics of the various reaction paths for glycine indicates that the catalyzed reaction proceeds preferentially via the concerted reaction mechanism of the hydroxyl-bound configuration. This involves an eight-membered ring of the transition structure instead of the four-membered ring of the others. The step from the amino-bound configuration to glycylglycine is the rate-determining step of the concerted mechanism. It has an estimated activation energy of 51.2 kcal mol$^{-1}$. Although the catalytic reaction can also occur via the stepwise reaction mechanism, this path is not favored.

## 1. Introduction

Peptide bond formation is an essential step in the synthesis of proteins and peptides. Understanding this process allows the control of construction and organization of these polymers with useful applications in medical, biological, and food sciences.[1] Its reaction mechanism has attracted much attention over the last five decades. It is relevant to the synthesis of peptides from amino acids or their esters under prebiotic conditions[2] and numerous attempts from the experimental and computational side were performed to examine the basic steps of peptide bond formation.[3] Of even more practical importance is that many current works deal with designing peptides as parts of biocompatible units and take advantage of their self-assembly features. Peptides are also increasingly used as sensing devices.[1a–c,4]

For the acid/base-catalyzed aminolysis of alkyl esters, the mechanism of peptide bond formation has been studied experimentally in aqueous solution by Jencks et al.[3c–e] The basic step is the nucleophilic attack of the lone electron pair of the amino group onto the carbon atom of the carboxyl group followed by proton transfer from the amino group to one of the oxygen atoms of the carboxyl group. In the proposed concerted and/or stepwise reaction mechanisms, a possible formation of a relatively stable zwitterionic intermediate is considered. The relative stability of this adduct depends on the acid–base properties of the solvent, and its lifetime can be an important factor in the whole reaction mechanism.

Despite the intensive experimental works mentioned above and various studies using silica,[5] clays[5,6], and aluminas[5,7] as catalysts for the peptide formation, mechanistic discussions are rare and no detailed molecular picture is available for these processes. Nevertheless, some mechanisms have been suggested in the past to interpret the experimental evidence of the formation of small oligopeptides, albeit at the level of very simple schemes by Zamaraev et al.,[6a] for adsorption of glycine on zeolites and kaolinite and by Basiuk et al. for silica and alumina.[7a] Recently, zeolites have found potential applications in amino acid separation,[8] immobilized peptide synthesis,[9] and biomedical sensors.[10]

Theoretically, the mechanism of the uncatalyzed amide bond formation has been investigated by Oie et al. and Jensen et al.,[3g,h] who have shown that stepwise and concerted mechanisms may compete since both involve comparable activation energies. The latter authors also performed a study for the glycine + glycine reaction, and the main conclusion was that the model system glycine + glycine appears to be a good representative of a dipeptide system. Moreover, the mechanisms of amide bond formation in various catalytic systems have been

[a] O. Phuakkong, K. Bobuatong, Prof. Dr. P. Pantu, Prof. Dr. J. Limtrakul
Laboratory for Computational and Applied Chemistry, Department of Chemistry, Faculty of Science and Center of Nanotechnology
Kasetsart University Research and Development Institute
Kasetsart University, Bangkok 10900 (Thailand)
Fax: (+66) 2-562-5555 ext 2159
E-mail: Jumras.l@ku.ac.th

[b] O. Phuakkong, K. Bobuatong, Prof. Dr. P. Pantu, Dr. B. Boekfa, Prof. Dr. J. Limtrakul
Center for Advanced Studies in Nanotechnology and Its Applications in Chemical, Food and Agricultural Industries
Kasetsart University, Bangkok 10900 (Thailand)

[c] O. Phuakkong, K. Bobuatong, Prof. Dr. P. Pantu, Dr. B. Boekfa, Prof. Dr. J. Limtrakul
NANOTEC Center of Excellence, National Nanotechnology Center
Kasetsart University, Bangkok 10900 (Thailand)

[d] Dr. B. Boekfa
Chemistry Department, Faculty of Liberal Arts and Science
Kasetsart University Kamphaeng Saen Campus
Nakhon Pathom 73140 (Thailand)

[e] Prof. Dr. M. Probst
Institute of Ion Physics and Applied Physics
University of Innsbruck, 6020 Innsbruck (Austria)

[**] A Density Functional Theory Study

Supporting information for this article is available on the WWW under http://dx.doi.org/10.1002/cphc.201100047.

theoretically investigated. Rimalo et al. examined the role of Lewis and Brønsted catalysts on peptide formation using HF and $AlF_3$,[11] anorthite and sanidine[12] as the catalytic models, respectively. It has been found that the synergy of those catalysts dramatically lowers the activation barrier for the amide bond formation, a fact relevant in the prebiotic synthesis of peptides on the surface of oxide minerals that are rich in Lewis/Brønsted sites.

Brønsted acid sites are usually well characterized in the interior of zeolites. To our knowledge, their catalytic role in the peptide bond formation process has never been addressed together with a realistic representation of the zeolite. Therefore, we investigated the reaction mechanisms and kinetics of the zeolite-catalyzed peptide bond formation between two glycine molecules as the simplest model of such a reaction.

Quantum chemical calculations are reliable theoretical tools for studying chemical reactions which cannot be readily characterized by experimental techniques. Moreover, it is possible to compute valuable information about the nature of the transition states and the stable intermediate states as well as details of thermodynamics, kinetics of reaction, and spectroscopic properties such as the frequencies of vibration[13] of the system. Thus, direct insight into the reaction mechanism is possible, provided that the data are checked against available experimental results.

Zeolites usually possess hundreds of atoms per unit cell which makes the use of sophisticated methods, such as periodic ab initio calculations, computationally too expensive. The recent development of hybrid methods, such as the embedded cluster or combined quantum mechanics/molecular mechanics (QM/MM) methods,[13,14] has brought accurate results on large systems within reach.[14h,15] This was, for example, demonstrated in a study of the interaction of glycine with H-ZSM-5 zeolite.[15f] Complementary to this development, density functionals like the M06 set[16] can be applied to account for a more accurate treatment of the interactions in these systems, as has, for example, been done when studying the reactions of hydrocarbons inside zeolites.[14e,i,17] Herein we proceed along similar lines but apply a newer density functional and discuss its performance.

The aims of the present work are: 1) to investigate the peptide bond formation on zeolite and 2) to study the effect of the zeolite framework on the reaction. Two possible reaction mechanisms are investigated, a concerted and a stepwise one. The results of this study may be helpful for understanding the fundamentals of peptide formation of amino acid catalyzed by zeolite.

## 2. Results and Discussion

It was assumed that the reaction can either occur via a concerted reaction mechanism (Figure S1 in the Supporting Information) or by a stepwise reaction mechanism through the formation of the diolic intermediate (Figure S2 in the Supporting Information).

### 2.1. Concerted Reaction Mechanism

The peptide bond formation of two glycine molecules catalyzed by faujasite zeolite (Figure 1) via a concerted reaction mechanism is shown in Figure S1 in the Supporting Information. Depending on the site of initial adsorption, three possible energy profiles are presented for the concerted reaction in Figure 2a. The reaction is catalyzed by the Brønsted acidic proton acting as a proton donor to the oxygen atom of the amino group (amino-bound, Figure 3a), the carboxyl group (carboxyl-bound, Figure 4a), and the hydroxyl group (hydroxyl-bound, Figure 5a) of the glycine molecule, respectively. All of them are involved in the nucleophilic attack of the amino group on the

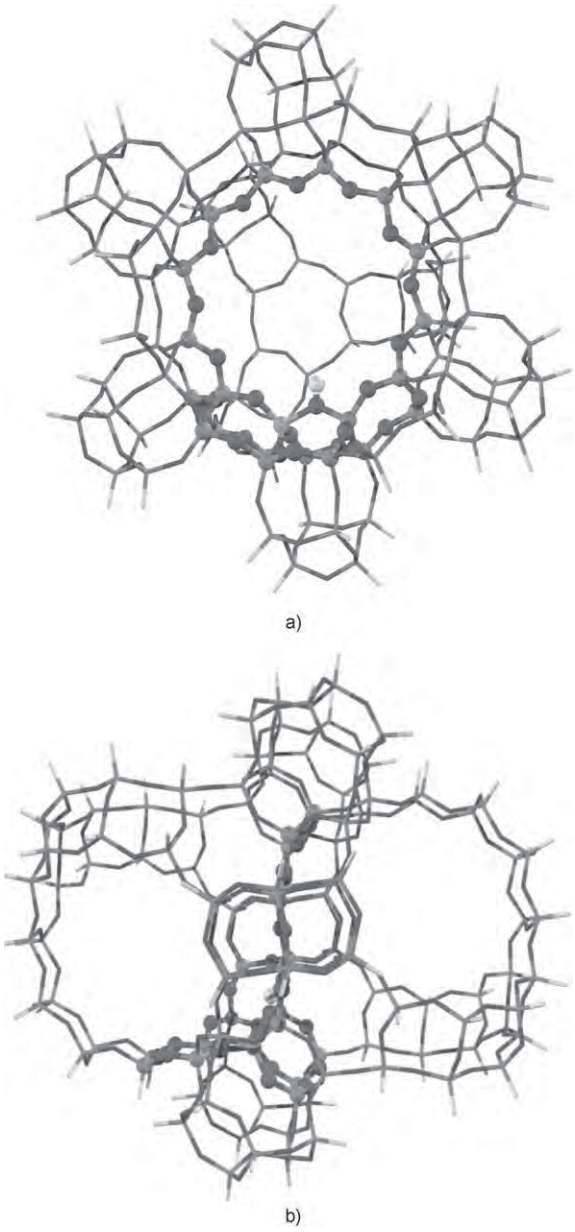


**Figure 1.** The 120T cluster models of H-FAU. Atoms belonging to the 21T quantum cluster are drawn as balls and sticks. a) Front view showing the 12-membered-ring window connecting the two supercages. b) Side view showing the two supercages connected to the 120T quantum cluster.

  

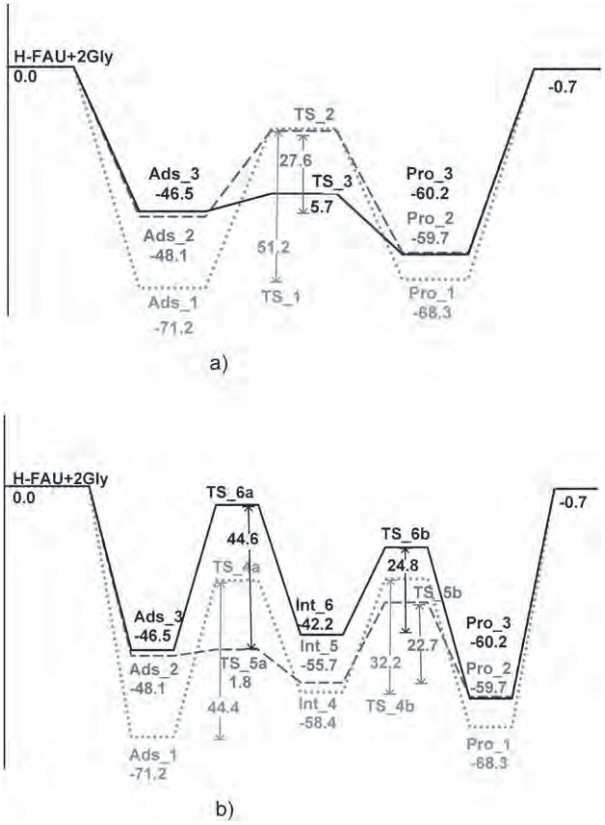


**Figure 2.** Energy profile (kcal mol$^{-1}$) of the peptide bond formation from different configurations of two glycine molecules interacting with H-FAU zeolite model 120T//21T calculated at the M08-HX/6-31G(d,p) level. Amino-bound configuration (•••••), carboxyl-bound configuration (– – –), and hydroxyl-bound configuration (——): a) concerted reaction mechanism; b) stepwise reaction mechanism.

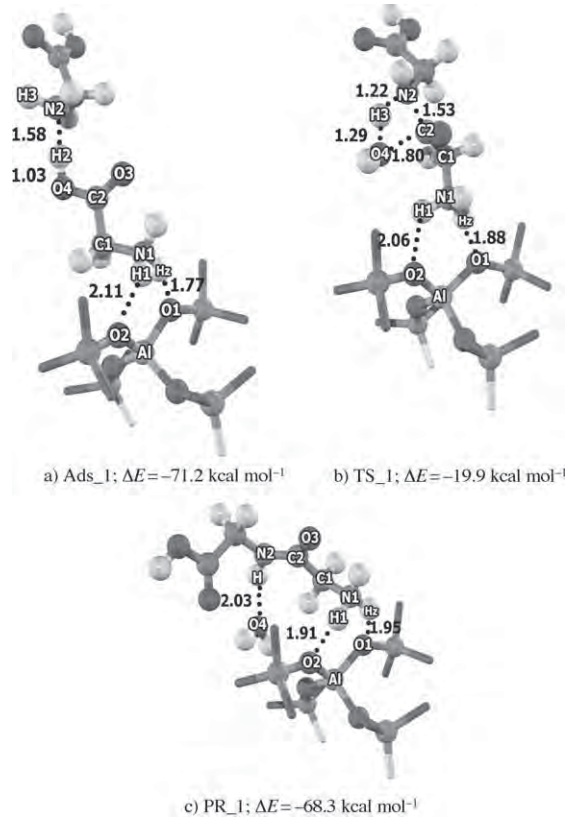


**Figure 3.** Optimized geometries of adsorption complexes, transition states, and products. a) Adsorption complex of the amino-bound configuration in the concerted reaction mechanism, Ads_1. b) Transition structure of the amino-bound configuration in the concerted reaction mechanism, TS_1. c) Adsorption complex of the products glycylglycine and water in the amino-bound configuration in the concerted reaction mechanism, Pro_1.

carboxyl carbon atom and the indirect transfer of a hydrogen atom from the nucleophilic amino group to a hydroxyl of another glycine molecule, which results in adsorbed glycylglycine and an adsorbed water molecule which is desorbed in the final step.

### *2.1.1. Interactions of Two Glycine Molecules in Different Configurations with H-FAU Zeolite*

The calculated adsorption energies of two glycine molecules in different configurations on H-FAU zeolites are shown in the energy profile (Figure 2a) and in Table S1 in the Supporting Information, together with selected geometrical parameters.

The reaction proceeds as follows: First, two glycine molecules adsorb on the Brønsted acidic proton of the active zeolite site. This can occur via the amino group (amino-bound, Ads_1, Figure 3a), the carboxyl group (carboxyl-bound, Ads_2, Figure 4a) or the hydroxyl group (hydroxyl-bound, Ads_3, Figure 5a). In the first two configurations the adsorption (amino-bound and carboxyl-bound) of glycine is accompanied by a barrierless proton transfer from the active site to its C=O and $-NH_2$ groups. This causes the second hydroxyl group of glycine and the $-NH_3^+$ group to interact through two strong hydrogen bonds; the computed adsorption energies are −71.2 and −48.1 kcal mol$^{-1}$, respectively. In the hydroxyl-bound configuration glycine is adsorbed at the active site by hydrogen bonding between –OH of glycine and the Brønsted acidic proton. Its adsorption energy is −46.5 kcal mol$^{-1}$. It is difficult to directly compare calculated adsorption energies of glycine in zeolites with experimental results, and, to the best of our knowledge, there are no experimental data available on the glycine adsorption energy. The result for the amino-bound configuration can be compared with experimental data for ammonia which is protonated in zeolite with adsorption energies in the range of 24.9–25.6 kcal mol$^{-1}$.[18] Glycine is a more basic substance than $NH_3$. Moreover, the other glycine molecule is involved in the adsorption of the first one via hydrogen bonding between $-NH_3$ and the hydrogen atom of the carboxylic group of the first glycine, enhancing the adsorption energy of this configuration. Therefore, the adsorption energy of the amino-bound configuration over H-FAU should exceed that for ammonia, which agrees well with the known adsorption trend of this zeolite. The result shows that these adsorption energies are determined by both chemical (heat of protonation) and physical (confinement) factors. The latter, which arise from van der Waals interactions, cannot be ignored.

The first configuration is amino-bound (Ads_1, Figure 3a). Selected geometrical parameters of this configuration are pre-

  

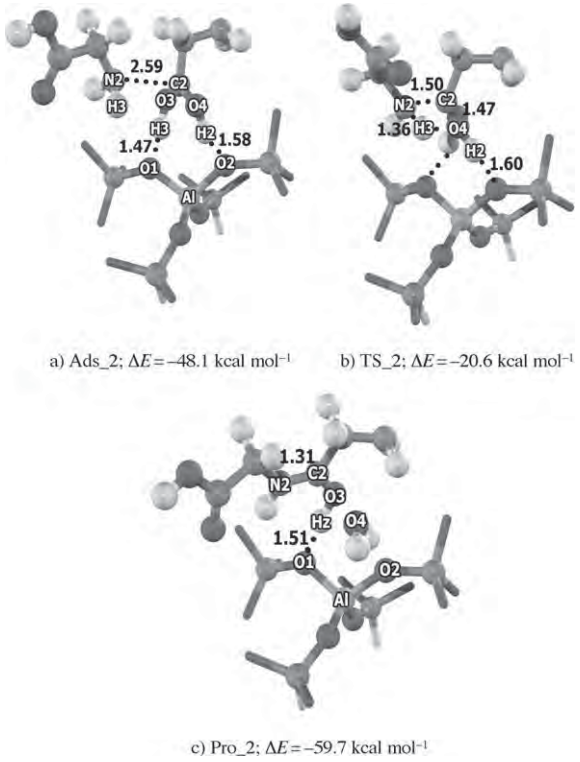


**Figure 4.** Optimized geometries of adsorption complexes, transition states, and products. a) Adsorption complex of the carboxyl-bound configuration in the concerted reaction mechanism, Ads_2. b) Transition structure of the carboxyl-bound configuration in the concerted reaction mechanism, TS_2. c) Adsorption complex of products glycylglycine and water of carboxyl-bound configuration in the concerted reaction mechanism, Pro_2.

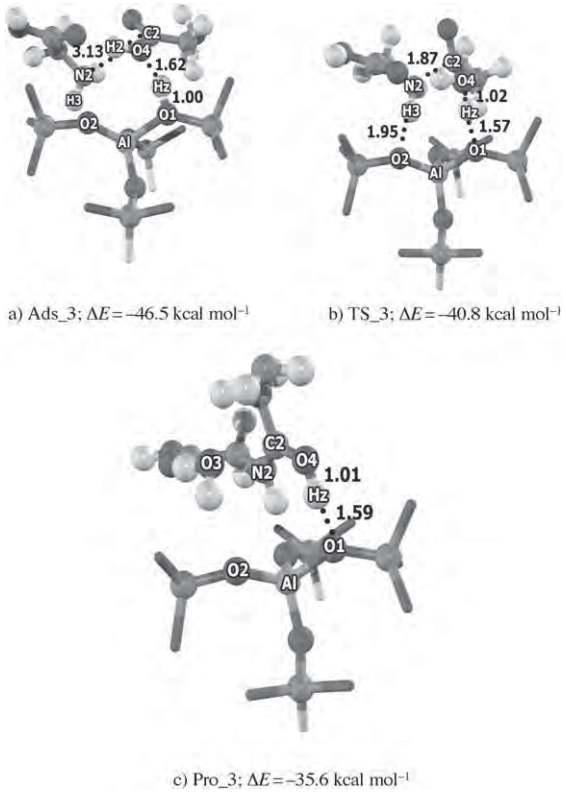


**Figure 5.** Optimized geometries of adsorption complexes, transition states, and products. a) Adsorption complex of the hydroxyl-bound configuration in the concerted reaction mechanism, Ads_3. b) Transition structure of the hydroxyl-bound configuration in the concerted reaction mechanism, TS_3. c) Adsorption complex of the products glycylglycine and water of the hydroxyl-bound configuration in the concerted reaction mechanism, Pro_3.

sented in Table S1 in the Supporting Information. The Brønsted acid of the zeolite O1–Hz bond is broken while the N1–Hz bond is formed. The O1···Hz distance in the amino configuration is about 1.77 Å. Both distances of N1–H1 and N1–Hz are virtually the same, indicating that there is a complete transfer of Brønsted acid. The second glycine is adsorbed by the hydrogen bond with a distance between H2···N2 of about 1.58 Å. The two hydrogen-bound adducts of glycine and zeolite (N1–Hz···O1 and N1–H1···O2) generate an "ion-pair-like structure" resulting in the highest adsorption energy of $-71.2$ kcal mol$^{-1}$.

For the carboxyl-bound configuration (Ads_2, Figure 4a), the adsorption of glycine involves a barrierless proton transfer from the active site to C=O. The O1–Hz bond distance of the Brønsted acidic proton is increased from 0.97 to 1.47 Å as compared to isolated H-FAU, indicating the weakening of the C=O bond. The C=O bond of glycine is elongated from 1.20 Å to 1.27 Å as compared to the isolated glycine molecule. The partial charge of the C atom changes from $+0.8$ in isolated glycine to $+0.9$ (Table 1). This shows that the catalyst facilitates the nucleophilic attack by the lone pair of the amine. Since the C2···N2 distance between the nitrogen atom of the $-NH_2$ group and this carbon atom (2.59 Å) is shorter than in the hydroxyl-bound configuration (3.13 Å) this co-adsorption complex is also stronger.

In the hydroxyl-bound configuration (Ads_3, Figure 5a) the hydrogen atom (H2) of the hydroxyl group of the first glycine points outward to interact with the oxygen atom (O5) of the carboxyl group of another glycine, with an O5···H2 distance of 1.58 Å and an O4–H2–O5 angle of 174.3°. The C2–O3 bond distance and the positive charge on the C atom at the reaction center are slightly increased with respect to the isolated glycine molecule. In summary, the carboxyl-bound configuration is more perturbed by the Brønsted acidic proton of H-FAU zeolite, explaining why the hydroxyl-bound configuration is the least stable one of the three configurations.

### 2.1.2. Peptide Bond Formation

The reaction pathways of the concerted mechanism for the three different configurations are shown in Figure S1 with selected geometries given in Table S1 of the Supporting Information. At the transition state of the amino-bound (TS_1, Figure 3b) and carboxyl-bound (TS_2, Figure 4b) configurations the concerted mechanism proceeds via four-center transition structures. This step is the nucleophilic attack of the lone electron pair of the amino group onto the carbon atom of the carboxyl group while simultaneously the proton transfer from the amino group to one of the oxygen atoms of the hydroxyl group takes place. The activation barriers in this step were cal-

  

**Table 1.** Activation barriers, $\Delta E_{ac}$ [kcal mol$^{-1}$], intrinsic rate constants for concerted and stepwise reaction mechanism, $k$, of peptide bond formation from two glycine molecules over H-FAU at 298 K [s$^{-1}$] and atomic charges, $q$(C), on the carbon atom of the carboxyl group of glycine at the reaction center (charges are in $e$).

| | Concerted | | | Stepwise | | | | | |
|---|---|---|---|---|---|---|---|---|---|
| | Amino | Carboxyl | Hydroxyl | Amino | | Carboxyl | | Hydroxyl | |
| | TS_1 | TS_2 | TS_3 | TS_4a | TS_4b | TS_5a | TS_5b | TS_6a | TS_6b |
| $\Delta E_{ac}$ | 51.2 | 27.6 | 5.7 | 44.4 | 32.2 | 1.8 | 22.7 | 44.6 | 24.8 |
| $k$ | $1.48\times10^{-26}$ | $6.37\times10^{-9}$ | $4.21\times10^{3}$ | $6.15\times10^{-22}$ | $1.95\times10^{-9}$ | $6.30\times10^{10}$ | $1.81\times10^{-3}$ | $2.35\times10^{-20}$ | $7.67\times10^{-5}$ |
| $q$(C) | 0.73 | 0.76 | 0.80 | 0.76 | 0.74 | 0.92 | 0.76 | 0.76 | 0.74 |

culated to be 51.2 and 27.6 kcal mol$^{-1}$, respectively, at which the adsorbed glycylglycine and a water molecule are formed.

In the transition state of the amino-bound configuration (TS_1, Figure 3b), C2 and N2 atoms form the peptide bond (C2···N2 distance: 1.53 Å) and the transfer of H3 from N2 to the oxygen atom of the hydroxyl group ends with an O4–H3 distance of 1.22 Å. The activation barrier of the amino-bound configuration, 51.2 kcal mol$^{-1}$, is similar to 47.7–52.7 kcal mol$^{-1}$ for the uncatalyzed reaction of two glycine molecules obtained by MP2 calculations.[3h] This means that protonation of the amino group by the Brønsted acidic proton does not significantly enhance the electrophilicity of the C=O group. In summary, the high barrier is a consequence of the most stable adsorption configuration together with the strained four-center ring at the transition state.

The carboxyl-bound configuration is about 23.1 kcal mol$^{-1}$ higher in adsorption energy. Since the transition state energy is similar, this brings the activation barrier down to 27.6 kcal mol$^{-1}$ (Table 1). The transition structure is also a four-membered ring.

The hydroxyl-bound configuration is the least stable one and its transition state is also the lowest (TS_3, Figure 5b). The total activation barrier is therefore only 5.7 kcal mol$^{-1}$. The reason for such a low barrier is the presence of an eight-membered ring in the transition structure in which a double proton transfer occurs: one Brønsted acidic proton from the H-FAU zeolite toward the glycine OH group and the other one from $NH_3$ back to the H-FAU zeolite in order to regenerate the active site. The C–O2 distance is elongated from 1.37 Å to 2.05 Å and the peptide bond is generated by the C–N bond formation when the C···N distance decreases from 3.20 Å to 1.61 Å.

From the energetic data we calculated the intrinsic rate constants, $k$, to be $1.48\times10^{-26}$, $6.37\times10^{-9}$, and $4.21\times10^{3}$ s$^{-1}$ for the amino-bound, the carboxyl-bound, and the hydroxyl-bound configurations, respectively.

The peptide bond formation is endothermic with a reaction energy of 2.9 kcal mol$^{-1}$ for the amino-bound configuration and exothermic with a reaction energy of 11.6 kcal mol$^{-1}$ for the carboxyl-bound and 13.7 kcal mol$^{-1}$ for the hydroxyl-bound configurations. The latter one is different from the first two because of the back donation of the proton from glycine to O4 instead of O3, which is the most stable position of the proton in H-FAU zeolite.[19] The endothermicity compares well with the value of 2.0–10.0 kcal mol$^{-1}$ from a theoretical study of the uncatalyzed reaction reported by Jensen et al.[3h]

### 2.2. Stepwise Reaction Mechanism

Alternatively, the peptide bond formation of two glycine molecules can proceed via a stepwise mechanism [Eqs. (1)–(4)]:

$$2\,\text{Glycine} + \text{H-FAU} \rightarrow 2\,\text{Glycine–H-FAU} \quad (1)$$

$$2\,\text{Glycine–H-FAU} \rightarrow \text{Diol–H-FAU} \quad (2)$$

$$\text{Diol–H-FAU} \rightarrow \text{Glycylglycine–}H_2O\text{–H-FAU} \quad (3)$$

$$\text{Glycylglycine–}H_2O\text{–H-FAU} \rightarrow \text{Glycylglycine} + H_2O + \text{H-FAU} \quad (4)$$

First, step (1) is the adsorption of two glycine molecules on the active site of the H-FAU. Then, in step (2), the nucleophilic attack of the amino group on the carboxyl carbon atom coincides with the intramolecular hydrogen transfer in order to form a diolic intermediate. Step (3) involves the diolic intermediate and the intramolecular rearrangement to form glycylglycine and the water molecule adsorbed over H-FAU which is desorbed in the final step (4).

The energy profile of the reaction mechanisms from three starting orientations of the first glycine adsorption is shown in Figure 2b and selected geometric parameters are listed in Table S3 in the Supporting Information.

#### *2.2.1. Interactions of Two Glycine Molecules in Different Configurations with H-FAU Zeolite*

The same three configurations for the adsorbtion of two glycine molecules adsorbing on the active site are possible. Adsorption in the amino-bound (AD_1, Figure 3a), carboxyl-bound (AD_2, Figure 4a), and hydroxyl-bound (AD_3, Figure 5a) configuration is identical to the concerted mechanism discussed above. The adsorption energies are −71.2, −48.1, and −46.5 kcal mol$^{-1}$ for the amino-bound, carboxyl-bound, and hydroxyl-bound glycine interaction, respectively.

#### *2.2.2. Peptide Bond Formation*

Starting from the amino-bound configurations, the peptide bond is generated simultaneously with hydrogen transfer in the four-membered transition structure (TS_4a, Figure 6a). The amino hydrogen atom from the second glycine is moved to the carboxyl oxygen atom on the first glycine as the C2–N2 bond is formed. At the first transition state, the C2···N2 dis-

  

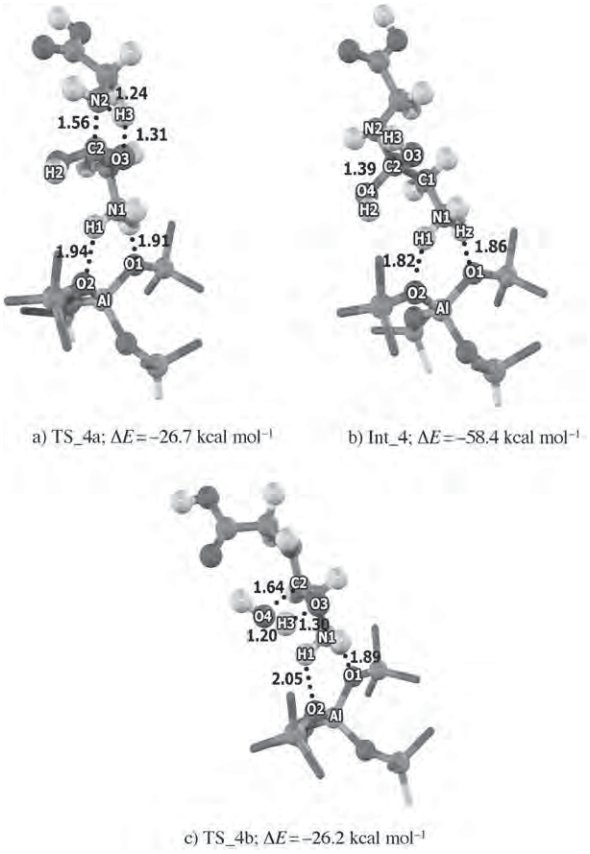


**Figure 6.** Optimized geometries of adsorption complexes, transition states, and products. a) First transition structure of the amino-bound configuration in the stepwise reaction mechanism, TS_4a. b) Intermediate of the amino-bound configuration in the stepwise reaction mechanism, Int_4. c) Second transition structure of the amino-bound configuration in the stepwise reaction mechanism, TS_4b.

For the carboxyl-bound configuration, the peptide formation involves only a nucleophilic attack of the amine nitrogen to the carboxyl carbon (TS_5a, Figure 7a). An activation energy of

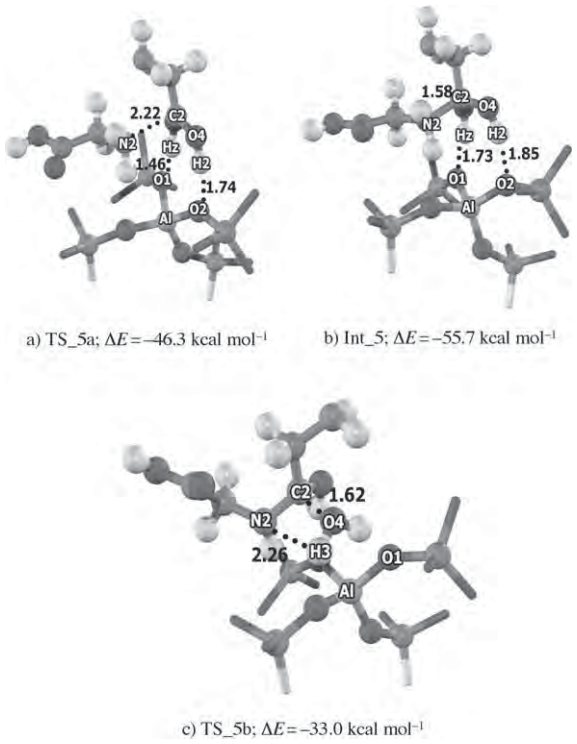


**Figure 7.** Optimized geometries of adsorption complexes, transition states, and products. a) First transition structure of the carboxyl-bound configuration in the stepwise reaction mechanism, TS_5a. b) Intermediate of the carboxyl-bound configuration in the stepwise reaction mechanism, Int_5. c) Second transition structure of the carboxyl-bound configuration in the stepwise reaction mechanism, TS_5b.

tance is 1.56 Å and N2–H3 is elongated to 1.24 Å. The activation barrier (44.4 kcal mol$^{-1}$) is smaller than for the hydrogen transfer in the concerted reaction mechanism (51.2 kcal mol$^{-1}$) from the amino group to the more basic oxygen atom of the carboxyl group and is preferred over the transfer to the less basic hydroxyl group. The diolic intermediate (Int_4, Figure 6b), with a tetrahedral sp$^3$ configuration on the carbon atom at the peptide bond, is produced and adsorbed over the deprotonated active site. Its energy is −58.4 kcal mol$^{-1}$.

At the second transition state (TS_4b, Figure 6c), water is eliminated from the planar four-membered ring transition structure and a distorted tetrahedral configuration at the carbon atom of the peptide bond of the diolic intermediate rearrangement is formed. Its activation energy is 32.2 kcal mol$^{-1}$. At the C2 atom previously linked to the N2 atom, $H_2O$ is formed through hydrogen transfer from one hydroxyl group to the leaving one. The hydroxyl cleavage is accompanied by an extension of the C2–O4 distance from 1.39 Å to 1.64 Å and a contraction of the C–N bond from 1.43 Å to 1.39 Å. The water molecule is co-adsorbed between the framework and the newly formed glycylglycine (Pro_1). The relative energy of the product is −68.3 kcal mol$^{-1}$.

1.8 kcal mol$^{-1}$ is required. The intermolecular C2···N2 distance is shortened to 2.22 Å while the reacting molecules move further from the active site by 1.46 Å. In the intermediate (Int_5, Figure 7b) the C2–N2 bond length is 1.58 Å and its energy is −55.7 kcal mol$^{-1}$. The intermediate consequently loses a water molecule through hydrogen abstraction from the amino group to the leaving group with an energy barrier of 22.7 kcal mol$^{-1}$. In the four-membered transition structure (TS_5b, Figure 7c) the N2–H3 bond length is extended to 2.26 Å and the O3–H4 distance is contracted to 0.96 Å. The departure of the hydroxyl group is promoted by a C2–O4 bond length of 1.62 Å. The final step is then again the co-adsorption of protonated glycylglycine (Pro_2) and water molecules over the zeolitic framework. The relative energy for this step is −59.7 kcal mol$^{-1}$.

Concerning the hydroxyl-bound configuration, no transfer of the zeolitic proton is involved in the first transition state (TS_6a, Figure 8a). The diolic intermediate (Int_6, Figure 8b) is generated via the four-membered transition state. The conversion, like for the amino-bound configuration discussed above, consists of the proton transfer and the formation of the intermolecular C2···N2 bond. The protonic H3 from the second glycine N2 moves towards O3 of the first glycine molecule as

  

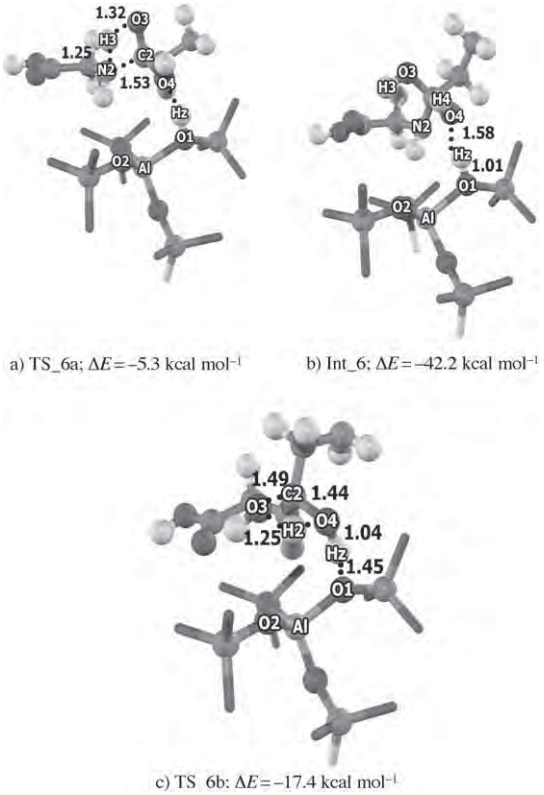


**Figure 8.** Optimized geometries of adsorption complexes, transition states, and products. a) First transition structure of the hydroxyl-bound configuration in the stepwise reaction mechanism, TS_6a. b) Intermediate of the hydroxyl-bound configuration in the stepwise reaction mechanism, Int_6. c) Second transition structure of the hydroxyl-bound configuration in the stepwise reaction mechanism, TS_6b.

shown in the distances of N2–H3 and O3–H3 of 1.25 Å and 1.32 Å, respectively. The C–O3 bond length is extended to 1.33 Å as O3 receives the proton H3. The intermolecular distance of C2–N2 is shortened from 3.13 Å to 1.53 Å. As the O1–Hz length is 1.01 Å and O4–Hz is 1.51 Å, the Brønsted proton is moving slightly closer to O2 of the first glycine and the reacting molecules are stabilized by adsorbing closer to the framework with a distance of 2.28 Å. At the adsorption complex of this configuration, the positive charge of the C atom at the reaction center (0.83) is in between the ones of the amino-bound and the carboxyl-bound configurations (0.82 and 0.890, respectively). The formed diolic intermediate has an adsorption energy of $-42.15$ kcal mol$^{-1}$. The four-membered transition structure (TS_6b, Figure 8c) is similar to the other configurations. The zeolitic proton is then transferred to the reacting molecule. The protonic H2 is abstracted from the leaving OH group and the transition structure adsorbs 2 Å closer to the framework. The process needs an activation energy of 24.8 kcal mol$^{-1}$ yielding as products protonated glycylglycine (Pro_3, Figure 5d) and water located over the active region of the zeolite.

The barriers at the first transition state, 44.4, 1.8, and 44.6 kcal mol$^{-1}$, result in intrinsic rate constants, of $6.15\times10^{-22}$, $6.30\times10^{10}$, and $2.35\times10^{-20}$ s$^{-1}$ for the amino-bound, carboxyl-bound, and hydroxyl-bound configurations, respectively. The activation barriers of the second transition state for the three configurations (32.2, 22.7, and 24.8 kcal mol$^{-1}$, respectively) lead to intrinsic rate constants of $1.95\times10^{-9}$, $1.81\times10^{-3}$, and $7.67\times10^{-5}$ s$^{-1}$, respectively.

For the stepwise reaction mechanism, the peptide bond formation is an exothermic reaction with a reaction energy of 0.7 kcal mol$^{-1}$. The energies required for desorption of the water molecule are 20.6, 14.2, and 15.0 kcal mol$^{-1}$ for the amino-bound, carboxyl-bound, and the hydroxyl-bound configuration, respectively.

The complete energy profiles for the peptide formation mechanisms of glycine on H-FAU are shown in Figure 2. The three types of adsorptions, amino-bound, carboxyl-bound, and hydroxyl-bound have, for 2 glycine molecules, energies of $-71.2$, $-48.4$, and $-46.5$ kcal mol$^{-1}$, respectively. The reaction is exothermic. In the concerted mechanism, the activation energies are 51.2, 27.6, and 5.7 kcal mol$^{-1}$ for amino-bound, carboxyl-bound, and hydroxyl-bound, respectively. In the stepwise mechanism the activation energies are 44.4 and 32.2 kcal mol$^{-1}$ for amino-bound, 1.8 and 22.7 kcal mol$^{-1}$ for carboxyl-bound and 44.6 and 24.8 kcal mol$^{-1}$ for hydroxyl-bound configurations. The reaction via the amino-bound adsorbate in the concerted mechanism is the energetically preferred one.

## 3. Conclusions

The catalysis of peptide bond formation of two glycine molecules on H-FAU zeolite has been studied with density functional theory at the M08-HX level. There are three possible adsorption orientations for the first adsorbed glycine molecule which lead to different reaction pathways, these are, amino-bound, carboxyl-bound, and hydroxyl-bound configurations. For each of them, the concerted and the stepwise reaction mechanisms have been investigated.

In the concerted reaction, both the C–N bond formation and the release of water by N–H and C–O bond cleavages take place simultaneously. The catalytic activity of H-FAU zeolite influences the transition states for each reaction. The interaction to the Brønsted acidic proton increases the charge deficiency on the carbon atom of the carboxyl group and thus facilitates the nucleophilic attack by the lone electron pair of the amine.

The peptide bond is then generated by the dehydration of glycine taking place in a single step without a prior zwitterionic intermediate. The order of the activation barriers is amino-bound (51.2 kcal mol$^{-1}$) > carboxyl-bound (27.6 kcal mol$^{-1}$) > hydroxyl-bound (5.7 kcal mol$^{-1}$). The barrier height is significantly reduced by the presence of an eight-membered ring in the transition structure instead of the four-membered ring.

For the stepwise reaction mechanism, the reaction takes place through a stable diolic intermediate. Already in the first step, the C–N bond is formed through nucleophilic attack of the nitrogen on a carbon atom and simultaneous hydrogen transfer from ammonia to a carboxyl oxygen atom, except for the carboxyl-bound configuration, where a nucleophilic attack of the amine nitrogen on the carboxyl carbon was found.

  

In the second step, a water molecule is released by C–O and O–H bond cleavages. In contrast to the first mechanism, in which a hydrogen atom is transferred to hydroxyl oxygen from the ammonia, the stepwise reaction mechanism involves transfer of hydrogen to the carboxyl oxygen.

The concerted reaction mechanism should therefore dominate the overall reaction with an estimated activation barrier of 51.2 kcal mol$^{-1}$, starting from the amino-bound configuration. The overall reaction is predicted to be slightly endothermic.

## Computational Methods

The cluster models of H-FAU are taken from the lattice structure of faujasite zeolite.[20] The active region consists of a 21T cluster, which is considered to be the smallest unit required to represent the acidic site of zeolite and the reactive molecules. In the 21T cluster, one of the silicon atoms in the faujasite zeolite is substituted by an aluminum atom, and a proton is added to one of the bridging oxygen atoms bonded directly to the aluminum atom, conventionally called the O1 position.[19,20] During the structure optimization, only the 5T part of the active site region [(≡SiO)$_2$(H)Al(OSi≡)$_2$] and the adsorbates are allowed to relax while the rest of the active region is fixed at the crystallographic coordinates. To represent the confinement effect of the zeolite pore structure, the extended structure of a 120T cluster (Figure 1) which includes two supercages is used in single point calculations. It is assumed that these models for the H-FAU zeolites are large enough to cover all the important framework effects that act on both the active site and on the adsorbates. Attempts have been made to demonstrate that the geometry constraints imposed in this work do not influence the results and the reliability of the M08-HX functional was compared with MP2 calculations. Some test calculations on glycine over the H-FAU zeolite have been performed relaxing 5T and 8T atoms (see Table S4 in the Supporting Information). All calculations were performed by means of the M08-HX density functional[21] and the 6-31G(d,p) basis set. For the transition structures, frequency calculations were performed in order to check whether the imaginary frequency mode corresponds to the reaction coordinate.

Atomic charges were computed from the natural population analysis (NPA). All calculations were performed using the Gaussian 03 code with the Minnesota density functionals module 3.1 by Zhao and Truhlar incorporated.[16a,22]

In order to analyze the kinetics of the reaction, classical transition state theory was used to derive the intrinsic rate constants $k$. They were calculated within the harmonic oscillator–rigid rotor approximation [Eq. (5)]:

$$k(T) = \frac{K_B T}{h} e^{-\Delta^{\neq} G^0/RT} \quad (5)$$

where $k_B$, $T$, $h$, $\Delta^{\neq}G^0$, and $R$ are the Boltzmann constant, the temperature of the system (taken to be 298 K), Planck's constant, Gibbs free energy of activation, and the gas constant, respectively.

## Acknowledgements

*This work was supported in part by grants from the National Science and Technology Development Agency (2009 NSTDA Chair Professor funded by the Crown Property Bureau under the management of the National Science and Technology Development Agency and NANOTEC Center of Excellence funded by the National Nanotechnology Center), Kasetsart University Research and Development Institute (KURDI), the Thailand Research Fund (TRF), and the Commission on Higher Education, Ministry of Education (the "National Research University Project of Thailand (NRU)" and the "National Center of Excellence for Petroleum, Petrochemical and Advanced Materials (NCE-PPAM)"). Support from the Graduate School Kasetsart University and from the RFBR-FWF projects 09-03-91001-a and I200-N19 is also acknowledged. The authors are grateful to Donald G. Truhlar and Yan Zhao for their support with the M08-HX functional. We thank P. Khongpracha for helpful suggestions.*

**Keywords:** density functional calculations · dipeptide · glycine · reaction mechanisms · zeolites

[1] a) J. Liu, Z. Cao, Y. Lu, *Chem. Rev.* **2009**, *109*, 1948–1998; b) Y. Ura, J. M. Beierle, L. J. Leman, L. E. Orgel, M. R. Ghadiri, *Science* **2009**, *325*, 73–77; c) K. J. Waldron, N. J. Robinson, *Nat. Rev. Microbiol.* **2009**, *7*, 25–35; d) I. Ben-Gera, G. Zimmermann, *Nature* **1964**, *202*, 1007–1008.

[2] a) L. E. Orgel, *Trends Biochem. Sci.* **1998**, *23*, 491–495; b) P. Davies, *Sci. Prog.* **2001**, *84*, 17–29; c) P. Davies, *Sci. Prog.* **2001**, *84*, 1–16.

[3] a) J. D. Bernal, *The Physical Basis of Life*, Routledge and Kegan Paul, London, **1951**; b) B. K. G. Theng, *The Chemistry of Clay-Organic Reactions*, Wiley, New York, **1974**; c) M. J. Gresser, W. P. Jencks, *J. Am. Chem. Soc.* **1977**, *99*, 6963–6970; d) C. C. Yang, W. P. Jencks, *J. Am. Chem. Soc.* **1988**, *110*, 2972–2973; e) M. M. Cox, W. P. Jencks, *J. Am. Chem. Soc.* **1981**, *103*, 572–580; f) A. C. Satterthwait, W. P. Jencks, *J. Am. Chem. Soc.* **1974**, *96*, 7018–7031; g) T. Oie, G. H. Loew, S. K. Burt, J. S. Binkley, R. D. MacElroy, *J. Am. Chem. Soc.* **1982**, *104*, 6169–6174; h) J. H. Jensen, K. K. Baldridge, M. S. Gordon, *J. Phys. Chem.* **1992**, *96*, 8340–8351.

[4] H. Yang, S.-Y. Fung, M. Pritzker, P. Chen, *Langmuir* **2009**, *25*, 7773–7777.

[5] J. Bujdak, B. M. Rode, *React. Kinet. Catal. Lett.* **1997**, *62*, 281–286.

[6] a) K. I. Zamaraev, V. N. Romannikov, R. I. Salganik, W. A. Wlassoff, V. V. Khramtsov, *Origins Life Evol. Biosphere* **1997**, *27*, 325–337; b) M. Meng, L. Stievano, J.-F. Lambert, *Langmuir* **2004**, *20*, 914–923; c) N. Lahav, D. White, S. Chang, *Science* **1978**, *201*, 67–69; d) M. Rao, D. G. Odom, J. Oro, *J. Mol. Evol.* **1980**, *15*, 317–331; e) A. J. A. Aquino, D. Tunega, M. H. Gerzabek, H. Lischka, *J. Phys. Chem. B* **2004**, *108*, 10120–10130.

[7] a) V. A. Basiuk, T. Y. Gromovoy, V. G. Golovaty, A. M. Glukhoi, *Origins Life Evol. Biosphere* **1991**, *20*, 483–498; b) J. Bujdák, B. M. Rode, *J. Mol. Evol.* **1997**, *45*, 457–466; c) J. Bujdak, B. M. Rode, *J. Mol. Catal. A* **1999**, *144*, 129–136; d) A. Rimola, L. Rodriguez-Santiago, P. Ugliengo, M. Sodupe, *J. Phys. Chem. B* **2007**, *111*, 5740–5747.

[8] a) J. E. Krohn, M. Tsapatsis, *Langmuir* **2005**, *21*, 8743–8750; b) J. E. Krohn, M. Tsapatsis, *Langmuir* **2006**, *22*, 9350–9356; c) F. Xu, Y. Wang, X. Wang, Y. Zhang, Y. Tang, P. Yang, *Adv. Mater.* **2003**, *15*, 1751–1753; d) S. Munsch, M. Hartmann, S. Ernst, *Chem. Commun.* **2001**, 1978–1979.

[9] G.-W. Xing, X.-W. Li, G.-L. Tian, Y.-H. Ye, *Tetrahedron* **2000**, *56*, 3517–3522.

[10] a) Y. Cui, Q. Wei, H. Park, C. M. Lieber, *Science* **2001**, *293*, 1289–1292; b) J. Kong, N. R. Franklin, C. Zhou, M. G. Chapline, S. Peng, K. Cho, H. Dailt, *Science* **2000**, *287*, 622–625.

[11] A. Rimola, S. Tosoni, M. Sodupe, P. Ugliengo, *Chem. Phys. Lett.* **2005**, *408*, 295–301.

[12] A. Rimola, M. Sodupe, P. Ugliengo, *J. Am. Chem. Soc.* **2007**, *129*, 8333–8344.

[13] R. Z. Khaliullin, A. T. Bell, V. B. Kazansky, *J. Phys. Chem. A* **2001**, *105*, 10454–10461.

[14] a) P. E. Sinclair, A. de Vries, P. Sherwood, C. R. A. Catlow, R. A. van Santen, *J. Chem. Soc. Faraday Trans.* **1998**, *94*, 3401–3408; b) M. Brändle, J. Sauer, *J. Am. Chem. Soc.* **1998**, *120*, 1556–1570; c) S. P. Greatbanks, I. H. Hillier, N. A. Burton, P. Sherwood, *J. Chem. Phys.* **1996**, *105*, 3770–3776; d) J. Limtrakul, T. Nanok, S. Jungsuttiwong, P. Khongpracha, T. N. Truong, *Chem. Phys. Lett.* **2001**, *349*, 161–166; e) T. Maihom, B. Boekfa, J. Sirijaraensre, T. Nanok, M. Probst, J. Limtrakul, *J. Phys. Chem. C* **2009**,

  

*113*, 6654 – 6662; f) T. Maihom, S. Namuangruk, T. Nanok, J. Limtrakul, *J. Phys. Chem. C* **2008**, *112*, 12914 – 12920; g) P. Treesukol, K. Srisuk, J. Limtrakul, T. N. Truong, *J. Phys. Chem. B* **2005**, *109*, 11940 – 11945; h) P. Pantu, S. Pabchanda, J. Limtrakul, *ChemPhysChem* **2004**, *5*, 1901 – 1906; i) B. Boekfa, S. Choomwattana, P. Khongpracha, J. Limtrakul, *Langmuir* **2009**, *25*, 12990 – 12999.

[15] a) S. Yuan, J. Wang, Y.-B. Duan, Y.-W. Li, H. Jiao, *J. Mol. Catal. A* **2006**, *256*, 130 – 137; b) A. Waclaw, K. Nowinska, W. Schwieger, *Appl. Catal. A* **2004**, *270*, 151 – 156; c) S. Kasuriya, S. Namuangruk, P. Treesukol, M. Tirtowidjojo, J. Limtrakul, *J. Catal.* **2003**, *219*, 320 – 328; d) K. Bobuatong, J. Limtrakul, *Appl. Catal. A* **2003**, *253*, 49 – 64; e) S. Namuangruk, P. Pantu, J. Limtrakul, *J. Catal.* **2004**, *225*, 523 – 530; f) B. Boekfa, P. Pantu, J. Limtrakul, *J. Mol. Struct.* **2008**, *889*, 81 – 88; g) C. Tuma, J. Sauer, *Phys. Chem. Chem. Phys.* **2006**, *8*, 3955 – 3965.

[16] a) Y. Zhao, D. G. Truhlar, *Theor. Chem. Acc.* **2008**, *120*, 215 – 241; b) Y. Zhao, D. G. Truhlar, *J. Phys. Chem. C* **2008**, *112*, 6860 – 6868.

[17] a) C. Kumsapaya, K. Bobuatong, P. Khongpracha, Y. Tantirungrotechai, J. Limtrakul, *J. Phys. Chem. C* **2009**, *113*, 16128 – 16137; b) B. Boekfa, P. Pantu, M. Probst, J. Limtrakul, *J. Phys. Chem. C* **2010**, *114*, 15061 – 15067; c) S. Wannakao, B. Boekfa, P. Khongpracha, M. Probst, J. Limtrakul, *ChemPhysChem* **2010**, *11*, 3432 – 3438.

[18] H. G. Karge, V. Dondur, J. Weitkamp, *J. Phys. Chem.* **1991**, *95*, 283 – 288.

[19] J.-R. Hill, C. M. Freeman, B. Delley, *J. Phys. Chem. A* **1999**, *103*, 3772 – 3777.

[20] D. H. Olson, E. Dempsey, *J. Catal.* **1969**, *13*, 221 – 231.

[21] a) Y. Zhao, D. G. Truhlar, *J. Chem. Theory Comput.* **2008**, *4*, 1849 – 1868; b) Y. Zhao, D. G. Truhlar, *J. Chem. Theory Comput.* **2011**, *7*, 669 – 676.

[22] *Gaussian 03* (*Revision B.05*), M. J. Frisch, G. W. Trucks, H. B. Schlegel, G. E. Scuseria, M. A. Robb, J. R. Cheeseman, J. A. Montgomery, Jr., T. Vreven, K. N. Kudin, J. C. Burant, J. M. Millam, S. S. Iyengar, J. Tomasi, V. Barone, B. Mennucci, M. Cossi, G. Scalmani, N. Rega, G. A. Petersson, H. Nakatsuji, M. Hada, M. Ehara, K. Toyota, R. Fukuda, J. Hasegawa, M. Ishida, T. Nakajima, Y. Honda, O. Kitao, H. Nakai, M. Klene, X. Li, J. E. Knox, H. P. Hratchian, J. B. Cross, C. Adamo, J. Jaramillo, R. Gomperts, R. E. Stratmann, O. Yazyev, A. J. Austin, R. Cammi, C. Pomelli, J. W. Ochterski, P. Y. Ayala, K. Morokuma, G. A. Voth, P. Salvador, J. J. Dannenberg, V. G. Zakrzewski, S. Dapprich, A. D. Daniels, M. C. Strain, O. Farkas, D. K. Malick, A. D. Rabuck, K. Raghavachari, J. B. Foresman, J. V. Ortiz, Q. Cui, A. G. Baboul, S. Clifford, J. Cioslowski, B. B. Stefanov, G. Liu, A. Liashenko, P. Piskorz, I. Komaromi, R. L. Martin, D. J. Fox, T. Keith, M. A. Al-Laham, C. Y. Peng, A. Nanayakkara, M. Challacombe, P. M. W. Gill, B. Johnson, W. Chen, M. W. Wong, C. Gonzalez, J. A. Pople, Gaussian, Inc., Pittsburgh, PA, **2003**.

Received: January 18, 2011
Published online on June 22, 2011

  

THE JOURNAL OF PHYSICAL CHEMISTRY A

ARTICLE

pubs.acs.org/JPCA

# Density Functional Theory Study of the Carbonyl-ene Reaction of Encapsulated Formaldehyde in Cu(I), Ag(I), and Au(I) Exchanged FAU Zeolites

Sippakorn Wannakao,[†,‡,§] Pipat Khongpracha,[†,‡,§] and Jumras Limtrakul*[,†,‡,§]

[†]Laboratory for Computational and Applied Chemistry, Department of Chemistry, Faculty of Science and Center of Nanotechnology, Kasetsart University Research and Development Institute, Kasetsart University, Bangkok 10900, Thailand

[‡]Center for Advanced Studies in Nanotechnology and Its Applications in Chemical, Food and Agricultural Industries, Kasetsart University, Bangkok 10900, Thailand

[§]NANOTEC Center of Excellence, National Nanotechnology Center, Kasetsart University, Bangkok 10900, Thailand

Supporting Information

**ABSTRACT:** Carbonyl-ene reactions, which involve C−C bond formation, are essential in many chemical syntheses. The formaldehyde−propene reaction catalyzed by several of the group 11 metal cations, $Cu^+$, $Ag^+$, and $Au^+$ exchanged on the faujasite zeolite (metal-FAU) has been investigated by density functional theory at the M06-L/6-31G(d,p) level. The Au-FAU exhibits a higher activity than the others due to the high charge transfer between the Au and the reactant molecules, even though it is located at a negatively charged site of the zeolite. This site enables it to compensate for the charge of the $Au^+$ ion. The NBO analysis reveals that the 6s orbital of the Au atom plays an important role, inducing a charge on the probe molecules. Moreover, the effect of the zeolite framework makes the Au-FAU more active than the others by stabilizing the high charge induced transition structure. The activation energy of the reaction catalyzed by Au-FAU is 13.0 kcal/mol whereas that of Cu and Ag-FAU is found to be around 17 kcal/mol. The product desorption needs to be improved for Au-FAU; however, we suggest that catalysts with high charge transfer might provide a promising activity.


## 1. INTRODUCTION

Reactions involving carbon−carbon bond formation are essential for most chemical upgrading processes. Among the well-known C−C bond formations, the carbonyl-ene reaction is one of the top choices for synthesis.[1,2] The carbonyl-ene reaction is induced by Lewis acid[3] and generally requires a strongly electrophilic carbonyl compound. The reaction of formaldehyde and propene is an example of the carbonyl-ene reaction that yields as a product 3-buten-1-ol. This product can be used in chemical processes, e.g., the copolymerization of propylene for producing polypropylene. In addition, the formaldehyde−propene reaction is involved in the synthesis of tetrahydrofuran, one of the most popular organic solvents in the laboratory.

Because of its low boiling point (−19.5 °C), formaldehyde is difficult to handle. Moreover, it rapidly polymerizes to solid paraformaldehyde and trioxane. Then, its shelf life is quite short. To retain formaldehyde in its monomer state, Lewis acid treatment is used to depolymerize the polymer form. Unfortunately, the treatment causes problems of corrosion, handling, and toxic waste, making it environmentally unfriendly. For these reasons, formaldehyde has become limited in its application for organic synthesis. Finding storage materials that retain the monomeric formaldehyde should be a way for solving these problems.

Porous materials such as zeolites and metal organic frameworks (MOF),[4−11] a new type of designable material, widely used as gas storage and separation materials, are environmentally friendly candidates for formaldehyde storage. Successful utilization of a porous material for formaldehyde storage was achieved by Okachi et al.[12] in 2004. These authors found that Na/faujasite zeolite suppresses the decomposition and self-polymerization of formaldehyde while its reactivity toward nucleophiles remains the same. Recently, Tomita et al.[13] have theoretically demonstrated that formaldehyde does not tend to self-polymerize in alkaline-exchanged faujasite zeolite. Our previous ONIOM calculation of the formaldehyde-propene reaction on Na-exchanged faujasite zeolite has revealed that alkaline-exchanged zeolite can significantly reduce the reaction barrier in the reaction mechanism

**Special Issue:** Richard F. W. Bader Festschrift

**Received:** March 2, 2011
**Revised:** September 10, 2011
**Published:** September 26, 2011

compared to an uncatalyzed process.[14] Thus, it can be suggested not only that zeolite can be used for storage but that alkaline-exchanged zeolite can also enable catalyzation of this reaction. Zeolite can be used for not only these purposes but also metal organic frameworks.

In our recent study, the formaldehyde−propene reaction in MOF-11, in which the active site is Cu(II) in the paddle wheel unit ($Cu_2(CO_2)_4$), was theoretically investigated.[15] It was found that MOF-11 can reduce the activation energy of the reaction from 34.3 to 24.1 kcal/mol. A bare $Cu^+$, however, is much more reactive with an activation barrier of only 6.4 kcal/mol. Therefore, MOF-11 can be utilized in catalytic applications only with a moderated activity. Finding a structure that retains the high activity of the metal would be promising, not only for its academic interest but also for industrial applications.

Metals loaded on zeolites have been widely studied as their properties can be fine-tuned by varying the metals. Bell and coworkers have synthesized and characterized Cu(I)-exchange zeolite Y for catalyzing the dimethyl carbonate (DMC) reaction from oxidative carbonylation of methanol.[16−19] They found that Cu−Y provided a high reactivity for the reaction. Moreover, Ag(I) and Au nanoparticles exhibit good performances in reactions involving C−C bond formation.[20−22] The monomeric Au cation on zeolites has been successfully prepared,[23−29] and many theoretical studies have been conducted.[30−35] Ichikawa et al.[23,25] used CO adsorption and Fourier transform IR (FTIR) to study Au/NaY, Au/Na-mordenite, and Au/Na-ZSM-5 and concluded that Au(I) is the dominant active site for the decomposition of NO with CO and the water gas shift. Fierro-Gonzalez and Gates[26] have also synthesized and characterized monomeric Au(I) and Au(III) in zeolite NaY without zero valence Au clusters.

There is often little correlation between the catalytic activities of different cations on many reactions, even if the ions are chemically related. Thus, each cation has to be tested either theoretically or experimentally for any reaction of interest. Theoretical studies not only save a great deal of time and money compared to complicated experimental screening, but they also provide insight into why a particular cation has a higher activity, and thus a guide to synthesize the catalyst with the required characteristics. As a consequence, in this work, we investigate the formaldehyde-propene carbonyl-ene reaction on the Cu, Ag, and Au cation exchanged on FAU zeolite (M-FAU, M = Cu, Ag, and Au) by means of density functional theory with the M06-L functional.[36−38] Even though metal cations exchanged in zeolites have been widely studied, to the best of our knowledge, there is no theoretical study for the C−C bond formation processes with this series of metal-exchanged zeolites as a catalyst. This work thus investigates the possibility of using group 11 metal-exchanged zeolites as highly active catalysts for the carbonyl-ene reaction. We also make a comparison with other Lewis acid catatlysts (MOF-11 and Na-FAU).

## 2. MODELS AND METHOD

The faujasite zeolite is composed of sodalite building blocks that contain 192T (T is either a Si or an Al atom) atoms in the supercage unit cell.[39] The Cu(I) cation can be located in many different cation-exchange sites, as shown in Figure 1. Site I is located in the hexagonal prism, which is not accessible for the reaction to proceed. Site II is inside the FAU supercage on the hexagonal face and site III is also located in the supercage, but on the four-membered ring of the sodalite cage. An experimental

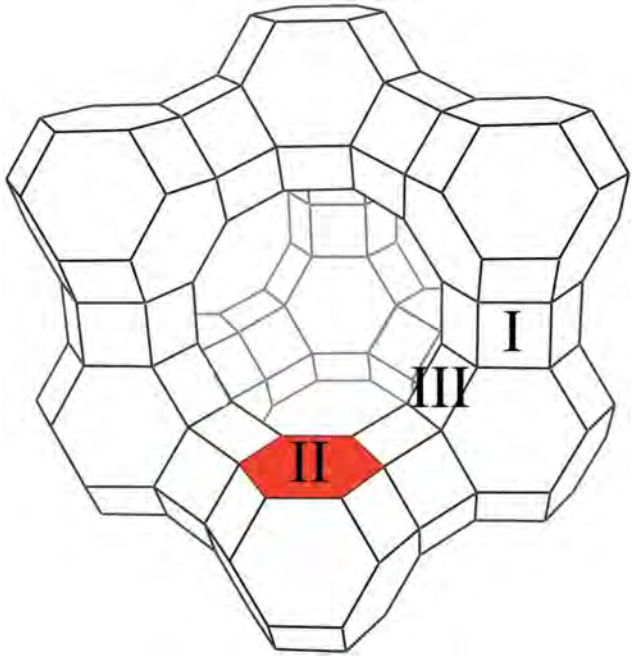


**Figure 1.** Cation exchanging sites of the faujasite zeolite (see text for explanations).

study by Drake et al.[40] shows that Cu(I) can replace all acidic protons of the H−Y zeolite, resulting in a ratio Cu/Al = 1.0. Moreover, these authors also concluded that site II is the site most occupied by $Cu^+$ ion. Site II was therefore chosen to represent the catalytically active site in this study. Furthermore, this site has also been studied for other metal cations in several previous reports.[19,30]

The selected 16T model (Figure 2) of site II consists of 6T from the hexagonal ring and the side extended four-membered rings to avoid interaction between terminating hydrogen atoms. To avoid the Al−OH group, which was not observed in experiments, Si atoms adjacent to the Al atom were included in the model. The metal ions were located in the middle of the hexagonal ring, as shown in Figure 2. Geometry optimizations were performed at the M06-L/6-31G(d,p) level of theory and Stuttgart ECP[41] were employed for the Cu, Ag, and Au atoms. The M06-L functional has been tested and found to be accurate and affordable from the Minnesota functional series for the energetic properties of systems containing transition metals and even in more sophisticated cases such as metal oxide systems.[37,42−47] Recent studies of chemical reactions regarding zeolite systems has demonstrated that this well calibrated series of functionals provides results in good agreement with experimental values.[48−51] Moreover, a theoretical study of the chemical reaction on transition metal oxide-exchanged zeolite shows that the M06-L functional provides acceptable results for both structure and adsorption energies when compared to the MP2[52] method. To avoid too many degrees of freedom during the optimization, only the metal atoms and the 4T region with the three oxygen atoms adjacent to the metal atoms ($-Si_3O_3Al-$) were allowed to relax while the rest were kept fixed at their crystallographic positions. Transition states were located by the Berny algorithm[53,54] and confirmed by normal-mode analyses that provide only one imaginary frequency corresponding to the designated reaction coordination. Total spin was kept to be singlet


**Figure 2.** Structures of the Cu-, Ag-, and Au-FAU catalysts obtained from M06-L/6-31G(d,p) optimizations.

**Table 1. Partial Electronic Charges of the Metal Atom and the Probe Molecules**

| | | NPA-charges/e | | |
|---|---|---|---|---|
| step | | Cu-FAU | Ag-FAU | Au-FAU |
| catalysts | metal | 0.682 | 0.759 | 0.699 |
| Ads | C | 0.308 | 0.259 | 0.327 |
| | O | −0.584 | −0.547 | −0.557 |
| | HCHO | 0.052 | 0.044 | 0.141 |
| | metal | 0.656 | 0.707 | 0.521 |
| CoAds | C | 0.217 | 0.266 | 0.284 |
| | O | −0.617 | −0.589 | −0.593 |
| | CoAds | −0.004 | 0.066 | 0.161 |
| | metal | 0.741 | 0.666 | 0.506 |
| TS | C | −0.047 | −0.040 | −0.070 |
| | O | −0.831 | −0.786 | −0.759 |
| | TS | 0.073 | 0.077 | 0.268 |
| | metal | 0.632 | 0.679 | 0.411 |

during the reaction pathway for all systems. Interaction between probe molecules and catalysts are reported as relative energies that relative to energies of isolated reactants which can be calculated by the equation, $E = E_{complex} - (E_{reactant1} + E_{reactant2} + ...)$. The charge distributions and population analyses of the complexes were also determined at the M06-L/6-31G(d,p) level of theory by the natural atomic orbital (NAO) and natural bond orbital analysis (NBO) methods.[55,56] The framework was then extended to 120T, covering a supercage structure of FAU, to perform the single point calculation with the same level of theory as the one used for evaluating the effect of the zeolite framework. Zero-point energies were also corrected for the quantum cluster of the 16T model of the zeolite system (Table S3, Supporting Information). All quantum chemical calculations were carried out with the Gaussian 03[57] code, modified to incorporate the Minnesota Density Functionals module 3.1 by Zhao and Truhlar.

## 3. RESULTS AND DISCUSSION

**3.1. Metal-Exchanged Faujasite Zeolite.** The optimized structures of the Cu-FAU, Ag-FAU, and Au-FAU models used in this study are illustrated in Figure 2. Partial charges and the electronic configuration of the systems are documented in Table 1 and Table S2 (Supporting Information), respectively. The calculated charges were found to be +0.682e, +0.759e, and +0.699e for the Cu, Ag, and Au atoms, respectively. This shows the compensation between the metal charges and the surrounding oxygen atoms in the 6-membered ring. The complexation energies between the metal cations and the zeolite were found to be −179.2, −147.9, and −154.2 kcal/mol for Cu-, Ag-, and Au-FAU, respectively. It is worth noting that the complexation energies with the amount of charge transfer between $M^+$ and the zeolite framework was revealed by the charge reduction of the exchanged cations ($Cu^+ > Au^+ > Ag^+$).

The structures and mechanisms of the encapsulated formaldehyde metal-FAU carbonyl-ene reaction are now investigated. The symbol M@S signifies that the molecule M is adsorbed on the active site S. The proposed reaction mechanism is similar to those of our previous calculations for Na-FAU catalyst as well as for MOF-11. The reaction is assumed to proceed on a concerted mechanism in which both reactants are involved in the rate limiting step. All optimized geometries are given in the Supporting Information, Table S1.

**3.2. Encapsulated Formaldehyde in Metal-FAU.** To keep formaldehyde in its monomer state and to keep it activated, the reaction begins with the encapsulation of formaldehyde on the metal-FAU catalysts like in the previous studies.[14,15] The oxygen atom of formaldehyde interacts with the Lewis acid metal site of the catalyst. The C−O distance is elongated from 1.20 to 1.23 Å, which is the same as in the alkaline exchange and the MOF-11 studies. The adsorption energies are found to be −16.9, −18.0, and −20.0 kcal/mol for Cu-, Ag-, and Au-FAU, respectively. From the NBO calculations we find highly ionic bonding characteristics between the Au and the O atom of the formaldehyde molecule, formed by the 6s orbital (8.45%) of the Au atom and the 2p orbital (91.55%) of the O atom (Figure 3). The interaction between the O and the Cu or Ag contains a contribution from the lone pair electron of the O atom to the metal (Figure 4). An electron back-donation from the metal to formaldehyde could not be observed at any significant level. The total occupancy of the Cu and Ag atoms were nearly unchanged whereas the Au atom received more electrons at the 6s orbital after the formaldehyde was encapsulated. This might be due to

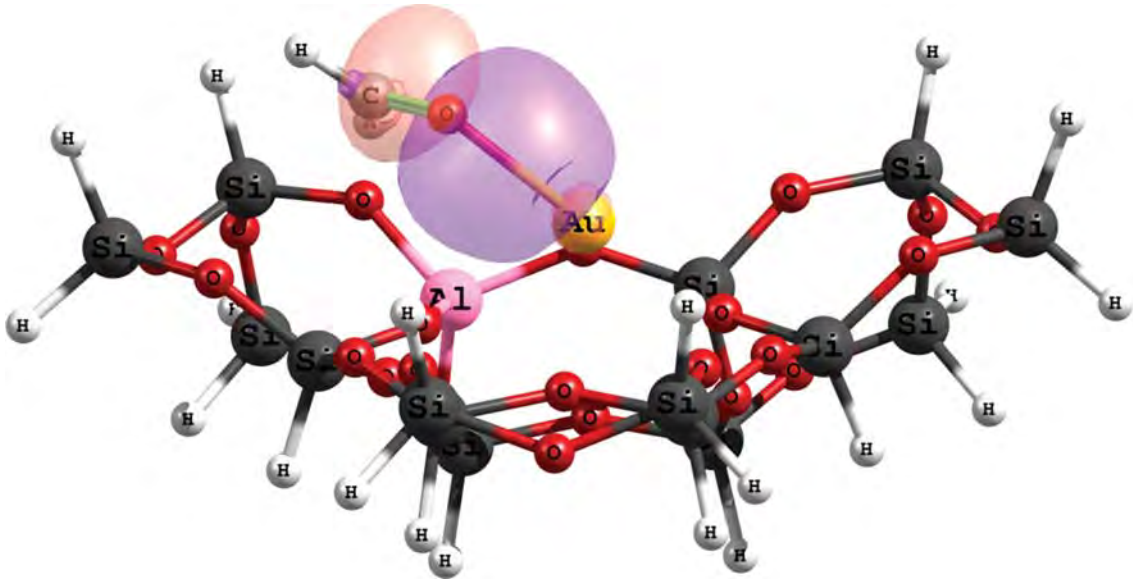


**Figure 3.** Illustration of the Au−O bonding character with contributions from (mostly) the 6s orbital of Au and the 2p orbital of the O atom. From the NBO calculations with the M06-L/6-31G(d,p) method.

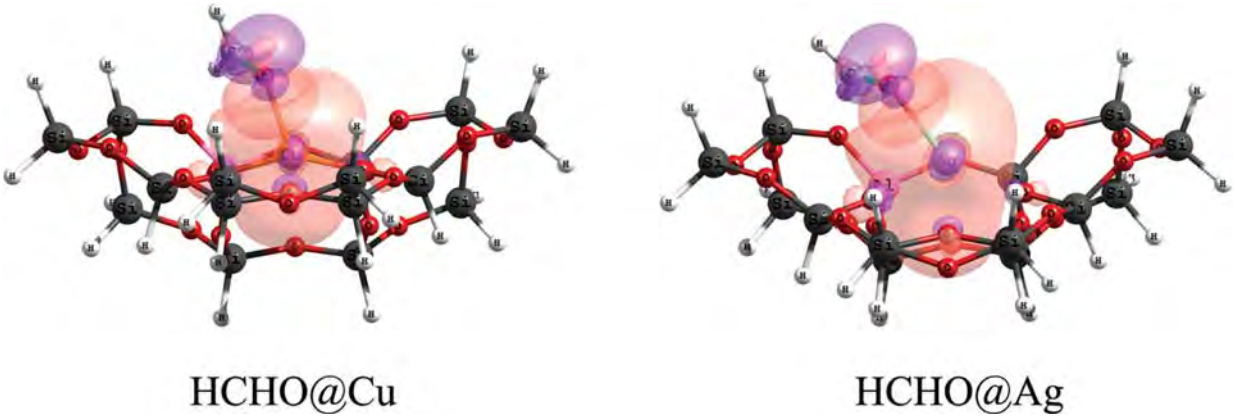


**Figure 4.** Illustration of the interaction between the 2p orbital of formaldehyde and the 4s orbital of Cu (left)/the 5s orbital of the Ag (right), analyzed from the NBO calculation with the M06-L/6-31G(d,p) method. The isosurface value is ±0.03 au.

the relativistic effect of a heavy metal atom like Au. Moreover, this may be the origin of the shorter length of the Au−O bond (2.26 Å) compared with the Ag−O bond (2.36 Å). The short Cu−O bond (2.07 Å) might originate from the smallest cation size of Cu when compared to that of others. The charge of the formaldehyde carbon atom was found to be +0.308e, +0.259e, and +0.327e in the Cu-, Ag-, and Au-FAU system, respectively. This indicates that Au-FAU causes the formaldehyde molecule to become an active electrophile, as a result the carbon of the HCHO@Au-FAU system favors the nucleophilic attack of another molecule.

An attempt has been made for predicting the carbonyl (CO) stretch vibrational frequencies of formaldehyde and its complexes with different Cu-, Ag-, and Au-FAU zeolites. Without scaling factors, our calculated CO vibrational frequencies of metal(I)/FAU complexes are predicted to be 1723, 1784, and 1747 $cm^{-1}$ for Cu-FAU, Ag-FAU, and Au-FAU, respectively. For all the studied complexes, the carbonyl (CO) stretch vibration is red-shifted by 85−146 $cm^{-1}$ with respect to the CO vibrational frequency (1869 $cm^{-1}$) in formaldehyde (cf. Table S4, Supporting Information). These values are higher than those calculated and experimental values for Cu and Ag embedded in other related types of zeolite, i.e., Cu and Ag-ZSM-5 reported by Datka et al.[58,59] However, our calculated C−O distances are longer for Cu- and Ag-FAU cases. This reflects one of the reasons the frequencies of our FAU zeolite are over shifted when compared to those values obtained from ZSM-5.

Metal cations without the zeolite structure (bare-metal cations) were investigated for comparison. The metal cations bind to the formaldehyde molecule with adsorption energies of −48.8, −32.2, and −38.8 kcal/mol for $Cu^+$, $Ag^+$, and $Au^+$, respectively. These energies correspond to the distance between the metal and the oxygen atom of the formaldehyde molecule, where Cu−O < Au−O < Ag−O (1.88, 2.20, and 2.23 Å). When the cations are adsorbed on the zeolite framework, the adsorption energies do not follow this trend due to the compensation

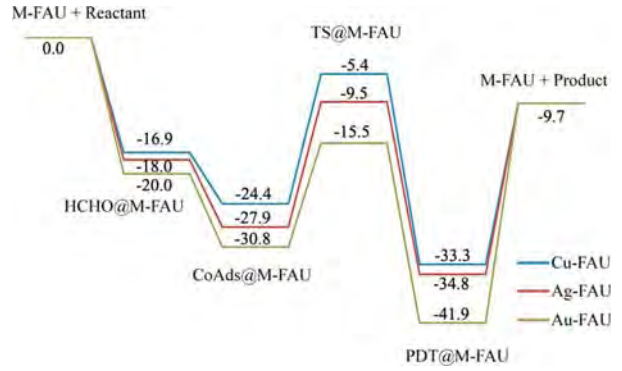


**Figure 5.** Zero-point corrected energy profiles of the reaction calculated by the 16T M06-L/6-31G(d,p) level of theory (all energies in kcal/mol).

charge transfer between the metals and the zeolite that we mentioned above. However, a large charge transfer character between formaldehyde and metal exchanged zeolite is still exhibited for the Au-FAU; it provides the highest adsorption energy. This indicated a good encapsulation capability of the formaldehyde even in a charge transferable solid support.

**3.3. Carbonyl-ene Reaction between Encapsulated Formaldehyde in Metal-FAU and Propene.** After the formaldehyde encapsulation, the reaction is followed by the coadsorption of propene to the encapsulated complex and then by a concerted transition state. The energetic reaction profile is summarized in Figure 5. In the coadsorption step, the propene bound to the encapsulated formaldehyde with the coadsorption energy increases by ~10 kcal/mol compared to the formaldehyde adsorption energies in all cases. The charge of the formaldehyde carbon atom is +0.217e, +0.266e, and +0.284e for the Cu-, Ag-, and Au-FAU, respectively. This again indicates that the formaldehyde carbon atom of the Au-FAU is ready to be attacked by the nucleophilic group. Propene and the encapsulated formaldehyde form a concerted transition structure in which new C−C1 and O−H bonds are formed simultaneously and the C3−H bond breaks (Table S1).

The C−O bond of formaldehyde is elongated from 1.23 Å to about 1.35 Å for the Cu and Ag systems whereas the one of the Au system is longer, 1.38 Å. This is compatible with the lowest activation energy for the reaction in Au-FAU, 15.3 kcal/mol, compared to 19.0 and 18.5 kcal/mol of that in Cu- and Ag-FAU, respectively. These results correlate well with the study of the same reaction with several Lewis acid catalysts by Yang et al.[60] They found that an electron withdrawing group at the formaldehyde C atom (providing a higher positive charge of the C atom) leads to a lower activation barrier for the reaction. In our case, the formaldehyde C atom is strongly induced to be highly positive by the metal cations. Moreover, these authors also showed that a more positive charge of the secondary C atom of propene, at the transition state, corresponds to a lower activation barrier. From our calculations, the charges of the propene secondary C atom at the transition state were +0.077e, +0.052e, and +0.157e for the Cu-, Ag-, and Au-FAU systems, respectively. The NBO analysis illustrates that the occupancy of the Au atom is almost unchanged when the propene is coadsorbed. Interestingly, the 6s orbital of the Au atom gains a significant occupation, from 0.45e to 0.59e, whereas the occupancies of Cu and Ag atoms remain almost unchanged when the reaction crosses the transition state.

**Table 2. Relative Energies with Respect to the Reactants of the Systems and Desorption Energies ($E_{des}$) and Activation Energies ($E_a$) Calculated with 16T/M06-L/6-31G(d,p), 120T/M06-L/6-31G(d,p)//16T/M06-L/6-31G(d,p), and Bare-Metal Systems//16T/M06-L/6-31G(d,p) without Zero-Point Energy Corrections**

| | relative energies (kcal/mol) | | | | | | | | |
|---|---|---|---|---|---|---|---|---|---|
| | Cu-FAU | | | Ag-FAU | | | Au-FAU | | |
| | 16T | 120T | bare | 16T | 120T | bare | 16T | 120T | bare |
| Ads | −16.5 | −20.0 | −45.0 | −19.0 | −21.1 | −30.0 | −21.6 | −24.5 | −37.7 |
| CoAds | −27.3 | −32.7 | −58.2 | −30.6 | −34.2 | −41.7 | −33.9 | −38.1 | −52.6 |
| TS | −8.4 | −15.4 | −49.3 | −12.5 | −17.0 | −29.5 | −18.9 | −25.1 | −46.6 |
| PDT | −39.7 | −48.3 | −72.1 | −41.0 | −46.2 | −56.0 | −48.8 | −55.1 | −65.2 |
| $E_{des}$ | 24.7 | 33.3 | 57.1 | 26.0 | 31.2 | 41.0 | 33.8 | 40.1 | 50.2 |
| $E_a$ | 18.9 | 17.4 | 8.8 | 18.0 | 17.2 | 12.2 | 15.0 | 13.0 | 6.1 |

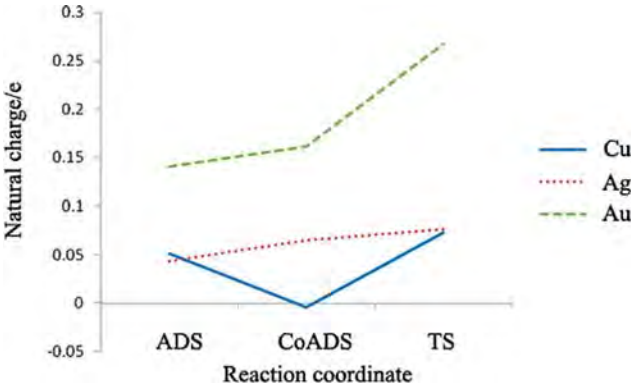


**Figure 6.** Evolution of the charge of the probe molecules (formaldehyde and propene) along the reaction coordinate.

Consequently, the relativistic effect, which can be inferred from the 6s orbital of the Au atom, might play an important role in the high activity of the Au system. The Au-FAU might have a problem with a high desorption energy (Table 2) when the full catalytic cycle is considered. However, we suggest that the catalyst that is active for this kind of reaction should have a character of high charge transfer to stabilize and activate the formaldehyde monomer.

We furthermore analyze the charges of the probe molecules bound to the metal-FAU systems (Table 1). The results show that the Au atom induces the highest charge of the probe molecules, in all cases and especially for the transition state, where the charge is +0.268e. With the Cu and Ag cations, the metals cannot induce charges of more than +0.100e in an elementary step. The charge evolution during the reaction pathway is shown in Figures 6 and 7.

**3.4. Zeolite Framework Effect.** In studies of zeolite systems, the framework effect, which contributes the confining van der Waals interactions, is found to be one of the important keys for understanding the adsorption phenomena and the catalytic activity. The extended 120T of the supercage structure of the faujasite zeolite was used for single point calculations to study the effects of the framework. The relative energies of the systems involved in the reaction are summarized in Table 2. We find that all systems are stabilized by the zeolite framework. Interestingly,

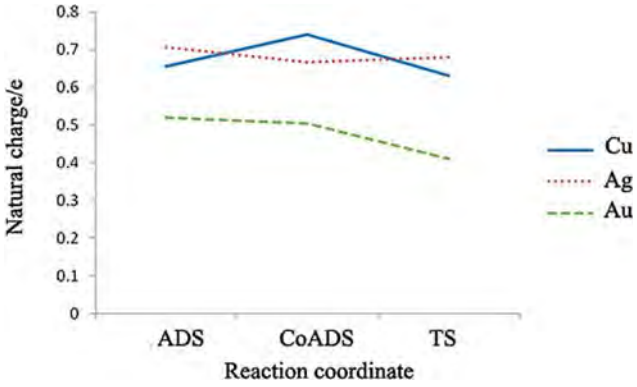


**Figure 7.** Evolution of the charge of the metal atoms along the reaction coordinate.

the Au-FAU framework structure reduces the activation barrier to only 13.0 kcal/mol and those of the Cu- and Ag-FAU systems remain around 17 kcal/mol (Table 2). This is consistent with a large induced charge flow from the Au atom and with the observation that the zeolite framework is more effective when the reaction proceeds via the ion pair intermediate.[48,61−65] From these results, one can state that the Au cation should work well for reactions promoted by Lewis acids in zeolite frameworks.

We also investigated systems without a zeolite framework. To avoid the effect of structural differences, single point calculations were performed on the optimized structures, but only with the metals and probe fragments (Table 2). The adsorption energies of the formaldehyde on the bare cations (−45.0, −30.0, and −37.7 kcal/mol for Cu, Ag, and Au) were found to be close to the optimized ones (−48.8, −32.2, and −38.8 kcal/mol). In comparison with our previous calculation on the bare-$Cu^+$ with the B3LYP functional,[15] we found that the single point calculations for the energetic profile of the $Cu^+$ ion were almost the same as the optimized one with B3LYP, especially the relative energy of the transition state (∼−49 vs −50 kcal/mol). This indicates that the structural difference does not affect the energetic properties as much as the effect of the charge compensation mentioned above. The activation energies of the extreme cases of metal cation systems were calculated to be 8.8, 12.2, and 6.1 kcal/mol for the $Cu^+$, $Ag^+$, and $Au^+$, respectively. Therefore, it can be concluded that the $Au^+$ ion shows a high activity for this reaction even after charge distribution between the cation and the zeolite occurred.

**3.5. Comparison with the Na-FAU and MOF-11 Systems.** From our previous study of the Na-exchanged FAU zeolite, we found that this alkaline exchanged zeolite can reduce the activation barrier from ∼34 kcal/mol for the uncatalyzed process to ∼25 kcal/mol. In comparison, the adsorption and coadsorption energies of the Na-FAU system were close to the results obtained for the transition metal exchanged systems. However, the transition metals provided higher activities by lowering the energy of the transition state, especially for the Au-FAU system. In contrast to the transition metals, the charge of Na was almost unchanged (∼+0.9e) during the whole reaction pathway whereas the charge transfers between the metals and probes are known to play an important role in the activity of transition metal exchanged zeolites.

The Cu site of the MOF-11 has also been used to catalyze this reaction. However, the activation energy was ∼24 kcal/mol whereas that of the bare $Cu^+$ ion was only 6.4 kcal/mol. This indicates that the MOF-11 structure cannot retain the high activity of the $Cu^+$ ion. In this work, the zeolite structure was found to be the more appropriate structure for loaded metal to catalyze this kind of reaction.

## 4. CONCLUSION

The carbonyl-ene reaction over Cu-, Ag-, and Au-exchanged FAU zeolites was investigated in quantum mechanical calculations with an efficient functional, M06-L. The $Au^+$ ion exhibits a high performance in the formaldehyde encapsulation process and shows a high catalytic activity. By analyzing the electronic configuration, we demonstrated that the 6s orbital of the Au atom plays an important role in this interestingly high activity: It accepts an electron and induces a large charge in the probe molecules. This inductive effect is enhanced by the framework of zeolite. Although the activity of the Cu- and Ag-FAU was not as high as that of the Au-FAU, the zeolite structures are suitable for use as a catalyst for this type of reaction. Moreover, these transition metals provide a higher activity than that of the alkaline-exchanged zeolites, which showed no significant charge transfer. In summary: the cation, which can maintain a charge transfer even in the presence of a charge compensating support is the most appropriate one for this reaction. From our results, we suggest that the Au-exchanged zeolites could be a potential catalyst for this type of reactions. However, the problem of high desorption energy should be improved for industrial applications.

## ■ ASSOCIATED CONTENT

**Supporting Information.** Optimized geometries, electronic structures, zero-point energies, and vibrational frequencies. This information is available free of charge via the Internet at http://pubs.acs.org.

## ■ AUTHOR INFORMATION

**Corresponding Author**

*E-mail: jumras.l@ku.ac.th. Tel: +66-2-562-5555, ext 2159.

## ■ ACKNOWLEDGMENT

This work was supported in part by grants from the National Science and Technology Development Agency (NSTDA Chair Professor and NANOTEC Center of Excellence), the Thailand Research Fund (to J.L.), the Kasetsart University Research and Development Institute (KURDI), the Commission on Higher Education, Ministry of Education ("the National Research University Project of Thailand (NRU)" and "Postgraduate Education and Research Programs in Petroleum and Petrochemicals and Advanced Materials"), and by a grant under the Royal Golden Jubilee Ph.D. program from the Thailand Research Fund (to S.W.). The Graduate School, Kasetsart University, is also acknowledged. The authors are grateful to Donald G. Truhlar and Yan Zhao for supplying them with the code for the M06-L functional.

## ■ REFERENCES

(1) Hoffmann, H. M. R. *Angew. Chem., Int. Ed. Engl.* **1969**, *8*, 556–577.

(2) Oppolzer, W.; Snieckus, V. *Angew. Chem., Int. Ed.* **1978**, *17*, 476–486.
(3) Yamanaka, M.; Mikami, K. *Helv. Chim. Acta* **2002**, *85*, 4264–4271.
(4) Düren, T.; Sarkisov, L.; Yaghi, O. M.; Snurr, R. Q. *Langmuir* **2004**, *20*, 2683–2689.
(5) Eddaoudi, M.; Kim, J.; Rosi, N.; Vodak, D.; Wachter, J.; O'Keeffe, M.; Yaghi, O. M. *Science* **2002**, *295*, 469–472.
(6) Frost, H.; Snurr, R. Q. *J. Phys. Chem. C* **2007**, *111*, 18794–18803.
(7) Furukawa, H.; Ko, N.; Go, Y. B.; Aratani, N.; Choi, S. B.; Choi, E.; Yazaydin, A. O.; Snurr, R. Q.; O'Keeffe, M.; Kim, J.; et al. *Science* **2010**, *329*, 424–428.
(8) Li, H.; Eddaoudi, M.; O'Keeffe, M.; Yaghi, O. M. *Nature* **1999**, *402*, 276–279.
(9) Rosi, N. L.; Eckert, J.; Eddaoudi, M.; Vodak, D. T.; Kim, J.; O'Keeffe, M.; Yaghi, O. M. *Science* **2003**, *300*, 1127–1129.
(10) Rowsell, J. L. C.; Yaghi, O. M. *Microporous Mesoporous Mater.* **2004**, *73*, 3–14.
(11) Yaghi, O. M.; O'Keeffe, M.; Ockwig, N. W.; Chae, H. K.; Eddaoudi, M.; Kim, J. *Nature* **2003**, *423*, 705–714.
(12) Okachi, T.; Onaka, M. *J. Am. Chem. Soc.* **2004**, *126*, 2306–2307.
(13) Tomita, M.; Masui, Y.; Onaka, M. *J. Phys. Chem. Lett.* **2010**, *1*, 652–656.
(14) Sangthong, W.; Probst, M.; Limtrakul, J. *J. Mol. Struct.* **2005**, *748*, 119–127.
(15) Choomwattana, S.; Maihom, T.; Khongpracha, P.; Probst, M.; Limtrakul, J. *J. Phys. Chem. C* **2008**, *112*, 10855–10861.
(16) Zhang, Y.; Bell, A. T. *J. Catal.* **2008**, *255*, 153–161.
(17) Zhang, Y.; Briggs, D. N.; de Smit, E.; Bell, A. T. *J. Catal.* **2007**, *251*, 443–452.
(18) Zhang, Y.; Drake, I. J.; Briggs, D. N.; Bell, A. T. *J. Catal.* **2006**, *244*, 219–229.
(19) Zheng, X.; Bell, A. T. *J. Phys. Chem. C* **2008**, *112*, 5043–5047.
(20) Baba, T.; Iwase, Y.; Inazu, K.; Masih, D.; Matsumoto, A. *Microporous Mesoporous Mater.* **2007**, *101*, 142–147.
(21) Sakurai, H.; Tsunoyama, H.; Tsukuda, T. *J. Organomet. Chem.* **2007**, *692*, 368–374.
(22) Tsunoyama, H.; Sakurai, H.; Ichikuni, N.; Negishi, Y.; Tsukuda, T. *Langmuir* **2004**, *20*, 11293–11296.
(23) Mohamed, M. M.; Salama, T. M.; Ichikawa, M. *J. Colloid Interface Sci.* **2000**, *224*, 366–371.
(24) Mohamed, M. M.; Salama, T. M.; Ohnishi, R.; Ichikawa, M. *Langmuir* **2001**, *17*, 5678–5684.
(25) Qiu, S.; Ohnishi, R.; Ichikawa, M. *J. Phys. Chem.* **1994**, *98*, 2719–2721.
(26) Fierro-Gonzalez, J. C.; Gates, B. C. *J. Phys. Chem. B* **2004**, *108*, 16999–17002.
(27) Gao, Z. X.; Sun, Q.; Chen, H. Y.; Wang, X.; Sachtler, W. M. H. *Catal. Lett.* **2001**, *72*, 1–5.
(28) Salama, T. M.; Shido, T.; Ohnishi, R.; Ichikawa, M. *J. Chem. Soc., Chem. Commun.* **1994**, 2749–2750.
(29) Qiu, S.; Ohnishi, R.; Ichikawa, M. *J. Chem. Soc., Chem. Commun.* **1992**, 1425–1427.
(30) Deka, A.; Deka, R. C.; Choudhury, A. *Chem. Phys. Lett.* **2010**, *490*, 184–188.
(31) Griffe, B.; Brito, J. L.; Sierraalta, A. *J. Mol. Catal. A: Chem.* **2010**, *315*, 28–34.
(32) Sierraalta, A.; Alejos, P.; Ehrmann, E.; Rodriguez, L. J.; Ferrer, Y. *J. Mol. Catal. A: Chem.* **2009**, *301*, 61–66.
(33) Sierraalta, A.; Hernandez-Andara, R.; Ehrmann, E. *J. Phys. Chem. B* **2006**, *110*, 17912–17917.
(34) Sierraalta, A.; Alejos, P.; Ehrmann, E. *Int. J. Quantum Chem.* **2008**, *108*, 1696–1704.
(35) Sierraalta, A.; Añez, R.; Diaz, L.; Gomperts, R. *J. Phys. Chem. A* **2010**, *114*, 6870–6878.
(36) Zhao, Y.; Truhlar, D. G. *J. Chem. Phys.* **2006**, *125*, 194101–194118.
(37) Zhao, Y.; Truhlar, D. G. *Acc. Chem. Res.* **2008**, *41*, 157–167.
(38) Zhao, Y.; Truhlar, D. G. *Theor. Chem. Acc.* **2008**, *120*, 215–241.
(39) Olson, D. H.; Dempsey, E. *J. Catal.* **1969**, *13*, 221–231.
(40) Drake, I. J.; Zhang, Y.; Gilles, M. K.; Teris Liu, C. N.; Nachimuthu, P.; Perera, R. C. C.; Wakita, H.; Bell, A. T. *J. Phys. Chem. B* **2006**, *110*, 11665–11676.
(41) Dolg, M.; Wedig, U.; Stoll, H.; Preuss, H. *J. Chem. Phys.* **1986**, *86*, 866–872.
(42) Valero, R.; Gomes, J. R. B.; Truhlar, D. G.; Illas, F. *J. Chem. Phys.* **2008**, *129*, 124710.
(43) Valero, R.; Gomes, J. R. B.; Truhlar, D. G.; Illas, F. *J. Chem. Phys.* **2010**, *132*, 124710.
(44) Valero, R.; Costa, R.; De P. R. Moreira, I.; Truhlar, D. G.; Illas, F. *J. Chem. Phys.* **2008**, *128*, 114103.
(45) Zhao, Y.; Truhlar, D. G. *J. Phys. Chem. C* **2008**, *112*, 6860–6868.
(46) Zhao, Y.; Truhlar, D. G. *J. Chem. Theory Comput.* **2009**, *5*, 324–333.
(47) Zheng, J.; Zhang, S.; Truhlar, D. G. *J. Phys. Chem. A* **2008**, *112*, 11509–11513.
(48) Boekfa, B.; Choomwattana, S.; Khongpracha, P.; Limtrakul, J. *Langmuir* **2009**, *25*, 12990–12999.
(49) Kumsapaya, C.; Bobuatong, K.; Khongpracha, P.; Tantirungrotechai, Y.; Limtrakul, J. *J. Phys. Chem. C* **2009**, *113*, 16128–16137.
(50) Maihom, T.; Boekfa, B.; Sirijaraensre, J.; Nanok, T.; Probst, M.; Limtrakul, J. *J. Phys. Chem. C* **2009**, *113*, 6654–6662.
(51) Maihom, T.; Pantu, P.; Tachakritikul, C.; Probst, M.; Limtrakul, J. *J. Phys. Chem. C* **2010**, *114*, 7850–7856.
(52) Wannakao, S.; Boekfa, B.; Khongpracha, P.; Probst, M.; Limtrakul, J. *ChemPhysChem* **2010**, *11*, 3432–3438.
(53) Gonzalez, C.; Schlegel, H. B. *J. Chem. Phys.* **1989**, *90*, 2154–2161.
(54) Schlegel, H. B. *J. Comput. Chem.* **1982**, *3*, 214–218.
(55) Reed, A. E.; Curtiss, L. A.; Weinhold, F. *Chem. Rev.* **1988**, *88*, 899–926.
(56) Reed, A. E.; Weinhold, F. *J. Chem. Phys.* **1983**, *78*, 4066–4073.
(57) Frisch, M. J.; Trucks, G. W.; Schlegel, H. B.; Scuseria, G. E.; Robb, M. A.; Cheeseman, J. R.; Montgomery, J. A., Jr; Vreven, T.; Kudin, K. N.; Burant, J. C.; Millam, J. M.; Iyengar, S. S.; Tomasi, J.; Barone, V.; Mennucci, B.; Cossi, M.; Scalmani, G.; Rega, N.; Petersson, G. A.; Nakatsuji, H.; Hada, M.; Ehara, M.; Toyota, K.; Fukuda, R.; Hasegawa, J.; Ishida, M.; Nakajima, T.; Honda, Y.; Kitao, O.; Nakai, H.; Klene, M.; Li, X.; Knox, J. E.; Hratchian, H. P.; Cross, J. B.; Adamo, C.; Jaramillo, J.; Gomperts, R.; Stratmann, R. E.; Yazyev, O.; Austin, A. J.; Cammi, R.; Pomelli, C.; Ochterski, J. W.; Ayala, P. Y.; Morokuma, K.; Voth, G. A.; Salvador, P.; Dannenberg, J. J.; Zakrzewski, V. G.; Dapprich, S.; Daniels, A. D.; Strain, M. C.; Farkas, O.; Malick, D. K.; Rabuck, A. D.; Raghavachari, K.; Foresman, J. B.; Ortiz, J. V.; Cui, Q.; Baboul, A. G.; Clifford, S.; Cioslowski, J.; Stefanov, B. B.; Liu, G.; Liashenko, A.; Piskorz, P.; Komaromi, I.; Martin, R. L.; Fox, D. J.; Keith, T.; Al-Laham, M. A.; Peng, C. Y.; Nanayakkara, A.; Challacombe, M.; Gill, P. M. W.; Johnson, B.; Chen, W.; Wong, M. W.; Gonzalez, C.; Pople, J. A. *Gaussian 03*, revision B.05; Gaussian, Inc.: Pittsburgh, PA, 2003.
(58) Datka, J.; Kozyra, P.; Kukulska-Zajac, E.; Kobyzewa, W. *Catal. Today* **2005**, *101*, 117–122.
(59) Broclawik, E.; Zalucka, J.; Kozyra, P.; Mitoraj, M.; Datka, J. *Catal. Today* **2011**, *169*, 45–51.
(60) Yang, Q.; Tong, X.; Zhang, W. *J. Mol. Struct. (THEOCHEM)* **2010**, *957*, 84–89.
(61) Injan, N.; Pannorad, N.; Probst, M.; Limtrakul, J. *Int. J. Quantum Chem.* **2005**, *105*, 898–905.
(62) Boekfa, B.; Pantu, P.; Limtrakul, J. *J. Mol. Struct.* **2008**, *889*, 81–88.
(63) Jansang, B.; Nanok, T.; Limtrakul, J. *J. Mol. Catal. A: Chem.* **2007**, *264*, 33–39.
(64) Maihom, T.; Namuangruk, S.; Nanok, T.; Limtrakul, J. *J. Phys. Chem. C* **2008**, *112*, 12914–12920.
(65) Sirijaraensre, J.; Limtrakul, J. *Phys. Chem. Chem. Phys.* **2009**, *11*, 578–585.

# THE VERSATILE SYNTHESIS METHOD FOR HIERARCHICAL MICRO- AND MESOPOROUS ZEOLITE: AN EMBEDDED NANOCARBON CLUSTER APPROACH

**Chularat Wattanakit[1,3,4], Chompunuch Warakulwit[1,3,4], Piboon Pantu[1,3,4], Boonruen Sunpetch[1,3,4], Metta Charoenpanich[2,3,4], Jumras Limtrakul[1,3,4*]**

[1]Department of Chemistry, Faculty of Science and Center of Nanotechnology, Kasetsart University Research and Development Institute, Kasetsart University, Bangkok 10900, Thailand

[2]Department of Chemical Engineering, Faculty of Engineering, Kasetsart University, Bangkok 10900,Thailand

[3]NANOTEC Center of Excellence, National Nanotechnology Center, Kasetsart University, Bangkok 10900, Thailand

[4]Center for Advanced Studies in Nanotechnology and Its Applications in Chemical, Food and Agricultural Industries, Kasetsart University, Bangkok 10900, Thailand

**Corresponding author's e-mail address:** jumras.l@ku.ac.th

***Abstract***. *In this work, we are reporting for the first time the synthesis of hierarchical micro- and mesoporous zeolite by using silica-carbon ($SiO_2$/C) composites prepared by pyrolysis of carbonaceous gases in the presence of silica gel. The pyrolysis effectively yielded carbon deposited onto the raw silica material. The obtained $SiO_2$/C composites were utilized as a bifunctional material, mesoporous template and silica source, for the zeolite synthesis. Tetrapropylammonium hydroxide (TPAOH) was used as a microporous template. The combination of the obtained composites and the TPAOH for the hydrothermal synthesis resulted in the formation of hierarchical micro- and mesoporous ZSM-5. The results from the SEM, TEM, and $N_2$ adsorption/desorption isotherms, and $^{27}$Al MAS NMR chracterizations of the synthesized samples obtained after the removal of the templates confirmed the successful formation of the micro- and mesoporous zeolites. The mesoporosity of the zeolites could be controlled by adjusting the carbon content in the $SiO_2$/C composites while the carbon content could be controlled by varying the deposition time and the concentration of the carbonaceous gases used. This controllable and efficient synthesis method is considered to be a promising method for creating hierarchical micro- and mesoporous zeolites.*

***Keywords:*** *Micro/mesoporous zeolite, ZSM-5, pyrolysis of carbonaceous gases, solid templating*

## INTRODUCTION

Zeolites have been widely used in the petrochemistry industry in a large number of applications such as cracking (Kung et al., 2000), isomerization (Houžvička et al., 1996; Trombetta et al., 1998) and hydrocarbon alkylation (Marcilly, 2000; Tanabe and Hölderich, 1999) due to their shape-selectivity, high thermal stability and suitable acidic properties (Beyerlein et al., 1988; Van Santen and Kramer, 1995). With reference to microporous zeolites (owing to their pore size being less than 2 nm, by IUPAC definition (Sing et al., 1985) or conventional zeolites, the active sites are located inside framework channels which play an important role for the shape-selective catalytic reaction. Based on such selectivity, the transformation of large reactant molecules or reactant molecules that yield large transition states and/or products could not succeed inside the micropores of conventional zeolites. Furthermore, the conventional zeolite catalysts also impose mass transfer limitations due to their micropore system. To overcome this problem, the combination of microporous and mesoporous characteristics within the structure of zeolites could be an alternative way to improve, not only, the viability to catalyze the reactions involving bulky reactants but also the viability to catalyze the reactions that involve the bulky transition states and/or products.

Hierarchical zeolites with networks of various pore sizes, i.e., micropore (< 2 nm), mesopore (2-50 nm) and macropore (> 50 nm), have attracted much attention as a result of their highly attractive properties, including superior mass/heat transfer characteristics (Ocampo et al., 2009; Zheng et al., 2009), enhanced resistance of the deactivation of the catalyst (Zhu et al., 2008), and lower restriction of the diffusion of molecules in the mesopores, which is mentioned above. Generally, the hierarchical dual micro- and mesoporous zeolites can be prepared by two approaches, non-templated (Groen et al., 2006; Pérez-Ramírez et al., 2009; Tao et al., 2006) and templated approaches (Egeblad et al., 2007; Jacobsen et al., 2000a; Kim et al., 2003; Perez-Ramirez et al., 2008; Tao et al., 2006; Xiao et al., 2006). For the former one, hierarchical zeolites are obtained by post synthesis treatments, e.g., extraction of metal atoms (demetalation) or silicon atoms (desilication) (Groen et al., 2006; Pérez-Ramírez et al., 2009; Tao et al., 2006). Nevertheless, these methods usually have some disadvantages, such as the required strong condition (due to the high stability of the zeolite structure) and difficulty in controlling the pore size (Egeblad et al., 2007). For the latter approach, the methods used can be mainly classified into three categories in terms of solid templating, supramolecular templating, and indirect templating (Egeblad et al., 2007). For the two previous cases, the porous structure of the zeolites is formed directly by solid or soft templates. For the case of indirect templating, the porous structure is formed indirectly by a controlled deposition of a zeolite onto a template material (Verhoef et al., 2001). Because the high purity

zeolite phase can be obtained by the direct templating method, various solid materials including carbon nanomaterials (Jacobsen et al., 2000a; Janssen et al., 2003; Perez-Ramirez et al., 2008; Schmidt et al., 2001), colloidal imprinted carbons (Kim et al., 2003), carbon aerogels (Tao et al., 2006), polymers (Wang et al., 2010; Xiao et al., 2006; Zhu et al., 2008), resins (Tosheva et al., 2000), solid biological templates (Davis et al., 1998) and various types of organized assemblies of surfactant templates (Mukti et al., 2009) have been used.

Compared with soft templates, it is generally known that hard templates have high confinement ability derived from their rigid structure (Tosheva et al., 2000). In addition, they usually contain many pore channels leading to the formation of zeolite with high porosity (Tosheva et al., 2000). Much attention has been focused on the synthesis of hierarchical zeolite by using carbon templates because either nanosized crystals or mesoporous zeolite single crystals with tunable porosity can be obtained simply by using porous carbon templates. The nanosized crystals can be produced in the confined space of porous carbons with little or no encapsulation of the carbon materials during synthesis (Tao et al., 2006) or in the voids of carbon blacks (Jacobsen et al., 2000a; Kustova et al., 2007) and carbon aerogels (Tao et al., 2005). While mesoporous zeolites can be produced by encapsulation of porous carbon materials during synthesis. After removal of the embedded carbon matrix, porous zeolites can be obtained (Jacobsen et al., 2000a). Nevertheless, it is possible to obtain a combination of nanosized and hierarchical mesoporous zeolite (Egeblad et al., 2007).

Recently, Kustova *et al.* (Kustova et al., 2007) prepared a hierarchical zeolite by using a silica-carbon composite from the decomposition of a sucrose solution which impregnated onto a silica raw material. Sequentially, the mesoporous zeolites were obtained after zeolite crystallization and combustion of the carbon residue. This method significantly extends the scope of the solid templating approach, a simple and inexpensive method. However, zeolites with low mesoporosity were obtained. This might be due to poorly dispersed sugar during the impregnation. Thus, the development of such a synthetic method remains a challenge. To the best our knowledge, the use of a silica-carbon ($SiO_2$/C) composite prepared by a pyrolysis of the carbonaceous gas has not previously been reported for the preparation of mesoporous zeolites. Herein, we approach this challenge and report for the first time the synthesis of hierarchical micro- and mesoporous ZSM-5 zeolites by using the $SiO_2$/C composites that were prepared by pyrolysis of carbonaceous gases in the presence of silica gel under an inert ambient. We believed that such pyrolysis could effectively improve the carbon deposition onto the silica yielding a good formation of hierarchical micro- and mesoporous zeolites.

# EXPERIMENTAL SECTION

## 1. MATERIALS

For the synthesis of zeolites, the chemicals used were silica gel with a particle size of 0.063-0.200 mm and pore volume of 1.0 $cm^3/g$ (Merck, silica gel 100), NaOH (Carlo Erba), tetrapropylammonium hydroxide (TPAOH, 20 wt%, Fluka), $NaAlO_2$ (Riedel-de Haën), acetylene ($C_2H_2$, 99.9%, Praxair), propane ($C_3H_8$, 99.5%, BOC Scientific) and nitrogen gas ($N_2$, 99.999%, Praxair). All chemicals were used as received without further purification.

## 2. PREPARATION OF BIFUNCTIONAL CARBONIZED SILICA ($SiO_2$/C COMPOSITES)

The carbon/silica composites were prepared by pyrolyses of carbonaceous gas (acetylene or propane, $C_xH_y$) over silica gel. Typically, for each synthesis, 5 g of silica gel was introduced into the middle zone of a fixed-bed tubular reactor. Nitrogen gas ($N_2$) was then introduced into the reactor with a flow rate of 180 or 190 ml/min depending on the desired concentration of the reactant gas. Nitrogen gas easily displaced air and therefore it formed an inert atmosphere in the chamber. The reactor temperature was gradually increased to 1123 K under the nitrogen flow. After that, the reactant gas ($C_xH_y$) was introduced into the reactor. The gas mixture concentration was 5 or 10 v/v% of $C_xH_y$ in $N_2$ with a total flow rate of 200 ml/min. After 1 or 2 h, the $C_xH_y$ flow was stopped. The work tube was cooled down to room temperature under the nitrogen flow. The obtained carbon/silica composites were used as bifunctional materials for the zeolite syntheses. The silica gel part of the composites was used as a silica source of the zeolites. The carbon residue formed in the composite was used as a template for the mesopores of the zeolites.

## 3. HYDROTHERMAL SYNTHESIS OF HIERARCHICAL MICRO- AND MESOPOROUS ZSM-5

$NaAlO_2$ was used as an alumina source. TPAOH was used as a structure-directing agent for the ZSM-5 micropores. The molar composition of the synthetic gel was 1 $Al_2O_3$ : 181 $SiO_2$ : 36 $TPA_2O$ : 15 $Na_2O$ : 1029 $H_2O$. Typically, for a synthesis, the aluminate solution was prepared by mixing 0.016 g of $NaAlO_2$ and 0.11 g of NaOH in 1.7 mL of deionized (DI) water. Then, the aluminate solution was then added into 6.77 g of 20 wt% of TPAOH in water under stirring. The mixture was stirred continuously until a clear solution was obtained. The prepared $SiO_2$/C composite (1 g of $SiO_2$) was sequentially added into the solution. The obtained mixture was then transferred into a Teflon-lined stainless-steel autoclave and then crystallized at 453K for 3 days. The resulting material was collected by filtration (using Whatman, No. 42 filter paper) and then washed with DI water until the pH of the filtrate was about 8. The obtained product was then dried at 383 K for 10 h. Finally, the organic template and the carbon particles were removed by calcination in air at 823 K for 20 h.

### 4. CHARACTERIZATIONS

Several different carbon contents in the $SiO_2$/C composite materials achieved by varying the concentration of the gas mixture and the pyrolysis time were investigated by a thermal gravimetric analysis (TGA). The textural properties of the composites were determined by using a $N_2$ adsorption/desorption isotherms analysis performed at 77 K on a Micromeritics ASAP 2010 instrument. For this characterization, the samples were degassed at 623 K in a vacuum for 20 hours before measurements were taken. The specific surface areas ($S_{BET}$) of the samples were calculated by the Brunauer-Emmett-Teller (BET) method. The total pore volume ($V_{tot}$) was estimated by measuring the amount of adsorbed nitrogen at 0.97 $P/P_0$. The *t*-plot method was used to calculate the micropore volume ($V_{micro}$). The volume of mesopore and macropore ($V_{meso+macro}$) was calculated from the difference between the $V_{tot}$ and $V_{micro}$ (Lippens and de Boer, 1965). The size distribution of the mesopores was obtained by applying a Barret-Jovner-Halenda (BJH) model (Barrett et al., 1951).

The MFI structure of the synthesized zeolites was confirmed by an X-Ray Diffraction (XRD) measurement performed on a Rigaku TTRAX III, 18kW diffractometer using Cu Kα radiation. The measurement was operated at an accelerating voltage of 30 kV and a current of 40 mA. The diffraction patterns were collected at 2θ angles ranging from 5° to 50° with a scan speed of 1.2 deg/min and a step size of 0.02 deg. The morphology of the samples was investigated by scanning electron microscopy (SEM, JEOL- JSM 6301F). The pores of the samples were observed by transmission electron microscopy (TEM, JEOL JEM-2010). The nature of the Al species in the zeolite framework was characterized by a $^{27}$Al magic-angle spinning (MAS) NMR spectroscopy ($^{27}$Al MAS NMR) was recorded at 78.20 MHz, using a Bruker Biospin (DPX-300, 300 MHz) spectrometer with a 2 μs pulse, 4 s delay time and 800 scans.

## RESULTS AND DISCUSSION

### 1. $SiO_2$/C COMPOSITES

The carbon content in the composites, “carbon (wt%)”, synthesized by using various experimental conditions measured by TGA analysis, is shown in Table 1. The amount of carbon deposited was found to correspond well with the deposition time and the concentration of hydrocarbon gas (acetylene and propane) used. Increasing the deposition time and the concentration of hydrocarbon gas resulted in increasing the carbon content. Therefore, it can be suggested that the amount of deposited carbon can be varied by simply varying the deposition time and concentration of carbonaceous gases. Furthermore, it was found that acetylene yielded a higher amount of carbon deposit than propane in the same experimental conditions. In the case of propane, in order to obtain the same carbon content as in the case of acetylene, a longer deposition time is required. For

example, in order to obtain about 10 wt% of carbon content, at the 5 v/v% of $C_xH_y$, the deposition time required for acetylene and propane were 60 and 120 min, respectively. Although propane has a higher molar ratio of carbon atoms than acetylene, its thermal stability during the pyrolysis process is higher than that of acetylene ($\Delta G_f^o$ of propane and acetylene are 45.72 and 40.62 kcal/mol at 1000 K, respectively (Alberty and Burmenko, 1986; Chao et al., 1973)), this results in less reactive and less carbon deposit when propane is utilized. The nature of carbon deposit on silica gel was investigated by XRD characterization (data is not shown). The crystalline peak was not found in the XRD pattern, indicating that such carbon deposit is amorphous carbon.

The textural properties, including the specific surface area calculated by the BET method ($S_{BET}$), the total pore volume ($V_{tot}$), the mesopore volume ($V_{meso}$), and the mesopore diameter ($D_{BJH}$) of the raw silica gel and the prepared $SiO_2$/C composites obtained by using the $N_2$ adsorption/desorption method are shown in Table 1. By using the *t*-plot method, the micropore volume ($V_{micro}$) was calculated to be nearly zero in all cases. The mean pore size obtained from the maximum BJH pore size distribution ($D_{BJH}$) of the starting silica gel was found to be ca. 11 nm. Its $N_2$ adsorption/desorption isotherms were of type IV (see Figure S1). Since parts of porosity could be obtained as the free space occurred as a result of carbon combustion during the calcination step. Thus, in order to clarify that the use of $SiO_2$/C composite significantly yielded mesoporosity rather than microporosity, the ratios of mesopore volume to micropore volume, $V_{meso+macro}/V_{micro}$ , were calculated for all zeolite samples and reported in Table 2. The significant increase of $V_{meso+macro}/V_{micro}$ ratios resulted from increasing the carbon content in the $SiO_2$/C composites, thus verifying that using $SiO_2$/C composite significantly yielded the mesopore formation rather than the micropore formation.

Due to the decrease of $V_{meso}$ and the appearance of the black color of the composites, it can be suggested that carbon was not only deposited inside the mesopores of the silica gel but also onto the outer surface of the silica gel. From the textural properties characterized by $N_2$ adsorption/desorption analysis, in the cases of acetylene, it was found that increasing the deposition time and the concentration of the reactant gas decreased the $V_{meso}$ of the silica gel. This result was in contrast to that of the propane cases where increasing the concentration of the reactant gas did not result significantly in the decreasing of the $V_{meso}$ of the silica gel (see 5% $C_3H_8$-120 min-$SiO_2$/C and 10% $C_3H_8$-120 min-$SiO_2$/C samples). The results indicated that carbon mainly deposited on the outer surface of silica gel in the case of propane (compared to that of acetylene). The values of $D_{BJH}$ were found to corresponding quite well with the $V_{meso}$ values.

## 2. HIERARCHICAL MICRO- AND MESOPOROUS ZSM-5 PREPARED FROM $SiO_2$/C COMPOSITES

### 2.1. POWDER X-RAY DIFFRACTION ( XRD)

The XRD pattern of the raw silica gel, a reference zeolite sample (commercial ZSM-5, ALSI-PENTA Zeolithe GmbH (APZ)), and the synthesized samples are shown in Figure 1. The pattern of the silica gel indicates the amorphous structure. The XRD patterns of the synthesized samples are comparable to that of the reference ZSM-5 confirming the characteristic of the MFI structure. In addition, it was observed that the diffraction peaks of the samples were sharp and contained a very low background signal. This indicated that the samples were synthesized with high crystallinity and purity.

### 2.2. SCANNING ELECTRON MICROSCOPY (SEM) AND TRANSMISSION ELECTRON MICROSCOPY (TEM)

The SEM and TEM images showing the morphology and the porosity of the selected zeolite samples (0% carbon-ZSM-5, 5% $C_2H_2$-60 min-ZSM-5, 5% $C_2H_2$-120 min-ZSM-5, and 10% $C_2H_2$-120 min-ZSM-5 samples) compared to those of the commercial ZSM-5 are shown in Figure 2 (see Figure S2 for 5% $C_3H_8$-120 min-ZSM-5, 10% $C_3H_8$-120 min-ZSM-5 samples). The commercial ZSM-5 had large crystal sizes of over than 4 μm (see Figure 2a). The SEM image of the sample 1 shows the formation of small well-faceted cubic zeolite crystals with the size widely distributed in the range of 150-400 nm (see Figure 2b). Because, under the synthesis conditions, the concentration of the structure-directing agent or TPAOH was high, it can thus be suggested that a large amount of nuclei could be formed leading to the formation of small crystals. The sample prepared by using of the $SiO_2$/C composite with low carbon content of about 10 wt% comprised nearly cubic crystals with the size of about 200-500 nm (see Figure 2c). In the case of the synthesized micro- and mesoporous ZSM-5 obtained by using the $SiO_2$/C composites with high carbon content, e.g., 5% $C_2H_2$-120 min-$SiO_2$/C and 10% $C_2H_2$-120 min-$SiO_2$/C which contain 18 and 29 %w/w, respectively, the ZSM-5 nanocrystal aggregates were formed with the size widely distributed in the range of about 500-900 nm (see Figures 2d and 2e). The size of each nanocrystal was less than 50 nm. As we found during the TEM measurement that this aggregate structure could be preserved during a sonication, thus, these aggregates were considered as fully bound-nanocrystal aggregates. It should be noted that the presence of high carbon content lead to a relatively high nucleation rate compared to the growth rate, as a result, the formation of small zeolite crystals was preferable compared to that of large crystals (Jacobsen et al., 2000b).

The bright area in the TEM image of the zeolites is indicative of the porosity (Janssen et al., 2001; Zhu et al., 2008). The TEM images of the samples synthesized by using of the $SiO_2$/C composites show more bright spots compared to those of the sample synthesized without using $SiO_2$/C composite and the commercial ZSM-5 implying the presence of the mesopores. In addition, it was observed that the amount of the bright spots in the

TEM images of the samples corresponded well with the amount of carbon content. This result implies that increasing the carbon content in the $SiO_2$/C composites resulted in increasing the mesopores in the samples.

### 2.3. SURFACE AREA AND POROSITY CHARACTERISTICS

The $N_2$ adsorption/desorption isotherms and the distribution of the pore sizes with respect to the mesopore calculated by the BJH method (derived from adsorption branch isotherms) of the synthesized samples and the commercial ZSM-5 are shown in Figures 3a and 3b, respectively. From the $N_2$ adsorption/desorption isotherms of samples, the adsorption at low relative pressure corresponding to the micropore filling (Schneider, 1995) was observed for all samples. A significant adsorption/desorption at high relative pressure ($P/P_0>0.9$) of 0% carbon-ZSM-5 sample indicates the presence of interparticle voids (Figure 3a). Because the crystal size of this sample was small, the amount of interparticle voids or macropore volume was high. The isotherms of 5% $C_2H_2$-60 min-ZSM-5, 5% $C_2H_2$-120 min-ZSM-5, 10% $C_2H_2$-120 min-ZSM-5, 5% $C_3H_8$-120 min-ZSM-5, and 10% $C_3H_8$-120 min-ZSM-5 samples significantly differ from those of 0% carbon-ZSM-5 sample and commercial ZSM-5. The presence of the hysteresis loop at $0.4<P/P_0<0.9$ in the isotherms of 5% $C_2H_2$-60 min-ZSM-5, 5% $C_2H_2$-120 min-ZSM-5, 10% $C_2H_2$-120 min-ZSM-5, 5% $C_3H_8$-120 min-ZSM-5, and 10% $C_3H_8$-120 min-ZSM-5 samples caused by a capillary condensation in the mesopore void space (Gregg and Sing, 1982), clearly demonstrates the formation of the mesopores in the samples whereas the $N_2$ isotherms of the commercial ZSM-5 exhibited the type I isotherms belonging to pure microporous material. The interpreted distributions in the pore sizes with respect to the mesopores of the samples show a significant increase of the mesopores in the 5% $C_2H_2$-60 min-ZSM-5, 5% $C_2H_2$-120 min-ZSM-5, 10% $C_2H_2$-120 min-ZSM-5, 5% $C_3H_8$-120 min-ZSM-5, and 10% $C_3H_8$-120 min-ZSM-5 samples compared to the 0% carbon-ZSM-5 sample and the commercial ZSM-5. The size of the mesopores of 5% $C_2H_2$-60 min-ZSM-5, 5% $C_2H_2$-120 min-ZSM-5, 10% $C_2H_2$-120 min-ZSM-5, 5% $C_3H_8$-120 min-ZSM-5, and 10% $C_3H_8$-120 min-ZSM-5 samples was distributed depending on the carbon content. Increasing the carbon content in the samples increases the amount of the mesopores and spreads the size distribution of the mesopores.

Table 2 shows the surface area and porosity of the prepared samples. By introducing the carbon content into the silica, the surface areas of the micropores of sample 1 and the commercial ZSM-5 were slightly higher than that of the other samples (ca. 15%) while their external surface areas were significantly lower than that of 5% $C_2H_2$-60 min-ZSM-5, 5% $C_2H_2$-120 min-ZSM-5, 10% $C_2H_2$-120 min-ZSM-5, 5% $C_3H_8$-120 min-ZSM-5, and 10% $C_3H_8$-120 min-ZSM-5 samples, especially for the commercial ZSM-5. The calculated pore volumes of the samples are related to the measured surface area. Increasing the carbon content in the $SiO_2$/C composites

resulted in a significant increase of the total pore volume which was reflected by the increase of the mesopore volume. As mentioned above, the micropores were formed by the presence of the TPAOH template, thus, the micropore volume of the samples that were prepared by using $SiO_2$/C composites only slightly decreased from that of sample 1. The results confirm the success of introducing the mesopores into the ZSM-5 zeolite yielding hierarchical micro- and mesoporous ZSM-5 by the presence of the carbon deposit in the silica source prepared by pyrolysis of hydrocarbon gas such as acetylene and propane.

### 2.4. $^{27}$Al MAS NMR

A typical $^{27}$Al MAS solid state NMR spectrum of the zeolite samples prepared in this work showing the environment around the aluminum atoms in the framework of the synthesized ZSM-5 is depicted in Figure 4. The spectrum contains a strong peak at the chemical shift of about 55 ppm corresponding to the tetrahedrally coordinated aluminum in the framework. A peak at the chemical shift at 0 ppm, which corresponds to the extra framework octahedrally coordinated aluminum, was not observed in synthesized samples. This result indicates that all aluminum atoms of the synthesized zeolites were incorporated into the zeolite framework during the synthesis.

Conclusively, by using silica-carbon ($SiO_2$/C) composites prepared by pyrolysis of carbonaceous gases in the presence of silica gel, it is possible to tailor hierarchical micro- and mesoporous zeolite with significant mesoporosity and acceptable mesopore size distribution compared to that obtained by using other carbon materials, e.g. carbon black (Jacobsen et al., 2000a), carbon nanotube (Schmidt et al., 2001), carbon nanofiber (Janssen et al., 2003) in which high amount of carbon precursors is generally required and that obtained by using sucrose mesopore-directing agent (Kustova et al., 2007) in which sugar solution is difficult to be dispersed into the pores of silica gel during the impregnation, thus, leading the formation of low mesoporosity zeolite. Hence, these developed synthesis method could potentially extend the scope of the solid carbon templating approach and mesopore-directing agent approach. In addition, this method could be scaled up due to the ease of C/$SiO_2$ composite preparation.

## CONCLUSION

In summary, the hierarchical micro- and mesoporous ZSM-5 zeolites were successfully synthesized by using the $SiO_2$/C composites that were prepared by pyrolysis of hydrocarbon gas in the presence of silica gel. The $SiO_2$/C composite acted as a bifunctional material, a mesoporous template and a silica source, for the zeolite synthesis. The results from the SEM, TEM, $N_2$ adsorption/desorption isotherms, and $^{27}$Al MAS NMR chracterizations revealed the successful synthesis of hierarchical micro- and mesoporous ZSM-5 by using the

composites. It was found that the mesoporosity of the zeolites could be controlled by adjusting the carbon content of the $SiO_2$/C composites. Increasing the carbon content in the composites resulted in significantly increasing the total pore volume, which was reflected in the increase of the mesopore volume whereas the micropore volume of the samples was not significantly altered. Because this controllable and efficient synthetic method is expected to be generalized for other types of zeolites, it is considered to be a promising method for creating hierarchical micro- and mesoporous zeolites that could overcome mass transport limitation of the catalytic process, especially in the reaction including the bulky molecule.

**ACKNOWLEDGEMENTS**

This work was supported in part by grants from The National Science and Technology Development Agency (2009 NSTDA Chair Professor funded by The Crown Property Bureau under the management of The National Science and Technology Development Agency and NANOTEC Center of Excellence funded by The National Nanotechnology Center), Kasetsart University Research and Development Institute (KURDI), The Thailand Research Fund (TRF), and The Commission on Higher Education, Ministry of Education (The "National Research University Project of Thailand (NRU)" and The "National Center of Excellence for Petroleum, Petrochemical and Advanced Materials (NCE-PPAM)"). C.W. also thanks The Thailand Research Fund (TRF) for a Royal Golden Jubilee Ph.D. Fellowship (3.C.KU/50/A.2).

## REFERENCES

Alberty, R. A. and E. Burmenko, "Standard Chemical Thermodynamic Properties of Alkyne Isomer Groups," J. Phys. Chem. Ref. Data **15**(4), 1339-1349 (1986).

Barrett, E. P., L. G. Joyner and P. P. Halenda, "The Determination of Pore Volume and Area Distributions in Porous Substances. I. Computations from Nitrogen Isotherms," J. Am. Chem. Soc. **73**(1), 373-380 (1951).

Beyerlein, R. A., G. B. McVicker, L. N. Yacullo and J. J. Ziemiak, "Influence of Framework and Nonframework Aluminum on the Acidity of High-Silica, Proton-Exchanged FAU-Framework Zeolites," J. Phys. Chem. **92**(7), 1967-1970 (1988).

Chao, J., R. C. Wilhoit and B. J. Zwolinski, "Ideal Gas Thermodynamic Properties of Ethane and Propane," J. Phys. Chem. Ref. Data **2**(2), 427-438 (1973).

Davis, S. A., H. M. Patel, E. L. Mayes, N. H. Mendelson, G. Franco and S. Mann, "Brittle Bacteria: A Biomimetic Approach to the Formation of Fibrous Composite Materials," Chem. Mater. **10**(9), 2516-2524 (1998).

Egeblad, K., C. H. Christensen, M. Kustova and C. H. Christensen, "Templating Mesoporous Zeolites," Chem. Mater. **20**(3), 946-960 (2007).

Gregg, S. J. and K. S. W. Sing, "Adsorption Surface Area, and Porosity." Academic Press Ltd, London (1982).

Groen, J. C., J. A. Moulijn and J. Perez-Ramirez, "Desilication: On the Controlled Generation of Mesoporosity in MFI Zeolites," J. Mater. Chem. **16**(22), 2121-2131 (2006).

Houžvička, J., O. Diefenbach and V. Ponec, "The role of Bimolecular Mechanism in the Skeletal Isomerisation of *n*-butene to Isobutene," J. Catal. **164**(2), 288-300 (1996).

Jacobsen, C. J. H., C. Madsen, J. Houzvicka, I. Schmidt and A. Carlsson, "Mesoporous Zeolite Single Crystals," J. Am. Chem. Soc. **122**(29), 7116-7117 (2000a).

Jacobsen, C. J. H., C. Madsen, T. V. W. Janssens, H. J. Jakobsen and J. Skibsted, "Zeolites by Confined Space Synthesis - Characterization of the Acid Sites in Nanosized ZSM-5 by Ammonia Desorption and $^{27}$Al/$^{29}$Si-MAS NMR spectroscopy," Microporous Mesoporous Mater. **39**(1-2), 393-401 (2000b).

Janssen, A. H., A. J. Koster and K. P. de Jong, "Three-Dimensional Transmission Electron Microscopic Observations of Mesopores in Dealuminated Zeolite Y," Angew. Chem. Int. Ed. **40**(6), 1102-1104 (2001).

Janssen, A. H., I. Schmidt, C. J. H. Jacobsen, A. J. Koster and K. P. de Jong, "Exploratory study of mesopore templating with carbon during zeolite synthesis," Microporous Mesoporous Mater. **65**(1), 59-75 (2003).

Kim, S.-S., J. Shah and T. J. Pinnavaia, "Colloid-Imprinted Carbons as Templates for the Nanocasting Synthesis of Mesoporous ZSM-5 Zeolite," Chem. Mater. **15**(8), 1664-1668 (2003).

Kung, H. H., B. A. Williams, S. M. Babitz, J. T. Miller, W. O. Haag and R. Q. Snurr, "Enhanced Hydrocarbon Cracking Activity of Y Zeolites," Top. Catal. **10**(1), 59-64 (2000).

Kustova, M., K. Egeblad, K. Zhu and C. H. Christensen, "Versatile Route to Zeolite Single Crystals with Controlled Mesoporosity: In situ Sugar Decomposition for Templating of Hierarchical Zeolites," Chem. Mater. **19**(12), 2915-2917 (2007).

Lippens, B. C. and J. H. de Boer, "Studies on Pore Systems in Catalysts. V. The t Method," J. Catal. **4**(3), 319-323 (1965).

Marcilly, C., "Where and How Shape Selectivity of Molecular Sieves Operates in Refining and Petrochemistry Catalytic Processes," Top. Catal. **13**(4), 357-366 (2000).

Mukti, R. R., H. Hirahara, A. Sugawara, A. Shimojima and T. Okubo, "Direct Hydrothermal Synthesis of Hierarchically Porous Siliceous Zeolite by Using Alkoxysilylated Nonionic Surfactant," Langmuir **26**(4), 2731-2735 (2009).

Ocampo, F., H. S. Yun, M. M. Pereira, J. P. Tessonnier and B. Louis, "Design of MFI Zeolite-Based Composites with Hierarchical Pore Structure: A New Generation of Structured Catalysts," Cryst. Growth Des. **9**(8), 3721-3729 (2009).

Pérez-Ramírez, J., S. Abelló, A. Bonilla and J. C. Groen, "Tailored Mesoporosity Development in Zeolite Crystals by Partial Detemplation and Desilication," Adv. Funct. Mater. **19**(1), 164-172 (2009).

Perez-Ramirez, J., C. H. Christensen, K. Egeblad, C. H. Christensen and J. C. Groen, "Hierarchical Zeolites: Enhanced Utilisation of Microporous Crystals in Catalysis by Advances in Materials Design," Chem. Soc. Rev. **37**(11), 2530-2542 (2008).

Schmidt, I., A. Boisen, E. Gustavsson, K. Stahl, S. Pehrson, S. Dahl, A. Carlsson and C. J. H. Jacobsen, "Carbon Nanotube Templated Growth of Mesoporous Zeolite Single Crystals," Chem. Mater. **13**(12), 4416-4418 (2001).

Schneider, P., "Adsorption Isotherms of Microporous-Mesoporous Solids Revisited," Appl. Catal. A: Gen. **129**(2), 157-165 (1995).

Sing, K. S. W., D. H. Everett, R. A. W. Haul, L. Moscou, R. A. Pierotti, J. Rouquerol and T. Siemieniewska, "Reporting Physisorption Data for Gas/Solid Systems with Special Reference to the Determination of Surface Area and Porosity (Recommendations 1984)," Pure Appl. Chem. **57**, 603-619 (1985).

Tanabe, K. and W. F. Hölderich, "Industrial Application of Solid Acid-Base Catalysts," Appl. Catal. A: Gen. **181**(2), 399-434 (1999).

Tao, Y., H. Kanoh, L. Abrams and K. Kaneko, "Mesopore-Modified Zeolites: Preparation, Characterization, and Applications," Chem. Rev. **106**(3), 896-910 (2006).

Tao, Y., H. Kanoh and K. Kaneko, "Synthesis of Mesoporous Zeolite A by Resorcinol–Formaldehyde Aerogel Templating," Langmuir **21**(2), 504-507 (2005).

Tosheva, L., V. Valtchev and J. Sterte, "Silicalite-1 Containing Microspheres Prepared Using Shape-Directing Macro-Templates," Microporous Mesoporous Mater. **35-36**, 621-629 (2000).

Trombetta, M., G. Busca, S. Rossini, V. Piccoli, U. Cornaro, A. Guercio, R. Catani and R. J. Willey, "FT-IR Studies on Light Olefin Skeletal Isomerization Catalysis: III. Surface Acidity and Activity of Amorphous and Crystalline Catalysts Belonging to the $SiO_2$-$Al_2O_3$ System," J. Catal. **179**(2), 581-596 (1998).

Van Santen, R. A. and G. J. Kramer, "Reactivity Theory of Zeolitic Brønsted Acidic Sites," Chem. Rev. **95**(3), 637-660 (1995).

Verhoef, M. J., P. J. Kooyman, J. C. van der Waal, M. S. Rigutto, J. A. Peters and H. van Bekkum, "Partial Transformation of MCM-41 Material into Zeolites: Formation of Nanosized MFI Type Crystallites," Chem. Mater. **13**(2), 683-687 (2001).

Wang, L., Z. Zhang, C. Yin, Z. Shan and F.-S. Xiao, "Hierarchical Mesoporous Zeolites with Controllable Mesoporosity Templated from Cationic Polymers," Microporous Mesoporous Mater. **131**(1-3), 58-67 (2010).

Xiao, F.-S., L. Wang, C. Yin, K. Lin, Y. Di, J. Li, R. Xu, D. S. Su, R. Schlögl, T. Yokoi and T. Tatsumi, "Catalytic Properties of Hierarchical Mesoporous Zeolites Templated with a Mixture of Small Organic Ammonium Salts and Mesoscale Cationic Polymers13," Angew. Chem. Int. Ed. **45**(19), 3090-3093 (2006).

Zheng, J., X. Zhang, Y. Zhang, J. Ma and R. Li, "Structural Effects of Hierarchical Pores in Zeolite Composite," Microporous Mesoporous Mater. **122**(1-3), 264-269 (2009).

Zhu, H., Z. Liu, D. Kong, Y. Wang and Z. Xie, "Synthesis and Catalytic Performances of Mesoporous Zeolites Templated by Polyvinyl Butyral Gel as the Mesopore Directing Agent," J. Phys. Chem. C **112**(44), 17257-17264 (2008).

## FIGURE CAPTIONS

Figure 1. XRD patterns of (a) raw silica gel, (b) the reference zeolite sample (ZSM-5, ALSI-PENTA Zeolithe GmbH (APZ)), (c) 0% carbon-ZSM-5, (d) 5% $C_2H_2$-60 min-ZSM-5, (e) 5% $C_2H_2$-120 min-ZSM-5, (f) 10% $C_2H_2$-120 min-ZSM-5, (g) 5% $C_3H_8$-120 min-ZSM-5, and (h) 10% $C_3H_8$-120 min-ZSM-5

Figure 2. SEM and TEM images of (a) a commercial ZSM-5 (ALSI-PENTA Zeolithe GmbH (APZ)), (b) 0% carbon-ZSM-5, (c) 5% $C_2H_2$-60 min-ZSM-5, (d) 5% $C_2H_2$-120 min-ZSM-5, (e) 10%$C_2H_2$-120 min-ZSM-5

Figure 3. (a) $N_2$ adsorption/desorption isotherms of the synthesized zeolite samples and the commercial ZSM-5

(b) Size distribution of their mesopores calculated from the adsorption branch of the isotherm

Figure 4. Typical $^{27}$Al MAS NMR spectrum of the synthesized ZSM-5 sample. This spectrum is taken from 10% $C_2H_2$-120 min-ZSM-5 sample.

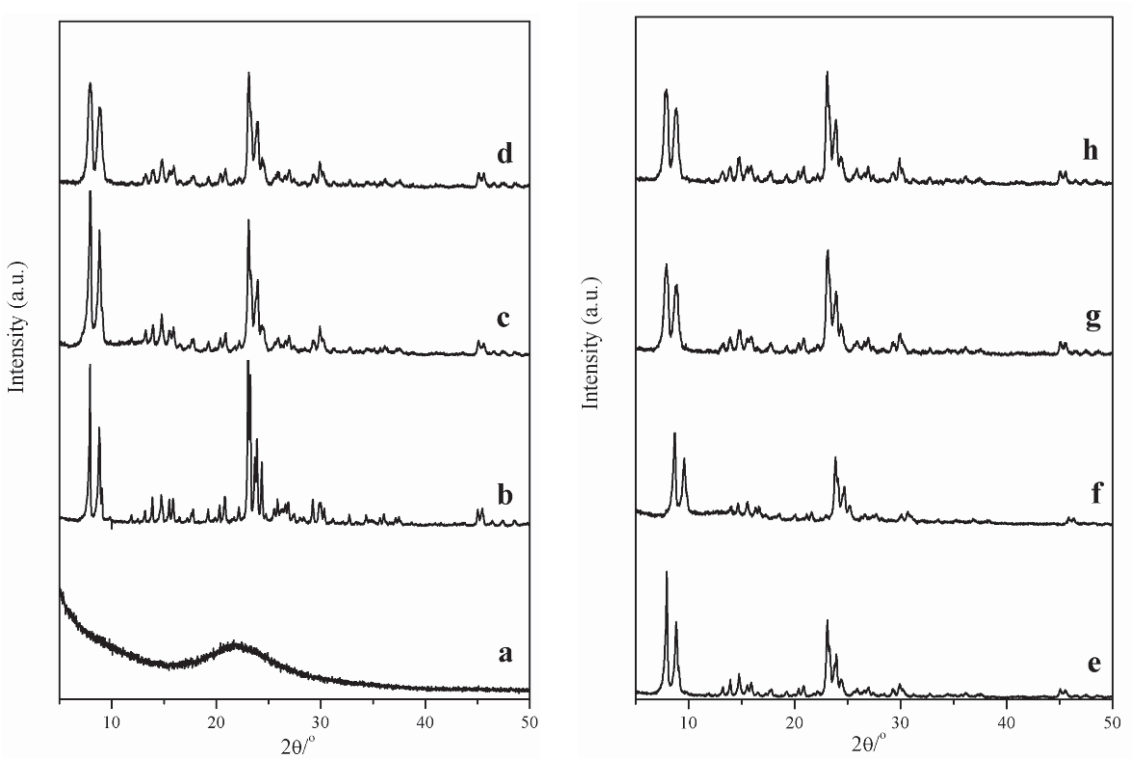
Intensity (a.u.)
d
c
b
a
10
20
30
40
50
2θ/°
Intensity (a.u.)
h
g
f
e
10
20
30
40
50
2θ/°

**Figure 1**.

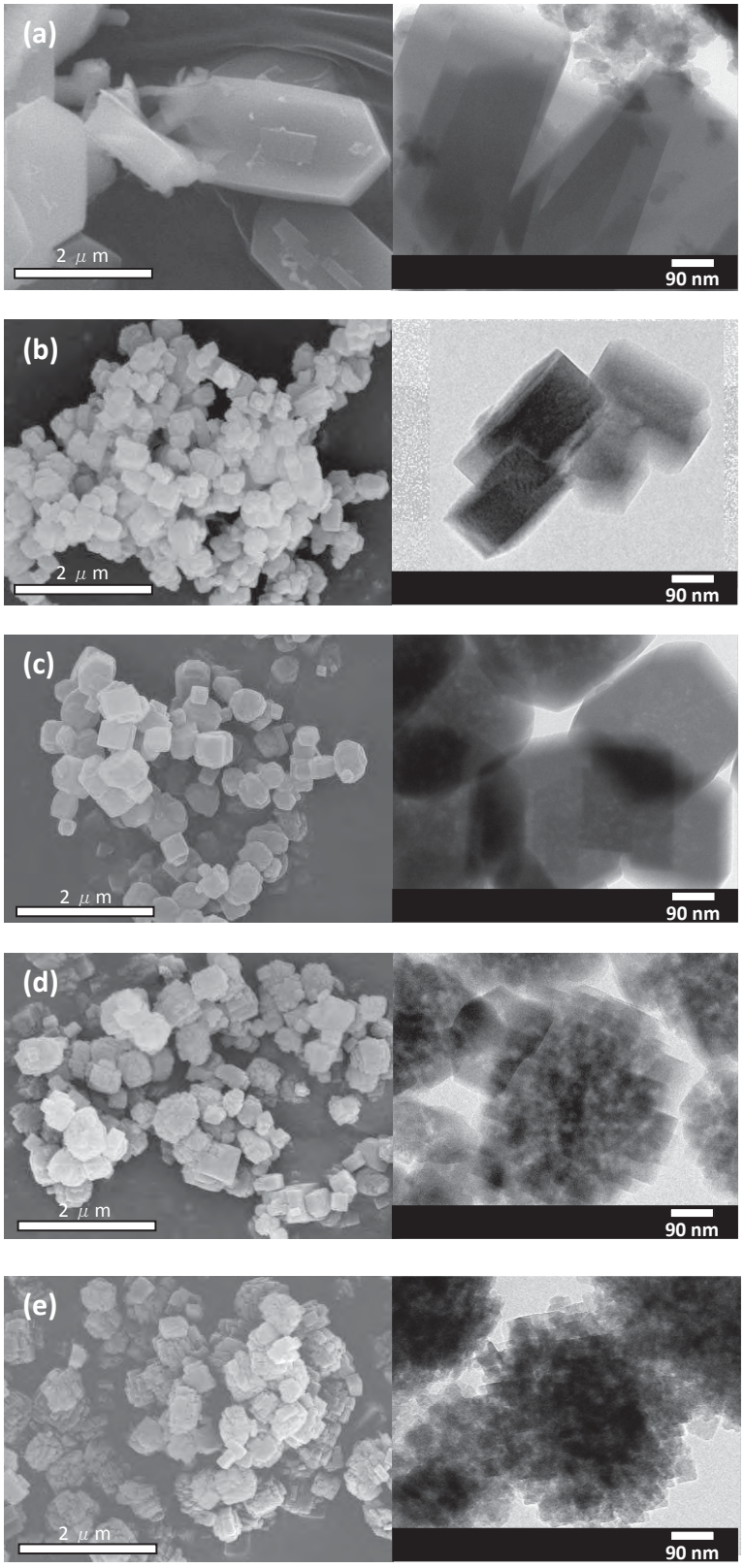


**Figure 2.**

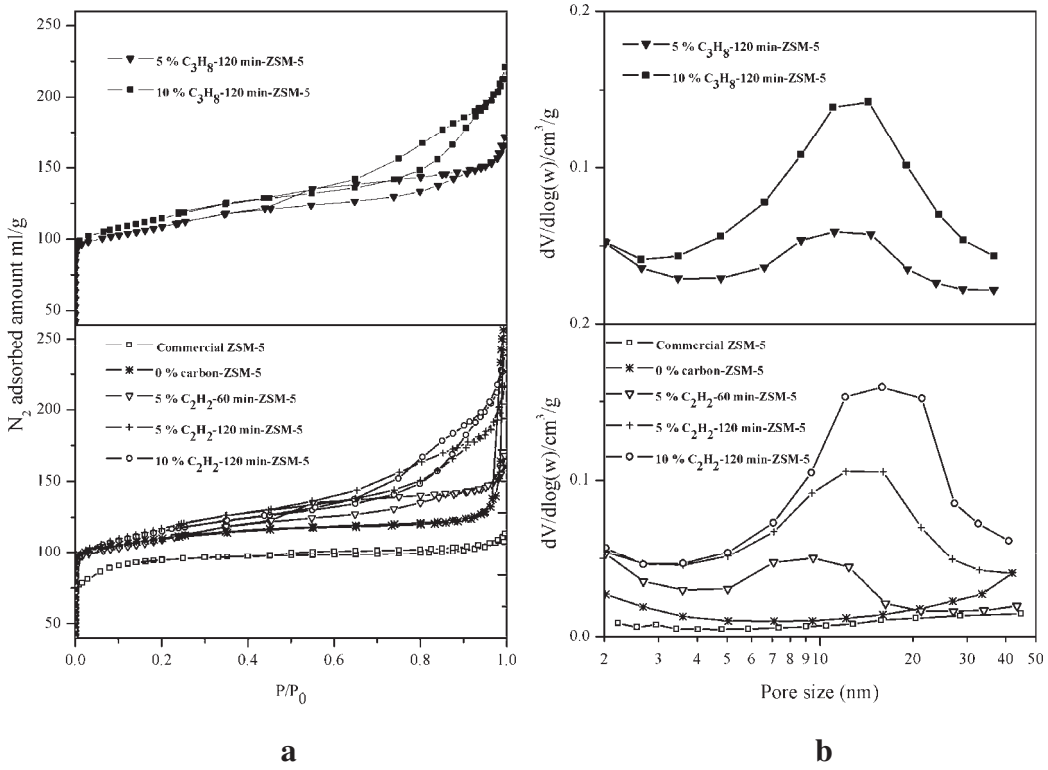


**Figure 3.**

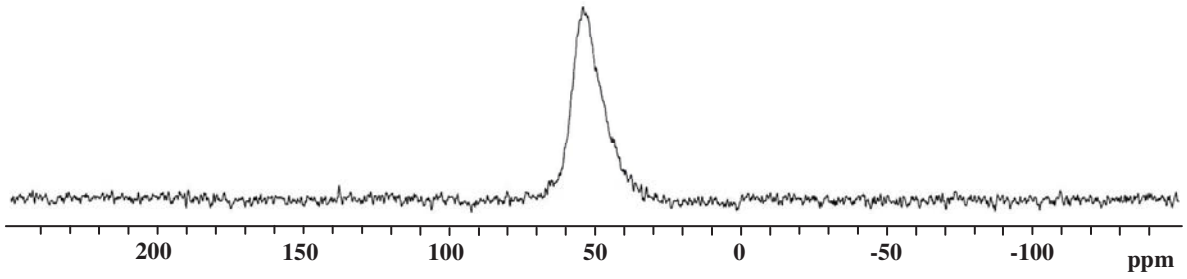


**Figure 4.**

**Table 1.** Carbon content and textural properties of the raw silica gel and the $SiO_2$/C composites prepared by using various experimental conditions.

| Sample | Carbon precursor | Deposition time (min) | Carbon (wt%) | $S_{BET}$[a] ($m^2$/g) | $V_{meso}$[b] ($cm^3$/g) | $D_{BJH}$[c] (nm) |
|---|---|---|---|---|---|---|
| $SiO_2$ | - | - | - | 366 | 1.00 | 11 |
| 5% $C_2H_2$-60 min-$SiO_2$/C | 5 v/v% $C_2H_2$ | 60 | 10 | 323 | 0.78 | 9 |
| 5% $C_2H_2$-120 min-$SiO_2$/C | 5 v/v% $C_2H_2$ | 120 | 18 | 361 | 0.67 | 8 |
| 10% $C_2H_2$-120 min-$SiO_2$/C | 10 v/v% $C_2H_2$ | 120 | 29 | 312 | 0.51 | 7 |
| 5% $C_3H_8$-120 min-$SiO_2$/C | 5 v/v% $C_3H_8$ | 120 | 11 | 276 | 0.83 | 11 |
| 10% $C_3H_8$-120 min-$SiO_2$/C | 10 v/v% $C_3H_8$ | 120 | 22 | 294 | 0.85 | 11 |

[a]$S_{BET}$: Specific surface area calculated by the BET method in the $P/P_0$ range of 0.05-0.35

[b]$V_{meso}$: Mesopore volume calculated by $V_{tot}$-$V_{micro}$. The total pore volume, $V_{tot}$, was calculated at $P/P_0$ of 0.99.

[c]$D_{BJH}$: Mesopore diameter calculated from adsorption branch of nitrogen isotherms using BJH method.

**Table 2**. Surface area and porosity of the synthesized ZSM-5 samples and the commercial ZSM-5.

| Sample | $S_{BET}$[a] ($m^2/g$) | $S_{micro}$[b] ($m^2/g$) | $S_{ex}$[c] ($m^2/g$) | $V_{tot}$[d] ($cm^3/g$) | $V_{micro}$[e] ($cm^3/g$) | $V_{meso+macro}$[f] ($cm^3/g$) | $V_{meso+macro}/V_{micro}$ ($cm^3/g$) |
|---|---|---|---|---|---|---|---|
| 0% carbon-ZSM-5 | 428 | 335 | 93 | 0.22 | 0.13 | 0.09[g] | 0.69 |
| 5% $C_2H_2$-60 min-ZSM-5 | 418 | 281 | 137 | 0.23 | 0.11 | 0.12 | 1.09 |
| 5% $C_2H_2$-120 min-ZSM-5 | 437 | 269 | 168 | 0.30 | 0.11 | 0.19 | 1.73 |
| 10% $C_2H_2$-120 min-ZSM-5 | 431 | 281 | 150 | 0.33 | 0.11 | 0.22 | 2.00 |
| 5% $C_3H_8$-120 min-ZSM-5 | 415 | 278 | 137 | 0.24 | 0.11 | 0.13 | 1.18 |
| 10% $C_3H_8$-120 min-ZSM-5 | 440 | 280 | 160 | 0.30 | 0.11 | 0.19 | 1.73 |
| Commercial ZSM-5 | 343 | 321 | 22 | 0.16 | 0.14 | 0.02 | 0.14 |

[a]$S_{BET}$: From the BET method ($P/P_0$=0.001-0.03). [b]$S_{micro}$: from the *t*-plot method. [c]$S_{ex}$: calculated by $S_{BET}$-$S_{micro}$.
[d]$V_{tot}$: at $P/P_0$ of 0.97. [e]$V_{micro}$: calculated by the *t*-plot method. [f]$V_{meso+macro}$: calculated by $V_{tot}$ - $V_{micro}$..
[g]the macropore volume resulted from the interparticle void space.

# บทความทางวิชาการที่เกี่ยวข้องกับ
# วัสดุที่มีรูพรุนชนิดอื่นๆ
# จำนวน 16 ผลงาน

Journal of Molecular Graphics and Modelling 28 (2009) 62–69

Contents lists available at ScienceDirect

Journal of Molecular Graphics and Modelling

journal homepage: www.elsevier.com/locate/JMGM

# Gas sensing properties of platinum derivatives of single-walled carbon nanotubes: A DFT analysis

P. Pannopard [a,b], P. Khongpracha [a,b], M. Probst [c], J. Limtrakul [a,b,*]

[a] Laboratory for Computational & Applied Chemistry, Chemistry Department, Faculty of Science, Kasetsart University, Bangkok 10900, Thailand
[b] Center of Nanotechnology, Kasetsart University Research and Development Institute, Kasetsart University, Bangkok 10900, Thailand
[c] Institute of Ion Physics and Applied Physics, Innsbruck University, Technikerstraße 25, 6020 Innsbruck, Austria

ARTICLE INFO

*Article history:*
Received 31 October 2008
Received in revised form 23 March 2009
Accepted 11 April 2009
Available online 20 April 2009

*Keywords:*
Sensor
$NO_2$
$NH_3$
Pt–CNT assemblies
Defected CNTs
DFT

ABSTRACT

The limitations of intrinsic carbon nanotube (CNT) based devices to examine toxic gases motivate us to investigate novel sensors which can possibly overcome sensitivity problems. Pt–CNT assemblies (with Pt deposited externally as well as internally Pt-doped ones) interacting with $NO_2$ and $NH_3$ are studied and compared with unmodified CNTs. DFT calculations show that Pt can enhance adsorption and charge transfer processes to a very large degree. Incoming gas molecules cause changes in the electronic structure and charge distribution of the Pt-substituted CNTs that are both larger and more far-reaching than in their unmodified counterparts. Their relatively high stability is unaffected by the complexation with $NO_2$ and $NH_3$. CNTs with defective surface were also investigated. The sensing performance of Pt-doped CNT is found to be superior to defected CNTs.



## 1. Introduction

Chemical sensors based on nanowires of semiconducting single-walled carbon nanotubes (SWCNTs) that perform well have been utilized for detecting pollutant and toxic gases like $NO_2$ and $NH_3$. Such nano-scale assemblies can achieve high sensitivity and fast response times, even at ambient temperature [1]. The fundamental sensing mechanism for these devices is the modulation of the conductivity of the SWCNT as a result of the charge transfer between it and analyzed gas. Former computational studies indicate that both $NO_2$ and $NH_3$ are physisorbed on unmodified-CNT surfaces, causing only a small charge transfer and mildly triggered conductance responses [2–5].

Therefore, there were many attempts to elucidate why experimentally strong signals are observed. Eventually, there are still several assumptions involved. Concerning $NO_2$ and $NH_3$, an indirect mechanism is regularly proposed. For instance, in the case of $NO_2$, $NO_3$ formation by the reaction of $NO_2$ with pre-adsorbed oxygen species or, for $NH_3$, activation by water vapor [1,3], is assumed to be the first step. Such complicated phenomena generally exclude the rational design of improved sensors. We did not consider them when we investigated modified CNTs with respect to their $NO_2$ and $NH_3$ sensing capabilities as discussed below.

Amongst the many possible strategies to tailor the selectivity and sensitivity of CNTs, the generation of new active sites on their surface is classically the premier strategy to overcome the drawback of the intrinsically inert CNT structure. The introduction of structural defects on the walls of CNTs, especially ones associated with vacancies, can be expected to enhance the sensitivity for small molecules like $NO_2$ and $NH_3$ [6–8]. Furthermore, embedding of foreign atoms or doping makes it possible to detect a wide range of gases by altering the dopants. B-, N- and Al-doped SWCNTs have proven to be highly sensitive to $NH_3$, $NO_2$, CO, $H_2O$ and HCOH [9–12]. Interestingly, the so-called decoration of a SWCNTs network with various transition metals allows the fabrication of single-chip devices [13]. This can enlarge the diversity of identified molecular species by combining CNTs decorated with different metals, each for one particular gas. Recent reports impart that the deposited metal–CNTs exhibit enhanced sensitivity, compared to bare CNTs [14]. For example, Pt- and Au-functionalized MWCNTs are more sensitive by an order of magnitude for $NH_3$ and $NO_2$ detection. Not only the catalytic role but also the engineering of transducer platforms are vital for sensor development. Typically, the efficiency of sensory support strongly depends on the amount of active locus on the surface which can boost the reactivity and sensitivity. In particular, for the metal–CNTs hybrid scaffold, the generation of small size metal clusters

* Corresponding author at: Laboratory for Computational & Applied Chemistry, Chemistry Department, Faculty of Science and Center of Nanotechnology, Kasetsart University Research and Development Institute, Kasetsart University, Bangkok 10900, Thailand. Tel.: +66 256 25555x2169; fax: +66 256 25555x2176.
*E-mail address:* jumras.l@ku.ac.th (J. Limtrakul).

1093-3263/$ – see front matter © 2009 Elsevier Inc. All rights reserved.
doi:10.1016/j.jmgm.2009.04.005

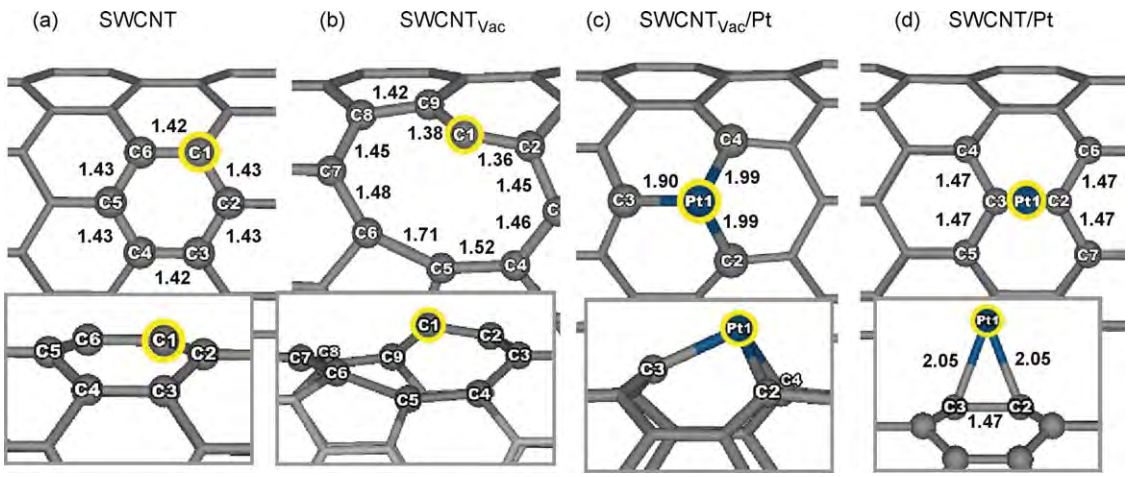


**Fig. 1.** (a) pristine SWCNT, (b) vacancy SWCNT, (c) Pt-doped SWCNT and (d) Pt-deposited SWCNT. Side views are shown under corresponding pictures. The yellow marks indicate the active site studied for the SWCNTs (a–d). Atom–atom distances (Å) around the active centers are also depicted.

with high content and uniform distribution is indeed realized. The surface adsorption of metal clusters on CNT-sidewalls is a well-known technique in sensing technology [13–16], nevertheless the large size of the metal clusters on the CNT produced by this technique often leads to an unfavorably small specific surface. Recent experiments and calculations indicate that defective CNTs are also capable of improving the Pt loading content and size distribution [17], and also that Pt atoms prefer to adsorb on a vacancy site, resembling conventional doping. Impurity doping works by changing the local chemical reactivity. Pt itself is well-known for its adsorption capabilities of small molecules [18–21]. We compare corresponding properties of pristine SWCNTs, of SWCNT with vacancies ($SWCNT_{Vac}$) and with Pt-deposited on perfect SWCNT (SWCNT/Pt). Ammonia ($NH_3$) and nitrogen dioxide ($NO_2$) have been chosen because of their importance as pollutants and industrial toxicants and also because they are good models for electron donors and electron acceptors, respectively.

## 2. Methodology

Fully optimized geometries and the properties of the systems were derived by means of density functional calculations in the spin-unrestricted generalized gradient approximation by using the DMol$^3$ code [22,23] with double-numerical polarized (DNP) basis sets. Concerning the density functional we faced certain restrictions with respect to CPU time and the implementation of periodic boundary conditions. This prohibits, for example, using new density functionals like MPWB1K [24–26]. Our calculations were performed with the PW91 [27] density functional which, while not including dispersion energy contributions, can efficiently be applied to large periodic systems. It has been used on a large number of comparable systems in good agreement with experimental information. The interactions between core and valence electrons are represented by DFT semicore pseudopotentials [28]. The real-space orbital cutoff was set to 4.0 Å, the force threshold for optimizations was 0.01 eV and the Brilloiouin zone *k*-point sampling was performed in a $1 \times 1 \times 2$ Monkhorst–Pack mesh [29]. These values of the parameters correspond to a medium-quality calculation which delivers the highest accuracy still computationally feasible for such large systems. Periodic-boundary conditions were applied with a tetragonal unit cell of $20 \times 20 \times 12.78$ Å$^3$. This is large enough to virtually avoid interactions with images in neighboring cells. An (8,0)SWCNT with 96 carbon atoms was chosen as a model of an unmodified SWCNT. This is a semiconducting SWCNT, a feature that is necessary for the sensor circuit. For this model, we calculated a HOMO–LUMO energy gap of 0.63 eV which agrees well with previous DFT studies [30,31]. From this SWCNT, the models for the Pt-deposited, and Pt-doped, and SWCNTs with vacancy defects were derived. They are shown and explained in Fig. 1.

We investigated different sites of the gas molecules above the hexagonal carbon ring structure of the CNT. $NO_2$ was oriented parallel or perpendicular to the SWCNT surface. For the latter one, we considered three orientations with N pointing to the SWCNT, with a single O atom or both O atoms pointing to the SWCNT. Likewise, $NH_3$ was placed above a carbon atom, between two carbons and above the center of a hexagonal ring. For each case, N, one H atom or all three H atoms were oriented towards the CNT surface. The N–H bonds were parallel to the hexagonal carbon framework or rotated away by 60°. Detailed graphs of the initial and optimized structures are available as supplementary information (S1 and S2, respectively).

The binding energies between the gas molecules and the SWCNT were calculated according to:

$$E_b = E_T(\text{support} : \text{gas}) - E_T(\text{support}) - E_T(\text{gas})$$

where $E_T$ (support:gas) is the total energy of a gas molecule adsorbed on the active site of support and $E_T$ (support) and $E_T$ (gas) are the total energies of the support and the gas molecule, respectively. All $E_T$ values refer to quantum chemical energies at optimized geometries. The electronic structure of the energetically most favorable complexes was analyzed in order to estimate the sensing susceptibility with respect to the following properties: partial and net charge transfers were obtained from a Mulliken population analysis. The partial and total density of states (PDOSs and DOSs) were calculated and the frontier molecular orbitals were analyzed. Electron density difference maps of optimized structures were calculated with a plane-wave basis set and ultrasoft pseudopotentials [32] as implemented in the CASTEP program [33].

## 3. Results and discussion

### 3.1. Energetics and optimized geometries

We start by considering the optimized geometries of pristine, defective, Pt-doped and Pt-deposited SWCNTs (Fig. 1) which serve as the sensing platforms. Fig. 1a shows the common SWCNT with a typical C–C bond length of about 1.42 Å and a nanotube diameter of 6.38 Å closely matching that of previous studies [30]. In Fig. 1b,

**Table 1**
Binding energies $E_b$ between Pt and SWCNT and $SWCNT_{Vac}$ and binding energies of $NO_2$ and $NH_3$ to the four types of SWCNTs. The structures are shown in Figs. 2 and 3, respectively. The energies are given in kcal/mol.

| Sensing support | | $E_b$ (SWCNT/Pt) |
|---|---|---|
| $SWCNT_{Vac}$/Pt | | 163.62 |
| SWCNT/Pt | | 53.39 |
| **Sensing support** | **$E_b$ (support:$NO_2$)** | **$E_b$ (support:$NH_3$)** |
| SWCNT | 1.96 | 1.33 |
| $SWCNT_{Vac}$ | 55.90 | 2.76 |
| $SWCNT_{Vac}$/Pt | 50.91 | 30.52 |
| SWCNT/Pt | 34.92 | 40.96 |

the single vacancy defected SWCNT is shown. It results from the 12-membered ring created by removing one carbon atom from the graphene sheet and the subsequent reconstruction to a 5-membered ring and a 9-membered ring. It holds one unsaturated carbon (C1), slightly sticking out from the tube surface. The rearrangement deforms the structure to obtain an elliptical cross section with major and minor diameters of 6.56 Å and 6.17 Å, respectively. Doping of the large Pt atom to the vacancy (Fig. 1c) causes a deformation of the nearby hexagonal rings in the doping region. The Pt–C distance is 1.9 Å and Pt protrudes outside of the SWCNT surface. Even though in this structure the SWCNT is apparently distorted (elliptic diameters: 6.49 Å and 6.28 Å), the Pt atom is bound with 163.62 kcal/mol (Table 1). This value is similar to the one reported in [17]. This stabilization can be ascribed to the saturation of the dangling C bonds and the formation of stable hexagonal rings. Consequently, the binding energy in Pt-deposited SWCNT is smaller (53.39 kcal/mol). Fig. 1d shows the energetically most favorable conformation with Pt residing above the C2–C3 bond [34–35] with a Pt–C distance of 2.05 Å. The geometry of the tube is changed due to strong Pt–CNT interaction causing nonidentical diameters with 6.48 Å and 6.29 Å of the longest and the shortest ones, respectively. In a long-lived sensor, the attachment of Pt to the SWCNT must be stable enough to withstand temperature and environmental effects. Although this is difficult to quantify, also the Pt-deposited SWCNT should still be a stable enough device.

### 3.1.1. $NO_2$

The most stable optimized geometries, their geometrical parameters and the binding energies of $NO_2$ adsorption on each support are given in Fig. 2 and Table 1. Nevertheless, there are some experimental and computational studies revealing that the nitro derivative on fullerenes can be found [36,37]. Though, due to the chemically inert CNT system, the functionalization of $NO_2$ on the CNT sidewall should be more difficult than that of a fullerene surface. One can see that the $NO_2$ molecule is merely physisorbed on the pristine SWCNT with the lowest absorption energy (1.96 kcal/mol) and a distance of 3.11 Å between N and C. The monomer geometries of the SWCNT and the $NO_2$ molecules are undisturbed.

In $SWCNT_{Vac}$, the unsaturated carbon atom (C1) binds to the nitrogen atom of $NO_2$ ($r_{C-N}$ = 1.46 Å) with an interaction energy of 55.90 kcal/mol. The binding can be attributed to the under-coordinated carbon atoms near the vacancy. C1 is the most negatively charged carbon and attracts the partially positively charged N atom of $NO_2$. Excess electrons are located in the antibonding orbitals of the $NO_2$ molecule causing a change of the N–O distance from 1.21 Å to 1.24 Å, The stability of the $SWCNT_{Vac}$/Pt:$NO_2$ complex (50.91 kcal/mol) is similar to that of $SWCNT_{Vac}$. Pt bonds to both oxygens of $NO_2$ causing an elongation of the N–O bond to 1.28 Å. The interaction between $NO_2$ and the Pt atom in SWCNT/Pt:$NO_2$ is similar to the one described above. In our SWCNT/Pt:$NO_2$ model, the SWCNT–Pt distances increased from 2.05 Å to 2.11 Å after $NO_2$ binding, indicating that the strong binding of $NO_2$ (34.92 kcal/mol) comes at the expense of a destabilization of the Pt–SWCNT stability.

### 3.1.2. $NH_3$

The most stable optimized geometries of $NH_3$ adsorbed on each support are shown in Fig. 3, together with the relevant distances. Their binding energies are tabulated in Table 1. In agreement with previous studies [5,9] in the preferred orientation, the hydrogen atoms of $NH_3$ point towards the SWCNT (Fig. 3a). $NH_3$ is noncovalently bound with only 1.33 kcal/mol and a C–H distance of about 3.3 Å. In contrast to $NO_2$, the interaction in $SWCNT_{Vac}$:$NH_3$ is only slightly stronger (2.76 kcal/mol) because in both cases a hydrogen bonded interaction is the only possibility. Here, the more negatively charged C1 acts as the electron donor and a C···H–N hydrogen bond can be formed (Fig. 3b). These weak interactions mean that materials consisting of both SWCNT and $SWCNT_{Vac}$ are inappropriate sensing platforms for $NH_3$ detection. In $SWCNT_{Vac}$/Pt:$NH_3$ and SWCNT/Pt:$NH_3$, $NH_3$ is strongly bound. In $SWCNT_{Vac}$/Pt:$NH_3$ and SWCNT/Pt:$NH_3$, ammonia is bound by 30.52 and 40.96 kcal/mol. The Pt–N distances are 2.29 and 2.14 Å, respectively. The strong binding of $NH_3$ to Pt via its nitrogen atom has a larger influence on the active region than the one caused by its

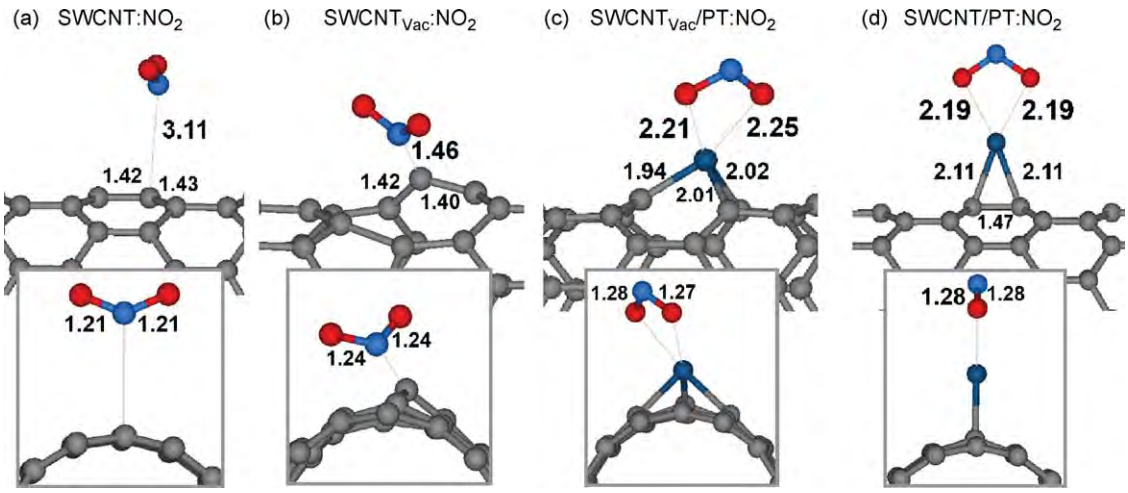


**Fig. 2.** Front and side views of the most favorable binding geometries of $NO_2$ on each support type, (a) pristine SWCNT, (b) vacancy SWCNT, (c) Pt-doped SWCNT and (d) Pt-deposited SWCNT, accompanied with their binding distances. Pt–C and some C–C distances (Å) are also given.

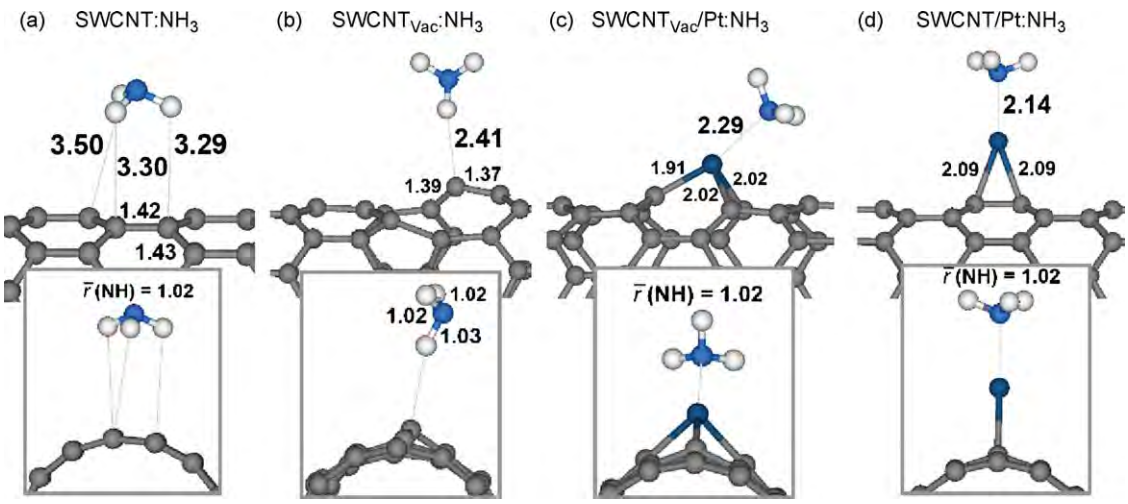


**Fig. 3.** Front and side views of the most favorable binding geometries of NH3 on each support type, (a) pristine SWCNT, (b) vacancy SWCNT, (c) Pt-doped SWCNT and (d) Pt-deposited SWCNT, accompanied with their binding distances. Pt–C and some C–C distances (Å) are also given..

weak H-bonded interaction with $SWCNT_{Vac}$, as can be seen from the redistribution of electron density (Fig. 4). As expected, the SWCNT–Pt distances increase somewhat from 2.05 Å to 2.09 Å after the $NH_3$ complexation. The N–H distances of all adsorbed $NH_3$ molecules are unaffected by the complexation and stay at 1.02 Å. The affinity of SWCNT/Pt to $NH_3$ approaches already the binding energy of the attached Pt to the SWCNT, which is a disadvantage since it might in practice lead to its destruction.

### 3.2. Electronic properties of the platform and sensitivity to $NO_2$ and $NH_3$

We investigated the effects of gas adsorption on the electronic properties of the SWCNTs by computing the charge transfers ($q_{Gas}$) between the gas molecule and support and the HOMO–LUMO energy gap modulations ($\Delta E_g$). The results are summarized in Table 2. The quantities in this table are defined as:

$$\Delta E_g = E_g\,(\text{support} : \text{gas}) - E_g\,(\text{bare support})$$
$$\Delta q_{SWCNT} = q_{SWCNT}\,(\text{support} : \text{gas}) - q_{SWCNT}\,(\text{bare support})$$
$$\Delta q_{Pt} = q_{Pt}\,(\text{support} : \text{gas}) - q_{Pt}\,(\text{bare support})$$

In addition, electron densities difference maps HOMO and LUMO orbitals and electronic densities of states (DOSs) have been derived. They are depicted in Figs. 4–8.

#### 3.2.1. $NO_2$

Since $NO_2$ is an electron-withdrawing molecule with an unusually large electron affinity between 2 eV and 3 eV [38], electrons are transferred from supports to it (Table 2). For $SWCNT_{Vac}$:$NO_2$, $SWCNT_{Vac}$/Pt:$NO_2$ and SWCNT/Pt:$NO_2$ these shifts amount to −0.27, −0.38 and −0.35*e*, respectively. The values for SWCNT/Pt:$NO_2$ and $SWCNT_{Vac}$/Pt:$NO_2$ are similar, but a more detailed analysis shows some differences. The positive value of $\Delta q_{SWCNT}$ in $SWCNT_{Vac}$/Pt:$NO_2$ (0.32*e*) is larger than the one in SWCNT/Pt:$NO_2$ (0.22*e*). Three-dimensional plots of the differential electron density can give detailed information of the rearrangement of the complex formation. Fig. 4 shows isosurfaces of certain density changes. It can be seen that $NO_2$ adsorption (Fig. 4a–d) on $SWCNT_{Vac}$/Pt causes a depletion of electron density (Fig. 4c) throughout, which is expected to change the electric properties of the nanotube dramatically. In contrast, electron relocation in SWCNT/Pt:$NO_2$ occurs only locally at the Pt–$NO_2$ moiety. The change of the energy gap ($\Delta E_g$) during the adsorption process is also related to the sensitivity of a sensor for a particular analyte. In Table 2, a negative sign of $\Delta E_g$ refers to a reduction of the energy gap in the complex compared to the bare support. We find that the energy gaps of all systems decrease after $NO_2$ adsorption by −0.32, −0.14, −0.25 and −0.41 eV for SWCNT:$NO_2$, $SWCNT_{Vac}$:$NO_2$, $SWCNT_{Vac}$/Pt:$NO_2$ and SWCNT/Pt:$NO_2$, respectively. This agrees

**Table 2**
Partial molecular and atomic charges $q(e)$ and values of the HOMO–LUMO gap $E_g$ (eV) of all studied complexes. Partial charge transfers and energy gap changes are indicated by the prefix delta (Δ). Refer to text for the definitions of the quantities.

| System | $E_g$ | $q_{SWCNT}$ | $q_{Pt}$ |
|---|---|---|---|
| SWCNT | 0.63 | 0.00 | |
| $SWCNT_{Vac}$ | 0.26 | 0.00 | |
| $SWCNT_{Vac}$/Pt | 0.39 | 0.12 | −0.12 |
| SWCNT/Pt | 0.58 | 0.05 | −0.05 |

| System | $E_g$ | $q_{SWCNT}$ | $q_{Pt}$ | $q_{Gas}$ | [a]$\Delta E_g$ | [b]$\Delta q_{SWCNT}$ | [c]$\Delta q_{Pt}$ |
|---|---|---|---|---|---|---|---|
| SWCNT:$NO_2$ | 0.31 | 0.05 | | −0.05 | −0.32 | 0.05 | |
| $SWCNT_{Vac}$:$NO_2$ | 0.12 | 0.27 | | −0.27 | −0.14 | 0.27 | |
| $SWCNT_{Vac}$/Pt:$NO_2$ | 0.14 | 0.44 | −0.06 | −0.38 | −0.25 | 0.32 | 0.06 |
| SWCNT/Pt:$NO_2$ | 0.17 | 0.27 | 0.08 | −0.35 | −0.41 | 0.22 | 0.13 |
| SWCNT:$NH_3$ | 0.63 | −0.01 | | 0.01 | 0.00 | −0.01 | |
| $SWCNT_{Vac}$:$NH_3$ | 0.28 | 0.01 | | −0.01 | 0.02 | 0.01 | |
| $SWCNT_{Vac}$/Pt:$NH_3$ | 0.29 | −0.09 | −0.18 | 0.27 | −0.10 | −0.21 | −0.06 |
| SWCNT/Pt:$NH_3$ | 0.62 | −0.06 | −0.22 | 0.28 | 0.04 | −0.11 | −0.17 |

[a] $\Delta E_g = E_g$ (support:gas) − $E_g$ (bare support).
[b] $\Delta q_{SWCNT} = q_{SWCNT}$ (support:gas) − $q_{SWCNT}$ (bare support).
[c] $\Delta q_{Pt} = q_{Pt}$ (support:gas) − $q_{Pt}$ (bare support).

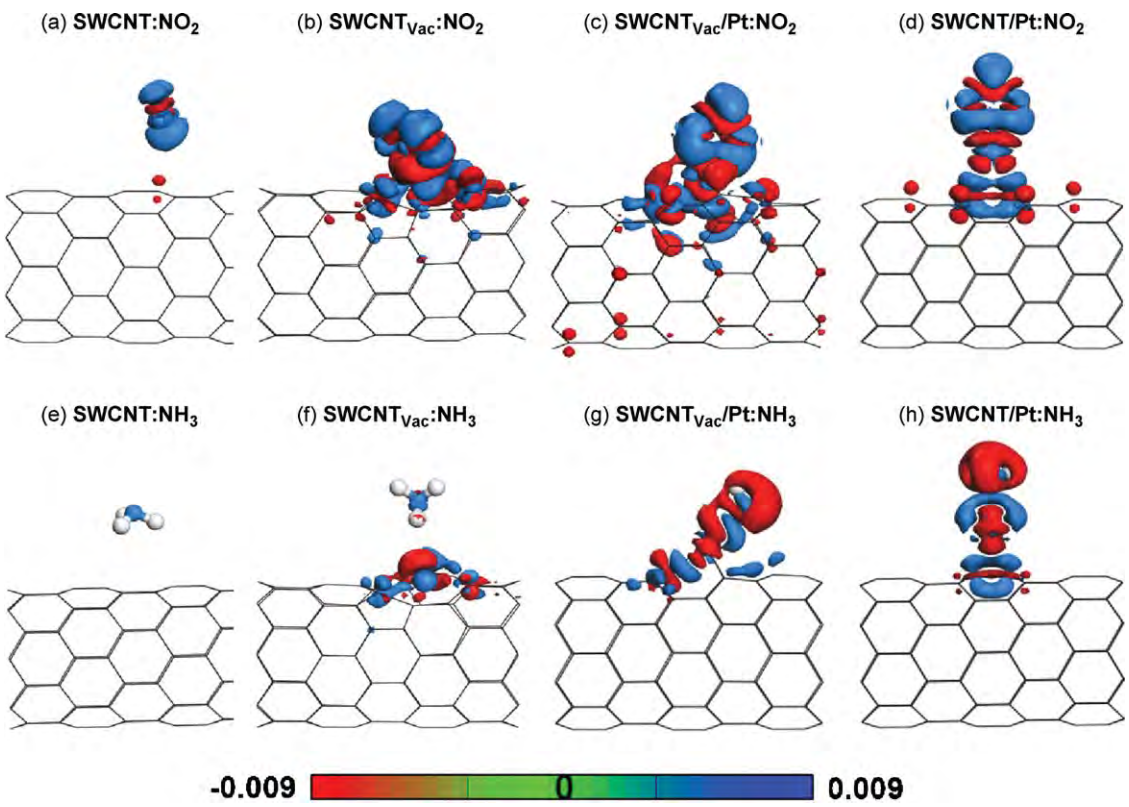


**Fig. 4.** Plots of the differential electron densities of all studied support-gas complexes, support-$NO_2$ complexes (a–d) and support-$NH_3$ complexes (e–h). The 3D-surfaces are plotted at isovalues of $\pm 0.009e/Å^3$. A red color denotes loss of density whereas blue denotes gain of electron density.

well with experimental reports that the conductivity of CNTs, defected-CNTs and Pt-doped–CNTs increase when exposed to $NO_2$ [1,4,14]. Electron density transfer to $NO_2$ generates holes in the support. The enhanced conductivities are directly related to the abundance of hole carriers, so these pristine and modified SWCNTs behave as p-type semiconductors as well and are also susceptible to become metallic after stimulated by $NO_2$, especially in the $SWCNT_{Vac}$:$NO_2$, $SWCNT_{Vac}$/Pt:$NO_2$ and SWCNT/Pt:$NO_2$ systems.

One can further see that the $\Delta E_g$ values are proportional to the amount of charge transfer, except for $\Delta E_g$ of SWCNT where $NO_2$ is very weakly bound. To clarify this further, we analyze the DOSs and PDOSs (Fig. 5). Comparing the DOS diagrams of SWCNT:$NO_2$ and SWCNT (Fig. 5e and a, respectively), one sees the appearance of an acceptor state in the middle of the HOMO–LUMO gap of the SWCNT, when $NO_2$ is bound [39]. When this state receives electrons from the valence band of the SWCNT the resistance of the system should decrease. Since this state is contributed from the $NO_2$ radical, as is indicated by the PDOSs and LUMO scheme of SWCNT:$NO_2$ (Figs. 5i and 6e, respectively), it is plausible that the measured energy gaps vary with the number of $NO_2$ molecules. SWCNT/Pt exhibits the highest change $\Delta E_g$ of its energy gap when $NO_2$ is bound to it (Table 2). However, that does not much affect the electronic structure of the SWCNT, as can be seen by the charge and electron density differences in Table 2 ($\Delta q_{SWCNT} = 0.22e$) and Fig. 4d, respectively. Moreover, the HOMO and LUMO orbitals (Fig. 6d and h, respectively), to which $\Delta E_g$ is related, have prominent contributions only in the area close to Pt and $NO_2$ and mostly involve the d-orbitals of Pt. Also the partial density of states distribution (Fig. 5n) shows the density near the Fermi level in SWCNT/Pt:$NO_2$ originating from these d-orbitals. The HOMO and LUMO of $SWCNT_{Vac}$/Pt:$NO_2$ (Fig. 6c and g, respectively) contain AO contributions from Pt and from the p-orbitals of the $NO_2$ oxygen atoms as well as from the nanotube mixed into the molecular orbitals of the whole system whereas in SWCN/Pt:$NO_2$, solely the first two and not the nanotube contribute to the frontier orbitals. Accordingly, despite the larger value of $\Delta E_g$, in SWCNT/Pt:$NO_2$, its localized response to $NO_2$ binding makes it less suitable as a sensor.

### 3.2.2. $NH_3$

In this section we discuss the sensitivity of the three supports to $NH_3$ detecting. The lone pair electrons at the N atom of $NH_3$ can readily be donated to the molecule interacting with it. Consequently, the charge of adsorbed $NH_3$ is positive by 0.01, 0.27 and $0.28e$ in SWCNT:$NH_3$, $SWCNT_{Vac}$/Pt:$NH_3$ and SWCNT/Pt:$NH_3$, respectively, except for $SWCNT_{Vac}$:$NH_3$ ($-0.01e$) where C···H–N resembles a hydrogen bond and H–N behaves as the electron acceptor. The complexes with weak adsorption via the H atom, i.e. SWCNT:$NH_3$ and $SWCNT_{Vac}$:$NH_3$, also exhibit insignificant charge transfers of only 0.01 and $-0.01e$, respectively. Together with the unnoticeable electron density difference, the energy gap is also unchanged. This is associated with the bare SWCNT character of the PDOSs near the Fermi level (Fig. 7i and j) and is also visible in the HOMO–LUMO pictures of both complexes (Fig. 8a, b, e and f). This infers that SWCNT and $SWCNT_{Vac}$ have very low sensibility to $NH_3$ gas.

Extraordinary large charge transfers are found in $SWCNT_{Vac}$/Pt:$NH_3$ and SWCNT/Pt:$NH_3$ with values of 0.27 and $0.28e$, respectively. Amounts and directions of $NH_3$ charge transfer of both complexes are quite similar and also their electron density difference maps are similar as shown in Fig. 4g and h, respectively. The better efficiency is derived from the existence of the Pt active site and N-contacted mode which enhance the outflow of nitrogen lone pair electron density. Generally, giving up electrons from $NH_3$ to a p-type semiconductor support reduces the hole carrier density and thus decreases the conductivity of the system, correlated with the widening of its HOMO–LUMO gap [1]. Even though the flows of

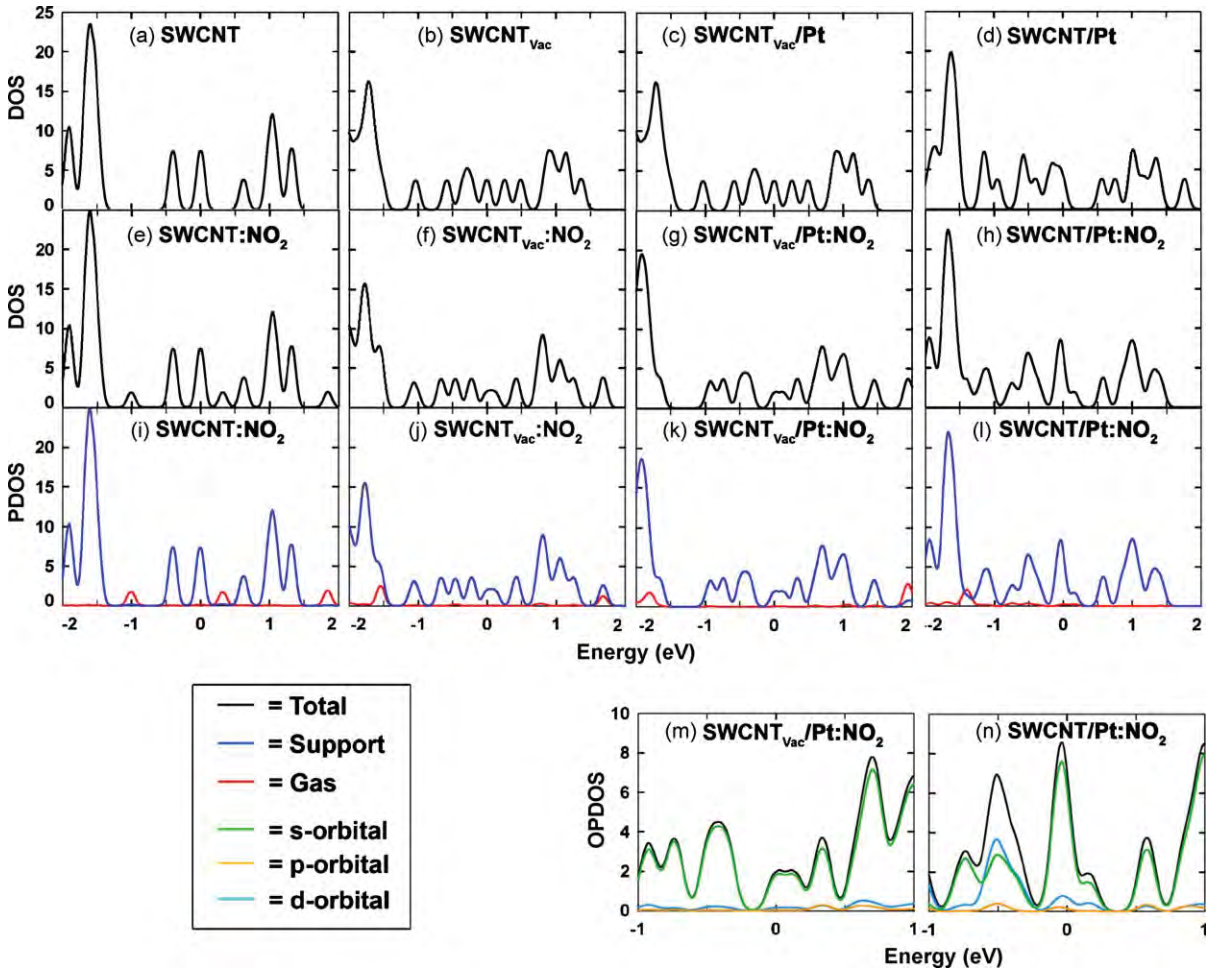


**Fig. 5.** Density of states (DOSs) for the studied supports (a–d) and their $NO_2$ complexes (e–h). Partial density of states (PDOSs) of all support-gas complexes (i–l) and orbital partial density of states (OPDOSs) of $SWCNT_{Vac}/Pt:NO_2$ and $SWCNT/Pt:NO_2$ (m and n) are also plotted for comparison. The Fermi levels (defined as the HOMO energies) are calibrated to locate at 0 eV.

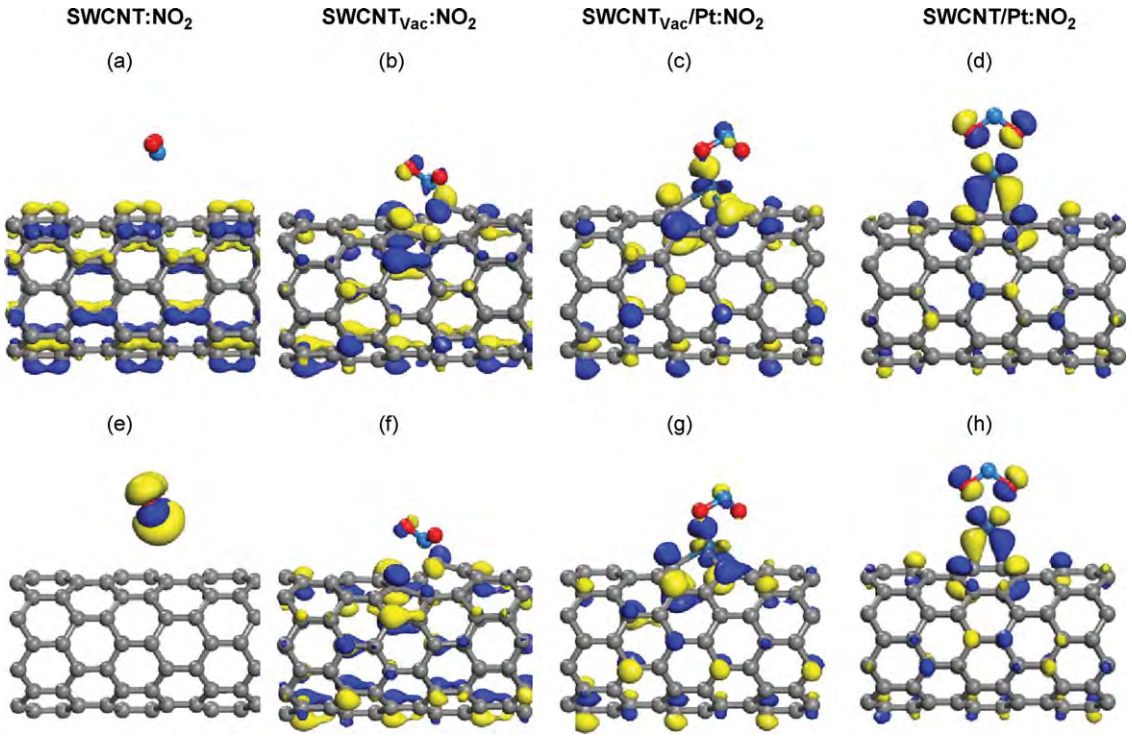


**Fig. 6.** Frontier molecular orbitals of the complexes with $NO_2$: HOMOs (a–d) and LUMOs (e–h).

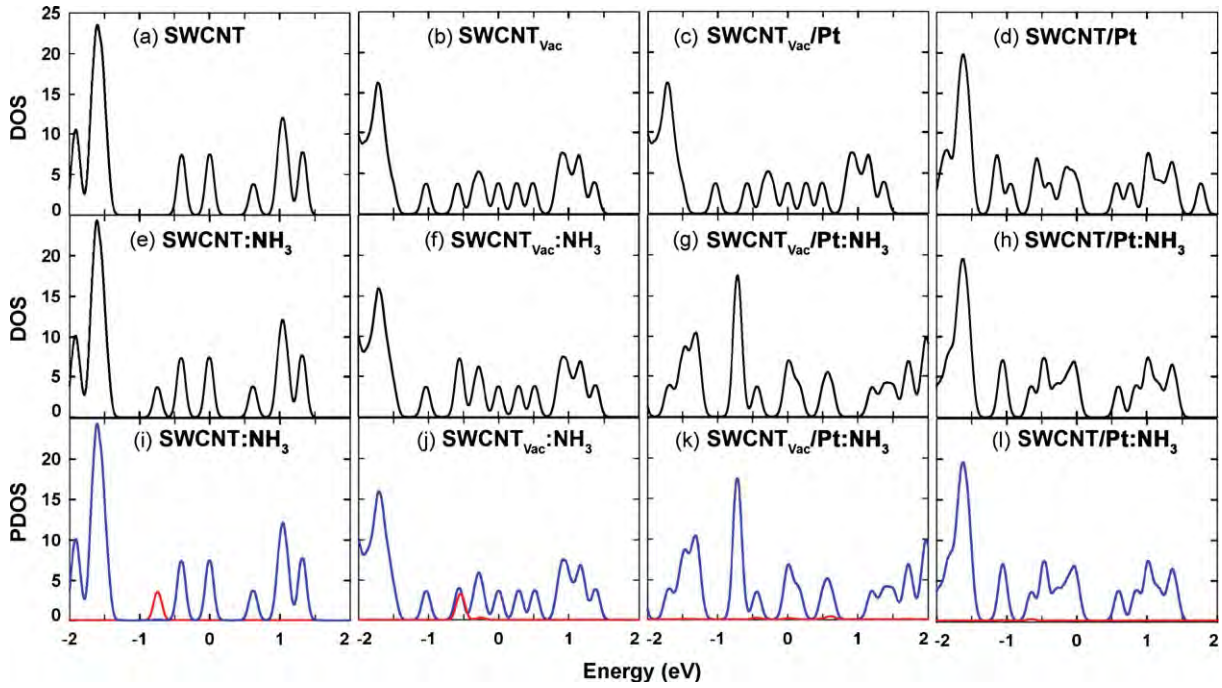


**Fig. 7.** Density of states (DOS) for all studied supports (a–d) and their $NH_3$ complexes (e–h). Partial density of states (PDOS) of all support-gas complexes (i–l) are also plotted for comparison (blue lines: support; red lines: contributions from $NH_3$). The Fermi levels (defined as HOMO energies) are calibrated to locate at 0 eV.

$NH_3$ electrons into SWCNT$_{Vac}$/Pt:$NH_3$ and SWCNT/Pt:$NH_3$ have the same direction, which indicates that they become less conductive, the signs of their $\Delta E_g$ values which represent how the conductivity changes are opposite. The energy gap of SWCNT/Pt:$NH_3$ is slightly widened (0.04 eV) whereas that of the SWCNT$_{Vac}$/Pt:$NH_3$ is significantly narrowed (−0.10 eV). These phenomena should principally interrelate to the electron redistribution in the support, especially of the SWCNT since the PDOSs near the Fermi level (Fig. 7k and l) and HOMO–LUMO features of both complexes (Fig. 8c, d, g and h) are merely contributed from it. Both $\Delta q_{SWCNT}$ values of SWCNT$_{Vac}$/Pt:$NH_3$ and SWCNT/Pt:$NH_3$ are negative (−0.21$e$ and −0.11$e$, respectively) due to the accumulation of electrons in the SWCNTs. Remarkably, the SWCNT$_{Vac}$/Pt:$NH_3$ tube can receive twice the electron density than SWCNT/Pt:$NH_3$ does. This can change its electrical characteristic from p-type to n-type, which explains the observed increase in the conductivity after $NH_3$ adsorption. The reason for the poorer electron transfer to SWCNT in SWCNT/Pt:$NH_3$ is the weaker interaction between SWCNT and

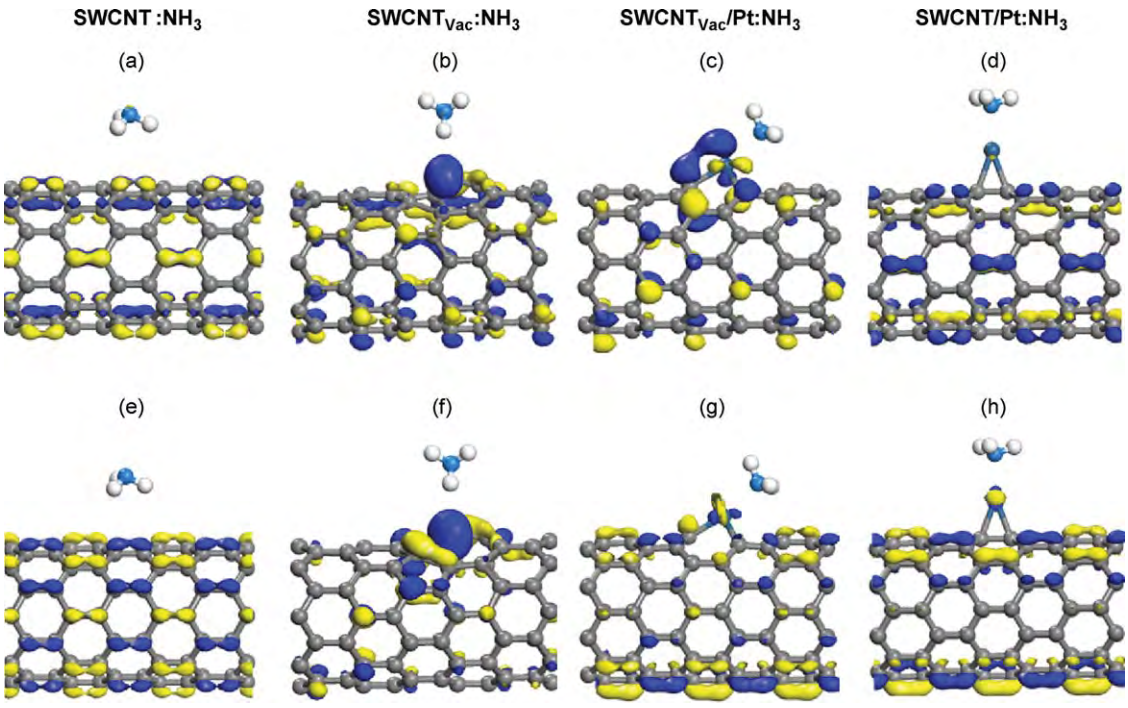


**Fig. 8.** Frontier molecular orbitals of all studied support-$NH_3$ complexes, HOMOs (a–d) and LUMOs (e–h).

Pt in the latter, which is further diminished by the adsorbed gas. The electron density acquired from $NH_3$ hardly moves to SWCNT as is shown by the accumulation of electron density on the Pt atom ($\Delta q_{Pt}$, $-0.17e$) after interacting with $NH_3$. Up until this point, $SWCNT_{Vac}$/Pt adequately satisfies the basic sensitivity requirements and induces more electronic change in terms of both the energy gap and partial charge transfer to the SWCNT than to the SWCNT/Pt.

## 4. Conclusion

We tried to study qualitatively the sensing performance of Pt–SWCNT with defective and pristine SWCNTs for $NO_2$ and $NH_3$ by means of first principle calculations. Overall, in both Pt-deposited and Pt-doped SWCNTs, platinum increases the charge transfer and other calculated properties. For the adsorption of $NO_2$, the Pt-doped SWCNT shows slightly smaller binding energies and gap changes than both the pristine SWCNT and the Pt-deposited SWCNT. Its electronic structure modulations are greater than that of the pristine SWCNT and its electron densities in the SWCNT unit are more disturbed than the ones of the Pt-deposited SWCNT. The binding of Pt to the SWCNT in the doped case is much stronger than if it is deposited on the surface. For $NH_3$ adsorption, the Pt-doped SWCNT shows the largest electron transfers to the SWCNT. We further compared the Pt-doped SWCNT with the well-known reactive defected SWCNT. Their abilities for capturing a $NO_2$ molecule are similar but for $NH_3$ the Pt-doped SWCNT is far better. The sensitivity of Pt-doped SWCNT is superior for both the detection of $NO_2$ and $NH_3$, because it exhibits larger energy gap changes and a larger charge transfer. These findings should be useful for the development of SWCNT-based nanosensor devices.

## Acknowledgements

This research was supported by grants from the Thailand Research Fund to PP (Royal Golden Jubilee Ph.D. fellowship 3.C.KU/50/A.1) and to JL, the National Science and Technology Development Agency (NSTDA Chair Professor and NANOTEC Center of Excellence and CNC Consortium), the Kasetsart University Research and Development Institute (KURDI), and the Commission on Higher Education (Postgraduate Education and Research Programs in Petroleum, Petrochemicals and Advanced Materials). Support for CPU time on the Tera cluster of the Thai National Grid Center is also acknowledged.

## Appendix A. Supplementary data

Supplementary data associated with this article can be found, in the online version, at doi:10.1016/j.jmgm.2009.04.005.

## References

[1] J. Kong, N.R. Franklin, C. Zhou, M.G. Chapline, S. Peng, K. Cho, H. Dailt, Nanotube molecular wires as chemical sensors, Science 287 (5453) (2000) 622–625.
[2] H. Chang, J.D. Lee, S.M. Lee, Y.H. Lee, Adsorption of $NH_3$ and $NO_2$ molecules on carbon nanotubes, Appl. Phys. Lett. 79 (23) (2001) 3863–3865.
[3] S. Peng, K. Cho, P. Qi, H. Dai, Ab initio study of CNT $NO_2$ gas sensor, Chem. Phys. Lett. 387 (4–6) (2004) 271–276.
[4] S. Santucci, S. Picozzi, F. Di Gregorio, L. Lozzi, C. Cantalini, L. Valentini, J.M. Kenny, B. Delley, $NO_2$ and CO gas adsorption on carbon nanotubes: experiment and theory, J. Chem. Phys. 119 (20) (2003) 10904–10910.
[5] J. Lu, S. Nagase, Y. Maeda, T. Wakahara, T. Nakahodo, T. Akasaka, D. Yu, Z. Gao, R. Han, H. Ye, Adsorption configuration of $NH_3$ on single-wall carbon nanotubes, Chem. Phys. Lett. 405 (1–3) (2005) 90–92.
[6] L. Valentini, F. Mercuri, I. Armentano, C. Cantalini, S. Picozzi, L. Lozzi, S. Santucci, A. Sgamellotti, J.M. Kenny, Role of defects on the gas sensing properties of carbon nanotubes thin films: experiment and theory, Chem. Phys. Lett. 387 (4–6) (2004) 356–361.
[7] J. Andzelm, N. Govind, A. Maiti, Nanotube-based gas sensors—role of structural defects, Chem. Phys. Lett. 421 (1–3) (2006) 58–62.
[8] F. Mercuri, A. Sgamellotti, L. Valentini, I. Armentano, J.M. Kenny, Vacancy-induced chemisorption of $NO_2$ on carbon nanotubes. A combined theoretical and experimental study, J. Phys. Chem. B 109 (27) (2005) 13175–13179.
[9] L. Bai, Z. Zhou, Computational study of B- or N-doped single-walled carbon nanotubes as $NH_3$ and $NO_2$ sensors, Carbon 45 (10) (2007) 2105–2110.
[10] S. Peng, K. Cho, Ab initio study of doped carbon nanotube sensors, Nano Lett. 3 (4) (2003) 513–517.
[11] R. Wang, D. Zhang, W. Sun, Z. Han, C. Liu, A novel aluminum-doped carbon nanotubes sensor for carbon monoxide, Theochem 806 (1–3) (2007) 93–97.
[12] R. Wang, D. Zhang, Y. Zhang, C. Liu, Boron-doped carbon nanotubes serving as a novel chemical sensor for formaldehyde, J. Phys. Chem. B 110 (37) (2006) 18267–18271.
[13] A. Star, V. Joshi, S. Skarupo, D. Thomas, J.-C.P. Gabriel, Gas sensor array based on metal-decorated carbon nanotubes, J. Phys. Chem. B 110 (42) (2006) 21014–21020.
[14] M. Penza, G. Cassano, R. Rossi, M. Alvisi, A. Rizzo, M.A. Signore, T. Dikonimos, E. Serra, R. Giorgi, Enhancement of sensitivity in gas chemiresistors based on carbon nanotube surface functionalized with noble metal (Au, Pt) nanoclusters, App. Phys. Lett. 90 (17) (2007) 173123/1–173123/3.
[15] S. Mubeen, T. Zhang, B. Yoo, M.A. Deshusses, N.V. Myung, Palladium nanoparticles decorated single-walled carbon nanotube hydrogen sensor, J. Phys. Chem. C 111 (17) (2007) 6321–6327.
[16] M.K. Kumar, S. Ramaprabhu, Nanostructured Pt functionlized multiwalled carbon nanotube based hydrogen sensor, J. Phys. Chem. B 110 (23) (2006) 11291–11298.
[17] S.J. Kim, Y.J. Park, E.J. Ra, K.K. Kim, K.H. An, Y.H. Lee, J.Y. Choi, C.H. Park, S.K. Doo, M.H. Park, C.W. Yang, Defect-induced loading of Pt nanoparticles on carbon nanotubes, App. Phys. Lett. 90 (2) (2007) 023114/1–023114/3.
[18] C. Zhou, J. Wu, A. Nie, R.C. Forrey, A. Tachibana, H. Cheng, On the sequential hydrogen dissociative chemisorption on small platinum clusters: a density functional theory study, J. Phys. Chem. C 111 (34) (2007) 12773–12778.
[19] L.C. Grabow, A.A. Gokhale, S.T. Evans, J.A. Dumesic, M. Mavrikakis, Mechanism of the water gas shift reaction on Pt: first principles, experiments, and microkinetic modeling, J. Phys. Chem. C 112 (12) (2008) 4608–4617.
[20] Y. Wang, P.B. Balbuena, Roles of proton and electric field in the electroreduction of $O_2$ on Pt(1 1 1) surfaces: results of an ab-initio molecular dynamics study, J. Phys. Chem. B 108 (14) (2004) 4376–4384.
[21] H. Orita, Y. Inada, DFT investigation of CO adsorption on Pt(2 1 1) and Pt(3 1 1) surfaces from low to high coverage, J. Phys. Chem. B 109 (47) (2005) 22469–22475.
[22] B. Delley, An all-electron numerical method for solving the local density functional for polyatomic molecules, J. Chem. Phys. 92 (1) (1990) 508–517.
[23] B. Delley, From molecules to solids with the $DMol^3$ approach, J. Chem. Phys. 113 (18) (2000) 7756–7764.
[24] T. Strassner, M.A. Taige, Evaluation of functionals O3LYP, KMLYP, and MPW1K in comparison to B3LYP for selected transition-metal compounds, J. Chem. Theory Comput. 1 (5) (2005) 848–855.
[25] Z. Slanina, P. Pulay, S. Nagase, $H_2$, Ne, and $N_2$ energies of encapsulation into C60 evaluated with the MPWB1K functional, J. Chem. Theory Comput. 2 (2006) 782–785.
[26] S.G. Stepanian, M.V. Karachevtsev, A.Yu. Glamazda, V.A. Karachevtsev, L. Adamowicz, Stacking interaction of cytosine with carbon nanotubes: MP2, DFT and Raman spectroscopy study, Chem. Phys. Lett. 459 (2008) 153–158.
[27] J.P. Perdew, Y. Wang, Accurate and simple analytic representation of the electron-gas correlation energy, Phys. Rev. B 45 (23) (1992) 13244–13249.
[28] B. Delley, Hardness conserving semilocal pseudopotentials, Phys. Rev. B: Condens. Matter Mater. Phys. 66 (15) (2002) 155125/1–155125/9.
[29] H.J. Monkhorst, J.D. Pack, Special points for Brillouin-zone integrations, Phys. Rev. B 13 (12) (1976) 5188–5192.
[30] O. Gulseren, T. Yildirim, S. Ciraci, Systematic ab initio study of curvature effects in carbon nanotubes, Phys. Rev. B: Condens. Matter Mater. Phys. 65 (15) (2002) 153405/1–153405/4.
[31] X. Blase, L.X. Benedict, E.L. Shirley, S.G. Louie, Hybridization effects and metallicity in small radius carbon nanotubes, Phys. Rev. Lett. 72 (12) (1994) 1878–1881.
[32] D. Vanderbilt, Soft self-consistent pseudopotentials in a generalized eigenvalue formalism, Phys. Rev. B 41 (11) (1990) 7892–8795.
[33] V. Milman, B. Winkler, J.A. White, C.J. Pickard, M.C. Payne, E.V. Akhmatskaya, R.H. Nobes, Electronic structure, properties, and phase stability of inorganic crystals: a pseudopotential plane-wave study, Int. J. Quantum Chem. 77 (5) (2000) 895–910.
[34] E. Durgun, S. Dag, V.M.K. Bagci, O. Gulseren, T. Yildirim, S. Ciraci, Systematic study of adsorption of single atoms on a carbon nanotube, Phys. Rev. B: Condens. Matter Mater. Phys. 67 (20) (2003) 201401/1–201401/4.
[35] G. Chen, Y. Kawazoe, Interaction between a single Pt atom and a carbon nanotube studied by density functional theory, Phys. Rev. B: Condens. Matter Mater. Phys. 73 (12) (2006) 125410/1–125410/6.
[36] L.Y. Chiang, J.B. Bhonsle, L. Wang, S.F. Shu, T.M. Chang, J.R. Hwu, Efficient one-flask synthesis of water-soluble [60]fullerenols, Tetrahedron 52 (14) (1996) 4963–4972.
[37] Z. Slanina, X. Zhao, L.Y. Chiang, E. Osawa, Biologically active fullerene derivatives: computations of structures, energetics, and vibrations of C60(OH)X and $C60(NO_2)Y$, Int. J. Quantum Chem. 74 (3) (1999) 343–349.
[38] The National Institute of Standards and Technology (NIST): Standard Reference Data Program (Chemistry WebBook, http://webbook.nist.gov).
[39] Y. Zhang, C. Suc, Z. Liu, J. Li, Carbon nanotubes functionalized by $NO_2$: coexistence of charge transfer and radical transfer, J. Phys. Chem. B 110 (45) (2006) 22462–22470.

# Structure and Dynamics of Water Confined in Single-Wall Nanotubes

**Tanin Nanok,[†,‡,§] Nongnuch Artrith,[†,‡,||] Piboon Pantu,[†,‡] Philippe A. Bopp,[⊥] and Jumras Limtrakul*[,†,‡]**

*Laboratory for Computational and Applied Chemistry, Department of Chemistry, Faculty of Science and Center of Nanotechnology, Kasetsart University, Bangkok 10900, Thailand, NANOTEC Center of Excellence, National Nanotechnology Center, Kasetsart University, Bangkok 10900, Thailand, and Department of Chemistry, Université Bordeaux 1, 351 Cours de la Libération, Building A12, F-33405 Talence cedex, France*

*Received: October 7, 2008; Revised Manuscript Received: November 28, 2008*

The structure and dynamics of water confined in model single-wall carbon- and boron-nitride nanotubes (called SWCNT and SWBNNT, respectively) of different diameters have been investigated by molecular dynamics (MD) simulations at room temperature. The simulations were performed on periodically extended nanotubes filled with an amount of water that was determined by soaking a section of the nanotube in a water box in an *NpT* simulation (1 atm, 298 K). All MD production simulations were performed in the canonical (*NVT*) ensemble at a temperature of 298 K. Water was described by the extended simple point charge (SPC/E) model. The wall−water interactions were varied, within reasonable limits, to study the effect of a modified hydrophobicity of the pore walls. We report distribution functions for the water in the tubes in spherical and cylindrical coordinates and then look at the single-molecule dynamics, in particular self-diffusion. While this motion is slowed down in narrow tubes, in keeping with previous findings (Liu et al. *J. Chem. Phys.* **2005**, *123*, 234701−234707; Liu and Wang. *Phys. Rev.* **2005**, *72*, 085420/1−085420/4; Liu et al. *Langmuir* **2005**, *21*, 12025−12030) bulk-water like self-diffusion coefficients are found in wider tubes, more or less independently of the wall−water interaction. There may, however, be an anomaly in the self-diffusion for the SWBNNT.



## I. Introduction

Carbon nanotubes (CNTs) have gained recognition as prominent building blocks of nanomaterials; they are used in a variety of nanotechnology applications due to their exceptional mechanical and electrical properties.[1,2] The transport of molecules in these nanoporous media could also exhibit interesting characteristics, different from the ones of transport in ordinary bulk media, since the interactions between the pore wall and the molecules become rather strong when the dimensions of the pore approach the size of the transported molecule. Although the mechanical and electrical properties of CNTs can be measured explicitly in experiments,[3] the understanding of the transport and conduction mechanisms through their pores is still incomplete. This is partly due to the difficulty of preparing CNTs with uniform pore sizes and distributions and of tracing the diffusive behavior inside. Computational studies thus play an important role in the interpretation of experimental data and provide predictive information on molecular transport through nanopores.

Because of the simplicity and hydrophobicity of their interior, CNTs are recognized as promising prototype models. They are frequently used as models for systems such as water transport in aquaporin water channels,[4] water migration in xylem vessels of plants,[5] the delivery of beneficial molecules to target cells[6−8] and other biological nanofluidic systems.

A previous molecular dynamics (MD) simulation study[9] on water conduction through the channel of single-walled carbon nanotubes (SWCNTs) showed that under normal conditions of pressure and temperature the filling of an empty (6,6)-CNT channel (8.1 Å in diameter and 13.4 Å in length) with water takes place within a few ten picoseconds. The channel then remained filled during the entire simulation time of 66 ns. The water molecules constrained in such a narrow space form a one-dimensionally ordered hydrogen-bond network that is not observed in bulk water. It was shown[10] that the channel occupancy and conductivity are dramatically decreased by a reduction of the attractive nanotube−water interactions. A 25% reduction leads to fluctuations between filled and empty sections in the tube and a 40% reduction to an emptying of the CNT channel.[9] This filling and conducting behavior has also been observed in an isoelectronic nanotube (a subnanometer boron nitride nanotube (BNNT)[11]) and other hydrophobic nanopores.[12,13]

Recently, several MD simulation studies have been performed on the diameter dependence of the CNT hydration. It was, for example, found that water confined in a critical-size armchair-(9,9) CNT can undergo a transition into a state having an ice-like mobility with an average number of hydrogen bonds close to that in bulk water under ambient temperature and pressure.[14] Unusual features, not seen in bulk ice, can also be observed with other CNT diameters under conditions of high water densities[15] and extremely high axial pressures (50 Mpa to 500 Mpa).[16] The radial distribution functions reveal highly ordered layered water structures in this case. For the dynamic properties, the radial and axial diffusivities of water encapsulated in SWCNTs are smaller than those of bulk water; both components

* Corresponding author. E-mail: fscijrl@ku.ac.th.
[†] Faculty of Science, Kasetsart University.
[‡] NANOTEC Center of Excellence, Kasetsart University.
[§] Present address: Institut für theoretische Physik, Universität Leipzig, Vor dem Hospitaltore, D-04103 Leipzig, Germany.
[||] Present address: Lehrstuhl für Theoretische Chemie, Ruhr-Universität Bochum, D-44780 Bochum, Germany.
[⊥] Université Bordeaux 1.

10.1021/jp8088676 CCC: $40.75 
Published on Web 12/30/2008

**TABLE 1: Details for the MD Simulation Runs of Water in Carbon- and Boron-Nitride Nanotubes in This Work[a]**

| tube | effective inner diameter (Å) | no. of water molecules | simulation time (ns) |
|---|---|---|---|
| (9,9)-nanotubes | 8.86 | 77 | 4 |
| (10,10)-nanotubes | 10.22 | 102 | 4 |
| (12,12)-nanotubes | 12.92 | 162 | 1 |
| (14,14)-nanotubes | 15.62 | 237 | 1 |
| (16,16)-nanotubes | 18.34 | 327 | 1 |
| (20,20)-nanotubes | 23.74 | 547 | 1 |

[a] The length is 36.89 Å in all cases.

decrease as the diameter of the SWCNTs decreases.[15,17,18] In other tubes with similar diameters, the flow of water was found to be strongly influenced by the hydrophilicity of the wall.[19,20] The strong interfacial water−nanotube attraction causes a significant reduction of the water flow rate.

Even though the structure and dynamics of water confined in SWCNTs have been extensively studied by MD simulations, most efforts have been directed toward small diameter tubes, in which the characteristics of bulk water cannot be attained even at the tube center. Thus, a more comprehensive understanding of the structural and dynamic properties of water confined in larger diameter SWCNTs seems to be desirable. Here, we study tubes with effective diameters (see below) between 8.86 to 23.74 Å and report on the influences of the attractive interactions between the wall and the confined water at an average density of 1.0 g/cm$^3$ under ambient conditions.

In the next section, the models and simulation details will be presented. Then, we will investigate the structure of the water in the tubes in terms of radial and cylindrical distribution functions. A study of the self-diffusion will then be presented.

## II. Models and Simulation Details

The armchair type SWCNTs considered in this study are modeled as rigid networks of uncharged Lennard-Jones (LJ) carbon atoms with C−C bond distances of 1.42 Å and a fixed nanotube length of 36.89 Å. To study the diameter dependence of the structural and dynamic properties of the confined water, the "effective diameter" (i.e., the diameter after excluding the van der Waals radius of a C atom, 1.70 Å) is varied from 8.86 to 23.74 Å, corresponding to the (*m*,*m*)-armchair SWCNTs with $m = 9$, 10, 12, 14, 16 and 20, respectively. *m* is an integer in the chiral vector $\mathbf{A} = m\mathbf{a}_1 + m\mathbf{a}_2$ of the hexagonal honeycomb

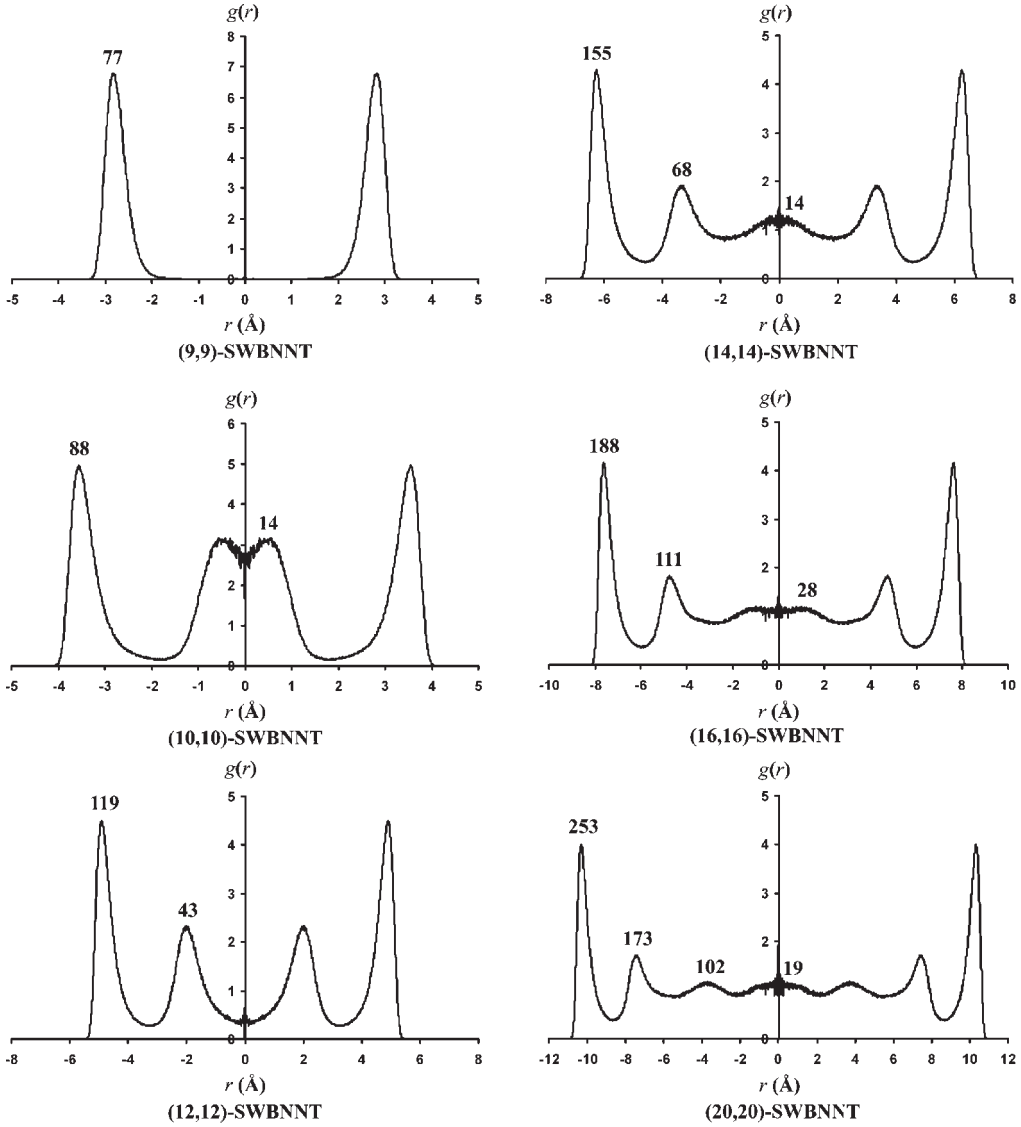


**Figure 1.** Local density distribution functions, in cylindrical coordinates, for the water molecules in the SWBNNTs. The numbers above the curves indicate the number of molecules present, on the average, in the various regions.

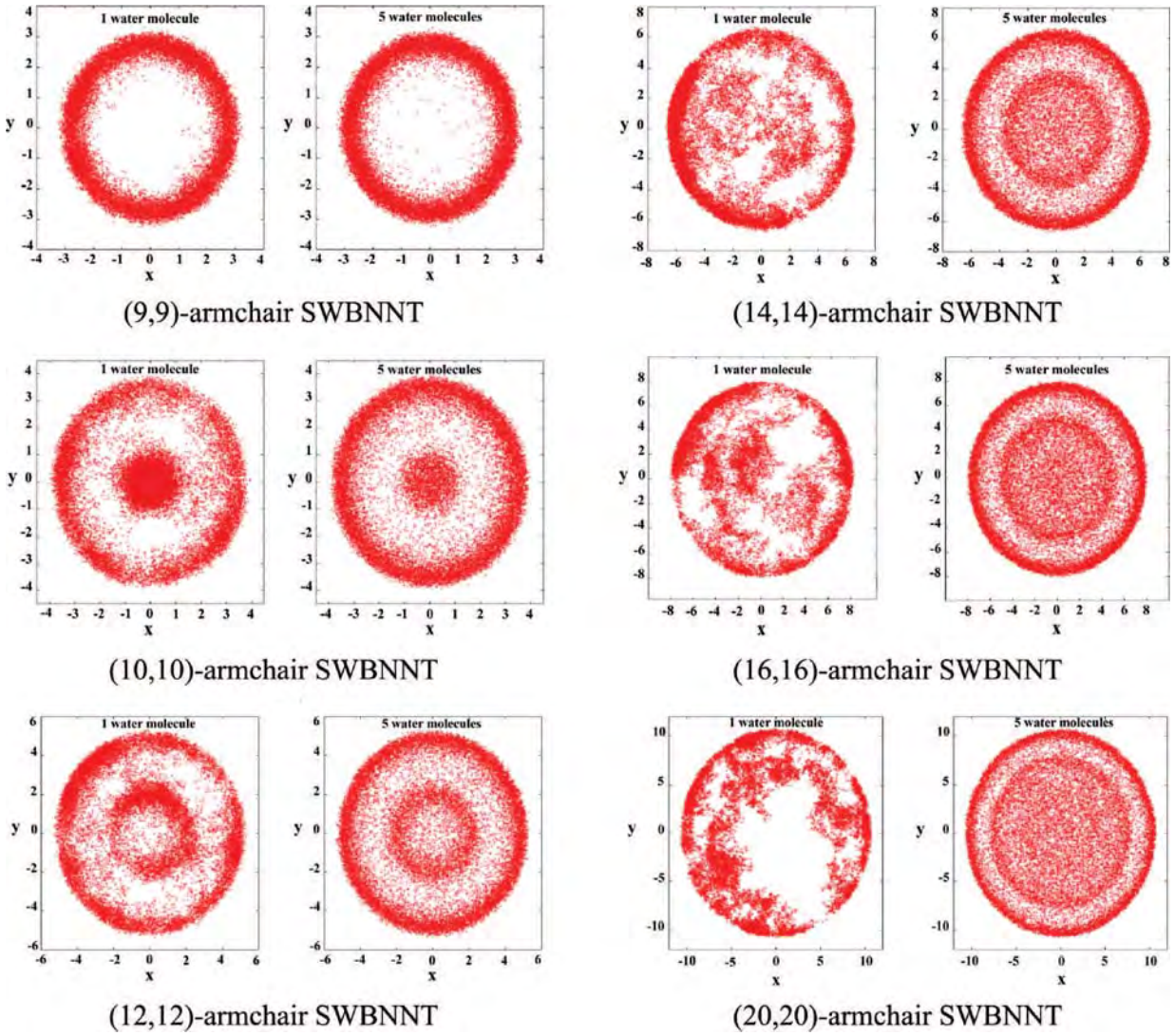


**Figure 2.** Trajectories of 1 (left) and 5 (right) arbitrarily selected water molecules in the SWBNNTs, corresponding to Figure 1, monitored during 1 ns. Note that the scale is not the same for all tubes.



lattice, where $\mathbf{a}_1$ and $\mathbf{a}_2$ are unit vectors. These nanotubes are filled with a total number of 77, 102, 162, 237, 327, and 547 water molecules, respectively, which leads to an average water density of 1.0 g/cm$^3$ in the tube.

Water is described by the extended simple point charge (SPC/E) model ($\varepsilon_{O-O} = 0.1554$ kcal/mol and $\sigma_{O-O} = 3.16$ Å).[21,22] The geometry of each water molecule is kept rigid using the SHAKE algorithm. The two hydrogen atoms are located at 1.0 Å from the oxygen with an H−O−H angle of 109.5°. Atomic charges of $-0.8476e$ and $+0.4238e$ are assigned to the oxygen and hydrogen sites, respectively.

The interactions between water and the nanotube wall are described by a 12-6 LJ potential. The LJ parameters for carbon ($\varepsilon_{C-C} = 0.0970$ kcal mol$^{-1}$ and $\sigma_{C-C} = 3.36$ Å) are taken from ref 14. The water−nanotube interaction parameters are derived by using the Lorentz−Berthelot combining rules i.e., $\varepsilon_{ij} = (\varepsilon_i\varepsilon_j)^{1/2}$ and $\sigma_{ij} = (\sigma_i + \sigma_j)/2$, where $\varepsilon_{ij}$ and $\sigma_{ij}$ symbolize the strength and size of the LJ potential parameters between sites $i$ and $j$.

The degree of "nanotube hydrophobicity" is varied for all tubes by changing the strength of the LJ potential parameter ($\varepsilon_{O-C}$) between water and wall as an independent parameter, keeping the size parameter ($\sigma_{C-C}$) unchanged. Hydrophobicity is said to increase when $\varepsilon_{O-C}$ is reduced. We study the case $\varepsilon_{O-C} = 0.1143$ kcal/mol, a 7% reduction compared to the full value $\varepsilon_{O-C} = 0.1230$ kcal/mol. These simulations are labeled a, e.g. (9,9)-SWCNTa; simulations with the full potential are labeled b. Furthermore, we study a case which models boron nitride nanotubes (SWBNNT) isostructural to the carbon tubes. Still keeping the $\sigma$-value constant, we set $\varepsilon = 0.1216$ and 0.1502 kcal/mol for the oxygen−boron and oxygen−nitrogen interactions, respectively, as in ref 11. Already the 7% decrease in hydrophobicity is found to lead to a loss of water conductivity in the small (5,5)-SWCNT.[11] Similarly, it is found that in (5,5)-armchair SWBNNT attractive interactions between water and nitrogen sites are primarily accountable for the good water conduction. Therefore, it seemed interesting to look at the diffusion and structural properties of water confined in large diameter tubes also of this type. Further details of the nanotube-simulations are given in Table 1. A pure SPC/E-water box at 298 K was also run for comparison.

The coordinates for the wall atoms of the nanotubes are generated by using the Materials Studio Visualizer program.[23] Short pieces of tube are then surrounded by about 2,000 SPC/E water molecules in a simulation box, *NpT* simulations are started with $p = 1$ atm and the temperature is lowered from high values to $T = 298$ K. In a few 10 ps, depending on tube size, the small sections of the tubes are filled with water. Several of these

pieces, for details see below, are then put together in a periodic box and equilibrated before starting the production runs.

All MD production simulations are performed in the canonical (*NVT*) ensemble at a temperature of 298 K using the Nosé-Hoover thermostat implemented in the DL_POLY program package,[24] version 2.17. The dimensions of the periodic simulation box for each system are twice the nanotube diameter in the *x*- and *y*-directions and the length of the tube in the *z*-direction. The principal axis of the nanotube is the *z*-axis of the simulation box. Periodic boundary conditions are applied to all three directions. The long-range electrostatic interactions between water molecules are computed using the Ewald method, and the short-range van der Waals interactions are computed up to a cutoff radius equal to the nanotube diameter for $m = 9$, 10, and 12, and equal to 18.44 Å for $m = 14$, 16, and 20. The equations of motion are integrated with a 0.25-fs time step. The production runs are conducted for at least 1 ns following the equilibration period of 0.25 ns. During the production runs, the coordinates and velocities are stored, usually every 50 fs, for further analyses.

## III. Results and Discussion

**(a) Structure.** Figure 1 shows the so-called cylindrical $g(r)$-functions across the boron-nitride nanotubes. The numbers above the curves refer to the average number of water molecules present in the various regions; the total number of molecules is listed in Table 1. In the (9,9) case only one peak appears, in keeping with the results by Mashl et al.[14] for their (9,9) single-wall nanotube, while starting from the (10,10) and in the larger tubes, the cylindrical RDF shows two peaks indicating layering. The distance between these two peaks is 2.89, 2.89, 2.91 and 2.92 Å in the (12,12), (14,14), (16,16), and (20,20) tubes, respectively, larger than the $r_{OO}$ distance of the first maximum of the $g(r_{OO})$-function in bulk water (2.76 Å). In the tubes with diameters above 18 Å the water density at the interior layer is very close to bulk density; inside a cylinder of 2.2 Å radius around the *z*-axis of the (20,20) tube it is exactly 1.0 g/cm$^3$.

Figure 2 gives a visual impression of the water arrangements (and motions) by showing the *x*- and *y*-coordinates of one (left) and five (right) arbitrarily selected water molecules plotted at regular time intervals during the simulations. The functions for the other two cases, SWCNTa and SWCNTb, are very similar to Figures 1 and 2 and are, therefore, not shown here. The boundary-layer peaks are only slightly enhanced with increasing wall−water interactions, as expected. As an example, we find an average of 250, 252, and 253 water molecules in the boundary layer in the cases of (20,20) SWCNTa, SWCNTb, and SWBNNT, respectively. The motions of the water molecules will be analyzed below.

When water molecules are confined in nanotubes, their neighborhoods differ from those in the bulk phase. A molecule is said here to have *n* neighbors if at a given time there are simultaneously *n* oxygen atoms with distances of $r_{OO}$ < the first minimum of the bulk $g(r_{OO})$ (i.e., 3.33 Å) from the central oxygen atom. This definition does of course not imply that the coordination of the central oxygen is necessarily tetrahedral. Figure 3 shows the distributions of the number of neighbors, as defined above, for the SWBNNTs, separately for water molecules in the center and near the wall of the tubes, and in pure water. In the (9,9) tube all water molecules are located close to the wall and there is no water in the center of the pore, see Figures 1 and 2. The water structure in this tube is indeed peculiar with an extremely strong preference for four neighbors. For the wider nanotubes, a regular pattern emerges with a more or less invariable distribution of neighbors in the outermost layer and distributions in the interior converging with increasing tube diameter toward the one for pure water.

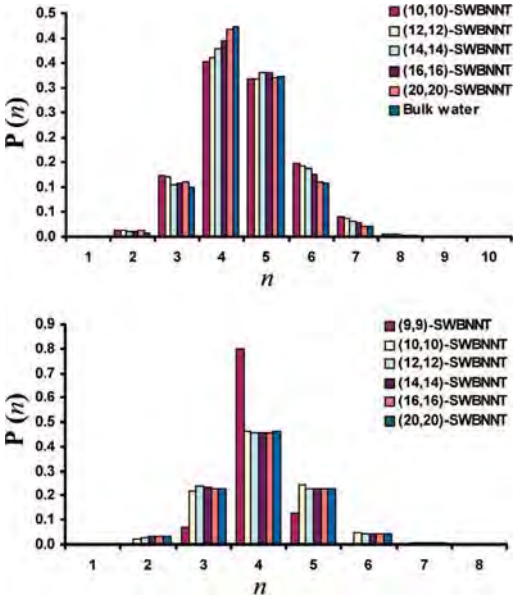


**Figure 3.** Distributions of the number of water neighbors of a water molecule in the interior (top) and in the outermost layer (bottom) in SWBNNT and, for comparison, in pure SPC/E water (top).

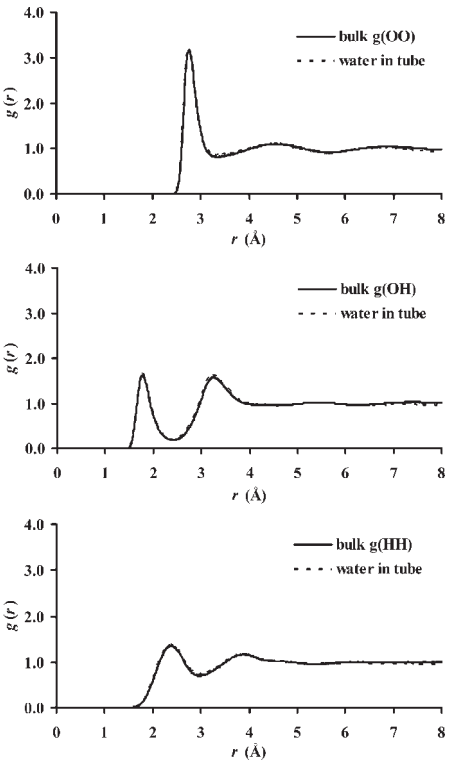


**Figure 4.** Radial distribution functions $g_{OO}$, $g_{OH}$, and $g_{HH}$ for pure water (solid) and for water molecules in the center (−2.2 Å < *r* < 2.2 Å) of the (20,20) SWBNNT (dashed).

In order to further analyze the water structure in the center of a large tube, Figure 4 compares the three radial distribution functions (rdf) $g(r_{OO})$, $g(r_{OH})$, and $g(r_{HH})$ obtained in our pure bulk water reference run (see Table 1) with the ones obtained for molecules in the center of the (20,20) SWBNNT. Only sites inside a cylinder of 2.2 Å radius around the *z*-axis (see Figure 1) are selected as centers for this function. Since the number

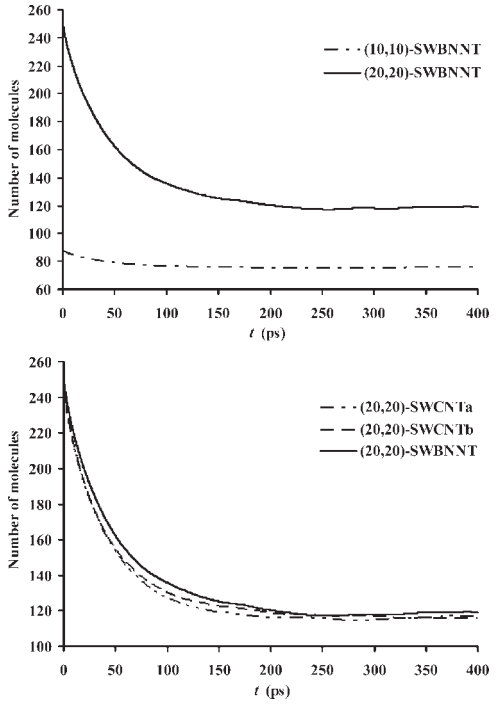


**Figure 5.** Average number of water molecules present in the outermost water layer at time 0 and still present there at later times, from simulation of (10,10) and (20,20) SWBNNT (top), and additionally, for comparison, for SWCNTa and SWCNTb (bottom).

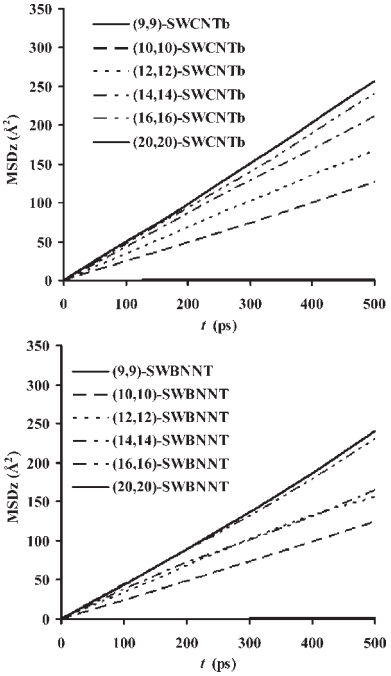


**Figure 6.** Mean square displacements of the oxygen atoms of water in the SWCNTbs (top) and SWBNNTs (bottom). For the self-diffusion coefficients, see Table 2 and Figure 7.

density is not constant across the tube, the normalization of these functions is somewhat arbitrary. The zone of roughly constant density inside the tube is about 8-Å wide, we thus selected to set $g(r \approx 6\ \text{Å}) = 1$ to ease comparisons. The figure shows that the three $g$-functions inside the tube are almost indistinguishable from the bulk ones. Thus, even with the strongest of our three wall−water interaction models, the water inside the larger tubes is, at least as far as the radial structure is concerned, very close to bulk water.

**(b) Dynamics.** Figure 5 shows the decay of the number of water molecules present in the boundary layer of the tube wall [defined as the water molecules with $r = \sqrt{(x^2 + y^2)}$ values larger than the minima in the distribution functions shown in Figure 1] at an initial time $t_0$, as a function of time. This figure shows, as examples, the results for a large and a small tube and also for a large tube with different interactions strengths (hydrophobicities) between water and wall. They confirm the visual impression obtained from Figure 2, namely that a given water molecules samples more or less the entire tube interior during the duration of our simulations.

The long time limit of these correlation functions is the expectation value of the initial molecules being present in the boundary layer when the system is totally mixed. It is seen that this value is reached, within the fluctuations, in all cases after about 150 ps. Functions of type

$$f(t) = a + b \cdot \exp(-t/\tau) \tag{1}$$

describe the correlation very well in all cases; the correlation times $\tau$ are all between 40 and 50 ps with the higher values for the stronger wall−water interactions. The sum $a + b$ obtained from the fits is, as it should be, close to the average total number of water molecules present in the boundary layer, which is also reported in Figure 1 from integrations of the distribution functions plotted there.

Figure 6 shows the averaged mean-square displacements of the oxygen atoms of the water molecules, corrected for the random drifts induced by the thermostat. The translational self-diffusion coefficients reported in Table 2 and Figure 7 have been obtained by fitting expressions

$$\left\langle (z - z_0)^2(t) \right\rangle = A + 2D_z t \tag{2}$$

to the mean-square displacement curves in $z$-direction at long times. We obtained a value of $D = 2.5 \pm 0.1 \times 10^{-5}$ cm$^2$s$^{-1}$ from our pure water simulation. This $D$-value is intermediate between the values reported by Mashl[14] ($2.69 \times 10^{-5}$ cm$^2$s$^{-1}$) and by experimental diffusion coefficient of water ($2.30 \times 10^{-5}$ cm$^2$ s$^{-1}$).[25] In passing, we also take good note of the remarks in these papers that the fact that the experimental $D$ is well reproduced by a given model for the pure liquid at a given state point does not necessarily mean that it will also do so in solutions, at an interface, or under different thermodynamic conditions. We nevertheless expect systematic trends (e.g., size dependences, or when the wall−water interactions are modified) to be reasonably well mirrored.

Figure 7 shows that no self-diffusion can be detected in the narrowest tubes during our simulation runs of a few nanoseconds. $D_z$ increases with increasing tube diameter and comes close to its bulk value in our widest tubes with diameters of about 24 Å, the convergence toward this value being faster for smaller wall−water interactions. In the case of the boron-nitride tubes the convergence is not monotonous. We were not able to pinpoint the particular structural features that may explain the plateau in $D_z$ observed between the (10,10) and (14,14) tubes (which we think is outside our uncertainties) in a convincing way. Even larger irregular variations of the self-diffusion have been observed by Mashl et al.[14] in narrower CNTs. No influence of the wall−water interactions can be distinguished in tubes wider than about 20 Å.

It is seen in Figure 6 that the linear regime of the mean-square displacement is reached typically after about 10 ps. Comparing this time with the typical time for water molecules to stay in the boundary layer discussed above (viz. 40 to 50 ps, see Figure 5), indicates that a separation of the total self-

**TABLE 2: Axial Self-Diffusion Coefficients $D_z$ ($cm^2\ s^{-1}$) of Water in Nanotubes at the Average Temperature of 298 K and the Water Density of 1.0 g/cm$^3$[a]**

| model | $D_z$ ($cm^2\ s^{-1}$) | model | $D_z$ ($cm^2\ s^{-1}$) | model | $D_z$ ($cm^2\ s^{-1}$) |
|---|---|---|---|---|---|
| bulk water | $2.50 \times 10^{-5}$ | | | | |
| (9,9)-SWCNTa | $3.00 \times 10^{-8}$ | (9,9)-SWCNTb | $9.80 \times 10^{-8}$ | (9,9)-SWBNNT | $8.60 \times 10^{-8}$ |
| (10,10)-SWCNTa | $1.20 \times 10^{-5}$ | (10,10)-SWCNTb | $1.30 \times 10^{-5}$ | (10,10)-SWBNNT | $1.20 \times 10^{-5}$ |
| (12,12)-SWCNTa | $2.00 \times 10^{-5}$ | (12,12)-SWCNTb | $1.70 \times 10^{-5}$ | (12,12)-SWBNNT | $1.60 \times 10^{-5}$ |
| (14,14)-SWCNTa | $2.30 \times 10^{-5}$ | (14,14)-SWCNTb | $2.10 \times 10^{-5}$ | (14,14)-SWBNNT | $1.60 \times 10^{-5}$ |
| (16,16)-SWCNTa | $2.40 \times 10^{-5}$ | (16,16)-SWCNTb | $2.40 \times 10^{-5}$ | (16,16)-SWBNNT | $2.40 \times 10^{-5}$ |
| (20,20)-SWCNTa | $2.70 \times 10^{-5}$ | (20,20)-SWCNTb | $2.60 \times 10^{-5}$ | (20,20)-SWBNNT | $2.50 \times 10^{-5}$ |

[a] The uncertainties are estimated to be of the order of $\pm 0.1 \times 10^{-5}$ $cm^2\ s^{-1}$.

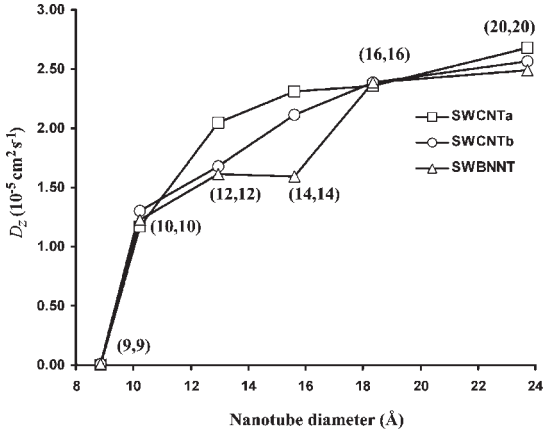


**Figure 7.** Axial self-diffusion coefficients $D_z$ ($10^{-5}$ $cm^2\ s^{-1}$) of water in nanotubes as a function of tube size.

diffusion into a component originating in the boundary layer molecules and a second one originating in the bulk would be justified. This work is presently ongoing.

## IV. Summary and Conclusions

Molecular dynamics computer simulations at room temperature of water-filled single-wall model nanotubes with diameters ranging from about 9 Å to about 24 Å have shown that, by and large, the influence of the wall on the local density of the water and on its self-diffusion does not extend much beyond the layer of molecules directly adsorbed to the wall. In particular circumstances, probably when the geometrical constraints by and the interactions with the wall favor the formation of particular water structures, anomalies cannot be ruled out even in tubes of intermediate widths.

Varying the strength of the wall−water interactions within reasonable limits for carbon or boron-nitride tubes does not alter these conclusions. The adsorbed water layer, on the other hand, is very strongly affected both in its structure and in its dynamics. The characteristic time for the exchange dynamics between the adsorbed layer and the rest of the water is of the order of about 40 to 50 ps, i.e. relatively long compared to the time needed for the diffusive regime to be reached in normal, unconfined water at the same thermodynamic conditions.

**Acknowledgment.** This work was supported in part by Grants from the Thailand Research Fund (to J.L. and P.A.B.) and the Kasetsart University Research and Development Institute (KURDI), the National Nanotechnology Center (NANOTEC Center of Excellence and CNC Consortium), the National Research Council of Thailand (NRCT), and the Commission on Higher Education (Postgraduate Education and Research Programs in Petroleum and Petrochemicals, and Advanced Materials to J.L. as well as Postdoctoral Research Scholar to T.N.). The support from the Graduate School Kasetsart University (to N.A.) is also acknowledged.

## References and Notes

(1) O'Connell, M. J. *Carbon Nanotubes: Properties and Applications*; CRC Press: Boca Raton, FL, 2006.
(2) Iijima, S. *Nature* **1991**, *354*, 56–58.
(3) Wang, Z. L.; Poncharal, P.; De Heer, W. A. *J. Phys. Chem. Solids* **2000**, *61*, 1025–1030.
(4) Sui, H.; Han, B. G.; Lee, J. K.; Walian, P.; Jap, B. K. *Nature* **2001**, *414*, 872–878.
(5) Kolesnikov, A. I.; Zanotti, J.-M.; Loong, C.-K.; Thiyagarajan, P.; Moravsky, A. P.; O. Loutfy, R. O.; Burnham, C. J. *Phys. Rev. Lett.* **2004**, *93*, 035503/1–035503/4.
(6) Chou, C.-C.; Hsiao, H.-Y.; Hong, Q.-S.; Chen, C.-H.; Peng, Y.-W.; Chen, H.-W.; Yang, P.-C. *Nano Lett.* **2008**, *8*, 437–445.
(7) Tajkhorshid, E.; Nollert, P.; Jensen Morten, O.; Miercke Larry, J. W.; O'Connell, J.; Stroud Robert, M.; Schulten, K. *Science (New York)* **2002**, *296*, 525–530.
(8) Bianco, A.; Kostarelos, K.; Prato, M. *Curr. Opin. Chem. Biol.* **2005**, *9*, 674–679.
(9) Hummer, G.; Rasaiah, J. C.; Noworyta, J. P. *Nature* **2001**, *414*, 188–190.
(10) Waghe, A.; Rasaiah, J. C.; Hummer, G. *J. Chem. Phys.* **2002**, *117*, 10789–10795.
(11) Won, C. Y.; Aluru, N. R. *J. Am. Chem. Soc.* **2007**, *129*, 2748–2749.
(12) Beckstein, O.; Biggin, P. C.; Sansom, M. S. P. *J. Phys. Chem. B* **2001**, *105*, 12902–12905.
(13) Allen, R.; Hansen, J.-P.; Melchionna, S. *J. Chem. Phys.* **2003**, *119*, 3905–3919.
(14) Mashl, R. J.; Joseph, S.; Aluru, N. R.; Jakobsson, E. *Nano Lett.* **2003**, *3*, 589–592.
(15) Liu, Y.; Wang, Q.; Wu, T.; Zhang, L. *J. Chem. Phys.* **2005**, *123*, 234701–234707.
(16) Koga, K.; Tanaka, H.; Zeng, X. C. *Nature* **2000**, *408*, 564–567.
(17) Liu, Y.; Wang, Q. *Phys. Rev.* **2005**, *72*, 085420/1–085420/4.
(18) Liu, Y.; Wang, Q.; Zhang, L.; Wu, T. *Langmuir* **2005**, *21*, 12025–12030.
(19) Joseph, S.; Aluru, N. R. *Nano Lett.* **2008**, *8*, 452–458.
(20) Won, C. Y.; Aluru, N. R. *J. Phys. Chem. C* **2008**, *12*, 1812–1818.
(21) Berendsen, H. J. C.; Grigera, J. R.; Straatsma, T. P. *J. Phys. Chem.* **1987**, *91*, 6269–6271.
(22) Guillot, B. *J. Mol. Liq.* **2002**, *101*, 219–260.
(23) Accelrys, Inc. *Materials Studio, 4.2 V*; Accelrys, Inc.: San Diego, CA, 2007.
(24) Smith, W.; Forester, T. R.; Todorov, I. T.; Leslie, M. *The DL_POLY 2.0, User Manual, Version 2.17*; CCLRC, Daresbury Laboratory: Daresbury, U.K., 2006.
(25) Price, W. S.; Ide, H.; Arata, Y. *J. Phys. Chem. A* **1999**, *103*, 448–450.

JP8088676

# Stable nanoporous alkali halide polymorphs: a first principles bottom-up study

**W. Sangthong,[abc] J. Limtrakul,[bc] F. Illas[a] and S. T. Bromley*[ad]**

***Received 29th May 2008, Accepted 2nd October 2008***
***First published as an Advance Article on the web 7th November 2008***
**DOI: 10.1039/b809129c**

The stability of nanoclusters and nanocluster-based polymorphs of a large range of alkali halides were investigated using state-of-the-art plane wave density functional theory (DFT) calculations. Specifically, the most energetically stable cluster isomers of $(MX)_{12}$ (M = Li, Na, K, Rb, Cs, X = F, Cl, Br, I) were considered (*i.e.* the slab and cage) with respect to two bulk polymorphs: rock-salt (rs-MX) and a nanoporous analogue of the zeolite sodalite (SOD-MX). In both cases, these bulk materials can be regarded as being assembled from their respective cluster building block (slab → rs, cage → SOD). For all alkali halides the dense rs-MX phase was found to be more stable than the low-density nanoporous SOD-MX phase. For the $(MX)_{12}$ clusters, the dense slab cluster isomers were also generally found to be the most stable cluster type except, however, for the LiX series where the cage isomer was energetically preferred. The energy difference between the rs-MX and the SOD-MX bulk polymorphs (per MX unit) was found to follow the same trend as that between the respective $(MX)_{12}$ slab and cage clusters. Correspondingly, the cage-based SOD-LiX phases were all found to be only marginally metastable with respect to the rs-LiX forms ($\Delta E_{\text{SOD-rs}} \leq 0.05$ eV per LiX). From DFT calculations on the low enthalpy landscape of LiF polymorphs, the energy *versus* volume equations of state of rs-LiF and SOD-LiF were compared with those of a number of other LiF polymorphs showing SOD-LiF to be stable with respect to compression and expansion and very competitive energetically with a number of denser phases. Classical molecular dynamics calculations were also performed to confirm the thermal stability of the SOD-LiF phase, further strengthening our prediction as to the viability of these novel low density nanoporous ionic materials.

## Introduction

The modification of the structure of inorganic crystalline solids through varying the external pressure is now a widely used experimental technique that has led to the discovery of a number of new phases with potential applications.[1,2] Theoretical methods have also been widely used to study the behavior of experimentally known ground-state phases of numerous materials under pressure.[3] Although experiments are now able to effectively maintain negative pressure conditions to explore the possibility of phases lower in density than the ground state, this technique does not yet allow one to investigate a wide class of very low density porous crystalline materials (*e.g.* zeolites[4]), which are regularly synthesised *via* bottom-up routes in solution. In order to theoretically explore the feasibility of new crystalline polymorphs, other than those obtained through pressure-induced transformations of the most stable phase, global optimisation algorithms may be employed to study the energy landscape of materials.[5–7] In relation to the present work on alkali halide polymorphs, we note in particular the recent careful investigations of a range of known and new hypothetical polymorphs of the alkali halides by Schön and co-workers[8,9] based on empirical potential based global optimisation followed by refined energy evaluation by DFT calculations. Crystal global optimisations generally start from the assumption of a bulk periodic crystal cell occupied by atoms, and make use of different algorithms to modify the atomic positions and cell dimensions towards possible minima. Such approaches may be described as top-down approaches. Increasing evidence indicates that the atomic structure of materials at the nanoscale, where the assumption of long-range crystalline periodicity breaks down, can be significantly different from that exhibited by bulk materials. Recent work, for instance, provides evidence that materials exhibiting the well-known wurtzite structure such as AlN, GaN, and SiC may exhibit a new graphitic phase as nanofilms.[10] Likewise, ZnO nanostructures have been predicted to experience different types of structural transformations specific to the nanoscale.[11,12] Compelling evidence that both $SiO_2$ and MgO may exhibit different stable alternative phases in thin films grown on metal substrates has also been reported.[13,14]

Recently, some of us reported on the prediction of low density nanoporous polymorphs of MgO, ZnO[15] and $SiO_2$[16] based on the assembly of highly stable nanoclusters. In contrast to top-down global optimisations, this approach follows the ideas contained in the ground-breaking work of Jena and co-workers on metal clusters[17] and can be regarded as a bottom-up means to materials prediction. Although both top-down and bottom-up approaches aim to find new stable polymorphs the former directly searches through the space of possible polymorphs whereas the latter aims first to find stable building blocks (*e.g.* through global optimisation

[a]*Departament de Química Física & Institut de Química Teòrica i Computacional (IQTCUB), Universitat de Barcelona, C/Martí i Franquès 1, E-08028 Barcelona, Spain*
[b]*Center of Nanotechnology, Kasetsart University, Bangkok 10900, Thailand*
[c]*Department of Chemistry, Kasetsart University, Bangkok 10900, Thailand*
[d]*Institució Catalana de Recerca i Estudis Avançats (ICREA), 08010 Barcelona, Spain*

of cluster isomers[15,16]) and then materials that may be regarded as arising from their assembly. Although both approaches are quite complementary, the focus on those materials which can be regarded as formed from stable cluster building blocks may provide more insight into ways in which these materials maybe fabricated *via* bottom-up routes. The prediction of stable polymorphs of MgO and ZnO as low density zeolitic analogues, derived from the bottom-up assembly of highly stable $(MO)_{12}$ cluster building blocks,[15] strongly suggests that similar nanoporous phases are likely to be stable for different types of materials.

In this work, we explore a wide range of ionic alkali halides for which, in many cases, small clusters have been experimentally generated.[18–20] Following the work of Carrasco *et al.*,[15] we use DFT calculations to study the relative stability of energetically lowest lying $(MX)_{12}$ (X = halogen, M = alkali metal) cluster isomers with respect to that of two polymorphs, which can be considered as formed from the assembly of these clusters: the rock-salt (rs-MX), and SOD-MX (the latter phase having strong topological similarity with the silicate zeolite sodalite[4,15]) phases. We compare the energetic trends of the cluster isomers and their respective bulk phases, throughout the full range of materials which reveals an intriguing link between nanoscale and macroscopic stabilities. The Li-based materials are shown, in particular, to be most likely to exhibit new viable low density nanoporous phases.

## II. Computational details

In order to explore low density phases of the alkali halides, two different sets of DFT calculations were carried out. In the first, the differences between the most energetically stable cluster isomers were calculated, and in the second we obtained the energy *versus* volume equation of state (EOS) of the extended bulk polymorphs. In the case of the clusters, for all alkali halides we considered three low energy $(MX)_{12}$ isomers: (i) a $4 \times 2 \times 1$ slab, (ii) a tube formed from four stacked $X_3M_3$ hexagons, and (iii) a discrete SOD cage. In order to attain a balanced description of both discrete and extended systems, it is convenient to use the same computational approach and, whenever possible, the same basis set. This can be achieved by first choosing a reliable exchange-correlation functional that can be used in molecular and periodic calculations and, secondly, by expanding the total electron density in a plane wave basis using an appropriate unit cell. A plane wave basis is computationally efficient and for which the quality can be conveniently and generally defined by a single parameter. The Perdew–Wang (PW91) form[21,22] of the generalised gradient approach (GGA), as implemented in the VASP code,[23–25] has been chosen for the exchange-correlation potential. Due to its formulation, the PW91 functional is known to be particularly suitable for solids.[26] Furthermore, for the comparison of the stabilities of solids of the same composition but with significantly different densities and ionic coordination environments (especially relevant for comparing rs-MX and SOD-MX polymorphs) the PW91 functional has also been shown to perform extremely well for other materials.[27] Specifically for the alkali halides other work has shown that the PW91 can reproduce experimental data with high accuracy[28] (see also Table 2).

For the discrete systems, using a plane wave basis set requires simply placing the clusters inside a large enough box, which is periodically repeated. The box chosen has to be large enough so that the distance between repeated $(MX)_{12}$ clusters is sufficient to make inter-cluster interactions negligible (in our calculations >1 nm). For the solids, although in principle we may use the same $(MX)_{12}$ units and reduce the vacuum space between the periodically repeated units in such a way that a bulk structure is created, it was computationally more convenient to use the typical cubic unit cell for rs-MX and a cubic unit cell containing 12 atoms of a cage for SOD-MX. For the bulk systems, it is also necessary to carry out appropriate integrations in reciprocal space, this is accomplished by using a Monkhorst–Pack grid of special *k*-points ($7 \times 7 \times 7$ for the rock-salt structure and $3 \times 3 \times 3$ for the low density phases). In the present work, we included plane waves with kinetic energies up to 415 eV in the basis set. The effect of core electrons on the valence density was taken into account through the plane augmented wave method[29] as implemented by Kresse and Joubert.[30] For all MX bulk structures, density functional optimisations of atomic positions and cell shape were carried out for different volumes of the unit cell and the volume *versus* energy data fitted using the Birch–Murnaghan EOS[31] in order to obtain the minimum energy and optimum cell parameters. For all calculations (both solids and clusters) no explicit use of symmetry was employed.

## III. Relative stability of $(MX)_{12}$ alkali halide clusters

The main purpose of the present work is to analyse the possibility of low density bulk phases of alkali halides and their relative stability with respect to the face-centered cubic (fcc) structure, which is almost always the most stable alkali halide polymorph. We note that for the most voluminous cation ($Cs^+$) with the three larger anions: $Cl^-$, $Br^-$, $I^-$, the body-centered cubic (bcc) phase is the ground state bulk phase. With relation to our bottom-up approach, however, the clusters $(CsCl)_{12}$, $(CsBr)_{12}$, $(CsI)_{12}$, all appear to be most stable as $4 \times 3 \times 2$ fcc slab isomers. For each alkali halide, we energy minimised the slab, the cage and tube (see Fig. 1) as $(MX)_{12}$ isomers. In all cases the $(MX)_{12}$ tube was never found to be the most stable isomer, with the lowest energy

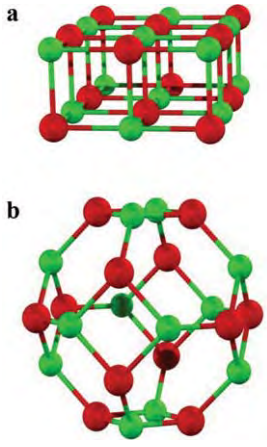


**Fig. 1** Schematic representation of the structure of the slab (a) and cage (b) structures of the $(MX)_{12}$ alkali halide clusters. Red spheres represent the fluoride anion whereas the green spheres represent the lithium cations.

 

**Table 1** Total energy (binding energy with respect to constituent spherical non spin-polarised atoms) per MX unit (in eV) of the slab and cage isomers of the $(MX)_{12}$ alkali halide clusters

| MX | Slab | Cage |
|---|---|---|
| LiF | −9.25 | −9.28 |
| LiCl | −7.16 | −7.18 |
| LiBr | −6.46 | −6.48 |
| LiI | −5.70 | −5.72 |
| NaF | −8.14 | −8.09 |
| NaCl | −6.43 | −6.38 |
| NaBr | −5.81 | −5.76 |
| NaI | −5.14 | −5.09 |
| KF | −7.86 | −7.79 |
| KCl | −6.39 | −6.31 |
| KBr | −5.83 | −5.74 |
| KI | −5.22 | −5.13 |
| RbF | −7.76 | −7.69 |
| RbCl | −6.32 | −6.23 |
| RbBr | −5.77 | −5.68 |
| RbI | −5.17 | −5.08 |
| CsF | −7.73 | −7.69 |
| CsCl | −6.34 | −6.25 |
| CsBr | −5.80 | −5.72 |
| CsI | −5.22 | −5.13 |

isomers being either the cage or slab only. Results for the relative energy of the slabs and cages for the series (M = Li–Cs and X = F–I) are reported in Table I.

For both slab and cage isomers, it is found that with the same alkali cation ($M^+$) and varying the halide anion ($X^-$), the optimised energies increase with decreasing ionic radius ratio ($r_{M^+}/r_{X^-}$) and follow an almost linear correlation (see Fig. 2a,b). Correspondingly, the most stable clusters are those of $(MF)_{12}$ type while the least stable are those of $(MI)_{12}$ composition. In contrast along each series: $(MF)_{12}$, $(MCl)_{12}$, $(MBr)_{12}$, $(MI)_{12}$ (*i.e.* fixing the halide type and varying the alkali metal ion) we see that, although for $(MCl)_{12}$, $(MBr)_{12}$, $(MI)_{12}$ the energy varies very little, for $(MF)_{12}$ both the cages and slabs clusters are significantly more stabilised (see Fig. 2a,b). Of all alkali halides, LiF is found to provide the most stable clusters for both slab and cage structures with energies (per MX unit) of −9.25 and −9.28 eV per LiF, respectively. This result together with the energetic preference of LiF for the cage isomer over the slab already provides an indication that LiF can be regarded as a special case.

In Fig. 3 we report the energy difference (per MX unit) between the cage and the slab isomers for each fixed halide (X) while varying the metal type (M). In most cases we find that the cubic slab isomer is most stable. This concurs with previous work showing an energetic preference for cubic isomers in alkali halide clusters containing Na, K, and Rb using a variety of theoretical methods including global optimisation techniques with empirical potentials, *ab initio* Hartree–Fock and Møller–Plesset second-order perturbation theory.[32–36] These works also often found

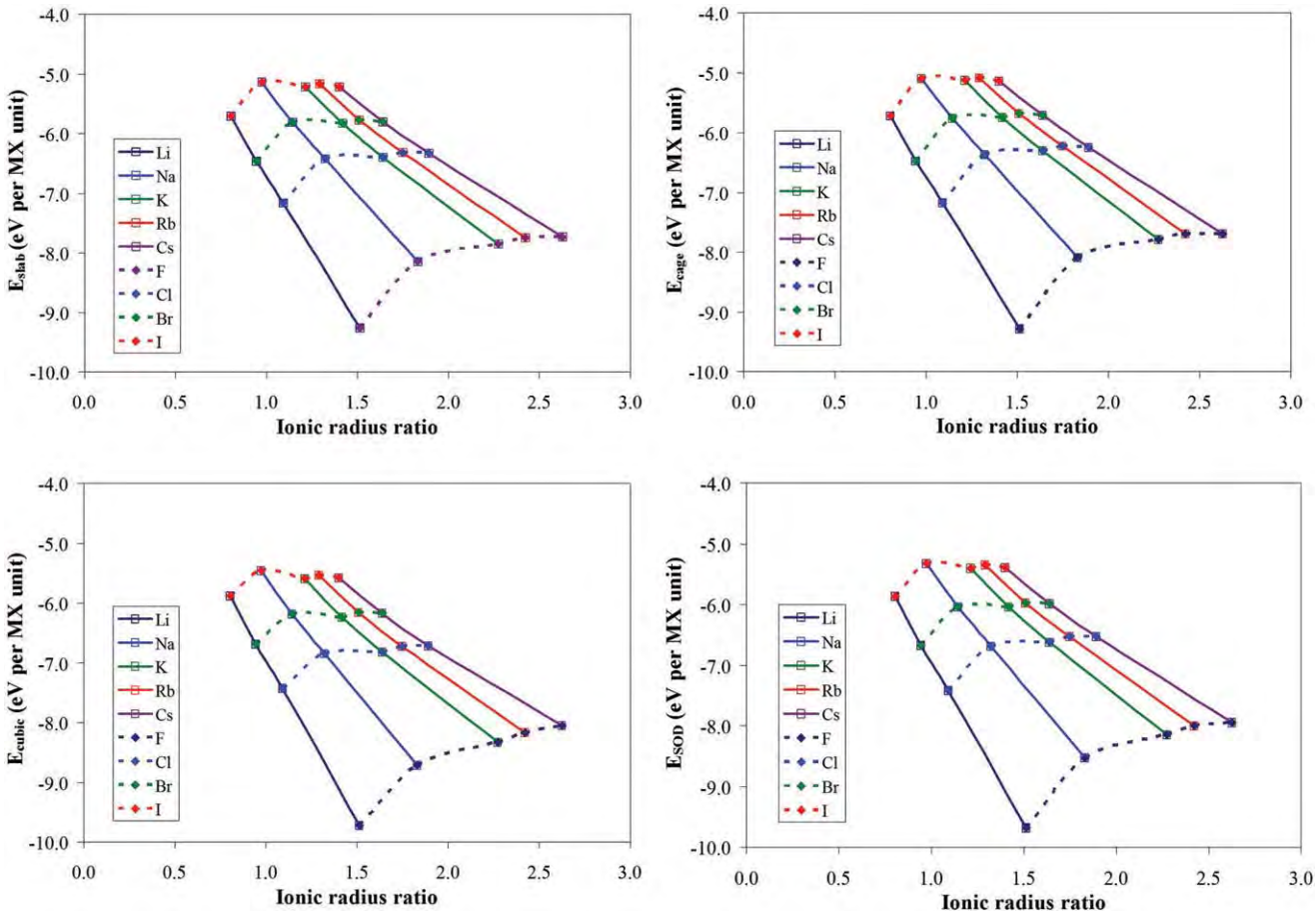


**Fig. 2** Total energy of the alkali halides as clusters (left-top: slab; right-top: cage) and materials (left-bottom: RS; right-bottom: SOD) as a function of the cation and anion type with respect to cation-to-anion radius.

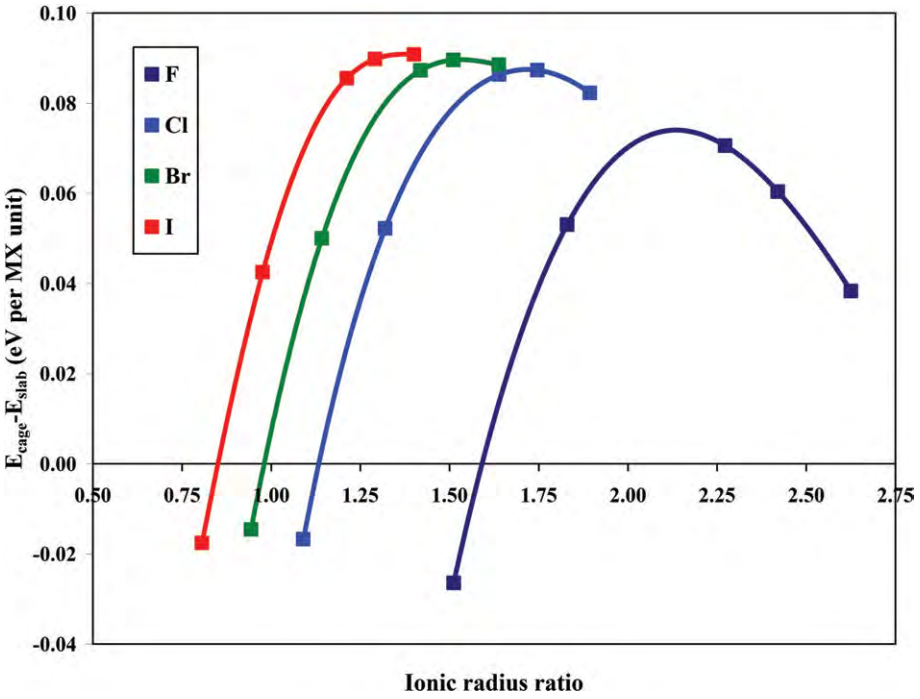


**Fig. 3** Energy difference (eV per MX) between the slab and cage structure of the $(MX)_{12}$ alkali halide clusters as a function of the cation-to-anion ionic radius ratio. Each set of points relates to a series maintaining the halide and varying the alkali metal from $Li^+$ to $Cs^+$ from left to right (the lines are parabolic fits to the points to guide the eye).

evidence for competition between the energetic stability between rock-salt and tubular hexagonal ring-based structures with the latter being generally favoured for Li-containing clusters. On idealised ionic packing grounds, it has been argued that the relative energy between the dense cubic and more open tubular structures may be rationalised by consideration of the ratio between the cationic and anionic radii.[33,37] Essentially, the argument is analogous to that used in the approximate rationalisation of dense crystal structures[38] whereby increasing differences in cation and anion radii leads to the inability of the ions to pack as closely as when of similar size, thus leading to more open crystal structures. In clusters, as there are no restrictions on periodicity, we may expect that the respective ions when of significantly different size may use non-bulk-like means to optimise their ionic packing. The reported emergence of non-bulk-like tubular low energy cluster isomers is in line with such packing rationalisations for the LiX series due to the very small relative size of the $Li^+$ ion with respect to all the halide ions. However, as noted above, for the size $(MX)_{12}$ we find tubular clusters are not the ground state isomer for any alkali halide and further that for the $(LiX)_{12}$ series the more open SOD cage structure appears to be the optimal manner to "pack" $Li^+$ and $X^-$ ions. Specifically, the cage structure is found to be more stable than both the slab and tubular cluster isomers for all the $(LiX)_{12}$ clusters, and for the remainder the cubic slab is the $(MX)_{12}$ ground state. For $(LiX)_{12}$ the energy differences between cubic slab and cage isomers are rather small, lying in the range between $-0.015$ to $-0.026$ eV per LiX. However, from Li to Cs for a fixed halide, the energy difference between the two clusters increases steeply with increasing cation *versus* anion ionic radius ratio up to a maximum difference. For I the energy difference increase stops at this maximum point for CsI, whereas for Br-, Cl- and F-containing clusters the energy difference maximises and then starts to reduce again. For the F series this effect is most notable with an energy difference between slab and cage reaching a maximum for KF and then decreasing significantly for RbF and CsF. Again, we can rationalise this trend with respect to ionic radii ratios, whereby at the maximum of the curves in Fig. 3 we have ions of a very similar size (and thus a preference for close-packed slabs) and away from these maxima such packing is not possible and the more open cage isomer becomes progressively more competitive.

Although ionic packing arguments are useful, they are only general idealised guides to structural preferences that omit many details (*e.g.* polarisation-induced ion distortions) of the bonding in real systems, which is governed by the electronic structure. To gain some more detailed insight into the bonding and ionic polarisation in the cage and slab clusters, we have also analysed the changes in the electronic structure upon increasing the formal cation–anion radius ratio using the electron localisation function (ELF). The ELF was introduced by Becke and Edgecombe[39] and has been extensively used to analyse chemical bonding in a range of systems.[40–42] The topological analysis of the ELF allows one to distinguish between core and valence electrons and, in this last case, between lone pairs, covalent bonding between two atoms or multi-centered bonds. In the case of the alkali halide clusters, the chemical bonding is highly ionic as is reflected in the ELF maps shown in Fig. 4. When going from the extremes of LiF to CsF, through KF as an intermediate case, one can note interesting changes in the ELF maps for both cage and slab cluster isomers. The ELF maps for the slab cluster show rather spherical ELF basins, which are indicative of a highly ionic character, although

 

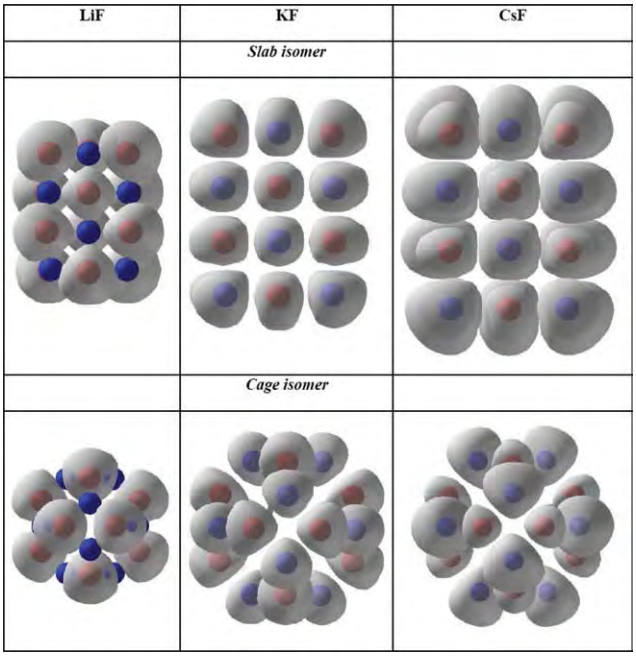


**Fig. 4** ELF maps for the slab and cage structures of LiF, KF and CsF. The red centres indicate the positions of the alkali metal ions and the blue centres the halide ion positions. The grey area shows the form of the ELF basins for each ion.

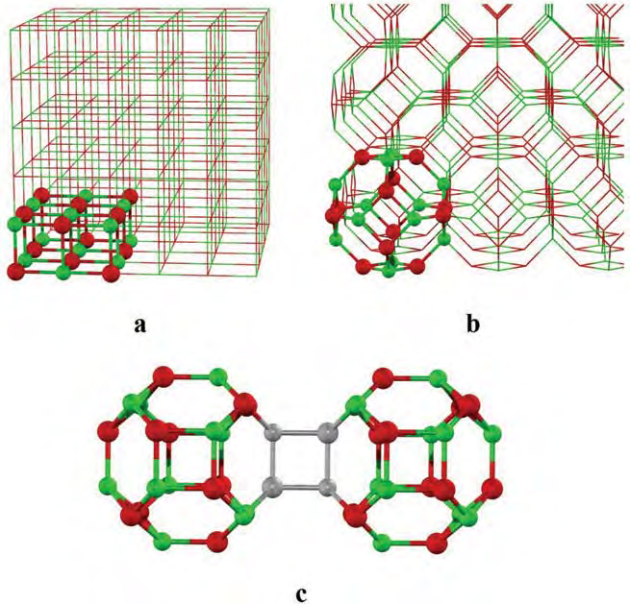


**Fig. 5** rs-MX and SOD-MX structures of alkali halides viewed as the assembling of $(MX)_{12}$ slabs (a) and $(MX)_{12}$ cage clusters (b). In (c) we highlight (in grey) one of the 12 linkages per cage involved in the assembly of the cage cluster into the SOD-MX material. Red spheres represent the fluoride anion whereas the green spheres represent the cations.

with an increasing and noticeable deformation when going from LiF to CsF. For the cage clusters the situation is rather different, the ELF maps are largely deformed from the symmetric spherical shape, even for LiF. This is a clear indication that, in spite of similar stability, the chemical bond between the alkali metal and the halogen atom in the slab and cage clusters is different, with a more marked polarised and directional character in the cage structures. The directional character of the chemical bond in the cage structures is enhanced when going from LiF to CsF. This may seem counter-intuitive since one would expect the ionic character to increase along the series in response to the decrease of the alkali atom ionisation potential. However, one must also consider the different polarisation of the electron density upon increasing the cation atomic radius. In any case, the ELF maps in Fig. 4 show that a clear difference exists in the chemical bond of alkali halides in the slab and cage structures.

## IV. Rock-salt structure *versus* sodalite structure of bulk alkali halides

Two types of bulk structures have been considered for the alkali halide materials (rs-MX and SOD-MX) both of which may be thought of as arising from assembling slab or cage clusters, respectively (see Fig. 5c). SOD-MX may be constructed by assembling twelve $(MX)_{12}$ cages by square links in such a way that an equivalent empty cage is created in the center of the resulting unit (see Fig. 4c). In the SOD-MX phase, the alkali and halide atoms are four-coordinated centers whereas in the rs-MX, the usual octahedral coordination is maintained. It should be noted that the sodalite (SOD) is not the only low density phase that may be generated by using $(MX)_{12}$ clusters as building blocks. Other low density nanoporous zeolite-like materials (*e.g.* LTA or faujasite[4]) can also be constructed from this simple building block,[15] however, these structures are generally less stable than SOD and have not been further considered.

For all the alkali halides series, the energy minimum for the SOD-MX structure has a volume per MX unit, which is significantly larger than that of the rs-MX structure with a concomitant lower density. Moreover, the SOD-MX phase is always higher in energy than the rs-MX polymorph, which is qualitatively different from the $(MX)_{12}$ slab and cage clusters where the cage structure was predicted to be more stable for the lithium halides. Nevertheless, as with the clusters, LiF is found to be the most stable compound in both rs-MX and SOD-MX phases with the calculated total energies being rather close: −9.73 and −9.68 eV per LiF, respectively. In order to investigate energetic trends, following the above analysis of the clusters, we have considered the dependence of the total energy of the rs-MX and SOD-MX phases with respect to the ionic radii ratio of the respective alkali metal and halide. For both phases, the total energy of the most stable polymorph, for a given cation while varying the anion, increases almost linearly with decreasing the ionic radii ratio (see Fig. 2c,d) in line with the trend observed for the clusters. Following the variation in cluster energetics, we also observe relatively little change in the energy of either bulk phase with the MCl, MBr, or MI composition, whereas the SOD-MF and rs-MF phases are particularly stable.

Examining the energy difference between rs-MX and SOD-MX phases at their corresponding optimised geometries, Fig. 6 shows that the energy difference between the rs-MX and SOD-MX phases also follows the same trend as the energy difference between the slab and cage $(MX)_{12}$ clusters (Fig. 3). This interesting finding strongly suggests that the relative energy

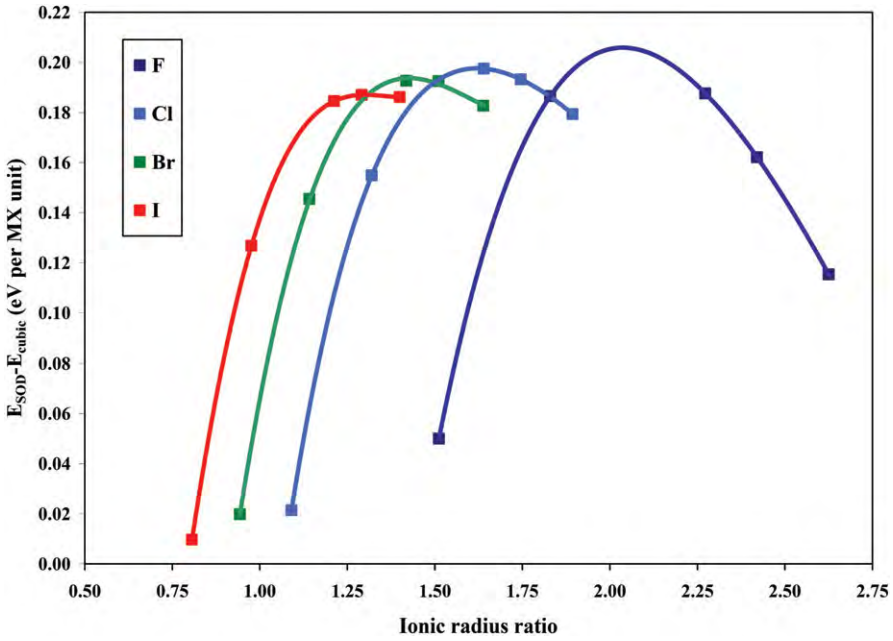


**Fig. 6** Energy difference (eV per MX) between the rs-MX and SOD-MX alkali halide materials as a function of the cation–anion ionic radius ratio. Each set of points relates to a series maintaining the halide and varying the alkali metal from $Li^+$ to $Cs^+$ from left to right (the lines are parabolic fits to the points to guide the eye).

of the rs-MX and SOD-MX crystal structures is largely determined by the same driving forces that cause the energy difference between the slab and cage building blocks. Contrary to the cluster energetics, the SOD-MX phase is always less stable than the rs-MX phase. However, for the most stable SOD-MX materials (*i.e.* those containing the smallest cation, Li) the minimum energies of the SOD-LiX phases (LiF, LiCl, LiBr and LiI) are only 0.01–0.05 eV per LiX above the ground state rs-LiX structure. These very small energy differences suggest that for these compositions the SOD-LiX structure could be a viable synthesis target. Furthermore, in line with the behavior observed in Fig. 3 for the clusters, we also find the SOD-CsF phase (exhibiting a significant difference between anion and cation radius) is only 0.12 eV per CsF higher than the rs-CsF phase.

## V. Stability of SOD-LiF

In order to compare the present results with previous work, we have calculated the energy *versus* volume EOS for rs-LiF and SOD-LiF together with a range of other reported phases in the literature. In particular we compare our bottom-up generated LiF-SOD phase with three new LiF phases predicted by Doll *et al.*[8] by global optimisation. These authors have also carried out periodic Hartree–Fock and LDA calculations for the different polymorphs predicted from their global optimisation studies. Interestingly, the low density SOD-LiF structure was not located by this method although it is very competitive in energy with respect to their newly predicted low energy LiF-phases (*i.e.* LiF-I, LiF-II and LiF-III). The probable reason for this omission is not due to any failure in the global optimisation methodology employed but rather due to the concentration on relatively dense materials with typically smaller unit cells. Whereas periodic Hartree–Fock calculations incorrectly predict wurtzite as the most stable LiF polymorph, both LDA calculations by Doll *et al.*[8] and the present GGA calculations correctly predict rs-LiF to be the most stable structure, in agreement with experiment. The energetic stability order of the remaining polymorphs predicted by LDA and GGA is, however, rather different. This is not so surprising since LDA is known to overestimate binding energies. Consequently, polymorphs with different crystal structures and variable coordination environments around each atom are affected differently by the LDA error. The GGA energies are likely to be considerably more accurate[26–28] and it is likely that the phase diagram in Fig. 7 provides a more realistic picture of the energy landscape of LiF polymorphs. In Table 2 we also compare the present GGA calculations for rs-LiF with other reported DFT calculations and experimental data also showing that the present PW91 calculations give a good account of the cell volume and bulk modulus.

The GGA calculated energy *versus* volume EOS curves predict that the SOD-LiF structure is marginally lower in energy than the LiF-I phase and significantly lower in energy than the LiF-II and LiF-III phases generated by Doll *et al.*[8] Only four phases appear to lie lower in energy than the SOD-LiF phase: rs-LiF, 5-5-LiF, wz-LiF (wurtzite), and zb-LiF (zincblende), all of which are significantly denser than SOD-LiF. The 5-5 phase (also known as the hexagonal phase in other studies[43,15]) was first proposed by Schön in the context of global optimisation of alkali metal oxide phases.[5] Interestingly, from a bottom-up perspective, the 5-5 phase can also be regarded as being generated from the assembly of hexagonal tubular clusters. Structurally, the 5-5 phase lies between wurtzite and rocksalt and is thought to be a relatively unstable phase with respect to its collapse into rocksalt, and, thus, 5-5-LiF is probably only viable as a real material at very low temperatures and low pressures.[5,8,43] Although the EOS curve of SOD-LiF shows that the structure is

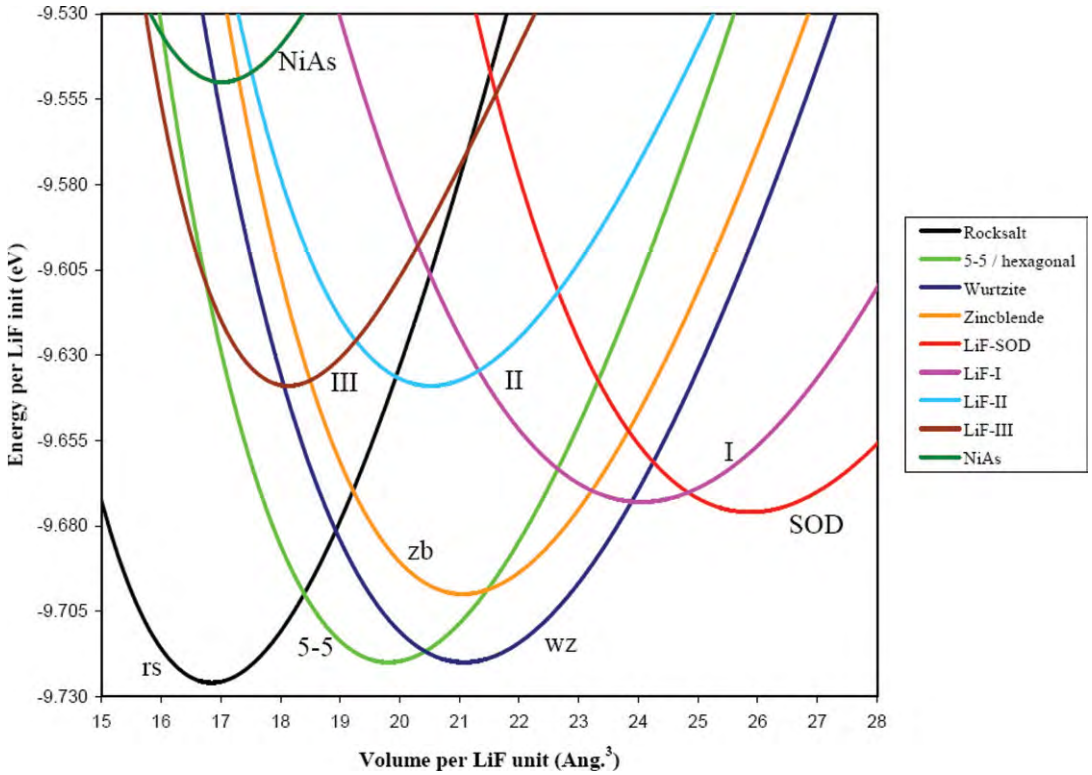


**Fig. 7** Energy *versus* volume phase diagram for various polymorphs of LiF. The legend entries are ordered from top to bottom with respect to increasing minimum total energy ($E_o$).

**Table 2** Properties of a range of LiF polymorphs calculated from the EOS fits to the GGA-DFT calculated data shown in Fig. 6: (i) $E_0$, minimum total energy (eV per LiF), (ii) $\Delta E_0$, total energy differences (eV per LiF), (iii) $V_0$, volume at minimum energy (Å$^3$ per LiF), (iv) $B_0$, the bulk modulus (GPa per LiF). The equilibrium volume and bulk modulus (where available) of rs-LiF are compared with experimental values and other reported DFT calculations in the first five rows

| | $E_0$ | $\Delta E_0$ | $V_0$ | $B_0$ |
|---|---|---|---|---|
| rs-LiF (exp.) | | | 16.32[47] | 69.9[48] |
| rs-LiF (present work) | −9.726 | 0.000 | 16.85 (+3.2%) | 68.6 (−1.9%) |
| rs-LiF (BPW91-GGA)[49] | | | 17.48 (+7.1%) | 63.9 (−8.6%) |
| rs-LiF (LDA)[49] | | | 14.38 (−11.9%) | 71.4 (+2.1%) |
| rs-LiF (LDA)[8] | | | 15.29 (−6.3%) | — |
| wz-LiF | −9.720 | 0.006 | 21.08 | 48.3 |
| 5-5-LiF | −9.701 | 0.025 | 16.94 | 60.4 |
| zb-LiF | −9.700 | 0.026 | 21.06 | 51.8 |
| SOD-LiF | −9.676 | 0.050 | 25.87 | 41.7 |
| LiF-I | −9.673 | 0.054 | 24.05 | 36.0 |
| LiF-II | −9.639 | 0.087 | 20.52 | 48.6 |
| LiF-III | −9.639 | 0.087 | 18.13 | 72.5 |

stable with respect to a range of pressures (both negative and positive in relation to the ground state) this only strictly applies at 0 K. Considering that SOD-LiF is one of the lowest density phases yet predicted for a purely ionic material, it is of interest as to whether the structure would be also stable to collapse to a denser more stable phase at finite temperatures.

In order to test the finite temperature stability of LiF-SOD we have employed constant pressure and temperature (NPT) molecular dynamics (MD). Due to the current unavailability of NPT-MD simulations within the VASP code and the very high computational expense of performing such simulations in a fully *ab initio* manner, we employed classical MD. For these simulations we employed the GULP code[44] and the interionic potentials of Catlow *et al.*[45] with a 3 Å cut-off and a 0.25 Å smoothing taper to avoid discontinuities in the energy and first and second derivatives. Importantly, considering the ELF analysis in section II, the potentials account for ionic polarisation *via* the shell model of Dick and Overhauser.[46] Firstly, we note that energy minimisations of atomic position and cell parameters using these potentials confirm that the SOD-LiF phase is metastable (by 0.03–0.17 eV per LiF) with respect to the lower energy denser phases (rs-LiF, wz-LiF, zb-LiF, 5-5-LiF) in qualitative agreement with the GGA-DFT optimisations, which confirms that the SOD-MX phase is not artificially stabilised by the

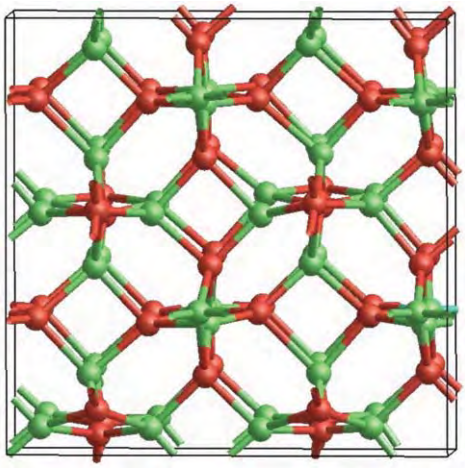

**Fig. 8** Snapshot from the MD simulation of the SOD-LiF phase showing a typical configuration of the $2 \times 2 \times 2$ super cell at 300K. Red spheres represent the fluoride anions and green spheres represent the lithium cations.

potentials. Furthermore, although fitted with respect to rs-LiF, the potentials also give optimised SOD-LiF cell parameters ($a$, $b$, $c = 5.17$ Å; $\alpha$, $\beta$, $\gamma = 90°$) in reasonable agreement with the GGA-DFT results ($a$, $b$, $c = 5.37$Å; $\alpha$, $\beta$, $\gamma = 90°$). After first equilibrating the SOD-LiF system for 30 ps, we simulated the behaviour of a SOD-LiF $2 \times 2 \times 2$ supercell at 300 K at zero external pressure for over 2 nanoseconds. Throughout the MD simulation we found that the bonding topology of the SOD-LiF structure remained fully intact with the root mean squared deviations from the optimal cell parameters being only 0.12 Å with respect to unit cell dimensions and 1.44 degrees with respect to unit cell angles (see typical MD snapshot in Fig. 8). Surprisingly, unlike the 5-5-LiF phase, which is probably unstable, these calculations suggest that the SOD-LiF phase, if synthesised, would be stable under ambient conditions.

## V. Conclusions

The possible existence of low density phases of bulk alkali halides has been investigated using a bottom-up approach together with state-of-the-art plane wave DFT calculations. To this end, the relative energies of the lowest energy cluster isomers of $(MX)_{12}$ have been studied throughout the MX series. The slab form of the $(MX)_{12}$ cluster may be viewed as the precursor of the rock-salt (rs-MX) structure while the assembling of $(MX)_{12}$ cages can lead to a low density phase reminiscent of the sodalite zeolite (SOD-MX). The slab $(MX)_{12}$ isomer is found to be energetically more stable than the cage, except for the LiX (X = F, Cl, Br, I) series where the cage is the most stable $(MX)_{12}$ cluster isomer. For a given halide series the energy difference between slab and cage isomers increases up until a maximum is reached and then decreases towards CsX. In the bulk analogues, the same behaviour with respect to the energy difference between rs-MX and SOD-MX is also observed. In both cases, the trends may be approximately rationalised in terms of ionic packing. In all alkali halides the SOD-MX phase was found to be stable with respect to compression and expansion at 0 K through calculation of their volume *versus* energy EOS. Furthermore, in the LiX (X = F, Cl, Br, I) series, where the cage is the ground state $(LiX)_{12}$ cluster, the SOD-LiX material is found to be particularly low in energy with respect to the lowest energy rs-LiX phase ($E_{\text{SOD-rs}}$ energy differences ranging between 0.01–0.05 eV per LiX). Taking the LiF-SOD phase as a case study, we have further employed MD simulations to confirm that the structure of this nanoporous alkali halide is thermally stable at 300 K. Considering that the lowest energy cluster for $(LiX)_{12}$ is a cage, together with the demonstration that for LiF, a nanoporous phase based upon its assembly, is stable with respect to 0 K pressure variation and at finite temperature, we suggest that these highly ionic yet low density materials may be realistic, yet challenging, synthesis targets through an appropriate bottom-up route.

## Acknowledgements

This study has been supported in part by the Spanish Ministry of Education and Science (grants CTQ2005-08459-CO2-01 and UNBA05-33-001) by the Generalitat de Catalunya (grants 2005SGR00697, 2005PEIR0051/69). This work was further supported in part by grants from the Thailand Research Fund (to W.S. and J.L.) and the Commission on Higher Education, Ministry of Education under Postgraduate Education and Research Programs in Petroleum and Petrochemicals, and Advanced Materials. Support from the National Nanotechnology Center (NANOTEC Center of Excellence) under the National Science and Technology Development Agency and KURDI is also acknowledged.

## References

1 L. Liu, W. A. Bassett, *Elements, Oxides, and Silicates. High-Pressure Phases with Implications for the Earth's Interior*, Oxford University Press, New York, 1986.
2 R. J. Hemley, *Ultrahigh-Pressure Mineralogy: Physics and Chemistry of the Earth's Deep Interior, vol. 37 of Reviews in Mineralogy*, The Mineralogical Society of America, Washington, DC, 1998.
3 A. Schleife, F. Fuchs, J. Furthmüller and F. Bechstedt, *Phys. Rev. B*, 2006, **73**, 245212.
4 *Atlas of Zeolite Framework Types, Sixth Edition*, ed. Ch. Baerlocher, LynneB. McCuskerand D. H. Olson, 6th revised edition, Elsevier, Amsterdam, 2007.
5 J. C. Schön, *Z. Anorg. Allg. Chem.*, 2004, **630**, 2354.
6 S. M. Woodley, P. D. Battle, J. D. Gale and C. R. A. Catlow, *Phys. Chem. Chem. Phys.*, 1999, **1**, 2535.
7 A. R. Oganov and C. W. Glass, *J. Chem. Phys.*, 2006, **124**, 244704.
8 K. Doll, J. C. Schön and M. Jansen, *Phys. Chem. Chem. Phys.*, 2007, **9**, 6127.
9 Z. P. Cancarevic, J. C. Schön and M. Jansen, *Chem.–Asian J.*, 2008, **3**, 561.
10 C. L. Freeman, F. Claeyssens, N. L. Allan and J. H. Harding, *Phys. Rev. Lett.*, 2006, **96**, 066102.
11 L. Zhang and H. Huang, *Appl. Phys. Lett.*, 2007, **90**, 023115.
12 A. J. Kulkarni, M. Zhou, K. Sarasamak and S. Limpijumnong, *Phys. Rev. Lett.*, 2006, **97**, 105502.
13 J. Weissenrieder, S. Kaya, J. L. Lu, H. J. Gao, S. Shaikhutdinov, H. J. Freund, M. Sierka and J. Sauer, *Phys. Rev. Lett.*, 2005, **95**, 076103.
14 J. Goniakowski, C. Noguera and L. Giordano, *Phys. Rev. Lett.*, 2004, **93**, 215702.
15 J. Carrasco, F. Illas and S. T. Bromley, *Phys. Rev. Lett.*, 2007, **99**, 235502.
16 J. C. Wojdel, M. A. Zwijnenburg and S. T. Bromley, *Chem. Mater.*, 2006, **18**, 1464.
17 S. N. Khanna and P. Jena, *Phys. Rev. Lett.*, 1992, **69**, 1664.

 

18 J. E. Campana, T. M. Barlak, R. J. Colton, J. J. DeCorpo, J. R. Wyatt and B. I. Dunlap, *Phys. Rev. Lett.*, 1981, **47**, 1046.
19 R. Pflaum, P. Pfau, K. Sattler and E. Recknagel, *Surf. Sci.*, 1985, **156**, 165.
20 Y. J. Twu, C. W. S. Conover, Y. A. Yang and L. A. Bloomfield, *Phys. Rev. B*, 1990, **42**, 5306.
21 J. P. Perdew, J. A. Chevary, S. H. Vosko, K. A. Jackson, M. R. Pederson, D. J. Singh and C. Fiolhais, *Phys. Rev. B*, 1992, **46**, 6671.
22 J. A. White and D. M. Bird, *Phys. Rev. B*, 1994, **50**, 4954.
23 G. Kresse and J. Hafner, *Phys. Rev. B*, 1993, **47**, 558.
24 G. Kresse and J. Furthmüller, *Comput. Mater. Sci.*, 1996, **6**, 15.
25 G. Kresse and J. Furthmüller, *Phys. Rev. B*, 1996, **54**, 11169.
26 J. P. Pedew and K. Burke, *Int. J. Quantum Chem.*, 1996, **57**, 309.
27 D. R. Hamann, *Phys. Rev. Lett.*, 1996, **76**, 660.
28 E. Apra, M. Causa, M. Príncipe, R. Dovesi and V. R. Saunders, *J. Phys.: Condens. Matter*, 1993, **5**, 2969.
29 P. E. Blöchl, *Phys. Rev. B*, 1994, **50**, 17953.
30 G. Kresse and D. Joubert, *Phys. Rev. B*, 1999, **59**, 1758.
31 F. Birch, *Phys. Rev.*, 1947, **71**, 809.
32 J. P. K. Doye and D. J. Wales, *Phys. Rev. B*, 1999, **59**, 2292.
33 A. Aguado, A. Ayuela, J. M. Lopez and J. A. Alonso, *Phys. Rev. B*, 1997, **56**, 15353.
34 T. Croteau and J. Patey, *J. Chem. Phys.*, 2006, **124**, 244506.
35 C. Ochsenfeld and R. Alrichs, *Ber. Der Bunsen-Gesellschaft*, 1994, **98**, 34.
36 M. Lintuluoto, *J. Mol. Struct. (Theochem)*, 2002, **540**, 177.
37 A. Wootton and P. Harrowell, *J. Chem. Phys.*, 2004, **121**, 7440.
38 D. Pettifer, *Bonding and Structure of Molecules and Solids*, Clareden, Oxford, 1995.
39 A. D. Becke and K. E. Edgecombe, *J. Chem. Phys.*, 1990, **92**, 5397.
40 B. Silvi and A. Savin, *Nature*, 1994, **371**, 683.
41 A. Savin, R. Nesper, S. Wengert and T. P. Fässler, *Angew. Chem., Int. Ed. Engl.*, 1992, **36**, 1809.
42 X. Krokidis, S. Noury and B. Silvi, *J. Phys. Chem. A*, 1997, **101**, 7277.
43 S. Limpijumnong and W. R. L. Lambrecht, *Phys. Rev. B*, 2001, **63**, 104103.
44 J. D. Gale, *J. Chem. Soc., Faraday Trans.*, 1997, **93**, 629.
45 C. R. A. Catlow, K. M. Diller and M. J. Norgett, *J. Phys. C: Solid State Phys.*, 1977, **10**, 1395.
46 B. G. Dick and A. W. Overhauser, *Phys. Rev.*, 1958, **112**, 90.
47 V. A. Streltsov, V. G. Tsirelson, R. P. Ozerov and O. A. Golovanov, *Kristallografiya*, 1987, **33**, 90.
48 C. V. Briscoe and C. F. Squire, *Phys. Rev.*, 1957, **1175**, 106.
49 G. Sandrone and D. A. Dixon, *J. Phys. Chem. A*, 1998, **102**, 10310.

# Predicting transition pressures for obtaining nanoporous semiconductor polymorphs: oxides and chalcogenides of Zn, Cd and Mg

**Winyoo Sangthong,[abc] Jumras Limtrakul,[bc] Francesc Illas[a] and Stefan T. Bromley*[ad]**

***Received 22nd March 2010, Accepted 29th May 2010***
***First published as an Advance Article on the web 6th July 2010***
**DOI: 10.1039/c0cp00002g**

The energy *versus* volume equations of state are calculated for seven known and hypothetical polymorphic forms of ZnX, CdX, and MgX (where X = O, S, Se, Te). From these data the phases of lowest enthalpy are extracted with respect to decreasing pressure starting at the ground state for all compositions. Following these paths of minimum enthalpy, with respect to the polymorphs considered, we predict the transition pressures required to convert the ground-state phase into the novel, as yet hypothetical, nanoporous SOD phase (an analogue of the silicate zeolite sodalite). Our results suggest that the SOD phase would be thermodynamically stable for all compositions considered under suitable negative pressures. Of all the compositions considered CdX and MgX with relatively large anions (*i.e.* Se and Te) are specifically predicted to be the most amenable materials for the experimental preparation of the SOD phase.

## Introduction

Binary ionic insulating materials of composition AB are known to exhibit only a small number of dense ground-state phases and are perhaps expected to be the least likely type of system in which to find new low-density polymorphs. Detailed theoretical explorations of the energy and enthalpy landscape of a number of such materials (*e.g.* the alkali halides and oxides) have, however, predicted that some moderately low-density phases should be only slightly metastable at standard pressure, and thermodynamically stable at slightly negative pressures.[1–3] Closely following these predictions, low-temperature atomic deposition on specially prepared substrates, causing conditions of effective negative pressure *via* lattice mismatch effects, has led to the production of LiBr and LiCl in the wurtzite structure (wz-LiBr and wz-LiCl) rather than the denser rocksalt (rs-LiBr and rs-LiCl) polymorph;[4,5] the latter being the ground-state phase under ambient pressure and temperature conditions. Although these are remarkable steps forward in the synthesis of new low-density inorganic polymorphs, potentially more exciting is the possibility of negative pressure conditions leading to new relatively low-density solid phases that are not known to be exhibited by any existing material. The so-called 5–5 or hexagonal phase (referred to hereafter by the abbreviation "hex-AB", where the AB is a 1 : 1 binary compound) consisting of aligned $A_3B_3$ hexagonal tubes, with density lower than rocksalt but higher than wurtzite, for example, was independently theoretically proposed as a metastable polymorph of NaCl[3] and later of MgO.[6] Although a hex-AB bulk phase has not yet been stabilized experimentally, it has been predicted to be potentially stable under suitable negative pressures (typically in the range −1 to −5 GPa) and low temperatures for a number of alkali halides[1] and alkali oxides.[2] Additionally, hex-MgO has been predicted to be formed in localized regions upon mechanically induced buckling of rs-MgO nanotubes.[7]

Other than AB insulators the binary wide-bandgap semiconductor ZnO has attracted significant recent attention with respect to its possible novel low-density polymorphism. ZnO can be prepared in small quantities as the rs-ZnO structure,[8] and can exist as both zinc blende (zb-ZnO) and wz-ZnO (the ground state) structural forms under standard conditions. Density functional (DF) calculations have also predicted that hex-ZnO may be stablised in unstrained ultra-thin nanorods and nanowires,[9] and in thicker nanorods under tensile strain.[10] A phase very similar to hex-ZnO but expanded in the crystallographic *c*-direction so as to make it closely analogous to the layered *h*-BN phase, with a density very similar to wz-ZnO, was also predicted by DFT calculations to be stable in thin films of ZnO.[11] We note that this phase, although often referred to as a graphitic ZnO phase, strictly does not have the same layer ordering as in graphite. Following Limpijumnong *et al.*[10] we will thus refer to this phase as "layered". Experimental deposition of monolayers of ZnO on Ag substrates confirmed that the layered-ZnO phase was stable up to three monolayers where upon the denser wz-ZnO phase appeared to form.[12] More recent DF calculations have predicted that another polymorph, the BCT (Body Centred Tetragonal) phase (also known as the β-BeO phase due to its existence as a high-temperature stable polymorph of BeO[13]), having a lower density than wurtzite, may be stabilized in slightly thicker nanoscale films of ZnO.[14] Other DF calculations have further predicted that BCT-ZnO may be stabilised

[a] *Departament de Química Física & Institut de Química Teòrica i Computacional (IQTCUB), Universitat de Barcelona, C/Martí i Franquès 1, E-08028 Barcelona, Spain*
[b] *Center of Nanotechnology, Kasetsart University Research and Development Institute (KURDI), Kasetsart University, Bangkok 10900, Thailand*
[c] *Department of Chemistry, Faculty of Science, Center of Nanotechnology, Kasetsart University, Bangkok 10900, Thailand*
[d] *Institució Catalana de Recerca i Estudis Avançats (ICREA), 08010 Barcelona, Spain*

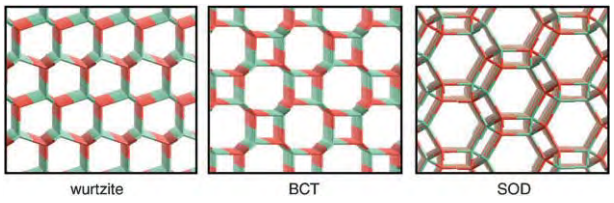


**Fig. 1** Views of the three lowest density polymorphs considered. Left: wurtzite along the *a*-axis, middle: BCT along the *a*-axis, and right: SOD along the [111] direction.

in wz-ZnO nanorods under a tensile strain of 7 GPa (*i.e.* −7 GPa uniaxial pressure) in the [0001] direction.[15] We note that the BCT phase has also been predicted as a polymorphic phase potentially accessible under conditions of negative pressure greater (*i.e.* more negative) than that required to obtain the hexagonal phase for a range of alkali halides and oxides.[1,2] Searches of the low-energy landscape of the insulator boron nitride (BN) have also found BCT-BN as a possible metastable phase.[16] The BCT structure is shown in Fig. 1.

Having an even lower density than BCT, the SOD polymorph (with an analogous structure to the silicate sodalite structure[17]), has also been predicted by DF calculations to be only moderately metastable under conditions of zero pressure and temperature for both ZnO[18] and many alkali halides.[19] The SOD structure (see Fig. 1) is particularly interesting due to its nanoporous structure consisting of interlinked cages, and, surprisingly for such a low density structure, shows high thermal stability.[19] Recently, it has also been suggested that SOD-ZnO may form the structural basis for the most energetically stable nanoparticles for $(ZnO)_N$ for $N \geq 60$.[20] Although the SOD structural type is, as yet, experimentally unknown in any AB material, if its synthesis is viable, it would be particularly interesting for semiconductor materials where it immediately suggests the possibility of introducing dopant atoms into the cages to enable tailoring of physical and chemical properties for a range of applications (*e.g.* opto-electronics, sensors).

In the present work, we considerably extend the exploration of predictive polymorphism in AB materials by studying the oxides and chalcogenides (sulfides, selenides, and tellurides) of Mg, Zn and Cd. Apart from MgO and MgS, it is of note that the remaining members of this set of materials are semiconductors with experimentally determined bandgaps ranging between 1.4 eV (CdTe) and 3.6 eV (MgSe). In particular, we explore the relative energetic and enthalpic stability of the low-density nanoporous SOD polymorph with respect to seven other polymorphic forms: (i) rs, (ii) hex, (iii) layered, (iv) wz, (v) zb, (vi) NiAs, and (vii) BCT. We note that the layered phase is only considered when the hex polymorph is unstable to spontaneous "de-layering" for a particular composition. For all polymorphs in all compositions we use DF calculations to assess the viability of forming the SOD phase under negative pressure conditions *via* calculating the transition pressures for obtaining the SOD phase from the respective ground state phase. Trends in the transition pressures are used to predict the semiconductor materials for which the SOD polymorph could be most easily prepared.

## Computational details

The energies and structures of all considered phases of MgX, ZnX and CdX (where X = O, S, Se, Te) were calculated using DFT employing the GGA (Generalised Gradient Approximation) PW91 exchange–correlation potential[21] as implemented in the VASP code.[22] Integrations in reciprocal space were accomplished by using Monkhorst–Pack[23] grids of special *k*-points (rs: 7 × 7 × 7, wz: 7 × 7 × 7, zb: 3 × 3 × 3, hex: 7 × 7 × 7, NiAs: 7 × 7 × 7, 3 × 3 × 3: BCT, 3 × 3 × 3: SOD). The effect of core electrons on the valence density was taken into account through the projector augmented wave method[24] with a 415 eV plane wave energy cut-off for valence states. All reported calculated energies refer to constituent spherical non-spin-polarised atoms in eV per formula unit. Calculated volume *versus* energy data was fitted using the third-order Birch–Murnaghan equation of state (EOS).[25] The corresponding expression for the enthalpy with respect to pressure was then used to calculate the transition pressures (taken to be the pressure where the enthalpies of two phases were equal). In some cases where there are transitions to intermediate phases going from the ground-state phase to the SOD phase, the pressure of the final transition (*i.e.* the one at the most negative pressure) is reported.

## Results and discussion

### ZnX series

Figs. 2a–d show the calculated total energy *versus* volume plots for the ZnX series. All EOS fitting parameters of the various considered phases of ZnX are given in Tables 1(a–d). The predicted series of ground-state phases are found to vary as wz-ZnO, zb-ZnS, zb-ZnSe and zb-ZnTe following the experimentally observed stability trend.[26] The energy difference between wz-ZnX and zb-ZnX is always found to be very small ($\leq$0.017 eV/ZnX) indicating that both phases are likely to be found as ZnX polymorphs under non-extreme thermodynamic conditions, also matching with the experimentally observed phases. Other than the wz-ZnX to zb-ZnX crossover, the trends in energetic stability with respect to wz-ZnX upon changing the anion from O to Te are very similar. For all phases apart from zb-ZnS, the change of anion from O to S results in an energetic destabilisation with respect to wz-ZnS. The largest O-to-S energetic shift is found for rs-ZnS (+0.33 eV/ZnX) and the smallest for BCT-ZnS (+0.03 eV/ZnX). Going along the series ZnS, ZnSe, ZnTe, there are few further changes in relative energetic stability with the order of energetic stability maintained throughout the set of considered polymorphs. The relatively lower density BCT-ZnX and SOD-ZnX phases are particularly unaffected by the anion change from S through to Te, with both only varying by up to a maximum of 0.017 eV/ZnX with respect to wz-ZnX. Throughout the same anion variation the denser phases, rs-ZnX and NiAs-ZnX, both become slightly more energetically stable with respect to wz-ZnX by 0.055 eV/ZnX.

The evolution of stability of the hex-ZnO phase with increase in anion size is subtlety different from the other considered phases in that it is also mechanically destabilized

 

upon the ZnO-to-ZnS compositional change. Although hex-ZnO is truly the bonded tubular hexagonal phase, lying at a density between that of wz-ZnO and rs-ZnO, for ZnX (with X = S, Se, Te) the hexagonal phase has an energetic preference to form the layered-ZnX phase. This tendency can be seen in the EOS plots in Figs. 2b–d where the energetic minimum of the layered-ZnX phase EOS lies at almost the same volume as that for wz-ZnX. Also the shape of the EOS curves for the layered-ZnX phases are distinctly asymmetrical about the energetic minima with the higher volume side of the curves being flatter due to the relative energetic ease of de-layering (also reflected in the relatively low fitted B0 values in Tables 1b–d).

A more general mechanical instability is shown by the BCT phase. In all cases considered the low volume (high pressure)

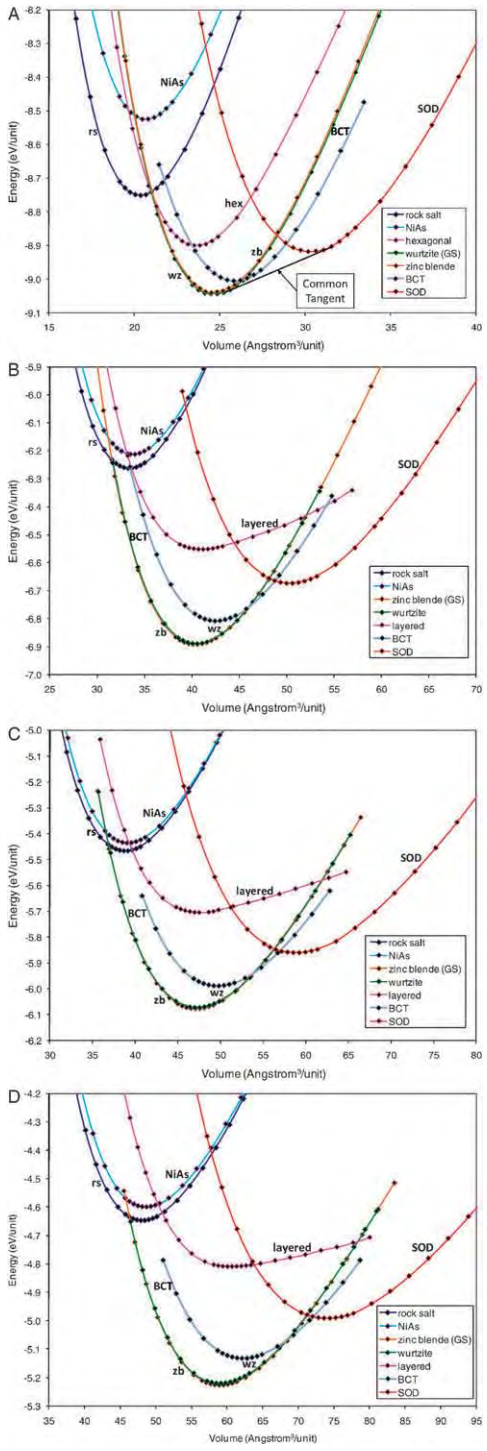


**Fig. 2** (a) Energy *versus* volume plots for the seven considered phases of ZnO. GS in the legend denotes the experimental ground-state phase. An example of the common tangent construction between the EOS curves of wz-ZnO and SOD-ZnO is also shown. (b) Energy *versus* volume plots for the seven considered phases of ZnS. GS in the legend denotes the experimental ground-state phase. (c) Energy *versus* volume plots for the seven considered phases of ZnSe. GS in the legend denotes the experimental ground-state phase. (d) Energy *versus* volume plots for the seven considered phases of ZnTe. GS in the legend denotes the experimental ground-state phase. Note that for (a)–(d) (*i.e.* S–Te) the hex-ZnTe is found to be unstable to spontaneous transformation to the layered phase which is reflected in the figure labelling—see also main text.

**Table 1** (a–d) Fitted parameters to the EOS data of the ZnX series polymorphs: total energy ($E0$, eV/ZnX), volume per unit ($V0$, Å$^3$/ZnX), bulk modulus ($B0$, GPa), and the pressure derivative ($B'$). Bold entries indicate the experimental ground-state phases

(a) ZnO

| | $E0$ | $V0$ | $B0$ | $B'$ |
|---|---|---|---|---|
| rs-ZnO | −8.75 | 20.35 | 166.2 | 4.57 |
| NiAs-ZnO | −8.52 | 20.69 | 159.5 | 4.55 |
| zb-ZnO | −9.04 | 24.68 | 130.7 | 4.52 |
| **wz-ZnO** | −9.05 | 24.68 | 129.6 | 4.57 |
| hex-ZnO | −8.90 | 23.60 | 130.5 | 5.15 |
| BCT-ZnO | −9.00 | 25.82 | 113.5 | 3.52 |
| SOD-ZnO | −8.92 | 30.26 | 105.1 | 4.51 |

(b) ZnS

| | $E0$ | $V0$ | $B0$ | $B'$ |
|---|---|---|---|---|
| rs-ZnZ | −6.26 | 33.33 | 86.1 | 4.55 |
| NiAs-ZnZ | −6.21 | 33.74 | 86.5 | 4.62 |
| **zb-ZnS** | −6.89 | 40.40 | 69.7 | 4.48 |
| wz-ZnS | −6.89 | 40.46 | 69.4 | 4.40 |
| hex-ZnS | −6.56 | 41.75 | 32.3 | 7.91 |
| BCT-ZnS | −6.81 | 42.73 | 60.9 | 3.18 |
| SOD-ZnS | −6.67 | 50.28 | 54.6 | 4.39 |

(c) ZnSe

| | $E0$ | $V0$ | $B0$ | $B'$ |
|---|---|---|---|---|
| rs-ZnSe | −5.46 | 38.75 | 70.6 | 4.72 |
| NiAs-ZnSe | −5.43 | 39.15 | 70.6 | 4.65 |
| **zb-ZnSe** | −6.08 | 47.15 | 57.1 | 4.60 |
| wz-ZnSe | −6.07 | 47.21 | 56.7 | 4.55 |
| hex-ZnSe | −5.70 | 47.96 | 27.6 | 9.54 |
| BCT-ZnSe | −5.99 | 49.70 | 51.0 | 4.00 |
| SOD-ZnSe | −5.86 | 58.75 | 44.4 | 4.59 |

(d) ZnTe

| | $E0$ | $V0$ | $B0$ | $B'$ |
|---|---|---|---|---|
| rs-ZnTe | −4.65 | 48.09 | 53.9 | 4.85 |
| NiAs-ZnTe | −4.60 | 48.61 | 53.3 | 4.72 |
| **zb-ZnTe** | −5.23 | 58.98 | 43.6 | 4.73 |
| wz-ZnTe | −5.22 | 58.99 | 43.3 | 4.72 |
| hex-ZnTe | −4.81 | 61.73 | 16.9 | 9.87 |
| BCT-ZnTe | −5.13 | 62.22 | 38.5 | 4.44 |
| SOD-ZnTe | −4.99 | 73.89 | 33.2 | 4.69 |

points on the EOS for each BCT-AB phase considered could only be continued up to a limited lower volume bound before a spontaneous transition occurred to the respective rock salt phase. Due to this transition to BCT-rs the EOS for BCT was fitted only for those points before the transition occurred, explaining the somewhat truncated appearance of the EOS curves for some BCT compositions.

### CdX series

The calculated total energy *versus* volume plots for the polymorphs of the CdX series are shown in Figs. 3a–d. Tables 2(a–d) gives all EOS fitting parameters of the various considered phases of CdX. Unlike the ZnX series, the ground state for CdO is found to be rock salt, as also observed in experiment.[26] Upon traversing the series of anions from O toTe, the trend in energetic stabilities with respect to wz-CdX is quite similar to that of the ZnX series. Again, apart from zb-CdX all other phases are relatively destabilized with respect to wz-CdS in increasing anion size. Contrasting with the ZnX series trend, this continues in a monotonically increasing fashion for all the relatively dense phases (rs-CdX, NiAs-CdX, hex-CdX). Note that, unlike ZnX, although the hex-CdX phase has a tendency to delayer (as seen in the asymmetric EOS curves) their energetic minima correspond to the hexagonal phase and not the layered-CdX phase. The lower density phases of BCT-CdX and SOD-CdX, after their initial destabilization upon going from the CdO to CdS, maintain fairly constant energy differences ($0.06 \pm 0.01$ eV/CdX and $0.15 \pm 0.01$ eV/CdX, respectively) with wz-CdX. For CdS and CdSe, the wurtzite phase is the ground state. The relative stabilization of the zb-CdX phase upon increasing anion size, however, causes zb-CdTe to become the predicted ground-state phase. The ground-state trend with anion variation (*i.e.* rs-CdO, wz-CdS, wz-CdSe, zb-CdTe) matches the observed trend in experiment.[26]

### MgX series

The calculated total energy *versus* volume curves of the considered polymorphs of the MgX series are shown in Figs. 4a–d. All corresponding EOS fitting parameters are documented in Tables 3(a–d). Following experiment, for the relatively smaller O and S anions rs-MgO and rs-MgS are found to be the most stable phases. With increasing anion size from O to Te, we note a number of changes in the relative energetic stability of the considered polymorphs. For consistency with our previous discussions and taking wz-MgX as a reference point, we find the dense rs-MX and hex-MgX phases become continually and rapidly destabilized going through the series (with an overall relative shift of 0.28 eV/unit and 0.24 eV/unit, respectively). Conversely, the two other relatively dense polymorphs (NiAs-MgX and zb-MgX) become more stabilized with respect to wz-MgX (although with NiAs-MgTe becoming slightly destabilized again going from X = Se to Te). At the same time, the least dense phases of BCT-MgX and SOD-MgX change little in their relative energetic stability with respect to wz-MgX (between 0.04–0.06 eV/unit for BCT-MgX and 0.13–0.17 for SOD-MgX), similar to that found for the ZnX and CdX series. The relative destabilization of the rs-MgX phase with increasing anion size results in the emergence of wz-MgX as a new predicted ground-state phase upon going from X = S to X = Se, and subsequently Te. The concurrent

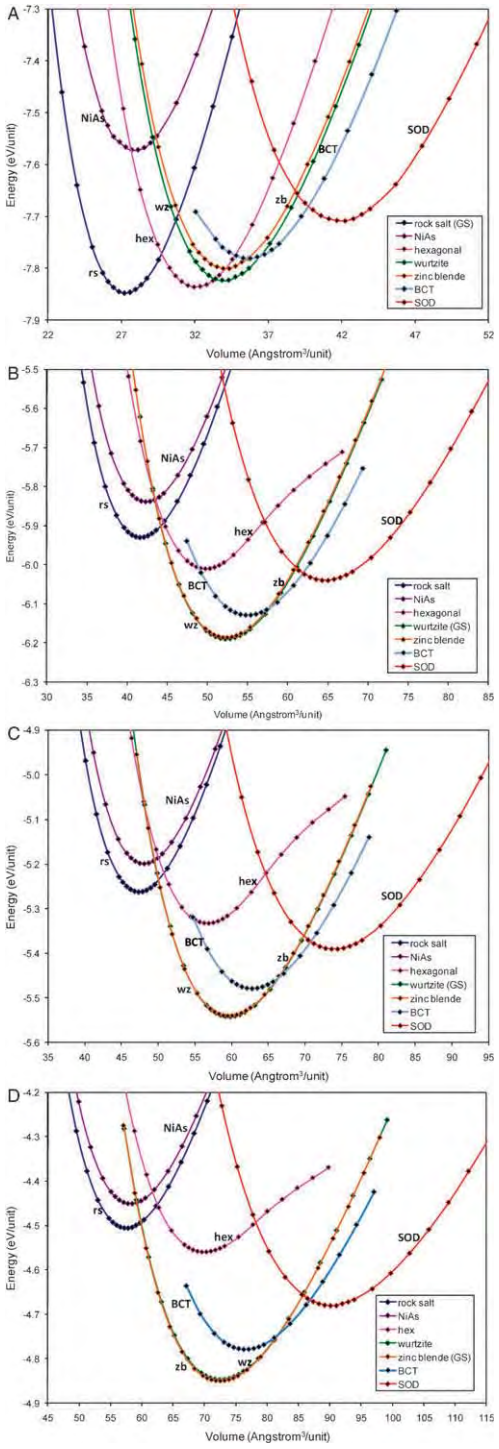


**Fig. 3** (a) Energy *versus* volume plots for the seven considered phases of CdO. GS in the legend denotes the experimental ground-state phase. (b) Energy *versus* volume plots for the seven considered phases of CdS. GS in the legend denotes the experimental ground-state phase. (c) Energy *versus* volume plots for the seven considered phases of CdSe. GS in the legend denotes the experimental ground-state phase. (d) Energy *versus* volume plots for the seven considered phases of CdTe. GS in the legend denotes the experimental ground-state phase.

**Table 2** (a–d) Fitted parameters to the EOS data of the CdX series polymorphs: total energy ($E0$, eV/CdX), volume per unit ($V0$, Å$^3$/CdX), bulk modulus ($B0$, GPa), and the pressure derivative ($B'$). Bold entries indicate the experimental ground-state phases

(a) CdO

| | $E0$ | $V0$ | $B0$ | $B'$ |
|---|---|---|---|---|
| **rs-CdO** | −7.85 | 27.25 | 128.6 | 4.89 |
| NiAs-CdO | −7.57 | 27.86 | 120.5 | 4.85 |
| hex-CdO | −7.83 | 31.89 | 103.6 | 5.58 |
| wz-CdO | −7.82 | 33.99 | 93.2 | 4.84 |
| zb-CdO | −7.80 | 34.10 | 93.2 | 4.73 |
| BCT-CdO | −7.78 | 35.60 | 74.8 | 2.92 |
| SOD-CdO | −7.71 | 41.80 | 75.5 | 4.72 |

(b) CdS

| | $E0$ | $V0$ | $B0$ | $B'$ |
|---|---|---|---|---|
| rs-CdS | −5.93 | 41.67 | 72.6 | 4.81 |
| NiAs-CdS | −5.84 | 42.38 | 71.0 | 4.77 |
| hex-CdS | −6.01 | 49.92 | 52.9 | 5.21 |
| zb-CdS | −6.19 | 52.29 | 53.8 | 4.65 |
| **wz-CdS** | −6.19 | 52.33 | 53.6 | 4.63 |
| BCT-CdS | −6.13 | 55.03 | 48.1 | 3.91 |
| SOD-CdS | −6.04 | 64.71 | 42.8 | 4.66 |

(c) CdSe

| | $E0$ | $V0$ | $B0$ | $B'$ |
|---|---|---|---|---|
| rs-CdSe | −5.26 | 47.37 | 60.8 | 4.87 |
| NiAs-CdSe | −5.20 | 48.07 | 60.1 | 4.83 |
| hex-CdSe | −5.33 | 56.92 | 43.0 | 5.68 |
| zb-CdSe | −5.54 | 59.63 | 45.2 | 4.76 |
| **wz-CdSe** | −5.54 | 59.68 | 45.0 | 4.72 |
| BCT-ZnSe | −5.48 | 62.76 | 40.4 | 4.30 |
| SOD-ZnSe | −5.39 | 73.92 | 35.8 | 4.77 |

(d) CdTe

| | $E0$ | $V0$ | $B0$ | $B'$ |
|---|---|---|---|---|
| rs-CdTe | −4.51 | 57.51 | 47.2 | 5.00 |
| NiAs-CdTe | −4.45 | 58.20 | 46.6 | 4.97 |
| hex-CdTe | −4.56 | 70.24 | 30.6 | 6.06 |
| **zb-CdTe** | −4.85 | 72.49 | 35.4 | 4.87 |
| wz-CdTe | −4.85 | 72.54 | 35.2 | 4.83 |
| BCT-CdTe | −4.78 | 76.58 | 30.7 | 3.88 |
| SOD-CdTe | −4.68 | 90.29 | 27.6 | 4.89 |

stabilization of zb-MgX and NiAs-MgX also results in a complicated competition for the ground state. Experimentally, it is found that both MgS and MgSe can be crystallized in three polymorphs (rocksalt, zinc blende and wurtzite)[27,28] implying that the crossover in stability is very gradual and that competition between these three phases is particularly close for MgS and MgSe. Although experimentally the rs-to-wz crossover has not quite occurred for MgSe (where rs-MgSe is found to be the ground state), in our calculations we find that zb-MgSe and wz-MgSe are slightly more stable than rs-MgSe, by only 0.03 eV/MgSe and 0.04 eV/MgSe, respectively. For MgTe, the experimental ground state is still not fully decided between NiAs-MgTe and wz-MgTe.[29] Our prediction of a wz-MgTe ground state is thus currently not possible to unambiguously confirm but matches well with other GGA-based DF calculations.[29] In comparable situations GGA DF calculations have proved to be superior to calculations using local density approximation based functionals;[30] the latter predicting NiAs-MgTe as the ground state.[31]

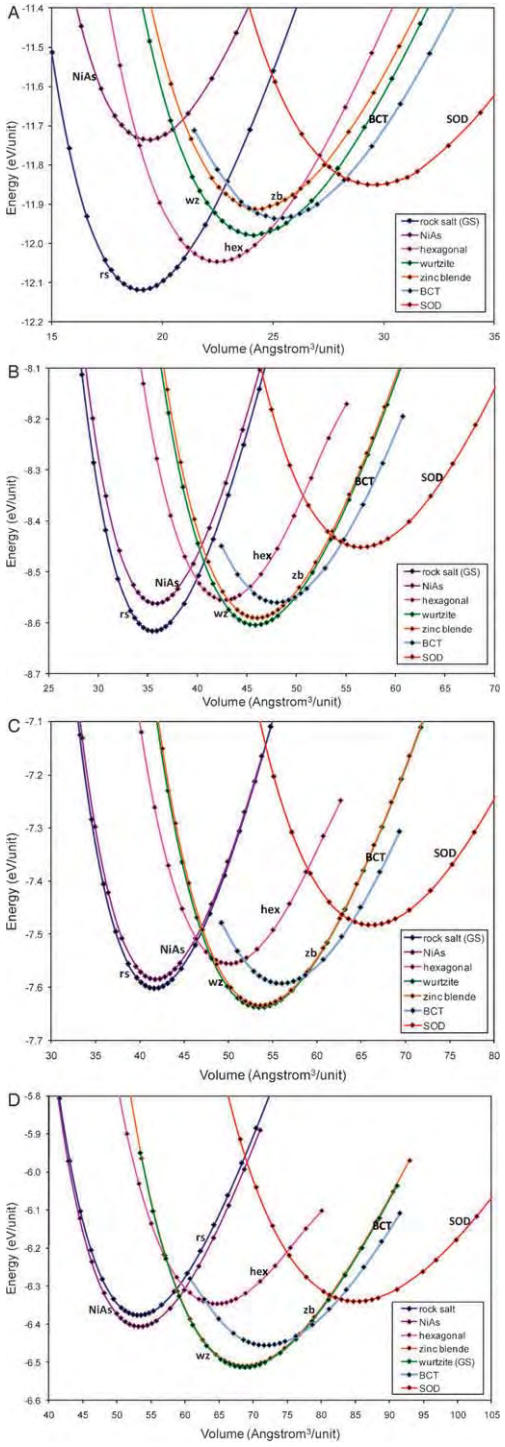


**Fig. 4** (a) Energy *versus* volume plots for the seven considered phases of MgO. GS in the legend denotes the experimental ground-state phase. (b) Energy *versus* volume plots for the seven considered phases of MgS. GS in the legend denotes the experimental ground state phase. (c) Energy *versus* volume plots for the seven considered phases of MgSe. GS in the legend denotes the experimental ground-state phase. (d) Energy *versus* volume plots for the seven considered phases of MgTe. GS in the legend denotes the experimental ground-state phase. Note that for MgTe both wz-MgTe and NiAs-MgTe have been proposed as the possible experimental ground state[29]—see also main text.

**Table 3** (a–d) Fitted parameters to the EOS data of the MgX series polymorphs: total energy ($E0$, eV/MgX), volume per unit ($V0$, Å$^3$/MgX), bulk modulus ($B0$, GPa), and the pressure derivative ($B'$). Bold entries indicate the experimental ground-state phases.

(a) MgO

| | $E0$ | $V0$ | $B0$ | $B'$ |
|---|---|---|---|---|
| **rs-MgO** | −12.12 | 19.03 | 153.1 | 4.17 |
| NiAs-MgO | −11.74 | 19.34 | 147.4 | 4.18 |
| hex-MgO | −12.05 | 22.45 | 126.0 | 4.50 |
| wz-MgO | −11.98 | 24.15 | 117.8 | 4.12 |
| zb-MgO | −11.91 | 24.31 | 117.6 | 4.12 |
| BCT-MgO | −11.93 | 25.25 | 102.2 | 3.17 |
| SOD-MgO | −11.85 | 29.53 | 95.6 | 4.11 |

(b) MgS

| | $E0$ | $V0$ | $B0$ | $B'$ |
|---|---|---|---|---|
| **rs-MgS** | −8.62 | 35.58 | 74.6 | 4.10 |
| NiAs-MgS | −8.56 | 35.77 | 73.9 | 4.13 |
| hex-MgS | −8.55 | 42.81 | 57.6 | 4.34 |
| zb-MgS | −8.60 | 45.84 | 55.6 | 4.14 |
| wz-MgS | −8.59 | 45.99 | 55.9 | 4.11 |
| BCT-MgS | −8.56 | 47.99 | 47.8 | 2.88 |
| SOD-MgS | −8.45 | 56.53 | 44.57 | 4.08 |

(c) MgSe

| | $E0$ | $V0$ | $B0$ | $B'$ |
|---|---|---|---|---|
| **rs-MgSe** | −7.60 | 41.64 | 61.2 | 4.15 |
| NiAs-MgSe | −7.59 | 41.80 | 60.9 | 4.16 |
| hex-MgSe | −7.55 | 50.08 | 47.5 | 4.49 |
| zb-MgSe | −7.64 | 53.51 | 45.2 | 4.16 |
| wz-MgSe | −7.63 | 53.63 | 45.5 | 4.13 |
| BCT-MgSe | −7.59 | 55.97 | 38.2 | 2.89 |
| SOD-MgSe | −7.48 | 66.12 | 36.2 | 4.11 |

(d) MgTe

| | $E0$ | $V0$ | $B0$ | $B'$ |
|---|---|---|---|---|
| rs-MgTe | −6.38 | 53.25 | 46.4 | 4.27 |
| NiAs-MgTe | −6.41 | 53.30 | 46.5 | 4.25 |
| hex-MgTe | −6.35 | 64.65 | 33.7 | 4.99 |
| zb-MgTe | −6.51 | 68.74 | 34.3 | 4.21 |
| **wz-MgTe** | −6.51 | 78.73 | 34.3 | 4.18 |
| BCT-MgTe | −6.45 | 71.74 | 27.9 | 2.63 |
| SOD-MgTe | −6.34 | 85.16 | 27.1 | 4.18 |

Although our DF calculations failed to predict that wz-MgSe is the ground state, we stress that the general experimental trend in ground-state MgX polymorphic stability with change in anion type is reproduced. This small energetic preference for wz-MgSe over rs-MgSe, is unlikely to affect our predicted transition pressures to obtain SOD-MgSe as the transition would almost certainly proceed indirectly *via* wz-MgSe in any case (as for CdO and MgS).

Further, considering: (i) the likely sensitive energetic balance of factors determining the ground-state crossover point for the MgX series, (ii) the success of our methodology with respect to the relative stabilities of the ground states of the corresponding ZnX and CdX series, and (iii) that the main objective of this study is concerned with predicting trends in (energetic and enthalpic) stability, rather than to try to achieve an exactingly accurate match to experimental data, we feel that the computational set-up employed is more than adequate for our present purposes.

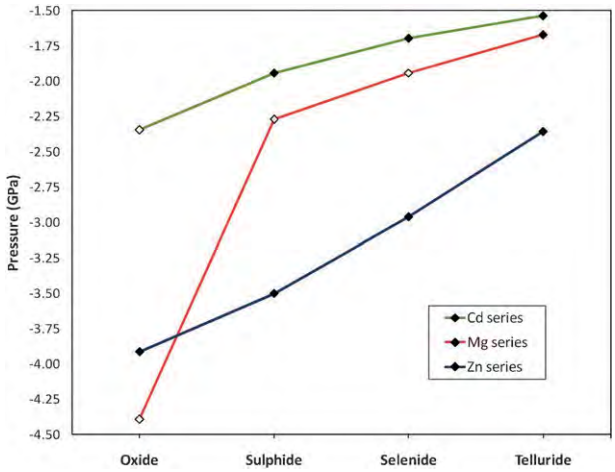


**Fig. 5** Transition pressures going from the ground state to the respective SOD phase. Solid data points denote direct ground-state-to-SOD transitions and open data points denote indirect transitions *via* other phases—see main text for details.

## SOD phase transition pressures

Based upon the Birch–Murnaghan fitted EOS data in Tables 1, 2 and 3, for every considered phase and composition we have derived the corresponding expression for the enthalpy. For each composition we started from the ground state and decreased the pressure while extracting a path following the phases with the lowest enthalpy. In all cases the aim was to find the pressure at which the SOD phase may possibly be stabilized, and for which compositions this was relatively most facile.

For the full ZnX series, CdS, CdSe, CdTe and MgTe, the lowest enthalpy path only included the ground-state phase and the corresponding SOD phase. In other words, for these compositions, no other phase competes with SOD on enthalpic grounds when applying negative pressures to the ground state at 0 K. The calculated pressure required for this transition varies greatly from −3.93 GPa for wz-ZnO to SOD-ZnO to −1.54 GPa for zb-CdTe to SOD-CdTe (see solid data points in Fig. 5 for a graph of all calculated direct transition pressures). The fact that this transition is predicted to be direct is perhaps less surprising when we consider that in all these cases the ground-state phase is either zinc blende or wurtzite and thus the only real competitor to SOD in our considered series could be the BCT phases (having a density intermediate between wurtzite/zinc blende and SOD). We further note that even in the cases where the lowest enthalpy transition from the ground state to the SOD phase is *via* other phases, this is always either *via* wurtzite for CdO, MgS, and MgSe or *via* the hexagonal phase for MgO, and never *via* BCT (transition pressures from an intermediate phase are shown as open data points in Fig. 5). That BCT is never enthalpically more stable than SOD is a strong indication that SOD may be the most thermodynamically stable phase under suitable negative pressures. The enthalpic stability of SOD over BCT with respect to negative pressure can also be seen graphically *via* the common tangent construction. This construction finds points on two EOS curves with: (i) the same gradient, and

 

(ii) which can be joined by a single tangent line. This common tangent line then corresponds to one of equal pressure and enthalpy respectively with the gradient of the line equating to the negative of the transition pressure between the two phases. Evidently the shallower the common tangent line connecting two EOS curves the lower the magnitude of the transition pressure and the more thermodynamically favoured it is over transitions to phases with EOS curves above the tangent line. In Fig. 2a we show the common tangent between the EOS curves of wz-ZnO and SOD-ZnO clearly passing under the EOS of BCT-ZnO. We note that very recent work has predicted that many polymorphs lie in the density region between wurtzite and SOD for a number of materials including ZnO, ZnS and CdS.[32] In all cases however none of these phases were found to lie below the common tagnet line between wurtzite and SOD, which further confirms our proposition that SOD is likely to be thermodynamically stable under conditions of negative pressure.

Apart from the relatively large negative pressure required to traverse from rs-MgO to SOD-MgO *via* hex-MgO, the overall trend in transition pressures follows the trend CdX, MgX, and ZnX in terms of decreasing relative ease in obtaining the SOD phase from the ground state. In each series it can also be seen that the SOD phase may be obtained more easily with increasing anion size. These trends result in CdTe (−1.54 GPa), MgTe (−1.68 GPa) and CdSe (−1.70 GPa) being the most promising candidates for obtaining the SOD phase *via* application of negative pressure. Considering that it has been estimated that effective negative pressures of about −1 GPa can be achieved in low temperature deposition solid state syntheses,[2] we are thus hopeful that the SOD phase may soon be experimentally prepared.

## Summary and conclusions

We systematically survey the low-energy and enthalpic polymorphic landscape of the oxides and chalcogenides of Zn, Cd, and Mg in order to establish pressure conditions under which the novel nanoporous SOD phase may be stabilised. Specifically, for all compositions we use gradient corrected DF calculations to derive the EOS of eight AB polymorphs: (i) rs, (ii) NiAs, (iii) hex, (iv) layered (v) zb, (vi) wz, (vii) BCT, and (viii) SOD. The extracted enthalpies of each phase allow us to follow the lowest enthalpy path for each composition and thus the transition pressures under which SOD may be obtained. We find that in all cases the low-density SOD phase is thermodynamically stable under conditions of negative pressure. Conversely, the potentially competing BCT phase is never thermodynamically stable. Transition pressures to obtain the SOD phase are predicted to be most facile for the CdX series and the MgS, MgSe, MgTe set. Due to the decrease in the magnitude of the negative pressure required to obtain the SOD phase with increasing anion size the most favourable candidates (of those compositions considered) for SOD formation are predicted to be CdTe, MgTe and CdSe with transition pressures calculated to be in the range −1.54 to −1.70 GPa.

## Acknowledgements

This study has been supported in part by the Spanish Ministry of Education and Science (grants FIS2008-02238) and by the Generalitat de Catalunya (grants 2009SGR1041 and XRQTC). This work was further supported in part by grants from the National Science and Technology Development Agency (2009 NSTDA Chair Professor funded by the Crown Property Bureau under the management of the National Science and Technology Development Agency and NANOTEC Center of Excellence funded by the National Nanotechnology Center), The Thailand Research Fund, The Commission of Higher Education, Ministry of Education (“National Research University of Thailand” and “Postgraduate Education and Research Programs in Petroleum and Petrochemicals, and Advanced Materials”). Support from the Kasetsart University Research and Development Institute (KURDI) is also acknowledged. The Barcelona Supercomputer Center is gratefully acknowledged for time on the Marenostrum supercomputer. Alexey Sokol is kindly acknowledged for useful discussions.

## References

1 Ž. Čančarević, J. C. Schön and M. Jansen, *Chem.–Asian J.*, 2008, **3**, 561.
2 J. C. Schön, *Z. Anorg. Allg. Chem.*, 2004, **630**, 2354.
3 J. C. Schön and M. Jansen, *Comput. Mater. Sci.*, 1995, **4**, 43.
4 Y. Liebold-Ribeiro, D. Fischer and M. Jansen, *Angew. Chem., Int. Ed.*, 2008, **47**, 4428.
5 A. Bach, D. Fischer and M. Jansen, *Z. Anorg. Allg. Chem.*, 2009, **635**, 2406.
6 W. R. L. Lambrecht, S. Limpijumnong and B. Segall, *MRS Internet J. Nitride Semicond. Res.*, 1999, **4S1**, p. G6.8.
7 A. N. Enyashin, I. R. Shein and A. L. Ivanovskii, *Phys. Rev. B: Condens. Matter Mater. Phys.*, 2007, **75**, 193408.
8 F. Decremps, J. Pellicer-Porres, F. Datchi, J. P. Itie, J. P. A. Polian, F. Baudelet and J. Z. Jiang, *Appl. Phys. Lett.*, 2002, **81**, 4820.
9 L. Zhang and H. Huang, *Appl. Phys. Lett.*, 2007, **90**, 023115.
10 A. J. Kulkarni, M. Zhou, K. Sarasamak and S. Limpijumnong, *Phys. Rev. Lett.*, 2006, **97**, 105502.
11 C. L. Freeman, F. Claeyssens, N. L. Allen and J. Harding, *Phys. Rev. Lett.*, 2006, **96**, 066102.
12 C. Tusche, H. L. Meyerheim and J. Kirschner, *Phys. Rev. Lett.*, 2007, **99**, 026102.
13 D. K. Smith and C. F. Cline, *Acta Crystallogr.*, 1965, **18**, 393.
14 B. J. Morgan, *Phys. Rev. B: Condens. Matter Mater. Phys.*, 2009, **80**, 174105.
15 J. Wang, A. J. Kulkarni, K. Sarasamak, S. Limpijumnong, M. J. Ke and M. Zhou, *Phys. Rev. B: Condens. Matter Mater. Phys.*, 2007, **76**, 172103.
16 K. Doll, J. C. Schön and M. Jansen, *Phys. Rev. B: Condens. Matter Mater. Phys.*, 2008, **78**, 144110.
17 Ch. Baerlocher, L. B. McCusker and D. H. Olson, *Atlas of Zeolite Framework types*, Elsevier, Amsterdam, 6th edn, 2007.
18 J. Carrasco, F. Illas and S. T. Bromley, *Phys. Rev. Lett.*, 2007, **99**, 235502.
19 W. Sangthong, J. Limtrakul, F. Illas and S. T. Bromley, *J. Mater. Chem.*, 2008, **18**, 5871.
20 B. Wang, X. Wang and J. Zhao, *J. Phys. Chem. C*, 2010, **114**, 5741.
21 J. Perdew, K. Burke and Y. Wang, *Phys. Rev. B: Condens. Matter*, 1996, **54**, 16533.
22 G. Kresse and D. Joubert, *Phys. Rev. B: Condens. Matter Mater. Phys.*, 1999, **59**, 1758.
23 H. J. Monkhorst and J. D. Pack, *Phys. Rev. B: Solid State*, 1976, **13**, 5188.
24 P. E. Blöchl, *Phys. Rev. B: Condens. Matter*, 1994, **50**, 17953.
25 F. Birch, *Phys. Rev.*, 1947, **71**, 809.

26 C.-Y. Yeh, W. Lu, S. Froyen and A. Zunger, *Phys. Rev. B: Condens. Matter*, 1992, **46**, 10086.
27 T. Li, H. Luo, R. G. Greene, A. L. Ruoff, S. S. Trail and F. J. DiSalvo, *Phys. Rev. Lett*., 1995, **74**, 5232.
28 L. Konczenwicz, P. Bigenwal, T. Cloitre, M. Chibane, R. Ricou, P. Testuo, O. Briot and R. L. Aulombard, *J. Cryst. Growth*, 1996, **117**, 159.
29 Y. Cai, S. Wu, J. Yu and R. Xu, *Phys. Rev. B: Condens. Matter Mater. Phys*., 2006, **74**, 214112.
30 D. R. Hamann, *Phys. Rev. Lett*., 1996, **76**, 660.
31 S. Duman, S. Bağcı, H. M. Tütüncü and G. P. Srivastava, *Phys. Rev. B: Condens. Matter Mater. Phys*., 2006, **73**, 205201.
32 M. A. Zwijnenburg, F. Illas and S. T. Bromley, *Phys. Rev. Lett*., 2010, **104**, 175503.

 

Electrochimica Acta 55 (2010) 8116–8120

Contents lists available at ScienceDirect

Electrochimica Acta

journal homepage: www.elsevier.com/locate/electacta

# Single point electrodeposition of nickel for the dissymmetric decoration of carbon tubes

G. Loget[a], G. Larcade[a], V. Lapeyre[a], P. Garrigue[a], C. Warakulwit[b], J. Limtrakul[b], M.-H. Delville[c], V. Ravaine[a], A. Kuhn[a,*,1]

[a] Université Bordeaux, ISM, ENSCBP, 33607 Pessac Cedex, France
[b] Center of Nanotechnology and Chemistry Department, Kasetsart University, Bangkok 10900, Thailand
[c] CNRS, UPR-9048, Université de Bordeaux, ICMCB, 87 Avenue du Dr. A. Schweitzer, 33608 Pessac Cedex, France

ARTICLE INFO

*Article history:*
Received 3 December 2009
Received in revised form 12 January 2010
Accepted 15 January 2010
Available online 25 January 2010

*Keywords:*
Janus particles
Bipolar electrochemistry
Single point electrodeposition
Carbon tubes
Capillary electrophoresis

ABSTRACT

Dissymmetric micro- and nanoobjects are of enormous interest in many areas ranging from molecular electronics to targeted drug delivery. So far it has been quite difficult to synthesize dissymmetric objects at these scales and most approaches are based on using interfaces to break the symmetry. Only a few bulk procedures are known so far to produce the so-called Janus-type objects. We report here a simple approach for the bulk generation of dissymmetric micro- and nanoobjects, especially carbon tubes (CTs), based on a known, but so far underestimated electrochemical principle, namely bipolar electrodeposition. A suspension of CTs is introduced in a capillary containing an aqueous nickel salt solution and a high electric field is applied to orientate and polarize the individual tubes. During their transport through the capillary under sufficient polarization, each tube is the site of water oxidation at one end, and of $Ni^{2+}$ reduction at the other one. The resulting nickel deposit at one end of the tube allows manipulation of the objects with the help of a magnetic field.



## 1. Introduction

Dissymmetric functionalization of micro- and nanoobjects is of major importance for many applications, ranging for example from directed self-assembly and electronic paper to sensing and catalysis. Various approaches to generate dissymmetric particles, also called Janus-type particles, have been reported in the recent literature. They have been obtained either by protection/deprotection mechanisms [1], focused laser-induced reactions [2], co-jetting of parallel polymer solutions under the influence of an electrical field [3], anisotropic electroless deposition [4], or with microfluidic techniques [5]. However, so far, most of the methods used to generate such objects need to break the symmetry by introducing interfaces like in the case of sputtering [6,7], stamp coating [8,9], and Langmuir–Blodgett-based techniques [10]. This makes the preparation of large quantities rather difficult because the majority of the techniques usually lead to monolayer equivalents of material as the modification occurs in a two-dimensional reaction space.

Thus, there is an increasing interest in developing truly three-dimensional techniques, in order to replace the two-dimensional approaches, and thus allowing a scale-up of the production of Janus objects to larger quantities by using bulk procedures [11]. Examples for such kind of approaches are based on the dissymmetric generation of charge carriers in semiconductors such as $TiO_2$ by using light [12] or antenna chemistry based on the irradiation of carbon nanotubes with microwaves [13]. However, in these cases a fine tuning of the driving force of the reactions is not possible.

In this context, an attractive way to break the symmetry in a three-dimensional reaction space is based on the concept of bipolar electrochemistry described by Fleischmann et al. [14]. This appealing approach relies on the fact that when a conducting object is placed in a strong electric field between two electrodes a polarization occurs that is proportional to the electric field $E$ and the characteristic dimension $r$ of the object as illustrated in Fig. 1. This concept has recently found interesting applications as driving force in electrochemiluminescent reactions [15], as detection mode in capillary electrophoresis [16] and for bipolar patterning [17,18]. In the present study we are using the approach to trigger point selective nickel electrodeposition on carbon tubes (CT) in analogy to our earlier work on the dissymmetric decoration of carbon nanotubes with gold nanoparticles [19]. In comparison to this previous work we want to demonstrate here that it is possible to generalize the approach by using another substrate (carbon microtubes)

* Corresponding author. Tel.: +33 5 40 00 65 73; fax: +33 5 40 00 27 17.
*E-mail address:* kuhn@enscbp.fr (A. Kuhn).
[1] ISE member.

0013-4686/$ – see front matter © 2010 Elsevier Ltd. All rights reserved.
doi:10.1016/j.electacta.2010.01.070

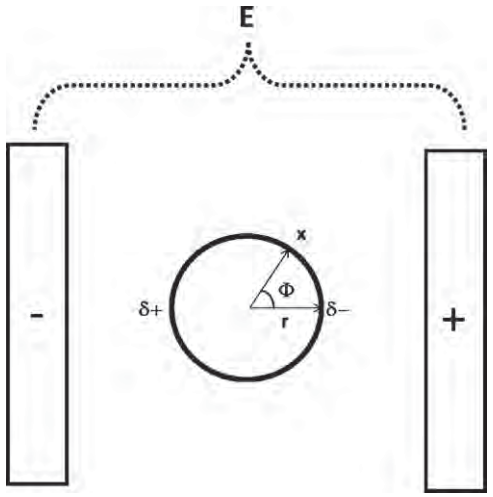


**Fig. 1.** Schematic illustration of the polarization of a conducting spherical particle in an electric field between two electrodes.

and another metal (Ni) which is much more difficult to reduce than the gold ions. In addition, we wanted to deposit a ferromagnetic metal in order to be able to manipulate the resulting objects with a magnetic field.

The simple equation [14] governing this polarization also immediately illustrates the practical problems that will arise when applying this concept to small objects.

$$\eta_x = Er\cos\Phi \quad (1)$$

With $\eta_x$ being the polarization at a given point $x$ at the surface of the object, $E$ the total electric field and $r$ the radius of the particle, one can easily calculate that the maximum potential difference $\Delta V_{max}$ between the two opposite sides of the object is given by:

$$\Delta V_{max} = 2Er \quad (2)$$

In order to carry out two different redox reactions at the opposite sides of the object $\Delta V_{max}$ has to be in a first order approximation equal to the difference of the formal potentials of the two redox reactions. In the present case, the redox reactions that should take place in an aqueous environment are the following ones:

$$Ni^{2+} + 2e^- \rightarrow Ni_{(s)}{}^0 \quad E^\circ = -0.26\,V \quad vs \quad NHE$$

$$2H_2O_{(l)} \leftrightarrow 4H_{(aq)}{}^+ + O_{2(g)} + 4e^- \quad E^\circ = +1.23\,V \quad vs \quad NHE$$

It immediately follows that the polarization has to generate a potential difference of approximately 1.5 V. This becomes an intrinsic problem of the approach when dealing with micro- or nanometer sized objects, as in this case $E$ needs to achieve values of up to MV/m, conditions that seem to be incompatible with a normal laboratory environment and especially with aqueous solutions because of the inherent side reactions accompanied by macroscopic bubble formation at both electrodes that disturbs the orientation of the objects in the electric field. Bradley et al. could partly circumvent the problem by using organic solvents in order to enlarge the potential window of the electrolyte and thus it was possible to generate metal layers in a dissymmetric way on different objects in the micrometer and sub-micrometer range [20,21]. However it was also necessary to immobilize the objects on a substrate in order to prevent them from rotating, which means that it is again a 2D and not a bulk process. Recently we could demonstrate that it is possible to get around these problems and to extend the approach to truly nanosized objects by using a capillary electrophoresis set-up to apply the high electric field [19]. With this capillary assisted bipolar electrodeposition (CABED) process we were able to generate a nanosized gold cluster selectively on one end of multiwall carbon nanotubes. This spatially controlled single point electrodeposition is extended in the present contribution to nickel as a metal and a different type of carbon tubes in order to demonstrate the possibility to generalize this attractive approach as an alternative to generate dissymmetric micro- and nanoobjects of different compositions in a straight forward and well-controlled way.

## 2. Experimental

### 2.1. Preparation of carbon tube suspensions

The carbon tubes used in this study were produced by chemical vapor deposition with a porous aluminum oxide membrane serving as a template [22]. After acid digestion of the template (Fig. 2a) the quite homogeneous tubes were recovered as a powder (Fig. 2b).

Suspensions of CTs can be produced in a different way compared to the procedure that we have used in former studies for other types of carbon [23–25]. About 0.1 mg of CTs was added to absolute ethanol (1.5 mL). To accelerate the formation of a suspension the mixture was sonicated, but only for a short time (1 min) in order to avoid excessive breaking of the tubes. After 3 h of sedimentation, 0.5 mL of the supernatant was taken and added to a solution of 10 mM $NiSO_4$ in ultrapure water.

### 2.2. Bipolar nickel deposition on carbon nanotubes

For CE experiments, all solutions or suspensions were introduced into the capillary by filling it manually with a syringe. The capillary used here is a fused silica capillary with a length of 30 cm and an inner diameter of 100 μm. The distance from the capil-

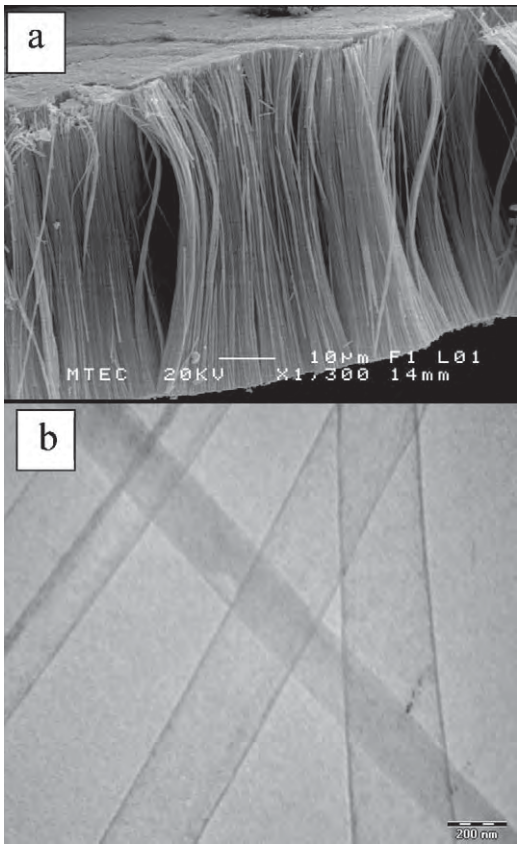


**Fig. 2.** (a) Scanning electron micrograph of the CT sample after dissolution of the $Al_2O_3$ template and (b) transmission electron micrograph of typical tubes obtained after suspension in water.

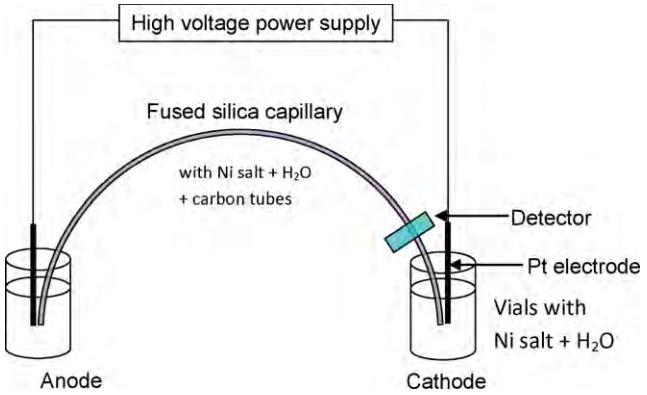


**Fig. 3.** Schematic illustration of the capillary electrophoresis set-up used in this study.

lary inlet (left side in Fig. 3) to the detection window (right side) was 24 cm in this case. The applied voltage was 30 kV whilst the temperature was maintained at 25 °C. The CE experiment was first performed by rinsing the capillary with ultrapure water. Then the diluted aqueous suspension of the carbon tubes was introduced into the capillary. The reason for using a diluted suspension for the CE experiment is due to the narrow capillary (100 μm). Introducing suspensions that are too concentrated leads to clogging of the capillary. The combination of electrophoretic migration and electroosmotic flow determines the transport of the CTs through the capillary. The flow characteristics were determined by recording the absorbance variations in the UV detector (254 nm) as a function of time.

The bipolar electrochemical nickel deposition on CTs is achieved by introducing the CT/$NiSO_4$ (10 mM) suspension into the capillary at the anodic side. No buffer solution was used in order to keep the conductivity of the medium as low as possible. Because the addition of the nickel salt increases the ionic strength it can result in the aggregation of the CTs, and, therefore, the suspension has to be sonicated for a short time in an ultrasound bath in order to maintain the CTs well dispersed just before introduction into the capillary. For such salt concentrations the typical currents in the electrophoresis set-up were around 1 μA.

The sample leaving the capillary at the cathodic side was collected directly at the outlet. This collected sample was put on a TEM grid or another substrate and dried. Because the suspension still contains nickel salt, drying of the suspension leads to salt crystallization which extremely disturbs the further microscopic analysis. Therefore, after the suspension was dropped onto the TEM grid, the solution, still containing salt, was soaked through the grid by placing a cleaning tissue under the grid. After that, the remaining particles on the grid were washed three times with ultrapure water using the same procedure. The washed objects were then characterized by optical microscopy, scanning electron microscopy or transmission electron microscopy.

## 3. Results and discussion

The potentials given in the above redox equations are standard potentials and, as the experiment is carried out far from standard conditions in terms of concentrations and partial gas pressures, large deviations from the theoretical threshold value of 1.5 V can be expected. This also means that the calculated electric fields might be different, especially when somewhat longer objects like the CTs are used. Using carbon tubes instead of carbon nanotubes for this experiment also has the advantage that the obtained objects can be easily visualized directly under the optical microscope and their movement, due to the presence of a magnetic field, can be followed in real time. The anisotropic tube structure results in a stronger polarization that induces at the same time an orientation of the tubes parallel to the electric field, which is preserved during their whole journey through the capillary. Thus, it is easier to perform such a bipolar electrochemical deposition with CTs compared to spherical objects that might change their orientation during the experiment and in this way lead to random metal deposition at the object's surface.

The experiment has been carried out at the maximum potential difference that could be delivered by the capillary electrophoresis set-up, which is 30 kV. When this potential difference is applied between the two ends of a capillary with a total length of 30 cm, an electric field of roughly 100 kV/m is generated in the capillary. For CTs with a typical length of 20 μm the maximum polarization that can be obtained between the two ends of the carbon tube is of the order of 2 V. This value is higher than the minimum potential difference required for driving the two redox reactions when the calculation is based on the standard potentials, and therefore the bipolar electrodeposition should occur under these conditions. The experiment shows indeed striking evidence for a dissymmetric deposition of nickel at one end of the tubes (see Fig. 4a) and the counter reaction at the other side of the tubes involves the formation of oxygen bubbles which dissolve in the surrounding medium.

The picture in Fig. 4b is representative of the majority of the tubes reaching the capillary outlet; however, in a more general sense, not 100% are always modified. The percentage of modified tubes obviously depends on the experimental parameters and there are several possible origins for a non-quantitative modification. First of all, the nickel deposit can detach from the tube during the collection and rinsing procedure. Second, the tubes can be more or less conducting depending on their morphology and defects. In

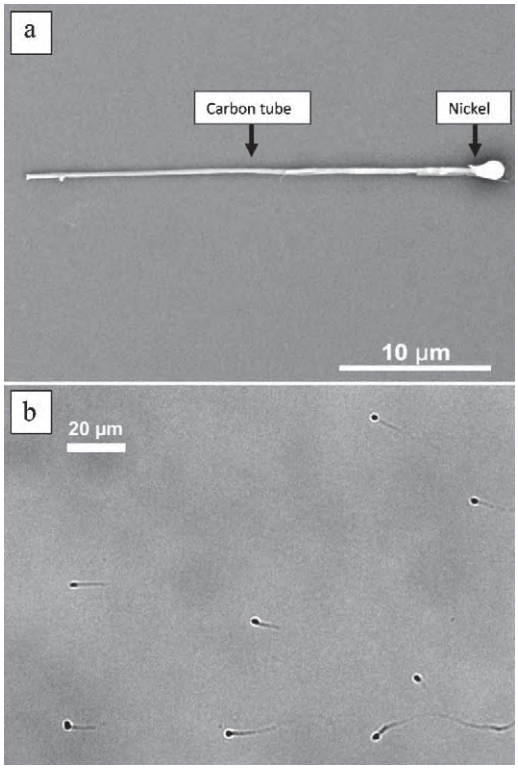


**Fig. 4.** Site selective bipolar electrodeposition of nickel at one end of a carbon tube (a) electron microscope image of a selected tube from a diluted sample and (b) optical microscope image of an ensemble of nickel modified tubes still suspended in the aqueous solution.

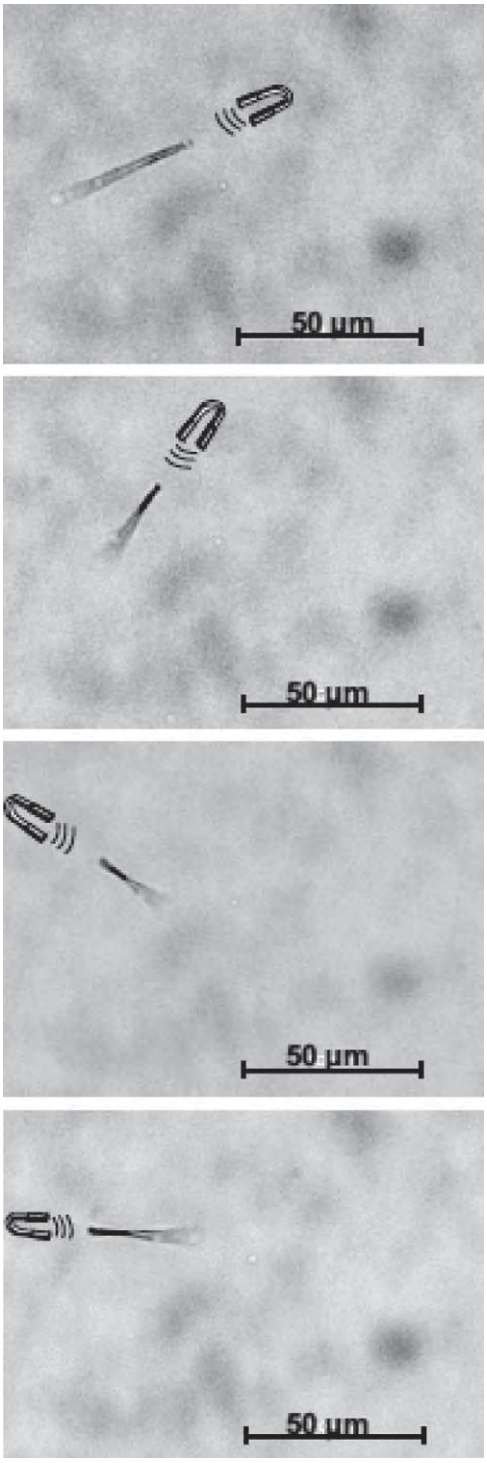


**Fig. 5.** Manipulation of a nickel modified carbon tube suspended in water by using an anti-clockwise rotating magnetic field.

the extreme case of an insulating tube, no deposition can occur and even for conducting tubes the conductivity has to be better than that of the surrounding electrolyte to induce a sufficient potential difference. The third reason is that the polarization scales with the length of the tube, and therefore shorter tubes might experience a potential difference between the two ends that is below the threshold value necessary to achieve metal deposition on one side and water oxidation on the other side. In order to approach 100% of modification the experiment should be carried out with tubes as long as possible and an external potential as high as possible. When optimizing these parameters one can achieve in a routine experiment that more than half of the tubes are modified (see, for example, Fig. 4b).

It is important to note that, in contrast to the former experiments [20,21], in this set-up the high voltage is not a problem, although we do not use organic solvents but water, because the electrodes are positioned at the outside of the capillary. This means that an eventual macroscopic hydrogen or oxygen evolution at the cathode or anode respectively does not disturb the experiment as it takes place in the bulk solution reservoirs and not in the capillary. Furthermore the currents are in the µA range because there is no added supporting electrolyte present and thus the total amount of developed gas is rather small.

In contrast to our former study using site selective deposition of gold on carbon nanotubes [19] we have used in this study on purpose a ferromagnetic metal. This allows us to manipulate the modified tubes with a magnetic field. Fig. 5 illustrates the possibility to turn the tube around an axis perpendicular to the tube's main axis. Such picture sequences are rather difficult to obtain because during application of the rotating magnetic field the object has to be followed simultaneously in the *x*, *y* and *z* direction with the additional problem that not the entire object is in the same focal plane. Triggering a well controlled rotation of the object would be difficult when using homogeneously modified tubes, but can be easily carried out with the present objects due to their dissymmetric nature. Therefore one can imagine using this process of single point electrodeposition for the generation of nano- and microobjects playing a crucial role in the construction of miniaturized mechanical devices such as motors.

## 4. Conclusions

The concept of bipolar electrochemistry has been adapted to modify in a dissymmetric way carbon tubes with a ferromagnetic nickel cap. The method employed to create these Janus-type objects is based on a slightly modified capillary electrophoresis experiment, (i) allowing the application of the mandatory high voltages, (ii) without having to use organic solvents and (iii) especially avoiding gas bubble formation in the reaction chamber, which otherwise would completely prevent the alignment of the tubes in the electric field. In contrast to the majority of literature processes used for the generation of dissymmetric objects the present process does not need any interface or surface to break the symmetry, but is a bulk process which allows one to easily imagine a scale-up of the production.

Looking into the future, the CABED process can be generalized to other types of nanoobjects and also deposits of a very different nature such as other metals, semiconductors, or polymers. The approach therefore opens up the way to a whole new family of experiments leading to complex nanoobjects with a sophisticated design allowing original applications, among others for example in the area of autonomous micro- and nanoswimmers [26–28]. In addition, the procedure reported here could also be adapted to sort conducting, semiconducting, and insulating carbon tubes, as the latter ones will not be modified with metal, whereas the first two categories of species will undergo a potential-dependent metal modification.

## Acknowledgments

This work is part of the CUBIHOLE project funded by the European NanoSci-Era+ action under contract ANR-08-NSCI-008-01 and has also been supported by the French Ministry of Research, CNRS, and ENSCBP. C.W. and J.L. thank the National Science and Technology Development Agency (NSTDA Chair Professor and National

Nanotechnology Center) and the Thailand Research Fund for support. We also thank P. Pannopard for providing us with CT samples.

## References

[1] A. Perro, S. Reculusa, F. Pereira, M.-H. Delville, C. Mingotaud, E. Duguet, E. Bourgeat-Lami, S. Ravaine, Chem. Commun. 44 (2005) 5542.
[2] E. Hugonnot, M.-H. Delville, J.-P. Delville, Appl. Surf. Sci. 248 (2005) 470.
[3] K.-H. Roh, D.C. Martin, J. Lahann, Nat. Mater. 4 (2005) 759.
[4] J.-Q. Cui, I. Kretzschmar, Langmuir 22 (2006) 8281.
[5] T. Nisisako, T. Torii, T. Takahashi, Y. Takizawa, Adv. Mater. 18 (2006) 1152.
[6] H. Takei, N. Shimizu, Langmuir 13 (1997) 1865.
[7] Y. Lu, H. Xiong, X. Jiang, Y. Xia, M. Prentiss, G.M. Whitesides, J. Am. Chem. Soc. 125 (2003) 12724.
[8] O. Cayre, V.N. Paunov, O.D. Velev, J. Mater. Chem. 13 (2003) 2445.
[9] V.N. Paunov, O.J. Cayre, Adv. Mater. 16 (2004) 788.
[10] K. Fujimoto, K. Nakahama, M. Shidara, H. Kawaguchi, Langmuir 15 (1999) 4630.
[11] L. Hong, A. Cacciuto, E. Luijten, S. Granick, Nano Lett. 6 (2006) 2510.
[12] H. Reiche, W.W. Dunn, A.J. Bard, J. Phys. Chem. 83 (1979) 2248.
[13] J.G. Duque, M. Pasquali, H.K. Schmidt, J. Am. Chem. Soc. 130 (2008) 15340.
[14] M. Fleischmann, J. Ghoroghchian, D. Rolison, S. Pons, J. Phys. Chem. 90 (1986) 6392.
[15] F. Mavré, K.-F. Chow, E. Sheridan, B.-Y. Chang, J.A. Crooks, R.M. Crooks, Anal. Chem. 81 (2009) 6218.
[16] O. Ordeig, N. Godino, J. Del Campo, F.X. Muñoz, F. Nikolajeff, L. Nyholm, Anal. Chem. 80 (2008) 3622.
[17] C. Ulrich, O. Andersson, L. Nyholm, F. Björefors, Anal. Chem. 81 (2009) 453.
[18] C. Ulrich, O. Andersson, L. Nyholm, F. Björefors, Angew. Chem. Int. Ed. 47 (2008) 3034.
[19] C. Warakulwit, T. Nguyen, J. Majimel, M.-H. Delville, V. Lapeyre, P. Garrigue, V. Ravaine, J. Limtrakul, A. Kuhn, Nano Lett. 8 (2008) 500.
[20] J.-C. Bradley, H.-M. Chen, J. Crawford, J. Eckert, K. Ernazarova, T. Kurzeja, M. Lin, M. McGee, W. Nadler, S.G. Stephens, Nature 389 (1997) 268.
[21] J.-C. Bradley, M. Zhongming, Angew. Chem. Int. Ed. 38 (1999) 1663.
[22] C. Warakulwit, Ph.D. Thesis, Kasetsart University Bangkok and University Bordeaux 1, 2007.
[23] P. Garrigue, M.-H. Delville, C. Labrugère, E. Cloutet, P.J. Kulesza, J.P. Morand, A. Kuhn, Chem. Mater. 16 (2004) 2984.
[24] D. Fattakhova-Rohlfing, A. Kuhn, Carbon 44 (2006) 1942.
[25] C. Warakulwit, J. Majimel, M.-H. Delville, P. Garrigue, J. Limtrakul, A. Kuhn, J. Mater. Chem. 18 (2008) 4056.
[26] N. Mano, A. Heller, J. Am. Chem. Soc. 127 (2005) 11574.
[27] U.K. Demirok, R. Laocharoensuk, K.M. Manesh, J. Wang, Angew. Chem. Int. Ed. 47 (2008) 9349.
[28] D. Pantarotto, W.R. Browne, B.L. Feringa, Chem. Commun. (2008) 1533.

# Persistence of magic cluster stability in ultra-thin semiconductor nanorods

**Winyoo Sangthong,[abcd] Jumras Limtrakul,[bcd] Francesc Illas[a] and Stefan T. Bromley*[ae]**

*Received (in Zürich, Switzerland) 28th September 2009, Accepted 23rd November 2009*
*First published as an Advance Article on the web 14th December 2009*
**DOI: 10.1039/b9nr00282k**

**The progression from quasi zero-dimensional (Q0D) nanoclusters to quasi one-dimensional (Q1D) nanorods, and, with increasing length, to nanowires, represents the most conceptually fundamental transition from the nanoscale to bulk-like length scales. This dimensionality crossover is particularly interesting, both scientifically and technologically, for inorganic semiconducting (ISC) materials, where striking concomitant changes in optoelectronic properties occur.[1,2] Such effects are most pronounced for ultra-thin[3] ISC nanorods/nanowires, where the confining and defective nature of the atomic structure become key. Although experiments on ISC materials in this size regime have revealed especially stable (or "magic") non-bulk-like Q0D nanoclusters,[4,5] all ISC Q1D nanostructures have been reported as having structures corresponding to bulk crystalline phases. For two important ISC materials (CdS and CdSe) we track the Q0D-to-Q1D transition employing state-of-the-art electronic structure calculations demonstrating an unexpected persistence of magic cluster stability over the bulk-like structure in ultra-thin nanorods up to >10 nm in length. The transition between the magic-cluster-based and wurtzite nanorods is found to be accompanied by a large change in aspect ratio thus potentially providing a route to nano-mechanical transducer applications.**

The impressive scientific and technological advances resulting from the intense research effort into inorganic semiconducting (ISC) nanosystems is exemplified by the continuing developments based on nanoscale CdS. Inspired by the technological promise of its tunable (opto)electronic properties,[1,2] recent work on 1D nano-CdS has given rise to a wide range of device applications such as lasers,[6] transistors[7] and waveguides.[8] Enhancement of finite size effects in 1D nano-CdS systems such as defect-induced optical response and quantum confinement,[9] can be achieved through restricting the length to form a nanorod and/or by reducing the diameter of nanowires or nanorods to the ultra-thin, or strongly-confined regime. For ISC Q1D nanosystems this size range can be defined as that where the dimensions of a nanorod or nanowire are significantly below the Bohr exciton radius (~3 nm for CdS and ~5 nm for CdSe) where one expects the greatest deviation from bulk properties. A number of recent experimental studies have reported the preparation of 1D CdS[10,11] and CdSe[12,13] nanorods with diameters <5 nm. Thus far, however, all such ultra-thin CdS and CdSe nanorods have had reported diameters >1.5 nm and, where measured (*e.g.* by high-resolution transmission electron microscopy (HRTEM) and X-ray diffraction), seemed to possess the bulk wurtzite (wz) atomic structure with the (001) direction aligned along the length of the rods. Relatively thick CdS and CdSe nanorods and nanowires (≥30 nm diameter) can be grown directly from the vapour phase from pure material powders,[14] but typically ultra-thin Q1D nanosystems are made from colloidal growth and assembly of ligated clusters in solution (*i.e.* oriented attachment[3]). Although ligands are important for shape and size control, they can also affect the atomic structure of ISC nanosystems[15] and thus for studying the intrinsic size-dependent behaviour of pure ISC materials it is desirable that they should be removed. Below, we concentrate our discussion mainly on ligand-free Q0D and Q1D nanosystems of CdS, although we note that strongly analogous results are also found for the corresponding CdSe systems.

Considering the wealth of experimental studies and, further, the role of 1D nano-CdS as a model system for studying the fundamental physics of anisotropic quantum confinement, surprisingly few detailed calculations have been performed on infinite CdS nanowires,[16–18] and, as far as we are aware, none on CdS nanorods. In contrast, computational modelling studies of Q0D CdS nanosystems are relatively abundant and have tended to proceed *via* two distinct routes: (i) top-down, where nanoparticle atomic structures are derived from cutting fragments from either the wz or zincblende (zb) bulk phases,[19,20] or (ii) bottom-up, where the most energetically stable nanocluster structures are sought without recourse to bulk crystalline structural stabilities.[5,21] Largely due to the use of its simplifying structural assumption, the former approach has permitted studies of size-dependent optical and electronic properties of wz- or zb-structured $(CdS)_N$ nanoparticles over a wide size range.[19,20] Technically, due to the explosion in the number of possible structures with increasing size, the bottom-up approach to modelling CdS nanoclusters is significantly more difficult and the ground-state energy minimum structures of $(CdS)_N$ nanoclusters are reasonably well established up to only $N = 16$ with some suggestions for $28 < N < 35$.[4,5] Unlike the assumed crystalline structures adopted in the top-down approach none of the reported ground-state nanocluster structures in this latter size regime are found to be wz-like or zb-like. Recent work has also suggested that wz-structured CdS nanoparticles up 2 nm in diameter are unstable with respect to amorphisation.[22] In Q1D nanowires and high-aspect-ratio nanorods the surface/volume ratio is significantly lower than in Q0D systems of the same composition and we may expect a more rapid convergence to bulk-like crystalline structures. That this may not be the case for ultra-thin nanowires was first proposed in 1998 by Tosatti *et al.* for elemental metal systems using simple atomistic models.[23] For

[a]*Departament de Química Física & Institut de Química Teòrica i Computacional (IQTCUB), Universitat de Barcelona, C/Martí i Franquès 1, E-08028 Barcelona, Spain*
[b]*Department of Chemistry, Kasetsart University, Bangkok 10900, Thailand*
[c]*Center of Nanotechnology, Kasetsart University, Bangkok 10900, Thailand*
[d]*NANOTEC Center of Excellence, National Nanotechnology Center, Kasetsart University, Bangkok 10900, Thailand*
[e]*Institució Catalana de Recerca i Estudis Avançats (ICREA), 08010 Barcelona, Spain*

 

compound materials of nanotechnological interest, such as the numerous types of ISC, however, neither experiment nor theory has reported any tendency for ultra-thin Q1D nanosystems to deviate from bulk-like structures.

In an effort to bridge the gap between experiment and theory, with respect to the inherent behaviour of ultra-thin Q1D nanosystems of pure ISC materials, we employed large state-of-the-art scale density functional theory (DFT) calculations to follow the Q0D-to-Q1D transition for ultra-thin CdS. In order to tackle both ends of this range we have combined both bottom-up and top-down modelling approaches by calculating the stability of both small nanoclusters and infinite nanowires. The main feature of our approach, however, is that we explicitly follow the transition between these extremes by computing how the stabilities of cluster-assembled nanorods vary with increasing length. Specifically, we have investigated the energetic stability and atomistic and electronic structure of ultra-thin nanorods and nanowires assembled from experimentally detected $(CdS)_{13}/(CdSe)_{13}$ magic clusters (*i.e.* clusters exhibiting pronounced abundance peaks in cluster beams[4,5]) with a diameter 1.0–1.2 nm, with respect to the corresponding bulk-like wz-structured Q1D systems. Of note is that the prominent high abundance of clusters with 13 units is observed both in laser ablation experiments producing ligand-free clusters,[4,5] and in solution-based nucleation experiments[4] where the clusters are ligated. Although the structure of the magic cluster(s) corresponding to these peaks cannot, as yet, be directly ascertained from experiment, following previous studies,[4,5] we assume that it most likely corresponds to the bare $(CdS)_{13}/(CdSe)_{13}$ isomer with the lowest energy.

To calculate the relative stabilities and properties of nanorods and nanowires built from wz and magic nanocluster building blocks we employed periodic density functional (DF) theory using the PW91 implementation[24] of the Generalized Gradient Approach (GGA) form of the exchange–correlation potential using the VASP code.[25] A plane wave basis set with a kinetic energy cut-off of 415 eV was used, with the effect of the atomic core on the valence electron density taken into account by the projector augmented wave (PAW) approach.[26,27] The calculations for all cluster isomers and nanorods were carried out by placing each system inside a large enough box so as to make the interaction between repeated images negligible in all directions (10 Å was found to be sufficient). The infinite nanowires, similarly spaced in all directions perpendicular to the axes of the wires, were also considered. For the infinite nanowire a $1 \times 1 \times 9$ Monkhorst–Pack mesh[28] of special $k$-points was employed, whereas for the finite nanorods and clusters Γ-point calculations were performed. In all cases the atomic structure of the system was fully relaxed until the forces were smaller than 0.01 eV $Å^{-1}$. In constructing the infinite nanowires, a magic cluster or wz cluster was initially placed in a periodic cell such that the axis of symmetry was aligned along the $z$-direction with a $z$-spacing of a suitable bond length. In order to prevent artificial geometric constraints due to the use of only one cluster as a repeat unit in the subsequent structural optimisations of the nanowires a two-cluster supercell (*i.e.* 52 atoms) was employed. Firstly, the nanowires were optimised (both the internal atomic structure and supercell length) to their closest energy minimum to the as-constructed structure (cluster-assembled nanowires). Subsequently, we mechanically annealed the cluster-assembled nanowires by gradually compressing and stretching them (by up to 30% of their original length) by appropriately varying the $z$-dimension of the supercell of the initial cluster-assembled nanowires; for every fixed $z$-value optimising the nanowire structure. Every time a structural change occurred (causing a new minimum energy atomic configuration), the annealing procedure was again performed around the minimum energy configuration of the newly obtained structure. This process was repeated until stretching and compressing the nanowires did not change their minimum energy structure. The resulting nanowires are referred to as annealed nanowires below.

In Fig. 1 we show the structures and calculated relative energetic stabilities of three selected $(CdS)_{13}/(CdSe)_{13}$ cluster isomers: a) the likely ground-state "magic" cluster, b) a cage-like cluster, and c) a wz cluster fragment. The $(CdS)_{13}$ magic cluster has been predicted by calculations to have the form of a distorted cage filled by a single 4-coordinated sulfur atom bonded to four 4-coordinated cadmium atoms giving rise to a $C_3$ structure.[4,5] Particularly interesting for the present study is the fact that the magic cluster structure lies ~1 eV below the wz nanocluster. Our calculations further confirm that the magic cluster structure is also the likely ground state for CdSe with a very similar energetic stability over the corresponding wz-structured isomer. The cage-like cluster isomer is an example of the numerous cluster isomers having energetic stabilities between that of the wz cluster and the likely ground-state magic cluster.[5,21] Although, in principle, one could consider many Q1D nanosystems based on these isomers, herein, we concentrate on comparing arguably the most important clusters (i) the wz cluster (giving rise to wz-structured Q1D nanosystems as observed for many Q1D CdS/CdSe nanosystems experimentally), (ii) the most stable cluster isomer, assumed to correspond to the magic-cluster abundance peak in experiments.

In previous studies we showed that stable clusters of other materials (*e.g.* ZnO, LiF) when considered as nanosized building blocks, can, when appropriately assembled, lead to predictions of novel stable bulk polymorphs.[29,30] Here, although the symmetry of the magic $(CdS)_{13}$ cluster does not easily lend itself to assembly in three dimensions, we may take advantage of its axial $C_3$ symmetry to form ultra-thin 1D nanowires and nanorods by forming Q1D stacks of axially aligned clusters. The wz $(CdS)_{13}$ isomer also has three-fold

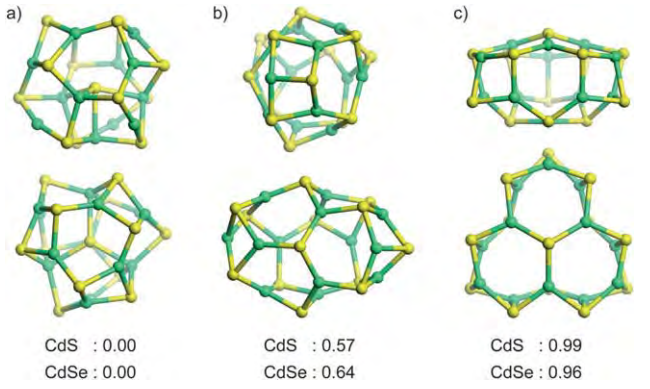


**Fig. 1** Optimised structures of three $N = 13$ nanocluster isomers, where the upper and lower rows correspond to different views of the same three clusters: a) magic-, b) cage-, and c) wurtzite-based clusters. Below each cluster the relative energy (in eV) is given for both CdS and CdSe compositions with respect to the energy of the magic-cluster. As for all figures yellow balls represent sulfur or selenium atom positions and green balls cadmium atom positions. All reported energies of clusters, nanorods and nanowires refer to binding energies with respect to constituent spherical non spin-polarised atoms.

symmetry allowing us to also construct axially aligned ultra-thin nanowires and nanorods with the wz structure (with their long axis aligned with the (001) direction in the wz crystal as found in experiments) of exactly the same atomic composition as in the magic-cluster case for direct comparison. It was found in both cases considered that annealed nanowires were significantly more stable than cluster-assembled wires. The wz cluster-assembled nanowire was found to be a shallow, relatively high lying, energy minimum having a layered hexagonal structure (see Fig. 2) analogous to that found in bulk boron nitride (*h*-BN) which has also been predicted theoretically to be stable for ultra-thin nanorods and nanowires of ZnO[31] and in thicker ZnO nanorods under tensile strain.[32] We note that this relatively dense phase should be differentiated from a similar low-density hexagonal phase with larger interlayer spacing,[33,34] which was not observed in our investigation. Upon annealing, the hexagonal layered nanowire transforms into new structure with a deeper lying energetic minimum having a more bulk-like wz structure with a correspondingly longer (+28%) unit cell length (Figs. 2, 3a1 and 3b1). For the magic-cluster-assembled nanowire, the annealing procedure proceeds *via* an intermediate nanowire structure and finally leads to a more stable nanowire structure having a slightly shorter (-6%) unit cell length (Figs. 2, 3a2 and 3b2) but which is still significantly longer (+20%) than the annealed wz nanowire. Unlike for $(CdS)_{13}$ nanoclusters, but following experimental observations for thicker CdS nanowires and nanorods, Fig. 2 clearly shows that the wz structure is the most stable structure for $(CdS)_{13}$-based nanowires. The comparable diameters of the wz and magic-cluster-based ultra-thin nanowires results in similarly strong quantum confinement with an increase in the band gap with respect to the bulk wz band gap by a factor of 2.5 (see Fig. 4). In contrast, the absolute energy levels of the annealed wz nanowire are deeper than for the magic-cluster-based nanowire probably due to the energetically preferred atomic structure of the former.

In order to analyze the transition from the most stable 01D nanosystem for $(CdS)_{13}$ (*i.e.* the magic-cluster structure) to the most stable infinite nanowire (*i.e.* bulk-like wz-structured) we considered

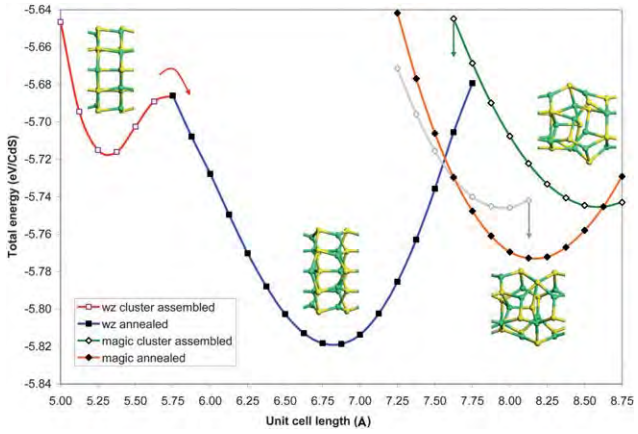


**Fig. 2** Energy (in eV/CdS) *versus* length curves for the infinite CdS nanowires. Total energy of the cluster-assembled and annealed nanowires constructed from the $(CdS)_{13}$ wz and magic clusters as a function of the unit cell length (half the super cell length used in the calculations) along the nanowire *z*-direction. The arrows indicate the energetically downhill annealing path. The inset figures show the structure of a unit cell of the cluster-assembled and final annealed nanowires.

$[(CdS)_{13}]_n$ nanorods of all four CdS nanowire structures considered above (*i.e.* wz- and magic-cluster-based, both annealed and cluster-assembled) from the size of a one-cluster unit ($n = 1$ or 26 atoms) to a six-cluster unit ($n = 6$ or 156 atoms). In Fig. 5 we show the change in total energy of the four nanorods per CdS unit with increasing length. Interestingly, unlike for the nanowires, for up to $n = 3$, the cluster-assembled wz nanorod was found to be more stable than the nanorod with the annealed wz structure. For all considered sizes, however, the annealed magic-cluster nanorod was found to be most energetically stable. As the length of the nanorods increases, the energy difference between the annealed wz and magic-cluster-based nanorod structures gradually reduces implying that a transition to the wz structure occurs for larger *n*. In order to predict at what length this transition occurs, we have extrapolated the energy *versus* length trends of the magic-cluster-based and wz nanorods by fitting the data points to an inverse power law (see inset to Fig. 5, fitted with $R^2 > 0.99$). We find that the persistence of the excess stability of the annealed magic nanorods with respect to the annealed wz nanorods lasts until approximately 13 cluster units; equating to 338 atoms and to more than 10 nm length with respect to the length of the annealed magic nanorod. We have also calculated the energy difference between annealed wz and magic-cluster-based $[(CdSe)_{13}]_6$ nanorods which is very similar to that found for CdS indicating analogous behaviour in both Q1D systems. Relative energies of all nanorods and nanowires are given in Table 1. To understand these trends we have examined the atomic and electronic structure of the nanorods.

The higher crystallinity of the annealed wz $[(CdS)_{13}]_6$ nanorod is clear from the radial distribution function (RDF) taken with respect to the position of a central sulfur atom showing prominent peaks at well-determined distances (see RDF for the annealed wz $[(CdS)_{13}]_6$ in Fig. 3c1 with respect to the structure shown in Fig. 3d1). In contrast, the corresponding RDF of the annealed magic-cluster-based $[(CdS)_{13}]_6$ nanorod (see Fig. 3c2 with respect to structure shown in Fig. 3d2). This lower crystallinity is also manifested in the oscillatory diameter of the annealed magic-cluster-based Q1D nanosystems (Fig. 3b2) due to the recognisable magic-cluster $(CdS)_{13}$ repeat units (see highlighted segment in Fig. 3d1). In contrast, the annealed wz Q1D nanosystems have a much more regular stacked structure with a uniform diameter (see Fig. 3d1). This crystalline layering has been observed by HRTEM in CdS and CdSe nanorods of larger diameters than those studied here.[10,13] Based upon our results we predict that such layering will be absent in well-annealed bare CdS and CdSe nanorods of diameters <1.5 nm and lengths <13 nm. Of potential technological importance, such annealed magic-cluster-based nanorods would also have significantly higher aspect ratios than wz nanorods of the same composition (~50% higher in the case of $[(CdS)_{13}]_6$). Under pressure cycling, ultra-thin CdSe nanorods have previously been shown to exhibit dramatic structural transitions between the six-fold coordinated rocksalt phase and the four-fold coordinated wz phase[35] often leading to fracturing. In the present case, although accompanied by a large aspect ratio change, the atomic-level transition is much more subtle and may thus be more robust for repetitive utilization in nano-mechanical transducers. We also note that we have confirmed the experimental observation that rocksalt nanorods are only stable under external pressure for the ultra-thin regime by attempts to optimise ultra-thin rocksalt-structured nanorods. We found in all cases that the such nanorods spontaneously relaxed into distorted non-cubic structures

 

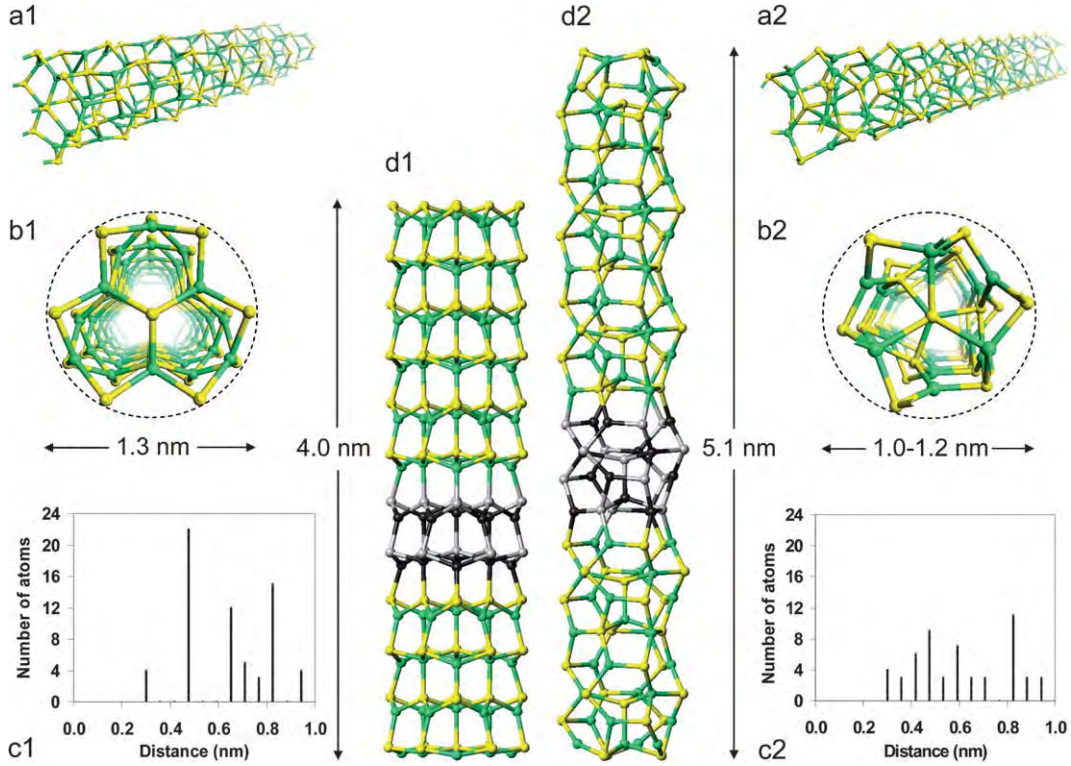


**Fig. 3** Summary of the structural features of annealed wz and magic-cluster-based CdS nanowires and nanorods. Perspective views of the annealed wz- (a1) and magic-cluster-based (a2) nanowires, cross-section of the of the annealed wz (b1) and the magic-cluster-based (b2) nanowire/nanorod, radial distribution function of the annealed wz (c1) and magic-cluster-based (c2) $[(CdS)_{13}]_6$ nanorod, atomic structure of the annealed wz (d1) and the magic-cluster-based (d2) $[(CdS)_{13}]_6$ nanorods (the $(CdS)_{13}$ repeat unit is highlighted in each case). Quoted distances include the radii of two sulfur ions to better compare with estimates made by HRTEM. The two distances in b2 indicate the maximum and minimum of the oscillatory diameter of the annealed magic-cluster-based nanorods and nanowires.

(usually with final structures similar to wz) which were always significantly less stable than the other nanorods considered herein.

Experimentally, CdS and CdSe nanorods possessing a layered wz structure oriented along the (001) direction are known to have very large electric dipole moments along the length of the rod[36] which are thought to be important for their self-assembly.[37] Maintaining a large dipole is not energetically favourable and it is known in similarly structured infinite 2D wz nanoslabs (where such a dipole is unsustainable) in other materials, that the atomic structure can reconstruct in ways to drastically reduce the moment across the slab.[33,34] In our case we estimate the dipole moment in the annealed wz CdS nanorods to be reduced by approximately 5% when going to the annealed magic-cluster-based CdS nanorods indicating that dipole reduction is not a significant structure-directing influence in the ultra-thin Q1D systems considered.

Along their length, both magic-cluster and wz annealed nanorods have the same atomic nearest neighbour coordination per $(CdS)_{13}$ unit: four four-coordinated and nine three-coordinated sulfur atoms and four four-coordinated and nine three-coordinated cadmium atoms. At their ends, termination induces three two-coordinated cadmium atoms in both annealed nanorod types and a further three two-coordinated sulfur atoms in the annealed wz nanorods only. Two-coordinated sulfur atoms appear to be an inherent terminating structural feature of bare annealed wz nanorods which cannot be repaired by local reconstruction. In order to retain a wz-like structure, while avoiding such under-coordination of the sulfur atoms, wholesale reconstruction seems to be the only option. Such a reconstruction leads to nanorods with a hexagonal layered structure and the resulting lower under-coordination of the sulfur atoms is a likely reason why such nanorods are more stable than annealed wz nanorods for $n$ <4 (see Fig. 5). Electronically, both the wz- and magic-cluster-based nanorods have a large number of states in the region of the gap of their respective infinite nanowire counterparts due to their defective end terminations. In line with the higher under-coordination in the annealed wz nanorods, the energy level spectrum is destabilised with respect to that of the annealed magic-cluster-based nanorods (see Fig. 4). We can view the annealed magic-cluster nanorods as structurally reconstructed versions of the annealed wz nanorods which helps to heal the less energetically favourable sulfur terminations in the latter. This reconstruction, although stabilising with respect to the nanorod ends also causes the internal atomic structure of the nanorod to be non-wz-like. Thus, with increasing length, a greater and greater percentage of the atoms in the annealed magic-cluster nanorods will be found in a structure known to be energetically less stable than the wz structure in the infinite limit and the percentage of atoms involved in an energetically preferable terminating reconstruction will become correspondingly lower. Evidently, at some length this situation will no longer be more stable than an annealed wz structure with a less favourable terminating end reconstruction. At this point, structural transition between the annealed magic-cluster structure and the annealed wz nanorod will be energetically favourable (at a length of ~10 nm, as predicted by our

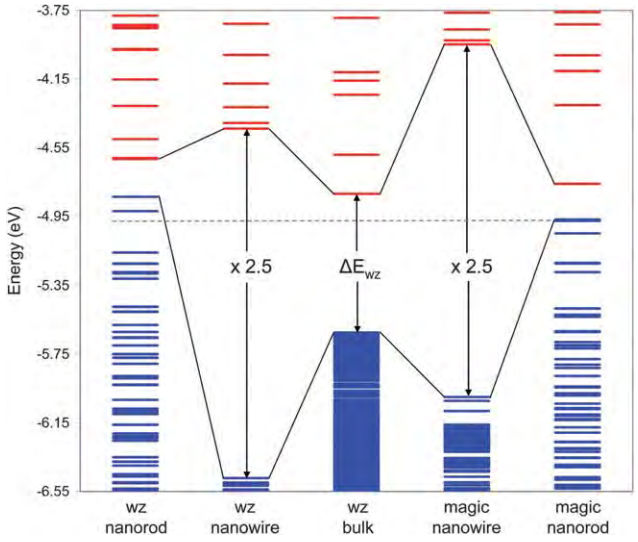


**Fig. 4** Summary of the electronic structure of annealed wz- and magic-cluster-based CdS nanowires and nanorods. Calculated energy levels (eV) of CdS systems (from left to right): annealed wz $[(CdS)_{13}]_n$ nanorod, infinite annealed wz nanowire, wz bulk crystal, infinite annealed magic-cluster-based nanowire, annealed magic-cluster-based $[(CdS)_{13}]_n$ nanorod. Blue denotes occupied levels (sulfur s–p states) and red unoccupied levels (cadmium s states). The gaps of the nanowires are shown to be red-shifted by a 2.5× multiplicative factor with respect to the bulk CdS wz bandgap ($\Delta E_{wz}$) due to quantum confinement. We note that, as is typical for DFT calculations, the band gaps are systematically underestimated and thus the figure provides an indication of relative changes in electronic structure (*i.e.* Q1D with respect to bulk) only.

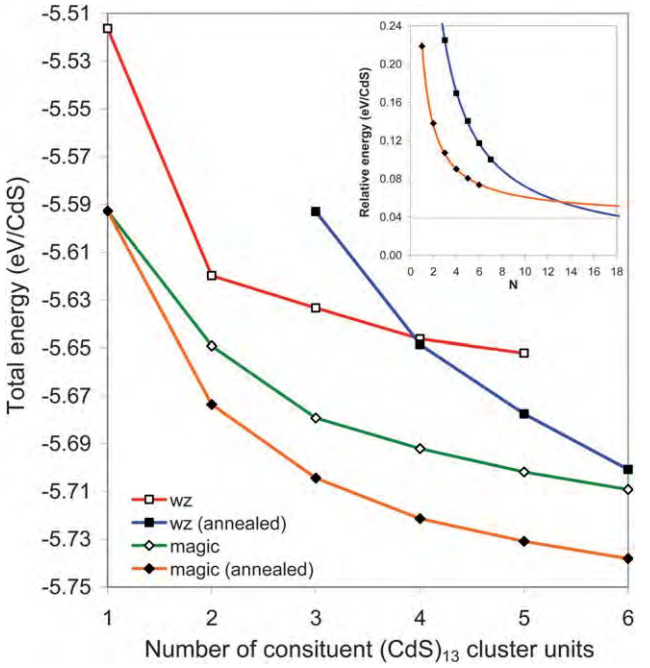


**Fig. 5** Energy (eV/CdS) of the cluster-assembled and annealed $[(CdS)_{13}]_n$ nanorods constructed from the $(CdS)_{13}$ wz and magic-cluster units as a function of $n$. The inset shows extrapolated energetic relative stability of the wz and magic-cluster-based annealed $[(CdS)_{13}]_n$ nanorods as a function of $n$ with respect to the energy of the calculated energy of the infinite annealed wz nanowire. The horizontal grey line shows the energy of the infinite magic-cluster annealed nanowire.

calculations). We note that this strong dependence of the overall CdS/CdSe ultra-thin nanowire structure, and, furthermore, aspect ratio, on the terminating surface atomic/electronic structure may provide a means for influencing the predicted nanorod structural crossover by reversible attachment of suitable ligands.

In summary, we have compared the stability of ultra-thin bare CdS nanowires and nanorods having the bulk wz structure with those based on the assembly of particularly stable $(CdS)_{13}$ magic-cluster building blocks using first principles calculations. Although the wz structure is energetically favoured in relatively thick CdS nanorods and in the limit of infinitely long ultra-thin nanowires, in ultra-thin nanorods the magic-cluster-based structure is found to be persistently more energetically stable than the correspondingly sized bulk-like wz nanorods up to a length of 10 nm. This nanoscale structural transition is also predicted to be found in ultra-thin Q1D CdSe and in both materials should be experimentally verifiable by HRTEM. As the length-dependent transition is also accompanied by a large change in the aspect ratio of the nanorods, if physically realized, this effect may find potential application in nano-mechanical transducers. We believe that our explicit demonstration of the persistence of the stability non-bulk like atomic structures in Q0D nanoclusters to Q1D ultra-thin nanorods in two nanotechnologically important ISC materials is likely to be general to many other materials. We hope that our work may help to encourage experimental efforts in this area to fabricate ultra-thin Q1D nanosytems (particularly with diameters ~1 nm) in a range of materials, many of which we predict will have novel non-bulk-like atomic structures and potentially useful new nanoscale properties.

**Table 1** Calculated energies (eV per formula unit) of all considered nanorods and nanowires of CdS and CdSe

| Composition | wz cluster assembled | wz cluster annealed | Magic cluster assembled | Magic cluster annealed |
|---|---|---|---|---|
| $Cd_{13}S_{13}$ | −5.516 | — | −5.593 | — |
| $Cd_{26}S_{26}$ | −5.620 | — | −5.649 | −5.674 |
| $Cd_{39}S_{39}$ | −5.633 | −5.593 | −5.679 | −5.704 |
| $Cd_{52}S_{52}$ | −5.646 | −5.649 | −5.692 | −5.721 |
| $Cd_{65}S_{65}$ | −5.652 | −5.678 | −5.702 | −5.731 |
| $Cd_{78}S_{78}$ | — | −5.701 | −5.709 | −5.738 |
| $Cd_{91}S_{91}$ | — | −5.718 | — | — |
| CdS nanowire | −5.720 | −5.818 | −5.747 | −5.780 |
| $Cd_{13}Se_{13}$ | −5.062 | — | −4.988 | — |
| $Cd_{78}Se_{78}$ | — | −5.177 | — | −5.140 |
| CdSe nanowire | — | −5.211 | — | −5.246 |

## Acknowledgements

We acknowledge support from the Spanish Ministry of Education and Science (grant FIS2008-02238), time on the *MareNostrum* supercomputer (*Barcelona Supercomputing Center/Centro Nacional de Supercomputación*) and grants from the Thailand Research Fund (to WS and JL) and the National Science and Technology Development Agency (NSTDA Chair Professor and NANOTEC Center of Excellence). Support from the Thai Commission on Higher Education, Ministry of Education under Postgraduate Education and Research Programs in Petroleum and Petrochemicals, and Advanced Materials is also acknowledged.

 

## References


1 L.-S. Li, J. Hu, W. Yang and A. P. Alivisatos, *Nano Lett.*, 2001, **1**, 349–351.
2 H. Yu, J. Li, R. A. Looms, L.-W. Wang and W. Buhro, *Nat. Mater.*, 2003, **2**, 517–520.
3 L. Cademartiri and G. A. Ozin, *Adv. Mater.*, 2008, **20**, A1–8.
4 A. S. R. Kasuya, Y. A. Barnakov, I. M. Dmitruk, T. Nirasawa, V. A. Romanyuk, V. Kumar, S. V. Mamykin, K. Tohji, B. Jeyadevan, K. Shinoda, T. Kudo, O. Terasaki, Z. Liu, R. V. Belosludov, V. Sundararajan and Y. Kawazoe, *Nat. Mater.*, 2004, **3**, 99–102.
5 E. Sanville, A. Burnin and J. BelBruno, *J. Phys. Chem. A*, 2006, **110**, 2378–2386.
6 X. F. Duan, Y. Huang, R. Agarwal and C. M. Lieber, *Nature*, 2003, **421**, 241–245.
7 X. F. Duan, C. M. Niu, V. Sahi, J. Chen, J. W. Parce, S. Empedocles and J. L. Goldman, *Nature*, 2003, **425**, 274.
8 C. J. Barrelet, A. B. Greytak and C. M. Leiber, *Nano Lett.*, 2004, **4**, 1981–1985.
9 Y. Wang and N. Herron, *J. Phys. Chem.*, 1991, **95**, 525–532.
10 W. Cai, Z. Li and J. Sui, *Nanotechnology*, 2008, **19**, 465606(1–6).
11 A. Ghezelbash, B. Koo and B. Korgel, *Nano Lett.*, 2006, **6**, 1832–1836.
12 N. Pradhan, X. Huifang and X. Peng, *Nano Lett.*, 2006, **6**, 720–724.
13 F. S. Riehle, R. Bienert, R. Thomann, G. A. Urban and M. Krüger, *Nano Lett.*, 2009, **9**, 514–518.
14 C. H. Ye, G. W. Meng, Y. H. Wang, Z. Jiang and L. D. Zhang, *J. Phys. Chem. B*, 2002, **106**, 10338–10341.
15 S. D. Elliott, M. P. Moloney and Y. K. Gun'ko, *Nano Lett.*, 2008, **8**, 2452–2457.
16 J. B. Li and L. W. Wang, *Phys. Rev. B: Condens. Matter Mater. Phys.*, 2005, **72**, 125325(1–15).
17 S. –P. Huang, W. –D. Cheng, D.-S. Wu, J.-M. Hu, J. Shen, Z. Xie, H. Zhang and Y.-J. Gong, *Appl. Phys. Lett.*, 2007, **90**, 031904(1–3).
18 H. Pan and Y. P. Feng, *ACS Nano*, 2008, **2**, 2410–2414.
19 S. Datta, M. Kabir, T. Saha-Dasgupta and D. D. Sarma, *J. Phys. Chem. C*, 2008, **112**, 8206–8214.
20 J. Frenzel, J.-O. Joswig and G. Siefert, *J. Phys. Chem. C*, 2007, **111**, 10761–10761.
21 S. M. Woodley, A. A. Sokol and C. R. A. Catlow, *Z. Anorg. Allg. Chem.*, 2004, **630**, 2343–2353.
22 C. E. Junkermeier, J. P. Lewis and G. W. Bryant, *Phys. Rev. B: Condens. Matter Mater. Phys.*, 2009, **79**, 125323(1–8).
23 O. Gülseren, F. Ercolessi and E. Tosatti, *Phys. Rev. Lett.*, 1998, **80**, 3775–3778.
24 J. Perdew, K. Burke and Y. Wang, *Phys. Rev. B: Condens. Matter*, 1996, **54**, 16533–16539.
25 G. Kresse and J. Hafner, *Phys. Rev. B: Condens. Matter*, 1993, **47**, 558–561.
26 P. E. Blöchl, *Phys. Rev. B: Condens. Matter*, 1994, **50**, 17953–17979.
27 G. Kresse and D. Joubert, *Phys. Rev. B: Condens. Matter Mater. Phys.*, 1999, **59**, 1758.
28 H. J. Monkhorst and J. D. Pack, *Phys. Rev. B: Solid State*, 1976, **13**, 5188–5192.
29 J. Carrasco, F. Illas and S. T. Bromley, *Phys. Rev. Lett.*, 2007, **99**, 235502(1–4).
30 W. Sangthong, J. Limtrakul, F. Illas and S. T. Bromley, *J. Mater. Chem.*, 2008, **18**, 5871–5879.
31 L. Zhang and H. Huang, *Appl. Phys. Lett.*, 2007, **90**, 023115(1–3).
32 A. J. Kulkarni, M. Zhou, K. Sarasamak and S. Limpijumnong, *Phys. Rev. Lett.*, 2006, **97**, 105502(1–4).
33 C. L. Freeman, F. Claeyssens and N. L. Allen, *Phys. Rev. Lett.*, 2006, **96**, 066102(1–4).
34 C. Tusche, H. L. Meyerheim and J. Kirschner, *Phys. Rev. Lett.*, 2007, **99**, 026102(1–4).
35 D. Zaziski, S. Prilliman, E. C. Scher, M. Casula, J. Wickham, S. M. Clark and A. P. Alivisatos, *Nano Lett.*, 2004, **4**, 943–946.
36 L.-S. Li and A. P. Alivisatos, *Phys. Rev. Lett.*, 2003, **90**, 097402(1–4).
37 A. V. Titov and P. Král, *Nano Lett.*, 2008, **8**, 3605–3612.

CARBON 48 (2010) 1524–1530

available at www.sciencedirect.com

ScienceDirect

journal homepage: www.elsevier.com/locate/carbon

# Density functional theory evidence for an electron hopping process in single-walled carbon nanotube-mediated redox reactions

*Teeranan Nongnual* [a,b], *Somkiat Nokbin* [a,b], *Pipat Khongpracha* [a,b], *Philippe Anthony Bopp* [c], *Jumras Limtrakul* [a,b,*]

[a] *Laboratory for Computational and Applied Chemistry, Chemistry Department, Faculty of Science, Kasetsart University, Bangkok 10900, Thailand*

[b] *NANOTEC Center of Excellence, National Nanotechnology Center, Kasetsart University, Research and Development Institute, Bangkok 10900, Thailand*

[c] *Department of Chemistry, Université Bordeaux 1, FR-33405 Talence Cedex, France*

ARTICLE INFO

*Article history:*
Received 18 September 2009
Accepted 18 December 2009
Available online 24 December 2009

ABSTRACT

The electron hopping mechanism in the single-walled carbon nanotube (SWCNT)-mediated redox reaction between anthraquinonyl ($AQH_2$) and 4-arylhydroxyl amine (4AHA) groups is studied by density functional theory calculations. The (8, 0) SWCNT is used to mimic the real system of interest. It is found that electrons from the oxidized $AQH_2$ group can be transferred to the oxidizing 4AHA group, at the other end of the nanotube, by a hopping process through the mediating SWCNT. Disparity of electron densities ascribable to non-localized electrons confirms this finding. The disparity, partial electron density difference, and Hirshfeld partial charges analyses show that the SWCNT can hold 87% of the extra electron density of the hypothetical negative intermediate produced from the oxidation of the $AQH_2$ process. Chemical attachments of these two redox reagents to the SWCNT also cause new impurity states within the band gap, thereby giving more metallic characteristics to the system. These findings provide a detailed understanding of the electron hopping process and agree well with a previous experimental study.



## 1. Introduction

Among all nanoscale morphologies of carbon, multi-walled carbon nanotubes (MWCNTs) were first observed under transmission electron microscopy (TEM) by Iijima in 1991 [1]. After that, single-walled carbon nanotubes (SWCNTs) were produced independently by Iijima and Ichihashi [2] and Bethune et al. [3] in 1993. Since these discoveries of low-dimensional carbon nanostructures, carbon nanotubes (CNTs) have attracted much interest in modern nanoscience and nanotechnology due to their novel and structure-dependent properties. Over the years, the physical and chemical properties of CNTs have been well-documented with more and more sophisticated methods. The novel properties of these CNTs allow their application as nanoelectronic devices [4], sensors [5], field emission sources [6], and composite materials [7]. The CNTs also function as nanowires to transport electrons between an electrode and electroactive proteins chemically

* *Corresponding author:* Address: NANOTEC Center of Excellence, National Nanotechnology Center, Kasetsart University, Research and Development Institute, Bangkok 10900, Thailand. Fax: +66 2562 5555x2176.
E-mail address: jumras.l@ku.ac.th (J. Limtrakul).

0008-6223/$ - see front matter © 2009 Elsevier Ltd. All rights reserved.
doi:10.1016/j.carbon.2009.12.049

attached on each end of the tube [8]. The transport distances, controlling the rate of electron transfer, are larger than 150 nm from the enzymatic active center to the electrode [9].

The chemical functionalization reactions for CNTs are categorized into three methods, which are: direct attachment to the graphitic surface, ester linkage, and covalent binding using diazonium reagents with high selectivity. The diazonium media method was further developed by Compton's group to initiate chemisorptions of aryl diazonium salts by direct reduction with hypophosphorous acid in the presence of carbon powder [10–12]. The method was further extended to the application on MWCNTs with anthraquinone-1-diazonium chloride and 4-nitrobenzenediazonium tetrafluoroborate, resulting in the synthesis of 1-anthraquinonyl–MWCNTs (AQ–MWCNTs) and 4-nitrophenyl–MWCNTs (NB–MWCNTs) [13].

Recently, Wong and Compton [14] reported a redox reaction on the same MWCNT for the first time. This MWCNT is functionalized with two redox-active species, directly attached by the diazonium salt method. The 4-arylhydroxyl amine (4AHA) and $AQH_2$ species are generated in the first oxidation cycle from $NO_2$–$C_6H_4$–MWCNT and AQ–MWCNT, respectively. This redox reaction consists of a reversible oxidation and an irreversible reduction; it is studied by the cyclic voltammetry technique. These authors proposed a redox reaction mechanism where $AQH_2$ is the oxidizing agent with the oxidation peak at $E_a = -0.385$ V while NHOH–$C_6H_4$ is the reducing group lessening the oxidation peak at $E_a = 0.125$ V

$$AQH_2\text{–MWCNT–}C_6H_4\text{–NHOH} \rightarrow AQ\text{–MWCNT–}C_6H_4\text{–}NH_2 + H_2O$$

The pathway of electron transfer from $AQH_2$ to the 4-arylhydroxyl amine group is investigated to determine whether it is via intermolecular electron tunneling between reagents or by electron hopping via the CNT. The hopping was proposed to be more favorable because of the shorter distance through the tube compared to a process through the solvent. This phenomenon is unique for both oxidizing and reducing groups confined to the same CNT.

Here, we report a theoretical study on the possible processes of electron hopping between two redox reagents functionalized on the same CNT. The mediating MWCNT (in the real system) is simplified to a semiconducting SWCNT for computational efficiency. Periodic calculations are performed to obtain computed electronic properties as realistic as possible. Although time-dependent calculations can yield more details about the electron transfer, such calculations are not practicable for such a large system due to computational limitations. We have thus limited ourselves to static calculation and have tried to overcome the limitations by focusing on six hypothetical subsystems, using static analysis techniques such as the disparity of the electron densities and the nucleophilic Fukui function plot. This yields enough information to establish and characterize the electron transfer process in the whole system.

We also focus only on the redox reaction and not on the chemical attachment and the preparation steps. Thus, the following redox reaction from $AQH_2$–SWCNT–4AHA, terminated at AQ–SWCNT–4AA, is proposed. It can be subdivided into a reversible oxidation and an irreversible reduction (see Fig. 1), where 4-arylamine is noted as 4AA.

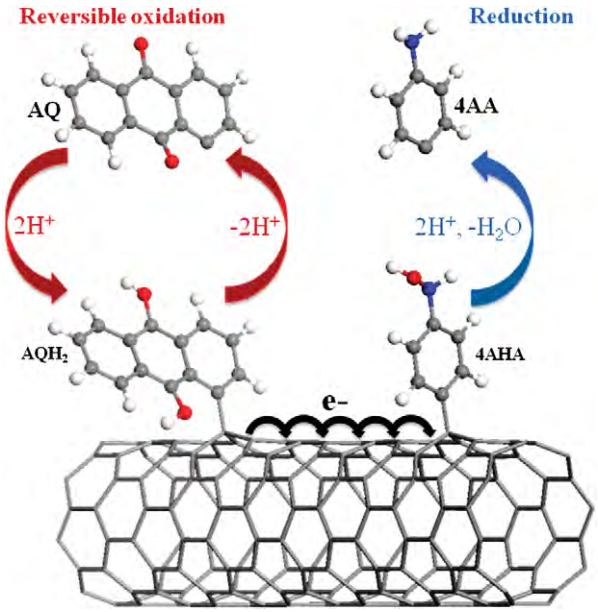


**Fig. 1 – Proposed mechanism for the SWCNT-mediated redox reaction, consisting of a reversible oxidation and an irreversible reduction. The SWCNT accepts electrons from the $AQH_2$ species and donates the electrons to the 4-arylhydroxyl amine.**

*Total reaction:*

$$AQH_2\text{–SWCNT–4AHA} \rightarrow AQ\text{–SWCNT–4AA} + H_2O$$

*Oxidation:*

$$AQH_2\text{–SWCNT–4AHA} \leftrightarrow AQ\text{–SWCNT–4AHA} + 2H^+ + 2e^-$$

*Reduction:*

$$AQ\text{–SWCNT–4AHA} + 2H^+ + 2e^- \rightarrow AQ\text{–SWCNT–4AA} + H_2O$$

## 2. Calibration of the SWCNTs and computational method

The periodic calculations were carried out using the density functional theory (DFT) method as implemented in the DMol3 package [15,16]. For all functionals that we investigated, the generalized gradient approximation (GGA) and an all-electron double numerical basis set with polarized function (DNP) were chosen for these spin-unrestricted computations. These functionals can be applied to large periodic systems and are known to bring about reliable qualitative results. The density functionals used in this work do not include dispersion energy contributions. The DNP basis set corresponds to a double-$\zeta$ quality basis set with a p-type polarization function added to hydrogen and d-type polarization functions added to heavier atoms, and is comparable to 6-31G** Gaussian basis sets, providing a better accuracy, particularly for the hydrogen removal step. The real space global cutoff radius was set to be 3.70 Å. For the geometrical optimizations, all atoms were fully optimized until all the forces on the atoms were less than 0.05 eV $Å^{-1}$. The Brillouin zone was sampled using the Monkhorst–Pack scheme [17].

### 2.1. Calibration of the SWCNTs

In the present approach, a suitably calibrated SWCNT is used to mimic the multi-walled tubes used in the experiments for the computations. The important feature is that the MWCNTs used in the experiments have electronic band gaps like semiconductors. The criterion for the calibration is thus, that the gap of the model-tube should be in the range of 0.5–1.5 eV [18]. The calibration is started with a study of naked ($n$, 0) zigzag SWCNTs, investigated with three functionals and comparing the energy gaps ($E_{gap}$) with each other and with the ones obtained in previous studies. Each initial structure is generated in a supercell periodic box of $20 \times 20 \times 8.52$ Å$^3$, composed of two repeated unit cells of SWCNT along the tube axis. The closest distance between two neighboring SWCNTs is larger than 10 Å in order to be able to ignore intertube interactions in the calculations.

The calibrations are performed in the GGA in the Perdew–Burke–Ernzerhof (PBE) [19], Becke's exchange and Lee, Yang, and Parr's correlation functional (BLYP) [20,21], and non-local exchange–correlation functional (PW91) [22] with the maximum $k$ points of $1 \times 1 \times 50$. The BLYP method is immediately disqualified due to its large average deviation of ±0.079 eV in $E_{gap}$ compared to previous theoretical data [23–28]. The PBE and PW91 methods give the same $E_{gap}$ within a small deviation of ±0.007 eV and a smaller deviation of ±0.044 eV compared to the same data. Although these two methods are very similar, the PBE functional is chosen in our calculations, following the recent theoretical studies [29,30] of periodic systems.

The diameter of the zigzag SWNCTs is then varied systematically and the band gaps studied with the same procedure to find the smallest nanotube representative of the experimental system. Three ($n$, 0) SWCNTs with $n$ mod 3 = 0 are found to be metallic, obeying the empirical ($n$, $n$ + 3$i$) rule for metallic carbon nanotubes, also known as the 1/3 rule: (6, 0) with an $E_{gap}$ of 0.00 eV ($E_{gap,\ calc}$ = 0.00 eV, Ref. [23]); (9, 0) with an $E_{gap}$ of 0.17 eV ($E_{gap,\ expt}$ = 0.080 ± 0.005 eV, Ref. [24] and $E_{gap,\ calc}$ = 0.17 eV, Ref. [25]); and (12, 0) with an $E_{gap}$ of 0.14 eV ($E_{gap,\ expt}$ = 0.042 ± 0.004 eV, Ref. [24] and $E_{gap,\ calc}$ = 0.078 eV, Ref. [23]) (where *expt* is experimental data, *calc* is theoretical data, and $i$ is an integer). The (7, 0) SWCNT also presents a metallic character with an 0.15 eV energy gap (0.21 eV, Ref. [26] and 0.19 eV, Ref. [27]). Thus, the (6, 0), (7, 0), (9, 0), and (12, 0) SWCNTs are certainly not usable as models because of their metallic character.

The (8, 0) SWCNT is found to be the smallest zigzag carbon nanotube that displays a semiconducting behavior with an acceptable energy gap of 0.62 eV. The calculated value is in good agreement with previous data for the $E_{gap}$ (0.643 eV, Ref. [23]; 0.62 eV, Ref. [25]; 0.59 eV, Ref. [27]; and 0.63 eV, Ref. [28]) and confirms that the $E_{gap}$ of $n$ mod 3 = 2 tubes is larger than that $n$ mod 3 = 1 [27]. In order to be able to neglect the intermolecular interaction between the two redox species, the six repeated unit cells along the z-direction of the carbon nanotube are used for the calculations of functionalized tubes. Therefore, the SWCNT-mediated redox models in this work are generated from the validated (8, 0) SWCNT and calculated by periodic calculations with the PBE method.

### 2.2. Redox systems

As seen above, an (8, 0) SWCNT is chosen. For the full redox system, it is functionalized by two redox groups more than 12 Å apart from each other to minimize, and eventually neglect, the intermolecular interaction between these two species. A supercell with $40 \times 40 \times 24.15$ Å$^3$, comprising six periodic lengths for the zigzag SWCNT, is adopted in the calculation with the PBE function (see Fig. S3(a)). Each supercell contains two redox groups, which are covalently bonded to the sidewall of the SWCNT. The smallest distance between two neighboring SWCNTs is larger than 30 Å. In order to save computational time, the $k$ points are reduced to be $1 \times 1 \times 10$, following the previous study [30], to calculate the electronic properties of the full redox system. Only the $\Gamma$ point in the Brillouin zone is also considered for the geometric optimization and orbital analysis.

Even though the individual processes in the overall redox reaction take place concurrently, we simplify the problem by dividing the full redox pathway into six hypothetical states (see Fig. S1), which are: $AQH_2$–SWCNT–4AHA (substrate: *subs*), $[AQH–SWCNT–4AHA]^{1-}$ (*intermediate-1*), $[AQ–SWCNT–4AHA]^{2-}$ (*intermediate-2*: *int-2*), $[AQ–SWCNT–Ph–NH]^{1-}$ (intermediate-3: *int-3*) and AQ–SWCNT–4AA (product: *prod*) (AQ = anthraquinonyl, 4AHA = 4-arylhydroxyl amine, 4AA = 4-arylamine, SWCNT = (8, 0) zigzag SWCNT). The intermediate-1 state can be considered in two configurations, which are termed intermediate-1-a (*int-1-a*) and intermediate-1-b (*int-1-b*) for the removal of H*a* and H*b*, respectively.

Mimicking a half-cell redox reaction, the singly functionalized tubes with two electrons from the oxidation reaction, $[AQ–SWCNT]^{2-}$ (*AQ-tube*) and $[4AHA–SWCNT]^{2-}$ (*4AHA-tube*), are also investigated to consider the possibility of the transfer of these electrons (see Fig. S2). This half-cell redox system is optimized and investigated using the same parameter as the full redox system described above.

## 3. Results and discussion

The diazonium method provides a well-defined chemical bond between the molecule and a carbon atom of the tube rather than the less well-defined interaction between an entire group and the tube surface found in the adsorption of π-conjugated molecules. Indeed, the optimized geometry of the functionalized SWCNTs in the full redox system shows that the reacting groups with closing carbon atoms of the nanotube change their geometries with an average displacement of 0.19 Å for the AQ derivatives and 0.22 Å for the 4AHA derivatives. While the remaining atoms, which are far from the reacting species, of the tube remain roughly at the same positions within, on an average, 0.06 Å. These averages are calculated for all atoms of a desired part changing their relative positions in each step of the mechanism. We also found that the phenyl plane of the 4AHA group (including its derivatives: Ph–NH, and 4AA) is parallel to the perpendicular axis (reference line), which is vertical to the tube axis of the SWCNT medium, as shown in Fig. S4. The angle between the anthraquinonyl plane of the $AQH_2$ group in *subs* and the reference line is sharp, about 30°, due to the steric effect to

the adjacent hydrogen atom (H*b*) of the hydroxyl moiety of the $AQH_2$ group (see Fig. S3(a)). Whenever this hydrogen atom is cleaved, the repulsive force on the ketone becomes smaller. Thus, a less sharp angle is found, about 10°. However, the AQ group is not exactly sharp to the reference line, because the carbonyl oxygen atom is a hindrance for such an orientation.

The electronic properties of the redox systems are reported in Table 1. The results show that the two configurations of intermediate-1 have relative energy which differs by −0.95 kcal $mol^{-1}$, the *int-1-b* being more favorable than *int-1-a* due to a smaller steric effect between the hydrogen atom of the AQH group (H*b*) and the nanotube. The proposed mechanism pathway of the redox reaction through *int-2* is presented in snapshots. It starts from the *subs* configuration and goes through *int-1-b*, *int-2*, and *int-3* to *prod*. In more detail: The O–H*b* of the *subs* is first cleaved, as demonstrated in the *int-1-b*, with one electron remaining. Sequentially, the O–H*a* is removed, resulting in the *int-2*. This is a half-cell redox reaction, with, overall, two electrons left. The *int-3* is an intermediate state, corresponding to the *int-2* to *prod* reduction, where a hydroxyl group of the 4AHA is dehydrated by an acidic proton addition, and the Ph–NH group remains. The nucleophilic nitrogen atom of the *int-3* is then also attacked by another electrophilic proton, resulting in the *prod* configuration. The reduction reaction cannot be reversible: A negative −0.26*e* local Hirshfeld charge is found on the nucleophilic nitrogen atom of the Ph–NH part of *int-3*. This makes an attack between this site and an oxygen atom of water highly unlikely.

The chemical attachment of the two redox reagents to the SWCNT creates new impurity states within the band gap. From the pristine SWCNT, $E_{gap}$ = 0.62 eV, the band gap in the redox systems is lowered to less than 0.16 eV, thereby introducing a more metallic character to the system. This eases electron delocalization in the modified system. The electron density difference and Hirshfeld partial charges analyses show that the tube can hold 87% of the extra electron density of the hypothetical negative intermediate produced from the oxidation of the $AQH_2$ (see entry 5 in Table 1). In addition, the remaining charge at the AQ in the *int-2* is −0.19*e*, leading to a reverse reduction of the AQ to the $AQH_2$.

The frontier molecular orbitals of the redox system are illustrated in Fig. S5. An electron ionization and reception occurs at the SWCNT, which can be clearly observed at both the HOMO and LUMO for the substrate. In the intermediate steps, an electronic connection between the AQ and the 4AHA molecules is clearly shown at the HOMO level. An electron movement is proposed as a theoretical mechanism pathway. The first electron from the oxidation reaction of the $AQH_2$ to AQH is initially excited to occupy the LUMO level of the *int-1-b*. In this state, both the AQ group and the nanotube are occupied, as shown in the LUMO level in Fig. S5(b). After that, the second electron is generated from the oxidation of the AQH to AQ, resulting in two excited electrons occupying strongly only in the AQ part in the LUMO level of the *int-2*. This case confirms the reversible reaction of the AQ to $AQH_2$. These two electrons then transfer to the 4AHA part, resulting in the strong occupation in the 4AHA side (Ph–NH) as shown in the LUMO level in Fig. S5(d). The Ph–NH group is eventually reduced by the extra electron at that level, resulting in the 4AA. The HOMO of the *prod* shows that the electrons are distributed mostly at the 4AA and no longer occupy the AQ side. In addition, an electron in the *int-1-b* and *int-2*, which is strongly localized at the AQ part, confirms that it can reversely reduce. This is the reduction reaction from AQ to $AQH_2$. On the other hand, an electron is rarely available at the 4AHA group (Ph–NH) in the *int-2* and *int-3*, leading to an irreversible reduction.

The plots of the difference of the Hirshfeld charge are presented in Fig. 2(a). These plots are calculated from the difference of each atomic charge between the negatively-charged structure and its neutralized version, neglecting relaxations, resulting in the charge difference of the negative atomic charge. An electron in the intermediate states has a high probability of presence at the AQH, leading to the reverse reduction of AQH to $AQH_2$. Two electrons in the *int-2* step have high probabilities at the AQ, 4AHA, and at the bridge in the nanotube, as shown in Fig. 2(a)-2. Therefore, it is clearly verified that the AQ and 4AHA groups can be reduced to $AQH_2$ and 4AA, respectively.

Fig. 2(b) shows the calculated disparity of the electron densities, following the definition; $\Delta\rho(\mathbf{i} \rightarrow \mathbf{j}) = \rho(\mathbf{j}) - \rho(\mathbf{i})$, where $\Delta\rho(\mathbf{i} \rightarrow \mathbf{j})$ is the change of negative charge densities between the negatively-charged structure, $\rho(\mathbf{j})$, and its neutralized version, $\rho(\mathbf{i})$, resulting in the density of only the negative charge. This plot clearly shows the connection between the reducing

**Table 1 – Hirshfeld partial charge (in elementary changes *e*), energy gap (eV), and relative energy (kcal $mol^{-1}$) calculated with the PBE method and DNP basis set for pristine SWCNT, substrate, intermediate, product, and single-functionalized systems (D = direct, I = indirect energy gap).**

| Entry | Structure | Hirshfeld charge | | | | Energy gap (eV) | Relative energy (kcal $mol^{-1}$) |
|---|---|---|---|---|---|---|---|
| | | Partial charge | | | Total | | |
| 1 | Pristine SWCNT | – | – | – | – | 0.62 D | – |
| 2 | Substrate | $AQH_2$ = 0.05 | SWCNT = −0.07 | 4AHA = 0.03 | 0.01 | 0.00 | – |
| 3 | Intermediate-1-a | AQH = −0.06 | SWCNT = −0.91 | 4AHA = −0.02 | −0.99 | 0.04 D | 0.00 |
| 4 | Intermediate-1-b | AQH = −0.16 | SWCNT = −0.81 | 4AHA = −0.02 | −0.99 | 0.04 I | −0.95 |
| 5 | Intermediate-2 | AQ = −0.19 | SWCNT = −1.73 | 4AHA = −0.07 | −1.99 | 0.10 I | – |
| 6 | Intermediate-3 | AQ = −0.07 | SWCNT = −0.77 | Ph–NH = −0.16 | −1.00 | 0.16 I | – |
| 7 | Product | AQ = −0.01 | SWCNT = −0.03 | 4AA = 0.05 | 0.01 | 0.00 | – |
| 8 | $[AQ–SWCNT]^{2-}$ | AQ = −0.27 | SWCNT = −1.72 | – | −1.99 | 0.00 | – |
| 9 | $[4AHA–SWCNT]^{2-}$ | – | SWCNT = −1.92 | 4AHA = −0.07 | −1.99 | 0.00 | – |

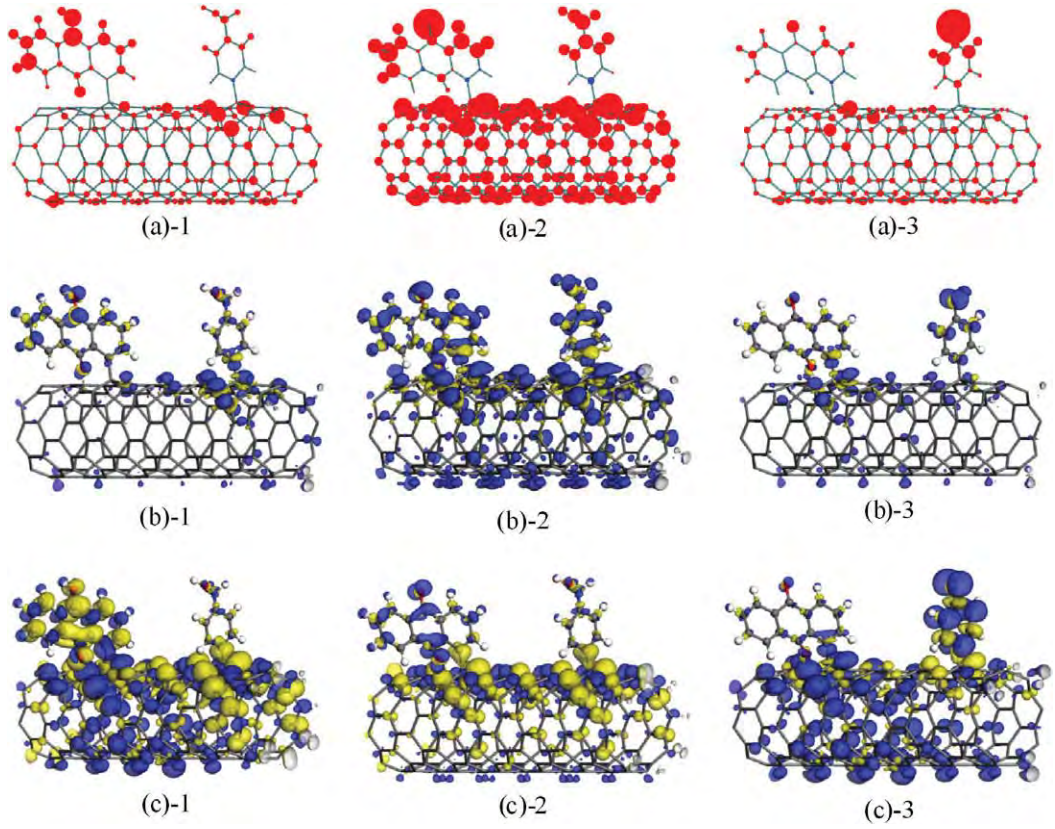


**Fig. 2 – Hirshfeld charge difference (a), where the red color represents a negative charge and the blue color a positive charge. Disparity of electron densities (b), where the blue and yellow colors represent electron accumulation and depression zones, respectively. Nucleophilic Fukui function plot (c). (1 stands for *int-1-b*, 2 for *int-2*, and 3 for *int-3*. (b) and (c) are plotted with an isovalue of ±0.004*e* Å$^{-3}$.) (For interpretation of the references to color in this figure legend, the reader is referred to the web version of this article.)**

group and the oxidizing group. The electron density obviously occupies only the redox molecules and their junction to the SWCNT medium.

The nucleophilic Fukui function plots, as demonstrated in Fig. 2(c), confirm the electron hopping process of the redox reaction via the nanotube. The mechanism starts with a high nucleophilic character of the AQ and its connection. Then, the reducing negative behavior at the AQ leads to an increase at 4AHA. However, the two carbon atoms of the nanotube connected to the AQ and 4AHA species are of the non-conjugated $sp^3$ type. The negative charge density is high at the bridging single bonds of both of the carbon atoms, as depicted in Fig. 2(c)-1–(c)-3, opening a route for the electron transfer from the reducing AQ group to the other. Therefore, the electron transfer between two redox groups can occur by electron hopping via the SWCNT.

The partial electron density difference plots, as shown in Fig. 3, are calculated from the difference of the electron densities between the whole structure and its three divided parts, which are an AQ derivative, a 4AHA derivative, and the tube. The definition; $\Delta\rho(\mathbf{R}) = \rho(\mathbf{R}) - \rho(\mathbf{o}) - \rho(\mathbf{r}) - \rho(\mathbf{m})$ (where $\Delta\rho(\mathbf{R})$ is the partial electron density difference of the redox system; **R** is all redox parts, **o** is the oxidation part, **r** is the reduction part, and **m** is the medium part) is considered and implied to both resonance character and an electron transferable of the system. The plot of *int-1-b* in Fig. 3(b) shows a high electron resonance of the π-conjugated system, covering the electron transfer, after the H*b* is cleaved. In Fig. 3(a) and (e), the electron transfer is observed between the two functionalized groups and the tube, confirming the electron movement possibility. The electron transfer between two redox groups is shown as the linkage at the tube in *int-2* and *int-3*.

In order to show that both functionalized groups must indeed be present on the same tube, the electron transfer of the singly functionalized tubes (known as the half-cell redox system), the *AQ-tube* and the *4AHA-tube*, is calculated and compared to the full redox system. The Hirshfeld partial charges analyses show that the charge density on the tube is virtually the same in the *AQ-tube* (−1.72*e*) and in the full redox system (−1.73*e*), which eases comparison: a more negative charge is left on the AQ group in the single-functionalized tube due to the lack of further electron accepting groups. When the accepting group, 4AHA, is added to the *AQ-tube* to obtain the full redox system, the remaining electron density in the AQ group is lowered by 30% and donated to the 4AHA (see entries 5 and 8 in Table 1). The plots of the deviation of electron densities of these single-functionalized systems are presented in Fig. S6. The plots show that an electron from the single AQ can transfer to the tube in the *AQ-tube*; and an electron in the tube can also transfer to the single 4AHA group in

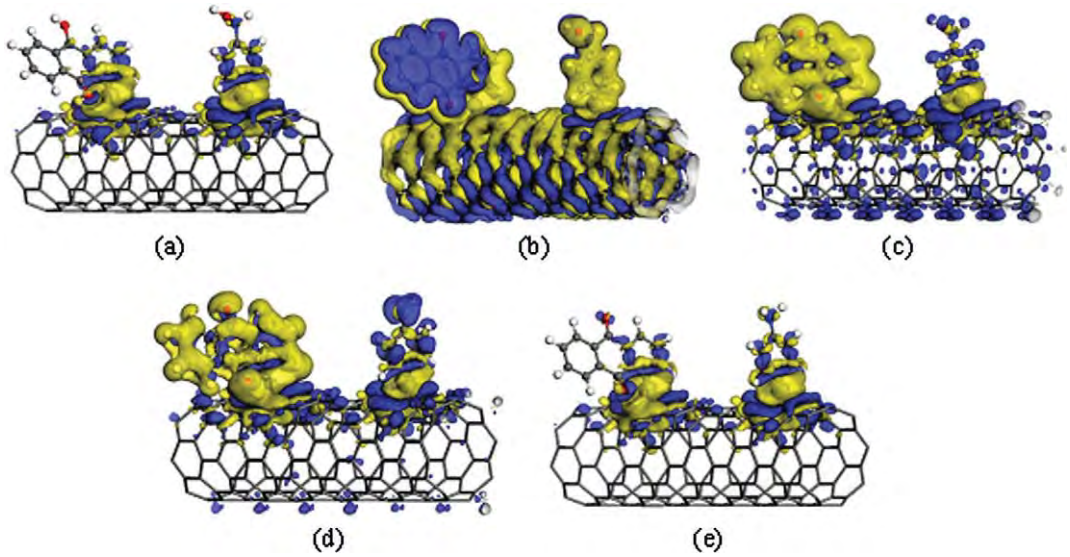


**Fig. 3 – Partial electron density difference of *subs* (a), *int-1-b* (b), *int-2* (c), *int-3* (d), and *prod* (e), plotted for an isovalue of ±0.004*e* Å$^{-3}$.**

the *4AHA-tube*. Two electrons in both singly functionalized systems have high probabilities along the tube, but the electronic junction can be observed only in the full redox system, as described above.

## 4. Conclusions

DFT calculations with the PBE functional are used to investigate the reaction mechanism of electron hopping in the SWCNT-mediated redox reaction of anthraquinonyl ($AQH_2$) and 4-arylhydroxyl amine (4AHA) groups. Our findings can be summarized into three main points. First, the disparity of electron densities, partial electron density difference, and Hirshfeld partial charges analysis show that the SWCNT can hold 87% of the extra electron density of the hypothetical negative intermediate produced from the oxidation of $AQH_2$. Second, the chemical attachment of these two redox reagents to the SWCNT also causes new impurity states to appear within the band gap, thereby introducing a more metallic character to the system. Third, the electrons from the oxidized $AQH_2$ group can be transferred to the oxidizing 4AHA group at the other end of the nanotube by a hopping process through the mediating SWCNT. This mechanism is confirmed by the non-localized distribution of the hopping excited electrons. These findings provide a detailed understanding of the electron hopping process and agree well with previous experimental study. This work is not only complementing experimental study by giving an interpretation in terms of electronic wave functions, but also demonstrates a promising application of the CNT materials in the nanotechnology field.

## Acknowledgements

This work was supported in part by Grants from the National Science and Technology Development Agency (2009 NSTDA Chair Professor funded by the Crown Property Bureau under the Management of the National Science and Technology Development Agency and NANOTEC Center of Excellence funded by the National Nanotechnology Center), Kasetsart University Research and Development Institute (KURDI), the Thailand Research Fund (TRF), and the Commission of Higher Education, Ministry of Education under Postgraduate Education and Research Programs in Petroleum and Petrochemicals and Advanced Materials and the Development and Promotion of Science and Technology Talents Project (DPST). The Kasetsart University Graduate School is also acknowledged. PAB particularly thanks the TRF and NSTDA Chair Professor for the generous support of his visits to Thailand and the Memorandum of Understanding between Kasetsart and Bordeaux 1 Universities. The computational calculations are supported by the Thai National Grid Center (TNGC) under the Software Industry Promotion Agency (SIPA).

## Appendix A. Supplementary data

Supplementary data associated with this article can be found, in the online version, at doi:10.1016/j.carbon.2009.12.049.

## REFERENCES

[1] Iijima S. Helical microtubules of graphitic carbon. Nature 1991;354(6348):56–8.
[2] Iijima S, Ichihashi T. Single-shell carbon nanotubes of 1-nm diameter. Nature 1993;363(6430):603–5.
[3] Bethune DS, Klang CH, de Vries MS, Gorman G, Savoy R, Vazquez J, et al. Cobalt-catalysed growth of carbon nanotubes with single-atomic-layer walls. Nature 1993;363(6430):605–7.
[4] Tans SJ, Verschueren ARM, Dekker C. Room-temperature transistor based on a single carbon nanotube. Nature 1998;393(6680):49–52.
[5] Kong J, Franklin NR, Zhou C, Chapline MG, Peng S, Cho K, et al. Nanotube molecular wires as chemical sensors. Science 2000;287(5453):622–5.

[6] de Heer WA, Châtelain A, Ugarte D. A carbon nanotube field-emission electron source. Science 1995;270(5239):1179–80.
[7] Baughman RH, Zakhidov AA, de Heer WA. Carbon nanotubes – the route toward applications. Science 2002;297(5582):787–92.
[8] Gooding JJ, Wibowo R, Liu JQ, Yang W, Losic D, Orbons S, et al. Protein electrochemistry using aligned carbon nanotube arrays. J Am Chem Soc 2003;125(30):9006–7.
[9] Patolsky F, Weizmann Y, Willner I. Long-range electrical contacting of redox enzymes by SWCNT connectors. Angew Chem Int Edit 2004;43(16):2113–7.
[10] Pandurangappa M, Lawrence NS, Compton RG. Homogeneous chemical derivatisation of carbon particles: a novel method for funtionalising carbon surfaces. Analyst 2002;127(12):1568–71.
[11] Wildgoose GG, Pandurangappa M, Lawrence NS, Jiang L, Jones TGJ, Compton RG. Anthraquinone-derivatised carbon powder: reagentless voltammetric pH electrodes. Talanta 2003;60(5):887–93.
[12] Leventis HC, Streeter I, Wildgoose GG, Lawrence NS, Jiang L, Jones TGJ, et al. Derivatised carbon powder electrodes: reagentless pH sensors. Talanta 2004;63(4):1039–51.
[13] Heald CGR, Wildgoose GG, Jiang L, Jones TGJ, Compton RG. Chemical derivatisation of multiwalled carbon nanotubes using diazonium salts. Chem Phys Chem 2004;5(11):1794–9.
[14] Wong ELS, Compton RG. Chemical reaction of reagents covalently confined to a nanotube surface: nanotube-mediated redox chemistry. J Phys Chem C 2008;112(22):8122–6.
[15] Delley B. An all-electron numerical method for solving the local density functional for polyatomic molecules. J Chem Phys 1990;92(1):508–17.
[16] Delley B. From molecules to solids with the DMol$^3$ approach. J Chem Phys 2000;113(18):7756–64.
[17] Monkhorst HJ, Pack JD. Special points for Brillouin-zone integrations. Phys Rev B 1976;13(12):5188.
[18] O'Connell MJ, Bachilo SM, Huffman CB, Moore VC, Strano MS, Haroz EH, et al. Band gap fluorescence from individual single-walled carbon nanotubes. Science 2002;297(5581):593–6.
[19] Perdew JP, Burke K, Ernzerhof M. Generalized gradient approximation made simple. Phys Rev Lett 1996;77(18):3865.
[20] Becke AD. Density-functional exchange-energy approximation with correct asymptotic behavior. Phys Rev A 1988;38(6):3098.
[21] Lee C, Yang W, Parr RG. Development of the Colle–Salvetti correlation-energy formula into a functional of the electron density. Phys Rev B 1988;37(2):785.
[22] Perdew JP, Wang Y. Accurate and simple analytic representation of the electron-gas correlation energy. Phys Rev B 1992;45(23):13244.
[23] Gülseren O, Yildirim T, Ciraci S. Systematic ab initio study of curvature effects in carbon nanotubes. Phys Rev B 2002;65(15):1534051–4.
[24] Ouyang M, Huang JL, Cheung CL, Lieber CM. Energy gaps in "metallic" single-walled carbon nanotubes. Science 2001;292(5517):702–5.
[25] Blase X, Benedict LX, Shirley EL, Louie SG. Hybridization effects and metallicity in small radius carbon nanotubes. Phys Rev Lett 1994;72(12):1878–81.
[26] Zólyomi V, Kürti J. First-principles calculations for the electronic band structures of small diameter single-wall carbon nanotubes. Phys Rev B 2004;70(8).
[27] Valavala PK, Banyai D, Seel M, Pati R. Self-consistent calculations of strain-induced band gap changes in semiconducting ($n$, 0) carbon nanotubes. Phys Rev B 2008;78(23).
[28] Pannopard P, Khongpracha P, Probst M, Limtrakul J. Gas sensing properties of platinum derivatives of single-walled carbon nanotubes: a DFT analysis. J Mol Graph Model 2009;28(1):62–9.
[29] Zhao JX, Ding YH. Chemical functionalization of single-walled carbon nanotubes (SWNTs) by aryl groups: a density functional theory study. J Phys Chem C 2008;112(34):13141–9.
[30] Wu X, Zeng XC. First-principles study of a carbon nanobud. ACS Nano 2008;2(7):1459–65.

J. of Supercritical Fluids 51 (2009) 230–237

Contents lists available at ScienceDirect

The Journal of Supercritical Fluids

journal homepage: www.elsevier.com/locate/supflu

# Formation of retinyl palmitate-loaded poly(L-lactide) nanoparticles using rapid expansion of supercritical solutions into liquid solvents (RESOLV)

Amporn Sane[a,b,*], Jumras Limtrakul[a,c]

[a] NANOTEC Center of Excellence, National Nanotechnology Center, Kasetsart University and Center of Nanotechnology, Kasetsart University Research and Development Institute, Kasetsart University, Bangkok 10900, Thailand
[b] Department of Packaging and Materials Technology, Faculty of Agro-Industry, Kasetsart University, Bangkok 10900, Thailand
[c] Department of Chemistry, Faculty of Science, Kasetsart University, Bangkok 10900, Thailand

ARTICLE INFO

*Article history:*
Received 10 May 2009
Received in revised form 5 September 2009
Accepted 5 September 2009

*Keywords:*
Poly(L-lactide)
Retinyl palmitate
Nanoparticles
Encapsulation
RESOLV
Supercritical fluids

ABSTRACT

Poly(L-lactide) (PLLA) nanoparticles loaded with retinyl palmitate (RP) were successfully prepared by rapid expansion of a supercritical carbon dioxide ($CO_2$) solution into an aqueous receiving solution containing a stabilizing agent (RESOLV). Three stabilizing agents, Pluronic F127, Pluronic F68, and sodium dodecyl sulfate (SDS) have been employed and the Pluronic F127 was found to be more effective for stabilizing PLLA/RP nanoparticles than Pluronic F68 and SDS, as RESOLV into a 0.1 wt% Pluronic F127 solution produced a stable nanosuspension consisting mainly of well-dispersed, individual nanoparticles. The effect of rapid expansion processing conditions (i.e., degree of saturation ($S$), pre-expansion temperature ($T_{pre}$), and concentrations of PLLA and RP ($C_{PLLA}$, $C_{RP}$)) on the particle size, form, and RP loading was systematically investigated. It was found that spherical PLLA/RP nanoparticles with an average size range of ~40–110 nm and RP loadings of 0.9–6.2 wt% were consistently produced by RESOLV. The size of PLLA/RP nanoparticles increased from ~30–80 to ~30–160 nm as the solution degree of saturation changed from $S < 1$ to $S > 1$, independent of $T_{pre}$, $C_{PLLA}$, and $C_{RP}$. The entrapment capacity of RP in PLLA nanoparticles was predominantly determined by $T_{pre}$ and $C_{RP}$. Increasing the $T_{pre}$ from 70 to 100 °C and the $C_{RP}$ from 0.05 to 0.15 wt% increased the encapsulated RP content at least twofold. Our results show that the technique with benign supercritical $CO_2$ should be generally applicable to nanoparticle fabrications of other important active ingredients, especially in liquid form, in polymeric nanoparticles.



## 1. Introduction

Encapsulation of active compounds, including drugs, cosmetics, and nutraceuticals, in nanoparticles of biodegradable and biocompatible polymers (e.g., chitosan, poly(D,L-glycolide), poly(D,L-lactide-co-glycolide), and polylactic acid or polylactide) has greatly attracted attention in the pharmaceutical, cosmetic, and food industries for multipurpose delivery applications, especially, controlling release, targeting, and increasing stability of active components [1,2]. Incorporation of such active ingredients in the polymeric nanoparticles with a controllable and narrow size distribution increases therapeutic benefits, leading to the small dosages required and avoiding undesirable side effects. Conventional techniques for encapsulating active substances in polymeric nanoparticles based on nano-emulsion templates [3] still have several limitations, including using organic solvents that need to be removed from the final products, generating broad particle size distributions, and requiring large quantities of surfactants. Rapid expansion of supercritical solutions (RESS) technology is generally recognized as a well-established technique for producing nano to micron-sized particles from a single component, especially from organics and polymers [4–8]. When a supercritical solution containing a dissolved solute is rapidly ($10^{-6}$ s) expanded across a micro-orifice, the solvent density dramatically decreases, leading to precipitation of the solute from the solvent (typically carbon dioxide) [9–11]. Due to very high supersaturation during the rapid expansion in the post-expansion environment, the process favors the formation of small particles with narrow size distributions. Besides single-compound particles, RESS has also been investigated for producing composite particles [12–24]. Tom et al. [12] reported the preparation of composite microparticles (10–100 μm) by co-precipitation of poly(D,L-lactic acid) and lovastatin. Microencapsulation of naproxen in poly(L-lactide) particles with a size range of 10–75 μm was published by Kim et al. [15] and Mishima et al. [16] described the encapsulation of lipase and lysozyme in polymer (e.g., poly(ethylene glycol), poly(methyl methacrylate),

* Corresponding author at: Department of Packaging and Materials Technology, Faculty of Agro-Industry, Kasetsart University, Bangkok 10900, Thailand.
Tel.: +66 2562 5099; fax: +66 2562 5092.
*E-mail address:* amporn.s@ku.ac.th (A. Sane).

0896-8446/$ – see front matter © 2009 Elsevier B.V. All rights reserved.
doi:10.1016/j.supflu.2009.09.003

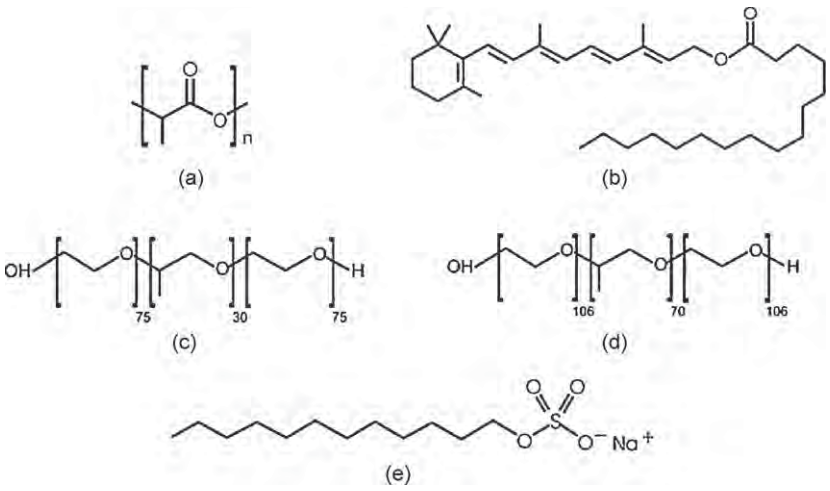


**Fig. 1.** Chemical structures of chemicals used in this study: (a) poly(L-lactide), (b) retinyl palmitate, (c) Pluronic F68, (d) Pluronic F127, and (e) sodium dodecyl sulfate.

and poly(L-lactic acid)) microparticles. Recently, Türk and Hils [20] were the first to report the feasibility of RESS for producing phytosterol-loaded poly(L-lactic acid) nanoparticles with the size of ~50 nm. This group found that the polymer content of the composite nanoparticles decreased with increasing pre-expansion temperature. Thus far, the RESS technique has been studied for encapsulating only crystalline solid, but not liquid, compounds in polymeric particles.

A modification of conventional RESS is the so-called RESOLV (rapid expansion of supercritical solutions into liquid solvents) process, in which the supercritical solution containing a solute is directly expanded into a liquid receiving solution (typically aqueous solution) that may or may not contain a stabilizing agent [6,25–28]. Organic particles produced using RESOLV were found to be smaller than those prepared by RESS due to expansion of the supercritical solution into a receiving liquid preventing the particles from collision and, hence, coalescence [5,6]. Particles with a bimodal size distribution (5–50 and 120–200 nm) were obtained from β-sitosterol [5], and phytosterol [29], and nanoparticles (~25–90 nm) were produced from ibuprofen, naproxen, fluorinated tetraphenylporphyrin, fluorinated acrylate polymer, poly(L-lactic acid), and poly(methyl methacrylate) [6,26–28]. Unlike RESS, RESOLV has not yet been investigated for encapsulating active components in polymeric nanoparticles. Thus, it remains a challenge to incorporate an active ingredient, especially in liquid form, in polymeric nanoparticles using the RESOLV process.

The aim of this work was to study the feasibility of RESOLV on encapsulation of a liquid active compound in biodegradable polymeric nanoparticles. In this study, retinyl (vitamin A) palmitate and poly(L-lactide) were chosen as a liquid active compound and a particle matrix, respectively. Retinyl palmitate, a vitamin A ester derivative in the retinoid group, is widely used in pharmaceutical and cosmetic applications. However, the therapeutic use of retinoids is still limited due to their light instability and adverse effects at high uptake [30]. Therefore, encapsulation is an alternative to protect retinyl palmitate from photo degradation induced by UVA and UVB radiation. Poly(L-lactide) has been widely used as a matrix material for drug delivery systems due to its biodegradability and biocompatibility [31–33]. In this work, we report on (i) the use of RESOLV to produce retinyl palmitate-loaded poly(L-lactide) nanoparticles and (ii) the effect of RESOLV processing conditions on size, morphology, and retinyl palmitate loading of the obtained particles.

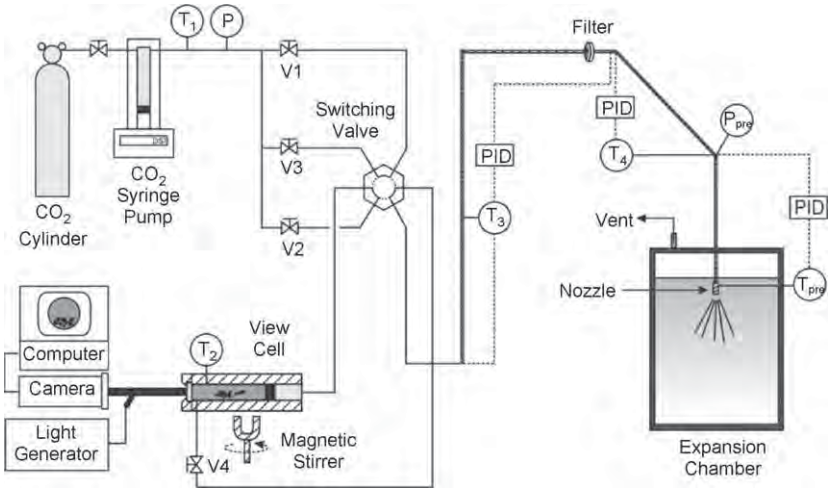


**Fig. 2.** Schematic of phase-behavior and RESOLV apparatus.

## 2. Experimental

### 2.1. Materials

Low-molecular-weight poly(L-lactide) (PLLA) with a number-average molecular weight of 1100 and a polydispersity index of 1.15 was supplied by Polymer Source. Retinyl palmitate (RP), sodium dodecyl sulfate (SDS), Pluronic F68 (F68) and Pluronic F127 (F127) were purchased from Sigma–Aldrich. The chemical structures of these compounds are shown in Fig. 1. Acetonitrile (HPLC grade) was obtained from Lab-Scan Analytical Sciences. Carbon dioxide ($CO_2$) with high purity grade (≥99.98%) was purchased from Chattakorn Lab Center (Thailand). Water was distilled before using it as a receiving solution.

### 2.2. Phase-behavior measurements

The phase-behavior measurements of PLLA and PLLA + RP in supercritical $CO_2$ were performed prior to RESOLV experiments because the phase state of a solute–solvent mixture has been found to be an important variable for RESS [4,7]. A schematic of the apparatus used in this work is shown in Fig. 2. Note that the same apparatus was used for both phase-behavior and RESOLV experiments. The central feature of the apparatus is a variable-volume view cell based on the design of McHugh and co-workers [34]. A syringe pump (Isco, Model 500HP) connected to one end of the view cell used $CO_2$ as the working fluid and pushed the piston to compress the PLLA or PLLA + RP solution on the other side of the piston. The solution mixture in the cell was observed through a view port with a rigid borescope (Gradient Lens, Model HBR-080-327-100) equipped with a light source (Gradient Lens, Model Luxxor 24), a digital CCD camera (Watec, Model WAT-202D), and a computer (Fig. 2). For a typical cloud-point (i.e., liquid–liquid transition) experiment, the view cell was charged with 0.008–0.023 g of RP and/or 0.015–0.046 g of PLLA, as well as ~15.2 g of $CO_2$. The cell was pressurized to 340 bar and heated to ~50 °C under continuous mixing using a magnetic stirrer until a homogeneous, clear solution was obtained. To determine the cloud point, the pressure of the solution was slowly decreased during continuous mixing until the transparent solution became cloudy. In this work, the cloud point was defined as the point at which the solution just became hazy. Upon reaching the temperature of ~100 °C, the heating was stopped and the cloud points were remeasured as the solution was slowly cooled down.

### 2.3. RESOLV experiments

Rapid expansion experiments were carried out by expanding a supercritical solution of PLLA + RP in supercritical $CO_2$ across a nozzle (50 μm dia., L/D = 4) into an aqueous solution containing a stabilizing agent (Fig. 2). To do an experiment, the variable-volume view cell was loaded with 0.030–0.091 g of PLLA and 0.015–0.046 g of RP. The cell was then sealed and charged with ~30.4 g of $CO_2$ using the syringe pump. After the mixture was pressurized to the desired pre-expansion pressure ($P_{pre}$), the cell was heated to 50–60 °C. Next, the mixture was stirred until a homogeneous solution was obtained. $CO_2$ was then allowed to flow from the syringe pump, bypassing the view cell, and finally expand across the nozzle into air. The fluid in the tubing leading to the nozzle and nozzle assembly was heated to the desired pre-expansion temperature ($T_{pre}$) using cable heaters. During this step, the pre-expansion temperature and pressure were measured upstream of the nozzle (Fig. 2). After steady-state conditions (as indicated by constant $T_{pre}$ and $P_{pre}$) were established, the flow of pure $CO_2$ was diverted via the 6-port switching valve (Valco Instruments, Model 6C6UWEY) to the high pressure cell, indirectly pushing the PLLA + RP solution in supercritical $CO_2$ out of the cell by means of the movable piston in the cell. The solution was subsequently expanded through the nozzle into 50 mL of aqueous solution containing 0.1 wt% stabilizer (F68, F127, and SDS) by submerging the nozzle ~2 cm below the liquid surface.

### 2.4. Particle size and morphological characterization

Suspension samples from RESOLV experiments were characterized by the dynamic light scattering (DLS) method using a Zetasizer (Malvern Instruments, Model Nano ZS90) for measuring the hydrodynamic diameter ($d_h$) of PLLA/RP particles [35,36]. The $d_h$ was computed from the translational diffusion coefficient ($D$) using the Malvern software package based on the theory of Brownian motion and the Stokes–Einstein equation:

$$d_h = \frac{kT}{3\pi\eta D} \quad (1)$$

where $k$ is the Boltzmann's constant, $T$ the absolute temperature, and $\eta$ is the suspending medium viscosity. The particle size and morphology were also determined using field emission scanning electron microscopy (FESEM, Hitachi, Model S4700). The FESEM sample was prepared by depositing ~100 μL of the RESOLV suspension onto a conductive carbon tape attached to an aluminum stub and then dried under vacuum (1 bar) at ambient temperature overnight.

### 2.5. Determination of RP loading

The quantities of RP and PLLA in composite particles obtained by RESOLV were determined via UV/vis spectrophotometry as follows. The suspension was centrifuged (10,000 rpm, 10 °C) in order to separate the particles and dried under vacuum (1 bar) at room temperature for at least 2 days. The dried powder sample was then dissolved in acetonitrile and analyzed by a UV/vis spectrophotometer (Thermo Fisher Scientific, Model HeλIOS Gamma Series). PLLA and RP have well-characterized absorption bands with $\lambda_{max}$ values of 211 ± 0.5 and 325 ± 0.5 nm, respectively, allowing for the accurate determination of PLLA and RP concentrations. The amounts of individual components in the particles were determined from the corresponding absorbance standard curves generated by known concentrations of PLLA and RP. The percentage of RP encapsulated (RP loading) in the particles was calculated by means of the following equation:

$$\text{RP loading (wt\%)} = \frac{\text{encapsulated RP (g)}}{\text{PLLA (g)} + \text{encapsulated RP (g)}} \times 100 \quad (2)$$

## 3. Results and discussion

### 3.1. Phase-behavior experiments of PLLA + RP in $CO_2$

Cloud-point pressures of PLLA and PLLA + RP in supercritical $CO_2$ were measured over a temperature range of ~50–100 °C as a function of PLLA and RP concentrations. Results are shown as a pressure–temperature diagram in Fig. 3. Initially, the pressure was taken to 340 bar at ambient temperature, and then the cell was heated at constant pressure until the polymer melted and completely dissolved (at a temperature range of ~50 – 60 °C). The concentrations of PLLA used in this study were 0.1 and 0.3 wt% because it was found that its solubility in supercritical $CO_2$ was ~0.4 wt% at pressure and temperature up to 340 bar and 100 °C, respectively. Consequently, the RP concentrations of 0.05 and 0.15 wt% were chosen such that the ratios of RP and PLLA ranged between 1:6 and 1:2. It is important to note that PLLA is significantly less soluble in supercritical $CO_2$ than RP and, therefore, the poly-

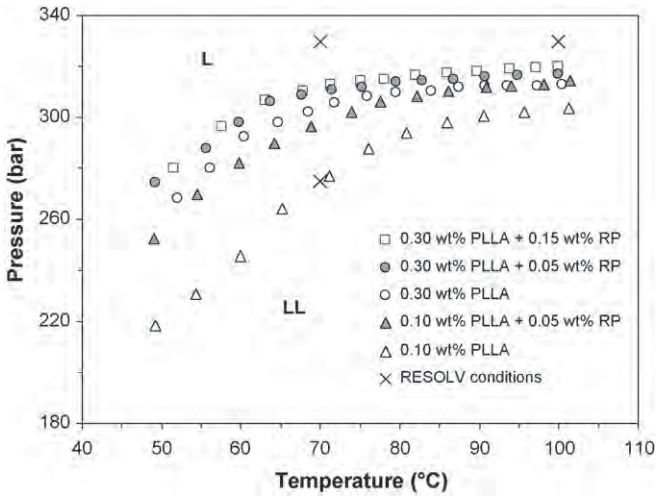


**Fig. 3.** Cloud-point curves for PLLA and PLLA + RP solutions in supercritical $CO_2$ and RESOLV experiments for PLLA + RP supercritical solutions in relation to their relevant cloud-point curves.

mer is the major component precipitated during decreasing the system pressures just below the cloud-point curve, whereas the RP remains dissolved within the solvent. As seen in Fig. 3, the measured cloud-point curves show a typical lower critical solution temperature (LCST) behavior, with the cloud-point slopes, $(\delta P/\delta T)_x$, up to 2.8 bar/°C. The LCST curve is interrupted at lower temperatures due to the solidification of PLLA and shifted toward higher pressures when increasing the concentrations of PLLA and RP. It is possible that the phase-behavior of this ternary PLLA + RP + $CO_2$ system exhibits multi-phase equilibria such as (i) LLV behavior especially in the vicinity of critical point of $CO_2$ due to the liquid–liquid immiscibility of PLLA-rich and RP-rich phases and (ii) SLLV behavior at low pressures due to the crystallization of PLLA. Therefore, the phase-behavior of this ternary system could be very complicated. Unfortunately, complete phase-behavior measurements of ternary mixtures are rather scarce, and most studies have focused only on portions of the liquid–liquid region. The cloud-point pressures of a 0.1 wt% PLLA solution in supercritical $CO_2$ increased from 219 to 303 bar as the temperature increased from 49.2 to 101.2 °C. The pressures increased by ~40 bar when increasing the concentration of PLLA to 0.3 wt%. The addition of RP at 0.05 wt% increased the cloud-point pressures of a 0.1 wt% PLLA solution by ~30 bar due to the presence of ternary solubility diminution of PLLA. This depressed solubility could be attributed to (i) the decrease in vapor pressure of low-molecular-weight PLLA due to the presence of liquid RP in $CO_2$ [37] and (ii) the occurrence of LV phase equilibrium for both PLLA + $CO_2$ and RP + $CO_2$ binary systems [38]. However, for 0.3 wt% PLLA, the cloud-point pressures were only slightly affected by the increase in the RP concentration from 0.5 to 0.15 wt%. The cloud-point pressures of a 0.1 wt% PLLA solution in $CO_2$ obtained in this work are approximately 120 bar higher than those in a mixture of tetrahydrofuran (THF) and $CO_2$ (20:80, w/w) reported by Sane and Thies [7] due to the cosolvent effect of THF. Significant increases in cloud-point pressures of PLLA in $CO_2$ solutions containing ~20 wt% of a cosolvent (either chlorodifluoromethane or dichloromethane) up to ~600–700 bar were reported when the polymer molecular weights increased to 2000, 50,000, and 100,000 [39,40]. Additionally, the solubility of low-molecular-weight PLLA in $CO_2$ is lower than that of higher-molecular-weight fluoropolymer poly(heptadecafluorodecyl acrylate) [4], but still relatively higher when compared to that of other higher-molecular-weight polymers such as poly(D,L-lactide-co-glycolide) [41], poly(methyl acrylate), and poly(vinyl acetate) [42].

### 3.2. Formation of PLLA/RP nanoparticles using RESOLV

RESOLV experiments were carried out by directly expanding PLLA + RP solutions in supercritical $CO_2$ at different experimental conditions (see Fig. 3) into liquid receiving solutions containing 0.1 wt% stabilizing agent (F68, F127, SDS). The RESOLV processing conditions included the degree of saturation ($S$) (varied by adjusting $P_{pre}$), pre-expansion temperature ($T_{pre}$), and PLLA and RP concen-

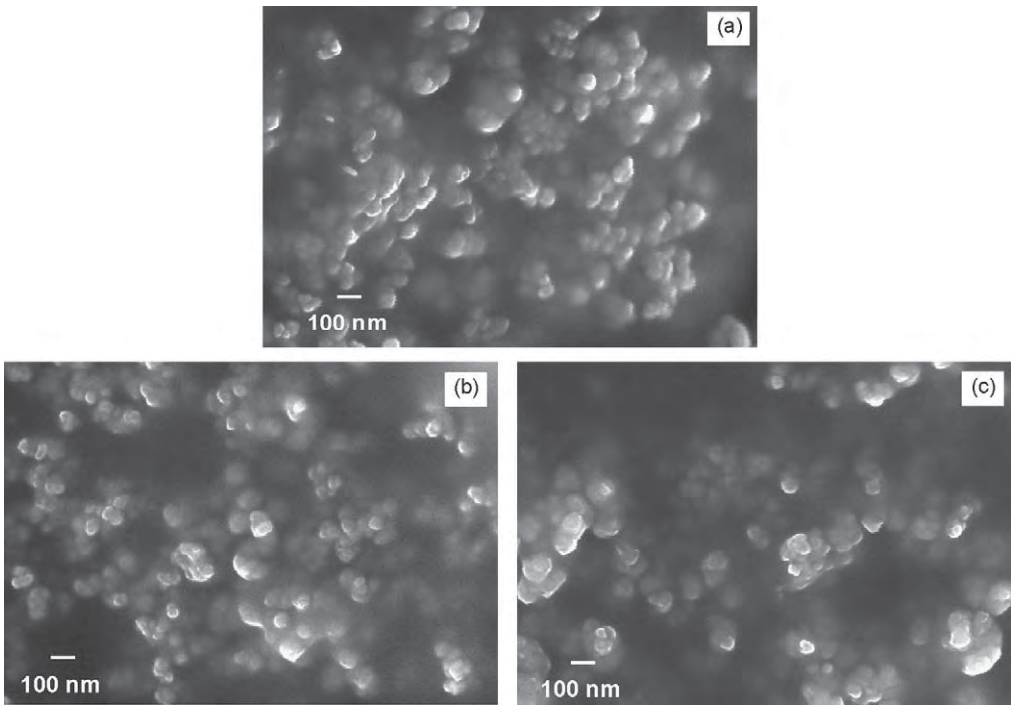


**Fig. 4.** FESEM micrographs of nanoparticles obtained from RESOLV of a 0.3 wt% PLLA + 0.05 wt% RP solution in $CO_2$ with $T_{pre}$ = 70 °C, $P_{pre}$ = 330 bar ($S$ < 1) into aqueous receiving solutions containing 0.1 wt% stabilizing agent: (a) F68, (b) F127, and (c) SDS.

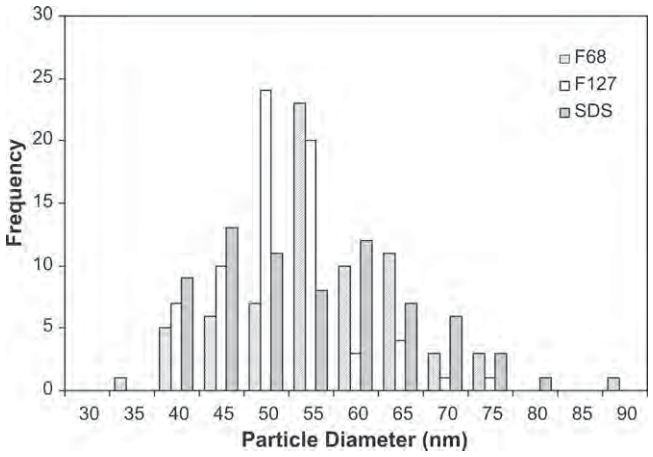


**Fig. 5.** PSDs measured from FESEM micrographs of nanoparticles obtained by RESOLV of a 0.3 wt% PLLA + 0.05 wt% RP solution in $CO_2$ with $T_{pre}$ = 70 °C, $P_{pre}$ = 330 bar ($S$ < 1) into aqueous receiving solutions containing 0.1 wt% stabilizing agent (F68, F127, and SDS).

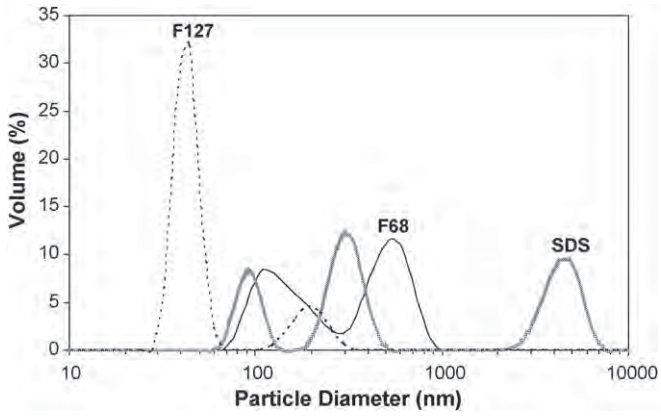


**Fig. 6.** PSDs from DLS analysis of stabilized nanoparticles prepared by RESOLV of a 0.3 wt% PLLA + 0.05 wt% RP solution in $CO_2$ with $T_{pre}$ = 70 °C, $P_{pre}$ = 330 bar ($S$ < 1) into aqueous receiving solutions containing 0.1 wt% stabilizing agent (F68, F127, and SDS).

trations ($C_{PLLA}$, $C_{RP}$). The $S$ is defined as the ratio of the actual solute concentration to the equilibrium concentration at pre-expansion conditions ($T_{pre}$, $P_{pre}$).

### 3.2.1. Effect of stabilizers on dispersibility of PLLA/RP nanoparticles

Because PLLA and RP are insoluble in water, aqueous solutions were used as the receiving solutions. However, there was a severe agglomeration of PLLA/RP particles in pure water owing to their hydrophobic nature (see Fig. 1a and b). From our previous work, the dispersibility of nanoparticles in a given receiving solution depends on the wettability of the surface of nanoparticles to the receiving solution [6]. The wettability of solid particles is affected by the type of surfactants and surface tension of the aqueous surfactant solutions [43,44]. In addition, decreasing surface tension of aqueous surfactant solutions usually provides improved wetting properties. Therefore, appropriate stabilizing agents for the PLLA/RP particle dispersion in this work had to be identified. F68, F127, and SDS were chosen as stabilizers for RP-encapsulated PLLA particles because F68 and F127 are nonionic, polymeric surfactants, while SDS is a conventional anionic surfactant (Fig. 1c–e). The stabilizer concentration of 0.1 wt% used in RESOLV was chosen based on the typical concentrations used in aqueous dispersions of nanoparticles and submicron-sized particles [25,45–47]. From FESEM characterization, spherical nanoparticles with a diameter ($d_p$) range of ~35–90 nm and an average size ($\bar{d}_p$) of ~50 ± 10 nm, independent of stabilizer type (Figs. 4 and 5 and Table 1), were reproducibly obtained by RESOLV of a 0.3 wt% PLLA + 0.05 wt% RP solution at $T_{pre}$ = 70 °C, $P_{pre}$ = 330 bar, and $S$ < 1 (i.e., above the cloud-point curve). The obtained nanoparticles were in the forms of individual particles and agglomerates (Fig. 4). Note that all the particle sizes were statistically determined from multiple FESEM images with the same magnification (60,000×) and the sharpness (contrast and focus) of the images were adjusted to enhance the particle–background and particle–particle boundaries before the size measurements. For the sizes of primary particles within the agglomerates, only partially overlapping particles were considered, while those with fully overlapping boundaries or uneven brightness/contrast were manually excluded. When measuring the hydrodynamic diameter ($d_h$) range and the mean hydrodynamic size ($\bar{d}_h$) using the DLS technique, however, broader particle size distributions (PSDs) were obtained and the size became dependent on the stabilizer type, as shown in Fig. 6 and Table 1. The measured hydrodynamic sizes ranged from 30 nm to 7.5 μm with bimodal and trimodal distributions. The particles stabilized in a 0.1 wt% F127 solution were substantially smaller (30–68 and 106–342 nm) than those suspended in 0.1 wt% F68 (59–300 and 342–800 nm) and 0.1 wt% SDS (59–142, 164–531, and 2000–7460 nm) solutions, indicating that the F127 is more effective for dispersing the PLLA/RP nanoparticles in the aqueous solution. Because DLS cannot be used to distinguish between individual particles and agglomerates, unlike FESEM, the larger measured sizes obtained from DLS were primarily due to the agglomeration of the PLLA/RP nanoparticles. F68 was a less effective stabilizer than F127 because slightly larger submicron-sized agglomerates were still present in the suspensions. This could be explained by the surface tension of receiving solutions, as the surface tension of a 0.1 wt% F68 solution (50 mN/m, 25 °C) is slightly higher than that of a 0.1 wt% F127 solution (41 mN/m, 25 °C) [48], thus providing less wettability and dispersibility to the PLLA/RP nanoparticles. However, this trend was not observed when using SDS as the particle stabilizer even though a 0.1 wt% SDS solution possesses the lowest surface tension of 33 mN/m (25 °C) [49], indicating that steric stabilization provided by nonionic polymeric surfactants is more efficient for stabilizing the PLLA/RP nanoparticles than ionic stabilization by SDS. Accordingly, F127 was chosen and used as the stabilizer for investigating the processing conditions on PLLA/RP particle size, morphology, and RP loading.

**Table 1**
Particle sizes obtained from DLS and FESEM measurements of nanoparticles prepared by RESOLV of a 0.3 wt% PLLA + 0.05 wt% RP solution in $CO_2$ with $T_{pre}$ = 70 °C, $P_{pre}$ = 330 bar ($S$ < 1) into aqueous receiving solutions containing 0.1 wt% stabilizing agent.

| Receiving solution | DLS | | FESEM | |
|---|---|---|---|---|
| | $d_h$ range (nm) | $\bar{d}_h$ (nm) | $d_p$ range (nm) | $\bar{d}_p$ ± S.D. (nm) |
| 0.1 wt% F68 | 59–300 | 148 | 35–87 | 54 ± 9 |
| | 342–800 | 531 | | |
| 0.1 wt% F127 | 30–68 | 43 | 37–72 | 49 ± 7 |
| | 106–342 | 198 | | |
| 0.1 wt% SDS | 59–142 | 923 | 39–77 | 53 ± 10 |
| | 164–531 | 310 | | |
| | 2000–7460 | 4460 | | |

### 3.2.2. Effect of rapid expansion conditions on PLLA/RP nanoparticles

To determine the effect of RESOLV processing conditions (i.e., $S$, $T_{pre}$, $C_{RP}$, and $C_{PLLA}$) on size, morphology, and RP loading of PLLA/RP particles, experiments were carried out by expanding PLLA + RP solutions in supercritical $CO_2$ into 0.1 wt% F127 solu-

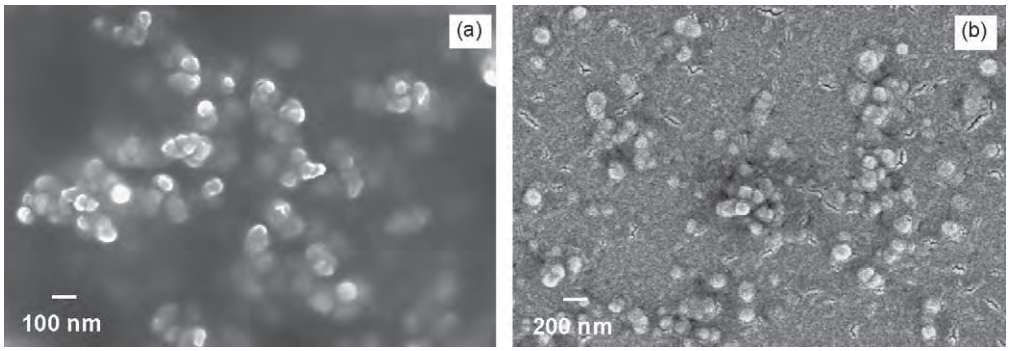


**Fig. 7.** FESEM micrographs of PLLA/RP nanoparticles prepared by RESOLV of a 0.3 wt% PLLA + 0.05 wt% RP solution in $CO_2$ with $T_{pre}$ = 70 °C, $P_{pre}$ = 275 bar ($S$ > 1) into a 0.1 wt% F127 solution.

tions at different processing conditions (see Fig. 3). FESEM was used to characterize the size and form of particles while UV/vis spectrophotometry was used to determine the RP loading of the particles. As shown in Table 2, PLLA/RP nanoparticles with the average size ranging from ~40 to ~110 nm were produced. The effect of $S$ was investigated by rapidly expanding PLLA + RP solutions at $T_{pre}$ = 70 °C and two different pressures (275 and 330 bar) such that one solution was initially supersaturated ($S$ > 1) and the other was subsaturated ($S$ < 1), respectively. The nanoparticles with an average size of 49 ± 7 nm (Fig. 4b and Table 2) were obtained when expansion of a 0.3 wt% PLLA + 0.05 wt% RP solution occurred from the unsaturated solution, while the particles with a bimodal size distribution and two average sizes of 45 ± 7 and 106 ± 19 nm (Fig. 7) were obtained when expansion occurred from the supersaturated solution. The significant increase in the particle size with $S$ can be seen in Fig. 8. A similar trend was also obtained in the cases of RESOLV of 0.1 wt% PLLA + 0.05 wt% RP and 0.3 wt% PLLA + 0.15 wt% RP solutions, as shown in Table 2. The obtained results are consistent with both (i) the phase separation kinetics and (2) the classical nucleation theory and growth mechanism [4,50] as follows. Larger nanoparticles (~110 nm) are formed when RESOLV is carried out such that the supercritical solution is supersaturated at pre-expansion conditions because the solution has already phase separated into polymer-rich and solvent-rich phases upstream of the nozzle, leading to (i) the formation of liquid-like droplets and even coalescence of the droplets and (ii) the nucleation of the liquid-like droplets followed by growth process via droplet diffusion and coagulation [9,50] until the solvent diffuses out of the polymer-rich droplets to the continuous phase and the formed structures solidify at sufficient pressure and temperature quenches. Furthermore, the smaller nanoparticles (~40–60 nm) are also present possibly due to the subsequent nucleation from the solvent-rich phase when a sufficient pressure drop has occurred upon expansion. On the other hand, only smaller nanoparticles (~50–60 nm) are formed when the expansion was initiated from unsaturated conditions, suggesting that the nucleation does not occur until a significant pressure drop has reached inside the nozzle or possibly not even until downstream of the nozzle. Our trend is consistent with RESS works reported by Blasig et al. [4] and Sane and Thies [7]. However, the PLLA/RP particles obtained from RESOLV are considerably smaller than those fluoropolymer and PLLA particles prepared by RESS, indicating that expansion into a receiving solution effectively hinders the particle growth in the free jet.

RESOLV of unsaturated solutions of 0.1 wt% PLLA + 0.05 wt% RP at $T_{pre}$ of 70 and 100 °C produced nanoparticles with average sizes of 48 ± 7 and 51 ± 9 nm, respectively (Fig. 9 and Table 2). However, changing the $T_{pre}$ from 70 to 100 °C slightly increased the average sizes of the nanoparticles from 49 ± 7 to 63 ± 10 nm and 56 ± 10 to 62 ± 15 nm when expanding the unsaturated solutions of 0.3 wt% PLLA + 0.05 wt% RP and 0.3 wt% PLLA + 0.15 wt% RP, respectively (Table 2). In addition, increasing $C_{PLLA}$ from 0.1 to 0.3 wt% and $C_{RP}$ from 0.05 to 0.15 wt% also yielded minor increases of particle sizes from 51 ± 9 to 63 ± 10 nm ($T_{pre}$ = 100 °C, $P_{pre}$ = 330 bar) and from 49 ± 7 to 56 ± 10 nm ($T_{pre}$ = 70 °C, $P_{pre}$ = 330 bar), respectively, as shown in Table 2. Both $T_{pre}$ and $C_{RP}$ influenced the extent of nanoparticle agglomeration, as the agglomeration was found to increase with $T_{pre}$ and $C_{RP}$. Therefore, our results indicate that $T_{pre}$, $C_{PLLA}$, and $C_{RP}$ do not play a significant role in the determination of the size of PLLA/RP nanoparticles, consistent with our previous work on RESOLV of fluorinated tetraphenylporphyrin (TBTPP) [6]. However, the average size of those TBTPP nanoparticles (28 ± 9 nm) is considerably smaller than that of PLLA/RP nanoparticles. This could be explained by the collision-coalescence theory

**Table 2**
Experimental conditions and sizes of PLLA/RP nanoparticles produced by RESOLV of a PLLA + RP solution in supercritical $CO_2$ into a 0.1 wt% F127 receiving solution.

| $C_{PLLA}$ (wt%) | $C_{RP}$ (wt%) | $T_{pre}$ (°C) | $P_{pre}$ (bar) | $S$ | $\bar{d}_p$ ± S.D. (nm) |
|---|---|---|---|---|---|
| 0.1 | 0.05 | 70 | 330 | <1 | 48 ± 7 |
| | | 70 | 275 | >1 | 43 ± 7, 95 ± 17 |
| | | 100 | 330 | <1 | 51 ± 9 |
| 0.3 | 0.05 | 70 | 330 | <1 | 49 ± 7 |
| | | 70 | 275 | >1 | 45 ± 7, 106 ± 19 |
| | | 100 | 330 | <1 | 63 ± 10 |
| | 0.15 | 70 | 330 | <1 | 56 ± 10 |
| | | 70 | 275 | >1 | 48 ± 9, 110 ± 20 |
| | | 100 | 330 | <1 | 62 ± 15 |

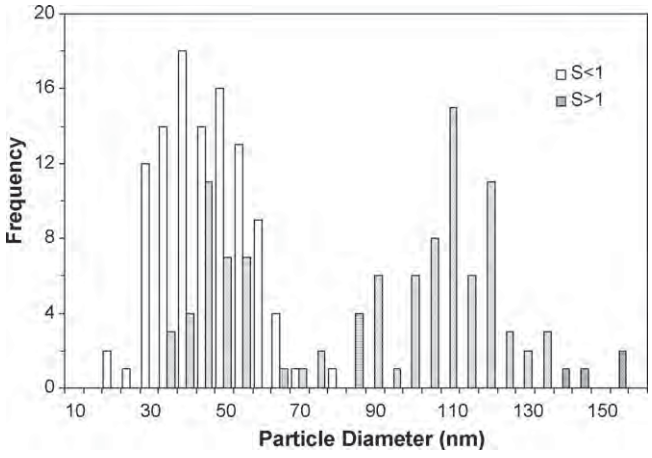


**Fig. 8.** PSDs of PLLA/RP nanoparticles prepared by RESOLV into a 0.1 wt% F127 solution of a 0.3 wt% PLLA + 0.05 wt% RP solution in $CO_2$ with $T_{pre}$ = 70 °C: $P_{pre}$ = 275 bar ($S$ > 1) and $P_{pre}$ = 330 bar ($S$ < 1).

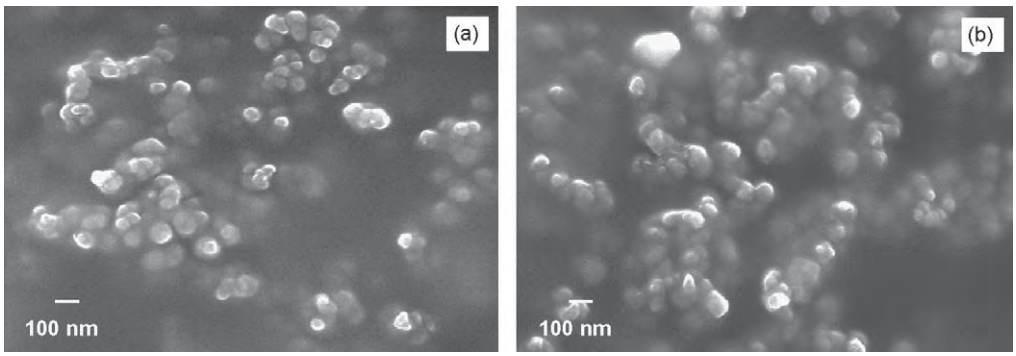


**Fig. 9.** FESEM micrographs of PLLA/RP nanoparticles produced by RESOLV into a 0.1 wt% F127 solution of a 0.1 wt% PLLA + 0.05 wt% RP solution in $CO_2$ with $P_{pre}$ = 330 bar ($S$ < 1): (a) $T_{pre}$ = 70 °C and (b) $T_{pre}$ = 100 °C.

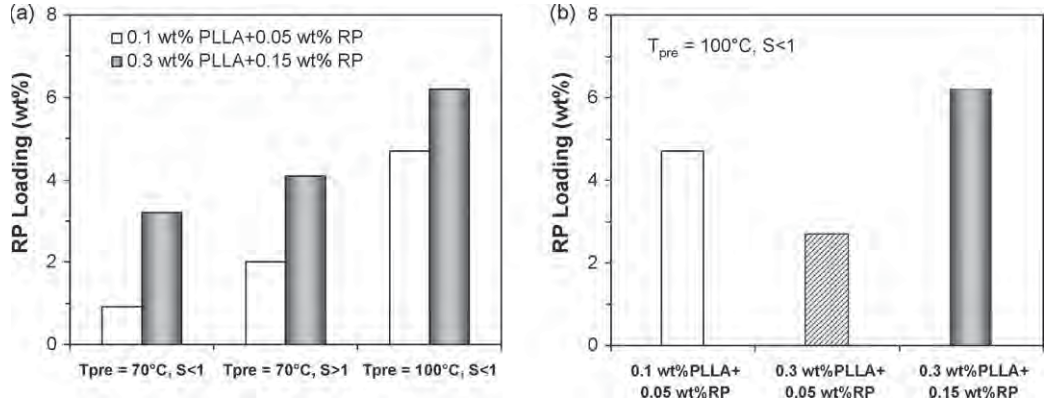


**Fig. 10.** Influence of RESOLV processing conditions: (a) $T_{pre}$ and $S$ and (b) $C_{PLLA}$ and $C_{RP}$ on RP loading levels of PLLA/RP nanoparticles.

developed by Friedlander and co-workers [51–53] in which the coalescence rate and the size of inorganic nanoparticles strongly increase with the solid-state diffusion coefficient ($D_s$), as recently applied to describe the growth of TBTPP and PLLA particles during rapid expansion across the nozzle and traveling in the free jet by Sane and Thies [6,7]. Since $D_s \propto \exp(-T_m/T)$ [54], decreasing absolute melting temperature ($T_m$) at a constant absolute temperature of particles ($T$) yields a rapid increase of the diffusion coefficient, leading to higher particle coalescence rate and larger particles. Consequently, the particles obtained from lower melting PLLA (120 °C, and lower in the presence of liquid RP) are larger than those of higher melting TBTPP (348 °C) because of the higher coalescence rate of PLLA particles during rapid expansion across the nozzle and traveling in the free jet before submerging under the receiving solution.

The extent of RP encapsulated in PLLA nanoparticles produced by RESOLV ranged from 0.9 to 6.2 wt%, depending on $T_{pre}$, $S$, $C_{PLLA}$, and $C_{RP}$ (Fig. 10). An increase of $T_{pre}$ from 70 to 100 °C during expanding a 0.1 wt% PLLA + 0.05 wt% RP solution at $P_{pre}$ = 330 bar ($S$ < 1) resulted in increasing the RP loading from 0.9 to 4.7 wt% (Fig. 10a). Similar to the case of RESOLV of a 0.3 wt% PLLA + 0.15 wt% RP solution at the same $P_{pre}$, the RP loading level increased from 3.2 to 6.2 wt% when increasing the $T_{pre}$ from 70 to 100 °C. This indicates that the entrapment of RP in the PLLA nanoparticles is favored when rapid expansion occurs at a higher $T_{pre}$. The increment of RP loading could be attributed to the decreases in RP and PLLA solubility leading to the solute precipitation initiated at higher pressures during expansion, the enhanced mass transfer between RP and PLLA components, and the small increase in particle size and agglomeration at the higher $T_{pre}$. The trend of increasing RP loading with increasing $T_{pre}$ agrees with results from RESS of PLLA + phytosterol reported by Türk and Hils [20]. In addition, the RP loading of nanoparticles obtained from RESOLV of a 0.1 wt% PLLA + 0.05 wt% RP solution with $T_{pre}$ = 70 °C slightly increased from 0.9 to 2.0 wt% when increasing the degree of saturation from $S$ < 1 to $S$ > 1 (Fig. 10a). Similar to the case of RESOLV of a 0.3 wt% PLLA + 0.15 wt% RP solution, increasing the $S$ resulted in the slight increase of the RP content from 3.2 to 4.1 wt%. Therefore, the $S$ had less impact on the RP loading than the $T_{pre}$. The smaller increase in the RP loading with the $S$ probably resulted from the supersaturated solution phase separated (L-LL) before entering the nozzle [4], and PLLA-rich droplets already formed, and even coalesced, within the $CO_2$-rich phase prior to expansion across the nozzle. As expected, the amount of RP trapped in the PLLA nanoparticles reduced with increasing $C_{PLLA}$ while increased with increasing $C_{RP}$ due to the availability of individual components during the rapid expansion. As shown in Fig. 10b, RESOLV at $T_{pre}$ of 100 °C and $P_{pre}$ of 330 bar ($S$ < 1) with $C_{RP}$ of 0.05 wt%, decreasing $C_{PLLA}$ from 0.3 to 0.1 wt% resulted in increased RP loading from 2.7 to 4.7 wt%. In addition, the encapsulated RP increased from 2.7 to 6.2 wt% when increasing $C_{RP}$ from 0.05 to 0.15 wt%.

## 4. Conclusions

In this work, PLLA nanoparticles containing RP were successfully produced in a single step using the RESOLV technique. F127 was a more effective stabilizer for dispersing the PLLA/RP nanoparticles than F68 and SDS. RESOLV into 0.1 wt% F127 solutions produced stable nanosuspensions containing mainly well-dispersed, spherical, individual nanoparticles with an average size range of ~40–110 nm and RP loadings of 0.9–6.2 wt%. The size of the PLLA/RP nanoparticles increased with $S$, relatively independent of $T_{pre}$, $C_{PLLA}$, and $C_{RP}$. The extent of RP encapsulated in the nanoparticles increased with increasing $T_{pre}$, $S$, and $C_{RP}$ while decreased with increasing

$C_{PLLA}$. Theoretical studies based on these results are necessary to better understand the relation between the processing conditions and the RP loaded PLLA nanoparticles. Finally, RESOLV is considered as a promising technique for producing stable suspensions of well-dispersed and uniform polymeric nanoparticles loaded with a liquid compound, with the process being amenable to commercial scale-up.

## Acknowledgements

This work was sponsored by the Thailand Research Fund (TRF). The authors would like to acknowledge the National Science and Technology Development Agency (NSTDA Chair Professor and NANOTEC Center of Excellence), Ministry of Science and Technology of Thailand as well as the Kasetsart University Research and Development Institute (KURDI) for financial support. We also acknowledge Dr. Markus Weber (now of Stettemerstrasse, Schaffhausen, Switzerland) and Prof. Mark C. Thies (Clemson University) for designing and supporting, respectively, the rapid expansion nozzles.

## References

[1] A.S. Agnihotri, N.N. Mallikarjuna, T.J. Aminabhavi, Recent advances on chitosan-based micro- and nanoparticles in drug delivery, J. Control. Release. 100 (2004) 5–28.
[2] V.J. Mohoraj, Y. Chen, Nanoparticles—a review, Trop. J. Pharm. Res. 5 (2006) 561–573.
[3] N. Anton, J.-P. Benoit, P. Saulnier, Design and production of nanoparticles formulated from nano-emulsion templates—a review, J. Control. Release. 128 (2008) 185–199.
[4] A. Blasig, C. Shi, R.M. Enick, M.C. Thies, Effect of concentration and degree of saturation on RESS of a $CO_2$-soluble fluoropolymer, Ind. Eng. Chem. Res. 41 (2002) 4976–4983.
[5] M. Türk, P. Hils, B. Helfgen, K. Schaber, H.-J. Martin, M.A. Wahl, Micronization of pharmaceutical substances by the rapid expansion of supercritical solutions (RESS): a promising method to improve bioavailability of poorly soluble pharmaceutical agents, J. Supercrit. Fluids 22 (2002) 75–84.
[6] A. Sane, M.C. Thies, The formation of fluorinated tetraphenylporphyrin nanoparticles via rapid expansion processes: RESS vs. RESOLV, J. Phys. Chem. B 109 (2005) 19688–19695.
[7] A. Sane, M.C. Thies, Effect of material properties and processing conditions on RESS of poly(L-lactide), J. Supercrit. Fluids 40 (2007) 253–263.
[8] M. Türk, Manufacture of submicron drug particles with enhanced dissolution behavior by rapid expansion processes, J. Supercrit. Fluids 47 (2009) 537–545.
[9] M. Weber, M.C. Thies, Understanding the RESS process, in: Y.-P. Sun (Ed.), Supercritical Fluid Technology in Materials Science and Engineering: Syntheses, Properties, and Applications, Marcel Dekker, New York, 2002, pp. 387–437.
[10] B. Helfgen, M. Türk, K. Schaber, Hydrodynamic and aerosol modelling of the rapid expansion of supercritical solutions (RESS-process), J. Supercrit. Fluids 26 (2003) 225–242.
[11] M. Weber, M.C. Thies, A simplified and generalized model for the rapid expansion of supercritical solutions, J. Supercrit. Fluids 40 (2007) 402–419.
[12] J.W. Tom, G.-B. Lim, P.G. Debenedetti, R.K. Prud'homme, Applications of supercritical fluids in the controlled release of drugs, ACS Symp. Ser. 514 (1993) 238–257.
[13] J.W. Tom, P.G. Debenedetti, R. Jerome, Precipitation of poly(L-lactic acid) and composite poly(L-lactic acid)-pyrene particles by rapid expansion of supercritical solutions, J. Supercrit. Fluids 7 (1994) 9–29.
[14] H. Ksibi, P. Subra, Powder coprecipitation by the RESS process, Adv. Powder Technol. 7 (1996) 21–28.
[15] J.-H. Kim, T.E. Paxton, D.L. Tomasko, Microencapsulation of naproxen using rapid expansion of supercritical solutions, Biotechnol. Prog. 12 (1996) 650–661.
[16] K. Mishima, K. Matsuyama, D. Tanabe, S. Yamauchi, T.J. Young, K.P. Johnston, Microencapsulation of proteins by rapid expansion of supercritical solution with a nonsolvent, AIChE J. 46 (2000) 857–865.
[17] J. Jung, M. Perrut, Particle design using supercritical fluids: literature and patent survey, J. Supercrit. Fluids 20 (2001) 179–219.
[18] M. Türk, P. Hils, R. Lizow, K. Schaber, Stabilization of pharmaceutical substances by rapid expansion of supercritical solutions (RESS), in: Proceedings of the Sixth International Symposium on Supercritical Fluids, vol. 3, Versailles, France, April 28–30, 2003, pp. 1911–1922.
[19] S.-D. Yeo, E. Kiran, Formation of polymer particles with supercritical fluids: a review, J. Supercrit. Fluids 34 (2005) 287–308.
[20] M. Türk, P. Hils, Formation of composite drug–polymer particles by co-precipitation during the rapid expansion of supercritical fluids, J. Supercrit. Fluids 39 (2006) 253–263.
[21] M. Bahrami, S. Ranjbarian, Production of micro- and nano-composite particles by supercritical carbon dioxide, J. Supercrit. Fluids 40 (2007) 263–283.
[22] K. Mishima, Biodegradable particle formation for drug and gene delivery using supercritical fluid and dense gas, Adv. Drug Deliv. Rev. 60 (2008) 411–432.
[23] C. Vemavarapu, M.J. Mollan, T.E. Needham, Coprecipitation of pharmaceutical actives and their structurally related additives by the RESS process, Powder Technol. 189 (2009) 444–453.
[24] M.J. Cocero, A. Martín, F. Mattea, S. Varona, Encapsulation and co-precipitation processes with supercritical fluids: fundamentals and applications, J. Supercrit. Fluids 47 (2009) 546–555.
[25] M.J. Meziani, H.W. Rollins, L.F. Allard, Y.-P. Sun, Protein-protected nanoparticles from rapid expansion of supercritical solution into aqueous solution, J. Phys. Chem. B 106 (2002) 11178–11182.
[26] M.J. Meziani, P. Pathak, R. Hurezeaun, M.C. Thies, R.M. Enick, Y.-P. Sun, Supercritical-fluid processing technique for nanoscale polymer particles, Angew. Chem. Int. Ed. 43 (2004) 704–707.
[27] P. Pathak, M.J. Meziani, T. Desai, Y.-P. Sun, Nanosizing drug particles in supercritical fluid processing, J. Am. Chem. Soc. 126 (2004) 10842–10843.
[28] M.J. Meziani, P. Pathak, T. Desai, Y.-P. Sun, Supercritical fluid processing of nanoscale particles from biodegradable and biocompatible polymers, Ind. Eng. Chem. Res. 45 (2006) 3420–3424.
[29] M. Türk, R. Lietzow, Stabilized nanoparticles of phytosterol by rapid expansion from supercritical solution into aqueous solution, AAPS Pharm. Sci. Technol. 5 (2004), Article 56.
[30] M. Cafara, C. Marianecci, A. Codeca, P. Squillaci, M. Scaizo, F. Cerreto, E. Santucci, Retinyl palmitate-loaded vesicles: influence on vitamin light-induced degradation, J. Drug Del. Sci. Technol. 16 (2006) 407–412.
[31] L.Y. Lee, C.H. Wang, K.A. Smith, Supercritical antisolvent of biodegradable micro- and nanoparticles for controlled delivery of paclitaxel, J. Control. Release. 125 (2008) 96–106.
[32] A.-M. Layre, R. Gref, J. Richard, D. Requier, H. Chacun, M. Appel, A.J. Domb, P. Couvreur, Nanoencapsulation of a crystalline drug, Int. J. Pharm. 298 (2005) 323–327.
[33] B. Conti, F. Pavenetto, I. Genta, Use of polylactic acid for the preparation of microparticulate drug delivery system, J. Microencapsulat. 19 (1992) 153–159.
[34] B.M. Hasch, S.-H. Lee, M.A. McHugh, The effect of copolymer architecture on solution behavior, Fluid Phase Equilib. 83 (1993) 341–348.
[35] B. Berne, R. Pecora, Dynamic Light Scattering: With Applications to Chemistry, Biology, and Physics, Dover Publications, Mineola, New York, 2000.
[36] A. Bootz, V. Vogel, D. Schubert, J. Kreuter, Comparison of scanning electron microscopy, dynamic light scattering and analytical ultracentrifugation for the sizing of poly(butyl cyanoacrylate) nanoparticles, Eur. J. Pharm. Biopharm. 57 (2004) 369–375.
[37] Ö. Güçlü-Üstündağ, F. Temelli, Solubility behavior of ternary systems of lipids in supercritical carbon dioxide, J. Supercrit. Fluids 38 (2006) 275–288.
[38] F.P. Lucien, N.R. Foster, Solubilities of solid mixtures in supercritical carbon dioxide: a review, J. Supercrit. Fluids 17 (2000) 111–134.
[39] J.M. Lee, B.-C. Lee, S.-J. Hwang, Phase behavior of poly(L-lactide) in supercritical mixtures of carbon dioxide and chlorodifluoromethane, J. Chem. Eng. Data 45 (2000) 1162–1166.
[40] B.-C. Lee, Y.-M. Kuk, Phase behavior of poly(L-lactide) in supercritical mixtures of dichloromethane and carbon dioxide, J. Chem. Eng. Data 47 (2002) 367–370.
[41] H.-S. Byun, H.-Y. Lee, Cloud-point measurement of the biodegradable poly(D,L-lactide-co-glycolide) solution in supercritical fluid solvents, Korean J. Chem. Eng. 23 (2006) 1003–1008.
[42] F. Rindfleisch, T.P. DiNoia, M.A. McHugh, Solubility of polymers and copolymers in supercritical $CO_2$, J. Phys. Chem. 100 (1996) 15581–15587.
[43] G.D. Parfitt, Fundamental aspects of dispersion, in: G.D. Parfitt (Ed.), Dispersion of Powder in Liquids, 2nd ed., Wiley & Sons, New York, 1973, pp. 1–43.
[44] M.J. Rosen, Surfactants and Interfacial Phenomena, Wiley & Sons, New York, 1989.
[45] P.E. Luner, S.R. Babu, S.C. Mehta, Wettability of a hydrophobic drug by surfactant solutions, Int. J. Pharm. 128 (1996) 29–44.
[46] E. Lemos-Senna, D. Wouessidjewe, S. Lesieur, D. Duchêne, Preparation of amphiphilic cyclodextrin nanospheres using the emulsification solvent evaporation method: influence of the surfactant on preparation and hydrophobic drug loading, Int. J. Pharm. 170 (1998) 119–128.
[47] Y. Lin, T.W. Smith, P. Alexandridis, Adsorption of a rake-type siloxane surfactant onto carbon black nanoparticles dispersed in aqueous media, Langmuir 18 (2002) 6147–6158.
[48] BASF Corporation, http://www2.basf.us/performancechemical/bcperfpluronic_grid.html (accessed July 2009).
[49] A. Bose, Wetting by solutions, in: J.C. Berg (Ed.), Wettability, Marcel Dekker, New York, 1993, pp. 149–181.
[50] W. Zhuang, E. Kiran, Kinetics of pressure-induced phase separation (PIPS) from polymer solutions by time-resolved light scattering. Polyethylene + n-pentane, Polymer 39 (1998) 2903–2915.
[51] S.K. Friedlander, M.K. Wu, Linear rate law for the decay of the excess surface area of a coalescing solid particle, Phys. Rev. B 49 (1994) 3622–3624.
[52] S.K. Friedlander, Synthesis of submicron solid particles: aerosol reactors, in: Smoke, Dust, and Haze: Fundamentals of Aerosol Dynamics, 2nd ed., Oxford University Press, New York, 2000, pp. 331–358.
[53] K.E.J. Lehtinen, R.S. Windeler, S.K. Friedlander, Prediction of nanoparticle size and the onset of dendrite formation using the method of characteristic times, J. Aerosol Sci. 27 (1996) 883–896.
[54] E.G. Seebauer, C.E. Allen, Estimating surface diffusion coefficients, Prog. Surf. Sci. 49 (1995) 265–330.

Journal of Molecular Liquids 147 (2009) 64–70

Contents lists available at ScienceDirect

Journal of Molecular Liquids

journal homepage: www.elsevier.com/locate/molliq

# Potential energy surface and molecular dynamics simulation of gold(I) in liquid nitromethane

Natcha Injan [a,b], Tünde Megyes [c], Tamas Radnai [c], Imre Bako [c], Szabolcz Balint [c], Jumras Limtrakul [b], Daniel Spangberg [d], Michael Probst [a,*]

[a] Institute of Ion Physics and Applied Physics, Innsbruck University, Austria
[b] Chemistry Department and Center of Nanotechnology, Kasetsart University, Bangkok, Thailand
[c] Chemical Research Centre of the Hungarian Academy of Sciences, Budapest, Hungary
[d] Angström Laboratory, Uppsala University, Uppsala, Sweden

ARTICLE INFO

Available online 17 November 2008

*Keywords:*
Au(I)
Ion solvation
Nitromethane
Potential energy functions
Molecular dynamics simulations
Cluster calculations
Quantum chemistry
Solvation shell

ABSTRACT

Potential energy functions for Au(I)-nitromethane (NM, $CH_3NO_2$) and NM–NM interactions were calculated by fitting analytical expressions to quantum chemically derived energies. These functions were then used in a molecular dynamics simulation of one Au(I) cation in 499 nitromethane molecules in the NVT ensemble at room temperature. A comparative simulation with a generic NM–NM potential energy function was also performed for comparison and gave the same results with respect to the calculated properties. It was found that the first solvation shell around the gold ion contains 9–10 nitromethane molecules in an environment with no strong symmetry.

Complementary, cluster calculations on $AuNM_n^+$ were performed. The especially strong binding of nitromethane in $AuNM_2^+$ and the validity of the pair approximation are discussed.



## 1. Introduction

A renewed interest in the properties of gold ions [1] in non-aqueous solution can be noticed and stems from various new applications and problems. New applications of gold solutions in nanotechnology and cluster science deal, for example, with gold nanowires and with the catalytic properties of gold nanoclusters. Many applications utilize the ability of gold to change easily between the oxidation states 0, 1 and 3. Potentially useful nanostructures can also be formed by self-assembly of ligands around gold ions. Gold surfaces in contact with various solvents play an important role in electrochemistry and in technology and, last but not least, gold is a biocompatible metal. On the other side, gold — like other heavy metals are — is an environmental liability. Since it is omnipresent in electronics devices it has to be separated and recovered before dumping or burning outdated boards and other scrap. Optimal processes for retrieving gold under such circumstances are still under investigation [2].

Gold exists in solutions predominantly as colloidal gold and as Au (I) and as Au(III) cations. Au cations in both of these oxidation states are normally complexed in solution and can easily transform or disproportionate into each other with Au(III) being normally the more stable and more strongly complexed oxidation state. Gold ions can also easily be reduced to neutral gold atoms which can form nanoclusters. There exist a large number of experimental works on gold ions in connection to nanotechnology but very few molecular dynamics studies on solutions of gold ions have been performed, however. Farges et al. [3] performed an EXAFS study on aqueous Au(III) chloride and found that gold exists as $AuX_4$ complexes (X = Cl, OH) at higher and at $AuCl_4^-$ at lower pH values. Bryce et al. [4] studied gold(I) thiosulfate in aqueous solution by means of EXAFS measurements and density functional. They found a linear S–Au(I)–S coordination. Their calculations used a continuum model for the effect of water. Concerning MD simulations of liquid nitromethane (NM) and the resulting properties we refer to a recent paper [5] where classical and Car–Parrinello simulation results are compared with diffraction data. NM is one of the good solvent of gold ions. Therefore this work investigate to study the specific properties of Au(I)–$NM_n$ cluster via quantum chemical calculations and the behaviors of Au(I) in liquid NM by molecular dynamics simulations.

## 2. Theory

### 2.1. Quantum chemical calculations

Most of our quantum chemical calculations were performed with the LANL2DZ [6] basis set for Au and the D95V [7] basis set for N, O, C and H. This choice of basis sets was motivated by the necessity of including relativistic effects for Au and the requirement that the LANL2DZ [6] basis set and ECP which is often used successfully for Au

* Corresponding author. Tel.: +43 6643244486.
*E-mail address:* michael.probst@uibk.ac.at (M. Probst).

0167-7322/$ – see front matter © 2008 Elsevier B.V. All rights reserved.
doi:10.1016/j.molliq.2008.10.016

[2,8] must be combined with a same-quality basis for the lighter elements. This also allows us to perform quantum chemical calculations on the larger clusters. As a method we employed Hartree–Fock (HF) and MP2. Primarily because of the use of an ECP for the Au core electrons, the BSSE (basis set superposition error) of the binding energy at the HF level is small. For calculations at the MP2 level it was found that after correcting for the BSSE, (which is larger than for HF), both HF and MP2 binding energies are very similar, which is typical for systems dominated by electrostatics. The method and basis sets as mentioned above were performed to investigate the geometry, electronic structure, and the binding energy of $AuNM_n^+$ clusters with $n=1$–10. Because NM is a molecule with a high dipole moment (4.6 debye) its electrostatic potential (Fig. 1) is divided into a positive half-space ($CH_3$) and a negative one ($NO_2$). This defines the electrostatics qualitatively . The chemical aspects of the coordination of Au(I) to $NO_2$ are discussed in paragraph 3 in detailed. All quantum chemical calculations were carried out with the Gaussian 03 [9] computer program.

### 2.2. $Au^+$–NM and NM–NM potential energy surface

The $Au^+$–NM and NM–NM intermolecular potential functions were developed for investigating the dynamics of Au(I) in liquid NM. We constructed an analytical pair potential for $Au^+$–NM by fitting the parameters of functions of the interatomic distances to energies derived from quantum chemical calculations. Details of these calculations were given in Section 2.1 above. Au(I) coordinates (Fig. 2) were generated along straight lines around a rigid NM molecule. In principle, it is not important how the conformation space is sampled unless important parts of it are left out. The subdivision of the sampling coordinates into straight lines only allows for an easy visualization of the potential energy in sets of distinct curves. The $q_i$ partial charges of NM were taken from [10] as shown in Table 3, for reasons of consistency ($q_{Au}=1$ a.u.). The equation and its parameters describing the $Au^+$–NM potential energy surfaces were obtained by minimizing the least-square deviation between the energies from the analytical formula and their quantum-chemically calculated counterparts.

We also calculated NM–NM energy surfaces at B3LYP/6–31 + G(d) level and constructed a NM–NM potential energy function, in the same way as described above. This served the purpose of providing an independent check since the intermolecular part of the NM potential energy function previously used for simulations of liquid NM [5,10] was derived from physical data of crystals of triazines [11,12]. Its accuracy is therefore difficult to judge and besides the issue of transferability sometimes such potential energy functions are not accurate for liquid state simulations where much more mutual orientations of neighboring molecules play a role than in the crystalline phase. We refer to this potential energy function subsequently as the 'generic NM pair potential'. The charges $q_{ij}$ were fixed at the values given in [10] in order of being able to use the Au–NM energy function described above.

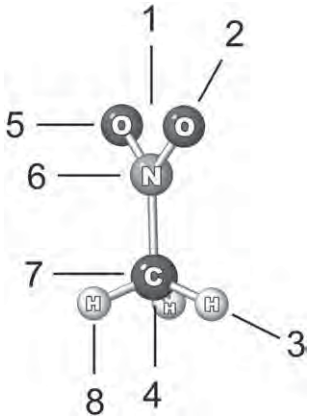


**Fig. 2.** Positions of Au around NM used for the construction of the $Au^+$–NM potential energy function. The solid lines refer to movement of $Au^+$. The numbers of the lines refer to the energy curves in Fig. 5.

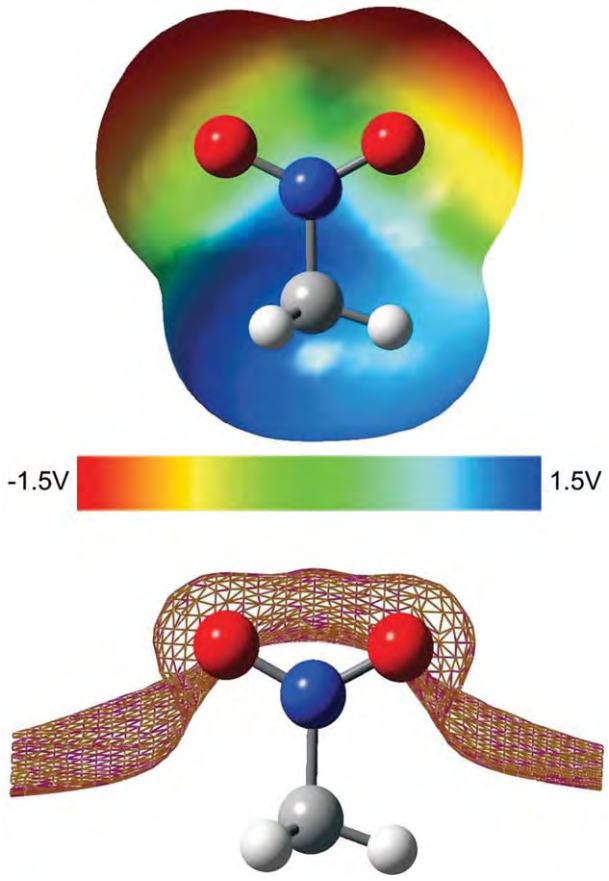


**Fig. 1.** Electrostatic potential of NM (upper part) and the surface of zero ESP (lower part).

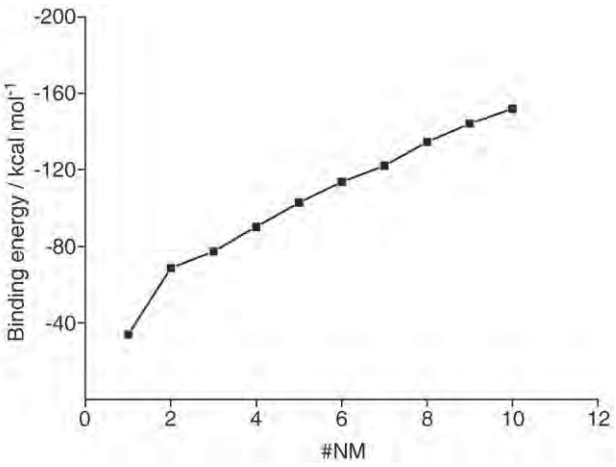


**Fig. 3.** Total ligand–cation binding energies defined as $E=E(Au(NM)_n^+)-E(Au^+)-nE$ (NM) in the $Au(NM)_n^+$ clusters with $n=1$ to 10. It can be seen that for $n>4$ the binding energies in the tri- to deca-coordinated complexes increase regularly.

**Table 1**
Atomic partial charge (NPA) and electronic configurations (NEC) of the atoms in NM, $AuNM^+$ and $AuNM_2^+$. See text for details.

| | NM | | | | | $AuNM^+$ | | | | | $AuNM_2^+$ | | | | |
|---|---|---|---|---|---|---|---|---|---|---|---|---|---|---|---|
| | NPA | NEC | | | | NPA | NEC | | | | NPA | NEC | | | |
| Au | 1.00 | 6s | 0.00 | 5d | 10.00 | 0.96 | 6s | 0.08 | 5d | 9.96 | 0.84 | 6s | 0.4 | 5d | 9.81 |
| N | 0.57 | 2s | 1.15 | 2p | 3.25 | 0.61 | 2s | 1.16 | 2p | 3.20 | 0.61 | 2s | 1.2 | 2p | 3.20 |
| C | −0.38 | 2s | 1.12 | 2p | 3.25 | −0.37 | 2s | 1.13 | 2p | 3.23 | −0.37 | 2s | 1.1 | 2p | 3.23 |
| O* | −0.48 | 2s | 1.79 | 2p | 4.67 | −0.65 | 2s | 1.77 | 2p | 4.86 | −0.63 | 2s | 1.8 | 2p | 4.52 |
| O | −0.40 | 2s | 1.75 | 2p | 4.64 | −0.30 | 2s | 1.75 | 2p | 4.54 | −0.28 | 2s | 1.8 | 2p | 4.85 |
| H | 0.23 | 1s | 0.77 | | | 0.25 | 1s | 0.75 | | | 0.25 | 1s | 0.8 | | |
| H | 0.23 | 1s | 0.77 | | | 0.25 | 1s | 0.75 | | | 0.25 | 1s | 0.8 | | |
| H | 0.23 | 1s | 0.77 | | | 0.25 | 1s | 0.75 | | | 0.25 | 1s | 0.8 | | |

### 2.3. Molecular dynamics

We performed two MD simulations, one with the newly developed potential energy function for the NM–NM interaction and one with a previously published NM–NM potential energy function taken from the literature [11]. The cubic box contained 499 rigid NM molecules and one $Au^+$ cation. The boxlength of 35.561 Å corresponded to the volume occupied by 500 NM molecules at 300K and atmospheric pressure. A continuous negative charge distribution was neutralizing the box. Periodic boundary conditions were employed, together with the minimal image convention for the short-range forces. For the electrostatic forces the Ewald summation was used. The simulation was performed in the NVT ensemble at 300 K. A timestep of 0.5 fs was chosen and the production run was performed for 77.5 ps after equilibrating the system for 22.5 ps. Before that, several equilibration cycles at high temperature with crude temperature scaling were employed to relax the system.

## 3. Results and discussions

### 3.1. The Au–NM interaction

Despite a long history of applying quantum chemical theory and calculations to gold–ligand systems some aspects of the energetics and the bond-directionality of transition metal cation–ligand interactions remain an interesting problem.

In some respect, Au(I)–ligand systems are simpler than most other transition metal–ligand systems because Au(I) has a completely filled $d^{10}$-shell, like Cu(I) and Ag(I). Even on the Hartree–Fock level, however, orbital effects are encountered: If NM ligands are added subsequently into the solvation shell of Au(I), the second NM molecule is about as strongly (or even slightly stronger, depending on the method of calculation) bound than the first one. Such a behavior is not found for singly charged alkaline ions where saturation effects start right away and in fact the decrease

$$\Delta E_n^{\mathrm{inc}} = E_n^{\mathrm{inc}} - E_{n-1}^{\mathrm{inc}}$$

in the incremental binging energies

$$E_n^{\mathrm{inc}} = E\left(\mathrm{Au(NM)}n^+\right) - E\left(\mathrm{Au(NM)}_{n-1}^+\right) - E(\mathrm{NM})$$

is largest when going from one to two ligands ($\Delta E_1^{\mathrm{inc}}$). In other words, for 'purely electrostatic' systems like alkali cations the binding energy per ligand in the 1:1 complex is always more than the one in 1:2 complexes while for Au(I) the opposite is found, as Fig. 3 shows. The natural bond orbital analysis (NBO, [13]) shows that no chemical bond is formed between Au(I) and the coordinating oxygen atom of NM. The charge transfer from one NM molecule to Au is 0.04*e* for $AuNM^+$ and 0.08*e* for $AuNM_2^+$. The Au 6*s* population in $AuNM_2^+$ is 0.35*e* while the 5*d* population decreases to 9.81*e* as shown in Table 1. A similar small overall charge transfer with a large increase in density of the highest *s* AO has been observed for $Cu(I)/H_2O$ long ago by Rosi and Bauschlicher. In two publications on this subject [14,15], they show (their Tables III and I, respectively) the increase in 4*s* density in $Cu(H2O)_2^+$. These authors already give a probably correct reason for the nonadditive behavior. They state that even without forming a bond, the mixing of $s^1$–$d^9$ into the wavefunction reduces the Cu(I)–O repulsion, thus allowing the ligand to approach closer. In the linear O–Cu(I)–O system the cost of the *s*–*d* mixing is shared between two ligands, offsetting the usual saturation effects. The same argument can be applied to Au(I). It is known [8,16] that, due to relativistic effects, the 6*s*–5*d* splitting in Au is much smaller than in Ag or Cu (in fact, the color of gold results from this [16]. These effects cause a lowering of the 6*s* and an increase of the 5*d* energy, thus facilitating the *s*–*d* mixing. The interaction of Au(I) with one and two water molecules

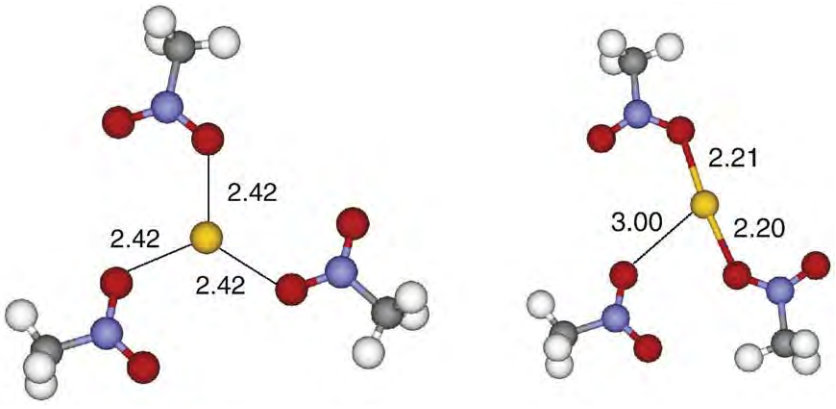


**Fig. 4.** Geometries of $C_3$h-symmetric (left) and fully geometry-optimized (right) $AuNM_3^+$, together with Au–O distances (Å).

**Table 2**
Atomic partial charges (NPA) and 6s and 5d populations (NEC) of Au in $AuNM_3^+$: geometry-optimized (left) and forced $C_3h$-symmetric structure (right).

| $AuNM_3^+$ (opt. geom.) | | | | | $AuNM_3^+$ ($C_3h$ geom.) | | | | |
|---|---|---|---|---|---|---|---|---|---|
| NPA | NEC | | | | NPA | NEC | | | |
| 0.86 | 6s | 0.30 | 5d | 9.83 | 0.91 | 6s | 0.13 | 5d | 9.94 |

has also recently been investigated [17] by Lee and coworkers. Their interpretation uses the same arguments but is more involved.

In some sense, therefore, the non-additivity discussed above is a relativistic effect. Non-relativistic quantum chemical calculations on Au are not recommended. Relativistic calculations on Au are not per se a problem, since the main effects like mass-velocity and Darwin are already well dealt with by using an atom-derived relativistic effective core potential like [6] and only for very accurate results high-level calculations that solve the full-electron Dirac equation are necessary.

This situation is further illustrated by comparing the fully geometry-optimized $AuNM_3^+$ complex with one in which $C_3h$ symmetry is enforced. In the former, one O–Au–O angle is nearly linear and the Au–O distance to the third oxygen is considerably longer (Fig. 4). There linear O–Au–O arrangement goes together with a 6*s* population of 0.30*e* compared to 0.13*e* in the $C_3h$ complex (Table 2).

In order to see if this highly nonadditive behavior for low coordination numbers has consequences for larger complexes, we performed geometry optimizations on $AuNM_n$ with $1 \le n \le 10$. From the interaction energies (Fig. 3), it can be seen that for $n>3$, the energetics resemble a low charge-density cation like $K^+$. Despite of the large value of $\Delta E_n^{inc}$ for $n=1$, NM molecules beyond $n=2$ are also bound in the first shell because they increase the overall binding energy. This justifies the construction of a pair potential like normally used for large, singly charged cations without problems. Its construction is outlined in Section 2.2. One might argue that nevertheless it has to be differentiated between the first two NM molecules and the rest in the sense that larger clusters $AuNM_n^+$ consist of $AuNM_2^+$ solvated by $n-2$ more loosely bound NM molecules. However, one sees that in $AuNM_3^+$ the energy of the trigonal planar geometry (Fig. 4) is only slightly higher than the T-shaped one and for $n=4$ the tetrahedral arrangement is already 2 kcal/mol more stable than the square planar one. Therefore $AuNM_2^+$ should not be considered as an 'inert core', dynamical considerations notwithstanding. The $AuNM_n^+$ clusters were all optimized without constraints. Up to $n=8$ they are compact and even the $AuNM_{10}^+$ cluster shows not two solvation shells but eight shorter (4.02 Å) and two longer (~5.11 Å) Au–O distances in a capped double prism typical of coordination number 10. Therefore, even without taking into account the pV term which in condensed phase systems makes 'spongy' structures less favourable, a high coordination number of Au(I) in NM can be expected. We should mention that at least for the gas phase this is different to the $Au(I)/H_2O$ system where calculations indicate that more than two water molecules build a second shell [18], partially due to the larger water–water interaction. Finally it should be mentioned that a recent combined experimental and theoretical study [19] on $Cu/H_2O$ and $Ag/H_2O$ hydration in the gas phase showed that the situation for $Cu^+$ is similar to the one encountered for $Au^+$ while the *d*/*s* gap in $Ag^+$ is much larger.

We can conclude that the quantum chemical cluster calculations indicate that, despite the peculiarities of the Au(I)–NM interaction, MD simulations with pair-additive potentials are justified for the condensed phase.

**Table 3**
Charges and fitted parameters (kcal/mol and Å) for the $Au^+$–NM pair potential.

| | q | A | B | C | D |
|---|---|---|---|---|---|
| C | −0.305 | 8905.8000 | −19,646.0000 | 166,150.0000 | 3.1885 |
| H | 0.146 | 650.5703 | −149.5139 | 81.1500 | 1.0576 |
| N | 0.821 | 0.0044 | 235.6198 | 2500.2000 | 1.8507 |
| O | −0.477 | 11,814.0000 | −10,535.0000 | 69,080.0000 | 3.1399 |

See text for explanations.

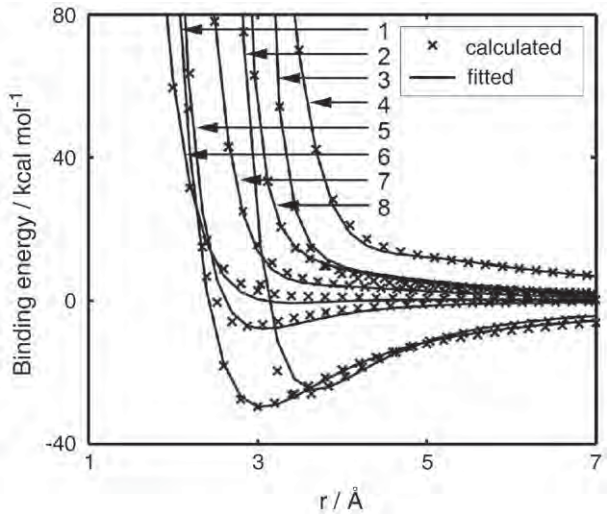


**Fig. 5.** Au–NM interaction: Quantum chemical (x) and fitted (solid lines) energies. The numbers 1–8 refer to Fig. 2.

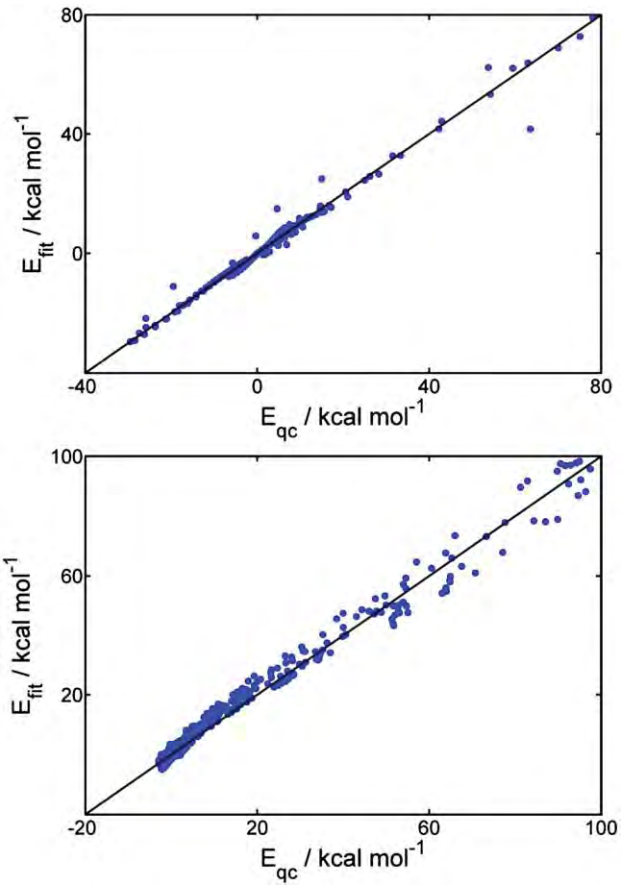


**Fig. 6.** Fitting accuracy of the $Au^+$–NM potential (upper part) and the NM–NM potential energy function (lower part).

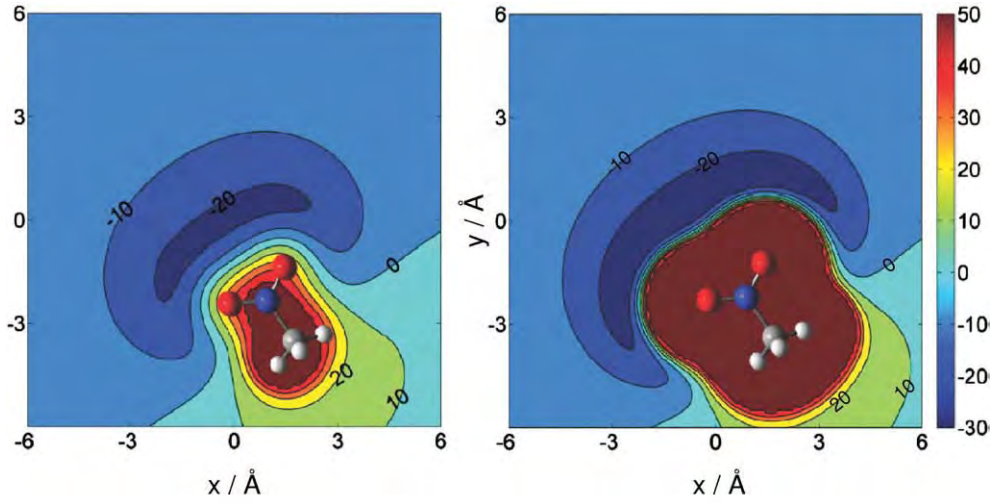


**Fig. 7.** $Au^{+}$–NM Potential energy according to Eq. (1) in the $C_s$ plane of NM (right) and 2 Å above (left). Energies in kcal/mol and $x/y$ coordinates in Å.

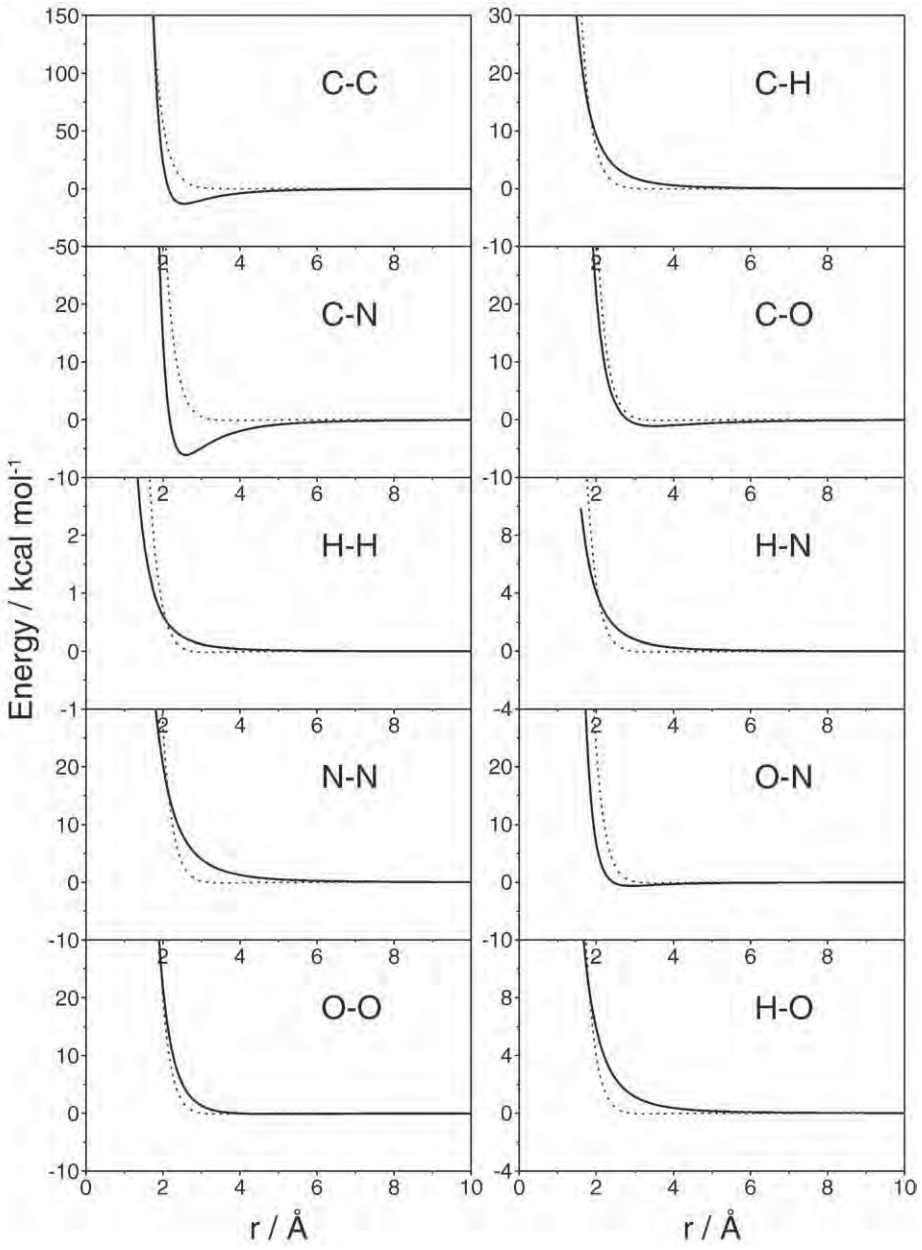


**Fig. 8.** Comparison of the atom–atom terms of our (solid lines) and the generic (dashed lines) NM–NM potential energy functions.

**Table 4**
Values of the parameters of the analytical NM–NM pair potential expression (Eq. (2)).

| j | k | A | B | C |
|---|---|---|---|---|
| C | C | 23,563.0 | 0.0 | −1112.2000 |
| C | H | 0.0 | 0.0 | 146.5868 |
| C | N | 12,299.0 | 0.0 | −548.6524 |
| C | O | 0.0 | 2375.6 | −844.1313 |
| H | H | 0.0 | 0.0 | 9.7094 |
| H | N | 0.8246 | 0.0 | 64.1848 |
| H | O | 0.0 | 0.0 | 93.0748 |
| N | N | 0.0 | 0.0 | 323.2490 |
| N | O | 3104.0 | 0.0 | −87.7924 |
| O | O | 270.4317 | 1366.2 | −353.2470 |

Energies in kcal/mol and distances in Å.

### 3.2. $Au^+$–NM potential energy surface

We used the analytical energy expression:

$$V_{\text{fit}}^{CH_3NO_2-Au^+} = \sum_{k\in NM} q_k / r_k + A_k / r_k^8 + B_k / r_k^6 + C\exp(-Dr_k) \quad (1)$$

for explaining the $Au^+$–NM intermolecular potential. The powers of $r$ of −8 and −6 in Eq. (1) do not have special physical significance but they gave a slightly better fitting than other combinations. These two terms in take care for the steep short-range parts while the exponential term models the shallow potential at medium distances. The values of the parameters $A$ to $D$ were obtained from the fitting calculations as described in Section 2.2. The values of the parameters are given in Table 3.

In Fig. 5, we show the fitted energy together with the ab-initio data. The fitting accuracy (Fig. 6) is generally good.

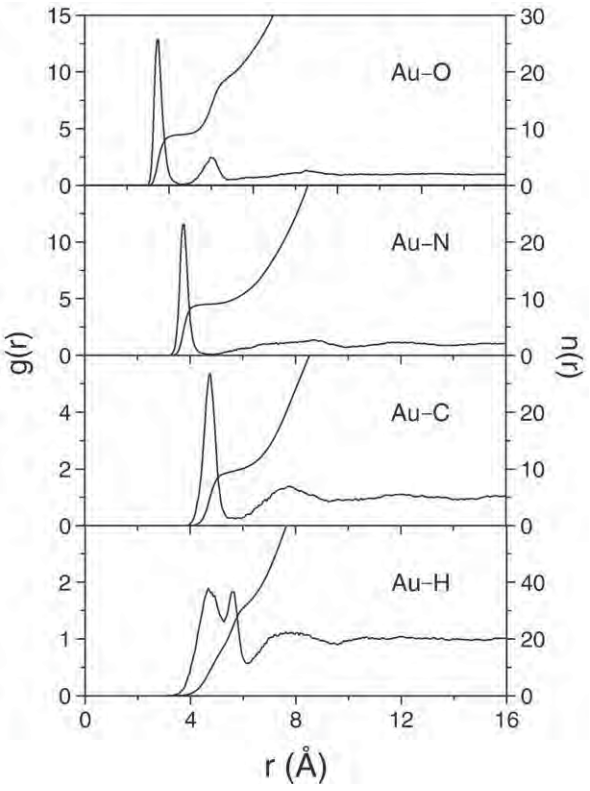


**Fig. 9.** Au–NM radial distribution functions from the simulation utilizing the newly constructed NM–NM potential energy function.

**Table 5**
Characteristic values of the radial distribution functions for the $Au^+$–nitromethane system with the (a) new and (b) generic NM–NM potential energy functions.

| Pair | 1st shell | | | | | 2nd shell | | | | |
|---|---|---|---|---|---|---|---|---|---|---|
| | $r_{max}$ | $g(r_{max})$ | $r_{min}$ | $g(r_{min})$ | $n(r_{min})$ | $r_{max}$ | $g(r_{max})$ | $r_{min}$ | $g(r_{min})$ | $n(r_{min})$ |
| *(a)* | | | | | | | | | | |
| Au–O | 2.62 | 12.86 | 3.42 | 0.11 | 8.96 | 4.52 | 2.47 | 5.07 | 0.51 | 18.88 |
| Au–N | 3.77 | 11.57 | 4.67 | 0.07 | 9.01 | 8.72 | 1.36 | 10.06 | 0.73 | 49.37 |
| Au–C | 4.77 | 5.35 | 5.52 | 0.27 | 9.44 | 7.72 | 1.39 | 9.26 | 0.84 | 37.87 |
| Au–H | 4.67 | 1.89 | 6.17 | 0.57 | 32.43 | 7.62 | 1.12 | 9.56 | 0.90 | 121.01 |
| *(b)* | | | | | | | | | | |
| Au–O | 2.62 | 13.44 | 3.52 | 0.08 | 9.84 | 4.62 | 2.69 | 5.17 | 0.37 | 20.48 |
| Au–N | 3.77 | 12.56 | 4.92 | 0.06 | 10.00 | 8.47 | 1.34 | 9.91 | 0.69 | 47.96 |
| Au–C | 4.67 | 5.39 | 5.92 | 0.14 | 10.60 | 7.67 | 1.53 | 10.16 | 0.72 | 49.34 |
| Au–H | 4.62 | 1.98 | 6.17 | 0.52 | 33.86 | 8.22 | 1.25 | 9.61 | 0.89 | 125.24 |

Fig. 7 shows a contour plot of two cuts through the analytical Au–NM potential energy surface according to Eq. (1), in the symmetry plane of NM and 2 Å above it.

### 3.3. NM–NM potential energy surface

Our own pair potential energy expression for the NM–NM interactions is a polynomial in $1/r$

$$V_{\text{fit}}^{CH_3NO_2-CH_3NO_2} = \sum_{j\in NM1}\sum_{k\in NM2} q_{jk} / r_{jk} + A_{jk} / r_k^8 + B_{jk} / r_k^5 + C_{jk} / r_k^4 \quad (2)$$

Fig. 8 shows that Eq. (2) provides a reasonable reproduction of the NM–NM interactions. Due to the higher dimensionality of the NM–NM system compared to the NM–Au system (6 internal degrees of freedom versus 3), much several thousand energy points had to be calculated and we do not show the various potential energy curves here. The number of non-zero parameters (Table 4) for the ten atom pairs is not overwhelming. Again, the atomics charges in the NM molecules were not changed.

A comparison between the two potential energy functions in terms of the various atom–atom pair terms is given in Fig. 8. Since the partial charges are the same in both cases, the electrostatic contributions were excluded. Our potential energy function is given in Eq. (2) while

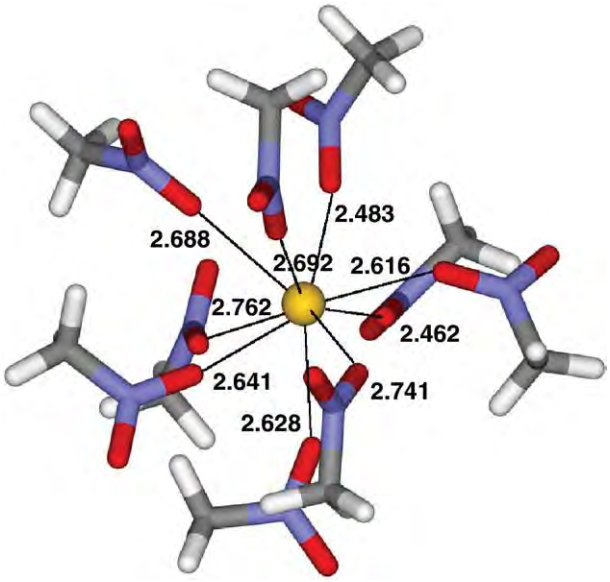


**Fig. 10.** Typical configuration of NM around $Au^+$.

the generic one [10] uses an $\exp(-r)$ term for the repulsion and an $r^{-6}$ term for attractive interactions beside the electrostatic terms.

Two main differences are present: In all curves the $\exp(-x)$ term leads to a steeper repulsive part. This is a consequence of the values of the parameters and not of the functional form since $r^{-8}$ is infinite for $r=0$ while $\exp(-r)$ terms are finite. Further, all terms in the generic potential exhibit no or only extremely shallow minima, in contrast to the pronounced minimum for C–N in our potential energy function. Due to the fact of the completely different ways in which both energy expressions were derived, detailed comparisons are difficult but it can be safely stated that the generic expression acts as a 'soft sphere plus coulomb'-type of potential. The largest deviations between both potential energy functions can be seen for C–N and C–C. These centers are, however, shielded by hydrogen atoms and not in close contact with each other.

Since it also turned out (see below) that the MD results from both Sorescu's [10] and our potential energy function are very similar to each other, one can conclude that electrostatic interactions dominate also in our model and the softer repulsive part plays a minor role.

### 3.4. Molecular dynamics simulation

The trajectory was analyzed in terms of radial distribution functions (RDFs). Fig. 9 shows all Au–NM pair correlation functions. The characteristic values of the RDFs are listed in Table 5. There the running integration numbers $n_{xy}$, defined according to

$$n_{xy}(r) = 4\pi\rho_0 \int_0^r r^2 g_{xy}(r)\mathrm{d}r \tag{3}$$

are also given. All RDFs with the exception of $g_{\mathrm{Au-H}}$ have one sharp first peak that goes down to near zero after its maximum. The splitting of $g_{\mathrm{Au-H}}$ might be an artifact from the rigidity of our NM model. The number of N atoms under the first peak is about 10 for the generic NM pair potential energy function [11] and 9.01 if our new one is used. Such a difference — even if the Au–NM interactions are the same in both potentials — is not surprising. These respective values for $n_{\mathrm{Au-O}}$ are consistent with the values for $n_{\mathrm{Au-C}}$ and $n_{\mathrm{Au-N}}$. Such a large solvation number is a consequence of the large distance (2.62 Å) at which $g_{\mathrm{Au-O}}$ has its maximum. The second O atom of the NM molecules is found under the second peak of $g_{\mathrm{Au-O}}$ at distances of about 4.62 Å. Consequently, $n_{\mathrm{Au-O}}$ is 18.88 (our potential) and 20.48 after this second peak. This is somewhat remarkable since the attractive potential at the site of one O atom and between two O atoms is similar (Fig. 7) and the quantum chemical details that might lead to a preference of coordination to a single oxygen (Section 3.1) are, of course, absent in our simple pair potential. Looking at the conformations (a typical snapshot is plotted in Fig. 10) one sees, however, that the more distant O atoms can interact favorably with the electropositive methyl groups, thus allowing for the crowded solvation shell. As mentioned above, virtually identical results for RDFs, coordination numbers and typical geometries are obtained if we use the NM–NM potential from [11] instead of the newly constructed one.

## 4. Summary

Energetic and geometric features of various gold(I)–nitromethane clusters were calculated and discussed in the light of the peculiar properties of Au(I). Ab-initio pair energy surfaces for Au(I)–NM and NM–NM were derived by fitting simple analytical functions to quantum chemically calculated energies. These functions were then used to perform a molecular dynamics simulation of one Au(I) cation in 499 nitromethane molecules in the NVT ensemble at room temperature. A comparative simulation with an older, generic NM–NM potential energy function was also performed and gave nearly identical results with respect to the analyzed quantities. The first solvation shell around the gold ion consists of 9–10 nitromethane molecules with a distance of about 2.6 Å for the first and about 4.6 Å for the second O atom to $Au^+$.

## Acknowledgements

Support from the projects WTZ A13/2006, GVOP-3.2.1.-2004-04-0210/3.0, NAP VENEUS05 OMsFB-00650/2005, OTKA K 68498 and from the organizations NANOTEC Center of Excellence, CNC Consortium, TRF, KURDI and CHE is gratefully acknowledged. NI thanks the University Development Commission (UDC) and the Graduate School of Kasetsart University for financial support.

## References

[1] P. Pyykko, Gold Bull. 37 (2004) 136.
[2] P. Pyykko, Inorg. Chim. Acta 358 (2005) 4113–4130.
[3] F. Farges, J.A. Sharps, G.E. Brown, Geochim. Cosmochim. Acta 57 (1993) 1243–1252.
[4] R.A. Bryce, J.M. Charnock, R.A.D. Pattrick, A.R. Lennie, J. Phys. Chem. A 107 (2003) 2516–2523.
[5] T. Megyes, S. Balint, T. Grosz, T. Radnai, I. Bako, L. Almasy, J. Chem. Phys. 126 (2007) 164507.
[6] P.J. Hay, W.R. Wadt, J. Chem. Phys. 82 (1985) 299–310.
[7] T.H. Dunning, P.J. Hay, in: H.F. Schaefer III (Ed.), Modern Theoretical Chemistry, Plenum, New York, 1976, p. 1.
[8] P. Pyykko, Angew. Chem. Int. Ed. 43 (2004) 4412–4456.
[9] M.J. Frisch, G.W. Trucks, H.B. Schlegel, G.E. Scuseria, M.A. Robb, J.R. Cheeseman, J.A. Montgomery Jr., T. Vreven, K.N. Kudin, J.C. Burant, J.M. Millam, S.S. Iyengar, J. Tomasi, V. Barone, B. Mennucci, M. Cossi, G. Scalmani, N. Rega, G.A. Petersson, H. Nakatsuji, M. Hada, M. Ehara, K. Toyota, R. Fukuda, J. Hasegawa, M. Ishida, T. Nakajima, Y. Honda, O. Kitao, H. Nakai, M. Klene, X. Li, J.E. Knox, H.P. Hratchian, J.B. Cross, V. Bakken, C. Adamo, J. Jaramillo, R. Gomperts, R.E. Stratmann, O. Yazyev, A.J. Austin, R. Cammi, C. Pomelli, J.W. Ochterski, P.Y. Ayala, K. Morokuma, G.A. Voth, P. Salvador, J.J. Dannenberg, V.G. Zakrzewski, S. Dapprich, A.D. Daniels, M.C. Strain, O. Farkas, D.K. Malick, A.D. Rabuck, K. Raghavachari, J.B. Foresman, J.V. Ortiz, Q. Cui, A.G. Baboul, S. Clifford, J. Cioslowski, B.B. Stefanov, G. Liu, A. Liashenko, P. Piskorz, I. Komaromi, R.L. Martin, D.J. Fox, T. Keith, M.A. Al-Laham, C.Y. Peng, A. Nanayakkara, M. Challacombe, P.M.W. Gill, B. Johnson, W. Chen, M.W. Wong, C. Gonzalez, J.A. Pople, Gaussian Inc., Wallingford CT.
[10] D.C. Sorescu, B.M. Rice, D.L. Thompson, J. Phys. Chem. A 105 (2001) 9336–9346.
[11] D.C. Sorescu, B.M. Rice, D.L. Thompson, J. Phys. Chem. B 104 (2000) 8406–8419.
[12] D.C. Sorescu, B.M. Rice, D.L. Thompson, J. Phys. Chem. B 101 (1997) 798–808.
[13] J.E. Carpenter, F. Weinhold, J. Mol. Struct.,Theochem. 169 (1988) 41–62.
[14] M. Rosi, C.W. Bauschlicher, J. Chem. Phys. 90 (1989) 7264–7272.
[15] M. Rosi, C.W. Bauschlicher, J. Chem. Phys. 92 (1990) 1876–1878.
[16] H. Schmidbaur, S. Cronje, B. Djordjevic, O. Schuster, Chem. Phys. 311 (2005) 151–161.
[17] H.M. Lee, M. Diefenbach, S.B. Suh, P. Tarakeshwar, K.S. Kim, J. Chem. Phys. 123 (2005) 074328.
[18] J.U. Reveles, P. Calaminici, M.R. Beltran, A.M. Koster, S.N. Khanna, J. Am. Chem. Soc. 129 (2007) 15565–15571.
[19] T. Iino, K. Ohashi, K. Inoue, K. Judai, N. Nishi, H. Sekiya, J. Chem. Phys. 126 (2007) 194302.

# Adsorption of M Species and $M_2$ Dimers (M = Cu, Ag, and Au) on the Pristine and Defective Single-Walled Carbon Nanotubes: A Density Functional Theory Study

**Chan Inntam*[,†] and Jumras Limtrakul[‡,§,||]**

*Chemistry Department, Faculty of Science, Ubon Ratchathani University, Ubon Ratchathani, 34190 Thailand, Chemistry Department and Center of Nanotechnology, Kasetsart University, Bangkok 10900, Thailand, and Center for Advanced Studies in Nanotechnology and Its Applications in Chemical, Food and Agricultural Industries, Kasetsart University, Bangkok 10900, Thailand*

*Received: September 23, 2010; Revised Manuscript Received: November 3, 2010*

We studied the adsorption of neutral M, charged M, and $M_2$ dimers (M = Cu, Ag, Au) on the pristine single-walled carbon nanotubes (SWNTs) as well as on the Stone−Wales and vacancy sites by means of the B3LYP/6-31G (d,p) hybrid density functional method. Our results for neutral metal atoms on the pristine and defective SWNTs agree very well with previous periodic calculations. The binding affinity trend of metal species toward the pristine and defective SWNTs is in the order of $M^+ > M^- > M$. This implies that the transfer of electron density between metal species and the nanotubes, the electrostatic attraction, and the Pauli repulsion play an important role in the M−SWNT system. From the Mulliken population analysis, the transfer of electron density induces a positive charge of the metal species and a negative charge of the carbon atoms of nanotubes. As far as the adsorption energy is concerned, the metal species are likely to deposit on the defect site, particularly on the vacancy site, rather than on the pristine tube. To explore the reactivity of the M−SWNT complexes which can serve as a gas sensor as well as a catalyst, the interaction between a CO molecule and a metal atom deposited on the atomic vacancy was also examined. We also found that the adsorption energy per atom decreases from the metal atom to metal dimers in line with the fact that metal−metal cohesion dominates over metal−SWNT interaction. Finally, based on calculated interaction energies, dimerization of adsorbed atoms on the defect sites is not particularly favored compared to dimerization on the pristine tube except for that of Ag and Au atoms on the vacancy site.

## 1. Introduction

Single-walled carbon nanotubes (SWNTs)[1,2] have attracted a great deal of interest due to their unique structural, electrical, and mechanical properties.[3−7] They have been the focus of many recent studies on sensor materials, optics, catalysts, and nanoelectronic devices.[8−19] The electronic properties of the SWNTs depend on the structure and chirality of the nanotubes, resulting in a semiconducting or metallic nature. However, these properties can be modified by metal doping or functionalization of the nanotubes. Recently, various transition metal atoms have been doped and decorated on the sidewall of SWNTs to investigate the reactivity and the characteristic of such complexes[20−23] as well as to developing novel techniques for the decoration of SWNTs with metal nanoparticles.[24−30] These are of particular interest as the metal atom and metal-nanoparticle-decorated SWNTs exhibit high sensitivity, being able to detect the presence of gases at concentrations below the order of parts per million (ppm), and high reactivity materials. For example, Rh-decorated SWNTs were found to bind strongly with the $NO_2$ molecule at low temperature (200 K).[31] After some modifications, this material can be considered as a CNT-based sensor for detecting $NO_2$ at room temperature.

The interaction between transition metal atoms and SWNTs has been investigated through experimental and theoretical approaches.[15,18,20−22,32−42] Durgun et al.[22] systematically studied the adsorption of 23 transition metal atoms on the perfect (8,0) and of 4 transition metal atoms on the perfect (6,6) SWNTs. They found that the interaction of two species depends on the hybridization between the $p_z$ orbital of carbon and the d orbitals of transition metals. Also, various kinds of defects found in the SWNTs, e.g., vacancies, Stone−Wales (SW), dangling bonds, and rehybridization,[43−45] can affect the properties of nanotubes and the nature of transition metal adsorption as reported by Yang et al.[46] They studied theoretically the adsorption of the Ni atom on the perfect and defective (5,5) and (10,0) SWNTs. It was reported that the presence of defects enhances the interaction between Ni and SWNTs, especially the single vacancy. Nevertheless, most theoretical studies of SWNTs and transition metals have focused either on the pristine tube or neutral metal atoms. Studies on the interactions of charged metal atoms, both of cation and anion species, as well as the small metal coinages have not been reported. The fundamental knowledge based on the interaction of charged metal species and small metal clusters on the sidewall of SWNTs is crucial. The results can provide an in-depth understanding of the nature of transition metal−nanotube interaction for producing metal nanoparticles with controlled sizes and shapes as well as for fabricating functional nanodevices.

In this article, we study systematically the interactions of the neutral metal atom M, metal M cation, and metal M anion (M = Cu, Ag, and Au) on the sidewall of (5,5) SWNTs using a density functional theory at the B3LYP level of calculation. To

* To whom correspondence should be addressed, inntam@gmail.com.
† Chemistry Department, Faculty of Science, Ubon Ratchathani University.
‡ Chemistry Department and Center of Nanotechnology, Kasetsart University.
§ Center for Advanced Studies in Nanotechnology and Its Applications in Chemical, Food and Agricultural Industries, Kasetsart University.
|| Present address: Laboratory for Computational and Applied Chemistry (LCAC) and Center of Nanotechnology, Kasetsart University.

10.1021/jp109098q 
Published on Web 11/19/2010

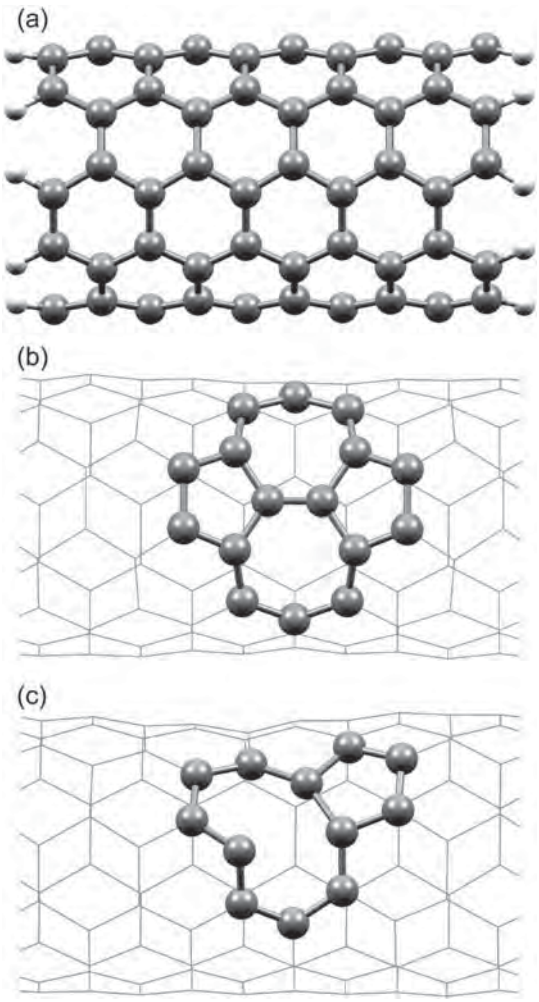


**Figure 1.** Sketches of the cluster models of SWNTs: (a) the pristine SWNTs ($C_{100}H_{20}$), (b) the Stone−Wales defect ($C_{100}H_{20}$), (c) the vacancy defect ($C_{99}H_{20}$).

elucidate the influence of the defect sites on the adsorption of such metal species, the metal deposition on the pristine and intrinsic defective SWNTs, vacancy, and Stone−Wales (SW), is considered. Also, the adsorption of metal dimers ($Cu_2$, $Ag_2$ and $Au_2$) on such sites is investigated for inspecting the initial stage of metal deposition on the sidewall of SWNTs. Moreover, this study can provide us the preferred adsorption site and stable geometries of deposited metal atoms and metal dimers, the nature of the metal−SWNTs bonding, and the propensity of adsorbed species to aggregate or to form metal dimers in the presence of vacancy and SW defects on the sidewall of SWNTs. It is believed that a fundamental understanding obtained by this work is of particular importance for fabricating hybrid metal−SWNT materials and for manufacturing chemical sensors.

## 2. Computational Details

In this work, the armchair (5,5) SWNTs were employed for exploring the adsorption of metal atoms and metal dimers. A quantum cluster model consisting of 100 carbon atoms of the nanotubes with H atoms capped at the ends of the fragment were applied to represent the SWNT structure, resulting in a $C_{100}H_{20}$ cluster model. These capped H atoms were used to avoid dangling bonds at the open ends. For the defective SWNTs, the Stone−Wales (SW) and atomic vacancy defects were generated by modifying the pristine $C_{100}H_{20}$ cluster model as shown in Figure 1. The SW defect creates a pentagon and heptagon pair by rotating a C−C bond in a hexagon by 90°. The atomic vacancy is formed by removing one carbon atom of the hexagon, consequently yielding a $C_{99}H_{20}$ cluster model. After geometry optimizations of such cluster models, the stable complexes were employed for studying the adsorptions of metal species, metal dimers, and a CO molecule on the sidewall of SWNTs.

**TABLE 1: Calculated Bond Lengths $r_e$ (M−M) (pm) and Dissociation Energies Per Atom $D_e$ (kcal mol$^{-1}$/atom) of Free $M_2$ Dimers (M = Cu, Ag, Au)**

| | | | $r_e$ (M−M) | | $D_e$ | |
|---|---|---|---|---|---|---|
| $M_2$ | symmetry | ground state | calcd | exptl | calcd | exptl |
| $Cu_2$ | $D_{\infty h}$ | $^1\Sigma^+_g$ | 202.4 | 222[a] | 25.6 | 23.2[a] |
| $Ag_2$ | $D_{\infty h}$ | $^1\Sigma^+_g$ | 261.6 | 248,[a] 253[b] | 17.4 | 19.1[a] |
| $Au_2$ | $D_{\infty h}$ | $^1\Sigma^+_g$ | 256.8 | 247[a] | 21.8 | 26.5[a] |

[a] Reference 51 [b] References 52 and 53.

All calculations were performed based on the density functional theory (DFT), employing Becke's three-parameter hybrid exchange functional combined with the Lee, Yang, and Parr correlation functional (B3LYP)[47,48] method implemented in a Gaussian 03[49] program. The basis sets used in the calculation were 6-31G(d,p) for C, capped H, and Cu atoms. The relativistic effective core pseudopotential of Hay and Wadt was employed for Ag and Au atoms.[50] Spin-unrestricted calculations were performed for all open-shell systems.

Adsorption energies, $E_{ads}$, presented in this study were calculated with respect to the sum of the corresponding spin-polarized ground-state energy of a free metal species, $M_1$ or $M_2$, in its equilibrium geometry and the energy of the relaxed cluster models as follows

$$E_{ads} = E[M_n\text{−SWNTs}] - E[\text{SWNTs}] - E[M_n] \quad (1)$$

where $E[M_n\text{−SWNTs}]$ is the total energy of the metal atom ($M_1$) or dimer ($M_2$) adsorbed on the pristine or defective SWNTs, $E$[SWNTs] is the total energy of either pristine $C_{100}H_{20}$ or defective SWNTs, $E[M_n]$ is the total energy of the corresponding free metal species, $M_1$ or $M_2$. As we focus on the structural properties of various metal species deposited on the SWNTs as well as the dimerization of adsorbed metal atoms, the basis set superposition error (BSSE) was neglected for this study. All optimized geometries were confirmed by frequency analyses at the same level of calculation.

## 3. Results and Discussion

**3.1. Metal Dimers.** Free metal dimers ($Cu_2$, $Ag_2$, and $Au_2$) with a singlet ground state ($^1\Sigma^+_g$) were characterized by the density functional theory (DFT) calculation. Their experimental bond lengths[51] are 222, 248 (253[52,53]), and 247 pm for $Cu_2$, $Ag_2$, and $Au_2$, respectively. The corresponding experimental dissociation energies ($D_e$)[51] are 23.2, 19.1, and 26.5 kcal mol$^{-1}$/atom. Our calculated bond lengths and dissociation energies of these metal dimers are documented in Table 1. For the $Cu_2$ dimer, the bond length is about 20 pm shorter than the experimental value and consequently shows the overestimated dissociation energies. The calculated bond lengths of $Ag_2$ and $Au_2$ employing the ECP of Hay and Wadt somewhat overestimate the experimental values reflecting the underestimated dissociation energies.

**3.2. Adsorption of Neutral Metal Atoms on the Sidewall SWNTs.** In this study, the adsorptions of neutral Cu, Ag, and Au atoms on both the pristine and defective SWNTs, Stone−

**TABLE 2: Calculated Parameters (bond lengths in pm, atomic charges $q$ in electrons, and adsorption energies $E_{ads}$ in kcal mol$^{-1}$) of Adsorption Complexes Concerning the Neutral Metal Atom M Deposited on the Pristine and Defective SWNTs**

| | | pristine SWNTs | defective SWNTs | |
|---|---|---|---|---|
| | metal | $C_{100}H_{20}$ cluster | Stone−Wales ($C_{100}H_{20}$) | vacancy ($C_{99}H_{20}$) |
| $r(M-C_{sur})$[a] | Cu | 203.6, 206.2, 210.5 | 196.7, 199.0 | 183.2, 185.7, 190.0 |
| | Ag | 345.3, 363.6, 365.4 | 240.5 | 212.0, 220.6, 220.8 |
| | Au | 273.5 | 218.5 | 200.6, 204.1, 210.7 |
| $q_M$[b] | Cu | 0.27 (−0.34, −0.31, 0.09) | 0.46 (−0.44, −0.43) | 0.48 (−0.23, −0.33, −0.28) |
| | Ag | −0.06 (0.01, 0.01) | 0.00 (−0.31) | 0.29 (−0.20, −0.19, −0.22) |
| | Au | −0.22 (−0.14, 0.06, 0.05) | −0.10 (−0.46) | 0.58 (−0.36, −0.36, −0.34) |
| $E_{ads}$ | Cu | −40.9 | −53.8 | −131.3 |
| | Ag | −0.5 | −4.0 | −10.8 |
| | Au | −4.0 | −15.0 | −26.3 |

[a] Distances between the metal atom M and nearby $C_{sur}$ atoms. [b] Charges of the metal atom M. Values in parentheses are the charges of nearby $C_{sur}$ atoms.

Wales (SW), and vacancy sites, are investigated. The various positions of the metal atoms deposited on the sidewall of SWNTs, cf. Figure 1, were considered for investigating the most stable geometry. For the atomic vacancy site as shown in Figure 1c, the most stable geometry of the $C_{99}H_{20}$ cluster was found to present a pentagon−enneagon defect. This defect was formed by the recombination of two dangling bonds which were generated after a removal of a $C_{sur}$ from the $C_{100}H_{20}$ cluster. This result agrees very well with previous theoretical studies.[23,54,55] Our calculated parameters concerning the most stable adsorption complex are summarized in Table 2.

For adsorption on the pristine SWNTs ($C_{100}H_{20}$ cluster), we found that the Cu and Ag atoms preferred to adsorb over the C−C bond tilted to the tube axis (bridge site) while the Au atom adsorbs directly above the surface carbon atom, $C_{sur}$ (on-top site). The distances of Cu−$C_{sur}$ (203.6−210.5 pm) are shorter than those of the Au−$C_{sur}$ (273.5 pm) and the Ag−$C_{sur}$ (345.3−365.4 pm). This indicates that the Cu atom interacts strongly with $C_{sur}$ atoms of the hexagon rather than the Ag and Au atoms. These results correspond with their adsorption energies, $E_{ads}$. The calculated adsorption energies of Cu, Ag, and Au atoms are −40.9, −0.5, and −4.0 kcal mol$^{-1}$, respectively. The different interaction of these three metal atoms can be explained by the transfer of electron density from the metal atom to nanotubes. On the basis of the Mulliken population analysis, the Cu atom exhibits strong positive charges (+0.27 e) while Ag and Au atoms are −0.06 e and −0.22 e, respectively. This implies that there are more electrons transferring from the Cu atom to the nanotubes which results in the stronger interaction. On the other hand, the Pauli repulsion weakens the interaction between the nanotubes and the metal atoms, particularly for the 5d metals (Au atom). Recently, the adsorption of the Cu atom on the armchair (5,5) SWNTs was studied by Zhang et al.[56] using the PBE functional[57] with the DNP basis set. Their calculated adsorption energy is −28.1 kcal mol$^{-1}$ for the adsorption on both of the bridge and on-top sites. However, the most stable adsorption complexes found in this study were not considered in their work. Therefore, the differences of Cu−$C_{sur}$ bonds as well as the functional considered cause a significant variation of adsorption energy. In addition, our results are in agreement with the previous periodic calculation studied by Durgun et al.[58] The interaction of the Au atom on the sidewall of pristine (6,6) SWNTs was reported to be −6.9 kcal mol$^{-1}$. Khongpracha et al.[34] investigated the Au atom adsorbed on the tip of a single-walled carbon nanohorn (SWNH) as well as on the tip of single-walled carbon nanotubes (SWNTs). The calculated adsorption energies with the PBE functional[57] are −10.8 and −16.2 kcal mol$^{-1}$ for SWNH and SWNTs systems, respectively. These values are more stable than our work due to the different functional and the curvature effect. The interaction of the metal atoms was found to be even stronger on the SWNTs with high curvature.[59]

For the interaction between the metal atoms and the defective SWNTs, both of the Stone−Wales (SW) and the vacancy site were found to be the more favorable adsorption site rather than the pristine SWNTs. On the SW defect, the pyramidalization angle of the $C_{sur}$ atom was reported to play an important factor for governing the interaction with the metal atoms.[46] In this study, the Cu atom bonded to two $C_{sur}$ atoms which involved the highest pyramidalization angles with distances of 196.7 and 199.0 pm (cf. Figure 2). The adsorption energy was calculated to be −53.8 kcal mol$^{-1}$. In contrast to the adsorption complex of Cu, Ag and Au atoms bonded over a $C_{sur}$ atom of the nanotubes. The Ag−$C_{sur}$ and Au−$C_{sur}$ distances are 240.5 and 218.5 pm, respectively. The corresponding adsorption energies were estimated to be −4.0 and −15.0 kcal mol$^{-1}$. Interestingly, the atomic adsorption on the vacancy site of SWNTs is even stronger than that on the SW defect for all metal atoms. We observed that the metal atoms prefer to be adsorbed above a position in which a $C_{sur}$ atom was removed and form bonds with three nearby $C_{sur}$ atoms of the nanotubes. These three $C_{sur}$ atoms with dangling bonds are unstable and prefer to bond with the metal atom. Again, the interaction of the Cu atom on the vacancy site is stronger than that of the Au and Ag atoms, respectively. As one can see from Table 2, the Cu−$C_{sur}$ distances are 183.2, 185.7, and 190.0 pm, which are shorter than those of the Au−$C_{sur}$ (200.6, 204.1, and 210.7 pm) and Ag−$C_{sur}$ (212.0, 220.6, and 220.8 pm). The estimated adsorption energies corresponding to Cu (−131.3 kcal mol$^{-1}$), Au (−26.3 kcal mol$^{-1}$), and Ag (−10.8 kcal mol$^{-1}$) are in accordance with the metal−$C_{sur}$ distances. Our Cu−$C_{sur}$ distances are similar to the work of Zhuang et al.[23] using the GGA functional in combination with periodic calculations. However, our calculated adsorption energy is more stable by ∼56 kcal mol$^{-1}$ (∼43%). The formation energy of the vacancy is also different from our result, being more stable than their result by ∼49%. This is probably due to the difference of the exchange-correlation functional. They also employed the spin-polarized projector augmented-wave (PAW) method for describing the electron−ionic core interaction. The $E_{ads}$ values of the metal atom on the vacancy site are about twice as strong as those on the SW defect. The M−$C_{sur}$ distances from the adsorption complex on the vacancy site are also shorter than those on the SW defect and the pristine SWNTs. Moreover, the Mulliken population analysis confirms that the transfer of electron density from the metal atom to nearby $C_{sur}$ atoms is greater in the defect sites. Therefore, we

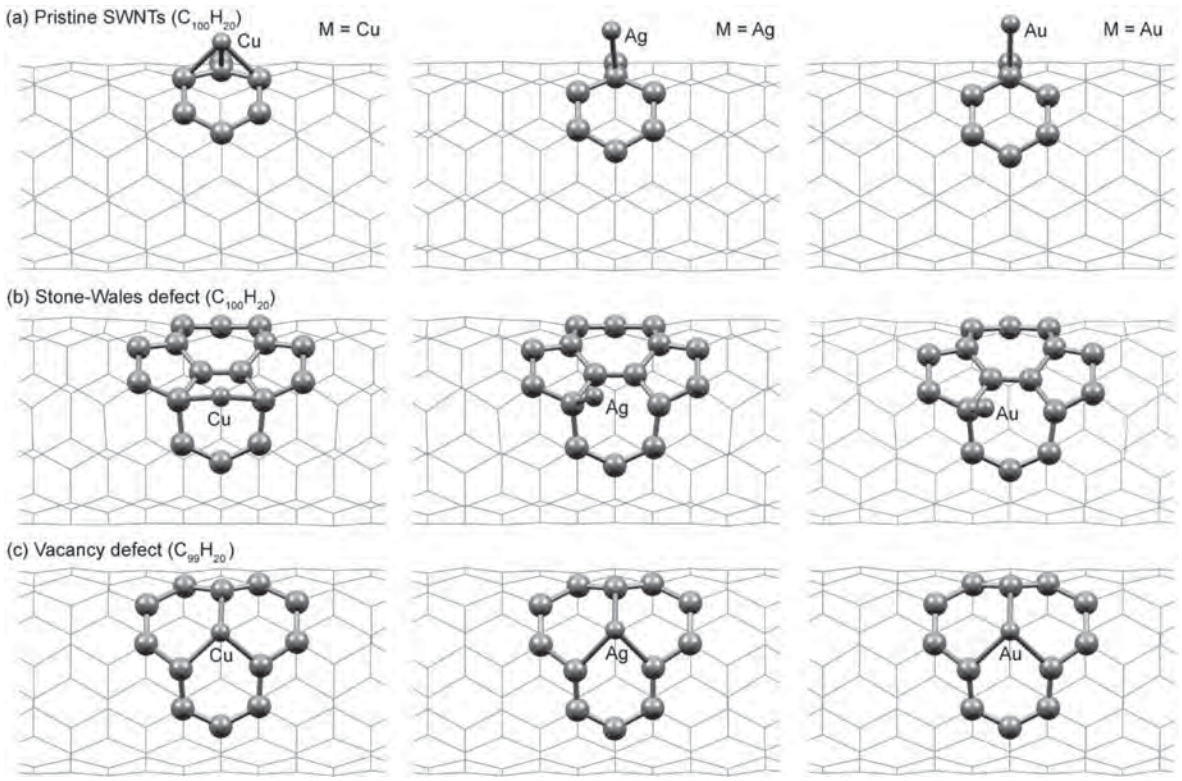


**Figure 2.** Adsorption complexes of M (M = Cu, Ag, and Au) species deposited on the SWNTs: (a) the pristine SWNTs ($C_{100}H_{20}$); (b) the Stone−Wales defect ($C_{100}H_{20}$); (c) the vacancy defect ($C_{99}H_{20}$).

**TABLE 3: Calculated Parameters (bond lengths in pm, atomic charges $q$ in electrons, and adsorption energies $E_{ads}$ in kcal mol$^{-1}$) of Adsorption Complexes Concerning the Metal Cation M$^+$ Deposited on the Pristine and Defective SWNTs[a]**

| | | pristine SWNTs | defective SWNTs | |
|---|---|---|---|---|
| | metal | $C_{100}H_{20}$ cluster | Stone−Wales ($C_{100}H_{20}$) | vacancy ($C_{99}H_{20}$) |
| $r$(M−$C_{sur}$) | $Cu^+$ | 200.5, 202.5, 205.9 | 196.6, 198.3 | 183.6, 183.8, 189.9 |
| | $Ag^+$ | 239.5, 278.7 | 229.1 | 209.4, 210.1, 217.3 |
| | $Au^+$ | 221.4 | 214.1 | 200.7, 201.2, 209.5 |
| $q_M$ | $Cu^+$ | 0.65 (−0.35, −0.34, 0.09) | 0.58 (−0.45, −0.45) | 0.54 (−0.25, −0.26, −0.32) |
| | $Ag^+$ | 0.30 (−0.34) | 0.26 (−0.39) | 0.39 (−0.22, −0.28, −0.33) |
| | $Au^+$ | 0.05 (−0.48) | 0.08 (−0.50) | 0.68 (−0.36, −0.36, −0.37) |
| $E_{ads}$ | $Cu^+$ | −130.8 | −154.4 | −210.0 |
| | $Ag^+$ | −62.3 | −76.0 | −71.3 |
| | $Au^+$ | −102.8 | −121.5 | −128.4 |

[a] See Table 2 for the definitions.

conclude that the metal atoms prefer to adsorb on the defect sites, particularly on the vacancy, rather than on the pristine SWNTs.

**3.3. Adsorption of Charged Metal Species on the Sidewall SWNTs.** In order to describe the metal particles aggregation procedure such as the electroless deposition on the sidewall of SWNTs, the interactions of metal cation and metal anion species on the pristine and defective SWNTs were investigated. The results of these metal species are listed in Table 3 and Table 4. Most of these adsorption complexes are similar to those obtained from the neutral metal complexes as shown in Figure 2.

When the interactions of neutral metal atoms are compared, it is clear that all the metal cations bind quite strongly on the pristine and defective SWNTs. The strong interaction is in accordance with the shorter M−$C_{sur}$ distances as well as the more positive charges of the metal. For the pristine tube, we found that the $Cu^+$ ion interacts on three $C_{sur}$ atoms with distances of 200.5, 202.5, and 205.9 pm, which are shorter than those of the neutral Cu complex by about 3−4 pm. Therefore, the interaction of the $Cu^+$ ion and the $C_{sur}$ bearing negative charge is stronger than that of the neutral Cu complex system. This greater electrostatic interaction contributes to the strong adsorption energy of the $Cu^+$ complex, −130.8 kcal mol$^{-1}$. Similar results are also obtained for the adsorption of $Ag^+$ and $Au^+$ ions. The $Ag^+$ and $Au^+$ ions interact directly on top of the $C_{sur}$ atom with distances of 239.5 and 221.4 pm, respectively. As expected, the adsorptions of $Ag^+$ and $Au^+$ species on the pristine SWNTs are more favorable than those for the neutral Ag and Au atoms. The estimated adsorption energies of $Ag^+$ and $Au^+$ ions are −62.3 and −102.8 kcal mol$^{-1}$, respectively. For the adsorption on the SW defect, the metal cation binds strongly on the SW defect rather than on the pristine tube. The adsorption complex of the $Cu^+$ ion corresponds to the deposition on the bridge site with strong $Cu^+$−$C_{sur}$ bonds (196.6 and 198.3 pm) whereas the adsorption complexes of $Ag^+$ and $Au^+$ ions are similar to those of the pristine SWNT system. The distances between the metal and $C_{sur}$ shorten by about 5, 10, and 7 pm for the $Cu^+$, $Ag^+$ and $Au^+$ ions, respectively. Consequently, the adsorption energies are more stable by about 18−22% ($Cu^+$, −154.4; $Ag^+$, −76.0; $Au^+$, −121.5 kcal mol$^{-1}$). The interaction

**TABLE 4: Calculated Parameters (bond lengths in pm, atomic charges $q$ in electrons, and adsorption energies $E_{ads}$ in kcal mol$^{-1}$) of Adsorption Complexes Concerning the Metal Anion M$^-$ Deposited on the Pristine and Defective SWNTs[a]**

| | | pristine SWNTs | defective SWNTs | |
|---|---|---|---|---|
| | metal | $C_{100}H_{20}$ cluster | Stone−Wales ($C_{100}H_{20}$) | vacancy ($C_{99}H_{20}$) |
| $r$(M−C) | $Cu^-$ | 195.1, 195.1 | 196.7, 199.8 | 181.3, 184.4, 189.9 |
| | $Ag^-$ | 343.0, 359.0 | 236.6 | 211.8, 217.2, 220.2 |
| | $Au^-$ | 241.4 | 222.9 | 200.5, 203.0, 211.7 |
| $q$ | $Cu^-$ | 0.18 (−0.28, −0.28) | 0.36 (−0.42, −0.41) | 0.37 (−0.25, −0.26, −0.32) |
| | $Ag^-$ | −0.36 (0.02, 0.02) | −0.13 (−0.31) | 0.14 (−0.19, −0.20, −0.24) |
| | $Au^-$ | −0.48 (−0.26) | −0.28 (−0.41) | 0.43 (−0.38, −0.33, −0.36) |
| $E_{ads}$ | $Cu^-$ | −104.4 | −128.2 | −209.9 |
| | $Ag^-$ | −15.8 | −24.4 | −39.1 |
| | $Au^-$ | −8.7 | −17.3 | −32.3 |

[a] See Table 2 for the definitions.

of metal cations on the vacancy site becomes even stronger than that on the SW defect and the pristine tube. The adsorption energies were calculated to be −210.0, −71.3, and −128.4 kcal mol$^{-1}$ for $Cu^+$, $Ag^+$, and $Au^+$, respectively. However, the adsorption energy of the $Ag^+$ ion on the vacancy site is slightly less stable than that on the SW defect by 4.7 kcal mol$^{-1}$. Compared with the adsorption complexes on the pristine tube, the M−$C_{sur}$ distances shorten by 17, 27, and 17 pm for $Cu^+$, $Ag^+$, and $Au^+$ ions, respectively. It is worth mentioning that in this case the metal cations are the electron acceptors and the nanotubes are the electron donors. Thus, the interaction is substantially enhanced by the electron transfer from the SWNTs to the metal cations. Accordingly, we can conclude that the interaction of the metal cations on the SWNTs, both for the pristine and defective tubes, is significantly stronger than that of the neutral metal atom by about 80−100, 60−70, and 100−105 kcal mol$^{-1}$ for Cu, Ag, and Au species, respectively.

For the metal anion species, we found that the interaction of the metal anion species is stronger than that of the neutral metal atoms on the same type of SWNTs but is weaker than that of the metal cation species. For instance, the estimated adsorption energies of Cu complexes are −40.9, −104.4, and −130.8 kcal mol$^{-1}$ for Cu, $Cu^-$, and $Cu^+$ species, respectively. Even distances of $Cu^-$−$C_{sur}$ (195.1 and 195.1 pm) are shorter than that of $Cu^+$−$C_{sur}$; the adsorption complex of the $Cu^-$ ion is less stable than that of the $Cu^+$ ion which is due partly to the charge repulsion between the $Cu^-$ ion and the electron-rich CNT as well as the electron transfer between the metal and the nanotubes. For the adsorption of the $Ag^-$ and $Au^-$ species, the M−$C_{sur}$ distances lengthen by 92 and 20 pm and weaker adsorption energies are obtained ($Ag^-$, −15.8; $Au^-$, −8.7 kcal mol$^{-1}$) compared with the interaction of the $Ag^+$ and $Au^+$ species. For the adsorption on the SW defect, all metal anion species bind on this site more preferably than on the pristine tube. The greater electron transfer provides strong positive charges of the M species as well as more negative charges of the $C_{sur}$ atoms as documented in Table 4. The adsorption energies of the metal anion species on the SW defect were calculated to be −128.2, −24.4, and −17.3 kcal mol$^{-1}$ for $Cu^-$, $Ag^-$, and $Au^-$ species, respectively. For the adsorption on the vacancy site, a stronger interaction by about 81.7 kcal mol$^{-1}$ ($Cu^-$ ion), 14.7 kcal mol$^{-1}$ ($Ag^-$ ion), and 15.0 kcal mol$^{-1}$ ($Au^-$ ion) is found with respect to the interaction on the SW defect. However, the interaction of metal anions is less stable than that of the metal cations on both the pristine and defective tubes by about 26, 32−52, and 93−104 kcal mol$^{-1}$ for Cu, Ag, and Au species, respectively. Note that the estimated adsorption energies of $Cu^+$ and $Cu^-$ species on the vacancy site are isoenergetic, about −210 kcal mol$^{-1}$. This is probably due to the very similar geometry of these two complexes. Furthermore, the transfer of electron density and the Pauli repulsion plays a major role in describing the interaction of these two species on the vacancy site. The transfer of electron density dominates over the Pauli repulsion for the vacancy site as compared with the SW defect and the pristine tube, especially for 3d metal atoms. Thus, the interaction of the $Cu^-$ ion which provides more electrons toward the tubes is the same as that of the $Cu^+$ ion on the vacancy site.

**3.4. Adsorption of the CO Molecule on M−SWNT Complexes.** To explore the reactivity of the M−SWNTs complexes which can serve as a gas sensor as well as a catalyst, the interaction between a CO molecule and a metal atom deposited on the atomic vacancy (M−$C_{99}H_{20}$, Figure 2c) was investigated. The M−$C_{99}H_{20}$ complex was chosen as it is the most stable adsorption complex which can be presented on the sidewall of nanotubes at room temperature. Therefore, this complex can be efficiently employed for monitoring the CO molecule. The adsorptions of the CO molecule through the C atom (OC···M−$C_{99}H_{20}$) and the O atom (CO···M−$C_{99}H_{20}$) on the Cu−$C_{99}H_{20}$ complex (cf. Figure 3) were considered. Then we applied the most stable geometry obtained from the Cu−$C_{99}H_{20}$ system to study the adsorption of the CO on Ag−$C_{99}H_{20}$ and Au−$C_{99}H_{20}$ complexes. The corresponding geometrical parameters of these adsorption complexes are reported in Table 5.

The previous DFT calculations utilizing cluster and slap models reported that the adsorption of the CO molecule on the SWNTs was very weak, particularly on the pristine SWNTs.[18,36,60−62] However, the deposition of a transition metal on the sidewall of SWNTs can stabilize the CO adsorption. A similar result is obtained from our calculations. For the Cu−$C_{99}H_{20}$ complex, the adsorption of CO through the C atom (OC···M−$C_{99}H_{20}$) is more energetically favorable than through the O atom (CO···M−$C_{99}H_{20}$) by about 22 kcal mol$^{-1}$ (cf. Table 5). This agrees reasonably well with the shortening of the Cu−C bond length (186.2 pm) as well as the lengthening of the adsorbed CO bond length (∼1 pm). We also observed a linear CO adsorption on the Cu atom (Cu−C−O angle ∼180°). On the basis of the estimated adsorption energies, the presence of Cu as well as Ag and Au atoms stabilizes the adsorption of CO on the sidewall of SWNTs. The calculated adsorption energies of CO on the Cu−$C_{99}H_{20}$, Ag−$C_{99}H_{20}$, and Au−$C_{99}H_{20}$ complexes are −26.3, −18.9, and −26.6 kcal mol$^{-1}$, respectively. The corresponding distances of Ag−C and Au−C are 208.9 and 198.4 pm, respectively. Moreover, the adsorption of CO affects the properties of the M−$C_{99}H_{20}$ complex. For instance, the interaction between the Cu atom and $C_{99}H_{20}$ weakens significantly, as seen from the lengthening of Cu−$C_{sur}$ (∼5−7 pm), upon the adsorption of CO. This also results in the change of $C_{sur}$ atomic charges which are less negative due to the reduction

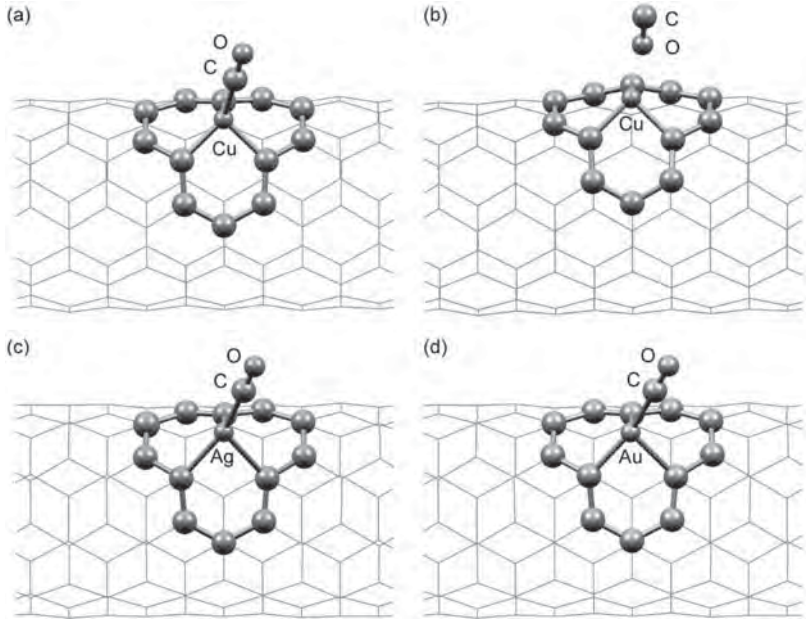


**Figure 3.** Adsorption of the CO molecule on the M−$C_{99}H_{20}$ (M = Cu, Ag, and Au) complexes: (a) OC···Cu−$C_{99}H_{20}$ complex; (b) CO···Ag−$C_{99}H_{20}$ complex; (c) OC···Ag−$C_{99}H_{20}$ complex; (d) OC···Au−$C_{99}H_{20}$ complex.

**TABLE 5: Calculated Parameters (bond lengths in pm, atomic charges $q$ in electrons, and adsorption energies $E_{ads}$ in kcal mol$^{-1}$) of Adsorption Complexes Concerning a CO Molecule Attached on the M−$C_{99}H_{20}$ (M = Cu, Ag, and Au)**

| | X = Cu−$C_{99}H_{20}$ | | X = Ag−$C_{99}H_{20}$ | X = Au−$C_{99}H_{20}$ |
|---|---|---|---|---|
| | X−CO (Figure *3*a) | X−OC (Figure *3*b) | X−CO (Figure *3*c) | X−CO (Figure *3*d) |
| $r$(C−O)[a] | 114.7 | 114.1 | 114.2 | 114.9 |
| $r$(M−CO)[b] | 186.2 | 237.5 | 208.9 | 198.4 |
| $r$(M−$C_{sur}$)[c] | 188.6, 193.1, 197.1 | 185.3, 187.2, 192.7 | 211.9, 226.0, 228.6 | 202.3, 219.7, 226.9 |
| $q_M$[d] | 0.23 (0.36, −0.28) | 0.45 (0.23, −0.17) | 0.18, (0.29, −0.26) | 0.50, (0.13, −0.28) |
| $q_C$[e] | −0.25, −0.22, −0.16 | −0.31, −0.26, −0.21 | −0.18, −0.16, −0.15 | −0.39, −0.19, −0.11 |
| $E_{ads}$ | −26.3 | −4.0 | −18.9 | −26.6 |

[a] Bond length of CO molecule. [b] Distance between the metal atom and the CO molecule. [c] Distances between the metal atom M and nearby $C_{sur}$ atoms. [d] Charges of the metal atom M. Values in parentheses are charges of the C and O atoms of the CO molecule, respectively. [e] Charges of $C_{sur}$ atoms surrounding the metal atom M.

of electron density of the Cu−C bond. Similar results are obtained from the OC···Ag−$C_{99}H_{20}$ and OC···Au−$C_{99}H_{20}$ complexes in which the Ag−$C_{sur}$ and Au−$C_{sur}$ bond lengthens by as much as 8 and 16 pm due to the adsorption of CO.

The interaction between CO and the supported M metal can be clearly explained by the classical mechanism known as the $\pi$-back-bonding mechanism.[63,64] The bonding orbitals were formed between an occupied CO orbital and an unoccupied metal orbital and between occupied metal d-orbitals and the unoccupied $\pi$*-orbital of CO. This interaction is comparable to the $\sigma$-donation from the $\sigma$ orbital of CO to sd-hybrid orbitals of the metal M and $\pi$-back-donation from the d-orbitals of the metal M to $\pi$*-orbital of CO. This $\sigma$-donation forms a new bond between the metal and the C atom of the CO molecule whereas the $\pi$-back-donation weakens the CO bond due to the nature of antibonding $\pi$* orbitals. This is obvious from the lengthening of the CO bond in all adsorption complexes. For our work, we found that the CO bond lengthens by as much as 2.1 pm when it is adsorbed on the Au−$C_{99}H_{20}$ complex.

**3.5. Adsorption of Metal Dimers on the Pristine and Defective SWNTs.** In this section, we studied the adsorption of the $Cu_2$, $Ag_2$, and $Au_2$ dimers on the pristine and defective SWNTs, the Stone−Wales, and the vacancy sites. In order to inspect the most favorable geometry of a metal dimer adsorbed on the nanotubes, the metal dimers oriented parallel (mode A) and standing (mode B) to the tube axis were considered as shown in Figures 4−6. The results concerning the geometric and energetic properties are listed in Table 6 and Table 7. Combining these with the results of the metal atoms can provide us with information concerning a propensity of dimerization on the various sites of SWNTs, which is expected to be the beginning step for the nanoparticles deposited on the nanotubes.

On the pristine SWNTs, the adsorption of the $Cu_2$ dimer in parallel orientation (mode A) is more stable than that of the standing orientation (mode B) as shown in Figure 4a. The corresponding adsorption energies were calculated to be −35.4 and −26.6 kcal mol$^{-1}$/atom for mode A and mode B, respectively. The adsorption complex in mode A involves the forming of three bondings between Cu and $C_{sur}$ atoms with distances of 192.2, 200.6, and 215.6 pm. This interaction is quite strong and leads to the reduction of electron density of the Cu−Cu bond. It is clearly seen from the lengthening of this bond (∼219.7 pm) compared with the gas phase $Cu_2$ (202.4 pm). In contrast to mode A, only one bonding of Cu and the $C_{sur}$ atom is formed in the adsorption mode B. Consequently, a smaller change in the distance of Cu−Cu (210.2 pm) is obtained. The Mulliken population analysis is also consistent with the results above. Both of the Cu atoms act as electron donors in mode A but only the Cu atom bound to the $C_{sur}$ does so for mode B. For the $Ag_2$ and $Au_2$ dimers, however, the results are different. When adsorbed on the pristine SWNTs, we found that the standing orientation of the $Ag_2$ and $Au_2$ dimers is energetically favorable

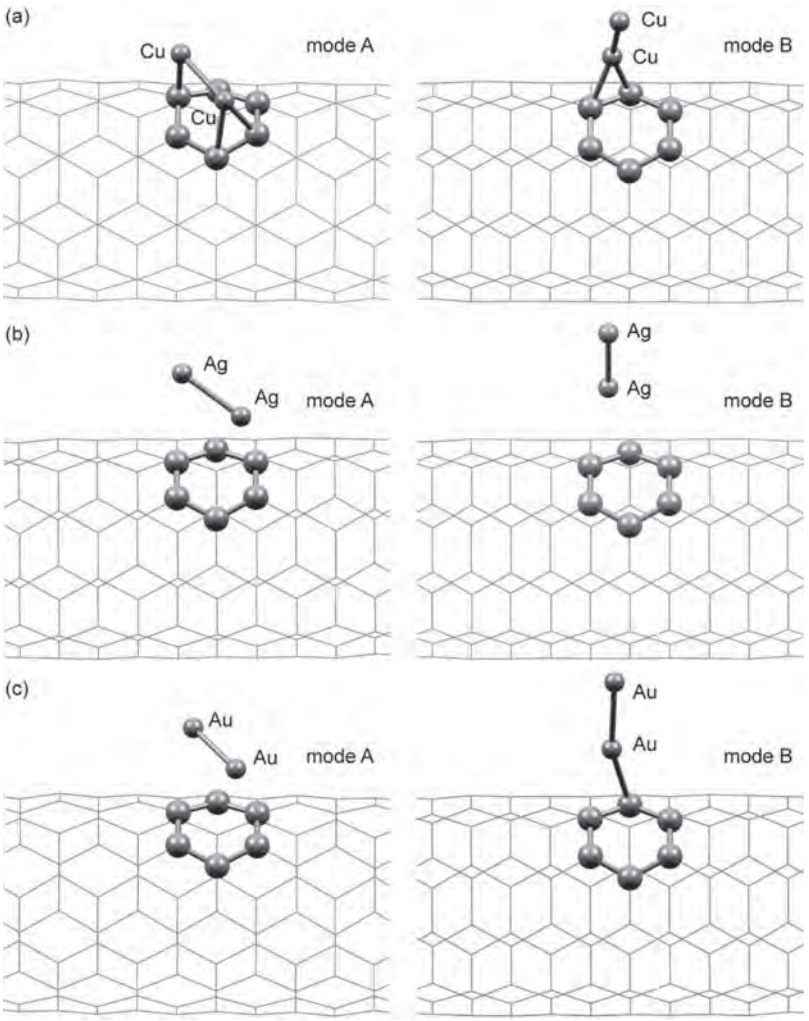


**Figure 4.** Adsorption complexes of the $M_2$ (M = Cu, Ag, and Au) dimers deposited on the pristine $C_{100}H_{20}$ cluster in adsorption mode A and mode B: (a) $Cu_2-C_{100}H_{20}$ complex; (b) $Ag_2-C_{100}H_{20}$ complex; (c) $Au_2-C_{100}H_{20}$ complex.

**TABLE 6: Calculated Parameters (bond lengths in pm, atomic charges $q$ in electrons, and adsorption energies $E_{ads}$ in kcal mol$^{-1}$) of Adsorption Complexes Concerning the Metal Dimer $M_2$ Deposited on the Pristine SWNTs[a]**

| | | pristine $C_{100}H_{20}$ | |
|---|---|---|---|
| | metal | mode A | mode B |
| $r$(M−C)[b] | Cu | 192.2, 200.6, 215.6 | 195.0, 198.2 |
| | Ag | 366.2, 405.9, 415.0, 423.6 | 276.8, 282.7 |
| | Au | 343.0, 370.6, 389.4, 398.3 | 241.3, 246.6 |
| $r$(M−M)[c] | Cu | 219.7 | 210.2 |
| | Ag | 261.6 | 261.9 |
| | Au | 257.7 | 257.3 |
| $q$[d] | Cu | 0.23 (−0.56); 0.18 (−0.33) | 0.46 (−0.57, 0.07); −0.34 |
| | Ag | −0.04 (0.0); −0.02 (0.0) | 0.06 (−0.08, −0.03); −0.19 |
| | Au | −0.07 (0.00,0.01, 0.03); −0.07 | −0.02 (−0.19, −0.10); −0.19 |
| $E_{ads}$ | Cu | −35.4 | −26.6 |
| | Ag | −0.5 | −2.0 |
| | Au | −0.8 | −6.7 |

[a] See Figure 4 for the definition of the adsorption modes. [b] Distances between the metal atom M and the nearby $C_{sur}$ atom. [c] Bond length of the metal dimer $M_2$. [d] Charges of each atom M of the metal dimer $M_2$. Values in parentheses are the charges of the $C_{sur}$ atom close to the metal atom M.

over the parallel orientation (cf. Figure 4b and Figure 4c). These results can be explained by the Pauli repulsion between the SWNTs and the metal dimers which is more pronounced than for the $Cu_2$ dimer system. Generally, the Pauli repulsion is less for small atoms as well as for an orientation of dimer in the standing mode. However, the interaction of the $Au_2$ dimer on the SWNTs is stronger than that of the $Ag_2$ dimer. The estimated adsorption energies of these complexes in mode B are −6.7 and −2.0 kcal mol$^{-1}$/atom for the $Au_2$ and $Ag_2$ dimer, respectively. The Au−$C_{sur}$ distances are about 36 pm shorter than the Ag−$C_{sur}$ distances. Moreover, binding on the nanotubes causes an increase of the metal−metal bond compared to the corresponding gas phase. Nevertheless, the adsorptions of the $Ag_2$ and $Au_2$ dimers on the pristine SWNTs are less stable than those on the defective sites (see below).

On the defective SWNTs, the orientations of metal dimers related to mode A and mode B were continually considered. Nevertheless, only some stable geometries were obtained as illustrated in Figure 5 and Figure 6. The adsorption complex of $Cu_2$ on the SW defect was found to be more stable in mode A than in mode B. The corresponding adsorption energies were calculated to be −46.0 and −30.7 kcal mol$^{-1}$/atom, respectively. The reason is due to the bonding between the Cu atom and the $C_{sur}$ atoms of SWNTs as explained above. In mode A, two Cu atoms bind strongly with the $C_{sur}$ atoms with distances of 188.3, 196.9, and 213.0 pm. Consequently, the Cu−Cu bond lengthens by 19.3 pm compared with the gas phase $Cu_2$ (202.4 pm). For mode B, the adsorption of the $Cu_2$ dimer is less stable due to

**TABLE 7: Calculated Parameters (bond lengths in pm, atomic charges $q$ in electrons, and adsorption energies $E_{ads}$ in kcal mol$^{-1}$) of Adsorption Complexes Concerning the Metal Dimer $M_2$ Deposited on the Defective SWNTs[a]**

| | | Stone−Wales $C_{100}H_{20}$ | | vacancy $C_{99}H_{20}$ | |
|---|---|---|---|---|---|
| | metal | mode A | mode B | mode A | mode B |
| $r$(M−C) | Cu | 188.3, 196.9, 213.0, 219.3 | 200.2, 205.9 | 181.6, 186.2, 198.4 191.7, 217.3, 220.8 | |
| | Ag | | 259.4 | 207.5, 210.1, 229.2, 230.5 | 220.0 |
| | Au | | 224.0 | 214.6, 207.1, 208.9, 201.3 | 202.4 |
| $r$(M−M) | Cu | 221.7 | 211.3 | 231.2 | |
| | Ag | | 262.4 | 272.0 | 264.6 |
| | Au | | 259.1 | 292.0 | 259.8 |
| $q$ | Cu | 0.22 (−0.50, −0.21); 0.30 (−0.30, −0.13) | 0.46 (−0.12, −0.21); −0.28 | 0.42 (−0.41, 0.10, −0.24); 0.36 (−0.21, −0.22) | |
| | Ag | | 0.04 (−0.18), −0.20 | 0.17 (−0.38); 0.26 (−0.23, −0.26) | 0.05 (−0.26); −0.23 |
| | Au | | −0.05 (−0.44); −0.20 | 0.60 (−0.64, −0.36, −0.35); −0.01 | 0.08 (−0.42); −0.20 |
| $E_{ads}$[b] | Cu | −46.0 | −30.7 | −79.1 | |
| | Ag | | −3.8 | −0.8 | −10.8 |
| | Au | | −10.6 | −28.2 | −23.5 |

[a] See Table 6 for the definitions. [b] The absence of $E_{ads}$ indicates that metal dimers do not bind to the tubes in the corresponding adsorption mode.

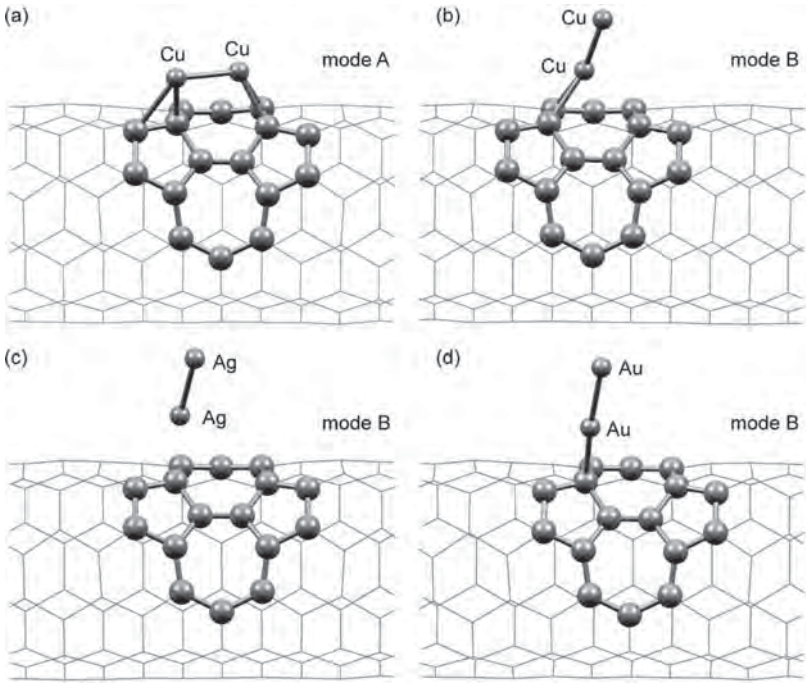


**Figure 5.** Adsorption complexes of the $M_2$ (M = Cu, Ag, and Au) dimers deposited on the Stone−Wales (SW) defect: (a) $Cu_2$−$C_{100}H_{20}$ complex in mode A; (b) $Cu_2$−$C_{100}H_{20}$ complex in mode B; (c) $Ag_2$−$C_{100}H_{20}$ complex in mode B; (d) $Au_2$−$C_{100}H_{20}$ complex in mode B.

only one Cu atom bonded to the $C_{sur}$ atoms. As expected, longer Cu−$C_{sur}$ distances (200.2 and 205.9 pm) are obtained from the adsorption complex in mode B. In contrast to the adsorption of the $Cu_2$ dimer, the optimized geometries of $Ag_2$ and $Au_2$ adsorbed on the SW defect are obtained only by the standing orientation, although various initial orientations of the dimers were applied. The strong Pauli repulsion in the parallel orientation of metal dimers probably destabilizes the adsorptions complex. As shown in Figure 5, the adsorption complex in mode B corresponds to the metal atom adsorbed directly on top of one $C_{sur}$ atom. The Ag−$C_{sur}$ and Au−$C_{sur}$ distances are 259.4 and 224.0 pm, respectively. The corresponding adsorption energies were estimated to be −3.8 and −10.6 kcal mol$^{-1}$/atom for $Ag_2$ and $Au_2$. These results are in accordance with the smaller changes in the metal−metal bond length compared with the gas phase dimers, 0.8 pm for $Ag_2$ and 2.3 pm for $Au_2$.

Table 7 shows the results concerning the metal dimer adsorption on the vacancy site, $C_{99}H_{20}$ cluster. We found that the metal dimers adsorb more strongly on the vacancy site than on the pristine tube and on the SW defect. The most stable geometry of $Cu_2$ and $Au_2$ complexes corresponds to the strong interaction between one metal atom and the nearby $C_{sur}$ atoms as illustrated in Figure 6. The corresponding adsorption energies of the $Cu_2$ and $Au_2$ dimers were calculated to be −79.1 and −28.2 kcal mol$^{-1}$/atom, respectively. This strong interaction is in accordance with the change in geometry of the metal dimer. Compared with the gas phase dimers, distances of Cu−Cu and Au−Au increase significantly by 28.8 and 45.2 pm, respectively. As described above, the electron density of such a metal−metal bond decreases dramatically. For the adsorption complex of $Ag_2$, the dimer interacts on the $C_{suf}$ atom in the upright position by one Ag atom. The corresponding Ag−$C_{sur}$ and Ag−Ag distances are 220.0 and 264.6 pm, respectively. The adsorption energy of $Ag_2$ was estimated to be −10.8 kcal mol$^{-1}$/atom. This similar mode of adsorption complex is also found for the $Au_2$ dimer, but it is less stable than the adsorption complex in mode A by

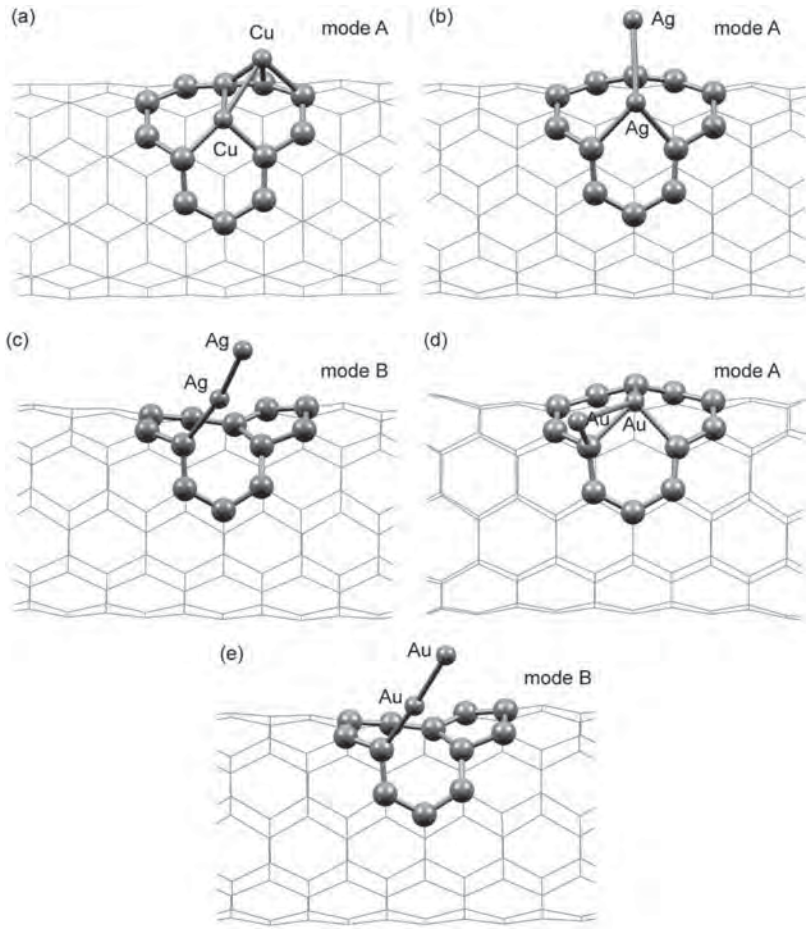


**Figure 6.** Adsorption complexes of the $M_2$ (M = Cu, Ag, and Au) dimers deposited on the vacancy defect ($C_{99}H_{20}$): (a) $Cu_2-C_{99}H_{20}$ complex in mode A; (b) $Ag_2-C_{99}H_{20}$ complex in mode A; (c) $Ag_2-C_{99}H_{20}$ complex in mode B; (d) $Au_2-C_{99}H_{20}$ complex in mode A; (e) $Au_2-C_{99}H_{20}$ complex in mode B.

about 5 kcal $mol^{-1}$/atom. It is worth mentioning that the orientation of the metal dimer in the upright position (mode B) diminishes the Pauli repulsion as well as the distortion in geometry of the metal dimer with respect to the other adsorption modes. Moreover, the electron transfer from the metal dimers to the SWNTs appeared from our results as the metal atom in contact with the $C_{sur}$ atom exhibits positive charges while the charges of nearby $C_{sur}$ atoms are negative. This implies that the transfer of electron density and the Pauli repulsion play a crucial role for determining the most stable adsorption complex.

Finally, we discuss the crucial stage as to whether indeed defect sites on SWNTs are stronger attractors for nucleation than the pristine tube. The stability of a dimer $M_2$ adsorbed at any site under inspection ($M_2$/$SWNTs_{site}$) with respect to two adatoms M, one of them bound to this site ($M_1$/$SWNTs_{site}$) and the other attached to the surface of the pristine SWNTs site ($M_1$/$SWNTs_{prist}$), is characterized by the following dimer dissociation energy on a surface site (per atom).[65,66]

$$E_{dis} = [E(M_1/SWNTs_{prist}) + E(M_1/SWNTs_{site}) - E(M_2/SWNTs_{site}) - E(SWNTs_{prist})]/2 \quad (2)$$

From Table 8, one sees that on the pristine tube $E_{dis}$ is 17−24 kcal $mol^{-1}$/atom, slightly larger for $Au_2$ than for $Cu_2$ and $Ag_2$. These values are close to the gas phase values, $D_e$ (Table 1). The dimer dissociation energies on all sites are not significantly different except for $Ag_2$ and $Au_2$ adsorbed on the vacancy site.

**TABLE 8: Comparison of Adsorption Energies ($E_{ads}$) of the Neutral Metal Atom and the Metal Dimer (kcal $mol^{-1}$/atom) on Pristine and Defective SWNTs as Well as the Dissociation Energies ($E_{dis}$) of Adsorbed Dimers**

| site | metal | $D_e$[a] | $E_{ads}$ ($M_1$)[b] | $E_{ads}$ ($M_2$)[c] | $E_{dis}$ ($M_2$)[d] |
|---|---|---|---|---|---|
| pristine tube | Cu | 25.6 | −40.9 | −35.4 | 20.1 |
| | Ag | 17.4 | −0.5 | −2.0 | 17.5 |
| | Au | 21.8 | −4.0 | −6.7 | 24.5 |
| SW defect | Cu | 25.6 | −53.8 | −46.0 | 20.0 |
| | Ag | 17.4 | −4.0 | −3.8 | 19.0 |
| | Au | 21.8 | −15.0 | −10.6 | 22.9 |
| vacancy site | Cu | 25.6 | −131.3 | −79.1 | 18.6 |
| | Ag | 17.4 | −10.8 | −10.8 | 22.6 |
| | Au | 21.8 | −26.3 | −28.2 | 34.9 |

[a] Table 1. [b] Table 2. [c] Table 6 and Table 7. [d] $E_{dis} = [E(M_1/SWNTs_{prist}) + E(M_1/SWNTs_{site}) - E(M_2/SWNTs_{site}) - E(SWNTs_{prist})]/2$.

The stability of the adsorbed $Cu_2$ dimer on any sites decreases as seen from the depressing of $E_{dis}$ by 5−7 kcal $mol^{-1}$/atom with respect to the gas phase value. This can be described by the strong interaction of the $Cu_2$ dimer on the SWNTs which causes an increase of the Cu−Cu bond length. Different results, however, are obtained for the adsorption of $Ag_2$ and $Au_2$ dimers. They are stabilized on all sites of SWNTs because the $Ag_2$ and $Au_2$ dimers which are in upright orientation do not substantially distort from the gas phase geometry. This is in accordance with the orientation of the metal dimer present in the most stable geometry (cf. Figures 4−6). Therefore, the adsorption on the SWNTs stabilizes the gas phase dimer for $Ag_2$ and $Au_2$ dimers but destabilizes for the $Cu_2$ dimer with respect to the gas phase

energies. Thus far, one may speculate that only $Ag_2$ and $Au_2$ dimers are stable on the sidewall of SWNTs with respect to dissociation on the surface and do not dissociate to monatomic species. In addition, the results demonstrate that the propensity for dimerization on pristine sites is virtually the same as that on SW and vacancy sites except for the Ag and Au atoms on the vacancy site. The calculated dimer dissociation energy shows that the stability of Ag and Au dimers on the vacancy site is higher than that on the pristine tube by 5.1 and 10.4 kcal $mol^{-1}$, respectively.

## 4. Conclusion

The interactions of atomic metal species and metal dimers on the different surfaces of the SWNTs was studied by means of DFT combined with the quantum cluster model representing the nanotube structure. We identified the most favorable adsorption site and geometry of adsorption complexes as well as the propensity of dimerization of the adsorbed metal atom.

For the interaction of atomic metal species on the pristine and defective SWNTs, we found that the metal cation binds more strongly than the metal anion and the neutral metal atom, respectively. The transfer of electron density between the metal species and the nanotubes as well as the electrostatic attraction, counteracted by the Pauli repulsion, mainly contributes to such strong interaction. On the pristine SWNTs, the Cu species interact strongly with several $C_{sur}$ atoms of the nanotubes while most of the Ag and Au species bind directly on top of a $C_{sur}$ atom. Consequently, the adsorption complexes of Cu species are more stable than those of the Au and Ag species. Moreover, the defects presented on the SWNTs affect the structural and energetic properties of the adsorption complexes. All metal species are likely to deposit on the defect sites, on the vacancy site in particular, rather than on the pristine tube. The adsorption on the vacancy site is notably stronger than that on other sites for two reasons. The Pauli repulsion between this site and metal species is lessened and the electron densities of the metal species as well as that of the vacancy are easier to polarize. The Mulliken population analysis confirms qualitatively that the transfer of electron density between the metal species and the nanotubes induces a positive charge of the metal species as well as a negative charge of nearby $C_{sur}$ atoms. From the study of CO adsorption on the $M-C_{99}H_{20}$ complex, additionally, the metal atom deposited on the atomic vacancy is potentially used as the hybrid metal−SWNTs material for monitoring the CO molecule.

For the adsorption of metal dimers, a similar order of interaction is obtained for all types of SWNTs: $Cu_2 > Au_2 > Ag_2$. The weakness of the metal dimer bonding during the adsorption is mainly due to the transfer of electron density from the bonding of $M_2$ to the nanotubes. This results in the increase of the M−M distance. However, such a M−M bond does not break down reflecting that the interaction of metal−metal is stronger than that of metal−SWNTs. The effective adsorption energy per atom is also found to decrease from the metal atom to the metal dimer. On various sites of SWNTs, the adsorption complexes of the $Cu_2$ dimer involve the interaction of two Cu atoms on the $C_{sur}$ atoms and consequently exhibit the strongest adsorption energy: −35.4 (pristine tube), −46.0 (SW defect), and −79.1 kcal $mol^{-1}$/atom (vacancy defect). In contrast to the $Cu_2$ dimer, most of the adsorption complexes of $Ag_2$ and $Au_2$ dimers correspond to the upright orientation of the metal dimers with respect to the tube axis. This orientation reduces the Pauli repulsion between the metal dimers and the nanotubes. However, the adsorptions of the $Ag_2$ and $Au_2$ dimers are weaker than that of the $Cu_2$ dimer for all sites of SWNTs.

On the basis of calculated interaction energies, we conclude that dimerization of adsorbed atoms on the SW defect is not particularly favored compared to dimerization on the pristine tube. However, the dimerization of Ag and Au atoms on the vacancy site is more stable than that on the pristine tube by 5.1 and 10.4 kcal $mol^{-1}$, respectively. In general, cluster growth is a complicated phenomenon; it is significantly affected by the type of metal as well as the type of sites on the sidewall of SWNTs involved in the very first stage of the metal nucleation. Therefore, high-level electronic structure calculations of adequate models are of special importance for providing information on the metal dimerization processes.

**Acknowledgment.** This work was supported by the Thailand Research Fund and the Commission on Higher Education (TRF-CHE: No. MRG5080253), the NSTDA Chair Professor, and NANOTEC Center of Excellence funded by the National Nanotechnology Center, the Commission on Higher Education, Ministry of Education (the "National Research University Project of Thailand (NRU)". The authors are grateful to Dr. Christian Herbst for helpful discussions.

## References and Notes

(1) Iijima, S. *Nature* **1991**, *354*, 56.
(2) Iijima, S.; Ichihashi, T. *Nature* **1993**, *363*, 603.
(3) Hamada, N.; Sawada, S.; Oshiyama, A. *Phys. Rev. Lett.* **1992**, *68*, 1579.
(4) Byon, H. R.; Choi, H. C. *J. Am. Chem. Soc.* **2006**, *128*, 2188.
(5) Chen, Z.; Appenzeller, J.; Lin, Y. M.; Sippel-Oakley, J.; Rinzler, A. G.; Tang, J.; Wind, S. J.; Solomon, P. M.; Avouris, P. *Science* **2006**, *311*, 1735.
(6) Lastella, S.; Mallick, G.; Woo, R.; Karna, S. P.; Rider, D. A.; Manners, I.; Jung, Y. J.; Ryu, C. Y.; Ajayan, P. M. *J. Appl. Phys.* **2006**, *99*, 024302.
(7) Singh, K. V.; Pandey, R. R.; Wang, X.; Lake, R.; Ozkan, C. S.; Wang, K.; Ozkan, M. *Carbon* **2006**, *44*, 1730.
(8) Liu, J.; Tian, S.; Knoll, W. *Langmuir* **2005**, *21*, 5596.
(9) Jeng, E. S.; Moll, A. E.; Roy, A. C.; Gastala, J. B.; Strano, M. S. *Nano Lett.* **2006**, *6*, 371.
(10) Kose, M. E.; Harruff, B. A.; Lin, Y.; Veca, L. M.; Lu, F.; Sun, Y. P. *J. Phys. Chem. B* **2006**, *110*, 14032.
(11) Collins, P. G.; Bradley, K.; Ishigami, M.; Zettl, A. *Science* **2000**, *287*, 1801.
(12) Kong, J.; Franklin, N. R.; Zhou, C. W.; Chapline, M. G.; Peng, S.; Cho, K. J.; Dai, H. J. *Science* **2000**, *287*, 622.
(13) Rozhin, A. G.; Sakakibara, Y.; Tokumoto, M.; Kataura, H.; Achiba, Y. *Thin Solid Films* **2004**, 464.
(14) Sakakibara, Y.; Rozhin, A. G.; Kataura, H.; Achiba, Y.; Tokumoto, M. *Jpn. J. Appl. Phys.* **2005**, *44*, 1621.
(15) Cuong, N. T.; Fujiwara, A.; Mitani, T.; Chi, D. H. *Comput. Mater. Sci.* **2008**, *44*, 163.
(16) Feldman, A. K.; Steigerwald, M. L.; Guo, X.; Nuckolls, C. *Acc. Chem. Res.* **2008**, *41*, 1731.
(17) Miyata, Y.; Yanagi, K.; Maniwa, Y.; Kataura, H. *J. Phys. Chem. C* **2008**, *112*, 13187.
(18) Yeung, C. S.; Liu, L. V.; Wang, Y. A. *J. Phys. Chem. C* **2008**, *112*, 7401.
(19) Li, J.; Lu, Y.; Ye, Q.; Cinke, M.; Han, J.; Meyyappan, M. *Nano Lett.* **2003**, *3*, 929.
(20) Mercuri, F.; Sgamellotti, A. *Inorg. Chim. Acta* **2007**, *360*, 785.
(21) Wang, G.; Huang, Y. *J. Phys. Chem. C* **2008**, *112*, 9128.
(22) Durgun, E.; Dag, S.; Bagci, V. M. K.; Gülseren, O.; Yildirim, T.; Ciraci, S. *Phys. Rev. B* **2003**, *67*, 201401.
(23) Zhuang, H. L.; Zheng, G. P.; Soh, A. K. *Comput. Mater. Sci.* **2008**, *43*, 823.
(24) Lin, Y.; Watson, K. A.; Fallbach, M. J.; Ghose, S.; Smith, J. G.; Delozier, D. M.; Cao, W.; Crooks, R. E.; Connell, J. W. *Acs Nano* **2009**, *3*, 871.
(25) Guo, D.-J.; Li, H.-L. *J. Colloid Interface Sci.* **2005**, *286*, 274.
(26) Qu, L.; Dai, L. *J. Am. Chem. Soc.* **2005**, *127*, 10806.
(27) Quinn, B. M.; Dekker, C.; Lemay, S. G. *J. Am. Chem. Soc.* **2005**, *127*, 6146.
(28) Zhao, Q.; Nardelli, M. B.; Lu, W.; Bernholc, J. *Nano Lett.* **2005**, *5*, 847.
(29) Zhang, G.; Qi, P.; Wang, X.; Lu, Y.; Mann, D.; Li, X.; Dai, H. *J. Am. Chem. Soc.* **2006**, *128*, 6026.

(30) Qu, L.; Dai, L.; Osawa, E. *J. Am. Chem. Soc.* **2006**, *128*, 5523.
(31) Larciprete, R.; Petaccia, L.; Lizzit, S.; Goldoni, A. *J. Phys. Chem. C* **2007**, *111*, 12169.
(32) Okada, S. *Chem. Phys. Lett.* **2007**, *447*, 263.
(33) Inoue, S.; Matsumura, Y. *Carbon* **2008**, *46*, 2046.
(34) Khongpracha, P.; Probst, M.; Limtrakul, J. *Eur. Phys. J. D* **2008**, *48*, 211.
(35) Pannopard, P.; Khongpracha, P.; Probst, M.; Limtrakul, J. *J. Mol. Graphics Modell.* **2008**, *26*, 1066.
(36) Zhao, J.-X.; Ding, Y.-H. *Mater. Chem. Phys.* **2008**, *110*, 411.
(37) An, W.; Turner, C. H. *J. Phys. Chem. C* **2009**, *113*, 7069.
(38) Inoue, S.; Suto, H.; Wongwiriyapan, W.; Kimura, T.; Murata, Y.; Honda, S.; Katayama, M. *Appl. Phys. Express* **2009**, *2*, 035005.
(39) Ni, M. Y.; Zeng, Z.; Ju, X. *Microelectron. J.* **2009**, *40*, 863.
(40) Pannopard, P.; Khongpracha, P.; Probst, M.; Limtrakul, J. *J. Mol. Graphics Modell.* **2009**, *28*, 62.
(41) Zhao, J.-X.; Ding, Y.-h. *Mater. Chem. Phys.* **2009**, *116*, 21.
(42) Yagi, Y.; Briere, T. M.; Sluiter, M. H. F.; Kumar, V.; Farajian, A. A.; Kawazoe, Y. *Phys. Rev. B* **2004**, *69*, 075414.
(43) Charlier, J.-C. *Acc. Chem. Res.* **2002**, *35*, 1063.
(44) Li, X.; Niu, J.; Zhang, J.; Li, H.; Liu, Z. *J. Phys. Chem. B* **2003**, *107*, 2453.
(45) Ishigami, M.; Choi, H. J.; Aloni, S.; Louie, S. G.; Cohen, M. L.; Zettl, A. *Phys. Rev. Lett.* **2004**, *93*, 196803.
(46) Yang, S. H.; Shin, W. H.; Lee, J. W.; Kim, S. Y.; Woo, S. I.; Kang, J. K. *J. Phys. Chem. B* **2006**, *110*, 13941.
(47) Becke, A. D. *J. Chem. Phys.* **1993**, *98*, 5648.
(48) Lee, C.; Yang, W.; Parr, R. G. *Phys. Rev. B* **1988**, *37*, 785.
(49) Frisch, M. J. T., G. W.; Schlegel, H. B.; Scuseria, G. E.; Robb, M. A.; Cheeseman, J. R.; Montgomery, J. A., Jr.; Vreven, T.; Kudin, K. N.; Burant, J. C.; Millam, J. M.; Iyengar, S. S.; Tomasi, J.; Barone, V.; Mennucci, B.; Cossi, M.; Scalmani, G.; Rega, N.; Petersson, G. A.; Nakatsuji, H.; Hada, M.; Ehara, M.; Toyota, K.; Fukuda, R.; Hasegawa, J.; Ishida, M.; Nakajima, T.; Honda, Y.; Kitao, O.; Nakai, H.; Klene, M.; Li, X.; Knox, J. E.; Hratchian, H. P.; Cross, J. B.; Adamo, C.; Jaramillo, J.; Gomperts, R.; Stratmann, R. E.; Yazyev, O.; Austin, A. J.; Cammi, R.; Pomelli, C.; Ochterski, J. W.; Ayala, P. Y.; Morokuma, K.; Voth, G. A.; Salvador, P.; Dannenberg, J. J.; Zakrzewski, V. G.; Dapprich, S.; Daniels, A. D.; Strain, M. C.; Farkas, O.; Malick, D. K.; Rabuck, A. D.; Raghavachari, K.; Foresman, J. B.; Ortiz, J. V.; Cui, Q.; Baboul, A. G.; Clifford, S.; Cioslowski, J.; Stefanov, B. B.; Liu, G.; Liashenko, A.; Piskorz, P.; Komaromi, I.; Martin, R. L.; Fox, D. J.; Keith, T.; Al-Laham, M. A.; Peng, C. Y.; Nanayakkara, A.; Challacombe, M.; Gill, P. M. W.; Johnson, B.; Chen, W.; Wong, M. W.; Gonzalez, C.; Pople, J. A. *Gaussian 03, revision E.01*; Gaussian, Inc.: Wallingford, CT, 2004.
(50) Hay, P. J.; Wadt, W. R. *J. Chem. Phys.* **1985**, *82*, 299.
(51) Morse, M. D. *Chem. Rev.* **1986**, *86*, 1049.
(52) Simard, B.; Hackett, P. A.; James, A. M.; Langriedge-Smith, P. R. R. *Chem. Phys. Lett.* **1991**, *186*, 415.
(53) Krämer, H. G.; Beutel, V.; Weyers, K.; Demtröder, W. *Chem. Phys. Lett.* **1992**, *193*, 331.
(54) Rossato, J.; Baierle, R. J.; Fazzio, A.; Mota, R. *Nano Lett.* **2005**, *5*, 197.
(55) Lu, A. J.; Pan, B. C. *Phys. Rev. Lett.* **2004**, *92*, 105504.
(56) Zhang, B.-X.; Yang, C.; Feng, Y.-F.; Yu, Y. *Acta Phys. Sin.* **2009**, *58*, 4066.
(57) Perdew, J. P.; Burke, K.; Ernzerhof, M. *Phys. Rev. Lett.* **1996**, *77*, 3865.
(58) Durgun, E.; Dag, S.; Ciraci, S.; Gulseren, O. *J. Phys. Chem. B* **2004**, *108*, 575.
(59) Gulseren, O.; Yildirim, T.; Ciraci, C. *Phys. Rev. Lett.* **2001**, *87*, 116802.
(60) Peng, S.; Cho, K. *Nano Lett.* **2003**, *3*, 513.
(61) Star, A.; Joshi, V.; Skarupo, S.; Thomas, D.; Gabriel, J.-C. P. *J. Phys. Chem. B* **2006**, *110*, 21014.
(62) Silva, L. B.; Fagan, S. B.; Mota, R. *Nano Lett.* **2004**, *4*, 65.
(63) Blyholder, G. *J. Phys. Chem.* **1964**, *68*, 2772.
(64) Treesukol, P.; Srisuk, K.; Limtrakul, J.; Truong, T. N. *J. Phys. Chem. B* **2005**, *109*, 11940.
(65) Del Vitto, A.; Sousa, C.; Illas, F.; Pacchioni, G. *J. Phys. Chem.* **2004**, *121*, 7457.
(66) Inntam, C.; Moskaleva, L. V.; Neyman, K. M.; Nasluzov, V. A.; Rösch, N. *Appl. Phys. A: Mater. Sci. Process.* **2006**, *82*, 181.

JP109098Q

THE JOURNAL OF PHYSICAL CHEMISTRY C

ARTICLE

pubs.acs.org/JPCC

# Healing of a Vacancy Defect in a Single-Walled Carbon Nanotube by Carbon Monoxide Disproportionation

Teeranan Nongnual and Jumras Limtrakul*

Laboratory for Computational and Applied Chemistry, Department of Chemistry, Faculty of Science, Center of Nanotechnology, Kasetsart University Research and Development Institute, Center for Advanced Studies in Nanotechnology and Its Applications in Chemical, Food and Agricultural Industries, and NANOTEC Center of Excellence, National Nanotechnology Center, Kasetsart University, Bangkok 10900, Thailand

**ABSTRACT:** We propose a new mechanism for the bimolecular healing of the vacancy defect in single-walled carbon nanotubes (SWCNTs). The mechanism is of particular importance to avoid the errors often encountered in the electronic properties of carbon nanotubes. Using density functional theory (DFT) calculations with the Perdew−Burke−Ernzerhof (PBE) functional, we investigate the reaction mechanism of the healing process of the monatomic vacancy defect in the (8, 0) SWCNT via carbon monoxide disproportionation. It is found that the proposed mechanism is theoretically possible and it has the following advantages: (1) The activation energy is only 9.37 kcal·mol$^{-1}$ for the 4-membered-ring-opening step at high CO concentrations; (2) no catalyst is needed, and thus no purification step is needed to remove the catalyst; (3) the CO can be used as a reactant; (4) no oxygen byproduct is found; and (5) there is a high selectivity of CO for vacancy defect sites. Our finding establishes that a CNT with a vacancy defect, as it is generally obtained from the syntheses or from uses as a nanomaterial device, can be healed completely and resumes its function as a perfect CNT displaying the original electronic properties.

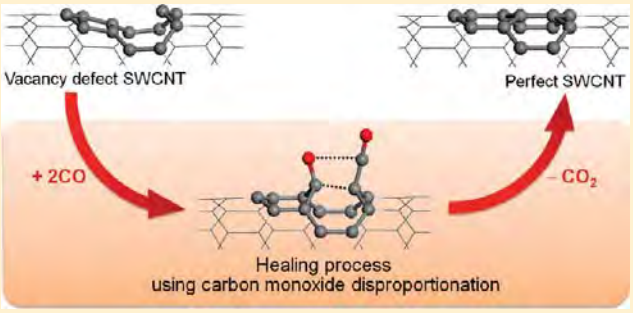


## INTRODUCTION

Carbon nanotubes (CNTs) have played a crucial role in nanomaterial science since the confirmation of the discovery of single-walled carbon nanotubes (SWCNTs) by Iijima and Ichihashi[1] and Bethune et al.[2] The structure of a SWCNT can be conceptualized by wrapping a one-atom-thick layer of graphite, called graphene, into a seamless cylinder represented by a chiral vector with a pair of indices ($n$, $m$). This discovery led to the categorization of carbon nanotubes into three common types, which are zigzag, armchair, and chiral. Due to the small electronic band gap of the semiconducting single-walled carbon nanotubes (S-SWCNT) that obeys the $(n - m) \neq 3i$ rule, it is easier there than in metallic carbon nanotubes to create new impurity states within the band gap. CNT-based devices such as molecular sensors[3,4] have been created by use of this unique characteristic. Many previous studies related to S-SWCNT sensors focused on the change in the electronic properties or in the band gap after the adsorption of a molecule on the ideal nondefective pure or doped carbon nanotube.[5−8]

SWCNTs are usually studied theoretically as if they were perfectly crystalline wires even though the highest quality tubes that can be synthesized contain at least one defect per 4 $\mu$m, on average, with a distribution weighted toward areas of curvature.[9] The ozone titration method indicated that SWCNTs contain a fractional defect level of 5.5% ± 2.5%, as measured by the presence of oxidized carbon atoms at these sites.[10] Defects such as these can be created at the stage of SWCNT growth, chemical treatment, or irradiation.[11] The presence of these defects can degrade the performance and reliability of CNT-based devices. In addition, the defects can significantly cause two important errors in the sensing; essentially due to a shift of the band gap of the defect in the carbon nanotube and an under- or overbinding between the adsorbed molecule and the defect.

The crystallographic defects in carbon nanotubes can be divided into three main groups, which are native atomic rearrangements, impurities or adatoms, and atomic vacancies. This study reviews the healing techniques for these defects. The well-known atomic rearrangement defect, the Stone−Wales (SW) defect,[12] in which pentagon and heptagon pairs (5−7−7−5 rings) are observed, can be healed by a rearrangement that returns the tube back to pristine. The SW defects can be practically repaired under an applied current of 2.4 $\mu$A·nm$^{-1}$ for thermal electronic excitation.[13] Impurity defects such as squares, three-atom protrusions, or 7−5−5−7 hillocklike defects can shed the extra atoms spontaneously under high-temperature conditions or by use of an electron beam.[14,15] $H_2$ adsorption on the hillocklike defect can heal it by fetching the adatoms and releasing $C_2H_2$ with an energy barrier of 1.26 eV.[16] $O_2$ and $CO_2$ molecules can also etch a 7−5−5−7

**Received:** November 6, 2010
**Revised:** February 5, 2011
**Published:** March 01, 2011

  

defect and an isolated C adatom, respectively, on sufficiently large CNTs, releasing two CO molecules.

Molecular dynamics simulations were used to investigate two kinds of large vacancy defects induced by compressive or torsional buckling of SWCNTs.[17] It was found that this defect was reconstructed during unloading of the external carbon sources or by increasing the temperature, forming nonhexagonal rings and SW defects, resulting in a self-healing process. Dynamic electron microscopy tracking of the healing process confirmed the closing of multivacancies of up to approximately 20 missing atoms.[15] Metallic carbon nanotubes with a monatomic vacancy (12-membered ring) induced by illumination can be electronically excited with self-healing abilities, forming 5- and 9-membered rings.[18] The defect healing process of the $sp^2$ carbon cap, which resulted in the removal of the 5−7, adatom, and monovacancy defects,[19,20] occurred via ring isomerization during SWCNT growth. These studies demonstrated the vacancy self-healing ability, but a perfect tube was not reached at the end. If the vacancy defect has not been healed completely, even during CNT growth, a foreign carbon atom must be introduced from external carbon sources in order to repair this defect.

A new method of SWCNT production has been introduced that uses a gas-phase catalytic process reaching 79 mol % of carbon nanotubes.[21] The carbon nanotube is grown by thermal decomposition of the catalyst, iron pentacarbonyl, in a heated flow of high-pressure carbon monoxide (known as the HiPco method). Tubes with diameters as small as 0.7 nm, the same as that of a fullerene, were produced.

A solid carbon growth mechanism was proposed, involving CO disproportionation (the Boudouard reaction) with $Fe(CO)_n$ as a catalyst.

CO disproportionation:

$$CO(g) + CO(g) \rightarrow C(s) + CO_2(g)$$

Ambient CO is used as a carbon source in the commercial HiPco method. A CO molecule can be detected by deformed CNTs but not by pristine CNTs. The radial-deformed SWCNTs change electronic properties, allowing functionalization of the tube surface to detect the presence of CO molecules.[22] In addition, metal-decorated carbon nanotubes were proposed as promising candidates for sensors: titanium-coated carbon nanotube,[23] aluminum-doped SWCNTs,[24] and Au-supported single-walled carbon nanotube and nanohorn.[25] Defect graphene sheets were also used to detect CO gas with adsorption energy of −2.33 eV, compared to that of the perfect graphene sheets of −0.12 eV.[26]

According to the need for an external carbon source for vacancy healing, we introduce an alternative mechanism of bimolecular healing by CO disproportionation without a metal catalyst, mimicking the HiPco method, in order to leave a carbon atom filling the vacancy site on the side walls of a SWCNT. In other words, the defect carbon nanotube acts as a catalyst supporting the disproportionation of two CO molecules and then heals itself by the carbon atom it produced.

## METHODOLOGY

The model and periodic calculations were chosen following our recent calibration[27] with semiconducting SWCNTs with concern to computational efficiency. The (8, 0) SWCNT was chosen because it is the smallest representative S-SWCNT. Its

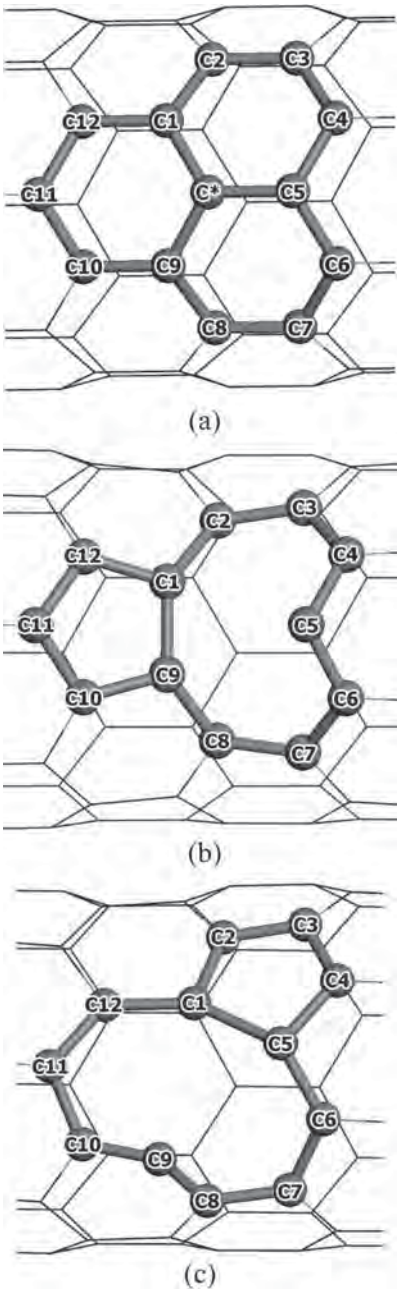


**Figure 1.** Optimized geometries of (a) pSWCNT, (b) symmetrical dSWCNT, and (c) asymmetrical dSWCNT labeled systematically with C1−C12, presenting the 5- and 9-membered rings at the defect site, and C*, the leaving carbon atom, leading to the defect of the SWCNT.

geometrical structure was generated in a supercell periodic box of 20 × 20 × 12.78 $Å^3$, composed of three repeated unit cells of SWCNT along the tube axis. The closest distance between two neighboring SWCNTs was set to be 13.77 Å in order to be able to ignore intertube interactions in the calculations. Since all carbon atoms in the S-SWCNT have the same topology, the monatomic vacancy defect in the (8, 0) SWCNT (dSWCNT) was built by removing one carbon atom (C* as shown in Figure 1a), resulting in the defect site called bicyclo[7,3,0]dodecane (5- and 9-membered rings) numbered C1 to C12 (Figure 1b). The distance


dx.doi.org/10.1021/jp110616c |J. Phys. Chem. C 2011, 115, 4649–4655

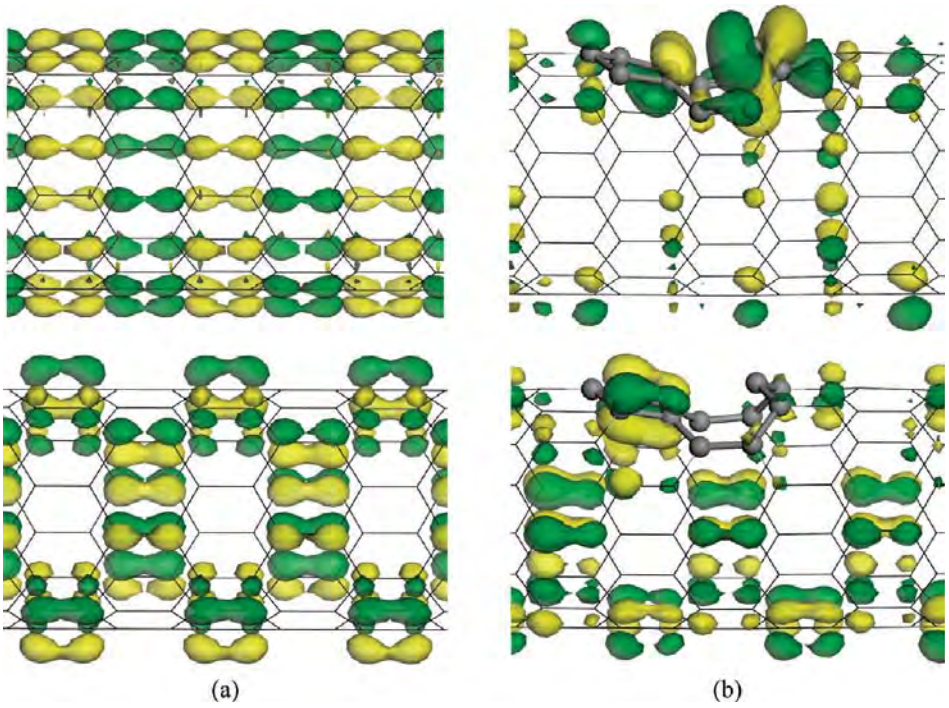


**Figure 2.** Lowest unoccupied molecular orbital (LUMO, top) and highest occupied molecular orbital (HOMO, bottom) of (a) pSWNCT and (b) symmetrical dSWCNT, plotted with an isovalue of $\pm 0.03$ e·Å$^{-3}$.

between two adjacent defect or reaction sites on the same carbon nanotube was larger than 10 Å, in order to neglect the intermolecular interactions between defect sites. The periodic calculations were carried out by the density functional theory (DFT) method with the Perdew−Burke−Ernzerhof (PBE) functional[28] as implemented in the DMol$^3$ package.[29,30] The generalized gradient approximation (GGA) and an all-electron double numerical basis set plus d-functions (DND) were chosen for these spin-unrestricted computations. The DND basis set corresponds to a double-ζ quality basis set with d-type polarization functions added to heavier atoms; it is comparable to the 6-31G* Gaussian basis sets. The real-space global cutoff radius was set to be 3.70 Å. The Brillouin zone was sampled by the Monkhorst−Pack scheme.[31] For geometrical optimizations and orbital analysis, only the Γ point was considered in the Brillouin zone and all atom positions were fully optimized until all the forces on the atoms were less than 0.05 eV·Å$^{-1}$. In order to gain accuracy, the $k$ points were increased to be $1 \times 1 \times 10$ to calculate the electronic properties. All possible mechanisms were searched.

The binding energy ($E_b$) of all reaction steps was calculated from the following equation, where $n$ is the number of $CO_x$ molecules ($n$ = 0, 1, or 2; $CO_x$ = CO or $CO_2$):

$$E_b(\text{dSWCNT-}n\text{CO}_x) = [E(\text{dSWCNT}) + nE(\text{CO}_x)] - E(\text{dSWCNT-}n\text{CO}_x) \quad (1)$$

## RESULTS AND DISCUSSION

A new mechanism of healing the monatomic vacancy defect in dSWCNT is proposed here that uses CO disproportionation. The mechanism pathway is proposed as follows, where the perfect (8, 0) SWCNT is noted as pSWCNT:

CO adsorption process:

$$\text{dSWCNT} + 2\text{CO} \rightarrow \text{dSWCNT-CO-CO}$$

CO coadsorption process:

$$\text{dSWCNT-CO} + \text{CO} \rightarrow \text{dSWCNT-CO-CO}$$

Healing and desorption processes:

$$\text{dSWCNT-CO-CO} \rightarrow \text{pSWCNT} + \text{CO}_2$$

The electronic properties of the pSWCNT were calculated, yielding an energy gap ($E_{gap}$) of 0.65 eV, which is close to our recent work[27] dealing with both experimental and theoretical data. This energy gap confirms the semiconducting behavior of the zigzag (8, 0) carbon nanotube, which obeys the $(n - m) \neq 3i$ rule.

After elimination of the C* atom, the 12-membered ring remains with different initial distances, C1···C9 of 2.440 Å and C1···C5 and C1···C9 of 2.467 Å. The tube curvature distorts the 120° hybridization angle of the sp$^2$ C*, and the C1−C*−C9 and C5−C*−C9 angles decreased by 3.15° and 0.31°, respectively. This leads to a first-aid self-healing process forming the 5- and 9-membered rings. These 5−9 rings can be considered as two optimized configurations: a symmetrical form with the C1−C9 bond and an asymmetrical form with the C1−C5 bond (symmetrically equivalent to the C9−C5 bond). The symmetrical form is favorable due to a shorter initial distance and a lower relative energy by 29.65 kcal·mol$^{-1}$. Therefore, the symmetrical dSWCNT is chosen in this study.


dx.doi.org/10.1021/jp110616c |J. Phys. Chem. C 2011, 115, 4649–4655

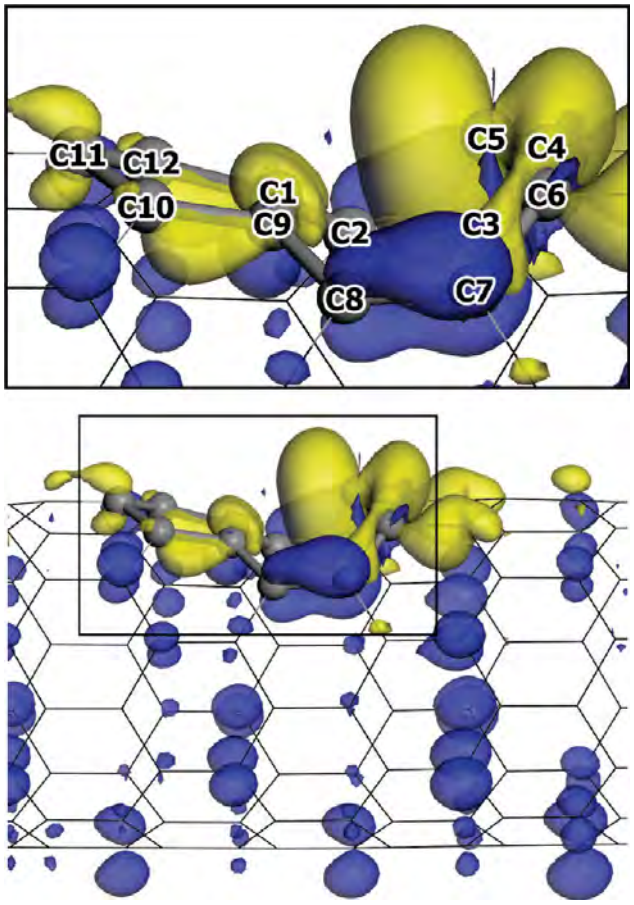


**Figure 3.** Nucleophilic Fukui function plot of symmetrical dSWCNT plotted with an isovalue of ±0.03 e·Å$^{-3}$. The plot was zoomed in and labeled as shown in the box.

The dSWCNT loses its semiconducting properties[32] with a new, metallic $E_{gap}$ of 0.43 eV (33.8% lower than that of the pSWCNT). This is caused by new energy states of the defect sites being introduced within the band gap. The defect energy states are shown clearly in the LUMO level of the dSWCNT (Figure 2), the electrons of which occupy mostly the defect site. Therefore, the vacancy defects, even a monatomic vacancy, play an important role in the electronic properties of carbon nanotubes, confirming that a healing process is needed in order to maintain the original properties.

The nucleophilic Fukui function plots of the dSWCNT are shown in Figure 3. The strong nucleophilic zones cover mainly the defect site, particularly at the C5. Its sp hybridization lifts the C5 position away from the tube axis in order to lower its electronic repulsion with the tube atoms (Figure 4a). The plots suggest the adsorption mechanism of an incoming CO molecule. Two adsorption orientations are observed, which are dSWCNT-CO and dSWCNT-OC. dSWCNT-OC is found to be unfavorable due to a repulsive force between the nucleophilic defect site of the dSWCNT and the oxygen atom of the CO. Thus, the CO adsorption is guided by the C5, which is the main active site, and the dSWCNT-CO direction is preferable for a nucleophilic attack to the carbon atom (partial positive charge) of the CO molecule. Fortunately, the CO molecule is much less attracted to a perfect site [$E_b$(dSWCNT-CO) on the perfect site is 0.50 kcal·mol$^{-1}$]. This is caused by the low polarity of the perfect carbon nanotube and the high polarity of the CO molecule. Therefore, the CO adsorption occurs highly selectively on the defect site.

Simultaneous adsorption of two CO reactants is considered in two cases, which correspond to high and low CO concentrations in the experiment. The calculations lead us to postulate two different pathways: the associative-coadsorption pathway (ACP) and the consecutive-coadsorption pathway (CCP).

For the ACP at high CO concentration, two CO molecules (the first and second are labeled as C′O′ and C″O″, respectively) are associatively coadsorbed on each of the two nucleophilic sites (C5 and assisted C1−C9), building a coadsorption (Coads) structure at C5−C′−O′ and C1−C″(−O″)−C9. The C″O″ Coads is doubly assisted by both the C1 and C9, then breaks the C1−C9 bond in the 5-membered ring, forming a 6-membered-ring cyclization of C″−C9−C10−C11−C12−C1, as shown in Figure 4b. The C″ and C5 atoms are then bonded via the transition state TS_1 (Figure 4c) with activation energy of 2.82 kcal·mol$^{-1}$ in order to create two new 6-membered rings, giving a more stable intermediate (Int_1) with a C″−C5 bond length of 1.539 Å, as shown in Figure 4d. This bonding also induces the O″ (partial negative charge) connected to C′ with a bond length of 1.373 Å, bringing about the 4-membered-ring cyclization of C″−O″−C′−C5. This causes a lengthening of the C″−O″, C′−C5, and C′−O′ bonds to 1.520, 1.556, and 1.198 Å, respectively. Next, the C″−O″ and C5−C′ bonds are broken with atomic distances of 2.065 and 1.655 Å, respectively, by the opening of the 4-membered-ring with an activation energy of 9.37 kcal·mol$^{-1}$ via TS_2 (Figure 4e). This step is supported by the strong electron resonance of O″−C′−O′. The C′−O″ bond is shortened from 1.373 to 1.280 Å whereas the C′−O′ bond is lengthened from 1.198 to 1.215 Å in order to symmetrically balance the dioxide group. Finally, the carbon dioxide molecule (O″−C′−O′) as a product leaves both the defect and perfect sites of the carbon nanotube immediately without any binding energy [$E_b$(dSWCNT-$CO_2$) are 0.54 and 0.46 kcal·mol$^{-1}$, respectively]. The C5···C′ atomic distance is lengthened to 3.590 Å, while the remaining carbon atoms of the dSWCNT, including C″, reconstructed the pSWCNT with identical carbon−carbon bonds of 1.421 Å, as shown in Prod (Figure 4f).

At low CO concentration, the CCP can be subdivided into two subpathways called here CCP-1 and CCP-2. The proposed CCP-1 involves the C5−C′−O′ bond as shown in Ads_1 (Figure 4g). C′O′ is adsorbed strongly on C5, giving a C′−C5 bond length of 1.320 Å with an $E_b$ of 48.47 kcal·mol$^{-1}$. Thus, the C′−O′ and C4−C5 (symmetrically the same as C5−C6) bonds are weakened from 1.141 to 1.176 Å and from 1.390 to 1.492 Å lengths, respectively. On the other hand, C1 (symmetrically the same as C9) can assist C5 for the adsorption, forming C1−C′(−O′)−C5 bonds and 5−6−7 fused rings, called CCP-2, as shown in Ads_2 (Figure 4h). This binding energy of the C′O′ adsorption is lower, with 43.33 kcal·mol$^{-1}$, than that in CCP-1, resulting in longer C′−O′ and C′−C5 bond lengths of 1.217 and 1.499 Å. The assisted C′−C1 bond is 1.538 Å in length. Even the assistance of C1 is explored; the dually assisted C1 and C9 for the C′O′ adsorption is not favorable because the C1−C9 bond of the 5-membered ring is hardly broken unless supported by the coadsorption. The C′O′ adsorption site at C5 via CCP-1 is favorable due to: the high nucleophilic C5 and the unstable sp$^3$ hybridization angle of C′−C1−C9 of 85.31° in the Ads_2 structure of CCP-2.

For CCP-2, no nucleophilic active site remains on the carbon nanotube defect for another CO adsorption; therefore, a subsequent

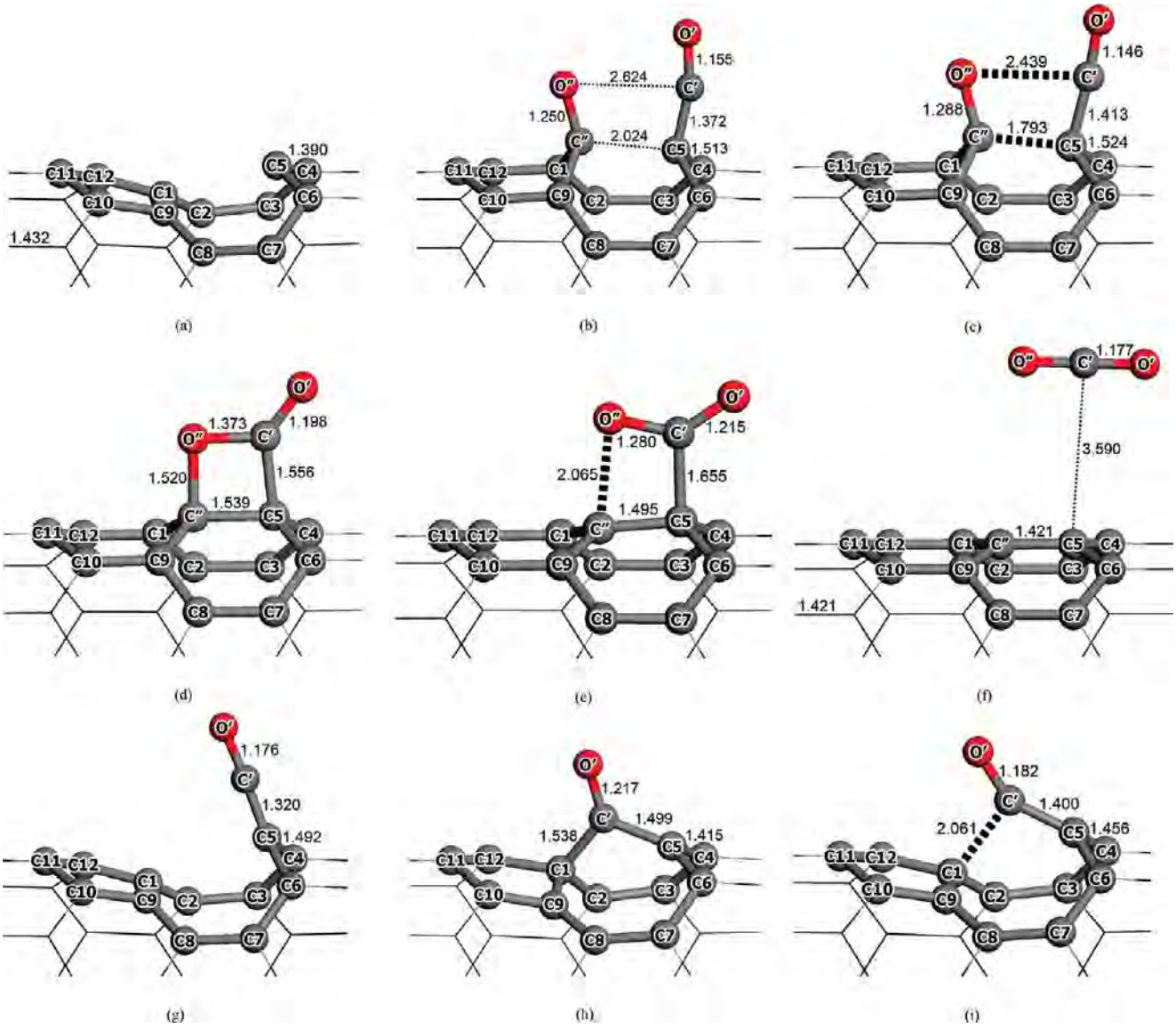


**Figure 4.** Optimized geometries of reaction steps in the proposed mechanisms (see Figures 5 and 6): (a) Subs; (b) Coads; (c) TS_1; (d) Int_1; (e) TS_2; (f) Prod; (g) Ads_1; (h) Ads_2; and (i) TS_3. Selected bond lengths and atomic distances are presented in angstrom units.

coadsorption from this step is impossible. Owing to the weakness of C1 in Ads_2, as described above, the C1−C′ bond is stretched with a length increasing from 1.538 to 2.061 Å. It is then broken through the transition state TS_3 (Figure 4i) by the 6-membered ring opening, forming Ads_1 with an activation energy of 14.49 kcal·mol$^{-1}$. In addition, this 6-membered ring opening requires a higher activation energy than that of the 4-membered ring opening in the ACP due to the lower stress in the larger ring. Surprisingly, the bypass CCP-2 merges with CCP-1 at this step. After the combination of these subpathways, the C″O″ molecule is then adsorbed on two remaining nucleophilic sites (C1 and C9), forming the same Coads structure as that in the ACP. Due to the repulsive force between the O″ and O′ atoms, the C′O′ group changes its position with a C′···O″ distance of 2.624 Å and C″···C5 distance of 2.024 Å. The C′O′ adsorption is also affected by the bond weakened from 1.320 to 1.372 Å. Thus, the reaction of the CCP continues from Coads to Prod following the ACP.

The energy profiles of the ACP and CCP are illustrated in Figures 5 and 6, respectively. For high CO concentrations, it is found that the ACP proceeds with overall activation energy of 9.37 kcal·mol$^{-1}$ of the 4-membered ring opening as the rate-determining step. On the other hand, -1 presents a barrierless CO adsorption whereas he CCP-2 introduces a new barrier of 14.49 kcal·mol$^{-1}$. Although CCP-1 is kinetically controlled, CCP-2 occurs with only 5.14 kcal·mol$^{-1}$ energy difference of the adsorption step. Therefore, for the lower CO concentration condition, a higher reaction temperature will be needed. The CCP process uses the carbon atom (C″) from the coadsorption of the second CO (C″O″) to fill in the vacancy in the healing. This mechanism thus proposes that a mole of monatomic vacancies of a SWCNT can be healed by two moles of CO, giving a mole of $CO_2$ as a product. In other words, the vacancy defect in the CNTs can convert two toxic CO molecules to a $CO_2$ molecule. Additionally, no oxygen molecule will be found as a


dx.doi.org/10.1021/jp110616c |J. Phys. Chem. C 2011, 115, 4649–4655

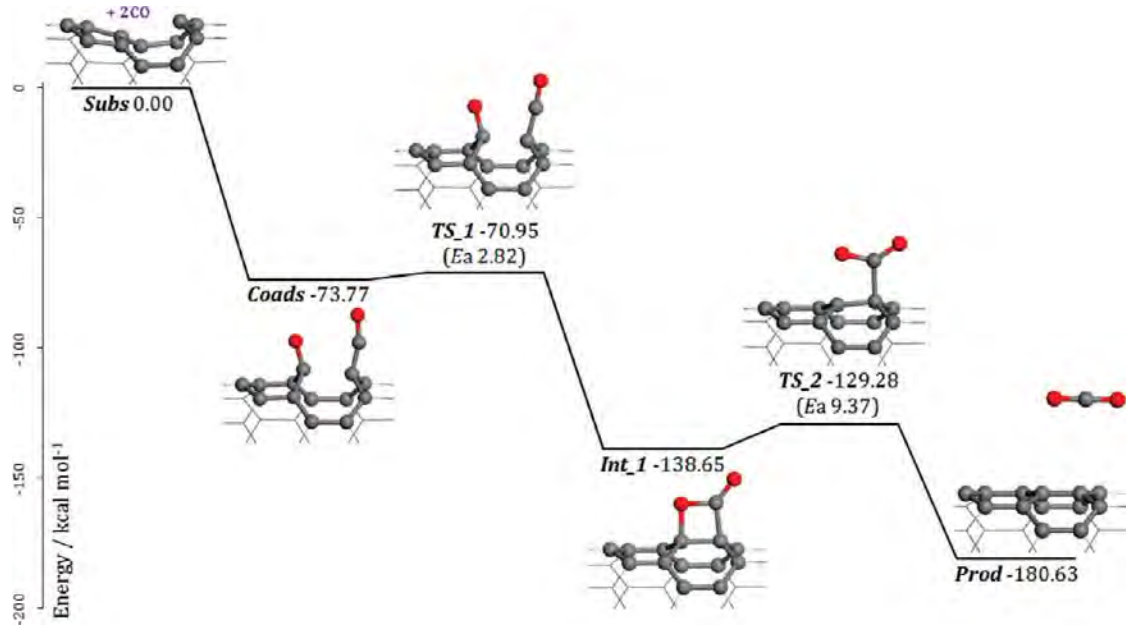


**Figure 5.** Energy profile of the associative-coadsorption pathway (ACP) of the healing process of the monatomic vacancy defect in the (8, 0) SWCNT by carbon monoxide disproportionation, as proposed at high CO concentrations.

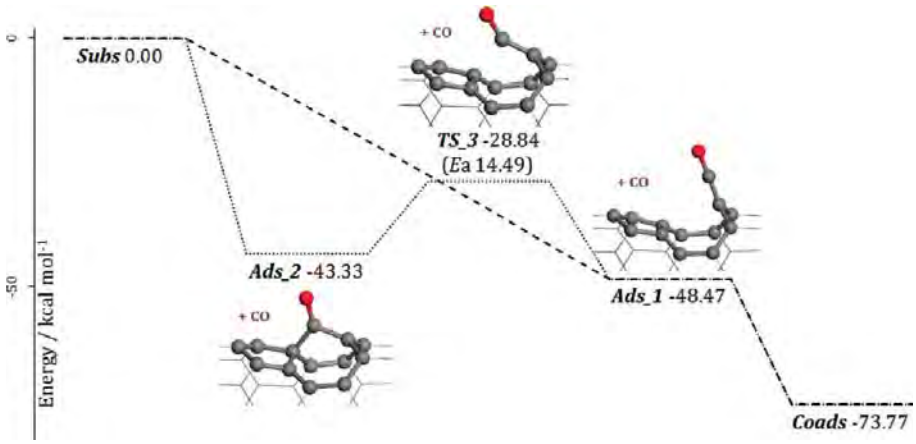


**Figure 6.** Energy profile of the consecutive-coadsorption pathway (CCP) of the healing process of the monatomic vacancy defect in the (8, 0) SWCNT by carbon monoxide disproportionation, as proposed at low CO concentrations. (---) CCP-1; (···) CCP-2.

byproduct. Thus, oxidation, oxidative combustion, and ozone etching of the SWCNTs can be avoided.

## CONCLUSION

DFT calculations with the PBE functional are used to investigate reaction mechanisms for the healing process of a monatomic vacancy defect in SWCNT via carbon monoxide disproportionation. At high CO concentrations, the reaction can proceed via the associative-coadsorption pathway with a barrierless CO coadsorption, while at low concentrations the consecutive-coadsorption pathway introduces a new barrier of 14.49 kcal·mol$^{-1}$. The advantages of the healing process are: low activation energy of 9.37 kcal·mol$^{-1}$ at the 4-membered ring opening step at high CO concentrations, no catalyst needed—thus no purification step is needed to remove the catalyst, the ambient CO can be used as a reactant, no oxygen byproduct is found, and there is high selectivity of CO for vacancy defect sites. Our findings prove that a vacancy defect in CNT, which occurs from syntheses or other uses as a nanomaterial device, can be healed to a perfect CNT holding the original electronic properties.

## AUTHOR INFORMATION

### Corresponding Author

*Fax +66 2562 5555, ext 2176; e-mail jumras.l@ku.ac.th.

## ACKNOWLEDGMENT

This work was supported in part by grants from the National Science and Technology Development Agency (2009 NSTDA Chair Professor funded by the Crown Property Bureau under the management of the National Science and Technology Development Agency and the NANOTEC Center of Excellence funded

by the National Nanotechnology Center), Kasetsart University Research and Development Institute (KURDI), the Thailand Research Fund (TRF), the Commission on Higher Education, Ministry of Education [the "National Research University Project of Thailand (NRU)" and the "National Center of Excellence for Petroleum, Petrochemical and Advanced Materials (NCE-PPAM)"], and the Development and Promotion of Science and Technology Talents Project (DPST). The Kasetsart University Graduate School is also acknowledged. The computational calculations were supported by the Thai National Grid Center (TNGC) under the Software Industry Promotion Agency (SIPA).

## REFERENCES

(1) Iijima, S.; Ichihashi, T. *Nature* **1993**, *363*, 603.
(2) Bethune, D. S.; Klang, C. H.; de Vries, M. S.; Gorman, G.; Savoy, R.; Vazquez, J.; Beyers, R. *Nature* **1993**, *363*, 605.
(3) Li, J.; Lu, Y.; Ye, Q.; Cinke, M.; Han, J.; Meyyappan, M. *Nano Lett.* **2003**, *3*, 929.
(4) Wang, J. *Electroanalysis* **2005**, *17*, 7.
(5) Krainara, N.; Nokbin, S.; Khongpracha, P.; Bopp, P. A.; Limtrakul, J. *Carbon* **2010**, *48*, 176.
(6) Kong, J.; Franklin, N. R.; Zhou, C.; Chapline, M. G.; Peng, S.; Cho, K.; Dai, H. *Science* **2000**, *287*, 622.
(7) Pannopard, P.; Khongpracha, P.; Probst, M.; Limtrakul, J. *J. Mol. Graphics Model.* **2009**, *28*, 62.
(8) Zhang, Y.; Zhang, D.; Liu, C. *J. Phys. Chem. B* **2006**, *110*, 4671.
(9) Fan, Y.; Goldsmith, B. R.; Collins, P. G. *Nat. Mater.* **2005**, *4*, 906.
(10) Mawhinney, D. B.; Naumenko, V.; Kuznetsova, A.; Yates, J. T.; Liu, J.; Smalley, R. E. *Chem. Phys. Lett.* **2000**, *324*, 213.
(11) Kang, D.; Kato, K.; Kojima, K.; Uchida, T.; Tachibana, M. *Appl. Phys. Lett.* **2008**, *93*, No. 133102.
(12) Stone, A. J.; Wales, D. J. *Chem. Phys. Lett.* **1986**, *128*, 501.
(13) Suekane, O.; Nagataki, A.; Nakayama, Y. *Appl. Phys. Lett.* **2006**, *89*, No. 183110.
(14) Tsetseris, L.; Pantelides, S. T. *Carbon* **2009**, *47*, 901.
(15) Borrnert, F.; Gorantla, S.; Bachmatiuk, A.; Warner, J. H.; Ibrahim, I.; Thomas, J.; Gemming, T.; Eckert, J.; Cuniberti, G.; Buchner, B.; Rummeli, M. H. *Phys. Rev. B* **2010**, 81.
(16) Tsetseris, L.; Pantelides, S. T. *J. Phys. Chem. B* **2009**, *113*, 941.
(17) Chen-Li, Z.; Hui-Shen, S. *J. Phys.: Condens. Matter* **2007**, *19*, No. 386212.
(18) Miyamoto, Y.; Berber, S.; Yoon, M.; Rubio, A.; Tománek, D. *Chem. Phys. Lett.* **2004**, *392*, 209.
(19) Page, A. J.; Ohta, Y.; Okamoto, Y.; Irle, S.; Morokuma, K. *J. Phys. Chem. C* **2009**, *113*, 20198.
(20) Page, A. J.; Ohta, Y.; Irle, S.; Morokuma, K. *Acc. Chem. Res.* **2010**, *43*, 1375.
(21) Nikolaev, P.; Bronikowski, M. J.; Bradley, R. K.; Rohmund, F.; Colbert, D. T.; Smith, K. A.; Smalley, R. E. *Chem. Phys. Lett.* **1999**, *313*, 91.
(22) da Silva, L. B.; Fagan, S. B.; Mota, R. *Nano Lett.* **2003**, *4*, 65.
(23) Mota, R.; Fagan, S. B.; Fazzio, A. *Surf. Sci.* **2007**, *601*, 4102.
(24) Wang, R.; Zhang, D.; Sun, W.; Han, Z.; Liu, C. *J. Mol. Struct. THEOCHEM* **2007**, *806*, 93.
(25) Khongpracha, P.; Probst, M.; Limtrakul, J. *Eur. Phys. J. D* **2008**, *48*, 211.
(26) Yong-Hui, Z.; et al. *Nanotechnology* **2009**, *20*, No. 185504.
(27) Nongnual, T.; Nokbin, S.; Khongpracha, P.; Bopp, P. A.; Limtrakul, J. *Carbon* **2010**, *48*, 1524.
(28) Perdew, J. P.; Burke, K.; Ernzerhof, M. *Phys. Rev. Lett.* **1996**, *77*, 3865.
(29) Delley, B. *J. Chem. Phys.* **1990**, *92*, 508.
(30) Delley, B. *J. Chem. Phys.* **2000**, *113*, 7756.
(31) Monkhorst, H. J.; Pack, J. D. *Phys. Rev. B* **1976**, *13*, 5188.
(32) O'Connell, M. J.; Bachilo, S. M.; Huffman, C. B.; Moore, V. C.; Strano, M. S.; Haroz, E. H.; Rialon, K. L.; Boul, P. J.; Noon, W. H.; Kittrell, C.; Ma, J.; Hauge, R. H.; Weisman, R. B.; Smalley, R. E. *Science* **2002**, *297*, 593.

Electrochimica Acta 56 (2011) 10562–10566

Contents lists available at ScienceDirect

Electrochimica Acta

journal homepage: www.elsevier.com/locate/electacta

# Straightforward single-step generation of microswimmers by bipolar electrochemistry

Z. Fattah [a], G. Loget [a,1], V. Lapeyre [a], P. Garrigue [a], C. Warakulwit [b], J. Limtrakul [b], L. Bouffier [a,1], A. Kuhn [a,*,1]

[a] Université Bordeaux, ISM, ENSCBP, 33607 Pessac, France
[b] Center for Advanced Studies in Nanotechnology for Chemical, Food and Agricultural Industries, Center of Nanotechnology and Chemistry Department, Kasetsart University, Bangkok 10900, Thailand

ARTICLE INFO

*Article history:*
Received 19 November 2010
Received in revised form 16 January 2011
Accepted 17 January 2011
Available online 22 January 2011

*Keywords:*
Microswimmers
Janus particles
Bipolar electrochemistry
Carbon tubes

ABSTRACT

Autonomous microswimmers are of enormous interest not only from an academic point of view, but also for future practical applications ranging from miniaturized motors to nanomedicine. A key step for the generation of such objects is their dissymmetric modification with a catalyst particle that activates the chemical conversion of a fuel molecule, leading ultimately to the propulsion of the object. So far it has been quite difficult to synthesize such dissymmetric objects and most approaches are based on using interfaces to break the symmetry. We demonstrate here that a very simple approach based on bipolar electrochemistry allows the bulk generation of carbon microtubes that are modified selectively at one end with a Pt cluster. The presence of this metal cluster allows the catalytic decomposition of hydrogen peroxide and the resulting oxygen bubbles trigger the propulsion of the object. The type of motion can be switched from linear to circular as a function of the exact position of the Pt cluster.


## 1. Introduction

In the frame of the intensive current efforts to develop micro- and nanomotors, one of the most fascinating domains is the research on autonomous swimmers, able to move in fluids under the influence of external parameters, like the presence of physical fields or chemical fuels [1]. In the latter case, which is the topic of the present work, the motion is generated by the conversion of locally available chemical energy into mechanical energy with the help of catalysts that are localized on one part of the swimmer. Many reports have appeared in the literature on the synthesis of heterogeneous objects at the micrometer or nanometer scale in order to carry out catalytic reactions at their different ends [2]. These systems are of great application potential in the field of nanoscience, due to their ability to accomplish various tasks at a tiny scale, inspired for example by natural biomachines such as kinesin (a linearly progressing motor in the cell) [3] or flagellar motion [4]. The recent research in nanotechnology has focused on a variety of such micro- and nanomotors, using different design principles and various catalysts in order to induce and control their motion [5–7].

Generally there are three methods to induce the motion of these objects:

(1) Biochemical fueling which is based on the functionalization of an object with catalytically active enzymes, converting natural fuel into kinetic energy [8,9]. (2) Physical fueling which implies applying an external electric [6,10], or magnetic field [4,11]. (3) Chemical fueling for objects of different design, such as gear-like structures [5], metal nanorods [7,12], nanorotors [13,14] and millimeter-sized plates [15]. In many of the cases the structure includes a metallic segment, that acts as the catalytic site for the decomposition of hydrogen peroxide to water and oxygen gas, which in turn generates the motion either by interfacial tension gradients [5,12], or recoil from oxygen bubbles [14,15]. In this context a key step in the design of the microswimmers is the dissymmetric placement of the catalyst, which is achieved most of the time using rather complex methods such as deposition through the pores of membranes [16] or vapor deposition processes [14]. Moreover, because these processes are occurring in a two-dimensional reaction space, the yield of product is quite limited and therefore not well-adapted for large-scale production.

In this contribution we propose a straightforward single-step procedure based on bipolar electrochemistry to prepare carbon microtubes (CMTs) that are modified in a dissymmetric way with a platinum catalyst. Depending on the exact location of the catalyst cluster this allows subsequently the propulsion of these objects either on a linear or circular trajectory.

Bipolar electrochemistry occurs when a conducting object is exposed to an electric field which induces a polarization that is sufficiently high to allow oxidation and reduction reactions at the

* Corresponding author. Tel.: +33 5 40 00 65 73; fax: +33 5 40 00 27 17.
*E-mail address:* kuhn@enscbp.fr (A. Kuhn).
[1] ISE member.

0013-4686/$ – see front matter © 2011 Elsevier Ltd. All rights reserved.
doi:10.1016/j.electacta.2011.01.048

opposite ends of the object, in the absence of direct contact between the object and the power supply [17,18].

This principle has found several interesting applications for pattering surfaces [19,20], sensing [21], generating electrochemiluminescence [18,22,23], membrane pore functionalization [24], establishing electrical contacts [25], propulsing micro objects [6] and as a powerful bulk procedure for creating dissymmetric objects (Janus-type particles) such as single point modified carbon micro- and nanotubes [11,26]. Here we will show that the procedure can be adapted not only to the selective formation of Pt clusters at one end of a CMT, but also to influence the orientation of the metal deposit with respect to the tube axis, which gives the possibility to generate two types of motion, a linear one and a circular one.

## 2. Experimental

### 2.1. Preparation and modification of carbon microtubes

The carbon microtubes used in this study were produced by chemical vapor deposition using a porous aluminum oxide membrane serving as a template [27]. After an acidic digestion of the template, the fairly homogeneous tubes were recovered as a powder. The suspension of CMTs was obtained by the addition of CMTs (0.3 mg) to absolute ethanol (1.25 ml). The formation of the suspension was accelerated by sonicating the mixture for a short time (1 min) in order to avoid excessive breaking of the tubes. After 30 min of sedimentation, 0.5 ml of the supernatant was taken and added to 1.5 ml of a freshly prepared 60 mM $H_2PtCl_6$ solution in ultrapure water (hexachloroplatinic acid hexahydrate, ACS reagent grade, purchased from Sigma–Aldrich Co.). The suspension was sonicated for a few seconds to disperse the tubes and directly employed for the bipolar electrodeposition process analogous to what has been described previously [11,26]. An electric field of 30 kV/m was applied to polarize the CMTs according to the relationship:

$$\Delta V_{max} = E\,l \quad (1)$$

where $\Delta V_{max}$ is the maximum potential difference generated between both sides of the microtube, $E$ is the total electric field and $l$ is the length of the CMT.

### 2.2. Characterization of modified carbon microtubes—observation of hydrogen peroxide decomposition and CMT motion

The suspension containing the modified carbon tubes was collected after the bipolar electrodeposition experiment and observed between two glass slides with a transmission optical microscope (Zeiss, Imager M1). Before the characterization with the scanning electron microscope (Hitachi, TM-1000), the suspension was dried on a conductive substrate.

For observing the movement of the modified carbon tubes, one drop of the suspension was dried on a glass slide and the swimmers were observed with the transmission optical microscope. 5 μl of a solution of 30 wt.% hydrogen peroxide in water (purchased from Sigma–Aldrich Co.) were then added on top of the slide with the tubes. Videos were recorded using a CCD camera.

## 3. Results and discussion

### 3.1. Microswimmer preparation

Let us first consider the two redox reactions that should take place at each side of the CMT:

$$Pt^{IV}Cl_6{}^{2-}{}_{(aq)} + 4e^- \rightarrow Pt^0{}_{(s)} + 6Cl^-{}_{(aq)} \quad E^\circ = +0.73\,V/_{NHE}$$

$$2H_2O_{(l)} \leftrightarrow 4H^+{}_{(aq)} + O_{2(g)} + 4e^- \quad E^\circ = +1.23\,V/_{NHE}$$

In order to trigger both reactions at the opposite ends of the tube we assume in a first order approximation that the polarisation has to generate a potential difference which is at least equal to the difference of the formal potentials of the two redox couples. In the present case this difference is 0.5 V and, according to Eq. (1), it is clear that an electric field of at least 25 kV/m must be applied in order to induce the deposition of platinum onto a 20 μm-long CMT.

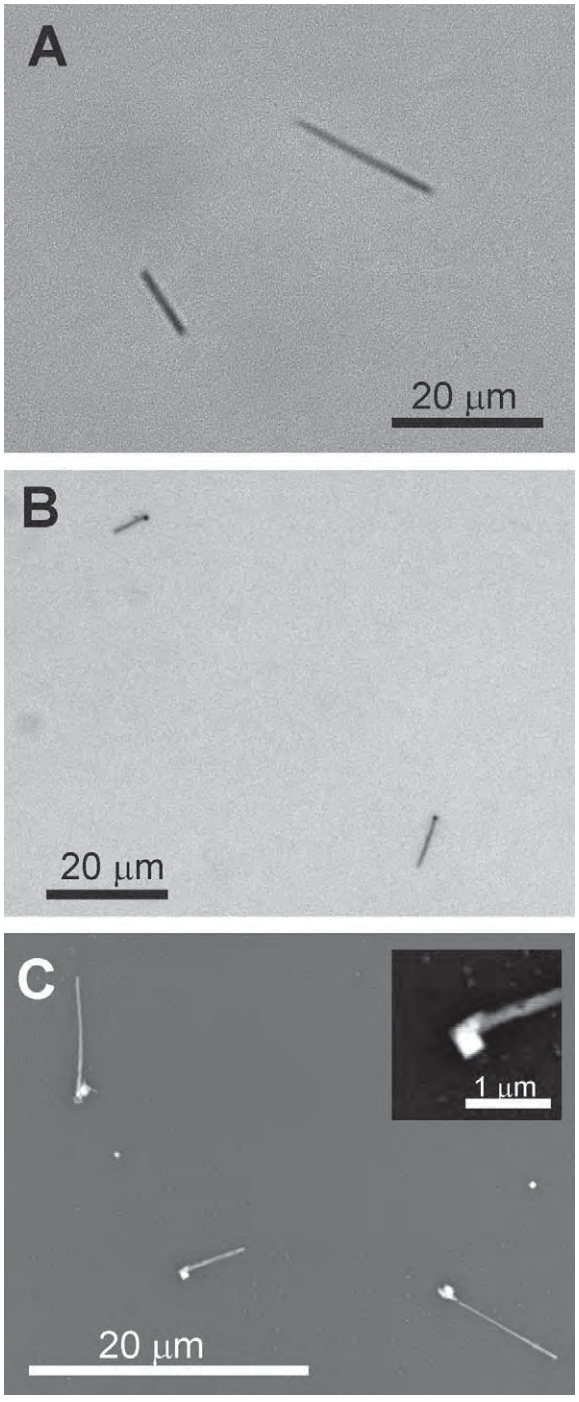


**Fig. 1.** Transmission optical micrograph (50 times magnification) of (A) unmodified carbon microtubes (CMTs) and (B) CMTs with either asymmetric (top left) or symmetric (bottom right) platinum deposits obtained by using bipolar electrodeposition. (C) Scanning electron microscopy image of platinum modified CMTs. Inset: magnified SEM image of the platinum deposit.

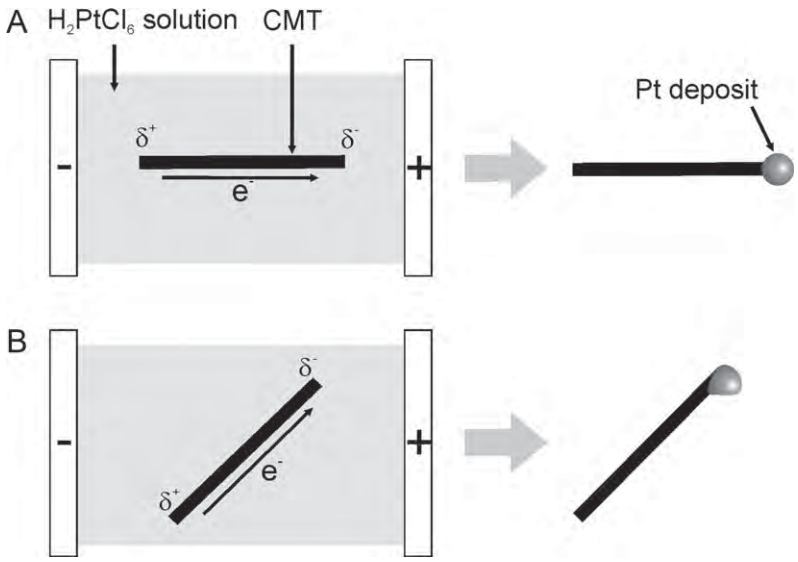


**Fig. 2.** Schematic illustration explaining the origin of different deposit locations obtained for CMTs as a function of their orientation in the electric field at the beginning of the electrodeposition process. (A) Aligned parallel to the electric field and (B) non-aligned with the electric field.

As reported previously, such high electric fields can be achieved with a capillary electrophoresis set-up [11]. Experimentally, we applied a slightly larger electric field (30 kV/m) to make sure that also a majority of shorter CMTs are modified. This corresponds to a good compromise because the difference of potential ($\Delta V$) between both sides of the CMT is higher than the thermodynamic threshold value necessary for the concomitant redox reactions, but still low enough to avoid bubble formation which would disturb the experiment and cause detaching of the Pt deposit from the CMTs' extremity.

### 3.2. Microswimmer characterization

The major reason for choosing carbon microtubes instead of carbon nanotubes [26] in this work is the ease of visualization of the achieved modification and especially of the generated motion by standard optical microscopy. An optical micrograph of two unmodified carbon microtubes is given in Fig. 1A. Both tubes are representative of the sample containing a population of tubes with a length ranging from 5 to 20 μm. Fig. 1B has been obtained after exposing the carbon tubes to the electric field in a solution containing the platinum salt. The experiment shows clear evidence for a dissymmetric deposition of platinum at one extremity of the tubes by the bipolar electrochemistry approach. Samples have been prepared at a quite high dilution in order to avoid superposition of several tubes. Careful examination of the samples highlights two slightly different topologies. The tube (length ~ 9 μm) located at the bottom of the right side of the picture is modified in a symmetrical way with the Pt particle centered on the C2 axis of the tube. On the other hand, the shorter tube in the top left corner (length ~ 6 μm) has been modified in a non-symmetrical fashion as the particle is positioned slightly off the tube axis.

This difference might be explained on the basis of a mixed influence of two competing kinetic parameters, which are the electromechanical alignment time against the kinetic activation of the bipolar reaction. Indeed, a linear potential sweep is applied in order to reach the final working potential $E_w$. Theoretically, this potential ramp should last for a time long enough to allow an alignment of the tubes along the direction of the electric field before reaching the threshold value where the bipolar reaction starts taking place. In this case the experiment should lead theoretically to the formation of a symmetric electrodeposit of the Pt (Fig. 2A) with respect to the tube axis, because the nucleation point is located at the point of maximum polarization.

But the reality is more complicated because the carbon tubes of a given sample have a length distribution due to the preparation mode of the CMTs. Practically, the kinetics of alignment of a population of microtubes in a given electric field depends of three main variables: the initial orientation and the length of each tube, as well as the viscosity of the surrounding environment (the latter depending on another series of variables: solvent, temperature, nature and concentration of the supporting electrolyte). The interesting point is that these experimental conditions can be adjusted in order to tune the electrodeposition morphology (symmetrical *versus* non-symmetrical functionalization). The initial orientation of the tubes is a statistical distribution, but the subsequent alignment could be favored by applying an initial potential difference lower than the threshold value necessary for the bipolar reaction, followed by a potential step above the threshold value once the tubes are all aligned. On the other hand, the solvent choice is of first importance as the timescale of reorientation of the CMT could be either very short in water or substantially longer by adding a co-solvent with a higher viscosity. A precise tuning of the monodispersity of the tube length does not seem to be necessary as two opposite factors influence the alignment: First, the length of the tube directly influences the polarization between both extremities of the CMT. All tubes are exposed to the same electric field (30 kV/m) and that means that the polarization of a 20 μm-long carbon tube is twice as large as the polarization of a tube of 10 μm. This polarization is the driving force of the alignment, but mechanical counter forces also depend on the tube lengths. Indeed, the longer CMTs exhibit a bigger surface area in contact with the surrounding environment and are, therefore, more affected by the solvent viscosity contribution, which slows down the alignment. Experimentally we find that these two contributions do not seem to be of the same magnitude, because the longer CMTs have a higher tendency to be functionalized in a non-symmetrical fashion, meaning that they need more time to orientate in the electric field and during this time the deposition already occurs at the point of highest polarization, which in this case is not located at the center of the tube end, but at the edge. Consequently the Pt electrodeposit resulting from the reduction of $H_2PtCl_6$ directly grows from the most favorable nucleation site and generates an off-centered platinum/carbon tube hybrid as illustrated in Fig. 2B. One can note that

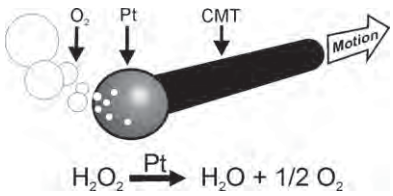


**Fig. 3.** Schematic illustration of the propulsion mechanism of a platinum-modified carbon tube moving in the opposite direction of the oxygen bubbles generated on the platinum catalyst.

this scenario is perfectly consistent with the extremely low surface mobility of the Pt atoms ($D_S = 10^{-18}$ cm$^2$ s$^{-1}$ determined on highly oriented pyrolitic graphite, HOPG), which is several orders of magnitude lower than that of the Ag atoms for example [28].

The modified carbon tubes have also been characterized by SEM and a representative picture is given in Fig. 1C. Three successfully functionalized small tubes with a length between 5 and 8 μm can be observed and at high magnification (inset) a typical Pt particle is visible. Theoretically, the size of the platinum cluster should depend on the CMT's length, but other considerations have to be taken into account: a carbon tube which is imperfectly aligned exhibits a high polarization located at the edge of each extremity instead of the center, leading to a non-centered nucleation point. In this case the driving force is not proportional to the overall tube lengths but to the projection of the tube in the plane of the electric field lines.

Although the present study did not focus on the crystallographic structure of the Pt deposit, the observation of non-symmetrical electrodeposits is in favor of a single crystal nucleation and growth, because the alternative pathway involving several nucleation sites distributed over the whole extremity of the microtube should generate a symmetrical Pt topology.

In summary, the described characterization by optical and electron microscopy clearly demonstrates the successful electrodeposition of platinum at one extremity of the carbon tubes and therefore the controlled generation of Janus-type microobjects, which then can be used to generate a movement by applying an external stimulus.

### 3.3. Microswimmer propulsion

Platinum metal is a well-known catalyst which has been extensively used in organic synthesis (for example for catalytic hydrogenation) as well as in electrocatalysis. We first tested the ability of the newly prepared material to decompose hydrogen peroxide. Dioxygen bubble generation was immediately observed as

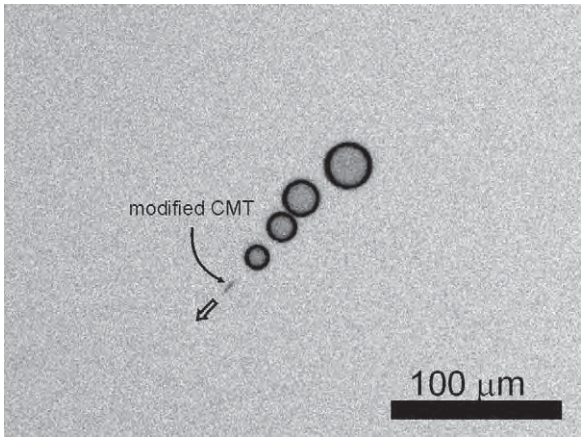


**Fig. 4.** Linear motion of the microswimmer leaving a bubble train behind observed under the optical microscope.

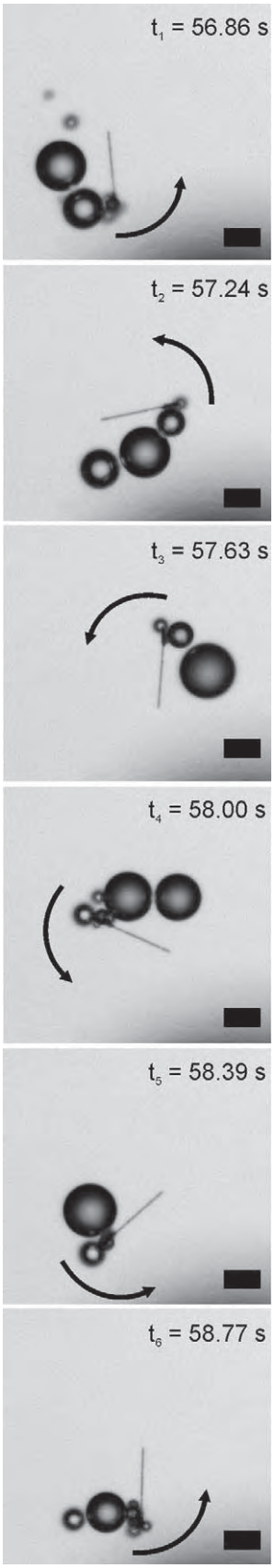


**Fig. 5.** Optical micrographs of a counter clockwise rotating microswimmer. Scale bar 10 μm.

soon as the Pt/CMT hybrid was in contact with the reactant solution according to the following dismutation equation:

$$H_2O_2 \rightarrow H_2O + 1/2O_2$$

The bubble production can be tuned by adjusting the hydrogen peroxide content and concentrated solutions like 30% $H_2O_2$ generated a very high activity. One can note that a control experiment with pure $H_2O$ instead of $H_2O_2$ did never lead to any bubbles due to purely mechanical effects.

Fig. 3 gives a schematic representation of the mechanism responsible for the motion. The ideal situation corresponds to a CMT functionalized with a perfectly symmetric Pt particle at one extremity. The $O_2$ bubbles will generate a local mechanical perturbation and a subsequent movement of the object in the opposite direction.

The propulsion of a CMT is experimentally very challenging to image for several reasons. (1) The generation of a large quantity of bubbles is necessary to move the microhybrid, but these bubbles disturb the optical resolution by changing instantly the nature of the local environment surrounding the CMT. (2) The propulsion usually takes place in a three dimension referential (*xyz*) and the optical microscope is only able to focus on a single plane (*xy*). (3) The rate of bubble formation and the acceleration of the CMT do not take place at the same timescale and it is therefore very frequent that the CMT moves out of the focal plane of the microscope. Fig. 4 shows an optical micrograph of a CMT in motion. The four dioxygen bubbles were formed successively from right to left and this results in an efficient propulsion of the carbon tube towards the bottom–left corner of the picture. As mentioned previously, this linear mode of motion is directly linked to the morphology of the platinum deposit. A Pt particle perfectly centered at the middle of a CMT extremity results in an isotropic production of $O_2$ bubbles and therefore a linear motion. However a non-symmetric deposit (for example like in Fig. 1B and C) will generate bubbles anisotropically with respect to the tube axis. As a result, the mode of motion does change from a translation to a rotation. Fig. 5 shows a selection of six high magnification optical images of a CMT performing one anticlockwise turn. These data are extracted from a large set of images in which the microhybrid is spinning several times around the unfunctionalized extremity of the microtube. A time interval of $2.01 \pm 0.14$ s/turn was estimated from 10 full turns which allows calculating a speed of $29.9 \pm 2.1$ rpm (or a frequency of $\sim$0.50 Hz). The sequence of images in Fig. 5 clearly demonstrates that the driving force of the rotation is the non-symmetric $O_2$ formation, as the CMT is rotating in the opposite direction with respect to the bubble evolution. It is noteworthy that this rotating CMT is a particularly long one (roughly 20 $\mu$m), thus confirming that the length of the microtube seems to be one of the variables influencing the formation of a non-symmetrical Pt electrodeposit. At this stage the advantage of the present modification approach using bipolar electrochemistry with respect to other experiments, where rotational motion has been generated on purpose [14], becomes very clear. By changing the potential ramp and the solvent viscosity during the deposition experiment it is in principle possible to generate on purpose objects that can either undergo dominantly linear or rotational propulsion.

## 4. Conclusion

A single-step procedure based on the concept of bipolar electrochemistry has been successfully employed to create Janus-type carbon microtubes with a platinum metal deposit at one end either in a symmetric or dissymmetric orientation with respect to the tube's axis. This bulk process is straightforward and well adapted to generate microswimmers with a high efficiency, whereas the majority of the literature processes are based on the use of interfaces or surfaces to generate such swimmers. Especially for rotational motion, sophisticated synthetic procedures have usually to be employed to generate the appropriate particles. In the present study, it is possible to generate swimmers that can perform both, rotational and linear motion as a function of the position of the Pt cluster with respect to the tube axis, which catalyzes the decomposition of hydrogen peroxide. The generated oxygen bubbles drive these microobjects either in a linear or a circular motion.

Bipolar electrochemistry can be also applied to generate such micro- and nanoobjects with a variety of other materials, in order to adapt the chemistry of the propulsion process for example to bioelectrochemical mechanisms [9]. Microswimmers elaborated using this or similar approaches [29] might one day move cargo in microfluidic devices, deliver pharmaceuticals, or track toxic molecules [30].

## Acknowledgments

This work is part of the CUBIHOLE project funded by the European NanoSci-Era+ action under contract ANR-08-NSCI-008-01 and has also been supported by the French Ministry of Research (MESR), CNRS, and ENSCBP. C.W. and J.L. thank the National Science and Technology Development Agency (NSTDA Chair Professor and National Nanotechnology Center NANOTEC), the Commission on Higher Education, the Ministry of Education and the Thailand Research Fund for support.

## References

[1] J. Wang, K.M. Manesh, Small 6 (2010) 338.
[2] S.J. Ebbens, J.R. Howse, Soft Matter 6 (2010) 726.
[3] G.A. Ozin, I. Manners, S. Fournier-Bidoz, A. Arsenault, Adv. Mater. 17 (2005) 3011.
[4] R. Dreyfus, J. Baudry, M.L. Roper, M. Fermigier, H.A. Stone, J. Bibette, Nature 437 (2005) 862.
[5] J.M. Catchmark, S. Subramanian, A. Sen, Small 1 (2005) 202.
[6] G. Loget, A. Kuhn, J. Am. Chem. Soc. 132 (2010) 15918.
[7] T.R. Kline, W.F. Paxton, T.E. Mallouk, A. Sen, Angew. Chem. Int. Ed. 44 (2005) 744.
[8] D. Pantarotto, W.R. Browne, B.L. Feringa, Chem. Commun. (2008) 1533.
[9] N. Mano, A. Heller, J. Am. Chem. Soc. 127 (2005) 11574.
[10] P. Calvo-Marzal, S. Sattayasamitsathit, S. Balasubramanian, J.R. Windmiller, C. Dao, J. Wang, Chem. Commun. 46 (2010) 1623.
[11] G. Loget, G. Larcade, V. Lapeyre, P. Garrigue, C. Warakulwit, J. Limtrakul, M.-H. Delville, V. Ravaine, A. Kuhn, Electrochim. Acta 55 (2010) 8116.
[12] W.F. Paxton, A. Sen, T.E. Mallouk, Chem. Eur. J. 11 (2005) 6462.
[13] S. Fournier-Bidoz, A.C. Arsenault, I. Manners, G.A. Ozin, Chem. Commun. (2005) 441.
[14] L. Qin, M.J. Banholzer, X. Xu, L. Huang, C.A. Mirkin, J. Am. Chem. Soc. 129 (2007) 14870.
[15] R.F. Ismagilov, A. Schwartz, N. Bowden, G.M. Whitesides, Angew. Chem. Int. Ed. 41 (2002) 652.
[16] N.S. Zacharia, Z.S. Sadeq, G.A. Ozin, Chem. Commun. (2009) 5856.
[17] M. Fleischmann, J. Ghoroghchian, D. Rolison, S. Pons, J. Phys. Chem. 90 (1986) 6392.
[18] F. Mavré, R.K. Anand, D.R. Laws, K.-F. Chow, B.-Y. Chang, J.A. Crooks, R.M. Crooks, Anal. Chem. 82 (2010) 8766.
[19] S. Ramakrishnan, C. Shannon, Langmuir 26 (2010) 4602.
[20] C. Ulrich, O. Andersson, L. Nyholm, F. Björefors, Anal. Chem. 81 (2009) 453.
[21] K.-F. Chow, B.-Y. Chang, B.A. Zaccheo, F. Mavré, R.M. Crooks, J. Am. Chem. Soc. 132 (2010) 9228.
[22] S.E. Fosdick, J.A. Crooks, B.-Y. Chang, R.M. Crooks, J. Am. Chem. Soc. 132 (2010) 9226.
[23] F. Mavré, K.-F. Chow, E. Sheridan, B.-Y. Chang, J.A. Crooks, R.M. Crooks, Anal. Chem. 81 (2009) 6218.
[24] A. Bouchet, E. Descamps, P. Mailley, T. Livache, F. Chatelain, V. Haguet, Small 5 (2009) 2297.
[25] J.-C. Bradley, J. Crawford, K. Ernazarova, M. McGee, S.G. Stephens, Adv. Mater. 9 (1997) 1168.
[26] C. Warakulwit, T. Nguyen, J. Majimel, M.-H. Delville, V. Lapeyre, P. Garrigue, V. Ravaine, J. Limtrakul, A. Kuhn, Nano Lett. 8 (2008) 500.
[27] C. Warakulwit, Ph.D. Thesis, Kasetsart University Bangkok and University Bordeaux 1, 2007.
[28] J.L. Zubimendi, L. Vázquez, P. Ocón, J.M. Vara, W.E. Triaca, R.C. Salvarezza, A.J. Arvia, J. Phys. Chem. 97 (1993) 5095.
[29] A. Ghosh, P. Fischer, Nano Lett. 9 (2009) 2243.
[30] M. Pumera, Nanoscale 2 (2010) 1643.

Journal of Molecular Liquids 159 (2011) 38–41

Contents lists available at ScienceDirect

Journal of Molecular Liquids

journal homepage: www.elsevier.com/locate/molliq

# $Au(CN)_2(CH_3NO_2)_n$ cluster anions: Energetics and geometrical features

Natcha Injan [a,b], Tünde Megyes [c], Tamas Radnai [c], Imre Bako [c], Szabolcz Balint [c], Jumras Limtrakul [b,*], Michael Probst [a,*]

[a] Institute of Ion Physics and Applied Physics, Innsbruck University, Austria
[b] Center of Nanotechnology, Chemistry Department and Center for Advanced Studies in Nanotechnology and Its Applications in Chemical, Food and Agricultural Industries Kasetsart University, Bangkok, Thailand
[c] Chemical Research Centre of the Hungarian Academy of Sciences, Budapest, Hungary

ARTICLE INFO

Available online 24 November 2010

*Keywords:*
Au(I) dicyano anion
Solvation shell structure
Nitromethane
Cluster calculations
Quantum chemistry
Ion solvation

ABSTRACT

Gold cyanides are widely used in chemical processes involving this coin metal since they are stable and soluble under a wide range of conditions. Nitromethane (NM) is the most widely used solvent for ionic complexes of Au. We have performed extensive quantum chemical calculations on $Au(CN)_2NM_n^-$ clusters with n = 1–10. For smaller values of n (<6), geometries with NM coordinating to the nitrogen atoms at both ends of the linear anion are the most stable ones while for higher values of n a geometrical pattern with chains or rings of NM molecules becomes competitive. We also analyze the electrostatic potentials of NM and $Au(CN)_2^-$ and the electronic structure of the anion.



## 1. Introduction

Gold ions in non-aqueous solution are known since the early days of gold mining but increasingly find new applications in modern technologies. Examples are the processing of electronic scrap [1], the decoration of nanomaterials with gold [2] and new types of gold clusters [3], amongst others. Due to the high complexation tendency of gold ions, bare Au(I) or Au(III) ions are normally not present in solution. $CN^-$ forms a soluble gold complex, Dicyanoaurate(I) anion ($Au(CN)_2^-$) which is widely used in industry. This gold complex is very stable and can be prepared as an alkaline salt, ($NaAu(CN)_2$ or $KAu(CN)_2$) by cyanidation of gold clusters [4]. However, in general little is known about the microscopic details of gold complexes in solution. In this work we study the interactions between $Au(CN)_2^-$ and its preferred solvent, nitromethane, by means of quantum chemical cluster calculations.

## 2. Methods

### 2.1. Quantum chemical calculations

We performed Hartree-Fock (HF) calculations with the LANL2DZ basis set [5] for Au(I) and the D95V basis set [6] for N, O, C and H. In a previous work [7] it was found that this combination is suitable to describe such systems in which the intermolecular interactions are governed by electrostatics. Often, anions require basis sets augmented with diffuse functions. In the case of $Au(CN)_2^-$, however, the negative charge of the dicyanoaurate(I) anion is quite evenly distributed over all atoms. This makes it possible to use a more compact basis set, at least concerning energetics and geometries, which are the aim of the present work. It also allows calculations on larger $Au(CN)_2^-$–$NM_n$ clusters which we studied with n up to 10. In many respects, calculations on the interaction of $Au(CN)_2^-$ anion with solvent molecules are less problematic than with bare Au(I) because the strong non-additive effects mentioned in [7] are not present for $Au(CN)_2^-$–NM. All quantum chemical calculations were carried out with the Gaussian 03 code [8].

## 3. Results and discussion

### 3.1. Structure and formation energy of $Au(CN)_2^-$

$Au(CN)_2^-$ itself is a linear molecule with $D_{\infty}h$ symmetry in which the C end of the cyanide group binds to Au. In order to form a $Au(CN)_2^-$ anion, one electron in a carbon sp orbital transfers to the unoccupied 6s orbital of Au(I). From an analysis of the natural populations (Table 1) it can be seen that Au(I) gains $0.36e^-$ from $CN^-$ group group and AuCN- obtains $0.31e^-$ from the second $CN^-$ group. Moreover, due to the strong ligand field of $CN^-$, only one $CN^-$ group can fully participate in the mixing of the 6s–5d orbital of Au(I). This differs, for example, in case of bare Au(I) where two nitromethane molecules participate in

* Corresponding authors. Tel.: +43 512 507 6260.
*E-mail address:* michael.probst@uibk.ac.at (M. Probst).

0167-7322/$ – see front matter © 2010 Elsevier B.V. All rights reserved.
doi:10.1016/j.molliq.2010.11.008

**Table 1**
Atomic partial charge (NPA) and electronic configurations (NEC) of the atoms in Au(I), $CN^-$, AuCN and $Au(CN)_2^-$. See text for details.

| | Au(I) | | | | | | | $CN^-$ | | | | | | |
|---|---|---|---|---|---|---|---|---|---|---|---|---|---|---|
| | NPA | NEC | | | | | | NPA | NEC | | | | | |
| Au | 1.00 | 6s | 0.00 | 5d | 10.0 | 6p | 0.00 | – | – | | | | | |
| C | – | – | | | | | | −0.18 | 2s | 1.56 | 2p | 2.56 | 3s | 0.04 |
| N | – | – | | | | | | −0.82 | 2s | 1.62 | 2p | 4.19 | 3s | 0.01 |
| | AuCN | | | | | | | $Au(CN)_2^-$ | | | | | | |
| | NPA | NEC | | | | | | NPA | NEC | | | | | |
| Au | 0.64 | 6s | 0.51 | 5d | 9.83 | 6p | 0.02 | 0.33 | 6s | 0.81 | 5d | 9.73 | 6p | 0.13 |
| C | −0.20 | 2s | 1.26 | 2p | 2.91 | 3s | 0.04 | −0.10 | 2s | 1.26 | 2p | 2.77 | 3s | 0.05 |
| N | −0.44 | 2s | 1.59 | 2p | 3.84 | 3s | 0.01 | −0.57 | 2s | 1.58 | 2p | 3.98 | 3s | 0.05 |

the mixing [7]. With the quantum-chemical methods described in 2.1, the formation energy between Au(I) cation and the first $CN^-$ group is exothermic by 180.6 kcal/mol. The calculated Au–C and C–N distances are 1.998 and 1.160 Å, respectively. To form the $Au(CN)_2^-$ anion, the 6s orbital of Au(I) in AuCN obtains $0.31e^-$ from a sp orbital of the C atom of the second $CN^-$ ligand. The attachment of the second cyano group releases 94.2 kcal/mol, about half as much energy as the first one, and leads to the mixing of the 6s,5d and 6p orbitals of Au. The structure of $Au(CN)_2^-$ can be compared to S–Au(I)–S complexes which have the same linear $D_{\infty}h$ – symmetry [9]. The calculated Au–C and C–N distances in $Au(CN)_2^-$ are 2.050 and 1.166 Å, respectively, in good agreement with X-ray diffraction data for the crystals $Nd[Au(CN)_2]_3 \cdot 3H_2O$ and $Am[Au(CN)_2]_3 \cdot 3H_2O$ in which the Au–C distances are 1.984 and 2.064 Å, respectively, for $Nd[Au(CN)_2]_3 \cdot 3H_2O$ and $Am[Au(CN)_2]_3 \cdot 3H_2O$. The C–N distances are 1.141 and 1.075 Å for $Nd[Au(CN)_2]_3 \cdot 3H_2O$ and $Am[Au(CN)_2]_3 \cdot 3H_2O$, respectively [10].

### 3.2. Electrostatic potential and electron densities

The $Au(CN)_2^-$–NM interaction is governed by the interaction of the high dipole moment (4.6 debye) of NM with the low charge density in $Au(CN)_2^-$. We use the electrostatic potentials (ESPs) of both molecules to quantify this for intermediate distances. The ESP of NM (Fig. 1a) is divided into a positive half-space ($CH_3$ side) and a negative one ($NO_2$ side). The ESP of $Au(CN)_2^-$ is negative everywhere except close to the nuclei (Fig. 1b). Consequently, the interaction of $Au(CN)_2^-$ with the $NO_2$ side of NM is repulsive and the one with the $CH_3$ side is attractive. The coordination of NM to $Au(CN)_2^-$ is described in more detail in the next section.

$Au(CN)_2^-$ consists formally of the singly positive Au(I) cation and the two singly negative cyanide ligands. The electron density (ρ) difference between $Au(CN)_2^-$ constituents was calculated according to:

$$\Delta\rho = \rho_{Total} - \rho_{Au^+} - \rho_{(CN)^-_{Right}} - \rho_{(CN)^-_{Left}} \quad (1)$$

at the optimized structure of $Au(CN)_2^-$. It reveals that the region around Au(I) gains electron density (Fig. 2) from the $CN^-$ groups. This increase of electron density takes place in a ring-shaped region perpendicular to the axis of the anion.

### 3.3. $Au(CN)_2^-/NM_n$ (n = 1–10) complexes: Geometries and binding energies

Unlike in the case of the free Au(I) ion [7], the 6s orbital of gold in $Au(CN)_2^-$ is nearly fully occupied (Table 1). Therefore, it does not

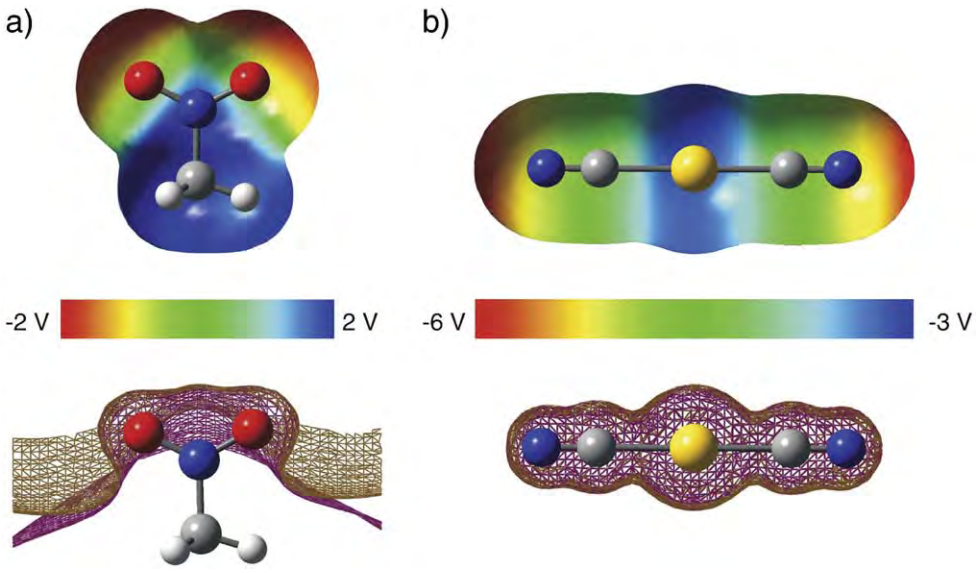


**Fig. 1.** Electrostatic potential (upper part) and the surface of near-zero (± $10^{-4}$ V)electrostatic potential (lower part) of a) nitromethane and b) $Au(CN)_2^-$.

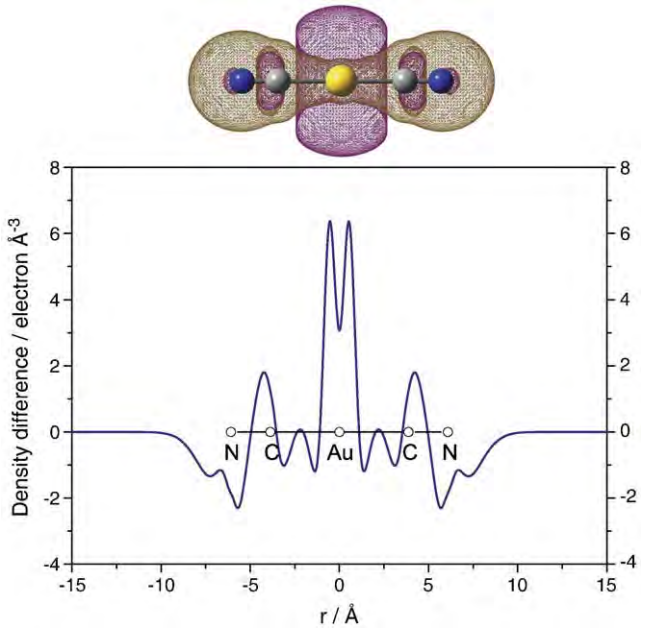


**Fig. 2.** Electron density difference between $Au(CN)_2^-$ complex and its constituents, Au (I) and the $CN^-$. Isosurface plot (upper part) and integral of $\Delta\rho(x,y,z)$ over y and z (lower part). The excess density (purple color, at $\Delta\rho = 0.4\times10^{-3}$ e/Å$^3$) is located around Au(I) while the $CN^-$ groups lose some electron density. (brown color, isosurface plotted at $\Delta\rho = -0.4\times10^{-3}$ e/Å$^3$).

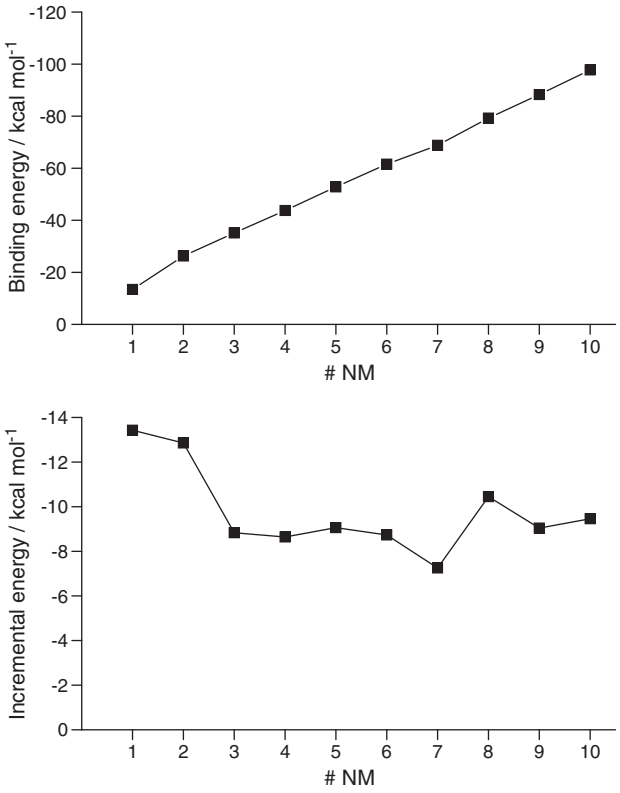


**Fig. 3.** (Upper) Total ligand–cation binding energies of the most stable structure defined as $E = E(Au(CN)_2^-\text{–}NM_n)\text{–}E(Au(CN)_2^-)\text{–}n\ E(NM)$ in the $Au(CN)_2^-\text{–}NM_n$ clusters with $1 \le n \le 10$. (Lower) Incremental energy defined as $\Delta E_n^{inc} = E_n^{inc} - E_{n-1}^{inc}$ where $E_n^{inc} = E(Au(CN)_2^-\text{–}NM_n)\text{–}E(Au(CN)_2^-\text{–}NM_{n-1})\text{–}E(NM)$.

change its hybridization when interacting with NM ligands. As a result, the binding energy per ligand decreases mostly (with the exception of n = 5 to 6) monotonically with the number (n) of ligands (Fig. 3) when the most stable structure for each n is considered. The optimized structures of $Au(CN)_2^-\text{–}NM_n$ with n = 1 to 10 are shown in Fig. 4. When a single NM molecule is added to $Au(CN)_2^-$, it prefers to be bound to $Au(CN)_2^-$ via end-on direction to form a linear $Au(CN)_2^-\text{–}NM$ complex. This end-on structure with a binding energy of −13.43 kcal/mol is about 5 kcal/mol more stable than the side-on structure with a T-shaped $Au(CN)_2^-\text{–}NM$ complex which is also a local minimum on the energy hypersurface. The energy difference is simply due to the fact that N in $Au(CN)_2^-$ has a higher negative partial charge than Au as is quantitatively shown in Fig. 1b. When a second NM molecule is added, $Au(CN)_2^-(NM)_2$ is formed as a linear complex with the NM molecules rather loosely bound to the anion. This linear form is 3.7 kcal/mol more stable than the one with two NM molecules binding to the same CN ligand. No local minima with NM coordinating to Au could be found for n>2 and for n = 3 we could locate only a single stable geometry. For n>3, the NM molecules can in principle either bind to the N atoms of the anion or form 'hydrogen-bonds' (we use this term simply to denote the C–H··· O pattern of arrangement between the highly polar NM molecules) to each other. From n = 4 to 7 these two geometrical patterns can be seen most clearly: The NM molecules can independently cluster on both N-sites or NM molecules can connect both sites. The respective energies are quite similar. For n>7, there are enough so that the two N binding sites of the anion are always bridged. For n = 8 and 9 half-ring structures are slightly preferred over more compact ones. Finally, for n = 10, the largest complex we investigated, a second shell of NM molecules starts to form.

The possibility of forming NM chains in the larger clusters is also reflected in the binding energies (Fig. 3). The incremental NM binding energy in the complexes with n = 8–10 is larger than for n = 7. Such a behavior is often found for solutes where solvent–solute and solvent–solvent binding energies are similar, which is the case for $Au(CN)_2(NM)_n^-$. Geometrically it reflects the competition between surface and interior states. In our system, due to the high directionality of the NM–NM interactions combined with the separation of the two N-sites of $Au(CN)_2^-$, the anion remains in the center of the complexes, at least until n = 10.

## 4. Conclusions

Our aim was to get an overall picture of dicyanoaurate(I) anion/nitromethane complexes. Structures and energies of clusters with up to 10 NM molecules were calculated. If less than 6 NM molecules are present, NM coordination to the nitrogen atoms at both ends of the linear is preferred while, for higher values of n, a geometrical pattern with chains or ring segments of NM molecules becomes competitive. The first solvation shell contains up to 9 NM molecules. At least for the cluster sizes we have investigated, no surface states are found with a central $Au(CN)_2^-$ being surrounded by NM molecules.

## Acknowledgements

Support from the Austrian Research Fund (I200-N29), from the Austrian Ministry of Science via an infrastructure grant to the LFU scientific computing platform and from the National Science and Technology Development Agency (2009 NSTDA Chair Professor, NANOTEC Center of Excellence, CNC Consortium) the Commission on Higher Education via the "National Research University Project of Thailand" (NRU) and the University Development Council (UDC) are

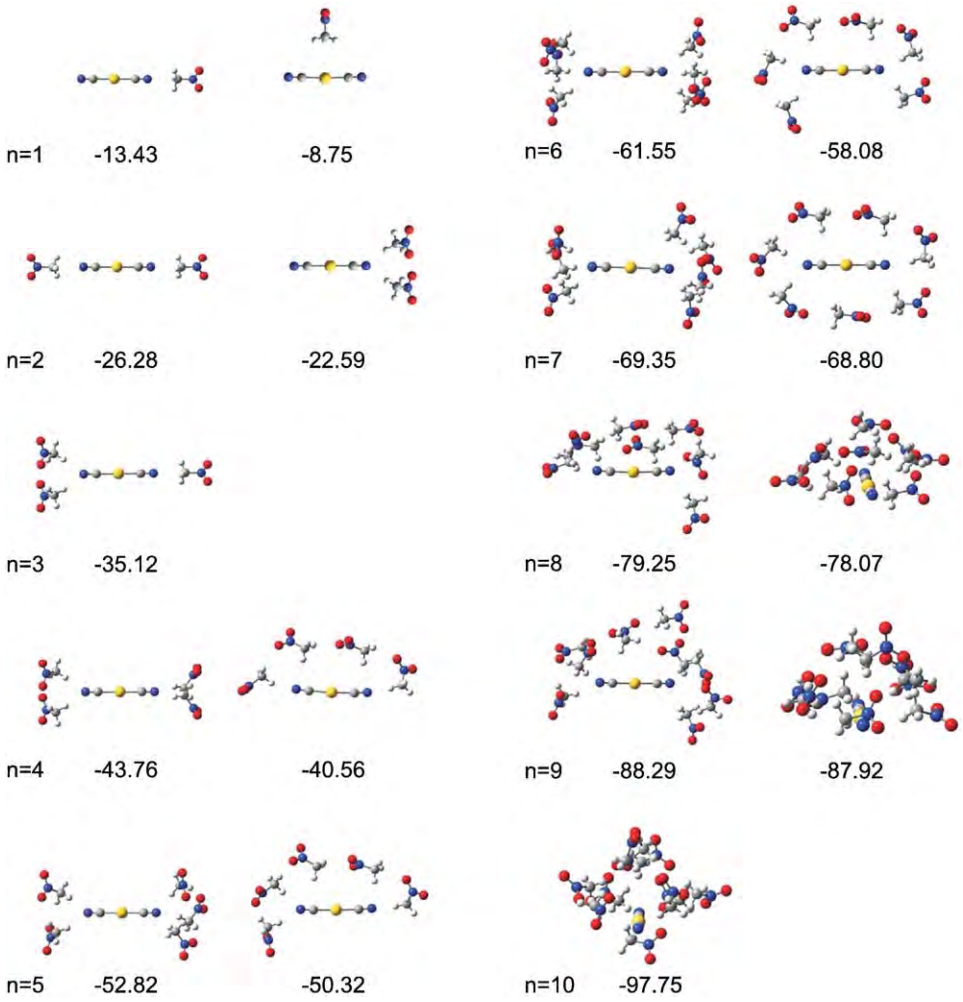


**Fig. 4.** Optimized geometries and binding energies of the most stable conformations of $Au(CN)_2^-$–$NM_n$ with $1 \leq n \leq 10$ calculated at the HF level. Energies are given in kcal/mol.

acknowledged. Support from the Kasetsart University Research and Development Institute (KURDI) and the Graduate School Kasetsart University to NI is also acknowledged.

## References

[1] J.R. Cui, L.F. Zhang, J. Hazard. Mater. 158 (2008) 228.
[2] C. Warakulwit, T. Nguyen, J. Majimel, M.-H. Delville, V. Lapeyre, P. Garrigue, V. Ravaine, J. Limtrakul, A. Kuhn, Nano Lett. 8 (2) (2008) 500.
[3] Z. Li, V. Ravaine, S. Ravaine, P. Garrigue, A. Kuhn, Adv. Funct. Mater. 17 (4) (2007) 618.
[4] A. Rubo, R. Kellens, J. Reddy, N. Steier, W. Hasenpusch, Ullmann's Encyclopedia of Industrial Chemistry, 'Alkali Metal Cyanides, , Wiley-VCH, Weinheim, 2006.
[5] P.J. Hay, W.R. Wadt, J. Chem. Phys. 82 (1985) 299.
[6] T.H. Dunning, P.J. Hay, in: H.F. Schaefer III (Ed.), Modern Theoretical Chemistry, Plenum Press, New York, 1976, p. 1.
[7] N. Injan, T. Megyes, T. Radnai, I. Bako, S. Balint, J. Limtrakul, D. Spangberg, M. Probst, J. Mol. Liquids 47 (2009) 64.
[8] M.J. Frisch, G.W. Trucks, H.B. Schlegel, G.E. Scuseria, M.A. Robb, J.R. Cheeseman, J.A. Montgomery Jr., T. Vreven, K.N. Kudin, J.C. Burant, J.M. Millam, S.S. Iyengar, J. Tomasi, V. Barone, B. Mennucci, M. Cossi, G. Scalmani, N. Rega, G.A. Petersson, H. Nakatsuji, M. Hada, M. Ehara, K. Toyota, R. Fukuda, J. Hasegawa, M. Ishida, T. Nakajima, Y. Honda, O. Kitao, H. Nakai, M. Klene, X. Li, J.E. Knox, H.P. Hratchian, J.B. Cross, V. Bakken, C. Adamo, J. Jaramillo, R. Gomperts, R.E. Stratmann, O. Yazyev, A.J. Austin, R. Cammi, C. Pomelli, J.W. Ochterski, P.Y. Ayala, K. Morokuma, G.A. Voth, P. Salvador, J.J. Dannenberg, V.G. Zakrzewski, S. Dapprich, A.D. Daniels, M.C. Strain, O. Farkas, D.K. Malick, A.D. Rabuck, K. Raghavachari, J.B. Foresman, J.V. Ortiz, Q. Cui, A.G. Baboul, S. Clifford, J. Cioslowski, B.B. Stefanov, G. Liu, A. Liashenko, P. Piskorz, I. Komaromi, R.L. Martin, D.J. Fox, T. Keith, M.A. Al-Laham, C.Y. Peng, A. Nanayakkara, M. Challacombe, P.M.W. Gill, B. Johnson, W. Chen, M.W. Wong, C. Gonzalez, J.A. Pople, Gaussian Inc., Wallingford CT.
[9] R.A. Bryce, J.M. Charnock, R.A.D. Pattrick, A.R. Lennie, J. Phys. Chem. A 107 (2003) 2516.
[10] Z. Assefa, K. Kalachnikova, R.G. Haire, R.E. Sykora, J. Solid State Chem. 180 (2007) 3121.

CHEMISTRY OF MATERIALS

ARTICLE

pubs.acs.org/cm

# Versatile Procedure for Synthesis of Janus-Type Carbon Tubes

Gabriel Loget,[†] Véronique Lapeyre,[†] Patrick Garrigue,[†] Chompunuch Warakulwit,[‡] Jumras Limtrakul,[‡] Marie-Hélène Delville,[§] and Alexander Kuhn[†,*]

[†]Université de Bordeaux 1, ISM, ENSCBP, 33607 Pessac Cedex, France

[‡]Center of Nanotechnology and Chemistry Department, Kasetsart University, Bangkok 10900, Thailand

[§]CNRS, UPR-9048, Université de Bordeaux 1, ICMCB, 87 Avenue du Dr. A. Schweitzer, 33608 Pessac Cedex, France

**ABSTRACT:** A bulk procedure based on bipolar electrochemistry is proposed for the generation of Janus-type carbon tubes. The concept is illustrated with carbon tubes that are selectively modified at their ends with various metals and conducting polymers. No surface or interface is required to break the symmetry and therefore this approach could be used for the mass production of Janus micro- and nano-objects. We show evidence that the technique is very versatile, allowing the choice of the kind of material that is deposited and whether the end product is mono- or bifunctionalized.

**KEYWORDS:** bipolar electrochemistry, carbon tubes, capillary electrophoresis, Janus particles, dumbbell structures

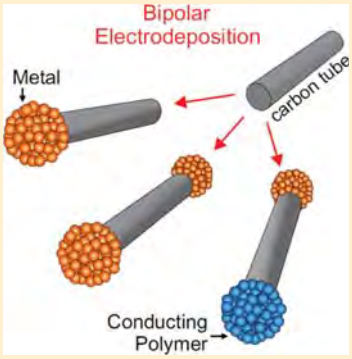


## INTRODUCTION

Elaboration of functionalized micro- and nanoparticles, especially dissymmetrical Janus-type objects, is of enormous interest. These particles have high application potential in many areas such as sensing, new electronic devices, and catalysis.[1] Nevertheless, most processes, used to achieve the site-selective functionalization of a particle at this scale, require the use of an interface to break the symmetry.[2] This makes the preparation of large quantities rather difficult because the majority of the techniques usually leads to monolayer equivalents of material, as the modification occurs in a two-dimensional reaction space. Thus, there is an increasing interest in developing alternative truly three-dimensional techniques, allowing a scale-up of the production of dissymmetrical particles. Examples of such kind of approaches are based on the generation of charge carriers in semiconductors using light,[3] or antenna chemistry.[4] An elegant method reported by Banin et al. consists of the precipitation of $HAuCl_4$ to grow selectively gold tips on cadmium selenide nanorods.[5]

In this context, another attractive way to selectively modify particles in a three-dimensional reaction space is based on the concept of bipolar electrochemistry, described by Fleischmann et al.[6] This appealing approach relies on the fact that when a conducting object is placed in a strong electric field between two electrodes, a polarization occurs that is proportional to the electric field and the characteristic dimensions of the object. When this polarization is strong enough, redox reactions can be carried out at the opposite ends of the object (Scheme 1a). This interesting theoretical concept[7] has recently found applications as the driving force in electrochemiluminescent reactions,[8−11] as detection mode in capillary electrophoresis,[12] for bipolar patterning,[13,14] for membrane pore functionalization,[15] as a mechanism for propelling micro-objects,[16] and in the fields of analytical chemistry and material science in general.[11,17] The potential difference between the two ends of a conducting object under the influence of an external electric field is given by the equation

$$\Delta V = Ed \tag{1}$$

with $E$ being the total external electric field and $d$ the particle size. To carry out two redox reactions at the opposite sides of the object, $\Delta V$ has to be in a first-order approximation at least equal to the difference between the formal potentials of the two redox reactions. Let us consider as an example for the dissymmetrical functionalization the formal potential ($E^0$) of the reduction of $Ni^{II}$ at one side

$$Ni^{II}{}_{(l)} + 2e^- \rightarrow Ni^0{}_{(s)} \tag{2}$$

and of the oxidation of water at the opposite side

$$2H_2O_{(l)} \rightarrow 4H^+{}_{(l)} + O_{2(g)} + 4e^- \tag{3}$$

From Table 1 it immediately follows that in this case the polarization has to generate a minimum potential difference of approximately

$$\Delta V_{min} = E^0_{Ni^0/Ni^{II}} - E^0_{H_2O/O_2} = 1.5\ V \tag{4}$$

This becomes an intrinsic problem of the approach when dealing with micro- or nanometer sized objects; as in this case $E$ needs to

**Received:** January 17, 2011
**Revised:** March 29, 2011
**Published:** April 21, 2011

**Scheme 1. (a) Concept of Bipolar Electrochemistry for the Generation of Janus-Type Objects; (b) Capillary Electrophoresis Set-up Used for the Dissymmetrical Electrodeposition**

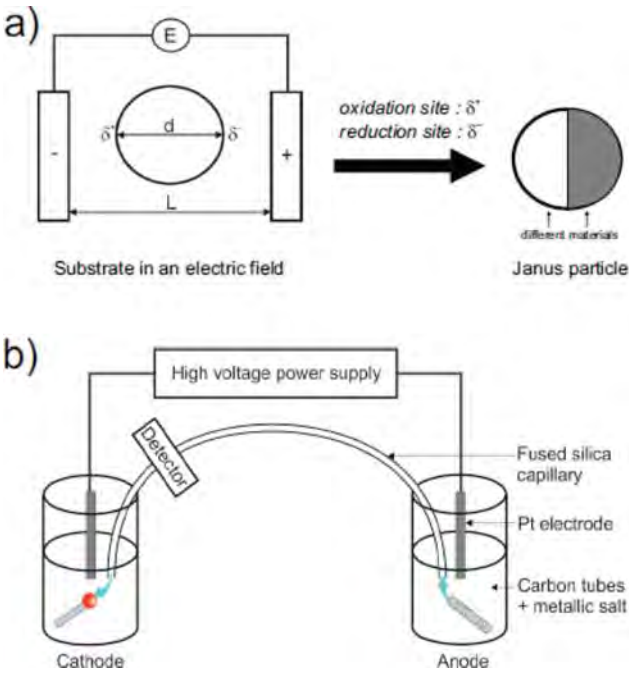


**Table 1. Formal Potentials of the Redox Couples Used for the Bipolar Electrodeposition Experiments**

| redox couple | $E^0$ [V vs NHE] |
|---|---|
| $[Au^{III}Cl_4]^-/Au^0$ | +0.99 |
| $Cu^I/Cu^0$ | +0.52 |
| $Ni^{II}/Ni^0$ | −0.26 |
| $Cu^{II}/Cu^I$ | +0.16 |
| $O_2/H_2O$ | +1.23 |

achieve values of up to MV $m^{-1}$ (see Eq 1), conditions that seem to be incompatible with a normal laboratory environment and especially with aqueous solutions because of the intrinsic side reactions accompanied by macroscopic bubble formation at both electrodes that disturbs the orientation of the objects in the electric field. Bradley et al. could partly circumvent the problem by using organic solvents to enlarge the potential window of the electrolyte and thus it was possible to generate metal deposits in a dissymmetrical way on different objects in the micrometer and submicrometer range.[18,19] However, it was also necessary to immobilize the objects on a surface to prevent them from rotating, which means that this is again a two-dimensional and not a bulk process. We could demonstrate that it is possible to get around these problems by using a capillary electrophoresis setup to apply the high electric field (Scheme 1b).[20] In this case the bipolar electrodeposition experiment consists of imposing a strong potential (several tens of kV) between two electrodes separated by a capillary, generating an electric field in the range of 100 kV $m^{-1}$. Under its influence, the conductive objects become polarized, and because of the electroosmotic flow through the capillary, they are moving from the anodic reservoir to the cathodic one. Electrodeposition is achieved in this way and the modified substrates are detected at the outlet with a UV−vis detector. In this work, we describe a generalization of the approach and we have chosen to illustrate this with micrometer-sized carbon tubes (CTs) because they can be easily visualized with an optical microscope. However, the approach can also be used for nanosized objects, as has been shown for the particular case of gold deposition on CNTs.[20] The so-called CABED procedure (Capillary Assisted Bipolar ElectroDeposition) was restricted so far to metal deposition, and most importantly, only one side of the carbon (nano)tubes could be modified.[21,22]

In the present work we demonstrate that the concept can be applied not only to a variety of metal deposits but also to the deposition of conducting polymers. In contrast to what has been reported in our previous work, we show here that by choosing the right potential sequence including relaxation times, we can not only deposit a material selectively on one side of the tubes but also trigger in a single experiment the deposition at both ends of the tube, resulting in structures that are either modified on both sides with the same material or with two different materials. This is the first time that such symmetric or dissymmetrical dumbbell-like structures are synthesized by bipolar electrochemistry using a bulk approach without the need of interfaces or surfaces to break the symmetry.

## EXPERIMENTAL SECTION

**Preparation of Carbon Tube Suspensions.** The CTs used in this study were produced by chemical vapor deposition with a porous aluminum oxide membrane serving as a template. After acid digestion of the template, the quite homogeneous tubes were recovered as a powder. For the suspensions containing $Au^{III}$ and $Ni^{II}$, about 0.1 mg of CTs was added to absolute ethanol (1.5 mL). To accelerate the formation of a suspension, the mixture was sonicated, but only for a short time (1 min), to avoid excessive breaking of the tubes. After 3 h of sedimentation, 0.5 mL of the supernatant was taken and added to 0.5 mL of 10 mM $NiSO_4$ or 10 mM $HAuCl_4$ in ultrapure water. The suspension with $Cu^I$ was prepared by adding about 0.1 mg of CTs to a solution of 10 mM CuI in acetonitrile. Suspensions with CuI and pyrrole were prepared by adding the same amount of CTs to a mixture of 10 mM CuI and freshly distilled 50 mM pyrrole in acetonitrile.

**Bipolar Electrodeposition on Carbon Tubes.** For electrodeposition experiments, all solutions or suspensions were introduced into the capillary by filling it manually with a syringe. The capillary used here is a fused silica capillary with a length of 24 cm and an inner diameter of 100 $\mu$m. The applied voltage was 30 kV for 5 min and the temperature was maintained at 25 °C. The CE experiment was first performed by rinsing the capillary with ultrapure water or acetonitrile. Then the CT suspension was introduced into the capillary. Because the addition of salt increases the ionic strength, it can result in the aggregation of the CTs, and therefore the suspensions were sonicated for a short time in an ultrasound bath before introduction into the capillary. For such salt concentrations, the typical currents in the electrophoresis setup were around 1 $\mu$A. The sample leaving the capillary at the cathodic side was collected directly at the outlet and transferred onto a TEM grid or another substrate, rinsed, and dried. The objects were then characterized by optical microscopy and scanning electron microscopy (SEM).

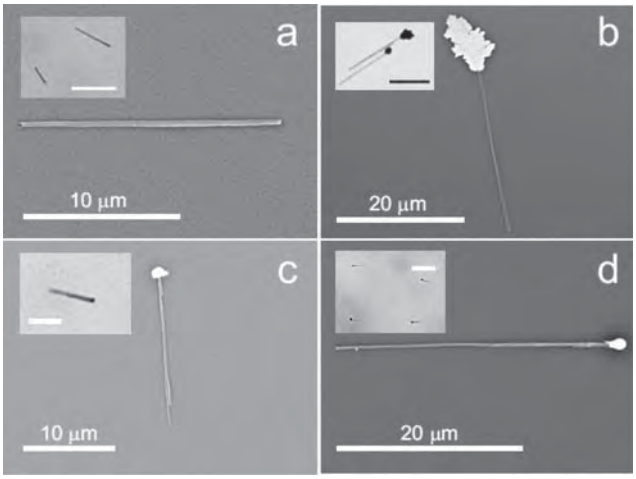


**Figure 1.** SEM images of CTs (a) without modification; modified at one side with (b) copper, (c) gold, and (d) nickel. Inset: optical microscope image of the modified CTs; scale bars are:(a), (b), and (d) 20 $\mu$m; (c) 10 $\mu$m.

## RESULTS AND DISCUSSION

The Janus-type CTs are obtained from raw carbon tubes synthesized by chemical vapor deposition into pores of an aluminum oxide membrane. The thickness of the collected tubes is 200 nm and their length is 20−30 $\mu$m (Figure 1a). The modified CTs are collected at the outlet of the capillary after bipolar electrodeposition. Samples shown in Figure 1b−d were obtained using carbon tube suspensions in solutions of $Cu^{I}$ (10 mM) in acetonitrile, $Au^{III}$ (5 mM) in water, and $Ni^{II}$ (5 mM) in water, respectively. Since copper modification was achieved in a nonaqueous solution, the reactions that occur at the tube ends are

$$Cu^{I} + e^{-} \rightarrow Cu^{0}{}_{(s)} \quad (5)$$

at one side and:

$$Cu^{I} \rightarrow Cu^{II} + e^{-} \quad (6)$$

at the opposite side. Using the $E^{0}$ values given in Table 1, one can easily see that the overall reaction resulting from a combination of eqs 5 and 6 should occur spontaneously via a dismutation. However, the $Cu^{I}$ species seem to be sufficiently stabilized because of the presence of $I^{-}$ ions so that a potential difference is still needed between the two ends of the tube to drive the reaction.

Gold deposition was carried out in aqueous solution, involving the following reactions:

$$[Au^{III}C1_4]^{-} + 3e^{-} \rightarrow Au^{0}{}_{(s)} + 4Cl^{-} \quad (7)$$

and

$$2H_2O_{(1)} \rightarrow 4H^{+}{}_{(1)} + O_{2(g)} + 4e^{-} \quad (8)$$

Table 1 indicates that in this case the combination of eqs 7 and 8 is not a spontaneous reaction and therefore a minimum potential difference between the two tube ends has to be generated to achieve dissymmetrical deposition:

$$\Delta V_{min} = E^{0}_{Au^{0}/AuCl_4^{-}} - E^{0}_{H_2O/O_2} = 0.24\ V \quad (9)$$

Obviously, because the experiments are carried out in far from standard conditions in terms of pH, concentrations, and partial gas pressures, deviations from the theoretical values of the potential threshold are expected. For all these experiments the same external electric field value $E$ = 125 kV $m^{-1}$ was applied, which gives typically for a 30 $\mu$m object a $\Delta V$ = 3.75 V. This value is definitely high enough, compared to the theoretical $\Delta V_{min}$ values previously calculated, to drive all these redox reactions. Looking at the SEM pictures of CTs collected at the capillary outlet (Figure 1b−d), it is obvious that the corresponding metal has been deposited. Because we used the same $E$, the same capillary length, and an identical experiment time, the variation in deposit size can be understood via the different growth kinetics which depend essentially on (i) the required $\Delta V_{min}$ and (ii) the salt concentration. Nickel modification, which requires the highest driving force ($\Delta V_{min}$ = 1.5 V), results in the smallest deposit size because for the given overall electric field the driving force is smaller and therefore the reaction proceeds more slowly. As stated above, copper deposition should occur almost spontaneously and therefore the required minimum voltage is certainly the smallest one compared to the other metals. This means that in this case the external field generates the highest driving force and leads to the biggest deposit. Another parameter that is important for the apparent deposit size is the growth morphology and its density. Copper is growing in a much more ramified structure, which leads for the same amount of reduced metal to a much bigger deposit compared to what is obtained for nickel and gold. This new family of monofunctionalized dissymmetric particles can be used for the localized functionalization of carbon tubes with organic molecules, for binding carbon tubes to a surface and for the development of nanodevices such as nanomotors because the orientation of tubes modified with a ferromagnetic material can be controlled with a magnetic field,[21] or a decomposition reaction can be driven by a catalytically active metal present at one tube end.[22]

During these bipolar electrodeposition runs, the end of the tube opposite to the one where the metal deposition takes place is positively polarized and therefore cannot be a site of reduction. If one wants to modify in a single experiment both ends with the same metal, polarization has to be reversed after the first deposition step so that the side that was the oxidation site becomes the reduction site. Since a classic electrophoresis set-up does not allow reversal of the polarization between the electrodes, we employed another approach consisting of the introduction of a relaxation time after the first polarization (without applied potential) to induce a statistical reversal of the CTs in the capillary. The optical microscope pictures in Figure 2 were obtained with the same carbon tube dispersion and the same electric field value as for the previous dissymmetrical deposition of copper, but with a regular interruption of the potential. When the potential is continuously applied or when the relaxation time between the pulses is short (Figure 2b,d), the CTs do not have the possibility to turn around in the capillary. Actually, once these anisotropic objects are polarized in the electric field, it would cost too much energy for them to flip in the opposite direction. This means that the tubes are all aligned parallel to the electric field and will not tumble or turn during their journey through the capillary. Therefore, this results exclusively in dissymmetrical deposits. In contrast, when the pulses are sufficiently separated in time (Figure 2a,c), the tubes are no longer polarized during the relaxation period without applied field and therefore have time to statistically change their orientation, thus leading to a symmetric deposition. In this case, after the first pulse, only one end of the tube is modified with $Cu^{0}$, but during the 5 minutes


dx.doi.org/10.1021/cm2001573 |*Chem. Mater.* 2011, 23, 2595–2599

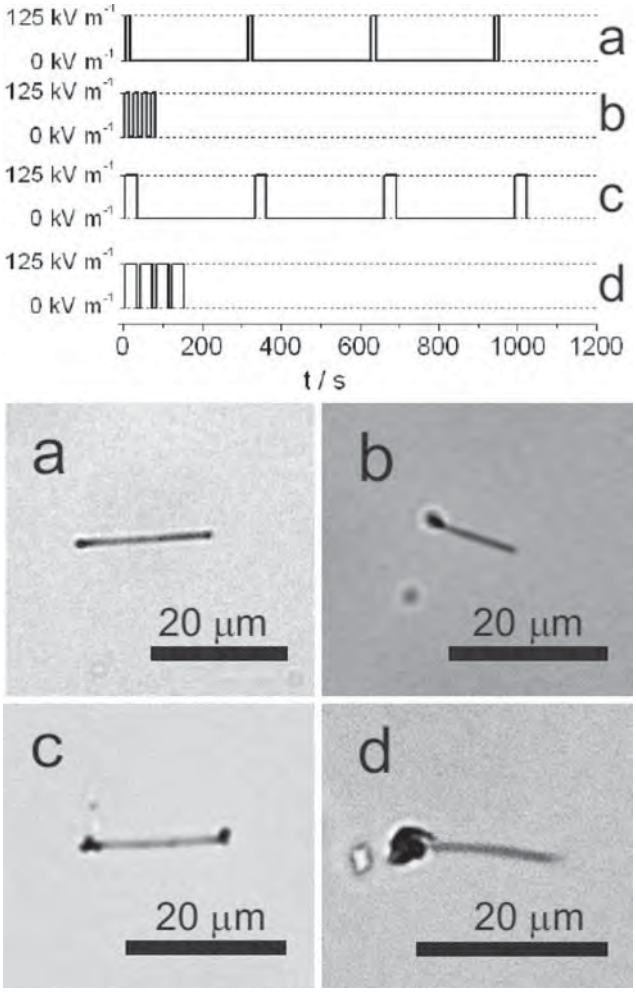


**Figure 2.** Pulsed bipolar electrodeposition with a suspension of CTs in 10 mM CuI in acetonitrile. The electric signal imposed between the electrodes is reported at the top and the corresponding optical microscope images of the modified carbon tubes at the bottom. The electric field was 125 kV·m. Time of potential pulses are 12 s (a and b) and 30 s (c and d); the time between the pulses are 5 min (a and c) and 10 s (b and d).

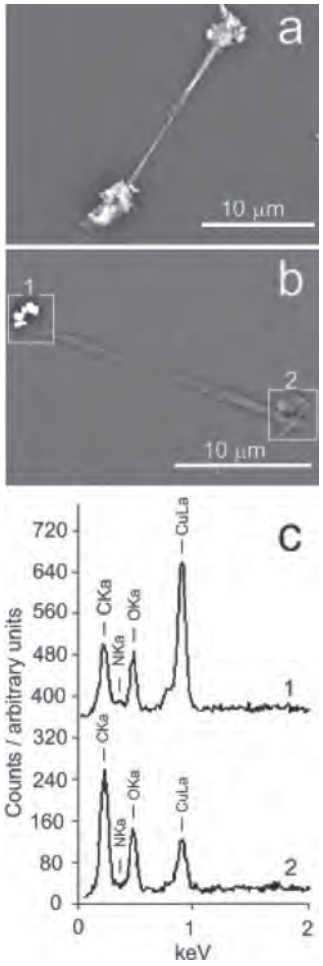


**Figure 3.** SEM pictures of modified dumbbell-like CTs. (a) Symmetric dumbbell-like object with copper deposits on both sides. (b) Dissymmetrical dumbbell-like object with one copper end (square 1) and one polypyrrole end (square 2). (c) EDX spectra recorded for the copper end (1) and for the polypyrrole end (2).

without polarization the tubes are allowed to reorientate in the capillary. Statistically, half of them will do so. Therefore, when the second pulse is applied, for half of the tubes the end where previously the oxidation of $Cu^{I}$ into $Cu^{II}$ took place becomes the reduction site where metal is formed. For these tubes, the counter reaction, which is the oxidation of $Cu^{I}$ into $Cu^{II}$, now takes place at the end of the tube that had been already modified with copper during the first potential pulse. Another possible counter reaction could be the oxidation of the already present copper deposit. However, it is more difficult to oxidize $Cu^{0}$ than $Cu^{I}$ because the oxidation potential is more positive (see Table 1) and therefore the dominating counter reaction is $Cu^{I} \rightarrow Cu^{II}$, thus preserving the already existing metal deposit.

If this long relaxation is repeated many times, statistically all tubes have turned around several times and consequently are modified on both sides. Striking evidence for the symmetric deposition of copper at both ends of the CT is shown in the SEM image of Figure 3a. The symmetric dumbbell-like functionalization of CTs can be extended to metals other than copper and these new materials can find exciting applications for self-assembly.

In the above experiments, the oxidation that occurs at the anodic end of the CTs produces gas or other oxidation products, but the involved reactions do not lead to a modification. We were therefore looking for an additional strategy, which would make use of this oxidation reaction to deposit also a material on the positively polarized side, concomitant with the reductive metal deposition on the negatively polarized side. One obvious type of material that can be obtained by oxidation is a conducting polymer. Because of their intrinsic reactivity, the metal salt and the monomer have to be chosen carefully. A mixture of $Cu^{I}$ and pyrrole was found to be stable in acetonitrile for at least 12 h. For longer times a brownish color that was due to the spontaneous polymerization of pyrrole appeared. CTs were added to this freshly prepared solution and bipolar electrodeposition was achieved using the same parameters that were applied for the dissymmetrical deposition of $Cu^{0}$. A SEM picture of a typical CT is shown in Figure 3b, the metallic end being clearly visible since the color contrast between metal and the carbon tube is very important. The polypyrrole (Ppy) end is less conductive than copper and thus exhibits a weaker contrast with respect to the


dx.doi.org/10.1021/cm2001573 |*Chem. Mater.* 2011, 23, 2595–2599

carbon tube. To make sure that the type of deposit at both ends is different, we performed, in addition, EDX experiments. The analysis has been carried out at the two opposite ends of the carbon tube. Figure 3c shows that the upper left end of the tube is characterized by a strong Cu signal around 1 keV compared to a much weaker carbon signal which originates most likely from the underlying carbon tube and the supporting grid. At the other end of the tube the carbon signal is much more prominent due to the presence of the conducting polymer. When both peaks are compared to the background oxygen signal, it becomes clear that their ratio is significantly different for the two ends of the tube, demonstrating the presence of the two different materials. However, on the Ppy side there is still a small contribution of Cu. This signal can be assigned to ionic copper species that become trapped in the polymer matrix during the pyrrole oxidation, it being known that copper forms stable complexes with polypyrrole, based on a Cu−N bond.[23]

This result opens up the way to a new family of bifunctional Janus-type materials that can be created by bipolar electrodeposition. Indeed, one can easily imagine that various metal-conducting polymer combinations can be deposited, leading to structures that could show interesting features. The pictures of Figures 1, 2, and 3 are representative of the majority of the tubes reaching the capillary outlet; however, in a more general sense, not 100% of the tubes are modified. The percentage of modified tubes obviously depends on the experimental parameters and there are several possible origins for a nonquantitative modification. The deposits might for example detach from the tube during the collection and rinsing procedure. Also, the tubes can be more or less conducting depending on their morphology and defects, which will lead to differences in polarization. When this kind of problem is minimized by careful sample handling, quantitative modification can be achieved.

## CONCLUSION

In summary, we present the generalization of a new bulk method based on bipolar electrochemistry that allows the highly controlled and localized functionalization of CTs. For the first time we could synthesize with one and the same process Janus-type carbon tubes that can be divided into three families, as a function of the used experimental parameters: (i) monofunctionalized dissymmetrical tubes, (ii) symmetric dumbbell-like tubes, and (iii) dissymmetrical dumbbell-like tubes. The deposit size and location can be very easily tuned by changing the strength and time variations of the electric field. Various materials can be deposited, assigning localized features to carbon tubes, thus leading to promising materials in domains such as sensing, electronic devices, self-assembly, and catalysis. Because this process is a true bulk process, one can imagine a scale-up of the production. Although we demonstrated the validity of the approach for the particular example of carbon tubes, this technique might be adapted to a large range of other micro- and nanoparticles of various size and shape.

## AUTHOR INFORMATION

### Corresponding Author

*Phone: +33540006573. Fax: +33540002717. E-mail: kuhn@enscbp.fr.

## ACKNOWLEDGMENT

This work has been cofunded by the French National Agency (ANR) and the European Commission in the frame of the "NanoSci-E+" transnational programme (CUBI-HOLE project, ANR's number: ANR-08-NSCI-008). It has also been supported by the French Ministry of Research, CNRS, and ENSCBP. C.W. and J.L. thank the National Science and Technology Development Agency (NSTDA Chair Professor and National Nanotechnology Center), the National Research University Project of Thailand (NRU) and the Thailand Research Fund for support.

## REFERENCES

(1) Walther, A.; Muller, A. H. E. *Soft Matter* **2008**, *4*, 663–668.
(2) Pradhan, S.; Xu, L.; Chen, S. *Adv. Funct. Mater* **2007**, *17*, 2385–2392.
(3) Reiche, H.; Dunn, W. W.; Bard, A.J. *J. Phys. Chem.* **1979**, *83*, 2248–2251.
(4) Duque, J. G.; Pasquali, M.; Schmidt, H. K. *J. Am. Chem. Soc.* **2008**, *130*, 15340–15347.
(5) Mokari, T.; Sztrum, C. G.; Salant, A.; Rabani, E.; Banin, U. *Nat. Mater.* **2005**, *4*, 855–863.
(6) Fleischmann, M.; Ghoroghchian, J.; Rolison, D.; Pons, S. *J. Phys. Chem.* **1986**, *90*, 6392–6400.
(7) Duval, J.; Kleijn, J. M.; Van Leeuwen, H. P. *J. Electroanal. Chem.* **2001**, *505*, 1–11.
(8) Mavré, F.; Chow, K.-F.; Sheridan, E.; Chang, B.-Y.; Crooks, J. A.; Crooks, R. M. *Anal. Chem.* **2009**, *81*, 6218.
(9) Chow, K.-F.; Mavré, F.; Crookes, J. A.; Chang, B.-Y.; Crooks, R. M. *J. Am. Chem. Soc.* **2009**, *131*, 8364–8365.
(10) Chow, K.-F.; Mavré, F.; Crooks, R. M. *J. Am. Chem. Soc.* **2008**, *130*, 7544–7545.
(11) Mavré, F.; Anand, R. K.; Laws, D. R.; Chow, K. F.; Chang, B. Y.; Crooks, J. A.; Crooks, R. M. *Anal. Chem.* **2010**, *82*, 8766–8774.
(12) Ordeig, O.; Godino, N.; Del Campo, J.; Munos, F. X.; Nikolajeff, F; Nyholm, L. *Anal. Chem.* **2008**, *80*, 3622–3632.
(13) Ulrich, C.; Andersson, O.; Nyholm, L.; Björefors, F. *Anal. Chem.* **2009**, *81*, 453–459.
(14) Ramakrishnan, S.; Shannon, C. *Langmuir* **2010**, *26*, 4602–4606.
(15) Bouquet, A.; Deschamp, E.; Maillet, P.; Livache, T.; Chatelain, F.; Haguet, V. *Small* **2009**, *5*, 2297–2303.
(16) Loget, G.; Kuhn, A. *J. Am. Chem. Soc.* **2010**, *132*, 15918–15919.
(17) Loget, G.; Kuhn, A. *Anal.Bioanal.Chem.* **2011**, in press, DOI 10.1007/s00216-011-4862-1.
(18) Bradley, J.-C.; Chen, H.-M.; Crawford, J.; Eckert, J.; Ernazarova, K.; Kurzeja, T.; Lin, M.; Nadler, W.; Stephens, S. G. *Nature* **1997**, *389*, 268–271.
(19) Bradley, J.-C.; Ma, Z. *Angew. Chem., Int. Ed.* **1999**, *38*, 1663–1666.
(20) Warakulwit, C.; Nguyen, T.; Majimel, J.; Delville, M.-H.; Lapeyre, V.; Garrigue, P.; Ravaine, V.; Limtrakul, J.; Kuhn, A. *Nano Lett.* **2008**, *8*, 500–504.
(21) Loget, G.; Larcade, G.; Lapeyre, V.; Garrigue, P.; Warakulwit, C.; Delville, M.-H.; Ravaine, V.; Kuhn, A. *Electrochim. Acta* **2010**, *55*, 8116–8120.
(22) Fattah, Z.; Loget, G.; Lapeyre, V.; Garrigue, P.; Warakulwit, C.; Limtrakul, J.; Bouffier, L.; Kuhn, A. *Electrochim. Acta* **2011**, in press, 10.1016/j.electacta.2011.01.048.
(23) Inoue, M. B.; Nebesny, K. W.; Fernando, Q.; Castillo-Ortega, M.; Inoue, M. *Synth. Met.* **1990**, *38*, 205–212.

# Structural and electronic bistability in ZnS single sheets and single-walled nanotubes

Norawit Krainara,[1,2] Jumras Limtrakul,[2] Francesc Illas,[1] and Stefan T. Bromley[1,3,*]

[1]*Departamento de Química Física & Institut de Química Teòrica i Computacional (IQTCUB), Universitat de Barcelona, Barcelona, Spain*

[2]*Department of Chemistry and Center for Advanced Studies in Nanotechnology and Its Applications in Chemical, Food and Agricultural Industries, Kasetsart University, Bangkok 10900, Thailand*

[3]*Institució Catalana de Recerca i Estudis Avançats (ICREA), Barcelona, Spain*

(Received 28 April 2011; published 30 June 2011)

We investigate a single sheet graphene analogue and a single-walled nanotube of ZnS using electronic structure calculations. Unlike the nearly perfectly flat structures of graphene and graphene analogues of other binary compounds (e.g., BN, ZnO, SiC), ZnS sheets are predicted to attain higher stability as complex, radically reconstructed structures. This predisposition to reconstruct also persists when ZnS sheets are rolled up into single-walled nanotubes. Smooth nanotubes and flat single sheets of ZnS have significantly smaller band gaps than their reconstructed counterparts, and are found to be metastable minima that are accessible from the reconstructed structures via external strain. This bistable electromechanical coupling may have significant technological potential (e.g., nanosensors, optomechanical switches).

DOI: 10.1103/PhysRevB.83.233305 PACS number(s): 61.46.Fg, 64.70.Nd, 62.23.Kn, 62.25.−g

Since the fabrication of atomically thin, nearly perfectly planar nanosheets of carbon (i.e., graphene[1]), two-dimensional (2D) materials have attracted huge scientific and technological interest. The formation of single flat sheets is facilitated in carbon, and similarly in boron nitride (BN),[2] by thermodynamic driving forces to form quasi-2D bulk crystal structures consisting of weakly interacting hexagonal ordered atomic layers (i.e., graphite and h-BN, respectively). Other technologically important materials, such as SiC, ZnO, and ZnS, exhibit fourfold-coordinated three-dimensional (3D) bulk crystal structures (i.e., zincblende or wurtzite), but these have been predicted to energetically favor layered phases[3] analogous to h-BN in thin films, which has been experimentally confirmed for ZnO.[4] Calculations have shown that isolated sheets of SiC,[5] and ZnO[6] are most stable as planar structures, just like for graphene and BN single sheets. Only for Si and Ge predicted a possible weak instability of single hexagonal planar sheets to slight puckering theory has (displacements of ±0.22 Å [Si] and ±0.32 Å [Ge] with respect to the planar sheet).[7]

Herein, using electronic structure calculations, we consider single hexagonal sheets of the II-IV semiconductor ZnS. We predict that 2D ZnS energetically prefers complex, significantly reconstructed sheets having out-of-plane displacements of ±1.95 Å. We find that these large distortions also persist even after rolling up such sheets into single-walled nanotubes (SWNTs). We further show that the application of tension/compression to 2D ZnS sheets and ZnS SWNTs can induce a structural transition between lower-energy reconstructed ZnS structures and their metastable planar/smooth forms. These structural transformations are also found to induce large band gap changes (>2 eV), showing how the mechanical and electronic properties of these systems are strongly coupled. Considering the impressive optoelectronic properties of current ZnS nanostructures[8] and the continuing advances in nanofabrication, the electronic and mechanical bistability of ZnS nanosheets and SWNTs is of potential technological importance (e.g., nanosensors, optomechanical switches).

Structures and properties were calculated using periodic density functional theory (DFT) as implemented in the Vienna Ab initio Simulation Package (VASP) code.[9] Calculations used the PW91[10] exchange-correlation potential, a plane-wave kinetic energy cutoff of 500 eV, and the projector augmented wave method.[11] Repeated image interactions were made negligible by ensuring a 15 Å separation between systems. For the nanosheets, both hexagonal cells of 32 atoms (a 4 × 4 supercell with respect to (w.r.t) the flat sheet) and rectangular 4 × 6 cells of 48 atoms (4 × 6 supercell w.r.t. the flat sheet) were employed, using 7 × 7 × 1 and 5 × 5 × 1 Monkhorst-Pack (MP)[12] meshes of $k$-points, respectively. In the (12,0) SWNT calculations, 48 atom supercells and 1 × 1× 9 MP $k$-point meshes were used. In all cases, the atomic structure of the system was fully relaxed until the forces were smaller than 0.005 eV/Å. To search for lowest-energy structures, we employed two methods. First, using a mechanical annealing technique,[13] systems were gradually compressed and stretched (up to ±30%) while optimizing the atomic positions at each stage. Every time a structural change occurred, the procedure was repeated around the newly obtained minimum energy configuration until no structural change occurred. Second, we employed microcanonical molecular dynamics with classical interatomic potentials[14] using the General Utility Lattice Program (GULP) code.[15] Systems were preheated to between 500 and 2000 K, and, during runs of 25–50 ps, sample configurations were energy-minimized and then further optimised using DFT.

We find that the strict graphene analogue of the ZnS single sheet has all atoms in a single plane with an optimized Zn-S bond distance of 2.246 Å and a 2D hexagonal supercell parameter of $a = b = 15.562$ Å. This structure is an energy minimum, with all vibrational modes having positive frequencies, and it is resilient to bending (see SWNT results below) and to small local distortions of its structure. For the latter, we prepared a number of sheets with randomly selected atoms displaced above and below the plane of the sheet, with out-of-plane displacements $\leqslant$0.03 Å, and found that the planar sheet was recovered after re-optimization.

 

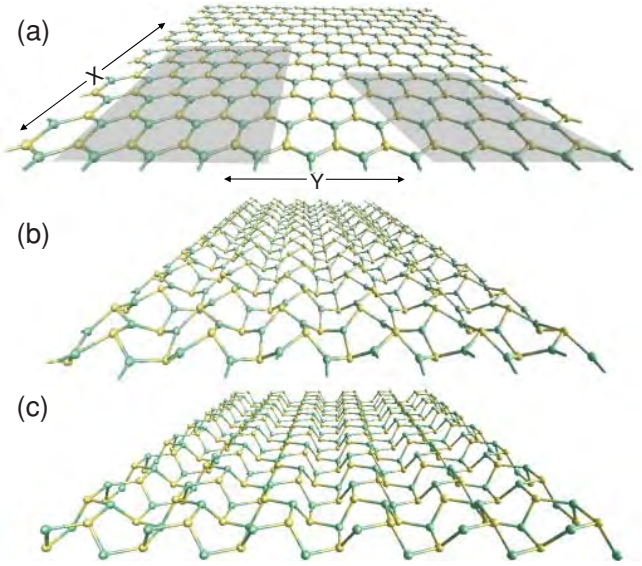


FIG. 1. (Color online) Structures of 2D ZnS systems: (a) flat sheet, (b) lowest-energy reconstructed sheet, (c) uppermost atoms of the $(11\bar{2}0)$ surface of wz-ZnS. Shaded areas show atoms in the cubic (left) and hexagonal (right) supercells. The X-Y axes in (a) relate to the applied strain directions. Lighter7darker grey balls indicate sulphur/zinc atom positions respectively.

Using a rectangular supercell (see Fig. 1), we applied strains perpendicular to in-plane directions and observed that small strains (less than ±5%) applied to the ZnS flat sheet also increased its energy, which, upon release, relaxed back to the planar minimum (see Fig 1(a)). Upon application of out-of-plane atomic distortions larger than 0.03 Å, the sheet re-optimized to a variety of lower-energy reconstructed geometries. The lowest-energy reconstructed structure found was 0.08 eV/ZnS lower in energy than the perfectly planar minimum. The significance of the magnitude of this energy difference can be appreciated by noting that it is approximately ten times larger than the calculated energy difference between zincblende ZnS (zb-ZnS) and wurtzite ZnS (wz-ZnS). This reconstructed sheet can also be obtained by increasing the in-plane compressive strain applied to the ZnS flat sheet in the *X* direction to beyond 5% (see Fig. 2(a)). The structure of the new energy minimum retains the bonding topology of the flat sheet and also exhibits all its Zn atoms in locally

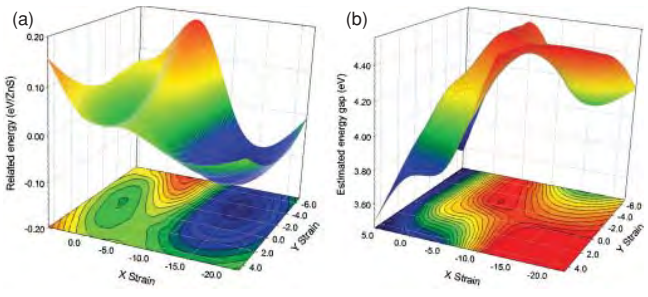


FIG. 2. (Color online) 2D ZnS flat sheet response to in-plane strain (%) with respect to: (a) relative total energy (eV/ZnS), and (b) estimated direct band gap (eV). Surfaces were generated from ∼50 *a*/*b*-constrained energy minimizations.

planar bonded configurations. The planes defined by the Zn centers and their three S nearest neighbors, however, are now not common to all Zn centers in the sheet, but instead they vary their inclination according to the alternating positions of the S atoms above and below the original plane of the flat sheet. These lateral out-of-plane atomic displacements involved in the reconstruction (up to ±1.95 Å) are found to be an order of magnitude larger than those of the relatively simple concerted buckling predicted for ZnS nanotubes (±0.1 Å)[18,20] and multilayer nanofilms (±0.265 Å),[16] with respect to corresponding perfectly planar systems. The high complexity of the reconstructed structure is reflected in the 16 atom unit cell (4 × 2) required to describe it, as compared to the two atoms per unit cell for the flat hexagonal ZnS sheet. The reconstructed structure (see Fig. 1(b)) has considerably smaller lattice supercell parameters with respect to the flat sheet ($a$ = 14.542 Å, $b$ = 13.971 Å), a slightly distorted near-hexagonal cell angle of 61.3°, and larger Zn-S bond distances, ranging between 2.264 and 2.278 Å. The S sublattice reconstruction is found to resemble that of the $(11\bar{2}0)$ surface of the wz-ZnS crystal (see Fig. 1(c)), which is calculated to be the most energetically stable bulk termination for ZnS.[14] The pattern of relaxation of the $(11\bar{2}0)$ wz-ZnS surface (e.g., a reduction in the S-Zn-S angles) described by Hamad *et al.*,[14] however, is much more exaggerated in 2D ZnS due to the absence of an attached underlying substrate. Other reconstructed single ZnS sheets found in our searches also resembled other bulk surfaces, such as the (110) surface of zb-ZnS, but all were found to be relatively higher in energy.

In both flat and reconstructed sheets, the Bader partitioned atomic charges are found to be very similar (flat: $Q_{Zn/S}$ = ±0.92e, reconstructed: $Q_{Zn/S}$ = ±0.90e), and, in the latter case, like those of zb-ZnS ($Q_{Zn/S}$ = ±0.90e). Thus, although some limited increase in charge transfer may occur, the main driving force behind this reconstruction is more likely to come from other influences. Assuming ZnS to be mainly covalent, we may envisage the 2D ZnS reconstruction as the result of the known tendency of S centers for $sp^3$ hybridization and an ensuing preference for tetrahedral coordination environments (as in "zb-ZnS"-abbreviation introduced at line). Interestingly, the reluctance of S (and Zn) to adopt more planar $sp^2$ hybridized multiple bonds has also been invoked in other studies to explain the relatively lower calculated energetic stability of stacks of planar ZnS sheets,[3] and smooth ZnS SWNTs[21] with respect to analogous structures in other materials (e.g., C, BN, and SiC). These studies, however, make no suggestion that sheet-based ZnS structures could thus reconstruct via $sp^3$ hybridization to become nonplanar to lower their energy. In a more ionic picture, we may consider the considerable mismatch between the small positive Zn ions and the considerably larger negative S ions tending to destabilize a regular hexagonal planar packing. In this picture, large, electron-rich S ions, by protruding away from the plane of the flat sheet, would be able to lower their energy through increased out-of-plane polarization. Classical interionic potentials (IPs) specifically parameterized to model S and Zn centers in tetrahedrally coordinated bulk environments in ZnS[14] also confirm that the reconstructed sheet is energetically more stable than the planar sheet. Here, this indeed occurs due to the classically incorporated polarizability of the $S^{2-}$ ions and not via

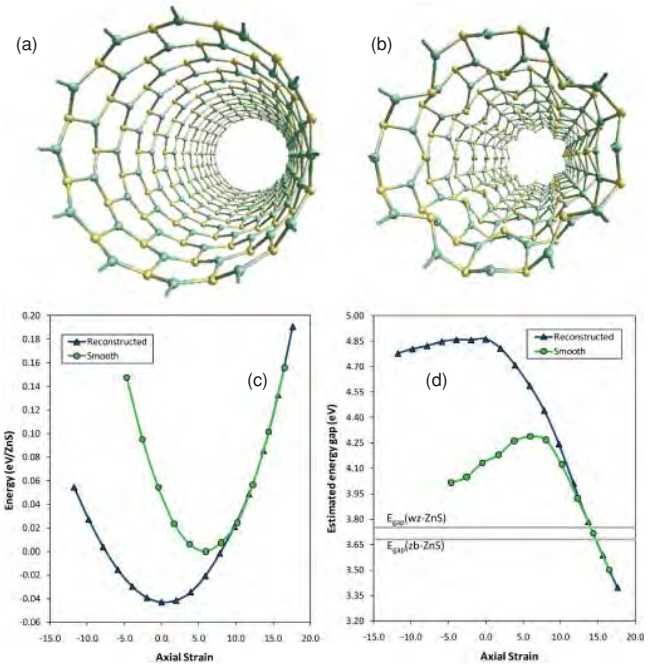


FIG. 3. (Color online) ZnS SWNT structures: (a) slightly buckled (smooth), and (b) reconstructed. Reconstructed SWNT response to axial strain (%) with respect to: (c) relative total energy, and (d) estimated direct band gap (exp. wz-ZnS and zb-ZnS band gaps also shown).

any specific directional parameters designed to promote a tetrahedral coordination environment of $Zn^{2+}$ ions, showing that sulfur polarization may also play an important role in stabilizing reconstructed ZnS nanostructures.

Rolling up flat 2D graphene sheets gives rise to smooth carbon SWNTs. Previous theoretical studies on ZnS SWNTs have reported minor concerted atomic displacements, similar to those found in BN SWNTs,[17] whereby all relatively less electronegative (smaller) ions/atoms move slightly inward (with respect to the mid-tube axis), and the remaining more electronegative (larger) ions/atoms move slightly outward (i.e., Zn and S respectively, each by $\leqslant$0.1 Å).[18–21] This small concerted radial buckling is also predicted to be most pronounced for small-diameter SWNTs, and to quickly diminish toward zero with increasing SWNT size.[18] In strong contrast to these reports, we find that slightly radially buckled ZnS SWNTs can, like the planar ZnS sheets, significantly lower their energy via radical structural reconstruction. We find that a slightly radially buckled (12,0) SWNT (see Fig. 3(a)) has a diameter of 1.50 nm, with slightly longer Zn-S bond lengths (2.253–2.258 Å) than in the corresponding smooth sheet. Our structural search approaches both give several more energetically stable reconstructed configurations, the most stable of which is shown in Fig. 3(b). This reconstructed (12,0) ZnS SWNT has very similar Zn-S bond lengths (2.265–2.278 Å) to the reconstructed sheet, and it is 0.04 eV/ZnS lower in energy than the slightly buckled (12,0) SWNT, with a significantly reduced diameter ($\sim$1.37 nm, taken as an average of maximum and minimum diameters). Like the reconstructed sheet, the Zn centers of the reconstructed SWNT lie in almost perfectly planar environments with respect to their three neighboring S atoms protruding, that protrude inwardly and outwardly (by $\sim\pm$1.0 Å with respect to a cylindrical surface lying symmetrically between the most inner and outer S atoms). As for the 2D ZnS sheets, we also find that the application of strain (parallel to the axis of the tube) can induce an interconversion between the reconstructed and slightly buckled SWNTs. Specifically, an axial tensile strain of $\geqslant$9% applied to the reconstructed SWNT and application of $\geqslant$4% axial tensile strain to the slightly buckled SWNT lead to the same strained structure. From this elongated geometry, relaxation, or application of axial compressive strain, can lead to either of the two SWNT energy minima (see Fig. 3(c)).

Consistent with the electronic structure of bulk ZnS, and previous studies of slightly buckled ZnS SWNTs[19,20] and ZnS nanofilms,[16] our reconstructed ZnS sheets and SWNTs both have direct gamma point gaps. Although the calculated absolute band gaps are underestimated by Generalized Gradient Approach (GGA) DFT, we use the difference between the calculated (2.07 eV) and experimental (3.75 eV)[22] wz-ZnS band gaps as an approximate corrective shift, which is applied to all reported gaps. The resulting values are only intended as a rough guide to actual band gaps and should in no way be regarded as accurate quantitative predictions. At their respective minimum energy geometries, where the band gaps are largest, larger gaps are found for the reconstructed ZnS sheet (4.70 eV) and (12,0) SWNT (4.86 eV) as compared to their relatively smooth counterparts (4.21 eV and 4.28 eV, respectively), i.e., $\sim$0.5 eV difference in each case. It is thus clear that the (opto)electronic and mechanical degrees of freedom in these systems are strongly coupled. Considering strain, not only as a means to traverse between minima, but more generally as an adjustable system variable, we see that these systems also allow for large continuous and reversible band gap variation (see Figs. 2(b) and 3(d)). For example, starting with the reconstructed (12,0) SWNT at its minimum energy geometry, we may, by increasing the axial compression continuously up to 18%, decrease its band gap in a near-linear fashion, eventually inducing an overall decrease of $\sim$1.5 eV. Based upon our band gap estimates, this mechanically induced band gap engineering would allow access to a wide range of UV photon energies (approximately between 3.3 and 4.8 eV), with possible applications in tunable wide-band optoelectronic devices. We note that similar calculations (e.g., C,[23] BN,[24] SiC[25]), and experiments in the case of C,[26] on other (n,0) SWNT systems have also shown strain-induced band gap variations. Specific to ZnS, however, it is possible to employ strain to switch between two stable energy minima, each with a distinctly different gap.

ZnS sheets display a more complex nonlinear electronic response upon application of perpendicular in-plane tensile strains. In the rectangular sheet, different strains along the *a* and *b* lattice directions can combine to give a range of band gap changes with a slightly smaller range of band gap energies ($\sim$3.5–4.5 eV, see Fig. 2(b)) than in the SWNTs. In experiments, although it is possible to study unsupported single layers, it is much easier to study monolayers that are grown on supporting materials. Single wz-ZnS monolayers are often grown as passivating layers on nanostructures of other inorganic semiconductors with smaller band gaps (e.g., CdSe) in order to improve quantum yields.[27] The structures

of these single layers are, however, strongly bound to the semiconductor support and are likely to be epitaxially locked into a structure determined by that of the support.[27] Although our results suggest that epitaxial growth of ZnS may be facilitated due to its capacity to adapt its structure to better match that of a relatively rigid bulk support, once it has been prepared, this adaptiveness, and thus its elasto-optic response, will be largely diminished. From experimental and theoretical studies of single flat hexagonal sheets of BN and ZnO grown on Ag(111) metal surfaces, the sheet-support interaction seems to be relatively much weaker.[4,28,29] For a monolayer of ZnS grown on a very weakly interacting support (e.g., a suitable noble metal), we would thus expect to observe significant geometric reconstruction. By varying the sheet-support interaction strength (e.g., by varying support material, temperature, etc.), the degree of reconstruction and the electronic response could be varied. Predictive calculations as to appropriate choices of support are currently being pursued. A change in the anion in ZnS by one position in its respective group (i.e., S $\rightarrow$ O) is known to give a system (i.e., ZnO) that can only stably exhibit the flat sheet.[3–5] Our preliminary calculations for systems where a cation is exchanged for Cd and/or the anion is exchanged for Se also appear to exhibit similar bistable behavior to that found for ZnS, thus illustrating the versatility and generality of this effect.

In summary, we predict that the low-energy structures of hexagonal ordered single sheets of ZnS, and nanostructures formed thereof, exhibit strongly reconstructed geometries that are distinct from the relatively smooth structures of graphene-based systems and analogous systems of other studied AB materials (e.g., BN, SiC, ZnO). We find that application of compressive and/or tensile strain allows for reversibe passage between the reconstructed ZnS systems and smooth structured higher-lying energy minima. In both ZnS single sheet graphene analogues and SWNTs, this energetic and structural bistability is coupled to significant changes in the direct band gap. This remarkable nanoscale mechanical-electronic response may have a range of future applications, such as optoelectronic devices and sensors.

Supporting grants and institutions include FIS2008-02238, 2009SGR1041, and XRQTC, National Science and Technology Development Agency (NSTDA chair professorship, NANOTEC Center of Excellence), and the Commission on Higher Education (National Research University of Thailand, the Joint Ph.D. Program Thai doctoral degree (NK)). Computer time on MareNostrum (BSC) is acknowledged.

*Corresponding author: s.bromley@ub.edu

[1] K. S. Novoselov, A. K. Geim, S. V. Morozov, D. Jiang, Y. Zhang, S. V. Dubonos, I. V. Grigorieva, and A. A. Firsov, Science **306**, 5696 (2004).
[2] M. Corso, W. Auwärter, M. Muntwiler, A. Tamai, T. Greber, and J. Osterwalder, Science **303**, 217 (2004).
[3] C. L. Freeman, F. Claeyssens, N. L. Allan, and J. H. Harding, Phys. Rev. Lett. **96**, 066102 (2006).
[4] C. Tusche, H. L. Meyerheim, and J. Kirschner, Phys. Rev. Lett. **99**, 026102 (2007).
[5] E. Bekaroglu, M. Topsakal, S. Cahangirov, and S. Ciraci, Phys. Rev. B **81**, 075433 (2010).
[6] M. Topsakal, S. Cahangirov, E. Bekaroglu, and S. Ciraci, Phys. Rev. B **80**, 235119 (2009).
[7] S. Cahangirov, M. Topsakal, E. Aktürk, H. Şahin, and S. Ciraci, Phys. Rev. Lett. **102**, 236804 (2009).
[8] X. Fang, Y. Bando, U. K. Gautam, T. Zhai, H. Zeng, X. Xu, M. Liao, and D. Golberg, Crit. Rev. Solid State Mater. Sci. **34**, 190 (2009).
[9] G. Kresse and J. Hafner, Phys. Rev. B **47**, 558 (1993).
[10] J. P. Perdew, K. Burke, and Y. Wang, Phys. Rev. B **54**, 16533 (1996).
[11] P. E. Blöchl, Phys. Rev. B **50**, 17953 (1994).
[12] H. J. Monkhorst and J. D. Pack, Phys. Rev. B **13**, 5188 (1976).
[13] W. Sangthong, J. Limtrakul, F. Illas, and S. T. Bromley, Nanoscale **2**, 72 (2010).
[14] S. Hamad, S. Cristol, and C. R. A. Catlow, J. Phys. Chem. B **106**, 11002 (2002).
[15] J. D. Gale, Z. Kristallogr. **220**, 552 (2005).
[16] X. Zhang, H. Zhang, T. He, and M. Zhao, J. Appl. Phys. **108**, 064317 (2010).
[17] E. Hernández, C. Goze, P. Bernier, and A. Rubio, Phys. Rev. Lett. **80**, 4502 (1998).
[18] S. Pal, B. Goswami, and P. Sarkar, J. Phys. Chem. C **111**, 1556 (2007).
[19] X. Zhang, M. Zhao, S. Yan, T. He, W. Li, X. Lin, Z. Xi, Z. Wang, X. Liu, and Y. Xia, Nanotech. **19**, 305708 (2008).
[20] L. Li, M. Zhao, X. Zhang, Z. Zhu, F. Li, J. Li, C. Song, X. Liu, and Y. Xia, J. Phys. Chem. C **112**, 3509 (2008).
[21] Y. Li, Z. Zhou, Y. Chen, and Z. Chen, J. Chem. Phys. **130**, 204706 (2009).
[22] A. Ebina, E. Fukunaga, and T. Takahashi, Phys. Rev. B **12**, 687 (1975).
[23] P. K. Valavala, D. Banyai, M. Seel, and R. Pati, Phys. Rev. B, **78**, 235430 (2008).
[24] Y. Kinoshita, and N. Ohno, Phys. Rev. B **82**, 085433 (2010).
[25] Z. Wang, X. Zu, H. Xiao, F. Goa, and W. J. Weber, Appl. Phys. Lett. **92**, 183116 (2008).
[26] E. D. Minot, Y. Yaish, V. Sazonova, J.-Y. Park, M. Brink, and P. L. McEuen, Phys. Rev. Lett. **90**, 156401 (2003).
[27] B. O. Dabbousi, J. Rodriguez-Viejo, F. V. Mikulec, J. R. Heine, M. Mattoussi, R. Ober, K. F. Jensen, and M. G. Bawendi, J. Phys. Chem. B **101**, 9463 (1997).
[28] F. Müller, S. Hüfner, H. Sachdev, R. Laskowski, P. Blaha, and K. Schwarz, Phys. Rev. B **82**, 113406 (2010).
[29] R. Laskowski, P. Blaha, and K. Schwarz, Phys. Rev. B **78**, 045409 (2008).

DOI: 10.1002/cphc.201100642

# Formaldehyde Encapsulated in Lithium-Decorated Metal-Organic Frameworks: A Density Functional Theory Study

Thana Maihom,[a, b] Saowapak Choomwattana,[a, b] Pipat Khongpracha,[a, b, c] Michael Probst,[d] and Jumras Limtrakul*[a, b, c]

The stability of monomeric formaldehyde encapsulated in the lithium-decorated metal-organic framework Li-MOF-5 was investigated by means of density functional calculations with the M06-L functional and the 6-31G(d,p) basis set. To assess the efficiency of Li-MOF-5 for formaldehyde preservation, we consider the reaction kinetics and the thermodynamic equilibrium between formaldehyde and its trimerized product, 1,3,5-trioxane. We propose that trimerization of encapsulated formaldehyde takes place in a single reaction step with an activation energy of 34.5 kcal mol$^{-1}$. This is 17.2 kcal mol$^{-1}$ higher than the corresponding activation energy in the bare system. In addition, the reaction energy of the system studied herein is endothermic by 6.1 kcal mol$^{-1}$ and the Gibbs free energy ($\Delta G$) of the reaction becomes positive (11.0 kcal mol$^{-1}$). Consequently, the predicted reverse rate for the trimerization reaction in the Li-MOF-5 is significantly faster than the forward rate. The calculations show that the oligomerization of formaldehyde in Li-MOF-5 is a reversible reaction, suggesting that such a zeolite might be a good candidate material for preserving formaldehyde in its monomeric form.

## 1. Introduction

Formaldehyde, a well-known volatile organic compound (VOC), is widely used as an industrial feedstock for the production of fine chemicals, resins, and several domestic products such as paints. Nevertheless, its applicability is limited by its low boiling point of −19.5 °C. Moreover, formaldehyde rapidly self-polymerizes into chain polymers such as paraformaldehyde or into oligomers such as the cyclic trioxane. Its preservation in the monomeric form is difficult.

Na–X and Na–Y zeolites have been reported to be capable of storing formaldehyde.[1] These materials stabilize and also activate formaldehyde to undergo carbonyl–ene reactions with a variety of olefins as has also been clarified by theoretical studies.[2] In recent years, metal-organic frameworks (MOFs) were investigated as promising candidates for gas storage (e.g. $CO_2$ and $H_2$)[3] because of their flexibility and the possibility to tune their surface composition and pore structures by changing the metal center or the organic linker. Computational and experimental investigations[4–5] have shown that metal atoms or cations that either decorate the linkers or are incorporated into them can enhance the capacity of MOFs for gas storage. The most frequently used metal is Lithium (Li) because decorating MOF structures with it is especially simple. Li on MOF linkers forms an accessible open metal site that can interact well with incoming molecules. It can therefore be expected to interact with formaldehyde in a way similar to the Na cation in zeolites, which is known to prevent formaldehyde from self-polymerizing.

To the best of our knowledge, such a system has not yet been studied in detail. Therefore, we investigated it herein by means of density functional theory (DFT) calculations with the M06-L functional. We calculated the reaction mechanism and the corresponding energy profile defined by the structures of the adsorbed starting complex (three formaldehydes coordinated to Li), the transition state and the product trioxane. We also compared our findings to those obtained for the bare system.

## 2. Results and Discussion

### 2.1. Decoration of MOF-5 with Li and its Subsequent Application as Formaldehyde Adsorption Complex

Herein, MOF-5[6] (also called IRMOF-1) was chosen as host material. It consists of $Zn_4O$ clusters connected to 1,4-benzenedi-

[a] T. Maihom, S. Choomwattana, Dr. P. Khongpracha, Prof. Dr. J. Limtrakul
Laboratory for Computational and Applied Chemistry
Department of Chemistry
Faculty of Science and Center of Nanotechnology
Research and Development Institute
Kasetsart University
Bangkok 10900 (Thailand)
Fax: (+66) 2-562-5555
E-mail: Jumras.l@ku.ac.th

[b] T. Maihom, S. Choomwattana, Dr. P. Khongpracha, Prof. Dr. J. Limtrakul
NANOTEC Center of Excellence
National Nanotechnology Center
Kasetsart University
Bangkok 10900 (Thailand)

[c] Dr. P. Khongpracha, Prof. Dr. J. Limtrakul
Center for Advanced Studies in Nanotechnology and its Applications in Chemical, Food, and Agricultural Industries
Kasetsart University
Bangkok 10900 (Thailand)

[d] Prof. Dr. M. Probst
Institute of Ion Physics and Applied Physics
University of Innsbruck
6020 Innsbruck (Austria)

  

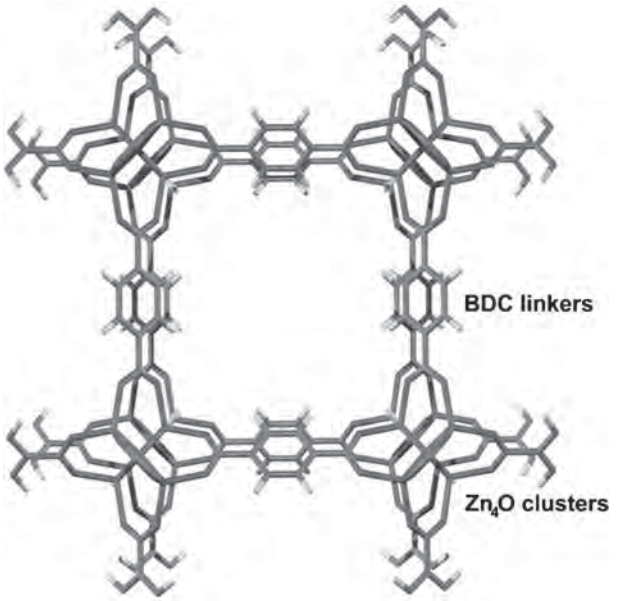


**Figure 1.** Unit cell of MOF-5.

carboxylate (BDC) organic linkers to form a cubic porous network with the unit formula $Zn_4O(BDC)_3$. The unit cell of MOF-5 is shown in Figure 1. Because of its large size, we used an abridged representative model to reduce the computational costs. A model consisting of two $Zn_4O$ clusters joined by one BDC linker is the simplest one that can reasonably mimic the active site of the MOF-5 linker (Figure 2a). It is comparable to the models that have been used in previous studies.[7] The remaining BDC linkers not taken into account were replaced by hydrogen atoms. The Li ion was placed on top of the benzene ring (Figure 2b) which has been found[4a,5] to be its preferred position on hexagonal aromatic hydrocarbon structures. The Li-MOF model has the sum formula $Zn_8O_{26}C_{18}H_{14}Li$.

The geometrical parameters of selected geometrical structures of pure MOF-5 and of Li-MOF-5 are given in Table 1. In

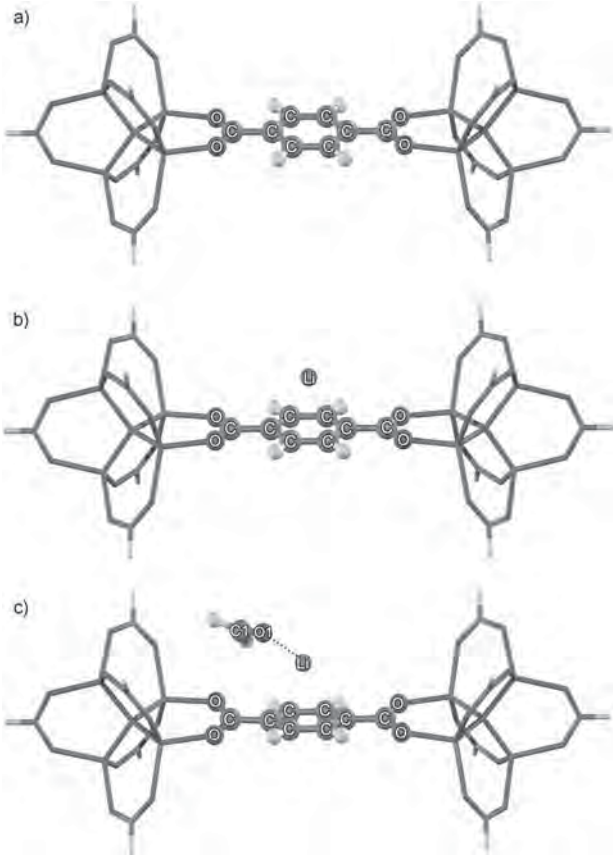


**Figure 2.** Optimized structures for a) pure MOF-5 (two $Zn_4O$ clusters joined by one 1,4-benzenedicarboxylate organic linker), b) Li-MOF-5 and c) formaldehyde adsorbed on Li-MOF (Ads_MOF).

the MOF-5 cluster, the average C–C bond distance ($<C–C>_{bz}$) in the benzene ring and the C–O–C bond angle ($<C–O–C>$) are 1.40 Å and 124.6°, respectively. These values are in a good agreement with the experimental results of 1.39 Å and 126.4°, respectively.[6c] For Li-MOF-5, the Li cation coordinates symmetrically through a $\eta^6$-type interaction to the hexagonal aromatic ring of the BDC linker. The average distance between the C atoms and Li ($<Li\cdots C>$) is 2.39 Å. The adsorption of the metal cation causes the average C–C bond distance and the O–C–O angle to increase by 0.01 Å and 3.0°, respectively. The natural atomic population of Li is $+0.941\,|e|$, which is consistent with the values between $+0.5\,|e|$ to $+1.0\,|e|$ for Li-doped systems[5]. This charge transfer also explains the abovementioned increase in the geometrical parameters. The calculated adsorption energy ($\Delta E_{Li}$) of a Li cation on MOF-5 is defined as follows in Equation (1):

**Table 1.** Optimized geometrical parameters of the species involved in the trimerization of formaldehyde in Li-MOF-5.

| Parameter | Isolated cluster | Isolated Li-MOF-5 cluster | Formaldehyde adsorption (Ads_MOF) | Formaldehyde adsorption (Coads_MOF) | Transition state (TS1_MOF) | Trioxane product (Prod_MOF) |
|---|---|---|---|---|---|---|
| Distances [Å] | | | | | | |
| $<C–C>_{bz}$ | 1.40 | 1.41 | 1.40 | 1.40 | 1.41 | 1.41 |
| $<Li\cdots C>$ | – | 2.39 | 2.51 | 3.03 | 2.53 | 2.55 |
| O1-Li | – | – | 1.90 | 1.93 | 1.82 | 2.17 |
| O2-Li | – | – | – | 1.97 | 3.85 | 2.18 |
| O3-Li | – | – | – | 1.98 | 3.36 | 2.20 |
| C1-O1 | 1.20 | – | 1.22 | 1.21 | 1.30 | 1.43 |
| C2-O2 | 1.20 | – | – | 1.21 | 1.24 | 1.42 |
| C3-O3 | 1.20 | – | – | 1.21 | 1.27 | 1.42 |
| O1-C2 | – | – | – | 4.57 | 2.25 | 1.42 |
| O2-C3 | – | – | – | 3.95 | 1.94 | 1.43 |
| O3-C1 | – | – | – | 4.50 | 1.61 | 1.42 |
| Angles [°] | | | | | | |
| $<O–C–O>$ | 124.6 | 127.6 | 126.8 | 125.4 | 126.9 | 126.7 |

  

$$\Delta E_{Li} = E(\text{Li}-\text{MOF}) - E(\text{Li}) - E(\text{MOF}) \quad (1)$$

where *E*(Li-MOF), *E*(Li) and *E*(MOF) are the total energies of the clusters of Li-MOF (Li adsorbed), the isolated Li cation and the pure MOF-5 model, respectively. The adsorption energy of $Li^+$ on MOF-5 is $-32.9\,kcal\,mol^{-1}$. The difference between this value and the measured value of $-38.5 \pm 3.2\,kcal\,mol^{-1}$ for the $Li^+$-$C_6H_6$ complex[8] is explainable by a somewhat diminished $\pi$ electron density over the benzene plane caused by the electrophilic nodes of the $Zn_4O$ clusters.

The adsorption complex of one formaldehyde coordinated to the Li ion in MOF-5 (Ads_MOF) is depicted in Figure 2c and its key optimized geometrical parameters are listed in Table 1. The formaldehyde molecule interacts with the Li ion through its lone pair electrons. This conformation resembles the ones found for formaldehyde adsorbed into Na-FAU zeolites[2] and coordinated to Cu complexed in the paddlewheels of MOF-11.[9] The lone pair interaction induces the average lengthening of Li···C distances from 2.39 to 2.51 Å. The intermolecular distance between the oxygen of formaldehyde and the Li ion in the MOF is 1.90 Å. The C–O···Li-MOF angle is 138.4°. In addition, the electron transfer from O1 to the Li ion results in a slight elongation of the intramolecular carbon–oxygen bond of formaldehyde from 1.20 to 1.22 Å. The natural population analysis (NPA) revealed that the positive charge on Li is reduced from +0.941 to +0.876 $|e|$. The calculated adsorption energy of this complex is $-28.0\,kcal\,mol^{-1}$.

### 2.2. Reaction Mechanism of Formaldehyde Trimerization

The steric constraints in the MOF cavities prevent the polymerization of formaldehyde into a chain polymer. Therefore, we only concentrated on the trimerization reaction equilibrium between formaldehyde and trioxane in Li-MOF-5 at room temperature and compared this to the bare system. Selected geometrical parameters for this reaction step are shown in Table 1.

The trimerization is considered to proceed in a single step without intermediates. In the bare system, three formaldehyde molecules align to each other in a twisted hexagonal complex in which the interaction between a carbon atom and an oxygen atom of the next molecule causes the inter- and intramolecular C–O distances to become almost equal (Figure 3a). The complexation energy is $-7.3\,kcal\,mol^{-1}$. In the Li-MOF-5 system, the adsorbed formaldehydes' arrangement is quite different, mainly due to the effect of the Li ion. Three molecules

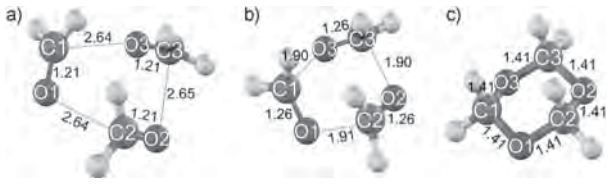


**Figure 3.** Optimized structures of the bare a) trimer (Complex_Bare), b) transition state (TS_Bare) and c) trioxane (Prod_Bare) for the trimerization reaction of unenclosed formaldehyde.

of formaldehyde coadsorb on the Li ion through coordination of the lone pair electrons of each formaldehyde oxygen atom to the Li ion (Figure 4a). The internuclear distances between the three formaldehyde oxygen atoms and $Li^+$ are 1.93, 1.97 and 1.98 Å, respectively. The coordination to $Li^+$ causes a slight elongation of the C=O double bonds from 1.20 in the isolated formaldehyde to 1.21 Å. The adsorption complex is additionally stabilized through hydrogen bonding from the hydrogen atoms of two formaldehyde molecules to the oxygen atoms of the linker. This causes the Li cation to shift slightly from the position above the middle of the benzene ring, as shown in Figure 4a. The total adsorption energy is $-66.8$ kcal $mol^{-1}$, indicating a considerable ability to stabilize monomeric formaldehyde.

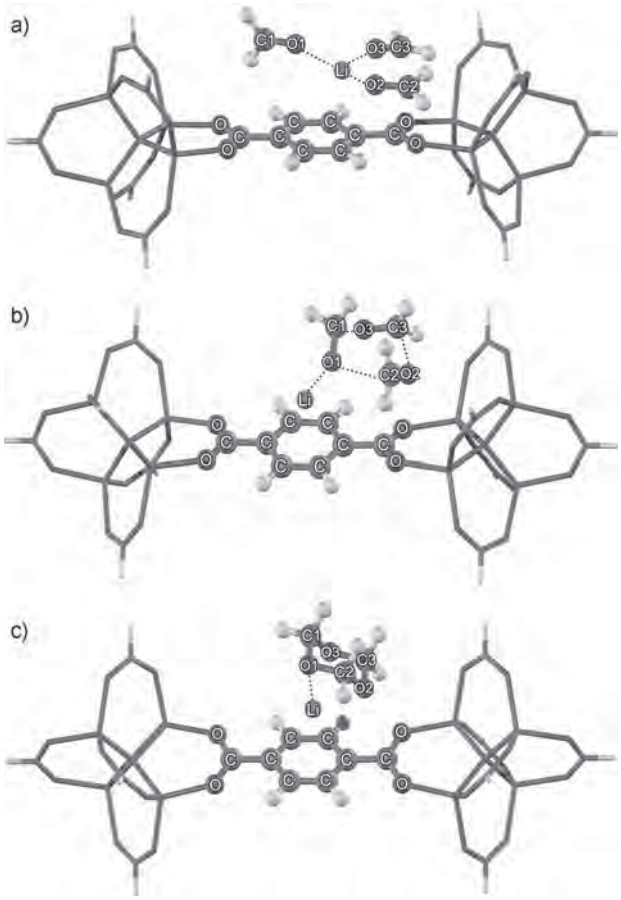


**Figure 4.** Optimized structures of the a) enclosed complex coordinated to Li (Coads_MOF), b) transition state (TS_MOF) and c) product (Prod_MOF) for the formaldehyde trimerization in the Li-MOF-5 system.

The cyclic trioxane product is created by the intermolecular C–O bond formation through the transition states shown in Figures 3b and 4b for the bare and the Li-MOF-5 systems, respectively. At both transition states, the intramolecular C=O double bonds of the formaldehyde molecules are stretched and the intermolecular C···O distances contract to form a new bond (Table 1). The hybridization of the formaldehyde C atoms changes from planar $sp^2$ to tetrahedral $sp^3$, as shown in Figur-

  

es 3b and 4b. In the bare system, the C=O double bonds increase from 1.21 to 1.26 Å while the intermolecular C···O distances decrease by about 0.75 Å. The activation barrier in this system was calculated to be 17.3 kcal mol$^{-1}$. Normal mode analysis reveals one imaginary frequency at 226.9*i* cm$^{-1}$ associated with the transition state. In contrast to the bare system, the formaldehyde C=O double bonds in the MOF system are unequally increased with distances of 1.30, 1.24 and 1.27 Å for C1=O1, C2=O2 and C3=O3, respectively. This is due to effect of the Li cation. Additionally, the intramolecular C···O distances decrease to 2.25, 1.94 and 1.61 Å for C2···O1, C3···O2 and C1···O3, respectively. The transition state was confirmed by one imaginary frequency at 277.0*i* cm$^{-1}$. The calculated activation energy is 34.5 kcal mol$^{-1}$, which is higher than that of the bare system. The overall energy of the trioxane product in the bare reaction with respect to the isolated reactants is −25.3 kcal mol$^{-1}$ which is in good agreement with a previous calculation.[2b] For Li-MOF-5, the strong interaction between the oxygens of trioxane and the $Li^+$ lead to an adsorption energy of −60.7 kcal mol$^{-1}$ (see Figure 4c) with respect to the reactants.

The complete energy profiles for the formaldehyde trimerization in Li-MOF-5 and in the bare system are shown in Figure 5. The calculated thermodynamic properties and the

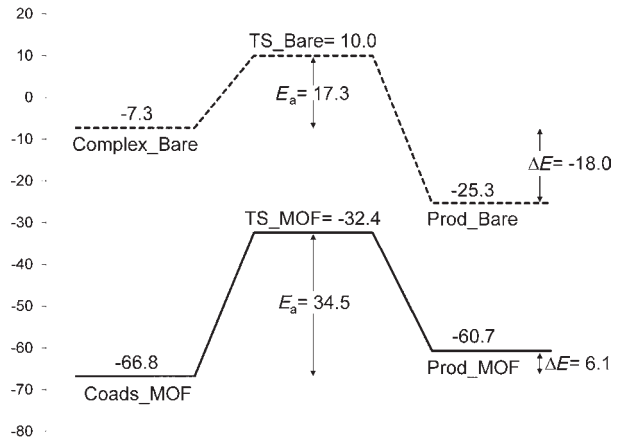


**Figure 5.** Energy profiles for the formaldehyde trimerization: bare system (----) and Li-MOF-5 system (——). The energies are in kcal mol$^{-1}$.

rate constants ($k_r$) are tabulated in Table 2. In the bare system, the overall reaction energy ($\Delta E$) is exothermic by −18.0 kcal mol$^{-1}$. The Gibbs free reaction energy ($\Delta G$) with respect to the isolated reactants is −2.0 kcal mol$^{-1}$ which is close to the experimentally estimated $\Delta G$ of about −1.8 kcal mol$^{-1}$.[10] The overall reaction $\Delta G$ value for the trimerization is negative (−13.3 kcal mol$^{-1}$), as necessary for a spontaneous reaction in which the product side is favoured as can also be seen from the fact that $k_r^+$ outpaces $k_r^-$. In contrast, for the Li-MOF-5 system the reaction is endothermic and the trimerization product is thermodynamically less stable than the reactants. The reaction energy is 6.1 kcal mol$^{-1}$ and the overall $\Delta G$ value is +11.0 kcal mol$^{-1}$. Therefore, the equilibrium for the Li-MOF-5 system lies strongly on the reactant side and in practice the reaction will hardly occur.

## 3. Conclusions

Density functional theory was used to investigate the adsorption and reaction of formaldehyde encapsulated into Li-decorated metal-organic frameworks by comparing them to the situation in the bare system. In order to demonstrate the preservation of formaldehyde in Li-MOF-5, the equilibrium between the adsorbed formaldehyde and trioxane was considered. The reaction is proposed to proceed in a single step without intermediates. The calculated activation barrier for the conversion of formaldehyde to trioxane in the Li-MOF-5 system was found to be 34.5 kcal mol$^{-1}$, which is 17.2 kcal mol$^{-1}$ higher than in the bare system. The reaction energy and reaction free energy in the non-encapsulated system are negative, but positive in the Li-MOF-5 system, due to the higher adsorption energy of individual formaldehyde molecules compared to trioxane on $Li^+$ cations. Consequently, the rate constant of the reverse reaction is also larger than the one for the forward reaction. It can be suggested that Li-decorated MOF-5 might be a good candidate material to preserve and stabilize monomeric formaldehyde. It might also have a similar effect on other small ketones and on molecules prone to polymerize easily in general.

## Computational Methods

The M06-L density functional[11] was used in all calculations. Recent studies of adsorption and reaction mechanisms in zeolites[12] and of $H_2$ adsorbed on light and transition metals that were doped on MOFs organic linkers[13] have been used to verify its usability. We checked this again for our systems. Single-point MP2 and M06-L calculations of the adsorption energy of $Li^+$ on MOF-5 give BSSE-corrected energies of −35.0 and 34.0 kcal mol$^{-1}$, respectively. The double-ζ 6-31G(d,p) basis set with polarization functions was employed for the H, C, O and Li atoms, while the Zn atom was described by the LANL2DZ pseudopotential and the corresponding basis set.[14] During geometry optimizations, only the 1,4-benzenedicarboxylate linker and the adsorbing molecule were allowed to relax while the rest of the structure was kept fixed at the crystallographic positions. Frequency calculations were performed at the same level of theory to identify the nature of all the stationary points and to obtain the zero point energy (ZPE) corrections. These calculations were also used to obtain thermodynamic properties. In addition, rate constants were calculated from the activation barriers and partition functions using classical transition-state theory (TST) according to Equa-

**Table 2.** Calculated reaction energy, thermodynamic properties and rate constant at 298.15 K for the trimerization of formaldehyde.

| Systems | $\Delta E$ [kcal mol$^{-1}$] | $\Delta H$ [kcal mol$^{-1}$] | $\Delta G$ [kcal mol$^{-1}$] | $k_r^+$ [s$^{-1}$] | $k_r^-$ [s$^{-1}$] |
|---|---|---|---|---|---|
| Bare | −18.0 | −21.5 | −13.3 | $1.86\times10^{-3}$ | $3.10\times10^{-13}$ |
| Li-MOF-5 | 6.1 | 2.4 | 11.0 | $7.31\times10^{-17}$ | $8.91\times10^{-9}$ |

  

tion (2):

$$k_r = \frac{k_B T}{h} \frac{q_{TS}}{q_{Int}} \exp(-\Delta E_a / RT) \quad (2)$$

where $\Delta E_a$ is the activation energy, $k_B$ is Boltzmann's constant, $h$ is Planck's constant, $T$ is the absolute temperature, $R$ is the universal gas constant, and $q_{TS}$ and $q_{Int}$ are the total partition functions for the transition state and the adsorption or product complex, respectively, in which electronic, translational, rotational and vibrational partition functions are included. In the case of the system with Li-MOF-5, the atoms of the immobile framework do not contribute to the translational and rotational parts of the partition function. The rate constants were derived for the temperature of 298.15 K. All calculations were performed with the Gaussian 03 code[15] modified by incorporating the Minnesota Density Functionals module 3.1 by Zhao and Truhlar.[11]

## Acknowledgements

*This work was supported in part by grants from the National Science and Technology Development Agency (NANOTEC Center of Excellence and NSTDA Chair Professor), the Thailand Research Fund (to J.L.), the Kasetsart University Research and Development Institute (KURDI), the Commission on Higher Education, Ministry of Education ("National Research University of Thailand" and "Postgraduate Education and Research Programs in Petroleum and Petrochemicals and Advanced Materials") as well as by the program Strategic Scholarships for Frontier Research network for the Joint Ph.D. Program Thai Doctoral degree from the Office of the Higher Education Commission, Thailand (to T.M. and S.C.). M.P. acknowledges support from the Austrian Ministry of Science (infrastructure grant to the LFU scientific computing platform) and the RFBR-FWF projects I200-N29 and 09-03-91001-a. The authors thank Donald G. Truhlar and Yan Zhao for providing them with the code for the M06-L functional.*

**Keywords:** density functional calculations · encapsulation · formaldehyde · metal-organic frameworks · zeolites

[1] T. Okachi, M. Onaka, *J. Am. Chem. Soc.* **2004**, *126*, 2306 – 2307.

[2] a) W. Sangthong, M. Probst, J. Limtrakul, *J. Mol. Struct.* **2005**, *748*, 119 – 127; b) M. Tomita, Y. Masui, M. Onaka, *J. Phys. Chem. Lett.* **2010**, *1*, 652 – 656.

[3] a) N. L. Rosi, J. Eckert, M. Eddaoudi, D. T. Vodak, J. Kim, M. O'Keeffe, O. M. Yaghi, *Science* **2003**, *300*, 1127 – 1129; b) O. M. Yaghi, M. O'Keeffe, N. W. Ockwig, H. K. Chae, M. Eddaoudi, J. Kim, *Nature* **2003**, *423*, 705 – 714; c) T. Düren, L. Sarkisov, O. M. Yaghi, R. Q. Snurr, *Langmuir* **2004**, *20*, 2683 – 2689; d) L. Pan, M. B. Sander, X. Huang, J. Li, M. Smith, E. Bittner, B. Bockrath, J. K. Johnson, *J. Am. Chem. Soc.* **2004**, *126*, 1308 – 1309; e) A. R. Millward, O. M. Yaghi, *J. Am. Chem. Soc.* **2005**, *127*, 17998 – 17999; f) J. L. C. Rowsell, E. C. Spencer, J. Eckert, J. A. K. Howard, O. M. Yaghi, *Science* **2005**, *309*, 1350 – 1354; g) S. Bourrelly, P. L. Llewellyn, C. Serre, F. Millange, T. Loiseau, G. Ferey, *J. Am. Chem. Soc.* **2005**, *127*, 13519 – 13521; h) D. J. Collins, H. C. Zhou, *J. Mater. Chem.* **2007**, *17*, 3154 – 3160; i) S. S. Han, W.-Q. Deng, W. A. Goddard III, *Angew. Chem.* **2007**, *119*, 6405 – 6408; *Angew. Chem. Int. Ed.* **2007**, *46*, 6289 – 6292; j) N. A. Ramsahye, G. Maurin, S. Bourelly, P. Lllewellyn, C. Serre, T. Loiseau, T. Devic, G. Ferey, *J. Phys. Chem. C* **2008**, *112*, 514 – 520; k) L. J. Murray, M. Dinca, J. R. Long, *Chem. Soc. Rev.* **2009**, *38*, 1294 – 1314; l) Y. H. Hu, L. Zhang, *Adv. Mater.* **2010**, *22*, E117 – E130.

[4] a) S. S. Han, W. A. Goddard III, *J. Am. Chem. Soc.* **2007**, *129*, 8422 – 8423; b) K. L. Mulfort, J. T. Hupp, *J. Am. Chem. Soc.* **2007**, *129*, 9604 – 9605; c) K. L. Mulfort, J. T. Hupp, *Inorg. Chem.* **2008**, *47*, 7936 – 7938; d) D. Zhao, D. Yuan, H. C. Zhou, *Energy Environ. Sci.* **2008**, *1*, 222 – 235; e) E. Klontzas, A. Mavrandonakis, E. Tylianakis, G. E. Froudakis, *Nano Lett.* **2008**, *8*, 1572 – 1576; f) P. Dalach, H. Frost, R. Q. Snurr, D. E. Ellis, *J. Phys. Chem. C* **2008**, *112*, 9278 – 9284; g) D. Wu, Q. Xu, D. Liu, C. Zhong, *J. Phys. Chem. C* **2010**, *114*, 16611 – 16617.

[5] a) A. Blomqvist, C. M. Araujo, P. Srepusharawoot, R. Ahuja, *Proc. Natl. Acad. Sci. USA* **2007**, *104*, 20173 – 20176; b) A. Mavrandonakis, E. Tylianakis, A. K. Stubos, G. E. Froudakis, *J. Phys. Chem. C* **2008**, *112*, 7290 – 7294.

[6] a) H. Li, M. Eddaoudi, T. L. Groy, O. M. Yaghi, *J. Am. Chem. Soc.* **1998**, *120*, 8571 – 8572; b) H. Li, M. Eddaoudi, M. O'Keeffe, O. M. Yaghi, *Nature* **1999**, *402*, 276 – 279; c) M. Eddaoudi, J. Kim, N. Rosi, D. Vodak, J. Wachter, M. O'Keeffe, O. M. Yaghi, *Science* **2002**, *295*, 469 – 472.

[7] K. Sillar, A. Hofmann, J. Sauer, *J. Am. Chem. Soc.* **2009**, *131*, 4143 – 4150.

[8] J. C. Amicangelo, P. B. Armentrout, *J. Phys. Chem. A* **2000**, *104*, 11420 – 11432.

[9] S. Choomwattana, T. Maihom, P. Khongpracha, M. Probst, J. Limtrakul, *J. Phys. Chem. C* **2008**, *112*, 10855 – 10861.

[10] Kagaku Binran, *Chemistry Handbook Basic 4th ed./Applied 5th ed.*, CSJ Publications, Maruzen, Tokyo, **2004**.

[11] a) Y. Zhao, D. G. Truhlar, *J. Phys. Chem. C* **2008**, *112*, 6860 – 6868; b) Y. Zhao, D. G. Truhlar, *Acc. Chem. Res.* **2008**, *41*, 157 – 167.

[12] a) T. Maihom, B. Boekfa, J. Sirijaraensre, T. Nanok, M. Probst, J. Limtrakul, *J. Phys. Chem. C* **2009**, *113*, 6654 – 6662; b) B. Boekfa, S. Choomwattana, P. Khongpracha, J. Limtrakul, *Langmuir* **2009**, *25*, 12990 – 12999; c) C. Kumsapaya, K. Bobuatong, P. Khongpracha, Y. Tantirungrotechai, J. Limtrakul, *J. Phys. Chem. C* **2009**, *113*, 16128 – 16137; d) T. Maihom, P. Pantu, C. Tachakritikul, M. Probst, J. Limtrakul, *J. Phys. Chem. C* **2010**, *114*, 7850 – 7856; e) B. Boekfa, P. Pantu, M. Probst, J. Limtrakul, *J. Phys. Chem. C* **2010**, *114*, 15061 – 15067; f) S. Wannakao, B. Boekfa, P. Khongpracha, M. Probst, J. Limtrakul, *ChemPhysChem* **2010**, *11*, 3432 – 3438; g) K. Bobuatong, M. Probst, J. Limtrakul, *J. Phys. Chem. C* **2010**, *114*, 21611 – 21617.

[13] a) S. J. Kolmann, B. Chan, M. J. T. Jordan, *Chem. Phys. Lett.* **2008**, *467*, 126 – 130; b) R. B. Getman, J. H. Miller, K. Wang, R. Q. Snurr, *J. Phys. Chem. C* **2011**, *115*, 2066 – 2075.

[14] P. J. Hay, W. R. Wadt, *J. Chem. Phys.* **1985**, *82*, 270 – 283.

[15] Gaussian 03, (Revision B.05), M. J. Frisch, G. W. Trucks, H. B. Schlegel, G. E. Scuseria, M. A. Robb, J. R. Cheeseman, J. A. Montgomery, Jr., T. Vreven, K. N. Kudin, J. C. Burant, J. M. Millam, S. S. Iyengar, J. Tomasi, V. Barone, B. Mennucci, M. Cossi, G. Scalmani, N. Rega, G. A. Petersson, H. Nakatsuji, M. Hada, M. Ehara, K. Toyota, R. Fukuda, J. Hasegawa, M. Ishida, T. Nakajima, Y. Honda, O. Kitao, H. Nakai, M. Klene, X. Li, J. E. Knox, H. P. Hratchian, J. B. Cross, V. Bakken, C. Adamo, J. Jaramillo, R. Gomperts, R. E. Stratmann, O. Yazyev, A. J. Austin, R. Cammi, C. Pomelli, J. W. Ochterski, P. Y. Ayala, K. Morokuma, G. A.Voth, P. Salvador, J. J. Dannenberg, V. G. Zakrzewski, S. Dapprich, A. D. Daniels, M. C. Strain, O. Farkas, D. K. Malick, A. D. Rabuck, K. Raghavachari, J. B. Foresman, J. V. Ortiz, Q. Cui, A. G. Baboul, S. Clifford, J. Cioslowski, B. B. Stefanov, G. Liu, A. Liashenko, P. Piskorz, I. Komaromi, R. L. Martin, D. J Fox, T. Keith, M. A. Al-Laham, C. Y. Peng, A. Nanayakkara, M. Challacombe, P. M. W. Gill, B. Johnson, W. Chen, M. W. Wong, C. Gonzalez, J. A. Pople, Gaussian, Inc., Wallingford, CT, **2004**.

Received: August 22, 2011
Revised: September 23, 2011
Published online on ■■ ■■, 2011

  

# ARTICLES

*T. Maihom, S. Choomwattana, P. Khongpracha, M. Probst, J. Limtrakul**

■■ – ■■

**Formaldehyde Encapsulated in Lithium-Decorated Metal-Organic Frameworks: A Density Functional Theory Study**

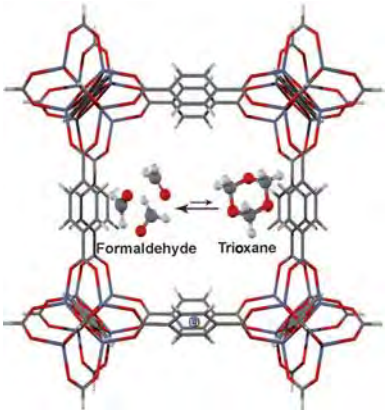


**Gotcha:** The equilibrium between adsorbed formaldehyde and trioxane in the Li-MOF-5 system (see picture) was investigated by means of density functional calculations with the M06-L functional.

  

# บทความที่นำเสนอ
# ในการประชุมวิชาการนานาชาติ

**Nanotech Conference 2009**

**ณ ประเทศสหรัฐอเมริกา**

**ระหว่างวันที่ 3-7 พฤษภาคม 2552**

**จำนวน 8 เรื่อง**

# The Quantum Confinement Effect on the Adsorption and Reaction of Aliphatic Hydrocarbons on 'Nano Reactor' ZSM-5 Zeolite: A Newly Developed Density Functional Theory (DFT) Investigation

B. Boekfa [a,b], S. Choomwattana [a,b], P. Maitarad [a,b], P. Limtrakul [a], J. Limtrakul [a,b,*]

[a]Laboratory for Computational and Applied Chemistry, Chemistry Department, Faculty of Science, Kasetsart University, Bangkok 10900, Thailand
[b]NANOTEC Center of Excellence, National Nanotechnology Center, Kasetsart University Research and Development Institute, Thailand
[*]E-mail: jumras.l@ku.ac.th, Tel: +662-562-5555 ext 2169, Fax: +662-562-5555 ext 2176

## ABSTRACT

Full quantum calculations with a newly developed functional, M06-L, on the ZSM-5 models of 5T, 12T, 34T, 46T and 128T were performed to simulate the nanoporous system. Methane and ethane are chosen to represent saturated hydrocarbons. The calculated adsorption energies are -7.0 kcal/mol for methane and -11.1 kcal/mol for ethane, which agree well with the experimental estimates of -6.7 and -9.1 kcal/mol. The M06-L method is also applied for the first time to systematically investigate the proton exchange reactions of methane and ethane within the nano-reactor of zeolite. The concerted mechanism is proposed for the reaction. The calculated activation energy of methane is 35.3 kcal/mol, which is comparable with the experimental data (33.4 kcal/mol), whereas the energy of ethane is 33.0 kcal/mol. The effect of nano-quantum confinement of the extended zeolite framework on adsorption and reaction mechanisms has been clearly demonstrated not only to better stabilize the adsorption complexes achieving the observed values but also to lower their activation energies to approach experimental benchmarking.

***Keywords***: zeolites, proton exchange reaction, M06-L functional, confinement effect, light alkanes

## 1 INTRODUCTION

In fine-chemical and pharmaceutical manufacture and in petroleum refining, zeolites, which have a combination of high stability with their excellent activity in acid-mediated reactions [1-3], have been applied in the process of heterogeneous catalysis. Especially, ZSM-5, patented in 1975, is widely used in chemical industries such as hydrocarbon cracking, isomerization, alkylation reaction and methanol to olefins (MTO) [4].

To clearly envision the structure, adsorption properties and chemical reaction mechanism, theoretical study can offer a practical tool that provides insight to the reaction mechanism complementing experimental investigations or, in certain cases, offer an understanding that is not possible by experimental investigations. Numerous experimental [5-9] and theoretical [10,11] researches have been devoted to understanding the chemistry of ZSM-5. Attempts have been made to develop the computational methodology that can precisely predict the physical and chemical properties of the zeolite itself and the reaction inside its nanocavity. The Density Functional Theory (DFT), especially B3LYP, has been widely used to study the interaction of hydrocarbons with zeolites. However, the limitation of the DFT calculations previously employed was that the contribution of dispersion interactions was not taken into account. This interaction contribution in the adsorption has been found to be essential in the chemical adsorptions and reactions inside the zeolite pore [8,12-17]. To overcome the enormous computational resource required for a DFT calculation on a large model, the ONIOM scheme combined with QM/MM calculation [18,19] is applied to such systems. This provides an acceptable balance between the accuracy of the results and the computational cost. The ONIOM scheme provides only an approximation [14,15,18-21] and, therefore, the quest for a more accurate method continues. Recently, the newly developed functional called M06-L was introduced by Zhao and coworkers [22]. It is recommended for transition metal thermochemistry, noncovalent interactions and for when a local functional is required; a local functional has a much lower cost for large systems [23-25]. With the improved combination of the computational method and the realistic model, we hypothesize that this method should be able to represent the interaction within the zeolite system.

The aim of this work is threefold: first, to present a theoretical study on the nature of the H-ZSM-5 adsorption complex of methane and ethane, second, to further describe the proton exchange reaction of methane and ethane catalyzed by the zeolite and third, to present, for the first time, the full quantum calculation application of the 'noncovalent interaction represented' M06-L method on the zeolite framework.

## 2 METHODOLOGY

ZSM-5 structure from the XRD data was trimmed down to become 5T, 12T, 34T, 46T and 128T cluster models (see Fig. 1). The 5T cluster ($AlSi_4O_4H_{13}$) is modeled to represent only the Brønsted active site. The T12 position was selected to be Al due to its being the most energetically favorable [26]. The 12T stands for the 10-membered-ring window of the zigzag nanochannel of the porous structure. The model was extended to 34T to cover the intersection of straight-zigzag channels, including some part of the zigzag channel. Adopted from our previous publications [12,13,20], the 46T model is similar to the 34T, but the framework

is extended surrounding the acid center in the zigzag channel. The largest model, 128T, envelops the whole model of 46T with another shell of tetrahedral subunits. The adsorption and reaction of methane and ethane on different H-ZSM-5 models are fully quantum calculated with the M06-L functional [22], along with the 6-31G(d,p) basis set. During the structure optimization on the 5T, 12T, 34T and 46T systems, the 5T portion of the active site region ($AlSi_4O_4H$) and the reacting molecule are allowed to relax while the rest is fixed at the crystallographic coordinates [27]. The transition states (TS) of the reaction were characterized by the existence of a single imaginary frequency. All calculations were performed using the Gaussian 03 code [28].

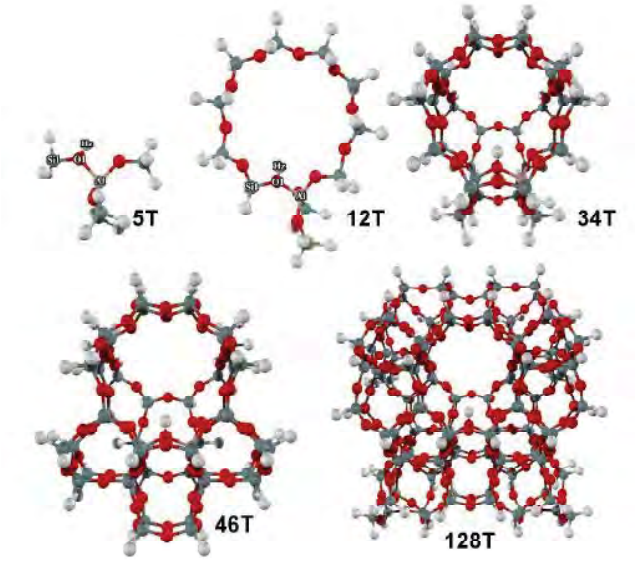


Figure 1: The evolution of H-ZSM-5 models, from the 5T unit to 128T clusters.

## 3 RESULTS AND DISCUSSION

### 3.1 Molecular Cluster and Nanocluster Models of H-ZSM-5 catalyst

The evolution of our H-ZSM-5 models, from the 5T unit to the 128T framework, is illustrated in Fig. 1. Selected structural parameters of each model are presented in Fig 2.

In the bare zeolite, one can observe the influence of the framework on the effective Brønsted acidity. From Figure 2, the acidity is insignificantly more pronounced in the extended zeolite framework according to the increased O1-Hz bond length by at most 0.2 pm. The calculated Al···H distances in the range of 234.9-237.4 pm are close to the experimental report by Klinoski of 238.0-248.0 pm of H-zeolite [29]. This good agreement confirms the validation of our models.

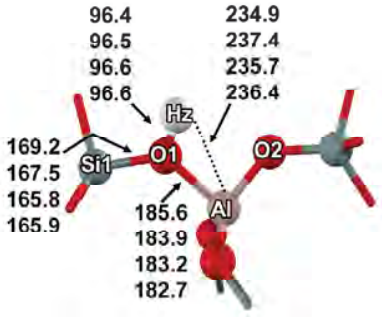


Figure 2: Optimized structure of various H-ZSM-5 models calculated with the M06-L/6-31G(d,p) method. Distance parameters shown in lines 1-4 are for 5T, 12T, 34T and 46T quantum clusters, respectively.

### 3.2 Adsorption of Light Alkanes on the Brønsted Acid Site

The adsorption energies of the methane and ethane complexes with various zeolite models are summarized in Table 1. As an underestimated value is expected from a small cluster, we found that the methane is bound by -2.9 kcal/mol to the acid site. This increases slightly and converges to -6.9 and -7.0 kcal/mol for the 34T and 46T, respectively. From the same zeolite models, ethane is bound by -10.8 and -11.1 kcal/mol to the acid site. The larger interaction for ethane than methane is found to agree favorably with the known adsorption trend as the molecular size increases. We also found that the adsorption energies are increased due to the presence of a larger framework effect in larger zeolite models. The experimental observation of methane and ethane adsorbed on H-ZSM-5 are -6.7 and -9.1 kcal/mol, respectively [16,17]. The calculated energies from the 34T and 46T clusters are therefore reasonably close to the experimental data.

| Model | Methane | Ethane |
|---|---|---|
| 5T | -2.9 | -4.6 |
| 12T | -5.1 | -7.7 |
| 34T | -6.9 | -10.8 |
| 46T | -7.0 | -11.1 |
| 128T [a] | -6.9 | -10.7 |
| Expt | -6.7 | -9.1 |

[a] The adsorption energies on the 128T cluster were computed with a single point calculation on the optimized structure of the 46T cluster.

Table 1: Interaction energies (kcal/mol) calculated at M06-L/6-31G(d,p) level of theory for the adsorptions of methane and ethane on various H-ZSM-5 models.

To determine the model size of the zeolite that can well represent the adsorption in the real system, the interaction energies from the single point calculation on the large quantum cluster of 128T on the optimized structure of the 46T are used as the energy benchmark. The energies are computed to be -6.9 and -10.7 kcal/mol for methane and ethane, respectively. Since the value from

the 34T model can be considered to be the same as the 128T model, the 34T and 46T models are assumed to be large enough to include the effect of the zeolite pore on chosen nonpolar adsorbates.

From our discussion above, it can be concluded that the full quantum calculation with the M06-L method and the 6-31G(d,p) basis set on the 34T and 46T models of H-ZSM-5 zeolite is the minimal requirement to reproduce the adsorption of methane and ethane within the zeolite pore.

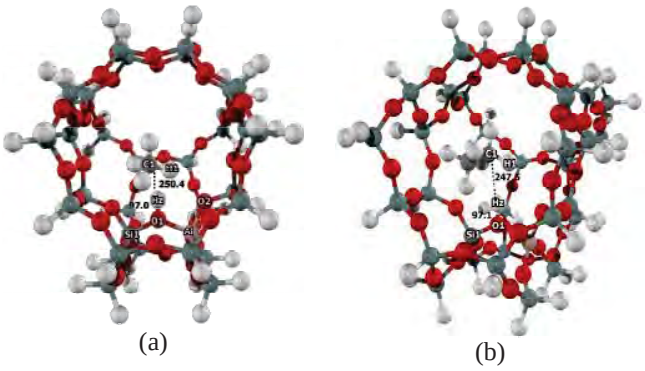


Figure 3: Optimized structure of (a) methane adsorption and (b) ethane adsorption on the 34T cluster model of H-ZSM-5 derived at the M06-L/6-31G(d,p) level of theory. Distances are in pm.

### 3.3 Proton Exchange Reaction of Light Alkanes

Reaction energies of the proton exchange reactions of methane and ethane with various models of H-ZSM-5 zeolite, calculated with the M06L/6-31G(d,p) method are documented in Table 2.

As for the small QM cluster of 5T, the actual activation energy for methane is computed to be 37.2 kcal/mol while the apparent activation energy is 34.3 kcal/mol. The same reaction studied on the small zeolite cluster reported the activation energy in the range of 30-40 kcal/mol [30-36]. Even the activation energies are in good agreement. The adsorption energies from this small quantum cluster are underestimated and found to be less than a half of the experimental data of 6.7 kcal/mol. With a larger zeolite model, the actual activation energies are 36.8, 35.4 and 35.2 kcal/mol, with the 12T, 34T and 46T quantum clusters, respectively. Their corresponding apparent activation energies are 31.7, 28.5, 28.2 kcal/mol. The reaction energies are considered to be 5.9, 11.0 and 10.3 kcal/mol with the 12T, 34T and 46T quantum cluster, respectively. The activation energy obtained from both the 34T and 46T clusters are virtually identical. Similar results are also derived for the single point calculation of the 128T cluster (the energy barrier of 35.2 kcal/mol and the apparent activation energy of 28.3 kcal/mol). Therefore, taking the framework effect into account improves the calculated result by increasing the underestimated adsorption energy and lowering the overestimated activation energy.

With the small quantum cluster (5T), the adsorption energy is -4.6 kcal/mol. The apparent activation energy is 32.5 kcal/mol whereas the actual one is 37.1 kcal/mol. Even though there is no experimental data for ethane on H-ZSM-5 zeolite, the calculated result is reasonable in that the reaction has a smaller energy barrier and is found to be more endothermic (about 6.5 kcal/mol). As the framework effect is considered in the 46T quantum cluster, the adsorption energy is -11.1 kcal/mol, which agrees well with the experimental data of -9.1 kcal/mol. Their corresponding actual and apparent activation energies are 32.8 and 21.7 kcal/mol, respectively. As expected, the adsorption and reaction energies calculated at the 128T model yield similar results (cf Table 2).

| Model | Methane | | | Ethane | | |
|---|---|---|---|---|---|---|
| | AD | TS | PR | AD | TS | PR |
| 5T | -2.9 | 34.3 (37.2) | 0.4 | -4.6 | 32.5 (37.1) | -1.9 |
| 12T | -5.1 | 31.7 (36.8) | -0.8 | -7.7 | 28.0 (35.7) | -2.7 |
| 34T | -6.9 | 28.5 (35.4) | -4.1 | -10.8 | 22.2 (33.0) | -8.3 |
| 46T | -7.0 | 28.2 (35.2) | -3.3 | -11.1 | 21.7 (32.8) | -7.7 |
| 128T[a] | -6.9 | 28.3 (35.2) | -2.8 | -10.7 | 22.3 (33.0) | -10.7 |

[a] The adsorption energies on the 128T cluster were computed with a single point calculation on the optimized structure of the 46T cluster.

Table 2: Reaction energies (kcal/mol) of the proton exchange reactions of methane and ethane with various models of H-ZSM-5 zeolite, calculated with the M06L/6-31G(d,p) method (activation energy in parenthesis).

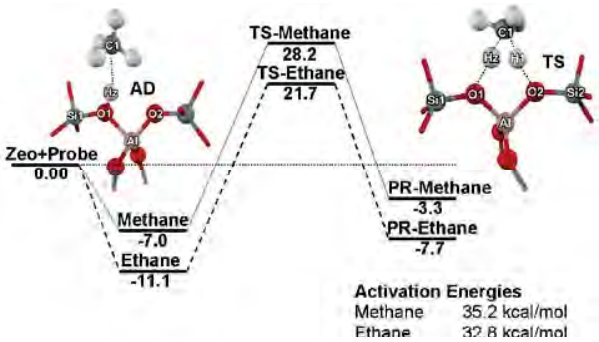


Figure 4: Energy profile for proton exchange reactions of methane and ethane on the 46T quantum cluster of H-ZSM-5, calculated with the M06-L/6-31G(d,p) method.

## 4 CONCLUSION

The chemical investigation on the adsorption and proton exchange reaction of methane and ethane with the H-ZSM-5 zeolite were performed with a newly developed density functional theory, M06-L. Since the dispersion interaction is included in the method, it can well reproduce the experimental estimate of the

adsorption and reaction of the nonpolar molecules, and also predict reliable information for the reactions that have not been experimentally studied. Based on the experimental report, the molecules are placed over the active site to proceed the adsorption and the reaction. With the validated combination of our 46T model and the M06L/6-31G(d,p) approach, the calculated adsorption energies of methane and ethane of -7.0 and -11.1 kcal/mol are in excellent agreement with the experimental observations of -6.7 and -9.1 kcal/mol, respectively. With the activation energy for the methane reaction calculated to be 35.2 kcal/mol, the method gives the apparent activation energy of 28.2 kcal/mol, which compares well with the experimental result. The actual and apparent activation energies for the ethane reaction are predicted to be 32.8 and 21.7 kcal/mol, respectively. To qualify our model for the prediction, we compared both adsorption and reaction results with the single point calculation for the realistic cluster model of 128T. We found that the 46T model gives virtually similar results for the reactions of both methane and ethane. Therefore, the full quantum calculation of the 46T cluster model with the newly developed functional, M06-L functional, is a practical and accurate model to systematically study the adsorption and reaction of hydrocarbons in “nano reactor” ZSM-5 zeolite.

## ACKNOWLEDGEMENTS

This research was supported by grants from the National Science and Technology Development Agency (NSTDA), the Thailand Research Fund (TRF), Kasetsart University Research and Development Institute (KURDI), the Commission on Higher Education, Ministry of Education, under the Postgraduate Education and Research Programs in Petroleum and Petrochemicals, and Advanced Materials as well as the Sandwich Program in the Strategic Scholarships Fellowships Frontier Research Network (CHE-PhD-SW-SUPV to SC). The authors are grateful to Donald G. Truhlar and Yan Zhao for supporting them with the M06-L functional. The Kasetsart University Graduate School is also acknowledged.

## REFERENCES

[1] B. W. Wojciechowsku and A. Corma "Catalytic Cracking: Catalysts, Chemistry, and Kinetics"; Dekker: New York, 1986.
[2] I. E. Maxwell and W. H. J. Stork "Introduction to Zeolite Science and Practice"; Elsevier: Amsterdam, 1991.
[3] G. A. Olah and A. Molnar "Hydrocarbon Chemistry"; John Wiley and Sons Inc.: New York, 1995.
[4] P. B. Venuto, Microporous Mater., 2, 297, 1994.
[5] A. Corma, J. Catal., 216, 298, 2003.
[6] E. G. Derouane and C. D. Chang, Microporous Mesoporous Mater., 35-36, 425, 2000.
[7] C. S. H. Chen and R. F. Bridger, J. Catal., 161, 687, 1996.
[8] D. J. Parrillo, C. Lee and R. J. Gorte, Appl. Catal., A, 110, 67, 1994.
[9] B. Smit and T. L. M. Maesen, Nature (London, U. K.), 451, 671, 2008.
[10] S. R. Blaszkowski, A. P. J. Jansen, M. A. C. Nascimento and R. A. van Santen, J. Phys. Chem., 98, 12938, 1994.
[11] S. R. Blaszkowski, M. A. C. Nascimento and R. A. van Santen, J. Phys. Chem., 100, 3463, 1996.
[12] J. Lomratsiri, M. Probst and J. Limtrakul, J. Mol. Graphics Modell., 25, 219, 2006.
[13] W. Panjan and J. Limtrakul, J. Mol. Struct., 654, 35, 2003.
[14] N. Injan, N. Pannorad, M. Probst and J. Limtrakul, Int. J. Quantum Chem., 105, 898, 2005.
[15] P. Pantu, B. Boekfa and J. Limtrakul, J. Mol. Catal. A: Chem., 277, 171, 2007.
[16] H. Papp, W. Hinsen, N. T. Do and M. Baerns, Thermochim. Acta, 82, 137, 1984.
[17] E. Yoda, J. N. Kondo and K. Domen, J. Phys. Chem. B, 109, 1464, 2005.
[18] S. Dapprich, I. Komiromi, K. S. Byun, K. Morokuma and M. J. Frisch, THEOCHEM, 461-462, 1, 1999.
[19] M. Svensson, S. Humbel, R. D. J. Froese, T. Matsubara, S. Sieber and K. Morokuma, J. Phys. Chem., 100, 19357, 1996.
[20] C. Raksakoon and J. Limtrakul, THEOCHEM, 631, 147, 2003.
[21] R. Rungsirisakun, B. Jansang, P. Pantu and J. Limtrakul, J. Mol. Struct., 733, 239, 2004.
[22] Y. Zhao, N. E. Schultz and D. G. Truhlar, J. Chem. Theory Comput., 2, 364, 2006.
[23] Y. Zhao and D. G. Truhlar, Theor. Chem. Acc., 120, 215, 2008.
[24] Y. Zhao and D. G. Truhlar, J. Phys. Chem. C, 112, 6860, 2008.
[25] Y. Zhao and D. G. Truhlar, Acc. Chem. Res., 41, 157, 2008.
[26] S. R. Lonsinger, A. K. Chakraborty, D. N. Theodorou and A. T. Bell, Catal. Lett., 11, 209, 1991.
[27] H. Van Koningsveld, H. Van Bekkum and J. C. Jansen, Acta Crystall. B43, 127, 1987.
[28] M. J. Frisch, et al. Gaussian 03, Revision C Gaussian, Inc., Wallingford CT, 2004.
[29] J. Klinowski, Chem. Rev., 91, 1459, 1991.
[30] E. M. Evleth, E. Kassab and L. R. Sierra, J. Phys. Chem., 98, 1421, 1994.
[31] V. B. Kazansky, M. V. Frash and R. A. van Santen, Catal. Lett., 28, 211, 1994.
[32] G. J. Kramer and R. A. van Santen, J. Am. Chem. Soc., 117, 1766, 1995.
[33] P. M. Esteves, M. A. C. Nascimento and C. J. A. Mota, J. Phys. Chem. B, 103, 10417, 1999.
[34] J. A. Ryder, A. K. Chakraborty and A. T. Bell, J. Phys. Chem. B, 104, 6998, 2000.
[35] X. Zheng and P. Blowers, J. Mol. Catal. A: Chem., 242, 18, 2005.
[36] X. Zheng and P. Blowers, J. Mol. Catal. A: Chem., 246, 1, 2006.

# A Mechanistic Investigation on 1,5- to 2,6-Dimethylnaphthalene Isomerization Catalyzed by Acidic Beta Zeolite: An ONIOM Study with a Newly Developed Density Functional Theory

Chawanwit Kumsapaya [a,b], Karan Bobuatong [a,b], Saowapak Choomwattana [a,b], Pipat Khongpracha [a,b], Yuthana Tantirungrotechai [c] and Jumras Limtrakul [a,b,*]

[a]Laboratory for Computational and Applied Chemistry, Chemistry Department, Faculty of Science, Kasetsart University, Bangkok 10900, Thailand
[b]NANOTEC Center of Excellence, National Nanotechnology Center, Kasetsart University Research and Development Institute, Thailand
[c]National Nanotechnology Center (NANOTEC), NSTDA, Khongluang, Pathumthani 12120, Thailand
*E-mail: jumras.l@ku.ac.th, Tel: +662-562-5555 ext 2169, Fax: +662-562-5555 ext 2176*

## ABSTRACT

2,6-Dimethylnaphthalene (DMN) is the key intermediate in the synthesis of poly(ethylene naphthalate) (PEN), a high-performance polymer. The detailed reaction mechanism of the catalyzed 1,5- to 2,6- DMN isomerization via 1,6-DMN by acidic beta zeolite is investigated at the ONIOM(M06-L/6-31G(d,p):UFF) level of theory. The M06-L method, a newly developed density functional theory, is applied for the first time to investigate such reaction within the nano-reactor of zeolite. The stepwise mechanism is proposed to proceed with three steps: protonation, methyl shift and proton back-donation. The methyl shift is the rate-determining step with the activation energies of 24.0 and 20.8 kcal/mol for 1,5- to 1,6-DMN and 1,6- to 2,6-DMN steps, respectively. The calculation confirmed the experiment that the 1,6-DMN formation is kinetically controlled. The calculated adsorption and activation energies are in good agreement with experimental data. Our findings demonstrate that the influence of the pore size of the beta zeolite perfectly fit for the enhancement of the isomerization of 1,5- into 2,6-DMN.

***Keywords***: dimethylnaphthalene, isomerization, density functional theory, zeolite, Beta

## 1 INTRODUCTION

A high-performance polymeric material, polyethylene naphthalate (PEN), has many more superior properties than common polyethylene terephthalate (PET) [1]. The current production process involves the condensation polymerization of ethylene glycol and dimethyl 2,6-napthalenedicarboxylate (2,6-NDC). The 2,6-NDC is in turn prepared from 2,6-dimethylnaphthalene (2,6-DMN) [2]. Its present large-scale production (30 kton/yr) is manufactured only by BP-Amoco using their patented process [3], involving four subsequent reactions in four separate reactors: alkylation, cyclization, dehydrogenation, and catalytic isomerization from 1,5- to 2,6-DMN [1, 4]. The final step is thought to be a limiting step which leads to the low availability and the high cost of 2,6-DMN [5]. The isomerization of 1,5- to 2,6-DMN occurs via an intramolecular 1,2-methyl shift [8-10]. This methyl shift is recognized as a key mechanistic step in the rearrangements of alkylbenzenes [8-9], which can be promoted by both Lewis and Brønsted acids.

Zeolite is a unique choice of catalyst for "green chemistry" industrial processes. Recently, Kraikul *et al*. conducted a catalytic activity test of H-beta, H-mordenite, and H-ZSM-5, on the isomerization of 1,5- to 2,6-DMN [5]. H-beta zeolite was found to provide the highest yield of 2,6-DMN. From further thermodynamic analysis, Kraikul *et al.* concluded that 1,5- to 1,6-DMN isomerization is the kinetically limiting step for the 1,5- to 2,6-DMN conversion. From the MD simulation to estimate the diffusional energy barrier of DMN in zeolites by Millini *et al.* [11], the diffusivity of DMN isomer is in the order 2,6-DMN > 1,6-DMN > 1,5-DMN. However, no chemical kinetics parameter is deduced from their study. Later, Suld and Stuart studied the isomerization kinetics of several alkylnapthalenes catalyzed by $BF_3$·HF [10]. Although there are some reports concerning the detailed investigation of this limiting step, the information of this reaction at the molecular level has not, to our knowledge, been published [1, 5-7], especially for the activation energy catalyzed by heterogeneous catalysts, zeolite in particular. In addition, although the isomerization from 1,5- into 2,6-DMN over the heterogeneous catalysts is known to occur with two methyl shift steps, the reaction mechanism has not been investigated in detail.

In this work, we report the mechanistic study of 1,5- to 2,6-DMN isomerization catalyzed by acidic beta zeolite by means of the hybrid Quantum Mechanics/Molecular Mechanics (QM/MM) approach, as well as the ONIOM (our-Own-N-layered Integrated molecular Orbital and molecular Mechanics) method [12-18]. Our several reports indicate ONIOM's good performance on the studies of adsorption and reaction in zeolite [19-29].

## 2 METHOD

The 120 tetrahedral subunit (120T) cluster, covering the active region, of the H-beta zeolite is used to represent the Brønsted acid site and the framework. This cluster is taken from the crystal lattice structures [30-31]. We focus on the 12T ring representing the main gateway to the intersection of two perpendicular 12T channel systems, where the reactions normally take place (see Fig. 1). A silicon atom at a T5 position in the zeolite is substituted by an aluminum atom. A proton is added to the bridging oxygen bonded

to the aluminum atom [30], labeled with O1 in this study. In the ONIOM model, an inner layer consists of a 14T cluster including the 12T and two adjacent Si atoms and a reacting molecule. An outer layer consists of the remainder of the extended framework up to 120T to take the confinement effect of the framework into account.

The ONIOM scheme consists of the inner layer of the active region calculated at the M06-L/6-31G(d,p) level and the outer layer of the framework calculated by the universal force field (UFF). M06-L, a DFT method developed by the Minnesota group [32-34]. This functional requires much less computational effort, thus it is practical for the calculation on large systems [34], such as for the interactions of the adsorbates with the acid site of zeolite. The UFF accounts for the van der Waals interaction for the framework [35], which contributes dominantly in adsorption-desorption mechanisms in zeolites [35-38]. During optimization, only the 5T region [(≡SiO)$_3$Al(OH)Si≡] was allowed to relax while the rest was fixed along the crystallographic coordinates. To obtain more reliable energies, single-point calculations at the 120T quantum cluster, i.e. 120T M06-L/6-31G(d,p)//120T ONIOM(M06-L/6-31G(d,p):UFF) are also computed. All calculations were performed using the Gaussian 03 code [39].

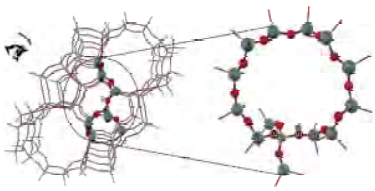

Figure 1: 120T model of H-beta zeolite. The oval dashed line encloses a nanoreactor (an intersection of two perpendicular 12MR channel systems). The 14T active region including the main gateway to the nanoreactor is shown in ball-and-stick style.

## 3 RESULTS AND DISCUSSION

### 3.1 Isomerization of 1,5- to 1,6-DMN

Fig. 2(a) summarizes the reaction mechanism of 1,5- to 1,6-DMN isomerization in the acidic beta zeolite. In this mechanism, a 1,5-DMN molecule is first adsorbed at the Brønsted acid site. Then, the adsorbed 1,5-DMN is protonated to form a σ-complex (Int_1), followed by the intramolecular methyl shift between the C5 and C6 positions. This results in the formation of a new σ-complex (Int_2) which donates proton back to the zeolite yielding a 1,6-DMN (Prod_1).

The adsorption takes place with the C5-C6 double bond interacting with the acidic proton (H1) (see Fig. 3(a)). The 1,5-DMN molecule was slightly perturbed by the zeolite cavity upon the adsorption. The C5-C6 double bond lengthens slightly. The adsorption energy of 1,5-DMN is computed to be -22.1 kcal/mol. Even though there is no report of experimental data, this value is in accord with the data of -20.4 kcal/mol for ethylbenzene in H-Y zeolites [40]. Next, the protonation in the adsorption complex, Ads_1, takes place at the C5 position. The protonated molecule is in the form of a carbenium ion in which the positive charge can delocalize over the benzene ring. At the transition state, TS_1, the zeolite proton moves toward the 1,5-DMN. The dimethylnaphthalenonium ion (Int_1) is then formed and stabilized by the resonance of the intact benzenoid nucleus [10]. The energy barrier for the protonation is 11. 7 kcal/mol and the corresponding reaction is endothermic by 5.8 kcal/mol. From Fig. 3(a), the geometry of the transition state (TS_1) is more similar to that of Int_1 than to that of Ads_1. Therefore, the reaction tends to proceed forward to the methyl shift step.

The reversible intramolecular 1,2-methyl shift moves the methyl group from α-position ($C_\alpha$) to the adjacent position ($C_\beta$). The TS_2 transition structure shows the shifting methyl group located in-between with C5 and C6 atoms. At this unstable tricentric transition state, the methyl group is moving toward the C6 atom. In the Int_2 structure, the Cm-C6 bond is formed. The calculated binding energy is -15.5 kcal/mol (see Fig. 4(a)). This is slightly less stable than that of Int_1 by 0.8 kcal/mol. Therefore, the reaction is almost thermoneutral. This may be attributed to the reduction of steric hindrance between the methyl group in the naphthalene ring and the zeolitic pore. The activation energy for the DMN methyl migration is 25.7 kcal/mol.

The final stage of the 1,5- to 1,6-DMN isomerization involves the proton (H2) back-donation from the C6 position of Int_2 to the O1 of the zeolite framework to form adsorbed 1,6-DMN (see Fig. 3(a)). This stage occurs very fast as evidenced by the predicted energy barrier of 2.6 kcal/mol (see Fig. 4(a)). The reaction is exothermic by 13.0 kcal/mol. It can be interpreted that the proton prefers to sit on the zeolite. The back transferred proton forms a chemical bond with the O1 atom. The C5-C6 bond resembles a double bond. Finally, 28.4 kcal/mol is required to remove the 1,6-DMN product from the acid site.

The energy profile of the 1,5- to 1,6-DMN isomerization are in Fig. 4(a). The methyl shift was found to be the rate-determining step. It has the highest activation energy of 25.7 kcal/mol compared with 11.7 and 2.6 kcal/mol for the protonation and the back-protonation steps. These results are in good agreement with the experimental observation in which the acid-catalyzed intramolecular 1,2-methyl shift is the rate- determining step for this isomerization with the activation energy of 20.3 kcal/mol [10].

### 3.2 Isomerization of 1,6- to 2,6-DMN

The reaction mechanism of 1,6- to 2,6-DMN isomerization is outlined in Fig. 2(b).


NSTI-Nanotech 2009, www.nsti.org, ISBN 978-1-4398-1784-1 Vol. 3, 2009

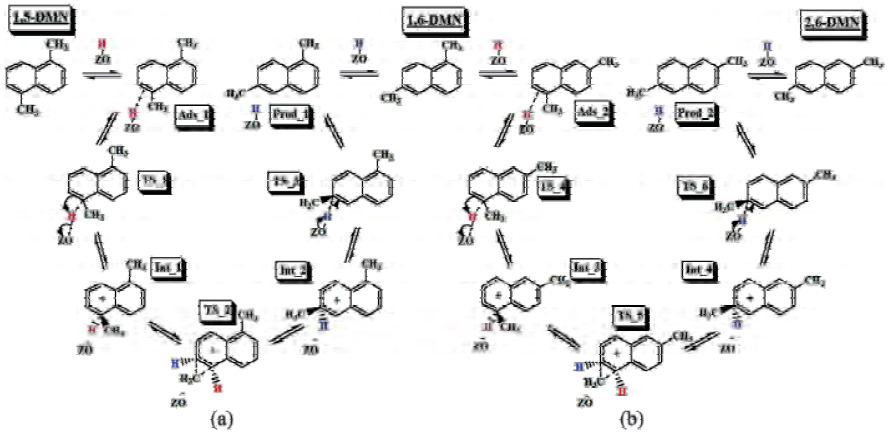


Figure 2: Reaction mechanism of (a) the 1,5- to 1,6-DMN and (b) the 1,6- to 2,6-DMN isomerization by acidic beta-zeolite. Schematically they consist of protonation, methyl shift and proton back-donation of the adsorbed species.

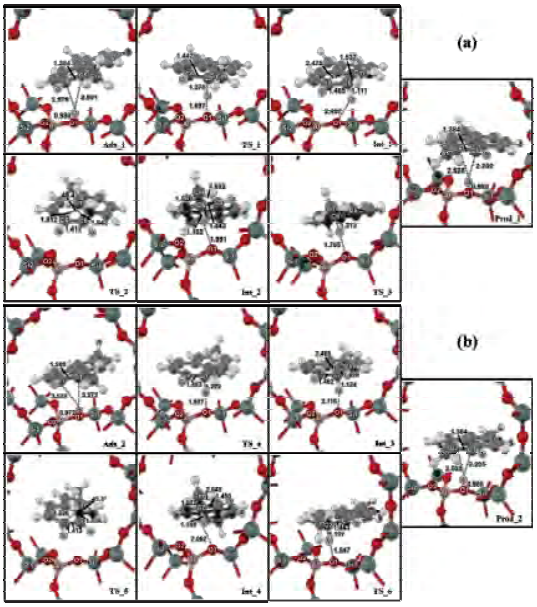


Figure 3: Optimized geometries of adsorbed reactants, transition states, intermediates and products of (a) 1,5- to 1,6-DMN and (b) 1,6- to 2,6-DMN isomerization over H-beta zeolite (14T/120T).

The energetic profiles for the overall steps of the 1,6- to 2,6-DMN isomerization are virtually similar to 1,5- to 1,6-DMN reaction and also summarized in Fig. 4(b). The methyl shift is found to be the rate-determining step for the isomerization with the energy barrier of 21.0 kcal/mol.

The isomerization from 1,5- to 2,6-DMN is shown in Fig. 2 in which is depicted the successive reactions from 1,5- to 1,6- and finally to 2,6-DMN. Comparison between the energy profiles of the 1,5- to 1,6-DMN and 1,6- to 2,6-DMN isomerizations can be made from Fig. 4. The methyl migration is the rate determining step in both reactions. The activation energy of the 1,5- to 1,6-DMN reaction is 25.7 kcal/mol, which is greater than 21.0 kcal/mol of 1,6- to 2,6-DMN reaction. This indicates that the former reaction proceeds more slowly than in the latter. The conclusion is in line with the thermodynamic observed by Kraikul *et al.* that the isomerization occurs rapidly with a higher isomerization rate [5] according to the ratio of 2,6-DMN:1,6-DMN of greater than 1. Our calculation also suggests the same trend. Although only the 14T cluster representing the active site of zeolite and the adsorbate are allowed to relax in M06-L/6-31G(d,p)//ONIOM(M06-L/6-31G(d,p):UFF) model, the information of the reaction such as adsorption and activation energies, are rational and compared well with the experimental data reports in the literature [5, 8, 10-11, 40-41].

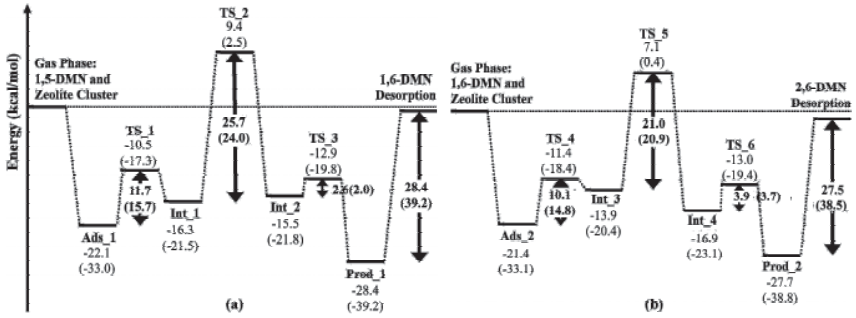


Figure 4: Overall energy profile of (a) 1,5- to 1,6-DMN and (b) 1,6- to 2,6-DMN conversions over H-beta zeolite, calculated with 120T M06-L/6-31G(d,p)//120T ONIOM(M06-L/6-31G(d,p):UFF). Values in parentheses are calculated at the ONIOM(M06-L/6-31G(d,p):UFF) method

## 4 CONCLUSION

The isomerization of 1,5- into 2,6-DMN over the acidic beta zeolite is investigated at the molecular level by using the 120T M06-L/6-31G(d,p)//120T ONIOM(M06-L/6-31G(d,p):UFF) method. This reaction involves two consecutive methyl shift processes through the conversion of 1,5- into 1,6-DMN and of 1,6- into 2,6- DMN, respectively. The reaction mechanism begins with the adsorption of the reactant on a Brønsted acid site of the zeolite followed by the protonation, 1,2-methyl shift and proton back-donation steps and the product desorption. The methyl shift is shown to be the rate-determining step with the 1,5- to 1,6-DMN isomerization reaction having a greater activation barrier than the 1,6- to 2,6-DMN reaction (25.7 vs. 21.0 kcal/mol). The predicted activation barriers agree with the experimental data. Under thermodynamic control, 2,6-DMN is expected to be the main product of the isomerization.

## ACKNOWLEDGEMENTS

The present work was supported in part by grants from the National Science and Technology Development Agency (NSTDA Chair Professor to JL), Thailand Research Fund (TRF), Kasetsart University Research and Development Institute (KURDI), the National Nanotechnology Center (NANOTEC Center of Excellence and Computational Nanoscience Consortium), the Commission on Higher Education, Ministry of Education, under the Postgraduate Education and Research Programs in Petroleum and Petrochemicals, and Advanced Materials as well as the Sandwich Program in the Strategic Scholarships Fellowships Frontier Research Network (CHE-PhD-SW-INDV to CK and CHE-PhD-SW-SUPV to SC). The authors are grateful to Donald G. Truhlar and Yan Zhao for supporting them with the M06-L functional. The Kasetsart University Graduate School is also acknowledged.

## REFERENCES

[1] L. D. Lillwitz , Appl. Catal. A Gen. 221, 337, 2001.
[2] C. Song, Cat. Tech. 6, 64, 2002.
[3] '2,6-dimethylnaphthalene (2,6-DMN): 99/00S7, Chem Systems Report', Chem Systems, 2000.
[4] K. Tanabe and W. F. Holderich, Appl. Catal. A 181, 399, 1999.
[5] N. Kraikul, P. Rangsunvigit and S. Kulprathipanja, Chem. Eng. J. 114, 73, 2005.
[6] N. Kraikul, P. Rangsunvigit, and S. Kulprathipanja, Appl. Catal. A. 312, 102, 2006.
[7] I. Ferino, R. Monaci, L. Pedditzi, E. Rombi, and V. Solinas, React. Kinet. Catal. Lett. 58, 307, 1996.
[8] D. A. McCaulay and A. P. Lien, J. Am. Chem. Soc. 74, 6246, 1952.
[9] M. Kilpatrick, J.A.S. Bett, and M. L. Kilpatrick, J. Am. Chem. Soc. 85, 1038, 1963.
[10] G. Suld and A. P. Stuart, J. Org. Chem. 29, 2939, 1964.
[11] R. Millini, F. Frigerio, G. Bellussi, G. Pazzuconi, C. Perego, P. Pollesel, and U. Romano, J. Catal. 217, 298, 2003.
[12] F. Maseras and K. Morokuma, J. Comput. Chem. 16, 1170, 1995.
[13] S. Humbel, S. Sieber, and K. Morokuma, J. Chem. Phys. 105, 1959, 1996.
[14] T. Matsubara, S. Sieber, and K. Morokuma, Int. J. Quantum Chem. 60, 1101, 1996.
[15] M. Svensson, S. Humbel, R. D. J. Froese, T. Matsubara, S. Sieber, and K. Morokuma, J. Phys. Chem. 100, 19357, 1996.
[16] M. Svensson, S. Humbel, R. D. J. Froese, T. Matsubara, S. Sieber, and K. Morokuma, J. Chem. Phys. 105, 3654, 1996.
[17] S. Dapprich, I. Komaromi, K. S. Byun, K. Morokuma, and M. J. Frisch, J. Mol. Struct. (Theochem) 461, 1, 1999.
[18] T. Vreven and K. Morokuma., J. Comput. Chem. 21, 1419, 2000.
[19] K. Bobuatong and J. Limtrakul, Appl. Catal. A 253, 49, 2003.
[20] W. Panjan and J. Limtrakul, J. Mol. Struct.(Theochem) 654, 35, 2003.
[21] C. Raksakoon and J. Limtrakul, J. Mol. Struct. (Theochem) 631, 147, 2003.
[22] S. Namuangruk, P. Pantu, and J. Limtrakul, J. Catal. 225, 523, 2004.
[23] J. Sirijaraensr, T.N. Truong, and J. Limtrakul, J. Phys. Chem. B 109, 12099, 2005.
[24] S. Namuangruk, P. Khongpracha, P. Pantu, and J. Limtrakul, J. Phys. Chem. B 110, 25950, 2006.
[25] B. Jansang, T. Nanok, and J. Limtrakul, J. Phys. Chem. B 110, 12626, 2006.
[26] W. Panyaburapa, T. Nanok, and J. Limtrakul, J. Phys. Chem. C 111, 3433, 2007.
[27] P. Pantu, B. Boekfa, and J. Limtrakul, J. Mol. Catal. A: Chem. 277, 171, 2007.
[28] B. Jansang, T. Nanok, and J, Limtrakul, J. Phys. Chem. C 112, 540, 2008.
[29] T. Maihom, S. Namuangruk, T. Nanok, and J. Limtrakul, J. Phys. Chem. C 112, 12914, 2008.
[30] A. H. de Vries, P. Sherwood, S.J. Collins, A.M. Rigby, M. Rigutto, and G. J. Kramer, J. Phys. Chem. B 103, 6133, 1999.
[31] R. Rungsirisakun, B. Jansang, P. Pantu, and J. Limtrakul, J. Mol. Struct. (Theochem) 733, 239, 2005.
[32] Y. Zhao and D. G. Truhlar, J. Chem. Phys. 125, 194101, 2006.
[33] Y. Zhao and D. G. Truhlar, Acc. Chem. Res. 41, 157, 2008.
[34] Y. Zhao and D. G. Truhlar, Theor. Chem. Acc. 120, 215, 2008.
[35] E. G. Derouane and C. D. Chang, Microporous Mesoporous Mater. 35-36, 425, 2000.
[36] A. Pelmenschikov and J. Leszczynski, J. Phys. Chem. B 103, 6886, 1999.
[37] L. A. Clark, M. Sierka, and J. Sauer, J. Am. Chem. Soc. 125, 2136, 2003.
[38] X. Rozanska, R.A. van Santen, F. Hutschka, and J. Hafner, J. Am. Chem. Soc. 123, 7655, 2001.
[39] M. J. Frisch, et al. Gaussian 03, Revision C Gaussian, Inc., Wallingford CT, 2004.
[40] D. M. Ruthven and M. Goddard, Zeolites. 6, 275, 1986.
[41] D. Barthomeuf and B. H. Ha, J. Chem. Soc., Faraday Trans. 69, 2158, 1973.

# Dehydration of Ethanol into Ethylene over H-MOR: A Quantum Chemical Investigation of Possible Reaction Mechanisms in the Presence of Water

Jittima Meeprasert [a,b,c], Saowapak Choomwattana [a,b,c], Piboon Pantu [a,b,c] and Jumras Limtrakul [a,b,c] *

[a] Laboratory for Computational and Applied Chemistry, Chemistry Department, Faculty of Science, Kasetsart University, Bangkok 10900, Thailand
[b] NANOTEC Center of Excellence, National Nanotechnology Center, Kasetsart University, Bangkok 10900, Thailand
[c] Center of Nanotechnology, Kasetsart University Research and Development Institute, Bangkok
*E-mail: jumras.l@ku.ac.th, Tel: +662-562-5555 ext 2169, Fax: +662-562-5555 ext 2176

## ABSTRACT

The conversion of ethanol to ethylene, which is one of the most important feed stocks for the petrochemical industry, is of particular commercial interest. Two mechanisms, stepwise and concerted, of the ethanol dehydration to ethylene in the presence of water have been investigated by the ONIOM model (14T/120T) with B3LYP/6-31g(d,p):UFF method. In the stepwise mechanism, the coadsorbed water assists the protonation of ethanol by the acidic zeolite proton to form an ethoxonium ion ($CH_3CH_2OH_2^+$). After that, the cation is dehydrated to form a surface ethoxide intermediate. The dehydration is found to be the rate-determining step with an activation barrier of 41.4 kcal/mol. The ethoxide is then deprotonated with a water molecule which results in the formation of the product of ethylene. The activation energy of the deprotonation is calculated to be 22.2 kcal/mol. The concerted mechanism differs in that the dehydration and the deprotonation occur simultaneously without the formation of the intermediate. In this mechanism, the activation barrier is higher at 54.7 kcal/mol. Therefore, we conclude that the stepwise mechanism should be the dominating one in hydrous ethanol dehydration.

***Keywords***: dehydration of hydrous ethanol to ethylene, H-MOR zeolite, confinement effects, ONIOM

## 1 INTRODUCTION

Petroleum has been and still is debatably the most important energy resource of the world. It and its derivates certainly are still needed for transportation (gasoline, diesel, jet fuel, etc.), and also have an important role in producing electricity. Of equal importance is its role as a raw material for many chemical products. Petroleum resources are inevitably becoming increasingly depleted and more expensive as consumption still continues to increase. The certainty of ever increasing scarcity of petroleum has in recent years resulted in concerted attention, efforts and research to develop alternative hydrocarbon resources.

Biomass, defined as the biological material of living organisms such as animals and plants, is becoming one such increasingly attractive alternative. Conversion of biomass can produce more valuable chemical compounds. A significant and important example of this is bio-ethanol, which is produced through the microbial fermentation of agricultural feedstock such as corn, sugarcane and cassava. Bio-ethanol has now become a highly attractive product in many countries with abundant agricultural resources.

Ethanol, in turn, used not only as a fuel, can be used also to produce more valuable hydrocarbon compounds, especially ethylene. This hydrocarbon compound is extremely important and is used industrially to synthesize a wide range of organic compounds. More than 200 years ago, acidic solution was used to be a catalyst for this reaction. Solid acid catalysts such as silica-alumina ($SiO_2/Al_2O_3$) and zeolites have also been used industrially, even before the twentieth century [10]. Zeolite has the advantage that it is environmentally friendly and can be reused and reactivated. Mordenite (H-MOR) and H-ZSM5 zeolite types are frequently used in ethanol dehydration [1,3,5,7,10-12]. Inaba *et al*. [6] found that H-MOR has a high selectivity for ethylene formation by intramolecular dehydration at temperatures of 400 °C, while H-ZSM-5 is effective for the formation of aromatics, parafins and C3+olefins. These results would indicate that H-ZSM-5 zeolite with a low $Si/Al_2$ ratio is more suitable to produce higher hydrocarbons from ethanol and, consequently, H-MOR is a more appropriate zeolite for the dehydration of ethanol into ethylene [11].

Generally, the dehydration of alcohol over zeolite is considered to start with the direct interaction of the hydroxyl group of alcohol with the Brønsted acid sites of zeolite [1-3,5,8,12]. Density functional theory (DFT) calculations with small quantum clusters were employed to study this mechanism and it is reported that ethanol dehydration proceeds via an intermediate ethoxide surface species [2]. This finding is in line with recent experimental results which confirm the presence of a stable ethoxy intermediate in this reaction [1,7]. Here, we use a 120T cluster representing the H-MOR framework and use the ONIOM (our Own N-layered-Integrated molecular Orbital and molecular Mechanics) method which recent theorectical studies [6,9,13] have shown that this method can be efficiently used for characterizing the reactivity of active sites inside zeolites.

Two different mechanisms for the dehydration of ethanol into ethylene reaction are considered. One is a concerted mechanism and the other proceeds in two steps. Moreover, we propose here that water is allowed to assist the reaction due to the fact that bio-ethanol or hydrous ethanol (a mixture of ethanol and water) is almost always used in industry and it is known from experimental studies

that water in ethanol feed enhances the catalytic activity and selectivity for ethylene formation [3,10,12].

## 2 MODELS AND METHODS

The structure of the 120T cluster was taken from the lattice of mordenite (H-MOR) zeolite (Figure 1). This cluster has been previously reported to be a satisfactory model for the adsorption of hydrocarbon compounds [6,9]. The ONIOM2 scheme, in which the whole model is subdivided into two layers, was adopted for computational efficiency. The inner layer is a fourteen-tetrahedral (14T) cluster consisting of the 12-membered-ring (MR) window of the straight channel of 6.5 Å × 7.0 Å where a silicon atom can be substituted by an aluminum atom to form the Brønsted acid site, which is confirmed by the occurrence of many chemical reactions in the 12MR channels of H-MOR only [9]. This layer, together with the reacting molecules, was treated with the B3LYP/6-31G(d,p) method. The rest of the model was treated with the Universal Force Field (UFF) to represent the confinement effect of the zeolite pore structure and to reduce the required computational time.

All calculations have been performed using the Gaussian 03 code. Geometry optimizations of all structures were performed at the ONIOM(B3LYP/6-31G(d,p):UFF) level of theory and allowing only the active site region 5T, $(H_3SiO)_4Al$ with the adsorbate to relax. For all transition states, vibrational spectra were calculated to ensure that only one imaginary frequency is present.

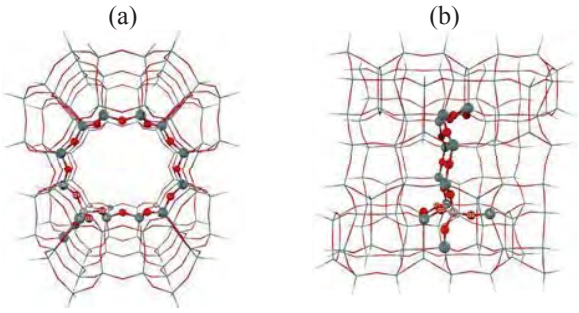


Figure 1: ONIOM model of 14T/120T cluster of H-MOR: (a) front view of the 12MR window of the straight channel and (b) side view showing the 12MR straight channel. Atoms belonging to the 14T quantum region are drawn as spheres.

## 3 RESULTS AND DISCUSSION

The initial step of hydrous ethanol dehydration to ethylene starts with ethanol and water molecules diffused into the pore of H-MOR zeolite and coadsorbed on the acidic and basic sites to form the coadsorption complex. The calculated adsorption energy is -24.0 kcal $mol^{-1}$. The value can be roughly compared with the experimental estimates of the heat of adsorption of ethanol in H-ZSM5, which is -31.1 kcal $mol^{-1}$ [8]. The ethanol molecule is protonated by the acidic proton of zeolite to form the ethoxonium ion ($CH_3CH_2OH_2^+$) which does not occur in the case of ethanol adsorption without water. Due to the formation of three hydrogen bonds in the coadsorption complex, the structures of ethanol and the one of the active site of H-MOR zeolite change considerably. In addition to the O4-Hz hydrogen bond, H1-O5 and H5-O3 hydrogen bonds with distances of 1.47 and 1.74 Å, respectively, are formed. The C1-C2 and C1-O4 bond distances of ethanol are 1.51 and 1.48 Å, respectively while, the O2-Hz and O4-Hz bond distances are 1.48 and 1.04 Å, respectively. After the adsorption process has taken place, the ethoxonium ion is converted to ethylene via the dehydration process. This process can proceed through either a concerted or a stepwise mechanism. In this study, these mechanisms for the dehydration of ethanol in the presence of coadsorbed water are investigated.

### 3.1 Concerted Mechanism

In this mechanism, the reaction is initialized by the coadsorption complex (RT_C) between ethanol and water over the Brønsted acid and its adjacent Lewis basic sites of H-MOR zeolite. Then, the deprotonation and the C-O bond destruction of the ethanol molecule occur simultaneously to give the ethylene product (Eq.1):

$$C_2H_5OH + H_2O + \text{H-MOR} \rightleftharpoons C_2H_4 + 2H_2O + \text{H-MOR} \quad (1)$$

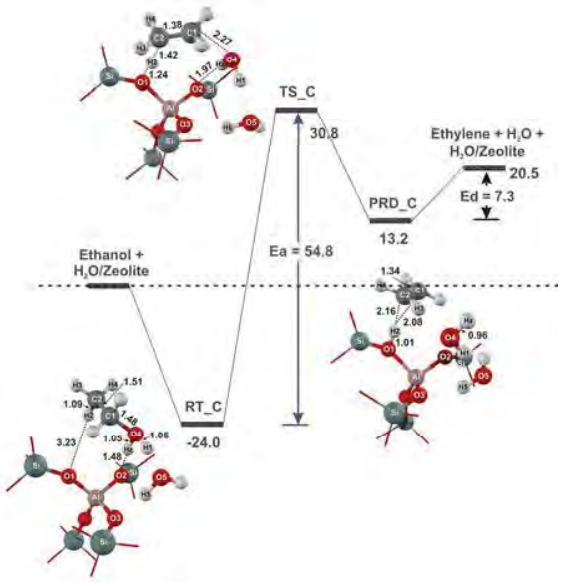


Figure 2: Calculated energy profile for the concerted mechanism of ethanol dehydration.

Figure 2 shows the optimized complexes and selected geometric parameters of the reactant, transition state and products. The coadsorbed water molecule facilitates the protonation of the ethanol molecule by the acidic proton of zeolite to form the ethoxonium ion ($CH_3CH_2OH_2^+$). The


NSTI-Nanotech 2009, www.nsti.org, ISBN 978-1-4398-1784-1 Vol. 3, 2009

adsorption energy of this complex is -48.8 kcal mol$^{-1}$. At the TS_C transition state configuration, the C1-O4 bond of the ethoxonium ion begins to break to form one water molecule and the ethyl group. For the formation of the latter, the C2-H2 bond distance changes from 1.09 to 1.42 Å. H2 attaches to O1 with a bond length of 1.24 Å. This transition state has one imaginary frequency at 1161.0 cm$^{-1}$. The activation barrier and the apparent activation energy for this step are calculated to be 54.8 and 5.9 kcal mol$^{-1}$, respectively. After forming the transition state, the proton (H2) of the ethyl group transfers completely from C2 to O1 to restore the acid site of zeolite and a double bond (1.38 Å) between C1-C2 is formed. The ethylene molecule remains adsorbed via the π-interaction while a water dimer is formed on the basic site of the zeolite (PRD_C). The adsorption energy of this complex is calculated to be -11.6 kcal mol$^{-1}$. The desorption of ethylene and one water molecule is an endothermic process which requires 7.3 kcal mol$^{-1}$.

## 3.2 Stepwise Mechanism

Alternatively, the dehydration of ethanol to ethylene can proceed in a stepwise mechanism through the formation of ethoxide intermediates that have also been observed in experiments [1,7]. The two processes involved are the dehydration of ethanol to ethoxide and the deprotonation of ethoxide to ethylene.

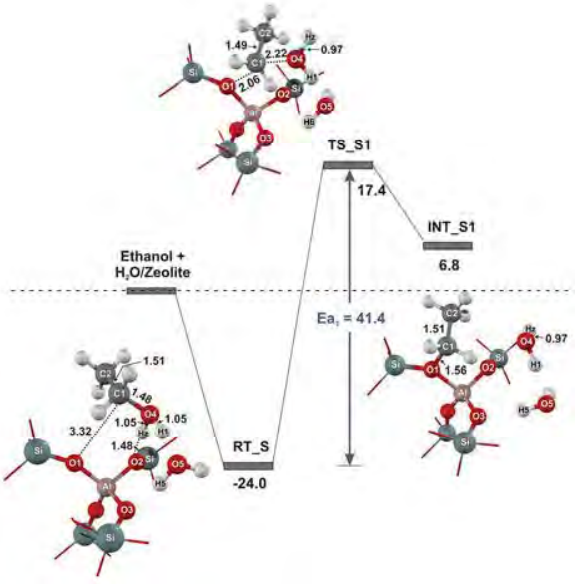


Figure 3: Calculated energy profile for the stepwise mechanism in the dehydration of ethanol to the ethoxide process.

*The dehydration of ethanol to the ethoxide process:* In this process, the ethanol molecule is dehydrated and an ethyl group is attached to the basic site of the zeolite. From there, the surface ethoxy species is formed within the presence of two water molecules (Eq. 2):

$$C_2H_5OH + H_2O + \text{H-MOR} \rightleftharpoons C_2H_5\text{-MOR} + 2H_2O \quad (2)$$

Figure 3 shows the optimized complexes and selected geometric parameters of the reactant, transition state and intermediates. The reaction starts with ethanol and water molecules coadsorbed on the acidic and basic sites of the zeolite, respectively. The adsorption energy of this complex is -48.8 kcal mol$^{-1}$. The coadsorbed water molecule facilitates the protonation of the ethanol molecule by the acidic proton of zeolite to form the ethoxonium ion ($CH_3CH_2OH_2^+$). At the TS_S1 transition state, the C1-O4 bond of ethoxonium (2.22 Å) is breaking to form a water molecule (Hz-O3-H1) while the ethyl group gets closer to the basic oxygen of zeolite with an O1-C1 distance of 2.06 Å. The O4-C1-O1 bond angle is 154.4°. The imaginary frequency of this transition state is 366.8 cm$^{-1}$. The activation barrier and the apparent activation energy for this step are calculated to be 41.5 and -7.7 kcal mol$^{-1}$, respectively. After the transition state, the intermediate of ethoxide and two water molecules (INT_S1) are formed. Their adsorption energy is -18.1 kcal mol$^{-1}$.

*The deprotonation of ethoxide to the ethylene process:* The dehydration process produces ethoxide in agreement with the experimental finding from IR spectroscopy [1,7]. In this process, the reaction starts with a surface ethoxy species and a water molecule. Then, the water-assisted deprotonation of ethoxide leads to the formation of ethylene. (Eq. 3):

$$C_2H_5\text{-MOR} + H_2O \rightleftharpoons C_2H_4 + H_2O + \text{H-MOR} \quad (2)$$

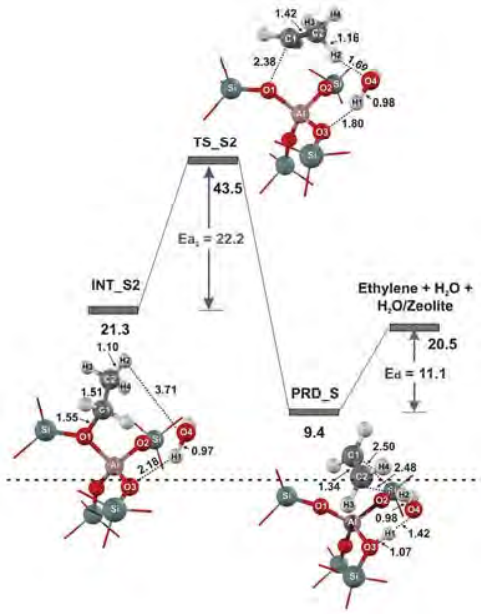


Figure 4. Calculated energy profile for the stepwise mechanism in the deprotonation of ethoxide to the ethylene process.

Figure 4 shows the optimized complexes and selected geometric parameters of the reactant, transition state and products. The reaction starts with ethoxide and water (INT_S2). This complex has an adsorption energy of -3.5 kcal mol$^{-1}$. In the transition state (TS_S2), the proton of ethoxide is transferred to the oxygen of the water molecule

that is hydrogen-bound to an oxygen atom of zeolite. The C1-C2 bond distance is slightly shortened by about 0.09 Å and the proton of the water molecule is transferred to the zeolite regenerating the acidic site (O3-H1 bond). This transition state has one imaginary frequency at 248.6 $cm^{-1}$. The calculated energy barrier and the apparent activation energy are 22.2 and 18.7 kcal $mol^{-1}$, respectively. The ethylene product is formed by adsorbing the water molecule via the π-interaction (PRD_S). The adsorption energy of this complex is -15.4 kcal $mol^{-1}$. The desorption of ethylene and water from the pore of H-MOR zeolite requires 37.5 kcal $mol^{-1}$. The overall reaction energy for the stepwise pathway is endothermic by 22.1 kcal $mol^{-1}$.

## 4 CONCLUSIONS

The dehydration of ethanol to ethylene over the mordenite zeolite in the presence of water has been investigated by using the ONIOM2 method. Two reaction mechanisms are considered. The stepwise mechanism occurs through the formation of ethoxide intermediates and can be separated into the dehydration of ethanol to ethoxide and the deprotonation of ethoxide to ethylene. The activation barrier of the first step is 41.5 kcal $mol^{-1}$, which is much higher than that of the second step (22.2 kcal $mol^{-1}$), and this is expected to be the rate determining step. For the concerted mechanism, without an ethoxide intermediate, the activation barrier is 54.8 kcal $mol^{-1}$. This is considerably higher than the barrier of the rate determining step of the stepwise mechanism (41.5 kcal $mol^{-1}$). On the basis of our calculations it can be concluded, therefore, that the dehydration of hydrous ethanol to ethylene over H-MOR zeolite is proceeding via a stepwise mechanism.

## ACKNOWLEDGEMENTS

The present work was supported in part by grants from the National Science and Technology Development Agency (NSTDA Chair Professor to JL), Thailand Research Fund (TRF), Kasetsart University Research and Development Institute (KURDI), the National Nanotechnology Center (NANOTEC Center of Excellence and Computational Nanoscience Consortium), the Commission on Higher Education, Ministry of Education, under the Postgraduate Education and Research Programs in Petroleum and Petrochemicals, and Advanced Materials as well as the Sandwich Program in the Strategic Scholarships Fellowships Frontier Research Network (CHE-PhD-SW-SUPV to SC). The Kasetsart University Graduate School is also acknowledged.

## REFERENCES

[1] R. Barthos, A. Széchenyi and F. Solymosi, "Decomposition and Aromatization of Ethanol on ZSM-Based Catalysts," J. Phys. Chem. B., 110, 21816-21825, 2006.

[2] S. R. Blaszkoski and R. A. van Santen, "Theoretical Study of C-C Bond Formation in the Methanol-to-Gasoline Process," J. Am. Chem. Soc., 119, 5020-5027, 1997.

[3] E. Costa, A. Ugeles, J. Aguado and P. J. Hernăndes, "Ethanol to Gasoline Process: Effect of Variables, Mechanism, and Kinetics," Ind. Eng. Chem. Process Des. Dev., 24, 239-244, 1985.

[4] F. Haase and J. Sauer, "Interaction of Methanol with Bronsted Acid sites of Zeolite Catalysts: An ab Initio Study," J. Am. Chem. Soc., 117, 3780-3789, 1995.

[5] M. Inaba, K. Murata, M. Saito and I. Takahara, "Ethanol Conversion to Aromatic Hydrocarbons over Several Zeolite Catalysis," React. Kinet. Catal. Lett., 88, 135-142, 2006.

[6] B. Jansang, T. Nanok and J. Limtrakul, "Interaction of Mordenite with an aromatic hydrocarbon: An embedded ONIOM study," Journal of Molecular catalysis A., 164, 33-39, 2007.

[7] J. N. Kondo, K. Ito, E. Yoda, F. Wakabayashi and K. Domen, "An Ethoxy Intermediate in Ethanol dehydration on Brønsted Acid Sites in Zeolite," J. Phys. Chem. B., 109, 10969-10972, 2005.

[8] C. C. Lee and R. J. Gorte, "Calorimetric Study of Alcohol and Nitrile Adsorbtion Complexes in H-ZSM-5," J. Phys. Chem. B., 101, 3811-3817, 1997.

[9] P. Pantu, B. Boekfa and J. Limtrakul, "The adsorption of saturated and unsaturated hydrocarbons on nanostructured zeolites (H-MOR and H-FAU): An ONIOM study," Journal of Molecular Catalysis A., 277, 171–179, 2007.

[10] C. B. Phillips and R. Datta, "Production of Ethylene from Hydrous Ethanol on H-ZSM-5 under Mild Conditions," Ind. Eng. Chem. Res., 36, 4466-4475, 1997.

[11] I. Takahara, M. Saito, M. Inaba and K. Murata, "Dehydration of ethanol into ethylene over solid acid catalysts," Catalysis Letters, 105, 249-252, 2005.

[12] A. K. Talukdar, K. G. Bhattacharyya and S. Sivasanker, "H-ZSM-5 Catalysed Conversion of Aqueous Ethanol to Hydrocarbons," Applied Catalysis A, 148, 357-371, 1997.

[13] T. Maihom, S. Namuangrak, T. Nanok and J. Limtrakul, "Theorectical Study on Structures and Reaction Mechanisms of Ethylene Oxide Hydration over H-ZSM-5: Ethylene Glycol Formation," J. Phys. Chem. C., 112, 12914-12920, 2008.

# The Theoretical Investigation of Oxidative Dehydrogenation of Ethane to Ethene over Fe-ZSM-5: A QM/MM Study

Karan Bobuatong [a,b], Jakkapan Sirijaraensre [a,b,c], Pipat Khongpracha [a,b], Piboon Pantu [a,b,c] and Jumras Limtrakul [a,b,c*]

[a] Laboratory for Computational and Applied Chemistry, Chemistry Department, Faculty of Science, Kasetsart University, Bangkok 10900, Thailand
[b] NANOTEC Center of Excellence, National Nanotechnology Center, Kasetsart University, Bangkok 10900, Thailand
[c] Center of Nanotechnology, Kasetsart University Research and Development Institute, Bangkok
*E-mail: jumras.l@ku.ac.th, Tel: +662-562-5555 ext 2169, Fax: +662-562-5555 ext 2176

## ABSTRACT

The complete detailed reaction mechanism for the oxidative dehydrogenation of ethane over Fe-ZSM-5 zeolite has been systematically investigated by means of the ONIOM(MP2/6-31G(d,p):UFF)//ONIOM(B3LYP/6-31G(d,p):UFF) scheme. Two types of reaction mechanisms for the oxidative dehydrogenation of ethane have been suggested: stepwise and concerted. The concerted mechanism, the concurrent abstraction of two hydrogen atoms from ethane was found to be unattainable. Two routes of the stepwise pathway were proposed. The reaction at the straight channel takes place via the alkoxide intermediate, while the key intermediate of the reaction occurring at the sinusoidal channel is an "ethyl radical" one. The activation energies of the reaction observed at the straight channel are 12.4 and 54.9 kcal/mol, which is quantitatively higher than those at the sinusoidal channel (10.3 and 4.8 kcal/mol). The stepwise reaction taking place via the radical intermediate has been proved to be a dominant step in generating the ethene molecule.

***Keywords***: ethene, Fe-ZSM-5 zeolite, ONIOM, oxidative dehydrogenation, ethane

## 1 INTRODUCTION

Ethene is one of the most important basic chemicals in the petrochemical industry as a feedstock for the production of ethylene oxide, ethylene dichloride, vinyl acetate, ethyl alcohol and other petrochemical products. Conventionally, ethane is produced in the petrochemical industry by stream cracking. This process occurs at a high temperature (750-950 $^0$C) [1]. Since the conventional production of ethylene has a high-energy consumption, much effort has been devoted to find an efficient route for the selective production of light olefins. Currently, the oxidative dehydrogenation of ethane is an alternative route to produce ethylene. This route carries on at a low temperature which would essentially reduce the formation of coke and also extend the lifetime of catalysts.

A range of heterogeneous catalysts have been used in this reaction for the purpose of achieving energy savings and increasing productivity. These include: metal oxides [3,4], zeolites [5,6], and metal-doped mesoporous materials [7,8].

The iron-modified zeolite of the MFI structure, Fe-ZSM-5, is proven to be one of the potential catalysts for the dehydrogenation of ethane. Held *et al*. [6] found that the ethane oxidation over the iron-modified zeolites; Y, MOR and ZSM-5 zeolites. They found that Fe-ZSM-5 provided the highest selectivity towards ethylene formation (in the range of 55% to 87%), whilst the Fe-MOR and Fe-FAU zeolite provides mainly the complete oxidation process. These results showed that the zeolite structure plays a key role in the catalytic activity of iron species for oxidative dehydrogenation reaction. However, the reaction mechanism of this reaction inside the pore of ZSM-5 zeolite has not been fully investigated.

The purpose of the present study is to analyze the reaction mechanisms of the oxidative dehydrogenation of ethane to ethene over Fe-ZSM-5 zeolite by means of the ONIOM (our-Own-N-layer Integrated molecular Orbital + molecular Mechanics) method. The results of this study may be helpful for understanding the fundamentals of how the oxidative dehydrogenation of ethane over zeolite works.

## 2 METHOD

The model of ZSM-5 zeolite, the 232T cluster, which covers the 10T active region and three different channel structures (the channel intersection, the straight channel, and the zigzag channel) where the reaction normally takes place, is taken from the lattice structure of the ZSM-5 zeolite [9]. The ONIOM2 scheme, in which the whole model is subdivided into two layers, is adapted. The active region, shown in Figure 1, consists of the 12T cluster, which is considered to be the smallest unit required for representing the reaction site of zeolite and the reactive molecules, is treated with the B3LYP level of theory using the 6-31G(d,p) basis set for H, C, O, Al and Si atoms and the effective core potential basis of Stuttgart and Bonn for the Fe atom [10]. In view of there being several reports that the sextet spin state was the most stable electronic configuration for the theoretical study on Fe-ZSM-5 [11-12], the total spin of the system was maintained at this state throughout all calculations. In order to obtain more reliable interaction energies, the single-point energy calculations at the ONIOM(MP2/6-31G(d,p):UFF)//ONIOM(B3LYP/6-31G(d,p):UFF) level were carried out. The rest of the extended framework is treated with the less demanding UFF force field [13]. It is

considered that these selected models for the ZSM-5 zeolites are large enough to cover all the important framework effects that act on both the active site and on the adsorbates.

All calculations have been performed using the Gaussian 03 code [14]. During the structure optimization, the 5T portion of the active site region and the adsorbate are allowed to relax while the rest of the active region is fixed at the crystallographic coordinates.

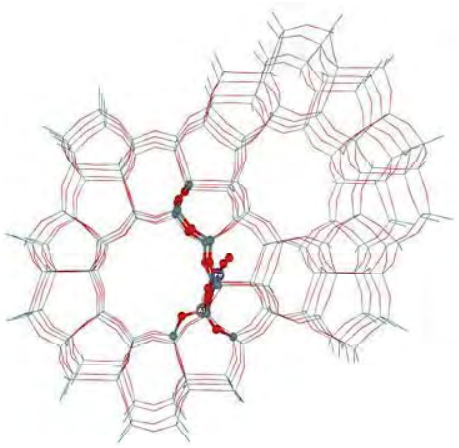

Figure 1: ONIOM2 layer of the 232T cluster model of Fe-ZSM-5. Atoms belonging to the12T quantum cluster are drawn as balls and sticks.

## 3 RESULTS AND DISCUSSION

### 3.1 Stepwise mechanism for ethane oxidative dehydrogenation

Due to the ZSM-5 zeolite consisting of two different types of pore: straight channel and sinusoidal channel, it is of interest to investigate the oxidative dehydrogenation of ethane taking place in different environments in order to get more insight into the role of the confinement effect of zeolite on the reaction.

*Effect of straight channel within the nanoreactor on chemical reactions, Stepwise I:* The reaction taking place in the straight channel at the junction of the sinusoidal channel and the straight one, molecular adsorption of ethane on the α-oxygen of Fe-ZSM-5, is observed by the mean of the ONIOM2 scheme. The adsorption complex of ethane (Ads_1) causes the slight lengthening of Fe-O1 and Fe-O2 bond distances by 0.001 Å. The computed adsorption energy is -8.5 kcal/mol. Dunne *et al*. [15] studied the calorimetric heats of adsorption and adsorption isotherm of methane and ethane on the silicalite which has the same crystal structure as ZSM-5 zeolite. The heat of adsorption of methane and ethane on the silicalite zeolite is 5.0 and 7.5 kcal/mol, respectively. This result shows that the difference of the energy is caused by the confinement effect of the zeolitic pore. In comparing the adsorption energy for the interaction of ethane and methane over the Fe-ZSM-5, the difference of values is 2.4 kcal/mol which is consistent with the difference in the adsorption from experimental data [15]. It can be concluded that the adsorption energy of ethane is qualitatively reliable. At the C-H cleavage transition state (TS_1), the activation energy required during the process of the (C1-H1 cleavage is 12.4 kcal/mol lower than the activation energy required during the C-H cleavage of methane over the Fe-ZSM-5 zeolite (15.3 kcal/mol) reported in previous work. The lowering of the activation energy is consistent with the weakening of the C-H bond of methane and ethane. The C-H bonding energy of methane is higher than that of ethane (435 vs. 420 kJ/mol). Therefore, cleavage of the C-H of ethane is preferable. After this step, the ethoxide and hydroxyl groups are formed. The alkoxide intermediate (Ads_2) is located in the intersection space and the H1-O1 bond also points to the direction of the free space in the intersection channel. The obtained ethoxide intermediate is much more stable than the initial state by 75 kcal/mol. The subsequent migration of hydrogen from the alkoxide group to the adjacent hydroxyl group (TS_2) leads to the formation of ethylene and water molecules. These indicate the migrating of

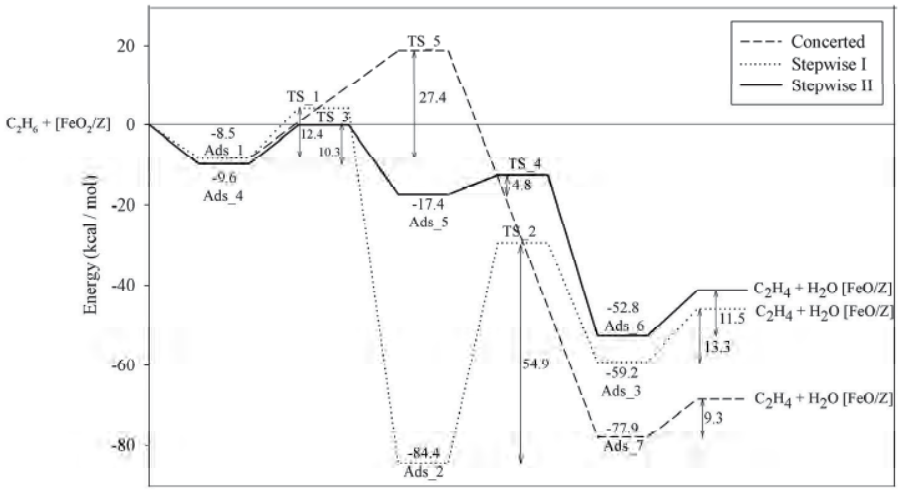


Figure 3: Compared energy profile for stepwise mechanism in the intersection, sinusoidal channel and concerted mechanism.


NSTI-Nanotech 2009, www.nsti.org, ISBN 978-1-4398-1784-1 Vol. 3, 2009

the C-H bond and the formation of the O-H bond, forming the ethylene and water molecules. This process is exothermic by 59.2 kcal/mol with a high-energy barrier of 54.9 kcal/mol.

*Effect of the sinusoidal channel within the nanoreactor on chemical reactions, Stepwise II:* The pathway of the oxidative dehydrogenation of ethane inside the sinusoidal channel is similar with that inside the straight channel in general, but their main differences will be highlighted. The reaction is initiated at the O2 site pointing toward the sinusoidal channel. The adsorption energy of ethane (Ads_5) in this channel is -9.6 kcal/mol. At the H abstraction transition state (TS_3), the energy barrier is calculated to be 10.3 kcal/mol, which is slightly lower than that of the C-H cleavage inside the straight channel. Variation of pore dimension at the transition state is shown to affect the direction of the reaction. Obviously, barrier height is decreased by about 30%. Comparison of the TS_1 in the straight channel shows that the form of the intermediate complex is affected by the pore shape. At this channel, the ethyl radical (Ads_6) is stabilized inside the sinusoidal channel. This phenomenon is called "intermediate shape selectivity" [16]. The ethyl radical intermediate is slightly more stable than the initial state by 7 kcal/mol. The formation of ethylene yields via the second H-abstraction by migrating one of the C-H bonds at the methyl site of the ethyl radical to the hydroxyl group bound on the iron site to form a water molecule. The coadsorption between water and ethylene molecules (Ads_6) are reached after the TS_4 requires only 4.8 kcal/mol, which is significantly lower than the activation energy for the corresponding step in the straight channel (TS_2). This result reveals that the ethyl radical is much more active than the alkoxide complex (Ads_2). The Ads_6 has the lowest energy, having the energy difference of about 35 kcal/mol with respect to Ads_5. Removal of water and propene from Ads_6 requires only 11.5 kcal/mol. The rate-limiting step of the reaction is the first H-abstraction step yielding the ethyl radical that reacts with the hydroxyl group attaching to the Fe site (Ads_5).

## 3.2 Concerted mechanism for ethane oxidative dehydrogenation

In addition to the stepwise mechanism in the formation of ethylene, we consider now the reaction pathway through a cyclic mechanism involving the simultaneous hydrogen abstraction of two hydrogen atoms from ethane to the iron oxygen atoms, yielding the $Fe(OH)_2$ site and the ethylene molecule. In this hypothesis, the ethane is coordinated on the α-oxygen atoms by a bidentate complex.

Such a TS is expected to involve double hydrogen abstractions with the breaking of the C-H bonds and the making of O-H bonds, leading to the formation of ethylene. However, in spite of intensive search, we were not able to locate the related cyclic minimum whilst the corresponding transition state structure (TS_5) is observed in which two hydrogen atoms are eliminated from the ethane to the α-oxygen atoms of the Fe site. In the bidentate complex, the ethane is twisted into an eclipsed conformation less stable than the minimum form: the staggered conformation, by

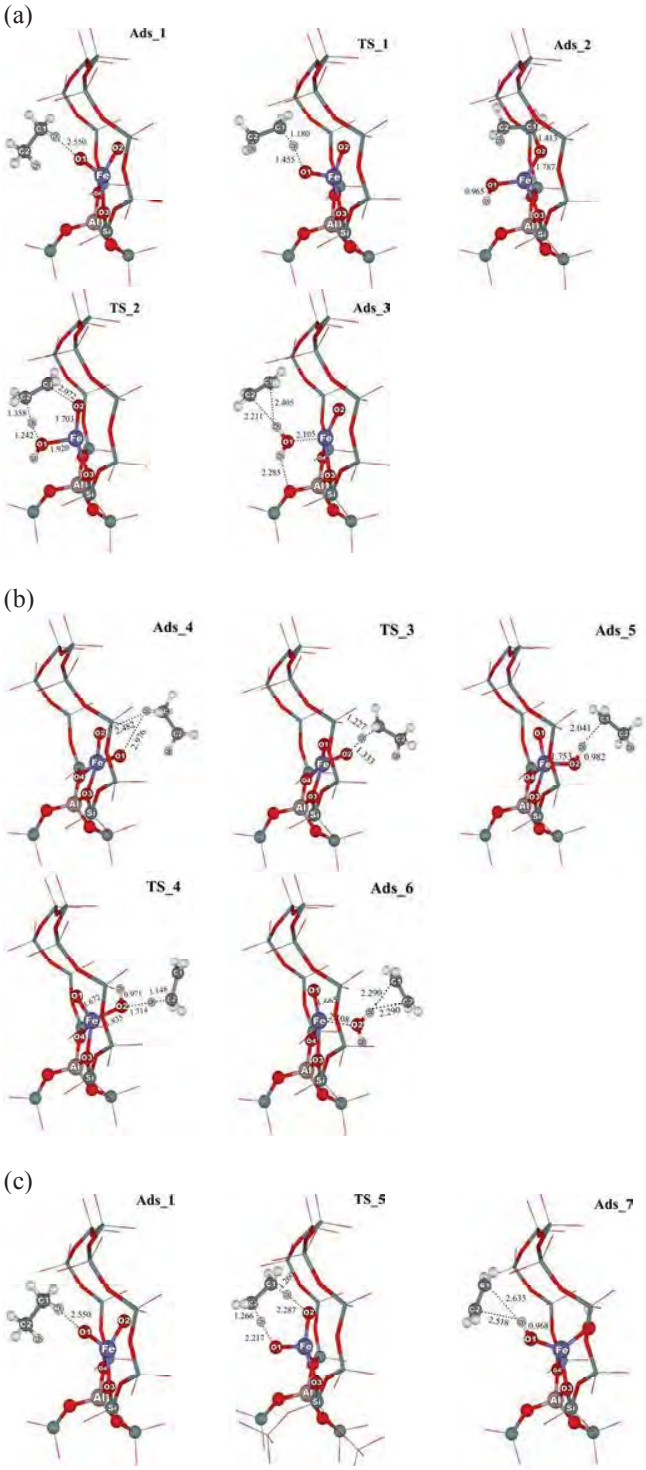


Figure 2: Optimized structures of adsorbed reactants, transition structures and products of (a) the stepwise mechanism in the intersection channel, Stepwise I, (b) the stepwise mechanism in the sinusoidal, Stepwise II, (c) the concerted mechanism.

3 kcal/mol [17]. Due mainly to steric hindrance, the interaction between eclipse-formed ethane and the α-oxygen atoms does not exist The route via the TS_5 yields ethylene attached to the $Fe(OH)_2$ site. The exothermicity of the reaction is -77.9 kcal/mol. The subsequent desorption of ethylene is weakly endothermic by 9.3 kcal/mol. These results suggest that only the single site of Fe is not favorable to perform the ethylene via a single step by abstracting two hydrogen atoms from ethane simultaneously. Formation of ethylene should be carried out via the stepwise mechanism.

## 4 CONCLUSION

The oxidative dehydrogenation reaction of ethane over Fe-ZSM-5 zeolite has been investigated using the ONIOM2 model. Two mechanisms, stepwise and concerted, have been evaluated. The concerted mechanism was found to be unfavorable. Our finding reveals that the stepwise mechanism taking place via the ethyl radical intermediate dominates the overall reaction of the oxidative dehydrogenation of ethane. However, this process competes against another plausible stepwise reaction that can proceed through the "alkoxide intermediate" at the straight channel. For the stepwise reaction with a radical intermediate occurring at the sinusoidal channel, it starts with the hydrogen abstraction of the ethane molecule to form the ethyl radical complex. The ethylene is generated via the second hydrogen abstraction in the second step. The activation energy of the first step is 10.3 kcal/mol, two fold higher than that of the second step (4.8 kcal/mol). These activation energies are quantitatively lower than those of the reaction via the alkoxide intermediate taking place at the straight channel (12.4 and 54.9 kcal/mol for the first and second H-abstractions, respectively). From calculated results, the activity of Fe ions is highly affected by the spaces in the vicinity of the active site. The ethane locating along the narrow channel would be readily dehydrogenated to ethylene faster than that on the open channel.

## ACKNOWLEDGEMENTS

The present work was supported in part by grants from the National Science and Technology Development Agency (NSTDA Chair Professor to JL), Thailand Research Fund (TRF), Kasetsart University Research and Development Institute (KURDI), the National Nanotechnology Center (NANOTEC Center of Excellence and Computational Nanoscience Consortium), the Commission on Higher Education, Ministry of Education, under the Postgraduate Education and Research Programs in Petroleum and Petrochemicals, and Advanced Materials. The Kasetsart University Graduate School is also acknowledged.

## REFERENCES

[1] L. Kniel, O. Winter, K. Stork, Ethylene: Keystone to the Petrochemical Industry, Marcel Dekker, New York, 1980.
[2] M. A. Banares, Catal. Today. 51 (1999) 319.
[3] M. Huff, L. D. Schmidt, J. Phys. Chem. 97 (1993) 11815.
[4] E. Jagielska, R. Mostowicz, S. Szarlik, Chemiczny 86 (2007) 340.
[5] N. Mimura, M. Okamoto, H. Yamashita, S. T. Oyama, K. Murata, J. Phys. Chem. B 110 (2006) 21764.
[6] A. Held, J. Kowalska, K. Nowinska, Appl. Catal. B 64 (2006) 201.
[7] Bi, Y.-L, V. C. Corberan, H. Zhuang, K. –J. Zhen, Stud. Surf. Sci. Catal. 153 (2004) 343.
[8] H. Yang, S. Liu, L. Xu, S. Xie, Q. Wang, L. Lin, Stud. Surf. Sci. Catal. 147 (2004) 697.
[9] H. van Koningveld, H. van Bekkum, H, J. C. Jansen, Acta Crystallogr. B 43 (1987) 127.
[10] J. A. Ryder, A. K. Chakraborty, A. T. Bell, J. Phys. Chem. B 106 (2002) 7059.
[11] W. Liang, A. T. Bell, M. Head-Gordon, A. K. Chakraborty, J. Phys.Chem. B 108 (2004) 4362.
[12] J. A. Ryder, A. K. Chakraborty, A. T. Bell, J. Catal. 220 (2003) 84.
[13] A. K. Rappe, C. J. Casewit, K. S. Colwell, W. A. Goddard, W. M. Skiff, J. Am. Chem. Soc. 114 (1992) 10,024.
[14] M. J. Frisch, et al. Gaussian 03, Revision C Gaussian, Inc, Wallingford CT, 2004.
[15] J. A. Dunne, R. Mariwala, M. Rao, S. Sircar, R. J. Gorte, A. L. Myers, Langmuir 12 (1996) 5888.
[16] L. A. Clark, M. Sierka, J. Sauer, J. Am. Chem. Soc. 126 (2004) 936.
[17] V. Pophristic, L. Goodman, Nature 411 (2001) 565.

# Mechanism of MOF-505 and Cu-ZSM-5 Promoted Mukaiyama Aldol Reaction: An ONIOM study

Sudarat Yadnum [a,b], Saowapak Choomwattana [a,b], Pipat Khongpracha [a,b], and Jumras Limtrakul [a,b*]

[a]Laboratory for Computational and Applied Chemistry, Chemistry Department,
Faculty of Science, Kasetsart University, Bangkok 10900, Thailand
[b]NANOTEC Center of Excellence, National Nanotechnology Center,
Kasetsart University Research and Development Institute, Thailand
*E-mail: jumras.l@ku.ac.th, Tel: +662-562-5555 ext 2169, Fax: +662-562-5555 ext 2176

## ABSTRACT

Density-functional theory (B3LYP/6-31G(d,p)) and ONIOM(B3LYP/6-31G(d,p):UFF) have been employed to investigate the reaction of the Mukaiyama aldol reaction and compare the catalytic efficiency between the metal-organic framework (MOF-505) and Cu-exchanged ZSM-5 zeolite. The Mukaiyama aldol reaction of encapsulated formaldehyde and silyl enol ether was studied on three model systems: (1) bare model: $O{=}CH_2/H_3SiOHC{=}CH_2$; (2) MOF-505: MOF-505/$O{=}CH_2/H_3SiOHC{=}CH_2$; and (3) Cu-exchanged zeolite: Cu-ZSM-5/$O{=}CH_2$ /$H_3SiOHC{=}CH_2$. The reaction is proposed to take place in a single concerted reaction step. It is found that both catalysts make the carbon atom in formaldehyde more electrophilic which leads to a lower energy barrier of the reaction as compared to the bare model system. For the comparison of the catalytic efficiency, it is found that Cu-ZSM-5 reduces the activation energy (6.3 kcal/mol) to be lower than that for MOF-505 (11.0 kcal/mol).

***Keywords***: Cu-ZSM-5 zeolite, Mukaiyama aldol reaction, confinement effects, metal-organic framework (MOF-505), ONIOM

## 1 INTRODUCTION

The Mukaiyama aldol reaction, an acid-catalyzed aldol reaction between a silyl enol ether and a carbonyl compound, has been an important and versatile tool in organic and biochemical domains [1]. For instance, Takasu et al. [2] reported the preference reaction on a [2+2] cycloaddition over the Mukaiyama aldol reaction in their study of the Lewis acid-catalyzed reactions between silyl enol ethers and α,β-unsaturated ethers. In the aspect of organic chemistry, formaldehyde is well known as one of the most versatile carbon electrophiles. However, its application is often limited because it rapidly tends to polymerize to solid paraformaldehyde and trioxane. In order to obtain formaldehyde monomer, thermal or Lewis acid pretreatment is therefore used to depolymerize paraformaldehyde or trioxane. Environmentally friendly porous materials such as zeolites were found to be promising candidates for the storage of molecular formaldehyde. For the reaction with larger molecules, porous materials like metal-organic frameworks (MOFs) become more advantageous because of the accessible variation of freely designed pore dimension and chemistry inside the cavity. As porous materials, MOFs also find applications in catalysis [3-7]. We approach the reaction mechanisms on a molecular level by means of quantum chemical calculations. Because both zeolites and MOFs are micro-mesoporous materials, the computational methods and schemes used for MOFs can be adopted from the ones used in the study of zeolites. Like in zeolites [8-11], only a small part of the framework affects the electronic properties of the reactive site, thus facilitating modeling using quantum chemical methods. To include the contribution of the environmental framework on the adsorption of the reactants, hybrid methods such as embedded cluster or combined quantum mechanics/ molecular mechanics (QM/MM) methods [12-19] as well as the ONIOM schemes are well suited to such systems. In this work, we study the reaction mechanism of the Mukaiyama aldol reaction between an encapsulated formaldehyde molecule and silyl enol ether on MOF-505 and Cu-ZSM-5 zeolite.

## 2 COMPUTATIONAL METHOD

Both Cu-ZSM-5 and MOF-505 structures are obtained from the XRD data. In the ONIOM model, the system is separated into two parts. The inner cluster consists of the active region, typically modeled in a small cluster calculated with density functional theory, to account for the interactions of adsorbates with the porous structure and their chemical reactions. The outer layer represents the environmental framework, described by a molecular mechanics force field, to account for the van der Waals interactions due to the extended structure. In this study, we study the reaction mechanism of the Mukaiyama aldol reaction between encapsulated formaldehyde molecule and silyl enol ether on MOF-505 and Cu-ZSM-5 zeolite. We have employed the ONIOM2 (B3LYP/6-31G(d,p):UFF) method to investigate the reaction on Cu-ZSM-5 and MOF-505. Since the active paddle wheel unit of MOF-505 is the effective part of the molecules of the system because formaldehyde can easily enter between the 3,3',5,5'-biphenyltetra-carboxylic

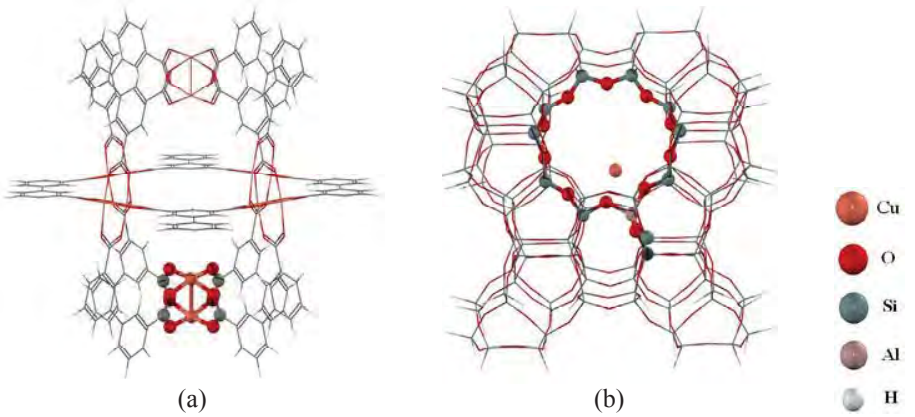


(a) (b)

Figure 1: Geometry of (a) MOF-505 and (b) Cu-ZSM-5
where the high layer (DFT region) is represented in ball-bond view and the low layer (UFF) is represented by line view.

acid unit, it is the inner ONIOM layer. The framework environment constitutes the outer ONIOM layer. For the ZSM-5 crystal structure (MFI framework), there are 12 symmetrically nonequivalent tetrahedral framework positions known as T-sites. The active region, consists of the 10T ring, representing the acidic site of zeolite and that of the reactive molecules whereas the rest of the framework is included into the calculation with the universal force field.

## 3 RESULTS AND DISCUSSION

We separate the topics into sections: 3.1-3.3. In the first section, we discuss the reaction without any Lewis acid catalyst. In section 3.2, the existence and reactivity of encapsulated formaldehyde in the MOF-505 ($O=CH_2$ @MOF-505) is described. We predict the interactions of MOF-encapsulated formaldehyde with silyl enol ether ($O=CH_2$ @MOF-505/$H_3SiOHC=CH_2$). In section 3.3, we describe the proposed mechanism of the Cu-ZSM-5 catalyzed reaction ($O=CH_2$@MOF-505/$H_3SiOHC=CH_2$). Finally, we make the comparison of the two catalyzed cases with the reaction without any Lewis acid catalyst.

### 3.1 The Mukaiyama aldol reaction between formaldehyde and silyl enol ether without a Lewis acid catalyst

For the mechanism of the uncatalyzed Mukaiyama aldol reaction of the parent system, the concerted pathway has been examined previously by Gung et al. [20] and Denmark et al. [21]. In agreement with results obtained by Gung et al., a boat-shaped six-membered-ring transition state is located for the concerted pathway. This concerted transition state involves a simultaneous C-C bond formation and the silicon group transfer. In the present work the reaction is predicted to be exothermic, by -26.6 kcal/mol. The reaction coordinate (the normal mode that has an imaginary frequency) indicates again the concerted mechanism of the Mukaiyama aldol reaction. The activation energy is 13.7 kcal/mol.

### 3.2 MOF encapsulated formaldehyde ($O=CH_2$@MOF-505) and the Mukaiyama aldol reaction between MOF-505 encapsulated formaldehyde and silyl enol ether ($O=CH_2$@MOF-505/$H_3SiOHC=CH_2$

The Cu unit ($Cu_1$-$Cu_2$) is barely changed upon the adsorption of formaldehyde (0.084 Å and 5° for changes in the $Cu_1$-$Cu_2$ bond distance and the O-Cu-O bond angle, respectively). According to the interaction between the hydrogen atoms of formaldehyde and the oxygen atoms of the framework, the corresponding distance between the formaldehyde oxygen and the Cu atom of MOF-505 active site is 2.32 Å. The carbon-oxygen bond of formaldehyde is elongated from 1.21 to 1.22 Å. For the Mukaiyama aldol reaction, a concerted mechanism was proposed in which the bond between the carbon atom of formaldehyde (C) and the silyl enol ether (C1) is found and the silicon group transferred. We suggest the fundamental step of the reaction as follows:

$$CH_2=O + \text{MOF-505} \rightarrow CH_2=O@\text{MOF-505} \quad (1)$$

$$SiH_3O\text{-}CH=CH_2 + CH_2=O@\text{MOF-505} \rightarrow O=CHCH_2CH_2OSiH_3@\text{MOF-505} \quad (2)$$

$$O=CHCH_2CH_2OSiH_3@\text{MOF-505} \rightarrow O=CHCH_2CH_2OSiH_3 + \text{MOF-505} \quad (3)$$

Initially, formaldehyde adsorbs over the paddlewheel active site of MOF-505 via a lone pair electron interaction with an adsorption energy of -14.3 kcal/mol. Then, the encapsulated formaldehyde interacts with silyl enol ether via a π interaction with a coadsorption energy of -23.2 kcal/mol, followed by the chemical reaction in order to produce 3-silyloxy-propanal. The activation energy is 11.0 kcal/mol. The transition structure of the proposed concerted pathway is confirmed with its mode of imaginary frequency which belongs to the C-C bond formation and the silicon group transfer. The product formation is exothermic by -46.8 kcal/mol. The adsorbed


NSTI-Nanotech 2009, www.nsti.org, ISBN 978-1-4398-1784-1 Vol. 3, 2009

propanal needs 20.2 kcal/mol to desorb from the active site in the final step (3). From our calculation, we propose MOF-505 to be a potential catalyst for the Mukaiyama aldol reaction of formaldehyde and silyl enol ether.

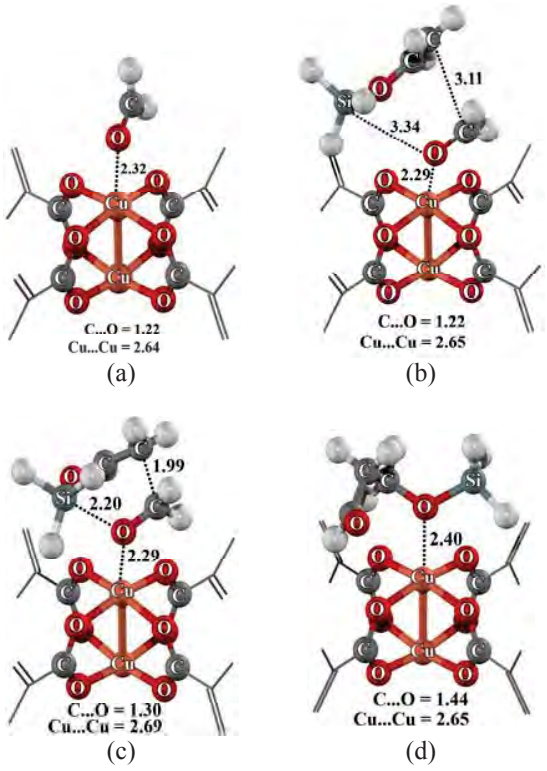


Figure 2: Optimized structures of (a) O=$CH_2$@MOF-505 (b) coadsorption complex (c) transition state and (d) product adsorption.

## 3.3 Cu-ZSM-5 encapsulated Formaldehyde (O=$CH_2$ @Cu-ZSM-5) and the Mukaiyama aldol reaction between Cu-ZSM-5 encapsulated formaldehyde and silyl enol ether (O=$CH_2$@Cu-ZSM-5/$H_3SiOHC=CH_2$)

Formaldehyde first interacts with the active Lewis acid site by its lone pair electron. The carbon-oxygen bond of formaldehyde is consequently elongated from 1.21 Å to 1.22 Å. The intermolecular distance, measured between the formaldehyde oxygen and the Cu atom of zeolite, is 1.89 Å and the corresponding adsorption energy for the complex is -31.8 kcal/mol. The C-O···Cu-ZSM-5 angle is 138.0°. We propose the reaction proceeds through the same mechanism that was previously described in the section 3.2. The reaction is initiated by the coadsorption of silyl enol ether on the encapsulated formaldehyde at the active site of the zeolite. The silyl enol ether molecule diffuses over the adsorbed formaldehyde on the Cu-ZSM-5 with a coadsorption energy of -52.7 kcal/mol. The activation energy is 6.3 kcal/mol. These results demonstrate that the zeolite framework contributes a larger effect on the stabilization of the adsorption and transition state than the one on the MOF structure. The adsorbed 3-silyloxy-propanal product is exothermic, -66.3 kcal/mol. The product desorption requires 39.6 kcal/mol in the final step. Therefore, Cu-ZSM-5 zeolite can be used as a catalyst in the Mukaiyama aldol reaction.

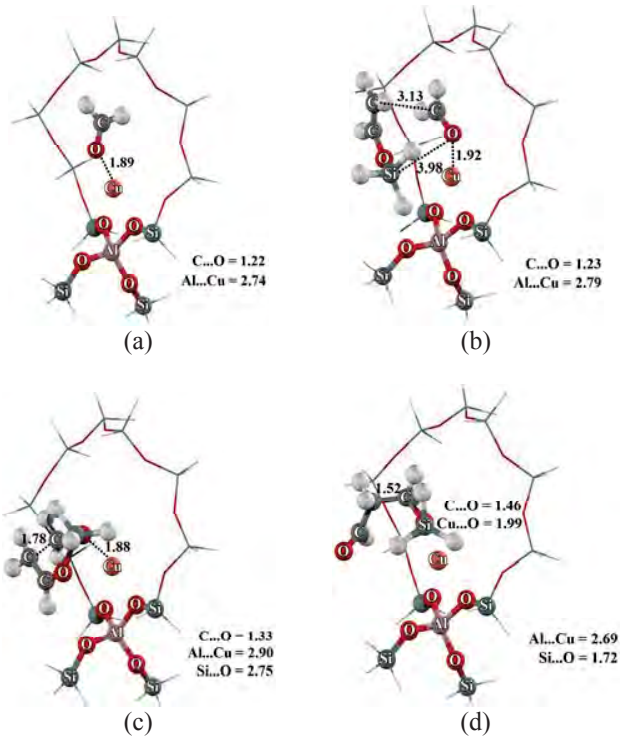


Figure 3: Optimized structures of (a) O=$CH_2$@Cu-ZSM-5 (b) coadsorption complex (c) transition state and (d) product adsorption.

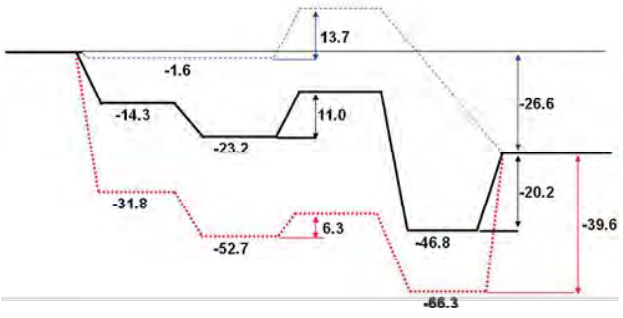


Figure 4: Calculated energy profile (kcal/mol) for the Mukaiyama aldol reaction between formaldehyde and silyl enol ether in the MOF-505 system (black solid line), the Cu-ZSM-5 system (red dot line) and the bare system (blue dash line).

The energy diagram of all three systems, i.e. uncatalyzed, MOF-505 and Cu-ZSM-5 catalyzed, were plotted in Fig. 4. For the bare system, the activation energy of the reaction is 13.7 kcal/mol whereas the barriers of the MOF-505 and the Cu-ZSM-5 systems are 11.0 and 6.3 kcal/mol, respectively. MOF-505 and Cu-ZSM-5 reduce the activation energy to be lower than that in the bare system. Cu in both catalysts induces the oxygen of formaldehyde to be more electronegative, which can be attacked by carbon nucleophile such as carbon in silyl enol ether.

## 4 CONCLUSIONS

Density-functional theory and the ONIOM approach are used for comparing the catalytic efficiency between the metal-organic framework (MOF-505) and the zeolite structure (Cu-ZSM-5) on the Mukaiyama aldol reaction of formaldehyde and silyl enol ether. The reaction mechanism is proposed to be intermediate-free concerted, consisting of the silicon group transfer and carbon-carbon bond formation. Both MOF-505 and Cu-ZSM-5 contain a Cu ion which behaves as a Lewis acid. Not only the acid in both catalysts is predicted to reduce the energy barrier, it was also found that environmental inclusion of the metal organic framework and zeolite has an effect on the structure and energetics of the adsorption complexes. As a consequence, it leads to a lower energy barrier ($\Delta E_{act}$ = 11.0 and 6.3 kcal/mol) of the reaction as compared to the bare model system (13.7 kcal/mol). The results indicate that Cu-exchanged ZSM-5 and MOF-505 can preserve formaldehyde in a monomeric form and also act as a Lewis acid which catalyzes the Mukaiyama aldol reaction of formaldehyde with olefin without the presence of potentially harmful acidic chemicals.

## ACKNOWLEDGEMENTS

This research was supported by grants from the National Science and Technology Development Agency (NSTDA), the Thailand Research Fund (TRF), Kasetsart University Research and Development Institute (KURDI), the Commission on Higher Education, Ministry of Education, under the Postgraduate Education and Research Programs in Petroleum and Petrochemicals, and Advanced Materials as well as the Sandwich Program in the Strategic Scholarships Fellowships Frontier Research Network (CHE-PhD-SW-SUPV to SC). The Kasetsart University Graduate School is also acknowledged.

## REFERENCES

[1] (a) R. Mahrwald, "Modern Aldol Reactions", Wiley-VCH: New York, 2004. (b) K. Miura and A. Hosomi, "In Main Group Metals in Organic Syntheses", 409-592, 2004.
[2] K. Takasu, M. Ueno, K. Inanaga and M. Ihara, J. Org. Chem. 69, 517, 2004.
[3] S. Hasegawa, S. Horike, R. Matsuda, S. Furukawa, K. Mochizuki, Y. Kinoshita and S. Kitagawa, J. Am. Chem. Soc. 129, 2607, 2007.
[4] M. Casarin, C. Corvaja, C. diNicola, D. Falcomer, L. Franco, M. Monari, L. Pandolfo, C. Pettinari, F. Piccinelli and P. Tagliatesta, Inorg. Chem. 43, 5865, 2004.
[5] L. Alaerts, E. Seguin, H. Poelman, F. Thibault-Starzyk, P. A. Jacobs and D. E. De Vos, Chem. Eur J. 12, 7353, 2006.
[6] B. Xiao, H. Hou and Y. Fan, J. Organomet Chem. 692, 2014, 2007.
[7] S. Choomwattana, T. Maihom, P. Khongpracha, M. Probst and J. Limtrakul, J. Phys. Chem. C. 112, 10855, 2008.
[8] J. Sauer, Chem. Rev. 89, 199, 1989.
[9] J. Sauer, P. Ugliengo, E. Garrone and V. R. Saunders, Chem. Rev. 94, 2095, 1994.
[10 J. Limtrakul, Chem. Phys. 193, 79, 1995.
[11] J. Limtrakul, P. Treesukol, C. Ebner, R. Sansone and M. Probst, Chem. Phys. 215, 77, 1997.
[12] J. Limtrakul, S. Jungsuttiwong and P. Khongpracha, J. Mol. Struct. 525, 153, 2000.
[13] P. E. Sinclair, A. De Vries, P. Sherwood, C. R. A. Catlow, and R. A. Van Santen, J. Chem. Soc. Faraday Trans. 3401, 1998.
[14] M. Braendle and J. Sauer, J. Am. Chem. Soc. 120, 1556, 1998.
[15] S. P. Greatbanks, I. H. Hillier, N. A. Burton, P. J. Sherwood, Chem. Phys. 105, 3770, 1996.
[16] R. Z. Khaliullin, A. T. Bell and V. B. Kazansky, J. Phys. Chem. A. 105, 10454, 2001.
[17] J. Limtrakul, T. Nanok, S. Jungsuttiwong, P. Khongpracha and T. N. Truong, Chem. Phys. Lett. 349, 161, 2001.
[18] A. H. De Vries, P. Sherwood, S. J. Collins, A. M. Rigby, M. Rigutto and G. J. Kramer, J. Phys. Chem. B. 103, 6133, 1999.
[19] M. Svensson, S. Humbel, R. D. J. Froese, T. Matsubara, S. Sieber and K. Morokuma, J. Phys. Chem. 100, 19357, 1996.
[20] B. W. Gung, Z. Zhu and R. A. Fouch, J. Org. Chem. 60, 2860, 1995.
[21] S. E. Denmark, B. D. Griedel, D. M. Coe and M. E. Schnute, J. Am. Chem. Soc. 116, 7026, 1994.

# Dissymmetric Metal Deposition on Carbon Nanotubes

C. Warakulwit[1,3], M.-H. Delville[2], V. Ravaine[1], J. Limtrakul[3], A. Kuhn[1]*

[1]Université Bordeaux 1, ISM, ENSCPB, Pessac, France, kuhn@enscpb.fr
[2]ICMCB, CNRS, Pessac, France, delville@icmcb-bordeaux.cnrs.fr
[3]Chemistry Department, Kasetsart University, Bangkok, Thailand, jumras.l@ku.ac.th

## ABSTRACT

Dissymmetric nanoobjects are of enormous interest in many areas ranging from molecular electronics to targeted drug delivery. So far it has been quite difficult to synthesize dissymmetric objects at the nanoscale and most approaches have been based on using interfaces to break the symmetry. Only a few bulk procedures are known so far to produce these Janus-type objects. We report here a simple approach for the bulk generation of dissymmetric nanoobjects, especially carbon nanotubes (CNTs), based on electrochemical principles. A stabilized suspension of nanotubes is introduced in a capillary containing an aqueous metal salt solution and a high electric field is applied to orientate and polarize the individual tubes. During their transport through the capillary under sufficient polarization each nanotube is the site of water oxidation at one end, and of metal ion reduction at the other one. The method can be generalized for very different types of deposits such as other metals, semiconductors or polymers. The approach therefore opens up the way to a whole new family of experiments leading to complex nanoobjects with an increasingly sophisticated design.

***Keywords***: Janus particles, bipolar electrochemistry, carbon nanotubes, capillary electrophoresis

## 1 INTRODUCTION

Dissymmetric functionalization of micro- and nanoobjects is of major importance to study, for example, directed self-assembly, but also for many applications ranging from electronic paper to sensing and catalysis. Various approaches to generate dissymmetric particles have been reported in the recent literature. These Janus-type particles have been obtained either by protection/deprotection mechanisms [1], focused laser-induced reactions [2], co-jetting of parallel polymer solutions under the influence of an electrical field [3], anisotropic electroless deposition [4], or with microfluidic techniques [5]. However, so far most of the methods used to generate such objects need to break the symmetry by introducing interfaces like in the case of sputtering [6,7], stamp coating [8,9], and Langmuir-Blodgett-based techniques [10]. This makes the preparation of large quantities rather difficult.

Thus, there is an increasing interest in developing alternative methods to replace the two-dimensional approaches by truly three-dimensional techniques allowing a scale-up of the production of Janus objects to larger quantities by using bulk procedures [11].

In this context an attractive method that uses the concept of bipolar electrochemistry [12] has been reported by Bradley et al. and allows generating metal layers in a dissymmetric way on different substrates [13,14]. In brief, when a conducting object is placed in a strong electric field between two electrodes a polarization occurs that is proportional to the electric field *E* and the characteristic dimension *r* of the object.

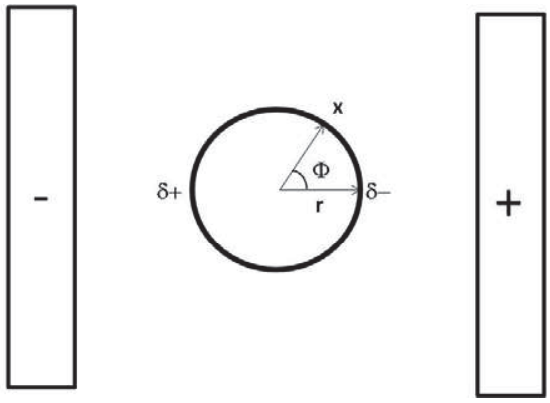


**Figure 1.** *Polarization of a conducting spherical particle in an electric field.*

The simple equation governing this polarization also immediately illustrates the practical problems that will arise when applying this concept to nanoobjects.

$$\eta_x = E\ r\ \cos\Phi \qquad (1)$$

With $\eta_x$ being the polarization at a given point x at the surface of the nanoobject, one can easily calculate that the maximum potential difference between the two opposite sides of the object is given by:

$$\Delta V_{max} = 2\ E\ r \qquad (2)$$

In order to carry out two different redox reactions at the opposite sides of the nanotube (oxidation at the left side and reduction at the right side) $\Delta V_{max}$ has to be at least equal to the difference of the formal potentials of the two redox reactions. Two typical redox reactions that could take place in an aqueous environment might be the following ones:

$$[AuCl_4]^-_{(aq)} + 3e^- \rightarrow Au^0_{(s)} + 4Cl^-_{(aq)} \qquad E° = +0.99\ V$$

$$2H_2O_{(l)} \leftrightarrow 4H^+_{(aq)} + O_{2(g)} + 4e^- \qquad E° = +1.23\ V$$

It immediately follows that the polarization has to generate a potential difference of at least 0.24 V. In order to achieve this difference on an object with *r* in the nanometer range, *E* reaches values of the order of MV/m. These conditions seem to be incompatible with a normal laboratory environment and especially with an aqueous solution. This might be partly the reason why previous work has been focused on objects in the micrometer or submicrometer range and the experiments had to be carried out in organic solvents [13, 14]. We show in this contribution that the approach can be extended to nanoobjects like carbon nanotubes, modified in aqueous solutions when a capillary electrophoresis set-up is used to apply the high electric field. This capillary assisted bipolar electrodeposition (CABED) process represents, therefore, an original alternative to generate dissymmetric nanoobjects of various compositions [15].

# 2 EXPERIMENTAL

## 2.1. Preparation of the nanotube suspensions

Aqueous suspensions of CNTs can be produced analogous to what has been reported for other types of carbon [16, 17]. The raw sample of carbon nanotubes used for this study was multi-wall carbon nanotubes produced by catalytic chemical vapor deposition (ARKEMA). About 0.1 mg of MWNTs was added to a polyoxometalate (POM) solution (10 mM $H_3PMo_{12}O_{40}$/0.1 M $H_2SO_4$). This solution was prepared from phosphomolybdic acid hydrate, $H_3PMo_{12}O_{40}.xH_2O$ (FLUKA) in 0.1 M $H_2SO_4$. The suspension was sonicated with a high intensity ultrasonic processor. After 1 hour of sonication a stable suspension of shortened CNTs is formed that can be further processed by fractionated centrifugation in order to select nanotubes with a quite narrow size distribution [18].

## 2.2. Bipolar gold deposition on carbon nanotubes

The starting solution used for the capillary electrophoresis (CE) experiment is an aqueous CNT/$HAuCl_4$ (1 mM) suspension. For CE experiments, all solutions or suspensions were introduced into the capillary by filling it manually with a syringe. The capillary used here is a fused silica capillary with a length of 45 cm and an inner diameter of 100 μm. The distance from the capillary inlet (left side in Figure 2) to the detection window (right side) in this case was 41 cm. The applied voltage was 30 kV whilst the temperature was maintained at 25°C. The CE experiment was first performed by rinsing the capillary with ultrapure water. Then the diluted aqueous suspension of the shortened, POM-modified carbon nanotubes was introduced into the capillary. The reason for using a diluted suspension for the CE experiment is due to the narrow capillary (100 μm). Introducing suspensions that are too concentrated leads to clogging of the capillary. The combination of migration and electroosmotic flow determines the transport of the CNTs through the capillary. The flow characteristics were determined by recording the absorbance variations in the UV detector (254 nm) as a function of time.

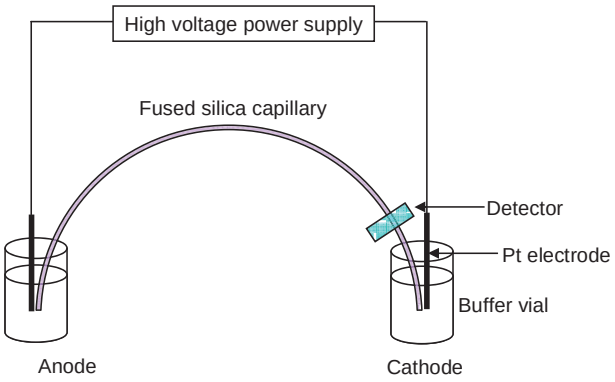


**Figure 2.** *Schematic illustration of the capillary electrophoresis set-up.*

The bipolar electrochemical gold deposition on CNTs is achieved by introducing the CNT/$HAuCl_4$ (1mM) suspension into the capillary at the anodic side. Because the addition of acid ($HAuCl_4$ here) can result in the aggregation of the POM-modified CNTs, the suspension has to be sonicated for 1 minute in an ultrasound bath in order to maintain the CNTs being well dispersed before introduction into the capillary.

The sample leaving the capillary at the cathodic side was collected directly at the outlet. This collected sample drop was put on a TEM grid and dried. Because the suspension still contains the gold salt ($AuCl_4^-$), drying of the suspension on the grid leads to gold salt crystallization


NSTI-Nanotech 2009, www.nsti.org, ISBN 978-1-4398-1782-7 Vol. 1, 2009

which extremely disturbs the further TEM analysis. Therefore, after the suspension was dropped onto the TEM grid, the solution still containing $HAuCl_4$ was soaked through the grid by placing a cleaning tissue under the grid. After that, the remaining particles on the grid were washed three times with ultrapure water using the same procedure. The washed particles were then characterized by TEM.

## 3 RESULTS AND DISCUSSION

The potentials given in the above redox equations are standard potentials and as the experiment is carried out far from standard conditions in terms of concentrations and partial gas pressures, large deviations from the threshold value of 0.24 V can be expected. This also means that the calculated electric fields in the MV range might be different, especially when somewhat longer objects like the CNTs are used. Using carbon nanotubes for this proof-of-principle experiment also has the advantage that, due to their anisotropy the polarization induces at the same time an orientation parallel to the electric field, that the nanotubes preserve during their whole journey through the capillary. Thus, it will be easier to perform such a bipolar electrochemical deposition with CNTs compared to spherical objects that might change their orientation during the experiment and in this way lead to random metal deposition at the object's surface.

The experiment has been carried out at the maximum potential difference that can be delivered by the capillary electrophoresis set-up, which is 30 kV. When this potential difference is applied between the two ends of a capillary with a total length of 45 cm, an electric field of 67 kV/m is generated in the capillary. The nanotube pieces obtained by the above mentioned sonication procedure have an average length of 500 nm [18]. One can therefore easily calculate that the maximum polarization that can be obtained between the two ends of a nanotube is of the order of 50 mV. This value is smaller than the minimum potential difference necessary for driving the two redox reactions when the calculation is based on the standard potentials and, therefore, no bipolar electrodeposition should occur under these conditions. Performing the experiment shows, however, striking evidence for a dissymmetric deposition of gold nanoparticles at one end of the nanotubes (see Figure 3). We explain this not only by the conditions that are far from the standard conditions used to define the E° values, but most likely the presence of adsorbed polyoxometalate molecules at the CNT surface has also an influence on the potential values as they can undergo complexation reactions with metal ions [19].

The pictures of Figure 3 are representative of the majority of the nanotubes reaching the capillary outlet; however, not 100% are modified. There are several possible origins for a non-quantitative modification. First of all, the gold deposit can detach from the tube during the collection and rinsing procedure, as seems to be the case for the small particles that can be seen in Figure 3A. Second, nanotubes can be more or less conducting depending on their morphology and defects. In the extreme case of an isolating tube, no deposition can occur and even for conducting tubes the conductivity has to be better than that of the surrounding electrolyte to induce a sufficient potential difference. The third reason is that the potential drop scales with the length of the tube, and therefore shorter tubes might experience a potential difference between the two ends that is below the threshold value.

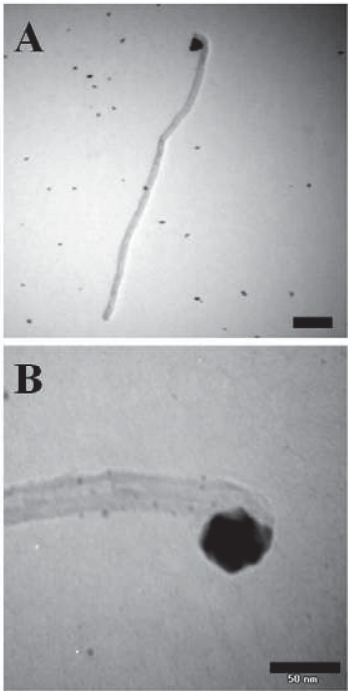


**Figure 3.** *Site selective bipolar electrodeposition of gold at one end of a carbon nanotube* ***A****) TEM image of a selected nanotube from a very diluted sample* ***B****) Magnification of the modified end of a nanotube; scale bars are 100 and 50 nm respectively.*

It is important to note that, in contrast to the former experiments [13, 14], in this set-up the high voltage is not a problem, although we don't use organic solvents but water, because the electrodes are positioned at the outside of the capillary. This means that an eventual macroscopic hydrogen or oxygen evolution at the cathode or anode respectively doesn't perturb the experiment as it take place in the bulk solution and not in the capillary. Furthermore the currents are in the nA range because there is no supporting electrolyte present and thus the total amount of developed gas is rather low.

## 4 CONCLUSION

In summary, the concept of bipolar electrochemistry has been adapted to modify in a dissymmetric way multiwall carbon nanotubes with a gold cap as illustrated in Figure 4. The method employed to create these Janus-type objects is based on a slightly modified capillary electrophoresis experiment, (i) allowing the application of the mandatory high voltages (ii) without having to use organic solvents and (iii) especially avoiding gas bubble formation in the reaction chamber, which otherwise would completely prevent the alignment of the nanotubes in the electric field.

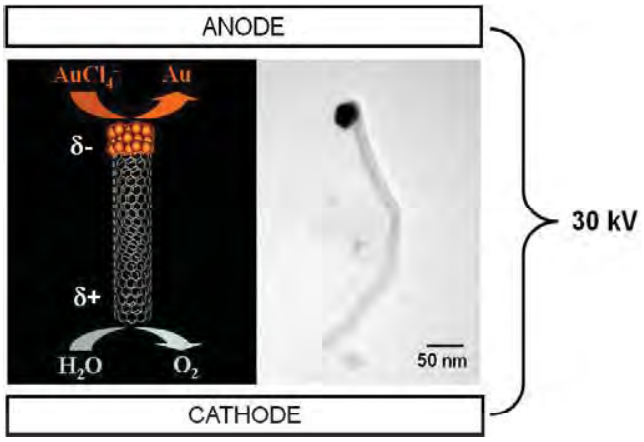


**Figure 4.** *Reaction scheme for the site selective generation of a metal cluster* ***(left)*** *and TEM image of a MWCNT, modified at one end with a gold cluster(****right)****.*

Most importantly, the procedure uses a real bulk-phase reaction in contrast to most of the literature methods based on interfaces to break the symmetry. This makes the method very attractive to scale-up the production of such dissymmetric objects.

Looking to the future, the CABED process can be generalized to other types of nanoobjects and also deposits of a very different nature such as other metals, semiconductors, or polymers. The approach therefore opens up the way to a whole new family of experiments leading to complex nanoobjects with an increasingly sophisticated design allowing original applications. In addition, the procedure reported here could also be adapted to sort conducting, semiconducting, and insulating carbon nanotubes, as the latter ones will not be modified with metal, whereas the first two categories of species will undergo a potential-dependent metal modification.

**Acknowledgment.** This work is supported by the French Ministry of Research, CNRS, and ENSCPB. We thank P. Poulin for various CNT samples. C.W. and J.L. also thank the National Science and Technology Development Agency (NSTDA), the Thailand Research Fund (TRF), Commission on Higher Education, Ministry of Education, the Kasetsart University Research and Development Institute (KURDI).

## REFERENCES

[1] Perro, A.; Reculusa, S.; Pereira, F.; Delville, M.-H.; Mingotaud, C.; Duguet, E.; Bourgeat-Lami, E.; Ravaine, S. J. Chem. Soc., Chem. Comm. 2005, 44, 5542.
[2] Hugonnot, E.; Delville, M.-H.; Delville, J.-P. Appl.Surf.Sci 2005, 248, 470.
[3] Roh, K.-H.; Martin, D. C.; Lahann, J. Nature Mat. 2005, 4, 759.
[4] Cui, J.-Q.; Kretzschmar, I. Langmuir 2006, 22, 8281.
[5] Nisisako, T.; Torii, T.; Takahashi, T.; Takizawa, Y. Adv.Mater. 2006, 18, 1152.
[6] Takei, H.; Shimizu, N. Langmuir 1997, 13, 1865.
[7] Lu, Y.; Xiong, H.; Jiang, X.; Xia, Y.; Prentiss, M.; Whitesides, G. M. J.Am.Chem.Soc. 2003, 125, 12724.
[8] Cayre, O.; Paunov, V. N.; Velev, O. D. J.Mater.Chem. 2003, 13, 2445.
[9] Paunov, V. N.; Cayre, O. J. Adv.Mater. 2004, 16, 788.
[10] Fujimoto, K.; Nakahama, K.; Shidara, M.; Kawaguchi, H. Langmuir 1999, 15, 4630.
[11] Hong, L.; Cacciuto, A.; Luijten, E.; Granick, S. Nano Lett. 2006, 6, 2510.
[12] Fleischmann, M.; Ghoroghchian, J.; Rolison, D.; Pons, S. J.Phys.Chem. 1986, 90, 6392.
[13] Bradley, J.-C.; Chen, H.-M.; Crawford, J.; Eckert, J.; Ernazarova, K.; Kurzeja, T.; Lin, M.; McGee, M.; Nadler, W.; Stephens, S. G. Nature 1997, 389, 268.
[14] Bradley, J.-C.; Zhongming, M. Angew. Chem.Int.Ed. 1999, 38, 1663.
[15] Warakulwit, C.; Nguyen, T.; Majimel, J.; Delville, M.-H. ; Lapeyre, V. ; Garrigue, P. ; Ravaine, V. ; Limtrakul, J. ; Kuhn, A. NanoLett. 2008, 8, 500.
[16] Garrigue, P.; Delville, M.-H.; Labrugère, C.; Cloutet, E.; Kulesza, P. J.; Morand, J. P.; Kuhn, A. Chem.Mater. 2004, 16, 2984.
[17] Fattakhova, D.; Kuhn, A. Carbon 2006, 44, 1942.
[18] Warakulwit, C.; Majimel, J.; Delville, M.-H. ; Garrigue, P. ; Limtrakul, J. ; Kuhn, A. J.Mater.Chem. 2008, 18, 4056
[19] Martel, D. ; Kuhn, A. ; Kulesza, P.J. ; Galkowski, M.T. ; Malik, M.A. Electrochim.Acta 2001, 46, 4197

# Electron Hopping Process in SWCNT-Mediated Redox Reaction: An Evidence Observed by DFT Theory

T. Nongnual[a,b,c], S. Choomwattana[a,b,c], S. Nokbin[a,b,c], P. Khongpracha[a,b,c], and J. Limtrakul[a,b,c*]

[a]Chemistry Department, Faculty of Science, Kasetsart University, Bangkok 10900, Thailand
[b]NANOTEC Center of Excellence, National Nanotechnology Center, Kasetsart University
[c] Center of Nanotechnology, Kasetsart University Research and Development Institute, Bangkok
*E-mail: jumras.l@ku.ac.th, Tel: +662-562-5555 ext 2169, Fax: +662-562-5555 ext 2176

## ABSTRACT

The electron hopping mechanism in SWCNT-mediated redox reaction of anthraquinonnyl ($AQH_2$-) and 4-arylhydroxyl amine (4AHA-) groups is systematically studied by DFT for the first time. It was found that electrons from the oxidized $AQH_2$ group can transfer to the oxidizing 4AHA group at the other end of the nanotube by the hopping process through the mediating SWCNT confirmed by the non-localized distribution of the hopping electrons. The electron density and Hirshfeld partial charges analysis shows that SWCNT can hold 87% of the extra electron density of the hypothetical negative intermediate forming by the oxidation of the $AQH_2$ process. Chemical attachments of these two redox reagents to the SWCNT also caused new impurity states within the band gap, thereby introducing more metallic characteristics to the system. These findings provide a detailed understanding of the electron hopping process and agree well with the previous experimental study.

***Keywords***: electron hopping process, SWCNT-mediated redox reaction, generalized gradient approximation (GGA), Perdew-Burke-Ernzerhof (PBE) method, carbon nanotube

## 1 INTRODUCTION

Among all nanoscale morphologies of carbon, multiwalled carbon nanotubes (MWCNTs) were first observed under transmission electron microscopy (TEM) by Iijima in 1991[1]. After that, single-walled carbon nanotubes (SWCNTs) were produced independently by Iijima[2] and Bethune[3] in 1993. Since their discoveries of the low-dimensional carbon nanostructures, carbon nanotubes (CNTs) have attracted much interest in modern nanoscience and nanotechnology due to their novel and structure-dependent properties. Over the years, the physical and chemical properties of CNTs have been well-documented as the results of more sophisticated methods. Novel properties of these CNTs endow their nanoscale applications as nanoelectronic devices[4], sensors[5], field emission sources[6], and composite materials[7], The CNTs also function as nanowires to transport electrons between the underlying electrode and electroactive protein chemically attached on each end of the tube[8]. The transport distances, controlling the rate of electron transfer, are greater than 150 nm from the enzymatic active center to the electrode[9].

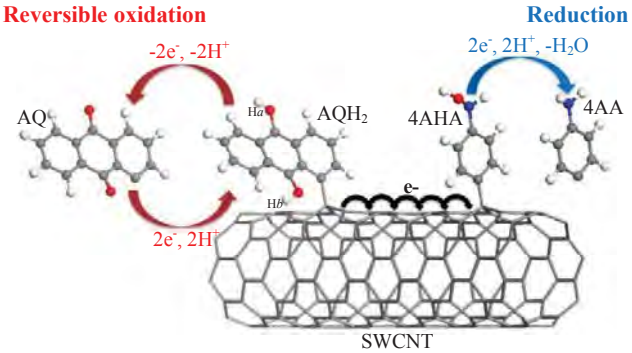


Figure 1: Proposed mechanism for the SWCNT-mediated redox reaction, consisting of the reversible oxidation and the irreversible reduction reactions. The SWCNT accepts electrons from the $AQH_2$ species and then donates the electrons to the 4-arylhydroxyl amine.

The chemical functionalization reactions for CNTs are categorized into three methods, which are: direct attachment to the graphitic surface, ester linkage, and covalent binding using diazonium reagents with high selectivity. The diazonium media method was also developed by Compton's group to initiate chemisorptions of aryl diazonium salts by direct reduction with hypophosphorous acid in the presence of carbon powder[10-12]. The method was further extended to the application on MWCNTs with anthraquinone-1-diazonium chloride and 4-nitrobenzenediazonium tetrafluoroborate, resulting in the synthesis of 1-anthraquinonyl-MWCNTs (AQ-MWCNTs) and 4-nitrophenyl-MWCNTs (NB-MWCNTs)[13].

Recently, Wong *et al.*[14] reported a redox reaction on the same nanovessel MWCNT for the first time. This MWCNT is functionalized from two redox-active species directly attached by the diazonium salt method. The 4-arylhydroxyl amine (4AHA) and $AQH_2$ species are generated in the first oxidation cycle from $NO_2$–$C_6H_4$–MWCNT and AQ–MWCNT, respectively. This redox reaction consists of a reversible oxidation and an irreversible reduction studied by the cyclic voltammetry technique. They proposed the redox reaction mechanism, where $AQH_2$ is an oxidizing agent while NHOH–$C_6H_4$ is a reducing group.

$$AQH_2 - \mathbf{MWCNT} - C_6H_4 - NHOH \rightarrow AQ - \mathbf{MWCNT} - C_6H_4 - NH_2 + H_2O$$

| Structure | Hirshfeld charge | | | | Energy gap / eV | Relative energy / kcal mol$^{-1}$ |
|---|---|---|---|---|---|---|
| | Partial charge | | | Total | | |
| pristine SWCNT | - | - | - | - | 0.62 D | - |
| substrate | $AQH_2$ = **0.05** | SWCNT = **-0.07** | 4AHA = **0.03** | 0.01 | 0.00 | - |
| intermediate-1-a | AQH = **-0.06** | SWCNT = **-0.91** | 4AHA = **-0.02** | -0.99 | 0.04 D | 0.00 |
| intermediate-1-b | AQH = **-0.16** | SWCNT = **-0.81** | 4AHA = **-0.02** | -0.99 | 0.04 I | -0.95 |
| intermediate-2 | AQ = **-0.19** | SWCNT = **-1.73** | 4AHA = **-0.07** | -1.99 | 0.10 I | - |
| intermediate-3 | AQ = **-0.07** | SWCNT = **-0.77** | Ph-NH = **-0.16** | -1.00 | 0.16 I | - |
| product | AQ = **-0.01** | SWCNT = **-0.03** | 4AA = **0.05** | 0.01 | 0.00 | - |

Table 1: Hirshfeld partial charge, energy gap (eV), and relative energy (kcal mol$^{-1}$) calculated with the PBE method and DNP basis set for pristine SWCNT, substrate, intermediate, and product states. (D = direct, I = indirect energy gap)

The mechanistic pathway of electron transfer from $AQH_2$ to the 4-arylhydroxyl amine group is also investigated, to determine whether it is intermolecular electron tunneling between reagents or by electron hopping via the CNT. Nevertheless, the hopping was proposed to be more favorable because of the shorter distance in the electron transfer. Such phenomenon is unique for both oxidizing and reducing groups confined on the same CNT.

Herein, we report the theoretical study on the possibility and the process of the electron hopping between two redox reagents that are functionalized on the same CNT. Even mediating MWCNT in the real system is simplified to the semiconducting SWCNT for computational efficiency; the periodic calculations are performed improve the electronic results so that they are more reasonable. In addition, we focus only on the redox reaction instead of the chemical attachment and the preparation steps. Thus, this redox reaction from $AQH_2$–**SWCNT**–4AHA terminated at AQ–**SWCNT**–4AA is proposed in the reversible oxidation and the irreversible reduction, where 4AA (4-arylamine) is noted.

Total reaction:

$AQH_2$ – **SWCNT** – 4AHA
$\rightarrow$ AQ – **SWCNT** – 4AA + $H_2O$

Oxidation:

$AQH_2$ – **SWCNT** – 4AHA
$\leftrightarrow$ AQ – **SWCNT** – 4AHA + $2H^+$ + $2e^-$

Reduction:

AQ – **SWCNT** – 4AHA + $2H^+$ + $2e^-$
$\rightarrow$ AQ – **SWCNT** – 4AA + $H_2O$

## 2 MODELS AND METHODOLOGY

The periodic calculations were carried out using the density functional theory (DFT) method as implemented in the DMol3 package[15,16]. The generalized gradient approximation (GGA) in the various methods and an all-electron double numerical basis set with polarized function (DNP) were chosen for the spin-unrestricted DFT computation. The real space global cutoff radius was set to be 3.70 Å. For geometrical optimization, the forces on all atoms were optimized to be less than 0.05 eV.Å$^{-1}$. The Brillouin zone was sampled using the Monkhorst-Pack scheme[17].

### 2.1 Diameter calibration of SWCNTs

Zigzag SWCNTs are calibrated in different diameters from (6,0) to (12,0). Each initial structure is generated in a supercell periodic box with $20 \times 20 \times 8.52$ Å$^3$ composed of two unit cells of SWCNT. The nearest distance between two neighboring SWCNTs is greater than 10 Å for ignoring an intertube interaction. The calibrations are performed by the GGA in the Perdew-Burke-Ernzerhof (PBE)[18], Becke's exchange and Lee, Yang, and Parr's correlation functional (BLYP)[19,20], and non-local exchange-correlation functional (PW91)[21] with *k* point $1 \times 1 \times 40$.

### 2.2 Redox system

An (8,0) SWCNT, the smallest semiconducting zigzag providing an acceptable energy gap, was chosen to be functionalized by two redox groups which were more than 12 Å

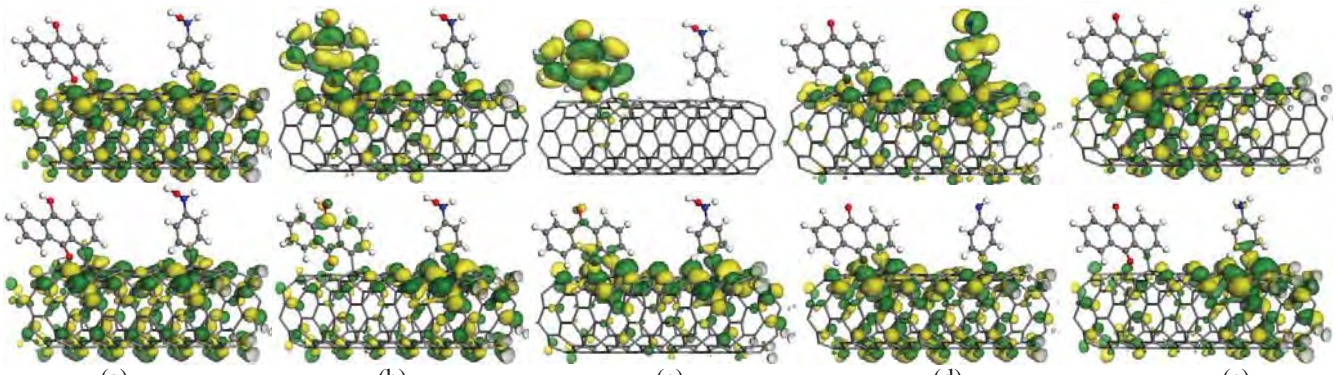

(a) (b) (c) (d) (e)

Figure 2: LUMO (top) and HOMO (bottom) plots of *subs* (a), *int-1-b* (b), *int-2* (c), *int-3* (d), and *prod* (e).

distant from each other to neglect an intermolecular interaction of these two species. A supercell with 40 × 40 × 24.15 Å$^3$ comprised of six periodic lengths for the zigzag SWCNT was adopted in the calculation with the PBE function. Each supercell consists of two redox groups, which are covalently bonded to the sidewall of the SWCNT. The nearest distance between two neighboring SWCNTs is greater than 30 Å. Only Γ point was considered in the Brillouin zone for the geometric optimization and orbital analysis but *k* points 1 × 1 × 10 was sampled to calculate electronic properties of the redox system. Even though the individual processes in the overall redox reaction take place concurrently, we simplify the problem by dividing the redox pathway into five hypothetical states, which are $AQH_2$-SWCNT-4AHA (substrate: *subs*), $[AQH\text{-}SWCNT\text{-}4AHA]^{1}$ (intermediate-1), $[AQ\text{-}SWCNT\text{-}4AHA]^{2-}$ (intermediate-2: *int-2*), $[AQ\text{-}SWCNT\text{-}Ph\text{-}NH]^{1-}$ (intermediate-3: *int-3*) and AQ-SWCNT-4AA (product: *prod*) (AQ = anthraquinonyl, 4AHA = 4-arylhydroxyl amine, 4AA = 4-arylamine, SWCNT = (8,0) zigzag SWCNT). The intermediate-1 state can be considered in two configurations, which are intermediate-1-a (*int-1-a*) and intermediate-1-b (*int-1-b*) for H*a* and H*b* removal, respectively.

## 3 RESULTS AND DISCUSSION

The diameter of carbon nanotubes and the periodic calculation with three functionals (PBE, BLYP, and PW91) was calibrated for searching a zigzag SWCNT suited to our models. Although all methods of investigating (n,0) zigzag SWCNTs give the same energy gap results, the PBE functional is chosen in our calculations following the previous theoretical studies. Moreover, it was found that the (6,0), (9,0), and (12,0) SWCNTs obey the $n - m = 3i$ metallic rule with *E*gap = 0.00, 0.17, and 0.14 eV, respectively. The (7,0) SWCNT presents as a semi-metallic character with a 0.15 eV energy gap. Fortunately, the (8,0) SWCNT is the first smallest zigzag carbon nanotube that provides semiconducting behavior with an acceptable 0.62 eV energy gap. Therefore, the SWCNT-mediated redox models in this paper are generated from the (8,0) SWCNT and calculated by periodic calculations with PBE method.

The electronic properties of the redox system are reported in Table 1. The results show the difference of relative energy of *int-1*, resulting in the *int-1-b* being more favorable than *int-1-a* due to the less steric effect between the hydrogen atom of AQH group and the nanotube media. Thus, the proposed mechanism pathway of the redox reaction starts with the *subs* configuration and forwards to *int-1-b*, *int-2*, *int-3*, and *prod*, respectively. Chemical attachments of these two redox reagents to the SWCNT cause new impurity states within the band gap, thereby introducing more metallic characteristics to the system. These properties lead to the ease of electron delocation among the modified system.

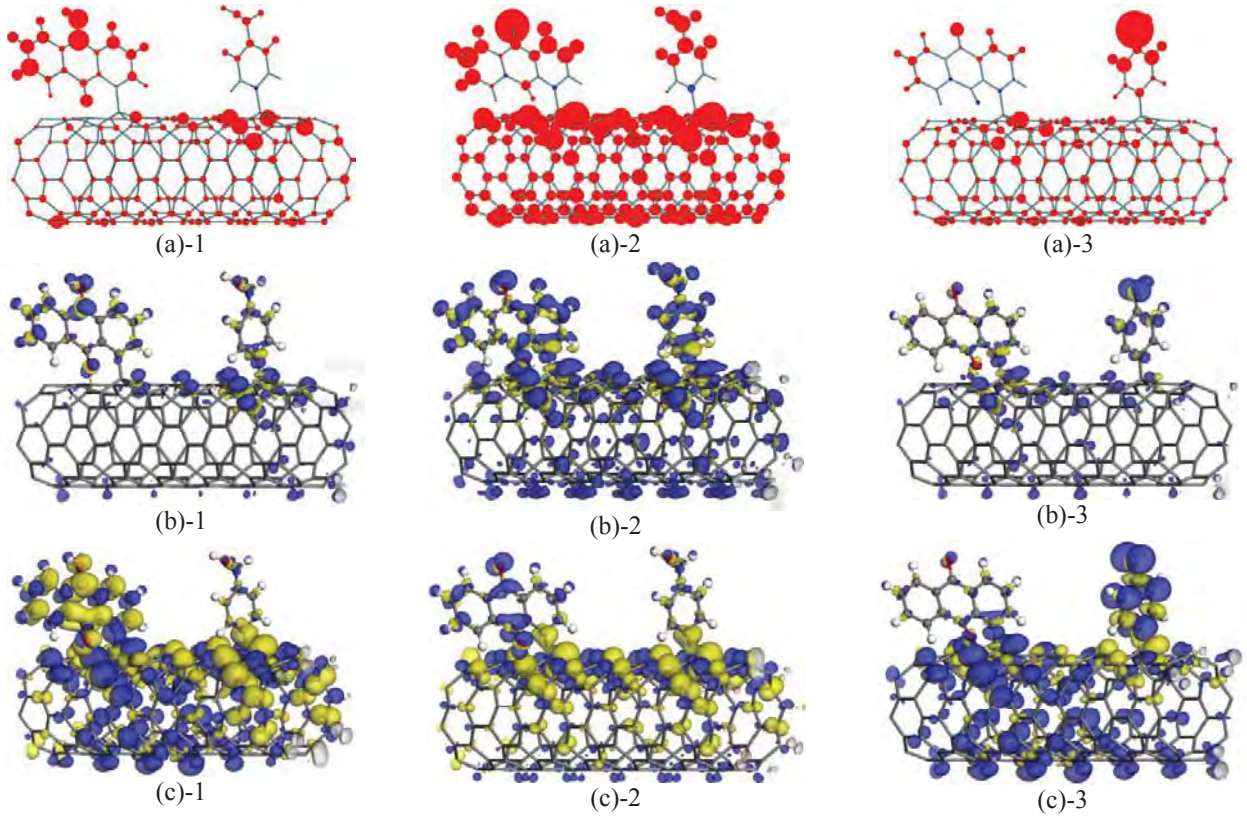


Figure 3: **Hirshfeld charge difference** of *int-1-b* (a)-1, *int-2* (a)-2, and *int-3* (a)-3 where the red color is a negative charge and the blue color is a positive charge. **Electron density difference** of *int-1-b* (b)-1, *int-2* (b)-2, and *int-3* (b)-3 is plotted for an isovalue of ±0.004 e/Å$^3$, where the blue and yellow color is represented for the electron accumulation and electron depression zones, respectively. **Nucleophilic Fukui function plot** of *int-1-b* (c)-1, *int-2* (c)-2, and *int-3* (c)-3.

The electron density difference and Hirshfeld partial charges analyses show that SWCNT can hold 87% of the extra electron density of the hypothetical negative intermediate forming that forms by the oxidation of the $AQH_2$ process.

The explanation of how an electron transfers from $AQH_2$ to 4AHA via SWCNT is illustrated in Figure 2. First, an electron ionization and reception occurs at SWCNT, which can be clearly observed at both the HOMO and LUMO for the substrate. At the intermediate steps, an electronic connection between the AQ and the 4AHA molecules on the SWCNT is shown clearly at the HOMO levels. An electron in the *int-1-b* and *int-2* that strongly remained at the AQ part can reversely reduce the AQ to $AQH_2$. Electrons move to the 4AHA side result in a reduction reaction, and the HOMO of the product shows that the electrons distribute mostly at 4AA and no longer occupy the AQ side. The opposite trend is observed for the LUMO of the product.

Hirshfeld charge density difference plots are presented in Figure 3(a). An electron in the intermediate states has a high occupation at the AQH, leading to the reverse reduction of AQH to $AQH_2$. Two electrons in the *int-2* step have a high occupation at the AQ, 4AHA, and the bridge in the nanotube media as shown in Figure 3(a)-2. Therefore, the AQ and 4AHA groups can be reduced to $AQH_2$ and 4AA, respectively. In Figure 3(b), the calculations are performed from the difference of the electron density between the negative-charge structure and its neutralized geometry, resulting in the density of only the negative charge. It is clearly presented about the negative charge from the reducing group connecting to the oxidizing group. The electron density obviously occupies only the redox molecules and their junction in the SWCNT media. The nucleophilic Fukui function plots as demonstrated in Figure 3(c) strongly confirmed the electron hopping process of the redox reaction via nanotube. The mechanism starts with high nucleophilic character at AQ and the connection. Then, the reducing negative behavior at AQ leads to the increase at 4AHA. Therefore, the electron transfer between two redox groups can occur apparently by electron hopping via the SWCNT.

## 4 CONCLUSIONS

The the PBE functional using the DFT calculation is used to investigate the reaction mechanism of electron hopping in the SWCNT-mediated redox reaction of anthraquinonnyl ($AQH_2$-) and 4-arylhydroxyl amine (4AHA-) groups. Our findings can be summarized into three main points. First, the electron density and Hirshfeld partial charges analysis shows that SWCNT can hold 87% of the extra electron density of the hypothetical negative intermediate forming by the oxidation of $AQH_2$ process. Second, chemical attachments of these two redox reagents to the SWCNT also caused new impurity states within the band gap, thereby introducing more metallic characteristics to the system. Third, the electrons from the oxidized $AQH_2$ group can transfer to the oxidizing 4AHA group at the other end of the nanotube by the hopping process through the mediating SWCNT. The mechanism is confirmed by the non-localized distribution of the hopping electrons. These findings provide a detailed understanding of the electron hopping process and agree well with the previous experimental study. This work is not only complementing experimental study by giving a fundamental interpretation but also demonstrating one other promising application of the CNT materials in the nanotechnology field.

## ACKNOWLEDGEMENTS

This research was supported by grants from the National Science and Technology Development Agency (NSTDA Chair Professor and NANOTEC Center of Excellence, National Nanotechnology Center), the Thailand Research Fund (TRF), Kasetsart University Research and Development Institute (KURDI), the Commission on Higher Education, Ministry of Education, under the Postgraduate Education and Research Programs in Petroleum and Petrochemicals, Advanced Materials as well as the Sandwich Program in the Strategic Scholarships Fellowships Frontier Research Network (CHE-PhD-SW-SUPV to SC), and the Development and Promotion of Science and Technology Talents Project (DPST). The Kasetsart University Graduate School is also acknowledged.

## REFERENCES

[1] S. Iijima, Nature. 354, 56, 1991.
[2] S. Iijima and T. Ichihashi, Nature. 363, 603, 1993.
[3] D. S. Bethune, C. H. Klang, M. S. de Vries, G. Gorman, R. Savoy, J. Vazquez and R. Beyers, Nature. 363, 605, 1993.
[4] S. J. Tans, A. R. M. Verschueren and C. Dekker, Nature. 393, 49, 1998.
[5] J. Kong, N. R. Franklin, C. Zhou, M. G. Chapline, S. Peng, K. Cho and H. Dai, Science. 287, 622, 2000.
[6] W. A. de Heer, A. Châtelain and D. Ugarte, Science. 270, 1179, 1995.
[7] R. H. Baughman, A. A. Zakhidov and W. A. de Heer, Science. 297, 787, 2002.
[8] J. J. Gooding, R. Wibowo, J. Q. Liu, W. Yang, D. Losic, S. Orbons, F. J. Mearns, J. G. Shapter and D. B. Hibbert, J. Am. Chem. Soc. 125, 9006, 2003.
[9] F. Patolsky, Y. Weizmann and I. Willner, Angew. Chem. Int. Ed. 43, 2113, 2004.
[10] M. Pandurangappa, N. S. Lawrence and R. G. Compton, Analyst. 127, 1568, 2002.
[11] G. G. Wildgoose, M. Pandurangappa, N. S. Lawrence, L. Jiang, T. G. J. Jones and R. G. Compton, Talanta. 60, 887, 2003.
[12] H. C. Leventis, I. Streeter, G. G. Wildgoose, N. S. Lawrence, L. Jiang, T. G. J. Jones and R. G. Compton, Talanta. 63, 1039, 2004.
[13] G. G. W. Charles G. R. Heald, Li Jiang, Timothy G. J. Jones, Richard G. Compton,, ChemPhysChem. 5, 1794, 2004.
[14] E. L. S. Wong and R. G. Compton, J. Phys. Chem. C. 112, 8122, 2008.
[15] B. Delley, J. Chem. Phys. 92, 508, 1990.
[16] B. Delley, J. Chem. Phys. 113, 7756, 2000.
[17] H. J. Monkhorst and J. D. Pack, Phys. Rev. B. 13, 5188, 1976.
[18] J. P. Perdew, K. Burke and M. Ernzerhof, Phys. Rev. Lett. 77, 3865, 1996.
[19] A. D. Becke, Phys. Rev. A. 38, 3098, 1988.
[20] C. Lee, W. Yang and R. G. Parr, Phys. Rev. B. 37, 785, 1988.
[21] J. P. Perdew and Y. Wang, Phys. Rev. B. 45, 13244, 1992.

# Comparing the Stabilities of Nanoclusters and Cluster-based Materials: Alkali Halides and the First Row Element Compounds

W. Sangthong [a,b,c], S.T. Bromley [c,d], F. Illas [c] and J. Limtrakul [a,b] *

[a] Department of Chemistry, Kasetsart University, Bangkok 10900, Thailand
[b] Center of Nanotechnology, Kasetsart University, Bangkok 10900, Thailand
[c] Departament de Química Física & Institut de Química Teòrica i Computacional (IQTCUB), Universitat de Barcelona, Cl Martí i Franquès 1, E-08028 Barcelona, Spain
[d] Institució Catalana de Recerca i Estudis Avançats (ICREA), 08010 Barcelona, Spain
*E-mail: jumras.l@ku.ac.th, Tel: +662-562-5555 ext 2169, Fax: +662-562-5555 ext 2176*

## ABSTRACT

We present state-of-the-art plane wave periodic density functional (DF) calculations aimed to unravel the structure and electronic properties of polymorphs of LiF, BeO, BN and C obtained by assembling $LiF_{12}$, $BeO_{12}$, $BN_{12}$ and $C_{24}$ $C_{12}$ building blocks with cage structure. Specifically, a nanoporous analogue of the sodalite zeolite (SOD) structure can be obtained in this way. The energy difference between the ground state phases and the SOD bulk polymorphs (per LiF, BeO, BN or $C_2$ unit; hereafter referred to simply as unit) was found to increase across the LiF, BeO, BN and C series with $\Delta E_{SOD\text{-}stab}$ = 0.05, 0.17, 0.68 and 1.07 eV/unit, respectively. The different electron distribution on each cluster is illustrated by the ELF analysis. The electronic properties results demonstrate that the cage-based polymorphs of these materials have band gaps significantly different from those in the most stable state phase, which could be interesting for nanotechnology applications.

***Keywords***: nanoclusters, sodalite, first row elements and density functional theory

## 1 INTRODUCTION

The appearance of pores in materials leads to a large number of applications as compared to the more dense bulk phases, zeolites being a paradigmatic example. Although experiments are now able to effectively maintain negative pressure conditions to explore the existence of phases with density lower than the ground state, this technique does not yet allow one to investigate a wide class of very low density porous crystalline materials. Nanoporous materials could be synthesized via a bottom-up route. Ultra-stable nanoclusters aggregation may result in various types of nanoporous materials. Hence, low density materials may possibly be obtained by aggregation of stable nanoclusters.

Assembling cage clusters, through edge to edge interactions, results in nanoporous materials similar to zeolites which are broadly used in industry. Recently, some of us reported on the prediction of low density nanoporous polymorphs of alkali halides [1], MgO, ZnO [2] and $SiO_2$ [3] based on the assembly of highly stable nanoclusters. The LiF, BeO, BN and C compounds formed from first row elements of the periodic table only provide simple models to expand the study about the stability of this type of zeolitic-like nanoporous materials.

Rock salt is the ground state phase of highly ionic LiF whereas BeO crystallizes in a wurtzite structure. Hexagonal structures are found to be stable in BN and C also appears in the form of graphite. In the present work, we report DF calculations aimed to study the geometry and electronic structure of the $LiF_{12}$, $BeO_{12}$, $BN_{12}$ and $C_{24}$ cage clusters of first row elements and to explore the stability of the new low density phases formed by assembling these building blocks relative to the ground state phase.

## 2 COMPUTATIONAL DETAILS

Two sets of plane wave density functional calculations have been carried out to explore the possibility of low density phases of the binary compounds of the first row elements (LiF, BeO, BN) and of C. The first one involves the stability of the $LiF_{12}$, $BeO_{12}$ $BN_{12}$ and $C_{24}$ cage clusters, whereas the second one concerns extended bulk systems built from these units. Energies, structures, and electronic states of cluster isomers and bulk phases of these compounds were calculated using the PW91 exchange-correlation potential [4-5] and the VASP code [6-8]. The PAW method [9] was used to represent the effect of the atomic cores and a 415 eV energy cutoff was used for the plane wave expansion. For the discrete systems, a large enough box has been constructed so that the distance between repeated clusters is larger than 1 nm. For the solids, the unit cell is defined by the crystal structure. The integrations in the reciprocal space is accomplished by using Monkhorst-Pack grids of special *k* points (7×7×7 for rock salt, wz, BN and graphite, 3×3×3 for low dense phases and Γ point for isolated clusters). For bulk phases the volume versus energy data was fitted using the Birch-Murnaghan EOS [10].

## 3 RESULTS & DISCUSSION

### 3.1 Stability of $(AB)_{12}$ cage clusters

The main purpose of the present work is to analyze the possible existence of low density bulk phases of the first row element binary compounds and their relative stability

with respect to the ground state phases. First, we analyze the possible structure of $LiF_{12}$, $BeO_{12}$, $BN_{12}$ and $C_{24}$ cage clusters consisting of 6 square faces and 8 hexagons. The geometry of these cage clusters is shown in Figure 1 and the optimized parameters are reported in Table 1.

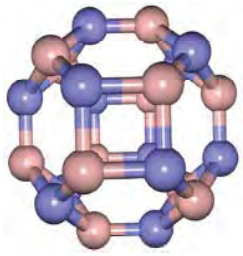

Figure 1: Geometry of $LiF_{12}$, $BeO_{12}$ and $BN_{12}$ cage clusters.

The geometry of these cage clusters is shown in Figure 1 and the optimized parameters are reported in Table 1.

| Parameters | LiF | BeO | BN | C |
|---|---|---|---|---|
| d (sq-hex), Å | 0.168 | 0.159 | 0.149 | 0.149 |
| d (hex-hex), Å | 0.163 | 0.153 | 0.144 | 0.138 |
| ∠ABA (sq),° | 95.0 (Li) | 98.3 (Be) | 98.4 (B) | 90.0 |
| | 84.9 (F) | 80.8 (O) | 80.3 (N) | 90.0 |
| ∠ABA (hex), ° | 122.0 (Li) | 124.9 (Be) | 125.8 (B) | 120.0 |
| | 117.4 (F) | 112.4 (O) | 110.9 (N) | 120.0 |
| LUMO, eV | -0.87 | -1.22 | -1.48 | -3.89 |
| HOMO, eV | -7.72 | -6.96 | -6.46 | -5.10 |
| E. Gap, eV | 6.85 | 5.74 | 4.98 | 1.21 |
| E./unit, eV | -9.28 | -13.44 | -16.24 | -16.28 |

Table 1: Structural parameters and electronic features of the $LiF_{12}$, $BeO_{12}$, $BN_{12}$ and $C_{24}$ cage clusters.

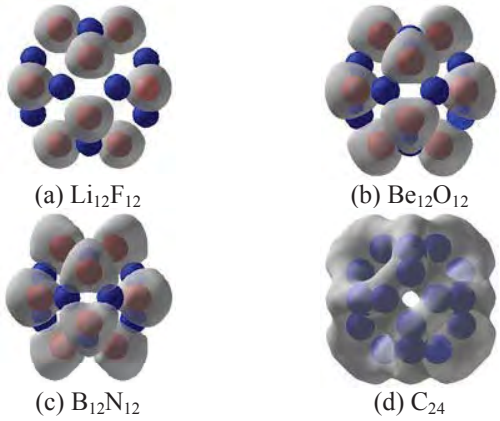

(a) $Li_{12}F_{12}$ (b) $Be_{12}O_{12}$

(c) $B_{12}N_{12}$ (d) $C_{24}$

Figure 2: Electron density map of $LiF_{12}$, $BeO_{12}$, $BN_{12}$ and $C_{24}$ cage clusters.

The geometry optimization results in a slight deviation of the molecular structure from a regular configuration except for the C24 cluster. These deviations result from charge transfer and ionicity in the chemical bond of the heteroatomic clusters. The bond distances increase with increasing ionicity. Bond angles are slightly different from the expected regular value because of the inhomogeneous electron localization. The energy gap, ΔE, between the HOMO and the LUMO and energy per unit for all cage clusters decreases from LiF to C.

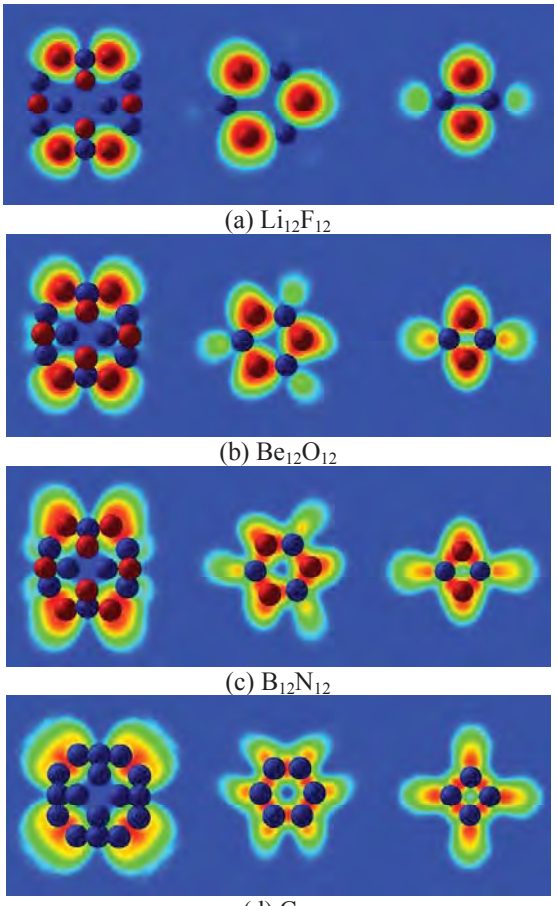

(a) $Li_{12}F_{12}$

(b) $Be_{12}O_{12}$

(c) $B_{12}N_{12}$

(d) $C_{24}$

Figure 3: Electron density maps in the three planes passing through $(AB)_{12}$ cage clusters.

To obtain additional detailed insight into the bonding and ionic polarization in the cage clusters, we have also analyzed the changes in the electronic structure upon increasing the formal cation/anion radii ratio using the Electron Localization Function (ELF). In the case of the first row element clusters, the chemical bonding is highly ionic in LiF and decreases when moving to C. From the ELF maps shown in Figure 2 one can note that when going from the extremes of LiF to CC, through BeO and BN as intermediate cases, interesting changes emerge. The ELF maps for the LiF cluster show rather spherical ELF basins, which are indicative of a highly ionic character, and they are increased and noticeably deformed when going from heteroatomic cages LiF, BeO, BN

to the case of C. In fact, for the carbon cage cluster the situation is rather different, the ELF maps are largely deformed from the symmetric spherical shape, the electron pair are clearly distributed all around the cluster. This is a clear indication that, in spite of a similar structure, the chemical bond between atoms in cage clusters is different, as expected, from chemical intuition.

A clear difference exists in the chemical bond of the first row element cage structures, which is further confirmed by the ELF maps in each plane reported in Figure 3

## 3.2 Relative stability of the sodalite phase

In order to compare the stability of the sodalite phase to that of the most stable polymorph and other possible phases, we explicitly considered other phases and determined the optimized parameters using the Birch-Murnaghan EOS. From the optimized parameters reported in Table 3 we find that the optimized volume per unit of the sodalite phase is larger than that of the ground state phase of LiF and BeO by 53% and 20%, respectively, whereas for for BN and C the volume of the most stable phase per unit is larger than that of the sodalite phase by 38% and 35%, respectively.

| Phase-AB | E0 | ΔE0 | V0 | B0 |
|---|---|---|---|---|
| RS-LiF (exp) | | | 16.32[a] | 69.9[b] |
| RS-LiF (present work) | -9.73 | 0.00 | 16.85 | 68.6 |
| SOD-LiF | -9.68 | 0.05 | 25.87 | 41.7 |
| WZ-BeO (exp)[c] | -12.73 | | 13.79 | 212 |
| WZ-BeO (present work) | -14.38 | 0.00 | 14.02 | 210.4 |
| SOD-BeO | -14.21 | 0.17 | 17.05 | 168.34 |
| HEX-BN (exp)[d] | | | | 36.7 |
| HEX-BN (present work) | -17.67 | 0.00 | 19.37 | 39.82 |
| SOD-BN | -16.99 | 0.68 | 14.61 | 290.05 |
| Graphite-C (exp)[e] | | | 35.15 | 42 |
| Graphite-C (exp)[f] | | | 35.12 | 33.8 |
| Graphite-C (present work) | -18.49 | 0.00 | 18.98 | 39.01 |
| SOD-C | -17.42 | 1.07 | 14.04 | 328.41 |

[a] Ref. 11, [b] Ref. 12, [c] Ref. 13, [d] Ref. 14, [e] Ref. 15, [f] Ref. 16

Table 2: Properties for various polymorphs (per unit) of LiF, BeO, BN and C as calculated from the EOS fits to the GGA-DFT calculated data: E0 is the minimum total energy (eV), $\Delta E_0$ the total energy differences (eV), V0 the volume at minimum energy ($Å^3$) and B0 the bulk modulus (GPa). V0 and B0 are compared with available experimental values.

In order to find the trend on the stability of the sodalite phase relative to the other phases considered in the present work, we plot in Figure 4 the energy difference (per unit) between the total energy of sodalite and the total energy of the most stable polymorph. From Figure 4 a clear monotonous trend is observed which makes it undoubtedly clear that the stability of the sodalite phase decreases along the LiF, BeO, BN and C series or that increasing covalent character of the chemical bond destabilizes the low density polymorph with respect to the more dense phases corresponding to the most stable polymorph. These results indicate that the sodalite form is likely to be easily synthesized from highly ionic compounds where for the remaining studied systems this will face increasing difficulties.

## 3.3 Electronic properties

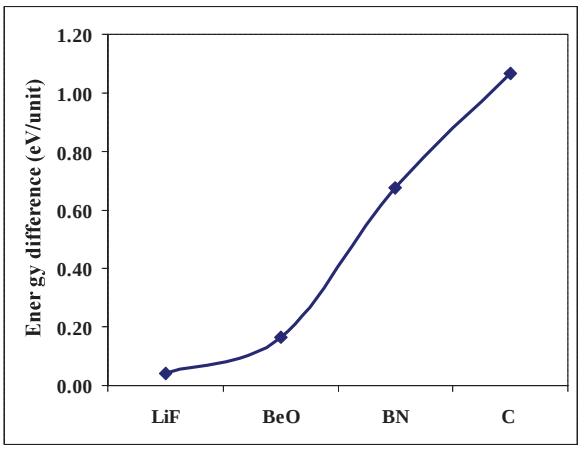


Figure 4: The energy differences between the sodalite phase and the ground state phase.

In order to investigate the electronic structures of the different polymorphs of LiF, BeO, BN and C more precisely, we have calculated the total density of states using the standard procedure. All band energies are given with respect to the Fermi energy ($E_F$) and shown in Figure 5. The Fermi energy is located at the top of the valence bands which is located at the Γ point and is set to zero. The DOS plots for rock salt and sodalite phases of LiF are presented in Figures 5a1 and 5a2, respectively. Below zero, there is a broad range of F states below the top of the valence band, whereas the conduction band consists of F and Li states. The difference between the maximum of the F valence band and the minimum of the Li conduction band results in a band gap of 8.83 eV and 6.36 eV for rock salt and sodalite phases, respectively. The band gap for the rock salt phase is underestimated with respect to the experimental value of 13.6 eV. This is a well known failure of the GGA functional. Nevertheless, one expects that the relative trends are well reproduced. The DOS plots of BeO for wurtzite and sodalite phases (Figures 5b1 and 5b2) display the same trend, the valence regions are mainly composed of O states while the conduction bands originate predominantly from Be states. The calculated energy gaps are 7.22 eV and 5.18 eV for wurtzite and sodalite phases, respectively. Again the band gap for wurtzite is underestimated with respect to the experimental value of 10.6 eV. The DOS for the two polymorphs of BN phases are reported in Figures 5c1 and 5c2 and also show that the top and the low energy part of the valence band is predominantly formed by the states of nitrogen atoms. The upper conduction band is dominated by contributions from both B and N states. The calculated band gap for hexagonal BN is 4.37 eV (experimental value = 5.4 eV) while the

calculated value for the sodalite phase is 4.38 eV. For the graphite phase (Figure 5d1), the DOS for the unit cell shows two groups of peaks with a band gap of 1.43 eV between them. The Fermi energy is placed at the top of the valence band (VB) so all states below it have two electrons per orbital, and all states above it are unoccupied. The energy gap of the sodalite form of carbon is calculated to be 2.44 eV.

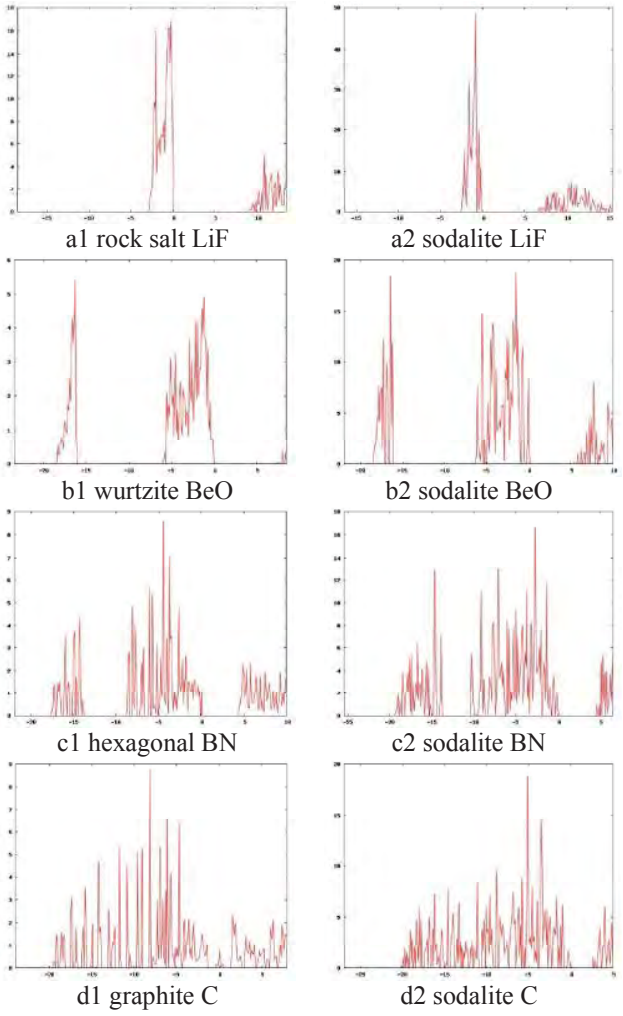


Figure 5: Total density of states of bulk phases of LiF, BeO, BN and C.

## 4 CONCLUSION

A bottom up approach and state-of-the-art plane wave periodic density functional calculations were utilized to investigate the possible existence of low density phases of the LiF, BeO, BN first row element binary compounds and of C. The existence of stable $(AB)_{12}$ or $C_{24}$ cage clusters, where AB= LiF, BeO, BN, suggest that these could act as building blocks to form novel nanoporous materials. The calculated HOMO-LUMO gaps of all clusters decreases along the LiF, BeO, BN, C series and can be understood from the ELF analysis. In fact, the ELF analysis of the bare cage clusters explains the difference in optimized geometry and electron distribution on each cluster. Bulk materials constructed from the cages may exhibit a sodalite structure; the total energy difference (per unit) between the most stable and the sodalite polymorphs was found to increase when going from LiF to C ($\Delta E_{SOD\text{-}stab}$=0.05, 0.17, 0.68, 1.07 eV/unit for LiF, BeO, BN and C, respectively). The calculated HOMO-LUMO gaps and electronic structure of all predicted nanoporous phases are different from those of the corresponding ground state phases. Merging state of the art density functional calculations and a bottom-up strategy provides a complementary way to motivate further synthesis and applications of new predicted nanoporous phases.

## ACKNOWLEDGEMENTS

This work was supported in part by grants from the National Science and Technology Development Agency (NSTDA), KURDI the Thailand Research Fund (to WS. and JL.) and the Commission on Higher Education, Ministry of Education under Postgraduate Education and Research Programs in Petroleum and Petrochemicals, and Advanced Materials. This study has been supported in part by the Spanish Ministerio de Ciencia e Innovacion grant FIS2008-02238/FIS.

## REFERENCES

[1] W. Sangthong, J. Limtrakul, F. Illas and S. T. Bromley, J. Mater. Chem., 2008, 18, 5871.
[2] J. Carrasco, F. Illas and S. T. Bromley, Phys. Rev. Lett., 2007, 99, 235502.
[3] J. C. Wojdel, M. A. Zwijnenburg and S. T. Bromley, Chem. Mater., 2006, 18, 1464.
[4] J. P. Perdew, J. A. Chevary, S. H. Vosko, K. A. Jackson, M. R. Pederson, D. J. Singh and C. Fiolhais, Phys. Rev. B, 1992, 46, 6671.
[5] J. A. White and D. M. Bird, Phys. Rev. B, 1994, 50, 4954.
[6] G. Kresse and J. Hafner, Phys. Rev. B, 1993, 47, 558.
[7] G. Kresse and J. Furthmu¨ ller, Comput. Mater. Sci., 1996, 6, 15.
[8] G. Kresse and J. Furthmu¨ ller, Phys. Rev. B, 1996, 54, 11169.
[9] P. E. Blöchl, Phys. Rev. B, 1994, 50, 17953.
[10] F. Birch, Phys. Rev., 1947, 71, 809.
[11] V. A. Streltsov, V. G. Tsirelson, R. P. Ozerov and O. A. Golovanov, Kristallografiya, 1987, 33, 90.
[12] C. V. Briscoe and C. F. Squire, Phys. Rev., 1957, 1175, 106.
[13] Hazen R M and Finger L W, J. Appl. Phys., 1986, 59, 3728.
[14] S. Bohr, R. Haubner, B. Lux, Diamond Relat. Mater., 1995, 4, 714.
[15] Y.X. Zhao and I.L. Spain, Phys. Rev. B, 1989, 40, 993.
[16] M. Hanfland, H. Beister, and K. Syassen, Phys. Rev. B, 1989, 39, 12 598.

**American Chemical Society National meeting & Exposition ครั้งที่ 239**

**ณ ประเทศสหรัฐอเมริกา**

**ระหว่างวันที่ 21-25 มีนาคม 2553**

**จำนวน 11 เรื่อง**

**918 - Propane cracking reaction over different types of nanostructured zeolites: A newly developed DFT approach**

***Sarawoot Impeng, Thana Maihom, Pipat Khongpracha, Dr. Somkiat Nokbin, Dr. Jumras Limtrakul, Prof. Dr. . Department of Chemistry, Faculty of Science, Kasetsart University Laboratory for Computational & Applied Chemistry, Physical Chemistry Division Chatuchak Bangkok Thailand, Center of Nanotechnology, Kasetsart University Research and Development Institute Chatuchak Bangkok Thailand, NANOTEC Center of Nanotechnology, National Nanotechnology Center, Kasetsart University Chatuchak Bangkok Thailand***

Propane cracking over different types of zeolites was investigated using the realistic nanocluster of 120T performed at the M06L/6-31G(d,p)//14T ONIOM(M06L/6-31G(d,p):UFF) level of theory. The adsorption energies of propane were predicted to be -7.6 and -9.9 kcal/mol for H-FAU and H-MOR, respectively. Using the experimental adsorption energies as the benchmark, our combined ONIOM scheme is found to represent the interaction of propane with zeolites. After adsorption, the zeolite's proton was inserted into a C-C bond of a propane molecule and yielded a methane and ethoxide intermediate. The intermediate was then deprotonated to form the ethylene product. The first step was found to be rate-determining with actual activation energies of 43.7 and 41.3 kcal/mol for H-FAU and H-MOR, respectively. The activation energies for the second step were 24.7 and 18.5 kcal/mol for H-FAU and H-MOR, respectively. Our findings suggested that the propane cracking was insensitive to the zeolite structure.

**Tuesday, March 23, 2010 07:00 PM**

**Inorganic Catalysts (07:00 PM - 09:00 PM)**

Close Window

**919 - Adsorption of a basic probe molecule over nanostructured zeolitic catalysts (H-FAU, H-MOR and H-MCM-22 ): A newly developed density functional M06-2X study**

***Supalak Khueanphet*, Bundet Boekfa, Dr. Tanin Nanok, Dr. *Jumras Limtrakul*, Prof. Dr. . Department of Chemistry, Faculty of Science, Kasetsart University Laboratory for Computational & Applied Chemistry, Physical Chemistry Division Chatuchak Bangkok Thailand, Center of Nanotechnology, Kasetsart University Research and Development Institute Chatuchak Bangkok Thailand, NANOTEC Center of Nanotechnology, National Nanotechnology Center, Kasetsart University Chatuchak Bangkok Thailand, Department of Chemistry Faculty of Liberal Art and Science, Kasetsart University Kamphaeng Saen Campus Nakhon Pathom Thailand***

The confinement effect on the adsorption of ammonia on different types of zeolite (H-FAU, H-MOR and H-MCM-22) has been studied with the newly developed Density Functional Theory, M06-2X, with 6-31G(d,p) basis set. The nanoporous zeolites, where chemical reactions take place, are represented by a small cluster of 14T up to a nanocluster of 120 tetrahedral atoms (T is Si or Al atoms). The adsorption energies of ammonia on H-FAU, H-MOR and H-MCM-22 are predicted to be -35.0, -41.1 and -41.7 kcal/mol, respectively, which are in the range of experiment observation of -35.9 kcal/mol for H-FAU and -38.2 kcal/mol of H-MOR. Therefore, the full quantum calculation with the new density functional theory, M06-2X/6-31G(d,p), is a practical and accurate model to study the confinement effect on the adsorption of the polar molecule in different pore sizes of zeolites.

Keywords: Confinement effect, Zeolites, Ammonia adsorption, M06-2X functional

**Tuesday, March 23, 2010 07:00 PM**

**Inorganic Catalysts (07:00 PM - 09:00 PM)**

Close Window

**917 - Skeletal isomerization of 1-butene over ferrierite zeolite: A quantum chemical analysis of structures and reaction mechanisms**

***Chularat Wattanakit*, Bundet Boekfa, Dr. Somkiat Nokbin, Dr. Piboon Pantu, Asst. Prof. *Jumras Limtrakul*, Prof. Dr. . Department of Chemistry, Faculty of Science, Kasetsart University Laboratory for Computational & Applied Chemistry, Physical Chemistry Division Chatuchak Bangkok Thailand, Center of Nanotechnology, Kasetsart University Research and Development Institute Chatuchak Bangkok Thailand, NANOTEC Center of Nanotechnology, National Nanotechnology Center, Kasetsart University Chatuchak Bangkok Thailand, Department of Chemistry Faculty of Liberal Art and Science, Kasetsart University Kamphaeng Saen Campus Nakhon Pathom Thailand***

The skeletal isomerization of 1-butene to isobutene has been investigated by a full quantum calculation using M06L/6-31G(d,p) method with a 37T H-FER cluster. The adsorption energies for 1-butene and isobutene, respectively, are predicted to be -22.0 and -16.7 kcal/mol. The monomolecular acid-catalyzed formation of isobutene has been considered. The mechanism starts with the protonation of the adsorbed 1-butene by an acidic proton to produce a surface secondary alkoxide intermediate and is subsequently transformed into primary alkoxide via the cyclic transition state. The isobutoxide is then altered to the isobutene product through *tert*-butyl cation. The activation barriers are 9.0 and 20.9 kcal/mol for the sequent first and second steps, respectively. For the third step, the barrier is 30.2 kcal/mol and is considered to be the rate-determining step, which agrees well with experiment,~30 kcal/mol. The shape selectivity due to the “nano-confinement” effect of the zeolite framework has been clearly demonstrated.

**Tuesday, March 23, 2010 07:00 PM**

**Inorganic Catalysts (07:00 PM - 09:00 PM)**

Close Window

# STRUCTURES AND REACTION MECHANISMS OF GLYCEROL DEHYDRATION OVER H-ZSM-5 ZEOLITE

*Kanokwan Kongpatpanich* [a, b, c], *Tanin Nanok* [a, b, c], *Bundet Boekfa* [b, c] *and Jumras Limtrakul* [a, b, c*]

[a] Laboratory for Computational and Applied Chemistry, Chemistry Department, Faculty of Science, Kasetsart University, Bangkok 10900, Thailand.
[b] Center of Nanotechnology, Kasetsart University Research and Development Institute, Kasetsart University, Bangkok 10900, Thailand.
[c] NANOTEC Center of Excellence, National Nanotechnology Center, Bangkok 10900, Thailand.

## Introduction

The global energy crisis that has been brought about by the continuing depletion of petroleum resources and the increase of environmental problems is acknowledged by researchers as a serious problem. This has led to the search for new, alternative and renewable resources. Biodiesel, an alternative non-toxic and biodegradable diesel fuel, can offer one alternative energy supply. At the present time, biodiesel costs are still higher than petroleum-based diesel mainly because of the cost of raw materials and the large amount of waste generated within the processes. Therefore, approaches that can utilize the waste from the processes are of particular interest. Several researches have been focused on new approaches for converting this valueless waste derived from biomass to higher value chemicals.[1]

Glycerol, a by-product from biodiesel production, has a relatively low global demand with a low market price which has a negative impact on biodiesel economics.[2] Since the demand for glycerol is outpaced by biodiesel production, a solution has to be found to increase the value of glycerol. One solution is to convert it to a more valuable chemical.[3] Acrolein or 2-propenal is a value-added chemical readily prepared from the catalytic dehydration of glycerol under a mild condition. Acrolein is an essential and versatile starting intermediate material widely used in the production of acrylic acid, DL-Methionine, super absorber polymers, and detergents.[4] For many years, acrolein has been produced by the oxidation of propylene over Bi/Mo mixed oxide catalysts, but the production is limited by the continuously increasing price of propylene.[5] Avoiding this route by using alternative carbon sources from biomass would be a green alternative for the chemical industry. Moreover, this route could improve the sustainability in environmental care and also is an economically attractive one.

Zeolite, with its selective properties, high thermal stability and intrinsic acidity[6] is one of the most important solid acid catalysts widely used in petroleum refinery industries and for the production of fine chemicals. Several studies have been conducted describing the dehydration of glycerol over different solid acids, for example $Nb_2O_5$, heteropoly acids, silica-supported heteropoly acids, and zeolites.[7-12] H-ZSM-5 zeolite has been found to have high catalytic activity and selectivity for the dehydration of glycerol into acrolein.[10-12] However, the reaction mechanism is still not clearly understood. Although there have been some theoretical studies of glycerol dehydration over homogeneous catalysts[13] but, as far we know, there are no theoretical studies reported about the detailed reaction mechanism of glycerol dehydration over solid acid, which may offer a different mechanism from the conventional ones.

In the present work, the full quantum chemical calculation was employed to study the dehydration of glycerol over H-ZSM-5 zeolite in order to better understand its chemistry and further control the industrial operating conditions.

## Methods

The structure of the 128T cluster model taken from the lattice structure of the ZSM-5 zeolite was employed to study the reaction mechanism. The cluster covers the straight channel, the zigzag channel, and the channel intersection. The intersection of the two channels allows a large space for the reaction to take place. Previous studies from our group indicate that the M06-2X functional developed by the Minnesota group[14, 15] show reliable results for the study of the interaction of organic molecules in the zeolite system.[16-18] Geometry optimizations were done over the 12T cluster at the M06-2X/6-31G(d,p) level of theory, with only the 5T cluster of the active site region and the adsorbing molecules being allowed to relax to reduce the required computational time. The frequency calculations were performed at the same level to verify that the transition state structure has only one imaginary frequency. Single-point calculation of the 128T cluster was done on the optimized structures to represent the confinement effect of the zeolite framework and to obtain more accurate energies. The standard enthalpy ($\Delta H$) and Gibbs free energy changes ($\Delta G$) of all structures in the first dehydration step were obtained from the frequency calculations. These data were used to predict the rate constants and the equilibrium constants. The rate constants were evaluated over the temperature range of 200-500 °C with the interval of 50 °C using a simple transition state theory (TST).[19] All calculations were performed using the Gaussian 03 code[20] incorporated with the Minnesota Density Functionals module 3.1 by Zhao and Truhlar.

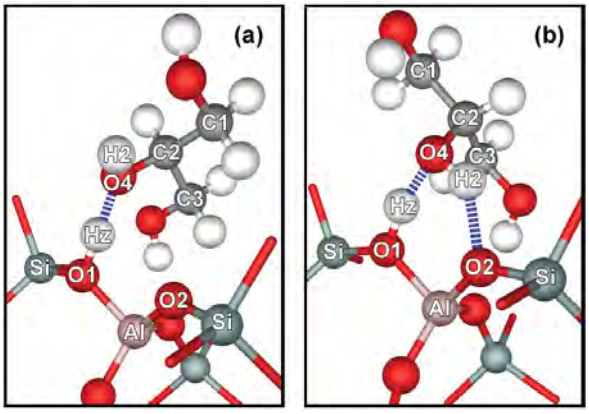


**Figure 1.** Optimized structures of (a) the side-on and (b) the end-on glycerol adsorption structures.

**Results and discussion**

Glycerol is a highly flexible $C_3$ molecule containing three hydroxyl groups. In the gas phase, it preferably forms a cyclic structure of intramolecular hydrogen bonds between three hydroxyl groups termed gG'gg'Gg(γγ) as the most stable conformer.[21] Therefore, we have chosen this conformer as a starting geometry for studying its entire reaction in the H-ZSM-5 zeolite. Prior to the exploration of the reaction mechanism for glycerol conversion to acrolein, the search for the adsorption structures leading to acrolein formation has been established. The protonation at the secondary hydroxyl group (OH) is placed for the crucial adsorption structures. Figures 1a and b show the side-on and end-on adsorption structures of glycerol adsorbed onto the Brønsted active site of H-ZSM-5. Glycerol has a completely different conformation from that found in the isolated gas phase. The cyclic intramolecular hydrogen bonding between the three hydroxyl groups has been separated and liberally stabilized by the partially negative-charged oxygen atoms of the zeolite framework. For the side-on structure, the secondary OH group interacts with the Brønsted proton via the lone-pair electron of its oxygen center and the OH group points away from the lattice oxygens of the zeolite framework. The lateral hydrogen bonding of the secondary OH group with the basic lattice oxygen is found, additionally, in the end-on structure. The adsorption energies for the side-on and end-on structures are estimated to be exothermic by 52.7 and 51.1 kcal/mol, respectively. These values are considerably larger than the experimental measurement for the exothermic methanol adsorption of 27.5 kcal/mol.[22] The effects of zeolite confinements and a number of hydrogen bondings experienced by glycerol are accountable for the highly exothermic adsorption energy. The strongest hydrogen bonding between the secondary OH group and the zeolite Brønsted active site results in the significant elongation of the O1-Hz zeolite bond distance from 0.97 Å to 1.06 and 1.07 Å for the side-on and end-on structures, respectively. The three-centered hydrogen bond angle, O1-Hz-O4, is close to a linear angle (177.2˚ and 165.0˚, for the side-on and end-on adsorption structures, respectively) and the O1-O4 distance is calculated to be 2.46 Å in both cases.

As mentioned above, the selective activation at the secondary OH group is substantially the initial reaction for acrolein production. We, thus, follow the schematic diagram of the reaction mechanisms guided by the previous infrared spectroscopic (IR) study.[12] The transformation of glycerol to acrolein can be consecutively divided into three main steps as follows:

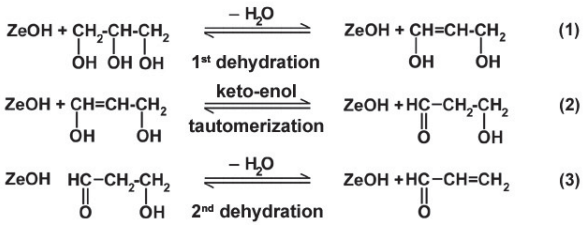


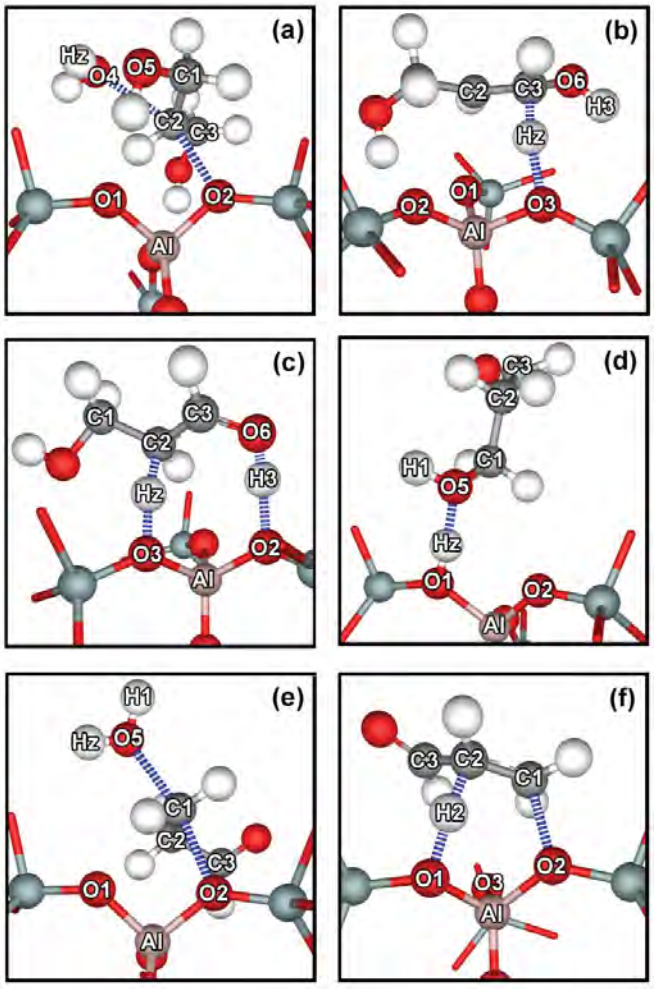


**Figure 2.** Optimized structures of the transition states and a stable intermediate (3-hydroxypropanal) along the reaction pathway for glycerol transformation to acrolein (a) ts_dehyd_1 (b) ts_alk_1 (c) ts_tauto_1 (d) keto_OH (e) ts_alk_2 and (f) ts_acrolein.

**(1) The first dehydration.** The protonation at the secondary OH group of glycerol is the key step for activating the first dehydration reaction. This process results in the weakening of the glycerol C2-O4 bond at the secondary position and, hence, promoting the OH group to be a good leaving group. To prevent the reversible proton back donation to the zeolite, that can occur readily under normal experimental conditions, we proposed the activated complex as shown in Figure 2a as the transition state structure, **ts_dehyd_1**, for the first dehydration reaction. The protonated glycerol molecule is oriented to have the secondary carbon C2 located in the middle, between the protonated OH group and the zeolite lattice oxygen O2. The strongly active mode of an imaginary frequency vibration of the transition state complex resembles the $S_N2$ mechanism in which the C2-O2 bond formation and the C2-O4 bond cleavage occur in the concerted fashion. When considering

the geometric parameters, it can be seen that a water molecule is completely developed (C2-O4 = 2.40 Å) during the formation of an alkoxide (C2-O2 = 2.28 Å). Therefore, this activated complex is considered as the late transition state complex which requires the activation energy of 41.4 kcal/mol with respect to the side-on adsorption complex. According to the well-known Hammond-Leffler postulate[23], any reaction that proceeds through the product-like transition state is likely to be the endothermic reaction. As expected, the reaction is endothermic by 25.5 kcal/mol. The secondary surface alkoxide species **alk_1** and a water molecule are the products of this reaction step. To shift the reaction forwards, it is necessary to desorb the water molecule from the system. The calculated desorption energy required for the removal of a water molecule adsorbed nearby the surface alkoxide is 16.4 kcal/mol. After the water molecule is eliminated from the system, the surface alkoxide can readily undergo the proton back donation to regenerate the zeolite Brønsted active site by returning a proton attached to the primary carbon C1 back to the basic zeolite oxygen O3 and releasing 1,3-dihydroxypropene **hyd_enol_1** as a resulting product. The reaction proceeds through the transition state **ts_alk_1** (see Figure 2b) and requires the activation energy of 25.0 kcal/mol. 1,3-dihydroxypropene has an enol-form structure and it can strongly adsorb onto the zeolite Brønsted active site via the hydrogen bonding interaction using its vinyl hydroxyl group.

**(2) The keto-enol tautomerization.** In order to tautomerize 1,3-dihydroxypropene, an enol form, into its keto form, the orientation of an adsorbed molecule is readjusted to interact with the Brønsted proton via the loosely bound π-bonding interaction, **pi_enol_1**. The π-bonding adsorption structure of the enol form can, then, easily tautomerize to the keto form 3-hydroxypropanal through a nearly barrierless transition state **ts_tauto_1** (see Figure 2c). The imaginary frequency vibration of the transition state demonstrates that the acidic proton that attached to the zeolite O3 transfers to the C2 of glycerol at the same time that the hydroxyl proton on the glycerol O5 transfers back to the zeolite O2 to regenerate the acidic site. The tautomerization from the enol to keto form is the exothermic reaction. The keto-product strongly adsorbs onto the Brønsted acid site via the hydrogen bonding using its carbonyl group, **keto_CO**.

**(3) The second dehydration.** The protonation at the primary OH group of 3-hydroxypropanal is the key activating process for the second dehydration reaction. Therefore, the adsorption structure of 3-hydroxypropanal (see Figure 2d) **keto_OH** via its OH group with the Brønsted acid site is adopted to be the starting geometry of this second dehydration step. Similar to the first dehydration step, the OH group is protonated by zeolite and acts as a leaving group. At the transition state **ts_alk_2** (see Figure 2e), the attack of the 3-hydroxypropanal primary carbon by the basic zeolite oxygen takes place in concomitance with an elimination of a water molecule. This step requires an activation energy of 38.6 kcal/mol. The primary alkoxide

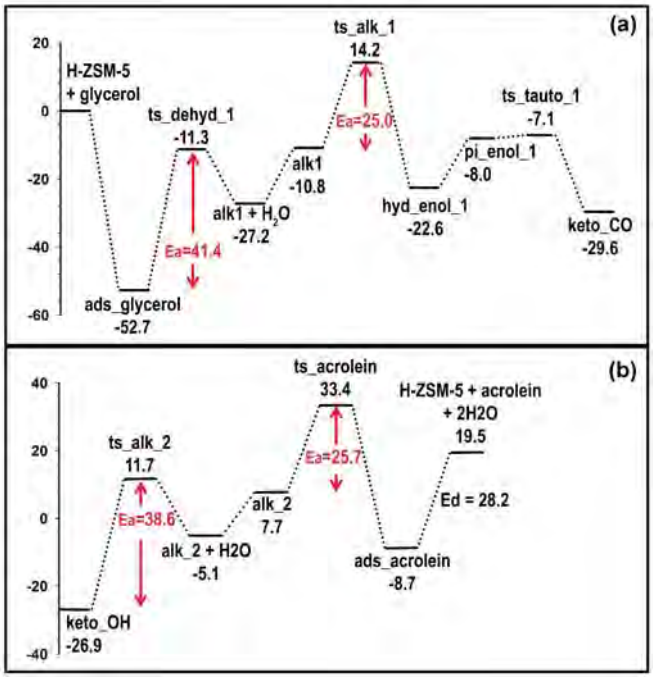


**Figure 3.** Relative energy profiles of (a) the first dehydration step and the keto-enol tautomerization and (b) the second dehydration step. Energies are in kcal/mol.

intermediate **alk_2** generated from this step is solvated by a single water molecule. To remove an adsorbed water molecule from the alkoxide species, it requires the desorption energy of 12.8 kcal/mol. The dehydrated alkoxide species undergoes proton back donation from the secondary carbon to the basic zeolite oxygen leading to the acrolein product formation. The transition state **ts_acrolein** (see Figure 2f) for acrolein formation requires an activation energy of 25.7 kcal/mol. Desorbing acrolein from the zeolite surface requires the desorption energy of 28.2 kcal/mol.

The overall energy profile for glycerol conversion to acrolein shown in Figures 3a and b indicates that the production of acrolein from glycerol over H-ZSM-5 is an endothermic process. The dehydration reaction is considered as the rate limiting step of the overall reaction because it requires the highest activation energy to overcome the reaction barrier. Instead, the hydration reaction which goes in the opposite direction of the dehydration reaction is found to be thermodynamically and kinetically favoured. Therefore, in order to shift the reaction from the left to the right, it is necessary to introduce a sufficiently high temperature to the system because the dehydration reaction is generally favoured at high temperature whereas the hydration reaction can readily occur at a low temperature.[11, 24] Table 1 shows the calculated rate constants ($k_{for}$ and $k_{rev}$) and the equilibrium constants ($K$) for the first dehydration reaction step over the temperature range of 200-500 °C. The rate constant increases with increasing the temperature. This behaviour is in good accordance with the typical endothermic reaction. Since the water molecule generated by the dehydration process

**Table 1.** Calculated rate constants ($k_{for}$ and $k_{rev}$) and the equilibrium constants ($K$) for the first dehydration reaction step over the temperature range of 200-500 °C.

| T (°C) | $k_{forward}$ | $k_{reverse}$ | $K_{eq}$ |
|---|---|---|---|
| **200** | $4.23\times10^{-6}$ | $4.43\times10^{4}$ | $9.55\times10^{-11}$ |
| **250** | $3.72\times10^{-4}$ | $3.39\times10^{5}$ | $1.10\times10^{-9}$ |
| **300** | $1.52\times10^{-2}$ | $1.83\times10^{6}$ | $8.33\times10^{-9}$ |
| **350** | $3.47\times10^{-1}$ | $7.58\times10^{6}$ | $4.58\times10^{-8}$ |
| **400** | $5.01\times10^{0}$ | $2.55\times10^{7}$ | $1.96\times10^{-7}$ |
| **450** | $5.03\times10^{1}$ | $7.30\times10^{7}$ | $6.90\times10^{-7}$ |
| **500** | $3.77\times10^{2}$ | $1.83\times10^{8}$ | $2.06\times10^{-6}$ |

can readily react with the active alkoxide intermediate, the continuous removal of water from the system is another crucial point for preventing the backward reaction. From the overall energy diagram, it can be concluded that 3-hydroxypropanal is a stable intermediate in acrolein production. Several works have reported that 3-hydroxypropanal is able to be dehydrated into acrolein when the temperature is increased and acrolein can be readily hydrated into 3-hydroxypropanal at lower temperatures.[25, 26]

## Conclusions

The structures and reaction mechanisms of glycerol dehydration over the H-ZSM-5 zeolite have been investigated using the newly developed density functional theory with the M06-2X functional. Three main reaction steps have been proposed to take place consecutively. The selective dehydration of glycerol at the secondary OH group is proved to be the first important step leading to acrolein formation. Even though the transition state of this step requires a relatively high activation energy compared to the other steps along the reaction pathway, the large amount energy released by glycerol adsorption could make the reaction becoming more efficient. Among several intermediates involved in the reaction, 3-hydroxypropanal is found to be the most stable intermediate. With respect to the gas phase glycerol, the acrolein formation is an endothermic reaction. In addition to increasing the reaction temperature, the removal of developed water from system could favor the forward reactions. The rate constants for the first dehydration over the temperature range of 200-500 ˚C are provided for comparing with future available kinetic experiments. Our findings are important for understanding the chemistry of glycerol dehydration over acidic zeolites.

**Acknowledgements.** This work was supported in part by grants from the National Science and Technology Development Agency (2009 NSTDA Chair Professor funded by the Crown Property Bureau under the management of the National Science and Technology Development Agency and NANOTEC Center of Excellence funded by the National Nanotechnology Center), The Thailand Research Fund, the Commission of Higher Education, Ministry of Education ("National Research University of Thailand" and "Postgraduate Education and Research Programs in Petroleum and Petrochemicals and Advanced Materials"). The support from the Kasetsart University Research and Development Institute (KURDI) and Graduate School Kasetsart University are also acknowledged. The authors are grateful to Donald G. Truhlar and Yan Zhao for their support with the M06-2X functional.

## References

(1) Corma Canos, A.; Iborra, S.; Velty, A., *Chem. Rev.* **2007,** *107*, 2411.
(2) Pagliaro, M.; Ciriminna, R.; Kimura, H.; Rossi, M.; Della Pina, C., *Angew. Chem. Int. Ed.* **2007,** *46*, 4434.
(3) Zheng, Y.; Chen, X.; Shen, Y., *Chem. Rev.* **2008,** *108*, 5253.
(4) Katryniok, B.; Paul, S.; Capron, M.; Dumeignil, F., *ChemSusChem* **2009,** *2*, 719.
(5) Pudar, S.; Oxgaard, J.; Chenoweth, K.; van Duin, A. C. T.; Goddard, W. A., *J. Phys. Chem. C* **2007,** *111*, 16405.
(6) Van Santen, R. A.; Kramer, G. J., *Chem. Rev.* **1995,** *95*, 637.
(7) Chai, S. H.; Wang, H. P.; Liang, Y.; Xu, B. Q., *J. Catal.* **2007,** *250*, 342.
(8) Atia, H.; Armbruster, U.; Martin, A., *J. Catal.* **2008,** *258*, 71.
(9) Tsukuda, E.; Sato, S.; Takahashi, R.; Sodesawa, T., *Catal. Commun.* **2007,** *8*, 1349.
(10) Zhou, C. J.; Huang, C. J.; Zhang, W. G.; Zhai, H. S.; Wu, H. L.; Chao, Z. S., *Stud. Surf. Sci. Catal.* **2007,** *165*, 527.
(11) Corma, A.; Huber, G. W.; Sauvanaud, L.; O'Connor, P., *J. Catal.* **2008,** *257*, 163.
(12) Yoda, E.; Ootawa, A., *Appl. Catal. A : General* **2009,** *360*, 66.
(13) Nimlos, M. R.; Blanksby, S. J.; Qian, X.; Himmel, M. E.; Johnson, D. K., *J. Phys. Chem. A* **2006,** *110*, 6145.
(14) Zhao, Y.; Truhlar, D. G., *Acc. Chem. Res.* **2008,** *41*, 157.
(15) Zhao, Y.; Truhlar, D. G., *Theor. Chem. Acc.* **2008,** *120*, 215.
(16) Maihom, T.; Boekfa, B.; Sirijaraensre, J.; Nanok, T.; Probst, M.; Limtrakul, J., *J. Phys. Chem. C* **2009,** *113*, 6654.
(17) Kumsapaya, C.; Bobuatong, K.; Khongpracha, P.; Tantirungrotechai, Y.; Limtrakul, J., *J. Phys. Chem. C* **2009,** *113*, 16128.
(18) Boekfa, B.; Choomwattana, S.; Khongpracha, P.; Limtrakul, J., *Langmuir* **2009**, DOI: 10.1021/la901841w.
(19) Choomwattana, S.; Maihom, T.; Khongpracha, P.; Probst, M.; Limtrakul, J., *J. Phys. Chem. C* **2008,** *112*, 10855.
(20) Frisch, M. J. T., G. W.; Schlegel, H. B.; Scuseria, G. E.; Robb, M. A.; Cheeseman, J. R.; Montgomery, Jr., J. A.; Vreven, T.; Kudin, K. N.; Burant, J. C.; Millam, J. M.; Iyengar, S. S.; Tomasi, J.; Barone, V.; Mennucci, B.; Cossi, M.; Scalmani, G.; Rega, N.; Petersson, G. A.; Nakatsuji, H.; Hada, M.; Ehara, M.; Toyota, K.; Fukuda, R.; Hasegawa, J.; Ishida, M.; Nakajima, T.; Honda, Y.; Kitao, O.; Nakai, H.; Klene, M.; Li, X.; Knox, J. E.; Hratchian, H. P.; Cross, J. B.; Bakken, V.; Adamo, C.; Jaramillo, J.; Gomperts, R.; Stratmann, R. E.; Yazyev, O.; Austin, A. J.; Cammi, R.; Pomelli, C.; Ochterski, J. W.; Ayala, P. Y.; Morokuma, K.; Voth, G. A.; Salvador, P.; Dannenberg, J. J.; Zakrzewski, V. G.; Dapprich, S.; Daniels, A. D.; Strain, M. C.; Farkas, O.; Malick, D. K.; Rabuck, A. D.; Raghavachari, K.; Foresman, J. B.; Ortiz, J. V.; Cui, Q.; Baboul, A. G.; Clifford, S.; Cioslowski, J.; Stefanov, B. B.; Liu, G.; Liashenko, A.; Piskorz, P.; Komaromi, I.; Martin, R. L.; Fox, D. J.; Keith, T.; Al-Laham, M. A.; Peng, C. Y.; Nanayakkara, A.; Challacombe, M.; Gill, P. M. W.; Johnson, B.; Chen, W.; Wong, M. W.; Gonzalez, C.; and Pople, J. A. *Gaussian 03, revision B.05*, Gaussian, Inc., Wallingford CT, 2004.
(21) Chelli, R.; Gervasio, F. L.; Gellini, C.; Procacci, P.; Cardini, G.; Schettino, V., *J. Phys. Chem. A* **2000,** *104*, 11220.
(22) Lee, C. C.; Gorte, R. J.; Farneth, W. E., *J. Phys. Chem. B* **1997,** *101*, 3811.
(23) Hammond, G. S., *J. Am. Chem. Soc.* **2002,** *77*, 334.
(24) Izumi, Y., *Catal. Today* **1997,** *33*, 371.
(25) Pressman, D.; Lucas, H. J., *J. Am. Chem. Soc.* **2002,** *64*, 1953.
(26) Clacens, J. M.; Pouilloux, Y.; Barrault, J., *Appl. Catal. A : General* **2002,** *227*, 181.

# Application of newly developed M06-2X functional for identifying a suitable industrially important petrochemical zeolite catalyst for a particular reaction

*Bundet Boekfa* [a,b,c] *, Piboon Pantu* [a,b]*, Pailin Limtrakul* [a]*, Michael Probst* [a,b]*, and Jumras Limtrakul* [a,b*]

[a] Laboratory for Computational & Applied Chemistry, Physical Chemistry Division, Department of Chemistry, Faculty of Science, Kasetsart University, Bangkok 10900, Thailand
[b] Center of Nanotechnology, Kasetsart University Research and Development Institute, Kasetsart University, Bangkok 10900, Thailand
[c] Chemistry Department, Faculty of Liberal Art and Science, Kasetsart University Kamphaeng Saen Campus, Nakhon Pathom 73140, Thailand

## Introduction

Zeolite, aluminosilicate materials with regular pore structure of molecular dimensions, is one of the most important heterogeneous catalysts widely used for environmental, pertrochemical and industrial applications.[1-7] Their activity and selectivity make them stand out from other catalysts in petrochemical industries. The aldol condensation is one of the C-C bond forming organic reactions that are widely used in the production of solvents and plasticizers, and in the synthesis of intermediates for perfumes and pharmaceuticals.[5,8,9] Acetone tautomerization to enol form is an important initial step of aldol condensation and C-C coupling. The activity of tautomerization (also known as enolization) is found to be dependent on the acidity and the ionic strength of the reaction media. [10-12]

Theoretical studies on keto-enol tautomerization of acetaldehyde and acetone over uncatalyzed and zeolite catalysts have reported that the bifunctional features of Brønsted acid and Lewis basic sites on H-ZSM-5 drastically reduce the barrier height for the tautomerization of acetaldehyde and acetone.[22,23] In addition, the interaction between the zeolite framework and an adsorbed molecule, which is generally called confinement effect,[13] also plays an important role for the adsorption and reactions on zeolites.[14-21] Therefore, the details of interactions between the reactants and the active site in the zeolite's framework and the influence of the topology close to the active site are important to completely understand the reaction mechanism inside zeolite pores. Recently, with the new density functional M06-2X, the role of the confinement effect on reactions of unsaturated aliphatic, aromatic and heterocyclic compounds has been studied by using full quantum calculations. [20,21]

The aim of this work is to study the confinement effect of the zeolite framework (H-ZSM-5) on the adsorption and reaction mechanism of acetone tautomerization using the M06-2X density functional. The effect of the quantum cluster size on the energy profile of the reaction will also be discussed.

## Methodology

Three different clusters were employed to model the H-ZSM-5 zeolite. First, the 5T cluster, $AlSi_4O_4H_{13}$, was the smallest cluster used to represent only the Brønsted acid site of zeolite. Second, 12T the quantum cluster was used to include the 10-membered-ring window over the acid site of the H-ZSM-5. A silicon atom was substituted with an aluminum atom at the most favorable position (T12). The last and most realistic model for this study was the 34T quantum cluster. This model includes the structure of the intersection cavity where the straight pore channel and the zigzag channel are crossed (Figure 1). In our previous works, the 34T quantum cluster was found to be sufficient to cover the non covalent effect of the zeolite.[20,21]

The M06-2X density functional was used in all calculations.[24,25] During geometry optimizations, only the 5T active region of ≡SiOHAl$(OSi)_2$OSi≡ and the probe molecule were allowed to relax while the rest of the structure was kept fixed at the crystallographic coordinates.[26] For geometry optimizations, the 6-31G(d,p) basis set was used. In order to get more accurate interaction energies, the single point calculations with the 6-311+G(2df,2p) basis set were carried out. Transition state structures were checked to verify that they had one imaginary frequency corresponding to the reaction coordinate. All calculations were performed with the Gaussian 03 code[27] modified to incorporate the Minnesota Density Functional module 3.1 by Zhao and Truhlar.

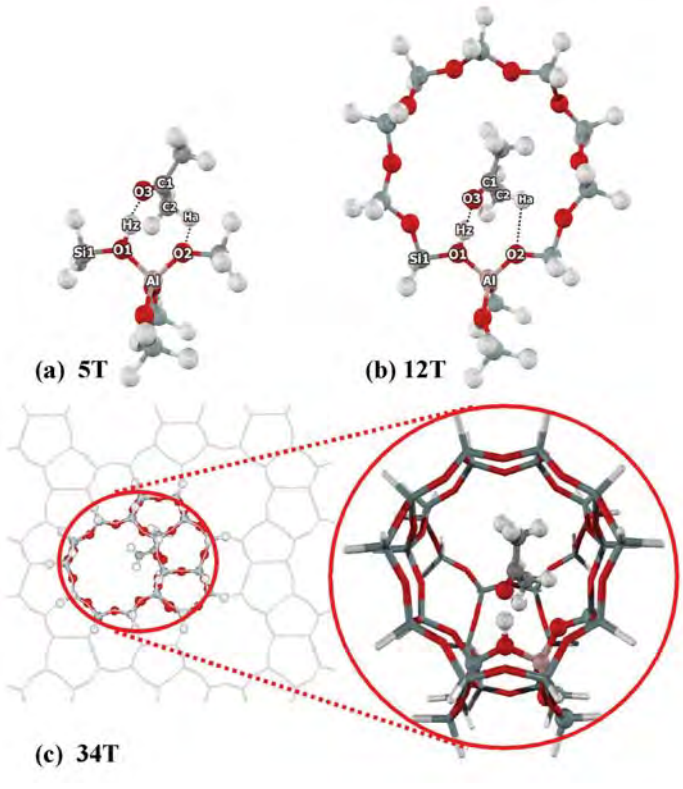


**Figure 1.** Quantum clusters used for modeling acetone adsorption and tautomerization on H-ZSM-5 zeolite (a) 5T, (b) 12T and (c) 34T model.

## Results and Discussion

**Nanocluster Models of Zeolite and Adsorption of Acetone.** All cluster models of H-ZSM-5 of zeolite, from the 5T unit to the 34T framework, are shown in Figure 1. The Brønsted acid O1-Hz bond lengths are 0.968, 0.970 and 0.970 Å, for the 5T, 12T and 34T cluster, respectively. The acidity is insignificantly changed with the O1-Hz bond length about 0.002 Å. The Al···Hz distances are between 2.33 – 2.36 Å, which compares well with the experimental values (2.38 – 2.48 ± 0.04 Å). [28,29]

The optimized structure of acetone adsorbed on the acid site at the intersection cavity of H-ZSM-5 zeolite is shown in Figure 2. An acetone molecule forms a hydrogen bond between its carbonyl oxygen atom, O3, and the Brønsted acidic proton, Hz, of zeolite. A weak interaction between a methyl hydrogen atom of acetone, Ha, and the adjacent oxygen atom, O2, is also present. Increasing the cluster sizes increases the interactions between acetone and the zeolite framework as evidenced by the increase of the O1-Hz bond distance from 0.97 Å to 1.05, 1.08 and 1.11 Å for the 5T, 12T and 34T, respectively and the increase of the C1-O3 double bond distance from 1.21 Å to 1.23 Å. The O1-Hz···O3 angle is near-linear (178.4, 179.1 and 177.6 degrees, respectively).

The adsorption energy of acetone on H-ZSM-5 was calculated at the M06-2X/6-311+G(2df,2p)//6-31G(d,p) level of theory. For the small 5T model, the adsorption energy is calculated to be -18.9 kcal/mol, which is much lower than the experimental report of -31.1 kcal/mol.[30] Increasing the cluster size results in higher adsorption energy. The calculated adsorption energies are -23.6 and –28.1 kcal/mol for the 12T and the 34T model respectively. The more realistic model, 34T gives the adsorption energy that agrees well with the experimental result. Solans-Monfort et al.[23] used ONIOM(B3LYP:MNDO) and ONIOM(B3LYP:AM1) approaches to study the interaction and reaction of acetaldehyde in ZSM-5 zeolite and reported the adsorption energy to be -7.4 and -9.3 kcal/mol, respectively. We also have tried the ONIOM(B3LYP/6-31G(d,p):UFF) and found the adsorption energy of acetone on the 12T/128T model of H-ZSM-5 is -26.3 kcal/mol. Although, the ONIOM model, with the right combination of high and low level methods, can give a good estimation of adsorption energy, it cannot account for all the non covalent effects of the zeolite because it uses a low level of calculations to represent the zeolite framework. The M06-2X, however, can account for all interactions with the zeolite framework quantum mechanically and the results show that the larger the quantum cluster size results the better they agree with the experimental result.

**Tautomerization of Acetone on H-ZSM-5 zeolite.** As discussed in the previous section, acetone is adsorbed on the active site of H-zeolite by strong hydrogen bonding. The reaction mechanism occurs concerted in one step in which the Brønsted acid proton is transferred to the carbonyl oxygen atom of acetone and the methyl C-H bond of acetone is dissociated giving a proton back to the negatively charged framework oxygen of zeolite, as shown in Figure 3. The enol product interacts with the zeolite via the π-adsorption complex. In all models, the transition state structure resembles the product structure. Figure 3 presents the energy profiles for the acetone tautomerization for the 34 quantum cluster of H-ZSM-5 zeolite. Selected geometric parameters of the intermediates and transition state are tabulated in Table 2 and are shown in Figures 4 and 5.

In the 34T cluster of ZSM-5 zeolite (Figure 3), the tautomerization reaction of acetone occurs in the intersection cavity of the 10T channel. The acetone molecule adsorbs by forming two hydrogen bonds, O1-Hz ··· O3 and C2-Ha ··· O2, with the zeolite acid site. The reaction proceeds via the concerted mechanism. The transition state structure (Figure

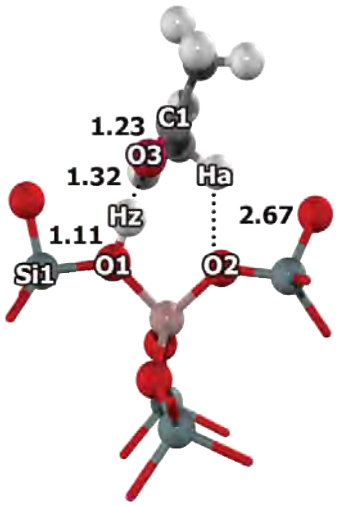


**Figure 2.** Optimized structure of the adsorption complex of acetone on the 34T cluster model of H-ZSM-5. For clarity atoms far from the acid site are omitted. Distances are in Å.

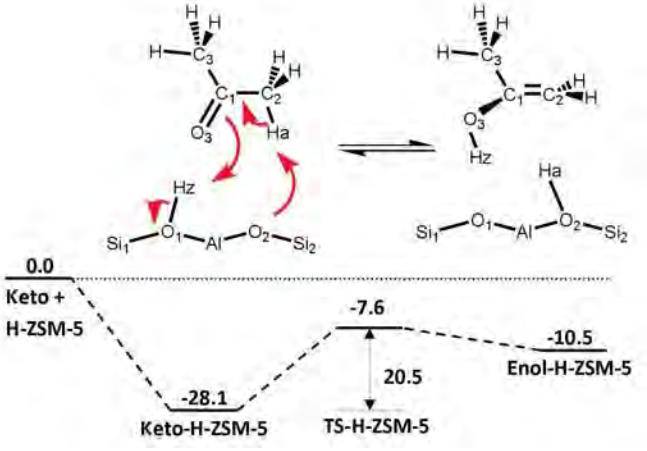


**Figure 3.** Potential energy diagram (kcal/mol) of the tautomerization of acetone on the 34T quantum cluster of H-ZSM-5.

4) is closer to the product structure. At the transition state, the hydroxyl Hz-O3 is already formed and the hydrogen atom of the methyl group (Ha) is dissociated and the C1-C2 double bond is formed. On the zeolite active site, the Brønsted O1-Hz bond is completely dissociated (O1-Hz distance =1.80 Å) and the O2-Ha bond is forming (O2-Ha distance =1.25 Å). An imaginary frequency at 917i $cm^{-1}$ associated with the transition state was found. Its vibrational motion corresponds to the moving of the Brønsted proton to the O3 of acetone and the proton Ha at the methyl group of acetone to the O2, oxygen of zeolite. The enol product (Figure 5) interacted with zeolite through the hydrogen bond between the Brønsted acid (Ha) and the π bond of enol (C1-C2). The unsymmetrical distances between Ha ··· C1 (2.25 Å) and Ha ··· C2 (1.76 Å) are found indicating a weak π interaction.

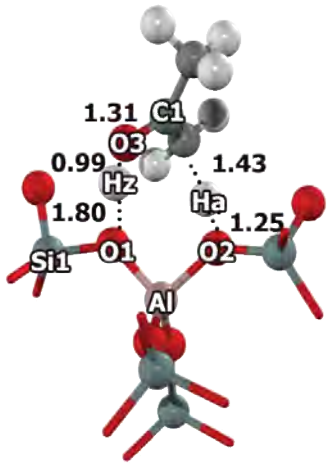


**Figure 4.** Optimized structure of the transition state complex of acetone on the 34T cluster model of H-ZSM-5. Distances are in Å.

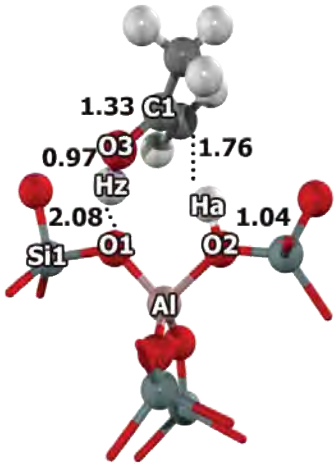


**Figure 5.** Optimized structure of the enol form of acetone on the 34T cluster model of H-ZSM-5. Distances are in Å.

**Table 1.** Reaction energies (kcal/mol) of the tautomerization reaction of acetone with various models of H-ZSM-5 zeolite, calculated with the M06-2X/6-311+G(2df,2p)//M06-2X/6-31G(d,p) level of theory (activation energy is in parenthesis).

| Model | Keto | TS | Enol |
|---|---|---|---|
| 5T | -18.9 | 0.9 (19.8) | -3.9 |
| 12T | -23.6 | -2.6 (21.0) | -6.7 |
| 34T | -28.1 | -7.6 (20.5) | -10.5 |

**Table 2.** Structure parameters for the tautomerization reaction of acetone on the 34T cluster of H-ZSM-5 (distances are in Å and angles are in degrees).

| | Bare | Keto | TS | Enol |
|---|---|---|---|---|
| **Distance** | | | | |
| Si1-O1 | 1.65 | 1.63 | 1.59 | 1.58 |
| Si2-O2 | 1.59 | 1.57 | 1.62 | 1.64 |
| Al -O1 | 1.82 | 1.78 | 1.71 | 1.69 |
| Al -O2 | 1.68 | 1.69 | 1.77 | 1.80 |
| Al-Oavg | 1.71 | 1.71 | 1.71 | 1.71 |
| Al···Hz | 2.35 | 2.45 | 3.19 | 3.52 |
| O1-Hz | 0.97 | 1.11 | 1.80 | 2.08 |
| Hz···O3 | | 1.32 | 0.99 | 0.97 |
| O1···O3 | | 2.42 | 2.74 | 2.52 |
| O3-C1 | 1.21 | 1.23 | 1.31 | 1.33 |
| C1-C2 | 1.52 | 1.49 | 1.38 | 1.36 |
| C2-Ha | 1.09 | 1.10 | 1.43 | 1.76 |
| C1···Ha | 2.14 | 2.10 | 2.07 | 2.25 |
| Ha···O2 | | 2.67 | 1.25 | 1.04 |
| **Angle** | | | | |
| Al-O1-Si1 | 130.6 | 128.4 | 127.6 | 127.4 |
| Al-O2-Si2 | 133.3 | 135.8 | 133.0 | 133.0 |
| O1-Hz-O3 | | 177.6 | 156.8 | 142.0 |
| O1-Al-O2 | 90.4 | 93.1 | 93.7 | 92.4 |

The calculated activation energy of acetone tautomerization in ZSM-5 zeolite is 20.5 kcal/mol. Previous MP2 studies reported that in the gas phase (isolated) acetone tautomerization required a high activation energy of 64.0 - 69.2 kcal/mol. [31,32] In the zeolite framework, the activation energy is greatly reduced. A similar result has been reported by using the ONIOM calculation.[23] It is interesting to note that in this study the activation energy of reverse reaction (enol to keto form) is also drastically reduced to only 2.9 kcal/mol (in the 34T model). For isolated acetone, the activation energy for the change from enol to the keto form is 52.4 kcal/mol and with the catalyzing effect of water molecules this energy is reduced to 20.9 kcal/mol.[32] The low activation energy for the enol to keto reaction is due to the interactions with the framework zeolite that can stabilize the transition state. This result was not observed in the previous ONIOM calculations.[23] Increasing the quantum cluster size results in the higher stabilization of adsorbed intermediates and the transition state and, thus, the lower activation energy.

## Conclusions

The effect of the zeolitic confinement on the adsorption and tautomerization of acetone has been studied by the new density functional theory, M06-2X. The adsorption energies are calculated to be -18.9, -23.6 and -28.1 kcal/mol for the 5T, 12T and 34T quantum cluster, respectively. We found that the extended framework significantly enhances the stabilities of adsorbed intermediates and the transition state. The large 34T model results in a better estimation of adsorption energy that is close to the experimental report of -31.1 kcal/mol. For the tautomerization of acetone on H-ZSM-5 zeolite, activation barriers are calculated to be 19.8, 21.0 and 20.5 kcal/mol, respectively. The reaction energies are 15.0, 16.9 and 17.6 kcal/mol, respectively. Moreover, the activation energy for the reverse reaction is also greatly reduced to 4.8, 4.1, 2.9 kcal/mol, respectively. The results obtained from this study indicate that the confinement effect from the large zeolite framework described by M06-2X functional is important to account for the interactions with the zeolite framework that lead to the stabilization of the transition state of the reaction mechanism.

**Acknowledgement.** This work was supported in part by grants from the National Science and Technology Development Agency (2009 NSTDA Chair Professor funded by the Crown Property Bureau under the management of the National Science and Technology Development Agency and NANOTEC Center of Excellence funded by the National Nanotechnology Center), The Thailand Research Fund, the Commission of Higher Education, Ministry of Education ("National Research University of Thailand" and "Postgraduate Education and Research Programs in Petroleum and Petrochemicals and Advanced Materials"). The support from the Kasetsart University Research and Development Institute (KURDI) and Graduate School Kasetsart University are also acknowledged. The authors are grateful to Donald G. Truhlar and Yan Zhao for their support with the M06-2X functional.

## References

(1) Wojciechowsku, B. W.; Corma, A. *Catalytic Cracking: Catalysts, Chemistry, and Kinetics*; Dekker: New York, 1986.
(2) Olah, G. A.; Molnar, A. *Hydrocarbon Chemistry*; John Wiley and Sons Inc.: New York, 1995.
(3) Maxwell, I. E.; Stork, W. H. J. *Introduction to Zeolite Science and Practice*; Elsevier: Amsterdam, 1991.
(4) Venuto, P. B. *Microporous Mater.* **1994**, *2(5)*, 297-411.
(5) Corma, A.; Garcia, H. *Chem. Rev. (Washington, DC, U. S.)* **2003**, *103(11)*, 4307-4365.
(6) Corma, A. *J. Catal.* **2003**, *216(1-2)*, 298-312.
(7) Hunger, M. *Microporous Mesoporous Mater.* **2005**, *82(3)*, 241-255.
(8) Panov, A. G.; Fripiat, J. J. *J. Catal.* **1998**, *178(1)*, 188-197.
(9) Biaglow, A. I.; Sepa, J.; Gorte, R. J.; White, D. *J. Catal.* **1995**, *151(2)*, 373-384.
(10) Flego, C.; Perego, C. *Appl. Catal., A* **2000**, *192(2)*, 317-329.
(11) Xu, T.; Munson, E. J.; Haw, J. F. *J. Am. Chem. Soc.* **1994**, *116(5)*, 1962-1972.
(12) Xu, M.; Wang, W.; Hunger, M. *Chem. Commun. (Cambridge, U. K.)* **2003,** *(6)*, 722-723.
(13) Derouane, E. G.; Chang, C. D. *Microporous Mesoporous Mater.* **2000**, *35-36*,425-433.
(14) Kasuriya, S.; Namuangruk, S.; Treesukol, P.; Tirtowidjojo, M.; Limtrakul, J. *J. Catal.* **2003**, *219(2)*, 320-328.
(15) Namuangruk, S.; Pantu, P.; Limtrakul, J. *J. Catal.* **2004**, *225(2)*, 523-530.
(16) Namuangruk, S.; Pantu, P.; Limtrakul, J. *ChemPhysChem* **2005**, *6(7)*, 1333-1339.
(17) Maihom, T.; Boekfa, B.; Sirijaraensre, J.; Nanok, T.; Probst, M.; Limtrakul, J. *J. Phys. Chem. C* **2009**, *113(16)*, 6654-6662.
(18) Pantu, P.; Boekfa, B.; Limtrakul, J. *J. Mol. Catal. A: Chem.* **2007**, *277(1-2)*, 171-179.
(19) Kumsapaya, C.; Bobuatong, K.; Khongpracha, P.; Tantirungrotechai, Y.; Limtrakul, J. *J. Phys. Chem. C* **2009**, *113(36)*, 16128-16137.
(20) Boekfa, B.; Choomwattana, S.; Khongpracha, P.; Limtrakul, J. *Langmuir* **2009**, DOI: 10.1021/la901841w.
(21) Boekfa, B.; Choomwattana, S.; Maitarad, P.; Limtrakul, P.; Limtrakul, J. *Nanotech Conference & Expo 2009* **2009**, *3*,268-271.
(22) Rodriguez-Santiago, L.; Vendrell, O.; Tejero, I.; Sodupe, M.; Bertran, J. *Chem. Phys. Lett.* **2001**, *334(1,2,3)*, 112-118.
(23) Solans-Monfort, X.; Bertran, J.; Branchadell, V.; Sodupe, M. *J. Phys. Chem. B* **2002**, *106(39)*, 10220-10226.
(24) Zhao, Y.; Truhlar, D. G. *J. Phys. Chem. C* **2008**, *112(17)*, 6860-6868.
(25) Zhao, Y.; Truhlar, D. G. *Acc. Chem. Res.* **2008**, *41(2)*, 157-167.
(26) Van Koningsveld, H.; Van Bekkum, H.; Jansen, J. C. *Acta Crystallogr., Sect. B: Struct. Sci.* **1987**, *B43(2)*, 127-132.
(27) Frisch, M. J.; Trucks, G. W.; Schlegel, H. B.; Scuseria, G. E.; Robb, M. A.; Cheeseman, J. R.; Montgomery, J. A., Jr.; Vreven, T.; Kudin, K. N.; Burant, J. C.; Millam, J. M.; Iyengar, S. S.; Tomasi, J.; Barone, V.; Mennucci, B.; Cossi, M.; Scalmani, G.; Rega, N.; Petersson, G. A.; Nakatsuji, H.; Hada, M.; Ehara, M.; Toyota, K.; Fukuda, R.; Hasegawa, J.; Ishida, M.; Nakajima, T.; Honda, Y.; Kitao, O.; Nakai, H.; Klene, M.; Li, X.; Knox, J. E.; Hratchian, H. P.; Cross, J. B.; Adamo, C.; Jaramillo, J.; Gomperts, R.; Stratmann, R. E.; Yazyev, O.; Austin, A. J.; Cammi, R.; Pomelli, C.; Ochterski, J. W.; Ayala, P. Y.; Morokuma, K.; Voth, G. A.; Salvador, P.; Dannenberg, J. J.; Zakrzewski, V. G.; Dapprich, S.; Daniels, A. D.; Strain, M. C.; Farkas, O.; Malick, D. K.; Rabuck, A. D.; Raghavachari, K.; Foresman, J. B.; Ortiz, J. V.; Cui, Q.; Baboul, A. G.; Clifford, S.; Cioslowski, J.; Stefanov, B. B.; Liu, G.; Liashenko, A.; Piskorz, P.; Komaromi, I.; Martin, R. L.; Fox, D. J.; Keith, T.; Al-Laham, M. A.; Peng, C. Y.; Nanayakkara, A.; Challacombe, M.; Gill, P. M. W.; Johnson, B.; Chen, W.; Wong, M. W.; Gonzalez, C.; Pople, J. A. *Gaussian 03, revision B.05; Gaussian, Inc.: Pittsburgh, PA*, 2003.
(28) Klinowski, J. *Chem. Rev.* **1991**, *91(7)*, 1459-1479.
(29) Freude, D.; Klinowski, J.; Hamdan, H. *Chem. Phys. Lett.* **1988**, *149(4)*, 355-362.
(30) Sepa, J.; Lee, C.; Gorte, R. J.; White, D.; Kassab, E.; Evleth, E. M.; Jessri, H.; Allavena, M. *J. Phys. Chem.* **1996**, *100(47)*, 18515-18523.
(31) Lee, D.; Kim, C. K.; Lee, B.; Lee, I. *J. Comput. Chem.* **1997**, *18(1)*, 56-69.
(32) Zakharov, M.; Masunov, A. E.; Dreuw, A. *J. Phys. Chem. A*, **2008**, *112(41)*, 10405-10412.

# QUANTUM-CHEMICAL ANALYSIS OF REACTIONS BETWEEN PYRIDINE AND THE INDUSTRIALLY IMPORTANT PETROCHEMICAL ZEOLITE CATALYST

*Pemikar Srifa*[a,b,c], *Somkiat Nokbin*[a,b], *Bundet Boekfa*[b,c,d] *and Jumras Limtrakul*[a,b,c*]

[a] Laboratory for Computational & Applied Chemistry, Physical Chemistry Division, Department of Chemistry, Faculty of Science, Kasetsart University, Bangkok 10900, Thailand
[b] Center of Nanotechnology, Kasetsart University Research and Development Institute, Kasetsart University, Bangkok 10900, Thailand
[c] NANOTEC Center of Nanotechnology, National Nanotechnology Center, Kasetsart University, Bangkok 10900, Thailand
[d] Chemistry Department, Faculty of Liberal Art and Science, Kasetsart University Kamphaeng Saen Campus, Nakhon Pathom 73140, Thailand

## Introduction

Acidic-Faujasite (H-FAU), one of the aluminosilicate zeolites containing the protonate sites, has been frequently used as the heterogeneous acid catalyst for petrochemical processes, especially the heavy oil cracking[1-3]. Due to its primitive building unit which is the fusion of two supercages[4,5], the large molecules such as heavy oil can be trapped by forming a strong hydrogen bond between those guest molecules and Brønsted bridging hydroxyl groups Si-OH-Al within the porous intersection of the catalyst before being reformed to smaller molecules. The catalytic properties of acidic sites around the area are thus a significant process to find out the catalytic proficiency of this zeolitic 'nanoreactor'.

Generally, zeolite acidity can be investigated by the adsorption of basic probe molecules on the Brønsted acidic site of zeolite using many straightforward methods such as microcalorimetry, temperature-programmed desorption (TPD), Nuclear Magnetic Resonance Spectroscopy (NMR) or other appropriate methods[6-11]. In the aspect of using pyridine as the probe molecule, these experiments explain that the pyridinium complex ($PYH^+$) first occurred during the adsorption process and is then stabilized by interacting with anionic zeolite ($Z^-$)[12-14].

In order to study the hidden agenda of these steps, theoretical investigation and experimental data have been combined, since it clearly provides not only the information on the proton transfer from the zeolite active site to an adsorbate but also the confinement effect of the framework: how the physical geometry, excluding the active site with the long range interaction of zeolite, affect the measured adsorption enthalpies[15,16]. Several theoretical elucidations using the quantum cluster calculation of pyridine adsorbed on zeolites have been reported[17-21]. Among these studies, there are some reports of our group related to the adsorption energy and geometry changes when pyridine adsorbed on different zeolitic cluster sizes using the embedded-ONIOM method[20,21] in which the long-range electrostatic interactions are represented on the outer layer of the calculated model. Although the results of this hybrid method are usually in agreement with experiments, the imbalance of the van der Waals interaction represented by the two methods combined in the ONIOM scheme may create an error, so the accuracy of system studied for the selected methods must be carefully checked. In the present study, to avoid the weakness of the proposed model, we thus employ full quantum methods with the newly developed hybrid density functional M06-2X, which cover the important weak interactions[22,23], for investigation of the interaction between pyridine and different model sizes of H-FAU. The effects of the infinite zeolitic framework on the cluster model are also included by a set of point charges generated by the embedded nanocluster model.

The goals of this study are to study the confinement effect from the zeolite on the adsorption properties of pyridine, and to demonstrate the combined interactions between the newly developed density functional theory, M06-2X, and the extended point charge. We will discuss the behavior of the different sizes of zeolite framework.

## Methods

Five different sizes of H-FAU model clusters, 5T, 14T, 38T, 54T and 120T cluster (T represents tetrahedral of Si or Al atoms) were employed to investigate the adsorption of pyridine, as shown in Figure 1. The most energetically favored Si position, T1, was replaced by an Al atom and used in all cluster sizes[24] to generate the Brønsted acid site. The 5T quantum cluster, $AlSi_4O_4H_{13}$, is considered as the smallest unit required to represent the Brønsted acid site of zeolite. The larger 14T cluster which covers the 12 membered-ring (12 MR) at the intersection window of the two supercages of H-FAU is then considered. The model was extended to 38T to cover the other shell of the Si unit around the 12MR. The

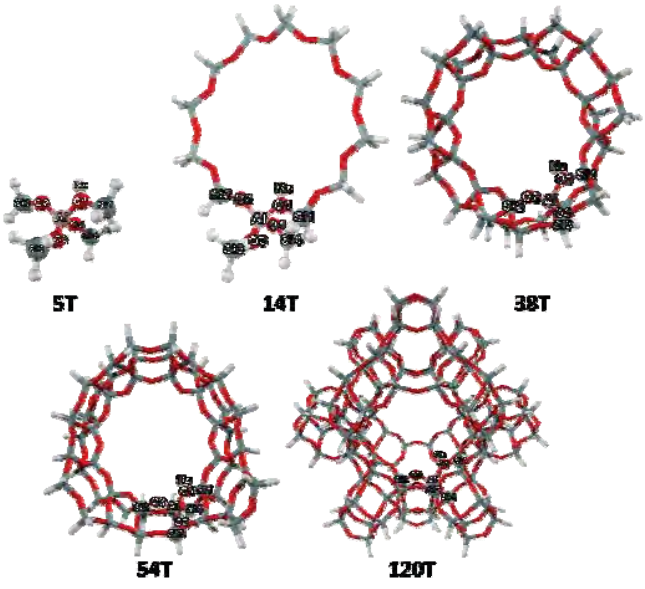


**Figure 1.** Presentation of H-FAU models in different sizes. Relaxation atoms are shown in balls, whereas the rest is symbolized with wireframes.

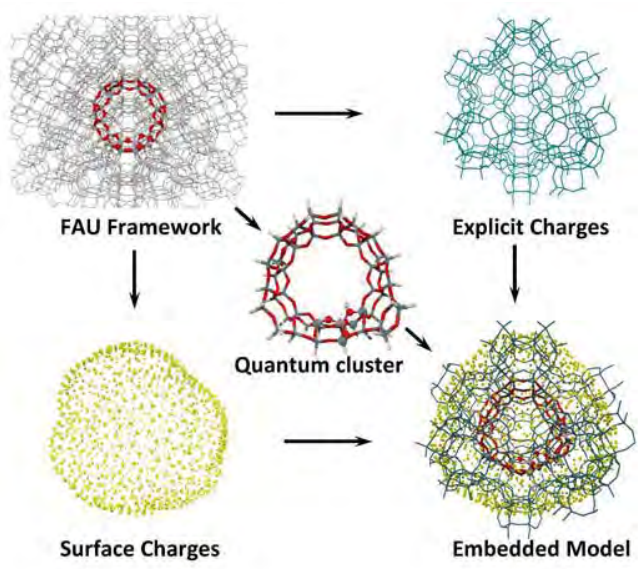


**Figure 2.** Surface charge representation of External electrostatic potential scheme.

54T is similar to the 38T, but the framework is more extended. Considered, in order to account for the important confinement effect of the zeolite, is that the larger model, 120T, acts as a nanoscopic reaction vessel which covers the two supercages in H-FAU. It can be expected that the largest 120T cluster represents the entire solid network of H-FAU.

The adsorptions of pyridine on different H-FAU models are calculated with the M06-2X functional and 6-31G(d,p) level of theory. Geometry optimizations are carried out for the 5T, 14T and 38T clusters with the criterion that the active region 5T and the probe molecule are allowed to relax while the rest remain fixed at the crystallographic positions. To determine the model size that can best represent the interaction properties, single-point energy calculations of the 54T and 120T at the M06-2X/6-31G(d,p) level were carried out to get more accurate energies, including the confinement effect of H-FAU.

To study the electrostatic contribution of the extended framework, the Madelung potential from the extended lattice is reproduced by point charges enclosed around the 54T cluster, as shown in Figure 2 (see ref. 21 for more details). The M06-2X calculation and the optimized electrostatic point charges method, called "embedded M06-2X approach", has been successfully applied to study the adsorption and reaction mechanism of unsaturated aliphatic, aromatic and heterocyclic compounds on H-ZSM-5 zeolites[25]. The calculated adsorption energies were obtained from the difference between the total energy of the complex and the isolated species in each system as described by $\Delta E_{ads} = E_{(Complex)} - E_{(Zeolite)} - E_{(Pyridine)}$. All quantum cluster calculations were performed by using the Gaussion 03 program[26] incorporated with the Minnesota Density Functionals module 3.1 by Zhao and Truhlar[22,23].

**Results and Discussion**

**Molecular cluster and adsorption structure of pyridine on H-FAU zeolite.** The selected geometrical parameters for 5T, 14T and 38T models are shown in Table 1. The lengthening of the O1-Hz bond, as a function of the cluster size, from 0.960 Å (5T) → 0.970 Å (14T) → 0.971 Å (38T) indicates the influence of the zeolite framework on acidity. The Al-O1-Si1 angle, one of the significant parameters for considering zeolite acidity, is found to be slightly increased from the 5T model by 0.4 and 1.7 degrees for the 14T and the 38T, respectively, demonstrated that the acidity values were increased as with the larger model. The calculated Al···Hz distances are measured in the range of 2.450-2.532 Å, which agree well with reported experimental observations by Klinoski of 2.380 - 2.480 Å[27], indicated the validation of the calculation models.

At the adsorption step, the pyridine adsorptions on H-FAU are clearly demonstrated the effects of the framework on the existence of adsorbate/adsorbent species in the system. For the small 5T cluster, we found only a simple hydrogen-bonded pyridine/zeolite complex in which the pyridine is held over the Brønsted acid site of H-FAU zeolite. The significant lengthening of the O1-Hz bond compared with the bare zeolite system can be observed (from 0.960 to 1.320 Å). The intermolecular distance between pyridine and zeolite, N-O1, is 2.489 Å. The N-Hz-O1 bond angle is found to be near-linear (178.6 degree), which describes the quite strong hydrogen bond interaction in the adsorbing complex. A weaker interaction between the hydrogen of pyridine, H1, and the adjacent oxygen, O2, is also presented. The changes of the zeolites structures are in accordance with Gutmann's rules[28,29], i.e., a lengthening of the O1-Hz bond, a shortening of the Al-O1 bond and, a lengthening of the Al-O2 bond.

**Table 1. Geometrical Parameters of Pyridine Adsorbed on Three Sizes of H-FAU Models. (Distances in Å, Angles in Degrees).**

| Parameter | System | | | | | |
|---|---|---|---|---|---|---|
| | 5T | | 14T | | 38T | |
| | Isolated | Complex | Isolated | Complex | Isolated | Complex |
| O1-Hz | 0.960 | 1.320 | 0.970 | 1.574 | 0.971 | 1.634 |
| O2-Hz | 2.692 | 2.489 | 2.822 | 2.864 | 3.004 | 3.058 |
| O2-H1 | - | 2.196 | - | 2.162 | - | 2.127 |
| Al-O1 | 1.926 | 1.850 | 1.946 | 1.812 | 1.968 | 1.821 |
| Al-O2 | 1.710 | 1.728 | 1.716 | 1.758 | 1.724 | 1.774 |
| Al-O3 | 1.709 | 1.718 | 1.711 | 1.730 | 1.718 | 1.737 |
| Al-O4 | 1.700 | 1.711 | 1.703 | 1.725 | 1.710 | 1.731 |
| Al-Hz | 2.450 | 2.525 | 2.499 | 2.789 | 2.532 | 2.865 |
| N-O1 | - | 2.489 | - | 2.649 | - | 2.685 |
| N-Hz | - | 1.357 | - | 1.074 | - | 1.063 |
| <Al-O1-Si1 | 130.6 | 128.3 | 130.9 | 128.5 | 132.3 | 131.0 |
| <Al-O1-Hz | 111.3 | 113.5 | 113.6 | 110.8 | 114.6 | 112.4 |
| <Al-O2-H1 | - | 120.4 | - | 122.0 | - | 115.9 |
| < N-Hz-O1 | - | 178.6 | - | 179.2 | - | 175.0 |

By enlarging the model to 14T, an ion-pair complex can be found. Increasing the model cluster was found to enhance the protonation of the Brønsted acidic site of zeolites to pyridine resulting in the formation of the pyridinium ion pair complex [$PYH^+$] by increasing of the O1-Hz bond to 1.574 Å corresponds with decreasing the N-Hz bond to 1.074 Å. The ion-pair interaction is also found on the more realistic 38T model, as shown in Figure 3. The longest O1-Hz bond (1.634 Å) and the shortest N-Hz bond (1.063 Å) indicate a stronger interaction between pyridine and H-FAU zeolite. The N-O1 intermolecular distances, on the one hand, are found to increase the model, expanding it from 2.489 Å (5T) to 2.685 Å (38T) while the O2···H1 distances, on the other hand, are decreased from 2.196 Å (5T) to 2.127 Å (38T). These suggest the greater stability of the adsorption complex in the larger cluster model. As a result, the interaction between pyridine and H-FAU is more stable as a function of the cluster size.

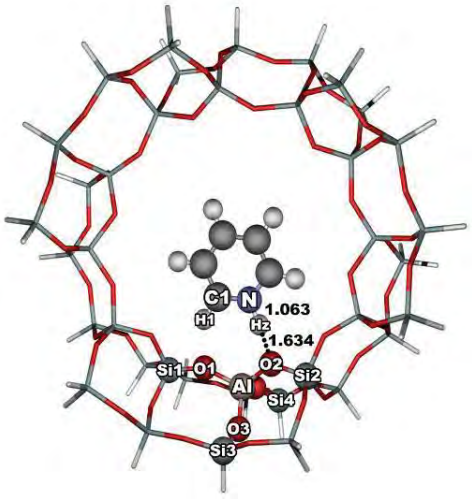


**(a)**

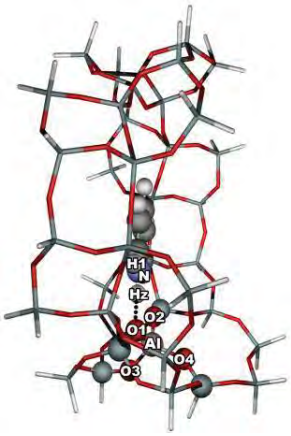


**(b)**

**Figure 3.** Presentation of the Pyridine interacting with the 38T model of H-FAU zeolite through the 12MR channel **(a)** and the side view **(b)**. All bond lengths are in angstroms.

**The energetic of pyridine on H-FAU zeolite.** All calculated pyridine adsorption energies have been summarized in Table 2. As expected, the interaction energy is stronger if the ion-pair is more pronounced. In energy features, the small cluster (5T unit) gives the adsorption energy of -24.9 kcal/mol, which is lower than the experimental data of -43.1 kcal/mol[30]. This is due to the rather weak interaction of the hydrogen-bonded configuration of the adsorption complex existing in the system. As for the 14T and 38T models, the adsorption energy increases considerably to -41.7 and -42.7 kcal/mol, respectively, resulting from the more stable ion-pair configuration of [$PYH^+$]/[$FAU^-$]. The adsorption energy slightly changes to -43.5 and -44.1 kcal/mol, respectively, by increasing the model sizes to 54T and 120T. The adsorption energy from the 54T model gives virtually the same results as the 120T model. This indicates that the 54T cluster is a good compromise between accuracy and the practical computational time.

Since the ion-pair complex existed in the larger model studied, the electrostatic potential from the infinite lattice of zeolite might play a bigger role on the ion-pair interaction of pyridine on H-FAU. Therefore, the "embedded M06-2X method" the combination between the M06-2X functional and the embedded approach was considered to examine the electrostatic potential effect. The optimized point charges are embedded into the quantum cluster 54T as shown in Figure 2. From Table 2, the adsorption energies from the M06-2X on 38T and the embedded M06-2X on 54T are -42.7 and -44.4 kcal/mol, respectively. The latter value agrees well with both the largest quantum cluster, 120T (-44.1 kcal/mol) and the experimental value (-43.1 kcal/mol). This suggests that the embedded M06-2X is more practical and accurate to study the adsorption of pyridine on zeolite. The embedding of the optimized point charges causes the adsorption energy obtained from the 54T cluster to be nearly identical with those of the120T cluster.

**Table 2. Comparison of Adsorption Energies (kcal/mol) of Pyridine on Various Model Sizes of H-FAU.**

| Model | Method | Adsorption Energy |
|---|---|---|
| 5T[a] | M06-2X | -24.9 |
| 14T[a] | M06-2X | -41.7 |
| 38T[a] | M06-2X | -42.7 |
| 54T[b] | M06-2X | -43.5 |
| 120T[b] | M06-2X | -44.1 |
| 54T[b] | Embedded M06-2X | -44.4 |
| Experimental value | | -43.1 |

[a] Energies calculated from full quantum optimization using the M062X/6-31G(d,p) level of theory.
[b] Energies obtained from single point calculation using geometries from 38T model clusters treated with the same method and basis set.

## Conclusions

The effect of the zeolitic nanocage on the adsorption properties of the important heterocyclic base, pyridine, of different sizes of H-FAU has been investigated by the M06-2X density functional with the 6-31G(d,p) basis set. The zeolitic 'nanoreactor' porous intersection, where chemical reactions take place, is represented by a small cluster of 5T up to a realistic nanocluster of 120 tetrahedral atoms. The adsorption energies were calculated to be -24.9, -41.7, -42.7, -43.5 and -44.1 kcal/mol for 5T, 14T, 38T, 54T and 120T, respectively and compare with the experimental value of -43.1 kcal/mol The results demonstrate that the newly developed hybrid density functional M06-2X is able to cover important weak interactions, especially the van der Waals interaction which is essential for describing the nano-confinement effect from the zeolite framework. Then, the adsorption energies are more accurate if the embedded nanocluster model is used. The effects of the infinite zeolitic framework on the cluster model are also included by a set of point charges generated by the embedded nanocluster model. The energy for the adsorption of pyridine on an embedded nanocluster model is predicted to be -44.4 kcal/mol, which is very close to experimental observations. The nano-confinement effect of the extended zeolite framework has been clearly demonstrated not only to stabilize the pyridine/zeolite complexes but also to improve their corresponding adsorption energies to approach the experimental benchmark. All results, for the model considered in this study, confirm that the embedded M06-2X method can be used effectively to study the reaction between the pyridine molecule and other zeolites for further comparison of the acidity of various zeolites.

**Acknowledgement.** This work was supported in part by grants from the National Science and Technology Development Agency (2009 NSTDA Chair Professor funded by the Crown Property Bureau under the management of the National Science and Technology Development Agency and NANOTEC Center of Excellence funded by the National Nanotechnology Center), the Commission of Higher Education, Ministry of Education ("National Research University of Thailand" and "Postgraduate Education and Research Programs in Petroleum and Petrochemicals and Advanced Materials"). The support from the Kasetsart University Research and Development Institute (KURDI) is also acknowledged. The authors are grateful to Donald G. Truhlar and Yan Zhao for their support with the M06-2X functional.

## References

(1) Ng, S.; Zhu, Y.; Humphries, A.; Zheng. L; Ding, F.; Yang, L.; Yui, S. *Energy Fuels* **2002**, *16*, 1196.
(2) Kuznicki, S. M.; McCaffrey, W. C.; Bian, J.; Wangen, E.; Koenig, A.; Lin, C. H. *Microporous Mesoporous Mater*. **2007**, *105*, 268-272.
(3) Stoyanov, S. R.; Gusarov, S.; Kuznicki, S. M.; Kovalenko, A. *J. Phys. Chem. C*. **2008**, *112*, 6794-6810.
(4) Breck, D. W. *U.S. Patent 3*, **1964**, 130,007.
(5) Costenoble, M. L.; Mortier, W. J.; Uytterhoeven, J. B. *J. Chem. Soc., Faraday Trans. I*. **1976**, *72*, 1877-1883.
(6) Gorte, R. J. *Catal. Today* **1996,** *28*, 405-414.
(7) Auroux, A. *Top. Catal*. **2002,** *19*, 3–4.
(8) Mishin, I. V.; Brueva, T. R.; Kapustin, G. I. *Adsorpt. Sci. Technol*. **2005,** *11*, 415–424.
(9) Jia, C.; Massiani, P.; Barthomeuf, D. *J. Chem. Soc. Faraday Trans*. **1993,** *89(19)*, 3659-3665.
(10) van Santen, R. A.; Kramer, G. J. *Chem. Rev*. **1995**, *95*, 637-660.
(11) Gorte, R. J. *Catal. Lett*. **1999**, *62*, 1–13.
(12) Parrillo, D. J.; Lee, C.; Gorte, R. J.; White, D.; Farneth, W. E. *J. Phys. Chem*. **1995**, *99*, 8745.
(13) Kubelkova, L.; Kotrla, J.; Florian, J. *J. Phys. Chem*. **1995**, *99*, 10285.
(14) Savitz, S.; Myers, A. L.; Gorte, R. J.; White, D. *J. Am. Chem. Soc*. **1998**, *120*, 5701.
(15) Derouane, E. G.; Fripiat, J. G. *J. Phys. Chem*. **1987**, *91*, 145.
(16) Derouane E.G.; Chang C. D. *Microporous Mesoporous Mater*. **2000**, *35*, 425–433.
(17) Rozanska, X.; van Santen, R. A.; Hutschka, F. *J. Catal*. **2001**, *200*, 79.
(18) Komiyama, M.; Kobayashi, M. *J. Phys. Chem. B* **1999**, *103*, 48.
(19) Ventura, M. C.; Akacem, Y.; Kassab E. *J. Phys. Chem. C* **2008**, *112*, 19045–19054.
(20) Lomratsiri, J.; Probst, M.; Limtrakul, J. *J. Mol. Graph. Model.* **2006,** *25*, 219–225.
(21) Injan, N.; Pannorad, N.; Probst, M.; Limtrakul, J. *Int J. Quantum Chem.* **2005**, 105, 898.
(22) Zhao, Y.; Truhlar, D. G. *J. Phys. Chem .C* **2008,** *112(17)*, 6860-6868.
(23) Zhao, Y.; Truhlar, D. G. *Theor. Chem. Acc*.**2008**, *120*, 215-241.
(24) Suzuki, K.; Noda, T.; Sastre, G.; Katada, N.; Niwa, M. *J. Phys. Chem. C* **2009**, *113*, 5672–5680.
(25) Boekfa, B.; Choomwattana, S.; Khongpracha, P.; Limtrakul, J. *Langmuir* **2009**, DOI: 10.1021/la901841w.
(26) Frisch, M. J. T.; Trucks, G. W.; Schlegel, H. B.; Scuseria, G. E.; Robb, M. A.; Cheeseman, J. R.; Montgomery, Jr., J. A.; Vreven, T.; Kudin, K. N.; Burant, J. C.; Millam, J. M.; Iyengar, S. S.; Tomasi, J.; Barone, V.; Mennucci, B.; Cossi, M.; Scalmani, G.; Rega, N.; Petersson, G. A.; Nakatsuji, H.; Hada, M.; Ehara, M.; Toyota, K.; Fukuda, R.; Hasegawa, J.; Ishida, M.; Nakajima, T.; Honda, Y.; Kitao, O.; Nakai, H.; Klene, M.; Li, X.; Knox, J. E.; Hratchian, H. P.; Cross, J. B.; Bakken, V.; Adamo, C.; Jaramillo, J.; Gomperts, R.; Stratmann, R. E.; Yazyev, O.; Austin, A. J.; Cammi, R.; Pomelli, C.; Ochterski, J. W.; Ayala, P. Y.; Morokuma, K.; Voth, G. A.; Salvador, P.; Dannenberg, J. J.; Zakrzewski, V. G.; Dapprich, S.; Daniels, A. D.; Strain, M. C.; Farkas, O.; Malick, D. K.; Rabuck, A. D.; Raghavachari, K.; Foresman, J. B.; Ortiz, J. V.; Cui, Q.; Baboul, A. G.; Clifford, S.; Cioslowski, J.; Stefanov, B. B.; Liu, G.; Liashenko, A.; Piskorz, P.; Komaromi, I.; Martin, R. L.; Fox, D. J.; Keith, T.; Al-Laham, M. A.; Peng, C. Y.; Nanayakkara, A.; Challacombe, M.; Gill, P. M. W.; Johnson, B.; Chen, W.; Wong, M. W.; Gonzalez, C.; and Pople, J. A.;. *Gaussian 03, revision B.05*, Gaussian, Inc., Wallingford CT, 2004.
(27) Klinowski, *J. Chem. Rev*. **1991**, *91*, 1459.
(28) Gutmann, V. *The Donor–Acceptor Approach to Molecular Interaction*, Plenum Press, New York, **1978**.
(29) Gutmann, V.; Resch, G.; Linert, W. *Coord. Chem. Rev.***1982**, *43*, 133–164.
(30) Parrillo, D. J.; Gorte, R. J. *J. Phys. Chem.* **1993**, *97*, 8786.

# WOXIDATIVE DEHYDROGENATION OF PROPANE OVER A VO2-EXCHANGED MCM-22: A NEWLY DEVELOPED DFT STUDY

*Sippakorn Wannakao[a,b], Bundet Boekfa[b,c], Pipat Khongpracha[a,b] and Jumras Limtrakul[a,b*]*

[a] Laboratory for Computational & Applied Chemistry, Physical Chemistry Division, Department of Chemistry, Faculty of Science, Kasetsart University, Bangkok 10900, Thailand
[b] Center of Nanotechnology, Kasetsart University Research and Development Institute, Bangkok 10900, Thailand
[c] Chemistry Department, Faculty of Liberal Arts and Science, Kasetsart University Kamphaeng Saen Campus, Nakhon Pathom 73140, Thailand

## Introduction

Propene is one of the most important starting materials in many chemical industry processes, for example, polymer synthesis processes. With the continuing scarcity of natural resources, the demand for propene will increase significantly in the near future. Concerted efforts to find inexpensive ways to produce propene are now high on research priority lists. Among those, oxidative dehydrogenation of the lower cost raw material, propane, is an outstanding method for the production of propene due to its lower energy consumption, lower coke and $CO_x$ byproducts and high selectivity to the desired product compared to the conventional dehydrogenation process.[1-3]

Vanadia supported catalysts have been proven to be active and selective for this reaction.[1-14] Silica supported vanadium oxide catalysts are highly propene selective catalysts because they do not favor direct combustion of the propane reactant to $CO_x$ species, compared to alumina and titania supports.[13,14] Zeolites and mesoporous silicas which are industrially important catalysts can also be used as the silica support catalysts.[14-18] Even though many theoretical studies of the propane oxidative dehydrogenation over vanadium oxides and silica supported catalysts were conducted, i.e., gas phase[19,20], cluster[21-23] and periodic[24,25] systems, to the best of our knowledge, porous silica supported vanadia catalysts have never been studied theoretically for the propane oxidative dehydrogenation reaction. For studying systems in the confined space, van der Waals interaction plays an important role in adsorption and catalysis processes. In our previous calculations on various reactions in zeolites, ONIOM (B3LYP:UFF) was found to reproduce the experimental data. Even due to the compensation between the overestimated framework confinement effect and the underestimated interaction in the active region, this method is accurate and economic in computational cost.[26-34] Recently, Zhao and Truhlar have developed a new type of DFT (M06-series) in which the dispersion force was taken into account.[35,36] In our recent studies, this method has been proved to be one of the useful methods for studying adsorption and reaction mechanisms of the van der Waals dominant species over zeolite systems.[37-39]

To understand the reaction which occurs in a confined space, a well calibrated $VO_2$-exchanged-MCM-22 ($VO_2$-MCM22) model which was recently experimentally studied[17], was used for studying the propane ODH reaction. In this work, M06-DFT has been employed to study the reaction mechanism of the propane oxidative dehydrogenation reaction over the catalyst. The reaction can be divided into two main steps, 1) methylene (-$CH_2$-) hydrogen activation and 2) propene formation. A reoxidation of the catalyst was not considered because it is not the rate limiting step for the propane oxidative dehydrogenation reaction.[40]

## Methods

The structure of the MCM-22 zeolite cluster was obtained from the crystal structure[41], represented by clusters of 14T (T = tetrahedral of Si or Al atoms). The cluster covers the 12-membered ring at the intersection of two channels which is considered to be an appropriate active site of the catalyst (see Figure 1). An Al atom was located at the T1 position, the most stable configuration of this model.[42] The Vanadium oxide specie $[VO_2]^+$ is placed at the highly accessible Brønsted acid site. All geometry optimizations were performed by the M06-L functional using the 6-31G(d,p) level of theory for H, C, O, Al and Si atoms, while the effective core potentials (ECP) of Stuttgart and Born[43] were employed for the V atom. To cover the confinement effect from the zeolite framework, the model is extended to a 120T structure. The 120T includes a supercage of MCM-22 where the adsorbates are trapped inside. During the optimization, only the active site of the catalyst ($VO_2/AlSi_4O_4$) and probe molecule were allowed to relax, while the rest was kept fixed as the original crystal structure. Normal mode analysis of the transition states have only one imaginary frequency whose mode corresponds to the designated reaction. The total spin was kept constant at the singlet state which was found to be the most stable state among the considered reaction steps.[19] All calculations were performed by the Gaussian 03 package[44] incorporated with the Minnesota Density Functionals module 3.1 by Zhao and Truhlar.

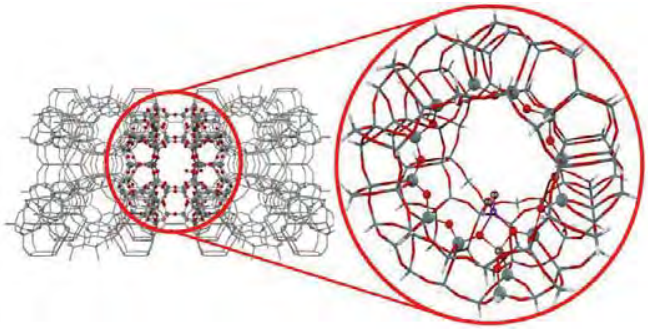

**Figure 1.** Illustration of the selected structure of $VO_2$-MCM-22. Balls represent the fully optimized quantum 14T cluster

and sticks represent an extended zeolitic framework of a realistic 120T quantum cluster.

**Table 1: Optimized Structural Parameters of Reaction Complexes During the Propane Oxidative Dehydrogenation Over $VO_2$-MCM-22 Which Were Obtained From M06L/6-31G(d,p) Calculations.**

| | Isolated | ADS | TS1 | INT1 | TS2 | INT2 |
|---|---|---|---|---|---|---|
| **Distance** | | | | | | |
| Al-V | 2.781 | 2.774 | 2.926 | 2.963 | 2.967 | 2.931 |
| V-O1 | 1.586 | 1.587 | 1.684 | 1.769 | 2.011 | 2.225 |
| V-O2 | 1.591 | 1.592 | 1.583 | 1.577 | 1.570 | 1.582 |
| Al-Oa | 1.766 | 1.768 | 1.765 | 1.742 | 1.753 | 1.758 |
| Al-Ob | 1.766 | 1.768 | 1.735 | 1.747 | 1.732 | 1.727 |
| V-Oa | 1.980 | 1.974 | 1.997 | 2.203 | 2.148 | 2.093 |
| V-Ob | 1.980 | 1.973 | 2.214 | 2.056 | 2.134 | 2.146 |
| C1-C2 | 1.519 | 1.518 | 1.527 | 1.509 | 1.466 | 1.425 |
| C1-H1 | 1.094 | 1.097 | 1.093 | 1.095 | 1.368 | 2.973 |
| C2-H2 | 1.097 | 1.096 | 1.452 | 3.267 | 3.739 | 3.930 |
| **Angle** | | | | | | |
| O1-V-O2 | 110.4 | 110.5 | 108.0 | 103.2 | 97.3 | 86.9 |
| Oa-Al-Ob | 90.2 | 90.1 | 90.4 | 90.0 | 90.4 | 91.2 |
| C1-C2-C3 | 112.6 | 112.7 | 114.9 | 115.3 | 119.5 | 121.2 |

## Results and Discussion

The optimized M06L/6-31G(d,p) structure of $VO_2$-MCM-22 whose molecular oxide specie acts as an active site embedded in the intersection cavity at the 12T membered ring of the supercage is illustrated in Figure 2. The active model is similar to that used in our previous study on isolated metal oxide on zeolite.[45]

The $[VO_2]^+$ ionic group lies between the two bridging oxygen atoms of the zeolite framework forming the tetrahedral arrangement at the vanadium atom which is the most stable configuration. The optimized V-O bond lengths are 1.586, 1.591, 1.980 and 1.980 Å for V-O1, V-O2, V-Oa and V-Ob, respectively (See Table 1). The distance between the V and Al atoms is 2.781 Å.

In the propane oxidative dehydrogenation reaction mechanism, the propane molecule is first adsorbed on $VO_2$-MCM-22 with a hydrogen bond between protons of propane (H1 and H2) and oxygen atoms (O1 and O2). The V-O1 bond was barely changed (1.586 to 1.587 Å)The computed adsorption energy -6.3 kcal/mol is obtained from the 14T quantum cluster. In order to see the effect of zeolitic framework on the reaction mechanism, the extended 120T quantum cluster calculation was performed on the structure optimized from the 14T quantum cluster. The extended framework enhances the adsorption energy to be -7.0 kcal/mol, which is about 10% higher than that from the 14T quantum cluster calculation. The computed adsorption energy is in the range of the experimentally observed values for heat of adsorption (~ -8 kcal/mol).[46]

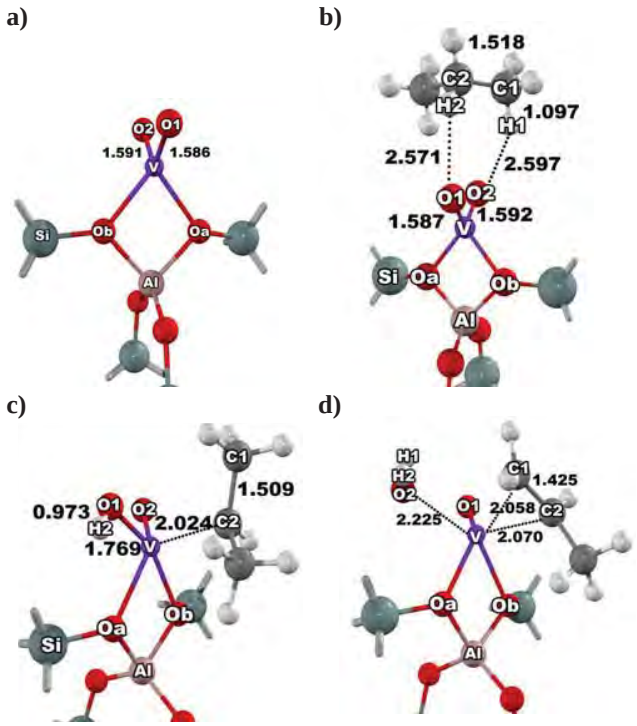


**Figure 2.** Optimized structures of $VO_2$-MCM-22 complexes **a)** bare model of $VO_2$-MCM-22 **b)** adsorption complex of $VO_2$-MCM-22 and propane (ADS) **c)** their corresponding intermediate (INT1) and **d)** the reaction products (INT2).

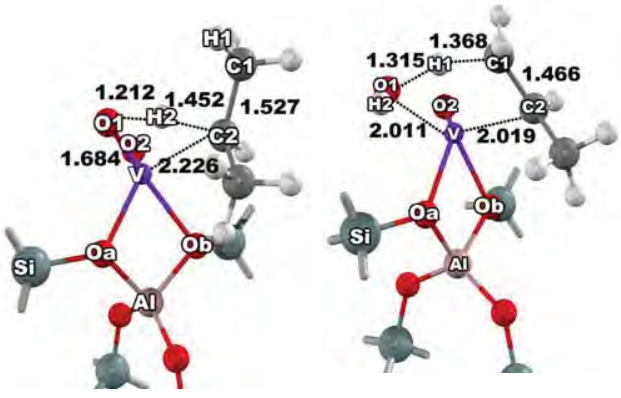


**a)** **b)**

**Figure 3.** The transition structures of the propane oxidative dehydrogenation reaction, **a)** TS1 and **b)** TS2.

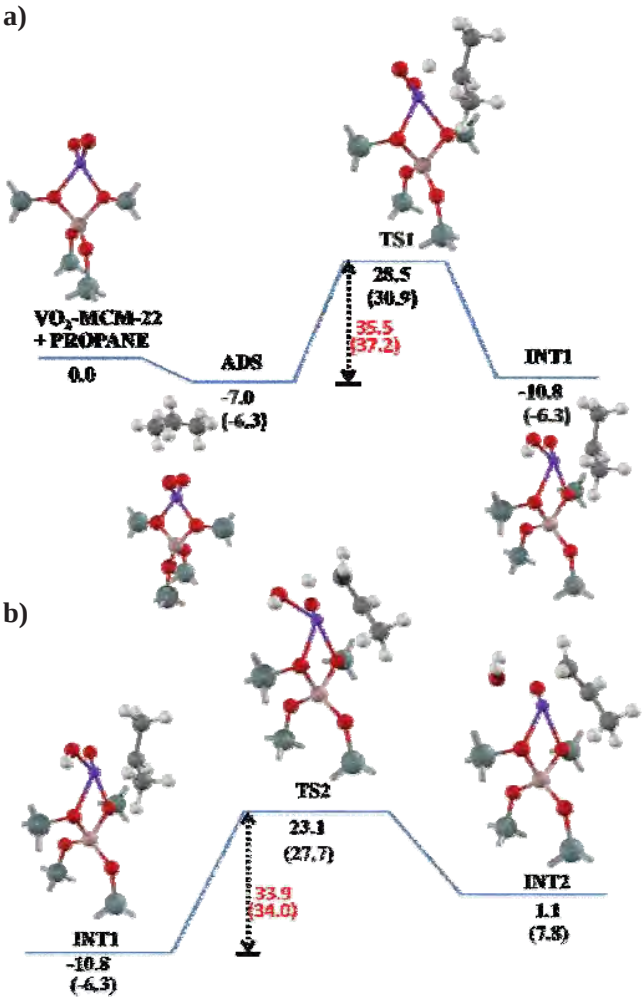


**Figure 4**. 120T M06-L/6-31G(d,p) energy profile (kcal/mol) for a) the hydrogen abstraction step and b) the propene formation step of the propane oxidative dehydrogenation reaction over $VO_2$-MCM-22. The values in parenthesis are calculated at the 14T M06-L/6-31G(d,p) level of theory.

In the next step, the hydrogen atom was abstracted from propane to an α-oxygen of $VO_2$-MCM-22 zeolite. Configuration of the transition structure was distorted from the tetrahedral structure (Figure 3). The O1-H2 and C2-H2 distances were found to be 1.212 and 1.452Å, respectively, while the V-O1 distance is longer than those of the bare catalyst (1.586 to 1.684 Å). The imaginary frequency of 1372i $cm^{-1}$ of the transition state corresponds to the moving of the H2 atom toward and backward between the O1 and C2 atoms. We found that the framework reduces the energy barrier whose the required actual activation barrier is 35.5 kcal/mol, while the apparent activation barrier is 28.5 kcal/mol (see Figure 4). This is in the range of experimental information of propane oxidative dehydrogenation over supported vanadia catalysts (20-30 kcal/mol).[12,47,48] The isopropyl radical intermediate [INT1] was found to be the product of this step with relative energy of -10.8 kcal/mol. The isopropyl radical intermediate is closely coordinated on the vanadium atom at the active site with a V-C2 distance of 2.024 Å.

In the last step, the isopropyl radical intermediate can be converted to propene via the second hydrogen abstraction from C1 to the O1H hydroxyl group on the vanadium atom yielding an adsorbed water molecule. At the transition state, the C1-H1 bond of the propyl radical is elongated from 1.093 to 1.368 Å, corresponding with the forming of H1---O1 which is decreased from 2.740 to 1.315 Å. The calculated actual activation barrier and apparent activation barrier are 33.9 and 23.1 kcal/mol, respectively. The barrier height for this step [TS2] is lower than that for the first hydrogen abstraction step [TS1]. Therefore, the first hydrogen abstraction can be considered as a rate determining step.

The water and propene products are strongly adsorbed to the vanadium atom [INT2]. To remove water and propene, it requires the energy of 27.0 and 57.2 kcal/mol, respectively. The energy profile is shown in the Figure 4. With the M06L functional, the adsorption and activation energies for oxidative dehydrogenation reaction of propane on $VO_2$-MCM-22 agree well with the range of experiment data.

## Conclusions

Reaction mechanisms of propane oxidative dehydrogenation over a 14T $VO_2$-exchanged MCM-22 model were investigated by a newly developed density functional theory (DFT), M06-L, with the effective core potential Stuttgart and Born, for the V atom, and 6-31G(d,p), for the rest, were employed for all calculations. To take the extended framework effect into account, 120T structures were used for single-point calculations at the same level of theory. The reaction began with a hydrogen abstraction on the $VO_2$ group, and acquired the HO-V-O intermediate. This was the rate determining step in which the activation energy was 35.5 kcal/mol. In the propene formation step, the hydroxyl group reacted with the isopropyl radical which required energy of 33.9 kcal/mol. The apparent activation energy was 28.5 kcal/mol, which was in good agreement with experimental results of propane oxidative dehydrogenation over other silica supports.

**Acknowledgements** This work was supported in part by grants from the National Science and Technology Development Agency (2009 NSTDA Chair Professor funded by the Crown Property Bureau under the management of the National Science and Technology Development Agency and NANOTEC Center of Excellence funded by the National Nanotechnology Center), The Thailand Research Fund, The Royal Golden Jubilee Ph.d Program, the Commission of Higher Education, Ministry of Education ("National Research University of Thailand" and "Postgraduate Education and Research Programs in Petroleum and Petrochemicals and Advanced Materials"). The support from the Kasetsart University Research and

Development Institute (KURDI) is also acknowledged. The authors are grateful to Donald G. Truhlar and Yan Zhao for their support with the M06-L functional.

**References**


(1) G. Centi, F. C., F. Trifiro` *Selective Oxidation by Heterogeneous Catalysis*,; Kluwer Academic, New York, 2001.
(2) Blasco, T.; Lopez Nieto, J. M. *Appl. Catal. A* **1997**, *157*, 117-142.
(3) Mamedov, E. A.; Cortés Corberán, V. *Appl. Catal. A* **1995**, *127*, 1-40.
(4) Chaar, M. A.; Patel, D.; Kung, H. H. *J. Catal.* **1988**, *109*, 463-467.
(5) Corma, A.; Nieto, J. M. L.; Paredes, N. *J. Catal.* **1993**, *144*, 425-438.
(6) Hardcastle, F. D.; Wachs, I. E. *J. Mol. Catal.* **1988**, *46*, 173-186.
(7) Wachs, I. E.; Weckhuysen, B. M. *Appl. Catal. A* **1997**, *157*, 67-90.
(8) Eon, J. G.; Olier, R.; Volta, J. C. *J. Catal.* **1994**, *145*, 318-326.
(9) Khodakov, A.; Olthof, B.; Bell, A. T.; Iglesia, E. *J. Catal.* **1999**, *181*, 205-216.
(10) Khodakov, A.; Yang, J.; Su, S.; Iglesia, E.; Bell, A. T. *J. Catal.* **1998**, *177*, 343-351.
(11) Kondratenko, E. V.; Baerns, M. *Appl. Catal. A* **2001**, *222*, 133-143.
(12) Argyle, M. D.; Chen, K.; Bell, A. T.; Iglesia, E. *J. Catal.* **2002**, *208*, 139-149.
(13) Kondratenko, E. V.; Cherian, M.; Baerns, M. *Catal. Today* **2006**, *112*, 60-63.
(14) Cavani, F.; Ballarini, N.; Cericola, A. *Catal. Today* **2007**, *127*, 113-131.
(15) Julbe, A.; Farrusseng, D.; Jalibert, J. C.; Mirodatos, C.; Guizard, C. *Catal. Today* **2000**, *56*, 199-209.
(16) Karakoulia, S. A.; Triantafyllidis, K. S.; Tsilomelekis, G.; Boghosian, S.; Lemonidou, A. A. *Catal. Today* **2009**, *141*, 245-253.
(17) Teixeira-Neto, A. A.; Marchese, L.; Landi, G.; Lisi, L.; Pastore, H. O. *Catal. Today* **2008**, *133-135*, 1-6.
(18) Dinse, A.; Khennache, S.; Frank, B.; Hess, C.; Herbert, R.; Wrabetz, S.; Schlögl, R.; Schomäcker, R. *J. Mol. Catal. A: Chem.* **2009**, *307*, 43-50.
(19) Engeser, M.; Schlangen, M.; Schröder, D.; Schwarz, H.; Yumura, T.; Yoshizawa, K. *Organometallics* **2003**, *22*, 3933-3943.
(20) Feyel, S.; Schröder, D.; Rozanska, X.; Sauer, J.; Schwarz, H. *Angew. Chem., Int. Ed.* **2006**, *45*, 4677-4681.
(21) Cheng, M. J.; Chenoweth, K.; Oxgaard, J.; Van Duin, A.; Goddard III, W. A. *J. Phys. Chem. C* **2007**, *111*, 5115-5127.
(22) Rozanska, X.; Fortrie, R.; Sauer, J. *J. Phys. Chem. C* **2007**, *111*, 6041-6050.
(23) Rozanska, X.; Kondratenko, E. V.; Sauer, J. *J. Catal.* **2008**, *256*, 84-94.
(24) Redfern, P. C.; Zapol, P.; Sternberg, M.; Adiga, S. P.; Zygmunt, S. A.; Curtiss, L. A. *J. Phys. Chem. B* **2006**, *110*, 8363-8371.
(25) Fu, H.; Liu, Z. P.; Li, Z. H.; Wang, W. N.; Fan, K. N. *J. Am. Chem. Soc.* **2006**, *128*, 11114-11123.
(26) Maihom, T.; Namuangruk, S.; Nanok, T.; Limtrakul, J. *J. Phys. Chem. C* **2008**, *112*, 12914-12920.
(27) Jansang, B.; Nanok, T.; Limtrakul, J. *J. Phys. Chem. C* **2008**, *112*, 540-547.
(28) Choomwattana, S.; Maihom, T.; Khongpracha, P.; Probst, M.; Limtrakul, J. *J. Phys. Chem. C* **2008**, *112*, 10855-10861.
(29) Jansang, B.; Nanok, T.; Limtrakul, J. *J. Mol. Catal. A: Chem.* **2007**, *264*, 33-39.
(30) Namuangruk, S.; Tantanak, D.; Limtrakul, J. *J. Mol. Catal. A: Chem.* **2006**, *256*, 113-121.
(31) Namuangruk, S.; Khongpracha, P.; Pantu, P.; Limtrakul, J. *J. Phys. Chem. B* **2006**, *110*, 25950-25957.
(32) Lomratsiri, J.; Probst, M.; Limtrakul, J. *Journal of Molecular Graphics and Modelling* **2006**, *25*, 219-225.
(33) Kasuriya, S.; Namuangruk, S.; Treesukol, P.; Tirtowidjojo, M.; Limtrakul, J. *J. Catal.* **2003**, *219*, 320-328.
(34) Bobuatong, K.; Limtrakul, J. *Appl. Catal. A* **2003**, *253*, 49-64.
(35) Zhao, Y.; Truhlar, D. G. *Theor. Chem. Acc.* **2008**, *120*, 215-241.
(36) Zhao, Y.; Truhlar, D. G. *Acc. Chem. Res.* **2008**, *41*, 157-167.
(37) Maihom, T.; Boekfa, B.; Sirijaraensre, J.; Nanok, T.; Probst, M.; Limtrakul, J. *J. Phys. Chem. C* **2009**, *113*, 6654-6662.
(38) Boekfa, B.; Choomwattana, S.; Khongpracha, P.; Limtrakul, J. *Langmuir* **2009** DOI:10.1021/la901841w.
(39) Kumsapaya, C.; Bobuatong, K.; Khongpracha, P.; Tantirungrotechai, Y.; Limtrakul, J. *J. Phys. Chem. C* **2009**, *113*, 16128-16137.
(40) Chen, K.; Iglesia, E.; Bell, A. T. *J. Catal.* **2000**, *192*, 197-203.
(41) Leonowicz, M. E.; Lawton, J. A.; Lawton, S. L.; Rubin, M. K. *Science* **1994**, *264*, 1910-1913.
(42) Zhou, D.; Bao, Y.; Yang, M.; He, N.; Yang, G. *J. Mol. Catal. A: Chem.* **2006**, *244*, 11-19.
(43) Dolg, M.; Wedig, U.; Stoll, H.; Preuss, H. *J. Chem. Phys.* **1986**, *86*, 866-872.
(44) Frisch, M. J. , Trucks, G. W.; Schlegel, H. B.; Scuseria, G. E.; Robb, M. A.; Cheeseman, J. R.; Montgomery, Jr., J. A.; Vreven, T.; Kudin, K. N.; Burant, J. C.; Millam, J. M.; Iyengar, S. S.; Tomasi, J.; Barone, V.; Mennucci, B.; Cossi, M.; Scalmani, G.; Rega, N.; Petersson, G. A.; Nakatsuji, H.; Hada, M.; Ehara, M.; Toyota, K.; Fukuda, R.; Hasegawa, J.; Ishida, M.; Nakajima, T.; Honda, Y.; Kitao, O.; Nakai, H.; Klene, M.; Li, X.; Knox, J. E.; Hratchian, H. P.; Cross, J. B.; Bakken, V.; Adamo, C.; Jaramillo, J.; Gomperts, R.; Stratmann, R. E.; Yazyev, O.; Austin, A. J.; Cammi, R.; Pomelli, C.; Ochterski, J. W.; Ayala, P. Y.; Morokuma, K.; Voth, G. A.; Salvador, P.; Dannenberg, J. J.; Zakrzewski, V. G.; Dapprich, S.; Daniels, A. D.; Strain, M. C.; Farkas, O.; Malick, D. K.; Rabuck, A. D.; Raghavachari, K.; Foresman, J. B.; Ortiz, J. V.; Cui, Q.; Baboul, A. G.; Clifford, S.; Cioslowski, J.; Stefanov, B. B.; Liu, G.; Liashenko, A.; Piskorz, P.; Komaromi, I.; Martin, R. L.; Fox, D. J.; Keith, T.; Al-Laham, M. A.; Peng, C. Y.; Nanayakkara, A.; Challacombe, M.; Gill, P. M. W.; Johnson, B.; Chen, W.; Wong, M. W.; Gonzalez, C.; and Pople, J. A.; Gaussian, Inc., Wallingford CT, **2004.**
(45) Pantu, P.; Pabchanda, S.; Limtrakul, J. *ChemPhysChem* **2004**, *5*, 1901-1906.
(46) Kamper, A.; Auroux, A.; Baerns, M. *Phys. Chem. Chem. Phys.* **2000**, *2*, 1069-1075.
(47) Chen, K.; Bell, A. T.; Iglesia, E. *J. Phys. Chem. B* **2000**, *104*, 1292-1299.
(48) Heracleous, E.; Machli, M.; Lemonidou, A. A.; Vasalos, I. A. *J. Mol. Catal. A: Chem.* **2005**, *232*, 29-39.

# ADSORPTION AND CRACKING REACTION OF *N*-HEXANE OVER H-ZSM-5: A M06-2X STUDY

*Thana Maihom[a,b,c], Piboon Pantu[a, b, c], Chaiwat Tachakritikul[d], and Jumras Limtrakul[a,b,c*]*

[a]Laboratory for Computational and Applied Chemistry, Physical Chemistry Division, Department of Chemistry, Faculty of Science, Kasetsart University, Bangkok 10900, Thailand
[b]Center of Nanotechnology, Kasetsart University Research and Development Institute, Bangkok 10900, Thailand
[c]NANOTEC Center of Excellence, National Nanotechnology Center, Kasetsart University, Bangkok 10900, Thailand
[d]PTT Research and Technology Institute, PTT Public Company Limited, Thailand

## Introduction

The catalytic cracking of hydrocarbons is an important reaction in the petrochemical industry. It is used to break down large hydrocarbons in crude oil into light hydrocarbons for the production of fuels. Zeolite catalysts, especially Y and ZSM-5, are widely used in cracking processes due to their advantages of high catalytic activity and selectivity.

The catalytic cracking of hydrocarbons is proposed to occur via a bimolecular and a monomolecular mechanism.[1-4] The bimolecular mechanism involves hydride-transfer between an alkane and an adsorbed carbenium ion followed by isomerization and β-scission. This mechanism prevails under high partial pressure of hydrocarbons and, especially, in large pore zeolites. A monomolecular cracking is believed to be an important mechanism for the cracking reaction of hydrocarbons in medium pore zeolites such as ZSM-5. In this mechanism, a carbonium-like ionic intermediate is formed through the direct protonation of Brønsted acid to the C–C bond.[3-9] It then leads to the scission of the C–C bond to produce alkane and alkene products. This mechanism is expected to be very sensitive to the acid strength of the Brønsted proton.

A number of theoretical studies have been carried out to investigate the cracking reaction of alkane over the zeolite catalysts.[6-10] Recently, Boronat et al.[9] have proposed that protolytic cracking of *n*-butane occurred in two steps. The first step is protonation to the C-C bond to form a carbonium ion intermediate having a two-electron three-centre C–H–C bridge adsorbed on the zeolite surface. The subsequent step is the decomposition of the carbonium ion to form an alkane and an alkene.

To understand hydrocarbon reactions, it is of particular interest to study the reactivity and stability of the carbonium ion intermediate on the zeolite surface. It is expected that the zeolite framework should have profound effects on reactive intermediates and the reaction mechanism for catalytic reactions over zeolite catalysts.[11-13] Therefore, it is suggested that it is essential to use relatively large clusters for investigations of reaction mechanisms in zeolites.

Recently, the new density functional M06-2X method has been found to successfully account for the effect of the zeolite framework on the adsorption and reaction of hydrocarbons over large quantum clusters of zeolites.[14-16] In this report, full quantum calculations on a large 34T cluster model of H-ZSM-5 using the M06-2X method are performed to investigate the mechanism of *n*-hexane protolytic cracking. The structures and energetics of reaction intermediates and transition states and the reaction mechanism are discussed.

## Models and Method

The structure of the 34T cluster model is used for representing the lattice of ZSM-5 zeolite,[17] which covers the intersection region of the straight and zigzag channels, as shown in Figure 1. One of the silicon atoms at the T12 site is replaced with an aluminium atom to generate the Brønsted acid site. This T12 site is found to be the most stable Al substitution site and has been generally used to model the active site of H-ZSM-5 zeolite. In our previous studies, this model had been employed for studying the adsorption and reactions of hydrogen exchange on unsaturated aliphatic, aromatic and heterocyclic compounds and gave reasonable results for adsorption and activation energies, compared with experimental values.[14,15]

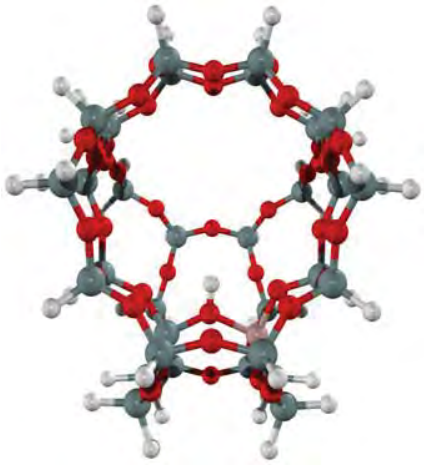

**(a)**

**(b)**

**Figure 1.** 34T cluster model of H-ZSM-5 zeolite: (a) sinusoidal channel view and (b) straight channel view.

All structure optimizations were performed with the M06-2X density functional[18-21] and the 6-31G (d,p) basis set. During optimization, only the 5T cluster of the active region, $[(\equiv SiO)_3Al(OH)Si\equiv]$ and the probe molecules are allowed to relax, while the remaining atoms are fixed at the crystallographic coordinates. Verification that the optimized transition state connects the intended reactant and product was made by normal mode analysis. All calculations were performed using the Gaussian 03 code[22] modified to incorporate the Minnesota Density Functional module 3.1 by Zhao and Truhlar.

## Results and Discussion

**Adsorption of *n*-Hexane.** Optimized adsorption structures of *n*-hexane on H-ZSM-5 zeolites obtained from the M06-2X method and the 6-31G(d,p) basis set are shown in Figure 2. It can be seen that the *n*-hexane molecule is weakly adsorbed on H-ZSM-5 zeolite through the interaction between two carbon atoms (C–C) and the Brønsted acid site (O1–H1). Four possible configurations of weak adsorption complexes were found. The calculated adsorption energies are –18.0, –17.6, –19.7 and –17.6 kcal/mol for the Ads1, Ads2, Ads3 and Ads4 geometries, respectively, with internuclear H1···C distances in the range of 2.71–3.66 Å. In this zeolite, the adsorption via the central C-C unit (Ads3) is slightly more stable (by 2 kcal/mol) than other structures. These predicted adsorption energies are in agreement with the experimental estimates of –19.6 kcal/mol.[23] These results suggest that the M06-2X/6-31G(d,p) method is suitable for studying the interactions of *n*-hexane in zeolites and should also be suitable for studying the *n*-hexane cracking.

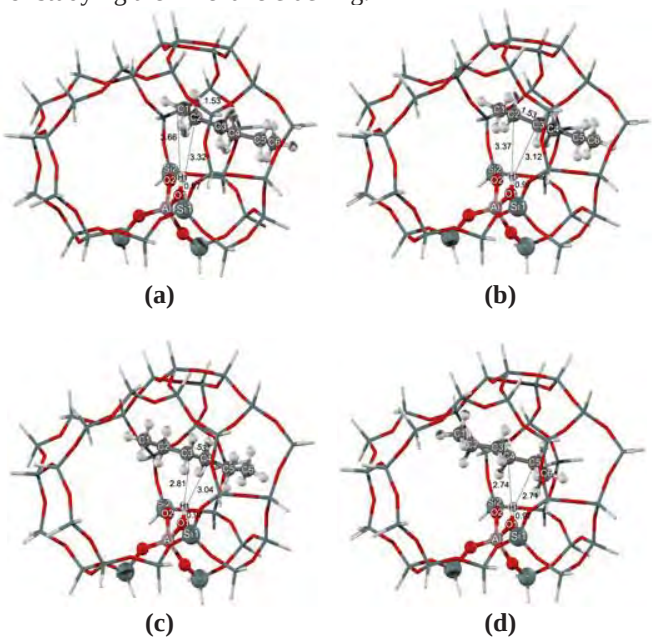


**Figure 2.** Optimized structures of *n*-hexane adsorbed over H-ZSM-5 zeolite (a) Ads1, (b) Ads2, (c) Ads3 and (d) Ads4.

**Reaction Mechanism of *n*-Hexane Cracking.** It has been reported that propane ($C_3H_8$) and propene ($C_3H_6$) are the major products of monomolecular *n*-hexane cracking on numerous zeolites.[24,25] Therefore, we concentrate on the protolytic cracking of the central C3–C4 bond only. The reaction profile and structures of intermediates and transition states are shown in Figure 3.

In the first step, the adsorbed *n*-hexane molecule is protonated by the acidic proton at the central C-C bond to form the adsorbed 3-C-hexonium intermediates via the three-center/two-electron bonds cationic transition state TS1. In this transition state, the C3–C4 bond of *n*-hexane is ruptured by the acidic proton. The O1–H1 bond distance is elongated from 0.98 to 1.74 Å while the C3–C4 bond distance is increased to 1.76 Å. The 3-C-hexonium intermediate having the C–H–C bridge adsorbed on the zeolite surface by forming hydrogen bond interactions with the basic oxygen atom of the zeolite. The C3–H1–C4 bridge angle is 101.4°. The bond distances of C3-H1 and C4-H1 are almost equal. The activation energy of this step is 44.5 kcal/mol. The adsorbed 3-C-hexonium intermediate is less stable than the adsorbed *n*-hexane by 43.1 kcal/mol. Boronat et al.[9] have also reported that the adsorbed 2-C-butonium intermediate is much less stable than the adsorbed *n*-butane.

The second step is the decomposition of the 3-C-hexonium intermediate to form the products of propane and propene via transition state TS2. At the transition state, the C3–H1–C4 bridge is broken. The C3–H1 distance increases to 1.88 Å while the H1–C4 bond is contracted to 1.11 Å. The adjacent C2–H2 bond is broken and the H2 proton is back-transferred to the oxygen of the zeolite framework. The hybridization of C2 changes from tetrahedral ($sp^3$) to planar ($sp^2$). The activation energy of this step is 11.9 kcal/mol. The products are propane and propene adsorbed on the acidic site through a π-bond interaction.

From the energy profile, the first step, which is the protonation of adsorbed *n*-hexane, is found to be the rate determining step with the activation energy of 44.5 kcal/mol. The 3-C-hexonium is found to be a true intermediate. This result is in agreement with the computational result of Boronat et al.[9] on *n*-butane cracking. Subsequently, the decomposition of the 3-C-hexonium to form a propane and a propene molecule is facile with an activation energy of 11.9 kcal/mol. The apparent activation energy is found to be 35.3 kcal/mol. This value is higher than the previous experimental reports of about 25 kcal/mol.[26,27] However, it is in good agreement with a recent report[26,27] in which an apparent activation energy of 35±2 kcal/mol was observed. In those works, the authors used purified *n*-hexane at very low partial pressures and relatively high reaction temperatures to ensure the monomolecular cracking mechanism. Lónyi et al.[28] have suggested that the activation energy of monomolecular cracking should be higher than that of the bimolecular cracking which supports the result of Babitz et al.[26] and van Bokhoven et al.[27] and agrees with our computed result.

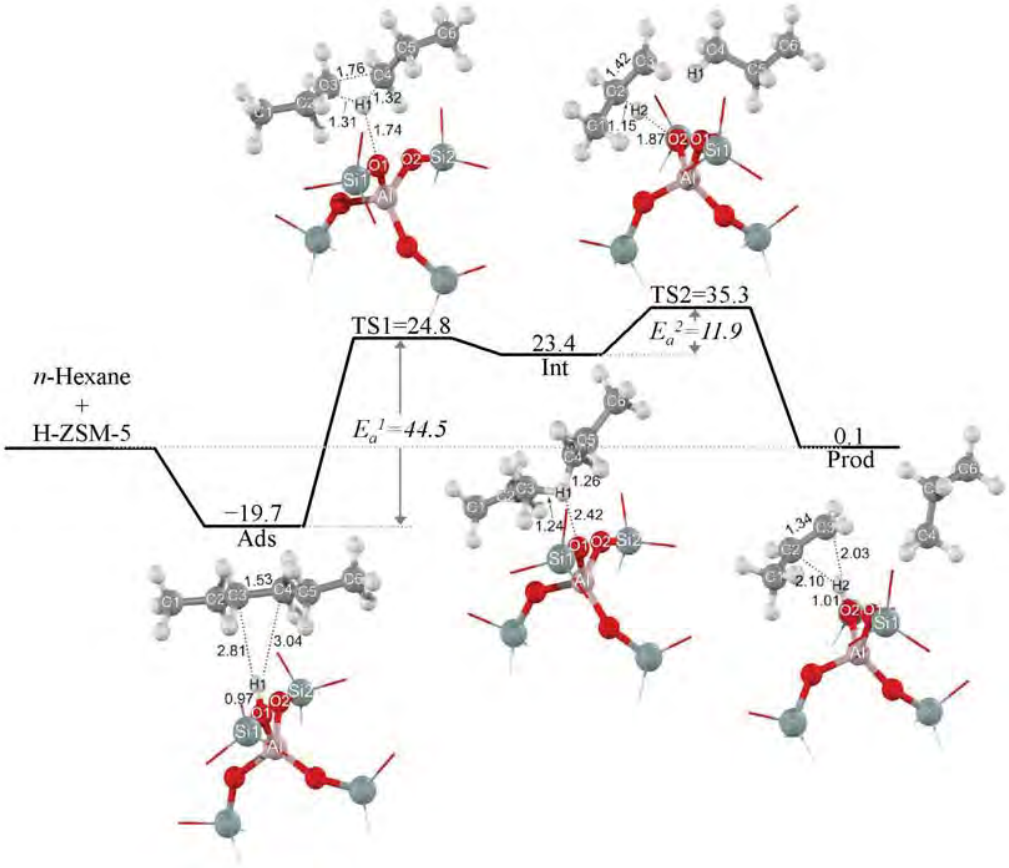


**Figure 3.** Energies and geometries of molecules and transition states involved in the *n*-hexane cracking mechanisms over H-ZSM-5 zeolite (energies are in kcal/mol).

## Conclusions

The monomolecular cracking reaction of *n*-hexane have been investigated by using the 34T H-ZSM-5 cluster model calculated at the M06-2X/6-31G(d,p) level of theory. This calculation provides reasonable adsorption energies of *n*-hexane in H-ZSM-5 that are in good agreement with the experimental measurements. In the first step of the reaction, the *n*-hexane C–C bond is protonated to form a 3-C-surface hexonium intermediate. Then, the 3-C-hexonium intermediate is decomposed to produce propane and propene products. The activation energies are 44.5 and 11.9 kcal/mol for the first and second step, respectively. The apparent activation energy is 35.3 kcal/mol which is in agreement with the experimental result of monomolecular cracking of n-hexane. These results also confirm that relatively large quantum clusters are needed for the study of hydrocarbon reactions in zeolites and the M06-2X method is one of the well-suited methods for this case.

**Acknowledgement.** This work was supported in part by grants from the National Science and Technology Development Agency (NSTDA Chair Professor and NANOTEC Center of Excellence), the Thailand Research Fund, the Kasetsart University Research and Development Institute (KURDI), the Commission on Higher Education, Ministry of Education, under the Postgraduate Education and Research Programs in Petroleum and Petrochemicals and Advanced Materials, PTT Research and Technology Institute, PTT Public Company Limited as well as under the program of Strategic Scholarships for Frontier Research Network for the Joint Ph.D. Program Thai Doctoral degree from the Office of the Higher Education Commission, Thailand (to TM). The authors are grateful to Donald G. Truhlar and Yan Zhao for supporting them with the code for the M06-2X functional.

## References

(1) Corma, A.; Planelles, J.; Sánchez-Marín, J.; Thomás, F. J. *Catal.* **1985**, *93*, 30.
(2) Krannila, H.; Haag, W. O.; Gates, B. C. *J. Catal.* **1992**, *135*, 115.
*(3)* Sie, S.T. *Ind. Eng. Chem. Res.* **1992**, *31*, 1881.
(4) Lercher, J. A.; Santen, R. A. v.; Vinek, H. *Catal. Lett.* **1994**, *27*, 91.
(5) Olah, A. G.; Halpern, Y.; Shen, J.; Mo, K. Y. *J. Am. Chem. Soc.* **1973**, *95*, 4960.
(6) Kazansky, V. B.; Frash, M. V.; Santen, R. A. v. *Appl. Catal. A* **1996**, *146*, 225.
(7) Zygmunt, S. A.; Curtiss, L. A.; Zapol, P.; Iton, L. E. *J. Phys. Chem. B* **2000**, *104*, 1944.
(8) Zheng, X.; Blowers, P. *J. Phys. Chem. A* **2005**, *109*, 10734.
(9) Boronat, M.; Corma, A. *Appl. Catal. A: General* **2008**, *336*, 2.

(10) Milas, I.; Nascimento, M. A. C. *Chem. Phys. Lett.* **2006**, *418*, 368.
(11) Brändle, M.; Sauer, J. *J. Am. Chem. Soc. , ,* **1998**, *120(7)*, 1556.
(12) Sinclair, P. E.; de Vries, A. H.; Sherwood, P.; Catlow, C. R. A.; R.A., V. S. *J. Chem. Soc., Faraday Trans.* **1998**, *94*, 3401.
(13) Clark, L. A.; Sierka, M.; Sauer, J. *J. Am. Chem. Soc.* **2003**, *125*, 2136.
(14) Maihom, T.; Boekfa, B.; Sirijaraensre, J.; Nanok, T.; Probst, M.; Limtrakul, J. *J. Phys. Chem. C* **2009**, *113*, 6654.
(15) Boekfa, B.; Choomwattana, S.; Khongpracha, P.; Limtrakul, J. *Langmuir* **2009**, Articles ASAP.
(16) Kumsapaya, C.; Bobuatong, K.; Khongpracha, P.; Tantirungrotechai, Y.; Limtrakul, J. *J. Phys. Chem. C* **2009**, *113* 16128.
(17) van Koningsveld, H.; Bekkum, H. v.; Jansen, J. C. *Acta. Crystallogr. B* **1987**, *43*, 127.
(18) Zhao, Y.; Schultz, N. E.; Truhlar, D. G. **2006**, *2*, 364.
(19) Zhao, Y.; Truhlar, D. G. **2008**, *41*, 157.
(20) Zhao, Y.; Truhlar, D. G. *Theor. Chem. Acc.* **2008**, *120*, 215.
(21) Zhao, Y.; Truhlar, D. G. **2008**, *112*, 6860.
(22) Frisch, M. J.; Trucks, G. W.; Schlegel, H. B.; Scuseria, G. E.; Robb, M. A.; Cheeseman, J. R.; Montgomery, J. A.; Jr.; Vreven, T.; Kudin, K. N.; Burant, J. C.; Millam, J. M.; Iyengar, S. S.; Tomasi, J.; Barone, V.; Mennucci, B.; Cossi, M.; Scalmani, G.; Rega, N.; Petersson, G. A.; Nakatsuji, H.; Hada, M.; Ehara, M.; Toyota, K.; Fukuda, R.; Hasegawa, J.; Ishida, M.; Nakajima, T.; Honda, Y.; Kitao, O.; Nakai, H.; Klene, M.; Li, X.; Knox, J. E.; Hratchian, H. P.; Cross, J. B.; Adamo, C.; Jaramillo, J.; Gomperts, R.; Stratmann, R. E.; Yazyev, O.; Austin, A. J.; Cammi, R.; Pomelli, C.; Ochterski, J. W.; Ayala, P. Y.; Morokuma, K.; Voth, G. A.; Salvador, P.; Dannenberg, J. J.; Zakrzewski, V. G.; Dapprich, S.; Daniels, A. D.; Strain, M. C.; Farkas, O.; Malick, D. K.; Rabuck, A. D.; Raghavachari, K.; Foresman, J. B.; Ortiz, J. V.; Cui, Q.; Baboul, A. G.; Clifford, S.; Cioslowski, J.; Stefanov, B. B.; Liu, G.; Liashenko, A.; Piskorz, P.; Komaromi, I.; Martin, R. L.; Fox, D. J.; Keith, T.; Al-Laham, M. A.; Peng, C. Y.; Nanayakkara, A.; Challacombe, M.; Gill, P. M. W.; Johnson, B.; Chen, W.; Wong, M. W.; Gonzalez, C.; Pople, J. A. *Gaussian 03*, revision B.05, Gaussian, Inc, Wallingford, CT, 2004.
(23) Eder, F.; Stockenhuber, M.; Lercher, J. A. *J. Phys. Chem. B* **1997**, *101*, 5414.
(24) Kotrel, S.; Rosynek, M. P.; Lunsford, J. H. *J. Phys. Chem. B* **1999**, *103*, 818.
(25) Narbeshuber, T. F.; H. Vinek; Lercher, J. A. *J. Catal.* **1995**, *157*, 388.
(26) Babitz, S. M.; B.A.Williams; Miller, J. T.; Snurr, R. Q.; W.O. Haag; Kung, H. *Appl. Catal. A Gen.* **1999**, *179*, 71.
(27) van Bokhoven, J. A.; Williams, B. A.; Ji, W.; Koningsberger, D. C.; Kung, H. H.; Miller, J. T. *J. Catal.* **2004**, *224* 50.
(28) Lónyi, F.; Kovács , A.; Valyon, J. *J. Phys. Chem. B* **2006**, *110*, 1711.

**394 - Density functional study of epoxide ring-opening reaction with methanol promoted by dicopper carboxylate in metal-organic framework**

***Sudarat Yadnum*, Saowapak Choomwattana, *Pipat Khongpracha*, Dr. Jumras Limtrakul, Prof. Dr. . Department of Chemistry, Faculty of Science, Kasetsart University Laboratory for Computational & Applied Chemistry, Physical Chemistry Division Chatuchak Bangkok Thailand, Center of Nanotechnology, Kasetsart University Research and Development Institute Chatuchak Bangkok Thailand, NANOTEC Center of Nanotechnology, National Nanotechnology Center, Kasetsart University Chatuchak Bangkok Thailand***

The ring-opening reaction mechanism of epoxide with methanol, an important process in alkoxy alcohol synthesis, was investigated with the new density-functional theory (M062X/6-31G(d,p)) for the systems of bare model and dicopper carboxylate “paddlewheels” with a metal-organic framework (MOF) as a catalyst. The concerted transition state concerning the C-O bond formation, C-O and O-H bond dissociation, and hydrogen transfer was proposed. For the bare system, the coadsorption energy is -8.1 kcal/mol and its reaction energy is -32.3 kcal/mol. In the catalyzed mechanism, epoxide is initially adsorbed over the dicopper carboxylate with an adsorption energy of -21.1 kcal/mol. Coadsorption energy between the epoxide and methanol is -28.7 kcal/mol. This catalyzed reaction is exothermic by -55.7 kcal/mol. The Cu-MOF was found to be an efficient catalyst in ring-opening reactions of epoxides with alcohols leading to a lower energy barrier (48.0 kcal/mol) as compared to that of the bare model system (60.1 kcal/mol).

**Sunday, March 21, 2010 07:00 PM**

**Chemistry of Materials (07:00 PM - 09:00 PM)**

Close Window

**1301 - Molecular dynamics simulation of *ortho*-, *para*- and *meta*-xylenes diffusion in MOF-5 with a model potential of Zn-O bonds for MOF materials**

***Chadchalerm Raksakoon*, *Saowapak Choomwattana*, *Jumras Limtrakul, Prof. Dr. . Department of Chemistry, Faculty of Science, Kasetsart University Laboratory for Computational & Applied Chemistry, Physical Chemistry Division Chatuchak Bangkok Thailand, Center of Nanotechnology, Kasetsart University Research and Development Institute Chatuchak Bangkok Thailand, NANOTEC Center of Nanotechnology, National Nanotechnology Center, Kasetsart University Chatuchak Bangkok Thailand***

We present a Zn-O bonds potential for Metal-Organic Framework in which the potential parameters are fitted to density functional theory data of B3LYP/6-31G(d,p) and ONIOM(B3LYP/6-31G(d,p):UFF) calculations on $Zn_4O$ and $Zn_4O(O_2C\text{-}C(CH)_2)_6$ models, respectively. To verify its accuracy, molecular dynamics (MD) simulations of *ortho*-, *para*- and *meta*-xylenes in MOF-5 at 300 K were performed with the combination of novel in-house potential energy surfaces (PES) and existing potentials to determine the maximum loading. The lattice dynamics is found at a loading of 58 molecules per unit cell and keeps increasing at higher loadings. Moreover, xylene isomers could be differentiated from their self-diffusion coefficients ($D_{self}$) in the framework. At the same loading, *p*-xylene is found to expand the lattice the most. Unlike in zeolites, where the pore window hindrance is the key difficulty, the diffusion in the open MOF-5 has to overcome p-p attraction of xylenes in the binding pockets.

**Thursday, March 25, 2010 03:30 PM**

**Computational Chemistry (01:30 PM - 04:30 PM)**

Close Window

**685 - Decomposition of nitrous oxide on transition metal-doped carbon nanotubes**

***Panvika Pannopard, Pipat Khongpracha, Dr. Chompunuch Warakulwit, Dr. Jumras Limtrakul, Prof. Dr. . Department of Chemistry, Faculty of Science, Kasetsart University Laboratory for Computational & Applied Chemistry, Physical Chemistry Division Chatuchak Bangkok Thailand, Center of Nanotechnology, Kasetsart University Research and Development Institute Chatuchak Bangkok Thailand, NANOTEC Center of Nanotechnology, National Nanotechnology Center, Kasetsart University Chatuchak Bangkok Thailand***

The catalytic activity of Carbon Nanotubes (CNTs) for greenhouse gas removal, like $N_2O$, is fine-tuned by metal doping. We take advantage of the superb capability of Sc, Ti and V transition metals in converting $N_2O$ to $N_2$ to improve the less reactive surfaces of CNTs. As such, the stable composite catalysts of Sc-, Ti- and V- doped on (5,5) Single-Walled Carbon Nanotubes (SWCNTs) along with the unmodified one were investigated by employing the practical tool $Dmol^3$ for periodic systems. Without metal doping, the concerted $N_2O$ decomposition on the bare tube proceeds via a high energy barrier (54.3 kcal/mol). However, such barriers can be overcome with the presence of active metals, i.e. reduced to 3.6, 8.0 and 10.2 kcal/mol for V-, Ti- and Sc- (5,5)SWCNTs, respectively. This superior reactivity is the result of the cooperative effect of the metal and SWCNT which enhances the electron transfers from the tube to $N_2O$.

**Tuesday, March 23, 2010 04:10 PM**

**Chemistry of Materials (01:30 PM - 04:30 PM)**

Close Window

**American Chemical Society National meeting & Exposition” ครั้งที่ 240**

**ณ ประเทศสหรัฐอเมริกา**

**ระหว่างวันที่ 22-26 สิงหาคม 2553**

**จำนวน 6 เรื่อง**

**441 - Structures and reaction mechanisms of propene oxide isomerization to propanal on H-FER zeolite: A theoretical study using the newly developed density functional theory**

***Dr. Bundet Boekfa**, Thana Maihom, Sippakorn Wannakao, Karan Bobuatong, **Prof. Jumras Limtrakul**. Laboratory for Computational & Applied Chemistry, Physical Chemistry Division, Department of Chemistry, Faculty of Science, Kasetsart University, Bangkok, Thailand; Center of Nanotechnology, Kasetsart University Research and Development Institute, Kasetsart University, Bangkok, Thailand; NANOTEC Center of Nanotechnology, National Nanotechnology Center, Kasetsart University, Bangkok, Thailand; Chemistry Department, Faculty of Liberal Arts and Science, Kasetsart University Kamphaeng Saen Campus, Nakhon Pathom, Thailand*

The isomerization mechanism of propene oxide over H-FER has been carried out via the utilization of 23T nanocluster models where T are Si or Al atoms, calculated by the newly developed Density Functional Theory, M08-HX. The calculated adsorption energy of propene oxide on H-FER is predicated to be -25.4 kcal/mol. The propene oxide isomerization to propanal is calculated to be an exothermic reaction with a reaction energy of 20.8 kcal/mol. The reaction mechanism is considered to proceed through a stepwise mechanism: (1) the epoxide ring protonation, and concurrently the ring-opening, and (2), the 1,2-hydride shift formatting the adsorbed carbonyl compound. The latter step is found to be the rate-determining step with the activation energies of 24 kcal/mol as compared with the former of 22 kcal/mol. The understanding gained of the adsorption and the reaction mechanism in the confinement of nanopore zeolite will be used to improve the catalytic performance.

**Tuesday, August 24, 2010 03:10 PM**
Inorganic Catalysts (01:30 PM - 05:10 PM)
**Location: Boston Convention & Exhibition Center**
**Room: Room 257B**

Close Window

**460 - Catalytic dehydrogenation of ethylbenzene to styrene over Fe-ZSM-5 zeolite: A newly developed density functional theory (M06-L) in ONIOM scheme**

***Dr. Bundet Boekfa**, Thana Maihom, Sippakorn Wannakao, Pailin Limtrakul, **Prof. Jumras Limtrakul**. Laboratory for Computational & Applied Chemistry, Physical Chemistry Division, Department of Chemistry, Faculty of Science, Kasetsart University, Bangkok, Thailand; Center of Nanotechnology, Kasetsart University Research and Development Institute, Kasetsart University, Bangkok, Thailand; NANOTEC Center of Nanotechnology, National Nanotechnology Center, Kasetsart University, Bangkok, Thailand; Chemistry Department, Faculty of Liberal Arts and Science, Kasetsart University Kamphaeng Saen Campus, Nakhon Pathom, Thailand*

The dehydrogenation mechanism of ethylbenzene to styrene over Fe-ZSM-5 zeolite was investigated by M06L/6-31G(d,p) //ONIOM(M06L/6-31G(d,p):UFF) model cluster of 46T//5T:46T where T are Si or Al atoms. The adsorption energy is calculated to be -29.0 kcal/mol, which compares well with the experimental observation. A hydrogen abstraction on the O-Fe-O group starts the reaction, and yields the ethylbenzene radical over HO-Fe-O. This step is the rate determining step with an activation energy of 14.2 kcal/mol. This is followed by the hydroxyl reacting with the ethylbenzene radical and results in the styrene product with activation energy of 6.9 kcal/mol. The reaction is exothermic reaction with a reaction energy of 56.5 kcal/mol. The catalytic dehydrogenation of Ethylbenzene to Styrene over Fe-ZSM-5 has been clearly demonstrated by the “noncovalent interaction represented” M06-L method on the zeolite framework.

**Wednesday, August 25, 2010 06:00 PM**
Molecular Systems for Efficient Solar Energy Conversion and Storage (06:00 PM - 09:00 PM)
**Location: Boston Convention & Exhibition Center**
**Room: Hall C**

Close Window

**455 - Structures and reaction pathways of methylation of 2-methylnaphthalene with methanol over H-BEA zeolite**

***Karan Bobuatong*, Dr. Bundet Boekfa, Sippakorn Wannakao, *Prof. Jumras Limtrakul*. Laboratory for Computational and Applied Chemistry, Department of Chemistry, Faculty of Science, Kasetsart University, Bangkok, Thailand; Center of Nanotechnology, Kasetsart University Research and Development Institute, Kasetsart University, Bangkok, Thailand***

The methylation of 2-methylnaphthalene (2-MN) with methanol to 2,6 dimethylnaphthalene (2,6-DMN) and 2,7-dimethylnaphthalene (2,7-DMN) catalyzed over H-BEA has been investigated using the M06-2X functional. Three different reaction pathways include, (1) the methylation of 2-MN to 2,6-DMN, (2) the methylation of 2-MN to 2-7-DMN, and (3) the intramolecular isomerization between 2,6-DMN and 2,7-DMN have been proposed. For the first two mechanisms, the methoxide formation from methanol is the initial step followed by the methyl migration to 2-MN leading to naphthalynic carbocations as the key intermediates, subsequently converted into 2,6-DMN and 2,7-DMN. The calculated reaction profiles of 2,6-DMN and 2,7-DMN formation are similar and in agreement with experimental observation that the selectivity to ratio of 2,6-DMN/2,7-DMN produced on H-BEA was almost 1. In the case of the competitive reaction, the intramolecular isomerization between these two isomers was found difficult to occur due to the unfavorable high-energy barrier required for the methyl migration.

**Wednesday, August 25, 2010 06:00 PM**
Molecular Systems for Efficient Solar Energy Conversion and Storage (06:00 PM - 09:00 PM)
**Location: Boston Convention & Exhibition Center**
**Room: Hall C**

Close Window

**337 - DFT study of oxidative dehydrogenation of propane over a $VO_2$-exchanged MCM-22 and ZSM-5 zeolites**

***Sippakorn Wannakao*, Thana Maihom, Dr. Winyoo Sangthong, Dr. Bundet Boekfa, Dr. Pipat Khongpracha, *Prof. Jumras Limtrakul*. Laboratory for Computational & Applied Chemistry, Physical Chemistry Division, Department of Chemistry, Faculty of Science, Kasetsart University, Bangkok, Thailand; Center of Nanotechnology, Kasetsart University Research and Development Institute, Kasetsart University, Bangkok, Thailand; NANOTEC Center of Nanotechnology, National Nanotechnology Center, Kasetsart University, Bangkok, Thailand; Chemistry Department, Faculty of Liberal Arts and Science, Kasetsart University Kamphaeng Saen Campus, Nakhon Pathom, Thailand***

The adsorption and the mechanism of the oxidative dehydrogenation (ODP) of propane over $VO_2$-exchanged 14T MCM-22 and 12T ZSM-5 zeolites were investigated by density functional theory calculations at the M06-L/6-31G(d,p) level of theory. The adsorption energies of propane are comparable to the ones derived from computationally much more demanding MP2 calculations and to experimental results while, as expected, the values from the B3LYP functional are too small. The reaction begins with the abstraction of a methylene hydrogen to the oxygen atom of $VO_2$ group, leading to a HO-V-O intermediate. This step is the rate determining step with apparent activation energies of 30.9 and 32.3 kcal/mol for MCM-22 and ZSM-5, respectively. The subsequent step is the propene together with the water formation. Although the catalyst reoxidation step was not included in rate limiting step, it was found to be important for releasing the product at the end of the reaction.

**Wednesday, August 25, 2010 06:00 PM**
Challenges for Density Functional Theory (06:00 PM - 09:00 PM)
**Location: Boston Convention & Exhibition Center**
**Room: Hall C**

Close Window

**442 - Reaction mechanisms of ethene formation via ethanol dehydration catalyzed by Fe-ZSM-5 zeolite: An ONIOM study with an M06-L functional**

***Thana Maihom*, Dr. Bundet Boekfa, Sippakorn Wannakao, *Prof. Jumras Limtrakul*. Laboratory for Computational & Applied Chemistry, Physical Chemistry Division, Department of Chemistry, Faculty of Science, Kasetsart University, Bangkok, Thailand; Center of Nanotechnology, Kasetsart University Research and Development Institute, Kasetsart University, Bangkok, Thailand**

Stepwise and concerted mechanisms of ethene formation through the ethanol dehydration over Fe-ZSM-5 zeolite have been investigated by the utilization of a nanocluster of a large 46T model where T are Si or Al atoms, calculated by the M06-L, incorporated into the ONIOM scheme (M06-L/6-31G(d,p):UFF). In the stepwise mechanism, the ethanol dehydration commences from the hydrogen abstraction of the ethanol OH group to form the ethoxide-hydroxide intermediate with a low activation energy of 19.2 kcal/mol. This is followed by the C-H bond of the methyl carbon of ethoxide intermediate being dissociated to produce the ethene-water product with activation barrier of 63.4 kcal/mol. For the concerted mechanism, the ethanol dehydration into ethene product occurs in a single step without the intermediate formation with the activation energy of 35.6 kcal/mol. These results suggested that the production of ethene from ethanol dehydration over Fe-ZSM-5 preferably occurs through the concerted mechanism.

**Tuesday, August 24, 2010 03:30 PM**
Inorganic Catalysts (01:30 PM - 05:10 PM)
**Location: Boston Convention & Exhibition Center**
**Room: Room 257B**

Close Window

**457 - Quantum chemical calculation of the hydrogenation reaction of encapsulated formaldehyde in Na-FAU zeolite**

***Dr. Winyoo Sangthong*, Sippakorn Wannakao, Saowapak Choomwattana, Thana Maihom, Dr. Bundet Boekfa, *Prof. Jumras Limtrakul*. Laboratory for Computational & Applied Chemistry, Physical Chemistry Division, Department of Chemistry, Faculty of Science, Kasetsart University, Bangkok, Thailand; Center of Nanotechnology, Kasetsart University Research and Development Institute, Kasetsart University, Bangkok, Thailand; NANOTEC Center of Nanotechnology, National Nanotechnology Center, Kasetsart University, Bangkok, Thailand; Chemistry Department, Faculty of Liberal Arts and Science, Kasetsart University Kamphaeng Saen Campus, Nakhon Pathom, Thailand***

Structures of Na-exchanged zeolite-encapsulated formaldehyde (HCHO@Na-zeolite) and their interactions with hydrogen molecule to produce methanol have been investigated by the recently developed density functional theory (M06-2X/6-31G(d,p)). Three model systems were utilized to study the hydrogenation reaction of hydrogen and formaldehyde: (1) formaldehyde in Na-exchanged zeolite: HCHO@Na-zeolite/$H_2$; (2) naked Na(I) as the catalyst: Na(I)/HCHO/$H_2$; (3) a bare model where only the reactants are present: HCHO/$H_2$. It was found that inclusion of the large electrostatic field generated by the naked Na(I) cation leads to a lower energy barrier (53.78 kcal/mol) of the reaction as compared to the bare model system (69.25 kcal/mol). Surprisingly, the inclusion of the extended zeolite framework had an effect on the structure and energetics of the adsorption complexes. Furthermore, stabilizing the transition state complex led to the lowest energy barrier (32.83 kcal/mol).

**Wednesday, August 25, 2010 06:00 PM**
Molecular Systems for Efficient Solar Energy Conversion and Storage (06:00 PM - 09:00 PM)
**Location: Boston Convention & Exhibition Center**
**Room: Hall C**

Close Window

# Nanothailand 2010: Nanotechnology for a Sustainable World

**ณ โรงแรมรามา การ์เด้นส์ กรุงเทพฯ ประเทศไทย**

**ระหว่างวันที่ 18-20 พฤศจิกายน 2553**

**จำนวน 15 เรื่อง**

# Healing of a Vacancy Defect in a Single-Walled Carbon Nanotube by Carbon Monoxide Disproportionation

Teeranan Nongnual[1,2,3], Jumras Limtrakul[1,2,3*]

[1]*Laboratory for Computational and Applied Chemistry, Department of Chemistry, Faculty of Science and Center of Nanotechnology, Kasetsart University Research and Development Institute, Kasetsart University, Bangkok 10900, Thailand*
[2]*NANOTEC Center of Excellence, National Nanotechnology Center, Kasetsart University, Bangkok 10900, Thailand*
[3]*Center for Advanced Studies in Nanotechnology and Its Applications in Chemical, Food and Agricultural Industries, Kasetsart University, Bangkok 10900, Thailand*

*Corresponding author: Tel. +66 2562 5555 ext 2169, Fax: +66 2562 5555 ext 2176,
E-mail address: jumras.l@ku.ac.th

**Keywords** Single-Walled Carbon Nanotube, Defect Healing, Carbon Monoxide Disproportionation

## Abstract

We proposed a new method of bimolecular healing of the vacancy defect in single-walled carbon nanotubes (SWCNTs). The creation of a new method was of particular importance to avoid the errors often encountered in the electronic properties of carbon nanotubes. Using DFT calculations with the PBE functional, we investigated the reaction mechanism of the monatomic vacancy defect in the (8, 0) SWCNT healing process using carbon monoxide disproportionation. Successful healing of the vacancy defect will enable numerous advantages: **(1)** The activation energy is relatively low, 9.37 kcal $mol^{-1}$, at the 4-membered-ring opening step under a high CO concentration condition; **(2)** no catalyst is needed, thus no purification step is needed to remove the catalyst; **(3)** only the CO ambient is used as a reactant; **(4)** no oxygen byproduct was found; and **(5)**, there was high selectivity of CO to vacancy defect sites. Our finding established that a CNT with a vacancy defect, which was generally obtained from the syntheses or other uses as a nanomaterial device, can be healed completely to resume its function as a perfect CNT holding the original electronic properties.

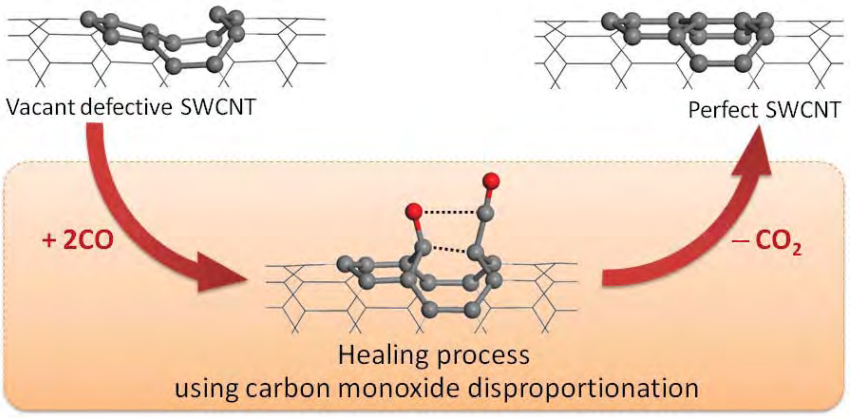


**Fig. 1** Structures and reaction mechanisms of bimolecular healing of the monatomic vacancy defect in single-walled carbon nanotubes (SWCNTs).

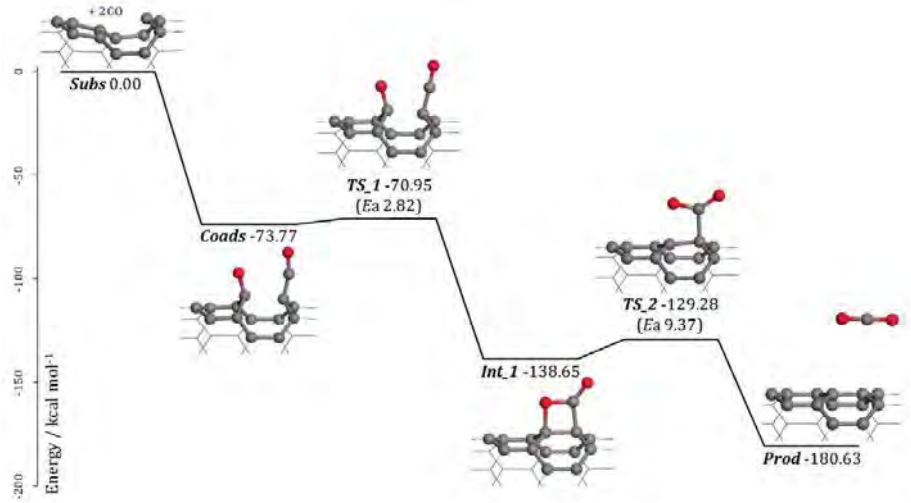


**Fig. 2** The Associative-Coadsorption Pathway (ACP) energy profile of the healing process of the monatomic vacancy defect in the (8, 0) SWCNT using carbon monoxide disproportionation was proposed under the high CO concentration.

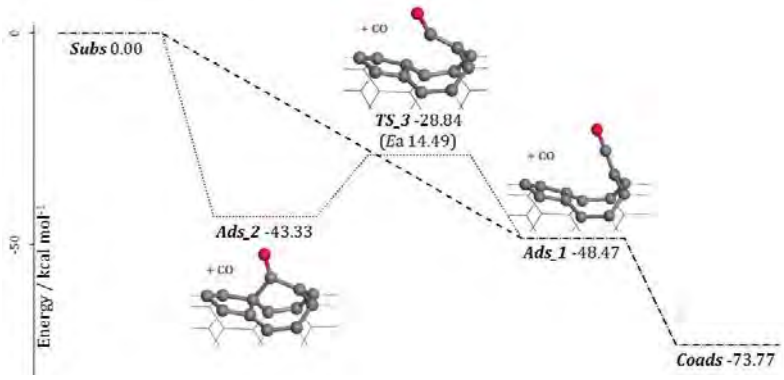


**Fig. 3** The Consecutive-Coadsorption Pathway (CCP) energy profile of the healing process of the monatomic vacancy defect in the (8, 0) SWCNT using carbon monoxide disproportionation was proposed under the low CO concentration. (Dashed line is the CCP-1; Dotted line is the CCP-2.)

## Acknowledgements

This work was supported in part by grants from the National Science and Technology Development Agency (2009 NSTDA Chair Professor funded by the Crown Property Bureau under the management of the National Science and Technology Development Agency and NANOTEC Center of Excellence funded by the National Nanotechnology Center), Kasetsart University Research and Development Institute (KURDI), the Thailand Research Fund (TRF), the Commission on Higher Education, Ministry of Education (the "National Research University Project of Thailand (NRU)" and the "National Center of Excellence for Petroleum, Petrochemical and Advanced Materials (NCE-PPAM)") and the Development and Promotion of Science and Technology Talents Project (DPST). The Kasetsart University Graduate School is also acknowledged. The computational calculations were supported by the Thai National Grid Center (TNGC) under the Software Industry Promotion Agency (SIPA).

## References

Page A. J., Y. Ohta, Y. Okamoto, S. Irle and K. Morokuma; "Defect Healing During Single-Walled Carbon Nanotube Growth: A Density-Functional Tight-Binding Molecular Dynamics Investigation." The Journal of Physical Chemistry C, 113, 20198–20207 (2009).

Nikolaev P., M. J. Bronikowski, R. K. Bradley, F. Rohmund, D. T. Colbert, K. A. Smith and R. E. Smalley; "Gas-Phase Catalytic Growth of Single-Walled Carbon Nanotubes from Carbon Monoxide." Chemical Physics Letters, 313, 91–97 (1999).

# Carbonyl-ene Reaction of Encapsulated Formaldehyde in Cu(I), Ag(I) and Au(I) Exchanged FAU Zeolites

Sippakorn Wannakao[1,2,3], Pipat Khongpracha[1,2,3], Jumras Limtrakul[1,2,3*]

[1]*Laboratory for Computational and Applied Chemistry, Department of Chemistry, Faculty of Science and Center of Nanotechnology, Kasetsart University Research and Development Institute, Kasetsart University, Bangkok 10900, Thailand*

[2]*NANOTEC Center of Excellence, National Nanotechnology Center, Kasetsart University, Bangkok 10900, Thailand*

[3]*Center for Advanced Studies in Nanotechnology and Its Applications in Chemical, Food and Agricultural Industries, Kasetsart University, Bangkok 10900, Thailand*

*Corresponding author: Tel. +66 2562 5555 ext 2169, Fax: +66 2562 5555 ext 2176,
E-mail address: jumras.l@ku.ac.th

**Keywords** Zeolite, Transition metal exchange, Formaldehyde, Chemical reaction, Density functional theory

## Abstract

Carbonyl-ene reaction is one of the common and very powerful tools for organic synthesis. In this work, we investigated the reaction mechanism of propene interacting with an encapsulated formaldehyde in Cu, Ag and Au-exchanged faujasite zeolites by means of the density functional theory using the newly developed and more accurate M06-L/6-31G(d,p) level of theory. Formaldehyde bound to the metal site provided adsorption energies of -15.8, -18.3 and -20.9 kcal/mol for Cu, Ag and Au-FAU, respectively. From NBO calculation, a high ionicity bonding characteristic between Au and O formed by 6s orbital of the Au atom and 2p orbital of the O atom was clearly observed. Moreover, Au-FAU was also the most active for the reaction which required 15.0 kcal/mol for the activation barrier while the rest were around 18.0 kcal/mol. These results provide significant information for utilizing these novel transition metal exchanged materials for organic synthesis processes.

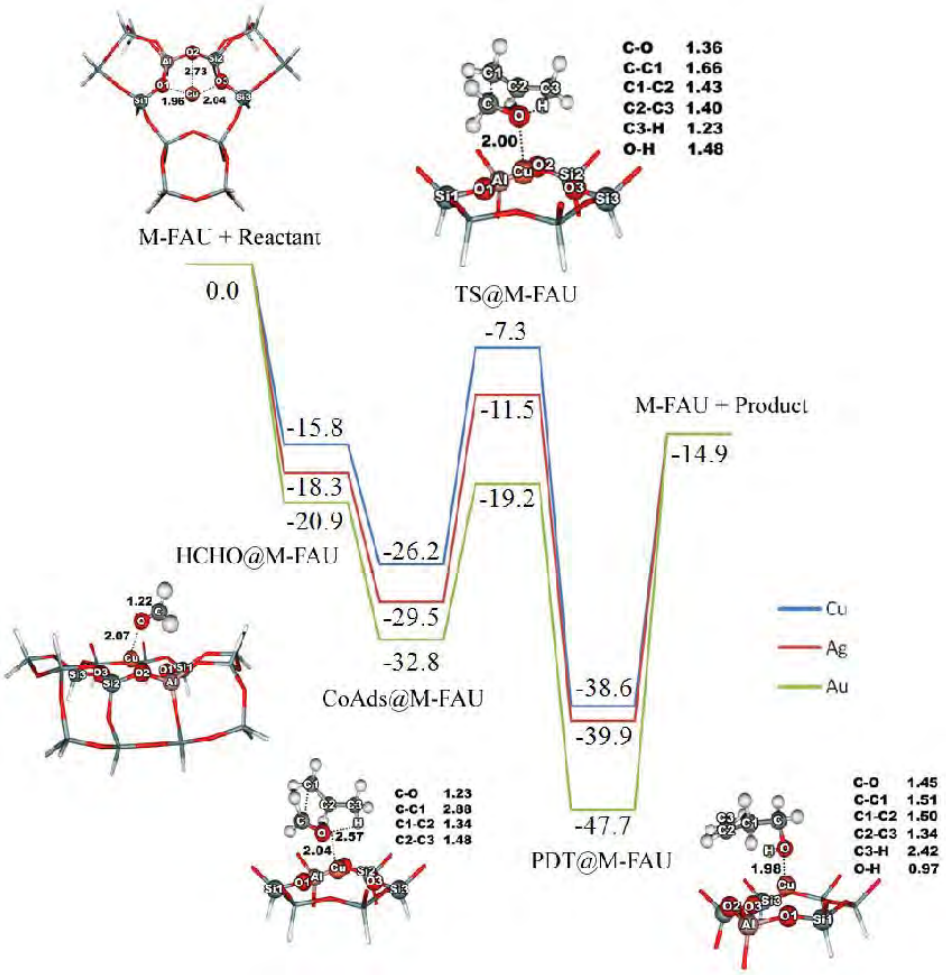


**Fig. 1** Reaction profile of the formaldehyde-propene carbonyl-ene reaction over Cu, Ag and Au-FAU zeolites. Energies are in kcal/mol units.


## Acknowledgements

This work was supported in part by grants from the National Science and Technology Development Agency (2009 NSTDA Chair Professor funded by the Crown Property Bureau under the management of the National Science and Technology Development Agency and NANOTEC Center of Excellence funded by the National Nanotechnology Center), the Royal Golden Jubilee Ph.D. program from the Thailand Research Fund (to S.W.) and the Commission on Higher Education, Ministry of Education (the "National Research University Project of Thailand (NRU)" and the "National Center of Excellence for Petroleum, Petrochemical and Advanced Materials (NCE-PPAM)"). The support from the Kasetsart University Research and Development Institute (KURDI) is also acknowledged. The authors are grateful to Donald G. Truhlar and Yan Zhao for their support with the M06-L functional.


## References


Sangthong W., M. Probst and J. Limtrakul; "Computational Study of the Carbonyl-ene Reaction of Encapsulated Formaldehyde in Na-FAU Zeolite", J. Mol. Struct., 748(1-3), 119-127 (2005).

Choomwattana S., T. Maihom, P. Khongpracha, M. Probst and J. Limtrakul; "Structures and Mechanisms of the Carbonyl-ene Reaction between MOF-11 Encapsulated Formaldehyde and Propylene: An ONIOM Study", J. Phys. Chem. C, 112 (29), 10855–10861 (2008).

Zhao Y. and D.G. Truhlar; "Density Functionals with Broad Applicability in Chemistry", Acc. Chem. Res., 41(2), 157-167 (2008).

# Theoretical Investigation of the Effect of the Zeolite Acidic Strength on the Reaction Mechanism of *n*-Hexane Cracking

Thana Maihom[1,2,3], Jumras Limtrakul[1,2,3*]

[1]*Laboratory for Computational and Applied Chemistry, Department of Chemistry, Faculty of Science and Center of Nanotechnology, Kasetsart University Research and Development Institute, Kasetsart University, Bangkok 10900, Thailand*
[2]*NANOTEC Center of Excellence, National Nanotechnology Center, Kasetsart University, Bangkok 10900, Thailand*
[3]*Center for Advanced Studies in Nanotechnology and Its Applications in Chemical, Food and Agricultural Industries, Kasetsart University, Bangkok 10900, Thailand*

*Corresponding author: Tel. +66 2562 5555 ext 2169, Fax: +66 2562 5555 ext 2176,
E-mail address: jumras.l@ku.ac.th

**Keywords** Cracking, Hexane, Zeolite, Acidic strength

## Abstract

The catalytic cracking of hydrocarbons is one of the important reactions in the petrochemical industry. It is used to break down large hydrocarbons in crude oil into light hydrocarbons for the production of fuels. It is generally accepted that the activity of this reaction is related to the acid strength of the zeolite. Therefore, it is of interest to study what role the zeolite's acid strength plays in the cracking reaction.

In this work, the effects of the acid strength on the cracking reaction have been investigated using the isomorphously substituted MFI zeolites: the H-[Al]-MFI and the H-[B]-MFI zeolites as catalysts at the M06-2X/6-311+G(2df,2p)//M06-2X/6-31G(d,p) level of theory. The calculated adsorption energies of n-hexane are –18.2 and –17.2 kcal/mol for H-[Al]-MFI and H-[B]-MFI, respectively. The former estimated adsorption energy is in excellent agreement with experimental measurement. The reaction mechanism of n-hexane cracking consists of two steps. In the first step, the acidic proton of the zeolites is protonated to the n-hexane C-C bond to form the highly unstable 3-C-hexonium intermediate in the nanocavity. For the second step, the 3-C-hexonium intermediate is decomposed to generate the propane and propene products. The first step is found to be the rate-determining step with activation energies of 45.8 and 54.2 kcal/mol for H-[Al]-MFI and H-[B]-MFI, respectively. The apparent and overall reaction energies are calculated to be 36.8 and 55.0 kcal/mol for H-[Al]-MFI zeolite and 45.3 and 62.5 kcal/mol for H-[B]-MFI zeolite. The activation energies in H-[Al]-MFI zeolite are lower due to their more acidic than H-[B]-MFI zeolite. The results verified that the intrinsic catalytic activity of n-hexane cracking is more sensitive to the acid strength of zeolites.

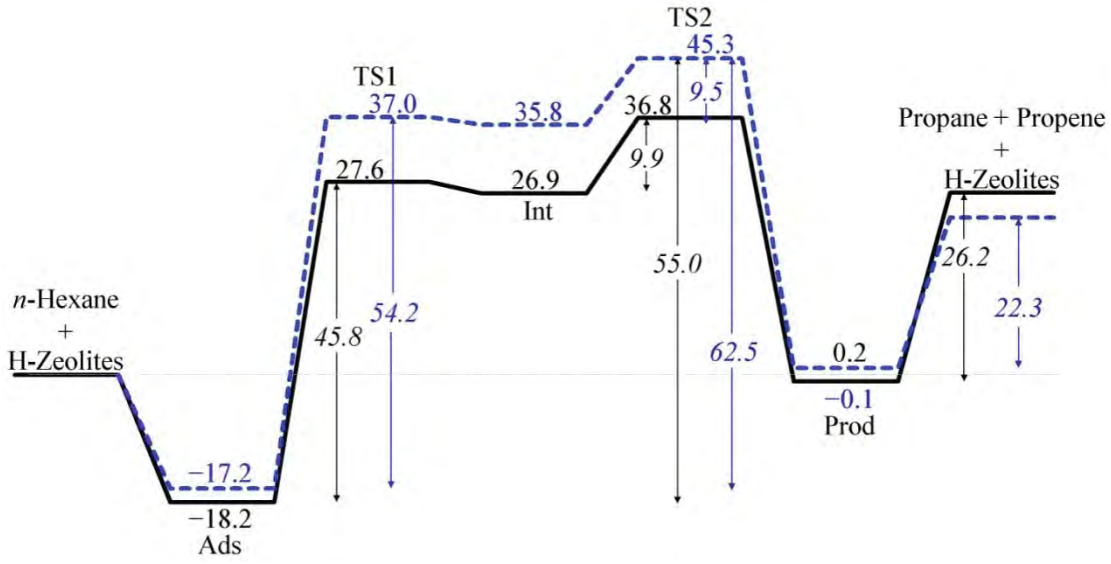


**Fig. 1** Energy profile for the n-hexane cracking mechanisms for both zeolites: H-[Al]-MFI zeolite (solid line) and H-[B]-MFI (dashed line) zeolite (energies are in kcal/mol).


## Acknowledgements

This work was supported in part by grants from the National Science and Technology Development Agency (NANOTEC Center of Excellence and NSTDA Chair Professor), the Kasetsart University Research and Development Institute (KURDI), the Commission on Higher Education, Ministry of Education (the "National Research University Project of Thailand (NRU)" and the "National Center of Excellence for Petroleum, Petrochemical and Advanced Materials (NCE-PPAM)") as well as under the program Strategic Scholarships for Frontier Research Network for the Joint Ph.D. Program Thai Doctoral degree from the office of the Higher Education Commission, Thailand (to TM). The authors are grateful to Donald G. Truhlar and Yan Zhao for supporting them with the code for the M06-2X functional.


## References


Maihom T., P. Pantu, C. Tachakritikul, M. Probst and J. Limtrakul; "Effect of the Zeolite Nanocavity on the Reaction Mechanism of n-Hexane Cracking: A Density Functional Theory Study" J. Phys. Chem. C , 114, 7850-7856 (2010).

Sirijaraensre J. and J. Limtrakul; "Effect of the Acidic Strength on the Vapor Phase Beckmann Rearrangement of Cyclohexanone Oxime over the MFI Zeolite: an Embedded ONIOM Study". Phys Chem Chem Phys 11 (3), 578-585 (2009).

Zhao Y. and D. G. Truhlar; "Benchmark Data for Interactions in Zeolite Model Complexes and Their Use for Assessment and Validation of Electronic Structure Methods" J. Phys. Chem. C. 112, 6860-6868 (2008).

Williams B. A., S. M. Babitz, J. T. Miller, R. Q. Snurr and H. H. Kung; "The Roles of Acid Strength and Pore Diffusion in the Enhanced Cracking Activity of Steamed Y Zeolites" Appl. Catal. A 177, 161-175 (1999).

# H-Bond Formation Assisted by a Single Au Atom and an $Au_{13}$ Cluster: A DFT Study

Anawat Thivasasith[1,2,3], Panvika Pannopard[1,2,3], Pipat Khongpracha[1,2,3], Chompunuch Warakulwit[1,2,3], Jumras Limtrakul[1,2,3*]

[1]*Laboratory for Computational and Applied Chemistry, Department of Chemistry, Faculty of Science and Center of Nanotechnology, Kasetsart University Research and Development Institute, Kasetsart University, Bangkok 10900, Thailand*
[2]*NANOTEC Center of Excellence, National Nanotechnology Center, Kasetsart University, Bangkok 10900, Thailand*
[3]*Center for Advanced Studies in Nanotechnology and Its Applications in Chemical, Food and Agricultural Industries, Kasetsart University, Bangkok 10900, Thailand*

*Corresponding author: Tel. +66 2562 5555 ext 2169, Fax: +66 2562 5555 ext 2176, E-mail address: jumras.l@ku.ac.th

**Keywords** H-bond formation, Cysteine-formic acid, Biosensor, Density functional theory (DFT), Gold atom, Gold cluster

## Abstract

An "$Au_{13}$-cysteine-formic acid" system was used as a simple model for a high sensitive biosensor. In this model, an $Au_{13}$ cluster linked with a cysteine molecule via a metal-thiolate (M-S) bond was chosen to represent a unit of Au clusters or Au nanostructures-based biosensor. The interaction between cysteine and formic acid was selected to be used as a very simple model representing an H-bond interaction that might be utilized in a biosensor. The geometries and electronic properties of the bare $Au_{13}$ cluster, cysteine (Cys), formic acid ($HCO_2H$) and their hybrid system were investigated by using density functional theory (DFT) calculations with the B3LYP functional. The calculations were performed by using the 6-31G** basis set for all the atoms except Au, for which the LANL2DZ was used. The calculations showed that the cysteine has high affinity to the single Au atom and the $Au_{13}$ cluster via the metal-thiolate bond with interaction energies of 46.04 kcal/mol and 63.27 kcal/mol, respectively. In the presence of the Au atom and the $Au_{13}$ cluster, the interaction energies between the Cys/$HCO_2H$ molecules were found to be higher (17.30 kcal/mol and 17.58 kcal/mol, respectively) than that of the bare complex (14.67 kcal/mol). Thus, the Au atom or the $Au_{13}$ cluster slightly affected the interaction energy between cysteine and formic acid. However, the modulation of the energy gap between the highest occupied molecular orbital (HOMO) and the lowest unoccupied molecular orbital (LUMO) of the system revealed that the presence of the Au atom and the $Au_{13}$ cluster increase the conductivity of the system by lowering the HOMO-LUMO gap (4.28 eV and 4.30 eV for the Au/Cys/$HCO_2H$ and the $Au_{13}$/Cys/$HCO_2H$ hybrid systems vs. 6.28 eV for the bare Cys/$HCO_2H$ complex).

## Acknowledgements

This work was supported in part by grants from the National Science and Technology Development Agency (2009 NSTDA Chair Professor funded by the Crown Property Bureau under the management of the National Science and Technology Development Agency and NANOTEC Center of Excellence funded by the National Nanotechnology Center), Kasetsart University Research and Development Institute (KURDI), the Thailand Research Fund (TRF) and the Commission on Higher Education, Ministry of Education (the "National Research University Project of Thailand (NRU)" and the "National Center of Excellence for Petroleum, Petrochemical and Advanced Materials (NCE-PPAM)"). The Graduate School, Kasetsart University is also acknowledged.

## References

Tiwari S. and P.C Mishra; "Vibrational Spectra of Cysteine Zwitterion and Mechanism of Its formation: Bulk and Specific Solvent Effects and Geometry Optimization in Aqueous Media" Spectrochimica Acta Part A: Molecular and Biomolecular Spectroscopy, 73, 719–729 (2009).

Larsson J. A., M. Nolan and J.C. Greer; "Interactions between Thiol Molecular Linkers and the $Au_{13}$.Nanopaticle" The Journal of Physical Chemistry B, 106, 5931-5931 (2002).

Pannopard P., P. Khongpracha, M. Probst and J. Limtrakul; "Structure and Electronic Properties of ''DNA–Gold–Nanotube'' Systems: A Quantum Chemical Analysis" Journal of Molecular Graphics and Modelling, 26, 1066-1075 (2007).

# Theoretical Studies of Nitrous Oxide Decomposition Reaction in Transition Metals (TM) Ion Exchanged ZSM-5 Zeolite

Boonruen Sunpetch[1,2,4], Bundet Boekfa[2,3,4], Piboon Pantu[1,2,4], Jumras Limtrakul[1,2,4*]

[1]*Laboratory for Computational and Applied Chemistry, Department of Chemistry, Faculty of Science and Center of Nanotechnology, Kasetsart University Research and Development Institute, Kasetsart University, Bangkok 10900, Thailand*
[2]*NANOTEC Center of Excellence, National Nanotechnology Center, Kasetsart University, Bangkok 10900, Thailand*
[3]*Chemistry Department, Faculty of Liberal Art and Science, Kasetsart University Kamphaeng Saen Campus, Nakhon Pathom 73140, Thailand*
[4]*Center for Advanced Studies in Nanotechnology and Its Applications in Chemical, Food and Agricultural Industries, Kasetsart University, Bangkok 10900, Thailand*

*Corresponding author: Tel. +66 2562 5555 ext 2169, Fax: +66 2562 5555 ext 2176,
E-mail address: jumras.l@ku.ac.th

**Keywords** Heterogeneous Catalysis, Metal-Exchanged Zeolite, nitrous oxide decomposition, ONIOM approach, M06 functional

## Introduction

Zeolites are used in a variety of applications such as petrochemical cracking, ion-exchange, and as a reducing toxic agent. Due to their excellent environmental catalyst, the transition metal (TM) loaded zeolites are used for the nitrous oxide ($N_2O$) decomposition reaction. In experiment, the nitrous oxide decomposition over transition metal ion exchanged zeolites has been studied extensively, but the detailed mechanism and reactivity are still being debated. Fe-ZSM-5 is one of the most widely studied transition metal-exchanged zeolites for nitrous oxide decomposition due to its high activity. The quantum calculation has been used to study the reaction of nitrous oxide decomposition. These works lead us to understand the reaction mechanism, however, the quantum models are quite small and the effects of the zeolite framework are not included. More recently the effects of the zeolite framework have been successfully studied with the newly developed density functional theory, M06 functional. The aim of this work is then: 1) to study the nitrous oxide decomposition on the nanostructure of ZSM-5 zeolite by including the confinement effect via the ONIOM (M06-2X:UFF) approach, and 2) to investigate the activity of different transition metal-exchanged zeolites.

## Computational Details

The nitrous oxide decomposition over transition metal exchanged zeolite has been studied via the ONIOM approach. The inner layer 12T active region was treated with the new density function theory. The outer layer model is extended up to a 96T quantum cluster to realistically represent the confinement effect of the zeolite framework, performed with the UFF force field. The structures of reactants, intermediates, transition states, and products were optimized at the M06 level of theory. The Effective Core Potentials (ECP) of Stuttgart and Born basis sets were assigned to metal center atoms (Ni and Fe) and the 6-31G(d,p) basis sets were applied for other remaining atoms. The total spin of the systems are

kept constant at high spin as sextet and quartet for Fe- and Ni-ZSM-5, respectively. In order to improve the accuracy of reaction energies, single point calculations at M06-2X/6-311+G(df,2p):UFF level of theory were carried out for optimized structures. All calculations were performed with the Gaussian 03 code modified to incorporate the Minnesota Density Functional module 3.1 by Zhao and Truhlar.

## Results and Discussion

The reaction mechanism of nitrous oxide decomposition over TM-ZSM-5 is summarized in Fig. 1. The initial active site is metal oxo species (I) which was reported as the active site for isolated Fe monodentate in ZSM-5. The first step is the adsorption of the first $N_2O$ molecule over the active site ([TMO]+, metal oxo species) through its O-end which is defined as structure II. The adsorbed $N_2O$ is decomposed through the transition state structure (III). The generated $N_2$ molecule adsorbed on the metal dioxo species (([OTMO]+, IV) was desorbed and the extremely active species (V) was generated. Then, the second $N_2O$ comes to adsorb on the metal dioxo isolated site and form the adsorption complex (VI). This complex was changed through the transition state structure (VII) to be the second $N_2$ molecule and 3 O-atoms bound about the TM atom (VIII). Finally, 2 O-atoms adsorbed in the form of an $O_2$ molecule (IX) were desorbed and regenerated the starting active oxo species (I). The decomposition of $N_2O$ through this reaction mechanism was applied to all metal species to make comparable reaction structures.

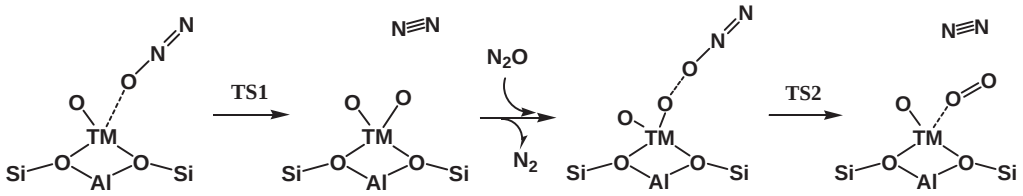


**Fig. 1** The proposed mechanism for $N_2O$ decompositions over TM-ZSM-5 (TM = Fe or Ni).

The nitrous oxide decomposition over Fe- and Ni-ZSM-5 is calculated with the ONIOM 12T:96T (M06-2X/6-311+G(df,2p):UFF//M06/6-31G(d,p):UFF) approach. The reaction of the nitrous oxide molecule locates in the intersection of ZSM-5, as shown in Fig. 2. The adsorption energies of nitrous oxide ($[TMO]^+$, metal oxo species) are -19.6 and -13.3 kcal/mol for Fe-ZSM-5 and Ni-ZSM-5, respectively. The optimized adsorption energies agree well with the experiment of -16 kcal/mol. Nitrous oxide decompositions in transition metal ion exchanged zeolitess are shown in Fig. 3.

The reaction energy profile of nitrous oxide decomposition over Fe-ZSM-5 and Ni-ZSM-5 are shown in Fig. 4. The apparent activation energies of $N_2O$ decomposition are calculated to be 36.5 and 51.6 kcal/mol for Fe- and Ni-ZSM-5, respectively. These results were in the same range as the work of Ryder that calculated the activation energy of $N_2O$ over FeO-ZSM-5 as 37.6 kcal/mol. The produced $N_2$ molecule was desorbed with the desorption energy 5.5 and 1.3 kcal/mol for Fe-, and Ni-ZSM-5, respectively.

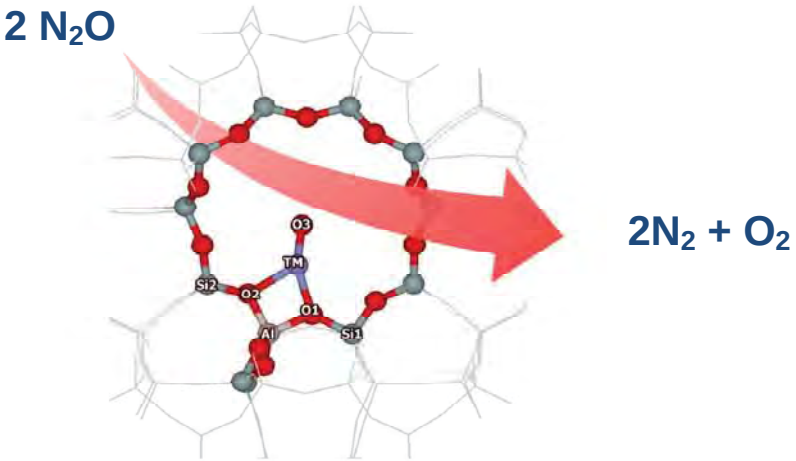


**Fig. 2** The structure of the nitrous oxide molecule on the 12T:96T model of Fe-ZSM-5.

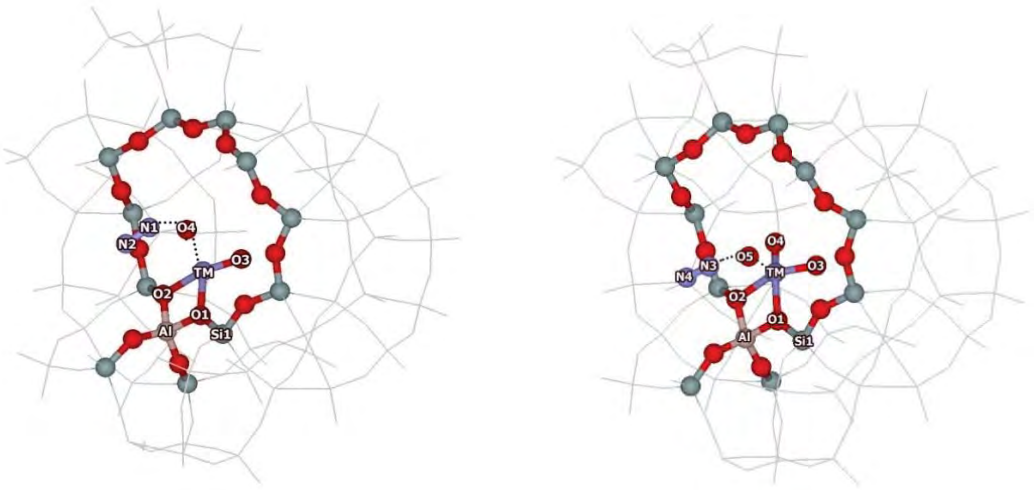


(a) (b)

**Fig. 3** Transition Structure of first (a) and second (b) nitrous oxide decomposition on TM-ZSM-5.

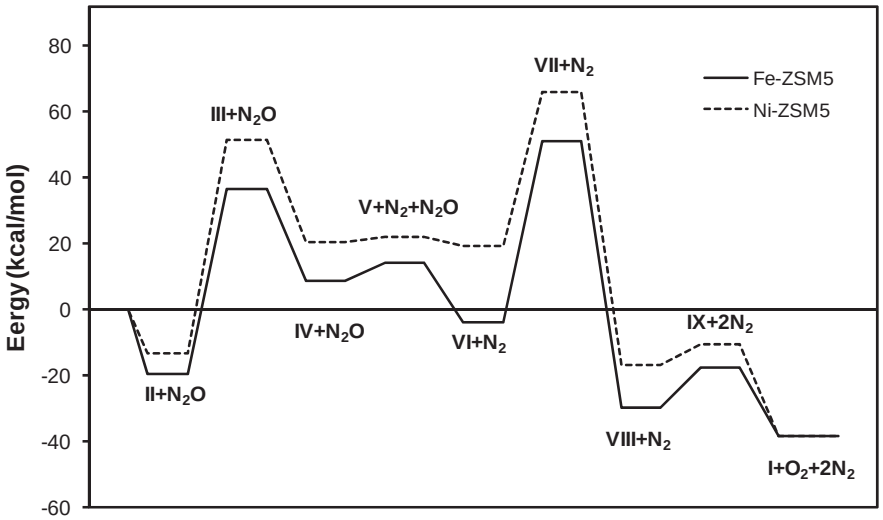


**Fig. 4** Energy profile of $N_2O$ decomposition over TMOx-ZSM-5.

The second $N_2O$ came to adsorb over the metal dioxo ZSM-5 through the oxygen atom (VI) with adsorption energies of -17.8 and 0.1 kcal/mol for Fe- and Ni-ZSM-5, respectively. The adsorption formed over metal dioxo ZSM-5 is less exothermic than the adsorption over metal oxo ZSM-5. This adsorbed $N_2O$ was decomposed through the transition structure (VII). The apparent activation energies for the second $N_2O$ decomposition are 37.0 and 46.8 kcal/mol for Fe- and Ni-ZSM-5, respectively. The product of this stage was the $N_2$ molecule adsorbed on $TMO_3$-ZSM-5 (VIII). The activation energies in this calculation are also close to the experimental results.

Finally, the $O_2$ molecule was released from the TM-ZSM-5 and reproduced the initial active oxo species (I). To eliminate this $O_2$ molecule from TMO-ZSM-5 required the energies of only 12.0 and 6.6 kcal/mol for Fe- and Ni-ZSM-5, respectively. Hence, the rate limiting step of $N_2O$ decomposition over TM-ZSM-5 in this study was the decomposition of first $N_2O$ for both Fe- and Ni-ZSM-5. The decomposition of $N_2O$ over Ni-ZSM-5 requires higher energy than Fe-ZSM-5. This activity trend agrees well with the trend of $N_2O$ decomposition on TM-ZSM-5 reported by Abu-Zied and coworkers that Fe-ZSM-5 is more active than Ni-ZSM-5.

## Conclusion

The catalytic cycle of nitrous oxide decomposition over transition-metal exchanged ZSM-5 zeolite is studied with the ONIOM 12T:96T approach. The models are calculated with the M06-2X:UFF//M06:UFF level of theory. The adsorption energies of nitrous oxide are calculated to be -19.6 and -13.3 kcal/mol for Fe-ZSM-5 and Ni-ZSM-5 zeolite, respectively. The nitrous oxide decomposed reactions are considered to proceed via two steps of mechanism: (1) the decomposition of the first nitrous oxide molecule on metal oxo species to produce nitrogen gas and the metal dioxo species, after that (2) the decomposition of the second nitrous oxide molecule to produce nitrogen gas, oxygen gas and metal oxo species. The reaction mechanisms are proposed to be exothermic. The first step of the reaction is calculated to be the rate of the reaction mechanism. The calculated apparent activation energies are 36.5 and 51.6 kcal/mol for Fe- and Ni-ZSM-5 zeolite, respectively. For the second step of the reaction the apparent activation energies are 37.0 and 46.8 kcal/mol, respectively. This calculation shows that Fe-ZSM-5 is more active than Ni-ZSM-5 for the reaction of nitrous oxide decomposition and agree well with experiment data. The ONIOM (M06:UFF) model, which includes the zeolite framework effect, can be used to calculate more reliable results.

## Acknowledgements

This work was supported in part by grants from the National Science and Technology Development Agency (2009 NSTDA Chair Professor funded by the Crown Property Bureau under the management of the National Science and Technology Development Agency and NANOTEC Center of Excellence funded by the National Nanotechnology Center), Kasetsart University Research and Development Institute (KURDI), the Thailand Research Fund (TRF), and the Commission on Higher Education, Ministry of Education (the "National Research University Project of Thailand (NRU)" and the "National Center of Excellence for Petroleum, Petrochemical and Advanced Materials (NCE-PPAM)").

## References

Boekfa B., S. Choomwattana, P. Khongpracha, and J. Limtrakul; "Effects of the Zeolite Framework on the Adsorptions and Hydrogen-Exchange Reactions of Unsaturated Aliphatic, Aromatic, and Heterocyclic Compounds in ZSM-5 Zeolite: A Combination of Perturbation Theory (MP2) and a Newly Developed Density Functional Theory (M06-2X) in ONIOM Scheme" Langmuir. 25(22), 12990–12999 (2009).

Choi S. H., B. R.Wood, J. A. Ryder and A. T. Bell; "X-ray Absorption Fine Structure characterization of the local structure of Fe in Fe-ZSM-5" J. Phys. Chem. B 107, 11843-11851 (2003).

Fellah M. F. and I. Onal; "$N_2O$ decomposition on Fe- and Co-ZSM-5: A density functional study." Catal. Today. 137, 410-417 (2008).

Heyden A., B. Peters, A. T. Bell and F. J. Keli; "Comprehensive DFT study of nitrous oxide decomposition over Fe-ZSM5" J. Phys. Chem. B. 109(5), 1857-1873 (2005).

Maihom T., P. Pantu, C. Tachakritikul, M. Probst and J. Limtrakul; "Effect of the Zeolite Nanocavity on the Reaction Mechanism of n-Hexane Cracking: A Density Functional Theory Study" J. Phys. Chem. C. 114 (17), 7850-7856 (2010).

Pantu P., S. Pabchanda and J. Limtrakul; "Theoretical investigation of the selective oxidation of methane to methanol on nanostructured Fe-ZSM-5 by the ONIOM method" Chem. Phys. Chem. 5, 1901-1906 (2004).

Ryder J., A. K. Chakraborty and A. T. Bell; "Density Functional Theory study of nitrous decomposition over Fe- and Co- ZSM5" J. Phys. Chem. B. 106, 7059-7064 (2002)

Wood B. R., J. A. Reimer and A.T. Bell; "Studies of $N_2O$ Adsorption and Decomposition on Fe–ZSM-5" J. Catal. 209, 151- 158 (2002).

Zhao Y. and D. G. Truhlar; "Benchmark Data for Interactions in Zeolite Model Complexes and Their Use for Assessment and Validation of Electronic Structure Methods" J. Phys. Chem. C. 112, 6860-6868 (2008).

# Corporative Effect of Zeolite Framework and Cation on Dehydrogenation of Methanol over Na-Exchanged Faujasite Zeolite: A Newly Developed Density Functional (M06-2X)

Winyoo Sangthong[1,2,3], Jumras Limtrakul[1,2,3*]

[1]*Laboratory for Computational and Applied Chemistry, Department of Chemistry, Faculty of Science and Center of Nanotechnology, Kasetsart University Research and Development Institute, Kasetsart University, Bangkok 10900, Thailand*

[2]*NANOTEC Center of Excellence, National Nanotechnology Center, Kasetsart University, Bangkok 10900, Thailand*

[3]*Center for Advanced Studies in Nanotechnology and Its Applications in Chemical, Food and Agricultural Industries, Kasetsart University, Bangkok 10900, Thailand*

*Corresponding author: Tel. +66 2562 5555 ext 2169, Fax: +66 2562 5555 ext 2176,
E-mail address: jumras.l@ku.ac.th

**Keywords** Zeolite, Methanol, Dehydrogenation, M06-2X

## Abstract

Methanol interacting with cluster models of Na-exchanged Faujasite zeolite ($CH_3OH$@Na-FAU) together with its dehydrogenation mechanisms to produce formaldehyde have been investigated by the recently developed and more accurate density functional theory (M06-2X/6-311+G(2df,p)//M06-2X/6-31G(d,p)). In order to be able to make a comparison, the dehydrogenation was also investigated for the uncatalyzed system and the bare Na(I). We propose two reaction mechanisms. The initial step of the stepwise mechanism comprises the proton transfer from the hydroxyl group to the zeolite framework as well as the formation of the methoxide species. This step requires an activation energy (ΔEact) of 52.8 kcal/mol, and is considered to be the rate determining step. The step following, the second step, is the formation of hydrogen from the proton of the zeolite framework and the hydrogen atom from the methoxy species. This requires an activation energy of 15.6 kcal/mol. For the concerted mechanism, the mechanism consists of the movement of the hydroxyl proton to simultaneously form a bond with the methyl hydrogen atom. The energy barriers are predicted to be 89.0, 96.7, and 81.7 kcal/mol for Na-exchanged faujasite, uncatalyzed system, and bare Na(I), respectively. The reason for this is that the electrostatic field generated by the naked Na(I) ion and the destabilizing role of the oxygen atom in the zeolite lattice surrounding the cation. The results are indicative of the stepwise pathway being favored over the concerted one and demonstrates that the inclusion of the extended zeolite framework has an effect on the structure and energetic of the reaction system. Furthermore, the zeolite framework has a corporative effect on the stabilizing of the transition state complex and the intermediate leading to the lowest energy barrier.

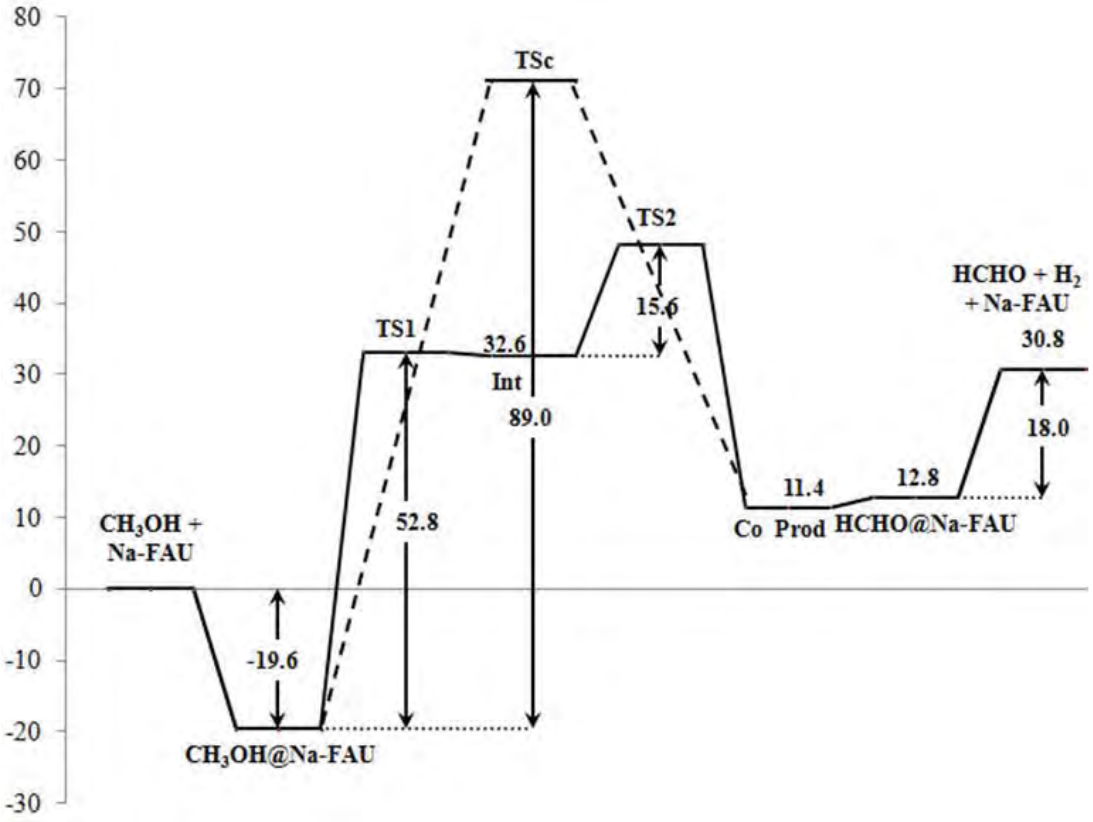


**Fig. 1** Energy profiles for the dehydrogenation reaction of methanol on the 30T quantum cluster of Na-FAU calculated with M06-2X/6-311+G(2df,2p) method: stepwise mechanism (solid line) and concerted mechanism zeolite (dashed line) (energies are in kcal/mol).


## Acknowledgements

This work was supported in part by grants from the National Science and Technology Development Agency (2009 NSTDA Chair Professor funded by the Crown Property Bureau under the management of the National Science and Technology Development Agency and NANOTEC Center of Excellence funded by the National Nanotechnology Center), the Thailand Research Fund (TRF) and the Commission on Higher Education, Ministry of Education (the "National Research University Project of Thailand (NRU)" and the "National Center of Excellence for Petroleum, Petrochemical and Advanced Materials (NCE-PPAM)"). Support from the Kasetsart University Research and Development Institute (KURDI) is also acknowledged.


## References


Plant D. F., A. Simperler and R. G. Bell; "Adsorption of Methanol on Zeolites X and Y. An Atomistic and Quantum Chemical Study." J. Phys. Chem. B, 110, 6170-6178 (2006).

Kang L. and K. Han; "Adsorption and Dehydrogenation of Methanol on Alkali-Cation-Exchanged Zeolite: A First-Principles Density Functional Study." Microporous and Mesoporous Materials, 127, 90-95 (2010).

Boekfa B., S. Choomwattana, P. Khongpracha, and J. Limtrakul; "Effects of the Zeolite Framework on the Adsorptions and Hydrogen-Exchange Reactions of Unsaturated Aliphatic, Aromatic, and Heterocyclic Compounds in ZSM-5 Zeolite: A Combination of Perturbation Theory (MP2) and a Newly Developed Density Functional Theory (M06-2X) in ONIOM Scheme." Langmuir, 25(22), 12990-12999 (2009).

# The Confinement Effect of the Zeolite Framework on the Isomerization Reaction of Propene Oxide over Nanostructured H-FER Zeolite Catalyst Using a Newly Developed "Embedded MP2:M06" Method

Bundet Boekfa[1,2,3], Jumras Limtrakul[1,3,4*]

[1]*NANOTEC Center of Excellence, National Nanotechnology Center, Kasetsart University, Bangkok 10900, Thailand*
[2]*Chemistry Department, Faculty of Liberal Arts and Science, Kasetsart University Kamphaeng Saen Campus, Nakhon Pathom 73140, Thailand*
[3]*Center for Advanced Studies in Nanotechnology and Its Applications in Chemical, Food and Agricultural Industries, Kasetsart University, Bangkok 10900, Thailand*
[4]*Laboratory for Computational and Applied Chemistry, Department of Chemistry, Faculty of Science and Center of Nanotechnology, Kasetsart University Research and Development Institute, Kasetsart University, Bangkok 10900, Thailand*

*Corresponding author: Tel. +66 2562 5555 ext 2169, Fax: +66 2562 5555 ext 2176,
E-mail address: jumras.l@ku.ac.th

**Keywords** Heterogeneous Catalysis, Zeolite, Isomerization reaction, embedded ONIOM, Confinement effect

## Abstract

The confinement effect of the zeolite framework on the adsorption and reaction mechanism has been studied with various methods: quantum cluster, ONIOM (Our own N-layered Integrated molecular Orbital + Molecular mechanics) and a newly developed embedded ONIOM method. The pore structure of H-FER is represented by models from 5T clusters up to realistic 34T clusters. The models are calculated with the newly developed and much accurate computational methods MP2/6-311+G(2df,2p):M06-2X/6-311+G(2df,2p), with the periodic charge from the infinite zeolite lattice included. To begin, the adsorption of propene oxide, propanal and propanone on H-FER zeolite are calculated and found to be -25.5, -24.5 and -26.0 kcal/mol, which agree well with experimental data for the propanone interacted with zeolite (-31.1 kcal/mol). The contributions of the confinement effect from the extended framework are 36, 38 and 67 % of adsorption energies for propene oxide, propanal and propanone over H-FER, respectively. In order to be able to account for the framework lattice, the more accurate "embedded MP2/6-311+G(2df,2p):M06-2X/6-311+G(2df,2p)" method is applied to study the reaction mechanism of propene oxide. The isomerization reaction mechanism of propene oxide is considered to proceed through a stepwise mechanism: (1) the epoxide ring protonation, and, concurrently, the ring-opening, and (2), the 1,2-hydride shift formatting the adsorbed carbonyl compound. Two different types of product, propanal and propanone, were observed. Exothermic reactions were detected with the heat of reaction -20.1 and -29.3 kcal/mol for propene oxide to propanal and propanone, respectively. The transition state complexes are stabilized by the framework. Consequently, it decreases the activation barrier by about 16 – 50%. For the propanal product, the ring opening step is found to be the rate-determining step with an activation barrier of 31.6 kcal/mol, whereas for the propanone product, the hydride shift formatting step is found to be the rate-determining step with a higher activation barrier of 48.9 kcal/mol. The results suggest that the "embedded MP2:M06" is a suitable tool for evaluating the adsorption and reaction mechanism in the nanoconfinement of zeolite.

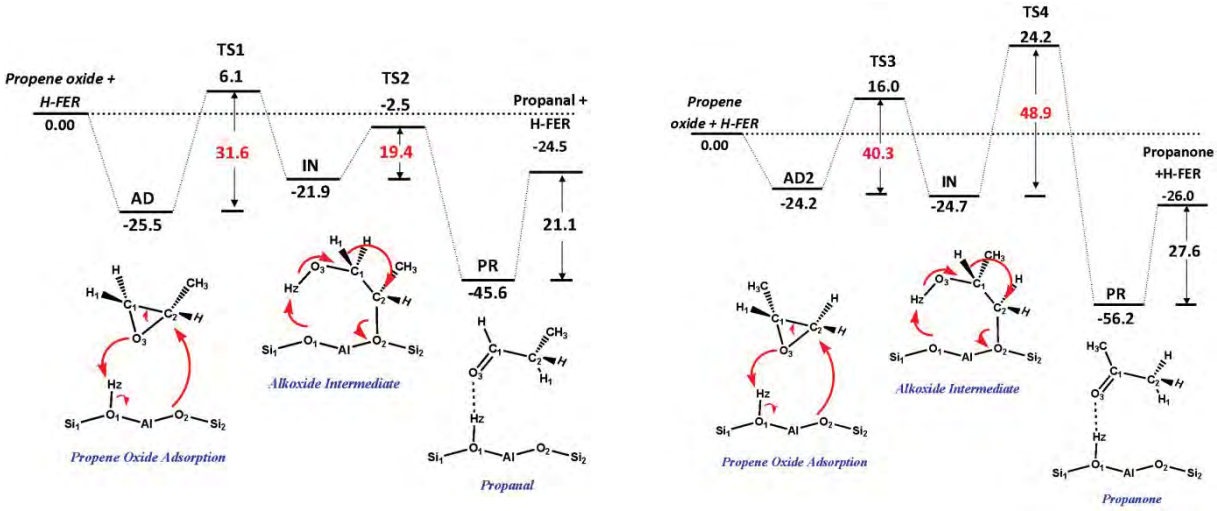


**Fig. 1** Potential energy diagram of the propene oxide isomerization to (a) propanal and (b) propanone on the 5T:34T ONIOM cluster of H-FER, calculated with the embedded MP2/6-311+G(2df,2p):M06-2X/6-311+G(2df,2p)//MP2/6-31G(d,p):M06-2X/6-31G(d,p) method. (kcal/mol).

## Acknowledgements

This work was supported in part by grants from the National Science and Technology Development Agency (2009 NSTDA Chair Professor funded by the Crown Property Bureau under the management of the National Science and Technology Development Agency and NANOTEC Center of Excellence funded by the National Nanotechnology Center), Kasetsart University Research and Development Institute (KURDI), the Thailand Research Fund (TRF), and the Commission on Higher Education, Ministry of Education (the "National Research University Project of Thailand (NRU)" and the "National Center of Excellence for Petroleum, Petrochemical and Advanced Materials (NCE-PPAM)").The authors are grateful to Donald G. Truhlar and Yan Zhao for their support with the M06-2X functional.

## References

Boekfa B., S. Choomwattana, P. Khongpracha, and J. Limtrakul; "Effects of the Zeolite Framework on the Adsorptions and Hydrogen-Exchange Reactions of Unsaturated Aliphatic, Aromatic, and Heterocyclic Compounds in ZSM-5 Zeolite: A Combination of Perturbation Theory (MP2) and a Newly Developed Density Functional Theory (M06-2X) in ONIOM Scheme" Langmuir 25(22), 12990–12999 (2009).

Derouane G. E. and C. D. Chang; "Confinement effects in the adsorption of simple bases by zeolites" Micropor. Mesopor. Mat. 35–36, 425–433 (2000).

Maihom T., B. Boekfa, J. Sirijaraensre, T. Nanok, M. Probst and J. Limtrakul; "Reaction Mechanisms of the Methylation of Ethylene with Methanol and Dimethyl Ether over H-ZSM-5: An ONIOM Study" J. Phys. Chem. C 113, 6654-6662 (2009).

Namuangruk S., P. Khongpracha, P. Pantu, and J. Limtrakul; "Structures and Reaction Mechanisms of Propene Oxide Isomerization on H-ZSM-5: An ONIOM Study". J. Phys. Chem. B 110, 25950-25957 (2006).

Pantu P., B. Boekfa and J. Limtrakul; "The adsorption of saturated and unsaturated hydrocarbon on nanostructured zeolite (H-MOR and H-FAU): An ONIOM study." J. Mol. Cat. A 277,171-179 (2007).

Zhao Y. and D. G. Truhlar; "Benchmark Data for Interactions in Zeolite Model Complexes and Their Use for Assessment and Validation of Electronic Structure Methods" J. Phys. Chem. C 112, 6860-6868 (2008).

# Structures and Reaction Mechanisms of Skeletal Isomerization of 1-Butene over Ferrierite Zeolite: An Embeded Nanocluster Approach

Chularat Wattanakit[1,2,4], Somkiat Nokbin[1,2,4], Bundet Boekfa[2,3,4], Piboon Pantu[1,2,4], Jumras Limtrakul[1,2,4*]

[1]*Laboratory for Computational and Applied Chemistry, Department of Chemistry, Faculty of Science and Center of Nanotechnology, Kasetsart University Research and Development Institute, Kasetsart University, Bangkok 10900, Thailand*

[2]*NANOTEC Center of Excellence, National Nanotechnology Center, Kasetsart University, Bangkok 10900, Thailand*

[3]*Chemistry Department, Faculty of Liberal Art and Science, Kasetsart University Kamphaeng Saen Campus, Nakhon Pathom 73140, Thailand*

[4]*Center for Advanced Studies in Nanotechnology and Its Applications in Chemical, Food and Agricultural Industries, Kasetsart University, Bangkok 10900, Thailand*

*Corresponding author: Tel. +66 2562 5555 ext. 2169, Fax: +66 2562 5555 ext. 2176, E-mail address: jumras.l@ku.ac.th

**Keywords** Skeletal isomerization, Ferrierite, 1-butene adsorption, Isobutene adsorption, Zeolites, DFT, M08-HX, SCREEP

## Introduction

The skeletal isomerization of linear butenes to isobutene has emerged as one of the most interesting topics with concentrated research in both the academic and industry fields. This intense interest has arisen because isobutene can be used in the preparation of intermediates for many productions, including fuel additives and antioxidants, e.g., ethyl tert-butyl ether (ETBE), isooctane and butylated hydroxyanisole (BHA). In general, the skeletal isomerization mechanisms of n-butene to isobutene on zeoites have been proposed in three pathways: the monomolecular mechanism, bimolecular mechanism and pseudomonomolecular mechanism (autocatalytic processes). Although many reaction mechanisms have been studied, the monomolecular mechanism still remains the most suitable one with medium pore zeolites, such as FER, TON and AEL to study the high selectivity of isobutene. Since the isobutoxide, secondary butoxide, the tert-butoxide and the tert-butyl cabenium species have been expected to be the intermediates for the skeletal isomerization of butene isomers. In both the experimental and theoretical studies, it has not been clearly reported whether the tert-butyl carbenium ion is a transition state or a stable intermediate, nor have the stabilities among these species been clearly reported. To address these unclear issues, the complete monomolecular mechanism and the stabilities of related intermediates for the skeletal isomerization of 1-butene to isobutene, including the formation of isobutoxide, 2-butoxide and tert-butyl species as intermediates, will be discussed by means of the DFT approach.

## Methodology

A 37T quantum cluster of the ferrierite zeolite (FER), consisting of 136 atoms ($Si_{37}O_{49}H_{50}$) (Fig. 1a), covering a two-dimensional pore system consisting of 10-membered ring (4.2 Å × 5.4 Å) channels intersected by 8-membered ring (3.5 Å × 4.8 Å) channels in which the isomerization of 1-butene takes place, was selected. All calculations were carried out by means of the density functional theory (DFT) at M08-HX/6-31G(d,p) level of theory. Furthermore, the confinement effects of the

zeolite framework were also demonstrated by the single point calculations at the M08-HX/6-31G(d,p) level of theory using the 114T and 5T models in which the framework effects were considered and neglected, respectively (Fig.s 1b and 1c). In order to be able to cover long range electrostatic interactions of the zeolitic framework beyond the largest model of 144T, the SCREEP model has been employed.

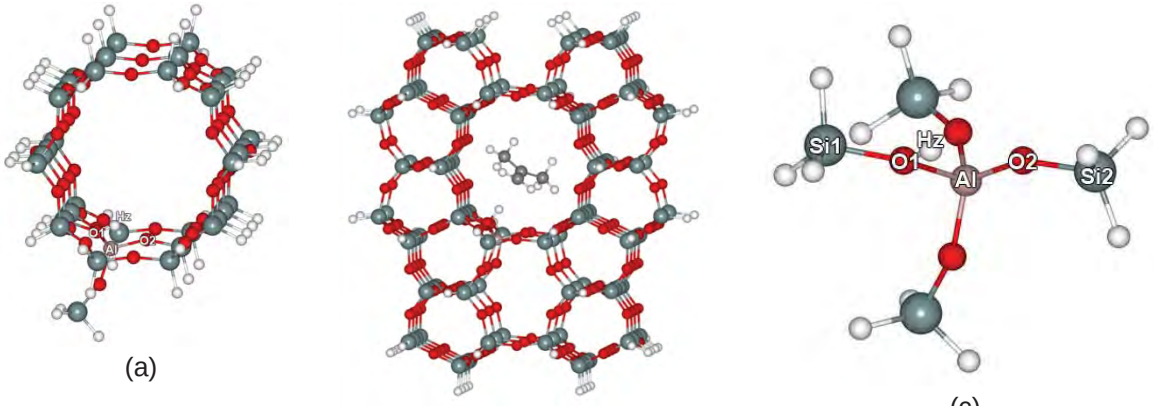


(a) (b) (c)

**Fig. 1** The different models used in the skeletal isomerization of 1-butene to isobutene in H-FER: (a) 37T, (b) 114T and (c) 5T models.

## Results and Discussion

### Adsorption of 1-Butene and Isobutene Over H-Fer

The adsorption energies of 1-butene and isobutene adsorption complexes, at the O1 position, on the 37T H-FER cluster are calculated to be -19.4 and -16.8 kcal/mol, respectively. The isobutene adsorption complex was reported to be less stable than the 1-butene adsorption complex by 2.6 kcal/mol due to steric repulsion between the zeolite frameworks and the methyl groups in the more bulky isobutene molecule. The significance of the confinement effects of the zeolite pore was also investigated by the single point calculations on the 5T, 114T and 114T+SCREEP clusters. For the 5T model, the adsorption energies for the 1-butene and isobutene were -10.2 and -9.6 kcal/mol, respectively, while increasing the cluster sizes to 114T (and 114T including the infinite lattice framework of zeolite) the corresponding adsorption energies were evaluated to be -20.0 (-20.8) and -16.9 (-17.8) kcal/mol, respectively. Our results suggest that the adsorption complexes can be significantly stabilized in the zeolite framework.

### Monomolecular Mechanism of The Skeletal Isomerization of 1-Butene To Isobutene

The reaction mechanism was proposed via four elementary steps as demonstrated in Fig. 2. The mechanism starts with the protonation of the adsorbed 1-butene (I) on the acidic site to provide the 2-butoxide intermediate (III) with an activation energy of 14.1 kcal/mol for the 37T model. The 2-butoxide was subsequently transformed into isobutoxide via the cyclic transition state (IV) which required an activation energy of 26.6 kcal/mol. Subsequently, the transformation of isobutoxide to tert-butyl cation existed through 1,2-hydride transfer with the activation energy of 35.0 kcal/mol and this step was determined to be the rate-determining step. The tert-butyl cation was less stable than isobutoxide and 2-butoxide by about 10.4 and 8.4 kcal/mol, respectively and was easily altered to be an isobutene product by activation energy of only 6.0 kcal/mol. Increasing the framework effect in the 114T cluster, SCREEP charges included, demonstrates that the tert-butyl cation is energetically favorable, similar to those of the isobutoxide and 2-butoxide. The effect of the framework shows significantly different stabilities of alkoxides and carbenium ion as well as the reaction energies. All the alkoxides were destabilized in the zeolite framework, whereas the carbenium ion in the framework effect was more stable than that without the framework effect. Therefore, this work confirms that the existence of tert-butyl cation in the pore of ferrierite was a true intermediate on the potential energy surface (PES) in the realistic system.

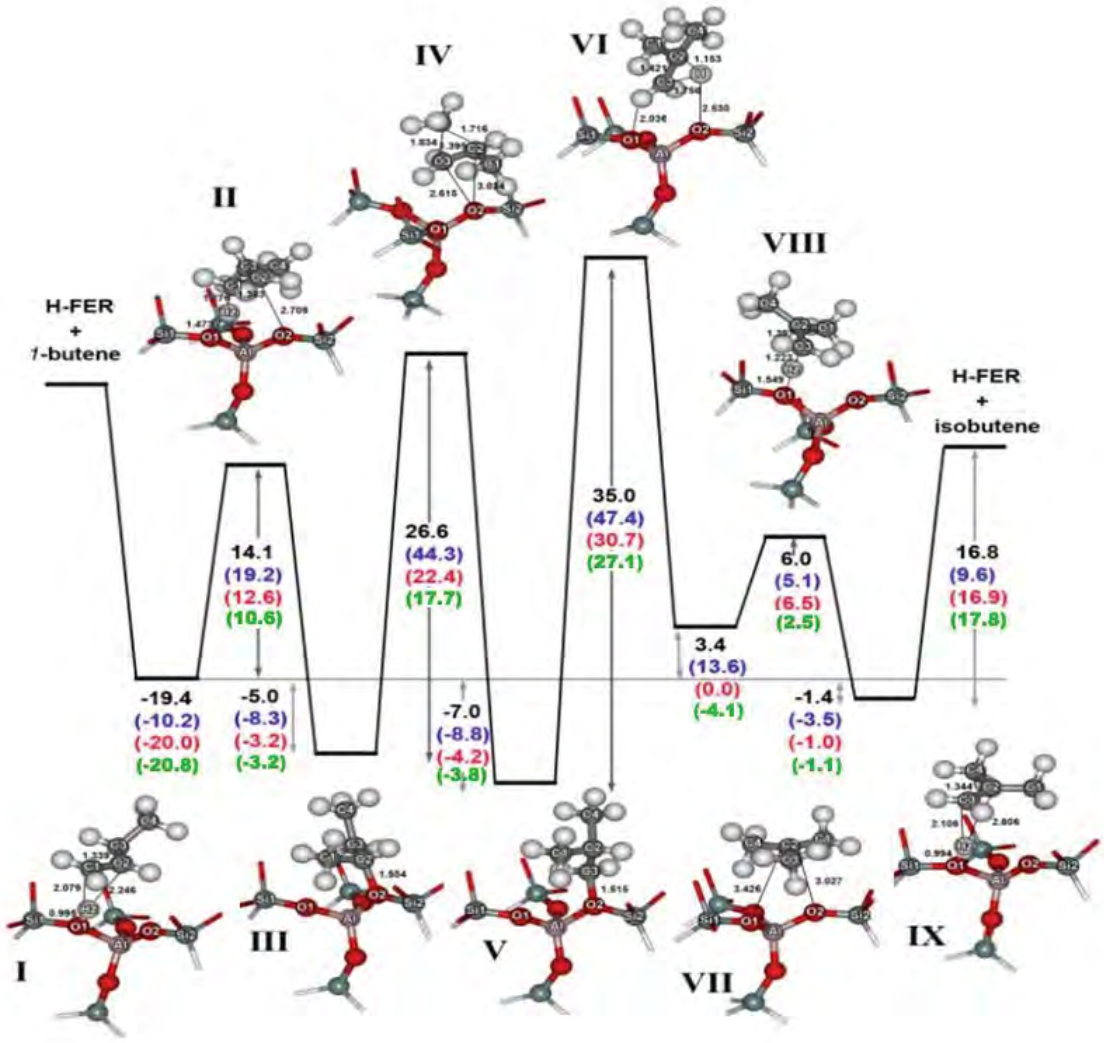


**Fig. 2** The reaction energy profile of 1-butene skeletal isomerization over 5T, 37T, 114T and 114T+SCREEP H-FER zeolite models. Energy values (kcal/mol) for 5T, 37T, 114T and 114T+SCREEP systems are written in blue, black, red and green, respectively.

## Conclusion

The complete reaction mechanisms of skeletal isomerization of 1-butene over ferrierite zeolite have been theoretically investigated using a newly developed density functional theory, M08-HX method with 6-31G(d,p) basis set. The reaction mechanisms of the skeletal isomerization of 1-butene to isobutene are proposed by the monomolecular reaction followed by four elementary steps. The rate-determining step related to the 1,2-hydride shift transition state (VI) in the conversion of isobutoxide to the tert-butyl cation intermediate with the corresponding apparent activation barriers of 38.6, 28.0, 26.5 and 23.3 kcal/mol, for the 5T over the 37T, and up to the more realistic models of 114T and 114T+SCREEP, respectively.

## Acknowledgements

This work was supported in part by grants from The National Science and Technology Development Agency (2009 NSTDA Chair Professor Funded by The Crown Property Bureau under The management of The National Science and Technology Development Agency and NANOTEC Center of Excellence funded by The National Nanotechnology Center), Kasetsart University Research and Development Institute (KURDI), The Thailand Research Fund (TRF), and The Commission on Higher Education, Ministry of Education (The "National Research University Project of Thailand (NRU)" and The "National Center of Excellence for Petroleum, Petrochemical and Advanced Materials (NCE-PPAM)"). CW wishes to thank The Thailand Research Fund (TRF) for a Royal Golden Jubilee Ph.D. Fellowship (3.C.KU/50/A.2).

## References

Boekfa B., S. Choomwattana, P. Khongpracha and J. Limtrakul; "Effects of the zeolite framework on the adsorptions and hydrogen-exchange reactions of unsaturated aliphatic, aromatic, and heterocyclic compounds in ZSM-5 zeolite: a combination of perturbation theory (MP2) and a newly developed density functional theory (M06-2X) in ONIOM scheme", Langmuir 25, 12990-12999 (2009).

Boronat M. and A. Corma; "Are carbenium and carbonium ions reaction intermediates in zeolite-catalyzed reactions?", Appl. Catal. A 336, 2-10 (2008).

Namuangruk S., D. Tantanak and J. Limtrakul; "Application of ONIOM calculations in the study of the effect of the zeolite framework on the adsorption of alkenes to ZSM-5", J. Mol. Catal. A 256, 113-121 (2006).

# DFT Analysis of the MOF Catalyzed Ring-Opening Reaction of Epoxides: An Important Process in Alkoxy Alcohol Synthesis

Sudarat Yadnum[1,2,3], Saowapak Choomwattana[1,2,3], Pipat Khongpracha[1,2,3], Chompunuch Warakulwit[1,2,3],Jumras Limtrakul[1,2,3*]

[1]*Laboratory for Computational and Applied Chemistry, Department of Chemistry, Faculty of Science and Center of Nanotechnology, Kasetsart University Research and Development Institute, Kasetsart University, Bangkok 10900, Thailand*
[2]*NANOTEC Center of Excellence, National Nanotechnology Center, Kasetsart University, Bangkok 10900, Thailand*
[3]*Center for Advanced Studies in Nanotechnology and Its Applications in Chemical, Food and Agricultural Industries, Kasetsart University, Bangkok 10900, Thailand*

*Corresponding author: Tel. +66 2562 5555 ext 2169, Fax: +66 2562 5555 ext 2176,
E-mail address: jumras.l@ku.ac.th

**Keywords** Metal-Organic Framework, M06L, ONIOM, Ring-Opening, Catalyst

## Abstract

The MOF-catalyzed ring-opening reactions of epoxides by methanol, an important route for alkoxy alcohol production, were investigated by using the density functional theory, a recently developed DFT “M06L” with 6-31G(d,p) basis set. The dicopper carboxylate “paddlewheels unit” model was used to represent an active site of MOF-505 catalyst. The interaction of the epoxide ring with methanol was found to take place in a single concerted reaction step. The transition state involving the forming of the C-O bond and the breaking of the C-O and O-H bonds, and hydrogen transfer was proposed. In the dicopper carboxylate catalyzed mechanism, the epoxide initially adsorbed over the dicopper carboxylate with an energy of -16.6 kcal/mol. Subsequently, the interaction energy of the co-adsorption of epoxide and methanol was observed to be -27.9 kcal/mol. This catalyzed reaction was calculated to be exothermic by -47.0 kcal/mol. The dicopper carboxylate, acting as a catalyst, is able to stabilize the “transition state complex” and hence leads to a lower energy barrier ($\Delta E_{act}$) (43.4 kcal/mol) as compared to that of the uncatalyzed reaction (52.0 kcal/mol). To take the framework effect into account, the ONIOM (our-Own-N-layered Integrated molecular Orbital + Molecular Mechanics) (M06L/6-31G(d,p): UFF) calculation was also carried out. The confinement effect of the extended MOF-505 framework was shown to stabilize the adsorption complexes (-27.9 kcal/mol to -32.3 kcal/mol) where the activation energy was not decreased.

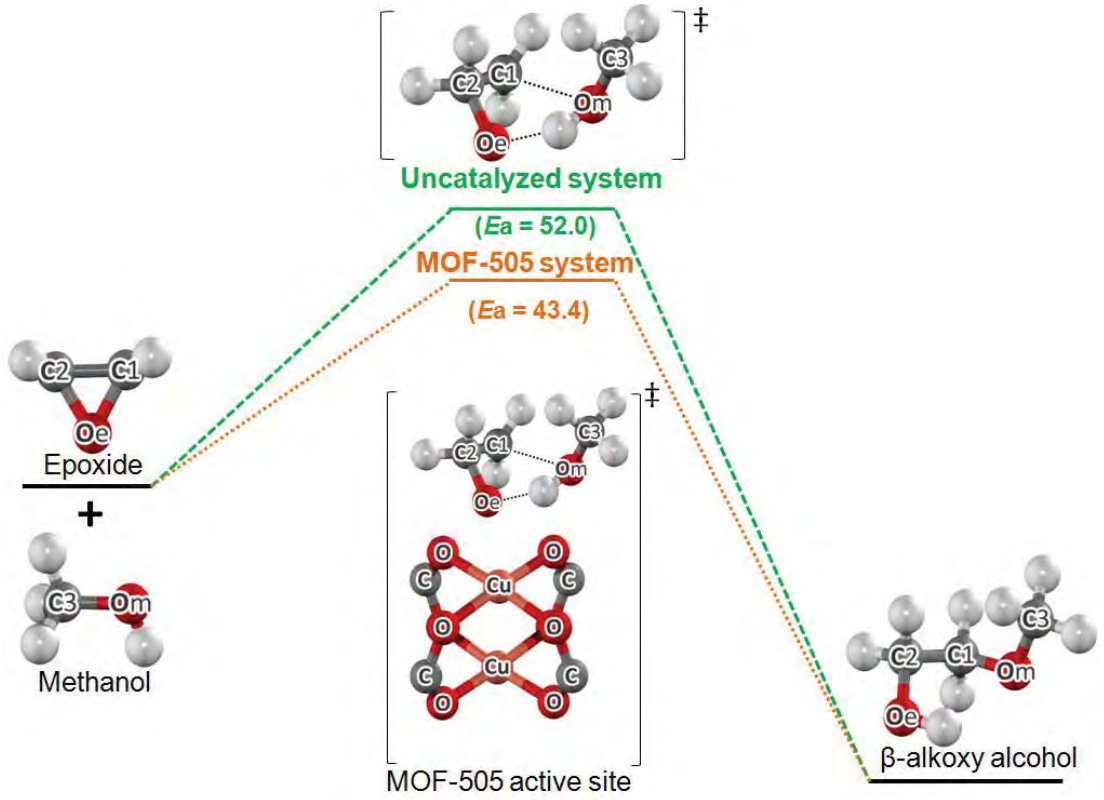


**Fig. 1** Structures and energy profile (kcal/mol) for the epoxide ring-opening in the dicopper carboxylate system (orange line) and the uncatalyzed system (green line).


## Acknowledgements

This work was supported in part by grants from the National Science and Technology Development Agency (2009 NSTDA Chair Professor funded by the Crown Property Bureau under the management of the National Science and Technology Development Agency and NANOTEC Center of Excellence funded by the National Nanotechnology Center), Kasetsart University Research and Development Institute (KURDI), the Thailand Research Fund (TRF), the Royal Golden Jubilee (RGJ) and the Commission on Higher Education, Ministry of Education (the "National Research University Project of Thailand (NRU)" and the "National Center of Excellence for Petroleum, Petrochemical and Advanced Materials (NCE-PPAM)"). The Kasetsart University Graduate School is also acknowledged. The program Strategic Scholarships for Frontier Research Network for the Joint Ph.D. Program Thai Doctoral degree (CHE-PhD-SW) from the office of the Higher Education Commission, Thailand (to S.C.) is also acknowledged.


## References


Jiang D., T. Mallat, F. Krumeich, A. Baiker; "Copper-Based Metal-Organic Framework for the Facile Ring-Opening of Epoxides." J. Catal., 257, 390-395 (2008).

Choomwattana S., T. Maihom, P. Khongpracha, M. Probst, J. Limtrakul; "Structures and Mechanisms of the Carbonyl-ene Reaction between MOF-11 Encapsulated Formaldehyde and Propylene: An ONIOM study." J. Phys. Chem. C, 112, 10855-10861 (2008).

# First-Principle-Derived Potential Energy Function for $Zn_4O$ Tetrahedron-Based Metal-Organic Frameworks

Chadchalerm Raksakoon[1,2,3], Saowapak Choomwattana[1,2,3], Jumras Limtrakul[1,2,3*]

[1]*Laboratory for Computational and Applied Chemistry, Department of Chemistry, Faculty of Science and Center of Nanotechnology, Kasetsart University Research and Development Institute, Kasetsart University, Bangkok 10900, Thailand*
[2]*NANOTEC Center of Excellence, National Nanotechnology Center, Kasetsart University, Bangkok 10900, Thailand*
[3]*Center for Advanced Studies in Nanotechnology and Its Applications in Chemical, Food and Agricultural Industries, Kasetsart University, Bangkok 10900, Thailand*

*Corresponding author: Tel. +66 2562 5555 ext 2169, Fax: +66 2562 5555 ext 2176,
E-mail address: jumras.l@ku.ac.th

**Keywords** Metal-Organic Framework, Force Field, Zn-O bond, Molecular Dynamics, Diffusion

## Abstract

The Zn-O intermolecular potential functions were newly developed for investigating the adsorption and diffusion of *o*-, *m*- and *p*- xylene isomers in metal-organic framework. We constructed the LJ potential for Zn-O by fitting the parameters of the functions of the intermolecular distances to energies derived from B3LYP/6-31G(d,p) calculations. Zn coordinates are generated along lines tetrahedrally coordinated to the O atom according to the vibrational modes taken from the more realistic model of $Zn_4O(O_2C\text{-}C(CH)_2)_6$ evaluated at the ONIOM (B3LYP/6-31G(d,p):UFF) level of theory.

Lennard-Jones equation: $$U_{12-6}(r) = \left(A/r^{12}\right) - \left(B/r^{6}\right)$$

The parameters of the equation employed describing the Zn-O potential energy surfaces were obtained by minimizing the least-square deviation between the energies from the LJ formula and their density functional theory calculated counterparts. Meanwhile, the atomic interactions of the rest of the framework are treated with Morse and harmonic potentials.

Morse potential: $$U_{Morse}(r) = E_0\left[\{1-\exp(-k(r-r_0))\}^2 - 1\right]$$

Harmonic potential: $$U_{harmonic}(r) = \frac{1}{2}k(r-r_0)^2$$

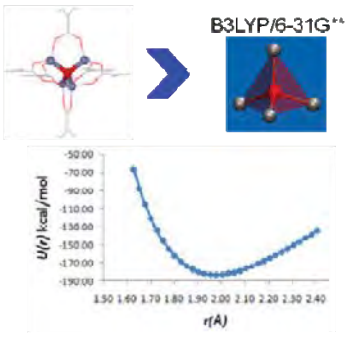


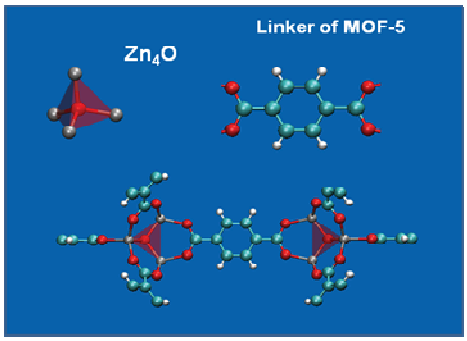


**Fig. 1** (Left) The potential energy surface of $Zn_4O$ in which the Zn-O is tetrahedrally, symmetrically stretched was calculated by B3LYP/6-31G (d,p) method. (Right) MOF-5 components: $Zn_4O$ inorganic node and 1,4-benzenedicarboxylate organic linker and its connectivity. (Zn = grey, O = red, C = cyan, H = white)

**Table 1** Comparison of the calculated lattice using our combined parameterized functions in various conditions and the X-ray crystallographic data

| Parameter | NVT | | | | NPT | | | | X-ray* |
|---|---|---|---|---|---|---|---|---|---|
| | 258 | 300 | 350 | 400 | 258 | 300 | 350 | 400 | |
| Zn-Oc | 1.951 | 1.953 | 1.953 | 1.951 | 1.951 | 1.950 | 1.952 | 1.953 | 1.941 |
| Zn-O | 1.929 | 1.928 | 1.929 | 1.927 | 1.928 | 1.928 | 1.927 | 1.927 | 1.922 |
| Zn-Zn | 3.191 | 3.191 | 3.191 | 3.189 | 3.190 | 3.189 | 3.179 | 3.198 | |
| O-C1 | 1.303 | 1.302 | 1.301 | 1.299 | 1.301 | 1.299 | 1.299 | 1.299 | 1.301 |
| C1-C2 | 1.492 | 1.495 | 1.493 | 1.494 | 1.489 | 1.491 | 1.491 | 1.490 | 1.486 |
| C2-C3 | 1.404 | 1.405 | 1.405 | 1.404 | 1.403 | 1.404 | 1.403 | 1.404 | 1.392 |
| C3-C3 | 1.401 | 1.401 | 1.401 | 1.402 | 1.397 | 1.404 | 1.401 | 1.398 | 1.388 |
| C3-H | 1.083 | 1.081 | 1.082 | 1.082 | 1.082 | 1.081 | 1.078 | 1.084 | |
| Lattice | 25.832 | | | | 25.755 | 25.738 | 25.727 | 25.718 | |

* Jesse L. C. Rowsell et al. Science 309(5739), 1350 – 1354 (2005).

Our combined parameterized functions are found to reproduce the lattice parameter of MOF-5 when compared to the experimental data. To verify its accuracy, molecular dynamics (MD) simulations of ortho-, para- and meta-xylenes in MOF-5 at the temperature of 300 K were performed with the combination of novel in-house potential energy surfaces (PES) and existing potentials to determine the maximum loading. Our calculation reveals that the lattice parameter decreases upon the loading amount increase. At a loading of 56 molecules per unit cell for o-xylene and 54 molecules per unit cell for m- and p-isomers, the lattice parameter begins to increase. This indicates that our derived force field can reproduce the breathing effect in MOF. Moreover, xylene isomers can be differentiated by their self-diffusion coefficients ($D_{self}$) in the framework of MOF-5. At the same loading, p-xylene is found to expand the lattice the most. Unlike in zeolites, where the pore window hindrance is the key difficulty, the diffusion in the open MOF-5 has to overcome π-π attraction of xylenes in the binding pockets. Our original potentials combination could, therefore, give an accurate prediction for other MOF-5 properties.

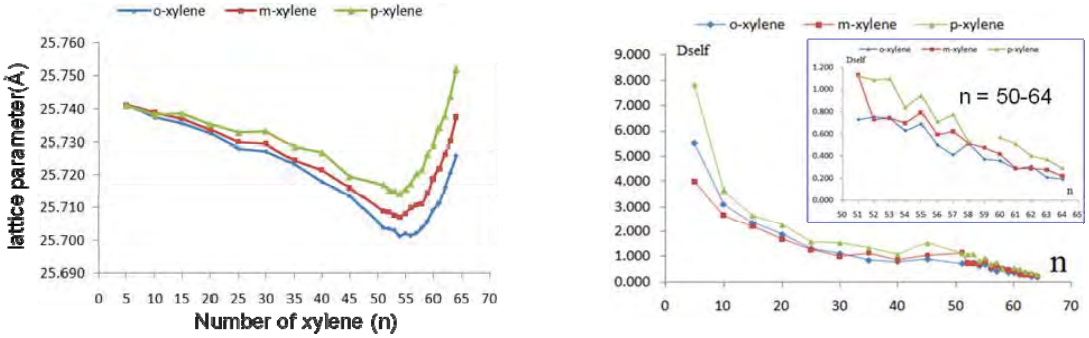


**Fig. 2** Loading amount-dependent variation of the simulated lattice constant of MOF-5 (Left) and self-diffusion coefficient of xylenes (Right) at T = 300 K.

## Acknowledgements

This work was supported in part by grants from the National Science and Technology Development Agency (2009 NSTDA Chair Professor funded by the Crown Property Bureau under the management of the National Science and Technology Development Agency and NANOTEC Center of Excellence funded by the National Nanotechnology Center), Kasetsart University Research and Development Institute (KURDI), the Thailand Research Fund (TRF), the Kasetsart University Graduate School and the Commission on Higher Education, Ministry of Education (the "National Research University Project of Thailand (NRU)" and the "National Center of Excellence for Petroleum, Petrochemical and Advanced Materials (NCE-PPAM)"). The CHE-PhD-SW from the office of the Higher Education Commission, Thailand (to S.C.) is also acknowledged.

## References

Li H., M. Eddaoudi, M. O'Keeffe, O. M. Yaghi; "Design and Synthesis of an Exceptionally Stable and Highly Porous Metal-Organic Framework" Nature, 402, 276-279 (1999).

Tafipolsky M., S. Amirjalayer, R. Schmid; "Ab Initio Parametrized MM3 Force Field for the Metal-Organic Framework MOF-5." J. Comp. Chem. 28(7), 1169–1176 (2007).

# Density Functional Analysis of the Confinement Effect in Nanoporous MCM-22 Petrochemical Catalyst: Nanocluster Model Approach

Pemikar Srifa[1,2,4], Somkiat Nokbin[1,2,4], Bundet Boekfa[2,3,4], Jumras Limtrakul[1,2,4*]

[1]*Laboratory for Computational and Applied Chemistry, Department of Chemistry, Faculty of Science and Center of Nanotechnology, Kasetsart University Research and Development Institute, Kasetsart University, Bangkok 10900, Thailand*
[2]*NANOTEC Center of Excellence, National Nanotechnology Center, Kasetsart University, Bangkok 10900, Thailand*
[3]*Chemistry Department, Faculty of Liberal Art and Science, Kasetsart University Kamphaeng Saen Campus, Nakhon Pathom 73140, Thailand*
[4]*Center for Advanced Studies in Nanotechnology and Its Applications in Chemical, Food and Agricultural Industries, Kasetsart University, Bangkok 10900, Thailand*

*Corresponding author: Tel. +66 2562 5555 ext 2169, Fax: +66 2562 5555 ext 2176,
E-mail address: jumras.l@ku.ac.th

**Keywords** Pyridine adsorption, MCM-22 zeolite, Acidity, Brønsted site, DFT, M06-2X

## Introduction

Acidic MCM-22 (H-MCM-22) is one of the porous aluminosilicate zeolites used as the acid catalyst for petrochemical processes. Basically, the catalytic properties of this material can be investigated by the adsorption of basic probe molecules such a pyridine on its Brønsted acidic site. Inside this adsorption process, the confinement effect of all physical interactions between adsorbed substrate and the zeolitic framework has played an important role on adsorption enthalpies. The confinement effect from the zeolite framework on the adsorption of pyridine has been recently investigated via QM:MM calculations named “B3LYP:UFF”. The calculated adsorption energies of pyridine over two types of zeolites, H-ZSM-5 and H-FAU agree well with experimental data. However, it is due to a larger extent from the fact that the overestimation of “van der Waals interactions” generated by the force field, UFF coupled nicely with the systemical compensation of the interactions from a small quantum cluster treated by the density functional, B3LYP method. However, one might expect somewhat underestimated adsorption energy derived from this hybrid model (B3LYP:UFF) when increasing the size of the quantum cluster, and especially when absorbing species are quite large organic molecules such as large aliphatic and aromatic hydrocarbons. Recently, the newly developed density functional theory, M06 functional, has been successfully applied to address and understand the confinement contributed from nanoporous materials. In this study the effect of zeolite confinement on the adsorption properties of pyridine interacted with nanoporous H-MCM-22 will be investigated and their results will be compared with experimental data. Thus, it can to some extent be employed to fine tune the acidity of zeolites and, hence, be useful for the zeolite’s community and for them to systemically select the right candidates for their reaction.

## Computational Details

Protonic H-MCM-22 zeolite was selected to study the pyridine adsorption reaction in order to examine the confinement effect of the H-MCM-22 zeolite. Five different cluster sizes, i.e., 5T, 14T, 38T, 54T and 120T clusters (T represents the tetrahedral of Si or Al atoms) were employed in this work, as shown in Fig. 1. In all models, one Si atom at the T1 position was replaced by an Al atom,

leading to the generation of the Brønsted acid site. All geometry optimizations of pyridine adsorption over the 5T, 14T and 38T models were calculated at the M06-2X/6-31G(d,p) level of theory. In order to get more accurate adsorption energies due to the confinement effect of H-MCM-22, single-point energy calculations of the optimized structures of the 38T systems embedded in the 54T and 120T systems were also carried out at the same level. All calculations were carried out using the Gaussian 03 code incorporated with the Minnesota Density Functionals module 3.1 by Zhao and Truhlar.

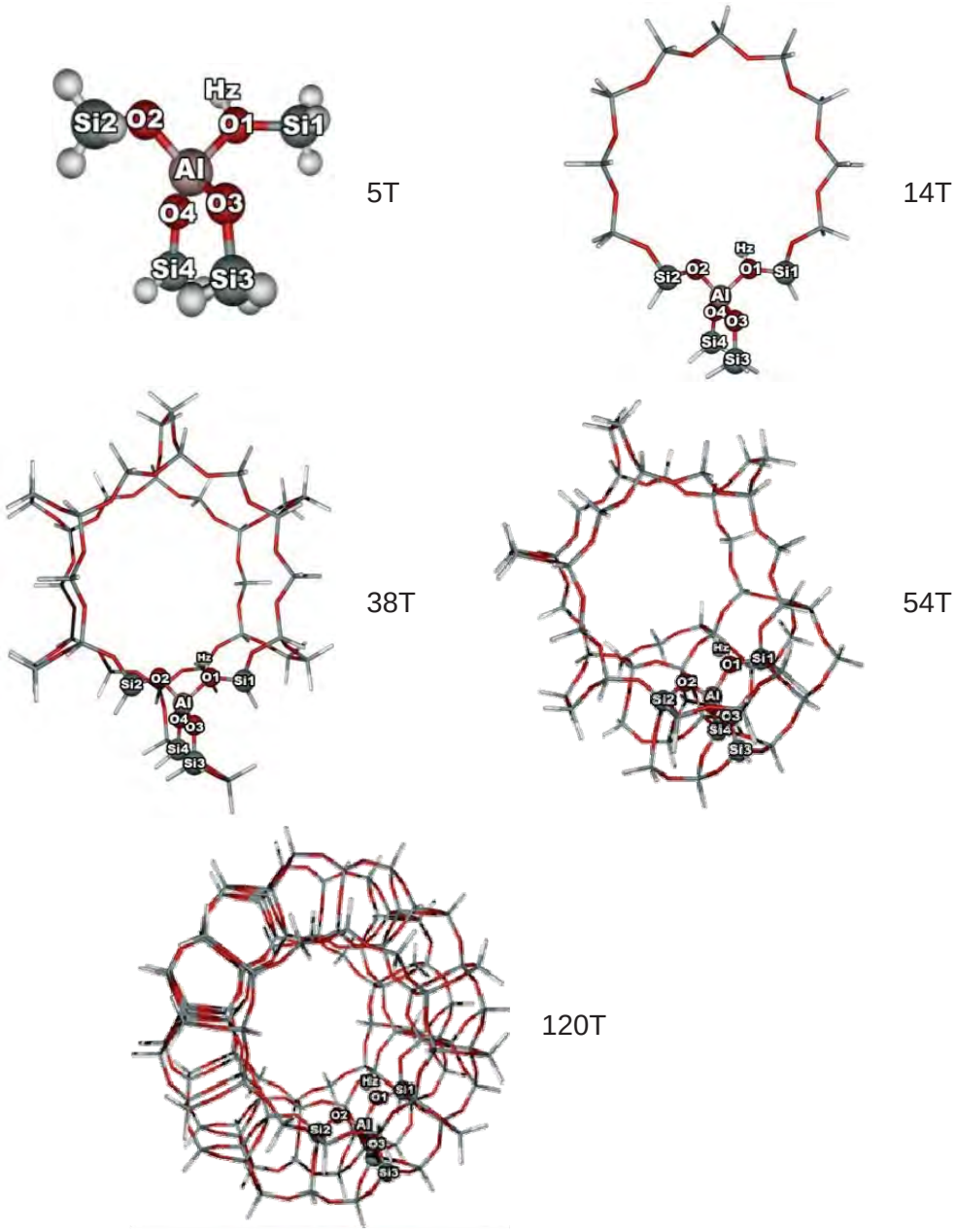


**Fig. 1** Presentation of H-MCM-22 models in different sizes generated from the finite lattice framework.

## Results and Discussion

Table 1 documents the selected geometries parameters of the 5T, 14T and 38T models. The calculated adsorption energies of pyridine on the zeolitic models are -20.9, -41.3, -46.1, -50.8 and -54.0 kcal/mol for 5T, 14T, 38T, 54T and 120T, respectively. Our results show that the adsorption energy of the 120T model is in very good agreement with the experimental value of -55.0 kcal/mol. This suggests that the confinement effect as well as the environmental framework of the zeolite play

vital roles in the pyridine adsorption energies which are related to the prediction of the acidity of zeolite.

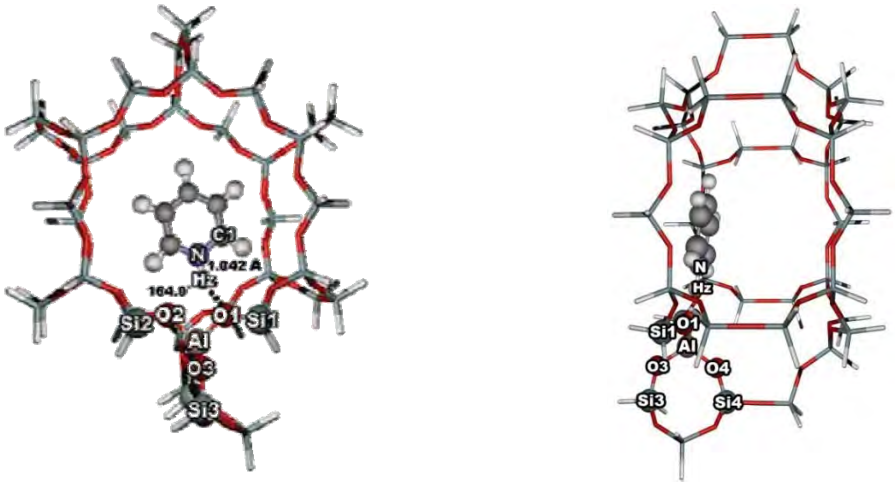


(a) (b)

**Fig. 2** Presentation of the pyridine adsorption on the 38T model of H-MCM-22 viewed through the 12 MR (a) and through the 10 MR, which is perpendicular to 12 MR (b). The bond lengths are in angstroms.

**Table 1** Geometrical parameters of pyridine adsorbed on three sizes of H-MCM-22 models. (Distances are in angstroms and angles are in degrees.)

| Parameter | System | | | | | |
|---|---|---|---|---|---|---|
| | 5T | | 14T | | 38T | |
| | Isolated | Complex | Isolated | Complex | Isolated | Complex |
| O1-Hz | 0.969 | 1.345 | 0.969 | 1.822 | 0.970 | 1.804 |
| O2-Hz | 2.347 | 2.631 | 2.565 | 2.138 | 2.567 | 2.226 |
| O2-H1 | - | 2.050 | - | 2.430 | - | 2.338 |
| Al-O1 | 1.841 | 1.754 | 1.815 | 1.720 | 1.813 | 1.716 |
| Al-O2 | 1.692 | 1.708 | 1.675 | 1.713 | 1.671 | 1.707 |
| Al-O3 | 1.708 | 1.721 | 1.708 | 1.726 | 1.704 | 1.725 |
| Al-O4 | 1.683 | 1.697 | 1.676 | 1.689 | 1.681 | 1.697 |
| Al-Hz | 2.314 | 2.553 | 2.408 | 2.651 | 2.397 | 2.686 |
| N-O1 | - | 2.496 | - | 2.783 | - | 2.795 |
| N-Hz | - | 1.153 | - | 1.042 | - | 1.042 |
| < Al-O1-Si1 | 127.7 | 124.1 | 125.1 | 123.3 | 126.9 | 125.1 |
| <Al-O1-Hz | 106.8 | 175.6 | 116.5 | 96.9 | 115.6 | 99.5 |
| <Al-O2-H1 | - | 123.6 | - | 146.7 | - | 145.2 |
| < N-Hz-O1 | - | 110.3 | - | 151.7 | - | 157.5 |

## Conclusion

The effect of the zeolitic nanocage on the adsorption properties of the important heterocyclic base, pyridine, of different sizes of H-MCM-22 has been investigated. The results demonstrate that the hybrid density functional M06-2X is able to encompass important weak interactions describing the nano-confinement effect from the zeolite framework, especially the van der Waals interaction. The nano-confinement effect of the extended zeolite framework has been clearly demonstrated not only to stabilize the pyridine/zeolite complexes but also to improve the corresponding adsorption energies to approach the experimental benchmark.

## Acknowledgements

This work was supported in part by grants from the National Science and Technology Development Agency (2009 NSTDA Chair Professor funded by the Crown Property Bureau under the management of the National Science and Technology Development Agency and NANOTEC Center of Excellence funded by the National Nanotechnology Center), the Thailand Research Fund (TRF), the Development and Promotion of Science and Technology Talents Project (DPST) and the Commission on Higher Education, Ministry of Education (the "National Research University Project of Thailand (NRU)" and the "National Center of Excellence for Petroleum, Petrochemical and Advanced Materials (NCE-PPAM)"). The support from the Kasetsart University Research and Development Institute (KURDI) is also acknowledged. The authors are grateful to Donald G. Truhlar and Yan Zhao for their support with the M06-2X functional.

## References

Boekfa B., S. Choomwattana, P. Khongpracha and J. Limtrakul; "Effects of the zeolite framework on the adsorptions and hydrogen-exchange reactions of unsaturated aliphatic, aromatic, and heterocyclic compounds in ZSM-5 zeolite: A combination of perturbation theory (MP2) and a newly developed density functional theory (M06-2X) in ONIOM scheme", Langmuir, 25(22), 12990-12999 (2009).

Derouane G. E. and C. D. Chang; "Confinement effects in the adsorption of simple bases by zeolites" Micropor. Mesopor. Mat. 35–36, 425–433 (2000).

Injan N., N. Pannorad, M. Probst and J. Limtrakul; "Pyridine adsorbed on H-faujasite zeolite: Electrostatic effect of the infinite crystal lattice calculated from a point charge representation", Int. J. Quantum Chem., 105(6), 898-905 (2005).

Maihom T., P. Pantu, C. Tachakritikul, M. Probst, and J. Limtrakul; "Effect of the Zeolite Nanocavity on the Reaction Mechanism of n-Hexane Cracking: A Density Functional Theory Study" J. Phys. Chem. C, 114, 7850–7856 (2010).

Parrillo J. D. and R. J. Gorte; "Characterization of Acidity in H-ZSM-5, H-ZSM-12, H-Mordenite, and H-Y Using Microcalorimetry" J. Phys. Chem. 97, 8786-8792 (1993)

Zhao Y. and D. G. Truhlar; "Density functionals with broad applicability in chemistry", Accounts Chem. Res., 41(2), 157-167 (2008).

# Reaction Mechanisms for ETBE Production Catalyzed by H-BEA as Nanoporous Zeolite

Panida Singra[1,2,3], Pipat Khongpracha[1,2,3], Jumras Limtrakul[1,2,3*]

[1]*Laboratory for Computational and Applied Chemistry, Department of Chemistry, Faculty of Science and Center of Nanotechnology, Kasetsart University Research and Development Institute, Kasetsart University, Bangkok 10900, Thailand*

[2]*NANOTEC Center of Excellence, National Nanotechnology Center, Kasetsart University, Bangkok 10900, Thailand*

[3]*Center for Advanced Studies in Nanotechnology and Its Applications in Chemical, Food and Agricultural Industries, Kasetsart University, Bangkok 10900, Thailand*

*Corresponding author: Tel. +66 2562 5555 ext 2169, Fax: +66 2562 5555 ext 2176,
E-mail address: jumras.l@ku.ac.th

**Keywords** Zeolite, Etherification reaction, Octane booster, Ethyl tert-butyl ether (ETBE)

## Introduction

Ethyl tert-butyl ether (ETBE) can be considered a prime candidate to be a high-octane additive for its remarkably friendly environmental properties. ETBE easily mixes with gasoline, to make gasoline burn cleanly and completely, and reduce the vehicle's greenhouse gas emission from the exhaust.

ETBE is readily synthesized by the etherification reaction of isobutene with ethanol. Conventionally, sulfonated acidic ion-exchange resin catalysts, such as Amberlyst-15 and Lewatit K2631 were used to catalyze the reaction for synthesis of the ETBE. Although these catalysts are very efficient, they have some disadvantages, such as low thermal stability and corrosion problems in the reactor. Hence, zeolites become more advantageous because of high thermal and chemical stability, and their ability to be recycled result in there being many investigations on zeolite catalysts. From a previous experimental study on the vapor phase synthesis of MTBE and ETBE, it was found that H-BEA is as active as Amberlyst-15. The order for the activity of commonly used zeolites decreases as follow: H-BEA > H-Y ≥ H-mordenite > H-ZSM-5.

Quantum chemical calculation is a useful tool in this work to investigate and analyze the reaction mechanisms for ETBE production via the etherification reaction of isobutene and ethanol, and compares uncatalyzed and catalyzed reactions by H-BEA, nanostructured zeolite.

## Methodology

The uncatalyzed reaction, the bare model system, is investigated with M06-2X/6-311+G(2df,2p) //M06-2X/6-31G(d,p) calculations.

For the catalyzed reaction, the 54T nanocluster is used as the model of the Brønsted acid site in the H-BEA zeolite framework. This model is taken from the BEA zeolite crystal lattice structures. For computational efficiency, the 54T nanocluster model is subdivided into two layers according to the Our-own-N-layered-integrated molecular orbital + molecular mechanics (ONIOM) scheme. An inner layer, high level, consists of a 14T cluster including the 12-membered ring and the other two Si atoms around the Al atom, as the active site region, is treated with the density function, namely M06-2X with the 6-31G(d,p) basis set. An outer layer, low level, consists of the rest of the extended framework, is treated with the universal force field (UFF). This force field has been found to provide a good description of the long-range van der Waals (vdW) interactions. In the structure

optimization, only the 5T cluster of the active site region, [(≡SiO)$_3$ Al(OH)Si≡], and the probe molecule are allowed to relax while the rest is fixed at the crystallographic coordinates. Frequency calculation at the same level of the active site region was carried out to verify transition states structure with only one imaginary frequency. In order to make the results more reliable, single point calculations are performed using M06-2X method, 6-311+G(2df,2p) basis set for the active site region, and 6-31G(d,p) basis set for the rest of the extended framework. All calculations were performed using the Gaussian 03 code.

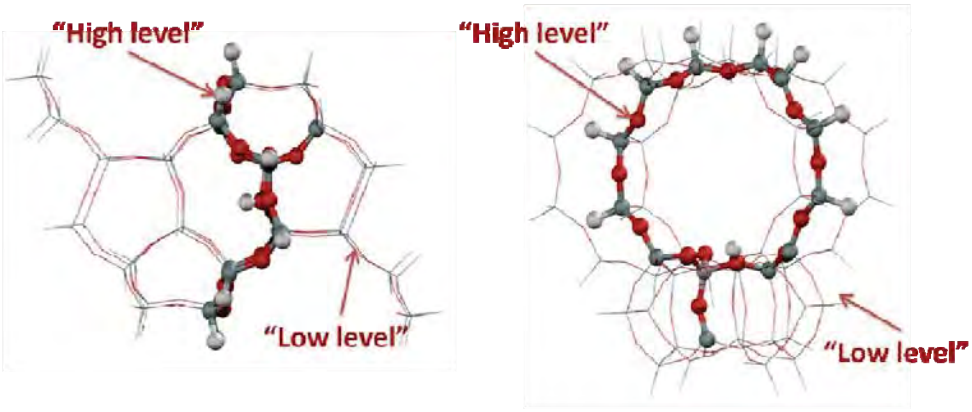


(a) (b)

**Fig. 1** Extended 54T cluster model of H- BEA (a) An intersection of two perpendicular 12-membered ring channel systems which serve as a nanoreactor (b) View along the main channel.

## Results and Discussion

The etherification reaction of isobutene and ethanol to ETBE catalyzed by H-BEA. The reaction is initiated by the coadsorption between isobutene and ethanol over the Brønsted acid site of BEA, the coadsorption complex (B_Ads_1), was stabilized by orbital interaction between the π bonding orbital of the C1=C2 bond of isobutene with the σ*-antibonding orbital of O1-Hz bond zeolite and interaction between H atom of ethanol with the O atom of zeolite. This was followed by the concerted transition state (B_TS_1), a protonation of the adsorbed isobutene and an ethanol molecule attraction to isobutene occurs simultaneously, resulting in adsorbed ETBE (B_Ads_2), which is desorbed in the final step. The uncatalyzed reaction is from the bare model system. The transition state concerns the O-H bond dissociation, O-C and H-C bond formation. The optimized geometric parameters of all species involved in the etherification of isobutene with ethanol are showed in Tables1 and 2.

**Table 1** Optimized geometric parameters of all species involved in the ETBE formation of the uncatalyzed reaction, the bare model system.

| Parameter | Ads_1 | TS_1 | Ads_2 |
|---|---|---|---|
| Distance (Å) | | | |
| C1-H | 2.57 | 1.40 | 1.09 |
| C2-H | 2.35 | 1.74 | 2.16 |
| H-O | 0.97 | 1.24 | 2.64 |
| C1-C2 | 1.34 | 1.42 | 1.53 |
| Angle (°) | | | |
| C2-C1-H | 65.1 | 76.3 | 109.7 |
| C1-C2-H | 83.8 | 51.2 | 28.4 |
| C1-H-O | 155.5 | 130.2 | 67.0 |
| C1-C2-O | 99.2 | 90.4 | 110.6 |

**Table 2** Optimized geometric parameters of all species involved in the ETBE formation of the catalyzed reaction by H-BEA zeolite.

| Parameter | zeolite | B_Ads_1 | B_TS_1 | B_Ads_2 |
|---|---|---|---|---|
| Distance (Å) | | | | |
| O1-Hz | 0.97 | 1.01 | 1.34 | 2.35 |
| C1-Hz | - | 1.97 | 1.35 | 1.09 |
| C2-Hz | - | 2.28 | 2.12 | 2.16 |
| C1-C2 | - | 1.35 | 1.38 | 1.52 |
| O3-C2 | - | 3.67 | 2.66 | 1.50 |
| O3-C3 | - | 1.42 | 1.42 | 1.46 |
| O3-H1 | - | 0.97 | 0.97 | 1.10 |
| H1-O2 | - | 2.20 | 1.97 | 1.38 |
| Angle (°) | | | | |
| Al-O1-Si | 131.8 | 130.2 | 129.2 | 130.0 |
| Al-O2-Si | 129.8 | 130.5 | 133.4 | 129.8 |
| O1-Hz-C1 | - | 172.4 | 156.2 | 161.6 |
| Hz-C1-C2 | - | 163.9 | 102.0 | 110.5 |

The H-BEA zeolite, as the catalyst changes the reaction path by lowering the energy barrier from 53.3 kcal/mol to 8.3 kcal/mol, which leads to increasing the rate of the reaction. The reaction for the ETBE production was exothermic and this study provides the calculated reaction energy of −18.4 kcal/mol. This result is reasonable and compares well with the experimental study of the enthalpy of reaction by −14.9±0.5 kcal/mol. The calculated relative energies of all reaction coordinates are summarized in Fig. 2.

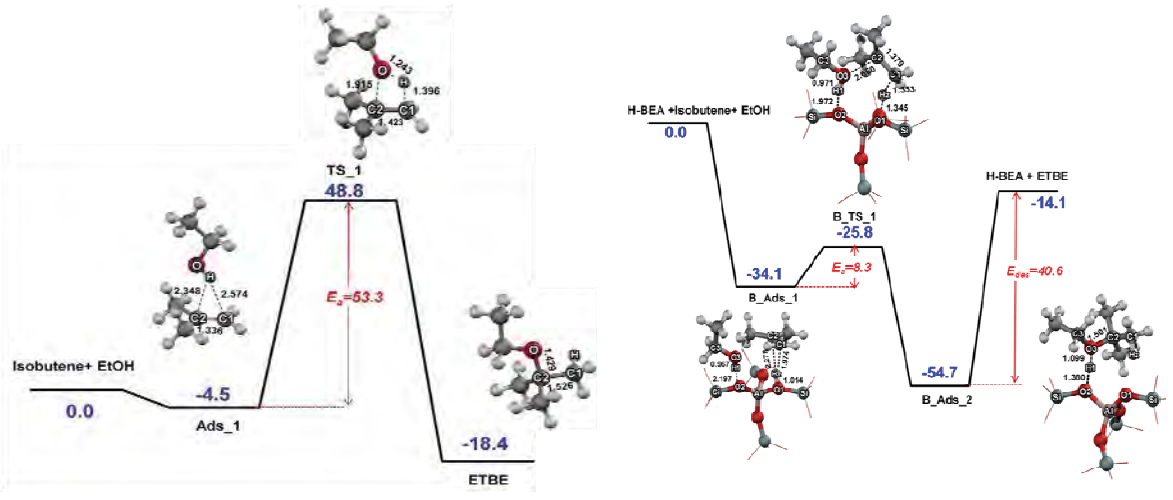


(a) (b)

**Fig. 2** Relative energies (kcal/mol) of all reaction coordinates in the etherification reaction of isobutene with ethanol to ETBE. (a) Uncatalyzed reaction, the bare model system, (b) Catalyzed reaction by H-BEA zeolite.

## Conclusion

The reaction mechanisms for ETBE production via the etherification reaction of isobutene and ethanol catalyzed reactions by H-BEA is investigated by using the ONIOM(M06-2X/6-31G(d,p):UFF) method. Single point calculations are performed using the M06-2X method, 6-311+G(2df,2p) basis set for the active site region, and 6-31G(d,p) basis set for the rest of the extended framework. For the uncatalyzed reaction, the bare model system is investigated with M06-2X/6-311+G(2df,2p)//M06-2X/6-31G(d,p) method. The overall reaction was estimated to be the exothermic of −18.4 kcal/mol. The H-BEA as a nanostructured zeolite was found to be an efficient catalyst in the etherification of isobutene with ethanol, culminating in a lower energy barrier (8.3 kcal/mol) as compared to that of the bare model system (53.3 kcal/mol).

## Acknowledgements

This work was supported in part by grants from the National Science and Technology Development Agency (2009 NSTDA Chair Professor funded by the Crown Property Bureau under the management of the National Science and Technology Development Agency and NANOTEC Center of Excellence funded by the National Nanotechnology Center), the Thailand Research Fund (TRF) and the Commission on Higher Education, Ministry of Education (the “National Research University Project of Thailand (NRU)” and the “National Center of Excellence for Petroleum, Petrochemical and Advanced Materials (NCE-PPAM)”). The support from the Kasetsart University Research and Development Institute (KURDI) is also acknowledged. The authors are grateful to Donald G. Truhlar and Yan Zhao for their support with the M06-2X functional.

## References

Collignon F. and G. Poncelet; “Comparative vapor phase synthesis of ETBE from ethanol and isobutene over different acid zeolites”, J. Catal., 202(1):68-77 (2001).

Collignon F., M. Mariani, S. Moreno, M. Remy and G. Poncelet; “Gas phase synthesis of MTBE from methanol and isobutene over dealuminated zeolites”. J. Catal., 166(1):53-66 (1997).

Doğu T., N. Boz, E. Aydın, Nuray Oktar, K. Murtezaoğlu and G. Doğu; “DRIFT studies for the reaction and adsorption of alcohols and isobutylene on acidic resin catalysts and the mechanism of ETBE and MTBE synthesis”. Ind. Eng. Chem. Res., 40(23):5044-5051 (2001).

Iborra M., J. F. Izquierdo, J. Tejero and F. Cunili; “Equilibrium Constant for Ethyl tert-Butyl Ether Vapor-Phase Synthesis”, J. Chem. Eng. Data, 34:1-5 (1989).

Jansang B., T. Nanok and J. Limtrakul; “Structure and Reaction Mechanism of Alkylation of Phenol with Methanol over H-FAU Zeolite: An ONIOM Study”. J. Phys. Chem. C, 112: 540-547 (2008).

Kumsapaya C., K. Bobuatong, P. Khongpracha, Y. Tantirungrotechai and J. Limtrakul; “Mechanistic Investigation on 1,5- to 2,6-Dimethylnaphthalene Isomerization Catalyzed by Acidic β Zeolite: ONIOM Study with an M06-L Functional”. J. Phys. Chem. C, 113:16128-16137 (2009).

Maihom T., B. Boekfa, J. Sirijaraensre, T. Nanok, M. Probst and J. Limtrakul; “Reaction Mechanisms of the Methylation of Ethene with Methanol and Dimethyl Ether over H-ZSM-5: An ONIOM Study”. J. Phys. Chem. C**,** 113:6654-6662 (2009).

Zhao Y. and D.G. Truhlar; “Density functionals with broad applicability in chemistry”, Accounts Chem. Res., 41(2), 157-167 (2008).

# Adsorption of a Basic Probe Molecule over Nanoporous Catalysts (H-FAU and H-MOR): an Embedded Nanocluster Approach

Supalak Khueanphet[1,2,4], Bundet Boekfa[2,3,4], Tanin Nanok[1,2,4], Jumras Limtrakul[1,2,4*]

[1]*Laboratory for Computational and Applied Chemistry, Department of Chemistry, Faculty of Science and Center of Nanotechnology, Kasetsart University Research and Development Institute, Kasetsart University, Bangkok 10900, Thailand*

[2]*NANOTEC Center of Excellence, National Nanotechnology Center, Kasetsart University, Bangkok 10900, Thailand*

[3]*Chemistry Department, Faculty of Liberal Art and Science, Kasetsart University Kamphaeng Saen Campus, Nakhon Pathom 73140, Thailand*

[4]*Center for Advanced Studies in Nanotechnology and Its Applications in Chemical, Food and Agricultural Industries, Kasetsart University, Bangkok 10900, Thailand*

*Corresponding author: Tel. +66 2562 5555 ext 2169, Fax: +66 2562 5555 ext 2176, E-mail address: jumras.l@ku.ac.th

**Keywords** Confinement effect, Zeolites, Ammonia adsorption, M06-2X functional

## Introduction

An acid site in zeolites acting with probe molecules has generated considerable interest because it represents the initial step of chemical reactions resulting from catalyzation by acidic zeolites. The heat of adsorption complexes that is created when a basic probe molecule is adsorbed on the nanostructure zeolitic pores is the sum of two significant terms, the chemisorption and the physisorption. The latter term relates to a large degree to the confinement effect arising from the van der Waals interaction, which is a main factor for the determination of selective adsorption and catalytic activity in the acid-catalyzed reaction of zeolites.

Derouane *et al.* investigated the confinement effect of ammonia adsorption on various silicalites and zeolites. This report led to some important studies on the adsorption of ammonia in zeolites using quantum cluster calculations that have since been reported. These works guide us to elucidate on the influence of zeolitic confinement on structure and mechanisms. However, most of the investigations lack inclusion of the effect of zeolite frameworks that include an important contribution of dispersion energy. Recently, the newly developed density functional theory coupled with accurate long range electrostatic interactions called “embedded M06-2X functional” has been successfully employed to describe the confinement effect of the zeolite framework. The goal of our work is to systemically investigate the confinement effect of ammonia adsorption on the different types of zeolite, namely H-FAU and H-MOR zeolites.

## Methodology

The cluster models, 5T, 14T, and 38T, were optimized by the M06-2X functional with the 6-31G(d,p) level of theory. During the optimization, the Brønsted acid site of H-FAU and H-MOR, for the 5T, ≡$(SiO)_3Al(OH)Si$≡, and ammonia were allowed to relax while the other atoms were kept fixed to their crystallographic coordinates. The long-range electrostatic potential was carried out by single-point calculations with the electronic embedding approach. The electrostatic potential from the extended lattice is generated by optimized point charges which enclose around the realistic quantum cluster of 38T. The adsorption energy is evaluated as:

$$\Delta E_{ads} = E_{H\text{-}Z} + E_{NH3} - E_{NH4\text{-}Z}$$

where $E_{H\text{-}Z}$, $E_{NH3}$, and $E_{NH4\text{-}Z}$ refer to the total energy of each structure.

In order to be able to derive more accurate results, all $\Delta E_{ads}$ were corrected for the basis set superposition error (BSSE) via the counterpoise correction. All calculations were performed by using the Gaussian 03 code modified M06 functional by Zhao Y. and D. G. Truhlar.

## Results and Discussion

### Comparisons of geometrical structures of different quantum cluster models

The adsorption of the ammonia on H-FAU and H-MOR zeolites was investigated with the M06-2X functional. The ammonia molecules are located at the 12T supercage of H-FAU and the 12T straight channel of H-MOR. The adsorption process of ammonia on the Brønsted acid site of zeolites is as follow: the proton (Hz) of the acid site was transferred to ammonia, and hence generates the ammonium ion adsorbed to the acid site of zeolites in the form of an ion-pair complex, $Z^-$- $NH_4^+$. The geometrical structures of cluster models are illustrated in Fig. 1.

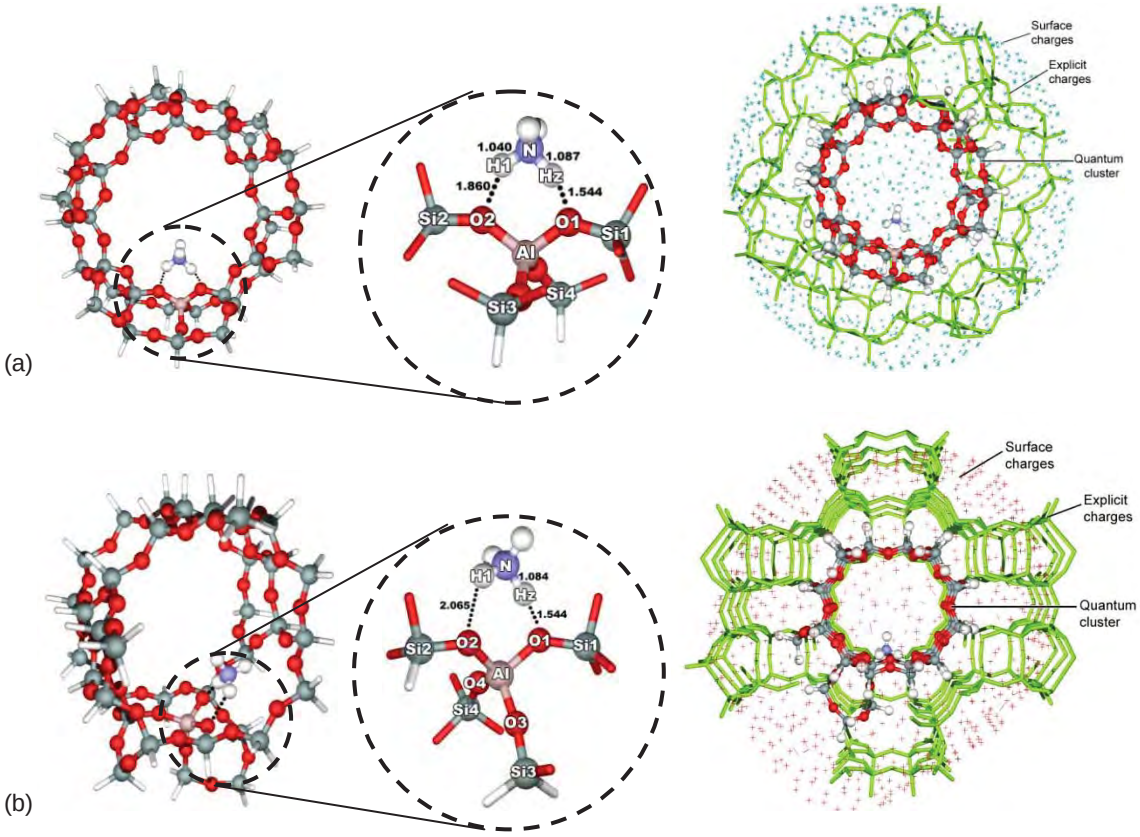


**Fig. 1** Adsorption complex of $NH_3$ in the 38T and embedded cluster models of H-FAU (a) and H-MOR (b), respectively. (Distances are in Å.)

The geometrical parameters of the optimized structures of H-FAU and H-MOR are documented in Tables 1 and 2, respectively. Without the confinement effect, the ammonia is adsorbed on the small quantum 5T cluster by forming a strong hydrogen bond between the nitrogen atom of ammonia and the proton Brønsted acid of zeolites. Increasing the models to 14T and 38T quantum clusters, the formation of the ion-pair of ammonia on the deprotonated zeolites can be observed. The shortening Al-O1 and a lengthening of Al-O2 bond distances are in accordance with Gutmann's rules. The O1-Hz bond distances are 1.109, 1.484 and 1.544 Å for the 5T, 14T, respectively, and 38T clusters of H-FAU, and are 1.130, 1.399 and 1.544 Å for the 5T, 14T and 38T

clusters, respectively of H-MOR. Therefore, it indicates that for the small quantum 5T cluster, hydrogen bonded complexes are found and for the larger 38T cluster the ion-pair is favored.

Another important evidence that can be used to be able to calibrate our models is the Al···Hz distances. Klinowski *et al.* used H-NMR to observe these distances and compiled an experimental range of 2.340 to 2.520 Å. Our predicted Al···Hz distances are in the range of 2.35 to 2.53 Å, that agree well with their experimental observation.

**Table 1** Selected geometric parameters of the adsorption complex of ammonia on H-FAU (Distances are in Å and angles are in degrees).

| Parameters | Models | | | | | |
|---|---|---|---|---|---|---|
| | 5T | | 14T | | 38T | |
| | Isolated | Complex | Isolated | Complex | Isolated | Complex |
| O1-Hz | 0.967 | 1.109 | 0.971 | 1.484 | 0.971 | 1.544 |
| O2-H1 | - | 2.023 | - | 1.856 | - | 1.860 |
| Al-O1 | 1.962 | 1.886 | 1.972 | 1.835 | 1.968 | 1.828 |
| Al-O2 | 1.721 | 1.757 | 1.719 | 1.792 | 1.724 | 1.800 |
| Al-O3 | 1.715 | 1.721 | 1.715 | 1.726 | 1.719 | 1.728 |
| Al-O4 | 1.707 | 1.719 | 1.709 | 1.725 | 1.710 | 1.723 |
| Al-$O_{avg}$ | 1.776 | 1.770 | 1.779 | 1.769 | 1.780 | 1.770 |
| Al···Hz | 2.481 | 2.471 | 2.511 | 2.651 | 2.532 | 2.669 |
| Si-O1 | 1.730 | 1.692 | 1.720 | 1.652 | 1.719 | 1.641 |
| N-O1 | - | 2.493 | - | 2.552 | - | 2.589 |
| N-Hz | - | 1.403 | - | 1.104 | - | 1.087 |
| N-H1 | - | 1.026 | - | 1.040 | - | 1.040 |
| <Al-O1-Si1 | 131.0 | 130.7 | 130.8 | 130.6 | 132.3 | 131.8 |
| <N-Hz-O1 | - | 165.8 | - | 160.6 | - | 159.0 |
| <N-H1-O2 | - | 137.4 | - | 139.9 | - | 141.2 |
| <H1-N-Hz | - | 98.3 | - | 102.0 | - | 103.3 |
| <O2-Al-O1 | 100.5 | 102.2 | 102.2 | 103.4 | 106.3 | 106.5 |

**Table 2** Selected geometric parameters of the adsorption complex of ammonia on H-MOR (Distances are in Å and angles are in degrees).

| Parameters | Models | | | | | |
|---|---|---|---|---|---|---|
| | 5T | | 14T | | 38T | |
| | Isolated | Complex | Isolated | Complex | Isolated | Complex |
| O1-Hz | 0.969 | 1.130 | 0.970 | 1.399 | 0.971 | 1.544 |
| O2-H1 | - | 2.023 | - | 2.026 | - | 2.065 |
| O4-H2 | - | 4.128 | - | 4.109 | - | 4.186 |
| Al-O1 | 1.868 | 1.809 | 1.848 | 1.758 | 1.834 | 1.737 |
| Al-O2 | 1.702 | 1.726 | 1.694 | 1.736 | 1.685 | 1.723 |
| Al-O3 | 1.685 | 1.690 | 1.683 | 1.685 | 1.673 | 1.682 |
| Al-O4 | 1.682 | 1.694 | 1.676 | 1.689 | 1.673 | 1.688 |
| Al-$O_{avg}$ | 1.734 | 1.730 | 1.725 | 1.717 | 1.716 | 1.708 |
| Al···Hz | 2.345 | 2.429 | 2.405 | 2.552 | 2.398 | 2.662 |
| Si-O1 | 1.705 | 1.664 | 1.692 | 1.621 | 1.679 | 1.600 |
| N-O1 | - | 2.480 | - | 2.503 | - | 2.604 |
| N-Hz | - | 1.364 | - | 1.128 | - | 1.084 |
| N-H1 | - | 1.025 | - | 1.030 | - | 1.030 |
| <Al-O1-Si1 | 130.1 | 129.7 | 130.3 | 131.8 | 132.7 | 133.1 |
| <N-Hz-O1 | - | 167.5 | - | 164.3 | - | 164.2 |
| <N-H1-O2 | - | 131.8 | - | 129.7 | - | 123.3 |
| <H1-N-Hz | - | 97.4 | - | 101.1 | - | 103.9 |
| <O2-Al-O1 | 94.5 | 97.6 | 97.6 | 100.5 | 96.2 | 97.6 |

**Adsorption energies of ammonia on the acidic site of H-FAU and H-MOR zeolites**

Table 3 shows calculated and adsorption energies (kcal/mol) on different types of zeolite of various cluster sizes. The models range from the small cluster of 5T up to the more realistic cluster models of 38T. Overall, it can be seen that $\Delta E_{ads}$ for the 5T model of all types of zeolites are virtually the same and there is only a slight change for the 14T cluster models. The significant alternations in $\Delta E_{ads}$ are observed at the larger cluster of 38T. The effect of the long range interactions is also included via optimized point charges added to the realistic nanocluster 38T, which we called "embedded nanocluster". Inclusion of the extended zeolitic framework covering the nanocluster has an effect on the adsorption properties and yields the adsorption energies which agree well with the available experimental data, -35.6 vs -35.8 kcal/mol for H-FAU and -39.5 vs -38.2 kcal/mol for H-MOR, respectively. Thus, it can to some extent be used to fine tune the acidity of zeolites and hence be useful for zeolite chemists to systemically select their right candidates for their reaction.

**Table 3** Calculated adsorption energies of ammonia on various cluster models of zeolites[a] (kcal/mol).

| Zeolite | $\Delta E_{ads}^{BSSE}$ | | | | Exp.[c] |
|---|---|---|---|---|---|
| | 5T[a] | 14T[a] | 38T[a] | Embedded 38T[b] | |
| H-FAU | -24.6 | -28.7 | -30.3 | -35.6 | -35.8±1.2 |
| H-MOR | -24.1 | -27.1 | -35.1 | -39.5 | -38.2±1.2 |

[a]Cluster models of 5T up to 38T are optimized for full QM calculation.
[b]Single-point calculations on embedded 38T.
[c]Experimental values from the Microcalorimetric method.

## Conclusion

The confinement effect for the adsorption of ammonia over different zeoiltes, H-FAU and H-MOR zeolites, has been clearly demonstrated with the newly developed Density Functional Theory, embedded M06-2X, with 6-31G(d,p) basis set. By increasing the cluster size of H-FAU and H-MOR, the adsorption energies of ammonia are slightly increased until close to the embedded cluster models. The adsorption energies for ammonia are calculated to be -35.6 and -39.5 kcal/mol, respectively, which agree well with experiment data. The nature of the local active site and surrounding framework of different zeolites are the main factors leading to the variation in the ammonia adsorption energy. Our findings suggest that the "embedded M06-2X" is a practical and accurate model to examine the confinement effects on the adsorption and reaction mechanisms.

## Acknowledgements

This work was supported in part by grants from the National Science and Technology Development Agency (2009 NSTDA Chair Professor funded by the Crown Property Bureau under the management of the National Science and Technology Development Agency and NANOTEC Center of Excellence funded by the National Nanotechnology Center), the Thailand Research Fund (TRF) and the Commission on Higher Education, Ministry of Education (the "National Research University Project of Thailand (NRU)" and the "National Center of Excellence for Petroleum, Petrochemical and Advanced Materials (NCE-PPAM)"). The support from the Kasetsart University Research and Development Institute (KURDI) is also acknowledged. The authors are grateful to Donald G. Truhlar and Yan Zhao for their support with the M06-2X functional.

## References

Boekfa B., S. Choomwattana, P. Khongpracha, and J. Limtrakul; "Effects of the Zeolite Framework on the Adsorptions and Hydrogen-Exchange Reactions of Unsaturated Aliphatic, Aromatic, and Heterocyclic Compounds in ZSM-5 Zeolite: A Combination of Perturbation Theory (MP2) and a Newly Developed Density Functional Theory (M06-2X) in ONIOM Scheme" Langmuir. 25(22), 12990–12999 (2009).

Derouane G. E. and C. D. Chang; "Confinement effects in the adsorption of simple bases by zeolites" Micropor. Mesopor. Mat. 35–36, 425–433 (2000).

Injan N., N. Pannorad, M. Probst, and J. Limtrakul; “Pyridine Adsorbed on H-Faujasite Zeolite: Electrostatic Effect of the Infinite Crystal Lattice Calculated From a Point Charge Representation” Int. J. Quantum. Chem. 105, 898–905 (2005).

Maihom T., P. Pantu, C. Tachakritikul, M. Probst, and J. Limtrakul; “Effect of the Zeolite Nanocavity on the Reaction Mechanism of n-Hexane Cracking: A Density Functional Theory Study” J. Phys. Chem. C, 114, 7850–7856 (2010).

Pantu P., B. Boekfa, and J. Limtrakul; “The adsorption of saturated and unsaturated hydrocarbons on nanostructured zeolites (H-MOR and H-FAU): An ONIOM study” J. Mol. Catal. A: Chem. 277, 171–179 (2007).

Parrillo J. D. and R. J. Gorte; “Characterization of Acidity in H-ZSM-5, H-ZSM-12, H-Mordenite, and H-Y Using Microcalorimetry” J. Phys. Chem. 97, 8786-8792 (1993)

Zhao Y. and D. G. Truhlar; “Density Functionals with Broad Applicability in Chemistry” Accounts. Chem. Res. 41, 157-167 (2007).

# Catalytic Dehydrogenation of Ethylbenzene to Styrene over a Tetrahedral Platinum Nanocluster: A DFT Study

Patanachai Janthon[1,2,3], Teeranan Nongnual[1,2,3], Piboon Pantu[1,2,3], Jumras Limtrakul[1,2,3*]

[1]Laboratory for Computational and Applied Chemistry, Department of Chemistry, Faculty of Science and Center of Nanotechnology, Kasetsart University Research and Development Institute, Kasetsart University, Bangkok 10900, Thailand
[2]NANOTEC Center of Excellence, National Nanotechnology Center, Kasetsart University, Bangkok 10900, Thailand
[3]Center for Advanced Studies in Nanotechnology and Its Applications in Chemical, Food and Agricultural Industries, Kasetsart University, Bangkok 10900, Thailand

*Corresponding author: Tel. (+66)02-562-5555 ext 2169, Fax: (+66)02-562-5555 ext 2176, E-mail address: jumras.l@ku.ac.th

**Keywords** Dehydrogenation, Ethylbenzene, Styrene, Tetrahedral Platinum, Density-Functional Theory

## Introduction

Styrene ($C_8H_8$) has been one of the highly significant chemicals used widely in the synthetic polymer industry[1]. The dehydrogenation of ethylbenzene over a potassium promoted iron (III) oxide catalyst at high temperature was mainly used for the production of commercial styrene. However, there were disadvantages in this process - endothermic reaction and rapid deactivation, but many researchers have developed new catalysts, adsorbents and catalyst supports to overcome these. Among the developments, the Pt(111) surface was a candidate catalyst for the dehydrogenation of ethylbenzene to styrene concerning the dissociation of ethylbenzene at low temperature on the surface forming styrene and hydrogen products[2]. But, this again had the disadvantage that the styrene desorption step was quenched by its strong binding to the surface, resulting in the polymerization of glued styrene molecules under an annealing temperature condition. The activity of unsupported Pt nanoclusters was studied by determining an activation of the small hydrocarbons such as methane[3-5]. This brought about the small Pt nanoclusters ($Pt_n$) which were more reactive than monatomic Pt by at least one order of magnitude. The tetrahedral Pt nanocluster ($Pt_4$) was also found to improve the oxidative dehydrogenation of propane[4].

In this work, we introduce the tetrahedral Pt nanocluster as a novel candidate catalyst for the dehydrogenation of ethylbenzene to styrene.

## Computational Details

Neutral $Pt_4$ with $C_2$ symmetry in a triplet state was used in our model. Full geometry optimizations for all pathways were performed using the B3LYP method including 6d functions and unrestricted spin polarization, implemented in the Gaussian 03 program. We have employed the LANL2DZ basis set for all Pt atoms, which uses 18-electron relativistic effective core potentials (ECP) to reduce the number of electrons explicitly. The 6-31G (d, p) basis set for all H and C atoms was added in the calculation, increasing the accuracy of the dehydrogenation processes.

## Results and Discussion

The dehydrogenation of ethylbenzene over the $Pt_4$ catalyst was categorized by the number of catalytic Pt atoms into three mechanistic pathways: single-site catalytic $Pt_4$ (SCP), double-site

catalytic $Pt_4$ (DCP), and triple-site catalytic $Pt_4$ (TCP) as shown in Fig. 1. The DCP pathway has been separated into two sub pathways, DCP_i and DCP_ii, which are dealing with the Int4 and Int5, respectively. Due to the same single-site, the SCP pathway was investigated by comparing the results with activation of the monatomic Pt catalyst. The dehydrogenation was investigated by dealing with the H' and H" dissociations.

**Fig. 1** The mechanism scheme for the dehydrogenation of ethylbenzene to styrene over $Pt_4$ catalyst: single-site catalytic $Pt_4$ (SCP, black solid line), double-site catalytic $Pt_4$ (DCP_i, red dash line and DCP_ii, blue dot line) and triple-site catalytic $Pt_4$ (TCP, purple dash-dot line)

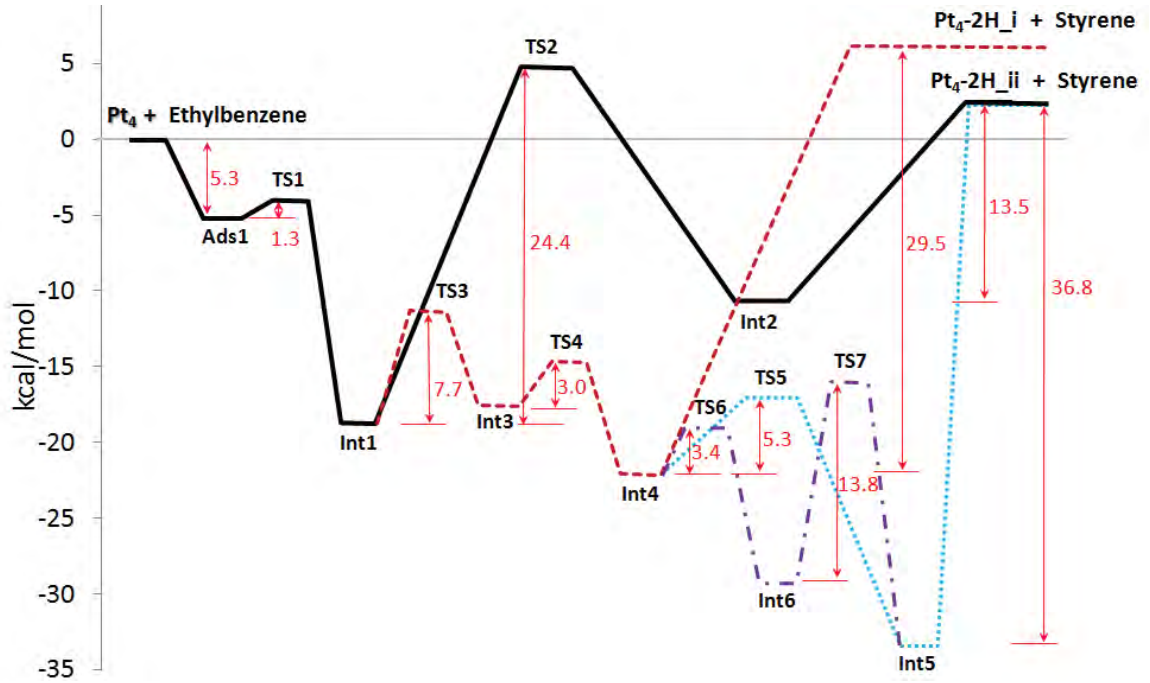


**Fig. 2** Energy profiles for the dehydrogenation of ethylbenzene to styrene over $Pt_4$ catalyst: SCP (black solid line), DCP_i (red dash line), DCP_ii (blue dot line) and TCP (purple dash-dot line).

For all catalytic $Pt_4$ pathways as shown in Fig. 2, the dehydrogenation started from the adsorption of ethylbenzene on the first catalytic site of the $Pt_4$ (Ads1) with the adsorption energy of -5.3 Kcal/Mol. The C-H' bond was then dissociated with the activation energy of 1.3 kcal/mol (TS1) forming the intermediate Int1. After that, the three main pathways were considered.

For the SCP pathway, the C-H" bond was broken, moving the H" to the same catalytic site with the activation energy of 24.4 kcal/mol (TS2) forming an unstable intermediate with the adsorbed styrene product (Int2). This is the rate determining step caused by an increasing steric effect of seven coordinates on the single platinum site. Surprisingly, the styrene and $Pt_4$-2H_ii were then easily desorbed with the desorption energy of 13.5 kcal/mol due to the high steric effect.

For the DCP pathway, the H' migrated to the second catalytic site with the activation energy of 7.7 kcal/mol (TS3) forming the intermediate Int3. The C-H" bond was then broken with the activation energy of 3.0 kcal/mol (TS4), moving the H" onto the first catalytic site (Int4) with the absorbed styrene product. Focusing on the DCP_I pathway, the styrene was desorbed with the desorption energy of 29.5 kcal/mol leaving the $Pt_4$-2H_I. On the other hand, the DCP_ii pathway forwarded by the H" moving to join with the H' on the second catalytic site with the activation energy of 5.3 kcal/mol (TS5) stabilizing the intermediate Int5. Thus, the desorption energy was increased to 36.8 kcal/mol leaving the $Pt_4$-2H_ii.

For the TCP pathway, the H" of the Int4 moved to the third catalytic site with the activation energy of 3.4 kcal/mol (TS6) forming the intermediate Int6. Next, the H" moved to join with the H' with the activation energy of 13.8 kcal/mol (TS7), merging to the Int5 as in the DCP_ii pathway.

The hydrogen migrations on the catalytic sites, using low activation energy in the range of 3.4 to 13.8 kcal/mol, can stabilize an intermediate. This led to the higher desorption energy for the styrene product. Therefore, the rate determining step of the DCP and the TCP pathways were associated with the styrene desorption step. In contrast, this H-moving step was not considered in the SCP pathway, therefore, the stabilization of an intermediate was not observed. Thus, its non-stabilized intermediate (Int2) can assist the styrene desorption more easily with lower desorption energy.

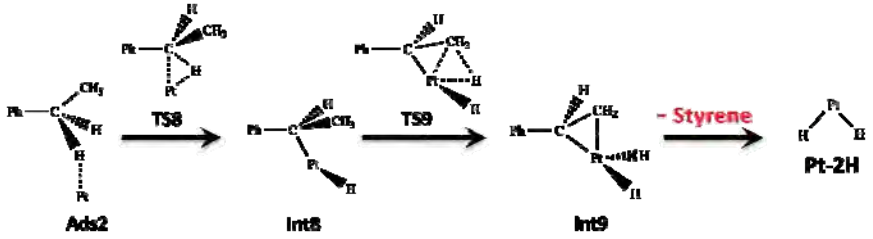


**Fig. 3** The mechanism scheme for the dehydrogenation of ethylbenzene to styrene over monatomic Pt catalyst.

**Fig. 4** Energy profile for the dehydrogenation of ethylbenzene to styrene over monatomic Pt catalyst.

Although the overall activation energy of the SCP pathway was the smallest, the DCP and TCP pathways were kinetically favorable. Therefore, the dehydrogenation was terminated at the Int5 and Int6 steps with styrene products attached to the catalytic site. To avoid this problem, the SCP pathway must be chosen, thus, the single site catalytic must be favorably controlled.

The dehydrogenation of ethylbenzene over the monatomic Pt catalyst was shown in Fig. 3 with the energy profile in Fig. 4. The C-H' bond was broken with the activation energy of 12.9 kcal/mol (TS8). The C-H" bond was then dissociated with the activation energy of 25.5 kcal/mol (TS9). This was the same as that of the SCP pathway. The styrene was then desorbed with the activation energy of 35.0 kcal/mol, which was the rate determining step. This activation energy is higher than that of the SCP pathway due to its lower steric effect to push the styrene out. It can be suggested that three vacant sites of the $Pt_4$ can assist the dehydrogenation of the H' and can increase the steric effect to the active site.

## Conclusion

We report here the first theoretical study of the dehydrogenation of ethylbenzene over the $Pt_4$ catalyst. Although the overall activation energy of the SCP pathway was the smallest, the DCP and TCP pathways were kinetically favorable without desorption of the styrene product. To avoid this problem, the SCP pathway must be chosen, thus, the single site catalytic must be favorably controlled. The H-migration step was not considered in the SCP pathway. For this reason, the stabilization of an intermediate was not observed. Therefore, the non-stabilized intermediate of SCP pathway (Int2) can assist the styrene desorption more easily with the lower desorption energy. This caused the overall activation energy of 24.4 kcal/mol that belonged to the C-H" to dissociate. In addition, we suggest the control for the SCP pathway by the assistance of an adsorbent blocking three sites with remaining one active site of the $Pt_4$ catalyst. Moreover, in order to recover the $Pt_4$ catalyst, the oxidative dehydrogenation should be introduced to eliminate the two adsorbed-H atoms remaining on the catalyst. This understanding can be applied for an alternative styrene synthesis.

## Acknowledgements

This work was supported in part by grants from the National Science and Technology Development Agency (2009 NSTDA Chair Professor funded by the Crown Property Bureau under the management of the National Science and Technology Development Agency and NANOTEC Center of Excellence funded by the National Nanotechnology Center), the Thailand Research Fund (TRF) (to J.L.), under the program "Strategic Scholarships for Frontier Research Network for the Joint Ph.D. Program Thai Doctoral degree" (CHE-PhD-SW) from the office of the Higher Education Commission, Thailand (to P.J.), Ministry of Education (the "National Research University Project of Thailand (NRU)" and the "National Center of Excellence for Petroleum, Petrochemical and Advanced Materials (NCE-PPAM)") and the Development and Promotion of Science and Technology Talents Project (DPST) (to T.N.). The Kasetsart University Graduate School is also acknowledged.

## References

1. Lee W. J. and G. F. Froment; "Ethylbenzene Dehydrogenation into Styrene: Kinetic Modeling and Reactor Simulation." Industrial & Engineering Chemistry Research. **47**(23), 9183-9194 (2008).
2. Ranke W. and W. Weiss; "Adsorption and thermal decomposition of ethylbenzene and styrene on Pt(111) studied by UPS and XPS." Surface Science. **465**(3), 317-330 (2000).
3. Xiao L. and L. Wang; "Methane Activation on Pt and $Pt_4$: A Density Functional Theory Study." The Journal of Physical Chemistry B. **111**(7), 1657-1663 (2007).
4. Trevor D. J., D. M. Cox, A. Kaldor; "Methane activation on unsupported platinum clusters." Journal of the American Chemical Society. **112**(10), 3742-3749 (1990).
5. Vajda S., M. J. Pellin, J. P. Greeley, C. L. Marshall, L. A. Curtiss, G. A. Ballentine, J. W. Elam, S. Catillon-Mucherie, P. C. Redfern, F. Mehmood, P. Zapol; "Subnanometre platinum clusters as highly active and selective catalysts for the oxidative dehydrogenation of propane." Nature Materials. **8**(3), 213-216 (2009).

# DFT Study on the Effect of Phosphate Ionic Core on Basicity of $PW_{12}O_{40}^{3-}$ Polyoxometalate

Saowapak Choomwattana[1,2,3], Jakkapan Sirijaraensre[1,2,3], Jumras Limtrakul[1,2,3*]

[1]*Laboratory for Computational and Applied Chemistry, Department of Chemistry, Faculty of Science and Center of Nanotechnology, Kasetsart University Research and Development Institute, Kasetsart University, Bangkok 10900, Thailand*
[2]*NANOTEC Center of Excellence, National Nanotechnology Center, Kasetsart University, Bangkok 10900, Thailand*
[3]*Center for Advanced Studies in Nanotechnology and Its Applications in Chemical, Food and Agricultural Industries, Kasetsart University, Bangkok 10900, Thailand*

*Corresponding author: Tel. +66 2562 5555 ext 2169, Fax: +66 2562 5555 ext 2176, E-mail address: jumras.l@ku.ac.th

**Keywords** Polyoxometalate, Tungstophosphate, Tungsten oxide, Density-Functional Theory, Pyrrole

## Abstract

The surface oxygen sites of α-Keggin phosphotungstate (PT) anion ($PW_{12}O_{40}^{3-}$) and neutral $W_{12}O_{36}$ cage were differentiated with pyrrole using the density-functional theory (DFT-GGA-PW91/DNP). It was found that the ionic core plays a dominant role on the intermolecular interaction as the adsorption energy of the two cases are about 10 kcal $mol^{-1}$ different. However, the preferred trend adsorption site of corner-sharing oxygen < terminal oxygen < edge-sharing oxygen is preserved even when the ionic core is removed. The strongest adsorption at the edge-sharing oxygen atom in $[PW_{12}O_{40}]^{3-}$ can be explained by the electron donation from the *p* orbital of POM O to the *p* vacant orbital of pyrrole H. From PDOS analyses, the phosphate anionic core induces the formation of intermolecular hydrogen bonding between the POM and pyrrole. The understanding can be applied for advanced studies on tailor-made polyoxometalate and catalytic mechanism with the POM.

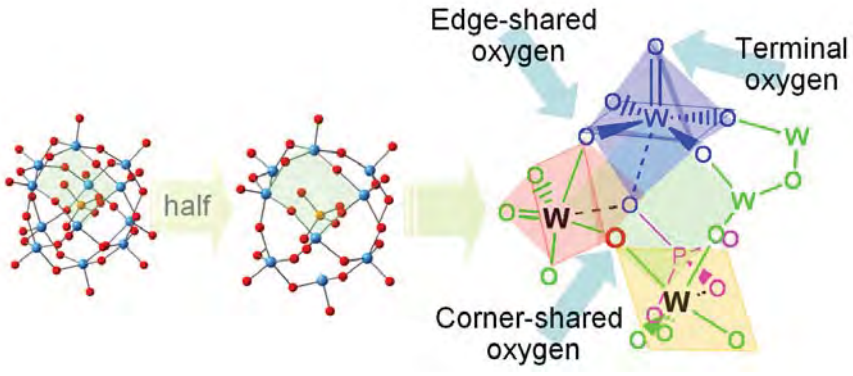


**Fig. 1** Three types of surface oxygen in PT anion: terminal, edge-shared and corner-shared.

**Table 1** Orientations and their adsorption energy (kcal $mol^{-1}$) of pyrrole complexes with $PW_{12}O_{40}^{3-}$ and $W_{12}O_{36}$.

| | System | |
|---|---|---|
| **Oxygen site** | $PW_{12}O_{40}^{3-}$ | $W_{12}O_{36}$ |
| Terminal | 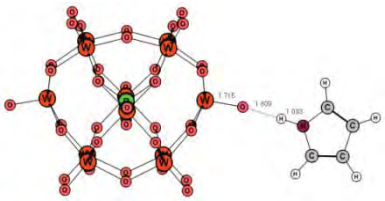 -17.08 | 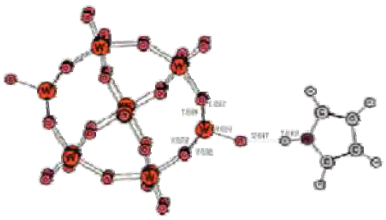 -9.90 |
| Edge-shared | 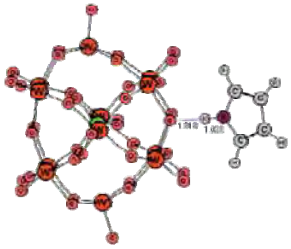 -18.61 | 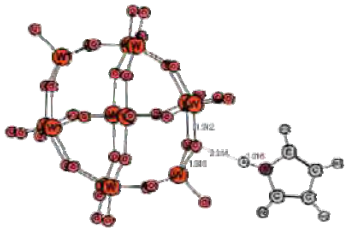 -10.24 |
| Corner-shared | 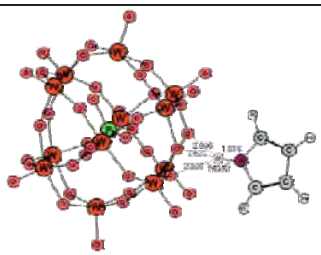 -15.17 | 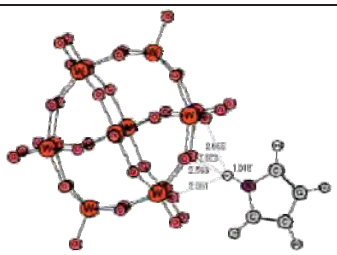 -8.85 |


## Acknowledgements

This work was supported in part by grants from the National Science and Technology Development Agency (2009 NSTDA Chair Professor funded by the Crown Property Bureau under the management of the National Science and Technology Development Agency and NANOTEC Center of Excellence funded by the National Nanotechnology Center), the Thai National Grid Center (TNGC) under the Software Industry Promotion Agency (SIPA), the Thailand Research Fund (TRF) (to J.L.), the Kasetsart University Research and Development Institute (KURDI), Graduate School Kasetsart University and the Commission on Higher Education, Ministry of Education (the "National Research University Project of Thailand (NRU)" and the "National Center of Excellence for Petroleum, Petrochemical and Advanced Materials (NCE-PPAM)"). The program Strategic Scholarships for Frontier Research Network for the Joint Ph.D. Program Thai Doctoral degree (CHE-PhD-SW) from the office of the Higher Education Commission, Thailand (to S.C.) is also acknowledged.


## References


Lavalley J. C.; "Infrared spectrometric studies of the surface basicity of metal oxides and zeolites using adsorbed probe molecules", Catal. Today 27(3-4), 377-401 (1996).

Nongnual T., S. Nokbin, P. Khongpracha, P. A. Bopp and J. Limtrakul; "Density functional theory evidence for an electron hopping process in single-walled carbon nanotube-mediated redox reactions", Carbon 48(5):1524-1530 (2010).

Soares-Santos P. C. R., L. Cunha-Silva, F. L. Sousa, L. Mafra, J. Rocha, A. M. V. Cavaleiro, T. Trindade, F. A. A. Paz, J. Klinowski and H. I. S. Nogueira; "Two novel supramolecular organic-inorganic adducts containing dibenzo-30-crown-10 and $H_3PM_{12}O_{40}$ (M = W or Mo)", J. Molec. Struct., 888(1-3), 99-106 (2008).

Zhang F. Q., X. M. Zhang, H. S. Wu and H. Jiao; "Structural and Electronic Properties of Hetero-Transition-Metal Keggin Anions: A DFT Study of $\alpha/\beta$-$[XW_{12}O_{40}]^{n-}$ (X = $Cr^{VI}$, $V^{V}$, $Ti^{IV}$, $Fe^{III}$, $Co^{III}$, $Ni^{III}$, $Co^{II}$, and $Zn^{II}$) Relative Stability", J. Phys. Chem. A, 111(1):159-166, (2006).

**American Chemical Society National meeting & Exposition” ครั้งที่ 241**

**ณ ประเทศสหรัฐอเมริกา**

**ระหว่างวันที่ 27-31 มีนาคม 2554**

**จำนวน 12 เรื่อง**

# SKELETAL ISOMERIZATION OF 1-BUTENE TO ISOBUTENE ON H-ZSM-5 ZEOLITE: A NEWLY DEVELOPED DENSITY FUNCTIONAL THEORY STUDY

*Bundet Boekfa*[a,c,d], *Kanokwan Kongpatpanich*[b,c,d], *Pailin Limtrakul*[b,c,d] *and Jumras Limtrakul*[b,c,d*]

[a] Chemistry Department, Faculty of Liberal Arts and Science, Kasetsart University Kamphaeng Saen Campus, Nakhon Pathom 73140, Thailand
[b] Laboratory for Computational and Applied Chemistry, Department of Chemistry, Faculty of Science and Center of Nanotechnology, Kasetsart University Research and Development Institute, Kasetsart University, Bangkok 10900, Thailand
[c] NANOTEC Center of Excellence, National Nanotechnology Center, Kasetsart University, Bangkok 10900, Thailand
[d] Center for Advanced Studies in Nanotechnology and Its Applications in Chemical, Food and Agricultural Industries, Kasetsart University, Bangkok 10900, Thailand

## Introduction

Isobutene is a raw material for the production of methyl *tert*-butyl ether (MTBE) and ethyl *tert*-butyl ether (ETBE), which is used as a potential additive in lead-free gasoline. Isobutene can be rearranged from the more abundant butene isomers, such as 1-butene and 2-butene, via the skeletal isomerization catalyzed by nanoporous catalysts[1-14].

Zeolites are considered to be one of the most promising catalysts due to their active and selective properties.[15-20] A survey of literature suggests that suitable catalysts of this reaction are the zeolites with a pore diameter between 4 and 5.5 Å, which are in the range of the 8- to 10-membered ring channels such as Ferrierite, Theta-1 and ZSM-5[3,9-10]. Among the various zeolites that were tested, ZSM-5 showed satisfsctory results with the isobutene conversion of nearly 90%. The general mechanisms proposed are based on either a bimolecular mechanism or a monomolecular mechanism. At a low number of acid sites and high temperature, it is reported that the skeletal isomerization of 1-butene toward isobutene is the monomolecular mechanism rather than dimerization, followed by cracking into light hydrocarbons[21].

The dimerization process was proposed to be an auto catalytic pathway via the active species of *tert*-butyl carbenium ions and trans-2-butene as input reactants[13]. For the monomolecular, a theoretical study was used to study this reaction on theta-1 zeolite[22]. These studies are helpful in predicting the reaction activity, however, the quantum cluster is small and the method does not take into account the van der Waals interaction.

The reaction mechanism of the skeletal isomerization of 1-butene provides useful knowledge to improve the catalytic performances of zeolite and increase the selectivity to the desired product. Unfortunately, 1-butene is very reactive and rapidly isomerizes or dimerizes even at room temperature. Therefore, the reaction mechanism of this reaction has so far been difficult to obtain from experiment.

Where a unit cell of zeolite contains hundreds of atoms, sophisticated methods of calculation, such as periodic ab initio, are computationally too expensive and even impractical. However, recently developed hybrid methods, such as the embedded cluster or the combined quantum mechanics/molecular mechanics (QM/MM) methods now make it possible to calculate larger zeolite systems with much greater accuracy. [23-28] The adsorption of butene was studied on various zeolites via QM/MM calculations[25-26,29]. These results show the importance of the confinement effect from the zeolite framework on the studies of the adsorption process and reaction mechanism. Recently the adsorption and reaction mechanism of hydrocarbon with a large quantum cluster has been successfully studied with the new density functional theory, M06-2X[30-32].

In this work the reaction mechanism of skeletal isomerization of 1-butene over H-ZSM-5 is explored by using a large quantum cluster, 120T, with the new density functional theory, M08-HX. In addition, the results are compared with the second-order Møller-Plesset perturbation theory, MP2.

## Methodology

The cluster models were taken from the lattice structure of ZSM-5 Zeolite[33]. The 23T (T being Si or Al tetrahedral atoms) cluster is modeled to cover the intersection channel of H-ZSM-5 zeolite where the probe molecules occur as shown in Figure 1. The Al atom is selected to substitute at the most favored position T12[34]. An additional single point calculation on the extended 128T cluster is performed to account for the framework effect. The Brønsted acid site ($Si_4O_4AlH$) and the adsorbate are allowed to relax while the rest is kept fixed at the crystallographic coordinate. All models were treated with the M08-HX/6-31G(d,p) level of theory. In order to validate the energies from the M08-HX functional, the single point calculations at MP2/6-31G(d,p) have been used as benchmarks. All calculations were performed using the Gaussian 03 code[35] incorporated with the Minnesota Density Functional module 3.1 by Zhao and Truhlar[36-37].

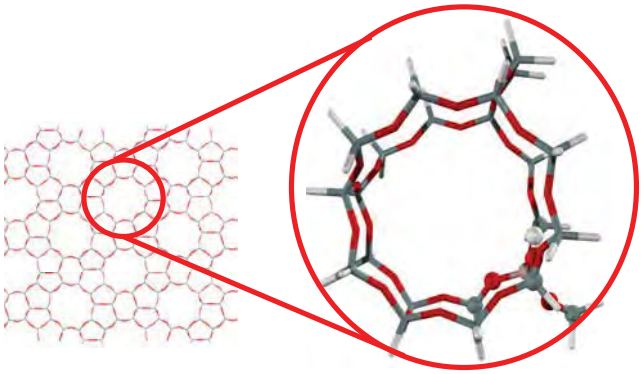

(a)

(b)

**Figure 1.** Presentation of the 23T cluster of H-ZSM-5 zeolite, (a) view from the straight channel and (b) view from the zigzag channel.

## Results and Discussion

**Model of H-ZSM-5 zeolite catalyst.** The 23T quantum is modeled to cover the intersection cavity where the reactions normally take place, as shown in Figure 1. The model was then calculated with the new density functional, M08-HX with the 6-31G(d,p) basis set. The O1-Hz bond distance is about 0.97 Å. While the Al···Hz distance is about 2.36 Å, which agrees well with the experimental observation (2.38-2.48 Å) [38].

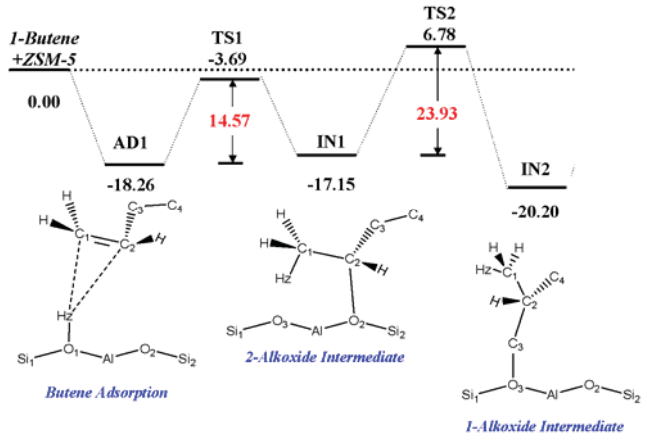


**Figure 2.** Potential energy diagram of the 1-butene to 1-alkoxide intermediate on the 120T//23T quantum cluster of H-ZSM-5, calculated with the M08-HX/6-31G(d,p) method (kcal/mol).

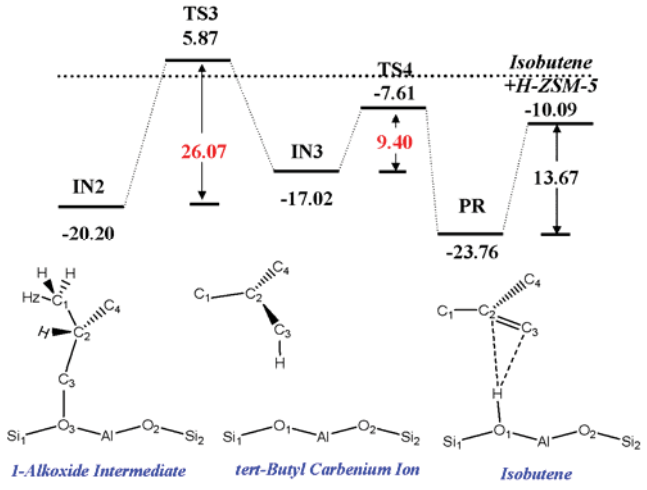


**Figure 3.** Potential energy diagram of the 1-alkoxide intermediate to isobutene on the 120T//23T quantum cluster of H-ZSM-5, calculated with the M08-HX/6-31G(d,p) method (kcal/mol).

**Reaction mechanism for 1-butene isomerization to isobutene.** The 1-butene molecule is located in the 10T membered ring at the intersection of H-ZSM-5 zeolite. It adsorbs on the Brønsted acid via a π-interaction, as shown in Figure 4(a). The slight increase of the Brønsted acid O1-Hz is observed to be about 0.02 Å corresponding with the slight elongation of the C-C double bond by about 0.01 Å. The intermolecular distance between the Brønsted acid and the carbon of the double bond are 2.18 and 2.22 Å for Hz···C1 and Hz···C2, respectively. The adsorption energy of 1-butene on the H-ZSM-5 model 120T//23T is computed to be -18.26 kcal/mol. To the best of our knowledge there is no experimental data available for the adsorption of butane on the protonic zeolites due to the oligomerization reaction. Only the heat of adsorption of n-butane on H-ZSM-5, which is reported to be -13.9 kcal/mol[39]. From our calculation, the adsorption of butane on H-ZSM-5 is calculated to be –11.5 kcal/mol with M08-HX/6-31G(d,p), which compared well with the experiment.

The isomerization mechanism of 1-butene to isobutene on H-FER is proposed as a stepwise reaction mechanism. The energy profile is shown in Figures 2 and 3. The mechanism consists of four steps: 1) protonation of the adsorbed 1-butene and form the secondary alkoxide intermediate, 2) the methyl shift via the cyclic transition state and form the primary alokoxide intermediate, 3) proton transfer and form the *tert*-carbenium cation and 4) protonation back to zeolite and desorption of isobutene.

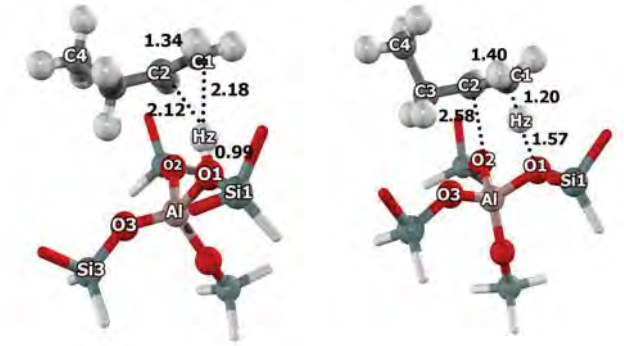


(a) AD1, ΔE= -18.26 kcal/mol (b) TS1, ΔE= -3.69 kcal/mol

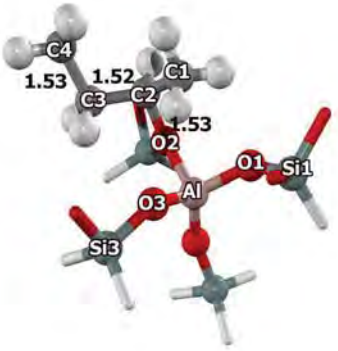


(c) IN1, ΔE= -17.15 kcal/mol

**Figure 4.** Optimized structures of 1-butene isomerization to isobutene on H-ZSM-5 zeolite: (a) the adsorption complex of 1-butene (AD1), (b) the transition structures (TS1), and (c) the secondary alkoxide intermediate (IN1). Distances are in Ås.

After adsorption of the 1-butene molecule, the secondary alkoxide intermediate [IN1, Figure 4(c)] is formed via the first step of the reaction [TS1, Figure 4(b)]. The O1-Hz bond is broken and the O2-C2 bond is formed. The C1-C2 double bond is elongated to become a single bond. The hybridization of C1 is changed from planar ($sp^2$) to tetrahedral ($sp^3$). The transition state is confirmed to be only one imaginary frequency at -217.4 $cm^{-1}$ related with the moving of the proton Hz form the zeolite to the carbon (C1) of the double bond of the 1-butene and forming of the bond between the carbon (C2) of the 1-butene and oxygen (O2) of the zeolite. The

activation energy is about 14.57 kcal/mol. The activation energy is in agreement with the experiment estimates of the activation energy for the isotope exchange of ethylene in zeolites of 15-20 kcal/mol[40]. The intermediate is the secondary alkoxide of the 1-butene. The strong covalent bond of C2-O2 is formed while the C1-C2 is elongated to become a single bond. The relative energy is -17.15 kcal/mol.

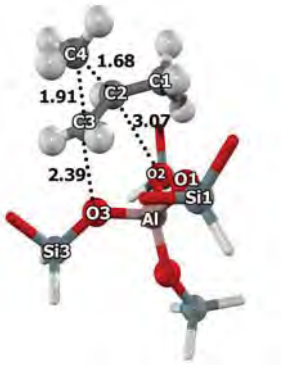


(a) TS2, ΔE= 6.78 kcal/mol

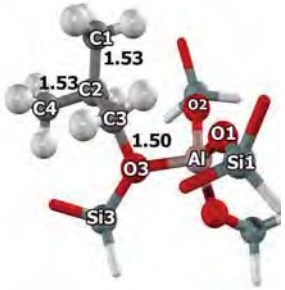


(b) IN2, ΔE= -20.20 kcal/mol

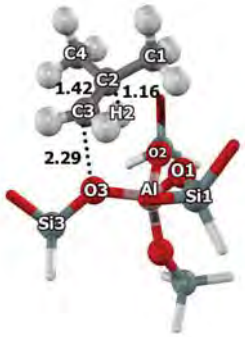


(c) TS3, ΔE= -5.87 kcal/mol

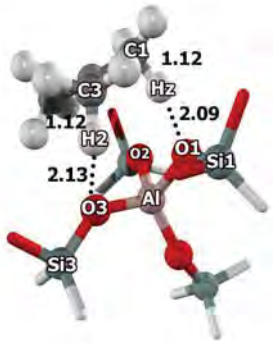


(d) IN3, ΔE= -17.02 kcal/mol

**Figure 5.** Optimized structures of 1-butene isomerization to isobutene on H-ZSM-5 zeolite: (a) the transition state (TS2), (b) the primary alkoxide intermediate (IN2), (c) the transition state (TS3), and (d) *tert*-butyl carbenium cation (IN3). Distances are in Ås.

The next step is the methyl shift via the cyclic transition state. The transition state [Figure 5(a)], the breaking of the C3-C4 and the O2-C2 bond corresponds with the formation of the C2-C4 and C3-O3 bond. One imaginary frequency is found at -101.3 $cm^{-1}$. The reaction is via the cyclic transition state, the C4 methyl group is breaking the bond from the C3 atom and is forming the bond with the C2 atom and breaking the C2-O2 bond and forming the C3-O3 bond. This step required the activation energy of 23.93 kcal/mol. The apparent activation energy is 6.78 kcal/mol. The product is the primary alkoxide intermediate as shown in Figure 5(b). The primary alkoxide intermediate is formed with the relative energy -20.20 kcal/mol. This shows that the IN2 is slightly stronger than IN1 because the bond of the primary alkoxide intermediate (C3-O3 1.50 Å) is shorter than the bond of the secondary alkoxide intermediate (C2-O2 1.53 Å).

The third step is the proton transfer and formation of the *tert*-carbenium cation [IN3, Figure 5(d)]. At this step, the covalent C3-O3 bond is breaking and one proton is moving from the C2 to the C3 atom. From a frequency calculation of the transition state geometry [TS3, Figure 5(c)], the imaginary frequency of -482.4 $cm^{-1}$ corresponds to the transition state. For the transition state it shows the hydrogen atom H2 is breaking the bond from the C2 atom to form the bond with the C3 atom and simultaneously breaking the C3-O3 bond. The activation energy is 26.07 kcal/mol. The *tert*-carbenium ion is found to be the intermediate with the relative energy of -17.02 kcal/mol. The symmetrical distances between C1-C2, C3-C2 and C4-C2 is about 1.42 Å. However, the *tert*-butyl carbenium ion does not have lower energy than the alkoxide intermediate and easily transfers to the isobutene via the proton shift back to the zeolite. The isobutene is the product as shown in Figure 6(b) with the activation barrier for this step of only 9.40 kcal/mol.

**Table 1. Comparison of Model Size and Computational Approach on the Adsorption and Activation Energies of 1-butene Isomerization to Isobutene on H-ZSM-5 Zeolite. Intrinsic Activation Energies are in Parenthesis. Energies are in kcal/mol.**

| **Model** | **23T** | **128T//23T** | **23T** |
|---|---|---|---|
| **Method** | **M08HX** | **M08HX** | **MP2 //M08HX** |
| AD1 | -16.99 | -18.26 | -16.35 |
| TS1 | 1.28 (18.26) | -3.69 (14.57) | 2.69 (19.05) |
| IN1 | -17.63 | -17.15 | -16.14 |
| TS2 | 10.76 (29.85) | 6.78 (23.93) | 9.81 (25.94) |
| IN2 | -21.51 | -20.2 | -18.82 |
| TS3 | 8.3 (29.81) | 5.87 (26.07) | 9.51(28.34) |
| IN3 | -12.61 | -17.02 | -8.32 |
| TS4 | -0.52 (12.06) | -7.61 (9.40) | 3.52 (11.85) |
| PR | -22.64 | -23.76 | -14.24 |

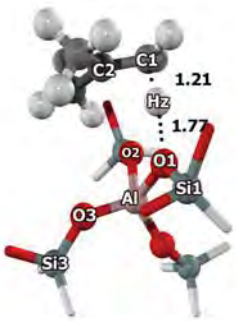


(a) TS4, ΔE= -7.61 kcal/mol

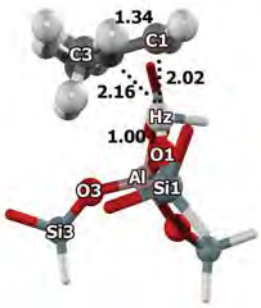


(b) PR, ΔE= -23.76 kcal/mol

**Figure 6.** Optimized structures of 1-butene isomerization to isobutene on H-ZSM-5 zeolite: (a) transition state (TS4), and (b) product isobutene adsorption (PR). Distances are in Ås.

The 1-butene to iso-butene reaction is an exothermic reaction. The rate determining step is the third step which shows the breaking of the bond formation of the primary alkoxide intermediate and the proton shift. To verify the accuracy of this method, the single point at MP2 is used to perform the energy of the density functional theory (see Table 1). The adsorption energies of 1-butene on H-ZSM-5 are calculated to be -16.99 and -16.35 kcal/mol with M08-HX/6-31G(d,p) and MP2/6-31G(d,p)//M08-HX/6-31G(d,p) methods, respectively. The activation energies of 1-butene isomerization are computed to be 18.26, 29.85, 29.81 and 12.10 kcal/mol with M08-HX. With the MP2//M08-HX, the activation energies are computed to be 19.05, 25.94, 28.34 and 11.85 kcal/mol. This suggests that the

M08-HX is a suitable method to study the reaction mechanism in the zeolite system.

**Conclusions**

The adsorption and skeletal isomerization of 1-butene to isobutene on the nanostructured H-ZSM-5 catalyst has been studied by the newly developed Density Functional Theory, M08-HX. The 128T quantum cluster model covers the intersection cavity of ZSM-5 zeolite. The adsorption energy of 1-butene is calculated to be -18.26 kcal/mol. The reaction mechanism of the skeletal isomerization of 1-butene is proposed to be four steps: 1) the protonation of adsorbed 1-butene to a secondary alkoxide intermediate, 2) the methyl shift between adjacent carbon-carbon atoms of the secondary alkoxide to form the primary alkoxide, 3) the proton transfer to form the *tert*-butyl carbenium ion, and 4) the deprotonation of the carbenium intermediate leading to isobutene as the product of the reaction. From the calculated results, the third step of the reaction is the rate determining step with an activation energy of 26.07 kcal/mol, which agrees well with the experimental value of 30.0 kcal/mol.

**Acknowledgement.** This work was supported in part by grants from the National Science and Technology Development Agency (2009 NSTDA Chair Professor funded by the Crown Property Bureau under the management of the National Science and Technology Development Agency and NANOTEC Center of Excellence funded by the National Nanotechnology Center), Kasetsart University Research and Development Institute (KURDI), the Thailand Research Fund (TRF), and the Commission on Higher Education, Ministry of Education (the "National Research University Project of Thailand (NRU)" and the "National Center of Excellence for Petroleum, Petrochemical and Advanced Materials (NCE-PPAM)").The authors are grateful to Donald G. Truhlar and Yan Zhao for their support with the M08-HX functional.

**References**

(1) Andy, P.; Gnep, N. S.; Guisnet, M.; Benazzi, E.; Travers, C. *J. Catal.* **1998**, *173*, 322.
(2) Asensi, M. A.; Corma, A.; Martíez, A. *J. Catal.* **1996**, *158*, 561.
(3) Guisnet, M.; Andy, P.; Boucheffa, Y.; Gnep, N. S.; Travers, C.; Benazzi, E. *Catal. Lett.* **1998**, *50*, 159.
(4) Guisnet, M.; Andy, P.; Gnep, N. S.; Benazzi, E.; Travers, C. *J. Catal.* **1996**, *158*, 551.
(5) Houžvička, J.; Hansildaar, S.; Ponec, V. *J. Catal.* **1997**, *167*, 273.
(6) Jousse, F.; Leherte, L.; Vercauteren, D. P. *Mol. Simul.* **1996**, *17*, 175.
(7) Jousse, F.; Leherte, L.; Vercauteren, D. P. *J. Mol. Catal. A: Chem.* **1997**, *119*, 165.
(8) Meriaudeau, P.; Bacaud, R.; Ngoc Hung, L.; Vu, A. T. *J. Mol. Catal. A: Chem.* **1996**, *110*.
(9) Mériaudeau, P.; Tuan, V. A.; Le, N. H.; Szabo, G. *J. Catal.* **1997**, *169*, 397.
(10) Seo, G.; Jeong, H. S.; Lee, J. M.; Ahn, B. J. *Stud. Surf. Sci. Catal.* **1997**, *105 B*, 1431.
(11) Trombetta, M.; Busca, G.; Rossini, S.; Piccoli, V.; Cornaro, U. *J. Catal.* **1997**, *168*, 349.
(12) De Ménorval, B.; Ayrault, P.; Gnep, N. S.; Guisnet, M. *Catal. Lett.* **2004**, *98*, 211.
(13) De Ménorval, B.; Ayrault, P.; Gnep, N. S.; Guisnet, M. *J. Catal.* **2005**, *230*, 38.
(14) de Ménorval, B.; Ayrault, P.; Gnep, N. S.; Guisnet, M. *Appl Catal A Gen* **2006**, *304*, 1.
(15) Bhan, A.; Iglesia, E. *Acc. Chem. Res.* **2008**, *41*, 559.
(16) Chen, C. S. H.; Bridger, R. F. *J. Catal.* **1996**, *161*, 687.
(17) Corma, A. *J. Catal.* **2003**, *216*, 298.
(18) Smit, B.; Maesen, T. L. M. *Nature (London, U. K.)* **2008**, *451*, 671.
(19) Venuto, P. B. *Microporous Mater.* **1994**, *2*, 297.
(20) Yaluris, G.; Rekoske, J. E.; Aparicio, L. M.; Madon, R. J.; Dumesic, J. A. *J. Catal.* **1995**, *153*, 65.
(21) Rutenbeck, D.; Papp, H.; Ernst, H.; Schwieger, W. *Appl Catal A Gen* **2001**, *208*, 153.
(22) Boronat, M.; Viruela, P.; Corma, A. *Phys. Chem. Chem. Phys.* **2001**, *3*, 3235.
(23) Namuangruk, S.; Pantu, P.; Limtrakul, J. *J. Catal.* **2004**, *225*, 523.
(24) Namuangruk, S.; Pantu, P.; Limtrakul, J. *ChemPhysChem* **2005**, *6*, 1333.
(25) Namuangruk, S.; Khongpracha, P.; Pantu, P.; Limtrakul, J. *J. Phys. Chem. B* **2006**, *110*, 25950.
(26) Pantu, P.; Boekfa, B.; Limtrakul, J. *J. Mol. Catal. A: Chem.* **2007**, *277*, 171.
(27) Boekfa, B.; Pantu, P.; Limtrakul, J. *J. Mol. Struct.* **2008**, *889*, 81.
(28) Pantu, P.; Boekfa, B.; Sunpetch, B.; Limtrakul, J. *Chem. Eng. Commun.* **2008**, *195*, 1477.
(29) Nieminen, V.; Sierka, M.; Murzin, D. Y.; Sauer, J. *J. Catal.* **2005**, *231*, 393.
(30) Boekfa, B.; Choomwattana, S.; Khongpracha, P.; Limtrakul, J. *Langmuir* **2009**, *25*, 12990.
(31) Boekfa, B.; Pantu, P.; Probst, M.; Limtrakul, J. *J. Phys. Chem. C* **2010**, *114*, 15061.
(32) Maihom, T.; Boekfa, B.; Sirijaraensre, J.; Nanok, T.; Probst, M.; Limtrakul, J. *J. Phys. Chem. C* **2009**, *113*, 6654.
(33) Van Koningsveld, H.; Van Bekkum, H.; Jansen, J. C. *Acta Crystallogr., Sect. B: Struct. Sci.* **1987**, *B43*, 127.
(34) Lonsinger, S. R.; Chakraborty, A. K.; Theodorou, D. N.; Bell, A. T. *Catal. Lett.* **1991**, *11*, 209.
(35) Frisch, M. J.; Trucks, G. W.; Schlegel, H. B.; Scuseria, G. E.; Robb, M. A.; Cheeseman, J. R.; Montgomery, J. A., Jr.; Vreven, T.; Kudin, K. N.; Burant, J. C.; Millam, J. M.; Iyengar, S. S.; Tomasi, J.; Barone, V.; Mennucci, B.; Cossi, M.; Scalmani, G.; Rega, N.; Petersson, G. A.; Nakatsuji, H.; Hada, M.; Ehara, M.; Toyota, K.; Fukuda, R.; Hasegawa, J.; Ishida, M.; Nakajima, T.; Honda, Y.; Kitao, O.; Nakai, H.; Klene, M.; Li, X.; Knox, J. E.; Hratchian, H. P.; Cross, J. B.; Adamo, C.; Jaramillo, J.; Gomperts, R.; Stratmann, R. E.; Yazyev, O.; Austin, A. J.; Cammi, R.; Pomelli, C.; Ochterski, J. W.; Ayala, P. Y.; Morokuma, K.; Voth, G. A.; Salvador, P.; Dannenberg, J. J.; Zakrzewski, V. G.; Dapprich, S.; Daniels, A. D.; Strain, M. C.; Farkas, O.; Malick, D. K.; Rabuck, A. D.; Raghavachari, K.; Foresman, J. B.; Ortiz, J. V.; Cui, Q.; Baboul, A. G.; Clifford, S.; Cioslowski, J.; Stefanov, B. B.; Liu, G.; Liashenko, A.; Piskorz, P.; Komaromi, I.; Martin, R. L.; Fox, D. J.; Keith, T.; Al-Laham, M. A.; Peng, C. Y.; Nanayakkara, A.; Challacombe, M.; Gill, P. M. W.; Johnson, B.; Chen, W.; Wong, M. W.; Gonzalez, C.; Pople, J. A. *Gaussian 03, revision B.05; Gaussian, Inc.: Pittsburgh, PA*, 2003.
(36) Zhao, Y.; Truhlar, D. G. *J. Phys. Chem. C* **2008**, *112*, 6860.
(37) Zhao, Y.; Truhlar, D. G. *Acc. Chem. Res.* **2008**, *41*, 157.
(38) Klinowski, J. *Chem. Rev.* **1991**, *91*, 1459.
(39) Yoda, E.; Kondo, J. N.; Domen, K. *J. Phys. Chem. B* **2005**, *109*, 1464.
(40) Cant, N. W.; Hall, W. K. *J. Catal.* **1972**, *25*, 161.

# STRUCTURES AND REACTION MECHANISMS OF n-BUTYL ALCOHOL CONVERSION TO iso-BUTYLENE OVER THETA-1 ZEOLITE: A DFT STUDY

*Jitwadee Wiangngean*[a,b,c], *Kanokwan Kongpatpanich*[a,b,c], *Sippakorn Wannakao*[a,b,c], *Bundet Boekfa*[b,c,d], *and Jumras Limtrakul*[a,b,c]*.

[a] Laboratory for Computational and Applied Chemistry, Department of Chemistry, Faculty of Science and Center of Nanotechnology, Kasetsart University Research and Development Institute, Kasetsart University, Bangkok 10900, Thailand
[b] Center for Advanced Studies in Nanotechnology and Its Applications in Chemical, Food and Agricultural Industries, Kasetsart University, Bangkok 10900, Thailand
[c] NANOTEC Center of Excellence, National Nanotechnology Center, Kasetsart University, Bangkok 10900, Thailand
[d] Chemistry Department, Faculty of Liberal Arts and Science, Kasetsart University Kamphaeng Saen Campus, Nakhon Pathom73140, Thailand

## Introduction

isobutylene is an important raw material for the production of oxygenated species such as methyl *tert*-butyl ether (MTBE) and ethyl *tert*-butyl ether (ETBE), which are currently used as octane enhancer additives of gasolines. In addition, isobutylene is a potential intermediate for petroleum and chemical industries**.** When taking into consideration environmental concerns, production of isobutylene from sustainable resources, such as biomass, is of tremendous interest. Bio-butyl alcohol is produced from biomass fermentation to be a clean fuel[1-2] as well as an industrially important intermediate to produce higher value chemicals.

Butyl alcohol dehydration was studied in many solid acid catalysts including acidic zeolites[3-4]. Furthermore, skeletal isomerization of linear butylenes has also been widely studied[5-8], but only a few studies describe the conversion of n-butyl alcohol to isobutylene[9-10]. The general mechanisms of linear butylene isomerization can be considered either monomolecular or bimolecular mechanisms. When a low number of acid sites appeared on the catalyst surface or at low temperatures, the isomerization mechanism typically favored the monomolecular mechanism[11-12]. Moreover, small pore zeolites such as theta-1 and FER lead to a high selectivity of the isomerization products over that of oligomerization. Recently, Zhang et al. have successfully studied the one-step dehydration and isomerization of n-butyl alcohol to iso-butylene over various types of zeolites. They found that both dehydration and isomerization occurred over acid sites and concluded that the theta-1 zeolite provides a high conversion of butyl alcohol together with a high selectivity of isobutylene product. Although many theoretical studies of dehydration and isomerization have been conducted, to the best of our knowledge, information of the direct conversion of n-butyl alcohol to isobutylene over zeolite systems has not been reported.

Theta-1 is a synthetic zeolite with a one dimensional channel[13]. The medium-pore size (4.4x5.5 Å) of theta-1 zeolite with a high silica ratio exhibits valuable properties and yields many important reactions such as isomerization, oligomerization.[14-16]**.** It is accepted that, the confinement effect from the zeolite framework is important to describe a reaction mechanism in the nanopore size of the zeolite[17-20]. Recently, the confinement effect of the zeolite framework on the adsorption and reaction mechanism have been successfully studied with M06 functional[21-24].

The aim of this study is to describe the reaction mechanism of the conversion of n-butyl alcohol to isobutylene over theta-1 zeolite which can occur in complicated stepwise and concerted ways using the dispersion included functional, M06-2X.

## Methodology

The quantum cluster structure was taken from the lattice structure of theta-1 zeolite. The 12T cluster model which represents its one direction pore character covering the straight channel of Theta-1 zeolite is shown in Figure 1. One Al atom was substituted in the T1 position and one H atom was attached to the neighboring oxygen, O11 to create a Brønsted acid site[25-26]. The Brønsted acid site ($Si_4O_4AlH$) and the probe molecule are allowed to relax while the rest is kept fixed at the crystallographic structure. The geometries of all the structures considered in this study have been optimized using the density functional, M06-2X, with the 6-31G(d,p) basis set. A normal-mode analysis of the transition state shows only one imaginary frequency that corresponds to the reaction mechansim. All calculations were performed with the Gaussian 03 code modified to incorporate the Minnesota Density Functional module 3.1 by Zhao and Truhlar[27]**.**

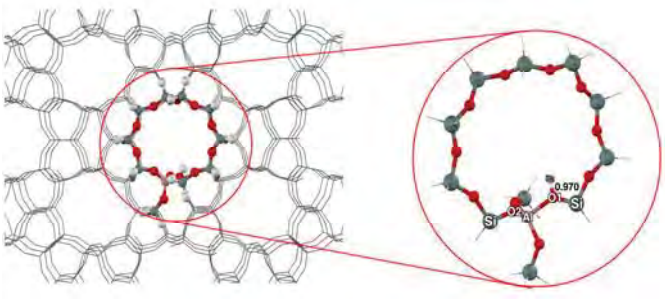


**Figure 1**. The 12T quantum cluster of the Theta-1 zeolite.

## Results and Discussion

The structures and reaction mechanisms of n-butyl alcohol dehydration and isomerization were investigated using the M06-2X/6-31G(d,p) level of theory. The butyl alcohol adsorbed on the Brønsted acid with a hydrogen bond in the straight channel of theta-1 zeolite is shown in Figure 2 (a, b). There are two stable forms of n-butyl alcohol on zeolite: end-on and site-on structures. The end-on structure (Ads1_endon) is adsorbed with the two hydrogen bonds; 1) The oxygen atom at the hydroxyl group of n-butyl alcohol and Brønsted acid site (O3 ··· Hz-O1) and 2) the hydrogen atom at the hydroxyl group of n-butyl alcohol and the oxygen of zeolite (O3-H···O2). Whereas only one strong hydrogen bond (O3 ··· Hz-O1) occurs in the side-on adsorption structure (Ads2_sideon). The O3…Hz distances are 1.403 and 1.407 Å for the end-on and the side-on structures, respectively. This distance corresponds with the calculated adsorption energies for the end-on and the side-on structures to be -31.5 and -29.1 kcal/mol, respectively. With this small difference of the adsorption energies, the n-butyl alcohol can possibly change its adsorption form without a significant energy change.

The conversion of n-butyl alcohol to isobutylene is achieved via the consecutive dehydration and skeletal isomerization. The dehydration of n-butyl alcohol over theta-1 zeolite can be considered as either a stepwise or a concerted mechanism. While skeletal isomerization is proposed in two pathways depending on the existence of the carbenium ion intermediate.

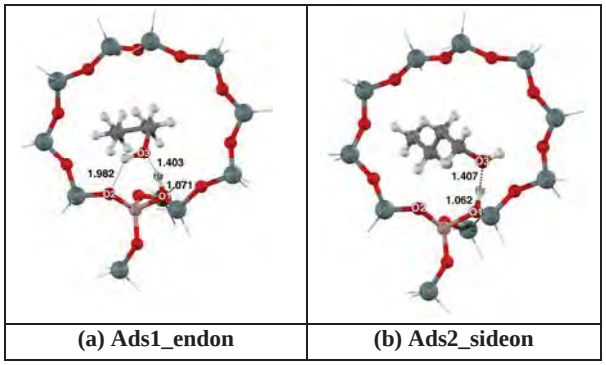


| (a) Ads1_endon | (b) Ads2_sideon |
|---|---|

**Figure 2.** The optimized structures of the adsorption complexes on the 12T cluster model of Theta-1: (a) endon n-butyl alcohol adsorption b) sideon n-butyl alcohol adsorption

**1. Dehydration of n-butyl alcohol on Theta-1 zeolite**

The dehydration of n-butyl alcohol on the theta-1 zeolite is proposed to be a stepwise mechanism. After the first step of adsorption, the Brønsted proton of zeolite interacts with the end-on n-butyl alcohol adsorption to form the alkoxide intermediate through the transition state (TS1_dehy). The transition state, the breaking of the C1-O3 **bond and forming the C1-O2 bond occur with one imaginary frequency at 401i $cm^{-1}$. This step requires the activation energy of 42.9 kcal/mol. The primary alkoxide intermediate is formed (Int_butox+$H_2O$) with the energy of -9.8 kcal/mol. The *desorption water of the alkoxide intermediate (Int2_butox) requires 1.7 kcal/mol. The next step is the primary alkoxide intermediate (Int2_butox) which changes to butylene via the transition state (TS_form). The breaking of the C1-O2 bond, the C2-H bond and forming the H-O1 bond of transition state require the activation energy of 33.4 kcal/mol. The n- butylene product occurs with the relative energy of 6.0 kcal/mol.

**2. Skeletal isomerization of butylene on Theta-1 zeolite**

After the dehydration occurs, the n-butylene can be converted to isobutylene via skeletal isomerization. The reaction mechanism is proposed to be four steps: 1) the protonation of adsorbed butylene to give the secondary butoxide intermediate (Int4_2-butox), 2) the conversion of the secondary alkoxide intermediate to a branched primary compound via a cyclic transition state (Int5_iso_butox), 3) the proton transfer to form the *tert*-butyl carbenium ion (Int6_tert) and 4) the deprotonation of the carbenium intermediate leading to the isobutylene product (Pro_isobut).

The first step, the transition state (TS_but_pro) proceeds via the forming of the C2-O2 bond and breaking of the C1-Hz bond. The C1-C2 bond changes from a double to a single bond. This step requires the activation energy of 19.9 kcal/mol. The secondary alkoxide intermediate (Int4_2-butox) is formed with a relative energy of 0.8 kcal/mol. The second step is the conversion of the secondary alkoxide intermediate to a branched primary compound via a cyclic transition state (TS_conver), the methy group transferring, with the activation energy of 32.1 kcal/mol. The primary butoxide intermediate (Int5_iso_butox) is the product of this step with the energy of -3.7 kcal/mol.(see Figure 6 for the structural information)

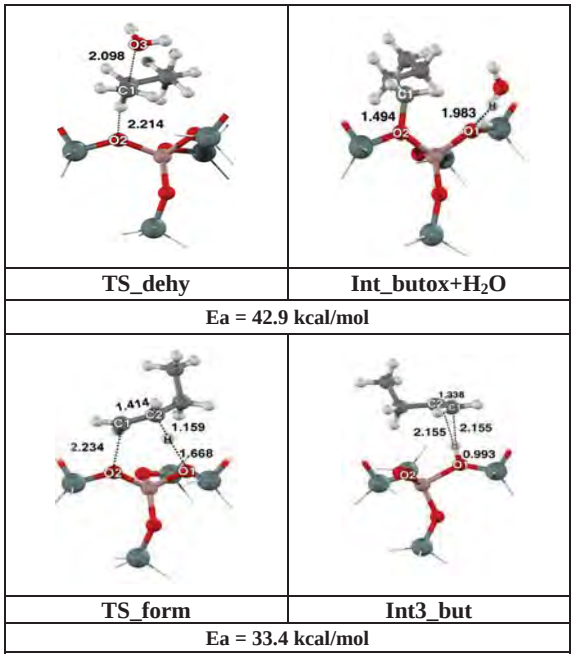


| TS_dehy | Int_butox+$H_2O$ |
|---|---|
| Ea = 42.9 kcal/mol | |
| TS_form | Int3_but |
| Ea = 33.4 kcal/mol | |

**Figure 3.** The optimized structures of the n-butyl alcohol dehydration step (stepwise mechanism) on the 12T cluster model of Theta-1

Next, the third step (The structures are shown in Figure 6) is the proton transfer to form the carbenium ion via the transition state (TS_cat). At this step, the C3-O1 bond breaks and one hydrogen atom transfers from the C2 to the C3 atom with the activation energy of 32.4 kcal/mol. The carbenium ion (Int6_tert) is not stable and can easily transform to isobutylene via the transition state (TS_H_shf) with the activation energy of only 0.5 kcal/mol. The final product is isobutylene (Prod_isobut) which interacted with the zeolite via the hydrogen bond between the π bond of butylene and the Brønsted acid of zeolite. The desorption energy of isobutylene on theta-1 is calculated to be 17.1 kcal/mol.

The concerted mechanism from the primary butoxide intermediate to isobutylene is proposed via the transition state (TS_decom) which is shown in Figure 7. The activation energy is 34.1 kcal/mol. These results show whether the mechanism from butylene to isobutylene should proceed via the carbenium ion or not, because of a very small amount of energy difference in the high temperature reaction process.

The overall reaction is calculated to be an endothermic reaction with the reaction energy of 16.9 kcal/mol. The first step of dehydrogenation of the butyl alcohol to the n-butylene is proposed to be the rate determining step of this reaction. This study will be beneficial for the further reaction mechanism to produce biomass to chemicals with zeolite catalysis.

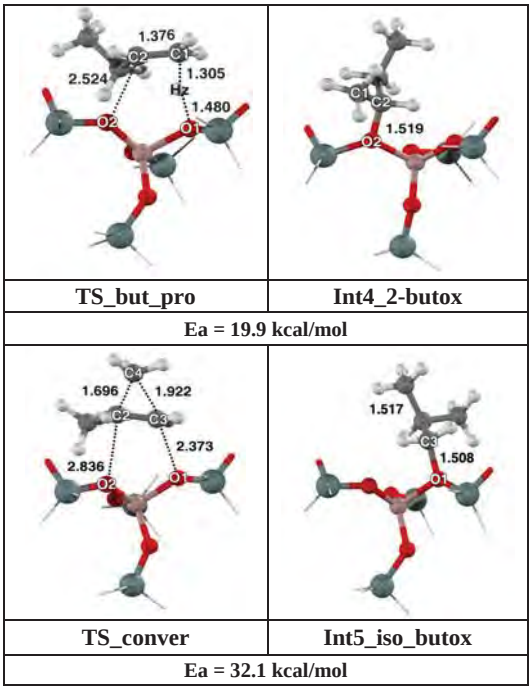


| TS_but_pro | Int4_2-butox |
|---|---|
| Ea = 19.9 kcal/mol | |
| TS_conver | Int5_iso_butox |
| Ea = 32.1 kcal/mol | |

**Figure 5**. The optimized structures of protonation of the butylene step and conversion of the secondary to branched primary alkoxide intermediate step on the 12 cluster model of Theta-1.

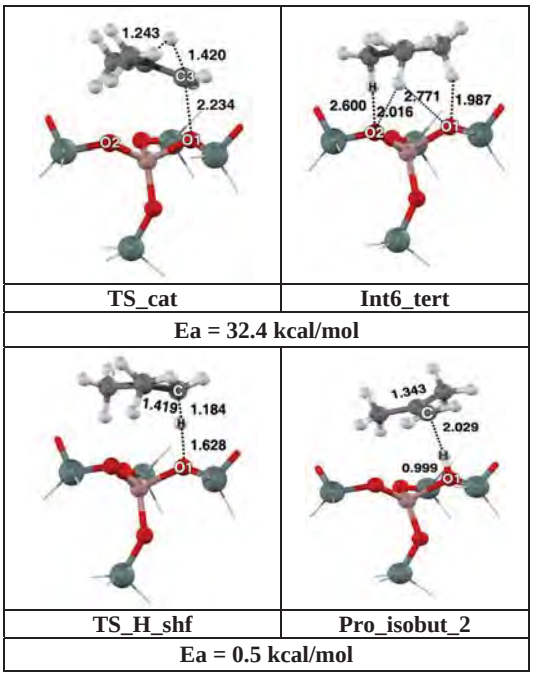


| TS_cat | Int6_tert |
|---|---|
| Ea = 32.4 kcal/mol | |
| TS_H_shf | Pro_isobut_2 |
| Ea = 0.5 kcal/mol | |

**Figure 6**. The optimized structures of the transition state and the intermediate complex on the isomerization mechanism proceeding via the carbenium ion.

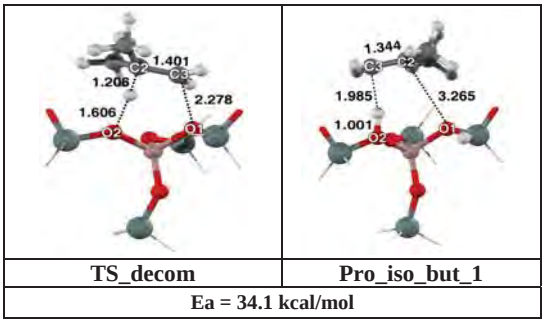


| TS_decom | Pro_iso_but_1 |
|---|---|
| Ea = 34.1 kcal/mol | |

**Figure 7**. The optimized structures of the decomposition of the branched primary alkoxide intermediate to the isobutylene step (concerted mechanism) on the 12 cluster model of Theta-1.

## Conclusions

Conversion of a bundle of biomass derived butyl alcohol to isobutylene over theta-1 zeolite has been a subject of great industrial significance. We investigated this by the M06-2X/6-31G(d,p) level of theory. The isobutylene production can proceed the stepwise mechanism of dehydration of butyl alcohol to produce butylene resulting in an isomerisation reaction to form isobutylene. First, the reaction began with the dehydration of butyl alcohol resulting from the butoxide intermediate forming 1-butylene with the activation barrier of 42.9 and 33.4 kcal/mol, respectively. The butoxide intermediate formation step is the rate determining step for the overall reaction. Next, the skeletal isomerization occurred through the carbenium ions. The four steps from butylene to isobutylene are proposed with activation energies of 19.9, 32.1, 32.4 and 0.5 kcal/mol, respectively. The obtained results suggest that the reaction mechanisms of direct conversion of n-butyl alcohol to isobutylene preferably proceeds via the concerted reaction pathway.

**Acknowledgement.** This work was supported in part by grants from the National Science and Technology Development Agency (2009 NSTDA Chair Professor funded by the Crown Property Bureau under the management of the National Science and Technology Development Agency and NANOTEC Center of Excellence funded by the National Nanotechnology Center), The Thailand Research Fund, the Commission of Higher Education, Ministry of Education ("National Research University of Thailand" and "Postgraduate Education and Research Programs in Petroleum and Petrochemicals and Advanced Materials"). The support from the Kasetsart University Research and Development Institute (KURDI) and Graduate School Kasetsart University are also acknowledged. The authors are grateful to Donald G. Truhlar and Yan Zhao for their support with the M06-2X functional.

## References

(1) Vane, L. M. *J. Chem. Technol. Biotechnol.* **2005**, *80*, 603-629.
(2) Qureshi, N.; Ezeji, T. C. *Biofuels, Bioproducts and Biorefining* **2008**, *2*, 319-330.
(3) Mashkina, A. V.; Khairulina, L. N. *Kinet. Catal.* **2002**, *43*, 684-690.
(4) West, R. M.; Braden, D. J.; Dumesic, J. A. *J. Catal.* **2009**, *262*, 134-143.
(5) Boronat, M.; Viruela, P.; Corma, A. *J. Phys. Chem. A* **1998**, *102*, 982-989.
(6) Onyestyak, G.; Valyon, J.; Pal-Borbely, G.; Rees, L. V. C. *Appl. Surf. Sci.* **2002**, *196*, 401-407.
(7) Namuangruk, S.; Tantanak, D.; Limtrakul, J. *J. Mol. Catal. A:Chem* **2006**, *256*, 113-121.
(8) Boronat, M.; Viruela, P.; Corma, A. *Phys. Chem. Chem. Phys.* **2001**, *3*, 3235-3239.

(9) Zhang, D. Z.; Al-Hajri, R.; Barri, S. A. I.; Chadwick, D. *Chem. Commun. (Cambridge, U. K.)* **2010**, *46*, 4088-4090.
(10) Macho, V.; Kralik, M.; Jurecekova, E.; Hudec, J.; Jurecek, L. *Appl. Catal., A* **2001**, *214*, 251-257.
(11) Seo, G.; Kim, N. H.; Lee, Y. H.; Kim, J. H. *Catal. Lett.* **1999**, *57*, 209-215.
(12) Čejka, J.; Wichterlová, B.; Sarv, P. *Appl. Catal., A* **1999**, *179*, 217-222.
(13) Barri, S. A. I.; Smith, G. W.; White, D.; Young, D. *Nature* **1984**, *312*, 533-534.
(14) Guisnet, M.; Andy, P.; Gnep, N. S.; Benazzi, E.; Travers, C. *Revue de l'Institute Francais du Petrole* **1999**, *54*, 23-28.
(15) Pirngruber, G. D.; Seshan, K.; Lercher, J. A. *Microporous Mesoporous Mater.* **2000**, *38*, 221-237.
(16) Fang, X.; Tong, G.; Liao, S.; Liu, Q.; Liu, P.; Yao, C.; Xie, L. *Petroleum Refinery Engineering* **2004**, *34*, 1-4.
(17) Kasuriya, S.; Namuangruk, S.; Treesukol, P.; Tirtowidjojo, M.; Limtrakul, J. *J. Catal.* **2003**, *219*, 320-328.
(18) Injan, N.; Pannorad, N.; Probst, M.; Limtrakul, J. *Int. J. Quantum Chem.* **2005**, *105*, 898-905.
(19) Namuangruk, S.; Tantanak, D.; Limtrakul, J. *J. Mol. Catal. A: Chem.* **2006**, *256*, 113-121.
(20) Pantu, P.; Boekfa, B.; Limtrakul, J. *J. Mol. Catal. A: Chem.* **2007**, *277*, 171-179.
(21) Wannakao, S.; Boekfa, B.; Khongpracha, P.; Probst, M.; Limtrakul, J. *ChemPhysChem* **2010**, *11*, 3432 – 3438.
(22) Boekfa, B.; Choomwattana, S.; Khongpracha, P.; Limtrakul, J. *Langmuir* **2009**, *25*, 12990-12999.
(23) Maihom, T.; Boekfa, B.; Sirijaraensre, J.; Nanok, T.; Probst, M.; Limtrakul, J. *J. Phys. Chem. C* **2009**, *113*, 6654-6662.
(24) Kumsapaya, C.; Bobuatong, K.; Khongpracha, P.; Tantirungrotechai, Y.; Limtrakul, J. *J. Phys. Chem. C* **2009**, *113*, 16128-16137.
(25) Boronat, M.; Zicovich-Wilson, C. M.; Viruela, P.; Corma, A. *J. Phys. Chem. B* **2001**, *105*, 11169-11177.
(26) Boronat, M.; Zicovich-Wilson, C. M.; Viruela, P.; Corma, A. *Chem.-Eur. J.* **2001**, *7*, 1295-1303.
(27) Frisch, M. J. T., G. W.; Schlegel, H. B.; Scuseria, G. E.; Robb, M. A.; Cheeseman, J. R.; Montgomery, J. A., Jr.; Vreven, T.; Kudin, K. N.; Burant, J. C.; Millam, J. M.; Iyengar, S. S.; Tomasi, J.; Barone, V.; Mennucci, B.; Cossi, M.; Scalmani, G.; Rega, N.; Petersson, G. A.; Nakatsuji, H.; Hada, M.; Ehara, M.; Toyota, K.; Fukuda, R.; Hasegawa, J.; Ishida, M.; Nakajima, T.; Honda, Y.; Kitao, O.; Nakai, H.; Klene, M.; Li, X.; Knox, J. E.; Hratchian, H. P.; Cross, J. B.; Adamo, C.; Jaramillo, J.; Gomperts, R.; Stratmann, R. E.; Yazyev, O.; Austin, A. J.; Cammi, R.; Pomelli, C.; Ochterski, J. W.; Ayala, P. Y.; Morokuma, K.; Voth, G. A.; Salvador, P.; Dannenberg, J. J.; Zakrzewski, V. G.; Dapprich, S.; Daniels, A. D.; Strain, M. C.; Farkas, O.; Malick, D. K.; Rabuck, A. D.; Raghavachari, K.; Foresman, J. B.; Ortiz, J. V.; Cui, Q.; Baboul, A. G.; Clifford, S.; Cioslowski, J.; Stefanov, B. B.; Liu, G.; Liashenko, A.; Piskorz, P.; Komaromi, I.; Martin, R. L.; Fox, D. J.; Keith, T.; Al-Laham, M. A.; Peng, C. Y.; Nanayakkara, A.; Challacombe, M.; Gill, P. M. W.; Johnson, B.; Chen, W.; Wong, M. W.; Gonzalez, C.; Pople, J. A. Gaussian 03, revision B.05; Gaussian, Inc.: Pittsburgh, PA, **2003**.

# Quantum Effect on the Reaction Mechanism of Propene Oxide Isomerization in H-ITQ-22: A DFT Investigation

*Kulwadee Theanngern*[a,b,c], *Bundet Boekfa*[b,c,d], *Pipat Khongpracha*[a,b,c] *and Jumras Limtrakul*[a,b,c*]

[a] Laboratory for Computational and Applied Chemistry, Department of Chemistry, Faculty of Science and Center of Nanotechnology, Kasetsart University Research and Development Institute, Kasetsart University, Bangkok 10900, Thailand
[b] NANOTEC Center of Excellence, National Nanotechnology Center, Kasetsart University, Bangkok 10900, Thailand
[c] Center for Advanced Studies in Nanotechnology and Its Applications in Chemical, Food and Agricultural Industries, Kasetsart University, Bangkok 10900, Thailand
[d] Chemistry Department, Faculty of Liberal Arts and Science, Kasetsart University Kamphaeng Saen Campus, Nakhon Pathom73140, Thailand

## Introduction

The reactive epoxide, driven from the constraint of the three-membered ring, makes it suitable to be a building block in the synthesis of organic compounds and polymers. The use of epoxide as a chemical starting material is of great current interest from both academic and industrial viewpoints. Propene oxide is one of the most important epoxides with a huge application in polymer industries[1-4]. The reaction of propene oxide that is attracting attention is the "ring-opening isomerization" to various oxygenated products, especially propanal and propanone[5-7]. This process can be catalyzed by either homogeneous or heterogeneous catalysts such as $Al_2O_3$, $Al_2O_3$-$SiO_2$, ZnO[8], Nafion-H, and zeolites[9-10]. The most current catalysts for this process are deficient in the versatility to be selective for the desired products. It is desirable to develop a catalytic process which is able to handle and give a beneficial selectivity.

Zeolite is an aluminosilicate porous material widely used in petroleum refineries and petrochemical industries[11-18]. Owing to its shape selectivity, intrinsic acidity and simple separation system, this material is one of the candidates for this process. Recently, Andras Fasi and co-workers studied the ring-opening isomerization of epoxide in various zeolites, including H-ZSM-5[9-10]. Their results showed that the reaction of epoxide in zeolite lead to the carbonyl compounds and propanal was the major product when H-ZSM-5 was employed as a catalyst. The comprehensive mechanistic study of this reaction in zeolite was initiated with the quantum chemical calculation[19]. Propene oxide isomerization over H-ZSM-5 zeolite was proposed in two mechanisms based on the reaction products, propanal and propanone. The ring-opening step was found to be the rate-determining step with activation barriers of 38.5 kcal/mol and 42.4 kcal/mol for propanal and propanone, respectively.

ITQ-22 (IWR) is the synthetic multipore zeolite with the dimension 8 x 10 x 12 membered ring pore structure[20]. Conventionally, this novel zeolite is applied for the isomerization of m-xylene, the disproportionation of m-xylene and the alkylation of benzene with isopropanol or propylene. The catalytic selectivity toward these reactions has proved to be better than ZSM-5 zeolite.

The exchange functional is required to realistically describe the interaction of ITQ-22 and the probing species. Therefore, the periodic calculation seems not to take into account some effects such as the van de Waals interaction, while the small quantum cluster is not able to represent the confinement effect of the zeolite framework.[21-23] The M06-2X functional recently developed by Zhao and Thrular[24-25] has been successfully applied to study the adsorption and reaction mechanisms of non-polar and aromatic molecules on zeolites.[26-29]

The aim of this work is to study the propene oxide isomerization over the multipore ITQ-22 zeolite using the density functional theory. The detailed reaction mechanism of propene oxide to propanal and propanone have been discussed.

## Methods

The geometry of the ITQ-22 zeolite was obtained from the crystallographic structure[20]. The 14T quantum cluster where T means the tetrahedral unit of Si or Al atoms was used for representing the active site of ITQ-22 zeolite. The cluster covers the 12-membered ring at the intersection cavity. One Si atom was replaced with an Al atom at the most appropriate T1 position and subsequently one proton was added to the system yielding a Brønsted acid site. All geometries were optimized with the M06-2X functional using the 6-31G(d,p) basis set. Only the active region, $\equiv SiO(H)Al(OSi)_4\equiv$, and the probe molecule were allowed to relax while the rest was kept fixed with the crystallographic structure. Only one imaginary frequency with its vibration corresponding to the transition structure was confirmed by frequency calculation. In order to examine the effect of the extended framework, single point calculations were performed on a 58T quantum cluster covered intersection and 8-, 10- and 12-MR windows of ITQ-22 as shown in Fig 1. All calculations were carried out by the Gaussian 03 package[30] incorporated with the Minnesota Density Functionals module 3.1 by Zhao and Truhlar.

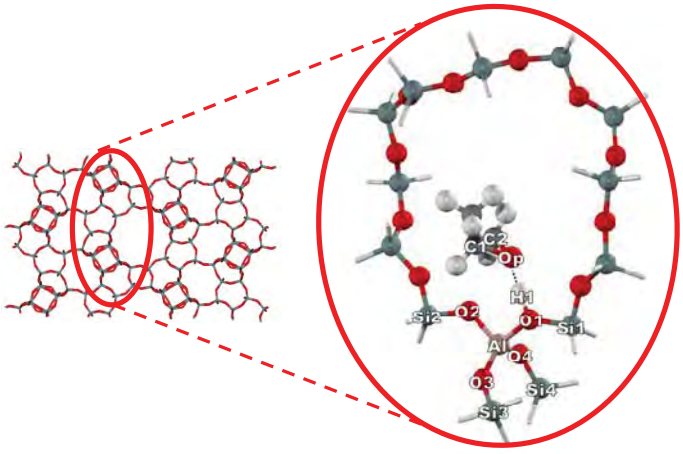


**Figure 1.** The selected structure of the 14T cluster of H-ITQ-22 zeolite.

## Results and Discussion

**The Zeolite Model and Adsorption Complexes.** The active site of ITQ-22 zeolite calculated by the 14T quantum cluster is shown in Figure 1. The optimized geometric parameters from the 14T quantum cluster are tabulated in Table 1. The Brønsted acid O1-Hz bond distance is 0.97 Å. The Al···Hz distance is 2.35 Å, which compared well with the experimental value (2.38-2.48 Å).

The propene oxide adsorbed on the Brønsted acid site with the hydrogen bond at the intersection of ITQ-22 is shown in Figure 2. Two optimum adsorption configurations are found, namely ADS_A and ADS_B with comparable adsorption energies of -24.09 and -24.51 kcal/mol, respectively. On both adsorption complexes, most of the geometric parameters are the same (see Table 1 and Table 2). The Brønsted acid O1-Hz bond distance is significantly increased from 0.97 to 1.06 Å. Strong hydrogen bond interactions in both configurations are confirmed by high adsorption energy; a short

intermolecular distance between the propene oxide and the Brønsted acid of zeolite H1···Op (1.42 and 1.41 Å) and the nearly linear arrangement of O1-H1-Op angle (174.69 and 175.49 degrees). The shorter H1···Op distance of ADS_B refers to the higher interaction with the zeolite. The calculated adsorption energies are in the range of the experimental data of acetone adsorbed on H-ZSM-5 zeolite (-31.1 kcal/mol). [31]

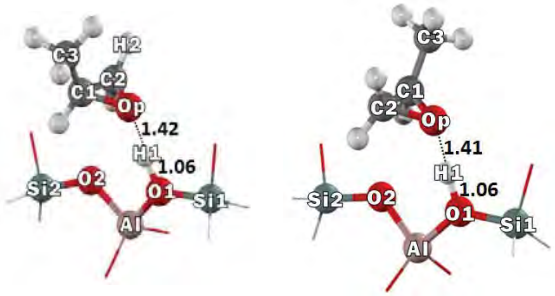


a) ADS_A
ΔE = -24.09 kcal/mol

b) ADS_B
ΔE = -24.51 kcal/mol

**Figure2.** Optimized structure of propene oxide on H-ITQ-22 zeolite: a) ADS_A and b) ADS_B. Distances are in Ås.

**The Reaction Mechanism of Isomerization of Propene Oxide.** The isomerization reaction of propene oxide occur via the C-O bond breaking in the propene oxide. Two different types of products, propanal and propanone, are produced from the breaking of the C-O bond at the tertiary carbon (C1-Op) and the other carbon atom (C2-Op). The energy profiles of both competitive routes are shown in Figure 3 and Figure 5.

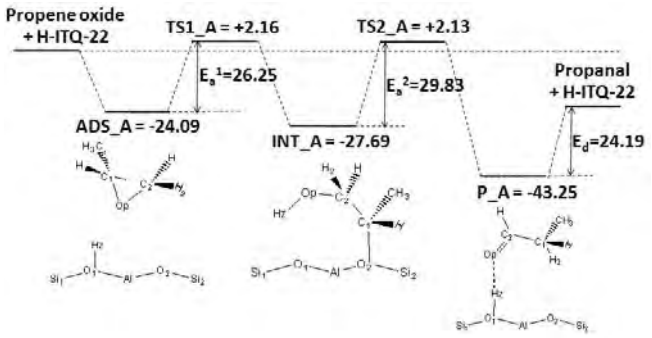


**Figure3.** The calculated energy profile for the isomerization of propene oxide to propanal over 14T clusters.

For a reaction that gives a propanal product, the reaction mechanism is proposed to be a stepwise mechanism. The optimized structures of all reaction intermediates are tabulated in Table 1. After the adsorption, ADS_A, the C1-Op bond is broken to produce a secondary alkoxide intermediate, INT_A. At the transition state structure, the C1-Op bond is broken and the coordination of C1 is changed from tetrahedral to the planar form. Only one imaginary frequency from the transition structure is observed at –497.41 $cm^{-1}$ corresponding with the moving of O1-H1 bond and the breaking of the C1-Op bond. The calculated activation barrier is 26.25 kcal/mol. The intermediate, INT_A, is formed subsequently to this step and has a relative energy -27.69 kcal/mol with respect to the starting reagent.

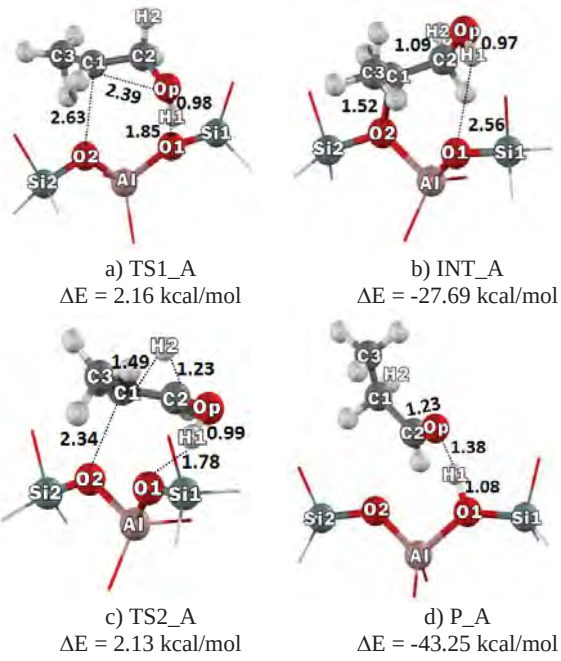


a) TS1_A
ΔE = 2.16 kcal/mol

b) INT_A
ΔE = -27.69 kcal/mol

c) TS2_A
ΔE = 2.13 kcal/mol

d) P_A
ΔE = -43.25 kcal/mol

**Figure 4.** Optimized structure of propene oxide to propanal on H-ITQ-22 zeolite: a) TS1_A, b) INT_A, c) TS2_A and d) P_A. Distances are in Ås.

**Table 1. Optimized Structural Parameters of the Adsorption and Reaction Complexes of Propene oxide to Propanal on H-ITQ-22 Zeolite. Distances are in Ås and Angles are in Degrees.**

| parameter | Bare | ADS_A | TS1_A | INT_A | TS2_A | P_A |
|---|---|---|---|---|---|---|
| Distances | | | | | | |
| O1-H1 | 0.97 | 1.06 | 1.85 | 2.56 | 1.78 | 1.08 |
| Al-H1 | 2.35 | 2.20 | 3.04 | 3.79 | 2.67 | 2.43 |
| Al-O1 | 1.89 | 1.83 | 1.74 | 1.71 | 1.75 | 1.84 |
| Al-O2 | 1.70 | 1.71 | 1.76 | 1.85 | 1.74 | 1.70 |
| O1-Si1 | 1.69 | 1.67 | 1.61 | 1.60 | 1.61 | 1.66 |
| O2-Si2 | 1.62 | 1.61 | 1.62 | 1.70 | 1.61 | 1.61 |
| H1-Op | | 1.42 | 0.98 | 0.97 | 0.99 | 1.38 |
| Op-C1 | 1.42 | 1.44 | 2.39 | 2.45 | 2.41 | 2.39 |
| Op-C2 | 1.42 | 1.44 | 1.38 | 1.40 | 1.34 | 1.23 |
| C1-C2 | 1.47 | 1.47 | 1.48 | 1.55 | 1.41 | 1.49 |
| C1-H2 | 1.09 | 2.23 | 2.02 | 2.15 | 1.49 | 1.10 |
| C2-H2 | 2.20 | 1.09 | 1.11 | 1.09 | 1.23 | 2.09 |
| O2-C1 | | 3.04 | 2.63 | 1.52 | 2.34 | 3.48 |
| O2-C2 | | 2.95 | 3.27 | 2.53 | 2.52 | 2.64 |
| Angles | | | | | | |
| Si1-O1-Al | 135.8 | 133.8 | 135.7 | 138.1 | 140.2 | 133.8 |

The next step is the 1,2 hydride shift where H transfers from the C2 atom to the C1 atom and concurrently the proton H1 moves back

to the zeolite. The transition state, TS2_A, is confirmed by one imaginary frequency at –709.25 $cm^{-1}$ where the vibration shows consecutive movement between the intermediate INT_A and the product. The activation barrier is calculated to be 29.83 kcal/mol. Therefore, this step is the rate-determining step of this pathway. The propanal product, P_A has a relative energy of -43.25 kcal/mol. The desorption energy of propanol from the ITQ-22 is calculated to be 24.19 kcal/mol. The propene oxide isomerization to propanal is exothermic reaction with the heat of reaction -19.06 kcal/mol.

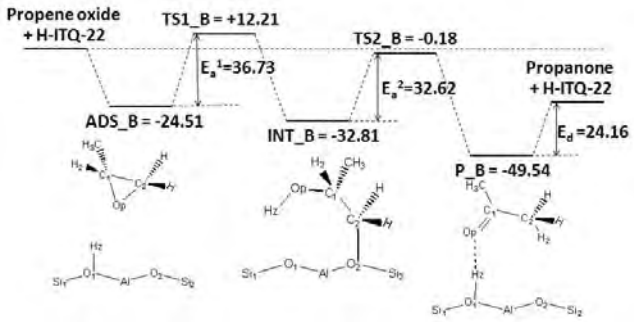


**Figure5.** The calculated energy profile for the isomerization of propene oxide to propanone over 14T clusters.

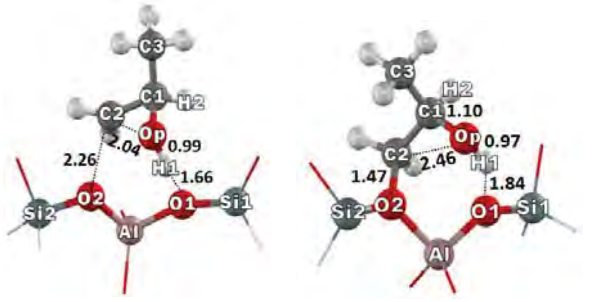


a) TS1_B
ΔE = 12.21 kcal/mol




b) INT_B
ΔE = -32.81 kcal/mol

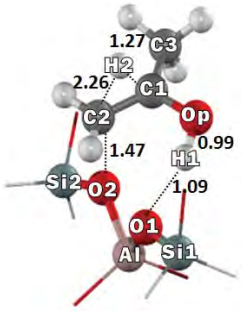


c) TS2_B
ΔE = -0.18 kcal/mol

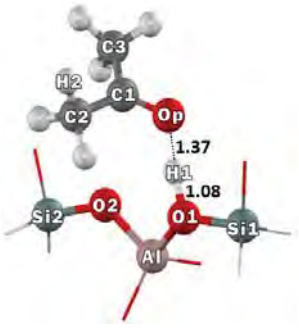


d) P_B
ΔE = -49.54 kcal/mol

**Figure 6**. Optimized structure of propene oxide to propanone on H-ITQ-22 zeolite: a) TS1_B, b) INT_B, c) TS2_B and d) P_B. Distances are in Å.

For the propanone production route, the reaction mechanism is similar to with the propanal route. The reaction is proposed to be a stepwise mechanism as shown in Figure 5. The optimized geometric parameters of all reaction intermediates are tabulated in Table 2. First, propene oxide adsorbed on the ITQ-22 zeolite forms the adsorption complex ADS_B. The propene oxide molecule is then protonated at the Op atom and the C2-Op bond is broken yielding the carbenium ion activated complex. For the transition state, TS1_B, requires the energy barrier of 36.73 kcal/mol, which is higher than that in the propanal step. This is due to the fact that a carbenium ion in the TS1_B is considered to be a primary carbenium ion that is less stable than a secondary carbenium ion, as in the TS1_A transition structure. The reaction generates the primary alkoxide intermediate, INT_B, with a relative energy of -32.81 kcal/mol. Next, the reaction goes through the transition state, TS2_B, which is a 1,2 hydride shift transfer from the C1 atom to the C2 atom and the return of the acidic proton H1. This step requires the energy barrier of 32.62 kcal/mol. The propanone product has a relative energy of -49.54 kcal/mol. The desorption energy of propanone from ITQ-22 is 24.16 kcal/mol. The propene oxide isomerization to propanone is an exothermic reaction with the heat of reaction -25.38 kcal/mol.

The isomerization of propene oxide to propanal and propanone on H-ITQ-22 has been successfully studied with the M06-2X functional. The rate determining step requires activation energies 29.83 and 36.73 kcal/mol for propanal and propanone, respectively. This leads to the conclusion that propanal is the major product from the propene oxide isomerization reaction. Our findings are also confirmed by the experiment data that higher selectivity of propanal over propanone is observed in propene oxide isomerization using zeolite as a catalyst[9].

**Table2. Optimized Structural Parameters of the Adsorption and Reaction Complexes of Propene Oxide to Propanone on H-ITQ-22 zeolite. Distances are in Å and Angles are in Degrees.**

| parameter | Bare | ADS_B | TS1_B | INT_B | TS2_B | P_B |
|---|---|---|---|---|---|---|
| | | | Distances | | | |
| O1-H1 | 0.97 | 1.06 | 1.66 | 1.84 | 1.83 | 1.08 |
| Al-H1 | 2.35 | 2.42 | 2.70 | 2.77 | 2.91 | 2.38 |
| Al-O1 | 1.89 | 1.83 | 1.75 | 1.72 | 1.75 | 1.83 |
| Al-O2 | 1.70 | 1.71 | 1.74 | 1.85 | 1.76 | 1.71 |
| O1-Si1 | 1.69 | 1.67 | 1.62 | 1.61 | 1.61 | 1.67 |
| O2-Si2 | 1.62 | 1.61 | 1.62 | 1.70 | 1.62 | 1.60 |
| H1-Op | | 1.41 | 0.99 | 0.97 | 0.98 | 1.37 |
| Op-C1 | 1.42 | 1.44 | 1.42 | 1.40 | 1.33 | 1.23 |
| Op-C2 | 1.42 | 1.44 | 2.04 | 2.46 | 2.38 | 2.39 |
| C1-C2 | 1.47 | 1.47 | 1.47 | 1.55 | 1.41 | 1.50 |
| C1-H2 | 2.21 | 1.09 | 1.09 | 1.10 | 1.27 | 2.11 |
| C2-H2 | 1.09 | 2.17 | 2.16 | 2.12 | 1.48 | 1.10 |
| O2-C1 | | 2.98 | 3.25 | 2.50 | 3.24 | 2.80 |
| O2-C2 | | 3.03 | 2.26 | 1.47 | 2.05 | 2.91 |
| | | | Angles | | | |
| Si1-O1-Al | 135.8 | 134.2 | 136.3 | 139.8 | 136.3 | 133.5 |

**Conclusion**

The selective isomerization of propene oxide over multi-nanopore zeolite, H-ITQ-22, has been investigated with the

M06-2X/6-31G(d,p) method. A 14T quantum cluster covered the intersection 12 membered ring was used to represent the acid site, where T is Si or Al atoms. The reaction mechanisms were proposed through the ring opening and the 1,2 hydride rearrangement. Two different pathways were systematically examined leading to the targeted products, namely propanal and propanone. The rate determining step leading to propanal was observed to be the 1,2 hydride rearrangement with an activation barrier of 29.8 kcal/mol, whereas, the ring-opening step was found to be the rate-determining step for propanone with an activation barrier of 36.7 kcal/mol. With chemically realistic and well-calibrated models together with an accurate DFT method, our findings clearly demonstrate that H-ITQ-22 zeolite is one of the good catalysts for the selective isomerization of propene oxide for the production of propanal.

**Acknowledgement.** This work was supported in part by grants from the National Science and Technology Development Agency (2009 NSTDA Chair Professor funded by the Crown Property Bureau under the management of the National Science and Technology Development Agency and NANOTEC Center of Excellence funded by the National Nanotechnology Center), Kasetsart University Research and Development Institute (KURDI), the Thailand Research Fund (TRF), and the Commission on Higher Education, Ministry of Education (the "National Research University Project of Thailand (NRU)" and the "National Center of Excellence for Petroleum, Petrochemical and Advanced Materials (NCE-PPAM)").The authors are grateful to Donald G. Truhlar and Yan Zhao for their support with the M06-2X functional.

**References**

(1) Smith, J. G. *Synthesis* **1984**, 629.
(2) Katsuki, T.; Sharpless, K. B. *J. Am. Chem. Soc.* **1980**, *102*, 5974.
(3) Cheng, Z.; Zhu, X.; Fu, G. D.; Kang, E. T.; Neoh, K. G. *Macromolecules* **2005**, *38*, 7187.
(4) Carlier, P. R. *Angew. Chem., Int. Ed.* **2004**, *43*, 2602.
(5) Ranu, B. C.; Jana, U. *J. Org. Chem.* **1998**, *63*, 8212.
(6) Karamé, I.; Tommasino, M. L.; Lemaire, M. *Tetrahedron Lett.* **2003**, *44*, 7687.
(7) Procopio, A.; Dalpozzo, R.; De Nino, A.; Nardi, M.; Sindona, G.; Tagarelli, A. *Synlett* **2004**, 2633.
(8) Molnár, Á.; Bucsi, I.; Bartók, M.; Resofszki, G.; Gáti, G. *J. Catal.* **1991**, *129*, 303.
(9) Fási, A.; Gömöry, A.; Pálinkó, I.; Kiricsi, I. *J. Catal.* **2001**, *200*, 340.
(10) Fási, A.; Pálinkó, I.; Gömöry, A.; Kiricsi, I. *J. Mol. Catal. A: Chem.* **2004**, *208*, 307.
(11) Andy, P.; Gnep, N. S.; Guisnet, M.; Benazzi, E.; Travers, C. *J. Catal.* **1998**, *173*, 322.
(12) Bhan, A.; Iglesia, E. *Acc. Chem. Res.* **2008**, *41*, 559.
(13) Corma, A. *J. Catal.* **2003**, *216*, 298.
(14) Hsia Chen, C. S.; Bridger, R. F. *J. Catal.* **1996**, *161*, 687.
(15) Luzgin, M. V.; Rogov, V. A.; Arzumanov, S. S.; Toktarev, A. V.; Stepanov, A. G.; Parmon, V. N. *Angew. Chem., Int. Ed.* **2008**, *47*, 4559.
(16) Smit, B.; Maesen, T. L. M. *Nature* **2008**, *451*, 671.
(17) Venuto, P. B. *Microporous Materials* **1994**, *2*, 297.
(18) Yaluris, G.; Rekoske, J. E.; Aparicio, L. M.; Madon, R. J.; Dumesic, J. A. *J. Catal.* **1995**, *153*, 65.
(19) Namuangruk, S.; Khongpracha, P.; Pantu, P.; Limtrakul, J. *J. Phys. Chem. B* **2006**, *110*, 25950.
(20) Corma, A.; Rey, F.; Valencia, S.; Jordá, J. L.; Rius, J. *Nature Materials* **2003**, *2*, 493.
(21) Namuangruk, S.; Tantanak, D.; Limtrakul, J. *J. Mol. Catal. A: Chem.* **2006**, *256*, 113.
(22) Pantu, P.; Boekfa, B.; Limtrakul, J. *J. Mol. Catal. A: Chem.* **2007**, *277*, 171.
(23) Pantu, P.; Boekfa, B.; Sunpetch, B.; Limtrakul, J. *Chem. Eng. Commun.* **2008**, *195*, 1477.
(24) Zhao, Y.; Truhlar, D. G. *J. Phys. Chem. C* **2008**, *112*, 6860.
(25) Zhao, Y.; Truhlar, D. G. *Acc. Chem. Res.* **2008**, *41*, 157.
(26) Boekfa, B.; Choomwattana, S.; Khongpracha, P.; Limtrakul, J. *Langmuir* **2009**, *25*, 12990.
(27) Kumsapaya, C.; Bobuatong, K.; Khongpracha, P.; Tantirungrotechai, Y.; Limtrakul, J. *J. Phys. Chem. C* **2009**, *113*, 16128.
(28) Maihom, T.; Boekfa, B.; Sirijaraensre, J.; Nanok, T.; Probst, M.; Limtrakul, J. *J. Phys. Chem. C* **2009**, *113*, 6654.
(29) Maihom, T.; Pantu, P.; Tachakritikul, C.; Probst, M.; Limtrakul, J. *J. Phys. Chem. C* **2010**, *114*, 7850.
(30) Frisch, M. J.; Trucks, G. W.; Schlegel, H. B.; Scuseria, G. E.; Robb, M. A.; Cheeseman, J. R.; Montgomery, J. A.; Vreven, T.; Kudin, K. N.; Burant, J. C.; Millam, J. M.; Iyengar, S. S.; Tomasi, J.; Barone, V.; Mennucci, B.; Cossi, M.; Scalmani, G.; Rega, N.; Petersson, G. A.; Nakatsuji, H.; Hada, M.; Ehara, M.; Toyota, K.; Fukuda, R.; Hasegawa, J.; Ishida, M.; Nakajima, T.; Honda, Y.; Kitao, O.; Nakai, H.; Klene, M.; Li, X.; Knox, J. E.; Hratchian, H. P.; Cross, J. B.; Adamo, C.; Jaramillo, J.; Gomperts, R.; Stratmann, R. E.; Yazyev, O.; Austin, A. J.; Cammi, R.; Pomelli, C.; Ochterski, J. W.; Ayala, P. Y.; Morokuma, K.; Voth, G. A.; Salvador, P.; Dannenberg, J. J.; Zakrzewski, V. G.; Dapprich, S.; Daniels, A. D.; Strain, M. C.; Farkas, O.; Malick, D. K.; Rabuck, A. D.; Raghavachari, K.; Foresman, J. B.; Ortiz, J. V.; Cui, Q.; Baboul, A. G.; Clifford, S.; Cioslowski, J.; Stefanov, B. B.; Liu, G.; Liashenko, A.; Piskorz, P.; Komaromi, I.; Martin, R. L.; Fox, D. J.; Keith, T.; Al-Laham, M. A.; Peng, C. Y.; Nanayakkara, A.; Challacombe, M.; Gill, P. M. W.; Johnson, B.; Chen, W.; Wong, M. W.; Gonzalez, C.; Pople, J. A. *Gaussian 03, revision B.05*, 2003.
(31) Šepa, J.; Lee, C.; Gorte, R. J.; White, D.; Kassab, E.; Evleth, E. M.; Jessri, H.; Allavena, M. *Journal of Physical Chemistry* **1996**, *100*, 18515.

# STRUCTURES AND REACTION MECHANISMS OF BUTADIENE CYCLOADDITION OVER METAL-EXCHANGED FAUJASITE

*Thittaya Yutthalekha* [a,b,c], *Kanokwan Kongpatpanich* [a,b,c], *Thana Maihom* [a,b,c], *Bundet Boekfa* [b,c,d], *and Jumras Limtrakul* [a,b,c]

[a] Laboratory for Computational and Applied Chemistry, Department of Chemistry, Faculty of Science and Center of Nanotechnology, Kasetsart University Research and Development Institute, Kasetsart University, Bangkok 10900, Thailand
[b] NANOTEC Center of Excellence, National Nanotechnology Center, Kasetsart University, Bangkok 10900, Thailand
[c] Center for Advanced Studies in Nanotechnology and Its Applications in Chemical, Food and Agricultural Industries, Kasetsart University, Bangkok 10900, Thailand
[d] Chemistry Department, Faculty of Liberal Arts and Science, Kasetsart University Kamphaeng Saen Campus, Nakhon Pathom73140, Thailand

## Introduction

4-vinylcyclohexene (4-VCH) is primary used as the important intermediate in the synthesis of polystyrene and other useful copolymers. Currently, styrene is manufactured largely from benzene through ethylbenzene. The dehydrogenation of 4-VCH is important as an alternative route for the manufacture of styrene[1]. 4-VCH is produced through Diels–Alder cycloaddition reaction of two 1,3-butadiene molecules. Several researchers have studied this reaction in various catalysts, such as the promoted $ZrO_2$ catalyst, Pd catalysts supported on alumina and polyoxometalate[2-7]. This route is potentially attractive because it does not require petroleum-based aromatic feedstock and it is a fairly clean process.

The Diels–Alder cycloaddition of 1,3-butadiene to 4-VCH is a well-known thermally-initiated cycloaddition reaction between two 1,3-butadiene molecules in which one serves as the a conjugated diene and the other as the dienophile. This cyclic adduct formation of butadiene molecules has an energy barrier of 24.7 kcal/mol. It is kinetically second-order in 1,3-butadiene[8]. The catalytic role of zeolites has been understood in term that zeolites being able to confine 1,3-butadiene within their pores due to their shape and size selective properties. Thus, by increasing the 1,3-butadiene concentration inside the zeolitic pores relative to that in the external gas phase, the zeolite can enhance the rates of bimolecular reactions. In theoretical investigations, several mechanisms have been proposed for this process; the most popular are the concerted (symmetry-allowed) mechanism and the stepwise mechanism, which the latter involves the formation of a bisallyl biradical intermediate. It has been shown that both mechanisms are similar in their energetics[9-10].

Zeolites consist of hundreds of atoms per unit cell where the use of such sophisticated methods as periodic calculation are too computationally demanding and expensive. The recently developed hybrid methods, for example the embedded cluster or combined quantum mechanics/molecular mechanics (QM/MM) methods, as well as the more general Our-own-N-layered Integrated molecular Orbital + molecular Mechanics (ONIOM) method has brought more economical methods to study the adsorptions and reactions on zeolites[11-17]. More recently, the newly developed method, M06 functional, is successfully applied to study the interaction and reactions of hydrocarbon on various zeolites. [18-20]

The cycloaddition reaction of 1,3-butadiene has been studied over a large-pore zeolites, such as NaX[21-22], NaZSM-20[23], NaBeta[23] and CuY[21,24]. Instead of the targeted cycloaddition of 1,3-butadiene, the Brønsted acid character of zeolite catalyzes the oligomerization yielding oligomeric residues such as polyolefinic species and alkenyl carbocations.[25] In the same manner as NaX, even the high butadiene conversion can be obtained but the selective for the cycloaddition adduct is relatively poor (<30%). The main products over NaX are oligomeric ones such as polyalkenes[22]. Moreover, $Cu^+$ exchanged zeolites were also active catalysts in many reactions, such as the direct decomposition of NO into $N_2$ and $O_2$, as well as in the selective photocatalytic reduction of $NO_x$, butene isomerization[26-27] and alkene oxidation[28]. The Diels–Alder cycloaddition of 1,3-butadiene over a $Cu^+$ exchanged zeolite gives an excellent yield of 4-VCH[25,29].

The goal of this work is to investigate the reaction mechanisms of 1,3-butadiene cycloaddition over Cu-exchanged Faujasite zeolite (Cu-FAU).

## Methods

The active region consists of the 8T (T=tetrahedral of Si or Al atoms) inside the supercage, which can be considered as the smallest unit required to represent the active site of Faujasite zeolite. This was taken from the zeolite crystal lattice structures. The Si atom at the most favored position, T2, is replaced with an Al atom and a transition metal ion was placed to compensate for the charge. In the present study, we have employed the M06-2X functional using the 6-31G(d,p) basis set for H, C, O, Al and Si atoms, while the Stuttgart RSC 1997 effective core potential (ECP) were used for the Cu atom. Normal mode analyses were carried out to verify the transition states to have one imaginary frequency whose mode corresponded to the reaction coordinate. The total spin was kept constant at the singlet ground states. The charge distribution in the complexes has been analyzed via the natural population analysis (NPA). The 49T extended framework was treated with the single point calculation to represent the confinement effect of the zeolite framework. All calculations in this work have been performed by using the Gaussian 03 program[30] incorporated with the Minnesota Density Functionals module 3.1 by Zhao and Truhlar[31-32].

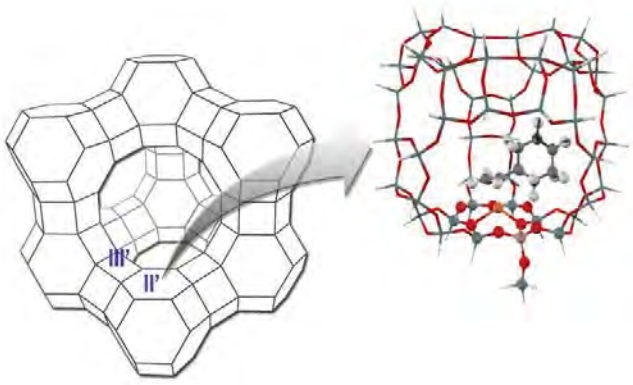


**Figure 1.** Model of the 49T cluster. The 8T quantum cluster is drawn as the bond and stick model.

## Results and Discussion

The location of the copper cations in the zeolite framework are sites II' & III' which accessible to reactants and contribute to the activity of the catalyst[33]. The metal ion lies between the three bridging oxygen atoms of the zeolite framework. The Al-Cu bond is

3.06 Å, which agrees with experiment data[33]. Bond distances for the nearest-neighbor O and Cu atoms are shown in the Figure 1.

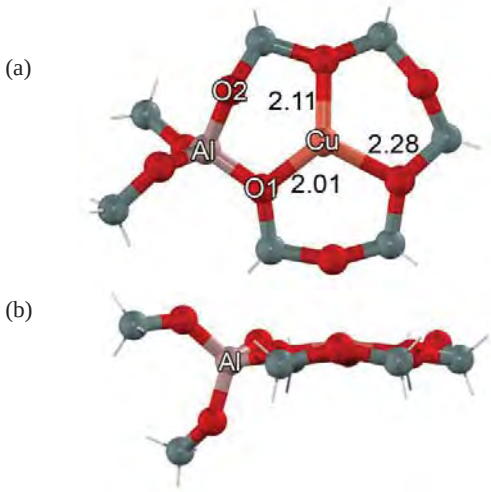


**Figure 2.** Optimized structure of the Cu-exchange faujasite complexes. (a) top view, (b) side view, Distances are in Å.

The optimized structures of Cu-FAU complexes and their reaction coordinates are shown in Figure 2 and the optimized geometrical parameters are tabulated in Table 1. The 1,3-butadiene adsorbs on Cu-FAU in the supercage over the 6T window of the FAU zeolite. The Al-Cu distance increases from 3.06 to 3.12 Å. The C1=C2 bond of the 1,3-butadiene was decreased to be 1.36 Å due to the π-back donation of electrons from the *d* orbitals of metal to the π* antibonding orbitals of 1,3-butadiene. The adsorption energy of 1,3-butadiene on the 8T cluster is -20.23 kcal/mol. To represent the confinement effect, the extended 49T quantum cluster gives the adsorption energy of -28.23 kcal/mol. There is no experimental data for the adsorption of butadiene on Cu-FAU. There is data only for the experiment of ethylene on Cu-FAU zeolite, which reports the adsorption energy to be -20.79 kcal/mol.

**Table 1. Optimized structural parameters of reaction complexes during the cycloaddition of 1,3-butadiene over a Cu(I) faujasite which were obtained from M06-2X/6-31G(d,p) calculations.**

| Distance | Bare | Ads | Coads | TS | PR |
|---|---|---|---|---|---|
| Al-Cu | 3.06 | 3.12 | 3.12 | 3.13 | 3.05 |
| Si-O1 | 1.63 | 1.63 | 1.63 | 1.64 | 1.63 |
| Si-O2 | 1.58 | 1.59 | 1.59 | 1.59 | 1.59 |
| Al-O1 | 1.80 | 1.79 | 1.79 | 1.80 | 1.79 |
| Al-O2 | 1.73 | 1.73 | 1.73 | 1.74 | 1.73 |
| C1-Cu | | 2.25 | 2.24 | 2.57 | 3.55 |
| C2-Cu | | 2.32 | 2.30 | 2.42 | 3.14 |
| C1-C1’ | | - | 3.36 | 2.02 | 1.53 |
| C2-C4’ | | - | 3.29 | 2.41 | 1.54 |
| C1-C2 | 1.33 | 1.36 | 1.36 | 1.40 | 1.53 |
| C2-C3 | 1.46 | 1.47 | 1.47 | 1.48 | 1.50 |
| C3-C4 | 1.33 | 1.34 | 1.34 | 1.34 | 1.35 |
| C1’-C2’ | | - | 1.34 | 1.39 | 1.51 |
| C2’-C3’ | | - | 1.47 | 1.41 | 1.33 |
| C3’-C4’ | | - | 1.34 | 1.38 | 1.51 |

In the next step, another 1,3-butadiene diffuses over the adsorbed 1,3-butadiene on the metal-exchanged faujasite zeolite (Co-ads) as shown in Figure 2(b). The calculated energy on the 8T quantum cluster is -23.64 kcal/mol. The framework effect of the 49T quantum cluster increases the adsorption energy to -33.40 kcal/mol. The extended framework gives the coadsorption of the 1,3-butadiene and stabilizes the adsorption complex by 5.17 kcal/mol.

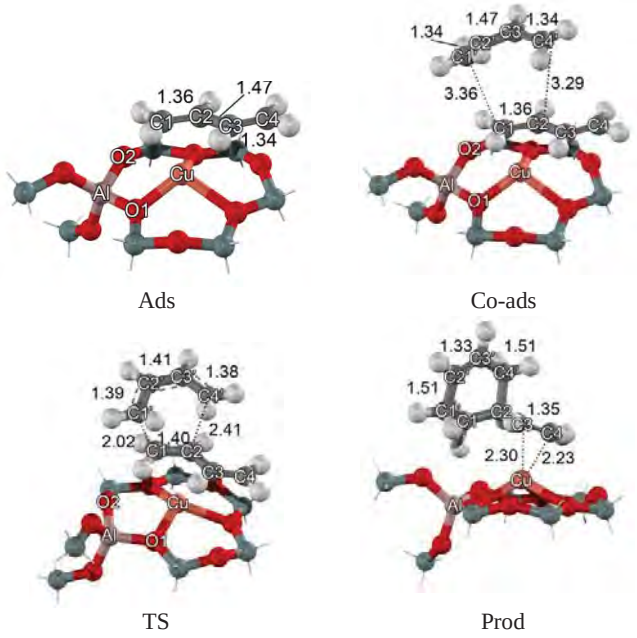


**Figure 3.** Optimized structures of the Cu-exchange faujasite complexes. Distances are in Å.

The cycloaddition reaction of two 1,3-butadiene give the 4-vinylcyclohexene product. The energy profile is shown in Figure 3. The transition state, the C1-C1’ and C2-C4’ bonds of the two 1,3-butadienes are decreased from 3.36 to 2.02 Å and 3.29 to 2.41 Å respectively. Only one imaginary frequency can be found at -559 $cm^{-1}$ corresponding with the forming of the C1-C1’ and C2-C4’ bonds of the two 1,3-butadienes. This step requires activation barriers of 21.28 kcal/mol with the 8T quantum cluster. The extended framework reduces the apparent activation barrier by 8.90 kcal/mol.

In the last step, the 4-vinylcyclohexene product is strongly adsorbed to the metal atom via double of C3-C4 bond. The relative energies of the product are -71.34 and -79.07 kcal/mol for the 8T and 49T quantum cluster, respectively. The desorption energies are 20.76 and 28.49 kcal/mol for the 8T and the 49T quantum cluster, respectively.

The charge distribution in the complexes, which are analyzed by the natural population analysis (NPA), show the charge of metal ions in the Faujasite supercage to be 0.78, which is compensated by the surrounding oxygen atoms in the 6-ring inside the supercage. When 1,3-butadienes adsorbed on the metal, the charge of $Cu^+$ was decreased to 0.72, indicating that the $Cu^+$ makes 1,3-butadiene to be a better dienophile.

**Table 2 Natural population analysis (NPA) parameters of reaction complexes during the cycloaddition of 1,3-butadiene over a Cu-FAU zeolite which were obtained from M06-2X/6-31G(d,p) calculations.**

| Atom | Bare | Ads | Coads | TS | PR |
|---|---|---|---|---|---|
| Cu | 0.78 | 0.72 | 0.72 | 0.70 | 0.70 |
| Al | 2.08 | 2.09 | 2.09 | 2.10 | 2.10 |
| O1 | -1.36 | -1.35 | -1.36 | -1.37 | -1.37 |
| O2 | -1.31 | -1.32 | -1.32 | -1.32 | -1.32 |
| C1 | | -0.49 | -0.49 | -0.49 | -0.49 |
| C2 | | -0.32 | -0.33 | -0.39 | -0.39 |
| C3 | | -0.26 | -0.27 | -0.27 | -0.27 |
| C4 | | -0.41 | -0.41 | -0.46 | -0.46 |
| C1’ | | - | -0.42 | -0.45 | -0.45 |
| C2’ | | - | -0.26 | -0.22 | -0.22 |
| C3’ | | - | -0.26 | -0.28 | -0.28 |
| C4’ | | - | -0.42 | -0.39 | -0.39 |

The Diels–Alder cycloaddition of 1,3-butadiene on Cu-FAU is calculated with the M06-2X functional. The reaction is proposed via a concerted mechanism with an activation energy of 22.09 kcal/mol. The 4-vinylcyclohexene product is strongly adsorbed on Cu-FAU. The reaction is exothermic with a reaction energy –50.58 kcal/mol. This calculation is useful to further produce styrene.

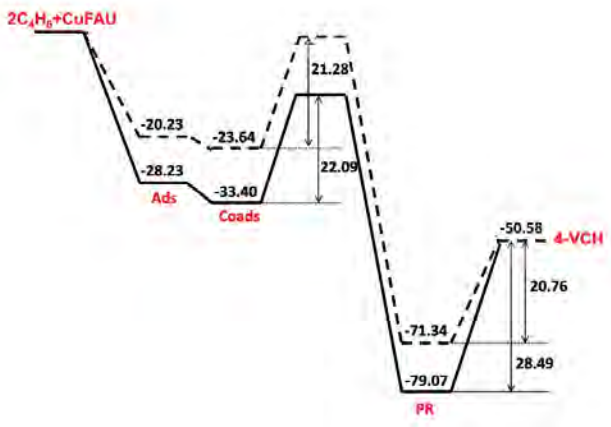


**Figure 3.** The energy profile (kcal/mol) for 8T (black line) and 49T (red line).

## Conclusions

The Diels–Alder cycloaddition of 1,3-butadiene over Cu-exchange zeolite has been investigated theoretically by the M06-2X density functional. The 49T cluster is modeled to cover the supercage of Cu-FAU zeolite. The reaction occurs via a concerted mechanism without an intermediate. The adsorption energies are calculated to be -33.40 kcal/mol. The activation barriers are calculated to be 22.09 kcal/mol due to the metal making diene a better dienophile. The reaction is exothermic reaction with reaction energy of 50.58 kcal/mol. These results show that Cu-exchanged faujasite zeolite is active for the Diels–Alder cycloaddition of 1,3-butadiene and that it can stabilize all species in the reaction systems.

**Acknowledgements.** This work was supported in part by grants from the National Science and Technology Development Agency (2009 NSTDA Chair Professor funded by the Crown Property Bureau under the management of the National Science and Technology Development Agency and NANOTEC Center of Excellence funded by the National Nanotechnology Center), The Thailand Research Fund, the Commission of Higher Education, Ministry of Education (“National Research University of Thailand” and “Postgraduate Education and Research Programs in Petroleum and Petrochemicals and Advanced Materials”). The support from the Kasetsart University Research and Development Institute (KURDI) and Graduate School Kasetsart University are also acknowledged. The authors are grateful to Donald G. Truhlar and Yan Zhao for their support with the M06-2X functional.

## References

(1) Haggin, J. *Chemical and Engineering News* **1994**, *72*, 31.
(2) Thomas, M. L.; Fraga-Dubreuil, J.; Coote, A. S.; Poliakoff, M. *Green Chem.* **2008**, *10*, 197.
(3) Alimardanov, K. M.; Abdullayev, A. F. *Pet. Chem.* **1995**, *35*, 508.
(4) Neumann, R.; Dror, I. *Applied Catalysis A: General* **1998**, *172*, 67.
(5) De Bruyn, M.; Neumann, R. *Advanced Synthesis and Catalysis* **2007**, *349*, 1624.
(6) Choi, Y. S.; Park, Y. K.; Chang, J. S.; Park, S. E.; Cheetham, A. K. *Catal. Lett.* **2000**, *69*, 93.
(7) Castellan, A.; Tauszik, G. R. *J. Catal.* **1977**, *50*, 172.
(8) Vaughan, W. E. *J. Am. Chem. Soc.* **1932**, *54*, 3863.
(9) Li, Y.; Houk, K. N. *J. Am. Chem. Soc.* **1993**, *115*, 7478.
(10) Von Doering, W. E.; Franck-Neumann, M.; Hasselmann, D.; Kaye, R. L. *J. Am. Chem. Soc.* **1972**, *94*, 3833.
(11) Kasuriya, S.; Namuangruk, S.; Treesukol, P.; Tirtowidjojo, M.; Limtrakul, J. *J. Catal.* **2003**, *219*, 320.
(12) Pantu, P.; Pabchanda, S.; Limtrakul, J. *ChemPhysChem* **2004**, *5*, 1901.
(13) Namuangruk, S.; Pantu, P.; Limtrakul, J. *ChemPhysChem* **2005**, *6*, 1333.
(14) Sangthong, W.; Probst, M.; Limtrakul, J. *J. Mol. Struct.* **2005**, *748*, 119.
(15) Namuangruk, S.; Khongpracha, P.; Pantu, P.; Limtrakul, J. *J. Phys. Chem. B* **2006**, *110*, 25950.
(16) Namuangruk, S.; Tantanak, D.; Limtrakul, J. *J. Mol. Catal. A: Chem.* **2006**, *256*, 113.
(17) Pantu, P.; Boekfa, B.; Limtrakul, J. *J. Mol. Catal. A: Chem.* **2007**, *277*, 171.
(18) Boekfa, B.; Choomwattana, S.; Khongpracha, P.; Limtrakul, J. *Langmuir* **2009**, *25*, 12990.
(19) Kumsapaya, C.; Bobuatong, K.; Khongpracha, P.; Tantirungrotechai, Y.; Limtrakul, J. *J. Phys. Chem. C* **2009**, *113*, 16128.
(20) Maihom, T.; Pantu, P.; Tachakritikul, C.; Probst, M.; Limtrakul, J. *J. Phys. Chem. C* **2010**, *114*, 7850.
(21) Maxwell, I. E.; Downing, R. S.; Van Langen, S. A. J. *J. Catal.* **1980**, *61*, 485.
(22) Chang, J. S.; Park, S. E.; Gao, Q.; Férey, G.; Cheetham, A. K. *Chem. Commun. (Cambridge, U. K.)* **2001**, 859.
(23) Dessau, R. M. *J. Chem. Soc., Chem. Commun.* **1986**, 1167.
(24) Maxwell, I. E.; de Boer, J. J.; Downing, R. S. *J. Catal.* **1980**, *61*, 493.
(25) Voskoboinikov, T. V.; Coq, B.; Fajula, F.; Brown, R.; McDougall, G.; Luc Couturier, J. *Microporous Mesoporous Mater.* **1998**, *24*, 89.
(26) Dimitrov, C.; Leach, H. F. *J. Catal.* **1969**, *14*, 336.
(27) Nieminen, V.; Kumar, N.; Datka, J.; Päivärinta, J.; Hotokka, M.; Laine, E.; Salmi, T.; Murzin, D. Y. *Microporous Mesoporous Mater.* **2003**, *60*, 159.
(28) Espeel, P. H.; De Peuter, G.; Tielen, M. C.; Jacobs, P. A. *J. Phys. Chem.* **1994**, *98*, 11588.
(29) Kugel, V. Y.; Lakhman, L. I.; Abramova, A. V.; Matiyeva, Z. M.; Smirnov, V. K.; Irisova, K. N.; Livenbuk, M. I.; Slivinskii, Y. V. *Pet. Chem.* **1997**, *37*, 297.
(30) Frisch, M. J.; Trucks, G. W.; Schlegel, H. B.; Scuseria, G. E.; Robb, M. A.; Cheeseman, J. R.; Montgomery, J.; J. A.; Vreven, T.; Kudin, K. N.; Burant, J. C.; Millam, J. M.; Iyengar, S. S.; Tomasi, J.; Barone, V.;

Mennucci, B.; Cossi, M.; Scalmani, G.; Rega, N.; Petersson, G. A.; Nakatsuji, H.; Hada, M.; Ehara, M.; Toyota, K.; Fukuda, R.; Hasegawa, J.; Ishida, M.; Nakajima, T.; Honda, Y.; Kitao, O.; Nakai, H.; Klene, M.; Li, X.; Knox, J. E.; Hratchian, H. P.; Cross, J. B.; Bakken, V.; Adamo, C.; Jaramillo, J.; Gomperts, R.; Stratmann, R. E.; Yazyev, O.; Austin, A. J.; Cammi, R.; Pomelli, C.; Ochterski, J. W.; Ayala, P. Y.; Morokuma, K.; Voth, G. A.; Salvador, P.; Dannenberg, J. J.; Zakrzewski, V. G.; Dapprich, S.; Daniels, A. D.; Strain, M. C.; Farkas, O.; Malick, D. K.; Rabuck, A. D.; Raghavachari, K.; Foresman, J. B.; Ortiz, J. V.; Cui, Q.; Baboul, A. G.; Clifford, S.; Cioslowski, J.; Stefanov, B. B.; Liu, G.; Liashenko, A.; Piskorz, P.; Komaromi, I.; Martin, R. L.; Fox, D. J.; Keith, T.; Al-Laham, M. A.; Peng, C. Y.; Nanayakkara, A.; Challacombe, M.; Gill, P. M. W.; Johnson, B.; Chen, W.; Wong, M. W.; Gonzalez, C.; Pople, J. A.; Gaussian, Inc., Wallingford CT: 2004.

(31) Zhao, Y.; Schultz, N. E.; Truhlar, D. G. *Journal of Chemical Theory and Computation* **2006**, *2*, 364.

(32) Zhao, Y.; Truhlar, D. G. *Accounts of Chemical Research* **2008**, *41*, 157.

(33) Drake, I. J.; Zhang, Y.; Briggs, D.; Lim, B.; Chau, T.; Bell, A. T. *Journal of Physical Chemistry B* **2006**, *110*, 11654.

# CATALYTIC DEHYDROGENATION OF ETHYLBENZENE TO STYRENE OVER A TETRAHEDRAL PLATINUM NANOCLUSTER: A DFT STUDY

*Patanachai Janthon[1,2,3], Teeranan Nongnual[1,2,3], Piboon Pantu[1,2,3] and Jumras Limtrakul[1,2,3,*]*

[1]Laboratory for Computational and Applied Chemistry, Department of Chemistry, Faculty of Science and Center of Nanotechnology, Kasetsart University Research and Development Institute, Kasetsart University, Bangkok 10900, Thailand
[2]NANOTEC Center of Excellence, National Nanotechnology Center, Kasetsart University, Bangkok 10900, Thailand
[3]Center for Advanced Studies in Nanotechnology and Its Applications in Chemical, Food and Agricultural Industries, Kasetsart University, Bangkok 10900, Thailand

## Introduction

Styrene ($C_8H_8$) has been one of the highly significant chemicals used widely in the synthetic polymer industry.[1-2] The dehydrogenation of ethylbenzene over a potassium promoted iron (III) oxide catalyst at high temperature was mainly used for the production of commercial styrene. However, there were disadvantages in this process - endothermic reaction and rapid deactivation, but many researchers have developed new catalysts, adsorbents and catalyst supports to overcome these.[3-10] Among the developments, the Pt(111) surface was a candidate catalyst for the dehydrogenation of ethylbenzene to styrene concerning the dissociation of ethylbenzene at low temperature on the surface forming styrene and hydrogen products. But, this again had the disadvantage that the styrene desorption step was quenched by its strong binding to the surface, resulting in the polymerization of glued styrene molecules under an annealing temperature condition.[11] The activity of unsupported Pt nanoclusters was studied by determining an activation of the small hydrocarbons such as methane.[12-13] This brought about the small Pt nanoclusters ($Pt_n$) which were more reactive than monatomic Pt by at least one order of magnitude. The tetrahedral Pt nanocluster ($Pt_4$) was also found to improve the oxidative dehydrogenation of propane.[14]

In this work, we introduce the tetrahedral Pt nanocluster consisting of one dehydrogenating Pt site, withdrawing two H atoms, as a novel candidate catalyst for the dehydrogenation of ethylbenzene to styrene.

## Methodology

Neutral $Pt_4$ with $C_2$ symmetry in a triplet state was used in our model. Full geometry optimizations for all pathways were performed using the B3LYP method including 6d functions and unrestricted spin polarization, implemented in the Gaussian 03 program.[15] We have employed the LanL2DZ basis set for all Pt atoms, which uses 18-electron relativistic effective core potentials (ECP) to reduce the number of electrons explicitly. The 6-31G(d,p) basis set for all H and C atoms was added in the calculation, increasing the accuracy of the dehydrogenation processes. In addition, neutral monatomic Pt in a triplet state was investigated using the same level of theory.

## Results and Discussion

The dehydrogenation mechanism was investigated concerning with the H' and H" dissociations over the $Pt_4$ catalyst. The dehydrogenation pathways were categorized by the number of Pt sites that these hydrogen atoms moving to. Three mechanistic pathways were proposed as shown in Figure 1. The DP pathway was separated into two sub pathways, DP_i and DP_ii, which are dealing with the *Int4* and *Int5*, respectively.

For all catalytic $Pt_4$ pathways, the dehydrogenation started from the adsorption of ethylbenzene on the dehydrogenating site of $Pt_4$

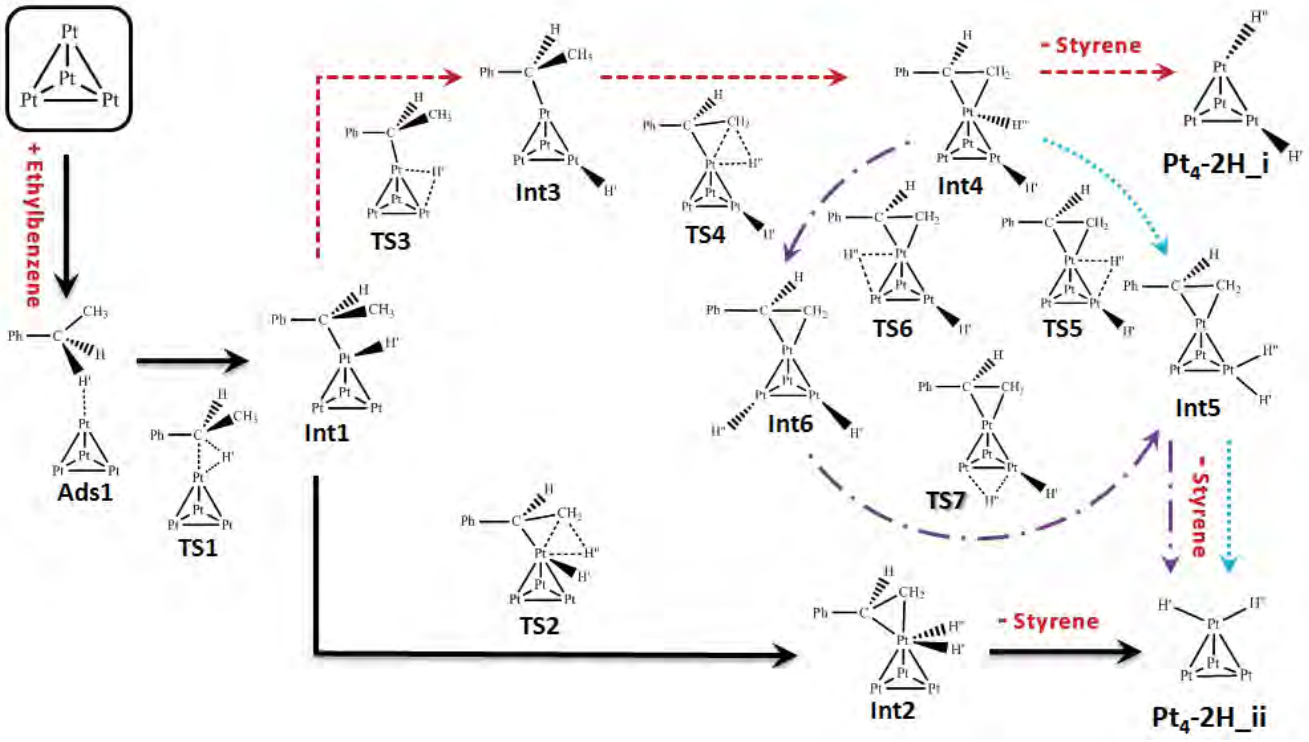


**Figure 1.** The mechanism pathways for the dehydrogenation of ethylbenzene to styrene over $Pt_4$ catalyst: single-catalytic-site $Pt_4$ (SP, black solid line), double-catalytic-site $Pt_4$ (DP_i, red dash line and DP_ii, blue dot line) and triple-catalytic-site $Pt_4$ (TP, purple dash-dot line)

(*Ads1*) with the adsorption energy of -5.3 kcal/mol. The C-H' bond was then dissociated with the activation energy of 1.3 kcal/mol (*TS1*) forming the intermediate *Int1*. After that, the three main pathways were considered.

For the SP pathway, the C-H" bond was broken, moving the H" to the first $Pt_4$ site - dehydrogenating site, with the activation energy of 24.4 kcal/mol (*TS2*) forming an unstable intermediate with the adsorbed styrene product (*Int2*). This is the rate determining step caused by an increasing steric effect of seven coordinates on the single platinum site. Surprisingly, the styrene and $Pt_4$-2H_ii were then easily desorbed with the desorption energy of 13.5 kcal/mol due to the high steric effect.

For the DP pathway, the H' migrated to the second $Pt_4$ site with the activation energy of 7.7 kcal/mol (*TS3*) forming the intermediate *Int3*. The C-H" bond was then broken with the activation energy of 3.0 kcal/mol (*TS4*), moving the H" onto the first $Pt_4$ site (*Int4*) with the absorbed styrene product. Focusing on the DP_i pathway, the styrene was desorbed with the desorption energy of 29.5 kcal/mol leaving the $Pt_4$-2H_i. On the other hand, the DP_ii pathway forwarded by the H" moving to join with the H' on the second $Pt_4$ site with the activation energy of 5.3 kcal/mol (*TS5*) stabilizing the intermediate *Int5*. Thus, the desorption energy was increased to 36.8 kcal/mol leaving the $Pt_4$-2H_ii.

For the TP pathway, the H" of the *Int4* moved to the third $Pt_4$ site with the activation energy of 3.4 kcal/mol (*TS6*) forming the intermediate *Int6*. Next, the H" moved to join with the H' on the second $Pt_4$ site with the activation energy of 13.8 kcal/mol (*TS7*), merging to the *Int5* as in the DP_ii pathway.

The hydrogen migrations on the $Pt_4$ sites (in the DP and the TP pathways) using low activation energy in the range of 3.4 to 13.8 kcal/mol, can stabilize an intermediate. This led the desorption energy for styrene product was higher. Therefore, the rate determining step of the DP and the TP pathways were associated with the styrene desorption step. In contrast, this H-moving step was not considered in the SP pathway, therefore, the stabilization of an intermediate was not observed. Moreover, this led the second dehydrogenation of the DP and the TP pathways (*TS4*) using less activation energy than the second dehydrogenation of the SP (*TS2*). Due to steric repulsion between adsorbed styrene and the hydrogen atoms that bonding to the same $Pt_4$ site, non-stabilized intermediate of SP (*Int2*) can assist the styrene desorption more easily with lower desorption energy.

Although the overall activation energy of the SP pathway was the smallest, the DP and TP pathways were kinetically favorable. Therefore, the dehydrogenation was terminated at the *Int5* and *Int6* steps with styrene products hardly attached to the catalytic site. To avoid this problem, the SP pathway must be chosen, thus, the single site catalytic must be favorably controlled.

The dehydrogenation of ethylbenzene over the monatomic Pt catalyst was shown in Figure 2. The C-H' bond was broken with the activation energy of 12.9 kcal/mol (*TS8*). The C-H" bond was then dissociated with the activation energy of 25.5 kcal/mol (*TS9*). This was the same as that of the SP pathway. The styrene was then desorbed with the activation energy of 35.0 kcal/mol, which was the rate determining step. This activation energy is higher than that of the SP pathway due to its lower steric effect to push the styrene out. It can be suggested that three vacant sites of the $Pt_4$ can assist the dehydrogenation of the H' and can increase the steric effect to the active site.


**Figure 2.** The mechanism for the dehydrogenation of ethylbenzene to styrene over monatomic Pt catalyst.

## Conclusion

We report here the first theoretical study of the dehydrogenation of ethylbenzene over the $Pt_4$ catalyst. Although the overall activation energy of the SP pathway was the smallest, the DP and TP pathways were kinetically favorable without desorption of the styrene product. To avoid this problem, the SP pathway must be chosen, thus, the single site catalytic must be favorably controlled. The H-migration step was not considered in the SP pathway. For this reason, the stabilization of an intermediate was not observed. Therefore, the non-stabilized intermediate of SP pathway (*Int2*) can assist the styrene desorption more easily with the lower desorption energy. This caused the overall activation energy of 24.4 kcal/mol regarding to the C-H" dissociation. In addition, we suggest the control for the SP pathway by the assistance of an adsorbent blocking three sites with remaining one active site of the $Pt_4$ catalyst. Moreover, in order to recover the $Pt_4$ catalyst, the oxidative dehydrogenation should be introduced to eliminate the two adsorbed-H atoms remaining on the catalyst. This understanding can be applied for an alternative styrene synthesis.

**Acknowledgements.** This work was supported in part by grants from the National Science and Technology Development Agency (NSTDA Chair Professor funded by the Crown Property Bureau under the management of the National Science and Technology Development Agency and NANOTEC Center of Excellence funded by the National Nanotechnology Center), the Thailand Research Fund (TRF) (to J.L.), under the program "Strategic Scholarships for Frontier Research Network for the Joint Ph.D. Program Thai Doctoral degree" (CHE-PhD-SW) from the Office of the Higher Education Commission, Thailand (to P.J.), Ministry of Education (the National Research University Project of Thailand (NRU) and "Postgraduate Education and Research Programs in Petroleum and Petrochemicals and Advanced Materials") and the Development and Promotion of Science and Technology Talents Project (DPST) (to T.N.). The Kasetsart University Graduate School is also acknowledged.

## References

(1) Lee, W. J.; and Froment, G. F. *Ind. & Eng. Chem. Res.* **2008**, *47(23)*, 9183-9194.
(2) Badstube, T.; Papp, H.; Kustrowski, P.; and Dziembaj, R. *Cat. Lett.* **1998**, *55*, 169–172.
(3) Morán, C.; González, E.; Sánchez, J.; Solano, R.; Carruyo, G.; Moronta, A. *J. Col. Interf. Sci.* **2007,** *315* (1), 164-169.
(4) Cavani, F.; Trifirò, F. *Appl. Cat. A: General* **1995,** *133* (2), 219-239.
(5) Yuichi, M.; Kazuyoshi, I.; Hiroshi, U.; Tadashi, H.; and Tomohiko, T. *App.Cat.***1982**, *2*, 67-74.
(6) Su, D. S.; Maksimova, N.; Delgado, J. J.; Keller, N.; Mestl, G.; Ledoux, M. J.; Schlögl, R. *Cat. Tod.* **2005**, *102–103*, 110–114.
(7) Su, D. S.; Delgado, J. J.; Liu, X.; Wang, D.; Schlögl, R.; Wang, L.; Zhang, Z.; Shan, Z.; and Xiao, F. S. *Chem. Asian J.* **2009**, *4*, 1108 – 1113.
(8) Keller, N.; Maksimova, N. I.; Roddatis, V. V.; Schur, M.; Mestl, G.; Butenko,Y. V.; Kuznetsov, V. L.; and Schlögl, R. *Angew. Chem. Int. Ed.* **2002**, *41(11)*, 1885-1888.
(9) Du, Y.; Li, J.; and Yang, X. *Cat. Com.* **2008**, *9*, 2331–2333.

(10) Sakurai, Y.; Suzaki, T.; Ikenaga, N.; and Suzuki, T. *Appl. Cat. A: General* **2000,** *192*, 281–288.
(11) Ranke, W.; and Weiss, W. *Surf Sci.* **2000**, *465(3)*, 317-330.
(12) Xiao, L.; and Wang, L. *J. Phys. Chem. B.* **2007**, *111(7)*, 1657-1663.
(13) Trevor, D. J.; Cox, D. M.; and Kaldor, A. *J. Am. Chem. Soc.* **1990**, *112(10)*, 3742-3749.
(14) Vajda, S.; Pellin, M. J.; Greeley, J. P.; Marshall, C. L.; Curtiss, L. A.; Ballentine, G. A.; Elam, J. W.; Catillon-Mucherie, S.; Redfern, P. C.; Mehmood, F.; and Zapol, P. *Nat. Mat.* **2009**, *8(3)*, 213-216.
(15) Frisch, M. J.; Trucks, G. W.; Schlegel, H. B.; Scuseria, G. E.; Robb, M. A.; Cheeseman, J. R.; Montgomery, J. A.; Jr.; Vreven, T.; Kudin, K. N.; Burant, J. C.; Millam, J. M.; Iyengar, S. S.; Tomasi, J.; Barone, V.; Mennucci, B.; Cossi, M.; Scalmani, G.; Rega, N.; Petersson, G. A.; Nakatsuji, H.; Hada, M.; Ehara, M.; Toyota, K.; Fukuda, R.; Hasegawa, J.; Ishida, M.; Nakajima, T.; Honda, Y.; Kitao, O.; Nakai, H.; Klene, M.; Li, X.; Knox, J. E.; Hratchian, H. P.; Cross, J. B.; Adamo, C.; Jaramillo, J.; Gomperts, R.; Stratmann, R. E.; Yazyev, O.; Austin, A. J.; Cammi, R.; Pomelli, C.; Ochterski, J. W.; Ayala, P. Y.; Morokuma, K.; Voth, G. A.; Salvador, P.; Dannenberg, J. J.; Zakrzewski, V. G.; Dapprich, S.; Daniels, A. D.; Strain, M. C.; Farkas, O.; Malick, D. K.; Rabuck, A. D.; Raghavachari, K.; Foresman, J. B.; Ortiz, J. V.; Cui, Q.; Baboul, A. G.; Clifford, S.;Cioslowski, J.; Stefanov, B. B.; Liu, G.; Liashenko, A.; Piskorz, P.; Komaromi, I.; Martin, R. L.; Fox, D. J.; Keith, T.; Al-Laham, M. A.; Peng, C. Y.; Nanayakkara, A.; Challacombe, M.; Gill, P. M. W.; Johnson, B.; Chen, W.; Wong, M. W.; Gonzalez, C.; Pople, J. A.*Gaussian 03*, revision E.01, Gaussian, Inc, Wallingford, CT, 2004.

**PETR** **Todd Gardner** **Thursday, March 31, 2011**

**113 - Density functional theory study of possible mechanisms of isooctene formation via isobutene dimerization over acidic beta zeolite**

***Panida Singra*, Kanokwan Kongpatpanich, Pipat Khongpracha PhD, *Professor Jumras Limtrakul PhD*. Laboratory for Computational and Applied Chemistry, Department of Chemistry, Faculty of Science and Center of Nanotechnology, Kasetsart University Research and Development Institute, Kasetsart University, Chatuchak, Bangkok, Thailand; NANOTEC Center of Excellence, National Nanotechnology Center, Kasetsart University, Chatuchak, Bangkok, Thailand; Center for Advanced Studies in Nanotechnology and Its Applications in Chemical, Food and Agricultural Industries, Kasetsart University, Chatuchak, Bangkok, Thailand***

Isobutene dimerization over beta zeolite has been investigated by using the recently developed and highly accurate M06-2X/6-31G(d,p) level of theory. The reaction starts with the protonation of isobutene by the Brønsted acid of zeolite and yields a "*tert*-butyl carbocation" intermediate. Subsequently, the C-C bond formation between the carbocation intermediate and the second isobutene molecule gives a "*tert*-octyl carbocation" intermediate and afterwhich it returns the proton back to the zeolite framework to give trimethylpentene isomers (isooctenes). The protonation of isobutene is observed to be the rate-determining step which requires an activation energy of 14.4 kcal/mol. Whereas the C-C bond formation more easily occurs with the activation energy of 4.0 kcal/mol and the sequential deprotonation requires activation energies of 1.2 and 5.4 kcal/mol for 2,4,4-trimethyl-1-pentene and 2,4,4-trimethyl-2-pentene,respectively. The calculated results found that 2,4,4-trimethyl-1-pentene was the kinetically primary product.

**Thursday, March 31, 2011 08:30 AM**
Chemistry of Petroleum and Emerging Technologies (08:30 AM - 11:20 AM)
**Location: Anaheim Marriott**
**Room: Grand Blrm G**

Close Window

# 241st ACS National Meeting, Anaheim, CA

**Document ID:** 19375

**Program Area:** INOR: Division of Inorganic Chemistry

**Symposium Title:** (INOR031) Inorganic Catalysts

**INSTITUTIONS**

1. Kasetsart University Kamphaeng Saen Campus, Chemistry Department, Faculty of Liberal Arts and Science, Nakhon Pathom, Nakhon Pathom, 73140, Thailand

2. Laboratory for Computational and Applied Chemistry, Faculty of Science and Center of Nanotechnology, Kasetsart University Research and Development Institute, Kasetsart University, Department of Chemistry, Jatujak, Bangkok, 10900, Thailand

3. NANOTEC Center of Excellence, National Nanotechnology Center, Kasetsart University, Jatujak, Bangkok, 10900, Thailand

4. Center for Advanced Studies in Nanotechnology and Its Applications in Chemical, Food and Agricultural Industries, Kasetsart University, Jatujak, Bangkok, 10900, Thailand

**AUTHORS**

1. Bundet Boekfa[1,3,4], Dr., PhD, Kasetsart University Kamphaeng Saen Campus, Chemistry Department, Faculty of Liberal Arts and Science, Nakhon Pathom, Nakhon Pathom, 73140, Thailand , +66 2562 5555 ext 2169, bundet.b@ku.ac.th

2. Jumras Limtrakul[2,3,4], Prof. Dr., PhD, Kasetsart University, Department of Chemistry, Laboratory for Computational and Applied Chemistry, Faculty of Science and Center of Nanotechnology, Kasetsart University Research and Development Institute, Kasetsart University, Jatujak, Bangkok, 10900, Thailand , +66 2562 5555 ext 2169, jumras.l@ku.ac.th

**Reason for Abstract Submission:** I am contributing this paper in response to the Call for Papers.

**Invitation from:** No response indicated

**Email of Inviter:** No response indicated

**Criteria are met:** Are met by at least one author

**Presenting author will register:** Yes

**Abstract will be withdrawn if author cannot attend:** Yes, I agree

**Abstract submitted only once:** Yes, I agree

**Equipment Needs:** No response indicated

**Comments to Organizers:** No response indicated

**Preferred Presentation Method:** Poster Preferred

**Should this Paper be Considered for a SCI-MIX?** No response indicated

**Student Type** No response indicated

**Title:** The Acid Location of the Brønsted Acid Site in ITQ-22 zeolite: A Newly Developed Density Functional Theory Study

**Abstract Body:** The location of Brønsted acid site, ≡Si-O(H)-Al≡, and the adsorption of pyridine on multipore zeolite H-ITQ-22 have been studied by the newly developed density functional theory, M08-HX. Different 44 Brønsted acid sites derived from the 16 different Al-substituted ITQ-22 zeolite were calculated with the 5T quantum cluster. Al1(O2H), Al14(O30H) and Al15(O33H) are the most favorable three positions for the Brønsted acid site. The extended 28T quantum cluster covered intersection cavity of ITQ-22 is used to study the adsorption of pyridine to determine the acid strength. The calculated adsorption energies are -46.5, -44.0 and -43.0 kcal/mol for Al1 (O2H), Al14(O30H) and Al15(O33H) positions, respectively compared well with the pyridine on H-ZSM-5 (-47.6 kcal/mol). The results of this study may be helpful for understanding the acidic of the zeolite for further applications.

**PrePrint:** No response indicated

# Preview

Draft Preview of Document 19366

THIS COPY IS A DRAFT ONLY. YOUR FINAL PRINTOUT WILL BE AVAILABLE AT TIME OF SUBMISSION

Print document.

## 241st ACS National Meeting, Anaheim, CA

**Document ID:** 19366

**Program Area:** INOR: Division of Inorganic Chemistry

**Symposium Title:** (INOR013) Inorganic Catalysts

**INSTITUTIONS**

1. Kasetsart University Kamphaeng Saen Campus, Chemistry Department, Faculty of Liberal Arts and Science, Nakhon Pathom, 73140, Thailand

2. Laboratory for Computational and Applied Chemistry, Faculty of Science and Center of Nanotechnology, Kasetsart University Research and Development Institute, Kasetsart University, Department of Chemistry, Jatujak, Bangkok, 10900, Thailand

3. NANOTEC Center of Excellence, National Nanotechnology Center, Kasetsart University, Jatujak, Bangkok, 10900, Thailand

4. Center for Advanced Studies in Nanotechnology and Its Applications in Chemical, Food and Agricultural Industries, Kasetsart University, Jatujak, Bangkok, 10900, Thailand

**AUTHORS**

1. Bundet Boekfa[1,3,4], Dr., PhD, Kasetsart University Kamphaeng Saen Campus, Chemistry Department, Faculty of Liberal Arts and Science, Nakhon Pathom, Nakhon Pathom, 73140, Thailand , +66 2562 5555 ext 2169, bundet.b@ku.ac.th

2. Jumras Limtrakul[2,3,4], Prof. Dr., PhD, Kasetsart University, Department of Chemistry, Laboratory for Computational and Applied Chemistry, Faculty of Science and Center of Nanotechnology, Kasetsart University Research and Development Institute, Kasetsart University, Jatujak, Bangkok, 10900, Thailand , +66 2562 5555 ext 2169, jumras.l@ku.ac.th

**Reason for Abstract Submission:** I am contributing this paper in response to the Call for Papers.

**Invitation from:** No response indicated

**Email of Inviter:** No response indicated

**Criteria are met:** Are met by at least one author

**Presenting author will register:** Yes

**Abstract will be withdrawn if author cannot attend:** Yes, I agree

**Abstract submitted only once:** Yes, I agree

**Equipment Needs:** No response indicated

**Comments to Organizers:** No response indicated

**Preferred Presentation Method:** Oral Preferred

**Should this Paper be Considered for a SCI-MIX?** No response indicated

**Student Type** No response indicated

**Title:** Strength and Brønsted acid sites of ITQ-34/Pyridine Complexes: A Newly Developed Density Functional Theory Study

**Abstract Body:** The newly developed density functional theory, M08-HX, was applied to investigate the strength and location of Brønsted acid sites, ≡Si-O(H)-Al≡, in the new ITQ-34 zeolite. The 25 Brønsted acid sites generated from the nine different Al-substitited ITQ-34 zeolite were calculated at the M08-HX/6-31G(d,p) level of theory. The 5T cluster model was employed for the acid site. The most favorable positions for the ITQ-34 were Al3(O4H), Al4 (O3H) and Al4(O13H). To determine the acid strength, the pyridine is selected to adsorb on the 28T quantum clusters. The calculated adsorption energies are -38.5, -41.4 and -42.3 kcal/mol for Al3(O4H), Al4(O3H) and Al4 (O13H) positions, respectively. The adsorption energies compared well with H-FAU zeolite (-43.1 kcal/mol). These important findings will be useful for applications of this new zeolite in areas of adsorption separation and catalysis adsorption.

**PrePrint:** No response indicated

Print document.

# Preview

Draft Preview of Document 19358

THIS COPY IS A DRAFT ONLY. YOUR FINAL PRINTOUT WILL BE AVAILABLE AT TIME OF SUBMISSION

Print document.

## 241st ACS National Meeting, Anaheim, CA

**Document ID:** 19358

**Program Area:** INOR: Division of Inorganic Chemistry

**Symposium Title:** (INOR013) Inorganic Catalysts

**INSTITUTIONS**

1. Laboratory for Computational and Applied Chemistry, Faculty of Science and Center of Nanotechnology, Kasetsart University Research and Development Institute, Kasetsart University, Department of Chemistry, Jatujak, Bangkok, 10900, Thailand

2. NANOTEC Center of Excellence, National Nanotechnology Center, Kasetsart University, Jatujak, Bangkok, 10900, Thailand

3. Center for Advanced Studies in Nanotechnology and Its Applications in Chemical, Food and Agricultural Industries, Kasetsart University, Jatujak, Bangkok, 10900, Thailand

**AUTHORS**

1. Sippakorn Wannakao[1,2,3], Kasetsart University, Department of Chemistry, Laboratory for Computational and Applied Chemistry, Faculty of Science and Center of Nanotechnology, Kasetsart University Research and Development Institute, Kasetsart University, Jatujak, Bangkok, 10900, Thailand , +66 2562 5555 ext 2169, jumras.l@ku.ac.th

2. Kanokwan Kongpatpanich[1,2,3] ,

3. Pipat Khongpracha[1,2,3] , Dr., PhD

4. Jumras Limtrakul[1,2,3], Prof.Dr., PhD, Kasetsart University, Department of Chemistry, Laboratory for Computational and Applied Chemistry, Faculty of Science and Center of Nanotechnology, Kasetsart University Research and Development Institute, Kasetsart University, Jatujak, Bangkok, 10900, Thailand , +66 2562 5555 ext 2169, jumras.l@ku.ac.th

**Reason for Abstract Submission:** I am contributing this paper in response to the Call for Papers.

**Invitation from:** No response indicated

**Email of Inviter:** No response indicated

**Criteria are met:** Are met by at least one author

**Presenting author will register:** Yes

**Abstract will be withdrawn if author cannot attend:** Yes, I agree

**Abstract submitted only once:** Yes, I agree

**Equipment Needs:** No response indicated

**Comments to Organizers:** No response indicated

**Preferred Presentation Method:** Oral Preferred

**Should this Paper be Considered for a SCI-MIX?** No response indicated

**Student Type** Graduate Student

**Title:** Activities of Au and $Au_2$ cation-exchanged zeolite for methane C-H bond activation: a DFT study

**Abstract Body:** The methane C-H activation, the initial step for many industrially important chemical processes, on gold and gold embedded in two different types of zeolites, Faujasite and ZSM-5 was studied for the first time with a newly developed functional, M06L. A cooperative effect of gold coupled with the nanopore of zeolite plays an important role for dictating methane activation. One of most convincing results was that the Au/ZSM-5 systems yield an unexpectedly low barrier (13.6 kcal/mole) as compared to bare gold systems (21.3 kcal/mole). As for FAU and $Au_2$-FAU complexes, the activity was not as good as the corresponding Au-ZSM-5 and $Au_2$-ZSM-5 systems. Our findings are very important for the search for a catalyst which is able to activate the C–H bond in alkanes.

**PrePrint:** No response indicated

Print document.

## 241st ACS National Meeting, Anaheim, CA

**Document ID:** 19325

**Program Area:** INOR: Division of Inorganic Chemistry

**Symposium Title:** (INOR013) Inorganic Catalysts

**INSTITUTIONS**

1. Laboratory for Computational and Applied Chemistry, Faculty of Science and Center of Nanotechnology, Kasetsart University Research and Development Institute, Kasetsart University, Department of Chemistry, Bangkok, 10900, Thailand

2. NANOTEC Center of Excellence, National Nanotechnology Center, Kasetsart University, Bangkok, 10900, Thailand

3. Center for Advanced Studies in Nanotechnology and Its Applications in Chemical, Kasetsart University, Bangkok, 10900, Thailand

**AUTHORS**

1. Phornphimon Maitarad[1,2], Dr., PhD

2. Pimpa Hormnirun[1,2,3] , Dr., PhD

3. Pipat Khongpracha[1,2,3] , Dr., PhD

4. Jumras Limtrakul[1,2,3], Prof.Dr., PhD, Kasetsart University, Department of Chemistry, Laboratory for Computational and Applied Chemistry, Department of Chemistry, Faculty of Science and Center of Nanotechnology, Kasetsart University Research and Development Institute,, Bangkok, 10900, 10900, Thailand , +66 2562 5555 ext 2169, jumras.l@ku.ac.th

**Reason for Abstract Submission:** I am contributing this paper in response to the Call for Papers.

**Invitation from:** No response indicated

**Email of Inviter:** No response indicated

**Criteria are met:** Are met by at least one author

**Presenting author will register:** Yes

**Abstract will be withdrawn if author cannot attend:** Yes, I agree

**Abstract submitted only once:** Yes, I agree

**Equipment Needs:** No response indicated

**Comments to Organizers:** No response indicated

**Preferred Presentation Method:** Oral Preferred

**Should this Paper be Considered for a SCI-MIX?** No response indicated

**Student Type** No response indicated

**Title:** Structure Activity Relationship and the Electronic Property of Bis(phenoxyimine) Ligated Zirconium Catalysts for Ethylene Polymerization: A Combined CoMFA and DFT study

**Abstract Body:** Comparative Molecular Field Analysis (CoMFA) and Natural Bond Orbital (NBO) analysis were applied on 16 Zr phenoxy-imine (FI) post-metallocene catalysts to explore the structural requirements for catalytic activity of ethylene polymerization. The obtained CoMFA model exhibited good $r^2_{cv}$ = 0.664 and $r^2$ = 0.963, and can well predict the test set. CoMFA steric-electrostatic maps and the NBO electronic distributions, as given by the second order perturbation $E^{(2)}$, can guide us to a new design for new potent catalysts. Firstly, the $\mathbf{R_1}$ substitution of the catalyst favors the less electron-donating group, next, the $\mathbf{R_2}$ substitution of the catalyst must be in the form of big bulky groups with high electron distributions and, finally, the hydrogen atom is suitable for $\mathbf{R_3}$ substitution. In summary, our obtained results not only can be used to rationally guide the design of new potent FI catalysts, but can also significantly save on the experimental synthesis.

**PrePrint:** No response indicated

# Preview

Draft Preview of Document 19372

THIS COPY IS A DRAFT ONLY. YOUR FINAL PRINTOUT WILL BE AVAILABLE AT TIME OF SUBMISSION

Print document.

## 241st ACS National Meeting, Anaheim, CA

**Document ID:** 19372

**Program Area:** INOR: Division of Inorganic Chemistry

**Symposium Title:** (INOR013) Inorganic Catalysts

**INSTITUTIONS**

1. Laboratory for Computational and Applied Chemistry, Faculty of Science and Center of Nanotechnology, Kasetsart University Research and Development Institute, Kasetsart University, Department of Chemistry, Jatujak, Bangkok, 10900, Thailand

2. NANOTEC Center of Excellence, National Nanotechnology Center, Kasetsart University, Jatujak, Bangkok, 10900, Thailand

3. Center for Advanced Studies in Nanotechnology and Its Applications in Chemical, Food and Agricultural Industries, Kasetsart University, Jatujak, Bangkok, 10900, Thailand

**AUTHORS**

1. Thana Maihom[1,2,3], Kasetsart University, Department of Chemistry, Laboratory for Computational and Applied Chemistry, Faculty of Science and Center of Nanotechnology, Kasetsart University Research and Development Institute, Kasetsart University, Jatujak, Bangkok, 10900, Thailand , +66 2562 5555 ext 2169, jumras.l@ku.ac.th

2. Jumras Limtrakul[1,2,3], Prof. Dr., PhD, Kasetsart University, Department of Chemistry, Laboratory for Computational and Applied Chemistry, Faculty of Science and Center of Nanotechnology, Kasetsart University Research and Development Institute, Kasetsart University, Jatujak, Bangkok, 10900, Thailand , +66 2562 5555 ext 2169, jumras.l@ku.ac.th

**Reason for Abstract Submission:** I am contributing this paper in response to the Call for Papers.

**Invitation from:** No response indicated

**Email of Inviter:** No response indicated

**Criteria are met:** Are met by at least one author

**Presenting author will register:** Yes

**Abstract will be withdrawn if author cannot attend:** Yes, I agree

**Abstract submitted only once:** Yes, I agree

**Equipment Needs:** No response indicated

**Comments to Organizers:** No response indicated

**Preferred Presentation Method:** Oral Preferred

**Should this Paper be Considered for a SCI-MIX?** No response indicated

**Student Type** Graduate Student

**Title:** Formaldehyde Encapsulated in Lithium-Decorated Metal-Organic Frameworks: A DFT Study

**Abstract Body:** Stability of the monomeric formaldehyde encapsulated on lithium-decorated metal-organic frameworks 5 (Li-MOF-5) has been investigated by means of the density functional method, M06-L/6-31+G (d,p).The reaction kinetics and thermodynamics equilibrium between the formaldehyde and its trimerization product, 1,3,5-trioxane are considered to assess the efficacy of Li-MOF-5 for formaldehyde preservation. The trimerization of formaldehyde takes place in a single reaction step. The calculated activation energy for the reaction on Li-MOF-5 is 33.7 kcal/mol, which is 16.4 kcal/mol higher than in the gas phase system. In addition, the calculated reaction energy with respect to the adsorption complex is endothermic by 5.9 kcal/mol and the reaction Gibbs free energy (ΔG) also becomes positive (11.0 kcal/mol). These results revealed that the formaldehyde trimerization on Li-MOF-5 is favorably a reversible reaction, suggesting that the Li-decorated MOF-5 is a good candidate material for preserving the monomeric formaldehyde.

**PrePrint:** No response indicated

Print document.

**INOR** **Michelle Millar, Nora Radu** **Tuesday, March 29, 2011**

**781 - Theoretical study of the oxidative dehydrogenation of ethylbenzene to styrene over Fe-ZSM-5**

***Dr. Supawadee Namuangruk PhD*, Dr. Pipat Khongpracha PhD, Prof. Dr. Jumras Limtrakul PhD. National science and technology development agency, National Nanotechnology Center, klongluang, Phatumthani, Thailand; Department of chemistry, Kasetsart University, Laboratory for Computational and Applied Chemistry, Jatujak, Bangkok, Thailand; National nanotecnology center, Kasetsart University, NANOTEC Center of Excellent, Jatujak, Bangkok, Thailand***

The reaction mechanisms of the catalytic reaction cycle for the oxidative dehydrogenation of ethylbenzene over Fe-ZSM-5 have been investigated by the ONIOM(M06/6-31G**:UFF) method. The complete reaction cycle consists of three sub-reactions: (i) nitrous oxide decomposition, (ii) oxidative dehydrogenation of ethylbenzene, and (iii) dehydration for active site regeneration. The calculated energy barriers of the rate-limiting steps for the reactions (i), (ii) and (iii) are 47.72, 21.19, and 35.67 kcal/mol indicating that the nitrous oxide decomposition is the controlling reaction in the whole reaction cycle. For the oxidative dehydrogenation of ethylbenzene yielding styrene (ii), we proposed newly two consecutive reaction pathways, Paths A and B. For the Path A, the mechanism is proceeded by consecutive cleavages of the primary and secondary C-H bonds, respectively, while the C-H bond cleavages order for the Path B is reversed. The first C-H bond cleavage of ethylbenzene for each path is found to be rate-limiting step where the calculated activation barrier is 21.19 kcal/mol for Path A which is higher than that for Path B (13.89 kcal/mol). The reaction rate constants calculated from the activation barriers of the rate-limiting steps are $9.45 \times 10^{11}$ and $4.63 \times 10^{12} s^{-1}$ at 273.15 K for Paths A and B, respectively. We predicted that styrene formation from oxidative dehydrogenation of ethylbenzene is carried out via a consecutive reaction starting from the secondary C-H bond cleavage followed by the primary C-H bond cleavages, respectively.

**Monday, March 28, 2011 08:00 PM**
Sci-Mix (08:00 PM - 10:00 PM)
**Location: Anaheim Convention Center**
**Room: Hall B**

**Tuesday, March 29, 2011 07:00 PM**
Inorganic Catalysts (07:00 PM - 10:00 PM)
**Location: Anaheim Convention Center**
**Room: Hall B**

Close Window

**American Chemical Society National meeting & Exposition” ครั้งที่ 242**

**ณ ประเทศสหรัฐอเมริกา**

**ระหว่างวันที่ 28 สิงหาคม -1 กันยายน 2554**

**จำนวน 10 เรื่อง**

# Reaction Mechanism of Isomerization of 1-Butene to Isobutene over Multipore H-ITQ-22 Zeolite: A DFT Study

*Bundet Boekfa[1,2,4], Piti Treesukol[1,2,4] and Jumras Limtrakul[2,3,4*]*

[1]Chemistry Department, Faculty of Liberal Arts and Science, Kasetsart University Kamphaeng Saen Campus, Nakhon Pathom 73140, Thailand
[2]Center for Advanced Studies in Nanotechnology and Its Applications in Chemical, Food and Agricultural Industries, Kasetsart University, Bangkok 10900, Thailand
[3]Laboratory for Computational and Applied Chemistry, Department of Chemistry, Faculty of Science and Center of Nanotechnology, Kasetsart University Research and Development Institute, Kasetsart University, Bangkok 10900, Thailand
[4]NANOTEC Center of Excellence, National Nanotechnology Center, Kasetsart University, Bangkok 10900, Thailand
[*]Corresponding author: Tel.: +662 562 5555 ext 2169, Fax: +662 562 5555 ext 2176, E-mail address: jumras.l@ku.ac.th

## Introduction

Zeolites are widely used for their range of applications in petroleum refineries and petrochemical industries[1-4]. With their size- and shape-selectivity and their ability, zeolites are the catalysts of choice for petrochemical catalysts such as hydrocarbon cracking, isomerization and oligomerization[1-3,5]. ITQ-22 (IWR) is a new synthetic multipore zeolite[6] with a pore structure that comprises 8-, 10- and 12-membered-ring pores of 4.52 x 3.32, 5.86 x 4.98 and 6.66 x 6.66 Å, respectively. This zeolite has proved to be an outstanding catalyst for isomerization-disproportionation of m-xylene, and alkylation of benzene with isopropanol and propylene[6].

1-butene isomerization over acidic catalysts is an important reaction for the production of isobutene, a raw material for methyl *tert*-butyl ether (MTBE) and ethyl *tert*-butyl ether (ETBE) production[7-12]. Many zeolites such as Ferrierite, ZSM-5 and Theta-1 zeolite[8,11] have been already used for those reactions. Corma et al. proposed the mechanism for this reaction on Theta-1 zeolite as a monomolecular mechanism[13]. Their activation energy is calculated to be 33-34 kcal/mol, which compares well with the experimental value of 30 kcal/mol. Tuma et al. used the hybrid MP2:DFT to study adsorption of the 1-butene, isobutene, *tert*-butyl cation and their alkoxide species in H-zeolite[14-15]. These studies lead us to understand the reaction in the specific pore of zeolite.

The zeolite framework effect or confinement effect, which is mainly composed of dispersive van der Waals interactions, has been proposed by Derouane[16] to explain the interactions between the zeolite framework and the adsorbed molecule. The conventional DFT functions are not able to describe the van der Waals effect from the zeolite framework. Recently, we have studied a number of adsorptions and reactions in the zeolite framework by using the recently developed M06-functionals including dispersion energy[17-24]. We found that these functionals can be used to describe the confinement effect of the zeolite framework. Combined with a second-order Møller-Plesset perturbation theory (MP2), the ONIOM (MP2:M06-2X) can successfully elucidate the adsorption and reaction mechanism of aliphatic, aromatic and heterocyclic compounds[20].

In this study, we examine the framework effects of this new multipore zeolite, H-ITQ-22, for the 1-butene isomerization into isobutene on the H-ITQ-22 zeolite by means of the well calibrated scheme of ONIOM (MP2:M06-2X). This study will provide the detailed understanding for the adsorption and reaction mechanism of butane isomerization in this new zeolite framework.

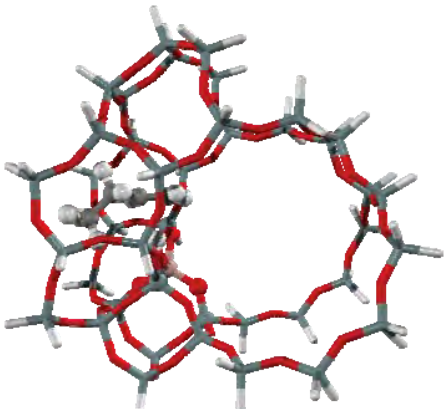

**Figure 1.** Presentation of 1-butene on H-ITQ-22 models 5T:42T ONIOM model. Atoms treated with the MP2 level of theory are shown in balls, whereas the areas treated with the M06-2X functional are shown in wireframes.

## Methodology

The adsorption and reaction of 1-butene on H-ITQ-22 zeolite have been studied with an ONIOM model[25]. An Al atom is selected to substitute the Si atom at the T1 position. The active 5T (T means tetrahedral of Si or Al atoms) represents the Brønsted acid site assigned to be the inner layer, where the extended 42T model is the outer layer. The 5T inner layer of the ONIOM model is calculated with the MP2/6-31G(d,p) level of theory while the 42T outer layer is performed with the M06-2X/6-31G(d,p) level of theory[20]. The ONIOM 5T:42T is shown in Fig. 1. Only the active region, $AlSi_4O_4H$ and the probe molecule are allowed to relax while the rest is kept fixed with the crystallographic structure[6]. All calculations were performed using the Gaussian 03 program[26] incorporated with the Minnesota Density Functionals module 3.1 by Zhao and Truhlar[17-18].

## Results and Discussion

**Butane and 1-butene adsorptions onto the Brønsted acid site of H-ITQ-22.** The ONIOM model for the H-ITQ-22 zeolite is illustrated in Fig. 1. The 42T quantum cluster is modeled to cover the intersection cavity (10T and 12T) where the guest molecule prefers to locate. The inner-layer 5T cluster, representing the Brønsted acid site, is calculated with the MP2 calculation while the outer-layer 42T cluster, representing the framework of zeolite, is calculated with the M06-2X functional. The acidic O1-Hz distance is calculated to be 0.97 Å. The Al ··· Hz bond distance is about 2.37 Å, which agrees well with the experiment data (2.38-2.48 Å)[27].

The optimized structures of butane and 1-butene on H-ITQ-22 zeolite are shown in Figures 2a and 2b, respectively. The butane molecule adsorbs in the 10T pore of H-ITQ-22 via interactions between the alkyl group and the Brønsted acid site of zeolite. The acidic O1-Hz bond distance is almost the same as in the isolated zeolite (0.97 Å). The distance between the carbon atom of butane and the Brønsted acid site (C2 ··· Hz) distance is 2.79 Å. The adsorption energy of butane on H-ITQ-22 is calculated to be -11.8 kcal/mol. This energy compares well with the experimental data of -11.9 kcal/mol for butane on H-MOR zeolite[28] and -12.6 kcal/mol for butane H-ZSM-5 zeolite[29].

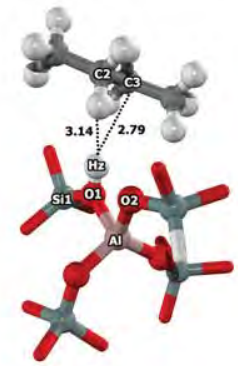


(a) Butane,
ΔE= -11.8 kcal/mol

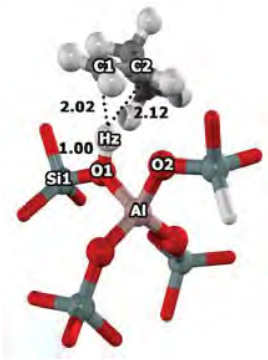


(b) 1-butene,
ΔE= -20.5 kcal/mol

**Figure 2.** Optimized structure of butane (a) and 1-butene (b) on H-ITQ-22 zeolite. Distances are in Ås.

The 1-butene molecule prefers to adsorb on the Brønsted acid site via the π-bond interaction of the double bond carbons. The acidic O1-Hz bond distance is increased to 1.00 Å. The distances between the double bond carbon and the Brønsted acid site (C1 - - Hz and C2 - - Hz) are 2.02 and 2.12 Å, respectively. The calculated adsorption energy is -20.6 kcal/mol. Only the adsorption of ethene on H-FAU from the experiment is reported to be -9.1 kcal/mol by Cant and Hall[30]. With the greater acidity of H-ITQ-22 and the larger probe molecule, our calculated adsorption energy of 1-butene on H-ITQ-22 is in the range of experimental data.

**1-butene Isomerization to Isobutene on H-ITQ-22** The isomerization reaction of 1-butene to isobutene on H-ITQ-22 is proposed as a stepwise mechanism via 4 steps: 1) the secondary alkoxide intermediate formation via the protonation of 1-butene, 2) the cyclic transition state via the methyl shift and the primary alkoxide intermediate formation, 3) the *tert*-carbenium cation formation via the proton shift and 4) the protonation back to zeolite and desorption of isobutene. Fig. 3 shows the energies profile for the 1-butene isomerization reaction.

The 1-butene molecule is adsorbed in the intersection pore at the 10T position of ITQ-22 [AD, Figure 2b] with an adsorption energy of -20.5 kcal/mol. The first transition state [TS1, Figure 4a] is the secondary alkoxide intermediate formation. The Brønsted acid O1-Hz bond is broken and the strong covalent bond O2-C2 is formed. This step requires an activation energy of about 17.1 kcal/mol. The intermediate [IN1, Figure 4b] strongly interacts with zeolite with a

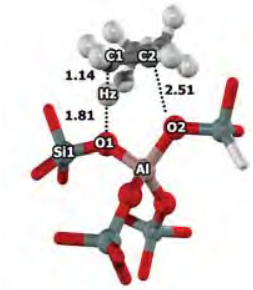


(a) TS1,
ΔE= -3.4 kcal/mol

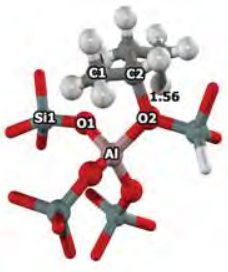


(b) IN1,
ΔE= -27.0 kcal/mol

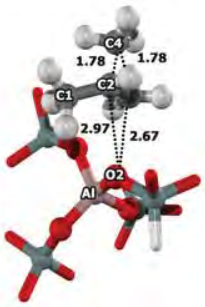


(c) TS2,
ΔE= 3.4 kcal/mol

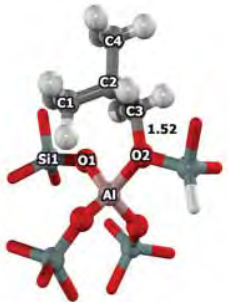


(d) IN2,
ΔE= -27.7 kcal/mol

**Figure 4.** Optimized structure of 1-butene isomerization to isobutene on H-ITQ-22 zeolite: a) the transition structure (TS1), b) the secondary alkoxide intermediate (IN1), c) the transition structure (TS2), d) the primary alkoxide intermediate (IN2). Distances are in Ås.

relative energy of -27.0 kcal/mol. The second transition state [TS2, Figure 4c] is the cyclic transition state via the methyl shift. The C4 atom breaks the bond with the C3 atom and forms a bond with the C2 atom. This corresponds with the breaking of the O2-C2 bond and the forming of the O2-C3 bond. The activation energy is calculated to be 30.4 kcal/mol. The primary alkoxide intermediate [IN2, Figure 4d] is the product with a relative energy of -27.7 kcal/mol.

The third transition state [TS3, Figure 5a] is the proton transfer from C2 to C3 with an activation energy of 38.2 kcal/mol. This step is the rate determining step of the 1-butene isomerization reaction

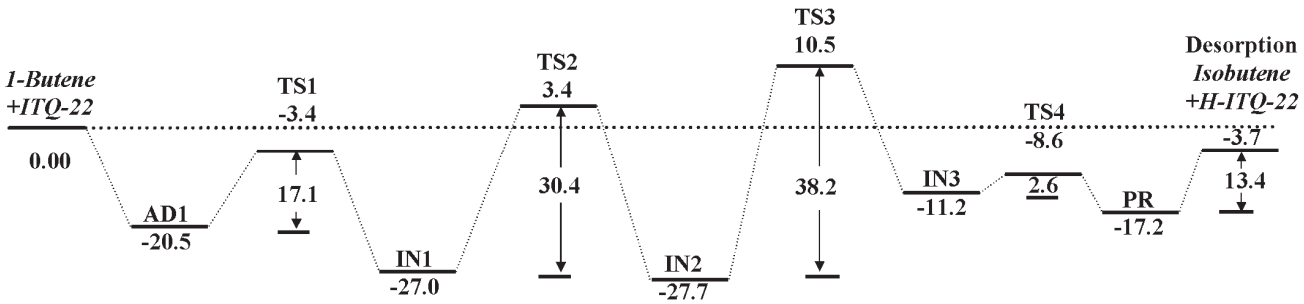


**Figure 3.** Potential energy diagram of the 1-butene to isobutene on the 5T:42T ONIOM (MP2:M06-2X) method (kcal/mol).

and gives the *tert*-butyl carbenium ion product [IN3, Figure 5b]. The *tert*-butyl carbenium is not stable and can move easily to isobutene via the forth transition state [TS4, Figure 5c]. The activation energy is only 2.6 kcal/mol. The isobutene product is adsorbed on H-ITQ-22 via a π-bonding interaction with a relative energy -17.2 kcal/mol [PR, Figure 5d]. The desorption energy of isobutene on H-ITQ-22 is 13.4 kcal/mol. The 1-butene isomerization to isobutene is an exothermic reaction with a heat of reaction (ΔH) of 4.1 kcal/mol.

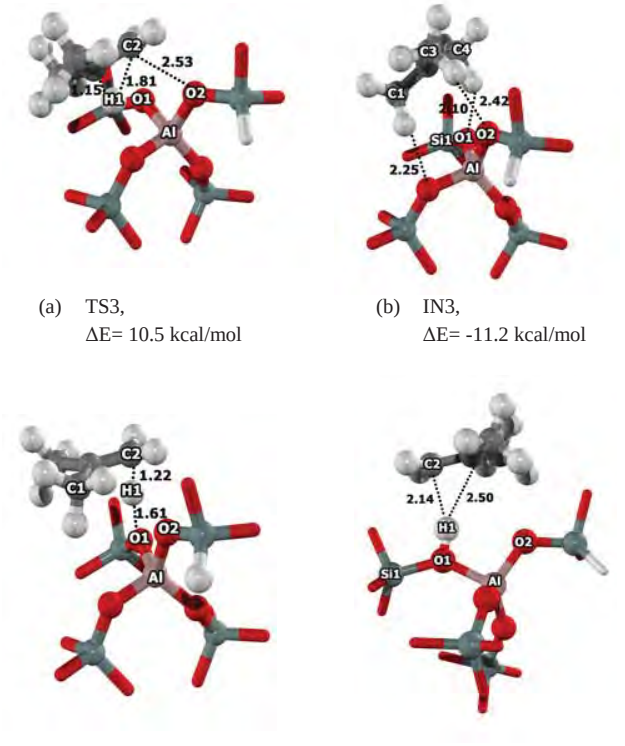


(a) TS3, ΔE= 10.5 kcal/mol

(b) IN3, ΔE= -11.2 kcal/mol

(c) TS4, ΔE= -8.6 kcal/mol

(d) PR, ΔE= -17.2 kcal/mol

**Figure 5.** Optimized structure of 1-butene isomerization to isobutene on H-ITQ-22 zeolite: a) the transition structure (TS3), b) the *tert*-butyl carbenium cation (IN3), c) the transition structure (TS4), d) the product isobutene adsorption (PR). Distances are in Å.

**Energetic Analysis between quantum cluster MP2 and ONIOM (MP2:M06-2X)** The energies profile for 1-butene isomerization to isobutene on H-ITQ-22 is shown in Figure 3 and the energies are shown in Table 1. The adsorption energies are calculated to be -20.5 and -11.2 kcal/mol for 5T:42T and 5T, respectively. The framework increases the adsorption energy by about 45%. The reaction mechanism of 1-butene to isobutene is proposed to be step four of the mechanisms. Without the framework effect, the activation energies are calculated to be 25.4, 51.3, 46.3 and 0.6 kcal/mol on the 5T cluster with the MP2 calculation. The activation energies are decreased to be 17.1, 30.4, 38.2 and 2.6 kcal/mol with the 5T:42T ONIOM (MP2:M06-2X). The framework stabilizes the transition structure by as much as 30-40 % and the values are in the range of the experimental data. We suggest that the ONIOM (MP2:M06-2X) is practical for the study of the framework effect on the adsorption and reaction mechanism in the ITQ-22 zeolite.

**Table 1. The Contribution Analysis on the 1-butene isomerization on 5T:42T of ITQ-22 calculated with the ONIOM (MP2:M06-2X). Intrinsic activation energies are in parenthesis. Energies are in kcal/mol.**

| Model | 5T:42T | 5T // 5T:42T |
|---|---|---|
| Method | ONIOM (MP2:M06-2X) | MP2//ONIOM (MP2:M06-2X) |
| AD | -20.5 | -11.2 |
| TS1 | -3.4 (17.1) | 14.2 (25.4) |
| IN1 | -27.0 | -24.7 |
| TS2 | 3.4 (30.4) | 26.6 (51.3) |
| IN2 | -27.7 | -24.9 |
| TS3 | 10.5 (38.2) | 21.4 (46.3) |
| IN3 | -11.2 | 4.6 |
| TS4 | -8.6 (2.6) | 5.2(0.6) |
| PR | -17.2 | 7.9 |

## Conclusions

The adsorption and isomerization reaction of 1-butene on H-ITQ-22 were theoretically studied using the ONIOM (MP2:M06-2X) approach. The adsorption energy of 1-butene on H-ITQ-22 is calculated to be -20.5 kcal/mol, which is in the range of experimental data. The reaction mechanism of 1-butene isomerization is proposed to be in four steps: 1) the secondary alkoxide intermediate formation via the protonation of 1-butene, 2) the cyclic transition state via the methyl shift and the primary alkoxide intermediate formation, 3) the *tert*-carbenium cation formation via the proton shift and 4) the protonation back to zeolite and desorption of isobutene. The activation energies are calculated to be 17.1, 30.4, 38.2 and 2.6 kcal/mol, respectively. The rate determining step is the *tert*-carbenium cation formation. This multi-pore H-ITQ-22 zeolite is suggested as one of the candidate materials for selective isomerization of 1-butene to isobutene and should be of particular interest to the petrochemical industry.

**Acknowledgement.** This work was supported in part by grants from the National Science and Technology Development Agency (2009 NSTDA Chair Professor funded by the Crown Property Bureau under the management of the National Science and Technology Development Agency and NANOTEC Center of Excellence funded by the National Nanotechnology Center), Kasetsart University Research and Development Institute (KURDI), the Thailand Research Fund (TRF), and the Commission on Higher Education, Ministry of Education (the "National Research University Project of Thailand (NRU)" and the "National Center of Excellence for Petroleum, Petrochemical and Advanced Materials (NCE-PPAM)"). The authors are grateful to Donald G. Truhlar and Yan Zhao for their support with the M06-2X functional.

## References

(1) Bhan, A.; Iglesia, E. *Acc. Chem. Res.* **2008**, *41*, 559.
(2) Corma, A. *J. Catal.* **2003**, *216*, 298.
(3) Smit, B.; Maesen, T. L. M. *Nature (London, U. K.)* **2008**, *451*, 671.
(4) Venuto, P. B. *Microporous Mater.* **1994**, *2*, 297.
(5) Yaluris, G.; Rekoske, J. E.; Aparicio, L. M.; Madon, R. J.; Dumesic, J. A. *J. Catal.* **1995**, *153*, 65.
(6) Corma, A.; Rey, F.; Valencia, S.; Jorda, J. L.; Rius, J. *Nat. Mater.* **2003**, *2*, 493.
(7) Andy, P.; Gnep, N. S.; Guisnet, M.; Benazzi, E.; Travers, C. *J. Catal.* **1998**, *173*, 322.
(8) Guisnet, M.; Andy, P.; Gnep, N. S.; Benazzi, E.; Travers, C. *J. Catal.* **1996**, *158*, 551.

(9) Houžvička, J.; Hansildaar, S.; Ponec, V. *J. Catal.* **1997**, *167*, 273.
(10) Jousse, F.; Leherte, L.; Vercauteren, D. P. *Mol. Simul.* **1996**, *17*, 175.
(11) Meriaudeau, P.; Bacaud, R.; Ngoc Hung, L.; Vu, A. T. *J. Mol. Catal. A: Chem.* **1996**, *110*.
(12) Mériaudeau, P.; Tuan, V. A.; Le, N. H.; Szabo, G. *J. Catal.* **1997**, *169*, 397.
(13) Boronat, M.; Viruela, P.; Corma, A. *Phys. Chem. Chem. Phys.* **2001**, *3*, 3235.
(14) Tuma, C.; Kerber, T.; Sauer, J. *Angew. Chem.-Int. Edit.* **2010**, *49*, 4678.
(15) Tuma, C.; Sauer, J. *Phys. Chem. Chem. Phys.* **2006**, *8*, 3955.
(16) Derouane, E. G.; Chang, C. D. *Microporous Mesoporous Mater.* **2000**, *35-36*, 425.
(17) Zhao, Y.; Truhlar, D. G. *J. Phys. Chem. C* **2008**, *112*, 6860.
(18) Zhao, Y.; Truhlar, D. G. *Acc. Chem. Res.* **2008**, *41*, 157.
(19) Bobuatong, K.; Probst, M.; Limtrakul, J. *J. Phys. Chem. C* **2010**, *114*, 21611.
(20) Boekfa, B.; Choomwattana, S.; Khongpracha, P.; Limtrakul, J. *Langmuir* **2009**, *25*, 12990.
(21) Boekfa, B.; Pantu, P.; Probst, M.; Limtrakul, J. *J. Phys. Chem. C* **2010**, *114*, 15061.
(22) Maihom, T.; Boekfa, B.; Sirijaraensre, J.; Nanok, T.; Probst, M.; Limtrakul, J. *J. Phys. Chem. C* **2009**, *113*, 6654.
(23) Pantu, P.; Boekfa, B.; Limtrakul, J. *J. Mol. Catal. A: Chem.* **2007**, *277*, 171.
(24) Wannakao, S.; Boekfa, B.; Khongpracha, P.; Probst, M.; Limtrakul, J. *ChemPhysChem* **2010**, *11*, 3432.
(25) Dapprich, S.; Komiromi, I.; Byun, K. S.; Morokuma, K.; Frisch, M. J. *THEOCHEM* **1999**, *461-462*, 1.
(26) Frisch, M. J.; Trucks, G. W.; Schlegel, H. B.; Scuseria, G. E.; Robb, M. A.; Cheeseman, J. R.; Montgomery, J. A., Jr.; Vreven, T.; Kudin, K. N.; Burant, J. C.; Millam, J. M.; Iyengar, S. S.; Tomasi, J.; Barone, V.; Mennucci, B.; Cossi, M.; Scalmani, G.; Rega, N.; Petersson, G. A.; Nakatsuji, H.; Hada, M.; Ehara, M.; Toyota, K.; Fukuda, R.; Hasegawa, J.; Ishida, M.; Nakajima, T.; Honda, Y.; Kitao, O.; Nakai, H.; Klene, M.; Li, X.; Knox, J. E.; Hratchian, H. P.; Cross, J. B.; Adamo, C.; Jaramillo, J.; Gomperts, R.; Stratmann, R. E.; Yazyev, O.; Austin, A. J.; Cammi, R.; Pomelli, C.; Ochterski, J. W.; Ayala, P. Y.; Morokuma, K.; Voth, G. A.; Salvador, P.; Dannenberg, J. J.; Zakrzewski, V. G.; Dapprich, S.; Daniels, A. D.; Strain, M. C.; Farkas, O.; Malick, D. K.; Rabuck, A. D.; Raghavachari, K.; Foresman, J. B.; Ortiz, J. V.; Cui, Q.; Baboul, A. G.; Clifford, S.; Cioslowski, J.; Stefanov, B. B.; Liu, G.; Liashenko, A.; Piskorz, P.; Komaromi, I.; Martin, R. L.; Fox, D. J.; Keith, T.; Al-Laham, M. A.; Peng, C. Y.; Nanayakkara, A.; Challacombe, M.; Gill, P. M. W.; Johnson, B.; Chen, W.; Wong, M. W.; Gonzalez, C.; Pople, J. A. *Gaussian 03, revision B.05; Gaussian, Inc.: Pittsburgh, PA*, 2003.
(27) Klinowski, J. *Chem. Rev.* **1991**, *91*, 1459.
(28) Eder, F.; Stockenhuber, M.; Lercher, J. A. *J. Phys. Chem. B* **1997**, *101*, 5414.
(29) Yoda, E.; Kondo, J. N.; Domen, K. *J. Phys. Chem. B* **2005**, *109*, 1464.
(30) Cant, N. W.; Hall, W. K. *J. Catal.* **1972**, *25*, 161.

# Decomposition of Nitrous oxide on Au-Embedded Graphene

*Anawat Thivasasith[1,2,3], Pipat Khongpracha[1,2,3], Chompunuch Warakulwit[1,2,3] and Jumras Limtrakul[1,2,3*]*

[1]Laboratory for Computational and Applied Chemistry, Department of Chemistry, Faculty of Science and Center of Nanotechnology, Kasetsart University Research and Development Institute, Kasetsart University, Bangkok 10900, Thailand
[2]Center for Advanced Studies in Nanotechnology and Its Applications in Chemical, Food and Agricultural Industries, Kasetsart University, Bangkok 10900, Thailand
[3]NANOTEC Center of Excellence, National Nanotechnology Center, Kasetsart University, Bangkok 10900, Thailand

*Corresponding author: Tel. +66 2562 5555 ext 2169, Fax: +66 2562 5555 ext 2176,
E-mail address: jumras.l@ku.ac.th

## Introduction

Metal nanostructures deposited on an exfoliated or a single graphene sheet have been the subject of numerous investigations due to their considerable promise in the various applications including catalysis[1], electrocatalyst and fuel cell[2], biosensors[3], and surface enhanced Raman scattering (SERs)[4]. Apart from metal nanostructures deposited onto a graphene sheet, recently the metal embedded graphene has attracted attention from both experimental[5] and theoretical[6] points of view due to its interesting electronic (and also magnetic) structures[6] and high thermal stability[5] opening up tremendous opportunities in advancing catalysis based on graphene[2]. A graphene sheet with a single-vacancy defect or the missing lattice atom, the simplest defect in any material[7], is good substrate material for metal embedded graphene. Many transition metal atoms can form strong covalent bonds with high binding energies ranging between 2-8 eV with an under-coordinate atom at a vacancy[6] indicating possible use in catalysis[7]. The catalytic activity of metal embedded graphene including Au-, Fe-, and Cu-embedded graphene was studied by using the CO oxidation as a benchmark probe[2]. To the best of our knowledge, the catalytic activity of the metal-embedded graphene for the decomposition of nitrous oxide ($N_2O$), an attractive subject from the environmental point of view, has not been investigated. Then, in this work, we aim to investigate the catalytic activity of a metal-embedded (Au) graphene, for the nitrous decomposition. This is because, in many cases, molecular oxygen can be adsorbed preferentially on small Au clusters[8] and $N_2O$ can also act as an oxygen donor.

## Model and Methods

The spin-unrestricted density functional theory (DFT) calculations were carried out using the DMol[3] package. All results were obtained by the generalized gradient approximation with the Perdew-Burke-Ernzerhof (PBE) functional. DFT semicore pseudopotentials (DSPPs) and a double numerical basis set including a d-polarization function (DND) were selected. Within the DSPP scheme implemented in DMol[3], all-electron calculations were performed for C and O atoms, and relativistic effects were included for Au. The real-space global orbital cutoff radius was set to 6 Å. A hexagonal graphene supercell (4×4 graphene unit cells) containing 32 atoms was set up to represent the system. One carbon atom was substituted by an Au atom. The minimum distance between the graphene sheet and its mirror images is greater than 20 Å, which is sufficiently large to avoid interactions between them. In the geometric optimization and the transition state (TS) searching steps, the Brillouin zone integration was performed with the Monkhorst-Pack 3×3×1 *k*-point sampling. The minimum-energy pathway for elementary reaction steps was computed using the nudged elastic band (NEB) method[9]. For the density-of-states (DOS) calculations, the 6×6×1 *k*-point sampling was used to achieve high accuracy. Charge distribution in each system was calculated with the Hirshfeld charge analysis method[10]. The adsorption energy $E_{ad}$ between the adsorbate and Au/graphene is defined as;

$$E_{ad} = E_{cpx} - ( E_{Au/graphene} + E_{adsorbate})$$

where the subscripts cpx, Au/graphene, and adsorbate denote the total energies of the adsorption complex and the corresponding substances.

## Results and Discussion

In this work, DFT calculations were performed to investigate the reaction mechanisms of the decomposition of the nitrous oxide molecule on the Au-embedded graphene models. The bond length between the Au atom and each of the three neighboring carbon atoms is 2.30 Å, and the height of the Au atom above the graphene base plane is 1.67 Å both of which are in good agreement with those of previous calculations based on the plane-wave basis[2,3]. Moreover by means of the Hirshfeld charge population analysis, there is about a 0.40e electron transfer (Q) from Au to the graphene sheet.

The spin density mainly accumulates on the Au atom and those three neighboring carbon atoms (Figure 1b). To gain a deeper insight into the electron structure of Au-embedded graphene, the spin-polarized local density of states are projected on Au-5d and Au-6s orbitals and the neighboring C-2p orbital is plotted, as shown in Figure 1c. Because of the formation of C-Au bonds and electron transfer from Au to C, Au-5d, Au-6s, and C-2p orbitals are partially filled. As a result, the high density of spin-polarized states around $E_F$ is localized on C-2p, Au-5d and Au-6s orbitals. This confirmed that the region at the gold atom is an active site for the incoming nitrous oxide molecule.

The nitrous decomposition on the Au-embedded graphene was proposed to occur via the concerted mechanism. The reaction intermediates related to this mechanism are shown in Figure 2a. At the initial step (IS), the $N_2O$ molecule approaches the Au- embedded graphene in a tilted direction (the Au-O-N angle = 131.6° ) and transfers an O atom to the Au-embedded graphene. At the transition state (TS) the O atom is pointing to the Au atom and the bond distance of O–Au is 2.12 Å. In comparison to the isolated $N_2O$ molecules, the O–N2 lengthens from 1.20 to 1.62 Å and N1–N2 shortens from 1.14 to 1.13 Å. The N1–N2–O is changed from a linear to a bent alignment on account of the changing of the electronic hybridization of the central atom in the $N_2O$ molecule. Finally, the product (PRO) that the bond between O and Au is formed (1.96 Å).

The adsorption of $N_2O$ with Au-embedded graphene, Figure 2a shows the most stable configuration of $N_2O$ on the Au-embedded graphene system with $E_{ad}(N_2O)$ = -4.26 kcal/mol. Meanwhile, there is about a 0.02e electron transfer from $N_2O$ to the Au-embedded defect graphene, which occupies in Au-5d orbitals. In this case, the electrons not only accumulate on the Au atom but also on C-Au bond. The O atom of $N_2O$ approaches the Au-embedded graphene and reaches TS. The activation energy barrier $E_a$ is estimated to be 26.26 kcal/mol (Figure 3). At this configuration, there is about a 0.04e electrontransfer from Au-5d and Au-6s to $N_2O$ (spin-polarized states are localized around $E_F$, figure 2b) which are occupied in $N_2O$-$2\pi^*$ orbitals and subsequently lead to the elongation of the O-N2 bond length from 1.13 to 1.62 Å (Figure 2a-TS). After the TS, the

intermediate complex (INT) is formed. At this point, there is about a 0.06 electron transfers from the Au-embedded graphene to O of $N_2O$ and this leads to the complete cleavage of the O–N2 bond from 1.13 to 3.30 Å. The process is found to be an endothermic process with respect to the initial state. Finally, the $N_2$ molecule is desorbed from the complex with the required energy of 0.24 kcal/mol.

In the previous studies, the $N_2O$ decomposition on the defect carbon nanotube had a reaction barrier of 40.3 kcal/mol[11] and 30.0 kcal/mol on the defect graphene at room temperature. In this work, a much lower activation energy barrier for the nitrous decomposition catalyzed by Au-embedded graphene of 26.3 kcal/mol is found. Due to the low activation barrier involved, the reaction is likely to proceed rapidly at room temperature. Moreover, the catalytic activity of this graphene-based catalyst may be tuned or enhanced by the curvature of a sheet due to its flexible character. Another important property of Au-embedded graphene is its plane structure with high surface area, which ensures its good catalytic efficiency and activity in reaction progresses.

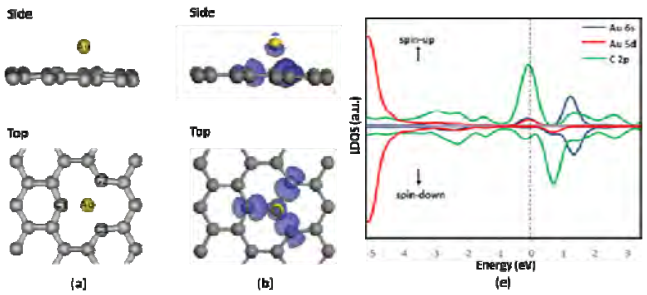


**Figure 1.** Electronic and geometric structure of Au-embedded graphene. (a) Side and top view of the geometric and (b) spin-density isosurface. (c) Spin-polarized local density of states projected on 5d (red curve) and 6s (blue curve) orbitals of Au as well as 2p (green curve) orbitals of neighboring carbon atoms.

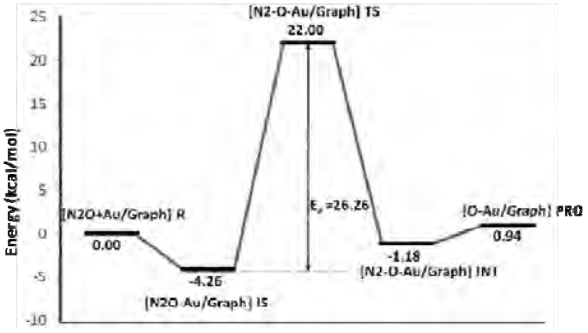


**Figure 3.** Schematic energy profiles corresponding to local configurations along the minimum-energy pathway via the $N_2O \rightarrow N_2+O$ route.

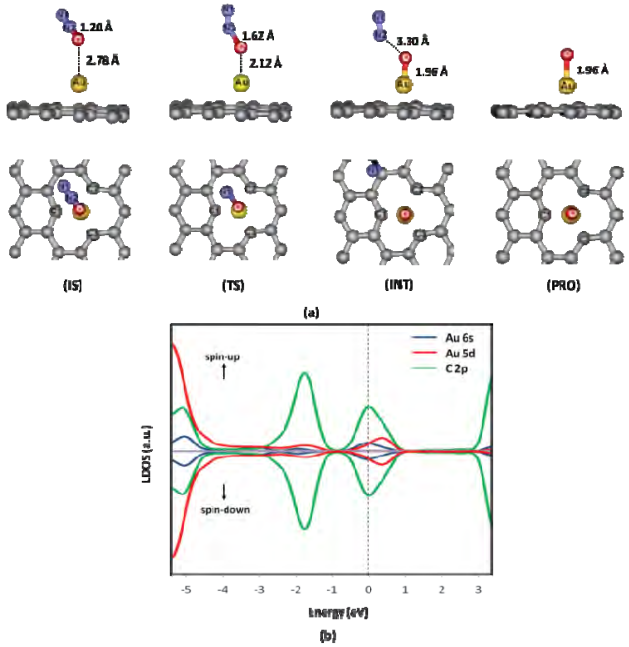


**Figure 2.** Local configuration of the adsorbates on the Au-embedded defect graphene at various intermediate states, (a) including the initial state (IS), transition state (TS), intermediate state (INT), and product state (PRO) along the minimum-energy pathway via the $N_2O \rightarrow N_2+O$ route. (b) Spin-polarized local density of state of transition state projected on 5d (red curve) and 6s (blue curve) orbitals of Au as well as 2p (green curve) orbitals of neighboring carbon atoms.

## Conclusions

The nitrous decomposition on Au-embedded graphene is predicted to occur at room temperature. The high catalytic activity of Au-embedded graphene may be attributed to the partially occupied s and d orbital localized in the vicinity of the Fermi level because of the interactions between the Au atom and the C neighboring atom of graphene. However, we can expect that the metal atom is not limited to Au. Other transition-metal- embedded graphene is expected to have high catalytic activity, such as Ag, Cu-embedded graphene. The proposed method transforms the inert graphene to a highly active material for catalysis. This opens a new avenue to fabricate low cost and highly efficient catalysts based on carbon.

**Acknowledgement.** This work was supported in part by grants from the National Science and Technology Development Agency (2009 NSTDA Chair Professor funded by the Crown Property Bureau under the management of the National Science and Technology Development Agency and NANOTEC Center of Excellence funded by the National Nanotechnology Center), Kasetsart University Research and Development Institute (KURDI), the Thailand Research Fund (TRF), and the Commission on Higher Education, Ministry of Education (the "National Research University Project of Thailand (NRU)" and the "National Center of Excellence for Petroleum, Petrochemical and Advanced Materials (NCE-PPAM)"). The Kasetsart University Graduate School is also acknowledged.

**References**


(1) Li, Y.; Fan, X.; Qi, J.; Ji, J.; Wang, S.; Zhang, G.; Zhang, F., *Mater. Res. Bull.* **2009**, *45* (10), 1413-1418.

(2) Muszynski, R.; Seger, B.; Kamat, P. V., *J. Phys. Chem. C* **2008**, *112* (14), 5263-5266.

(3) Hong, W.; Bai, H.; Xu, Y.; Yao, Z.; Gu, Z.; Shi, G., *J. Phys. Chem. C* **2010**, *114* (4), 1822-1826.

(4) Goncalves, G.; Marques, P. A. A. P.; Granadeiro, C. M.; Nogueira, H. I. S.; Singh, M. K.; Gracio, J., *Chem. Mater.* **2009**, *21* (20), 4796-4802.

(5) Gan, Y.; Sun, L.; Banhart, F., *Small* **2008**, *4* (5), 587-591.

(6) Krasheninnikov, A. V.; Lehtinen, P. O.; Foster, A. S.; Pyykk; ouml; P.; Nieminen, R. M., *Phys. Rev. Lett.* **2009**, *102* (12), 126807.

(7) Banhart, F.; Kotakoski, J.; Krasheninnikov, A. V., *ACS Nano* **2011,** *5* (1), 26-41.

(8) Tsunoyama, H.; Sakurai, H.; Tsukuda, T., *Chem. Phys. Letters* **2006**, *429* (4-6), 528-532.

(9) Lu, Y.-H.; Zhou, M.; Zhang, C.; Feng, Y.-P., *J. Phys. Chem. C* **2009**, *113* (47), 20156-20160.

(10) Song, E. H.; Wen, Z.; Jiang, Q., *J. Phys. Chem. C* **2011**, *115* (9), 3678-3683.

(11) Namuangruk, S.; Khongpracha, P.; Tantirungrotechai, Y.; Limtrakul, J., *J. Mol. Graph. Model.* **2007**, *26* (1), 179-186.

# DENSITY FUNCTIONAL THEORY STUDY ON CATALYTIC CRACKING OF *n*-HEXANE ON HETEROPOLY ACID COMPARISON WITH FAU ZEOLITE

*Saowapak Choomwattana*[1,2,3], *Thana Maihom*[1,2,3], *and Jumras Limtrakul* [1,2,3*]

[1]Laboratory for Computational and Applied Chemistry, Department of Chemistry, Faculty of Science and Center of Nanotechnology, Kasetsart University Research and Development Institute, Kasetsart University, Bangkok, Thailand
[2]NANOTEC Center of Excellence, National Nanotechnology Center, Kasetsart University, Bangkok, Thailand
[3]Center for Advanced Studies in Nanotechnology and Its Applications in Chemical, Food and Agricultural Industries, Kasetsart University, Bangkok, Thailand
*Corresponding author's e-mail address: jumras.l@ku.ac.th

## Introduction

In petroleum refining and petrochemical conversion, acid-catalyzed reactions of alkanes, including cracking, dehydrogenation, isomerization, and disproportionation is of significant importance. One reaction among those most thoroughly investigated is the cracking reaction. This one has the possibility for comparing experimental results with theory and the promising insight into the molecular mechanism of more complicated reactions. The key components of industrial petroleum cracking catalysts are solid proton-donor acids, including zeolites. Numerous researches concerning solid catalysts have been conducted due to their catalytic activity for the low-temperature reaction. What lies beneath the catalyst effectiveness is the strength of the acid. It influences both pathways and the nature of reacting species in the cracking reaction.

Both zeolites and heteropoly acids (HPA) are well known superacids. Without a doubt, zeolite is capable of cracking hydrocarbons. For instance, monomolecular cracking reactions over ZSM-5, Beta and Faujasite zeolites occur at the temperature of 623-773 K.[1] HPA is, on the other hand, less well known for the application in hydrocarbon cracking reactions due to its poor stability and lack of monodispersity. An example of this is the experimental work on the stability and catalytic property of phosphotungstic acid (HPW) on the *n*-hexane cracking reaction.[2] It was reported that, in a fixed bed reactor and the nitrogen-hexane mixture feed at atmospheric pressure, the catalyst was active at 473 K for only 8 minutes before it died completely. The drawbacks are possibly surmountable as many attempts, such as applying catalyst support and stabilizer,[3-5] have been made to improve the catalyst.

Regarding the molecular point of view, bimolecular and monomolecular mechanisms were proposed to explain the catalytic cracking of hydrocarbons,[6-8] while the classical bimolecular mechanism, consisting of hydride transfer, isomerization and β-scission, was suggested for the condition of high partial pressure of hydrocarbons and low reaction temperature. Monomolecular cracking is believed to be dominant in the cracking reaction of hydrocarbons under low pressure and high temperature reaction.[6,7] The key reacting species of the latter mechanism is a high-energy nonclassical two-electron three-center carbonium ion which is formed by the direct protonation of Brønsted acid to the C−C bond.[6,7] Subsequently, the carbonium ion collapses, leading to the scission of the C−C bond to produce alkane and alkene products. In our calculation, we reported in 2010 that the protonation step is found to be the rate-determining step.[9] Therefore, only the information of this step could lead to a reasonable prediction for the catalyst effectiveness.

Attempts have been made to develop the computational methodology that can precisely predict the physical and chemical properties of the catalyst itself and the catalyzed reactions. The new meta-hybrid density functional M06 series[10,11] have been recently developed for the accurate computation of the covalent and non-covalent binding energies of adsorbates with the zeolite acid site. The results were comparable to MP2 calculations at a high basis set but at much more affordable computer times. M06-L is the most accurate functional for transition metals and is especially efficient for calculations on large systems.[12] Therefore, it is practical for presenting systems.

In this work, the density functional theory, M06-L including dispersion energy, has been employed to determine transition states and the corresponding energy barriers of the reactions related to the first step of cracking *n*-hexane catalyzed by a protonated zeolite (H-FAU) and a heteropoly acid (HPA). Hexane is chosen as a reactant in this work because it is widely used experimentally as a benchmark in cracking reactions to study the catalyst acidity.[13,14] The direct comparison of the protolytic cracking of *n*-hexane on zeolite and heteropoly acid has been performed for the first time to provide insight into understanding these two catalysts for industrially important cracking reactions.

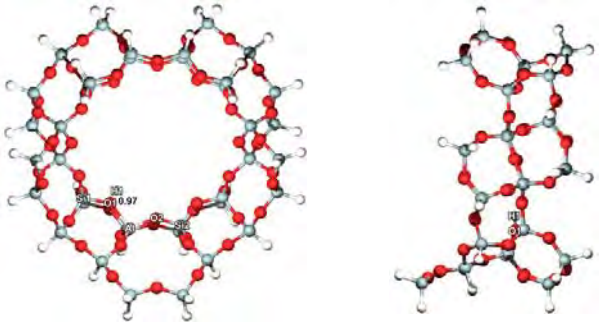

(a) (b)

**Figure 1.** 38T cluster model of H-FAU zeolite: (a) front view with the acidic bond distance and (b) side view.

(a) (b)

**Figure 2.** Cluster model of α-Keggin HPW heteropoly acid: (a) atomistic graphics with the acidic bond distance and (b) an orange tetrahedron representing the phosphate anionic core of the HPW.

## Models and Method

Nanocluster models of zeolite (H-FAU) and Heteropoly Acid (α-Keggin HPW) were generated from their lattice structures.[15,16] The 38T cluster model of H-FAU, illustrated in Figure 1 covers the 12-membered-ring window connecting two supercages of faujasite. It is symmetrically extended from the 12T of the 12-membered-ring to include 38 tetrahedral atoms. Silicon at the T2 position was replaced by aluminum to model a Brønsted acid site. For the phosphotungstic acid, the cluster model (see Figure 2a) whose molecular formula is $H_3PW_{12}O_{40}$, can be considered as a $W_{12}O_{36}$ cage (which is composed of 12 edge-sharing $WO_6$ metal-oxygen octahedra) enveloping a

phosphate ($PO_4^{3-}$) anion (Figure 2b). Similar to zeolites, the acidic proton, for the charge neutralization, of HPW heteropoly acid resides on framework oxygen atoms. We adopted the model from the work of Yang and co-workers[17] which proposed a rational model based on experimental works.[18]

For the zeolite system, only the 5T active region of "$SiOHAl(OSi)_2OSi$" and the reacting molecule are allowed to relax during geometry optimizations, while the rest of the structure is kept fixed at the crystallographic coordinates. For the HPW system, all atoms are allowed to relax during the optimizations. M06-L density functional was used in all calculations. The basis set of 6-31G(d,p) was employed for Al, Si, O, P and H atoms, while the W atom was described by the Effective Core Potentials (ECP) of Stuttgart RSC 1997 ECP.[19] All calculations were performed with the Gaussian 03 code[20] modified to incorporate the Minnesota Density Functionals module 3.1 by Zhao and Truhlar.

**Results and Discussion**

**Bare Catalysts.** H-FAU and HPW share a common character, Brønsted acid that is accessible, thus being proficient in acid catalysis. From a review of Mizuno and Misono,[21] it was stated that heteropoly acids such as HPW in the solid state are pure Brønsted acids and stronger acids than the conventional solid acids such as $SiO_2$-$Al_2O_3$, $H_3PO_4/SiO_2$, and HX and HY zeolites. By definition, one can analyze the Brønsted acidity from deprotonation energy calculated with the following equation:

$$\text{Deprotonation energy} = E(\text{H-Catalyst}) - E(H^+) - E(\text{Catalyst})$$

From our calculation, we found the same trend as the deprotonation energy of H-FAU and HPW; 310.9 and 263.1 kcal/mol, respectively. Even so, the O–H acidic bond in both catalysts is the same (0.97 Å, shown in Figures 1 and 2). The finding can be construed as the confinement effect of the zeolitic framework influences a stronger attraction of proton or other adsorbates to the framework oxygen, O1, thus requiring more energy to deprotonate the catalyst.

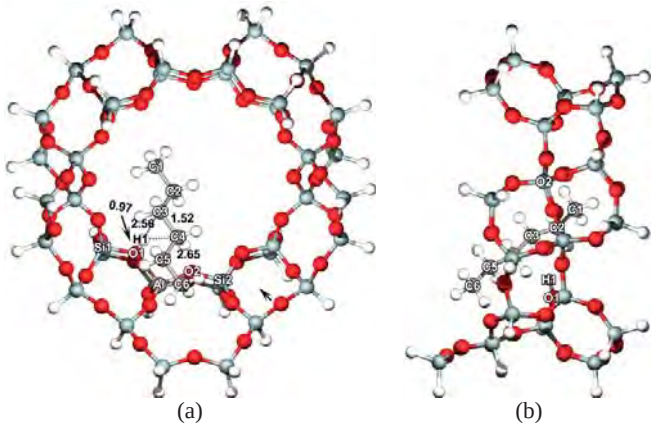


(a) (b)

**Figure 3.** Optimized structures of the adsorption state of *n*-hexane protolytic cracking over H-FAU: (a) front view and (b) side view.

***n*-Hexane adsorption.** Upon the adsorption (see Figures 3 and 4), there is no significant change in the bond lengths of the O1–H1 acidic bond and the cracking of the C3–C4 bond, when comparing to the isolated components. Nevertheless, the intermolecular distances between the alkane and the catalytic acid of the catalysts are different. The zeolite proton resides in 'the valley' of the oxygen framework. On the other hand, the curvature of the HPW active site is upward. The proton of HPW is therefore more accessible to the adsorbate. Consequently, the average intermolecular distance between *n*-hexane and the proton is 2.62 Å for H-FAU and 2.42 Å for HPW.

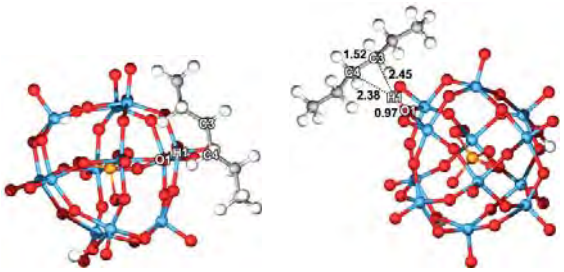


(a) (b)

**Figure 4.** Optimized structures of adsorption state involved in the protolytic cracking of *n*-hexane over HPW: These views are meant to imitate the view of *n*-hexane in Figures 3 (a) and (b), respectively.

Once the intermolecular distance is larger, the adsorption energy is generally expected to be less. In this present work, there is a contrary. The corresponding adsorption energies for H-FAU and HPW systems are −11.7 and −6.8 kcal/mol, respectively. The calculated adsorption energy of the H-FAU system agrees well with an experimental measurement of −12.7 kcal/mol.[21] The tendency contradiction between the intermolecular distance and the adsorption energy can be explained with the confinement effect of the zeolite pore that plays a dominant role in the adsorption. This is another proof of the major contribution of the confinement effect in the zeolite catalysis.

**Transition State of Protolytic Cracking of *n*-Hexane.** The adsorbed *n*-hexane molecule is protonated by the acidic proton at the central C−C bond to form the adsorbed 3-C-hexonium intermediate. Selected geometrical parameters for the reaction step and optimized structures are shown in Figures 5 and 6 for reactions in H-FAU and HPW, respectively.

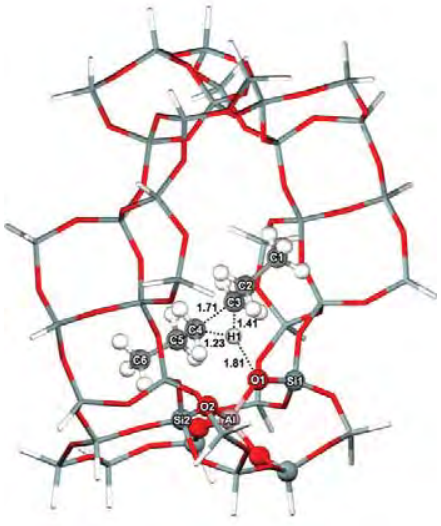


**Figure 5.** Optimized structure of the transition state of *n*-hexane protolytic cracking over H-FAU.

At the transition state, the H1 proton is protonated to the C3–C4 bond of *n*-hexane. The interaction that holds the transition complex of the proton-accepting reacting species and the proton-donating catalyst together can be considered as electrostatic.[23-25] In H-FAU, the Brønsted O1–H1 bond distance is elongated from 0.98 to 1.81 Å while the C3–C4 bond distance is increased to 1.71 Å. The C3−H1 and C4–H1 distances are 1.41 and 1.23 Å, respectively. The geometry of the transition state structure in HPW is similar to that in H-FAU with slight differences in the HPW system, i.e. a shorter Brønsted O1–H1 bond distance (1.61 Å) and proton transfer distances (C3–H1 = 1.41 Å and C4–H1 = 1.28 Å). The existence of true transition states has been confirmed by frequency calculations resulting in one imaginary frequency related to the movement of the acidic proton of zeolite (H1) to the *n*-hexane C3–C4 bond and the breaking of the C3–C4 bond.

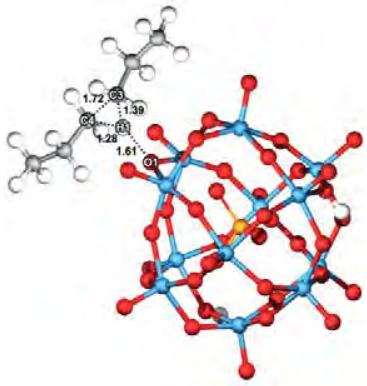


**Figure 6.** Optimized structure of *n*-hexane protolytic cracking over HPW.

The adsorption energies of *n*-hexane are predicted to be −11.7 and −6.8 kcal/mol for H-FAU and HPW, respectively, the former value is in good agreement with experimental measurements. This indicates that the models employed for zeolite as well as for HPW can be well represented by the M06-L functional. The cracking reaction is assumed to proceed via the first step of the C–C activation and is found to be the rate-determining step with activation energies of 44.7 and 41.4 kcal/mol for H-FAU and HPA, respectively. It is noted that the relative energy of the transition state is 33.0 kcal/mol for H-FAU and 34.6 kcal/mol for HPW. The apparent activation energy is only 1.63 kcal/ml different. The consequence is that the stability of the adsorption is the key factor to determine the height of the activation barrier.

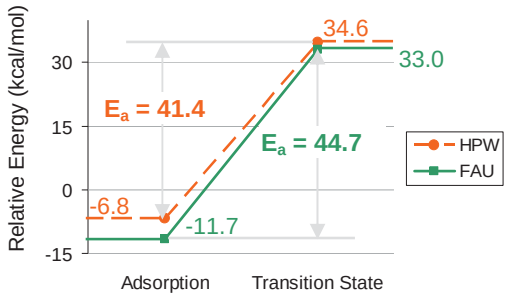


**Figure 7.** Energy profile for *n*-hexane protolytic cracking catalyzed by H-FAU zeolite (solid line) and HPW heteropoly acid (dashed line) comparing to the isolated systems.

With the comparable catalytic efficiency presented in the present study, HPW could be used instead of H-FAU. However, heteropoly acids lack the confinement effect that is provided by the zeolite pore. This weakness can be overcome by applying the acids into other porous materials. Nowadays, there is a number of publications reporting about the hybrid materials of heteropoly compounds (in either protonated or anionic form) and metal-organic frameworks (MOFs)[26-28] Utilizing the molecular design approach, one can vary the type of heteropoly acid and the composition combination of the MOFs to achieve the materials with a desired catalytic property of the acid and the tailored environment (i.e. size and shape of the pore and functionality) of the framework.

## Conclusions

The key step of the *n*-hexane cracking reaction over two different types of solid acid catalyst has been investigated by utilizing the 38T H-FAU and α-Keggin HPW cluster models calculated at the M06-L/6-31G(d,p) level of theory. These calculations give adsorption energies which represent the experimental data well. The key transition state of the protolytic cracking, which is the rate-determining step of the overall cracking reaction, was optimized and analyzed. The different activities of the Brønsted acid catalysts can be explained by the different adsorption energies which are mainly due to the presence of the confinement effect of the zeolite pore that facilitates the adsorption but raise the activation barrier at the same time. The present study shows the advantages and disadvantages of both catalysts. While the zeolite provides confinement effect and shape selectivity, it lacks variety, thus being difficult to modify to suit any new applications. Alternatively, heteropoly acid has no confinement effect and such a specific selectivity, but it is tunable by varying the elemental composition and the geometry. Not only for a better stability and dispersion, but for the combination of heteropoly acid into hybrid materials is promising for breakthrough applications.

**Acknowledgement.** This work was supported in part by grants from the National Science and Technology Development Agency (2009 NSTDA Chair Professor funded by the Crown Property Bureau under the management of the National Science and Technology Development Agency and NANOTEC Center of Excellence funded by the National Nanotechnology Center), the Thai National Grid Center (TNGC) under the Software Industry Promotion Agency (SIPA), the Thailand Research Fund (TRF) (to J.L.), the Kasetsart University Research and Development Institute (KURDI), Graduate School Kasetsart University and the Commission of Higher Education, Ministry of Education ("the National Research University Project of Thailand (NRU)" and "Postgraduate Education and Research Programs in Petroleum and Petrochemicals, and Advanced Materials"). The program "Strategic Scholarships for Frontier Research Network for the Joint Ph.D. Program Thai Doctoral degree (CHE-PhD-SW)" from the Office of the Higher Education Commission, Thailand (to S.C. and T.M.) is also acknowledged.

## References

(1) Kotrel, S.; Rosynek, M. P.; Lunsford J. H. *J. Phys. Chem. B* **1999**, *103(5)*, 818–824.
(2) Jalil, A.; Faiz, M.; Tabet, N.; Hamdan, N. M.; Hussain, Z. *J. Catal.* **2003**, *217(2)*, 292–297.
(3) Bhorodwaj, S. K.; Dutta D. K. *App Clay Sci*., **2011**, doi:10.1016/j.clay.2011.01.019.
(4) Fiuza, R. A.; Santos, I. V.; Fiuza, R. P.; José, N. M.; Boaventura, J. S.; *Macromol. Symp.* **2011**, *299-300(1)*, 234–240.
(5) Betz, D.; Altmann, P.; Cokoja, M.; Herrmann, W. A.;Kuhn, F.E. *Coord. Chem. Rev.* **2011**, doi:10.1016/j.ccr.2010.12.004.

(6) Haag, W. O.; Dessau, R. M. *Proc. 8th Intl. Cong. Catal. Berlin (Dechema, Frankfurt-am-Main)*, **1984**, 2, pp 305−316.
(7) Kotrel, S.; Knözinger, H.; Gates, B. C. *Micropor. Mesopor. Mater.* **2000**, *35−36*, 11-20.
(8) Corma, A.; Orchilles, A. V. *Micropor. Mesopor. Mater.* **2000**, *35−36*, 21-30.
(9) Maihom, T.; Pantu, P.; Tachakritikul, C.; Probst, M. and Limtrakul J. *J. Phys. Chem. C* **2010**, *114(17)*, 7850–7856.
(10) Zhao, Y. and Truhlar, D. G. *J. Phys. Chem. C* **2008**, *112*, 6860–6868.
(11) Zhao, Y. and Truhlar, D. G. *Acc. Chem. Res.* **2008**, *41(2)*, 157–167.
(12) Kumsapaya, C.; Bobuatong, K.; Khongpracha, P.; Tantirungrotechai, Y.; Limtrakul, J. *J. Phys. Chem. C* **2009**, *113(36)*, 16128–16137.
(13) Bourdillon, G.; Gueguen, C.; Guisnet, M. *Appl. Catal.* **1990**, *61(1)*, 123-139.
(14) Lercher, J. A.; Jentys, A. ; Brait, A. *Mol. Sieves Sci. Technol.* **2008**, *6*, 153-212.
(15) Alberti, A.; Davoli, P.; Vezzalini, G. Z. Z. *Kristallogr.* **1986**, *175*, 249–256.
(16) Soares-Santos P. C. R.; Cunha-Silva, L.; Sousa, F. L.; Mafra, L.; Rocha, J.; Cavaleiro, A. M. V.; Trindade, T.; Paz, F. A. A.; Klinowski, J. ; Nogueira, H. I. S. *J. Molec. Struct.* **2008**, *888(1-3)*, 99-106.
(17) Yang, J.; Janik, M. J.; Ma, D.; Zheng, A.; Zhang, M.; Neurock, M.; Davis, R. J.; Ye, C. and Deng, F. *J. Am. Chem. Soc.*, **2005**, *127*(51), pp 18274-18280.
(18) Ueda, T; Tatsumi, T; Eguchi, T.; Nakamura, N. *J. Phys. Chem. B* **2001**, *105(23)*, 5391–5396.
(19) Dolg, M.; Stoll, H.; Preuss, H.; Pitzer, R. M. *J. Phys. Chem.* **1993**, *97*, 5852–5859.
(20) *Gaussian 03, revision B.05*; Gaussian, Inc.: Pittsburgh, PA, **2003**.
(21) Mizuno, N.; Misono, M.*Chem. Rev.* **1998**, *98 (1)*, 199–218.
(22) Eder, F.; Stockenhuber, M.; Lercher, J. A. *J. Phys. Chem. B* **1997**, *101(27)*, 5414–5419.
(23) Galadima, A.; Anderson, J. A.; Wells, R. P. K. *Sci. World J.* **2009**, *4(3)*, 15-22.
(24) Bharad, J. V.; Madje, B. R.; Ubale, M. B. *Int. J. ChemTech Res.* **2010**, *2(1)*, 346-353.
(25) Vollmer, J. M.; Truong, T. N. J. *Phys. Chem. B* **2000**, *104(26)*, 6308–6312.
(26) Dang, D.-B.; Bai, Y.; He, C.; Wang, J.; Duan, C.-Y.; Niu, J.-Y. *Inorg. Chem.* **2010**, *49(4)*, 1280–1282.
(27) Ma, F.-J.; Liu, S.-X.; Liang, D.-D.; Ren, G.-J.; Zhang, C.-D.; Wei, F.; Su, Z.-M. *Eur. J. Inorg. Chem.* **2010**, *24*, 3756–3761.
(28) Juan-Alcaniz, J.; Ramos-Fernandez, E. V.; Lafont, U.; Gascon, J.; Kapteijn, F. *J. Catal.*,**2010**, *269(1)*, 229-241.

# Synthesis of Precisely Size-Controlled Gold Nanoparticles and Their Infusion into Mesoporous Silica SBA-15 by Compressed Carbon Dioxide Solution Technique

*Sarawoot Impeng[1,3,4], Amporn Sane[2,3,4], Chompunuch Warakulwit[1,3,4], Panvika Pannopard[1,3,4], Boonruen Sunpetch[1,3,4], Pipat Khongpracha[1,3,4], Jumras Limtrakul[1,3,4*]*

[1]Department of Chemistry, Faculty of Science and Center of Nanotechnology, Kasetsart University Research and Development Institute, Kasetsart University, Bangkok 10900, Thailand
[2]Department of Packaging and Materials Technology, Faculty of Agro-Industry, Kasetsart University, Bangkok 10900, Thailand
[3]NANOTEC Center of Excellence, National Nanotechnology Center, Kasetsart University, Bangkok 10900, Thailand
[4]Center for Advanced Studies in Nanotechnology and Its Applications in Chemical, Food and Agricultural Industries, Kasetsart University, Bangkok 10900, Thailand
*Corresponding author's e-mail address: jumras.l@ku.ac.th

## Introduction

Gold nanoparticles (AuNPs) especially with a diameter less than 5 nm have attracted great interest from scientific and industrial standpoints due to their excellent catalytic activity in various important chemical reactions including many oxidation and hydrogenation reactions at low temperatures. AuNPs supported on metal oxide were used as high active and durable catalysts for CO oxidation,[1] alcohols oxidation,[2] water-gas shift reaction,[3] C-C bond formation,[4] and so on. In particular, low temperature CO oxidation catalyzed by AuNPs deposited on reducible metal oxides[5] ($TiO_2$, $CeO_2$, $Fe_2O_3$, and $Co_3O_4$) and nonreducible metal oxides[1f,6] ($Al_2O_3$ and $SiO_2$) has been widely investigated. These studies reported that the catalytic activity depended on the size of AuNPs as well as the nature of supports. In many cases using the reducible supports for gold nanoparticles, the support or the Au-support interface was reported to play an important role on their catalytic activity leading such supported gold nanoparticles to be active catalysts.[1c] Particularly, AuNPs with a size smaller than 5 nm supported on nonreducible metal oxides were reported to be active. It is suggested that the catalytic activity of such gold nanoparticles is derived from the change of electronic structure or the higher density of reactive defective sites of the nanoparticles.[1f] For those reducible supports, however, the catalytic activity still depends on the size of AuNPs.[7]

Mesoporous silica materials have been considered as ideal catalyst supports because of their well-defined pore size as well as their high thermal and chemical stability. SBA-15 has been synthesized with a tunable structure, large pore diameter in the range of 2–30 nm and a wall thickness of 3.1–6.4 nm. This allows facile diffusion of the molecules into the porous structure of the silica, even for bulky molecules, making them desirable for depositing small metal nanoparticles inside. As the surface of mesoporous silica is highly negative charged; it is difficult to prepare AuNPs supported on SBA-15 with $AuCl_4^-$ being used as a precursor via direct deposition-precipitation and the impregnation technique.[2b] To overcome this limitation, the surface of mesoporous silica was modified with functional groups such as –SH[1f,8] and $–NH_2$.[9] Nevertheless, this method produced AuNPs with a broad size distribution as well as poorly controllable size and shape. Alternatively, AuNPs supported on a pure surface of mesoporous silica can be achieved by replacing the $AuCl_4^-$ precursor with $[Au(en)_2]^{3+}$ a cation precursor[1e] or using the colloidal deposition method.[2b,10] Employing colloidal AuNPs is of specific interest since the size distribution and shape of the nanoparticles can be effectively controlled as well as their catalytic activity that depends on the type of protecting ligands. Tsukuda *et al.* reported that AuNPs stabilized by poly(vinylpyrrolidone) (PVP) provided weak interaction between the nanoparticles and the protecting polymer such that part of the nanoparticle surface was exposed and readily accessible for catalytic conversion.[11]

Recently, Liu *et al.* successfully deposited AuNPs (with a diameter of ~1 nm) stabilized by triphenylphosphine into pure mesoporous silica (SBA-15, HMS, MCF) dispersed and stirred in an organic medium.[2b] However, low loading of AuNPs (less than 1 wt %) was still obtained because of high viscosity and surface tension of the dispersion medium. Thus, it remains a challenge for developing a new technique to infuse AuNPs into pure mesoporous silica SBA-15. A supercritical fluid could be an excellent medium for the infusion of AuNPs due to its tunable solvent strength, high diffusivity, as well as low viscosity and surface tension. Especially, supercritical carbon dioxide ($scCO_2$) has been considered as an attractive solvent due to it being inexpensive, non-toxic, and non-flammable with a low critical temperature (31 °C) and moderate critical pressure (73.8 bar).[12] In addition, the solvent power of $scCO_2$ can be improved by adding an organic cosolvent. Gupta and co-workers reported the success of infusion of Au nanocrystals (2.2 ± 0.3 nm) protected with dodecanethiol into mesoporous SBA-15 with high Au loadings of up to 2.5 wt % by using a mixture of toluene and $scCO_2$ (1:3 v/v) at a temperature and pressure of 35 °C and 241 bar, respectivly.[13] Nevertheless, the disadvantage of using gold nanostructures protected by thiols is their low catalytic activity due to the strong interaction between thiol and the gold surface. Then, the usage for catalytic application is still limited. Thus far, the infusion of AuNPs with supercritical fluids for catalytic application has still been limited. Therefore, the aim of this work was to study the feasibility of the compressed $CO_2$ solution technique to infuse PVP-stabilized AuNPs into pure mesoporous SBA-15 in order to obtain the gold-supported mesoporous silica as a high active catalyst.

## Experimental Section

**Materials.** Pluronic P123 triblock copolymer ($EO_{20}PO_{70}EO_{20}$), sodium borohydride ($NaBH_4$), and hydrogen tetrachloroaurate(III) trihydrate ($HAuCl_4.3H_2O$) were purchased from Sigma-Aldrich. Poly(vinylpyrrolidone) (PVP, MW = 40 000) was obtained from Fluka. Sodium silicate solution ($Na_2Si_3O_7$, 32 wt % $SiO_2$) was supplied by PQ Chemicals (Thailand). Analytical grade hydrochloric acid (HCl, 36.5–38.0 %) and absolute ethanol (98 %) were provided by J.T. Baker and Carlo Erba, respectively. $CO_2$ (purity >99.98%) was purchased from Chattakorn Lab Center (Thailand). All chemicals were used as received. Water was distilled and deionized before using in our experiments.

**Synthesis of SBA-15.** Mesoporous silica SBA-15 was synthesized by adapting the previously published method.[14] In a typical experiment, 0.845 g of Pluronic 123 was dissolved in 60 mL of deionized distilled water (DI water). During stirring of the solution, 3.125 g of sodium silicate solution was gradually added, followed by rapidly adding 5.4 mL of HCl to the Pluronic 123 solution. The mixture was continuously stirred and heated at 40 °C for 24 h. The mixture was autoclaved at 100 °C for 24 h and then filtered to collect as a white powder product. The product was neutralized by washing with DI water and then dried in a hot air oven at 140 °C for 3 h. Finally, the product was calcined at 550 °C for 6 h in order to obtain SBA-15.

**Preparation of PVP-stabilized Au nanoparticles.** The colloidal of PVP-stabilized Au (Au:PVP) nanoparticles were prepared by following the previous work reported by Tsunoyama *et al.*[4b,15] Typically, an aqueous mixture containing $HAuCl_4$ (1 mM, 50 mL) and PVP (5.56 g) was gently stirred for 30 min at 0 °C. Then, an aqueous solution of $NaBH_4$ (0.1 M, 5 mL) was rapidly added to the

mixture under vigorous stirring. At this step, the color of this solution immediately changed from pale yellow to dark brown, indicating the formation of the desired Au nanoparticles. The aqueous suspension of Au:PVP nanoparticles was kept at 0 °C under continuous stirring for 1 h. The colloidal suspension was centrifuged at 4000 rpm using a membrane tube with a 10 kDa molecular weight cut-off (MWCO) to separate and remove the inorganic impurities left in the mixture. The obtained dark brown product of Au:PVP nanoparticles was freeze-dried under vacuum conditions for 2 days.

**Infusion of Au nanoparticles into SBA-15.** The synthesized Au:PVP nanoparticles were infused into SBA-15 using a compressed solution containing $scCO_2$ and ethanol. Typically, the prepared SBA-15 (250 mg) was added into a variable-volume view cell. Au:PVP nanoparticles (5–10 mg) previously dispersed in ethanol (1–5 g) was then loaded into the cell. Next, $scCO_2$ (5–12 g) was loaded into the cell and the mixture was pressurized to 241 bar and heated at 35 °C. The obtained mixture was continuously stirred using a magnetic stirring bar for 3 h. Next, the mixture was depressurized and cooled down to ambient conditions. The resulting sample was dried in air to remove ethanol, and then calcined at 370 °C for 2 h to remove the PVP protecting-ligand from the AuNPs. The weight ratios of Au:PVP nanoparticles to SBA-15 used in this study were 1:25 and 1:50, while those of ethanol to $scCO_2$ were varied between 1:12 and 1:1.

**Characterization.** The powder sample of AuNPs-loaded SBA-15 was dispersed in ethanol and sonicated for 2 min. Then, the suspension was dropped onto a carbon-coated copper grid and dried at ambient conditions before being characterized by a transmission electron microscope (TEM, JEOL JEM-2010) with an accelerating voltage of 200 kV. Wide angle X-ray diffraction (XRD) data were collected via a PhiLips X'Pert Pro diffractometer with Cu Kα radiation (λ=0.1543 nm) operating with an accelerating voltage of 40 kV and current of 30 mA. Low angle XRD patterns were also collected using a Rigaku-TTRAX III diffractometer with Cu Kα radiation operating with 50 kV and 300 mA. $N_2$ adsorption-desorption isotherms were measured in a Micrometrics ASAP 2020 instrument at 77 K. All powder samples were degassed at 150 °C overnight before the measurements. The specific surface area was calculated using the Brunauer-Emmett-Teller (BET) method.[16] The total pore volume was estimated from the amount adsorbed at a relative pressure of about of 0.99, whereas the pore size distribution was determined from the adsorption branches of the isotherms by using the Barrett-Joyner-Halenda (BJH) method.[17] Thermogravimetric analysis (TGA) was performed using a Perkin Elmer TGA7 by heating from 30 to 370 °C with a rate of 10 °C/min and then maintained at 370 °C for 2 h under $N_2$ gas atmosphere.

## Results and Discussion

**Synthesis of SBA-15.** Mesoporous silica SBA-15 produced in this work was characterized by $N_2$ adsorption-desorption isotherms, TEM, and low angle XRD. Figure 1a shows $N_2$ adsorption-desorption isotherms of the synthesized SBA-15, revealing a typical type IV with an H1 hysteresis loop. In addition, the shape of isotherms exhibits the hysteresis loop with very sharp adsorption-desorption branches, indicating uniform pore size distribution of SBA-15.[18] In the hysteresis loop, $N_2$ adsorption quantity rapidly increased from 300 to 500 $cm^3g^{-1}$ at a relative pressure ($P/P_0$) of ~0.7 due to capillary condensation.[14a]

The BET specific surface area and total pore volume of the synthesized SBA-15 are 727 $m^2g^{-1}$ and 0.83 $cm^3g^{-1}$, respectively. The pore size distribution was determined from the adsorption branches of the isotherms by using the BJH method, it is 7.6 nm (see Figure 1b). These results agree well with that obtained in the previous report of SBA-15.[14]

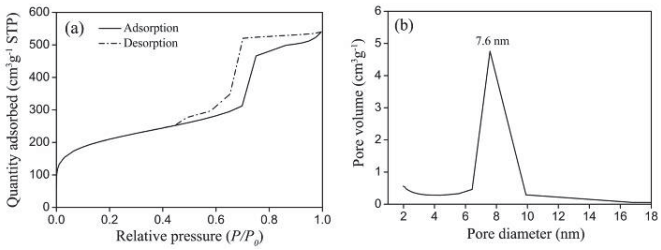


**Figure 1.** $N_2$ adsorption-desorption isotherms (a) and pore size distribution curve (b) of SBA-15

TEM analysis results illustrate that the synthesized SBA-15 has a well-ordered mesoporous channel (Figure 2a) and hexagonal honeycomb structures (Figure 2b) with the mean pore size and wall thickness of approximately 7–8 and 4–5 nm, respectively. Low angle XRD pattern of the SBA-15 exhibited three characteristic peaks at $2\theta$ values of 0.87, 1.49, and 1.74° (see Figure 3) which were respectively indexed to (100), (110), and (200) reflections of the two-dimensional hexagonal (*p6mm*) mesostructure,[14a] in accordance with the TEM results (Figure 2). The *d*-spacing estimated from the first peak ($d_{100}$) was 10.1 nm. The unit cell parameter ($a_0$) corresponding to the distance between two pore centers calculated using $a_0 = 2d_{100}/\sqrt{3}$ was equal to 11.7 nm. Furthermore, the wall thickness estimated from the difference of the $a_0$ value and the pore size determined by $N_2$ adsorption-desorption isotherm analysis, was approximately 4.1 nm, relatively close to that determined from TEM images.

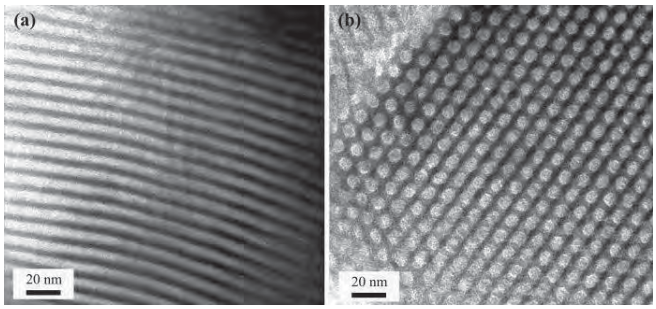


**Figure 2.** TEM images of pure SBA-15: (a) viewing normal to the pore axis; (b) viewing along the pore axis.

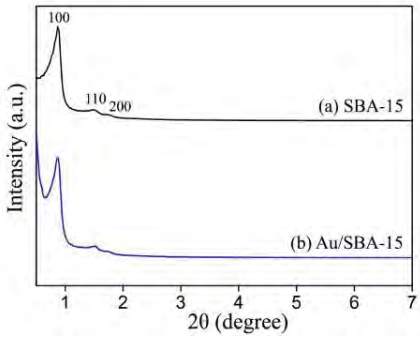


**Figure 3.** Low angle XRD patterns of: (a) SBA-15; (b) Au/SBA-15 composite (1:25 Au:PVP nanoparticles to SBA-15; 1:1 ethanol to $scCO_2$).

**Preparation of Au:PVP nanoparticles**. The synthesized Au:PVP nanoparticles were characterized by TEM and TGA analyses. Figure 4 shows a TEM image and the related particle size distribution of Au:PVP nanoparticles. The obtained nanoparticles were spherical and uniform with a narrow size distribution. The size of nanoparticles ranged from 1.0 to 4.0 nm with an average diameter of 2.3 ± 0.6 nm. The size of Au:PVP nanoparticles synthesized in this study was slightly larger than that previously reported by Tsunoyama *et al.* (1.3 ± 0.3 nm).[4b,15] TGA analysis of Au:PVP nanoparticles was also performed to determine a suitable calcination temperature for removing the PVP protecting-ligand without inducing aggregation of AuNPs after infusion into the SBA-15. TGA curves of Au:PVP nanoparticles are shown in Figure 5. It is shown that all of the PVP, the stabilizing polymer (67% in weight loss was found), was completely removed at the temperature of 370 °C indicating this temperature is suitable for calcination of the Au:PVP/SBA-15 composite.

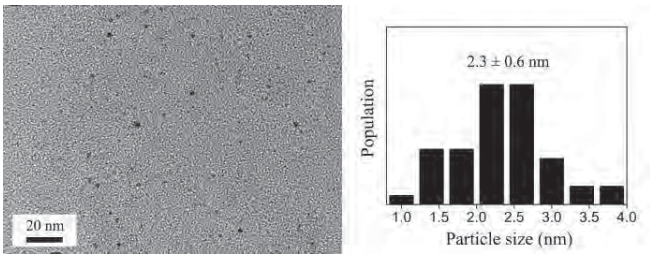


**Figure 4.** TEM image and size distribution of Au:PVP nanoparticles.

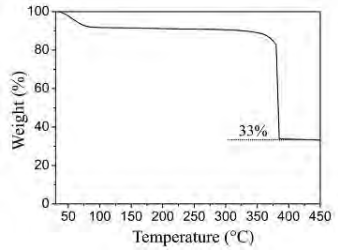


**Figure 5.** TGA curve of Au:PVP nanoparticles.

**Infusion of Au:PVP nanoparticles into SBA-15.** Our preliminary study has shown that Au:PVP nanoparticles were not well-dispersed in $scCO_2$, owing to the non-polar nature of $scCO_2$. In general, the polarity of $scCO_2$ can be increased by mixing with a polar solvent. Therefore, ethanol was added to $scCO_2$ to improve the dispersibility of Au:PVP nanoparticles. Infusion of Au:PVP nanoparticles into mesoporous SBA-15 was carried out at a temperature of 35 °C and a pressure of 241 bar because the mixture of ethanol and $scCO_2$ formed a homogeneous solution at this condition. Using a mixture of ethanol and $scCO_2$ (1:12 w/w), infusion of Au:PVP nanoparticles in SBA-15 was carried out with the Au:PVP nanoparticles to SBA-15 weight ratios of 1:25 and 1:50. After calcination of Au:PVP/SBA-15 composites at 370 °C for 2 h, the resulting Au/SBA-15 composites were characterized by TEM, low- and wide angle XRD, and $N_2$ adsorption-desorption isotherms. TEM results illustrated the trend of increasing the amount of Au loading in SBA-15 when the Au:PVP nanoparticles to SBA-15 weight ratio changed from 1:50 to 1:25, as shown in Figure 6. Furthermore, Au loading content seemed to depend on the concentration of ethanol present in the infusion medium. Increasing the ethanol concentration by changing the ethanol to $scCO_2$ weight ratio from 1:12 to 1:1 increased the Au loading content (compare between Figures 6b and 7a) when the Au:PVP nanoparticles to SBA-15 weight ratio remained constant at 1:25. Low angle XRD patterns of Au/SBA-15 composites exhibited similar characteristic peaks as pure SBA-15, as shown in Figure 3. Therefore, both low angle XRD and TEM results indicated that the infusion process used in this work did not damage the mesostructure of the SBA-15.

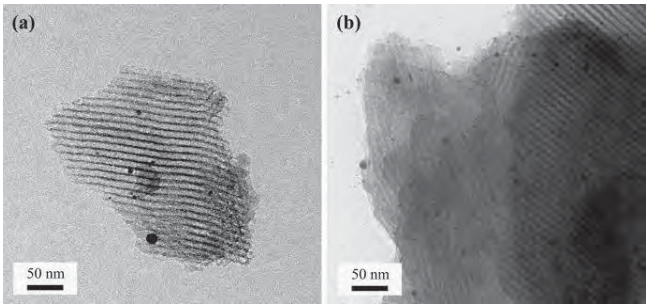


**Figure 6.** TEM images of Au/SBA-15 composites prepared by infusion of Au:PVP nanoparticles into SBA-15 using 1:12 ethanol to $scCO_2$ mixture with Au:PVP nanoparticles to SBA-15 weight ratios of: (a) 1:50; (b) 1:25 after calcination at a temperature of 370 °C.

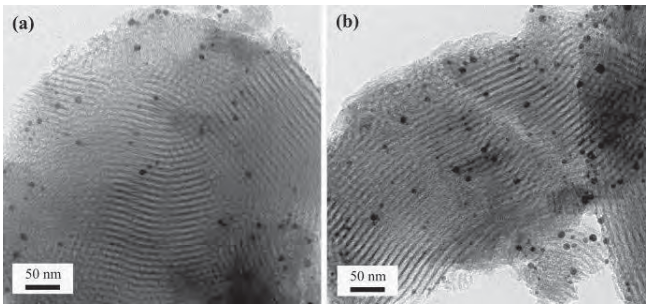


**Figure 7.** TEM images of Au/SBA-15 composites prepared by infusion of Au:PVP nanoparticles into SBA-15 using 1:1 ethanol to $scCO_2$ mixture and 1:25 Au:PVP nanoparticles to SBA-15, followed by calcination at temperatures of: (a) 370 °C; (b) 500 °C.

In addition, XRD analysis of the Au/SBA-15 composites showed only a broad peak at $2\theta$ of ~23° due to the amorphous nature of $SiO_2$, similar to that of pure SBA-15 (Figure 8). Rombi and co-workers reported that XRD patterns of Au/SBA-15 composites after calcinations at 560 °C in flowing air for 6 h showed intense peaks at $2\theta$ = 38.2, 44.7, and 64.6°, corresponding to the (111), (200), and (220) crystal planes of the face-centered cubic structure of Au; however, after calcinations at 300 °C, only a small broad peak still appeared around $2\theta$ = 38°.[1f] In our work, there were no characteristic peaks corresponding to the presence of Au. This could be due to the lower crystallinity of AuNPs and different calcination conditions (i.e., temperature, time, flowing gas) used for Au/SBA-15 composites.

It has been recognized that the location of metal nanoparticles, on the surface or in the channels of a mesoporous support, is important for the catalytic activities and applications.[19] In this work, AuNPs seemed to appear both on the surface and in the channels of SBA-15 (Figures 6b and 7a). It was found that, unlike AuNPs located in the channels of mesoporous SBA-15, those located on the surface of the mesoporous structures tended to aggregate or sinter when increasing the calcination temperature from 370 and 500 °C. In addition, the size of AuNPs located on the surface of mesoporous

SBA-15 somewhat increased with increasing calcination temperature, while that of AuNPs located inside the channel of SBA-15 remained unchanged (compared between Figures 7a and b). It can be deduced that most of AuNPs located inside the channel of SBA-15. Furthermore, $N_2$ adsorption-desorption isotherms of the Au/SBA-15 composite (1:25 Au:PVP nanoparticles to SBA-15; 1:1 ethanol to $scCO_2$) were similar to those of the SBA-15. The BET specific surface area of this composite is 622 $m^2g^{-1}$ while the reduction of the pore size distribution and total pore volume was not observed in the Au/SBA-15 composite. This result consequently confirmed again that the infusion of AuNPs into SBA-15 by using the compressed carbon dioxide solution approach is successful.

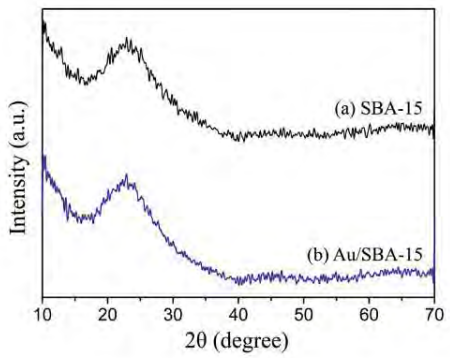


**Figure 8.** XRD patterns of: (a) SBA-15; (b) Au/SBA-15 composite (1:25 Au:PVP nanoparticles to SBA-15; 1:1 ethanol to $scCO_2$).

## Conclusions

We have demonstrated that compressed carbon dioxide solution technique can be used to infuse the AuNPs (2.3 ± 0.6 nm) into mesoporous SBA-15 at moderate experimental conditions (35 °C, 241 bar). The success of infusion of AuNPs into SBA-15 was confirmed by TEM and $N_2$ adsorption-desorption isotherms. Our infusion method could be a promising environmentally friendly technique for fabricating the composites of metal nanostructures/mesoporous materials. In addition, loading content of AuNPs in SBA-15 as well as their catalytic activity are currently under investigation.

**Acknowledgement.** This work was supported in part by grants from the National Science and Technology Development Agency (NSTDA Chair Professor and NANOTEC Center of Excellence), the Thailand Research Fund (TRF), the Kasetsart University Research and Development Institute (KURDI), the Commission on Higher Education, Ministry of Education [the "National Research University Project of Thailand (NRU)" and the "National Center of Excellence for Petroleum, Petrochemical and Advanced Materials (NCE-PPAM)"]. Faculty of Science and the Graduate School of Kasetsart University are also acknowledged. The authors are grateful to Assoc. Prof. Dr. Metta Chareonpanich for the $N_2$ adsorption-desorption measurements of the SBA-15 and Au/SBA-15 composite.

## References

(1) (a) Haruta, M.; Yamada, N.; Kobayashi, T.; Iijima, S. *J. Catal.* **1989,** *115*, 301. (b) Haruta, M.; Tsubota, S.; Kobayashi, T.; Kageyama, H.; Genet, M. J.; Delmon, B. *J. Catal.* **1993,** *144*, 175. (c) Haruta, M. *Chem. Rec.* **2003,** *3*, 75. (d) Comotti, M.; Li, W. C.; Spliethoff, B.; Schüth, F. *J. Am. Chem. Soc.* **2006,** *128*, 917. (e) Zhu, H.; Ma, Z.; Clark, J. C.; Pan, Z.; Overbury, S. H.; Dai, S. *App. Catal., A* **2007,** *326*, 89. (f) Rombi, E.; Cutrufello, M. G.; Cannas, C.; Casu, M.; Gazzoli, D.; Occhiuzzi, M.; Monaci, R.; Ferino, I. *Phys. Chem. Chem. Phys.* **2009,** *11*, 593. (g) Widmann, D.; Liu, Y.; Schuth, F.; Behm, R. J. *J. Catal.* **2010,** *276*, 292.

(2) (a) Hutchings, G. J.; Carrettin, S.; Landon, P.; Edwards, J. K.; Enache, D.; Knight, D. W.; Xu, Y. J.; Carley, A. F. *Top. Catal.* **2006,** *38*, 223. (b) Liu, Y.; Tsunoyama, H.; Akita, T.; Tsukuda, T. *J. Phys. Chem. C* **2009,** *113*, 13457. (c) Liu, Y.; Tsunoyama, H.; Akita, T.; Tsukuda, T. *Chem. Lett.* **2010,** *39*, 159. (d) Su, F. Z.; Liu, Y. M.; Wang, L. C.; Cao, Y.; He, H. Y.; Fan, K. N. *Angew. Chemie. Int. Ed.* **2008,** *47*, 334.

(3) (a) Fu, Q.; Deng, W.; Saltsburg, H.; Flytzani-Stephanopoulos, M. *App. Catal., B* **2005,** 56, 57. (b) Silberova, B. A. A.; Mul, G.; Makkee, M.; Moulijn, J. A. *J. Catal.* **2006,** *243*, 171.

(4) (a) Carrettin, S.; Guzman, J.; Corma, A. *Angew. Chem., Int. Ed.* **2005,** *44*, 2242. (b) Tsunoyama, H.; Sakurai, H.; Ichikuni, N.; Negishi, Y.; Tsukuda, T. *Langmuir* **2004,** *20*, 11293.

(5) (a) Grunwaldt, J. D.; Baiker, A. *J. Phys. Chem. B* **1999,** *103*, 1002. (b) Liu, H.; Kozlov, A. I.; Kozlova, A. P.; Shido, T.; Iwasawa, Y. *Phys. Chem. Chem. Phys.* **1999,** *1*, 2851. (c) Okumura, M.; Tsubota, S.; Haruta, M. *J. Mol. Catal. A* **2003,** *199*, 73. (d) Delannoy, L.; El Hassan, N.; Musi, A.; To, N. N. L.; Krafft, J. M.; Louis, C. *J. Phys. Chem. B* **2006,** *110*, 22471. (e) Kotobuki, M.; Leppelt, R.; Hansgen, D. A.; Widmann, D.; Behm, R. J. *J. Catal.* **2009,** *264*, 67. (f) Carrettin, S.; Concepción, P.; Corma, A.; López Nieto, J. M.; Puntes, V. F. *Angew. Chemie., Int. Ed.* **2004,** *43*, 2538. (g) Widmann, D.; Leppelt, R.; Behm, R. J. *J. Catal.* **2007,** *251*, 437.

(6) Chiang, C. W.; Wang, A.; Wan, B. Z.; Mou, C. Y. *J. Phys. Chem. B* **2005,** *109*, 18042.

(7) Haruta, M. *Gold Bull.* **2004,** *37*, 27.

(8) (a) Guari, Y.; Thieuleux, C.; Mehdi, A.; Reyé, C.; Corriu, R. J. P.; Gomez-Gallardo, S.; Philippot, K.; Chaudret, B. *Chem. Mater.* **2003,** *15*, 2017. (b) Petkov, N.; Stock, N.; Bein, T. *J. Phys. Chem. B* **2005,** *109*, 10737.

(9) (a) Yen, C. W.; Lin, M. L.; Wang, A.; Chen, S. A.; Chen, J. M.; Mou, C. Y. *J. Phys. Chem. C* **2009,** *113*, 17831. (b) Gu, J.; Fan, W.; Shimojima, A.; Okubo, T. *J. Solid State Chem.* **2008,** *181*, 957. (c) Bore, M. T.; Pham, H. N.; Switzer, E. E.; Ward, T. L.; Fukuoka, A.; Datye, A. K. *J. Phys. Chem. B* **2005,** *109*, 2873.

(10) (a) Zhu, J.; Kónya, Z.; Puntes, V. F.; Kiricsi, I.; Miao, C. X.; Ager, J. W.; Alivisatos, A. P.; Somorjai, G. A. *Langmuir* **2003,** *19*, 4396. (b) Zheng, N.; Stucky, G. D. *J. Am. Chem. Soc.* **2006,** *128*, 14278. (c) Turner, M.; Golovko, V. B.; Vaughan, O. P. H.; Abdulkin, P.; Berenguer-Murcia, A.; Tikhov, M. S.; Johnson, B. F. G.; Lambert, R. M. *Nature* **2008,** *454*, 981.

(11) Tsukuda, T.; Tsunoyama, H.; Sakurai, H. *Chem. Asian J.* **2011**, *6*, 736.

(12) Sane, A.; Limtrakul, J. *J. Supercrit.Fluids* **2009,** *51*, 230.

(13) Gupta, G.; Shah, P. S.; Zhang, X.; Saunders, A. E.; Korgel, B. A.; Johnston, K. P. *Chem. Mater.* **2005,** *17*, 6728.

(14) (a) Zhao, D.; Feng, J.; Huo, Q.; Melosh, N.; Fredrickson, G. H.; Chmelka, B. F.; Stucky, G. D. *Science* **1998,** *279*, 548. (b) Chareonpanich, M.; Nanta-ngern, A.; Limtrakul, J. *Mater. Lett.* **2007,** *61*, 5153.

(15) Tsunoyama, H.; Sakurai, H.; Negishi, Y.; Tsukuda, T. *J. Am. Chem. Soc.* **2005,** *127*, 9374.

(16) Brunauer, S.; Emmett, P. H.; Teller, E. *J. Am. Chem. Soc.* **1938,** *60*, 309.

(17) Barrett, E. P.; Joyner, L. G.; Halenda, P. P. *J. Am. Chem. Soc.* **1951,** *73*, 373.

(18) Tanev, P. T.; Pinnavaia, T. J. *Chem. Mater.* **1996,** *8*, 2068.

(19) Rioux, R. M.; Song, H.; Hoefelmeyer, J. D.; Yang, P.; Somorjai, G. A. *J. Phys. Chem. B* **2005,** *109*, 2192.

# Oxidation of Carbon Monoxide by Nitrous Oxide Decomposition on Fe-embedded graphene

*Sippakorn Wannakao[1,2,3], Thana Maihom[1,2,3], Pipat Khongpracha[1,2,3], Bundet Boekfa[2,3,4], and Jumras Limtrakul[1,2,3]**

[1]Laboratory for Computational and Applied Chemistry, Department of Chemistry, Faculty of Science and Center of Nanotechnology, Kasetsart University Research and Development Institute, Kasetsart University, Bangkok 10900, Thailand
[2]Center for Advanced Studies in Nanotechnology and Its Applications in Chemical, Food and Agricultural Industries, Kasetsart University, Bangkok 10900, Thailand
[3]NANOTEC Center of Excellence, National Nanotechnology Center, Kasetsart University, Bangkok 10900, Thailand
[4]Chemistry Department, Faculty of Liberal Arts and Science, Kasetsart University Kamphaeng Saen Campus, Nakhon Pathom 73140, Thailand
*Corresponding author's e-mail address: jumras.l@ku.ac.th

## Introduction

The production of poisonous carbon monoxide (CO) from the combustion of fuel, vehicles, and industrial processes, is considered to be one of the big current environmental issues to be solved.

Many experimental and theoretical studies[1-19], mostly based on transition metals have been made to study the reaction between CO and $O_2$. Among the automobile emitted gases, nitrous oxide ($N_2O$) is very harmful for the environment since it has been found to contribute to the greenhouse gas concern (ca. 300 times more warming potential than $CO_2$) and has also caused ozone depletion. Even though it is not as active as oxygen, the $N_2O$ can be used as one of the oxidizing agents for many reactions. Therefore, the study of the CO oxidation with the $N_2O$ decomposition by one catalyst seems to be the most promising ways of reducing two harmful automobile gases at the same time.

Graphene, is a one layer sheet of carbon atoms which has unique properties and is considered as the new generation of electronic materials.[20-21] With its large surface area, graphene can be used as a support for the heterogeneous catalysis. Many metals have been loaded to the graphene sheet and used to catalyze the CO oxidation with $O_2$, for example, Au, Fe, and Cu.[22-24] Among those, Fe-embedded graphene (Fe-Graphene) is a low cost catalyst that can enable reaction under a low temperature condition. Moreover, the Fe has been recognized as one of the active species for the decomposition of $N_2O$.

In this work, we employed the periodic density functional theory calculation for studying the oxidation of CO by using $N_2O$ decomposition on Fe-Graphene as an oxidizing catalyst. To the best of our knowledge, the Fe-Graphene for $N_2O$ decomposition has never been studied before. This work shows the possibility for utilizing the Fe-Graphene as a bi-functional catalyst for reducing both environmentally harmful gases. This is very important for developing an automobile catalytic converter that can clean up more than one gas by one process.

## Methodology

The spin unrestricted density functional theory with the generalized gradient approximation (GGA) with the Perdew-Burke-Ernzerhof (PBE) functional[25] that is implemented in the DMol3 code[26-27] was used in this study. The double numerical basis set including the d-polarization functional and the DFT semicore pseudopotentials (DSPPs) were employed. By the DSPP scheme, all electron calculations were performed for the C, N and O atoms, and relativistic effect was included for the Fe.

We selected the 4x4 supercell of graphene which was found in literature[22,24] to be sufficient for studying the reaction as a model for this study. The Fe atom was placed at the single vacant site that was introduced in the middle of the model (see Figure 1) due to the high Fe diffusion barrier of the defect compared to the perfect graphene.[23] In order to avoid the interaction of the mirror image, the distance between the sheets was set at 20 Å. The Brillouin zone intregation was calculated with 3 x 3 x 1 k-point sampling for the geometry optimizations. The global orbital cutoff with fine quality was selected. The population analysis was perform by the Hirshfeld charge analysis method[28]. Transition structures were confirmed by one imaginary frequency that corresponded with the reaction coordinate.

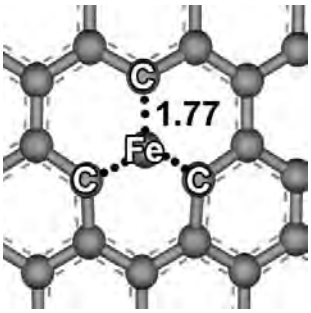


**Figure 1.** The embedded Fe atom on the single vacant site of the graphene

## Results and Discussion

The Fe atom was located on the single vacant site of the graphene with the optimized distance between the Fe atom and the adjacent C atoms being 1.77 Å. The charge of the Fe atom was +0.254e according to the Hirshfeld population analysis. This indicates the charge transfer from the Fe atom to the graphene vacant site.

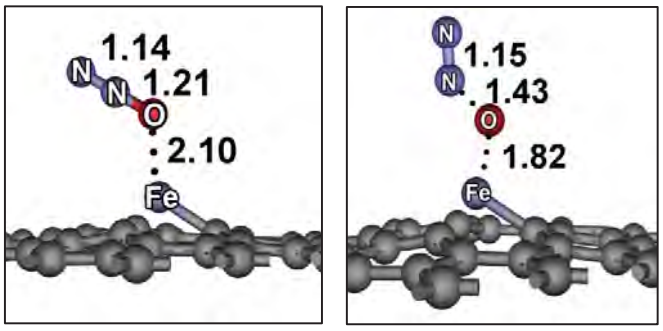


**Figure 2.** The adsorption structure of $N_2O$ (Left) and the transition structure of the $N_2O$ decomposition step (right)

The structure of the $N_2O$ adsorption and the transition state of the $N_2O$ decomposition are showed in Figure 2 above. The $N_2O$ adsorbed on the Fe site by the interaction between the lone pair electron of $N_2O$ oxygen atom and the Fe atom with the Fe–O distance of 2.10 Å and the corresponding adsorption energy was −10.0 kcal/mol. The distance between the O and N atom was elongated to

1.21 Å from 1.19 Å of the gas phase $N_2O$. The charge of the Fe atom was reduced to +0.139e that corresponded with the reducing of the negative charge of the O atom from –0.119e to –0.029e and the summarized charge of $N_2O$ was +0.321e. These indicate the charge transfer from the $N_2O$ molecule to the Fe active site. After the $N_2O$ adsorption, the reaction proceeded via the transition structure (TS1), which the N–O bond breaking to give the oxygen atom attached to the Fe site and the $N_2$ molecule. The O–Fe and O–N distance were 1.82 Å and 1.43 Å, respectively. This step required the activation energy of 8.0 kcal/mol. The Fe atom gained a more positive charge (+0.156e) that is consistent with the more negative O atom (–0.129e) and the summarized charge of the $N_2O$ molecule (–0.075e). This charge transfer might occur by the oxygen transfer from $N_2O$ to the Fe active site. After that, the $N_2$ molecule can easily desorbe by the low desorption energy of 1.7 kcal/mol with the Fe–O intermediate remaining stable with the relative energy of –37.2 kcal/mol. The Fe–O distance was 1.62 Å and the charge of the Fe and O atom were +0.201e and –0.252e respectively. This specie can be the oxidizing site for the CO oxidation.

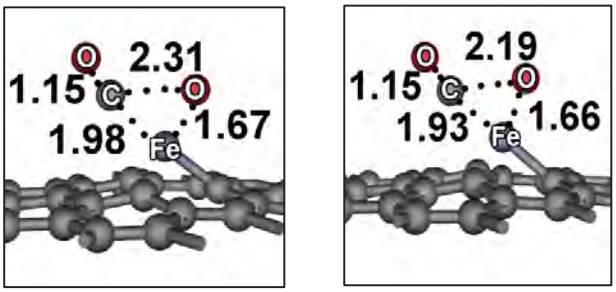


**Figure 3.** The adsorption structure of CO (Left) to the Fe–O site and the transition structure of the $CO_2$ formation step (right)

The CO molecule adsorbed on the Fe–O site with the C atom of the CO bound to the Fe atom with adsorption energy of –10.5 kcal/mol. The Fe–C distance was 1.98 Å while the Fe–O elongated to 1.67 Å. The C atom and the active O atom were ready to react with the distance between C and O of 2.31 Å. The charge of the CO molecule was +0.099e which was obtained from +0.159e of the C atom and –0.060e of the O atom while the Fe atomic charge was +0.125e. This shows that the charge was moving from the O atom of the CO through the C atom to the Fe active site (see Figure 3). The $CO_2$ formation can easily occur by the very low activation energy of 4.0 kcal/mol. The reacting C and O atoms moved close to 2.19 Å. The $CO_2$ desorption energy was 9.6 kcal/mol. The transformation of the $N_2O$ and CO to the highly stable product ($CO_2$ and $N_2$) was exothermic by -80.2 kcal/mol. The decomposition of $N_2O$ molecule was considered to be a rate limiting step due to its higher energy barrier during the reaction pathway that was mentioned above. The energy barrier was lower than that of the $O_2$ activation on the Fe-Graphene from the ref 23. Moreover, the transition structure of the $CO_2$ formation that we found in this work was more favorable than that cited in literature (4.0 kcal vs 25.6 kcal/mol).

From these results, one can imply that the Fe-Graphene exhibits properties of a bi-functional catalyst that can be used for reducing the $N_2O$ and oxidizing the CO by a single step. By the low activation energy, Fe-Graphene might convert these harmful vehicle gases at the ambient condition.

**Conclusions**

The oxidation of carbon monoxide using the nitrous oxide as an oxidizing agent on Fe-Graphene was studied by mean of density functional theory with the PBE functional. Graphene can induce the positive charge of the Fe atom and make it ready to react with the $N_2O$ molecule. The charge transfer between the Fe atom and $N_2O$ molecule was found to be important for the $N_2O$ decomposition step. The activation of $N_2O$ (activation energy was 8.0 kcal/mol) was more favorable than the activation of $O_2$ that was previously studied. After the $N_2O$ decomposition, the CO molecule easily reacts to the Fe–O intermediate obtaining the low activation energy of 4.0 kcal/mol. From this study, we suggest the Fe-Graphene as one candidate for reducing the toxic gases from vehicles at ambient conditions.

**Acknowledgement.** This work was supported in part by grants from the National Science and Technology Development Agency (NSTDA Chair Professor and NANOTEC Center of Excellence), the Thailand Research Fund (to J.L.), the Kasetsart University Research and Development Institute (KURDI), Graduate School KU, the Commission on Higher Education, Ministry of Education ("the National Research University Project of Thailand (NRU)" and "Postgraduate Education and Research Programs in Petroleum and Petrochemicals and Advanced Materials"), under the Royal Golden Jubilee Ph.D. program from the Thailand Research Fund (to S.W.).

**References**

(1) Ackermann, M. D.; Pedersen, T. M.; Hendriksen, B. L. M.; Robach, O.; Bobaru, S. C.; Popa, I.; Quiros, C.; Kim, H.; Hammer, B.; Ferrer, S.; Frenken, J. W. M. *Phys. Rev. Lett.* **2005**, *95*, 255505.
(2) Alavi, A.; Hu, P.; Deutsch, T.; Silvestrelli, P. L.; Hutter, J. *Phys. Rev. Lett.* **1998**, *80*, 3650.
(3) Bleakley, K.; Hu, P. *J. Am. Chem. Soc.* **1999**, *121*, 7644.
(4) Chen, M. S.; Cai, Y.; Yan, Z.; Gath, K. K.; Axnanda, S.; Goodman, D. W. *Surf. Sci.* **2007**, *601*, 5326.
(5) Eichler, A. *Surf. Sci.* **2002**, *498*, 314.
(6) Eichler, A.; Hafner, J. *Surf. Sci.* **1999**, *435*, 58.
(7) Kandoi, S.; Gokhale, A. A.; Grabow, L. C.; Dumesic, J. A.; Mavrikakis, M. *Catal. Lett.* **2004**, *93*, 93.
(8) Kimble, M. L.; Castleman Jr, A. W.; Mitrić, R.; Bürgel, C.; Bonacic-Koutecky, V. *J. Am. Chem. Soc.* **2004**, *126*, 2526.
(9) Krenn, G.; Bako, I.; Schennach, R. *J. Chem. Phys.* **2006**, *124*, 144703.
(10) Liu, D. J. *J. Phys. Chem. C* **2007**, *111*, 14698.
(11) Liu, W.; Zhu, Y. F.; Lian, J. S.; Jiang, Q. *J. Phys. Chem. C* **2007**, *111*, 1005.
(12) Nakai, I.; Kondoh, H.; Amemiya, K.; Nagasaka, M.; Nambu, A.; Shimada, T.; Ohta, T. *J. Chem. Phys.* **2004**, *121*, 5035.
(13) Nakai, I.; Kondoh, H.; Shimada, T.; Resta, A.; Andersen, J. N.; Ohta, T. *J. Chem. Phys.* **2006**, *124*, 224712.
(14) Oh, S. H.; Hoflund, G. B. *J. Catal.* **2007**, *245*, 35.
(15) Salo, P.; Honkala, K.; Alatalo, M.; Laasonen, K. *Surf. Sci.* **2002**, *516*, 247.
(16) Sljivancanin, Z.; Hammer, B. *Phys. Rev. B* **2010**, *81*, 121413.
(17) Stampfl, C.; Scheffler, M. *Surf. Sci.* **1999**, *433*, 119.
(18) Zhang, C. J.; Baxter, R. J.; Hu, P.; Alavi, A.; Lee, M. H. *J. Chem. Phys.* **2001**, *115*, 5272.
(19) Zhang, C. J.; Hu, P. *J. Am. Chem. Soc.* **2001**, *123*, 1166.
(20) Geim, A. K.; Novoselov, K. S. *Nat. Mater.* **2007**, *6*, 183.
(21) Novoselov, K. S.; Geim, A. K.; Morozov, S. V.; Jiang, D.; Zhang, Y.; Dubonos, S. V.; Grigorieva, I. V.; Firsov, A. A. *Science* **2004**, *306*, 666.
(22) Song, E. H.; Wen, Z.; Jiang, Q. *J. Phys. Chem. C* **2011**, *115*, 3678.
(23) Li, Y.; Zhou, Z.; Yu, G.; Chen, W.; Chen, Z. *J. Phys. Chem. C* **2010**, *114*, 6250.
(24) Lu, Y. H.; Zhou, M.; Zhang, C.; Feng, Y. P. *J. Phys. Chem. C* **2009**, *113*, 20156.
(25) Delley, B. *Phys. Rev. Lett.* **1996**, *77*, 3865.
(26) Delley, B. *J. Chem. Phys.* **1990**, *92*, 508.
(27) Delley, B. *J. Chem. Phys.* **2000**, *113*, 7756.
(28) Hirshfeld, F. L. *Theor. Chim. Acta* **1977**, *44*, 129.

# Precisely Size-controlled Metal Nanoparticles (Au, Pd and Pt) Inserted into Metal-Organic Frameworks (MOFs): Synthesis and Catalytic Properties

*Sudarat Yadnum[1,2,3], Pipat Khongpracha[1,2,3], Chompunuch Warakulwit[1,2,3] and Jumras Limtrakul[1,2,3*]*

[1]Laboratory for Computational and Applied Chemistry, Department of Chemistry, Faculty of Science and Center of Nanotechnology, Kasetsart University Research and Development Institute, Kasetsart University, Bangkok 10900, Thailand
[2]Center for Advanced Studies in Nanotechnology and Its Applications in Chemical, Food and Agricultural Industries, Kasetsart University, Bangkok 10900, Thailand
[3]NANOTEC Center of Excellence, National Nanotechnology Center, Kasetsart University, Bangkok 10900, Thailand
[*]Corresponding author: Tel.: +662 562 5555 ext 2169, Fax: +662 562 5555 ext 2176, E-mail address: jumras.l@ku.ac.th

## Introduction

Metal organic frameworks (MOFs) have attracted much attention in the past decade due to their high porosity and high specific surface area making them suitable for many applications, including gas storage, separations, and catalysis[1-7]. For the latter, the unique structure of MOFs, resulted from the combination of the long-range order of a solid-state template material with a tunable dimensionality and chemical tailoring of the inner surface of the channels and cavities, makes them promising candidates for embedding and supporting functional nanomaterials. A number of functional nanoparticles for embedding, e.g. Cu, Ru, Pd, Au, Ag and Pt metal nanoparticles, into the cavities of MOFs, are relevant for many applications, especially for heterogeneous catalysis, have been achieved by using various preparation methods. These methods include gas-phase infiltration, solid grinding (SG), and solution impregnation[8-15]. In many cases, the resulting metal@MOFs catalysts exhibited unique catalytic activity[16].

Among MOFs that have been previously reported, the MIL-101, a zeolite-type MOF, has been known to possess a large surface area (Brunauer-Emmett-Teller (BET) surface area of ca. 3000 $m^2 g^{-1}$), large pore size (of ca. 29-34 Å), and good chemical resistance to water and organic solvents. These properties are desirable for depositing small metal nanoparticles by using a colloidal deposition preparation method[17,18]. The MIL-101 supported gold nanoparticles (Au/MIL-101) was recently synthesized for catalytic application for aerobic oxidation of alcohols. The prepared Au/MIL-101 exhibited extremely high catalytic activities in the liquid-phase aerobic oxidation of a wide range of alcohols under ambient conditions in the absence of water or base[16]. The electron donation of the aryl rings of organic linker molecules composed in the MIL-101 to the surface of gold nanoparticles through the π-bond interactions is suggested to facilitate the formation of anionic Au leading to the favorable activation of $O_2$ on the Au surfaces[19-24]. This study raises the question of how the electron donation of the aryl rings to the surface of other metal nanoparticles, such as Pd and Pt, could affect the reaction catalyzed by those metal nanoparticles The insight into the combined role between an intrinsic catalytic activity of precisely size-controlled metal nanoparticles (Au, Pd and Pt) and the electron donation effect gained from the organic linker of MOFs on the activity and selectivity of the reaction remains a great challenge.

In this research, we aim to synthesize the noble metal nanoparticles of gold, palladium, and platinum encapsulated into the MIL-101, in order to be heterogeneous catalysts for oxidation of alcohols, by using colloidal deposition of the metal nanoparticles stabilized by poly(N-vinyl-2-pyrrolidone) (PVP). This method was used for preparing the Au/MIL-101 in the previous work[16]. The catalytic activity and selectivity of the obtained metal/MIL-101 hybrid materials in the aerobic oxidation of alcohols will be further investigated.

## Experimental Method

**Raw chemicals.** Chromium nitrate ($Cr(NO_3)_3.9H_2O$, Sigma-Aldrich, 99%), Terephthalic acid ($C_8H_6O_4$, Sigma-Aldrich, 98%), Polyvinylpyrrolidole (K-30, wt~40,000, Fluka), Sodium borohydride ($NaBH_4$, Sigma-Aldrich, 99%), Potassium tetrachloro palatinate (II) ($K_2PtCl_4$, Sigma-Aldrich, 99.9%), Gold (III) chloride trihydrate ($HAuCl_4.3H_2O$, Sigma-Aldrich, 99.9%), Palladium (II) chloride ($PdCl_2$, Sigma-Aldrich, 99.9%), Hydrofluoric acid (HF, 48%), Ethyl alcohol ($C_2H_5OH$, 98%) were used. The deionized water was made in our laboratory.

### Catalyst Preparation

**Synthesis of MIL-101.** The MIL-101 was prepared by using the previously published hydrothermal reaction method [25]. Briefly, $Cr(NO_3)_3 \cdot 9H_2O$ (5 mmol), HF (5 mmol), terephthalic acid (5 mmol), and DI water (24 mL) were mixed and reacted at 220 ºC for 8 h in an autoclave under vacuum. After that, the reaction mixture was allowed to cool down slowly to room temperature for 12 h. Next, in order to remove the residual carboxylic acid left in the form of large white crystals, the mixture was then filtered through a large-pore filter, a nylon membrane filter with pore diameter of 41 μm (Spectra/Mesh Nylon Macroporous filters). The MIL-101 product remained in the filtrate part. Later, the MIL-101 product was separated from the filtrate, which contained the unreacted terephthalic acid, by using a small-pore paper filter (Whatman, No. 1). The solid that remains on the filter paper was then washed by a solution of 95 % v/v ethanol in water and further taken out from the filter paper. The sample powder of MIL-101 was obtained after soaking the washed solid in a solution of 95 % v/v ethanol in water at 80 ºC for 24 h and followed drying at 150 ºC under vacuum overnight.

**Preparation of Au:PVP, Pd:PVP and Pt:PVP nanoparticles.** The metal colloids stabilized by PVP were synthesized by following Tsunoyama's method[26]. Typically, hydrogen tetrachloroaurate tetrahydrate ($HAuCl_4.3H_2O$), tetrachloropalladate ($PdCl_4$) and potassium tetrachloroplatinate ($K_2PtCl_4$) were used as metal sources. Poly(N-vinyl-2-pyrrolidone) (PVP) with an average molecular weight of ca. 40 kDa was used as a stabilizer. Sodium borohydride ($NaBH_4$) was used as a reducing agent. 555.5 mg (0.0139 mmol) of PVP was added into the aqueous solution of each metal source (1 mM, 50 mL). The resulting mixture was placed in an ice bath at 0 ºC and stirred for 30 min. Then, an aqueous solution of $NaBH_4$ (100 mM, 5 mL) was rapidly added into the mixture under vigorous stirring. After the addition of the $NaBH_4$ aqueous solution, the mixture was further stirred for 1h. For the case of Au:PVP, after addition of the $NaBH_4$ aqueous solution, the color of the reaction mixture immediately turned from pale yellow to dark brown, indicating the formation of small Au nanoclusters (NCs). For the Pd:PVP case and Pt:PVP, there is no change in color of the reaction mixtures observed. The resulting mixtures of metal:PVP were used as starting materials for the next colloidal deposition step.

**Synthesis of metal/MIL-101 by colloidal deposition of the metal nanoparticles stabilized by PVP.** Typically, in order to support the metal nanoparticles onto the MIL-101, 0.5 g of the synthesized MIL-101 powder was added to 4 mL of DI water and then dispersed in the water by sonicating in an ultrasonic bath for 20s. As-prepared mixtures of metal:PVP were sonicated for 20s before using. Two mixtures were then mixed and stirred in an ice

bath at 0 ºC for 4 h. The metal/MIL-101 was obtained after filtration of the finally obtained mixture by using a normal paper filter (Whatman, No. 1). The metal/MIL-101 sample was washed with DI water and then dried under $N_2$ gas.

**Characterization** Powder X-ray diffraction (XRD) patterns of the samples were obtained by a Rigaku diffractometer (TTRAX III) using Cu Kα radiation (for the low angle XRD pattern) operating at an accelerating voltage of 50 kV and a current of 300 mA and a Philips diffractometer (X'Pert Pro) with Cu-Kα radiation (for the high angle XRD pattern) operating at an accelerating voltage of 40 kV and a current of 30 mA. The BET surface area, pore size and pore volume measurements were performed by using the $N_2$ adsorption/desorption isotherms characterization measured at 77 K on a Micromeritics ASAP 2010 instrument. The size and morphology of MIL-101 and metal/MIL-101 were investigated by using a transmission electron microscope (TEM) and scanning electron microscope (SEM).

**Results and Discussion**

**Characterization of MIL-101.** Low angle powder X-ray diffraction pattern recorded from 2 to 7 degrees of 2θ by using the step-size of 0.01 degrees and the scan speed of 0.5 degrees/minute are shown in Figure 1a. The high angle XRD pattern recorded from 5 to 50 degrees using the step-size of 0.01 degrees and the scan speed of 0.5 degrees/minute are shown in Figure 1b. The diffraction peak positions and relative diffraction intensities of MIL-101 as synthesized were found to correspond with those obtained in the previous literature[25] reported for MIL-101, confirming the obtaining of MIL-101.

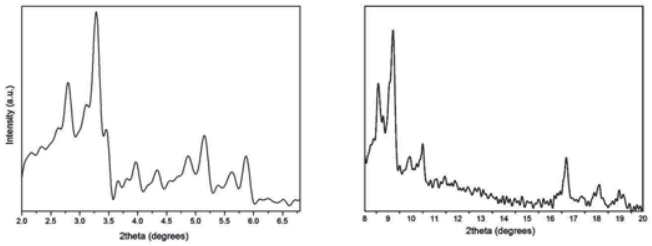


**a)** **b)**

**Figure 1.** (a) Low angle and (b) high angle XRD patterns of the synthesized MIL-101 sample.

The morphology of MIL-101 was studied by using scanning electron microscopy (SEM). The SEM images with low and high magnifications of the synthesized MIL-101 are shown in Figures 2a and 2b, respectively. It can be seen that the obtained powder of MIL-101 was composed of cubo-octahedral crystals with quite uniform size in the range of 1-2 μm in diameter (see Figure 2). This result agrees well with that obtained in the previous report of MIL-101[25].

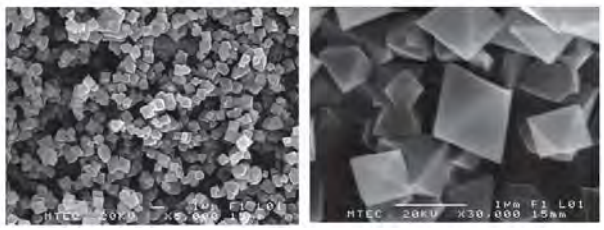

**a)** **b)**

**Figure 2.** (a) Low magnification and (b) high magnification SEM images of the as-synthesized MIL-101.

For the TEM investigation of MIL-101 sample, the dry powder of as-synthesized MIL-101 was dispersed in absolute ethanol for a few minutes by using an ultrasonic bath and then deposited on a carbon-coated Cu TEM grid. Then the grid was let in air until dry. TEM images of MIL-101 confirm the nearly perfect cubo-octahedral crystal structure of the synthesized MIL-101 (see Figure 3).

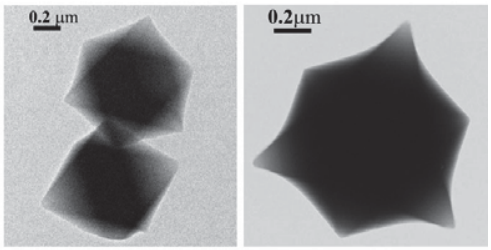


**Figure 3.** TEM images of the as-synthesized MIL-101 showing the nearly perfect cubo-octahedral crystal structure.

The BET surface area, pore size and pore volume of the MIL-101 samples were determined by using the $N_2$ adsorption/desorption measurement. Before the measurement, the sample was degassed under vacuum overnight at 100 ºC. The BET surface area ($S_{BET}$), pore size and pore volume ($V_{pore}$) of the obtained MIL-101 were 3,384 $m^2/g$, 25.428 Å and 1.611 $cm^3/g$, respectively. These values indicate that the synthesized MIL-101 has a high specific surface area and pore volume that could facilitate the inclusion of metal nanoparticles into the structure of MIL-101. Furthermore, the obtained BET surface area is in good agreement with the previously reported value of MIL-101[25].

**Characterization of metal/MIL-101.** Due to the small size (sub-ten nanometer) of the metal nanoparticles synthesized by using PVP as a stabilizer in which the XRD pattern of metal nanoparticles was not expected to be observed in the metal/MIL-101 sample, the XRD pattern of the metal/MIL-101 was not recorded. The SEM and TEM images of the synthesized Au/MIL-101, Pd/MIL-101 and Pt/MIL-101 are shown in Figures 4, 5 and 6, respectively. It can be seen from the SEM image (see Figures 4a, 5a and 6a) that the cubo-octahedral crystal structure of the MIL-101 still remained after addition of the metal:PVP nanoparticles followed by calcination at 200°C. This indicates that the colloidal deposition method used for supporting the metal nanoparticles onto the MIL-101 structure did not destroy the structure of MIL-101.

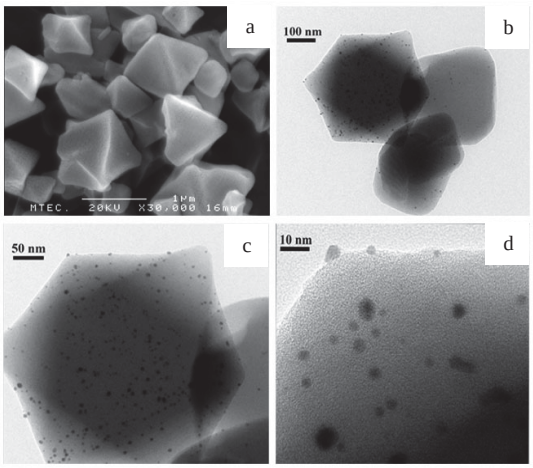


**Figure 4.** (a) SEM and (b-d) TEM images of the synthesized Au/MIL-101.

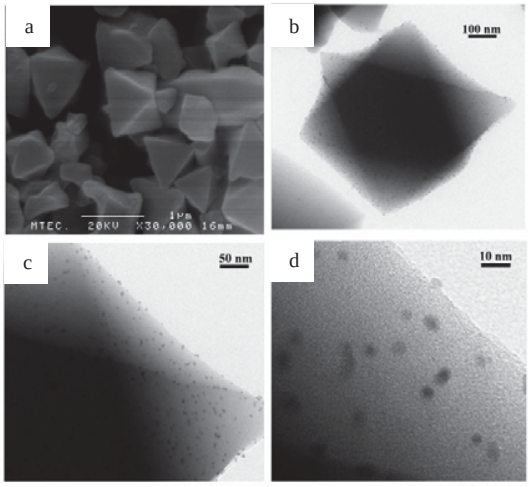


**Figure 5.** (a) SEM and (b-d) TEM images of the synthesized Pd/MIL-101.

From the TEM images of the metal/MIL-101 (Figures 4b-4d, 5b-5d and 6b-6d), it is found that the Au, Pd and Pt nanoparticles with average diameters of 2.59 ± 1.27, 2.80 ± 0.67 and 1.62 ± 0.41 nm, respectively (which are in good agreement with the MIL-101 pore size of about 2.9-3.4 Å[25]) were successfully supported onto the MIL-101 structure by using the simple colloidal deposition method used in this work. The high magnification TEM images of the metal/MIL-101 (Figures 4d, 5d and 6d) show that all the Au and Pd nanoparticles and some Pt nanoparticles were highly dispersed in the structure of MIL-101 support whereas a part of the Pt nanoparticles tended to form an aggregate structure during the preparation. Due to the MIL-101 pore size of about 2.9-3.4 Å, which is much smaller than the size of the aggregate structure found (the diameter is in the order of tens of nanometers), it is suggested that the Pt nanoparticles with aggregate structure were located onto the external surface of MIL-101 whereas the highly dispersed part was located in the porous channels of MIL-101. This aggregate structure further implies the weak interaction between the MIL-101 surface and Pt:PVP nanoparticles during the colloidal deposition.

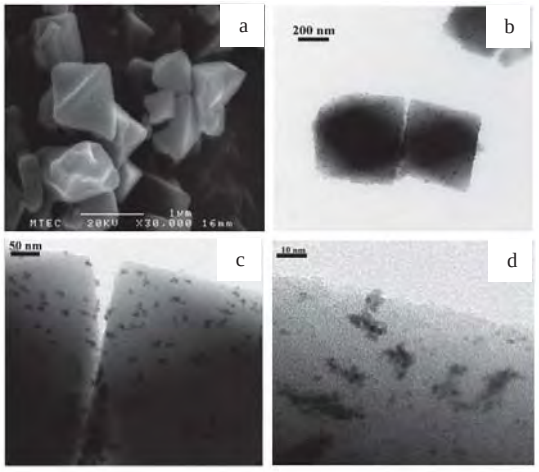


**Figure 6.** (a) SEM and (b-d) TEM images of the synthesized Pt/MIL-101

**Conclusions**

In this work, we prepared precisely size-controlled metal nanoparticles (Au, Pd and Pt) embedded into metal-organic frameworks (MIL-101) by using the simple colloidal deposition followed by calcination. The XRD, SEM, TEM and $N_2$ adsorption/desorption characterization of the as-synthesized MIL-101 confirmed the characteristic of MIL-101 showing the successful synthesis achieved by using the hydrothermal method. The SEM and TEM characterizations of the prepared Au/MIL-101, Pd/MIL-101, Pt/MIL-101 sample show that preparation method used allows preservation of the MIL-101 structure. The high magnification image TEM images of the prepared Au/MIL-101, Pd/MIL-101, Pt/MIL-101 sample show that Au, Pd and Pt nanoparticles with average diameters of 2.59 ± 1.27, 2.80 ± 0.67 and 1.62 ± 0.41 nm, respectively were successfully supported both in the porous channels and onto the external surface of MIL-101. Observation of a part of Pt nanoparticles with the aggregate structure leads us to suggest that the Pt:PVP nanoparticles had weaker interaction to the MIL-101 surface than other metal nanoparticles, Au:PVP and Pd:PVP nanoparticles. This implies the difference on intrinsic properties of metal nanoparticles which could further lead to the difference in catalytic activity and selectivity for oxidation of alcohols.

**Acknowledgment** This work was supported in part by grants from the National Science and Technology Development Agency (2009 NSTDA Chair Professor funded by the Crown Property Bureau under the management of the National Science and Technology Development Agency and NANOTEC Center of Excellence funded by the National Nanotechnology Center), Kasetsart University Research and Development Institute (KURDI), the Thailand Research Fund (TRF), the Commission on Higher Education, Ministry of Education (the "National Research University Project of Thailand (NRU)" and the "National Center of Excellence for Petroleum, Petrochemical and Advanced Materials (NCE-PPAM)") and the Development and Promotion of Science and the Royal Golden Jubilee (RGJ). The Kasetsart University Graduate School is also acknowledged.

**References**


(1) Mueller, U.; Schubert, M.; Teich, F.; Puetter, H.; Schierle-Arndt, K.; Pastre, J. *J. Mater. Chem* **2006**, *16*, 626.
(2) Kitagawa, S.; Kitaura, R.; Noro, S.-i. *Angew. Chem., Int. Ed* **2004**, *43*, 2334.
(3) Lee, J.; Farha, O. K.; Roberts, J.; Scheidt, K. A.; Nguyen, S. T.; Hupp, J. T. *Chem. Soc. Rev* **2009**, *38*, 1450.
(4) Zhao, X.; Xiao, B.; Fletcher, A. J.; Thomas, K. M.; Bradshaw, D.; Rosseinsky, M. J. *Science* **2004**, *306*, 1012.
(5) Dincă, M.; Long, J. R. *Angew. Chem., Int. Ed* **2008**, *47*, 6766.
(6) Yaghi, O. M.; O'Keeffe, M.; Ockwig, N. W.; Chae, H. K.; Eddaoudi, M.; Kim, J. *Nature* **2003**, *423*, 705.
(7) Furukawa, H.; Ko, N.; Go, Y. B.; Aratani, N.; Choi, S. B.; Choi, E.; Yazaydin, A. O.; Snurr, R. Q.; O'Keeffe, M.; Kim, J.; Yaghi, O. M. *Science*, **2010**, *329*, 424.
(8) Schroder, F.; Esken, D.; Cokoja, M.; van den Berg, M. W. E.; Lebedev, O. I.; Van Tendeloo, G.; Walaszek, B.; Buntkowsky, G.; Limbach, H.-H.; Chaudret, B.; Fischer, R. A. *J. Am. Chem. Soc.* **2008**, *130*, 6119.
(9) Mueller, M.; Hermes, S.; Kähler, K.; van den Berg, M. W. E.; Muhler, M.; Fischer, R. A. *Chem. Mater.* **2008**, *20*, 4576.
(10) Hermes, S.; Schröter, M.-K.; Schmid, R.; Khodeir, L.; Muhler, M.; Tissler, A.; Fischer, R. W.; Fischer, R. A. *Angew. Chem., Int. Ed.* **2005**, *44*, 6237.
(11) Houk, R. J. T.; Jacobs, B. W.; Gabaly, F. E.; Chang, N. N.; Talin, A. A.; Graham, D. D.; House, S. D.; Robertson, I. M.; Allendorf, M. D. *Nano Lett.* **2009**, *9*, 3413.
(12) El-Shall, M. S.; Abdelsayed, V.; Khder, A. E. R. S.; Hassan, H. M. A.; El-Kaderi, H. M.; Reich, T. E. *J. Mater. Chem* **2009**, *19*, 7625.
(13) Kleist, W.; Maciejewski, M.; Baiker, A. *Thermochim Acta*, **2010**, *499*, 71.
(14) Ishida, T.; Nagaoka, M.; Akita, T.; Haruta, M. *Chem.–Eur. J.***2008**, *14*, 8456.
(15) Jiang, H.-L.; Liu, B.; Akita, T.; Haruta, M.; Sakurai, H.; Xu, Q. *J. Am. Chem. Soc.* **2009**, *131*, 11302.
(16) Liu, H.; Liu, Y.; Li, Y.; Tang, Z.; Jiang, H. *J. Phys. Chem. C*, **2010**, *114*, 13362.
(17) Pan, Y.; Yuan, B.; Li, Y.; He, D. *Chem. Commun*, **2010**, *46*, 2280.
(18) Yuan, D.; Zhao, D.; Sun, D.; Zhou, H.-C. *Angew. Chem., Int. Ed.*, **2010**, *49*, 5357.
(19) Salisbury, B. E.; Wallace, W. T.; Whetten, R. L. *Chemical Physics* **2000**, *262*, 131.
(20) Okumura, M.; Kitagawa, Y.; Haruta, M.; Yamaguchi, K. *Chem. Phys. Lett.* **2001**, *346*, 163.
(21) Stolcic, D.; Fischer, M.; Ganteför, G.; Kim, Y. D.; Sun, Q.; Jena, P. *J. Am. Chem. Soc.* **2003**, *125*, 2848.
(22) Stiehl, J. D.; Kim, T. S.; McClure, S. M.; Mullins, C. B. *J. Am. Chem. Soc.* **2004**, *126*, 1606.
(23) Barton, D. G.; Podkolzin, S. G. *J. Phys. Chem. B* **2004**, *109*, 2262.
(24) Chowdhury, B.; Bravo-Suarez, J. J.; Mimura, N.; Lu; Bando, K. K.; Tsubota, S.; Haruta, M. *J. Phys. Chem. B* **2006**, *110*, 22995.
(25) Férey, G.; Mellot-Draznieks, C.; Serre, C.; Millange, F.; Dutour, J.; Surblé, S.; Margiolaki, I. *Science* **2005**, *309*, 2040.
(26) Tsunoyama, H.; Sakurai, H.; Negishi, Y.; Tsukuda, T. *J. Am. Chem. Soc.* **2005**, *127*, 9374.

# Shape-selective Hydrocarbon Cracking of *n*-hexane on MCM-22 zeolite

*Supakit Tiewcharoen*[1,2], *Bundet Boekfa*[1,2,4], *Piti Treesukol*[1,2], *Thana Maihom*[2,3,4] *and Jumras Limtrakul*[2,3,4]*

[1]Chemistry Department, Faculty of Liberal Arts and Science, Kasetsart University Kamphaeng Saen Campus, Nakhon Pathom 73140, Thailand
[2]Center for Advanced Studies in Nanotechnology and Its Applications in Chemical,Food and Agricultural Industries, Kasetsart University, Bangkok 10900, Thailand
[3]Laboratory for Computational and Applied Chemistry, Department of Chemistry, Faculty of Science and Center of Nanotechnology, Kasetsart University Research and Development Institute, Kasetsart University, Bangkok 10900, Thailand
[4]NANOTEC Center of Excellence, National Nanotechnology Center, Kasetsart University,Bangkok 10900, Thailand
*Corresponding author: Tel.: +662 562 5555 ext 2169, Fax: +662 562 5555 ext 2176, E-mail address: jumras.l@ku.ac.th

## Introduction

Zeolites are widely used as heterogeneous catalysts for petroleum refineries and the petrochemical industry. With its size and shape-selectivity, many petrochemical processes take advantage of this material as catalysts, for instance in hydrocarbon cracking, isomerization and oligomerization, etc. The hydrocarbon cracking is an important reaction to break down the large-hydrocarbon crude oil into light-hydrocarbons fuel[1-2].

The hydrocarbon cracking reaction on zeolites have been studied both experimentally[3-5] and theoretically[6-14]. The mechanism is proposed via both a monomoleculear mechanism and a bimolecular mechanism. With the low pressure of hydrocarbons and high reaction temperature, the mechanism is believed to be a monomolecular mechanism[3-4]. This mechanism proceeds through carbonium ion intermediate and gives alkane and alkene products. Maihom et al.[14] studied the *n*-hexane cracking on H-FAU and H-ZSM-5 with the M06-2X functional. The reaction mechanism was proposed to be two steps: 1) protonation to form a hexonium intermediate and 2) decomposition to propane and propene products. They found that the first step was the rate determining step with activation energies of 45.7 and 45.8 kcal/mol for H-FAU and H-ZSM-5, respectively. This study provided us the understanding of the mechanism occurring in the large- and medium- pore zeolites.

MCM-22 (MWW framework) is an outstanding large pore zeolite[15-16]. It contains two different pore sizes, two-dimensional sinusoidal 10T (1.4 Å x 5.1 Å) channels and large cylindrical supercages 12T (7.1 Å x 18.2 Å). Katada et al.[17] studied the cracking of *n*-hexane and octane on several zeolites, such as H-MOR, H-MCM-22, H-ZSM-5. The adsorption energies were measured to be 7.6, 14.6, and 11.0 kcal/mol for H-FAU, H-ZSM-5 and H-MCM-22 zeolite, respectively. For the cracking reaction of *n*-hexane, the activation energies were reported to be 41.1, 36.5 and 30.4 kcal/mol, respectively. These results illustrated the performance of H-MCM-22 zeolite on the hydrocarbon cracking reaction.

In this study, we performed the quantum chemical calculation to study the *n*-hexane cracking on H-MCM-22 zeolite. We employed the ONIOM methodology[18] which is capable of predicting the adsorption and reaction mechanism in the zeolite framework[19-23]. The single point energy at the large quantum cluster with M06-2X function[19-25] was carried out to improve the energy. Our calculations are in good agreement with the previous experimental data which provide the detailed understanding on the mechanism.

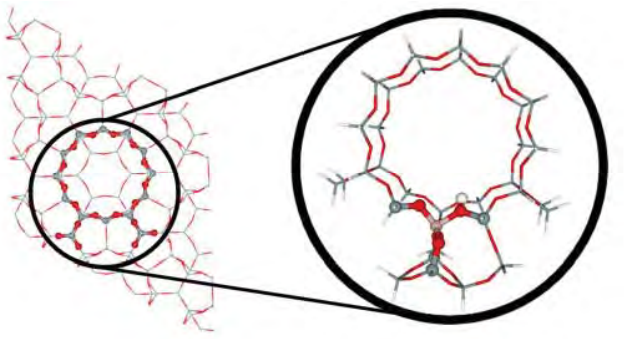

**Figure 1.** Presentation of H-MCM-22 models 5T:34T ONIOM model. Atoms treated with the M06-2X level of theory are shown in balls, whereas the areas treated with the HF functional are shown in wireframes.

## Methodology

The geometry of the H-MCM-22 zeolite was obtained from the crystallographic structure[16]. The Al atom substituted for the Si atom at the T1 position. The 34T quantum cluster was utilized to represent the 10T sinusoidal and 12T channels of the supercage of H-MCM-22, as shown in Fig. 1. For computational cost efficiency, the ONIOM scheme was applied on the 34T model of H-MCM-22 zeolite[20]. The 5T quantum region of the Brønsted acid site was assigned to be the inner layer while the 34T model was the outer layer. The geometries were optimized at the ONIOM model 5T:34T with the M06-2X/6-31G(d,p):HF/3-21G level of theory. To improve the energy, the single point at the high level M06-2X/6-31G(d,p) was performed. Only the active region ($AlSi_4O_4H$) and the probe molecule were allowed to relax while the rest was kept fixed with the crystallographic coordinate. All calculations were performed using the Gaussian 03 program[26] incorporated with the Minnesota Density Functionals module 3.1 by Zhao and Truhlar[25,27].

## Results and Discussion

**Molecular cluster and Adsorption of *n*-hexane with H-MCM-22.** The 34T quantum cluster of H-MCM-22 zeolite, shown in Figure 1, is modeled to cover the intersection region between the 10T sinusoidal and 12T channels of the supercage where the adsorbates prefer to locate. The Brønsted acid site in H-MCM-22 is modeled to be the inner layer 5T quantum cluster while the extended framework is represented by the lager 34T cluster. The Brønsted acid O1-Hz bond length is 0.97 Å. The Al ··· Hz distance is 2.44 Å, which compared well with the experimental data (2.38-2.48 Å)[28].

The *n*-hexane adsorbed on H-MCM-22 at the intersection region between the 10T sinusoidal and 12T channels of the supercage of MCM-22 [AD, Figure 2a]. In this study, the adsorption through the central C-C bond of *n*-hexane is focused because the main propane and propene products are produced from central C-C bond breaking. The O1-Hz bond is not significantly changed due to weak interaction. The distances between *n*-hexane and the proton of Brønsted acid are 2.75 and 2.82 Å for Hz ··· C3 and Hz ··· C4, respectively. The calculated adsorption energy of -11.1 kcal/mol with the M06-2X//ONIOM(M06-2X:HF) method agrees well with experiment report of -11.0 kcal/mol[17].

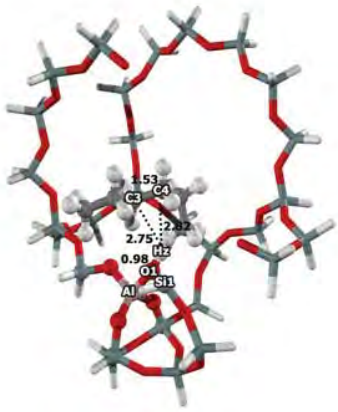


(a) Adsorption (AD),
ΔE= -11.1 kcal/mol

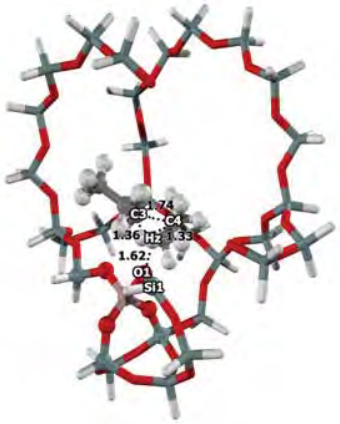


(b) Transition State (TS),
ΔE= 26.1 kcal/mol

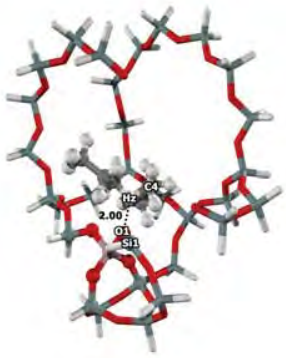


(c) 3-C-hexonium intermediate (IN),
ΔE= 24.4 kcal/mol

**Figure 2.** Optimized structure of Adsorption (a), Transition State (b) and 3-C-hexonium intermeidate (c) of *n*-hexane on H-MCM-22 zeolite. Distances are in Ås.

**The Cracking Reaction of *n*-hexane with H-MCM-22**. The cracking reaction of n-hexane is studied in the H-MCM-22 zeolite. Based on the previous calculation, the reaction mechanism is proposed through the two steps: (1) Protonation of n-hexane and (2) Decomposition of the Hexonium intermediate to produce propane and propene products. This study is focused on the protonation of n-Haxane which is the rate determination step of reaction.

The *n*-hexane molecule is adsorbed in the intersection region of H-MCM-22 with an adsorption energy -11.1 kcal/mol [AD, Figure 2a]. The transition state is the protonation of acidic proton to the central C-C bond of *n*-hexane to form the adsorbed 3-C-hexonium intermediate. At the transition state [TS, Figure 2b], the H1 migrates to the C3-C4 bond of *n*-hexane. The O1-Hz bond distance increases from 0.98 Å to 1.62 Å and the C3-C4 bond increases from 1.53 Å to 1.74 Å. The distances Hz-C3 and Hz-C4 are 1.36 and 1.33 Å. The transition state structure has been confirmed by a single imaginary frequency at 828.5i $cm^{-1}$. The calculated activation energy is 37.2 kcal/mol. This activation energy is lower than the previous calculations on H-ZSM-5 and H-FAU which are 45.8 and 45.7 kcal/mol, respectively. The lower activation energy for *n*-hexane cracking on H-MCM-22 agrees well with experimental data [17].

The product of this step is the 3-C-hexonium intermediate [IN, Figure 2c]. The O1-Hz distance is 1.90 Å while the Hz-C1 and Hz-C2 distances are 1.23 and 1.27 Å, respectively. The 3-C-hexonium interacts with the zeolite surface with the relative energy of 24.4 kcal/mol. The reaction is an endothermic reaction with the reaction energy of 24.4 kcal/mol. This energy is lower than the previous calculation, 33.6 and 26.9 kcal/mol for H-FAU and H-ZSM-5, respectively. This was due to the lower activation energy of the transition state in H-MCM-22.

For the bare 5T quantum cluster, the calculated adsorption energy of *n*-hexane on H-MCM-22 is -6.0 kcal/mol. The calculated activation energy for *n*-hexane cracking is 50.9 kcal/mol. The zeolite framework stabilizes the adsorption complex and the transition state structure by about 54 % for its adsorption energy and 37% for its activation energy. Our results show that H-MCM-22 can stabilize the adsorption structure and transition complexes that give lower activation energy for *n*-hexane cracking.

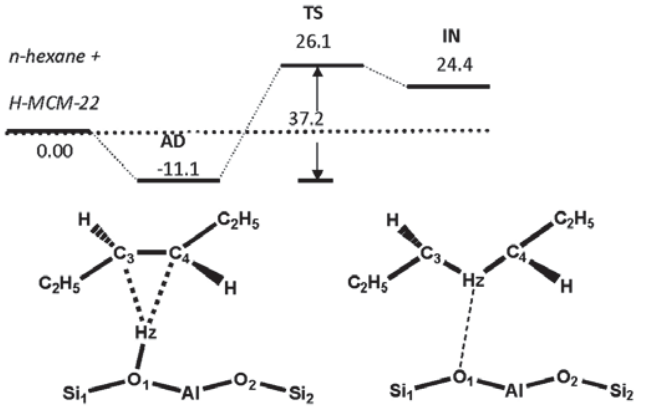


**Figure 3.** Potential energy diagram of the *n*-hexane to 3-c-hexonium intermediate on the 34T// ONIOM (5T:34T) with M06-2X//ONIOM (M06-2X:HF) method (kcal/mol).

**Conclusion**

The hydrocarbon cracking of *n*-hexane over H-MCM-22 zeolite has been calculated via the ONIOM (5T:34T) M06-2X/6-31G(d,p):HF/3-21G method. To improve the energy, the single point calculation at the large quantum 34T with M06-2X/6-31G(d,p) level of theory has been performed. The adsorption energy of *n*-hexane on the H-MCM-22 is predicted to be -11.1 kcal/mol, which lies between those of the H-FAU (−10.8 kcal/mol) and the ZSM-5 complexes (−18.2 kcal/mol), all of which are in good agreement with experimental data. The reaction mechanism of *n*-hexane to propane and propene is proposed via the 3-C-hexonium. Only the rate-determining step of the 3-C-hexonium formation is calculated. The calculated actual activation energy of *n*-hexane on H-MCM-22 is 37.2 kcal/mol, which is lower than the previous calculations on H-FAU and H-ZSM-5 of 45.7 and 45.8 kcal/mol, respectively. Thus, the results obtained with this hybrid-meta functional, parametrized to include the London dispersion energy, suggest that the H-MCM-22 zeolite is one of the promising candidate catalysts for hydrocarbon cracking.

**Acknowledgements** This work was supported in part by grants from the National Science and Technology Development Agency (2009 NSTDA Chair Professor funded by the Crown Property Bureau under the management of the National Science and Technology Development Agency and NANOTEC Center of Excellence funded by the National Nanotechnology Center), Kasetsart University Research and Development Institute (KURDI), the Thailand Research Fund (TRF), and the Commission on Higher Education, Ministry of Education (the "National Research University Project of Thailand (NRU)" and the "National Center of Excellence for Petroleum, Petrochemical and Advanced Materials (NCE-PPAM)"). The authors are grateful to Donald G. Truhlar and Yan Zhao for their support with the M06-L functional.

**References**

(1) Weitkamp, J. *Solid State Ionics* **2000**, *131*, 175.
(2) Stöcker, M. *Microporous Mesoporous Mater.* **2005**, *82*, 257.
(3) Kotrel, S.; Rosynek, M. P.; Lunsford, J. H. *J. Phys. Chem. B* **1999**, *103*, 818.
(4) Kotrel, S.; Knozinger, H.; Gates, B. C. *Microp. Macrop. Mat.* **2000**, *35-36*, 11.
(5) Corma, A.; Orchilles, A. V. *Microporous Mesoporous Mater.* **2000**, *3536*, 21.
(6) Collins, S. J.; Omalley, P. J. *J. Catal.* **1995**, *153*, 94.
(7) Collins, S. J.; O'Malley, P. J. *Chem. Phys. Lett.* **1995**, *246*, 555.
(8) Kazansky, V. B.; Frash, M. V.; van Santen, R. A. *Catal. Lett.* **1994**, *28*, 211.
(9) Blaszkowski, S. R.; Nascimento, M. A. C.; Van Santen, R. A. *J. Phys. Chem.* **1996**, *100*, 3463.
(10) Frash, M. V.; Van Santen, R. A. *Top. Catal.* **1999**, *9*, 191.
(11) Zheng, X.; Blowers, P. *J. Phys. Chem. A* **2005**, *109*, 10734.
(12) Boronat, M.; Viruela, P.; Corma, A. *J. Phys. Chem. B* **2000**, *104*, 1944.
(13) Boronat, M.; Corma, A. *Appl Catal A Gen* **2008**, *336*, 2.
(14) Maihom, T.; Pantu, P.; Tachakritikul, C.; Probst, M.; Limtrakul, J. *J. Phys. Chem. C* **2010**, *114*, 7850.
(15) Corma, A.; Corell, C.; Llopis, F.; Martínez, A.; Pérez-Pariente, J. *Applied Catalysis A, General* **1994**, *115*, 121.
(16) Leonowicz, M. E.; Lawton, J. A.; Lawton, S. L.; Rubin, M. K. *Science* **1994**, *264*, 1910.
(17) Katada, N.; Suzuki, K.; Noda, T.; Miyatani, W.; Taniguchi, F.; Niwa, M. *Appl Catal A Gen* **2010**, *373*, 208.
(18) Dapprich, S.; Komiromi, I.; Byun, K. S.; Morokuma, K.; Frisch, M. J. *THEOCHEM* **1999**, *461-462*, 1.
(19) Boekfa, B.; Choomwattana, S.; Khongpracha, P.; Limtrakul, J. *Langmuir* **2009**, *25*, 12990.
(20) Boekfa, B.; Pantu, P.; Probst, M.; Limtrakul, J. *J. Phys. Chem. C* **2010**, *114*, 15061.
(21) Maihom, T.; Boekfa, B.; Sirijaraensre, J.; Nanok, T.; Probst, M.; Limtrakul, J. *J. Phys. Chem. C* **2009**, *113*, 6654.
(22) Namuangruk, S.; Khongpracha, P.; Pantu, P.; Limtrakul, J. *J. Phys. Chem. B* **2006**, *110*, 25950.
(23) Pantu, P.; Boekfa, B.; Limtrakul, J. *J. Mol. Catal. A: Chem.* **2007**, *277*, 171.
(24) Zhao, Y.; Truhlar, D. G. *Theor. Chem. Acc.* **2008**, *120*, 215.
(25) Zhao, Y.; Truhlar, D. G. *Acc. Chem. Res.* **2008**, *41*, 157.
(26) Frisch, M. J.; Trucks, G. W.; Schlegel, H. B.; Scuseria, G. E.; Robb, M. A.; Cheeseman, J. R.; Montgomery, J. A., Jr.; Vreven, T.; Kudin, K. N.; Burant, J. C.; Millam, J. M.; Iyengar, S. S.; Tomasi, J.; Barone, V.; Mennucci, B.; Cossi, M.; Scalmani, G.; Rega, N.; Petersson, G. A.; Nakatsuji, H.; Hada, M.; Ehara, M.; Toyota, K.; Fukuda, R.; Hasegawa, J.; Ishida, M.; Nakajima, T.; Honda, Y.; Kitao, O.; Nakai, H.; Klene, M.; Li, X.; Knox, J. E.; Hratchian, H. P.; Cross, J. B.; Adamo, C.; Jaramillo, J.; Gomperts, R.; Stratmann, R. E.; Yazyev, O.; Austin, A. J.; Cammi, R.; Pomelli, C.; Ochterski, J. W.; Ayala, P. Y.; Morokuma, K.; Voth, G. A.; Salvador, P.; Dannenberg, J. J.; Zakrzewski, V. G.; Dapprich, S.; Daniels, A. D.; Strain, M. C.; Farkas, O.; Malick, D. K.; Rabuck, A. D.; Raghavachari, K.; Foresman, J. B.; Ortiz, J. V.; Cui, Q.; Baboul, A. G.; Clifford, S.; Cioslowski, J.; Stefanov, B. B.; Liu, G.; Liashenko, A.; Piskorz, P.; Komaromi, I.; Martin, R. L.; Fox, D. J.; Keith, T.; Al-Laham, M. A.; Peng, C. Y.; Nanayakkara, A.; Challacombe, M.; Gill, P. M. W.; Johnson, B.; Chen, W.; Wong, M. W.; Gonzalez, C.; Pople, J. A. *Gaussian 03, revision B.05; Gaussian, Inc.: Pittsburgh, PA*, 2003.
(27) Zhao, Y.; Truhlar, D. G. *J. Phys. Chem. C* **2008**, *112*, 6860.
(28) Klinowski, J. *Chem. Rev.* **1991**, *91*, 1459.

# ACTIVITY OF GOLD-SUPPORTED MFI ZEOLITES FOR NITROUS OXIDE DECOMPOSITION: A DENSITY FUNCTIONAL STUDY

*Thana Maihom[1,2,3],Pipat Khongpracha[1,2,3]and Jumras Limtrakul[1,2,3]**

[1]Laboratory for Computational and Applied Chemistry, Department of Chemistry, Faculty of Science and Center of Nanotechnology, Kasetsart University Research and Development Institute, Kasetsart University, Bangkok 10900, Thailand
[2]Center for Advanced Studies in Nanotechnology and Its Applications in Chemical, Food and Agricultural Industries, Kasetsart University, Bangkok 10900, Thailand
[3]NANOTEC Center of Excellence, National Nanotechnology Center, Kasetsart University, Bangkok 10900, Thailand
*Corresponding author's e-mail address: jumras.l@ku.ac.th

## Introduction

Nitrous oxide ($N_2O$), from industrial and motor vehicle exhausts, is well known as an environmental pollutant because it is a strong greenhouse effect gas and also plays an important role in the destruction of the stratospheric ozone layer. With increasing concern over environmental problems, the development of methods for reducing $N_2O$ has become not only extremely important but also attractive. The catalytic decomposition is one of the most promising ways to remove the $N_2O$. Among a variety of tested catalysts, metals such as Fe, Co, Cu and Ag containing zeolite structures included MFI, MOR, FER, and Y show promising activity features for $N_2O$ decomposition.[1-11]

Gold (Au) containing zeolites is one of the catalysts that has been verified for catalyzing the decomposition of $N_2O$. Previously, the experimental studies found that the Au/MFI can catalyze the decomposition of $N_2O$ to $N_2$ even in the presence of $O_2$.[12] Additionally, Au-zeolites also showed high activity for various reactions such as direct NO decomposition, CO activation and the water gas shift (WGS) reaction at low temperature.[13-17]

The different oxidation states of Au species have been proposed and investigated as catalytic active sites in the literature. Ichikawa et al.[18] have concluded that $Au^+$ was the dominant active site for the Au/NaY, Au/Na-MOR, and Au/Na-MFI zeolites where the reaction could take place. Sachtler et al.[19] analyzed the Au/MFI zeolite by using FTIR, XRD, HRAEM and CO-TPR and found that the $Au^+$ and $Au^{3+}$ were the dominant golds present; however, the $Au^+$ was irreversibly transformed to $Au^0$ at 500°C. In addition, Fierro-Gonzalez and Gates[20] have synthesized and characterized mononuclear $Au^+$ and $Au^{3+}$ complexes in NaY zeolite and also tested the activity for the NO reduction with CO. In that report, they found the $Au^{3+}$ complex was more active than the $Au^+$ complex. That finding emphasizes that the oxidation state of Au in zeolite seriously influences catalytic activity.

To the best of our knowledge, the decomposition of $N_2O$ on different species of Au in zeolite has not been theoretically studied and compared previously. In this work, we report the theoretical investigation on the activity of the Au cation and Au atom supported MFI zeolite for the decomposition of $N_2O$ by using the M06-L method. The reaction mechanism and relative energies and structures of intermediates and transition states are discussed.

## Models and Method

The MFI zeolites were represented by the 12T cluster model that was generated from its lattice structures.[21] The 12T cluster model of MFI, illustrated in Figure 1, covers the 10-membered-ring window at the interconnection between the straight channel and the zigzag channel. One aluminium atom was substituted for a silicon atom at the T12 site to generate the Brønsted acid site. In the model of Au/MFI, the Brønsted site of zeolite is exchanged by Au cation (Figure 1a). For the Au/H-MFI model, an Au atom was placed next to the Brønsted site of zeolite (Figure 1b).

The M06-L density functional[22-23] was used in all calculations. The series of this method has been shown to be very useful for studying adsorption and reaction mechanisms in the zeolites.[24-30] The basis set of 6-31G(d,p) was employed for the $N_2O$ molecule and all zeolitic atoms, while the Au atom was described by the Effective Core Potentials (ECP) of Stuttgart RSC 1997 ECP.[31] During geometry optimizations, only the 5T active region and the adsorbates were allowed to relax while the rest of the structure is kept fixed at the crystallographic coordinates. The total spin singlet state was employed for all calculations of the reaction coordinates. Transition states were confirmed to have one imaginary frequency corresponding to the reaction coordinate. All calculations were performed with the Gaussian 03 code[32] modified to incorporate the Minnesota Density Functionals module 3.1 by Zhao and Truhlar.

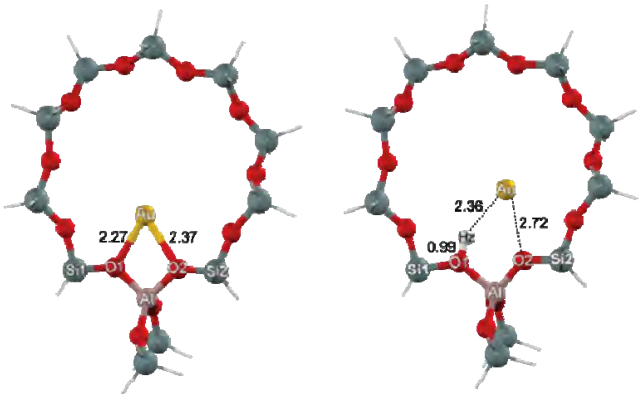


(a) (b)

**Figure 1.** Optimized geometric parameters of the Au supported MFI models: (a) Au/MFI zeolite (b) Au/H-MFI zeolite.

## Results and Discussion

**Structures of Au/MFI and Au/H-MFI.** Optimized structures of Au/MFI and Au/H-MFI zeolites are illustrated in Figures 1a and 1b, respectively. In the Au/MFI zeolite, the Au cation ($Au^+$) is coordinated with the two oxygen bridging atoms of zeolite having the bond distances of 2.27 and 2.37 Å for Au···O1 and Au···O2, respectively. The Al···Au distance is predicted to be 3.10 Å. The Mulliken population analysis for the partial atomic charge on the Au is calculated to be +0.189e. As for the Au/H-MFI zeolite, the Au atom interacts with a Brønsted proton (Hz) and the oxygen bridging (O2) of the zeolite. The acidic bond (O1–Hz) of zeolite is calculated to be 0.99 Å. The calculated distances of Au···Hz and Au···O2 are 2.36 and 2.72 Å, respectively. The electron transfer from the Hz and O2 to the Au atom cause the Mulliken charge on the Au atom to be negative (–0.366e).

**Adsorption of $N_2O$ on Au/MFI and Au/H-MFI.** The optimized adsorption structures of $N_2O$ on the Au cation of the Au/MFI zeolite is shown in Figures 2a. It can be seen that the $N_2O$ molecule interacts with the $Au^+$ by its lone pair electron. The oxygen–nitrogen (O–N1) bond of $N_2O$ is elongated from 1.19 to 1.26 Å. The distance between the nitrous oxide oxygen (O) and the $Au^+$ of

zeolite is 2.31 Å and the corresponding adsorption energy (ΔE) for this complex is –15.9 kcal/mol, which agrees well with the previous calculation.[33] The positive charge on Au is reduced from +0.189e to +0.102e by reason of the electrons transferred from O to Au.

Figure 3a depicts the adsorption structure of $N_2O$ interacted with the Au atom of the Au/H-MFI zeolite. The $N_2O$ is weakly adsorbed on zeolite through interactions between the π-bond of $N_2O$ and Au atom. The adsorption interactions are weak so that the structures of the Au/H-MFI zeolite and the adsorbed $N_2O$ are not significantly altered. The bond distances of O1–Hz, Au···Hz, Au···O2 of zeolite and the O–N1 bond of $N_2O$ differ slightly from the corresponding isolated molecules. The internuclear distances of Au···O and Au···N1 between the adsorbed $N_2O$ and the Au active site are comparable. The negative charge of the Au atom is increased from –0.366e to –0.423e. The calculated adsorption energy (ΔE) is –5.5 kcal/mol which is almost three times lower than that derived from the Au/MFI complex (ΔE = –15.9 kcal mol).

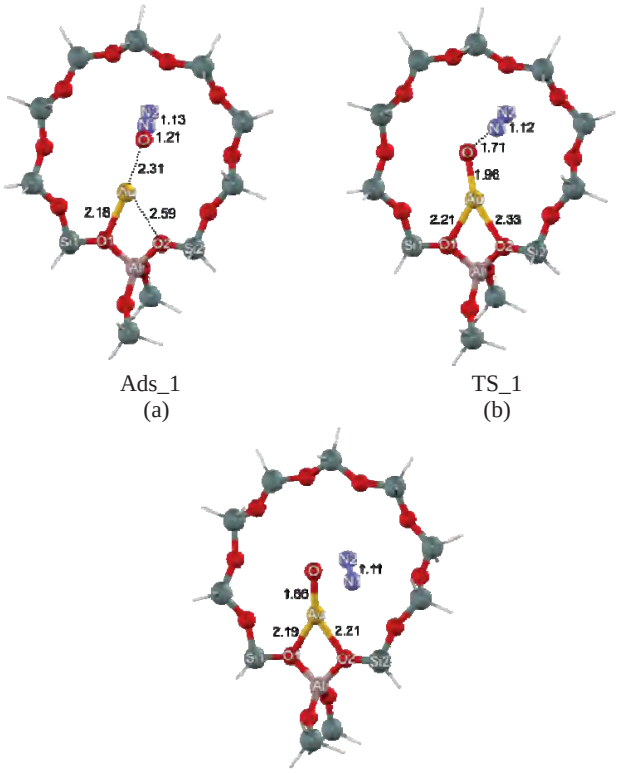


Ads_1 (a) TS_1 (b) Prod_1 (c)

**Figure 2.** Optimized structures of adsorption (Ads_1), transition state (TS_1) and product (Prod_1) involved in the decomposition of $N_2O$ over Au/MFI zeolite.

**Reaction Mechanism of $N_2O$ Decomposition on Au/MFI and Au/H-MFI zeolites.** The decomposition of $N_2O$ on Au/MFI is depicted in Figure 2. This reaction is initiated by the adsorption of nitrous oxide on the active Au cation site of MFI zeolite (Ads_1). Here, its adsorption energy is –15.9 kcal/mol. The adsorbed $N_2O$ is decomposed via the transition state of the N–O bond breaking (TS_1). In this transition state, TS_1, the N–O bond of $N_2O$ is cleaved and the Au···O distance is contracted leading to form a new bond (Figure 2b). The activation energy for this transition state is 41.9 kcal/mol. The transition state proceeds then by the deposition of an oxygen species on the Au center and the formation of a nitrogen molecule (Prod_1). In it, the Au···O distance is reduced to 1.86 Å. The adsorption energy of this complex with respect to the isolated reactants is 16.2 kcal/mol, significantly less than the adsorption energy of nitrous oxide.

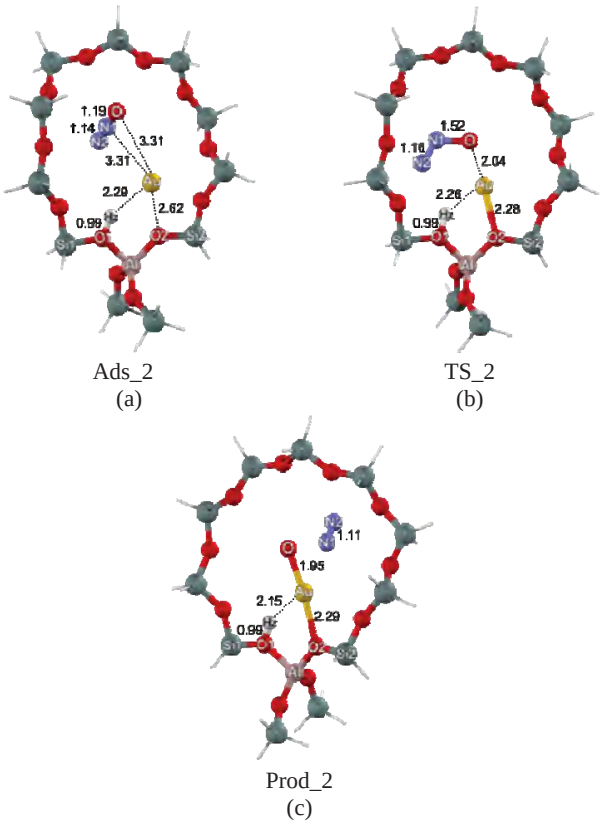


Ads_2 (a) TS_2 (b) Prod_2 (c)

**Figure 3.** Optimized structures of adsorption (Ads_2), transition state (TS_2) and product (Prod_2) involved in the decomposition of $N_2O$ over Au/H-MFI zeolite.

The equivalent decomposition of nitrous oxide on Au/H-MFI zeolite is shown in Figure 3. This reaction proceeds as the decomposition on Au/MFI discussed above. Ads_2 shows the $N_2O$ adsorption complex whose adsorption energy is evaluated to be –5.5 kcal/mol. Then, the N–O bond of the adsorbed nitrous oxide is cleaved and the Au–O bond is formed (TS_2). Again, the surface oxygen species is generated on the active Au center and a nitrogen molecule also formed in the zeolite framework. The activation energy is 15.2 kcal/mol, which is significantly lower than the $N_2O$ decomposition on Au/MFI reported earlier. The surface Au–O bond distance in the surface oxygen species is 1.95 Å (Prod_2). The calculated adsorption energy of this complex is –15.8 kcal/mol, which is more stable than $N_2O$ adsorption.

The activation energy for the decomposition of $N_2O$ on Au/H-MFI zeolite is found to be lower than on Au/MFI zeolite (cf. Figure 4). With respect to the adsorption complex, the decomposition product on Au/H-MFI is also more stable than the Au/MFI. This shows that the Au/H-MFI zeolite is kinetically and thermodynamically favored for the $N_2O$ decomposition over Au/MFI zeolite.

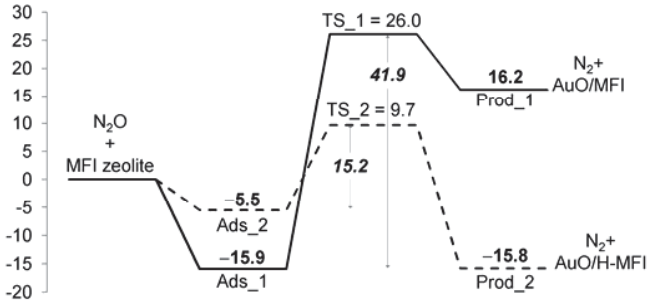


**Figure 4.** Energy profile for the $N_2O$ decomposition for both zeolites: Au/MFI zeolite (solid line) and Au/H-MFI (dashed line) zeolite (energies are in kcal/mol).

**Conclusion**

The density functional calculations, M06-L including dispersion energy, has been employed for investigating the $N_2O$ decomposition reaction over Au/MFI and Au/H-MFI zeolites. The reaction is proposed to proceed in a single step of the $N_2O$ N–O bond breaking to give the surface oxygen deposited on the Au active site and the nitrogen molecule. The calculated activation barriers ($E_a$) for N2O decomposition are observed to be $E_a$ = 41.9 and $E_a$ =15.2 kcal/mol for the reaction over Au/HMFI and Au/H-MFI zeolites, respectively. The latter $E_a$ is much lower than that of the former as a result of more negative charges of the gold atom found in the Au/H-MFI as compared to the Au/ZSM-5 adduct. The formation of the $N_2O$ decomposition product on Au/H-MFI (–15.8 kcal/mol) is also more stable in energy than on Au/MFI (16.2 kcal/mol). On the basis of these results, it can be concluded that the Au/H-MFI zeolite is more active for $N_2O$ decomposition than Au/MFI zeolite.

**Acknowledgement.** This work was supported in part by grants from the National Science and Technology Development Agency (2009 NSTDA Chair Professor funded by the Crown Property Bureau under the management of the National Science and Technology Development Agency and NANOTEC Center of Excellence funded by the National Nanotechnology Center), Kasetsart University Research and Development Institute (KURDI), the Thailand Research Fund (TRF), and the Commission on Higher Education, Ministry of Education (the "National Research University Project of Thailand (NRU)" and the "National Center of Excellence for Petroleum, Petrochemical and Advanced Materials (NCE-PPAM)"). The authors are grateful to Donald G. Truhlar and Yan Zhao for their support with the M06-L functional.

**References**

(1) Shelef, M.; *Chem. Rev.* **1995**, *95*, 209.
(2) Gomez, S.A.; Campero, A.; Martínez-Hernández, A.; Fuentes, G.A.; *Appl. Catal. A* **2000**, *197*, 157.
(3) Yahiro, H.; Iwamoto, M. *Appl. Catal. A* **2001**, *222*, 163.
(4) Parez-Ramirez, J.; Kapteijn, F.; Mul, G.; Moulijin, J.A. *Chem. Commmun.* **2001**, 693.
(5) Heyden, A.; Peters, B.; Bell, A.T.; Keil, F.J. *J. Phys. Chem. B* **2005**, *109*, 1857.
(6) Schidder, M.; Kumar, M.S.; Klementiev, K.; Pohl, M.M.; Brückner, A.; Grünert, W. *J. Catal.* **2005**, *231*, 314.
(7) Devades, M.; Kröcher, O.; Elsener, M.; Wokiaun, A.; Söges, N.; Pfeifer, M.; Demel, Y.; Mussmann, L. *Appl. Catal. B Environ.* **2006**, *67*, 187.
(8) Chupin, C.; van Veen, A.C.; Konduru, M.; Despres, J.; Mirodals, C. *J. Catal.* **2006**, *241*, 103.
(9) Pantu, P.; Boekfa, B.; Sunpetch, B.; Limtrakul, J. Chem. Eng. Comm. **2008**, *195*, 1477.
(10) Shibata, J.; Takada, Y.; Shichi, A.; Satokawa, S.; Satsuma, A.; Hattori, T. *Appl. Catal. B Environ.* **2004**, *54*, 137.
(11) Shibata, J.; Shimizu, K.; Takada, Y.; Shichi, A.; Yoshida, H.; Satokawa, S.; Satsuma, A.; Hattori, T. *J. Catal.* **2004**, 227, 367.
(12) Gao, Z.; Sun, Q.; Chen, H.; Wang X.; Sachtler, W.M.H. *Catal. Lett.* **2001**, *72*, 1.
(13) Qiu, S.; Ohnishi, R.; Ichikawa, M. *J. Chem. Soc., Chem. Commun.* **1992**, 1425–1427.
(14) Fierro-Gonzalez, J. C.; Gates, B. C. *J. Phys. Chem. B.* **2004**, *108*, 16999–17002.
(15) Salama, T. M.; Shido, T.; Ohnishi, R.; Ichikawa, M. *J. Chem. Soc., Chem. Commun.* **1994**, 2749–2750.
(16) Mohamed, M. M.; Salama, T. M.; Ichikawa, M. *J. Colloid Interface Sci.* **2000**, *224*, 366–371.
(17) Mohamed, M. M.; Ichikawa, M. *J. Colloid Interface Sci.* **2000**, *232*,381–388.
(18) Mohamed, M. M.; Salama, T. M.; Ichikawa, M. *J Colloid Interface Sci* **2000**, *224*, 366.
(19) Qiu, S.; Ohnishi, R.; Ichikawa, M. *J Phys Chem Lett* **1994**, *98*, 2719.
(20) Fierro-Gonzalez, J.C.; Gates, B.C. *J. Phys. Chem. B* 2004, *108*, 16999.
(21) van Koningsveld, H.; van Bekkum, H.; Jansen, J. C. *Acta. Crystallogr. B* **1987**, *43*, 127.
(22) Zhao, Y.; Truhlar, D. G. *J. Phys. Chem. C* **2008**, 112, 6860.
(23) Zhao, Y.; Truhlar, D. G. *Acc. Chem. Res.* **2008**, 41, 157.
(24) Maihom, T.; Boekfa, B.; Sirijaraensre, J.; Nanok, T.; Probst, M.; Limtrakul, J. *J. Phys. Chem. C* **2009**, 113, 6654.
(25) Boekfa, B.; Choomwattana, S.; Khongpracha, P.; Limtrakul, J. *Langmuir* **2009**, 25(22), 12990.
(26) Kumsapaya, C.; Bobuatong, K.; Khongpracha, P.; Tantirungrotechai, Y.; Limtrakul, J. *J. Phys. Chem. C* **2009**, 113, 16128.
(27) Maihom, T.; Pantu, P.; Tachakritikul, C.; Probst, M.; Limtrakul, J. *J. Phys. Chem. C* **2010**, 114, 7850.
(28) Boekfa, B.; Pantu, P.; Probst, M.; Limtrakul, J. *J. Phys. Chem. C* **2010**, 114, 15061.
(29) Wannakao, S.; Boekfa, B.; Khongpracha, P.; Probst, M.; Limtrakul, J. *ChemPhysChem* **2010**, 11, 3432.
(30) Bobuatong, K.; Probst, M.; Limtrakul, J. *J. Phys. Chem. C* **2010**, 114, 21611.
(31) Dolg, M.; Stoll, H.; Preuss, H.; Pitzer, R. M. *J. Phys. Chem.* **1993**, *97*, 5852.
(32) *Gaussian 03, revision B.05*; Gaussian, Inc.: Pittsburgh, PA, **2003**.
(33) Sierraalta, A.; Hernandez-Andara, R.; Ehrmann, E. *J. Phys. Chem. B* **2006**, *110*, 17912.

# STRUCTURES AND REACTION MECHANISMS OF BUTADIENE CYCLOADDITION OVER METAL-EXCHANGED FAUJASITE

*Thittaya Yutthalekha* [1,2,3], *Bundet Boekfa*[1,2,3,4] *and Jumras Limtrakul* [1,2,3*]

[1]Laboratory for Computational and Applied Chemistry, Department of Chemistry, Faculty of Science and Center of Nanotechnology, Kasetsart University Research and Development Institute, Kasetsart University, Bangkok 10900, Thailand
[2]Center for Advanced Studies in Nanotechnology and Its Applications in Chemical, Food and Agricultural Industries, Kasetsart University, Bangkok 10900, Thailand
[3]NANOTEC Center of Excellence, National Nanotechnology Center, Kasetsart University, Bangkok 10900, Thailand
[4]Chemistry Department, Faculty of Liberal Arts and Science, Kasetsart University Kamphaeng Saen Campus, Nakhon Pathom73140, Thailand
*Corresponding author's e-mail address: jumras.l@ku.ac.th

## Introduction

Butadiene cycloaddition reaction is one of the alternative routes for styrene production with the benefit of higher conversion[1] compared to the conventional route[2]. Benzene alkylation is ultimately required by both processes for dehydrogenation to styrene. The cycloaddition of butadiene to 4-vinylcyclohexene is a well-known thermally-initiated cycloaddition reaction between two butadienes in which one serves as the diene and the other serves as the dienophile. This reaction is believed to proceed via a concerted mechanism or two-step mechanism. From theoretical investigations, it has been shown that both mechanisms are similar in their energetics[3,4]. Several studies propose the use of various catalysts for the reaction, such as the promoted $ZrO_2$ catalyst, Pd catalysts supported on alumina, polyoxometalate and zeolite[5-10]. A previous study reported that the cycloaddition of butadiene over a Cu-exchanged zeolite produces an excellent yield of 4-vinylcyclohexene[11-14] while the Brønsted acid[13] site of zeolite and the alkaline-exchanged zeolite[15] such as NaX[11,16], yield the oligomeric compounds as major products.

Transition metals supported on zeolite have been found to be active catalysts for many processes[17-19]. Copper containing zeolites have long drawn strong attention because of their activity in the decomposition of NO. Moreover, Cu-exchanged in zeolites such as CuZSM-5, CuX, CuY and CuMCM-41 was found to activate multiple carbon–carbon bonds in alkenes (ethene, propene, butenes), ethyne, and benzene. The activation was evidenced by a measured red-shift of multiple bonds stretching by 80–130 $cm^{-1}$ for alkenes, 168 $cm^{-1}$ for ethyne, 16 $cm^{-1}$ for benzene[20-22]. The charge transfer phenomenon between the alkene molecule and the cationic active site resulted in the bond weakening, an important factor for catalyzing the reaction.

Zeolites are microporous aluminosilicates with a large number of atoms in the unit cell, where the use of such sophisticated methods as periodic calculation are too computationally demanding and expensive. In theoretical studies, small clusters are usually used for representing models of catalytic zeolite. However, these cluster models do not incorporate the framework effect, which has an important role for reactions inside zeolites. More recently, the newly developed M06 functional, in which the dispersion force was taken into account, is successfully applied to study the interaction and reactions of hydrocarbon on various zeolites[23-25].

To the best of our knowledge, only a small number of theoretical studies of the mechanisms on the systems of butadiene cycloaddition over Cu-exchanged Faujasite have been reported to date. The aim of this work is to study the effects of the metal inside zeolites and possible mechanisms for the reaction.

## Methods

The cluster model of Faujasite was obtained from their crystal lattice structures. To account for the framework effect of the zeolite pores, we applied the ONIOM2 approach to the 50T cluster representing the supercage of faujasite zeolite in which the reactions can occur. The 50T cluster which divides the faujasite structure into two layers is shown in Figure1. The inner layer consists of the 10T cluster and the reactive species, which were treated with the M06L functional using the 6-31G(d,p) basis set for H, C, O, Al and Si atoms, while the Stuttgart RSC 1997 effective core potential (ECP) were used for the Cu atom. The outer layer is the 40T extended structure of faujasite zeolite, treated with the UFF force field to account for the effect of the Faujasite framework on the adsorbed species inside the pore. Normal mode analyses were carried out to verify the transition states to have one imaginary frequency whose mode correspond to the reaction coordinate. The total spin was kept constant at the singlet ground states for Cu(I) whereas it was kept constant at the doublet ground states for Cu(II). NPA charges and electronic configuration were determined by Natural Bond Orbital (NBO) methods.

All calculations in this work have been performed by using the Gaussian 03 program incorporated with the Minnesota Density Functionals module 3.1 by Zhao and Truhlar[26-28].

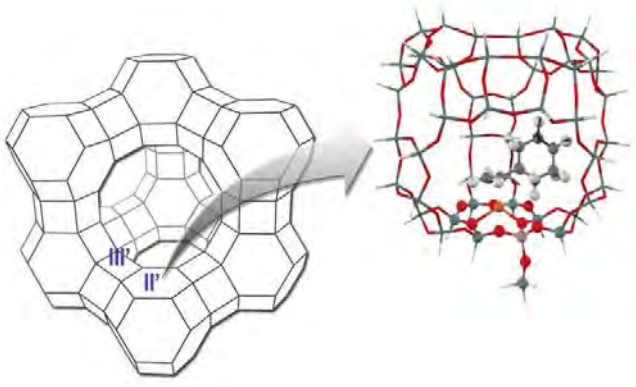


**Figure1.** Model of the 50T cluster, the 10T quantum cluster is drawn as the bond and stick model.

## Results and Discussion

**The metal exchanged zeolite Models and Adsorption Complexes.** The optimized structures of Cu-exchanged Faujasite, whose metal ion acts as an active site are shown in Figure1. The metal ion lies between the three bridging oxygen atoms of the zeolite framework. The Al-Cu bond is 3.06 Å, which agrees with previous work[28].

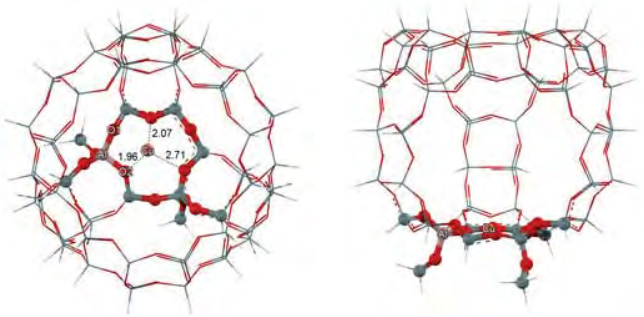


Cu(I)-FAU

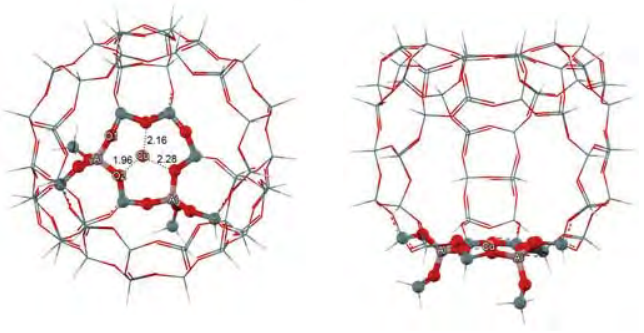


Cu(II)-FAU

**Figure1.** Optimized structures of the Cu(I) and Cu(II) exchanged Faujasite

The optimized structures of butadiene adsorbed via the π complex on the metal ion are shown in Figure2. For the Cu(II)-FAU system, the adsorption energy is calculated to be 37.36 kcal/mol, which is much higher than the Cu(I)-FAU system of -35.82 kcal/mol. The C1=C2 bonds of adsorbed 1,3 butadiene was increased to 1.39 and 1.37 Å for Cu(I)-FAU and Cu(II)-FAU system, respectively in comparison with the isolated molecule(1.33 Å). In the coadsorption complex, the Cu(II)-FAU system yields coadsorption energy of -50.48 kcal/mol while the Cu(I)-FAU system give coadsorption energy of -42.83 kcal/mol.

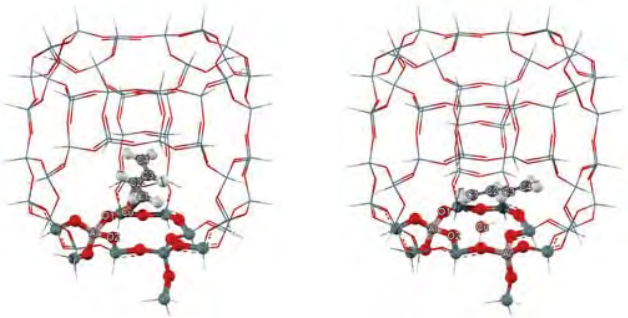

Cu(I)-FAU Cu(II)-FAU

**Figure2.** Adsorption complex structures (Å) of butadiene on Metal exchanged Faujasite

**The Reaction Mechanism of butadiene cycloaddition.** We investigated two different mechanisms of this reaction: stepwise mechanism and concerted mechanism, which are shown in Figure3.

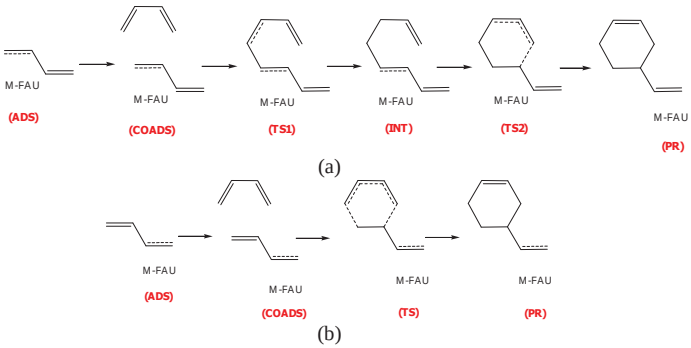


(a)




(b)

**Figure3.** Proposed mechanisms of butadiene cycloaddition:
(a) Stepwise mechanism
(b) Asynchronous concerted mechanism

**The stepwise mechanism**, the optimized structures are shown in Figure4 and the reaction energies are shown in Table1. This mechanism is composed of two steps. The first step, formation of the first C-C bond, is the rate determining step and followed rapidly by ring closure of the second C-C bond. The calculated activation energies are calculated to be 19.91 and 9.12 kcal/mol for Cu(I)-FAU and Cu(II)-FAU system, respectively.

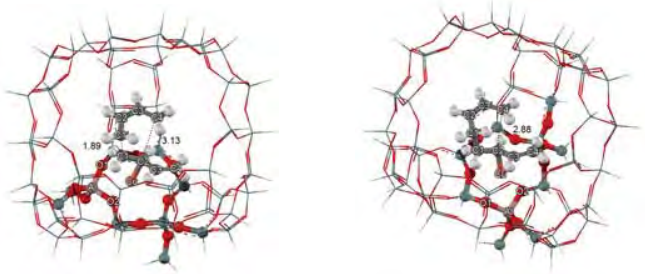


TS1-Cu(I)-FAU TS2-Cu(I)-FAU

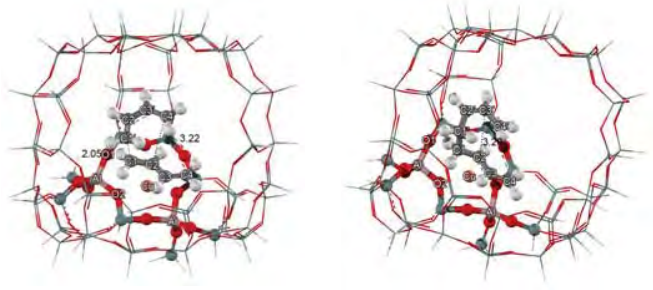


TS1-Cu(II)-FAU TS2-Cu(II)-FAU

**Figure4.** Transition state structures (Å) of butadiene cycloaddition on Metal exchanged Faujasite.

**Table1.** Reaction energies (kcal/mol) of the butadiene cycloaddition on Cu-FAU zeolite calculated with 10T:50T ONIOM (M06L:UFF), Activation energies are in parenthesis

| Model | Ads | Coads | TS1 | INT | TS2 | Pr |
|---|---|---|---|---|---|---|
| Cu(I)-FAU | -35.82 | -42.83 | -22.92 (19.91) | -24.40 | -22.81 (1.59) | -84.42 |
| Cu(II)-FAU | -37.36 | -50.48 | -41.35 (9.12) | -49.56 | -44.97 (4.59) | -88.30 |

**The concerted mechanism**, the optimized transition state structures are shown in Figure5 and the reaction energies are shown in Table1. The lower activation energy compared with the stepwise mechanism indicating that this mechanism is more favorable than the stepwise mechanism. The geometries of the transition states are asynchronous structures in which the distances between two molecules in cyclic transition are not equal. The activation energies are predicted to be 12.36 and 6.99 kcal/mol for Cu(I)-FAU and Cu(II)-FAU system, respectively.

**Table2.** Reaction energies (kcal/mol) of the butadiene cycloaddition on Cu-FAU zeolite calculated with 10T:50T ONIOM (M06L:UFF), Activation energies are in parenthesis.

| Model | Ads | Coads | TS | Pr |
|---|---|---|---|---|
| Cu(I)-FAU | -35.82 | -42.83 | -29.36 (12.36) | -84.42 |
| Cu(II)-FAU | -37.35 | -50.48 | -43.48 (6.99) | -88.30 |

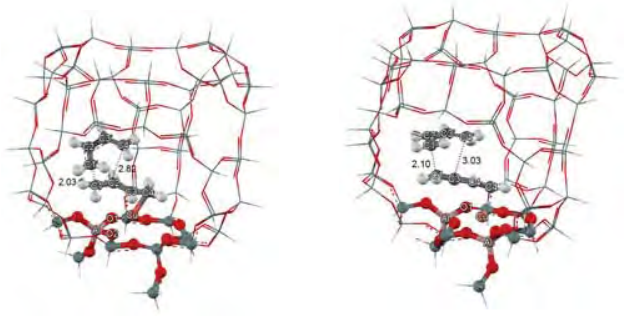


Cu(I)-FAU Cu(II)-FAU

**Figure5.** Transition state structures (Å) of butadiene cycloaddition on Metal exchanged Faujasite.

The interaction between butadiene and metal exchanged-Faujasite can be examined in visual detail by using NBO analysis derived at the 10T high level of ONIOM FAU-50T model. The NBO calculations which are shown in Figure6 and Table3 evidenced that, the activation of the adsorbed butadiene molecule was revealed by the π back donation of d electrons of metal to π* antibonding orbitals of a butadiene. As a result, butadiene acquired a negative charge, whereas the metal became more positive. Part of the charge transmitted to the molecule came from the metal itself and part from the zeolite framework which acted as an 'electron reservoir'.

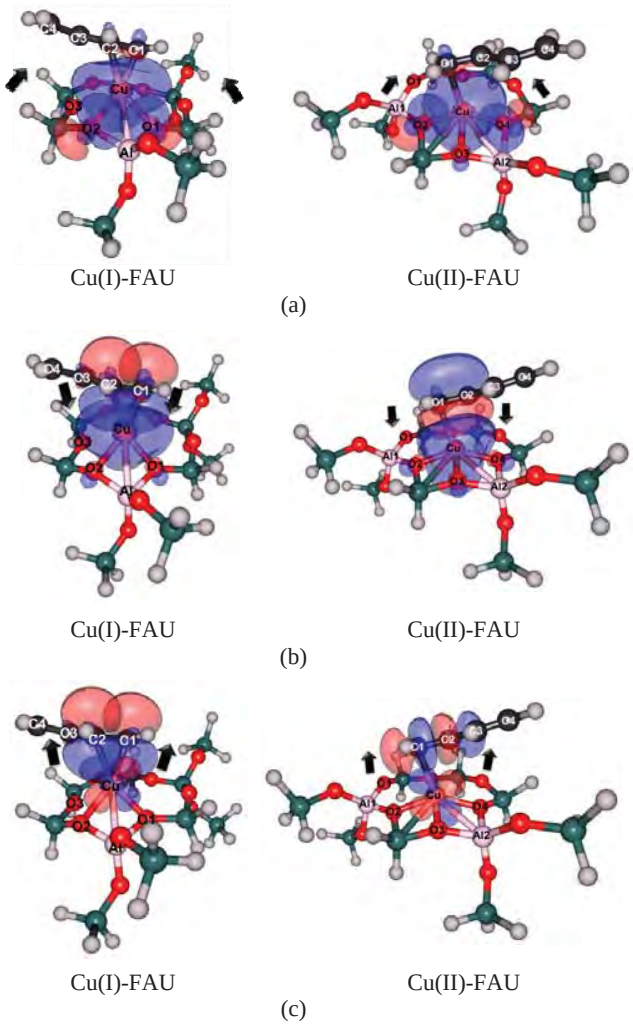

Cu(I)-FAU Cu(II)-FAU

(a)

Cu(I)-FAU Cu(II)-FAU

(b)

Cu(I)-FAU Cu(II)-FAU

(c)

**Figure6.** The interaction between butadiene and metal exchanged-Faujasite obtained from calculation at the 10T high level of ONIOM FAU-50T:

(a) The charge transfer of the nearest oxygen in zeolite to the metal cation.
(b) The σ-donation from bonding π electron or p orbital (in the case of Cu(I) ) of butadiene to the orbital of the metal.
(c) The d-π* electron back donation from d orbital of the metal to π* orbital of butadiene

**Table3.** Natural population analysis (NPA) parameters of adsorptions of butadiene and concerted transition state on Metal exchanged Faujasite which were obtained from M06L/6-31G(d,p) calculations.

| systems | Partial Charge | | | | | |
|---|---|---|---|---|---|---|
| | Cu | C1 | C2 | Al | O1 | O2 |
| Butadiene(BD) | - | -0.42 | -0.24 | - | - | - |
| Cu(I)-FAU | 0.73 | - | - | 2.09 | -1.32 | -1.32 |
| Cu(I)-FAU-BD | 0.69 | -0.56 | -0.33 | 2.08 | -1.30 | -1.30 |
| Cu(I)-FAU-TS | 0.78 | -0.43 | -0.27 | 2.10 | -1.32 | -1.31 |
| Cu(II)-FAU | 1.08 | - | - | 2.09 | -1.32 | -1.28 |
| Cu(II)-FAU-BD | 1.06 | -0.53 | -0.21 | 2.10 | -1.33 | -1.24 |
| Cu(II)-FAU-TS | 0.98 | -0.39 | -0.21 | 2.11 | -1.30 | -1.33 |

## Conclusions

The butadiene cycloaddition over metal-exchanged zeolite has been investigated by the ONIOM (M06L:UFF) approach. The basis set are the Stuttgart RSC 1997 effective core potential (ECP), for Cu atom, and 6-31G(d,p) for the rest. The reaction mechanism is proposed both stepwise and concerted mechanism. For the stepwise, the activation barriers are 19.1 and 1.59 kcal/mol for Cu(I)-Faujasite and 9.12 and 4.59 kcal/mol for Cu(II)-Faujasite. For concerted mechanism, the activation barriers are 12.36 and 6.99 kcal/mol for Cu(I) and Cu(II) Faujasite, respectively. The lower activation barrier on Cu(II)-Faujasite is due to the metal weakening the butadiene by electron back donation which comfirmed by the NBO analysis. This study gives better understanding of the structures and mechanistic properties at the molecular level of the metal-exchanged zeolite catalyst which are useful for further improvement of styrene production.

**Acknowledgements.** This work was supported in part by grants from the National Science and Technology Development Agency (2009 NSTDA Chair Professor funded by the Crown Property Bureau under the management of the National Science and Technology Development Agency and NANOTEC Center of Excellence funded by the National Nanotechnology Center), The Thailand Research Fund, the Commission of Higher Education, Ministry of Education ("National Research University of Thailand" and "Postgraduate Education and Research Programs in Petroleum and Petrochemicals and Advanced Materials"). The support from the Kasetsart University Research and Development Institute (KURDI) and Graduate School Kasetsart University are also acknowledged. The authors are grateful to Donald G. Truhlar and Yan Zhao for their support with the M06-2X functional.

## References

(1) Vaughan, W. E. *Journal of the American Chemical Society* **1932**, *54*, 3863.
(2) Christensen, C. H.; Johannsen, K.; Schmidt, I.; Christensen, C. H. *Journal of the American Chemical Society* **2003**, *125*, 13370.
(3) Li, Y.; Houk, K. N. *Journal of the American Chemical Society* **1993**, *115*, 7478.
(4) Von Doering, W. E.; Franck-Neumann, M.; Hasselmann, D.; Kaye, R. L. *Journal of the American Chemical Society* **1972**, *94*, 3833.
(5) Thomas, M. L.; Fraga-Dubreuil, J.; Coote, A. S.; Poliakoff, M. *Green Chemistry* **2008**, *10*, 197.
(6) Alimardanov, K. M.; Abdullayev, A. F. *Petroleum Chemistry* **1995**, *35*, 508.
(7) Neumann, R.; Dror, I. *Applied Catalysis A: General* **1998**, *172*, 67.
(8) De Bruyn, M.; Neumann, R. *Advanced Synthesis and Catalysis* **2007**, *349*, 1624.
(9) Choi, Y. S.; Park, Y. K.; Chang, J. S.; Park, S. E.; Cheetham, A. K. *Catalysis Letters* **2000**, *69*, 93.
(10) Castellan, A.; Tauszik, G. R. *Journal of Catalysis* **1977**, *50*, 172.
(11) Maxwell, I. E.; de Boer, J. J.; Downing, R. S. *Journal of Catalysis* **1980**, *61*, 493.
(12) Maxwell, I. E.; Downing, R. S.; Van Langen, S. A. J. *Journal of Catalysis* **1980**, *61*, 485.
(13) Voskoboinikov, T. V.; Coq, B.; Fajula, F.; Brown, R.; McDougall, G.; Luc Couturier, J. *Microporous and Mesoporous Materials* **1998**, *24*, 89.
(14) Kugel, V. Y.; Lakhman, L. I.; Abramova, A. V.; Matiyeva, Z. M.; Smirnov, V. K.; Irisova, K. N.; Livenbuk, M. I.; Slivinskii, Y. V. *Petroleum Chemistry* **1997**, *37*, 297.
(15) Dessau, R. M. *Journal of the Chemical Society, Chemical Communications* **1986**, 1167.
(16) Chang, J. S.; Park, S. E.; Gao, Q.; Férey, G.; Cheetham, A. K. *Chemical Communications* **2001**, 859.
(17) Dimitrov, C.; Leach, H. F. *Journal of Catalysis* **1969**, *14*, 336.
(18) Nieminen, V.; Kumar, N.; Datka, J.; Päivärinta, J.; Hotokka, M.; Laine, E.; Salmi, T.; Murzin, D. Y. *Microporous and Mesoporous Materials* **2003**, *60*, 159.
(19) Espeel, P. H.; De Peuter, G.; Tielen, M. C.; Jacobs, P. A. *Journal of Physical Chemistry* **1994**, *98*, 11588.
(20) Datka, J.; Kukulska-Zajac, E. *Journal of Physical Chemistry B* **2004**, *108*, 17760.
(21) Datka, J.; Kukulska-Zajac, E.; Kozyra, P. *Journal of Molecular Structure* **2006**, *794*, 261.
(22) Kukulska-Zajac, E.; Kozyra, P.; Datka, J. *Appl. Catal. A-Gen.* **2006**, *307*, 46.
(23) Boekfa, B.; Choomwattana, S.; Khongpracha, P.; Limtrakul, J. *Langmuir* **2009**, *25*, 12990.
(24) Kumsapaya, C.; Bobuatong, K.; Khongpracha, P.; Tantirungrotechai, Y.; Limtrakul, J. *Journal of Physical Chemistry C* **2009**, *113*, 16128.
(25) Maihom, T.; Pantu, P.; Tachakritikul, C.; Probst, M.; Limtrakul, J. *Journal of Physical Chemistry C* **2010**, *114*, 7850.
(26) Zhao, Y.; Schultz, N. E.; Truhlar, D. G. *Journal of Chemical Theory and Computation* **2006**, *2*, 364.
(27) Zhao, Y.; Truhlar, D. G. *Accounts of Chemical Research* **2008**, *41*, 157.
(28) Drake, I. J.; Zhang, Y.; Briggs, D.; Lim, B.; Chau, T.; Bell, A. T. *Journal of Physical Chemistry B* **2006**, *110*, 11654.

# Catalytic Dehydrogenation of Propane over Au(I) exchanged ZSM-5: Density Functional Theory Calculations

*Winyoo Sangthong[2,3,4] and Jumras Limtrakul,[1,2,3,4*]*

[1] Laboratory for Computational and Applied Chemistry, Department of Chemistry, Faculty of Science and Center of Nanotechnology, Kasetsart University Research and Development Institute, Kasetsart University, Bangkok 10900, Thailand
[2] Center for Advanced Studies in Nanotechnology and Its Applications in Chemical, Food and Agricultural Industries, Kasetsart University, Bangkok 10900, Thailand
[3] NANOTEC Center of Excellence, National Nanotechnology Center, Kasetsart University, Bangkok 10900, Thailand
[4] Center of Nanotechnology, Kasetsart University Research and Development Institute, Kasetsart University, Bangkok, 10900, Thailand
[*]Corresponding author: Tel.: +662 562 5555 ext 2169, Fax: +662 562 5555 ext 2176, E-mail address: jumras.l@ku.ac.th

## Introduction

Currently, the demand of alkenes has increased because they are important starting materials for chemical industrial procedures, especially propene[1]. Generally, propene could be obtained by dehydrogenation of propane. However, the conventional steam cracking process has the problem of a high energy-consuming process that also produces $CO_2$ and deactivation of the catalyst by coke production. Therefore, the research for alternative ways for the production of propene becomes imperative. One of the alternative ways is the direct catalytic non-oxidative dehydrogenation of propane over zeolitic catalysts. Transition metal supported on ZSM-5 increases the rate of non-oxidative propane conversion and the selectivity to unsaturated products[2-7]. $Au^+$ is found to be an active specie for dehydrogenation of propane[8]. Therefore, Au(I)-exchanged ZSM-5 could be considered as a new catalyst for propane dehydrogenation. In order to investigate this reaction mechanism, theoretical methodology can offer an understanding that has still not been studied by experimental investigations. In this work, we put forward a preliminary report of the efficiency enhancements for propane dehydrogenation by using Au(I)-ZSM-5 as a high-quality cooperative catalyst using the density functional theory with the well calibrated M06-L functional.

## Methodology

The crystal lattice structure of ZSM-5 was taken from the work of van Koningsveld, et al[9]. The Al atom is selected to substitute a Si atom at the T12 position, which is the most energetically favored position[10,11]. The 34T cluster is used to represent the active site of ZSM-5 and employed throughout this study, as shown in Fig.1. It includes the 10-membered ring representing the main gateway to the intersection between the straight channel and the zigzag channel, where the reactions normally take place. The atomic coordinates are treated with the density functional theory (DFT) method using the M06-L functional. The 6-31G(d,p) basis set was used for Al, Si, O, C and H atoms and the effective core potential basis of LANL2DZ was used for the singlet state of the Au atom. Only the 5T regions $[(\equiv SiO)_3Al(OH)Si\equiv]$ of zeolite and the reactants were allowed to relax during the geometry optimization, while the rest were fixed at the crystallographic coordinates. For metal exchanged zeolite, Au(I) was placed at the ion exchange site in the zigzag channel window. The frequency calculations were performed at the same level of theory to verify that the transition states had one imaginary frequency whose mode corresponds to a saddle point of the reaction coordinate. Single point calculations at the M06-L/6-311+G(2df,2p) level of theory were also carried out in order to obtain more reliable results. All calculations were performed by using the Gaussian 03 code, with the M06-L functional implemented by Donald G. Truhlar and Yan Zhao[12,13].

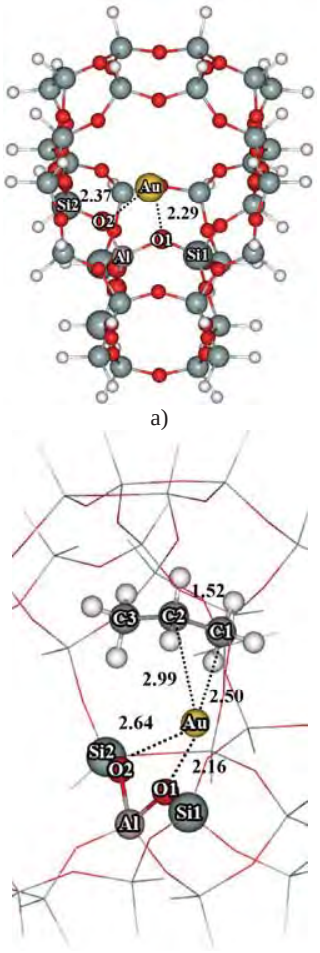


**Figure 1.** Structure of 34T cluster of Au(I)-ZSM-5 (a) and optimized adsorption structure of propane over Au(I)-ZSM-5 (b).

## Results and Discussion

**Structure of Au(I)-ZSM-5 and propane adsorption complex.** The model of the 34T Au(I)-ZSM-5 clusters and their optimized propane adsorption complexes are illustrated in Figures 1a and 1b. In the optimization, the atoms in the 5T region in the clusters are optimized with the exception of the atoms in the extended framework. The exchanged Au cation is located over the aluminum atom and bidentated two oxygen atoms, O1 and O2, close to the aluminum atom. The bond distances of Au···O1 and Au···O2 of Au(I)-ZSM-5 are calculated to be 2.29 Å and 2.37 Å, respectively.

In order to clearly demonstrate the propane conversion process, it is important to study propane physisorption over the active site of metal exchanged ZSM-5. The selected geometrical structures of this interaction are presented in Figure 1b. For the adsorption of propane on Au(I)- ZSM-5, we found that propane adsorbed on zeolite through interactions between methyl and methylene carbon atoms and the Lewis acid site. This interaction results in a small deviation of the

structure of the Au(I)-ZSM-5 such that the Au···O1 and Au···O2 distances in Au(I)-ZSM-5 are slightly changed and the C-C bond of propane differs slightly from the isolated molecules. The binding energy is calculated to be -29.0 kcal/mol. The C1···Au and C2···Au distances are 2.50 and 2.99 Å, respectively. In this study, we focus only on the adsorption on the central C1-C2 bond of propane because we decided to choose methylene hydrogen abstraction to be the first step of the dehydrogenation reaction.

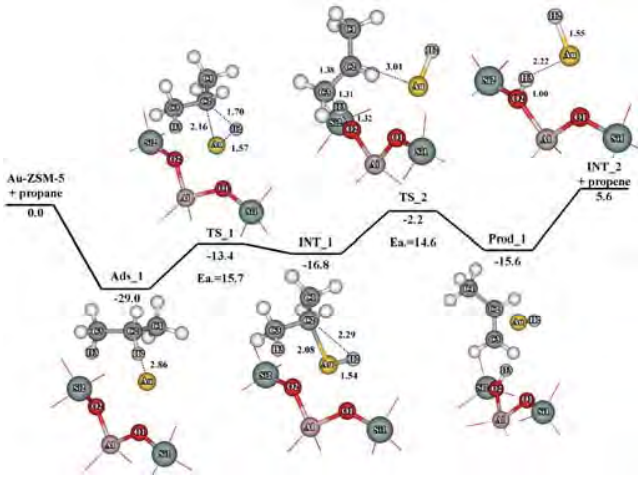


**Figure 2.** Energy profile for the methylene hydrogen abstraction and the formation of propene of the dehydrogenation of propane over the 34T cluster model of Au(I)-ZSM-5 calculated at M06-L/6-311+G(2df,p)//M06-L/6-31G(d,p).

**Methylene hydrogen activation.** The reaction starts with the C2-H2 bond of the adsorbed propane molecule as it is activated by the Au cation to form the gold-propyl hydride intermediate. The structures and energy profile of this step are shown in Figure 2. At the transition state (TS_1), the Au ion is inserted to the C2-H2 bond of propane. The C2-H2 bond distance is increased from 1.10 Å to 1.70 Å while the Au-C2 and Au-H2 distances are reduced to 2.16 Å and 1.57 Å, respectively. The activation energy of this step is 15.7 kcal/mol and has been confirmed by frequency calculations resulting in one imaginary frequency at 660.8i $cm^{-1}$, related to the breaking of the C2-H2 bond by the insertion of $Au^+$ yields the inserted propyl hydride intermediate (INT_1). The inserted propyl hydride intermediate stabilized on the zeolite surface with the relative energy of -16.8 kcal/mol with respect to the isolated reactants. The distances of Au-C2 and Au-H2 are 2.08 and 1.54 Å, correspondingly.

**The formation of propene.** The Au-propyl hydride intermediate can be converted to propene and the Au hydride intermediate through the abstraction of the hydrogen atom from the propyl hydride intermediate to the zeolite framework, to yield an adsorbed propene molecule and the Au hydride intermediate. At the transition state (TS_2), the H3 proton on the C3 atom is elongated to be transferred toward an oxygen atom (O2) of the zeolite framework and the C3-H3 bond and the Au-C2 are dissociated. Simultaneously, the C2-C3 single bond is being contracted to become the C2-C3 double bond. The C3-H3 bond is elongated to 1.31 Å and the O2-H3 distance is reduced to 1.32 Å. The Au-C2 bond is increased from 2.08 Å to 3.01 Å, and the C2-C3 bond distance is decreased from 1.51 Å to 1.38 Å. Normal mode analysis reveals one imaginary frequency at 1,281.5i $cm^{-1}$ of the transition state that corresponds to the movement of the H3 atom between the O2 and C3 atoms. The activation energy of this step is 14.6 kcal/mol. After the deprotonation is completed, the propene molecule and the Au hydride intermediate are produced (Prod_1). The desorption of the propene molecule requires an energy of 21.2 kcal/mol while the Au hydride intermediate remains adsorbed on the Brønsted acid site (INT_2).

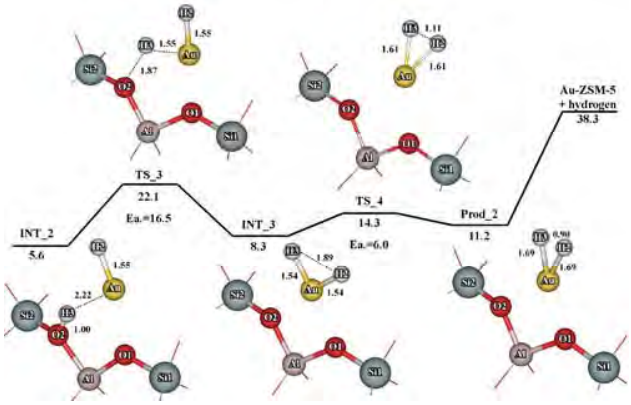


**Figure 3.** Energy profile for the hydrogen production and the regeneration of the active site over the 34T cluster model of Au(I)-ZSM-5 calculated at M06-L/6-311+G(2df,p)//M06-L/6-31G(d,p).

**Hydrogen production and the regeneration of the active site.** After the propene molecule desorbs from the surface, the Au hydride intermediate remains adsorbed on the Brønsted acid site. Finally, the active site is regenerated by the formation of the hydrogen molecule from the Au hydride intermediate (INT_2). The structures and energy profile of this reaction consist of two steps and are shown in Figure 3. First, the conversion of the Au hydride intermediate to the Au dihydride intermediate via the protonation reaction. At the transition state (TS_3), the H3 proton is transferred to the Au hydride intermediate. The Au-H3 distance is decreased to 1.55 Å and the O2-H3 bond distance is elongated to 1.87 Å. The transition structure has been confirmed by frequency calculations resulting in one imaginary frequency at 388.0 $cm^{-1}$, related to the O2-H3 bond breaking and the Au-H3 bond forming, simultaneously. The activation energy of this step is 16.5 kcal/mol. Dihydride groups (INT_3) on Au can form a bond to produce the hydrogen molecule. This step requires the energy of only 5.5 kcal/mol. Normal mode analysis reveals one imaginary frequency at 650.1i $cm^{-1}$ associated with the H2-H3 bond formed in the transition state structure (TS_4). The product of this step is the hydrogen molecule chemisorbed on Au(I)-ZSM-5 (Prod_2). The distance between Au and H2 is 1.69 Å and the Au-C3 distance is 1.69 Å. Finally, the hydrogen molecule desorbed from Au with the energy of 27.1 kcal/mol.

## Conclusion

Propane adsorption and its dehydrogenation reaction mechanism of the propane/Au(I)-ZSM-5 system have been investigated by DFT calculations with the M06-L functional. Propane adsorbs over Au(I)-ZSM-5 by the interaction of methyl and methylene carbon atoms and $Au^+$ with the binding energy 29.0 kcal/mol. For the reaction mechanism, the reaction begins with the methylene hydrogen abstraction yielding the Au inserted propyl methyl intermediate. The calculated activation energy is 17.8 kcal/mol. Eventually, propene can be produced by the proton transferred from the intermediate to the oxygen atom of the active site. This step requires the activation energy of 12.5 kcal/mol. The zeolitic framework plays an important role in the formation of propene from the stabilization of the

transition state. The intermediate of this step is AuH adsorbed over the Brønsted acid site. The active site is regenerated by the protonation of AuH with activation energy of 18.1 kcal/mol to form the dihydrogen intermediate. Then, the conversion of the dihydrogen intermediate to the hydrogen molecule requires the activation energy of 6.0 kcal/mol. Finally, the hydrogen molecule desorbs from Au(I)-ZSM-5 that requires the energy of 27.1 kcal/mol. This zeolite is suggested to be an interesting candidate material for dehydrogenation of propane to propene, which is more important in industrial chemical processes.

**Acknowledgements** This work was supported in part by grants from the National Science and Technology Development Agency (2009 NSTDA Chair Professor funded by the Crown Property Bureau under the management of the National Science and Technology Development Agency and NANOTEC Center of Excellence funded by the National Nanotechnology Center), Kasetsart University Research and Development Institute (KURDI), the Thailand Research Fund (TRF), and the Commission on Higher Education, Ministry of Education (the "National Research University Project of Thailand (NRU)" and the "National Center of Excellence for Petroleum, Petrochemical and Advanced Materials (NCE-PPAM)"). The authors are grateful to Donald G. Truhlar and Yan Zhao for their support with the M06-L functional.

**References**

1) Cavani, F.; Ballarini, N.; Cericola, A. *Catal. Today.* **2007**, 127, 113.
2) Nakamura, I.; Fujimoto, K. *Catal. Today*. **1996**, 31, 335.
3) Dooley, K. M.; Price, G. L.; Kanazirev, V. I.; Hart, V. I. *Catal. Today*. **1996**, 31, 305.
4) Berndt, H.; Lietz, G.; Volter, J. *Appl. Catal*. **1996**, 146, 365.
5) Biscardi, J. A.; Iglesia, E. *J. Catal*. **1999**, 182, 117.
6) Heemsoth, J.; Tegeler, E.; Roessner, F.; Hagen, A. *MicroporousMesoporous Mater*. **2001**, 46, 185.
7) Kazansky, V.; Serykh, A. *MicroporousMesoporousMater.* **2004**, 70, 151.
8) Chowdhury, A. K.; Wilkins, C. L. *J. Am. Chem. SOC.*, **1987**, 109(18), 5336.
9) van Koningsveld, H.; Tuinstra, F.; van Bekkum, H.; Jansen, J. C. *Acta Crystallogr., Sect. B.* **1989**, 45, 423.
10) Boekfa, B.; Choomwattana, S.; Khongpracha, P.; Limtrakul, J. *Langmuir.* **2009**, 25(22), 12990.
11) Maihom, T.; Boekfa, B.; Sirijaraensre, J.; Nanok, T.; Probst, M.; Limtrakul, J. *J. Phys. Chem. C.* **2009**, 113, 6654.
12) Zhao, Y.; Truhlar, D. G. *J. Phys. Chem. C.* **2008**, 112, 6860.
13) Zhao, Y.; Truhlar, D. G. *Acc. Chem. Res.* **2008**, 41, 157.